Distal Impact Ejecta Layers

A Record of Large Impacts in Sedimentary Deposits

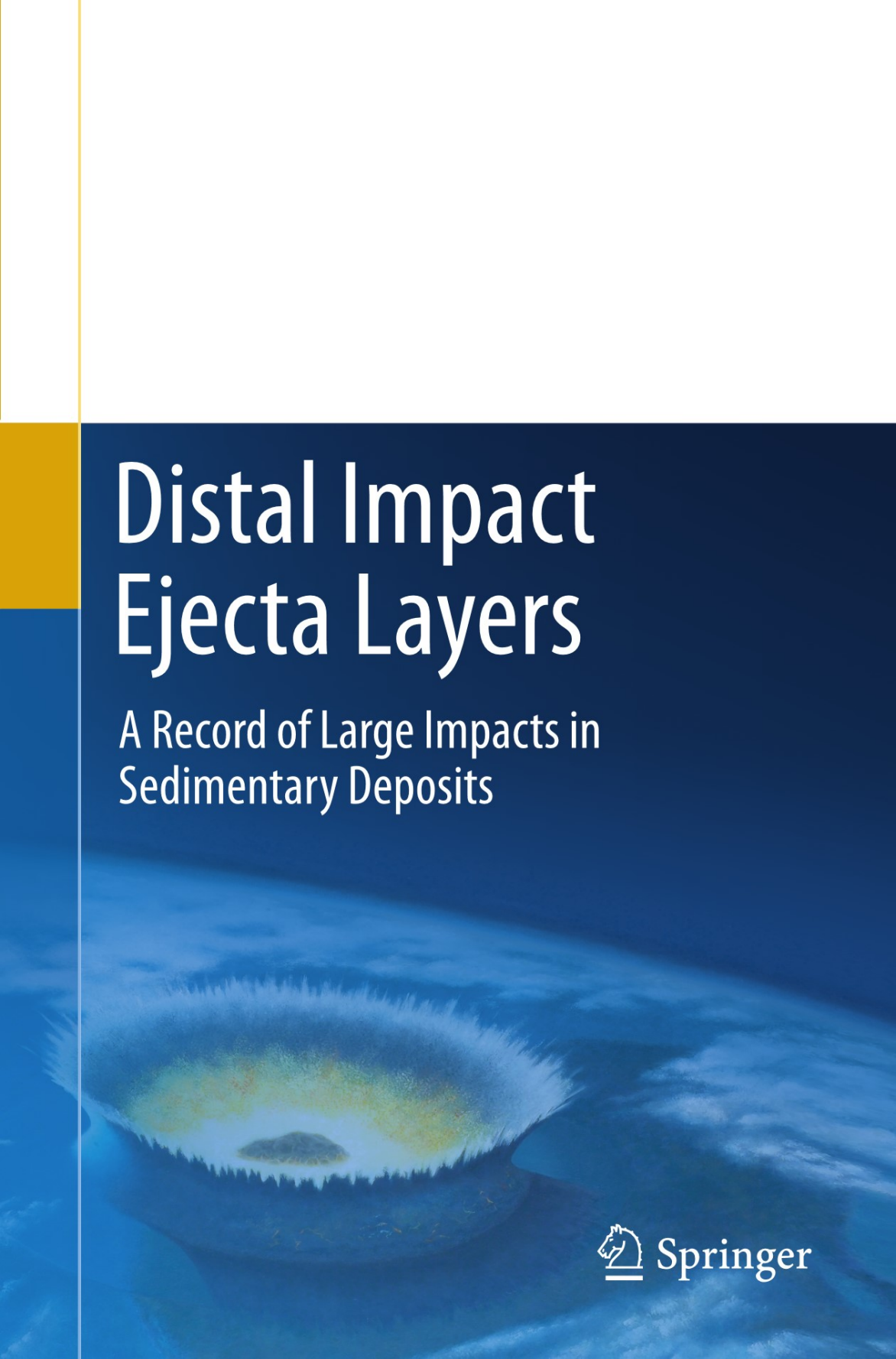

Springer

Impact Studies

For further volumes:
http://www.springer.com/series/4698

Billy P. Glass · Bruce M. Simonson

Distal Impact Ejecta Layers

A Record of Large Impacts in Sedimentary Deposits

Springer

ESF IMPACT

Billy P. Glass
Department of Geology
University of Delaware
Newark, DE
USA

Bruce M. Simonson
Department of Geology
Oberlin College
Oberlin, OH
USA

ISSN 1612-8338
ISBN 978-3-540-88261-9 ISBN 978-3-540-88262-6 (eBook)
DOI 10.1007/978-3-540-88262-6
Springer Heidelberg New York Dordrecht London

Library of Congress Control Number: 2012942024

Cover illustration: Dona Jalufka, Vienna, Austria

Printed on acid-free paper

Springer is part of Springer Science+Business Media (www.springer.com)

Preface

It is becoming increasingly clear that impact cratering has played a major role in the evolution of planetary bodies throughout the Solar System. In the specific case of the Earth, large impacts may have also played a role in the evolution of the atmosphere, oceans, and life. To date, the only well-documented example of such a connection is the correlation between the impact that produced the Chicxulub impact structure on the Yucatan Peninsula in Mexico and the mass extinction at the end of the Cretaceous. The key piece of evidence connecting the two is a thin layer of ejecta that blanketed the entire Earth and is so subtle that it was not detected until late in the twentieth century. Spurred on by the discovery of this layer, a number of additional ejecta layers have been discovered, and the appreciation of the usefulness of ejecta layers in understanding both impacts and other geological phenomena has expanded slowly but steadily.

Because the Earth is so geologically active, most terrestrial impact structures have been either deeply buried beneath sediment, eroded away by wind, water, and/or ice, or entirely eradicated by tectonic processes. Fortunately, tangible evidence of impact structures that no longer exist can be preserved in the stratigraphic record in the form of ejecta layers. Impact ejecta layers farther than five crater radii from their source craters are referred to as distal impact ejecta layers and they are the focus of this book. In addition to shedding significant light on the mechanics of impacts, distal impact ejecta layers provide a powerful tool for directly correlating impact events with oceanic, atmospheric, and/or biologic events recorded in the stratigraphic record. They can also be used for more conventional stratigraphic correlations at a regional or even global scale. Given the short-lived nature of an impact event, the recognition of distal ejecta from a single impact at multiple sites can be used to establish the contemporaneity of strata within an extremely short time span, even on a global scale. The correlation of distal impact ejecta layers may prove particularly useful in well-preserved Precambrian successions as high-resolution biostratigraphy is not possible and the uncertainty in isotopic age dating grows larger back through time. Furthermore, although large impacts were more frequent early in the Earth's history, no craters

older than ~2.4 Ga have been recognized and the only record of impacts older than 2.4 Ga are the distal spherule/ejecta layers.

Prior to the discovery of the impact ejecta layer at the Cretaceous-Tertiary (K-T) boundary (Alvarez et al. 1980), only four well-documented distal impact ejecta layers were known, namely the microtektite layers associated with the Australasian, Ivory Coast, and North American tektite strewn fields and the late Eocene clinopyroxene or cpx spherule layer. After the discovery that an impact ejecta layer coincided with the mass extinction at the end of the Cretaceous, numerous researchers searched for additional ejecta layers, mainly in association with other mass extinction events. Although most of these searches were fruitless, various additional impact ejecta layers were identified, most of which are not associated with mass extinctions. At least 26 reasonably well-defined distal impact ejecta layers are now known, the majority being spherule layers of Precambrian age. Given the stratigraphic correlations proposed between different formations both regionally and globally, the spherule layers recognized to date may represent only 22 impact events. At least 19 more layers have been proposed for which the evidence is inconclusive at present. Because of the rapid growth in the identification of definite and possible distal impact ejecta layers, we thought it was important to summarize our knowledge of these layers while it was still possible to do so in one book.

Based on our reading of the literature while writing this book, we have several suggestions for authors describing distal impact ejecta layers. First, authors should give sufficient information when proposing a new layer to establish unequivocally that it formed via an impact as opposed to some alternative process. Second, beyond simply convincing the reader that a layer has an impact origin, authors should strive to provide enough details on newly discovered layers to constrain models for how distal ejecta vary with distance from the source crater or, more specifically, to estimate the size of the source crater as well as how far the discovery site(s) may be from the source crater. In addition, researchers who are studying early Precambrian (spherule) layers should be aware that the presently available data suggest they differ from the later Precambrian and Phanerozoic distal ejecta layers in several respects. The most troubling difference is the extreme scarcity of evidence of shock metamorphism in the early Precambrian ejecta layers; no evidence of shock metamorphism whatsoever has been recognized to date in the Paleoarchean layers. This may be because of the generally larger size of the older events, the nature of the early Precambrian crust, alterations (diagenetic, metamorphic, and/or tectonic) of the layers due to their great age, or some combination thereof. This is a topic that clearly needs more study.

We have proposed a preliminary model for how distal impact ejecta vary with distance from their source crater primarily based on our knowledge of the Cenozoic microtektite/spherule layers and the K-T boundary impact ejecta layer (see Chap. 10). We challenge researchers to obtain appropriate data on ejecta layers that they are studying to test and improve the model. We would be happy to hear from readers who have data that can be used to test (support or contradict) our model.

Acknowledgments

The authors would like to thank W. U. Reimold, P. Schulte, and T. J. Goldin for critical reviews of Chaps. 2, 5, and 10, respectively. We also collectively thank the many researchers too numerous to mention who supplied us with images and/or information to use in this book. P. Claeys kindly provided chemical compositional data for the Late Devonian spherules in Belgium. BPG dedicates this book to Judy (my wife) who put her life on hold for five years and who proofread several drafts of each chapter (including text, tables, figure caption, and figures) and asked questions when something was not clear which often led to rewriting sections of the text or figure captions in order to make them clearer and easier to read. Judy has critically reviewed every paper that I have published during my entire career and this acknowledgment of her help and encouragement is long overdue. BMS likewise dedicates this book to Sue for her steadfast support and encouragement and to all his other family members who have good-naturedly endured years of hearing about "the book".

Billy P. Glass
Bruce M. Simonson

Contents

Chapter 1
Introduction

1.1 Introduction

Impact cratering is one of the most fundamental geological processes affecting solid bodies in the Solar System (Shoemaker 1977; French 1998; Pati and Reimold 2007). Planetary studies by astronauts and spacecrafts in the 1960s and 1970s led to the realization that the surfaces of the Moon, Mercury, asteroids, and most of the satellites of the outer planets are heavily cratered (Fig. 1.1). Impact craters are also common on much of Mars and, to a lesser extent, Venus. In contrast, as of 2011 only approximately 178 terrestrial impact craters had been identified (Earth Impact Database 2011; accessed 03/02/2011). So where are all the impact craters that must have been formed on Earth? The dearth of obvious impact craters on the Earth, compared with most of the other solid bodies in the Solar System, is due to the Earth having an active hydrological cycle and being tectonically and volcanically active, right up to the present time.

Studies of the Moon indicate that the cratering rate on the Moon and, therefore, the Earth was much higher prior to ~ 3.5 Ga ago. In fact, because the Earth is much bigger than the Moon its gravitational attraction is much stronger than the Moon's and as a result it has been more heavily bombarded than the Moon. The higher gravity of the Earth increases both the probability (impact rate) and average velocity (energy) of impacts compared with the Moon (Ivanov 2005). The average impact rate per unit area is estimated to be 1.67 times higher on Earth compared to the Moon (Ivanov 2005). The impact rate of the Moon, and presumably the Earth, dropped to close to its present rate ~ 3 Ga ago and has been relatively constant up to the present time (Fig. 1.2). We would expect that craters formed during the Paleoarchean would be more abundant than craters formed in more recent geological eras, but this is not observed in the geological record (Fig. 1.3). In fact, no Archean-age craters have been observed on Earth so far (Fig. 1.3). Presumably this is because the older impact structures have been destroyed through the eons by a variety of geological processes (tectonism, volcanism, erosion).

B. P. Glass and B. M. Simonson, *Distal Impact Ejecta Layers*, Impact Studies,
DOI: 10.1007/978-3-540-88262-6_1, © Springer-Verlag Berlin Heidelberg 2013

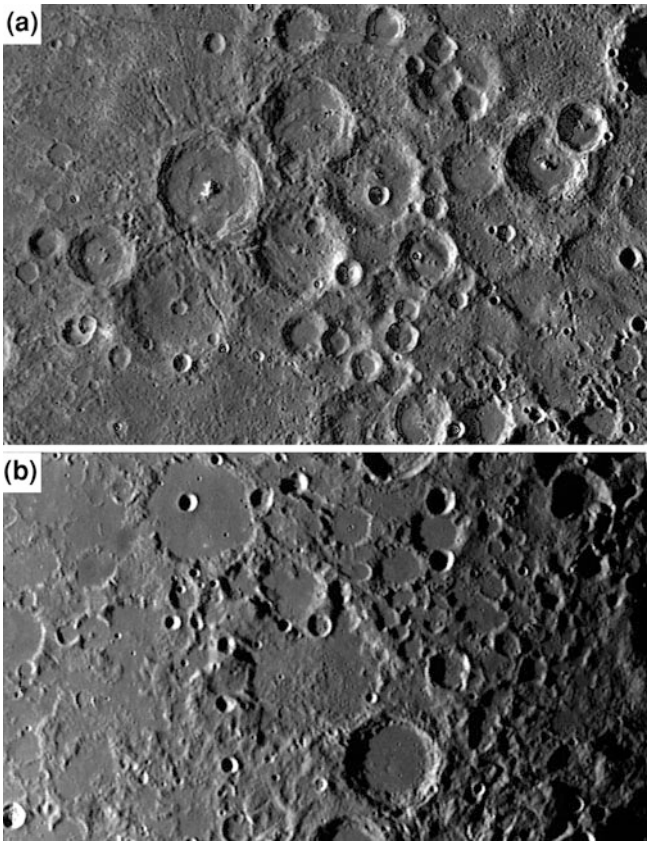

Fig. 1.1 Images of cratered planetary surfaces. **a** A Mercury Messenger spacecraft image of Mercury showing a heavily cratered terrain in the northwest quadrant near the equator. Features in the lower left corner of the image are ~250 km NNE of the high-albedo crater Kuiper. Courtesy of NASA/Johns Hopkins University Applied Physics Laboratory/Carnegie Institute of Washington. **b** A Galileo spacecraft image of a portion of the highly cratered lunar surface. Courtesy of Jet Propulsion Laboratory/NASA

Based on the flux of asteroids inferred from the lunar impact record, it is highly likely that there are still numerous impact structures and distal ejecta layers that have not yet been discovered.

Barringer crater (also known as **Meteor Crater**; Fig. 1.4), in Arizona, was the first terrestrial crater to be recognized as having an impact origin. This crater was studied by the well-known American geologist, G. K. Gilbert, in the 1890s. Numerous fragments of an iron meteorite were found scattered around the crater and Gilbert initially concluded that it was formed by the impact of a large iron meteorite. Gilbert believed that the bulk of the iron meteorite should have been buried under the crater; however, he was not able to find evidence of a large mass of iron meteorite beneath the crater floor as he expected. Because of this and

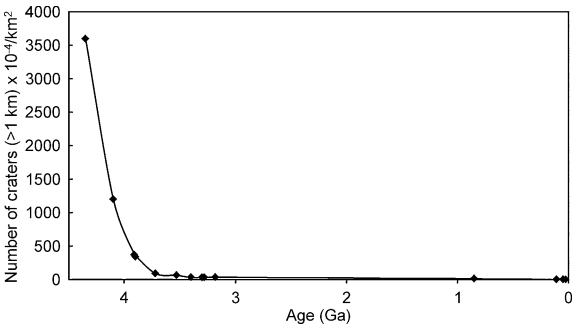

Fig. 1.2 Number of lunar craters (>1 km diameter) ($\times 10^{-4}$) per km^2 versus age. Data from Neukum and Ivanov (1994)

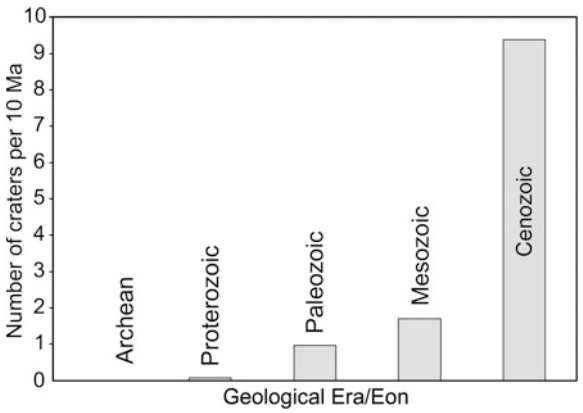

Fig. 1.3 Number of dated terrestrial impact craters per 10 Ma versus geological era/eon. Data from Earth Impact Database (2011); accessed 05/26/2011

because there are volcanoes near Barringer crater, Gilbert changed his mind and eventually concluded that the crater must be of volcanic origin and the presence of meteoritic fragments around the crater was merely a coincidence (Gilbert 1896). Ironically, at about the same time he correctly concluded that the craters on the Moon were of impact origin (Gilbert 1893).

A mining engineer, Daniel Moreau Barringer, became interested in the crater, which now bears his name, in the early 1900s. Like Gilbert, he believed that there must be a large mass of iron meteorite below the floor of the crater, which at that time was known by several names, including "Coon Butte Crater" or "Crater Mound". Barringer staked a claim on the structure and began searching for the large mass of meteoritic iron, or mother lode, beneath the crater. He sank several exploratory shafts without success. However, his studies of the crater led him to conclude that it had an impact origin (e.g., Barringer 1905).

Small craters, in Odessa, Texas, also associated with fragments of an iron meteorite, were recognized as impact craters by Barringer's son, D. M. Barringer, Jr., in the early 1920s (Barringer 1928). Over the next two decades, several additional small craters (<1 km in diameter) were recognized as impact craters. These include: the Kaalijarvi crater in Estonia; the Wabar crater in Saudi Arabia; the Henbury and Boxhole craters in the Northern Territory, Australia; Dalgaranga

Fig. 1.4 Barringer (Meteor) crater in Arizona, USA. This crater is ~1.2 km in diameter and has an age of ~49 ka. Courtesy of Charles O'Dale

Fig. 1.5 Wolfe Creek Crater in Western Australia. This crater is ~0.9 km in diameter and has an age of <300,000 years. Courtesy of VL Sharpton and the Lunar and Planetary Institute

and Wolfe Creek (Fig. 1.5) craters in Western Australia. Like Barringer and Odessa craters, meteorite fragments were found associated with all these craters. In addition, all of these craters are relatively young (<100,000 years old) and fresh in appearance.

An impacting body larger than ~50 m diameter (for a stony body) or ~20 m diameter (for an iron body) can penetrate the Earth's atmosphere with little or no deceleration and hit the ground with most of its cosmic velocity (French 1998), which is generally between 11 and 40 km/s (de Pater and Lissauer 2001). Upon impact the resultant shock waves generate pressures high enough to melt and vaporize most of the impacting body. In addition, meteoritic material is unstable on the Earth's surface and even if meteorite fragments did survive the impact, they

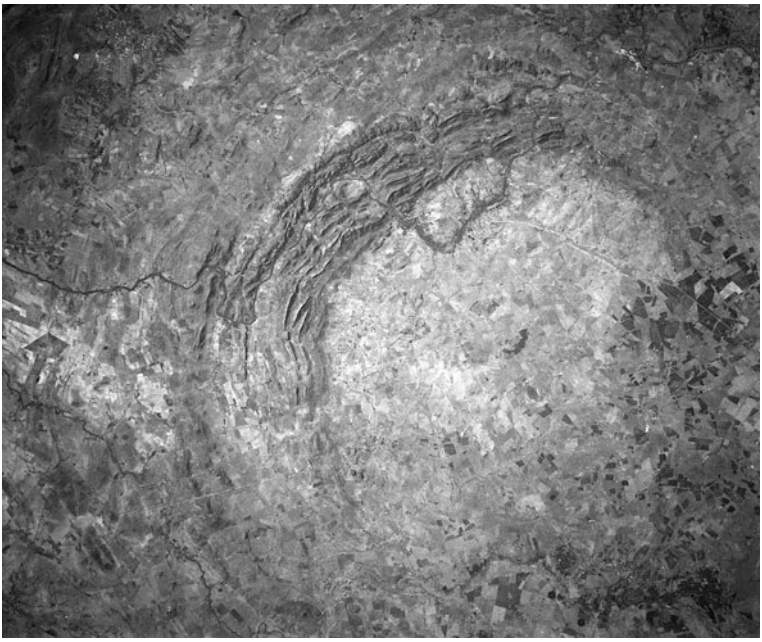

Fig. 1.6 Image of Vredefort impact structure in the Witwaterstrand Basin about 100 km south of Johannesburg, South Africa. The central core of uplifted granitic rocks (*white* to *light gray* region) is about 40 km in diameter. It is partly surrounded by a collar of upturned sedimentary rocks and basaltic lavas. The original impact structure is believed to have been as much as 300 km in diameter. It has an age of $\sim$2 Ga. Courtesy of the Lunar and Planetary Institute. NASA Space Shuttle Image STS511-33-56AA

would generally be quickly destroyed by weathering. Thus, meteorite fragments are not often found associated with older and/or larger impact structures.

Most of the older craters have been eroded down or filled in, and, in some cases, tectonically deformed—e.g., the **Sudbury impact structure**, Canada, and **Vredefort impact structure**, South Africa (Fig. 1.6). Since these older craters no longer have the topographic expression of a crater, they are referred to as impact structures. These older and generally larger impact structures not only do not have the topographic expression of a crater, but they rarely if ever have fragments of meteorites lying around them. Thus, other criteria are needed in order to establish their impact origin.

Impacts, involving projectiles or impacting bodies that are traveling at high enough velocity (generally greater than a few km/s) to generate shock waves upon impact, are called **hypervelocity impacts**. Two shock waves are generated during a hypervelocity impact: one that travels back through the projectile and one that travels down into the target rock. It is the shock wave that travels back through the projectile that melts and vaporizes it. A portion of the target rock near the point of impact can also be melted and vaporized, but a larger volume of target rock is

altered by the passage of the shock wave without being melted or vaporized. Although it is not melted, this rock is changed due to the high temperature, pressure, and strain-rate generated as the shock wave moves through it. Permanent changes produced in the rocks and minerals by this process are called shock-metamorphic effects. Nuclear and high-energy explosions can also generate shock waves which can produce shock-metamorphic effects in rock material. The phrase "impact metamorphism" can be used to refer to shock metamorphism produced in rock material as the result of a naturally-occurring impact event.

In the 1960s, impact-metamorphic effects were identified in craters of undoubted impact origin, such as Barringer crater. A large number of structures, including "cryptovolcanic" or "cryptoexplosion" structures, had been identified as having a possible impact origin. The origin of these structures was intensely debated for a decade or so (see, for example, Bucher 1963; Dietz 1963; Currie and Shafiqullah 1967; French 1968). With the discovery of impact-metamorphic features such as the high-pressure silica polymorphs coesite and stishovite, planar deformation features in quartz, diaplectic glass (such as maskelynite), and high temperature decomposition products (such as the breakdown of zircon to baddeleyite and silica), it became possible to confirm the impact origin of deeply eroded impact structures which did not have associated meteoritic fragments. After the early 1960s, the number of confirmed impact structures increased rapidly (French 1968) and by 2011 there were about 178 confirmed terrestrial impact structures. In addition to an increase in the number of known impact structures, the average size and age of the known impact structures also increased. As of 2011, the largest known impact structures are the ~300-km-diameter Vredefort structure (Fig. 1.6) in South Africa and the 250-km-diameter Sudbury structure in Ontario, Canada, which are 2.0 and 1.85 Ga old, respectively.

1.2 Distal Ejecta Layers: Formation and Nomenclature

During a hypervelocity impact, rock material is thrown or ejected from the point of impact to create an impact crater. Rock material thrown out of the forming crater is called **impact ejecta**. Some of the ejecta is thrown straight up and falls back into the crater to form what is called fallback ejecta. Most of the rest of the ejecta is deposited around the crater to form an ejecta blanket, which decreases in thickness away from the rim of the crater (Melosh 1989). Approximately 90 % of the ejecta are deposited within five crater radii of the crater rim (Montanari and Koeberl 2000). These ejecta are referred to as **proximal ejecta**. Ejecta farther away than five crater radii are called **distal ejecta**. However, the division between proximal and distal ejecta is arbitrary and gradational and Stöffler and Grieve (2007) define distal as being beyond the continuous ejecta blanket, which they say extends 2–3 crater radii from the crater. Distal ejecta layers are sometimes referred to as **impactoclastic layers** (e.g., Montanari and Koeberl 2000)

Distal ejecta are usually highly shock metamorphosed and most of the more distal ejecta are ejected as melt, which rapidly cools to form glassy bodies with **splash forms** (spheres, teardrops, dumbbells, discs), generally millimeter in size or smaller called **impact spherules**. Distal splash-form bodies composed of glass without any primary microlites/crystallites are called **tektites**, **minitektites**, or **microtektites** depending on their size (Glass 1990a; Prasad and Sudhaker 1999). If the splash-form bodies have partially crystallized upon cooling, they are called **microkrystites** (Glass and Burns 1988). If spherules have been diagenetically altered and it is no longer possible to determine if they were originally composed entirely of glass or were partially crystalline, then they should be referred to using the more general phrase spherules or impact spherules if their impact origin can be demonstrated. Another type of impact ejecta that can closely resemble spherules, especially after replacement, are **accretionary lapilli**. Since impact-generated accretionary lapilli are small rounded bodies, they could be called spherules; however, in order to distinguish them from impact spherules formed as melt droplets or vapor condensates, we will refer to them in this book as impact-generated accretionary lapilli. They generally consist of a coarse nucleus surrounded by concentric layers of fine dust-like grains to form a roughly spherical body and are similar to volcanic accretionary lapilli, except that some contain grains exhibiting evidence of shock metamorphism. Because they accreted mechanically, they do not show symmetric splash-form shapes. They occur more commonly in proximal ejecta layers and are found only rarely in distal ejecta. Impact-generated accretionary lapilli have been reported in the Cretaceous–Tertiary (K–T) boundary layer (e.g., Salge et al. 2000; Yancey and Guillemette 2008), the Alamo Breccia layer (Warme et al. 2002), and the Sudbury distal ejecta layer (Addison et al. 2005; Cannon et al. 2010).

Prior to 1980, only five distal impact ejecta layers had been discovered: the Australasian, Ivory Coast, and North American microtektite layers, the Central European tektite strewn field, and the upper Eocene clinopyroxene-bearing (cpx) spherule layer (Table 1.1). The discovery of the K–T boundary (now called the Cretaceous–Paleogene or K–Pg boundary) impact ejecta around 1980 increased the number of recognized distal impact ejecta layers to six. Some of the first impact ejecta layers to be recognized were discovered by accident. For example, the Australasian microtektite layer was discovered while studying the relationship between changes in planktic foraminifera assemblages and geomagnetic reversal stratigraphy in sediments in the Indian Ocean (Glass 1967) and the **K–T boundary ejecta layer** was discovered while trying to use Ir concentrations to determine the length of time it took for the clay layer at the K–T boundary to be deposited (Alvarez et al. 1980).

After acceptance of the K–T boundary impact ejecta layer and acceptance by many researchers that the K–T boundary impact may have been responsible for the mass extinction at the end of the Cretaceous, the number of geologists aware of distal impact ejecta layers greatly increased and several researchers began systematic searches for impact ejecta layers at other geological boundaries associated with mass extinctions. These searches were for the most part unsuccessful,

but the number of recognized distal impact ejecta layers increased as a result of a greater awareness of the importance of distal impact ejecta layers. Since discovery of the K–T boundary ejecta layer, as many as 26 additional possible/probable distal impact ejecta layers have been recognized, five during the writing of this book (i.e., since 2007; Table 1.1; Fig. 1.7).

Table 1.1 Distal impact ejecta layers listed chronologically according to date of first publication

Distal impact ejecta layer	Geographic location	First publication
Australasian microtektite	Indian Ocean, western equatorial Pacific Ocean, and adjacent seas	Glass (1967)
Ivory Coast microtektite	Eastern equatorial Atlantic	Glass (1968)
North American microtektite	Gulf of Mexico, Caribbean Sea, NW Atlantic Ocean	Donnelly and Chao (1973), Glass et al. (1973)
Clinopyroxene-bearing spherule	Global	John and Glass (1974), Keller et al. (1987), Glass and Burns (1987)
Cretaceous–Tertiary boundary ejecta	Global	Alvarez et al. (1980), Smit and Hertogen (1980), Bohor et al. (1984)
Acraman ejecta	South Australia	Gostin et al. (1986)
S2 spherule	South Africa	Lowe and Byerly (1986)
Warrawoona (S1) spherule[a]	Western Australia	Lowe and Byerly (1986)
S1 spherule[a]	South Africa	Lowe et al. (1989)
S3 spherule	South Africa	Lowe et al. (1989)
S4 spherule	South Africa	Lowe et al. (1989)
Nuussuaq (Disko) spherule	Western Greenland	Margolis et al. (1991b)
Dales Gorge spherule[b]	Western Australia	Simonson (1992)
Bee Gorge (Wittenoom) spherule	Western Australia	Simonson (1992)
Carawine spherule[c]	Western Australia	Simonson (1992)
Qidong spherule	Qidong, South China	Wang (1992)
Senzeille/Hony spherule	Belgium	Claeys et al. (1992)
Manson ejecta	South Dakota, USA	Izett et al. (1993)
Monteville spherule[c]	South Africa	Simonson and Hassler (1997)
Jeerinah spherule[c]	Western Australia	Simonson et al. (2000a)
Grænsesø spherule	South Greenland	Chadwick et al. (2001)
Late Triassic spherule	Bristol area, SW England	Walkden et al. (2002)
Mid-Devonian spherule	Morocco	Ellwood et al. (2003)

(continued)

Table 1.1 (continued)

Distal impact ejecta layer	Geographic location	First publication
Reivilo spherule[d]	South Africa	Simonson and Glass (2004)
Kuruman spherule[b]	South Africa	Rasmussen et al. (2005), Schröder et al. (2006)
Sudbury ejecta	Western Lake Superior area, USA and Canada	Addison et al. (2007), Pufahl et al. (2007)
S5 spherule	South Africa	Lowe and Byerly (2010)
S6 spherule	South Africa	Lowe and Byerly (2010)
S7 spherule	South Africa	Lowe and Byerly (2010)
Karelian spherule	Russia	Huber et al. (2011)
Paraburdoo spherule[d]	Western Australia	Hassler et al. (2011)

[a] These layers were probably formed by a single impact 3.47 Ga ago
[b] These layers were probably formed by a single impact ~2.49 Ga ago
[c] These layers were probably formed by a single impact 2.63 Ga ago
[d] These layers were probably formed by a single impact ~2.57 Ga ago

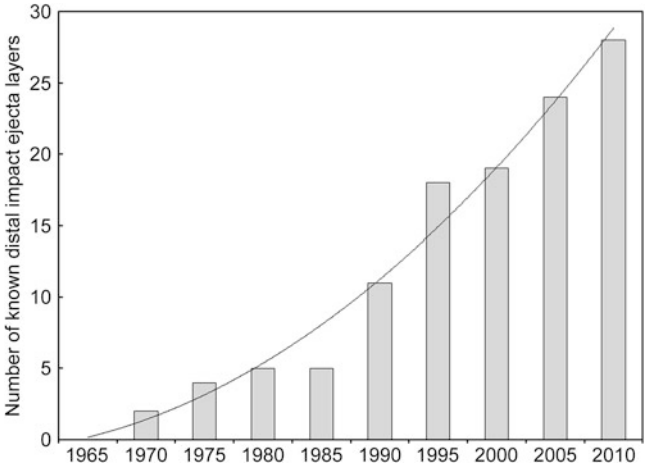

Fig. 1.7 Cumulative number of known and proposed impact ejecta/spherule layers from 1965 to 2010. See Table 1.1 for data

Distal impact ejecta can be found great distances from their source crater. Ivory Coast microtektites are found as far as 2530 km away from their source, the 10.5-km-diameter **Bosumtwi crater** (or **Ashanti crater**) in Ghana, Africa. This is about 240 crater diameters and at this distance there is no continuous ejecta layer; the microtektites were just scattered thinly over the sea floor. However, the thickness of ejecta deposited at a given distance is dependent on the size of the source crater. For a 100 km diameter crater, a distal ejecta layer at least 1 mm thick extends out ~3700 km or ~37 crater diameters. In this instance, a recognizable ejecta layer

covers an area ~5500 times the area of the source crater! Over most of this area, especially the parts farther away from the crater, impact spherules are the most abundant and easily recognizable part of the distal ejecta, although care is required in the identification of spherules as having an impact origin (see Chap. 3). In the case of major impacts, such as the one that produced the 180-km-diameter **Chicxulub impact structure**, the ejecta layer can be global in extent. An impact ejecta layer can be identified based on the presence of impact spherules, shock-metamorphosed minerals, and/or geochemical evidence of meteoritic contamination (see Chap. 3).

1.3 Importance of Distal Impact Ejecta Layers

New impact structures are being identified every year. However, based on estimated cratering rates and images of other planetary surfaces, especially the Moon, there must be many more impact events to be discovered (Grieve and Masaitis 1994); but, as discussed above, most of the impact craters formed on Earth have been destroyed. Distal impact ejecta layers from many of the larger impact structures are undoubtedly preserved in the stratigraphic record. Reimold and Koeberl (2008) pointed out that layers from many large impact events ought to be present in the extensive records of Phanerozoic rocks that have been drilled and studied in outcrops. Shock-metamorphosed minerals provide unequivocal evidence of impact events and can often be the last remnants of an impact (Langenhorst 2002). Even after the crater is completely erased, shock-metamorphosed minerals can be preserved in distal, sometimes global, ejecta layers; but they are rarely if ever easy to recognize in outcrops or drill cores. In contrast, impact spherules are the most common component of most distal impact ejecta layers and can be recognized in hand samples with a hand lens under favorable circumstances. Most spherules consist largely of glass, which is unstable and usually is replaced by other phases in a relatively short period of time, geologically speaking. However, diagenetically replaced spherules often retain original shapes and/or internal textures that are diagnostic of their having originated as molten droplets (e.g., see Simonson and Glass 2004 and references therein). Although glassy spherules can be produced volcanically, especially via fire fountains (Heiken 1972), we know of no terrestrial volcanic eruptions that produced layers consisting predominantly of formerly molten spherules like those found in distal impact ejecta layers.

Identification and mapping of distal ejecta layers can help fill in the missing record of many of the impact structures destroyed by tectonic processes and erosion, especially those of Precambrian age. In some cases, it may be possible to estimate the location and size of the source crater. In addition, an impact can be related to other geological events recorded in the same stratigraphic section as the ejecta. Correlating impact structures with other short-lived Earth events is difficult because most impact craters are not well dated. As of 2008, only eleven out of the then-known 174 known impact structures had been dated with uncertainties of 1 %

or less and for many craters no absolute age data were available at all (Jourdan et al. 2009). Even with uncertainties of 1 %, the age of a 200-Ma-old crater, for example, could be off by as much as 2 Ma. Since distal impact ejecta layers occur within the stratigraphic successions that contain the record of climatic and biological changes through time, if impacts caused any changes, those changes should be detectable at the same level as the distal impact ejecta layers.

Thus, distal impact ejecta layers can be used to evaluate the possible role that impact events may have played in causing biotic and climatic changes throughout geological history. The best example of the relationship between an impact and climatic/biologic changes is the K–-T boundary impact ejecta layer, which correlates with the mass extinction at the end of the Cretaceous (Alvarez et al. 1982). The layer was subsequently traced back to the Chicxulub impact structure (Hildebrand et al. 1991). However, if we only knew about the Chicxulub structure and not the layer, the connection between this impact and the end-Cretaceous mass extinction would be much more controversial than it is (see Schulte et al. 2010 and ensuing discussions).

Geochemical studies of spherule layers may also provide information regarding secular changes in the composition of projectiles through geological time. The ratios between siderophile elements, particularly the platinum group elements, can be a clue as to the type of projectile. More recently, Cr isotopic data have been used to identify the presence of extraterrestrial material and distinguish between projectiles of carbonaceous versus ordinary chondritic compositions (see Sect. 3.1.2.3). Not only could extraterrestrial impactors have changed in composition over time, variations in the number of distal ejecta layers through the geologic column could also reflect secular changes in the rate of impacts. Lastly, since most of the mass in distal ejecta comes from the Earth instead of the projectiles, spherule layers also have the potential to provide information about secular changes in the composition of Earth's crust through geological time (see next paragraph).

The search for distal ejecta layers of Archean age is especially important. Several authors have speculated that numerous large impacts during the Archean Eon may have played a major role in the evolution of the Earth's lithosphere, atmosphere, and hydrosphere, as well as the origin and evolution of the biosphere (Grieve 1987; Lowe et al. 1989; Simonson and Harnik 2000; Gilmour and Koeberl 2000; Glikson 2001, 2006, 2008). However, since no Archean impact structures have been identified, the search for distal impact ejecta layers is important for determining the impact history of the Archean and possible relationships between large impacts and changes in the lithosphere, hydrosphere, atmosphere, and biosphere. For example, textural and geochemical data suggest that Precambrian impact spherules were more basaltic in composition than are most Phanerozoic spherules (Lowe et al. 1989; Simonson and Harnik 2000). This suggests that Precambrian crust was more mafic than the Phanerozoic crust and is consistent with the widespread belief that most primitive crust was basaltic in composition whereas most continental crust was generated late in the Archean (e.g., Taylor and McLennan 2009). Spinel crystals in Paleoarchean spherules are much less oxidized than the spinel crystals in Phanerozoic spherules, which is probably a reflection of

the lower oxygen content of the Paleoarchean atmosphere (Byerly and Lowe 1994; Krull-Davatzes et al. 2010).

Impact cratering is not a process that was active only in the past; it has been active up until today and will continue to be active in the future (e.g., Pati and Reimold 2007). That impacts are continuing to happen was illustrated by the 1908 **Tunguska event**, which was the result of the explosion of an extraterrestrial body in the atmosphere over Siberia (Chyba et al. 1993; Gasperini et al. 2012). The shock wave flattened trees over an area $\sim 2200\ km^2$ (~ 50 km across) and damaged a trading post ~ 60 km away. More recently, in July 1994 fragments of the **Comet Shoemaker-Levy 9** impacted into the atmosphere of Jupiter, producing plumes as big as the Earth (Boslough et al. 1994). This event was witnessed by millions of television viewers all around the globe. On September 15, 2007, a bright fireball was observed and a big explosion was heard by inhabitants near the southern shore of Lake Titicaca in Peru (Tancredi et al. 2009). The explosion was the result of the impact of an extraterrestrial body which produced a crater ~ 14 m in diameter. Fragments of an ordinary chondrite were found close to the crater. These and other events have made it clear that catastrophic impact events are still occurring and could happen again in the future.

The study of past impacts and their geological, climatological, and biological effects can help us predict the effects of future impacts. According to Pati and Reimold (2007), "It is mandatory to improve knowledge of the past-impact record of the Earth to better constrain the probability of such events in the future." The most extensive, and, in many ways most informative, record of past impacts and their effects is likely to reside in distal impact ejecta layers.

Because distal impact ejecta layers are deposited instantaneously, they have the potential to be excellent marker horizons with regional to global extent. The K–T boundary layer is the best example of an impact ejecta layer which can be used for global stratigraphic correlation (see, e.g., Smit 1999; Claeys et al. 2002). Another example is the global (?) **late Eocene clinopyroxene-bearing spherule layer** (Glass 2002; Liu et al. 2009). The early Pleistocene **Australasian microtektite layer** is an excellent regional marker horizon for Quaternary sediments in much of the Indian Ocean, South China, Sulu, Celebes, and Philippine Seas, and adjacent western equatorial Pacific Ocean (Glass and Koeberl 2006). Moreover, spherule layers from four different large impacts have now been correlated with reasonable confidence between Paleoarchean, Neoarchean, and Paleoproterozoic strata in South Africa and Western Australia (Byerly et al. 2002; Simonson et al. 2009a, b; Hassler et al. 2011).

Studies of large impact structures and associated ejecta layers and the geological consequences of such large impacts are interdisciplinary by nature, involving such diverse fields as astronomy, meteoritics, geophysics, stratigraphy, sedimentology, petrography, geochemistry, cosmochemistry, paleobiology and other fields of earth and planetary science. Since the recognition, in the early 1980s, of the K–T boundary ejecta layer and its association with the mass extinction event at the end of the Cretaceous Period, the study of impact cratering and the effects of large cratering events has grown into an integrated discipline

involving most disciplines of geosciences and planetary science (Pati and Reimold 2007). Recognition of the importance of impact cratering as a geological process, which has had profound effects on the Earth's lithosphere, climate, and biosphere, has led to a new revolution in geology (see, e.g., Powell 2001; Pati and Reimold 2007; French and Koeberl 2010).

1.4 Objectives

The major purpose for writing this book is to summarize our present knowledge of distal impact ejecta layers (Chaps. 4–9). We want to do this now before the number of known impact ejecta layers is too great to easily summarize in one book. As of 2011, at least eleven Phanerozoic and fourteen Precambrian impact ejecta layers have been identified, but other distal ejecta layers have been proposed/suggested. So far, nine of these have been associated with known impact structures. In Chap. 10, we make some generalizations concerning how impact ejecta vary with distance from their source craters and present a model for how geographic variations in thickness and petrography of distal impact ejecta layers can be used to estimate the location and size of the source crater. We also discuss how distal impact ejecta layers have varied through geologic time and the possible significance of this variation. Chapters 2 and 3 deal with impact cratering, ejecta formation and distribution, and identification of impact ejecta layers. In the last chapter (Chap. 11) we summarize the known distal ejecta layers, discuss preservation of ejecta layers and some geological findings related to the discovery and study of ejecta layers. Finally we discuss some unanswered problems which deserve further study.

Pati and Reimold (2007) stated, "It is essential that sedimentologists and stratigraphers are alert to the possibility that impact deposits could be encountered in the rock record, as any new discovery will significantly contribute to our overall knowledge about impact flux onto this planet." It has been estimated that there are several hundred impact structures that still remain to be discovered (Grieve 1991). Many terrestrial impact structures have been destroyed by erosion, subduction, or other geological processes and their distal ejecta may be the only remaining record of these impacts. The recognition and study of distal ejecta layers will help us to understand and predict the effects of large impact events. It is our hope that this book will contribute to the understanding of distal ejecta layers and serve as a useful reference in the search for and study of these layers.

Chapter 2
Impact Crater Formation, Shock Metamorphism, and Distribution of Impact Ejecta

2.1 Introduction

As previously mentioned, an integral part of the cratering process is the formation and widespread distribution of ejecta. In order to comprehend how the distribution, thickness, and nature of an impact ejecta layer varies with distance from its source crater, one needs to understand the cratering process. Thus, we begin this chapter with a brief review of cratering mechanics. This leads into a discussion of shock metamorphism, which occurs during the cratering process and which is important in the identification of impact craters and distal ejecta layers. At the end of the chapter we briefly discuss some theoretical and experimental data on how ejecta, including the degree of shock metamorphism of the ejecta, vary with distance from the source crater. This last subject is addressed again in Chap. 10, but in Chap. 10 we compare observations on *how* distal ejecta vary with distance from source craters with theoretical and experimental data of how the thickness and nature of distal ejecta *should* vary with distance from the source crater.

2.2 Impact Cratering

2.2.1 Energy Considerations

A tremendous amount of energy is required to make a crater that is kilometers or tens of kilometers or larger in diameter and to throw ejecta over much, or all, of the globe. The source of this energy is the kinetic energy of the impacting body (projectile) which is equal to ½ mv^2, where "m" equals mass of the projectile and "v" equals its velocity. The typical velocity of most meteoroids or asteroids that enter the Earth's atmosphere is about 20 ± 5 km/s, but can range from ~11 km/s up to ~40 km/s; comets, however, can have impact velocities up to as high as 72 km/s with an average of ~30 km/s (French 1998; de Pater and Lissauer 2001;

B. P. Glass and B. M. Simonson, *Distal Impact Ejecta Layers*, Impact Studies,
DOI: 10.1007/978-3-540-88262-6_2, © Springer-Verlag Berlin Heidelberg 2013

Jeffers et al. 2001; Reimold and Koeberl 2008). A 5-km-diameter asteroid, with a density of 3.5 g/cm^3, traveling with an average velocity of 20 km/s will have a kinetic energy of $\sim 4.6 \times 10^{22}$ J. This is equivalent to 10 million megatons of TNT! An impact of this magnitude would, in a few seconds at one location, release more energy than is released on Earth through volcanism, earthquakes, and heat flow over a 32 year period. Such an impact would produce a crater ~ 100 km in diameter and throw ejecta around the entire globe. Fortunately, the impact of a body that size takes place only, on average, every 25 Ma (Neukum and Ivanov 1994).

2.2.2 Impact Crater Formation

The study of impact cratering is a relatively new field. The first detailed geological studies of the so-called **cryptoexplosion structures**, most of which are now identified as impact structures, were carried out in the mid-twentieth century and it was not until the early 1950s that the first petrographic criteria for identification of impact craters were established (Stöffler et al. 2006). The information given below is based on a four-fold approach involving: (1) geological field studies of impact structures; (2) laboratory studies of the petrography and chemistry of rocks from impact structures; (3) laboratory shock experiments used for calibration of shock pressures and temperature levels; and (4) numerical modeling of impact cratering, a relatively new, but successful method of studying the cratering process. Sedimentary rocks are present in the target rocks of ~ 70 % of the known terrestrial impact structures; however, the response of sedimentary rocks to hypervelocity impact is poorly understood (Osinski et al. 2008). A major problem is the role of melting versus decomposition of carbonates, which are present in the target rocks of ~ 30 % of the known impact structures.

Impacts involving impacting bodies (projectiles or impactors) traveling at high enough velocity (generally greater than a few km/s) to generate shock waves upon impact are called hypervelocity impacts. During a hypervelocity impact, the kinetic energy of the projectile is transferred into the surface, or target, rocks via shock waves, which are generated at the interface between the projectile and the Earth's surface (Gault et al. 1968). Another shock wave is generated in the projectile, which results in its destruction as discussed in one of the following sections. A shock wave, like a seismic wave, is a compressional wave; however, shock waves travel at higher velocities and, unlike seismic waves, are associated with material transport (Stöffler and Grieve 2007). Shock waves are non-isentropic and produce post-shock temperatures, which increase with increasing pressure. Shock waves that move upward and intersect the Earth's surface are reflected downward as rarefaction (or release) waves, which decompress the target rock. Some of the target rock is thrown up and away from the point of impact resulting in a depression or impact crater. After formation, the crater immediately begins to be modified by processes such as slumping, erosion, infill, and isostatic adjustment. Thus the crater-forming process can be divided into three stages: (1) contact and compression, (2) excavation, and

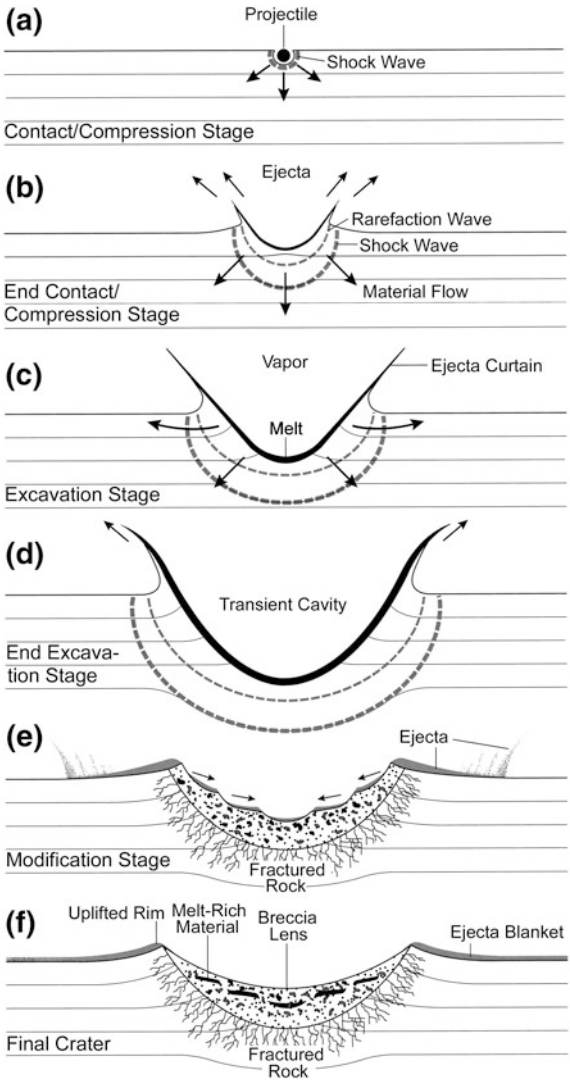

Fig. 2.1 Impact cratering stages. The contact/compression stage **a** begins when the projectile makes contact with the target rock and two shock waves are generated: one in the target rock and one in the projectile. It ends when the shock wave reaches the trailing edge of the projectile and a rarefaction wave is formed. The rarefaction wave causes the target material to be accelerated upward and outward forming an expanding cavity. This is the beginning of the excavation stage **b** Excavation continues **c** until the cavity reaches its maximum size forming the transient crater **d** After formation of the transient crater, the modification stage begins **e** as crater walls collapse and, in the case of larger craters, a central peak or uplift forms. **f** shows the final crater form prior to erosion and infilling. From French (1998), Fig. 3.3, with permission of the Lunar and Planetary Institute

(3) modification (Fig. 2.1) (Gault et al. 1968). These three stages are discussed in more detail in the following sections. It is important to keep in mind that the stages grade into each other and the division into stages is artificial.

2.2.2.1 Contact and Compression Stage

The shock wave that is generated at the contact between the projectile and target moves away from the leading edge of the projectile in a more or less hemispherical wave front. As the shock wave passes through the target rock it compresses it to

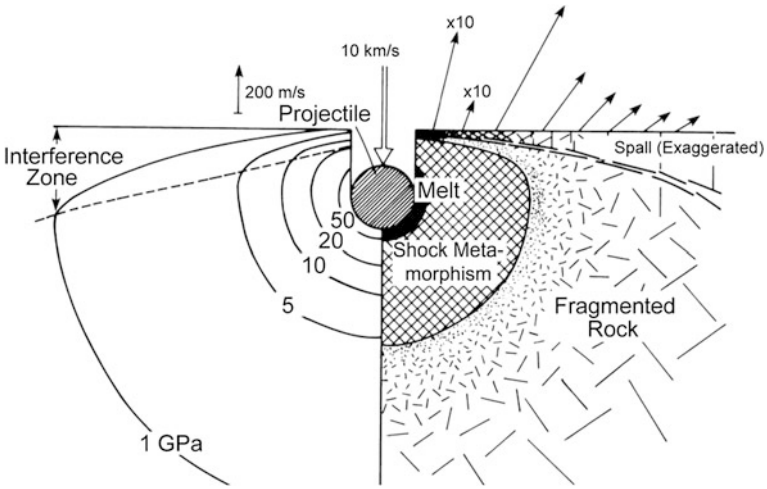

Fig. 2.2 Contact/compression stage of impact cratering. Initial shock wave pressure contours in GPa (*solid lines*) are shown on the *left side* of the figure and effects on the target rock (melting, shock metamorphism, fracturing) for the final stage of cratering are indicated on the *right side* of the figure. Note that the pressure drops off rapidly near the ground surface because of the free surface boundary conditions. Note also the near hemispherical shape of the deeper pressure contours. The *arrows* extending up from the surface on the *right* indicate the angle of ejection and velocity of ejecta. Velocities of ejecta are based on a projectile velocity of 10 km/s and are indicated by the length of the *arrows* (the length of the *vertical arrow* above the surface on the *left* is a scale indicating 200 m/s). The $\times 10$ above the two *arrows* on the right that are closest to the projectile indicates that those *arrows*, if drawn to scale, would be 10 times longer than shown. The spall zone shown on the *right* is a region near the surface where large blocks of unshocked to weakly shocked target rock can be accelerated to high velocities. From Melosh (1989), Fig. 5.4, by permission of Oxford University Press, Inc

very high pressures. Depending on the size and velocity of the projectile, the peak shock pressure can exceed 100 GPa (equal to 1000 kbar or 1 Mbar) (Melosh 1989). As the shock front moves away from the projectile it expands to cover a larger hemispherical area and decays in strength because it is spread over a greater volume of rock and because it undergoes irreversible energy losses in the shock-compressed rock. This results in a rapid drop in shock pressure with distance from the point of impact (Ahrens and O'Keefe 1977). Thus, around the point of impact, there is a series of concentric, approximately hemispherical shock zones, each defined by a given range in peak shock pressure and shock effects (Fig. 2.2).

Temperature in the target rock rises with increasing shock pressure and during large impacts the temperatures near the projectile can exceed 10,000 °C. Thus, near the point of impact, where the shock pressure is highest, the target rock can be vaporized upon unloading of the high pressure. Beyond that is a hemispherical shell where the shock pressure exceeds 50 GPa and the resulting temperature is high enough to melt the target rock. Surrounding that is a still larger volume of rock where the shock pressure is between about 5 and 50 GPa (Fig. 2.2). Here the

rocks undergo irreversible changes; that is, they are shock metamorphosed. Farther out where the pressure falls between about 1 and 5 GPa, the target rock can be broken into fragments. At even greater distances, the peak shock pressure falls below 1–2 GPa. At this distance, the velocity drops to that of the velocity of sound in the target rock and the shock wave transforms into an elastic or seismic wave (Melosh 1989). This transition occurs near where the crater rim will form.

As previously mentioned, upon contact with the target rock, a shock wave is also generated which travels back through the projectile. When the shock wave reaches the rear surface of the projectile, it is reflected forward through the projectile as a rarefaction wave. As the rarefaction wave passes through the projectile, it unloads the projectile from the high pressure. In a large impact, the pressure and associated temperature are so high that the projectile is almost completely melted and vaporized. When the rarefaction wave reaches the front of the projectile, it enters the compressed target rock. This is considered the end of the contact/compression stage. For a small impact, this stage lasts just fractions of a second. For larger impacts, it can last for several seconds. By the time the rarefaction wave reaches the front of the projectile it has penetrated up to one projectile diameter or more into the target rock (Melosh 1989; French 1998).

As the shock wave moves through the target rock it not only melts and crushes it, but it sets the target rock in motion radially away from the projectile. Thus, passage of the shock wave sets the stage for the excavation flow generated by the rarefaction wave, which follows the shock wave.

2.2.2.2 Excavation Stage

The **excavation stage** begins when the **rarefaction wave** propagates downward from the free surface (i.e., Earth's surface) producing an upward-directed pressure gradient behind the shock wave and adding an upward component to the radial velocity, which results in an upward and outward motion of the target rock. This is the excavation flow that is primarily responsible for opening the transient crater (Melosh 1989). Excavation flow velocities are highest near the point of impact and fall off approximately as the inverse power of the distance from the impact point. The maximum excavation flow velocity is between one-sixth and one-tenth of the projectile velocity (Melosh 1989), depending on the nature and composition of the target rock. Thus, for a projectile impacting with a velocity of 24 km/s, some of the ejecta could be ejected with a velocity as high as 4 km/s.

The diverging excavation flow ejects target material up and away from the growing crater form producing an inverted cone of ejecta material called an **ejecta curtain**. The lower edge of the ejecta curtain defines the outer lip of the growing crater (Melosh 1989). In small-scale laboratory experiments, this ejecta curtain has straight sides and forms an angle of about 45° with the target surface (Fig. 2.3). The apparently coherent ejecta curtain is due to a coincidence in alignment of the

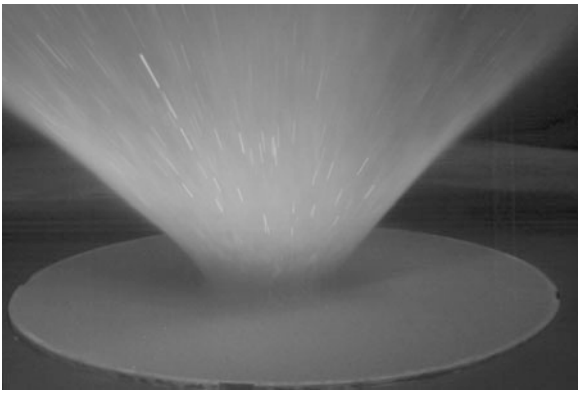

Fig. 2.3 Ejecta curtain produced in a laboratory experiment when a high velocity projectile was fired vertically into a horizontal target. Note that the ejecta curtain is at an approximately 45° angle to the target surface. NASA/JPL image courtesy of Peter Schultz

ejecta particles, each following its own trajectory (Melosh 1989). As the material is ejected, the crater form grows larger and the ejecta curtain moves outward from the center of the developing crater. The rarefaction waves, like the shock waves, lose energy as they move through the target rock. When the shock and rarefaction waves can no longer excavate or displace target rock, the crater ceases to grow. This is the end of the excavation stage and the beginning of the modification stage. The excavation stage takes a lot longer than the contact/compression stage; but still it takes only seconds to minutes, depending on crater size.

In the upper part of the target rock (**excavation zone**) the rock is shock metamorphosed to varied degrees, fractured, excavated, and ejected beyond the crater rim, as discussed above; but in the lower region (**displaced zone**), the rock is driven downward and outward in a semi-coherent manner (Grieve 1987; Melosh 1989) (Fig. 2.4). Rock from this region is not ejected. Roughly half of the volume of the cavity is produced by excavation and half by material that is pushed out of the way by the shock wave (Stöffler et al. 2006). It is important to note that the formation of even the largest known terrestrial impact structures did not result in the excavation of mantle material (Koeberl 2002).

During most impacts, the shock waves and following rarefaction waves move away from the projectile in a more-or-less hemispherical wave front resulting in ejecta being thrown out symmetrically around the crater as it is forming. This produces a generally circular crater with ejecta distributed symmetrically about it. At really low angles of impact, however, an elongate crater can be produced and the ejected material is not thrown symmetrically about the crater. The layer of ejecta found around an impact crater is called an **ejecta blanket**. The ejecta in the ejecta blanket exhibits a wide range of shock metamorphic effects and the blanket thins away from the crater. The ejection, transportation, and distribution of ejecta (especially distal ejecta), during both high and low angle impacts, are discussed in more detail in Sect. 2.4.

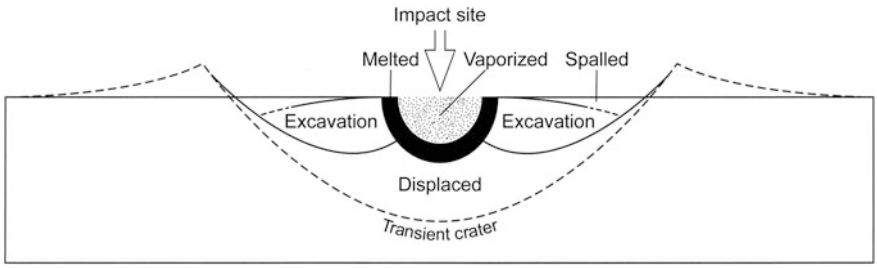

Fig. 2.4 Source regions for material ejected or moved aside to form a theoretical transient impact crater. Vaporized projectile and target rock (stippled) form closest to the point of impact. The vaporized rock expands upward and outward to form a vapor plume. Next to the vapor region a layer of melted rock (*solid black*) forms, which moves downward and outward across the transient crater floor. Most of the melt stays in the crater, but some lands adjacent to the crater and is deposited in the ejecta blanket. A small amount of the melt is ejected with the high velocity ejecta during the initial stage of crater formation and becomes part of the distal ejecta. Most of the rock from the excavation zone is ejected upward and outward beyond the crater rim to form an ejecta blanket adjacent to the crater. The ejected rock is excavated from a maximum depth that is approximately 1/3 of the transient crater depth. The remainder of the crater (displaced zone) is formed as rock is compressed and shoved downward and outward by the advancing shock wave. Rock that is displaced outward deforms adjacent rock, uplifting the surface near the rim. From Melosh (1989), Fig. 5.13, by permission of the Oxford University Press

2.2.2.3 Modification Stage

The modification stage begins as soon as the crater has been completely excavated. Excavation produces a bowl-shaped depression referred to as a **transient crater**. The walls of the transient crater generally collapse under the influence of gravity shortly after the crater is formed and the floor of the crater is raised by elastic and/or gravity-driven rebound (Stöffler et al. 2006). In smaller craters any rebound of the crater floor is small and loose rock debris on the crater walls slides into the crater and is deposited on the crater floor. In larger terrestrial craters, generally larger than about 4 km diameter, rebound can occur on a large scale forming a central uplift (central peak or a central ring of hills) in the interior of the crater and slump blocks slide down into the crater forming terraces. Both processes result in increase in diameter and decrease in depth of the crater. Formation of the central uplift is not well understood, but field studies indicate that deep-seated rock moves inward and upward in the central part of the crater immediately after formation of the transient crater. The mass movement may involve a process called **acoustic fluidization** (Melosh and Ivanov 1999). Still larger impact structures may have a ring structure with a series of concentric uplifted and down-dropped blocks or rings surrounding the central crater. The major part of the modification stage, during which the impact-related changes take place, lasts for only slightly longer than the excavation stage. The diameter of the resulting crater is generally about 20–30 times larger than the diameter of the projectile (French 1998). The actual crater size and morphology depend on the velocity, size, and nature of the projectile, the angle of impact, and the nature of the target rock.

On Earth, erosion and infill of a crater can begin shortly after formation due to a variety of geological processes involving the atmosphere and hydrosphere. In the case of craters formed in the marine setting, the infill deposits can include a significant component of material that was reworked and transported into the crater by strong resurge currents or tsunamis. On a longer timescale, the larger impact structures can be affected by isostatic rebound (Melosh 1989; Wichman and Schultz 1989).

The modification stage is not important in forming or distributing distal impact ejecta and will, therefore, not be discussed further.

2.2.3 Simple Craters, Complex Craters, and Multi-Ring Basins

Smaller craters, with bowl shapes, are called **simple crater**s, while larger craters with terraces and a central uplift or peak and/or possibly ring structures are called **complex crater**s (Fig. 2.5). Fresh simple craters have an apparent depth (from the original ground surface to the top of the breccia lens) that is one-eighth of the crater diameter. Complex craters have depth to diameter ratios that are generally smaller than 1 to 8. Depth to diameter ratios are smaller for sedimentary rock than for crystalline rocks (Grieve and Pesonen 1992). During the cratering process the surface layer adjacent to the point of impact is often thrown back over itself to form an overturned flap with a hinge line under the crater rim (Fig. 2.5). Thus, rocks near the top of the inner wall of the crater often exhibit an inverted stratigraphy with beds or layers repeated in a reverse order. In addition, ejecta from the surface layer of the target rock are thrown out first and ejecta from the deepest level are thrown out last. Thus, the ejecta blanket also has a reverse stratigraphy. The reverse stratigraphy is one of the characteristics of impact craters that help to distinguish them from volcanic craters.

The largest known planetary impact structures are **multi-ring basin**s. These features are a few 100 km up to more than 1,000 km in diameter (e.g., Spudis 1993). Multi-ring basins consist of multiple concentric uplifted rings (horsts) separated by down-faulted valleys (grabens). They are present on Mercury, Mars, the Moon, and some of the satellites of Jupiter (e.g., Callisto). They are not obvious on the Earth, but Vredefort (South Africa), Sudbury (Canada), Chicxulub (Mexico), Manicouagan (Canada), and Popigai (Russia) impact structures have been suggested as possible multi-ring basins (French 1998; Spray et al. 2004).

The diameter of an impact crater or structure is one of the most fundamental and important parameters used in energy scaling and numerical modeling of the cratering process. However, within the impact and geological communities there is no agreement as to which feature should be used to define the diameter of an impact structure (Turtle et al. 2005). There are a number of concentric features that can be used to define the diameter of an impact structure including: transient

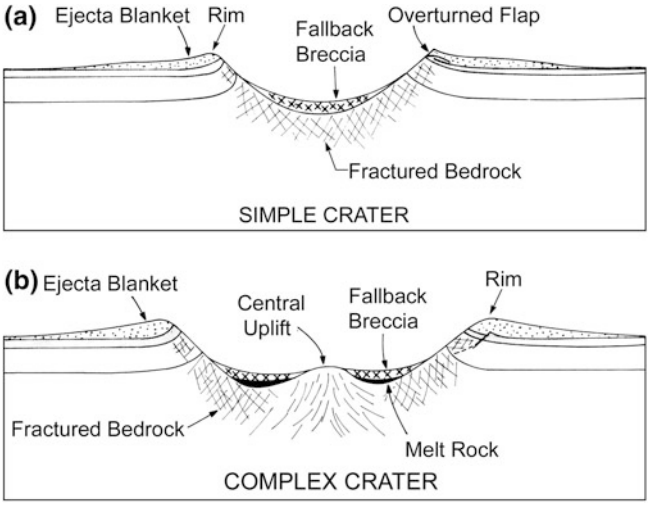

Fig. 2.5 Cross sections through a hypothetical simple impact crater (**a**) and a complex crater with a central uplift (**b**). Terrestrial craters smaller than 2–4 km diameter are generally simple bowl-shaped craters, whereas larger craters are generally complex with a central uplift or ring structure

crater, final rim, external rings, and outer limit of deformation. Therefore, care must be taken when comparing the diameter of one impact structure with that of another. For example, the size of Vredefort can be between 80 and 300 km depending on which feature is used to define its diameter.

2.3 Shock Metamorphism

Shock metamorphism refers to the permanent changes in geological materials resulting from the passage of a shock wave. Shock metamorphism also includes shock effects produced during laboratory experiments and nuclear explosions (e.g., see French and Short 1968). **Impact metamorphism** is a more restrictive term referring only to shock effects produced by hypervelocity impact (Chao 1967). The conditions of shock metamorphism are quite different from those produced by normal geological processes, including normal regional and contact metamorphism (French 1998) (Fig. 2.6). Normal metamorphism of crustal rock generally involves pressures <2–3 GPa and temperatures <1,000–1,200 °C (French 1998; Koeberl 2007); whereas shock waves can produce pressures >100 GPa near the impact point and >10 GPa in much of the surrounding rock, and temperatures that can exceed 10,000 °C near the impact point and between 500 and 3,000 °C in large volumes of the surrounding rock (Melosh 1989; French 1998). Another important difference is the strain rate, which is very slow in normal

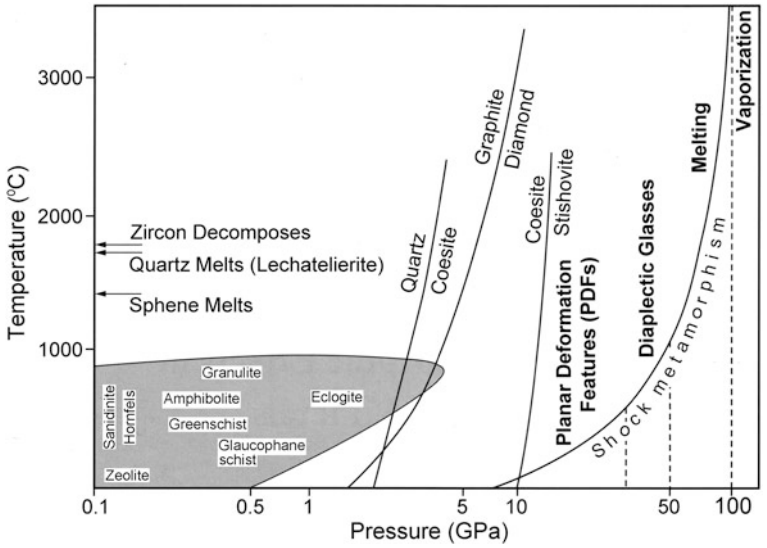

Fig. 2.6 Pressure-temperature diagram showing the conditions for regional metamorphism versus the conditions for shock metamorphism. Also shown are the pressure–temperature conditions required for formation of various shock metamorphism effects. From French (1998), Fig. 4.1, with permission from the Lunar and Planetary Institute

metamorphic processes ($<10^{-3}$/s), but rapid in shock metamorphism (up to 10^{6}/s). The high-strain rate produced during a cratering event is caused by a shock wave traveling at high velocity through the rock (compressing it to high pressure) followed immediately by a rarefaction wave, which reduces the pressure to zero or close to it; i.e., unloads the rock from high pressure. Thus, normal metamorphic processes take 100,000 s to millions of years, whereas the passage of a shock wave and, therefore, shock metamorphism, takes a fraction of a second for small impacts and up to a second or so for larger impacts. High residual temperatures can, however, remain for a long time and destroy much of the shock metamorphic effects produced by the high pressure and high-strain rate. The long time required for most normal metamorphic processes generally results in a mineral assemblage that is in equilibrium or close to it. Because shock metamorphism occurs rapidly, disequilibrium processes resulting in quenching and preservation of metastable minerals and glasses generally occur (French 1998).

In the past, the term **impactite** was used to refer to vesicular, glassy to finely crystalline material produced by melting of target rock by heat generated during a hypervelocity impact of an extraterrestrial body on the Earth (Gary et al. 1972). More recently, it has been proposed that the term impactite be used as a collective term to refer to all rocks affected by, or produced by, shock metamorphism (Stöffler and Grieve 2007). Proximal impactites include impact **melt rock**, impact breccia, and shocked rock. Impact melt rock is rock formed by solidification of impact melt. Melt rock contains variable amounts of clastic debris exhibiting

different degrees of shock metamorphism. Its groundmass consists of varying amounts of glass and crystallized melt.

There are three main types of impact breccias: **lithic breccia**, **impact melt breccia** (**melt-matrix breccia**), and **suevite**. Lithic breccias are melt-free breccias. Melt-matrix breccias are a type of melt-bearing breccia in which the melt occurs in the matrix that typically makes up 25–75 vol. % of the rock (French 1998). The melt can range from glassy to completely crystalline. Suevite has been described as a polymict, melt-bearing impact breccia which has a clastic matrix containing lithic and mineral clasts in various stages of shock metamorphism and cogenetic impact melt clasts (or glass bombs), which can be in a glassy or crystallized state (French 1998; Stöffler and Grieve 2007). However, in a more recent study of the matrix material, Osinski et al. (2004) concluded that the "suevite" is "…more akin to mixed impact melt breccias."

Shocked rock is unbrecciated rock that shows unequivocal effects of shock metamorphism, exclusive of whole rock-melting.

Distal impactites include impactoclastic airfall beds (Stöffler and Grieve 2007). According to Stöffler and Grieve (2007), an impactoclastic airfall bed is a fine-grained (pelitic) sedimentary layer "…containing a certain fraction of shock metamorphosed material, e.g., shocked minerals and melt particles…" which is "…deposited by interaction with the atmosphere over large regions of a planet or globally" (Fettes and Desmons 2007, p. 162). This definition appears to be too narrow as some of the distal ejecta layers consist largely or almost entirely of millimeter-sized, impact-generated spherules such as microtektites and microkystites (e.g., the Late Triassic spherule layer and all of the Archean spherule layers). These distal deposits generally contain a relatively high proportion of debris from the vaporized projectile and can have high concentrations of platinum group elements, including iridium. In larger impacts, the size of the Cretaceous-Tertiary impact and larger, unmelted shock metamorphosed grains as well as impact spherules can be found globally. In smaller impacts, the unmelted ejecta are restricted to an area closer to the source crater, while spherules can be ejected over much larger areas.

The degree of shock metamorphism produced by a given shock pressure depends on the equation of state of the material being shocked, which involves parameters including compressibility, specific energy, entropy, specific volume, and phase change (Stöffler et al. 2006). The transition from elastic to plastic behavior in rocks takes place at shock pressures of approximately 5–12 GPa and mechanical deformation and transition to high-pressure phases takes place at shock pressures generally between $\sim$10 and 60 GPa. In general, shock features produced at shock pressures below 10 GPa cannot be distinguished from similar features produced by normal geological processes (French and Koeberl 2010). At pressures above 40–100 GPa thermal effects begin to dominate (Stöffler et al. 2006). Whole rock melting takes place at shock pressures greater than $\sim$40 GPa for sedimentary rocks, $>\sim$60 GPa for felsic rocks, and >80 GPa for mafic rocks (Stöffler et al. 2006). Shock-induced vaporization and melting represent the highest degree of shock metamorphism. Shock pressures greater than 150 GPa cause vaporization of rock.

The primary shock effects produced during shock compression and decompression can be subdivided into the following categories: (1) vaporization and melting, (2) decomposition, (3) phase transformations, and (4) elastic–plastic deformation (e.g., French 1998; Langenhorst and Deutsch 1998).

2.3.1 Vaporization and Melting

During hypervelocity impacts, much of the projectile and some of the target rock adjacent to the projectile can be vaporized. The vapor can condense upon cooling and produce liquid droplets, which can be quenched to produce glassy spherules. Likewise, melt droplets can be ejected from the crater and can cool to form small (generally millimeter size or smaller) glassy spherules. Impact-generated melt droplets which cool too quickly to undergo crystallization form glass bodies without primary microlites/crystallites (e.g., tektites and microtektites), whereas melt droplets that cool slowly enough undergo partial crystallization to form spherules with primary microlites/crystallites (e.g., microkrystites; Fig. 2.7).

At shock pressures between about ~45 and 55 GPa it is possible for selective mineral melting to occur (French 1998). Occasionally, the post-shock temperatures will be high enough to melt most major mineral phases; but because of the rapid melting and quenching there is not enough time for mixing, and the resultant impactite may consist of a mixture of heterogeneous glasses with close to the original shapes and compositions of the melted mineral grains (French 1998). Such impactites are rare because of the narrow range of conditions required to form them (French 1998). More commonly, most of the melt flows and is mixed before quenching. Whole rock melting of most dense continental crustal rocks takes place at pressures exceeding 60–80 GPa (Stöffler et al. 2006). Whole rock melting of felsic crystalline rocks can start at pressures as low as 60 GPa; whereas whole rock melting of mafic rocks requires shock pressures >75–80 GPa.

Impact glasses are generally heterogeneous, exhibit flow banding or **schlieren**, contain some vesicles, and can contain unmelted or partially melted grains (Fig. 2.8). Schlieren are streaks of glass with different composition and, therefore, different color and refractive index from the glass in which they occur. In some cases the silica melt formed by shock melting of quartz grains does not mix with the rest of the melt and the resultant glass can contain lechatelierite particles (silica glass produced by the melting of quartz or other silica phases). **Lechatelierite** particles are ubiquitous in most terrestrial impact glasses, including tektites and microtektites (Fig. 2.9). Formation of lechatelierite during impact melting of dense crystalline rocks can occur at shock pressures between ~30 and 50 GPa (Gratz et al. 1996; Stöffler et al. 2006). The presence of lechatelierite indicates a temperature ≥1,750 °C (Stöffler and Langenhorst 1994). Lechatelierite can also be found in **fulgurites**, which are narrow tube-like bodies or branching networks of melted soil or sediment produced by lightning strikes.

Metallic spherules, ranging in size from a few micrometers up to 100 μm or more, have been found in impact glasses at several impact craters/structures

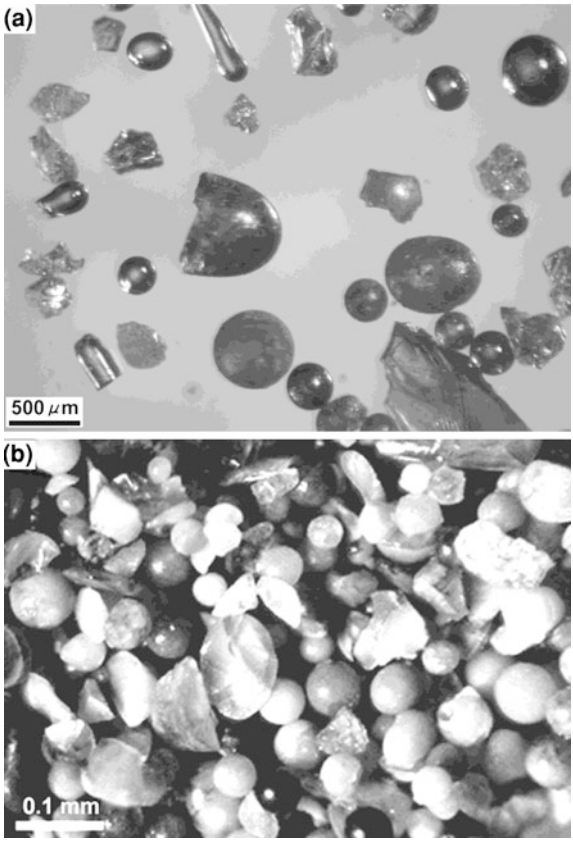

Fig. 2.7 Optical microscope images of microtektites and microkrystites. **a** Australasian microtektites from Core SO95-17957-2 taken in the South China Sea (10.9° N, 115.31° E). They are mostly splash forms or fragments of splash forms. Most of the whole splash forms are spheroids, but teardrop-, dumbbell-, and disc-shaped forms are also present. They are mostly transparent to translucent brown, but some are pale yellow to pale green. See Sect. 4.2 for more detail about the Australasian microtektites. **b** Upper Eocene clinopyroxene-bearing (cpx) spherules (microkrystites) from Ocean Drilling Project Hole 709C (Core 31, Section 4) in the equatorial western Indian Ocean (3.915°S, 60.552°E). All the cpx spherules appear to be spherical or fragments of spheres. Teardrop, dumbbell, and disc shapes have not been observed, but there are numerous examples of composite forms composed of two or more spheres fused together. The cpx spherules range from translucent to opaque. Most are light-colored, but many are dark in color and often mottled dark brown and light tan. All contain microlites of clinopyroxene and many contain skeletal microlites of nickel-rich spinel. See Sect. 4.6 for more details about the cpx spherules

including Barringer crater in the USA, Bosumtwi crater in Ghana, Henbury crater in Australia, the Wabar craters in Saudi Arabia, and Lappajärvi crater in Finland (see, e.g., El Goresy et al. 1968). The metallic spherules are Ni-rich (up to 90 wt % Ni) and presumably represent meteoritic contamination from the projectile. Similar metallic spherules have not been observed in distal impact glasses such as

microtektites and microkrystites. However, **Ni-rich spinel** microlites have been found in the upper Eocene **clinopyroxene-bearing spherules** (or **cpx spherules**), the Cretaceous-Tertiary (K-T) boundary spherules, and in some Precambrian spherules (e.g., Glass et al. 1985; Kyte and Smit 1986; Bohor et al. 1986; Lowe et al. 1989; Byerly and Lowe 1994; Pierrard et al. 1998). The relatively low Ti and high Ni, Mg, and Al contents of spinel crystals in the K-T boundary and upper Eocene cpx spherules are distinctly different from terrestrial spinels and indicate a meteoritic source (Kyte and Smit 1986; Pierrard et al. 1998). The high Fe_3+/Fe_2+ ratios of the K-T boundary and upper Eocene cpx spherules indicate highly oxidizing conditions during crystallization in the atmosphere (Robin et al. 1992).

The small size (generally <10 μm) and skeletal to dendritic crystal morphologies of the K-T boundary, upper Eocene cpx, and Precambrian spherules indicate rapid crystallization from a melt. The melt may have formed from condensation of vaporized projectile and target rocks (e.g., see Ebel and Grossman 2005). Although the Ni-rich spinels are not direct evidence of shock metamorphism, their occurrence in spherules indicates the presence of meteoritic contamination and supports an impact origin for the spherules.

2.3.2 Shock-Induced Decomposition or Dissociation

At high temperatures some mineral grains undergo **thermal decomposition** or dissociation, forming two or more phases. There are two types of shock-induced decomposition: (1) thermal decomposition that is caused primarily by the high residual temperature after the pressure has been released, and (2) decomposition caused by the action of the shock wave itself. The resultant grains can have the same bulk composition and shape as the original mineral grains. Zircon, for example, can be thermally decomposed to form microscopic **baddeleyite** (ZrO_2) crystals in an SiO_2 glass matrix (Fig. 2.10) (El Goresy et al. 1968). More recently it has been proposed that decomposition of zircon may not be solely the result of high temperature, but could also be shock-pressure induced, which is indicated by possible relics of a high-pressure ZrO_2 polymorph; i.e., **orthorhombic II ZrO_2** (Wittmann et al. 2006). Zircon decomposition takes place at a temperature above ~1,700 °C, produced by a shock pressure of ~90 GPa (Kusaba et al. 1985). Cr-rich spinels can breakdown to eskolaite (Cr_2O_3) and a Mg, Al phase (perhaps spinel) (El Goresy et al. 1968).

Al_2SiO_5 phases, such as kyanite, sillimanite, and andalusite, can breakdown to Al_2O_3 plus SiO_2 phases (Fig. 2.11). Liu (1974a) reported that kyanite dissociates into Al_2O_3 and SiO_2 phases at pressures >3 GPa. High pressure laboratory experiments show that kyanite breaks down to corundum plus stishovite at pressures between 14 and 17.5 GPa at temperatures between 1,000 and 2,000 °C (Schmidt et al. 1997). Some of the sillimanite in shocked gneisses from Haughton impact structure in Canada shows evidence of breakdown to mullite (Al_2O_3) plus amorphous SiO_2 (Martinez et al. 1993). Laboratory experiments show that at

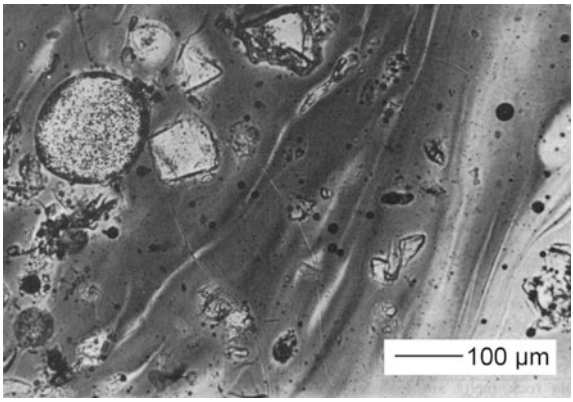

Fig. 2.8 Optical microscope image (transmitted light) of a thin section of impact glass in suevite from the Ries crater, Germany. The glass has a "granodioritic" composition and contains schlieren, vesicles, and mineral clasts (mostly quartz). From Stöffler (1984), Fig. 5. Reprinted with permission from Elsevier

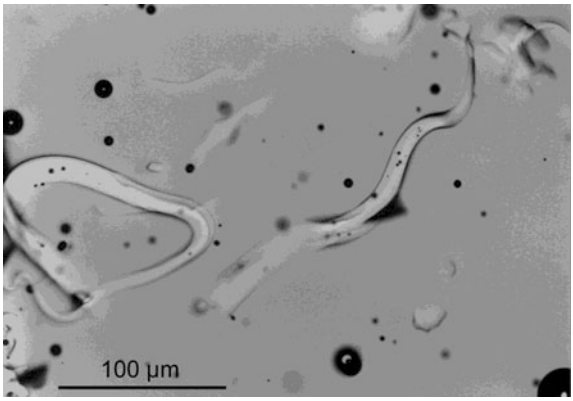

Fig. 2.9 Optical microscope image (unpolarized light) of a thin section of an Ivory Coast tektite containing lechatelierite and vesicles. The lechatelierite particles are *lighter gray* than the glass matrix and most in this section have been drawn out into ribbon-like shapes

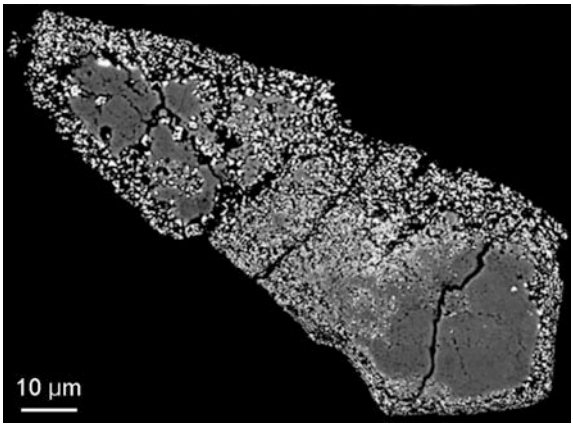

Fig. 2.10 Backscattered electron image of a shocked zircon (*dark gray*) which partly dissociated to ZrO_2 (*white*) and silica (*black*). The ZrO_2 is mostly, if not entirely, baddeleyite; but there may be trace amounts of a high-pressure ZrO_2 polymorph. The zircon is from core Yax-1 drilled into the Chicxulub impact structure (Yucatan Peninsula, Mexico). Courtesy of A. Wittmann

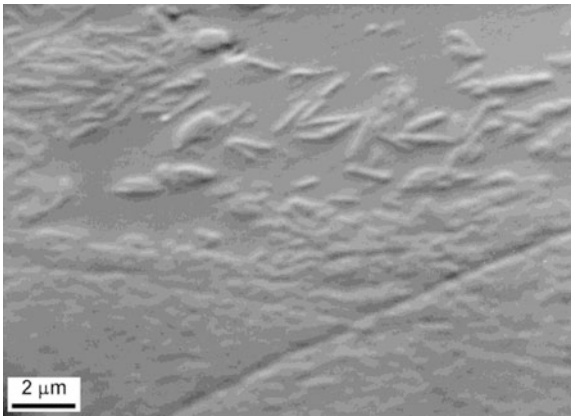

Fig. 2.11 Scanning electron image of a part of a shocked Al_2SiO_5 phase recovered from a Muong Nong-type Australasian tektite. The grain has decomposed into elongate microlites of corundum (Al_2O_3) in SiO_2 glass (smooth lower relief). The grain as a whole has an Al_2SiO_5 composition, but X-ray diffraction only indicates the presence of corundum

shock pressures above ~58 GPa gem-quality crystals of andalusite decompose into poorly crystallized γ-alumina, well-crystallized α-alumina (corundum) and X-ray amorphous silica (Schneider and Hornemann 1977). Schneider and Hornemann (1977) proposed that at shock pressures above 70 GPa andalusite will decompose into corundum and stishovite.

Biotite, some amphiboles and clinopyroxene, garnet, and staurolite can decompose into polyminerallic aggregates plus glass (Chao 1968; Feldman 1994). Some of the decomposition into several phases may involve migration of elements into and/or away from the shocked mineral grain—i.e., it is not always an isochemical process. Biotite can decompose into iron oxides (e.g., magnetite and ilmenite), pyroxene, alkali feldspar, and silica glass (Stöffler 1974). The decomposition of biotite takes place at shock loads between 20 and 50 GPa (Feldman 1994). The amphibole, hornblende, has been observed to break down, under shock loads of up to 30–35 GPa, into an aggregate composed of microscopic crystals of plagioclase, amphibole, clinopyroxene, magnetite, and, rarely, potassium feldspar (Feldman 1994). Under shock loads of 35–40 GPa, it has been observed that clinopyroxene decomposes into an aggregate composed of amphibole, plagioclase, clinopyroxene, and magnetite (Feldman 1994). Garnet begins to decompose or breakdown, beginning at 30 GPa, into spinel, hypersthene, and alkali feldspar, plus glass (Stähle 1975; Feldman 1994). In the Janisjärvi impact structure (Russia), staurolite was observed to have decomposed at ~20 GPa into an aggregate of sanidine, orthopyroxene, hercynite, and glass (Feldman 1994).

Laboratory studies have shown that olivine $(Mg, Fe)_2SiO_4$ dissociates to ringwoodite [$(Mg,Fe)SiO_3$-perovskite] plus **magnesiowüsite** (Mg, Fe)O at 23 GPa and 1,600 °C (Chen et al. 1996), and clinoenstatite ($MgSiO_3$) dissociates into a mixture of wadsleyite (β-Mg_2SiO_4) plus stishovite (SiO_2) at 25 GPa and 1,000 °C and ringwoodite (γ-Mg_2SiO_4) plus stishovite (SiO_2) at 28 GPa and 1,000 °C (Ito et al. 1972). However, as far as the authors know, these dissociates have not been observed in terrestrial shock metamorphosed rocks. Ringwoodite, wadsleyite, and stishovite are high-pressure polymorphs and are discussed in more detail in the following section.

2.3.3 Phase Transformation: High-Pressure Phases

As the shock wave passes through the target rock, some minerals can be transformed into high-pressure phases. High-pressure phases can be produced in a variety of ways, including: solid state transformation, high-temperature dissociation of a phase under pressure to produce one or more high-pressure phases, and melting and recrystallization while the pressure is still high. Some high-pressure phases have the same composition as common low-pressure phases and are called, therefore, **high-pressure polymorphs**. Because of the residual high temperatures that usually linger long after the shock wave passes through the rock, the high-pressure phases are often destroyed; but when they survive, they can provide reliable indicators of shock metamorphism. Some of the high-pressure phases that are produced by shock metamorphism can also be found in rocks brought up from great depths in the Earth's crust and upper mantle; however, the geologic setting, mineral association, and grain size can generally be used to distinguish between high-pressure phases produced by shock metamorphism and those produced at great depths in the Earth's crust and upper mantle. High-pressure phases can be found in metamorphosed rocks of ultra-high pressure origin (roots of eroded mountain ranges) and mafic volcanic rocks such as kimberlites. Because they are formed at great depths (>60 km), they are subjected to high pressures and high temperatures for long periods of time before they are exposed at the Earth's surface by tectonic uplift and erosion. Thus, they are generally coarsely crystalline in comparison with high-pressure polymorphs produced in fractions of a second by the passage of a shock wave.

The high-pressure polymorphs of quartz, i.e., **coesite** and **stishovite** (Tables 2.1 and 2.2), are the most commonly recognized high-pressure polymorphs found in shock metamorphosed rocks. Coesite was first produced in high-pressure laboratory studies in 1953, and was first recognized in nature in the shock metamorphosed rocks at Barringer crater, Arizona (Chao et al. 1960) (Table 2.2). Stishovite was also first recognized in shocked rocks from Barringer crater (Chao et al. 1962). Since their discovery, coesite and stishovite have been found at numerous impact structures, including the Ries impact structure in Germany (Chao et al. 1960; Shoemaker and Chao 1961) and the Vredefort impact structure in South Africa (Martini 1978). Coesite and stishovite have specific gravities of 2.93 and 4.23, respectively, whereas quartz has a specific gravity of 2.65. Stishovite reverts to an amorphous state at temperatures as low as 250–300 °C (Dachille et al. 1963; Fiske et al. 1994), and, therefore, is often destroyed by residual heat after an impact.

Under static conditions in high-pressure laboratory experiments, quartz is transformed to coesite at a pressure of >2 GPa and to stishovite at a pressure of 10–15 GPa. The short duration of shock compression impedes a direct solid-state transformation of quartz into coesite and stishovite. Rather, the quartz is melted at high pressure and coesite and stishovite can crystallize during decompression (Langenhorst 2002), and because of kinetics stishovite is actually formed at lower shock pressures than coesite: >12–15 GPa for stishovite versus >30 GPa for

Table 2.1 High-pressure phases produced by shock metamorphism: basic data

Mineral name/ phase	Composition	Crystal structure	Density [g/cm^3]	Low-pressure polymorph	First Synthesized
Coesite	SiO_2	Feldspar-like	2.93	Quartz, cristobalite	Coes (1953)
Stishovite[a]	SiO_2	Rutile	4.23	Quartz, cristobalite	Stishov and Popova (1961)
Seifertite	SiO_2	α-PbO_2-like	4.29	Quartz, cristobalite	Tsuchida and Yagi (1990)
Post-stishovite SiO_2 phase	SiO_2	Baddeleyite-like	4.3	Quartz, cristobalite	Dubrovinsky et al. (1997)
Diamond	C	Diamond	3.51	Graphite, coal	Bundy et al. (1955)
Lonsdaleite	C	Wurzite	3.41	Graphite, coal	Bundy and Kasper (1967)
Reidite	$ZrSiO_4$	Scheelite	5.2	Zircon	Reid and Ringwood (1969)
TiO_2II	TiO_2	Columbite	4.37	Rutile, anatase	Bendeliany et al. (1966)
Akaogiite	TiO_2	Baddeleyite	4.63	Rutile, anatase	Sato et al. (1991)
Majorite	$(Mg,Fe)SiO_3$	Garnet	3.74	Enstatite	Ringwood and Major (1966)
Akimotoite	$(Mg,Fe)SiO_3$	Ilmenite	3.82	Enstatite	Kawai et al. (1974)
$(Mg,Fe)SiO_3$-perovskite[b]	$(Mg,Fe)SiO_3$	Perovskite	4.08	Enstatite	Liu (1974b)
Wadsleyite[c]	$(Mg,Fe)_2SiO_4$	Spinel-like	3.45	Olivine	Ringwood and Major (1970)
Ringwoodite[c]	$(Mg,Fe)_2SiO_4$	Spinel	3.9	Olivine	Ringwood (1958)
A $KAlSi_3O_8$ phase	$KAlSi_3O_8$	Hollandite	3.84	K-feldspar	Ringwood et al. (1967)
Lingunite	$NaAlSi_3O_8$	Hollandite	3.8	Albite	Liu (1978)
Xieite	$FeCr_2O_4$	$CaTi_2O_4$	5.63	Chromite	Chen et al. (2003b)
Un-named $FeCr_2O_4$ phase	$FeCr_2O_4$	$CaFe_2O_4$	5.62	Chromite	Chen et al. (2003b)
Un-named $FeTiO_3$ phase	$FeTiO_3$	Li-niobate	Unknown	Ilmenite	Unknown
Tuite[d]	$Ca_3(PO_4)_2$	$Ba_3(PO_4)_3$	3.45	Merrillite	Murayama et al. (1986)

[a] In some of the older literature stishovite was called stipoverite.
[b] This phase is called liusite in some publications
[c] Wadsleyite and ringwoodite are sometimes referred to as the β-Mg_2SiO_4 phase and γ-Mg_2SiO_4 phase, respectively
[d] This phase is called γ-$Ca_3(PO_4)_2$ in some publications

Table 2.2 High-pressure phases produced by shock metamorphism: discovery and pressure conditions (see Table 2.1 for basic data about these phases)

Mineral name/phase (see Table 2.1 for chemical formula)	Location of first natural occurrence	Reference of first occurrence	Pressure conditions[a] [GPa]	Reference for shock pressure
Coesite	Barringer crater	Chao et al. (1960)	**30–60**	Stöffler and Langenhorst (1994)
Stishovite	Barringer crater	Chao et al. (1962)	**12–45**	Stöffler and Langenhorst (1994)
Seifertite	Shergotty meteorite	Sharp et al. (1999)	**70–90**	German et al. (1973)
			37–89	Dubrovinskaia et al. (2000)
Post-stishovite SiO_2 phase[c]	Shergotty meteorite	El Goresy et al. (2000)	>45?	El Goresy et al. (2000)
Diamond	Novo Urei ureilite meteorite	Yerofeev and Lachinov (1888)	**13–50+**	Hanneman et al. (1967)
Lonsdaleite	Canyon Diablo meteorite	Hanneman et al. (1967)	**70–140**	Stöffler (1972)
Reidite	Upper Eocene ejecta, NW Atlantic	Glass and Liu (2001)	**38–80**	Gucsik et al. (2004a)
			>20	Fiske et al. (1994)
TiO_2II	Ries crater	El Goresy et al. (2001a)	4–20	Sato et al. (1991)
			45–75	McQueen et al. (1967), Linde and DeCarli (1969)
Akaogiite	Ries crater	El Goresy et al. (2001b)	12–60	Sato et al. (1991), El Goresy et al. (2001b)
			17–24	Greshake et al. (2000)
Majorite	Coorara meteorite	Mason et al. (1968)	**13.5**	Stöffler (1972)
			16–22.5	Zhang et al. (2006a)
Akimotoite	Acfer 040 meteorite	Sharp et al. (1997)	19–25	Greshake et al. (2000)
		Tomioka and Fujino (1997)	23–25	Xie et al. (2006)
$(Mg,Fe)SiO_3$-perovskite	Tenham meteorite	Tomioka and Fujino (1997)	>23	Zhang et al. (2006a)
			25–60	Liu (1976), Saxena et al. (1996)

(continued)

Table 2.2 (continued)

Mineral name/phase (see Table 2.1 for chemical formula)	Location of first natural occurrence	Reference of first occurrence	Pressure conditions[a] [GPa]	Reference for shock pressure
Wadsleyite	Tenham meteorite	Tomioka and Fujino (1997)	13–20	Greshake et al. (2000)
			12–18	Agee et al. (1995)
Ringwoodite	Umbarger meteorite	Binns et al. (1969)	10–25	Agee et al. (1995)
			30–60+	Langenhorst (2002)
$KAlSi_3O_8$ with a hollandite structure	Basaltic achondrite	Mori (1994)	>23	Greshake et al. (2000)
			>9–10	Yagi et al. (1994)
Lingunite	Yamato 790729 meteorite	Mori (1990)	18–23	Ohtani et al. (2004)
Xieite	Suizhou meteorite	Chen et al. (2003a,b)	20–23	Chen et al. (2003a)
$FeCr_2O_4$ with a $CaFe_2O_4$ structure	Suizhou meteorite	Chen et al. (2003a,b)	>12.5	Chen et al. (2003b)
$FeTiO_3$ with a Li-niobate structure	Ries crater	Dubrovinsky et al. (2009)	<28	Dubrovinsky et al. (2009)
Tuite	Suizhou meteorite	Xie et al. (2002)	~23	Xie et al. (2002)
			>9–10	Murayama et al. (1986)

[a] Bold indicates shock pressure and normal font indicates static pressure
[b] A post-stishovite phase with an α-PbO_2-like structure
[c] A post-stishovite phase with a baddeleyite-like structure

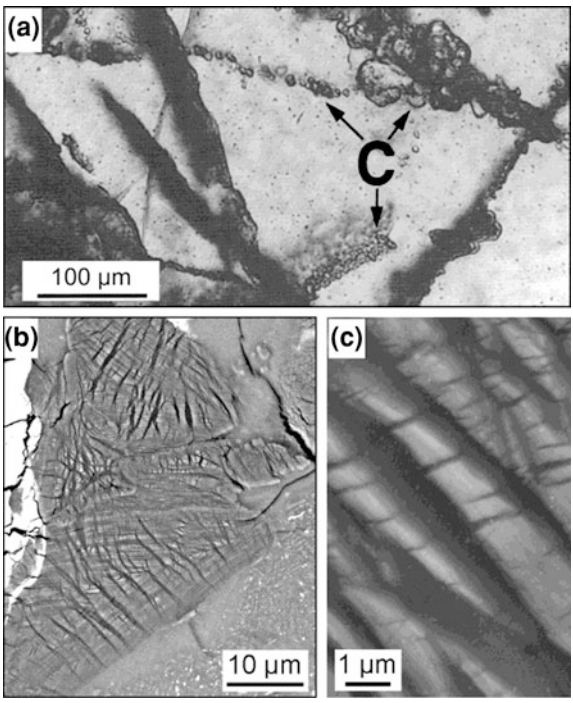

Fig. 2.12 High-pressure polymorphs of silica. **a** Optical microscope image of diaplectic quartz glass (*light gray*) with strings of small, high-relief crystals of coesite (c). From French (1998), Fig. 4.12, with permission of the Lunar and Planetary Institute. **b** SEM image of a large ($\sim 30 \times 50$ μm) silica grain (*darker gray*) containing seifertite (a post-stishovite SiO_2 polymorph) in a shock-melt vein in the Zagami shergottite. **c** High magnification SEM image of a portion of the seifertite-bearing grain in **b**. The bright lamellae are seifertite and the alternating darker lamellae are very dense SiO_2 glass. **b** and **c** are courtesy of El Goresy

coesite in dense rock (Stöffler and Langenhorst 1994). However, in porous rock, both coesite and stishovite form at shock pressures between 15 and 25 GPa (Greshake et al. 2000). Coesite can be found in ultra-high-pressure metamorphic rocks and in kimberlites. However, impact-produced coesite can generally be distinguished from coesite in ultra-high-pressure metamorphic rocks because of its much smaller grain size and its presence in a disequilibrium assemblage with other silica phases (e.g., coesite + quartz + silica glass) (Fig. 2.12a) (Grieve et al. 1996). Until recently, stishovite had only been found in impact craters and ejecta; however, small amounts of stishovite were recently found within diamonds (Wirth et al. 2007). Since diamonds are formed in deep-seated mantle rocks, stishovite still remains an excellent indicator of shock metamorphism when found in upper crustal rocks or sediments (French and Koeberl 2010).

Two post-stishovite polymorphs of silica (Tables 2.1 and 2.2) have been reported in the Shergotty meteorite (Fig. 2.12b) (Sharp et al. 1999; El Goresy et al. 2000). One phase has an α-PbO_2-type structure and has been named seifertite (El Goresy et al. 2008). The other phase has a baddeleyite-like structure. We are not aware of either phase having been found in shock metamorphosed terrestrial rocks.

Diamond (Tables 2.1 and 2.2) is a high-pressure polymorph of carbon that can be produced by shock metamorphism (Fig. 2.13). Shock-produced diamond and **lonsdaleite** (a rare hexagaonal diamond modification) form from carbon, such as graphite or coal, in the target rock. Impact diamonds form by solid-state transformation and can preserve the crystal form of the precursor phase, which is

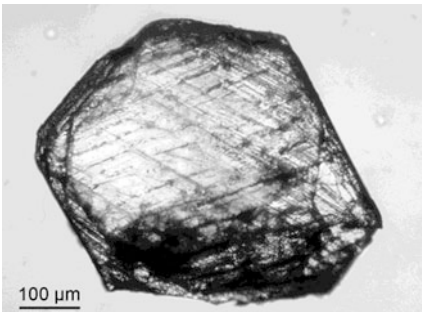

Fig. 2.13 An impact-produced diamond from the Popigai impact structure. The surface of the diamond exhibits some etching preferentially along twin boundaries and fissures, and flakes of graphite (*dark*) are present. The photograph was made under circular polarization. Courtesy of C. Koeberl

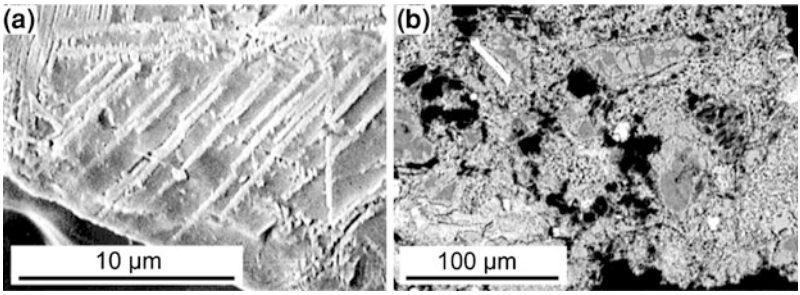

Fig. 2.14 High-pressure polymorphs of zircon (reidite) and rutile (TiO_2II). **a** Scanning electron image of a portion of the surface of a shock metamorphosed zircon crystal (*gray*) with microlites of reidite (*white*) aligned along crystallographic directions within the zircon. The shocked zircon was recovered from Chesapeake Bay impact structure ejecta in Ocean Drilling Program Site 904 in the northwest Atlantic off the coast of New Jersey (see Glass and Liu 2001). **b** Backscattered electron image of a shocked rock fragment containing TiO_2II ($\sim$40 µm long white crystal in the *upper left* quadrant) in a shocked rock fragment from the Australasian microtektite layer in a core from Ocean Drilling Program Site 1144 in the northern South China Sea (see Glass and Fries 2008)

commonly hexagonal graphite. Diamonds that are formed from graphite are pseudomorphs and are called **"apographitic" diamonds** (Masaitis et al. 1995; Langenhorst et al. 1999). Highly-ordered graphite can be transformed to diamond at pressures as low as 15 GPa and temperatures above $\sim$1,000 °C. Diamond formation in gneiss is estimated to take place at peak shock pressures in the range of $\sim$27–40 GPa with a post-shock temperature <2,000 K ($\sim$1,730 °C) (DeCarli 1998). Shock-produced diamonds can be formed in low-porosity rocks between 35 and 60 GPa (Greshake et al. 2000).

Impact-produced diamonds are polycrystalline, with sizes of individual crystals generally being <1 µm (e.g., Pratesi et al. 2003). Some impact diamonds from the

Popigai impact structure in northern Siberia were thought to contain up to 50–60 percent lonsdaleite, a rare hexagonal form of diamond (Masaitis 1998); however, TEM work was not able to confirm the presence of lonsdaleite, but rather seems to suggest the presence of stacking faults in the diamonds which apparently mimic the X-ray diffraction pattern of lonsdaleite (Koeberl et al. 1997a; Hough et al. 1998; Montanari and Koeberl 2000).

Diamonds of impact origin have been found in a number of impact structures, including: the Popigai impact structure in northern Siberia (Masaitis 1998; Koeberl et al. 1997a), the Ries impact structure in Germany (Hough et al. 1995), the Sudbury impact structure in Canada (Langenhorst et al. 1998), and the Lappajärvi impact structure in Finland (Langenhorst et al. 1999). The Popigai structure is regarded as the largest diamond deposit on Earth (Deutsch et al. 2000). The economic significance of the Popigai diamonds may be great, but, at the present time, it does not seem feasible to mine them commercially because of the lack of infrastructure in this remote area of northern Siberia (Deutsch et al. 2000; Reimold et al. 2005a). At the Ries impact structure, shock-produced diamonds have been found to be intergrown with silicon carbide in suevites (Hough et al. 1995). Although the occurrence of diamonds in near-surface rocks can be used as a reliable indicator of a hypervelocity impact, they must be used with care, as diamonds, like coesite, can form at depths >60 km in the Earth's crust and then later be uplifted and exposed at the Earth's surface.

Nanodiamonds (crystal sizes generally ~3–5 nm) have been found at some impact sites and have been used as an impact criterion; however, they have been found in some meteorites and they can be synthesized at low pressures by a variety of nonequilibrium chemical vapor-deposition techniques (Hazen 1999). Thus, the use of nanodiamonds as a diagnostic impact criterion is still being debated (see, e.g., Gilmour 1998; French and Koeberl 2010).

Several other high-pressure polymorphs of carbon have been reported since 2002. El Goresy et al. (2003) reported finding a new cubic (space group Pm3 m), dense, and super-hard polymorph of carbon in samples from the Ries and Popigai impact structures. More recently, Ferroir et al. (2010) found evidence two new ultrahard carbon phases in the Haverö ureillite meteorite. One is a rhombohedral carbon polymorph of the R3 m space group with a structure very close to that of diamond and the other is a theoretically predicted 21R diamond polytype.

In 2001, a high-pressure polymorph of zircon, with a scheelite structure, was discovered in ejecta from the Chesapeake Bay impact structure (Glass and Liu 2001). It was named **reidite** (Glass et al. 2002) after Alan F. Reid who first produced this phase in high-pressure laboratory experiments in 1969 (Reid and Ringwood 1969). Reidite (Fig. 2.14a) has since been found in shocked rocks from the Ries impact crater (Gucsik et al. 2004b). Reidite, like diamond, is formed by solid-state transformation. Shock compression experiments indicate that conversion of zircon to reidite begins at ~20 GPa with the amount of reidite increasing up to 100 % at about 52 GPa (Kusaba et al. 1985; Fiske et al. 1994). The pressure at which zircon begins to transform to reidite depends on the composition of the zircon (van Westrenen et al. 2004). Above 94 GPa, zircon begins to decompose

into ZrO_2 (baddeleyite) and SiO_2 (Kusaba et al. 1985), as discussed in the previous section. Reidite appears to be stable when heated to 1,100 °C at room pressure (Kusaba et al. 1985).

Two high-pressure polymorphs of rutile were discovered in shocked gneisses from the Ries crater: an α-PbO_2-structured TiO_2 phase and a baddeleyite-structured TiO_2 phase which has been named **akaogiite** (Tables 2.1 and 2.2; El Goresy et al. 2001a,b; Dubrovinsky et al. 2009). The α-PbO_2-structured TiO_2 phase, also known as **TiO_2 II**, has a columbite-type structure. This α-PbO_2 high-pressure TiO_2 polymorph has also been found in the Chesapeake Bay impact structure (Jackson et al. 2006), in shocked rock fragments from the Australasian microtektite layer (Fig. 2.14b) (Glass and Fries 2008), and in a sample from the Bosumtwi impact crater (McHone and Fries 2007). This phase has been produced in shock-loading experiments at shock pressures of 45 and 75 GPa (Table 2.2). When heated above 500 °C, the experimentally-produced α-PbO_2–structured TiO_2 polymorph quickly reverts back to rutile (Linde and DeCarli 1969). The baddeleyite-structured TiO_2 polymorph, akaogiite, is formed at static loads of 12–60 GPa (Sato et al. 1991) (Table 2.2).

A high-pressure polymorph of ilmenite ($FeTiO_3$) with a rhombohedral lattice similar to the Li-niobate structure of $MnTiO_3$ (Tables 2.1 and 2.2) was found in a shocked gneiss from the Ries impact structure, Germany (Dubrovinsky et al. 2009). This phase was found in association with akaogiite suggesting that it was subjected to a similar equilibrium peak shock pressure not exceeding 28 GPa. Dubrovinsky et al. (2009) argued that the original ilmenite was shock compressed to the perovskite polymorph which then inverted to the less dense Li-niobate structured phase during the decompression stage because the perovskite polymorph of $FeTiO_3$ is unquenchable.

The precursor phases for the high-pressure polymorphs discussed above are minerals commonly found in continental rocks and, therefore, the high-pressure polymorphs are good indicators of shock metamorphism for impacts involving continental crust. However, approximately 60 % of the Earth's crust is oceanic in nature and consists of mafic minerals such as pyroxene, olivine, and plagioclase feldspar. Since most of the terrestrial impacts must have taken place in oceanic crust, there is a need for shock metamorphic indicators for mafic minerals. There have been numerous studies of experimentally shocked mafic minerals and static high-pressure laboratory experiments on mafic minerals that can be used to estimate the pressure and temperature conditions under which they can be formed (see, for example, Stöffler et al. 1991; Agee et al. 1995; Xie et al. 2006 and papers listed therein; see also Sect. 2.3.6).

Studies of shock metamorphosed meteorites (chondrites and, to a lesser extent, achondrites) have provided numerous examples of high-pressure polymorphs of pyroxene, olivine, feldspar, and other mafic minerals. These high-pressure polymorphs are: **majorite**; **$(Mg,Fe)SiO_3$-perovskite; akimotoite; wadsleyite**; **ringwoodite**; **lingunite**, a high-pressure polymorph of feldspar with a hollandite structure; two post-spinel polymorphs of chromite; and **tuite**, a high-pressure polymorph of merrilite with a trigonal γ-$Ca_3(PO_4)_2$ structure (Tables 2.1 and 2.2).

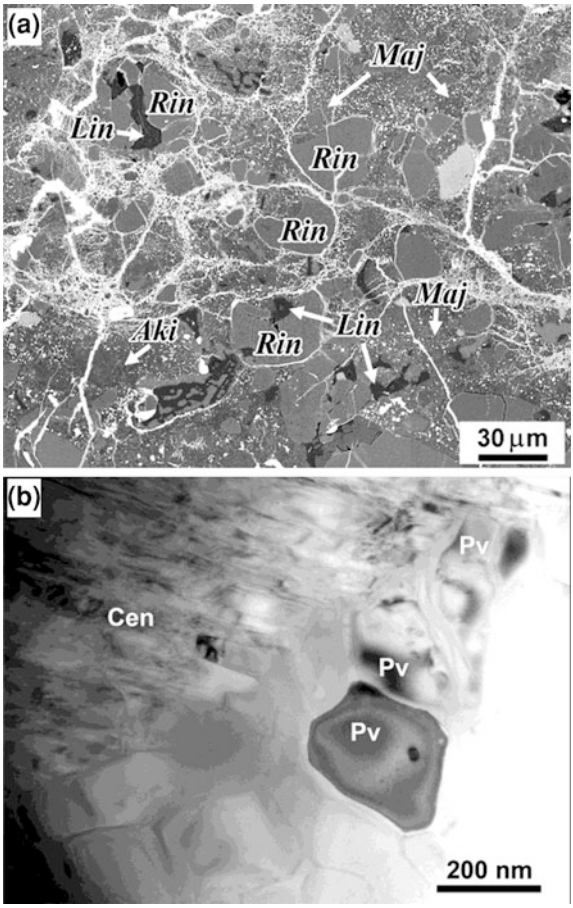

Fig. 2.15 Images of mafic high-pressure phases in shocked meteorites. **a** Backscattered electron image of a section of meteorite Y75267 (H6 chondrite) showing the presence of majorite (Maj), ringwoodite (Rin), akimotoite (Aki), and lingunite (Lin). Courtesy of Makoto Kimura. **b** Transmission electron microscope image showing (Mg,Fe)SiO_3-perovskite (Pv) and clinoenstatite (Cen) from the Tenham meteorite (L6 chondrite). Courtesy of Naotaka Tomioka

Ringwoodite, majorite, and wadsleyite are relatively common, but akimotoite, (Mg, Fe)SiO_3-perovskite, and alkali feldspars with a hollandite structure are less common (Xie et al. 2002).

Formation of high-pressure mafic phases in meteorites can take place by solid-state transformation or by crystallization from a shock-produced melt while still under high pressure. Most high-pressure mafic minerals found in meteorites occur adjacent to or in melt veins in highly shocked meteorites. These phases are generally quite small, <1 μm up to 100's of micrometers.

Most mafic minerals (e.g., olivine, pyroxene, garnets) are transformed to metastable phases or glass, or more likely simply melt when shocked at high enough pressure to produce high-pressure phases (Jones et al. 2003a). As of 2009, except for feldspar with a hollandite structure, the high-pressure mafic phases have not been found in terrestrial impact structures, although majorite has been observed in ultra-high-pressure metamorphosed terrestrial rocks (van Roermund et al. 2001). This may be due to different pressure–temperature histories of

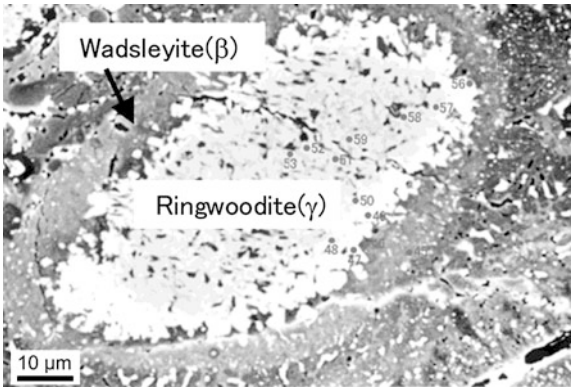

Fig. 2.16 Scanning electron photomicrograph of a grain of ringwoodite with a wadsleyite rim. This section is from an L6 chondrite (ALH78003). The numbers in the photomicrograph are where compositional data were obtained. Courtesy of Eiji Ohtani

terrestrial impacts compared with impacts on the meteorite parent bodies (Chen et al. 1996); or to a paucity of unweathered ultramafic lithologies in terrestrial impact structures. The precursor minerals for these impact-produced high-pressure phases are unstable at the Earth's surface. Thus, unless the transformation was greater than 50 %, the precursor phase, containing the microlites of the high-pressure phase, generally would be quickly altered, leaving scattered microlites of the high-pressure polymorph in clay or some other phase (Jones et al. 2003a). This would make detection of the high-pressure polymorphs of mafic minerals difficult.

Majorite, (Mg, Fe)SiO_3-perovskite, and akimotoite are high-pressure polymorphs of enstatite [(Mg, Fe)SiO_3] (Tables 2.1 and 2.2). Majorite has a garnet structure (Smith and Mason 1970). It was first reported by Mason et al. (1968) in the Coorara meteorite. It has since been found in numerous shock metamorphosed meteorites (Fig. 2.15a) and in ultra-high pressure terrestrial metamorphic rocks, but not in terrestrial impact craters or ejecta. Depending on the pressure–temperature conditions, majorite can form by crystallization from a melt at between $\sim$3 and 30 GPa and temperatures between $\sim$ 1,350 and 2,075 °C (Agee et al. 1995). Solid state transformation of pyroxene to majorite can take place between 20 and 24 GPa in temperatures in excess of 2,000 °C (Chen et al. 1996).

Akimotoite (Fig. 2.15a) is a high-pressure polymorph of enstatite with an ilmenite structure (Tables 2.1 and 2.2; Sharp et al. 1997; Tomioka and Fujino 1999). At static pressures, akimotoite occurs together with ringwoodite between 18 and 25 GPa in the $MgSiO_3$–Mg_2SiO_4 system (Gasparik 1992). Akimotoite has been found in or adjacent to shock-produced melt veins in numerous highly shocked meteorites including: the Tenham (Tomioka and Fujino 1999), Acfer 040 (Sharp et al. 1997), Umbarger (Xie and Sharpe 2004), Yamato 75267 (Kimura et al. 2003), Yamato 791384 (Ohtani et al. 2004), and Sixiangkou (Zhang et al. 2006a) chondrites and the Yamato 000047 shergottite (Imae and Ikeda 2010). Tomioka and Fujino (1999) proposed that the akimotoite that they found in the Tenham meteorite formed by solid state transformation and that the peak pressure and temperature generated by the shock event were in the range of 22–26 GPa and >2,000 °C. Akimotoite, along with ringwoodite, is found in veins in the Tenham

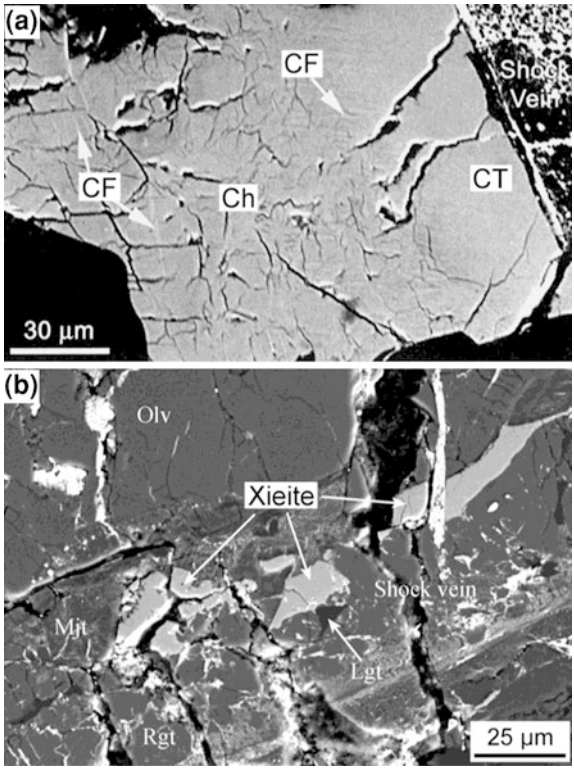

Fig. 2.17 Backscattered electron images of a shocked vein in the Suizhou meterorite (L6 chondrite) showing high-pressure $FeCr_2O_4$ polymorphs. **a** A shocked chromite grain (Ch) that has been partly converted to high-pressure (post-spinel) polymorphs, one with a $CaFe_2O_4$-type structure (CF) and one with a $CaTi_2O_4$-type structure (CT). Image is from Chen et al. (2003b), Fig. 3b. Copyright (2003) National Academy of Sciences. **b** A section showing several $FeCr_2O_4$ grains converted partly or completely to the high-pressure polymorph with a $CaFe_2O_4$-type structure, which has been given the mineral name xieite. This new mineral is found in association with olivine (Olv), majorite (Mjt), ringwoodite (Rgt), and lingunite (Lgt). Image is from Chen et al. (2008), Fig. 1a, with kind permission from Springer Science + Business Media

meteorite (Xie et al. 2006) and in the Acfer 040 meteorite (Sharp et al. 1997), where they are believed to have crystallized from a melt. Akimotoite is believed to have crystallized between 21 and 25 GPa in the Tenham meteorite (Xie et al. 2006). In the Sixiangkou meteorite crystallization in the veins is believed to have occurred at pressures of 20–24 GPa and a temperature >2,000 °C (Zhang et al. 2006a). According to Xie and Sharp (2004) crystallization in the Umbarger melt veins took place at ~18 GPa. These authors pointed out that this is much lower than the 45–90 GPa pressure that is suggested by the shock effects in the melt veins using criteria found, for example, in Stöffler et al. (1991). For further discussion of this problem, see Sect. 2.3.6.

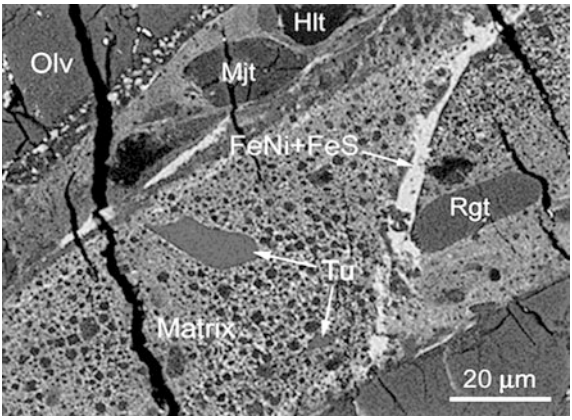

Fig. 2.18 Backscattered electron image of the Suizhou L6 chondrite showing two grains of tuite in a fine-grained matrix. The tuite (Tu) is associated with other high-pressure phases such as majorite (Mjt), ringwoodite (Rgt), and lingunite ($NaAlSi_3O_8$ with a hollandite structure, Hlt). Olv = olivine. Image from Xie et al. (2003), Fig. 2, with permission of the *European Journal of Mineralogy* (http://www.schweizerbart.de)

(Mg, Fe)SiO_3-perovskite (Fig. 2.15b) is a higher pressure polymorph of enstatite (Tables 2.1 and 2.2) which has been studied extensively because it has been inferred to be one of the most abundant minerals in the lower mantle (Chen et al. 2002). The (Mg, Fe)SiO_3-perovskite phase was discovered by Tomioka and Fujino (1997) in the Tenham chondrite meteorite. Sharp et al. (1997) also found evidence for this phase in the Acfer 040 meteorite. It is estimated that this phase crystallizes from a melt at between ~25–30 GPa, at a temperature of between ~1,900 and 2,100 °C (Agee et al. 1995). In high-pressure laboratory experiments it was found that $MgSiO_3$-perovskite is stable up to at least ~58 GPa, but above that pressure it begins to break down to MgO plus SiO_2 (stishovite) (Saxena et al. 1996). Some of the (Mg, Fe)SiO_3-perovskite phase in the Tenham meteorite is believed to have formed by solid state transformation of enstatite in the range between 22 and 26 GPa at a peak temperature higher than 2,000 °C (Tomioka and Fujino 1999).

Wadsleyite and ringwoodite are high-pressure polymorphs of olivine $(Mg,Fe)_2SiO_4$ (Table 2.1 and 2.2). Wadsleyite (Fig. 2.16) has a modified spinel structure (orthorhombic) and is also referred to as the β-Mg_2SiO_4 phase. Under static pressure at 1,000 °C, this phase forms at ~12 GPa (Ringwood and Major 1970). Ringwoodite (Figs. 2.15–2.18) has a spinel structure (isometric) and is referred to as γ-$(Mg, Fe)_2SiO_4$. Ringwoodite generally refers to the Mg-rich $(Mg, Fe)_2SiO_4$-spinel end member, but Xie et al. (2002) reported finding the Fe-rich end member in the Umbarger meteorite (L6 chondrite). In polarized transmitted light wadsleyite has a bluish-gray color, while ringwoodite has a distinctive purple or violet color (Walton and Herd 2007). Ringwoodite in shocked meteorites has been interpreted to form by both solid state transformation and crystallization from a melt (Ohtani et al. 2004; Miyahara et al. 2009, 2010). Under

static pressure at 1,000 °C, ringwoodite does not form below ~17 GPa (Suzuki et al. 2000). According to Xie et al. (2006) ringwoodite crystallized from a melt at a pressure of ~18 GPa in the Umbarger meteorite. Other investigators suggest that ringwoodite forms at shock pressures >25–30 GPa up to at least 60–75 GPa (Stöffler et al. 1991; Langenhorst and Deutsch 1998). For a given temperature, wadsleyite forms at a lower pressure than ringwoodite (Inoue et al. 2006). Laboratory experiments have shown that both wadsleyite and ringwoodite revert back to olivine at atmospheric pressure and a temperature of ~900 °C (Suzuki et al. 1980; Ming et al. 1991).

At high pressures, $KAlSi_3O_8$ and $NaAlSi_3O_8$ (alkali feldspars) are transformed to a denser phase with a hollandite structure (Tables 2.1 and 2.2). It is unclear whether there is a complete solid solution between $KAlSi_3O_8$ with a hollandite structure and $NaAlSi_3O_8$ with a hollandite structure. The Na-rich end member has been given the name, lingunite. Lingunite has since been found in some shocked meteorites (Fig. 2.15a, 2.17b, 2.18). Gillet et al. (2000) reported finding the $NaAlSi_3O_8$-hollandite high-pressure polymorph of plagioclase (lingunite) in the Sixiangkou meteorite (L6 chondrite). Tomioka et al. (2000) speculated that lingunite in the Tenham meteorite probably formed at about ~22–23 GPa at a temperature >1,200 °C or metastably at relatively low temperature where decomposition into stable phases was hindered due to sluggish kinetics. Langenhorst and Poirier (2000) reported finding the $KAlSi_3O_8$-hollandite high-pressure polymorph in the Zagami meteorite (basaltic shergottite). The high-pressure $KAlSi_3O_8$-hollandite phase forms at a pressure of 9–10 GPa (Yagi et al. 1994). Feldspar with a hollandite-type structure can form by solid state transformation of feldspar or from crystallization at high pressure of molten feldspar (Gillet et al. 2000).

A high-pressure phase of feldspar ($Ab_{41}An_{58}Or_1$) with a hollandite structure has been reported in strongly shocked anorthosite from the Manicouagan impact structure, Quebec, Canada (Langenhorst and Dressler 2003). The feldspar is mostly converted to diaplectic glass. There are some thin (<100 μm) grayish to brownish shock veins that pervade the rock in an irregular fashion. The veins contain some birefringent phases that could not be identified by optical microscopy but were identified as the high-pressure phase of feldspar with a hollandite structure using transmission electron microscopy. This is the first time that this phase has been reported in terrestrial impactites.

Two post-spinel polymorphs of chromite ($FeCr_2O_4$) have been found in the Suizhou meteorite (an L6 chondrite) (Fig. 2.17; Tables 2.1 and 2.2). One has a $CaTi_2O_4$-type structure and the other has a $CaFe_2O_4$-type structure (Chen et al. 2003a, b). The high-pressure chromite polymorph with an orthorhombic $CaTi_2O_4$-type structure has been named xieite. Xieite occurs as polycrystalline aggregates in association with coarser aggregates of ringwoodite, majorite, and lingunite in the Suizhou meteorite (Fig. 2.17b).

Both high-pressure $FeCr_2O_4$ phases were formed by solid-state transformation (Chen et al. 2003b). Xieite was formed at shock pressures of 18–23 GPa at temperatures between 1,800 and 1,950 °C (Chen et al. 2008).

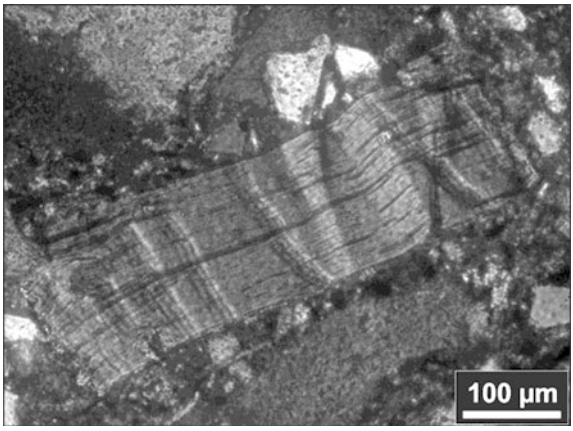

Fig. 2.19 Optical microscope image of kink bands in a biotite clast in a polymict breccia sample from the Rochechouart impact structure (France). The photograph is courtesy of L. Ferrière

Tuite, a high-pressure polymorph of whitlockite (sometimes called merrillite) with a trigonal γ-$Ca_3(PO_4)_2$ structure (Tables 2.1 and 2.2), has been found in the Suizhou meteorite (Fig. 2.18) (Xie et al. 2002, 2003). This phase was transformed from whitlockite by a shock-produced solid-state reaction at a pressure of $\sim$23 GPa and a temperature of $\sim$2,000 °C (Xie et al. 2002, 2003). Whitlockite has not been found on Earth; however, tuite can also form by decomposition of hydroxylapatite or fluorapatite at pressures above 12 GPa (Murayama et al. 1986), and these phases are fairly common on Earth.

2.3.4 Microscopic Shock-Deformation Features

As previously noted, during an impact event the shock wave travels through the target rock at supersonic velocities followed immediately by a rarefaction wave which decompresses the rock. This results in a tremendously high strain rate ($>10^7$ times higher than normal metamorphic processes), which can produce a variety of macroscopic and microscopic features in the target rock, some of which are unique to shock metamorphism. Microscopic shock-deformation features include: dislocations, kink bands, planar microstructures (including planar deformation features), mosaicism and X-ray asterism, and diaplectic glasses (Langenhorst and Deutsch 1998; French 1998).

2.3.4.1 Dislocations and Kink Bands

Dislocations are linear lattice defects. Formation and migration of dislocations are mechanisms of deforming crystals under high stress. Transmission electron microscope studies indicate that shock deformation can produce large numbers of dislocations per unit area in certain minerals like olivine and pyroxene

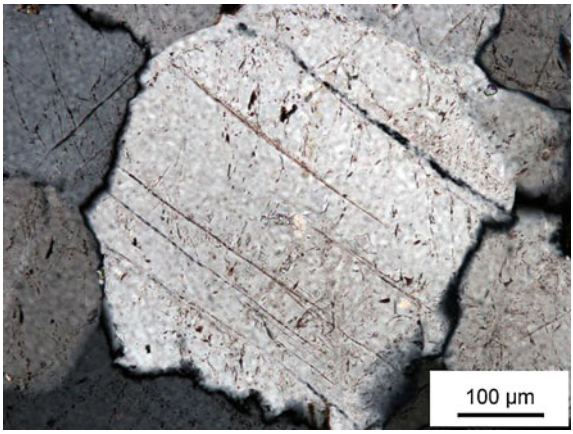

Fig. 2.20 Optical microscope image in transmitted light of a shocked quartz grain with one set of planar fractures (PFs) from the Aorounga impact structure, in Chad, Africa. Note that the spacing between the PFs is from ~40 to 200 µm and that the fractures are slightly curved and not exactly parallel. Courtesy of L. Ferrière

(Langenhorst and Deutsch 1998). Like planar deformation features discussed below, the dislocations are related to certain orientations within the crystal. In olivine, for example, the dislocations are almost always of pure screw character and have the Burgers vector [001] (Langenhorst and Deutsch 1998).

Kink bands (Fig. 2.19) are a type of microscopic deformation in which the orientation of the crystal lattice is changed or deflected by gliding or slippage and shortening along slippage planes. They are observed most commonly in phyllosilicate minerals (e.g., micas, chlorite), but are sometimes seen in olivine and pyroxene. Kink bands can form in biotite in non-porous rocks at shock pressures >0.5–1 GPa (Stöffler et al. 2006). Although kink bands are common in shock metamorphosed minerals with sheet structures, they can also be found in tectonically-deformed minerals. According to French and Koeberl (2010), kink bands in mica are not diagnostic of shock metamorphism since they can be formed by other geological processes. However, according to Langenhorst and Deutsch (1998), kink bands in shocked biotite exhibit strong asymmetry compared to kink bands in tectonically deformed biotite. They further state that the degree of asymmetry, frequency, and width of kink bands are correlated with shock pressure (Langenhorst and Deutsch 1998). In the Ries crater, the orientation of kink bands has been used to reconstruct the original position of ejected and overturned basement megablocks (Graup 1978).

2.3.4.2 Planar Microstructures

Numerous terms have been used to refer to optically recognizable planar microstructures produced by shock compression. Such features have been referred to as cleavage, deformation lamellae, planar elements, shock lamellae, planar cleavage fractures, planar features, and planar deformation structures (Stöffler and Langenhorst 1994, and references therein). In 1990, a group of experts in shock metamorphism proposed the phrase "planar deformation features" to describe

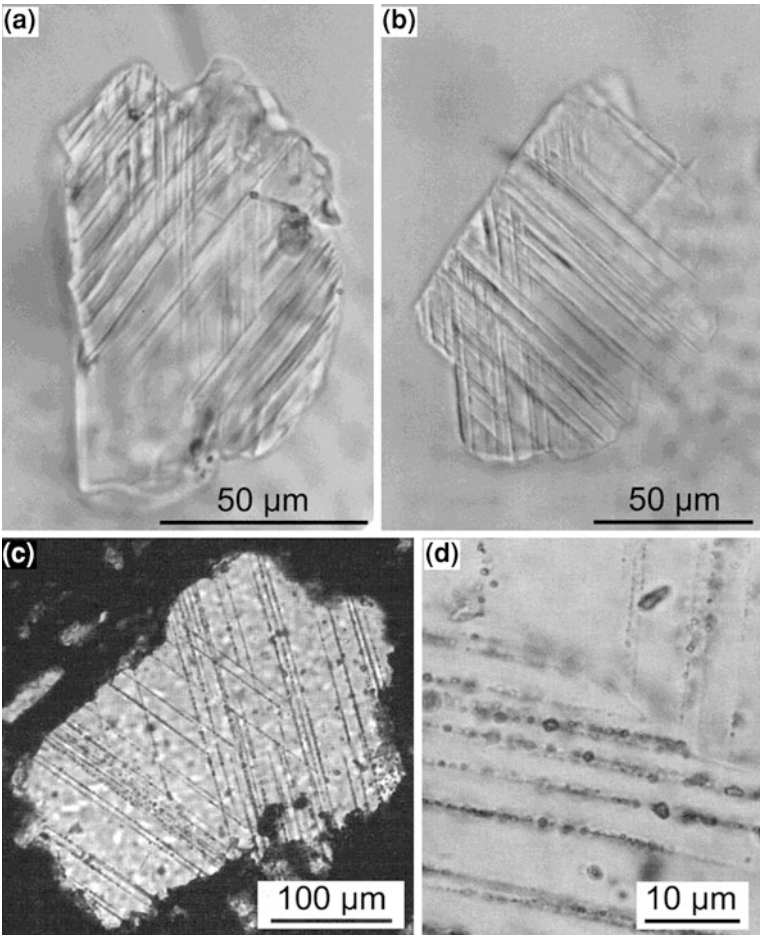

Fig. 2.21 Optical microscope images (plane polarized light) of shocked quartz grains exhibiting planar deformation features (PDFs). **a** Quartz grain with two well-defined sets of PDFs from Core LB-05A taken in Bosumtwi impact crater. **b** Quartz grain with two well-defined sets of PDFs from Core LB-05B taken in Bosumtwi impact crater. **c** Quartz grain with two sets of decorated PDFs in a breccia from Gardons impact structure, Norway. Image from French (1998), Fig. 4.20, with permission of the Lunar and Planetary Institute. **d** Detailed view of shocked quartz with decorated PDFs. The sample is from the Charlevoix impact structure, Quebec, Canada. Image from Robertson (1975), Fig. 3b

"optically recognizable, planar microstructures diagnostically produced by impact compression" (Grieve et al. 1990). Stöffler and Langenhorst (1994) proposed a broad term "planar microstructures" to include both planar fractures and planar deformation features. Both types of planar microstructures are parallel to rational crystallographic planes defined by Miller indices. Planar features in quartz, especially planar deformation features, have been one of the most widely used

Table 2.3 Typical crystallographic orientations of planar microstructures in shocked quartz (modified after Stöffler and Langenhorst, 1994)

Crystallographic form	Symbol	Miller indices	Polar angle
Basal pinacoid	**c**	**(0001)**	**0.00°**
Rhombohedron[a]		{10$\bar{1}$4}, {01$\bar{1}$4}	17.62°
Rhombohedron	**ω, ω'**	**{10$\bar{1}$3}, {01$\bar{1}$3}**	**22.95°**
Rhombohedron	**π, π'**	**{10$\bar{1}$2}, {01$\bar{1}$2}**	**32.42°**
Rhombohedron	**r, z**	**{10$\bar{1}$1}, {01$\bar{1}$1}**	**51.79°**
Hexagonal prism	m	{10$\bar{1}$0}	90.00°
Trigonal dipyramid	ξ	{11$\bar{2}$2}, {2$\bar{1}\bar{1}$2}	47.73°
Trigonal dipyramid	s	{11$\bar{2}$1}, {2$\bar{1}\bar{1}$1}	65.56°
Trigonal prism	a	{11$\bar{2}$0}, {2$\bar{1}\bar{1}$0}	90.00°
Trigonal dipyramid		**{22$\bar{4}$1}, {4$\bar{2}\bar{2}$1}**	**77.20°**
Rhombohedron	t	{40$\bar{4}$1}, {04$\bar{4}$1}	78.87°
Ditrigonal prism	k	{51$\bar{6}$0}, {6$\bar{1}$50}	90.00°
Trigonal trapezohedron	x	{51$\bar{6}$1}, {6$\bar{5}\bar{1}$1}	82.07°
		{6$\bar{1}$51}, {15 1}	
Trigonal trapezohedron		{31$\bar{4}$1}, {4$\bar{3}\bar{1}$1}	77.91°
		{4$\bar{1}$31}, {13$\bar{4}$1}	
Trigonal trapezohedron		{21$\bar{3}$1}, {3$\bar{2}\bar{1}$1}	73.71°
		{3$\bar{1}\bar{2}$1}, {12$\bar{3}$1}	

The most common orientations of planar microstructures are in bold
[a] From Ferrière et al. (2009a)

criteria for recognizing shock metamorphosed rocks, whether they be in impact structures or in distal impact ejecta. Planar microstructures have been observed in most rock-forming minerals (e.g., quartz, feldspar, olivine), as well as some accessory minerals such as zircon; however, most studies have concentrated on quartz. Quartz is an ideal mineral for this purpose, since it is abundant and stable. It is optically simple and it can record a variety of planar deformation features which can be correlated with shock pressure (Stöffler and Langenhorst 1994; French 1998).

2.3.4.2.1 Planar Fractures

Planar fractures (PFs) (Fig. 2.20) are sets (groups) of open fissures parallel to rational crystallographic planes. They can form in nearly all rock-forming silicates such as quartz, feldspar, amphibole, pyroxene, olivine, and garnet (Langenhorst and Deutsch 1998). In quartz, the most common orientations are parallel to crystallographic planes with low Miller indices such as (0001) or c (basal) and {10 1} or r (rhombohedral) (Stöffler and Langenhorst 1994). PFs can be regarded as high-pressure cleavage planes. The typical spacing between fractures is >20 μm. PFs develop at relatively low shock pressures, generally around 5–10 GPa (French

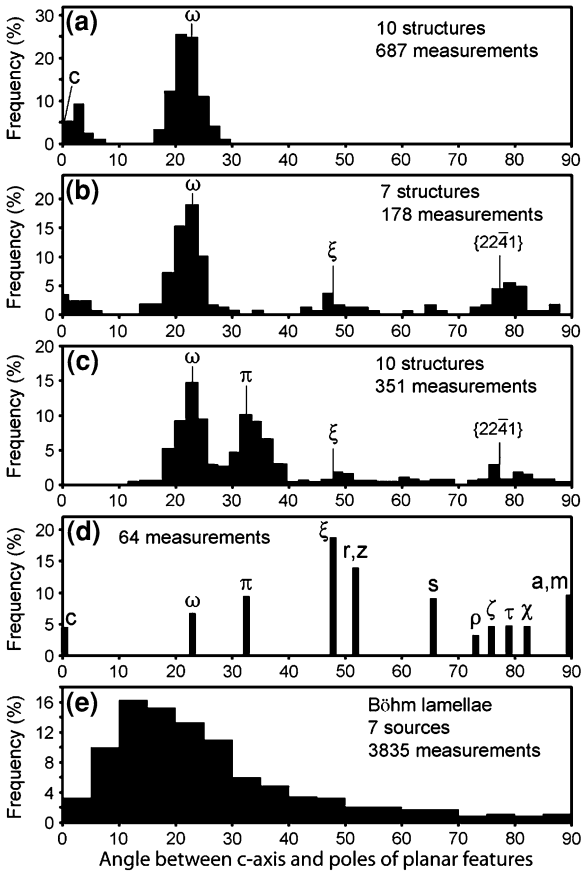

Fig. 2.22 Quartz PDF orientations for different degrees of shock metamorphism and types of target rocks. **a–c** Samples from craters in crystalline rocks. With increasing shock pressures, the number of different orientations increases. **a** The presence of just basal orientations (**c**) indicates shock pressures >7.5 GPa, but <10 GPa. The presence of both basal and ω $\{10\bar{1}3\}$ orientations indicates shock pressures >10 GPa. **b** The presence of $\{22\bar{4}1\}$ orientation along with other orientations indicates a minimum shock pressure of >14 GPa. **c** The presence of π $\{10\bar{1}2\}$ indicates shock pressures >16 GPa. **d** PDF orientations for quartz in sedimentary rock from the Tookoonooka impact structure in Australia. PDFs in quartz from sedimentary rocks have orientations dominated by high angles to the c-axis. **e** Planar features produced by normal regional metamorphism (Böhm lamellae) exhibit a broad range of orientations without any sharp peaks that center at specific crystallographic planes. PDF orientation data for **a–c** came from Robertson et al. (1968) and estimated minimum shock pressures are from Grieve and Robertson (1976); data for **d** came from Grieve and Therriault (1995); and data for **e** came from Carter and Friedman (1965)

1998; Koeberl 2007). Unfortunately, although rare, similar fractures can occur in tectonically deformed rocks. However, the presence of widespread and closely spaced PFs is strongly suggestive of shock metamorphism; and PFs can be used as

Table 2.4 Orientation of planar microstructures in shocked quartz in crystalline rock with increasing stage of shock metamorphism (after Stöffler and Langenhorst 1994)

Shock stage	Most common orientation	Additional orientations of PFs and PDFs	Optical properties of quartz
(1) Very weakly shocked	PFs: (0001)	PFs: rarely $\{10\bar{1}1\}$ PDFs: none	Normal
(2) Weakly shocked	PDFs: $\{10\bar{1}3\}$	PFs: $\{10\bar{1}1\}$, (0001) PDFs: rare	Normal
(3) Moderately shocked	PDFs: $\{10\bar{1}3\}$	PFs: $\{10\bar{1}1\}$, (0001) rare PDFs: $\{11\bar{2}1\}$, $\{11\bar{2}2\}$, (0001), $\{10\bar{1}0\}$ + $\{11\bar{2}1\}$, $\{10\bar{1}1\}$, $\{21\bar{3}1\}$, $\{51\bar{6}1\}$	Normal or slightly reduced refractive indices
(4) Strongly shocked	PDFs: $\{10\bar{1}2\}$, $\{10\bar{1}3\}$	PFs: rare or absent PDFs: $\{11\bar{2}1\}$, $\{11\bar{2}2\}$, (0001), $\{10\bar{1}0\}$ + $\{11\bar{2}1\}$, $\{10\bar{1}1\}$, $\{21\bar{3}1\}$, $\{51\bar{6}1\}$	Reduced refractive indices: 1.546–1.48
(5) Very strongly shocked	PDFs: $\{10\bar{1}2\}$, $\{10\bar{1}3\}$	None	Reduced refractive indices: <1.48

PFs planar fractures; *PDFs* planar deformation features
(0001) PDFs (Brazil twins) and at least four additional rare orientations may occur in stages (3) and (4)

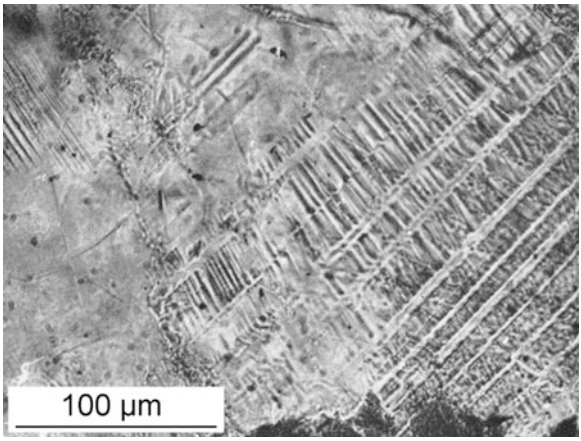

Fig. 2.23 Feldspar with multiple sets of PDFs and polysynthetic albite twin lamellae forming distinctive ladder texture (plane polarized light). The original polysynthetic twin lamellae (trending NW/SE) are still preserved in most of the grain shown here, but alternate twin lamellae have either been converted to diaplectic glass (maskelynite) or are crosscut by short, closely spaced PDFs to form a ladder appearance. This grain is from a moderately shocked amphibolite fragment in a suevite sample from the Ries crater, Germany. From Stöffler (1966), Fig. 4, with kind permission from Springer Science + Business Media

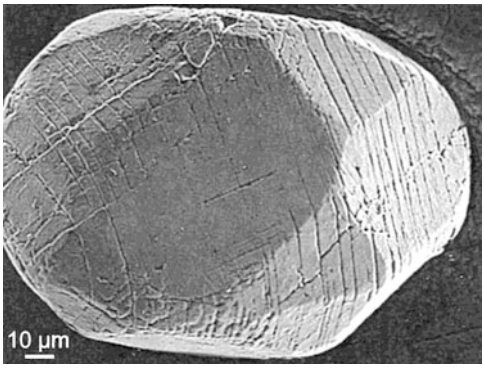

Fig. 2.24 SEM image of a shocked zircon exhibiting three sets of planar microstructures. The zircon is from a charnockite rock sample from the Vredefort impact structure, South Africa. From Kamo et al. (1996), Fig. 4h with permission from Elsevier

evidence of shock metamorphism if they are present in minerals without normal cleavage, or if they occur in planes which are not parallel to the normal cleavage directions of the host crystal (Langenhorst and Deutsch 1998).

2.3.4.2.2 Planar Deformation Features

Planar deformation features (PDFs) are regular planar microstructures (Fig. 2.21) that are oriented parallel to rational crystallographic planes of low Miller indices (Table 2.3; Fig. 2.22; Stöffler and Langenhorst 1994; Grieve et al.

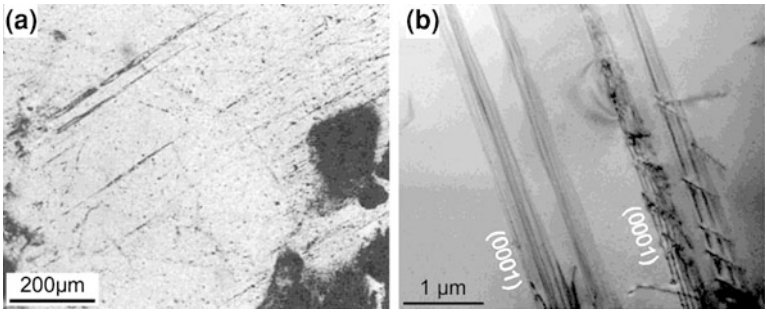

Fig. 2.25 Examples of shock-produced basal Brazil twins in shock metamorphosed quartz grains. **a** Basal Brazil twins (NE/SW trending) in charnockitic gneiss from Vredefort impact structure, South Africa (crossed polarizers). From Kamo et al. (1996), Fig. 2d, with permission from Elsevier. **b** Bright field transmission electron microscope image of Brazil twin boundaries, (0001) orientation, in quartz in charnockitic rock from the Charlevoix impact structure in Quebec, Canada. Courtesy of C. Trepmann

1996; Mossman et al. 1998). They often occur in multiple cross-cutting orientations or sets. Orientations of PDFs in quartz can be determined using a universal stage or spindle stage to determine the angle between the quartz c-axis and the poles (normal) to the PDF planes and then plotting the results as in Fig. 2.22 (for details see Montanari and Koeberl 2000; Ferrière et al. 2009a). Within each set, the PDFs occur as parallel, planar optical discontinuities that are narrower and more closely spaced than PFs. They are amorphous (glass) lamellae with the same composition as the host crystal. PDFs occur as <1–3 μm thick lamellae with a spacing of ~0.5–10 μm (Fig. 2.21; Goltrant et al. 1992; Stöffler and Langenhorst 1994). Because fresh PDFs in quartz consist of amorphous silica, they can be preferentially etched using, for example, HF, to accentuate the PDFs and make them visible in scanning electron microscope images (e.g., Gratz et al. 1996).

The most common orientations in quartz are: c(0001), $\omega\{10\bar{1}3\}$, $\pi\{10\bar{1}2\}$, r{10$\bar{1}$1}, and $\{22\bar{4}1\}$. Up to 18 sets of PDFs have been observed in a single quartz crystal, but 3–10 sets are commonly observed in shocked crystalline rock (Stöffler and Langenhorst 1994). The number of sets increases with increasing shock pressure and the orientations change with shock intensity. The $\omega\{10\bar{1}3\}$ orientation can form at shock pressures >10 GPa (Stöffler et al. 2006). At shock pressures >15–20 GPa, PDFs occur in more than one set of specific crystallographic orientations per grain (Stöffler et al. 2006; Koeberl 2007). Certain PDF orientations are present at different shock levels (Table 2.4); however, the orientation of the shock wave to the crystal orientation can also be a factor in determining the orientations of the PDFs (Langenhorst and Deutsch 1994).

Fresh (usually younger) unaltered PDFs occur in multiple sets of continuous planes that extend across most of the grain (Fig. 2.21a, b). However, in altered or metamorphosed grains the original amorphous silica in the PDF planes can be recrystallized back to quartz. In the process small (usually 1–2 μm) fluid

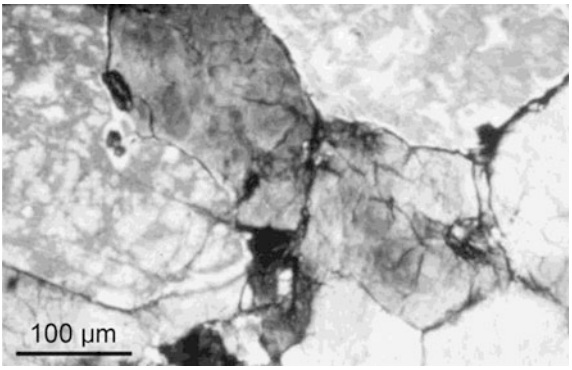

Fig. 2.26 Mosaicism in a shocked dunite. This is a specimen of Åheim dunite experimentally shocked to 29.3 GPa (Reimold and Stöffler 1978). The mosaicism is indicated by the blotchy (darker and lighter patches) within individual olivine crystals. Optical microscope image under crossed polarizers. Image courtesy of Uwe Reimold

inclusions or decorations develop along the original planes (Grieve and Therriault 1995). The resulting **decorated PDFs** preserve the orientation of the original PDFs (Fig. 2.21c, d). PDFs can still be recognized in 2 Ga old rocks that have experienced greenschist facies metamorphism (French 1998). At the Vredefort impact structure, remnants of PDFs can still be recognized in Archean granitoid gneisses which have survived amphibolite to granulite facies metamorphism (Gibson and Reimold 2000).

Porous sedimentary rocks respond differently to shock waves than do nonporous crystalline rocks (Kieffer 1971; French 1998). PDFs in shocked quartz in sedimentary rocks, where the individual quartz grains are more isolated and contrast with the matrix in terms of shock impedance (the product of the density of the shocked material at 1 bar times the shock wave velocity of the material), have orientations at higher angles to the c-axis than they do in quartz grains in crystalline rocks; and in some cases the ω orientations are missing or almost so (Fig. 2.22d; Grieve and Therriault 1995). In shocked Coconino Sandstone at Barringer (Meteor) Crater (Arizona, USA), PDFs are relatively rare and coesite is relatively abundant (Kieffer 1971; Robertson 1980). This may be due to more shock-wave energy being concentrated at grain interfaces and pore spaces in sedimentary rocks. These effects may be even more extreme in sediments.

Shock experiments on preheated target rocks have shown that the temperature of the target rock can have an effect on the nature of the shock metamorphic features and on the shock pressure required to form shock metamorphic features (see, e.g., Langenhorst and Deutsch 1994; Huffman and Reimold 1996; and references therein). For example, Huffman and Reimold (1996) found, in laboratory experiments, that the shock pressure required to produce multiple sets of PDFs in quartz is greater for specimens preheated to 440 °C than for specimens initially at 25 °C. In addition, the character of the PDFs changes, with the PDFs going from

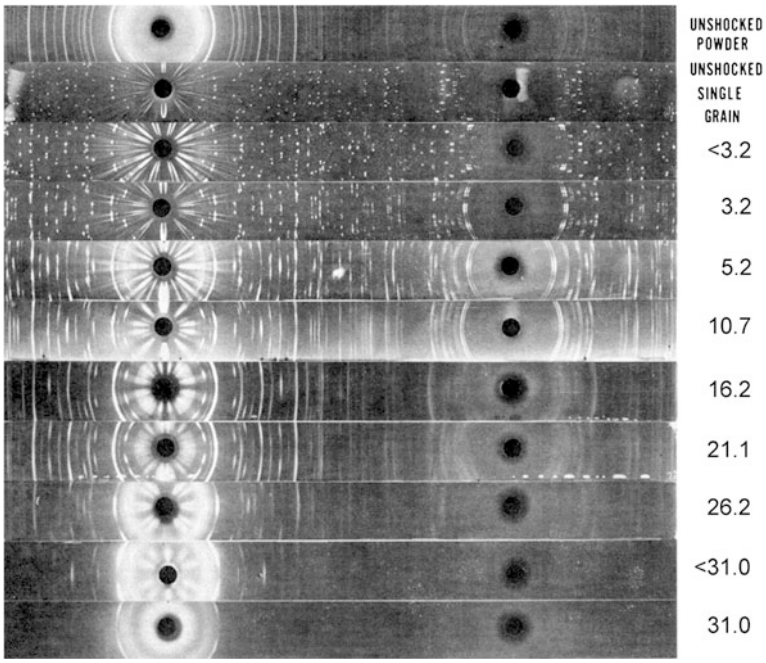

Fig. 2.27 Debye-Scherrer X-ray diffraction (XRD) patterns of unshocked quartz and quartz shocked at different pressures. Shock pressures (GPa) are indicated to the right of the XRD patterns. They are estimated to be accurate to within ±5 %. Unshocked powdered quartz produces solid lines and an unshocked single crystal of quartz produces spots. Single crystals of quartz shocked at various pressures produce patterns where the dots are smeared out to form streaks. In this experiment, the propagation of the shock wave was perpendicular to (0001). Note that the degree of streakiness, and broadening and fading of the streaks increases with increasing shock pressure. Above about 11 GPa, most of the streaks are solid lines and the pattern looks more like a powder pattern than a pattern for a single crystal. Above about 30 GPa the lines have mostly disappeared and the pattern looks like that of an amorphous phase. From Hörz and Quaide (1972), Fig. 8, with permission from Springer

narrow with sharp boundaries when the specimens are initially at 25 °C to wide with wavy boundaries when the specimens are initially at 440 °C. These temperature effects could be important in large impacts where shock metamorphism can occur at great depths involving rocks already at high temperature depending on the thermal gradient.

Feldspars can also exhibit planar microstructures, including PDFs. Short and closely spaced PDFs can be combined with longer and more widely spaced features, such as deformation bands and albite twins, to produce distinctive **ladder texture**s (Fig. 2.23) (French 1998). Planar microstructures, including PDFs, have been observed in several accessory minerals such as apatite, sillimanite, cordierite, garnet, scapolite, and zircon and in mafic minerals such as olivine, pyroxene, and amphibole (Stöffler 1972; Bohor et al. 1993; Langenhorst and Deutsch 1998; French and Koeberl 2010). Not much is known about PDFs in most of these

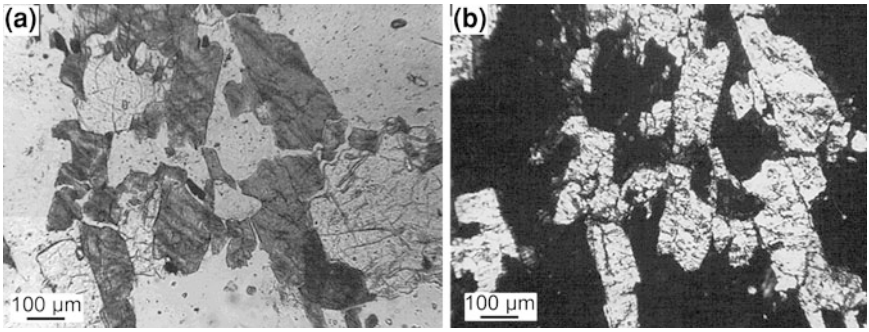

Fig. 2.28 Diaplectic quartz glass and diaplectic feldspar glass (maskelynite) in a shocked biotite gneiss in suevite from the Ries impact crater, Germany. **a** Diaplectic feldspar glass (*light gray*, low relief; e.g., *upper right*) and diaplectic quartz glass (*light gray*, higher relief, and fractured; e.g., *middle* to *lower right*). The biotite is *dark gray*. Plane polarized light. **b** Same as in **a**, but with cross polarized light. Note that quartz and feldspar are dark, indicating that they are amorphous, but the biotite is light in color due to birefringence, which indicates that it is still crystalline. From Stöffler and Langenhorst (1994), Fig. 22, with permission of *Meteoritics & Planetary Science*, ©1994 by the Meteoritical Society

minerals. However, minerals with low density (i.e., <3 g/cm^3) such as quartz and feldspar tend to develop more and thicker PDFs than do mafic minerals such as pyroxene and olivine (Langenhorst and Deutsch 1998).

Shocked zircons with well-defined planar microstructures have been described from the Cretaceous-Tertiary impact ejecta layer (Bohor et al. 1993; Krogh et al. 1993a, b; Kamo et al. 1996). Some authors have referred to these features as PDFs (Bohor et al. 1993; Krogh et al. 1993a, b). Kamo et al. (1996) describe similar planar features in zircons from the Vredefort impact structure "…as single or multiple sets of parallel, narrowly spaced ($\leq$5 µm), planar features that are continuous across the grain" (Fig. 2.24). In the above papers, the planar features were observed on the surfaces of etched zircons using scanning electron microscopy (SEM). Wittmann et al. (2006) describe conspicuous "trails of bubbles" in zircons from cores drilled into the Chicxulub impact structure as probably "decorated" PDFs which they propose were formed due to thermally induced crystallization of $ZrSiO_4$ glass in these features.

Leroux et al. (1999) studied experimentally shocked zircons using transmission electron microscopy (TEM). PDFs were observed by TEM in zircons shocked at 60 GPa. They consist of thin, 10–20 nm wide, planar defects filled with amorphous $ZrSiO_4$. The PDFs are very straight and oriented parallel to the {320} planes. According to Leroux et al. (1999) the PDFs form before the formation of the high-pressure phase reidite. Leroux et al. (1999) interpreted the optically resolved planar deformations as manifestations of shock-induced cleavage (planar fractures) rather than PDFs. However, Timms et al. (2012) mapped some planar features in lunar zircons, using electron backscatter diffraction, which are $<$5 µm wide with spacings typically between 0.1 and 25 µm. The planar features occur

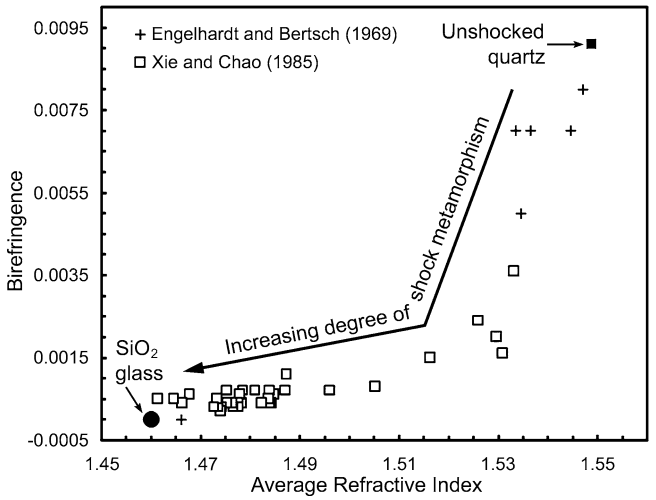

Fig. 2.29 Birefringence versus average refractive index for shocked quartz from the Ries impact crater, Germany. Birefringence and refractive index decrease with increasing shock metamorphism, from that of unshocked quartz to that of silica glass (lechatelierite). Data from Xie and Chao (1985), open squares, and Engelhardt and Bertsch (1969), plus symbols

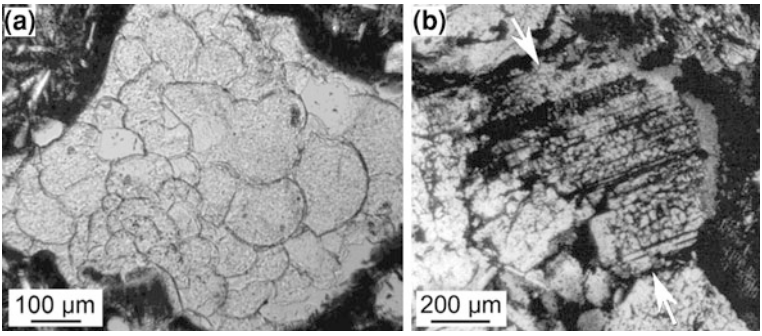

Fig. 2.30 Textures produced by post-impact thermal annealing. **a** Quartz with ballen texture in a fine-grained impact melt rock from the New Quebec impact structure, northern Ontario, Canada. Courtesy of R.A.F. Grieve. **b** Checkerboard feldspar (between arrows) in an inclusion in the Vredefort Granophyre from the Vredefort impact structure, South Africa. Crossed polarizers. From Buchanan and Reimold (2002), Fig. 9, with permission from the Meteoritical Society ©2002

along {001}, {110}, and {112} and were interpreted as PDFs. Wittmann et al. (2006) state that planar microstructures (PDFs) in zircon develop along with the transition to reidite. Development of planar microstructures begins at between 20 and 52 GPa with the most pronounced development of planar structures in the 60–80 GPa range.

2.3.4.2.3 Mechanical Twins

Another type of planar microstructure is **mechanical twins**. Shock-induced twinning can occur in minerals with low symmetry. Shock-induced twins are visible using an optical microscope and appear as narrow (<10 μm) polysynthetic bands and could be mistaken for exsolution lamellae (Langenhorst and Deutsch 1998). Shock-induced mechanical twins have been observed in quartz, amphibole, clinopyroxene, ilmenite, sphene, and probably calcite.

Shock-induced mechanical twins have been observed in quartz, using transmission electron microscopy, where they occur as **Brazil twins** (Fig. 2.25) oriented parallel to the basal or c (0001) orientation (Leroux et al. 1994; Joreau et al. 1996). Brazil twins can form in unshocked quartz, but they have not been observed parallel to the basal c direction (French 1998). Brazil twins have been produced experimentally at ~8 GPa and under high strain rates. According to Stöffler and Langenhorst (1994), Brazil twins parallel to c (0001) can be regarded as a unique shock metamorphic indicator; however, French and Koeberl (2010) state that such features "may suggest a shock history and should spur further study". Brazil twins were previously called PDFs because they could not be distinguished from PDFs using optical microscopy.

2.3.4.3 Mosaicism, X-Ray Asterism, and Diaplectic Glasses

The passage of a shock wave through a mineral grain can cause deformation of the crystalline structure which, in addition to the planar microstructures discussed above, can cause X-ray asterism, and produce mosaicism and diaplectic glass. These changes are the result of high-strain rate. **Mosaicism** refers to the internal fragmentation of a single crystal into a mosaic of slightly disoriented crystal domains resulting in a highly irregular patchy or mottled optical extinction pattern (Fig. 2.26), which is different from undulatory extinction common in tectonically deformed mineral grains. It is due to the very small size (usually in the submicroscopic range) of homogeneously extinguishing domains (Stöffler and Langenhorst 1994).

The degree of mosaicism can be determined using a petrographic microscope or by X-ray diffraction. Mosaicism can be measured using a petrographic microscope to determine the scatter in the orientation of the optical axes in different regions of a crystal exhibiting mosaicism. Using a Debye–Scherrer camera, a single unshocked crystal produces an X-ray diffraction (XRD) pattern consisting of discrete spots indicating a uniform crystalline structure. With increasing shock pressure the spots spread out to form arcs, and with still higher shock pressures the arcs become solid lines like those produced by a powder (Fig. 2.27; Hörz and Quaide 1972). The elongation of spots in the XRD pattern of a single crystal is called **X-ray asterism**. For quartz, X-ray asterism begins at shock pressures of about 3 GPa and increases up to about 30 GPa. The degree of asterism is a measure of the degree of mosaicism. Mosaicism can be produced by a variety of endogenic processes such

Fig. 2.31 Shatter cone segment in limestone from the Haughton impact structure on Devon Island in the Canadian Arctic. From Grieve (2006), Fig. 10.4, with permission of the Geological Society of Canada

as crystallization, growth, deformation, recrystallization, and replacement. Thus, it cannot be considered as a unique indicator of shock metamorphism at the present time (French and Koeberl 2010).

Beyond 30 GPa, in laboratory shock experiments, quartz lines are no longer present on the XRD patterns. This indicates complete destruction of the crystalline structure and formation of what is called diaplectic or **thetomorphic glass** (Fig. 2.28). **Diaplectic glass** is a dense glass that has the shape and composition of the original mineral grain but, unlike most glasses formed by melting, does not contain vesicles or flow structures (Stöffler and Langenhorst 1994; French 1998). Diaplectic glass with plagioclase composition was first recognized in meteorites by Tschermak (1872) and was given the name **maskelynite**. Most authors state that diaplectic glasses are formed by solid-state deformation; however, Langenhorst (1994) proposed that diaplectic glasses were formed by quenching of high-pressure melts. Regardless of the exact mechanism of formation, diaplectic glasses are good indicators of shock metamorphism. Diaplectic quartz glass forms at shock levels between 34 and 50 GPa in non-porous crystalline rocks, whereas maskelynite forms at shock pressures between 28 and 45 GPa (Stöffler et al. 2006).

Diaplectic glasses formed from minerals other than quartz or feldspar are rare but have been observed, e.g., cordierite (Stähle 1973). Diaplectic glasses can be distinguished from unshocked minerals and normal glasses formed by melting

Table 2.5 Shock stage and estimated pressure and post-shock temperature in quartzo-feldspathic rocks based on observed shock metamorphic effects (modified after Stöffler and Grieve 2007)

Shock metamorphic effects	Shock stage	Peak pressure [GPa]	Post-shock temperature [°C]
Fractured minerals	0		
		~5–10	~100
Quartz with planar fractures (PFs) and planar deformation features (PDFs); feldspar with PDFs	Ia		
		~20	~170
Quartz and feldspar with PDFs and reduced refractive index; stishovite and minor coesite	Ib		
		~35	~300
Zircon with PDFs (at least at TEM scale); diaplectic quartz and feldspar glass; coesite and traces of stishovite; reidite; cordierite glass	II		
		~45	~900
Zircon with PDFs (at least at TEM scale); normal feldspar glass (vesiculated) and diaplectic quartz glass; coesite; reidite; cordierite glass	III		
		~60	~1,500
Reidite; rock glasses or crystallized melt rocks (quenched from whole rock melts)	IV		
		~80–100	>2,500
Rock glasses (whole rock melts condensed from silicate vapor); zircon decomposed to baddeleyite and SiO_2	V		

based on refractive index measurements, X-ray diffraction, or Raman spectroscopy (see French and Koeberl 2010, and references therein).

With increasing shock pressure the birefringence and mean refractive index of mineral grains decrease (Stöffler and Langenhorst 1994). For quartz, the mean refractive index decreases from about 1.55 for unshocked quartz to about 1.46 for diaplectic quartz glass (Fig. 2.29). The refractive index of diaplectic glass is close to, but slightly higher than, that of silica glass or lechatelierite (~1.46). Physical properties of shocked quartz are affected by the number of PDFs present; the more of these amorphous lamellae that are present, the lower the refractive index and density of the quartz grain (Langenhorst and Deutsch 1998).

2.3.4.4 Post-Shock Thermal Effects

In addition to shock effects produced during compression and decompression, post-shock thermal effects can result from the residual high temperatures after an impact. In a broad sense, these effects can also be regarded as shock metamorphic indicators. Examples of post-shock effects include **ballen texture** in quartz and **checkerboard texture** in feldspar. Ballen and checkerboard textures are due to

Table 2.6 Shock stage and estimated pressure and post-shock temperature in shocked sandstone based on shock metamorphic effects (modified after Stöffler and Grieve 2007)

Shock metamorphic effects	Shock stage	Equilibrium shock pressure [GPa][a]	Post-shock temperature [°C]
Undeformed sandstone	0	0.2–0.9	~25
Compacted sandstone with remnant porosity	1a	~3.0 (2.2–4.5)	~250
Compacted sandstone compressed to zero porosity	1b	~5.5 (3.6–13)	~350
Dense (non-porous) sandstone with 2–5 vol % coesite, 3–10 vol % glass, and 80–95 vol % quartz	2	~13	~950
Dense (non-porous) sandstone with 18–32 vol % coesite, trace of stishovite, 0–20 vol % glass, and 45–80 vol % quartz	3	~30	>1,000
Dense (non-porous) sandstone with 10–30 vol % coesite, 20–75 vol % glass, and 15–45 vol % quartz	4		
Vesicular rock with 0–5 vol % coesite, 80–100 vol % glass (lechatelierite), and 0–15 vol % quartz	5		

[a] Ranges of pressure estimates given in parentheses

annealing effects. Ballen texture resembles a cauliflower-like fracture pattern (Fig. 2.30a). Ballen are somewhat spherical or elongate (ovoid) bodies that range in size from ~10–200 or more micromillimeters and which abut or penetrate each other (Ferrière et al. 2009b). They consist of α-cristobalite or α-quartz. Ferrière et al. (2009b) identified five different types of ballen based on mineralogy, texture, and optical properties. The different types of ballen are interpreted as having formed as the result of back-transformation of *β*-cristobalite and/or *β*-quartz to α-cristobalite and/or α-quartz over time (Ferrière et al. 2009b). Although some authors have suggested that ballen quartz can be used as an impact indicator, French and Koeberl (2010) stated that it is probably premature to call the presence of ballen quartz by itself a diagnostic indicator of shock metamorphism.

The checkerboard texture (also called sieved texture) in microcline and plagioclase feldspar is due to ~5–10 μm subgrains (with similar orientations) that are surrounded by an interstitial mesostasis with a different composition than the subgrains (Fig. 2.30b; Bischoff and Stöffler 1984; Langenhorst and Deutsch 1998). The uniform orientation of the subgrains is interpreted as a memory effect of the orientation of the precursor feldspar grain (Langenhorst and Deutsch 1998).

Table 2.7 Shock stage and estimated pressure and post-shock temperature in shocked mafic rock (basaltic-gabbroic) based on shock metamorphic effects (modified after Stöffler and Grieve 2007)

Shock effects and textural characteristics	Accompanying disequilibrium shock effects	Shock stage	Equilibration shock pressure [GPa]	Post-shock temperature [°C][a]
Unshocked (no unequivocal shock effects)	None	0		
			~1.5	~0
Fractured silicates; mechanical twinning in pyroxene and ilmenite; kink bands in mica; rock texture preserved	None	1		
			~20–22	~50–150
Plagioclase with planar deformation features and partially converted to diaplectic glass (maskelynite); high-pressure polymorphs of olivine and pyroxene	Incipient formation of localized mixed melt and glassy veins	2a		
			~28–34	~200–250
Maskelynite; mechanical twinning in pyroxene and ilmenite; mosaicism in olivine and other silicates	Localized mixed melt and melt veins (glassy or microcrystalline)	2b		
			~42–45	~900 (?)
Melted plagioclase with incipient flow structure and vesicles; mafics as in stage 2; high-pressure polymorph of rutile		3		
			~60	~1,100 (?)
Melted plagioclase with vesicles and flow structure; incipient contact melting of pyroxene; incipient recrystallization of olivine		4		
			~80	~1,500(?)
Melted plagioclase increasingly mixed with melt of mafics and ore minerals; olivine recrystallized; whole-rock melts at pressures of >100 GPa		5		

[a] Temperatures with a question mark are uncertain with errors of ~± 50 °C

Grainy, translucent, brownish quartz grains, called "toasted" quartz, have been found in shock metamorphosed rocks from several impact structures and in distal impact ejecta layers (Short and Gold 1996; Whitehead et al. 2002; Glass et al. 2004a). The translucent appearance and brownish color of the **toasted quartz** grains are probably caused by enhanced scattering of transmitted light due to the presence of numerous small (typically <1– ~ 5 μm) vesicles in the quartz grains (Whitehead et al. 2002; Ferrière et al. 2009c). Whitehead et al. (2002) concluded that the vesicles or fluid inclusions are located predominantly along PDFs. It has been proposed that toasted quartz is a post-shock feature, which is probably the result of hydrothermal or other post-shock modification (Short and Gold 1996) or that it forms in response to exsolution of water from glass, primarily in PDFs, during heat-driven recrystallization (Whitehead et al. 2002). More recently, Ferrière et al. (2009c) concluded that "…toasted quartz is formed by vesiculation after pressure release, at high post-shock temperatures, and, thus, represents the beginning of quartz breakdown due to heating."

2.3.5 Megascopic Shock-Deformation Features: Shatter Cones

Shatter cones are the only megascopic shock-deformation feature that is unique to impact or shock metamorphism (Dietz 1968; Sharpton et al. 1996; French 1998; Wieland et al. 2006). Shatter cones are distinctive curved, striated fractures in shocked rocks that typically form partial to rarely complete cones (Fig. 2.31). The striations branch and radiate down from the apices of the cones. When multiple cone features are partially superposed onto each other, this produces a unique pattern referred to as "horsetailing". Shatter cones occur in rocks beneath the crater floor, usually in the central uplifts of complex impact craters, or in the crater rims; but they can also be observed in rock fragments in impact breccias. They can form in all kinds of rocks, but the most well-formed and detailed shatter cones form in fine-grained rocks, especially carbonates (French 1998). Shatter cones can range from <1 cm to several meters in height. Shatter cones usually form at low shock pressures, generally between 2 and 10 GPa, but they may form at pressures as high as 40 GPa (Milton 1977; Roddy and Davis 1977; French 1998). At higher shock pressures (≥10 GPa) shatter cones may contain petrographic shock effects, such as quartz with PDFs or diaplectic glass (Dressler 1990). They are conical fragments of rock probably produced by tensile fractures which may have formed during shock unloading after passage of the shock wave through the rock (Wieland et al. 2006). Shatter cones are not usually found in distal ejecta.

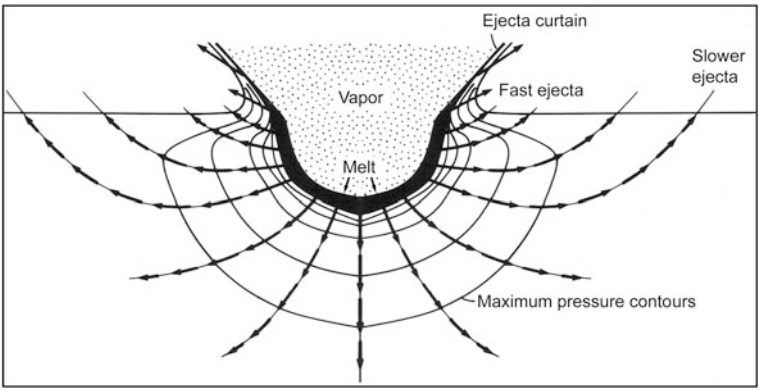

Fig. 2.32 Geometry of the excavation flow. The *arrows* indicate the direction of movement or flow of target rock set in motion by passage of the shock wave and following rarefaction wave. Also shown are peak pressure contours which decrease with distance from the point of impact. The material along each flow line moves along the same path and is ejected at the same angle and velocity. The ejecta that follow flow lines that leave the ground closest to the point of impact are ejected at higher velocities than those that are ejected farther from the point of impact. Note that material ejected along a given flow line cuts across the pressure contours and thus material ejected from a given flow line will contain a mixture of shock levels. However, as indicated in the diagram, high-velocity ejecta will contain a higher portion of melt and heavily shocked material than will the slower ejecta, which consist primarily of unshocked and weakly shocked rock. Modified after Melosh (1989), Fig. 5.9

2.3.6 Stages of Shock Metamorphism

Shock-recovery laboratory experiments have been used to calibrate shock effects under carefully controlled pressure and temperature conditions. However, the effects of some parameters, such as length of the pressure pulse, presence of phases with different shock impedance, and grain size, are not yet fully understood (Stöffler and Langenhorst 1994). Numerous calibration experiments have been performed on quartz and to a lesser extent feldspar and zircon. Among the rock-forming minerals, quartz exhibits the widest variety of shock metamorphic features (Langenhorst 2002). Estimations of the pressure and temperature conditions required to produce various shock metamorphic effects in quartz and feldspar have been used to develop criteria for recognizing different levels or stages of shock metamorphism in quartzo-feldspathic crystalline rocks (Table 2.5). Different calibration data are required for shock metamorphic stages in porous rocks, like sandstones, and for mafic rocks and chondrite meteorites, which contain little or no quartz (Stöffler 1984; Stöffler et al. 1991; Stöffler and Langenhorst 1994).

In porous rock (and sediments), the principal mechanism of energy deposition by a shock wave is due to the reverberation of shock and rarefaction waves through grains due to shock wave interaction with other grains (Kieffer et al. 1976). Collapsing pore walls become local hot spots where the initial deposition of energy from the shock wave is focused. Thus, high-pressure and high-temperature

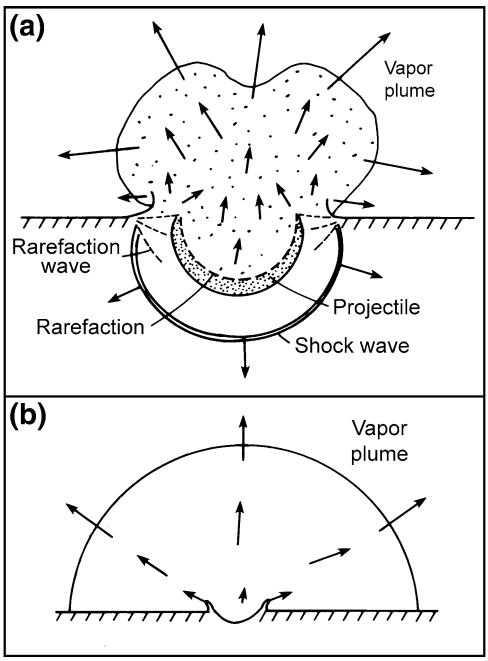

Fig. 2.33 Expansion of a vapor plume after a large impact. **a** Initial stage of vapor formation and expansion. Flow pattern may be complex as a result of variation in timing of the release of various parts of the projectile and target rock from high pressure. Pressure release and vapor formation first occur at the rim of the growing crater so that initial vapor expansion starts there. **b** This diagram illustrates the vapor plume at a later stage of crater formation, when the expanding vapor plume is approximately spherical. At this time the plume front has moved ahead of the ejecta curtain. The expansion velocity of the plume increases nearly linearly with distance from the center of the crater to a maximum at the edge of the plume. Reprinted from Melosh (1989), Fig. 5.6. By permission of Oxford University Press, Inc

transformations can take place locally in shocked rock where the average shock pressure is not high enough to cause transformations (Table 2.6).

In mafic rocks, where quartz is rare to absent, shock metamorphic stages are based on shock metamorphism of plagioclase, pyroxene, and olivine (Stöffler and Grieve 2007) (Table 2.7). In meteorites, calibration of the shock pressures at which high-pressure polymorphs (e.g., majorite, akimotoite, (Mg,Fe)SiO_3-perovskite, wadsleyite, ringwoodite) are formed has been done based on shock-recovery experiments (Stöffler et al. 1991) and on melt-vein crystallization (Agee et al. 1995; Asahara et al. 2004; Xie et al. 2006). The two methods do not agree. Xie et al. (2006) suggested that the discrepancy is probably due to the limitations of the shock-recovery experiments. They point out that the duration of shock experiments are only a few microseconds compared to large impact events where the high pressure can last up to a few seconds. Shock duration is critical for processes such as phase transformations. In other words, the over-pressure required for phase

transformations is dependent on the duration of the shock event. Thus, because of the short duration of high pressure during laboratory experiments, the pressure required for transformation must be higher than in a large impact event. On the other hand, crystallization in melt veins takes place after the peak shock pressure and thus the pressure at the time of crystallization is lower than the peak shock pressure. Shock-recovery experiments conducted on olivine and enstatite have not produced high-pressure polymorphs (Price et al. 1979; Chen et al. 1996; Langenhorst and Deutsch 1998).

2.4 Ejection and Distribution of Ejecta

Ejecta are removed from the evolving crater and distributed across the Earth's surface by a variety of mechanisms including: **jetting**, ejection of target material set in motion by the combined effects of the shock and rarefaction waves, **base surge**, and transport of fine-grained rock material and vaporized projectile and target rock by an expanding and collapsing vapor plume. The oblique convergence of the curved surface of a projectile with the target surface produces high pressure regions from which jets of highly shocked, melted, and vaporized projectile and target material are squirted at speeds generally greater than the velocity of the projectile (Melosh 1989). Jetting appears to be more important in oblique (relatively low angle) impacts. Jetted material is strongly contaminated with projectile material (Koeberl 2002).

The ejecta can be separated into two parts. The first, early part of the ejecta (formed during the first few seconds after the projectile makes contact with the target rock) is characterized by strong shock modification and consists only of vapor and melt (Shuvalov 2003). It is ejected at a wide range of ejection angles and forms the vapor plume. The total mass of this ejecta is only several percent of the total ejecta mass (Shuvalov 2003). However, this ejecta has high velocity and is ejected over a large area. The second part of the ejecta forms during the later stage of crater formation. The angle of ejection decreases from maximum angles of 60–80° at the beginning of ejection to a few degrees at the end of excavation (Shuvalov 2003). This ejecta forms an ejecta curtain consisting primarily of shock-modified and unshocked ejecta. Solid ejecta that is ejected at high velocity is subjected to high stress gradients and is, therefore, severely comminuted. Ejecta at any given distance from the source crater has experienced a wide range of peak pressures; however, the average shock pressure that the ejecta was subjected to generally increases with increasing distance from the crater (Schultz et al. 1981).

Most of the target material is ejected when it is set in motion up and outward from the impacted region by the rarefaction wave. The paths of the target material (set in motion by this process) cut across pressure contours (Fig. 2.32), so that material ejected along a given path is characterized by a variety of effects related to different shock levels. When material following a given path crosses the initial target surface it is ejected ballistically to form the ejecta curtain discussed previously. Note that the faster ejecta come from near surface deposits and have the

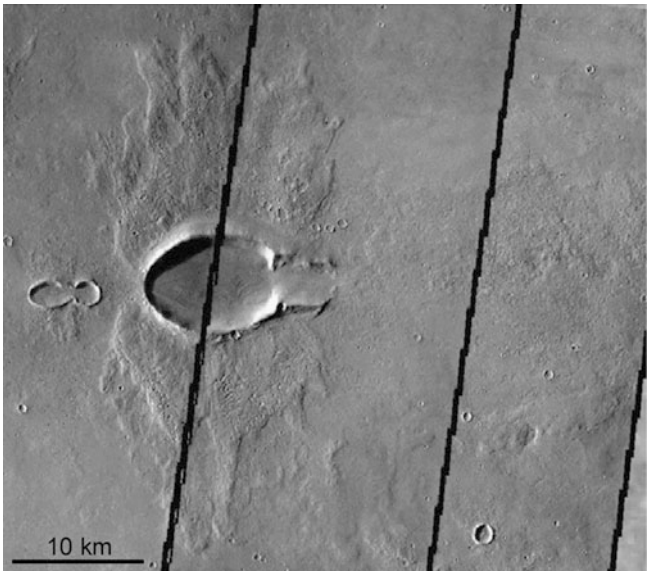

Fig. 2.34 A Martian crater with a butterfly ejecta pattern. The crater is elliptical (7.5 × 10 km). A smaller elliptical crater (2 × 3 km) with a butterfly ejecta pattern lies approximately 2 km uprange (to the *left*) from the larger crater. Note that the ejecta blanket is most prominent north and south of the larger and smaller crater. North is up. Mosaic of a THEMIS daytime IR image (Christensen PR, Gorelick NS, Mehall GL, Murray KC. THEMIS public data releases, planetary data system node, Arizona State University <http://themis-data.asu.edu>)

highest concentration of heavily shocked material (Fig. 2.32). The slower ejecta come from greater depths and are, on average, less shocked. Since the ejecta travels along ballistic paths, the higher the velocity of ejection, the farther the ejecta lands from the crater for a given angle of ejection. The distance (or range) is given by

$$R_b = 2R_p \tan^{-1}\left(\left(v_{e^2}/R_p g\right)\sin\Phi\cos\Phi\right)/\left(1 - \left(v_{e^2}/R_p g\right)\cos^2\Phi\right) \qquad (2.1)$$

where R_b is the ballistic range (or distance from the crater), R_p is the target planet's radius, v_e is ejection velocity of the ejecta, g is the acceleration due to gravity, and Φ is ejection angle (for most ejecta the ejection angle is about 45°). The equation is for planetary bodies without atmospheres. The Earth's atmosphere significantly affects the ejection and distribution of ejecta. Since the average degree of shock metamorphism increases with increasing velocity, the average degree of shock metamorphism of the ejecta increases with increasing distance from the crater (e.g., Vickery et al. 1992).

When impact velocities exceed ~ 10 km/s, most of the projectile and some of the target rock is vaporized upon pressure release (Melosh 1989). Vaporized projectile and target expand out of a growing crater at high speed forming a **vapor plume** or **fireball**. Pressure release starts near the rim of the growing crater so that vapor expansion begins there. The initial stage of expansion may be complex due to the timing of release of various parts of the projectile and target from high

pressure, but later the expanding vapor plume is nearly hemispherical (Fig. 2.33). The temperature in the core of the plume is initially in excess of 10,000 °C, but cools to less than about 1,000 °C within approximately one minute. At the edge of the plume the initial temperatures are much lower, but still in excess of ~700 °C (Pierazzo et al. 1998). The expansion is so rapid that the front of the plume tends to outrun the ejecta curtain (Melosh 1989). The density and velocity of the gas in the plume is so great that solid particles and melt can be accelerated up and outward from the crater. In addition, as the vapor cloud expands it will eventually begin to condense to form liquid droplets or solid dust particles.

Large impacts, involving projectiles ~10 km or larger in diameter, can produce an **ejecta couplet** (Vickery et al. 1992). The lower layer, produced by the main excavation flow, is composed primarily of splash-form spherules and it extends out at least 20 crater diameters. The upper layer is global in extent and it consists of the most highly shocked portion of the ejecta; i.e., material that was entrained in, or condensed from, the vapor plume (Vickery et al. 1992). It contains most of the vaporized impactor, spherules containing Ni-rich spinels, and shock metamorphosed rock and mineral grains. Vickery and Melosh (1990) proposed that if an impact is sufficiently energetic, all of the impactor can be ejected into space and lost from the Earth and, therefore, would not leave behind any siderophile enrichment (including Ir) in the ejecta layer.

Initial nucleation of the condensates does not occur until the vapor reaches an altitude equal to 7–20 impactor radii (O'Keefe and Ahrens 1983). For a given size body, the nucleation height increases with increasing velocity of the impactor. As an example, the nucleation height for a body with a radius of 5 km and impact velocity of 30 km/s is >35 km. Since the scale height of the Earth's atmosphere is only 7 km, this means that condensation would occur outside the Earth's atmosphere and the condensate droplets could be propelled on ballistic trajectories that would result in global distribution (O'Keefe and Ahrens 1983). However, much of the vapor may never condense, ending up as free atoms or molecules in space (Melosh 1989). The mean condensate diameter is proportional to the impactor size for a given velocity (O'Keefe and Ahrens 1983). It has been calculated that the maximum size of droplets that can condense out of a vapor plume, produced when a 10-km diameter projectile impacts with a velocity of 25 km/s, is ~400 μm in diameter (Melosh 1989). Some impact spherules (e.g., spinel-bearing Cretaceous-Tertiary (K-T) boundary spherules) may have formed by vapor condensation (Kyte and Smit 1986; Ebel and Grossman 2005).

In impacts large enough to form craters greater than ~3 km in diameter, the expanding gases can "blow out" the top of the atmosphere (Melosh 1989), which, for major impacts, can lead to global distribution of impact ejecta. The high-energy plume ejecta rises through the atmosphere in a column with a width that is less than or approximately equal to the width of the transient crater (Pierazzo et al. 1998). Particle velocities within the plume rapidly increase as the plume rises through the atmosphere and isotropically expands at the top of the atmosphere (Kring and Durda 2002).

In large impacts, the plume can entrain and transport unshocked to highly shocked solid grains and melt, which can be ejected out of the atmosphere into ballistic trajectories around the globe. Shocked mineral grains (e.g., shocked quartz with PDFs) and spherules can apparently be spread around the globe in this manner, since shocked quartz with multiple sets of PDFs are found around most of the globe in the K-T boundary layer. One would expect the high temperature in the plume to melt or vaporize shocked mineral grains, but thermal heterogeneities in the plume and/or brief interaction times probably prevent all of them from being destroyed (Kring and Durda 2002). The Ir anomaly found globally in K-T ejecta was also distributed via the vapor plume.

Base surge is a gravity-driven density current that flows down and outward from the rising mushroom cloud of a nuclear or volcanic explosion (Valetine 1998; Vazquez and Ort 2006; and references therein). It is a mixture of air and dust, originally in the fireball, that flows over the surrounding terrain. In the late 1960s and early 1970s, base surge was believed to be an important mechanism for depositing impact ejecta, especially around lunar craters (Melosh 1989). The deposition of suevite around the Ries crater in Germany may have been by a base-surge type of mechanism in which air suspension of the droplets of hot melt and clasts played a major role (Melosh 1989). Suevite-like ejecta deposits at other impact structures (e.g., Popigai, Chesapeake Bay) have also been suggested to have been deposited by base surges (Masaitis 2003; Gohn et al. 2008). On the other hand, Artemieva et al. (2009) proposed that the suevite outside the Ries crater may have been produced by phreatomagmatic explosions when the melt sheet inside the crater was flooded with water. Thus, the role of base surge in the deposition of impact breccia, especially suevitic breccias, remains controversial.

As previously mentioned, most of the ejecta are distributed more or less symmetrically around the source crater for near vertical impacts: however, most impacts are closer to 45°. Oblique impacts produce ejecta blankets with a bilateral symmetry (Gault and Wedekind 1978; Melosh 1989). As the impact angle decreases from close to 90°, the ejecta first begin to exhibit a preferential concentration downrange of the crater (Melosh 1989). At impact angles less than 45°, a wedge-shaped forbidden zone forms uprange from the crater. This wedge increases with decreasing impact angle. Below about 20° a second forbidden zone forms downrange of the crater. This bilateral pattern with concentration of ejecta in a sideways direction, with respect to the direction of the projectile, is called a **butterfly pattern** (Fig. 2.34). These patterns have been produced experimentally and are observed on the Moon, Mars, Venus and other planetary bodies and may be associated with some terrestrial craters as well (Gault and Wedekind 1978; Pierazzo and Melosh 2000; Herrick and Forsberg-Taylor 2003).

Distal ejecta, even from moderately sized craters (a few tens of kilometers in diameter) can be deposited thousands of kilometers from the source crater. In the case of large impact events, where debris is thrown over much or all of the Earth's surface, ejecta that is deposited more than about 400 km from the source crater was carried above the Earth's atmosphere before falling back to the Earth (Kring and Durda 2002). Size sorting will result in larger particles settling out first,

followed by finer dust-sized particles. If the ejecta are deposited in water, as most preserved ejecta layers were, there will be additional size and density sorting as the particles settle through the water column. Thus, distal ejecta deposits should be normally graded; however, bioturbation in Phanerozoic-aged deposits can rework the layer and destroy the size grading, especially if the initial thickness of the layer was less than a few centimeters. On the other hand, it has been suggested that under some conditions impact ejecta falling through the atmosphere and/or water may clump together and form density currents that flow to the ground or ocean floor more rapidly than the single particles themselves (Melosh 2004). Furthermore, the ejecta deposits may exhibit flow structures more indicative of the velocity of the density currents than of the environment in which they were deposited. This mechanism may be of importance with respect to the deposition of the thick Archean spherule layers found in Australia and South Africa (Melosh 2004) (for information about these spherule layers see Chaps. 8 and 9). Interestingly, at least one Paleoarchean spherule layer (S3; 30-cm thick) interpreted as an un-reworked direct fall-out deposit has normal grading and compositional grading that would not have occurred if clumping had taken place.

Spherule formation is an important part of the cratering process. Rock material initially shocked to high pressure approaches the liquid–vapor phase boundary from the liquid side as it undergoes decompression. The liquid then breaks up into an expanding spray of liquid droplets (Melosh and Vickery 1991). The liquid undergoes an initial fragmentation into clumps whose diameters are determined by a balance between the local kinetic energy and the surface tension of the liquid (Melosh and Vickery 1991). The diameter of the clumps (d_o) is given by the following equation: $d_o \approx (40\sigma/\rho_o)^{1/3}(Lv_i)^{2/3}$, where σ is the surface tension (typically $\sim 0.3\ \mathrm{Nm}^{-1}$), ρ_o is the liquid density ($\sim 2{,}500\ \mathrm{kg/m}^3$), L is the projectile diameter, and v_i is the impact velocity (Melosh and Vickery 1991). Following the initial breakup of the melt is a second generation of droplet formation which takes place in the more energetic part of the plume as vaporization begins. At this time the ejecta plume is still accelerating and the gas is moving faster than the melt clumps which results in breaking up the initial clumps into smaller melt droplets the size of which is determined from a balance between surface tension and aerodynamic forces. The equilibrium radius of the droplets is given by: $r_\infty \approx (0.11L^{1/2})/v_i$ (Melosh and Vickery 1991). Hassler et al. (2000) stated that there is an error in this equation and give the equation as $r_\infty \approx (0.08L^{1/2})/v_i$ based on a 1998 personal communication from Symes. According to Melosh and Vickery (1991), the radius derived from this equation should be valid for the high-energy portion of the ejecta as long as the impact velocity is close to 20 km/s. However, higher temperature of the melt, interaction with the ambient atmosphere, and atmospheric ablation after the droplets decouple from the plume can cause further reduction in size of the droplets (Melosh and Vickery 1991).

O'Keefe and Ahrens (1982) derived the following relationship for the mean radius of condensate droplets as a function of projectile diameter and impact velocity: $R_{cv} = 1.15 \times 10^{-5} d_p V^{2/3} (\varepsilon/U)^{-35/6}$, where R_{cv} is the mean condensate droplet radius, d_p is the diameter of the projectile, V is the impact velocity, ε is the

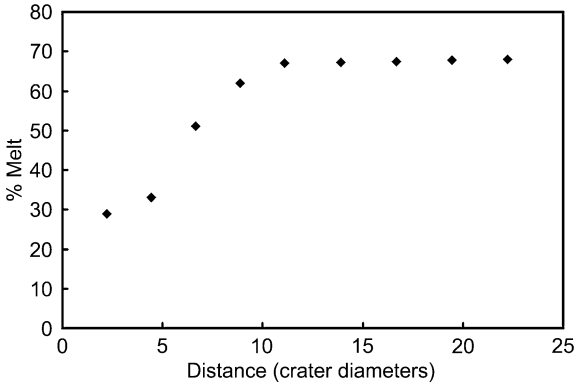

Fig. 2.35 Theoretically estimated percent melt in distal ejecta with distance (in crater diameters) from a crater the size of the 180-km-diameter Chicxulub impact structure (Yucatan Peninsula, Mexico). Data from Vickery et al. (1992)

average initial internal energy of the vapor, and U is the total energy of vaporization. Droplet radius and projectile diameter are in centimeters and impact velocity is in centimeters per second. Deviation from the mean droplet size increases with increasing impact velocity.

More recently, Johnson and Melosh (2012a) studied spherule formation in impact produced vapor plumes and found a simple linear relationship between average spherule size and size of the impactor. However, they found a complex dependence of spherule size on impact velocity, such that for a given size impactor, the average spherule size increases with increasing impact velocity up to ~27 km/s and decreases with increasing impact velocity at higher velocities. Johnson and Melosh (2012a) produced a figure (Fig. 13) that shows average diameter of spherules produced during impacts at impact velocities between 15 and 50 km/s for projectiles with diameters of 1, 10, 100, 1,000, and 10,000 km; but the calculations are based on a vapor plume (and, therefore, spherules) composed of silica (SiO_2). They found that a 10 km diameter asteroid impacting with a velocity of 21 km/s would produce spherules ~250 μm in diameter, which is comparable to the size of the spherules found globally in the K-T boundary layer. However, it would only require a 20 km/s impact velocity for a 10 km diameter projectile to produce basaltic spherules of the same size (Johnson and Melosh 2012a). In another publication, Johnson and Melosh (2012b) used the thickness of a global spherule layer to estimate the size of the impacting projectile and then used the average spherule size and projectile size to estimate the impact velocity (see Sect. 11.3.1).

2.5 Numerical Modeling of the Cratering Process

Over the last few decades, rapid progress in computer capabilities has made it possible to model impact cratering with increasing realism and complexity (Pierazzo and Collins 2003). Modeling complicated processes like impact cratering requires powerful computer codes that can model the propagation of shock waves as well as the behavior of a broad range in rock types over a wide

range of stress states. Computer programs used to model the cratering process are usually called "hydrodynamic computer codes" or simply **hydrocodes** (Anderson 1987). These computer programs are used to model the propagation of shock waves and compute velocities, strain, and stress as a function of time. They are called hydrocodes because initially they did not include strength effects; i.e., the materials were treated as fluids (Stöffler et al. 2006). For modeling impact cratering, hydrocodes have been modified to treat material strength and a wide range in rheological properties for material (rock) behavior. The hydrocode is used to monitor the effects of external and internal forces on a predefined mesh of cells that represents the geometry of the object under investigation (Pierazzo and Collins 2003). During each timestep, the program iterates through the mesh, cell by cell, and updates the grid positions to account for the effects of internal and external forces.

The foundations of hydrocode modeling, used to determine the forces acting on the mesh during each timestep, are: Newton's law of motion, the **equation of state**, and the **constitutive model**. The equation of state accounts for changes in density and irreversible thermodynamic processes like shock heating. The constitutive model describes the response of a material to deformation. In some recent hydrocodes, all information about ejecta particles (velocity and angle of ejection, pre-impact location, maximum temperature, and overpressure during impact) is conserved by markers (Shuvalov 2003). The distribution of size and different types of particles (i.e., melted, shock-modified, ejecta from specific depths, etc.) can be displayed for different timesteps. There is presently a major effort to bridge the gap between numerical models and field observations (see, e.g., Meteoritics and Planetary Science Vol. 39, No. 2, 2004).

2.6 Variations in Ejecta with Distance from the Source Crater

The thickness of the ejecta blanket decreases away from the source crater. McGetchin et al. (1973) compiled data, mainly from explosion experiments, which they used to derive an equation that relates the thickness of an ejecta blanket to size of the crater and distance from the crater for lunar impact basins. The thickness of the ejecta blanket (t) is a power function of the distance (r) from a crater with a transient crater radius *(R)* such that:

$$\mathrm{t} = 0.14\mathrm{R}^{0.74}(\mathrm{r}/\mathrm{R})^{-3.0} \tag{2.2}$$

with all dimensions in meters. A similar equation is given by Stöffler et al. (1975) based on experimental hypervelocity impacts into quartz sand. They derived the following equation:

$$\mathrm{t} = 0.06\mathrm{R}(\mathrm{r}/\mathrm{R})^{-3.26} \tag{2.3}$$

Both of these equations are intended for ejecta in the ejecta blanket (i.e., proximal ejecta). However, there are some data to suggest that such equations might also be useful for estimating the thickness of distal ejecta layers (Vickery et al. 1992; Glass and Pizzuto 1994). Thus, thickness of the ejecta layer should decrease exponentially with distance from the source crater; however, for large impacts involving global or near global distribution of ejecta, the thickness of the ejecta layer may be affected by the Earth's rotation and by processes occurring in the area of deposition (e.g., reworking by impact-generated tsunamis; see Sect. 2.7.3).

Based on cratering models, surface and near-surface deposits are thrown the farthest from the source crater and, on average, are the most shocked. Thus, the average degree of shock metamorphism should increase with increasing distance from the source crater. For distal ejecta, the degree of shock metamorphism can be indicated by the ratio of melted to unmelted ejecta which should increase with increasing degree of shock metamorphism and, therefore, with distance from the source crater. Vickery et al. (1992) have modeled the impact of the 180-km-diameter Chicxulub structure and calculated the percent melt in ejecta with distance from the crater. They found, for example, that the percent melt in the ejecta should be about 50 % at a distance of 1,200 km or $\sim$7 crater diameters (i.e., 1,200 km/180 km $\approx$ 7) from the crater (Fig. 2.35). In distal ejecta, the melted ejecta occur as impact spherules (e.g., microtektites and microkrystites). Thus, the percent impact spherules in a distal ejecta layer should increase with increasing distance from the source crater. Comparison of models predicting how distal impact ejecta should vary with distance from the source crater with observation of how distal ejecta vary with distance from the source crater is discussed in Chap. 10, after the descriptions of the known distal impact ejecta layers in Chaps. 4–9.

2.7 Complications

The model for transport and deposition of impact ejecta discussed above is simplistic and can be complicated in a number of different ways. Computer modeling suggests that there is a concentration of distal impact ejecta at the antipodal region, and, due to the Earth's rapid rotation, distal ejecta from large impacts can be concentrated in some areas and depleted in other areas relative to what would be predicted based on radial decay laws. During and/or after deposition the ejecta can be reworked by impact generated tsunamis, if the impact were adjacent to or in the ocean.

2.7.1 Effects of Earth's Rotation and Atmosphere on Transport and Distribution of Distal Ejecta from Large Impacts

The Earth's rotation can affect the transport and distribution of impact ejecta (Alvarez et al. 1995; Kring and Durda 2002), but the effect is generally small

except for large impacts (impacts producing craters larger than ~90 km in diameter) where the ejecta is transported over most or all of the globe. One effect of the Earth's rotation is that the eastward rotational velocity of the Earth (0.463 km/s) is added to the ejection velocity of eastbound ejecta and subtracted from the velocity of westbound ejecta; thus, eastbound ejecta goes up higher and stays up longer than does westbound ejecta (Alvarez et al. 1995). However, because the Earth is rotating eastward, particles ejected at high velocity and at high angles (e.g., greater than 60°) to the east land closer to the source crater than do particles ejected at the same velocity and angle to the west (Alvarez et al. 1995). Computer models have suggested that in major impacts, distal ejecta are concentrated at the antipodal region (Argyle 1989; Melosh et al. 1990; Kring and Durda 2002). Because of the Earth's rotation, the region of high concentration is smeared out to the west of the antipode (Kring and Durda 2002).

Modeling ejecta distribution from large impacts indicates that the **Coriolis effect** due to the Earth's rotation can also significantly affect ejecta distribution (Wrobel and Schultz 2003). For example, at high latitudes, all the particles ejected at high velocities and high angles (i.e., plume-entrained ejecta) from an impact "turn" toward the equator where they travel westward parallel to the equator, but without crossing the equator (Wrobel and Schultz 2003). Thus, deposition of plume-driven ejecta is severely limited east of the crater and enhanced west of the crater. On the other hand, low angle (45°) impact ejecta, with high enough velocity, will travel to the opposite hemisphere where it travels around the globe parallel to the equator. For high latitude impacts, this wrapping around the globe occurs around the pole in the opposite hemisphere from the impact. For low latitude impacts the wrapping of the ejecta around the globe can result in significant depositional increase (up to tenfold) in the amount of ejecta per unit area relative to expectation from simple exponential decay of ejecta amount/thickness with distance from the source crater (Wrobel and Schultz 2003) (additional discussion of this subject can be found in Sect. 4.6.11).

The thickness of an ejecta layer should decrease exponentially with distance from the source crater. In the case of Chicxulub, the source crater for the Cretaceous-Tertiary boundary ejecta layer, the ejecta layer should decrease in thickness by a factor of ~7 over a distance of 7,000–11,000 km; however, observations indicate that over those distances the ejecta layer is fairly uniform in thickness, ~2–3 mm (e.g., Smit 1999). Goldin and Melosh (2008) have proposed that density currents formed by loading of the atmosphere with infalling ejecta (mostly spherules) may result in lateral transport producing a more even distribution of the ejecta. Artemieva and Morgan (2009) reaffirmed that models that involve only ballistic transport of ejecta cannot explain the near uniform thickness of the distal Chicxulub ejecta layer. They proposed that the ejecta were emplaced non-ballistically by a mechanism termed "floating of impact debris in the atmosphere", a mechanism proposed by Colgate and Petschek (1985). According to these authors, re-entering ejecta heats the atmosphere, which expands upward and outward redistributing the ejecta.

2.7.2 Lobate and Ray-Like Ejecta Patterns

As previously mentioned, low angle or oblique impacts can throw ejecta preferentially downrange or to the sides (i.e., at right angles to the trajectory of the impacting body). This may have happened in the Australasian microtektite strewn field (see Sect. 4.2.4), which has a tri-lobed appearance. Because the ejecta are not distributed symmetrically in oblique impacts, variations in the thickness of the ejecta or number of spherules/unit area from a few sites (or even a few tens of sites) may not give a clear indication of the location of the source crater.

Long bright **ejecta rays** extending from younger impact craters on the Moon, Mercury, and other planetary bodies also indicate that ejecta is not always distributed uniformly about craters even when the impacts are not at low angles. The late Eocene clinopyroxene-bearing (cpx) spherule layer may have a ray-like pattern emanating from the Popigai impact structure (see Sect. 4.6.11), which is believed to be the source crater of the cpx spherules. Again, such a distribution pattern would make it difficult to determine the location of the source crater based on geographic variations in thickness of ejecta or abundance of spherules (number/unit area) at a few locations. Theoretically, if there are data on ejecta thickness or spherule abundance at enough sites to define the orientation of the lobes/rays, then the lobe or ray pattern should point back to the crater. However, in the case of the 0.8 Ma old Australasian microtektite strewn field, it required searching over a hundred deep-sea cores spread over more than 10 % of the Earth's surface (>50,000,000 km^2) in order to determine the lobate shape of that strewn field. This would be most difficult, if not impossible to do for older impact ejecta/spherule layers (i.e., older than ~100 Ma). However, computer models suggest that ray formation on Earth may not occur for larger impacts (i.e., impacts the size of Chicxulub or larger).

Computer models suggest that as impact spherules re-enter the atmosphere they decelerate due to atmospheric drag and begin to bunch up at an altitude of ~70 km (Goldin et al. 2010). The decelerating spherules compress the upper atmosphere creating a pressure gradient which leads to a lateral spreading of the spherules. Horizontal spreading velocities increase with higher spherule fluxes and smaller spherule sizes. Since spherule fluxes increase with the size of the impact, wider rays should form around larger craters; and for craters the size of Chicxulub or larger the rays will be so spread out that only a uniform layer of spherules should be deposited (Golden et al. 2010).

2.7.3 Reworking of Distal Impact Ejecta by Impact-Produced Tsunamis

Since ~70 % of the Earth's surface is covered by oceans, most extraterrestrial bodies that impact the Earth land in the ocean, but only large bodies could produce

a crater on the ocean floor in deep (>2 km) water. No impact craters have been identified on the deep ocean floor; however, they would be difficult to find and most of the older craters would have been destroyed by plate tectonic processes. As many as 20 impact craters have been discovered that were formed in shallow marine water on continental margins (Goto 2008). Impacts into marine environments can generate tsunamis which can interfere with deposition of the ejecta and/or rework the ejecta after initial deposition.

Tsunamis can be generated by impacts in several different ways, but probably the most important are crater-generated and submarine slide-generated tsunamis (Goto 2008). Crater-generated tsunamis are formed when water rushes into the crater after its formation. Piling up of the water in the center of the crater produces a water column which eventually collapses and propagates as a wave outward from the crater. Submarine slide-generated tsunamis can form when the shock wave or seismic wave generated by the impact triggers large-scale submarine slides. The magnitude of the impact-generated tsunamis is primarily dependent on the size of the submarine slide. Submarine slides can also generate gravity flows (e.g., turbidity currents). The velocity of a tsunami increases with increasing water depth, but even in the deep ocean basin (4 km depth) a tsunami only travels at a velocity of $\sim$0.2 km/s and thus is much slower than the velocity of distal ejecta. Therefore, a tsunami will generally arrive after deposition of the coarser ejecta. However, the finer ejecta which settles slowly through the atmosphere and water column usually arrive after passage of the tsunami. As the tsunami wave passes over the shallow sea floor it erodes and carries sediment up onto the adjacent land surface (run-up). As the velocity slows down, deposition will start to take place, with coarser debris deposited first. Later the water flows back out into the ocean basin (backwash) carrying with it continental debris as well as some of the marine debris carried inland by the run-up. There may be one or two other smaller run-ups followed by backwash.

Impact-generated tsunamis can rework ejecta from the same impact causing dilution of the ejecta and repetition of impact ejecta-enriched layers, which could be interpreted as multiple impact events. The topmost unit may consist of fine-grained ejecta from the vapor plume which is enriched in projectile material. Around the Gulf of Mexico, in neritic to upper-bathyal depths, impact ejecta from the Chicxulub crater appear to have been reworked by tsunamis generated by the impact (see Sect. 5.2.2.1 for description of these reworked ejecta deposits). Of course, the exact nature of a tsunami-reworked ejecta deposit will depend on the size of the tsunami, distance from the impact site, water depth at the deposition site, and nature of the adjacent continental shelf and inland area.

Seismic waves generated by a large impact on a continental margin can trigger gravity flow movements (e.g., submarine slides, slumping, turbidity currents) on the adjacent ocean floor. Seismic waves travel at velocities close to that of the ejecta, but there is a lag time between the arrival of the impact ejecta and the seismic wave due to the time it takes for the ejecta to settle through the atmosphere and water column. Thus, in deeper water environments (continental slope, continental rise, and adjacent ocean floor) near the impact site, ejecta will be deposited

after mass movements generated by arrival of the seismic waves. On the upper continental slope, the ejecta may be deposited on an older surface exposed by slumping or other mass movement triggered by the seismic waves. Since the seismic waves travel at high velocity compared with the velocity of tsunamis, there is a lag time between the arrival of a seismic wave and an impact generated tsunami. Therefore, under some conditions, it is possible to find a section where the lower part consists of gravity-flow deposits, the middle part consists of impact-generated tsunami deposits with reworked coarse ejecta, and the upper part consists of fine-grained ejecta (Smit 1999; Goto 2008).

Chapter 3
Distal Impact Ejecta Layers: Recognition, Confirmation, Dating, and Determining Source Craters

3.1 Recognition of Possible Distal Ejecta Layers

Discovery of a possible distal impact ejecta layer may begin in the field with recognition of a relatively thin (<1 m) lithologic layer that seems out of place or with the discovery of spherules in a well-defined layer, or in the laboratory with the discovery of a geochemical anomaly (e.g., high Ir) that suggests the presence of a meteoritic component.

3.1.1 Stratigraphy/Lithology

A thin layer with different lithology from the rocks above and below may be the first indication of the presence of an impact ejecta layer. Of course, other geological process can also produce widespread thin layers with a different lithology from the rock layers above and below it, e.g., volcanic ash layers or turbidites. However, as discussed below, distal impact ejecta layers can be distinguished from other such layers by the presence of grains showing evidence of shock metamorphism, and/or the presence of impact-generated spherules (e.g., microtektites), and/or geochemical anomalies indicating the presence of a meteoritic component. The ejecta layer may be coarser- or finer-grained than the host rocks and/or have a different composition from the host rock (e.g., a layer of clay within an otherwise carbonate section). Distal ejecta layers close to the source crater can contain abundant angular rock fragments in addition to glassy particles, including impact spherules. For example, the Acraman impact ejecta layer in South Australia was first recognized because it consists of a breccia layer in an otherwise fine-grained section of rock (Gostin et al. 1986; Williams and Gostin 2005; Fig. 3.1). The Acraman impact ejecta layer is found relatively close (between $\sim$3 and $\sim$6 crater diameters) to the **Acraman impact structure** in South Australia. At greater distances (in terms of crater diameters) from a source crater, ejecta consist mostly of glassy spherules.

B. P. Glass and B. M. Simonson, *Distal Impact Ejecta Layers*, Impact Studies,
DOI: 10.1007/978-3-540-88262-6_3, © Springer-Verlag Berlin Heidelberg 2013

Fig. 3.1 The Acraman impact ejecta layer in the Bunyeroo Formation, Adelaide Fold Belt, South Australia (see Sect. 7.2). The ejecta layer consists of angular coarse sand- to gravel-sized fragments of pink to red porphyritic volcanic rock between layers of green shale and is ~3–4 cm thick, as indicated by the coin which has a diameter of ~2.1 cm. The ejecta layer occurs about 80 m above the base of the Bunyeroo Formation which is a marine shale unit ~400 m thick. The ejecta layer stands out in sharp contrast to the rest of the Bunyeroo Formation due to its coarseness and reddish color

Other rounded particles, called accretionary lapilli, can also be found in some ejecta layers, but they are usually found in the proximal or more proximal part of the distal ejecta layer. Unlike impact-generated spherules, accretionary lapilli are not formed from melt droplets, but rather, as their name implies, by accretion of solid particles (e.g., glass fragments, mineral grains, rock fragments—see Sect. 3.2.1.1). In the more distal part of an impact ejecta layer, shock metamorphosed mineral grains can be sparse to non-existent, depending on the size of the impact and distance from the source crater. For example, over all of the Ivory Coast and most of the Australasian microtektite strewn fields only microtektites, but no shocked mineral grains, have been found so far. However, in the more distal parts of these strewn fields (>100 crater diameters from the source crater), the microtektites, which are the only ejecta component present (at least in the >63 μm size fraction), have been dispersed by bioturbation and the layer is not obvious by naked eye inspection.

Impact spherules can be up to several millimeters in size and spherule layers can often be easily recognized in the field (Fig. 3.2). Depending on the mineralogy of the spherules in comparison to that of the matrix, impact spherules may stand out in relief on weathered rock surfaces, and it may be possible to distinguish them from other types of spherules using a hand lens (Simonson 2003a; see Sect. 3.2.1). Cenozoic-aged, silica-rich, distal impact spherules (i.e., microtektites) are still mostly composed of glass. However, glass is unstable and older glass spherules have generally been altered to a wide variety of phases including: clay (e.g., K-T boundary spherules in the Western Interior, USA), pyrite (e.g., K-T boundary spherules and upper Eocene clinopyroxene-bearing spherules), glauconite (e.g., late Triassic spherules in England, and K-T boundary spherules), goyazite (e.g., K-T boundary

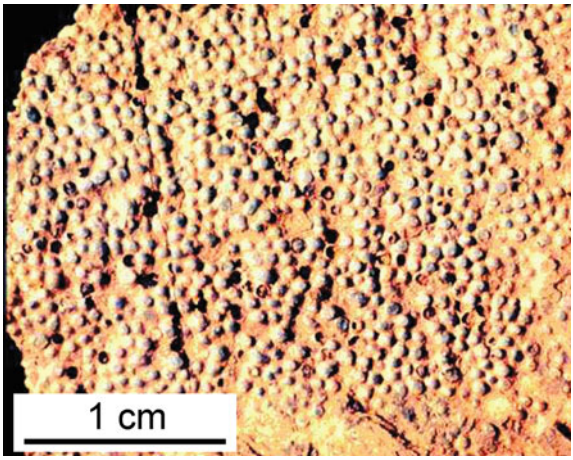

Fig. 3.2 Neoarchean impact spherules on the weathered surface of a specimen from the Bee Gorge spherule layer in the Hamersley Basin of Western Australia. The spherules stand out in relief due to differential weathering, which makes them clearly visible to the naked eye

spherules in the Western Interior, USA), carbonate and K-feldspar (e.g., K-T boundary and Neoarchean spherules), and chert or chlorite (e.g., Paleoarchean spherules). On the other hand, the Late Devonian spherules found in China and Belgium have remained glassy. Whether or not the glass phase is replaced with another phase depends on the composition of the glass, the environment of deposition, and the diagenetic environment. These factors also determine which phase replaces the glass.

Identification of impact spherules is discussed in Sect. 3.2.1.

3.1.2 Geochemistry

Impact craters are formed when asteroids and comets collide with the Earth. However, comets probably only account for ~1 % of the impacting bodies (Ivanov et al. 2002; Chapman 2004). During impacts of large extraterrestrial bodies (generally asteroidal), the impacting body is destroyed by melting and vaporization. Smaller bodies can sometimes survive their fiery passage through the Earth's atmosphere and subsequent collision with the ground, although they may be fragmented. Extraterrestrial objects that survive their trip through the atmosphere and impact with the ground are called **meteorites**. There are three main groups of meteorites; in decreasing order of abundance these are: stones, irons, and stony-irons. The stony meteorites are divided into **chondrites** and **achondrites**. Chondrites are primitive meteorites from undifferentiated asteroids and achondrites, irons, and stony-iron meteorites are from differentiated asteroids and other planetary bodies (Dodd 1986; McSween 1987). Chondrites are further divided into ordinary, enstatite, and carbonaceous chondrites, in decreasing order of abundance. Ordinary chondrites make up ~74 % (by number) of the meteorites that are observed to fall on the Earth (McBride 2001). Ordinary chondrites are divided into H (high iron), L (low iron), LL (low iron, low metal), R (Rumurutites), and K (Kakangari) types,

Table 3.1 Ni, Co, Cr and platinum group element contents for selected meteorite classes and the Earth's crust and mantle

Class	Ni (ppm)	Co (ppm)	Cr (ppm)	Os (ppb)	Ir (ppb)	Ru (ppb)	Pt (ppb)	Rh (ppb)	Pd (ppb)
Meteorites									
Carbonaceous chondrites									
CI	11000	505	2650	490	465	710	1000	140	560
CM	12300	560	3050	670	580	870	1100	160	630
CV	13200	640	3480	800	730	1200	1250	170	710
CO	14200	680	3520	805	740	1080	1240	n.d.	710
CH	25700	1100	3100	1150	1070	1600	1700	n.d.	n.d.
Ordinary chondrites									
H	17100	830	3500	835	770	1100	1580	210	845
L	12400	580	3690	530	490	750	1090	155	620
LL	10600	480	3680	410	380	n.d.	880	n.d.	560
R	14400	610	3640	690	610	960	<1000	n.d.	n.d.
K	14600	750	3600	550	550	850	n.d.	n.d.	n.d.
Enstatite chondrites									
EH	18400	870	3300	660	570	930	1290	n.d.	820
EL	14700	720	3030	670	560	770	1250	n.d.	730
Achondrites									
Eucrite	4	4.7	1780	0.008	0.096	n.d.	n.d.	n.d.	0.4
Howardite	25	18	5300	n.d.	n.d.	n.d.	n.d.	n.d.	10
Diogenite	25	16	5300	0.7	0.7	n.d.	n.d.	n.d.	2
Shergottite	79	40	1350	0.979	0.99	1.77	7.68	0.96	3.73
Nakhlite	90	48	1770	0.012	0.068	0.31	3.07	0.35	1.74
Chassignite	500	123	5240	1.8	1.42	16.6	6.18	6.7	25.2
Terrestrial rocks									
Continental crust									
Upper crust	45	8	37	0.03	0.03	1.06	n.d.	0.38	2
Whole crust	56	24	126	0.05	0.05	0.1	0.4	0.06	0.4
Oceanic crust									
Oceanic crust	135	47	270	<0.004	0.02	1.0	2.3	0.2	<0.2
Ultramafic rocks and mantle									
Ultramafic	1450	110	3090	3.1	3.2	n.d.	60	n.d.	10
Mantle	2108	105	3010	3.1	2.8	n.d.	n.d.	n.d.	n.d.

n.d. no data

Chondrite and eucrite, howardite, diogenite data are from Lodders and Fegley (1998); shergottite, nakhlite, and chassignite data are from Jones et al. (2003b); upper continental crust, whole continental crust, oceanic crust, ultramafic rocks, and mantle data are from Muñoz-Espadas et al. (2003), Wedepohl (1995), Taylor and McLennan (1985), Wedepohl and Muramatsu (1979), and Wänke et al. (1984), respectively

the enstatite chondrites into EH (high iron) and EL (low iron) types, and the carbonaceous chondrites into CI (Ivuna), CM (Mighei), CV (Vigarano), CO (Ornans), CK (Karoonda), and CH (high iron) types (Table 3.1; Lodders and Fegley 1998; Weisberg et al. 2006).

Most meteorites are enriched in siderophile elements, especially the **platinum group elements** (PGEs; Table 3.1) and have different isotopic ratios of some elements compared with those in the terrestrial crust. Thus, another way to identify possible impact ejecta layers is to search for evidence of meteoritic contamination. The presence of an extraterrestrial component can be indicated by anomalously high contents of siderophile elements or ^{3}He and/or by determining osmium and/or chromium isotopic ratios.

Over the last few decades **chemolithostratigraphic analysis** has become an important tool for the study of impactites, including distal impact ejecta layers (Koeberl 2007). Chemolithostratigraphic analysis involves geochemical and cosmochemical studies including: simple chemical characterization of target rocks, impactites, and distal ejecta layers; determination of the presence of extraterrestrial components in impactites and distal ejecta layers; identification of the impactor (projectile) type (e.g., chondrite, iron meteorite); and investigation of environmental changes associated with major impact events (Koeberl 2007 and references therein).

3.1.2.1 Siderophile and Platinum Group Elements

The detection of small amounts of meteoritic material within a distal ejecta layer composed of upper continental crust is difficult and it is even more difficult if there is a mafic or ultramafic component present in the target rocks (Koeberl 1998). Only elements that are abundant in meteorites but have low abundances in the Earth's crust can be used to determine the presence of a meteoritic component in an impactite or distal ejecta layer (Koeberl 2002, 2007). The most useful elements for detecting projectile presence and in identifying the projectile are siderophile elements such as, Ni, Co, and Au, platinum group elements (PGEs; Os, Ir, Ru, Pt, Rh, Pd), and Cr (Tagle and Hecht 2006; French and Koeberl 2010; Table 3.1). It is not only the high content of siderophile elements that indicates the presence of meteoritic contamination, but also the ratios between the siderophile element abundances.

Iridium is the PGE most used in scanning or searching for evidence of an impact event recorded in the rock record. Iridium, like other siderophile elements, is highly enriched in most meteorites compared with the siderophile elements in the Earth's crust, especially the continental crust (Table 3.1). The Ir content of chondrites ranges from $\sim$300 to 1000 ppb, whereas the continental crust usually has $<$0.1 ppb Ir. In addition, the Ir content can be determined with greater ease and sensitivity than the other PGEs (Sawlowicz 1993; Koeberl 2007). Even 0.1 wt % of a chondritic component will add 0.4 ppb Ir to an impactite (Koeberl 2007), which is at least one order of magnitude higher than the average upper continental crust value. Discovery of a positive Ir anomaly is what first suggested that the Cretaceous-Tertiary (K-T) boundary layer might be an impact ejecta layer (Alvarez et al. 1980). However, a layer enriched in one or more siderophile elements is only *suggestive* of the presence of a meteoritic component and is not

proof of an impact origin. Without any other chemical, mineralogical, or petrographic data, an Ir anomaly by itself cannot be used to establish the impact origin of a rock layer (French and Koeberl 2010). It must be demonstrated that the layer has meteoritic, not terrestrial, ratios between various siderophile elements, particularly the PGEs.

Nickel, Co, and Cr have often been used to search for meteoritic contamination in impactites (e.g., Palme et al. 1978). If the meteoritic content exceeds 0.1 wt %, it is possible to distinguish between chondrites and iron meteorites, since iron meteorites have Cr concentrations that are typically $\sim$100 times lower than those of chondrites (Koeberl 2007).

In the past, in order to determine the contribution by the projectile, siderophile element contents of the target rocks had to be determined. The indigenous concentrations were then subtracted from the abundances in the impactites in order to determine the amount and kind of meteoritic contamination. This is not possible in a distal ejecta layer for which there is no known source crater. However, Tagle and Hecht (2006) have proposed a method that they say is almost independent of target composition, especially if PGE ratios are considered. They have used this method on impact melt rocks. Melt rock compositions are relatively homogeneous, but the projectile component is unevenly distributed in the melt rock. Thus, measuring PGE contents of several melt rocks with different projectile/target ratios and plotting them against each other (e.g., Ru versus Rh) defines mixing trends that can be used to approximate the projectile elemental ratios (Fig. 3.3a; Tagle and Hecht 2006). The slopes determined by linear regression of these mixing trends are almost identical to the projectile elemental ratios. These ratios can then be compared to PGE ratios in different types of meteorites (Fig. 3.3b). Unfortunately, this method may not work on distal impact ejecta layers, unless the ejecta are uniform in composition with variable projectile/target ratios. Nor can this method be used on the impact spherules themselves, since the microtektites and microkrystites from a given layer generally have a wide range in composition and microtektites, like tektites, contain very little meteoritic component (usually <0.5 wt %).

Montanari and Koeberl (2000) pointed out that studies of impact glasses from some small craters indicate that the siderophile elements show strong and highly variable fractionation in interelement ratios compared with the ratios in the projectiles. Siderophile element fractionation may also occur in impact melts in larger craters and in distal impact ejecta (Montanari and Koeberl 2000). A variety of fractionation effects have been documented for the K-T boundary layer from around the globe (Evans et al. 1993). High PGE contents were found in the Acraman impact ejecta layer, but the PGE contents exhibit deviations from chondritic patterns. These deviations have been attributed to low temperature hydrothermal processes (e.g., Wallace et al. 1990b). However, Tagle and Hecht (2006) state that the PGE contents in their samples from the Popigai and Morokweng impact structures appear to be relatively unaffected by secondary mobilization processes.

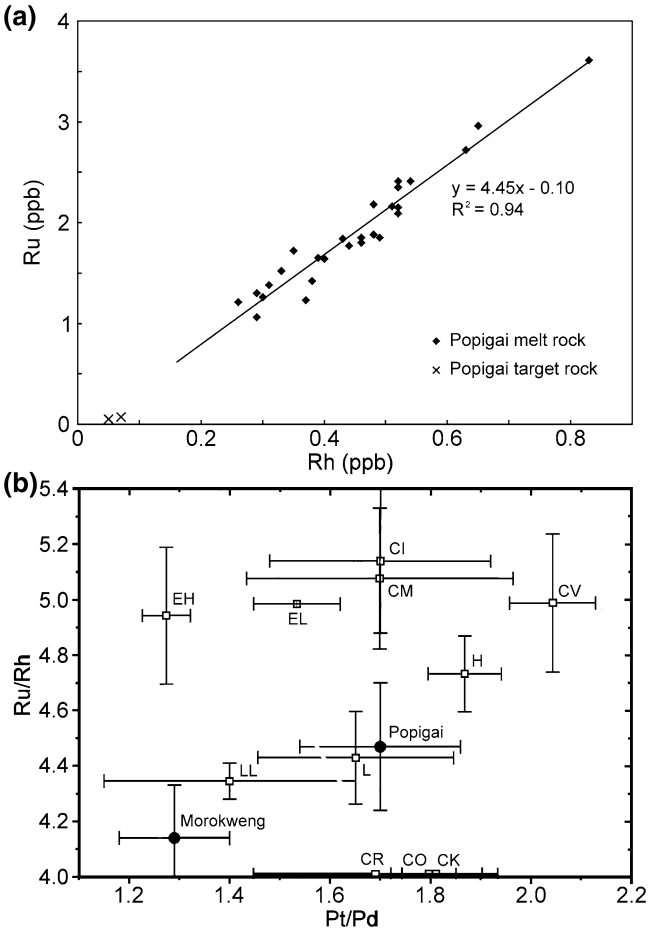

Fig. 3.3 Platinum group element plots used to identify the projectile for two impact craters. **a** Plot of Ru versus Rh for a group of melt rocks and two target rocks from the 35-Ma-old Popigai impact structure in northern Siberia (see Sects. 4.6.9 and 4.6.10). The slope of the best-fit line determined by linear regression is 4.45. This is interpreted to be the ratio between Ru and Rh in the projectile that produced the Popigai impact structure. The melt-rock data plot along a mixing line between the target rocks (Xs, lower left) and the projectile, which would plot to the upper right off the diagram (see Table 3.1 for the Ru and Rh contents of various chondrite meteorites). Data used to make this plot are from Tagle and Claeys (2005). **b** A plot of Ru/Rh versus Pt/Pd for various chondrite meteorites (see Table 3.1) and for melt rock from the Popigai and Morokweng impact structures. The 145-Ma-old Morokweng impact structure is in South Africa. The Ru/Rh ratio for the Popigai melt rock is the same as obtained in **a**. The Pt/Pd ratio was obtained in the same way. The data suggest that the Popigai projectile was an L chondrite and the Morokweng projectile was an LL chondrite. Modified after Tagle and Hecht (2006), Fig. 8

It is important to demonstrate that the siderophile enrichment occurs in a discrete layer over a wide area and in different sedimentary environments, as was

done for the K-T boundary layer (Alvarez et al. 1980). This would help rule out some local enrichment in siderophile elements that is unrelated to an impact.

3.1.2.2 Osmium Isotopic Method

The **osmium isotopic method** is another tool for detecting meteoritic contamination in impactites. It is based on ^{187}Os, one of seven stable isotopes of osmium, which is formed by beta decay of ^{187}Re, which has a half life of 42.3 ± 1.3 Ga (Koeberl et al. 2002a). Meteorites, with the exception of achondrites, have high Os contents and low Re contents compared with terrestrial crustal rocks (Table 3.2). This results in low Re/Os ratios ≤0.1 compared with terrestrial crustal rocks which have Re/Os ratios that are usually >10. In the Os isotopic method ^{187}Os is normalized to the abundance of ^{188}Os which is a non-radiogenic isotope. Because of the low Re/Os ratios in meteorites, the $^{187}Os/^{188}Os$ ratios increased slowly with time and, therefore, meteorites have low $^{187}Os/^{188}Os$ ratios (~0.11–0.18). As a result of the high Re/Os ratios in crustal rocks, the $^{187}Os/^{188}Os$ ratios increased rapidly with time resulting in an average $^{187}Os/^{188}Os$ ratio in upper crustal rocks of 1–1.2. Because meteorites have much higher Os contents than do terrestrial crustal rocks, even a small amount of meteoritic contamination in impactites leads to a large change in Os isotopic ratio (Fig. 3.4). However, contamination from an achondrite must be much greater in order to be detected, because achondrites have much lower PGE abundances compared with chondritic and iron meteorites (Koeberl 2007).

The first use of the osmium isotopic method to search for meteoritic contamination in impact material involved the measurement of Os isotopes in the K-T boundary clay (Luck and Turekian 1983), but the result was problematic due to low abundance of Os (Fehn et al. 1986). Development of the negative thermal ionization mass spectrometer a few years later allowed the measurement of Os isotopic ratios in samples of a few grams containing below ppb amounts of Os (e.g., Creaser et al. 1991). The first successful use of the osmium isotopic method involved the detection of ~0.6 % of a meteoritic component in Ivory Coast tektites from the Bosumtwi impact crater (Koeberl and Shirey 1993). This method has been used to confirm the presence of a meteoritic component in several additional craters (e.g., Aouelloul, Chicxulub, Gardnos, Kalkkop, Manson, Morokweng, Vredefort) (French et al. 1997; Koeberl et al. 1994; Koeberl and Shirey 1996; Koeberl 1998, 2002, 2004, 2007).

A problem with the osmium isotopic method is that mantle rocks have $^{187}Os/^{188}Os$ ratios similar to meteoritic ratios. Therefore, the presence of a mantle component in the target rocks must be ruled out in order to conclude that the measured ratios belong to a meteoritic source. Fortunately, PGE abundances in typical mantle rocks are at least two orders of magnitude lower than those in most meteorites. Thus, in order to have the same effect on the osmium isotopic ratios as meteoritic contamination would have, the mantle contribution would have to be about two orders of magnitude higher. The presence of that high of a mantle content

Table 3.2 Rhenium and osmium contents and osmium isotope data for meteorites and the Earth's crust

Class	Re (ppb)	Os (ppb)	Re/Os	$^{187}Os/^{188}Os$		Reference
				Value	Number	
Meteorites						
Carbonaceous chondrites						
CI	37	449	0.0826	0.12646	2	1
CM	49	614	0.0806	0.12564	3	1
CV	62	740	0.0837	0.12625	2	1
CO	62	780	0.0797	0.12657	2	1
CR	50	623	0.0800	0.12598	3	1
CK	44	687	0.0644	0.11980	1	1
Ordinary chondrites						
H	96	843	0.1145	0.12876	15	1
L	51	611	0.0834	0.12536	2	1
LL	31	366	0.0855	0.12801	2	1
R	43	690	0.0623			2
Enstatite Chondrites						
EH	53	605	0.0877	0.12818	6	1
EL	63	720	0.0874	0.12813	8	1
Achondrites						
Eucrite	0.010	0.008	1.213	n.d.	1	2
Diogenite	0.060	0.700	0.086	n.d.	1	2
Shergottite	0.096	1.130	0.085	n.d.	9	3
Nakhlite	0.027	0.012	2.238	n.d.	2	3
Chassignite	0.071	1.800	0.039	n.d.	1	3
Irons and Stony-Irons						
Irons	1040	11490	0.0905	1.084	13	4
Stony-irons	110	1018	0.1076	1.132	5	4
Terrestrial rocks						
Upper continental crust						
Loess[a]	0.474	0.035	14	0.92	16	5
Loess[a]	0.367	0.031	12	1.05	1	6
Loess[a]	0.213	0.040		1.22	35	7
Oceanic crust						
Upper crust[b]	1.526	0.021	73	0.213	43	8
Whole crust[c]	0.50	0.044	11	0.144	n/a	9

References: 1 = Walker et al. (2002), 2 = Lodders and Fegley (1998), 3 = Jones et al. (2003b), 4 = Hirata and Masuda (1992), 5 = Hattori et al. (2003), 6 = Peucker-Ehrenbrink and Jahn (2001), 7 = Honda et al. (2002) and Masatushi Honda personal communication, April 21, 2009, 8 = Peucker-Ehrenbrink et al. (2003), 9 = Bernhard Peucker-Ehrenbrink's website (www.whoi.edu/hpb/viewPage.do?id=1375&cl=5)

n.d. = no data, n/a = not applicable

[a] Loess is used as a proxy for the upper continental crust

[b] Based on analysis of oceanic crust from DSDP Site 504

[c] From a model of the oceanic crust based on data from DSDP Sites 468 and 504

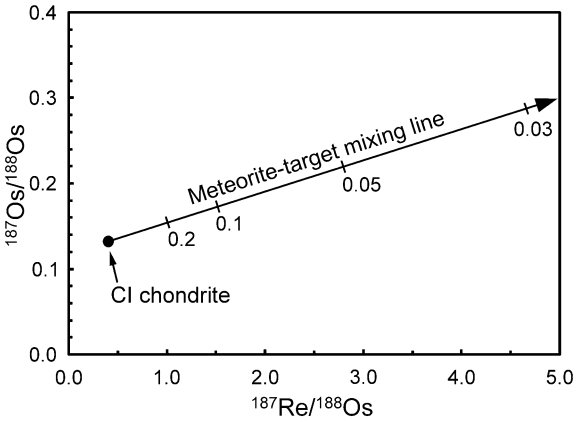

Fig. 3.4 $^{187}Os/^{188}Os$ versus $^{187}Re/^{188}Os$ showing the mixing relationship between a CI chondrite and a target rock with a $^{187}Os/^{188}Os$ ratio of 1.48 and a $^{187}Re/^{188}Os$ ratio of 30, which plots well outside the diagram. The numbers along the mixing line indicate the fraction of a CI chondrite required to produce the indicated isotopic ratios; i.e., 0.2 indicates a mixture of 20 % CI chondrite and 80 % target rock, 0.1 indicates 10 % CI chondrite and 90 % target rock, etc. Note that because Re and Os are orders of magnitude more abundant in most meteorites than in the Earth's crust (see Table 3.2), even small amounts of meteoritic contamination can be detected using this method. Modified after Koeberl and Shirey (1993), Fig. 3

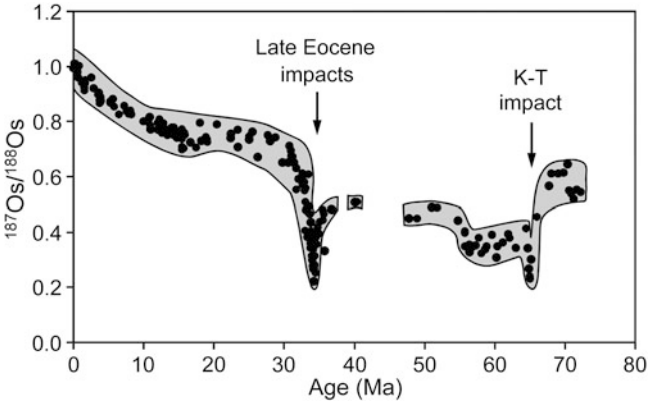

Fig. 3.5 Marine osmium isotope record for the last 75 Ma. The black dots represent data from different sources compiled by Klemm et al. (2005). Note the sharp drop in $^{187}Os/^{188}Os$ at approximately 65 Ma and 35 Ma corresponding to the Cretaceous-Tertiary boundary and late Eocene impacts, respectively. The drop in $^{187}Os/^{188}Os$ is consistent with an enhanced input of a meteoritic component at these times. Modified after Klemm et al. (2005), Fig. 1a

in an impactite should be evident in the clast population of a breccia, and/or from other geochemical data (especially Sr and Nd isotopes) in melt rock (Koeberl 2002).

The marine Os isotopic record of the past 80 Ma is a mixture of terrestrial and extraterrestrial sources. The marine Os isotopic record clearly shows evidence of

large meteoritic input at the K-T boundary and in the late Eocene (Fig. 3.5) (Peucker-Ehrenbrinck 1996; Klemm et al. 2005), which correlates with the K-T boundary ejecta layer and the late Eocene clinopyroxene-bearing (cpx) spherule layer (see Sects. 5.2 and 4.6, respectively).

The laboratory procedures (sample preparation, digestion, and measurement) of the osmium isotopic method are complex (Koeberl et al. 2002a). Furthermore, the osmium isotopic method does not allow determination of the projectile type (Koeberl 2002).

3.1.2.3 Chromium Isotopic Method

The Cr isotopic method is based on measurement of the relative abundance of ^{53}Cr, which was produced by the decay of ^{53}Mn with a half life of 3.7 Ma. The relative abundances of ^{53}Cr are measured as the deviations of the ^{53}Cr/^{52}Cr ratio in a sample relative to a terrestrial standard.

$$\varepsilon^{53}\mathrm{Cr} = \left[\left(^{53}\mathrm{Cr}/^{52}\mathrm{Cr}\right)_{\mathrm{sample}} / \left(^{53}\mathrm{Cr}/^{52}\mathrm{Cr}\right)_{\mathrm{standard}} - 1\right] \times 10,000 \qquad (3.1)$$

Thus, 1 ε unit is 1 part in 10^4. Measurements are made using a high-precision thermal ionization mass spectrometer. Terrestrial rocks exhibit very little variation in the ^{53}Cr/^{52}Cr ratio, because homogenization of the Earth was completed after all the primordial ^{53}Mn had decayed (Shukolyukov and Lugmair 1998, 2000). In contrast, most meteorite groups (ordinary and enstatite chondrites, primitive achondrites, and other differentiated meteorites) exhibit variable excesses of ^{53}Cr relative to terrestrial samples (Lugmair and Shukolyukov 1998). The range of ε^{53}Cr in most meteorites is about +0.1 to +1, depending on meteorite type (Table 3.3; Fig. 3.6). Carbonaceous chondrites, on the other hand, exhibit an apparent deficit in ε ^{53}Cr of about −0.4 (Shukolukov and Lugmair 1998, 2000). These variations in Cr isotopic compositions apparently reflect heterogeneous distribution of ^{53}Mn in the early solar system (Lugmair and Shukolyukov 1998). The negative ε value for carbonaceous chondrites is the result of using ^{54}Cr/^{52}Cr for a second order fractionation correction, since carbonaceous chondrites contain a presolar ^{54}Cr-rich component (Lugmair and Shukolyukov 1998). This excess ^{54}Cr component allows the carbonaceous chondrites to be distinguished from other meteorite types. Thus, in addition to confirming meteoritic contamination in a distal impact ejecta layer, the Cr isotopic method can be used to identify the kind of projectile (i.e., carbonaceous chondrite, enstatite chondrite, or other types of meteorites). The presence of an achondrite component in an impactite can only be determined using the Cr isotopic method (Koeberl 2007).

The Cr isotopic method has been used to determine the projectile type at several impact craters (e.g., East Clearwater in Canada; Rochechouart in France; Morokweng in South Africa; Lappajärvi in Finland) and several distal ejecta/spherule layers (e.g., upper Eocene cpx spherule layer, K-T boundary layer,

Table 3.3 Chromium concentrations and isotopic data for meteorites and terrestrial rocks

Sample	Location[a]	Cr (ppm)	ε^{53}Cr	Ref.
Terrestrial rocks				
Terrestrial crust		~185	≡0	1
Basalt	Deccan Traps, India	112	−0.04 ± 0.06	2
Basalt	Not given	16	0.03 ± 0.15	3
Pelagic clay	Western Pacific	34	−0.02 ± 0.09	2
Pelagic shale	Greenland[b]	38	0.00 ± 0.13	3
Clay	Caravaca, Spain[c]	40	−0.01 ± 0.07	2
Meteorites				
Carbonaceous chondrite CV3 (Allende)		3540	−0.41 ± 0.09	2
Carbonaceous chondrite CI (Orguell)		2530	−0.43 ± 0.09	2
Ordinary chondrites (H, L)		~3900	~0.48	2
Enstatite chondrites (EH)		2900	~0.17	2
Achondrites (eucrites)		1600–3200	0.7 ± 1.3	2
Achondrites (angrites)		800–1800	0.4 ± 0.7	2
Achondrites (SNC) Mars meteorites		1600–1800	~0.22	2
Achondrite (lunar anorthosite)		~240	0.00 ± 0.09	2
Iron meteorites[d]		112–200	0.81 ± 4.91	3

References: 1 = Koeberl et al. (2007a), 2 = Shukolyukov and Lugmair (1998), 3 = Frei and Rosing (2005)

[a] Location is only given for the terrestrial samples

[b] The Isua Supracrustal Belt in West Greenland. The data are an average of four samples

[c] Sample from 10–15 cm below the Cretaceous-Tertiary boundary

[d] The isotope data are for five iron meteorites, but the Cr concentration is for only two iron meteorites

several Precambrian spherule layers in South Africa and Western Australia) (Shukolyukov and Lugmair 1998, 2000; Shukolyukov et al. 2000; Simonson et al. 2009b; Lowe et al. 2003; Kyte et al. 2003, 2011).

Terrestrial Cr in the target rocks can be a problem (Kyte et al. 2003). A significant proportion of the Cr in an impactite or distal ejecta layer (generally at least 1 wt %) needs to be of extraterrestrial origin (Fig. 3.7). The analytical procedure for the Cr isotopic method is complicated and time-consuming (Koeberl 2007).

More recently, Trinquier et al. (2006) concluded that ^{54}Cr is a far better indicator of meteorite type than is ^{53}Cr. They used the ^{54}Cr isotopic method to identify the K-T boundary projectile as a CM2 chondrite.

3.1.2.4 Helium-3 and Fullerenes

Helium-3 is enriched in extraterrestrial material, particularly interplanetary dust particles, because of the presence of implanted solar wind helium (Nier and Schlutter 1990). The ^{3}He/^{4}He ratios can be used to determine the amount of extraterrestrial materials in sediments or sedimentary rocks. Farley et al. (1998)

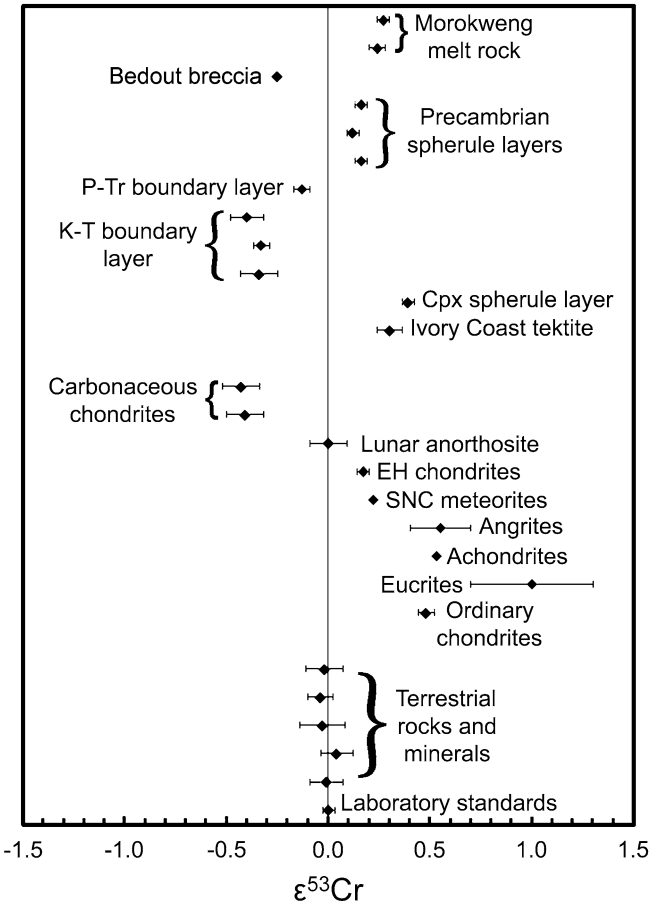

Fig. 3.6 Epsilon ^{53}Cr values for various meteorite groups and terrestrial samples, including distal impact ejecta and impact crater melt rock. The laboratory standard has an ε^{53}Cr value of zero by definition. Terrestrial rocks uncontaminated by extraterrestrial material and a lunar meteorite (anorthosite) also have zero values within error. Most meteorite groups have positive ε^{53}Cr values, but carbonaceous chondrites have negative values. Morokweng melt rock, some Precambrian spherule layers, the late Eocene cpx spherule layer, and an Ivory Coast tektite all have positive ε^{53}Cr values indicating formation by the impact of an ordinary chondrite, enstatite chondrite, or achondrite. The K-T boundary layer has a negative ε^{53}Cr value suggesting that the impacting body was a carbonaceous chondrite. A negative value for the Bedout breccia indicates the presence of a carbonaceous chondrite component, but, as of the time of writing, some investigators are not convinced of an impact origin for this structure (see Sect. 6.2.3). Likewise, the negative ε^{53}Cr value for the Permian–Triassic boundary layer at Graphite Peak, Antarctica, suggests that it has an impact origin and that the projectile was a carbonaceous chondrite; but, again, the impact origin for this layer is in dispute (see Sect. 6.2.2.5). Data used in the plot are from Shukolyukov and Lugmair (1998), Koeberl et al. (2002a), Koeberl et al. (2004a), Kyte et al. (2011), Becker et al. (2006)

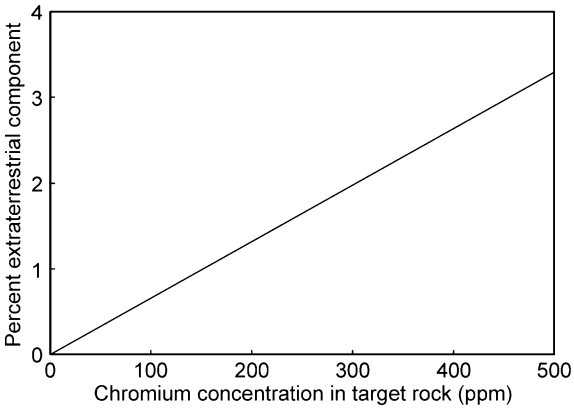

Fig. 3.7 Detection limits for an extraterrestrial component in an impactite using the Cr isotope method. The detection limit, assuming a chondritic projectile, is plotted (in percent) on the y-axis as a function of the Cr content in the terrestrial target rocks. For example, if there is 200 ppm of chromium in the target rock, then the extraterrestrial component in an impact would have to exceed ~1.4 % before it could be detected. Modified after Fig. 2 in Koeberl et al. (2002a)

reported an increase in ^{3}He in upper Eocene rocks at Massignano, Italy, which overlaps at least two positive Ir anomalies, one of which correlates with a Ni-rich spherule layer. Farley et al. (1998) proposed that the broad rise in ^{3}He abundance was the result of enhanced comet activity in the inner solar system, which probably resulted in a higher than normal impact rate. In a later publication Farley et al. (2006) found elevated ^{3}He abundances in middle Miocene deep-sea sediments, which they attributed to the breakup of an asteroid. This suggests that dust particles derived from both comets and asteroids can carry ^{3}He. Indeed, the late Eocene 100-km-diameter Popigai impact structure, which may be the source of the Ni-rich spherule layer at Massignano, appears to have been formed by the impact of a L or LL chondrite (Glass et al. 2004b; Tagle and Claeys 2005). An L or LL chondrite would be from an asteroid, not a comet. It must be stressed that ^{3}He is a proxy for extraterrestrial dust and elevated abundance of ^{3}He in a rock layer does not necessarily indicate an impact event.

Fullerenes are molecules composed entirely of carbon. One type consists of large hollow, spherical molecules (sometimes called **buckyballs**) made up of sixty or more carbon atoms. The central "cage" of these large carbon molecules can trap gases like helium. Fullerenes, especially C_{60} and C_{70}, have been reported from the Sudbury impact structure, Canada (e.g., Becker et al. 1996; Mossman et al. 2003), several other impact structures (Elsila et al. 2005), and the Cretaceous-Tertiary boundary layer (Heymann et al. 1994). Fullerenes can be formed by subjecting carbon or carbon-bearing gases to high temperatures, and do not require high pressure or shock waves (French and Koeberl 2010). Thus, fullerenes, by themselves, are not an indicator of impact or shock metamorphic conditions. Becker

and colleagues have stated that the evidence for impact is the presence of extraterrestrial ^{3}He "caged" in the fullerenes (e.g., Becker et al. 1996, 2001). However, the observation of ^{3}He in fullerenes in impactites has not been confirmed by other investigators (e.g., Koeberl et al. 2004b; Farley et al. 2005). Thus, at present, neither the presence of fullerenes, nor their contents, can be used as independent and diagnostic indicators of meteorite impact (French and Koeberl 2010).

After a distal impact ejecta layer is tentatively identified, based on lithology and/or a geochemical anomaly, its identification then must be confirmed.

3.2 Confirmation of Impact Origin for a Suspected Distal Impact/Spherule Layer

The discovery of a spherule layer and/or a positive PGE anomaly, especially if it occurs over a wide geographic area, may be an indication of a distal impact ejecta layer; but the identification must be confirmed. Identification of the first craters to be accepted as impact craters was based on the presence of meteorite fragments. This association was accepted as confirmation of their impact origin. Unfortunately, during formation of large impact structures with extensive ejecta layers the impacting body is mostly destroyed (vaporized/melted), and any fragments that might survive are quickly destroyed by post-impact weathering (French and Koeberl 2010). French and Koeberl (2010) point out that because there is a continuous flux of meteorite material onto the Earth's surface that is unrelated to large hypervelocity impact events, the presence of preserved meteorite impact fragments in, or adjacent to, a suspected impact crater does not necessarily indicate that a hypervelocity impact occurred as there is always the possibility of a coincidental association. The same argument can be made for meteorite fragments in a suspected impact ejecta layer. Although meteorite fragments rarely survive a large hypervelocity impact, detectable amounts of a melted/vaporized projectile component can be found in most distal impact ejecta layers. Geochemical determination that a spherule layer contains a meteoritic component strongly supports an impact origin; but for wider acceptance of an impact origin, it should be demonstrated that the spherules are impact spherules and don't have some other more common origin and/or that the layer contains grains exhibiting evidence of shock metamorphism (e.g., shocked quartz with planar deformation features; high-pressure polymorphs such as coesite, stishovite, reidite).

Identification of a distal impact ejecta layer, particularly in older rocks, can be difficult because of sediment reworking (e.g., by bioturbation or impact-generated tsunami), erosion, diagenetic alteration (particularly of glass), and even regional metamorphism. Finding impact signatures generally requires closely spaced samples (<10 cm intervals) and detailed petrographic and geochemical studies. Such detail is not commonly used when studying Mesozoic, Paleozoic, or Precambrian sediments/rocks (Claeys 1995).

3.2.1 Impact Spherules and Their Identification

Most impact spherules are generated during the early stages of crater formation when a portion of the target rock is melted and ejected. However, some impact spherules may have formed by vapor condensation—e.g., the Cretaceous-Tertiary boundary spherules containing Ni-rich spinels. The composition of the impact spherules will record that of the target rocks diluted in some instances by variable, sometimes significant, amounts of material from the projectile (meteoritic component). Spherules with compositions that cannot be matched with some mixture of normal continental crustal rocks (such as granite, shale, sandstone, and carbonates) or oceanic crustal rocks (basaltic and possibly ultramafic rocks), with or without a meteoritic component, should be regarded with suspicion. For example, spherules composed of >99 wt % silica or with high lead contents are not likely to be of impact origin. Unfortunately, in addition to impact spherules, there are a number of other naturally-occurring and manmade spherules, which, at first glance, can be, and some have been, mistaken for impact spherules. In this section, we define and describe the kinds of impact spherules, describe other naturally-occurring and manmade spherules, and discuss how they may be distinguished from impact spherules.

3.2.1.1 Impact Spherules: Kinds and Description

There are two kinds of silicate glassy impact spherules: microtektites which do not contain primary microlites/crystallites and microkrystites which do. Impact spherules can be produced by two mechanisms: as melt droplets or as condensate droplets. The two types of impact spherules combined with the two formation mechanisms result in four possible categories of impact spherules that can be found in distal impact ejecta layers: (1) microtektites produced as melt droplets, (2) microtektites formed as vapor plume condensate droplets, (3) microkrystites formed as melt droplets, and (4) microkrystites formed as plume condensate droplets. We believe that all four kinds have been found in distal impact ejecta deposits.

Most microtektites appear to have formed as impact melt droplets from continental impacts into silica-rich target rocks. Most spherules produced as condensate droplets from an impact plume appear to be microkrystites. This may be because melt droplets condensed from vapor plumes tend to have mafic compositions due to much of the vapor being from the projectiles, which are mostly chondritic in nature. Mafic melt droplets are more likely to undergo at least partial crystallization as they solidify and thus form microkrystites. In addition to clinopyroxene and plagioclase, for example, microkrystites formed as vapor condensate droplets often contain Ni-rich spinels. Microkrystites can also form as melt droplets from an impact into mafic (e.g., oceanic) crust. Formation of microkrystites by this process may have been more common in the Precambrian

(>2.4 Ga ago). Microtektites produced as vapor condensates may be rare, but we think that some microtektites found in the Late Eocene cpx spherule layer may have formed by such a process. For the sake of brevity, we will refer to microtektites and microkrystites formed from melt droplets as **melt-drop microtektites** and **melt-drop microkrystites** and we will refer to microkrystites and microtektites formed from condensate droplets as **condensate microkrystites** and **condensate microtektites**.

Melt-drop microtektites occur, for example, in the Australasian, Ivory Coast, and North American microtektite layers. These microtektites appear to be microscopic versions of larger glass bodies called tektites (see Sect. 4.1.2). They are commonly several hundred micrometers in size, but range up to millimeter size. They increase in number with decreasing size down to at least 60 μm. However, tektites in the same strewn field can range in size from ~1 cm up to 10 cm or more (<0.1 g to ~24 kg; Baker 1963; Chalmers et al. 1976; Koeberl 1992a), but they are too widely scattered to be used to define an ejecta layer. The larger tektites are the blocky, layered tektites called Muong Nong-type tektites (see Sect. 4.1.2). Melt-drop microtektites are mostly spherical in shape, but rotational forms (dumbbell, teardrop, and disc shapes; Figs. 2.7a and 3.8) are rare to common. It is important to note that the dumbbell shape is not simply two spheres stuck together, but is an elongate form in which the two ends have a greater diameter than the interior section (Fig. 3.8c). Dumbbells are formed by rapid rotation of melt droplets ejected into the atmosphere. If the rate of rotation is high enough for a given viscosity of the melt, the dumbbell can pull apart to form two teardrops. Melt-drop microtektites are usually transparent, but can be translucent or even opaque (depending primarily on the iron content). Their surfaces are generally pitted and grooved, but can be smooth (Fig. 3.9). Most of the surface features are due to solution, but some microtektites produced as melt droplets have high-velocity impact pits on their surfaces (Fig. 3.9f), especially close to the source crater. Melt-drop microtektites often contain spherical vesicles and lechatelierite particles. The abundance of lechatelierite particles varies from strewn field to strewn field and many individual microtektites do not contain lechatelierite. By definition, melt-drop microtektites do not contain primary microlites/crystallites (i.e., crystals that crystallized from the melt as it cooled), but close to the source crater they can contain relict mineral grains (Fig. 3.10); however, the only relict phase identified to date is quartz. Cenozoic tektites and microtektites are usually silica rich, but can have a broad range in composition, with the content of most of the other major oxides varying inversely with the silica content. They have low water contents (<0.02 wt %) and the iron is generally highly reduced with almost all occurring as Fe^{2+}.

Condensate microtektites may occur in the Late Eocene clinopyroxene (cpx) spherule or microkrystite layer. There are two main groups of microtektites found in the Late Eocene cpx spherule layer: (1) silica-rich (often >80 wt %), transparent colorless to pale brown microtektites up to a millimeter in size and (2) silica-poor (generally <70 wt %), transparent to opaque brown or yellow-green microtektites (Table 4.10). The silica-rich microtektites are mostly spherical, but teardrops and dumbbells are also present. They are similar to the Australasian, Ivory Coast, and

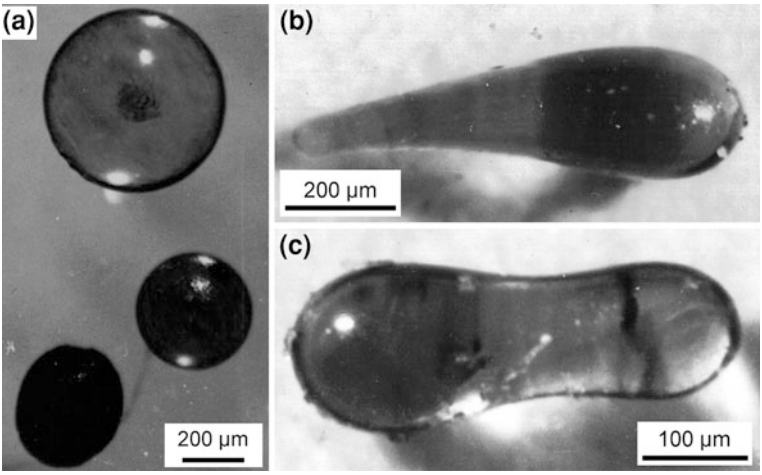

Fig. 3.8 Australasian microtektites showing different splash forms. **a** Two spheres and an oval. Spheres, oblate spheres, and prolate spheres are the most abundant splash forms in all microtektite layers. **b** A teardrop-shaped microtektite, which was probably formed when a dumbbell-shaped microtektite was pulled apart by centripetal force to form two teardrops due to rotation while still molten. **c** Dumbbell-shaped microtektite formed by rotation while still molten. These microtektites all came from Core V19-153 taken in the northwestern Indian Ocean off Sumatra

North American microtektites in most respects and we believe that they were also formed as melt droplets. The silica-poor microtektites are smaller and, based on the present data, have only spherical shapes and may not contain vesicles or lechatelierite particles. They are similar in size, shape, and composition to the cpx spherules. The high Ni, Co, and Cr content of many of the Si-poor microtektites indicate that they, like the cpx spherules, have a large meteoritic component from the projectile (see Sect. 4.6.10). Although similar in composition to the cpx spherules, there are some differences. For example, the Si-poor microtektites have higher average Al_2O_3, and lower average MgO and CaO contents (Table 4.10). We suggest that these microtektites may have, like the cpx spherules, formed as condensate droplets and that slight differences in composition may have prevented them from crystallizing.

Based on the above observations, we propose that melt-drop microtektites can be distinguished from condensate microtektites by: the presence of rotational forms (teardrops and dumbbells); the presence of vesicles, lechatelierite, and sometimes rare relict mineral grains; and compositionally, by the absence of an obvious meteoritic component. To put it another way, unlike the melt-drop microtektites, condensate microtektites do not occur in rotational forms, do not contain vesicles, lechatelierite, or relict mineral grains, but can have a significant meteoritic component.

Microkrystites thought to have formed as vapor condensates occur in the Late Eocene cpx (microkrystite) spherule layer, the Cretaceous-Tertiary (K-T) boundary

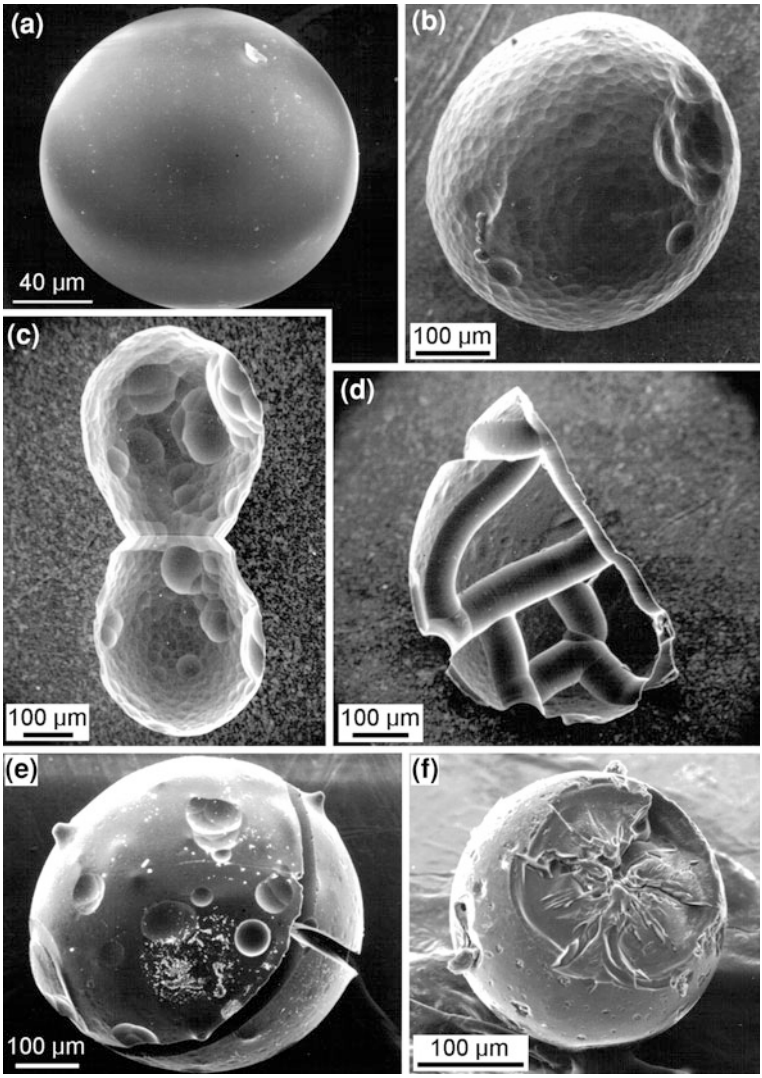

Fig. 3.9 Common surface features observed on Cenozoic microtektites. **a** Microtektite from the late Eocene clinopyroxene-bearing spherule layer with a smooth, shiny, featureless surface from Deep Sea Drilling Project Site 216 in the western equatorial Pacific Ocean. **b** Pitted Ivory Coast microtektite from Core K9-56 in the eastern equatorial Atlantic Ocean. **c** Pitted Ivory Coast microtektite (from Core K9-56) with V-shaped groove where two spherical microtektites were fused together. Rotation after fusion caused elongation to produce a dumbbell shape. Overlapping shallow pits, especially on the right in the upper half, produced a scalloped surface which is common on Ivory Coast microtektites. **d** Broken disc-shaped Ivory Coast microtektite (Core K9-56) with numerous U-shaped grooves. **e** Smooth to pitted Ivory Coast microtektite (Core K9-56) with cracks widened by solution. Also present are two prominent protrusions and a few smaller circular elevated areas. The prominent protrusions are probably silica-rich as indicated by compositional data obtained for similar protrusions on other microtektites. **f** Australasian microtektite with an impact crater on its surface. A small bleb attached to the surface on the left side is silica and iron rich. This microtektite is from Core V28-238 taken in the western equatorial Pacific Ocean

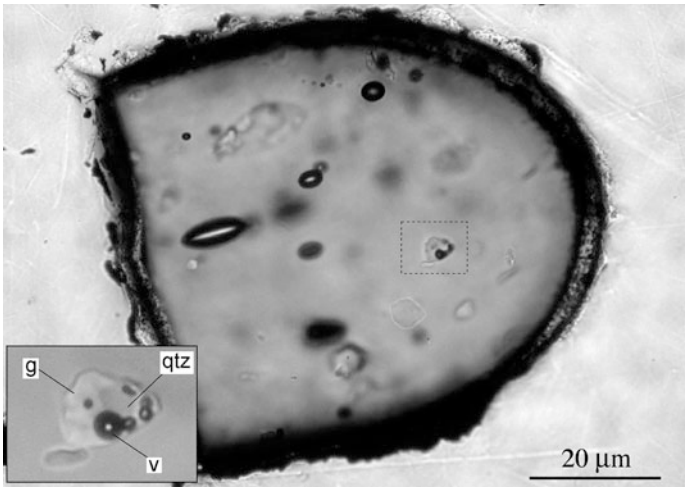

Fig. 3.10 Lechatelierite particles in an Australasian microtektite from Ocean Drilling Program Site 769 in the Sulu Sea. The elongate regions (up to 10 µm long) outlined in black are vesicles. The area outlined in the box is shown at higher magnification in the insert (*lower left corner*). *Qtz* quartz (*medium gray*); *v* vesicle (*black sphere with white center*); *g* glass: i.e., lechatelierite (*light gray*). Several other lechatelierite particles are present in the microtektite, but are out of focus. Image courtesy of Luigi Folco

layer (e.g., Ebel and Grossman 2005), and probably some of the Precambrian spherule layers. The glass and silicate phases making up the K-T boundary layer microkrystites have been replaced by other phases and most of the microkrystites have been flattened during compaction. The cpx spherules are mostly <200 µm in diameter (see, e.g., Fig. 4.34), and few, if any are larger than ~400 µm. They occur as spheres and composite forms (two or more fused together); no rotational forms have been observed. The cpx spherules appear to break more easily than do microtektites, and fragments are common (Fig 2.7b). Their surfaces are not pitted and grooved like microtektite surfaces, but they often exhibit crystalline features due to crystalline phases which were dissolved or which stand out in relief due to differential solution (Fig. 3.11). A variety of crystalline textures, primarily skeletal and dendritic (Fig. 3.12; see also Sect. 4.6.2), are observed on polished interior surfaces of the cpx spherules. The crystalline textures indicate rapid quenching from a high temperature. The cpx spherules do not contain vesicles or lechatelierite particles, although a crystalline silica phase is present in a few. On the other hand, Ni-rich spinel crystals have been found in many of the cpx spherules and K-T boundary layer microkrystites (Fig. 3.13). The Ni-rich spinels have compositions that differ from spinels found in terrestrial rocks (other than impactites) by their high-Ni content and, in the case of Phanerozoic spinels, by their high ferric/ferrous ratios, which indicate greater oxidation due to formation in the atmosphere (Pierrard et al. 1998).

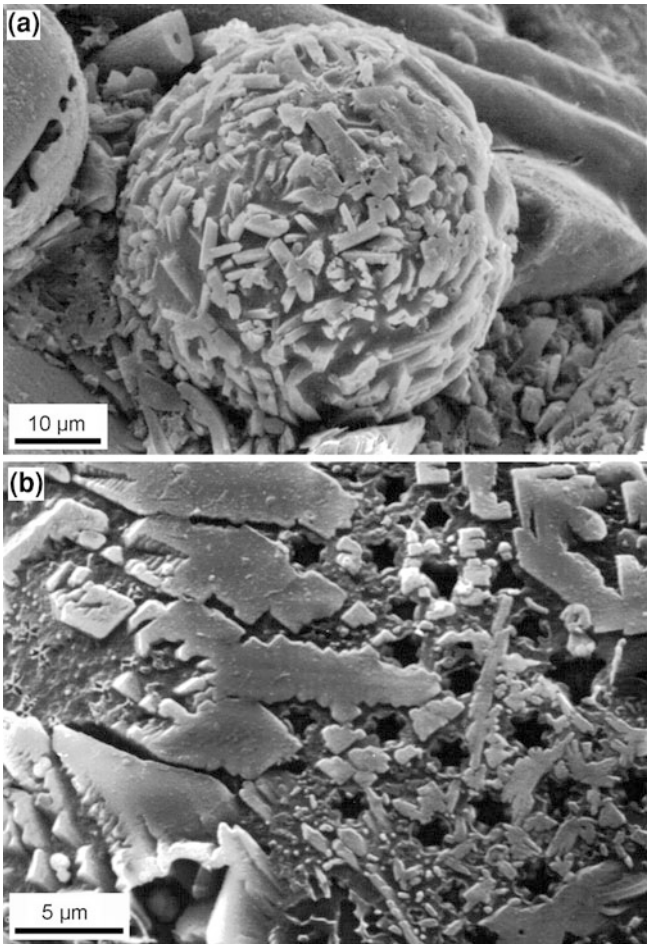

Fig. 3.11 Crystalline textures on the surfaces of clinopyroxene-bearing (cpx) spherules. **a** Scanning electron microscope (SEM) image of a small cpx spherule in the test of an agglutinated foraminifera. Lath-like crystals (*light gray*) stand out in relief above the glass matrix (*darker gray*). The cpx spherule is from Deep Sea Drilling Project Site 166 in the central equatorial Pacific Ocean. **b** SEM image of a portion of the surface of a cpx spherule removed from an agglutinated foraminiferal test. Clinopyroxene microlites (*light to medium gray*) with skeletal textures stand out in relief. Also present on the surface are a number of pits (black with diameter of ~1.5 μm) with six-fold symmetry. The origin of these pits is unknown

Some Precambrian spherules in spherule layers older than ~2.4 Ga have been interpreted as diagenetically-altered microkrystites. In the S3 spherule layer (South Africa; see Sect. 9.2.2), some of the spherules are microkrystites which contain Ni-rich spinels (chromite). The spinel-bearing microkrystites have been flattened parallel to bedding in this layer. They average about 650 μm in diameter, but a few are as large as 1 mm. Thus, they are larger than the cpx spherules and K-T

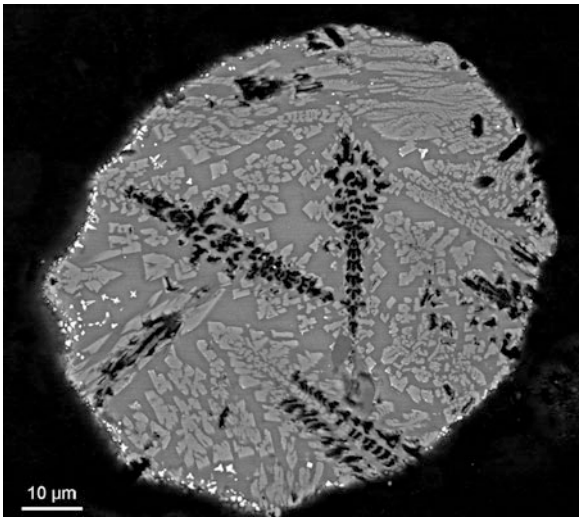

Fig. 3.12 Scanning electron microscope image of a polished interior surface of a clinopyroxene-bearing (cpx) spherule (i.e., microkrystite) from Ocean Drilling Program Site 709C in the western equatorial Indian Ocean. Clinopyroxene microlites (*light gray*) occur in a glass matrix (*darker gray*). Skeletal to octahedral Ni-rich spinel microlites (*white*) are concentrated around the margin (especially on the *left side*). Dark regions are where a more soluble phase has been removed by solution

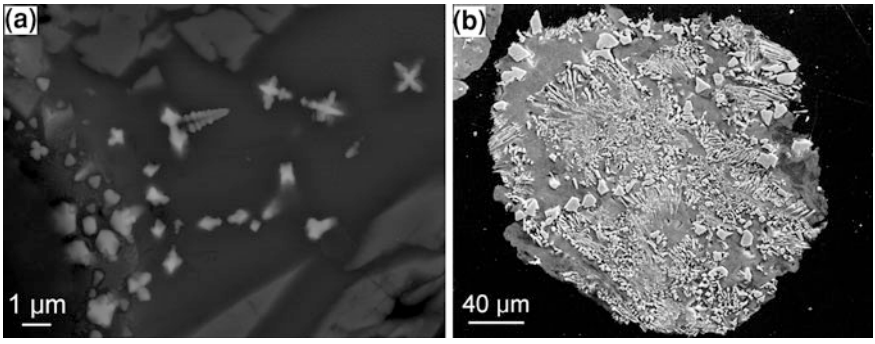

Fig. 3.13 Scanning electron microscope (back-scattered electron mode) images of spinel microlites on polished surfaces of microkrystites. **a** Portion of a dark opaque clinopyroxene-bearing (cpx) spherule (shown in Fig. 3.12) from Ocean Drilling Program Site 709C in the western equatorial Indian Ocean. The image shows dendritic, skeletal, and octahedral spinel microlites (*white*) and larger clinopyroxene microlites (*medium gray*) in a glass matrix (*dark gray*). **b** Octahedral and dendritic Ni-rich spinel microlites in an amorphous iron oxide matrix of a K-T boundary spherule from Petriccio, Italy. **b** is courtesy of Bruce Bohor

boundary microkrystites. Formation as droplets from a vapor plume would seem to explain why they only occur as spheres, but not teardrop or dumbbell shapes. It would also explain the absence of vesicles and lechatelierite particles and the presence of the Ni-rich spinels, which are mostly from the vaporized projectile.

Melt-drop microkrystites may occur in some of the older (>2.4 Ga) spherule layers (see Sect. 10.4). Like the melt-drop microtektites, some of the Precambrian spherules interpreted as being altered microkrystites have rotational (teardrop, dumbbell, disc) as well as spherical shapes, and like the melt-drop microtektites,

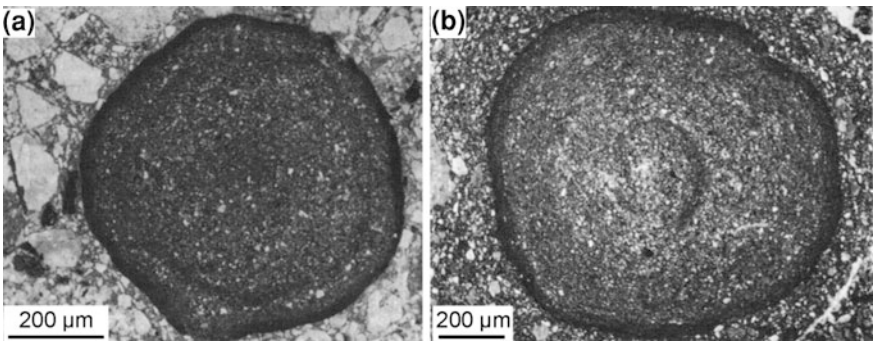

Fig. 3.14 Impact-produced accretionary lapilli in suevite samples from the Ries impact crater, Germany. **a** Accretionary lapillus with a very fine-grained outer layer and a concentric dark layer near the surface. **b** Accretionary lapillus with a core outlined by a dark band and surrounded by two concentric layers (*light* and *dark*) and a very fine-grained, dark outer layer. From Graup (1981), Fig. 14. Copyright (1981), with permission of Elsevier

some contain what appear to be relict vesicles, but do not contain Ni-rich spinels (see, e.g., Sects. 8.2.2.2 and 10.4; Simonson et al. 1998; Sweeney and Simonson 2008). The Middle Paleocene (~60 Ma) Nuussuaq spherules found in western Greenland (Jones et al. 2005a) are another possible example of microkrystites that formed as melt droplets. Many of these spherules have been altered, but, unlike the Precambrian examples, some of these spherules still retain their glassy nature. Some of the unaltered spherules contain crystals of plagioclase, pyroxene, and olivine in addition to dendritic Ni-rich spinel (Robin et al. 1996). Like the Precambrian examples, the Nuussuaq spherules contain vesicles and they are mostly spherical, but rotational shapes are present. Even though they contain Ni-rich spinels, the rotational shapes and presence of vesicles suggest that they were formed as melt droplets rather than as vapor condensate droplets.

Microtektites were originally described as being <1 mm in size (e.g., Cassidy et al. 1969; Glass 1967; Glass et al. 1979); however, splash-form tektite-like glass bodies up to several millimeters in size were recognized in the **North American microtektite layer** in 1987 (Thein 1987) and in the Australasian microtektite layer in 1999 (Prasad and Sudhakar 1999). Prasad and Sudhakar (1999) referred to the millimeter-sized splash forms as minitektites. We propose, therefore, the following size ranges: microtektites (<1 mm), minitektites (1 mm to 1 cm), and tektites (>1 cm). We also propose that microkrystites between 1 mm and 1 cm in diameter be called **minikrystites**; and if such bodies are found that are >1 cm in size, we propose that they be called **krystites**.

Also found in impact ejecta are small rounded bodies formed by accretion; i.e., accretionary lapilli. The impact-produced accretionary lapilli, formed by accretion of fine-grained ejecta particles, generally exhibit concentric layers. Impact-generated accretionary lapilli have been observed in ejecta from several impacts (e.g., Ries Crater, Germany; Chicxulub impact structure, Yucatan Peninsula, Mexico; Alamo Breccia ejecta, Nevada, USA). Impact-generated accretionary lapilli are

generally found close to the source crater, but, occasionally they are found in the more proximal part of a distal impact ejecta layer (e.g., Chicxulub and Sudbury ejecta layers). Accretionary lapilli range in diameter from <1 mm to 3 cm or more (Graup 1981; Warme et al. 2002; Schulte and Kontny 2005; Guillemette and Yancey 2006). Most are spherical, but some are more irregular in shape. They generally have a distinct core, which is surrounded by concentric layers of accreted grains (Fig. 3.14). The core is often coarser grained than the outer layers. The layering is generally visible due to variations in grain size. The long axes of the grains in the layers are preferentially aligned tangentially to the outer surface. Occasionally some of the grains in the lapilli exhibit evidence of shock metamorphism (Graup 1981; Warme et al. 2002; Addison et al. 2005). The grains may be composed of silicate minerals or carbonate phases or both depending on the nature of the target rock. The outermost layer is sometimes finer grained than the interior layers. Impact-produced accretionary lapilli are similar in appearance, internal structure, and mode of formation to volcanic accretionary lapilli. Formation of the accretionary lapilli appears to be facilitated by the presence of condensed water within the ejecta cloud or plume (Fisher and Schmincke 1994; Warme et al. 2002; Burns et al. 2003). Turbulence or changing conditions within the ejecta cloud can cause changes in the size of the accreted grains resulting in the observed concentric layering.

French and Koeberl (2010) stated, "There are several major problems in attempting to use spherules as independent evidence of meteorite impact events." According to them these are: 1) spherules alone do not provide diagnostic evidence of origin by impact, 2) many distal ejecta spherule layers do not contain grains that exhibit unambiguous shock metamorphic effects, 3) the spheroidal shape by itself is not a unique indicator of impact or even melting and 4) there are many naturally-occurring and artificial spheroidal objects with similar sizes to impact-generated spherules. We agree that finding spherules in a stratigraphic layer does not necessarily indicate that the layer is an impact ejecta layer; it must be demonstrated that the spherules are impact-generated spherules. However, that is not always easy to do as there are many kinds of naturally occurring and man-made spherules that can be, and sometimes have been, mistaken for impact spherules (for further discussion see below and Sect. 3.5). Most unaltered silicate glass impact spherules (e.g., Cenozoic microtektites) contain lechatelierite. However, the spherules in most impact spherule layers have been altered and the glass and other silicate phases have been replaced by other phases (e.g., the Cretaceous-Tertiary boundary spherules, the Late Triassic spherules in SW England, and all the Precambrian spherules). Most of the diagenetically-altered impact spherules have relict textures indicating quenching from a high-temperature melt and/or they contain Ni-rich spinels suggesting a meteoritic component. Such spherules can, and have been, identified as impact spherules on their own. The origin of most of these spherule layers has been supported by geochemical evidence of a meteoritic component (e.g., Ir, PGEs, Cr isotopes). Most, but not all, Cenozoic impact spherule layers have shock metamorphosed grains associated with them. On the other hand, shock metamorphosed grains have not been identified in most

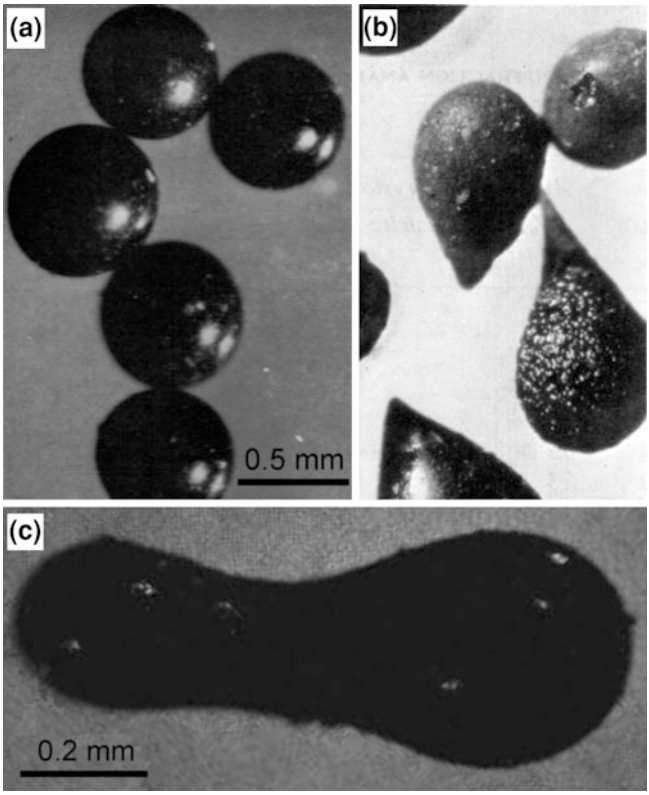

Fig. 3.15 Basaltic volcanic spherules from Deep Sea Drilling Project Site 32 in the northeastern Pacific. **a** Shiny black spheres. **b** Teardrop-shaped volcanic spherules. **c** Dumbbell-shaped volcanic spherule formed by rapid rotation while still liquid. **a** and **b** are from von der Borch (1971), Figs. 4a and 4c, respectively. Copyright (1971), with permission of Elsevier. **c** is from von der Borch (1970)

Precambrian spherule layers. We believe that shocked grains should be associated with all major spherule layers (see Chap. 10) and that the apparent absence of shocked grains is the result of diagenesis and/or low- to medium-grade metamorphism which destroyed or obscured some or all of the more commonly identified shock effects. However, a high-pressure polymorph of rutile, TiO_2II, has recently been found in several Neoarchean spherule layers (Smith et al. 2010). Evidence of shock metamorphism may eventually be found in some of the older Precambrian (Paleoarchean) spherule layers.

3.2.1.2 Other Naturally-Occurring Spherules

Naturally-occurring spherules can be formed in a variety of ways including: vulcanism, atmospheric ablation of meteorites (**cosmic spherules**), bio-precipitation

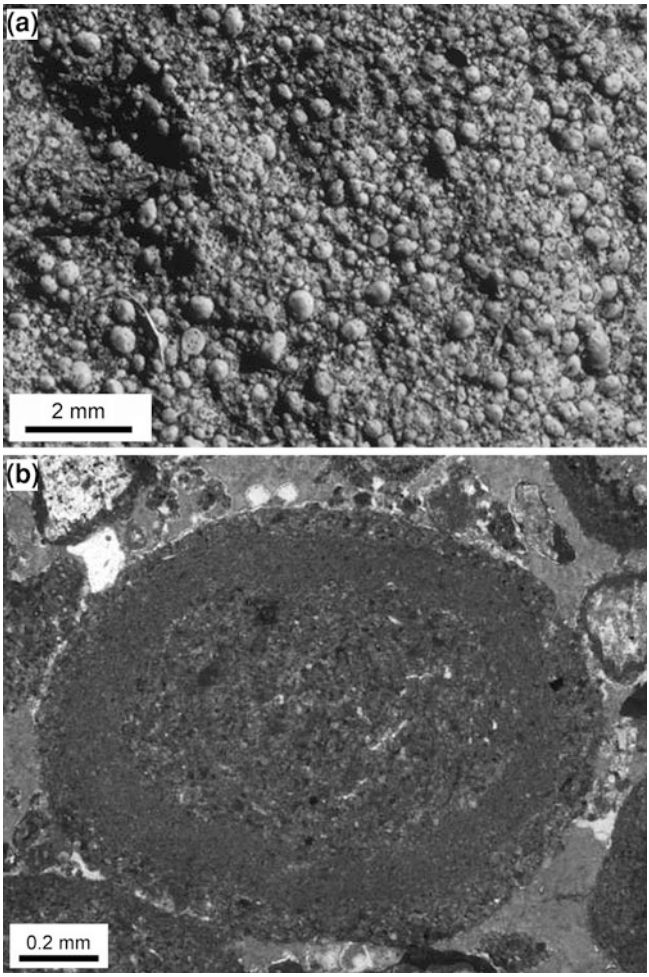

Fig. 3.16 Volcanic accretionary lapilli. **a** Accretionary lapilli-rich layer in the Tumbiana Formation in the Hamersley Basin in Western Australia. The Tumbiana Formation is stratigraphically beneath the Jeerinah Formation, which contains an impact spherule layer (see Sect. 8.2.6). **b** A polished section of an accretionary lapillus from the Tumbiana Formation showing the particulate nature and concentric growth bands. Note the lack of crystallization or devitrification textures. **a** and **b** are from Simonson (2003a), Figs. 1b and 9a, respectively

(**ooids**), biological processes (e.g., insect egg cases, microfossils), diagenesis (e.g., vesicle fillings, **framboids**, concretions, **pyrobitumen spherules**). In addition, rounded mineral grains can be mistaken for spherules. Identification of impact spherules is not always easy, especially if they have been diagenetically altered as is the case for spherules in most of the older spherule layers. Many of the above objects have at one time or another been mistaken for impact spherules.

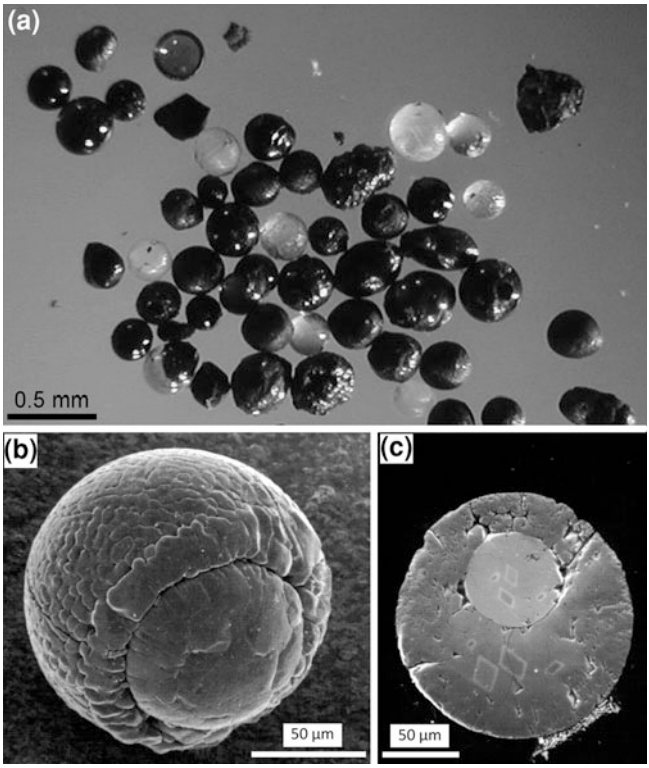

Fig. 3.17 Micrometeorites and cosmic spherules. **a** A group of micrometeorites/cosmic spherules recovered by melting ice at the South Pole. Most of the polar micrometeorites/cosmic spherules are glass- or stony-types; iron-types only make up 1–2 %, compared to 50 % or more in deep-sea sediments. Most of the glass- and stony-types have chondritic compositions. Courtesy of Susan Taylor. **b** A scanning electron microscope (SEM) image of a magnetite cosmic spherule with a large protruding Ni-rich metallic core recovered from deep-sea sediments. **c** An SEM image of a polished section of the iron cosmic spherule in **b**. The metallic core contains ~21 wt % nickel. Diamond shapes on the polished surface of the spherule are areas scanned by the electron beam

Volcanic fire fountaining can produce a rain of liquid droplets that quench in the atmosphere to form glassy bodies (spherules; Fig. 3.15; Wright and Hodge 1965; Heiken 1972; Melson et al. 1988) called volcanic lapilli, if they are between 2 and 64 mm in size. These volcanic spherules are generally spherical, but rotational shapes can also occur. They contain vesicles, and microlites and/or crystallites, but not lechatelierite. They have igneous (often basaltic) compositions and high water contents (up to several weight percent). Magma has time to become well-mixed and homogenized prior to eruption. Thus, volcanic spherules from a given eruption exhibit both inter- and intra-compositional homogeneity.

Volcanic accretionary lapilli consist of a core or nucleus surrounded by concentric layers of volcanic ash (Fig. 3.16). They form by the addition (accretion)

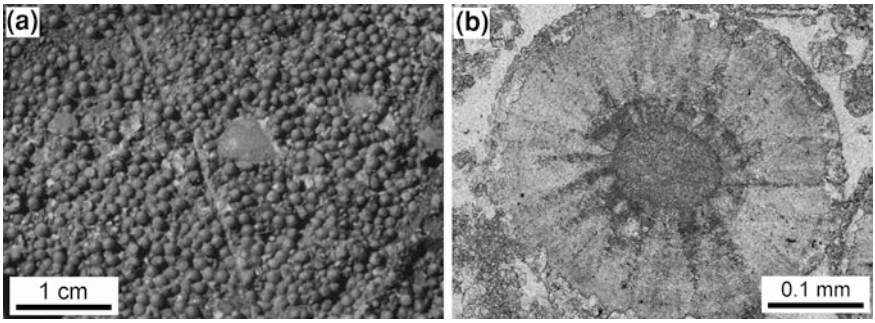

Fig. 3.18 Ooids. **a** Bedding surface of a layer of silicified ooids in the Carawine Dolomite in the Hamersley Basin, Western Australia. **b** Dolomite ooid from the Carawine Dolomite showing both radial texture and concentric growth bands around a coarser-grained nucleus. Note that the radial texture is due to fibrous fans which diverge out from the core instead of in from the edge as seen in some diagenetically-altered Cretaceous-Tertiary and Precambrian impact spherules. **a** and **b** are from Simonson (2003a), Figs.1c and 9c, respectively

of concentric layers of moist ash around a central nucleus. Volcanic accretionary lapilli are found close to their source and are associated with other volcanic ejecta.

Cosmic spherules are generally ablation droplets off meteorites which form as the meteorites traverse the atmosphere, initially traveling at cosmic velocity. However, some cosmic spherules may be micrometeorites that survived their flight through the atmosphere. In general, cosmic spherules consist of magnetite with or without Ni-rich metallic iron cores or silicate (glass and olivine) plus magnetite (Fig. 3.17). In addition, a small percent of cosmic spherules are Fe-rich glassy spherules, generally consisting of magnetite in a glass matrix (Taylor and Brownlee 1991; Taylor et al. 2000). Most cosmic spherules are magnetic. They are generally $<$100 μm in diameter, but can be larger (several hundred micrometers and rarely up to 1–2 mm) (Taylor and Brownlee 1991; Maurette et al. 1987). They have meteoritic compositions and do not generally occur in teardrop or, especially, dumbbell shapes; nor do they contain vesicles. In general, they occur in very low concentrations throughout the geologic column and, unlike impact ejecta, do not usually occur in discrete layers, although they can be concentrated in layers with extremely low accumulation rates.

Ooids (Fig. 3.18) are small rounded accretionary bodies with diameters generally between 0.5 and 1 mm. They form by precipitation in successive concentric layers, generally around a nucleus. Ooids usually have aragonite/calcite composition; however, in ancient rocks the ooids may have been replaced by another phase (silica for example) and the internal concentric layering may not be preserved. They have generally spherical, but not rotational, shapes although two ooids cemented together might look like a dumbbell.

Some calcareous, siliceous, and Ca-phosphate microfossils can superficially resemble impact spherules. An example of a spherical calcareous microfossil is the foraminifera taxa *Orbulina* (Fig. 3.19c), which can be up to $\sim$1 mm in diameter.

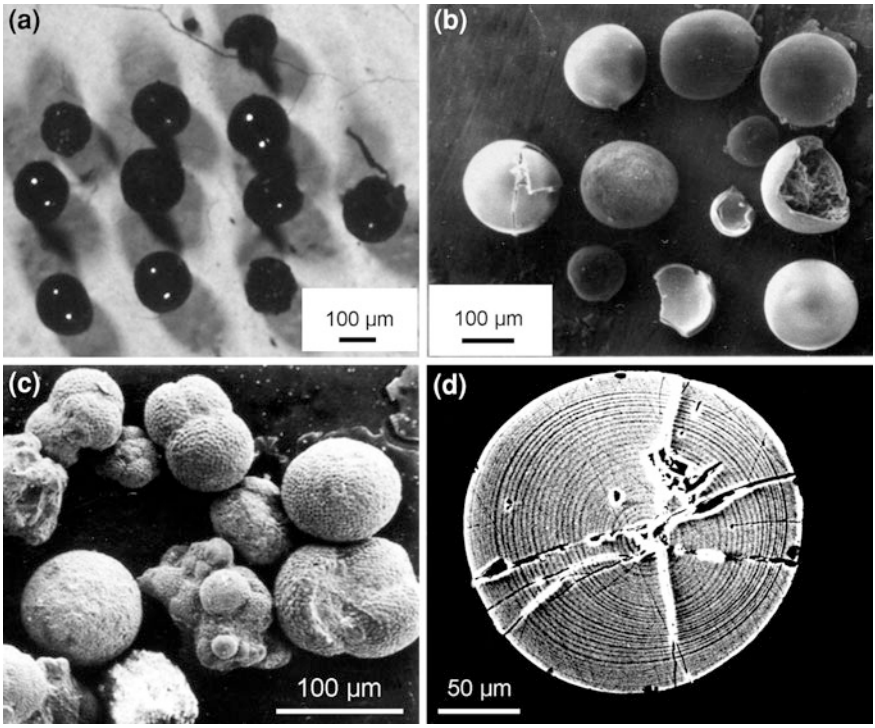

Fig. 3.19 Spherules of biogenic origin. **a** Optical microscope image of hollow spheres with organic walls (probably insect egg cases) recovered from the Cretaceous-Tertiary (K-T) boundary section near Gubbio, Italy. **b** Scanning electron microscope (SEM) image of spheres similar to those in A collected from the K-T boundary clay layer in the Bottaccione section near Gubbio. Note the hollow nature of one of the spheres that is broken and the fragment of another shell. **c** An SEM image of some Miocene planktonic foraminifera tests recovered from above the K-T boundary in the Bottaccione section near Gubbio. The spherical tests are probably *Orbulina*. **d** An SEM image of a polished section of a calcium phosphate spherule recovered from Early to Middle Devonian carbonate rocks (Telengit Suprahorizon) collected near Slair, Russia, showing well-defined thin concentric layers. It and other spheres were found in association with conodonts and are probably conodont pearls. The sample was provided by Emile Izokh. The images in **a**, **b**, and **c** are courtesy of Alessandro Montanari. **b** and **c** were used in Fig. 5.7.6.3 in Montanari and Koeberl (2000)

Radiolaria are a siliceous microfossil. Most produce silica (opaline) skeletons, which in some taxa are spherical (e.g., some actinommids) and can be several hundred micrometers in diameter. However, radiolarian skeletons are not solid, but rather consist of an open mesh-like structure. Calcium phosphate microfossils, called conodont pearls, are also spherical (Fig. 3.19d). They range from transparent yellow to translucent brown to opaque black and are up to ~700 µm in diameter. They are always found in association with conodonts. Other biogenetically-produced spherule-like objects are insect egg cases (Fig. 3.19a, b), which in some cases can be spherical and can have a translucent yellow to brown color.

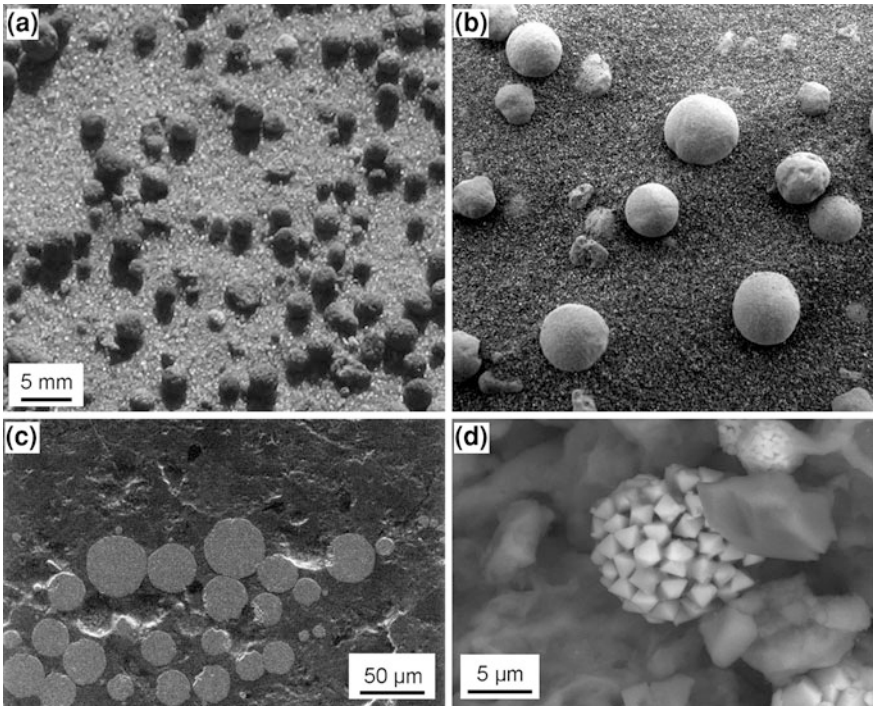

Fig. 3.20 Hematite concretions and pyrite framboids. **a** Millimeter-size hematite concretions in the Paria Wilderness of Vermillion Cliffs National Monument on the Utah/Arizona border, USA. Courtesy of Marjorie Chan. **b** Millimeter-size hematite concretions found on the Martian surface by the rover Opportunity. These spherules were nicknamed "blueberries" when first observed and some investigators suggested that one possibility was that they were impact spherules. After additional studies, it was concluded that the spherules are hematite concretions. The image is uncalibrated and no scale was given, but the spherules are typically between 4 and 6 mm in diameter (Squyres et al. 2004). Image provided by NASA/JPL/Cornell/USGS. **c** Scanning electron microscope (SEM) image of a polished section of a mudstone showing pyrite framboids (*light gray circular regions*). The mudstone sample is from the Late Cretaceous Hakobuchi Group, central Hokkaido, Japan. Courtesy of Hisanari Sugawara. **d** SEM image of a framboid in a rock fragment from Buncar Spring, Romania. Note that the framboid is composed of numerous small crystals of uniform size. Courtesy of Rachel Schelble

Detailed studies will show that they are organic material and that they are hollow, unless filled with fine-grained material or a mineral precipitate. Insect egg cases were misidentified as impact spherules in outcrop samples taken near the K-T boundary layer, where their abundance above and below the K-T boundary layer was used in an attempt to "show" that spherules were not confined to the K-T boundary layer (Montanari 1986).

Precipitation during sedimentation and/or diagenesis can produce a variety of spherule-like bodies, such as concretions and framboids, which, at first glance, could be confused with impact spherules (Fig. 3.20). Concretions (Fig. 3.20a) are

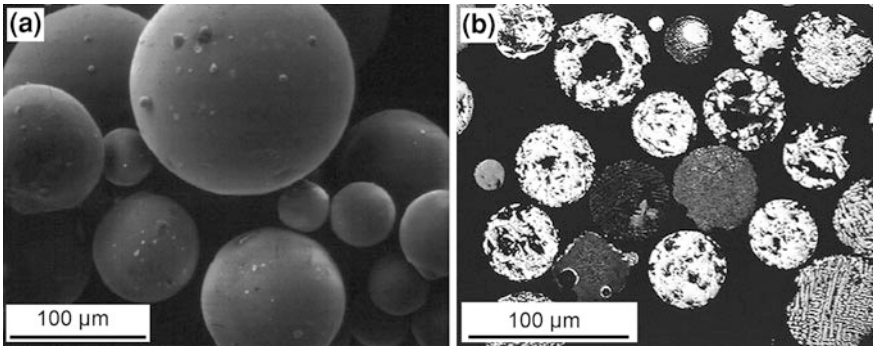

Fig. 3.21 Fly ash spheres. **a** Scanning electron microscope image of fly ash spheres. Note the smooth surfaces with some smaller particles attached to the surfaces, but without pits or grooves. Courtesy of James C. Hower. **b** Reflected light optical microscope image of polished sections of small, mostly solid, spinel-bearing fly ash spheres exhibiting a variety of crystalline textures. The spinel is most likely magnetite. Some of the darker spheres are composed of silicate glass and contain vesicles. These fly ash spheres are from a power plant that was burning high-sulfur, high-volatile C Illinois Basin coal. **b** is from the "Petrographic Atlas: Fly Ash" prepared by James C. Hower <http://mccoy.lib.siu.edu/projects/crelling2/atlas/> Frame F83

concentrations of mineral matter in sedimentary rocks that fill the pore space and produce bodies that are often harder and more resistant to weathering than the surrounding rock. They are generally ovoid or spherical in shape and can range in size from microscopic to a meter or more in diameter. They can be composed of a wide variety of phases including calcite, amorphous and/or microcrystalline silica (such as chert and flint), iron oxides or hydroxides (such as goethite or hematite), just to name a few. Sand-sized spherules were observed by the rover, Opportunity, on Mars (Fig. 3.20b). One of the first suggested hypotheses was that these spherules might be impact spherules, but after their compositions were determined it was generally accepted that they were hematite concretions (Squyres et al. 2004).

Framboids (Fig. 3.20c, d) are spherical masses of microcrystallites. They are generally composed of pyrite, but sometimes consist of greigite (Fe_3S_4), magnetite, or limonite. The microcrystallites produce a raspberry-like surface on the framboids (Fig. 3.20d). Framboids are generally quite small (<10 μm), but can be as large as ~100 μm in diameter.

High-temperature diagenesis of petroleum can produce pyrobitumen, which can occur as shiny black spherules or globules. The pyrobitumen spherules are relatively hard and break with conchoidal fracture. They can be associated with larger irregular masses of pyrobitumen.

Rounded quartz grains were misidentified as microtektites in DSDP Site 242 (e.g., Core 10, Section 4, and Core 15 Section 1; Keller et al. 1983). Although the overall shapes of the grains are spherical, detailed studies with an optical microscope revealed the presence of crystal faces and under cross polarizers they are birefringent and clearly are not glass (Glass et al. 1985).

Table 3.4 Chemical composition of fly ash (modified after Openshaw et al. 1992)

Oxide	Range (wt %)	Average (wt %)	Standard deviation	No. of analyses
SiO_2	2.2–68	44	13	58
TiO_2	0.5–2.6	1.3	0.5	39
Al_2O_3	3.4–39	23	6.5	60
Fe_2O_3	3.6–29	11	6.5	58
MnO	0–0.2	0.1	0.1	14
MgO	0.4–13	2.7	2.7	58
CaO	0.2–31.0	8.2	8.0	58
Na_2O	0.2–8.0	1.8	2.0	50
K_2O	0.2–8.1	2.0	1.8	49
P_2O_5	0.1–6.0	0.8	1.7	34
SO_3	0.1–7.3	1.6	1.9	47
C	0.1–26	4.0	7.3	12

3.2.1.3 Manmade Microscopic Spherical Glass Objects

There are a variety of microscopic manmade products that have spherical shapes (e.g., glass beads used in reflective paint, **fly ash**), and some have been mistaken for impact spherules, including microtektites. The most common type of manmade glass is the so-called soda lime glass. It generally contains about 70–75 wt % silica, 5–10 wt % CaO (or lime), 1–5 wt % MgO, and 13–17 wt % Na_2O (or soda). The high Na_2O content would be very difficult to produce by a random impact onto the Earth's surface. Other common manmade glasses are lead glass (sometimes inaccurately referred to as lead crystal), which is a silicate glass containing 20–35 wt % PbO; and borosilicate glass with 10–25 wt % B_2O_3.

Millimeter-sized, transparent, colorless, artificial glass spheres are added to paint used on road signs and highway markings to make them reflective at nighttime when headlights shine on them. Thus, outcrops along highways can be contaminated with glass beads from highway signs and road markings. These glass beads are mostly spherical; no dumbbell (except where two spheres fused together), teardrop, or disc shapes have been observed. Typical sizes generally range between ~200 and 800 μm in diameter (http://www.virginiadot.org/business/resources/Materials/MCS_Study_Guides/bu-mat-PaveMarkCh2.pdf; accessed 01/02/2012). They generally have shiny smooth surfaces without pits or grooves produced by solution; although they can have pits formed by abrasion, especially if they are from paint used in highway markings. These glass beads commonly have a soda-lime composition, but glass beads with other compositions are also used. The soda-lime glasses have a refractive index of ~1.50; beads with other compositions can have refractive indices as high as 1.90.

Another possible outcrop contaminant is fly ash, which is formed during combustion of coal in coal-burning power plants. As of 2005 more than 150 million tons/year were being produced globally (Matamoros-Veloza et al. 2005). Today most of the fly ash is collected by electrostatic or mechanical precipitation

Table 3.5 Characteristics that can be used to distinguish between impact spherules and other types of spherules

Spherule type	Shape	Surface	Petrography				Composition		
	(splash forms)[a]	(hypervelocity impact pits)	Vesicles	Lechatelierite	Primary crystallites[b]	Ni-rich spinels	Linear comp. trends[c]	Low water content	Low Fe^{3+}/Fe^{2+}
Impact spherules									
Microtektites									
Melt[d]	yes	sometimes	common	common	no	no	yes	yes	usually
Condensate[e]	no?	?	no?	no	no	no	?	?	no?
Microkrystites									
Condensate[f]	no	?	no	no	yes	common	ambiguous	?	no?
Melt[g]	yes	?	yes	no?	yes	yes?	yes?	yes?	yes?
Impact-generated accretionary lapilli									
Accretionary[h]	no	no	no	no	no	no	no?	no?	no?
Other naturally-occurring spherules									
Volcanic splash forms	yes	no	yes	no	yes	no	no	no	no
Accretionary volcanic lapilli	no	no	no	no	no	no	no	no	no
Ooids	no	no	no	no	no	no	no	no	no
Cosmic	no	no?	no	no	no	no	no	no	no
Biogenic[i]	no	no	no	no	no	no	no	no	no
Concretions	no	no	no	no	no	no	no	no	no
Framboids	no	no	no	no	no	no	no	no	no
Pyrobitumen	no	no	no	no	no	no	no	no	no

(continued)

Table 3.5 continued

Spherule type	Shape (splash forms)[a]	Surface (hypervelocity impact pits)	Petrography				Composition		
			Vesicles	Lechatelierite	Primary crystallites[b]	Ni-rich spinels	Linear comp. trends[c]	Low water content	Low Fe^{3+}/Fe^{2+}
Artificial									
Fly ash	no	no	yes	yes?	yes	yes	no?	no	no?
Glass spheres[j]	rarely	rare	yes	no	no	no	no	no	no

A stand-alone question mark means we have no data. A question mark after a "yes" or "no" means this is what we expect, but we have very little data

[a] Includes teardrop, dumbbell, and disc shapes in addition to spheres

[b] Crystallites and microlites formed by crystallization from the melt droplet that solidified to form the spherule

[c] Plots of major oxides versus silica form linear compositional trends. Ambiguous means that some oxides versus silica form linear trends, but there is a great deal of scatter

[d] Microtektites formed as melt droplets include the Australasian, Ivory Coast, and North American

[e] Some microtektites found in the Late Eocene cpx spherule layer may have formed as condensate droplets

[f] Microkystites believed to have formed as condensate droplets include the Late Eocene cpx spherules and the K-T boundary layer microkrystites

[g] Phanerozoic microkrystites formed from melt are not known, but there may be some Precambrian examples

[h] Impact-generated accretionary lapilli sometimes contain shock metamorphosed mineral fragments

[i] Includes spherical forms of radiolarian, foraminifera, insect egg cases, and conodont pearls

[j] Glass spheres like those used in reflective signs and road markings

in the chimneys of the power plants, but in the past fly ash was not collected and was deposited over large areas of the surrounding country. Some studies have shown that fly ash is widespread and can even be used as a historical or geological tracer (Rose 1996; Olson and Jones 2001; Jordanova et al. 2004). Spherules, believed to be of industrial origin, were found in all surface sediment samples in transects across the North Atlantic (Folger 1970).

Fly ash particles are mostly (up to at least 95 %) spherical and range in diameter between <1 and 200 μm (Fig. 3.21a), although most are between 2 and 20 μm diameter (Openshaw et al. 1992; Kutchko and Kim 2006). Fly ash is formed by melting of mineral matter in the coal. Fly ash is composed primarily of silicate glass; but crystalline phases can also be present, including: quartz, mullite, hematite, magnetite, magnesioferrite, maghemite, and even traces of additional spinel phases such as trevorite and magnesiochromite (Brownfield et al. 1999). These mineral phases can exhibit a variety of quench textures (Fig. 3.21b). Vassilev and Vassileva (1996) suggested that some of the quartz has been fused to form silica glass. Thus, it appears that some fly ash spheres may contain lechatelierite particles. Some fly ash spheres contain vesicles and some are even hollow. The hollow spheres tend to be larger and can make up as much as 15–20 % by volume of the fly ash (Openshaw et al. 1992; Kutchko and Kim 2006).

Magnetic material can make up to ~18 % of the fly ash and the magnetic component is enriched in Co, Cr, and Ni by factors of 2 to 5 over the nonmagnetic components (Vassilev and Vassileva 1996; Vassilev et al. 2004), which have Co, Cr, and Ni contents close to the average for the upper continental crust (Vassilev et al. 2004). This would suggest an extraterrestrial component, if their origin were not known. However, they are also enriched in elements such as Mn, Zr, As, and Zn (Vassilev et al. 2004), which is not compatible with meteoritic contamination. Fly ash is generally heterogenous and consists primarily of SiO_2, Al_2O_3, Fe_2O_3 and CaO, but it also contains minor amounts of TiO_2, MnO, Na_2O, K_2O, and SO_3 (Table 3.4).

The chemical composition and mineralogy of fly ash varies with the type of coal that was burned to produce it as well as the conditions of combustion. There are two main classes of fly ash: Class F and Class C (ASTM Standard C618 2008). Class F fly ash is formed primarily by the combustion of anthracite and bituminous coal. This fly ash contains a minimum of 70 wt % $SiO_2 + Al_2O_3 + Fe_2O_3$ and has low CaO content (<10 wt %). Class C fly ash is produced by the combustion of lignite or sub-bituminous coal. It contains a minimum of 50 wt % $SiO_2 + Al_2O_3 + Fe_2O_3$ and has high CaO content (generally >20 wt % and as high as 40 wt %).

3.2.1.4 Identification of Impact Spherules

The presence of impact spherules can be used to support the hypothesis that a stratigraphic layer is a distal impact ejecta layer; but there are numerous kinds of spherules with a variety of origins (Table 3.5). Therefore, in the absence of evidence of a meteoritic component or presence of grains exhibiting evidence of

shock metamorphism, it cannot be assumed that all spherule layers have an impact origin. It is necessary to demonstrate that the spherules in question are indeed impact spherules. If the spherules have not been altered, then the task should be relatively easy. However, the major phase in most impact spherules is glass, which is unstable and is usually replaced by other phases in deposits older than Cenozoic and even in some Cenozoic ejecta layers. It must be kept in mind that there are at least four categories or kinds of impact spherules. At the present time, we know of no criterion for identification that applies to all four categories (Table 3.5).

The most obvious characteristic of impact spherules, and the one which first draws the attention of the observer, is their shape. Most impact spherules are spherical in shape (including prolate and oblate forms), but, as previously pointed out, many other naturally-occurring objects can have spherical shapes as well. Microtektites and microkrystites formed as melt droplets can also have rotational shapes such as dumbbells, teardrops, and discs. The presence of these rotational shapes can help distinguish impact spherules formed as melt droplets from most other naturally-occurring spherules except for some volcanic splash forms (Fig. 3.15). Impact spherules formed as condensate droplets only have spherical shapes, although there are some rare agglutinates consisting of two or more spheres fused together.

Many of the other naturally-occurring spherules have surface features that can be used to help distinguish them from impact spherules. For example, concretions often have rough surfaces that easily distinguish them from the smooth or pitted and grooved surfaces of melt-drop microtektites and pyrite framboids are composed of pyrite microlites which give them a strawberry-like texture (Fig. 3.20d). Hypervelocity impact pits (or microcraters) are one surface feature that appears to be unique to melt-drop microtektites and which, might, therefore, be used to distinguish them from other naturally-occurring spherules (e.g., Fig. 3.9f). At the present time, we do not know if hypervelocity impact pits occur on the surfaces of other types of impact spherules.

Vesicles are common in melt-drop microtektites and appear to be present in some melt-drop microkrystites, but they have not been observed in microkrystites or microtektites formed as condensate droplets. The presence of vesicles can be used to distinguish melt-drop microtektites from most other naturally-occurring spherules, with the exception of splash-form volcanic spherules (Table 3.5).

Lechatelierite particles can be used to distinguish melt-drop microtektites from microtektites and microkrystites formed as condensate droplets and from all other naturally-occurring spherules (Table 3.5). However, the absence of lechatelierite particles does not necessarily mean that silicate glass spherules cannot be melt-drop microtektites. Lechatelierite particles are formed by melting of quartz grains. This means that the target rock must contain silt-sized (or larger) quartz grains. If it does not, then no lechatelierite particles can form. On the other hand, if the target rocks don't contain quartz grains, the impact-produced melt will be silica poor and the melt droplets are more likely to undergo partial crystallization to form microkrystites rather than microtektites.

Fig. 3.22 Basaltic impact spherules from the Lonar impact crater, India. Note the teardrop and dumbbell shapes, as well as spheres. Vesicles are exposed on some of the spherules. Courtesy of M. Shyam Prasad

The presence of primary microlites/crystallites can, by definition, be used to distinguish microkrystites from microtektites and from other naturally-occurring spherules except volcanic spherules. However, if Ni-rich spinel microlites are present they will indicate an impact, rather than volcanic, origin for the spherules.

If spherules are unaltered, compositional data (major oxide, trace element, water content, iron oxidation state) can be used to help determine whether or not they have an impact origin (Table 3.5). There is not time for impact melt to be thoroughly mixed and homogenized prior to being ejected. Individual melt-drop microtektites from a given impact can be fairly homogeneous, but as a group they generally exhibit a wide range in composition, depending on variations in composition of the target rock. Major oxide versus silica contents for melt-drop microtektites exhibit linear trends (e.g., Fig. 4.7). On the other hand, igneous magma has time to become well mixed and homogenized prior to eruption. Thus, volcanic spherules from a given eruption exhibit both inter- and intra-compositional homogeneity. This characteristic is utilized when using volcanic ash layers for stratigraphic correlation. Thus, compositional data from volcanic spherules plot in clusters rather than along linear trends. Most other naturally-occurring spherules have restrictive compositions which in most cases can be used to distinguish them from unaltered impact spherules. For example: ooids are composed of aragonite/calcite ($CaCO_3$); many cosmic spherules are composed of magnetite (Fe_3O_4) with

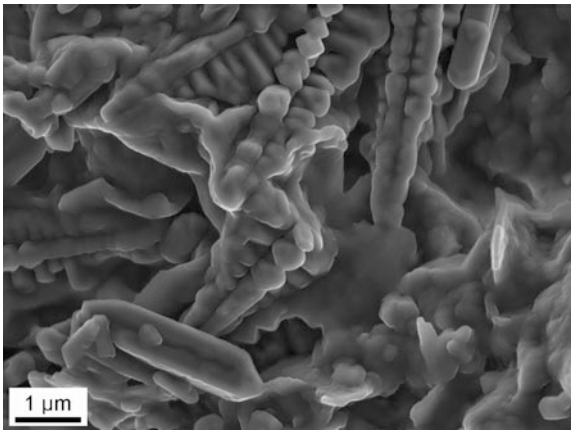

Fig. 3.23 Dendritic spinel microlites on the surface of a flattened, diagenetically-altered cpx spherule from the late Eocene section at Massignano, Italy

or without Ni-Fe metal; spherical biogenic microfossils are generally composed of calcite, silica (SiO_2), Ca phosphate, or organic matter; concretions can be composed primarily of iron oxides or silica; framboids are generally composed of iron sulfide unless replaced by another phase; and pyrobitumen spherules are organic and therefore carbon rich. Deutsch et al. (2010) proposed that some calcite spherules in the K-T boundary in the Gulf of Mexico are primary (unaltered) ejecta formed from carbonate melt. They proposed that it may be possible to develop criteria for distinguishing primary textures in melt-drop carbonate spherules from textures characteristic of alteration and diagenesis using back-scatter diffraction techniques.

Tektites and melt-drop microtektites have low water contents and usually low Fe^{3+}/Fe^{2+} (see Table 4.4). The water contents of tektites and melt-drop microtektites are usually <0.02 wt %. This is at least an order of magnitude lower than the water contents of volcanic glasses. The Fe^{3+}/Fe^{2+} ratios of tektites and melt-drop microtektites are usually <0.2, but some North American microtektites have higher ratios that overlap those of volcanic glasses (Giuli et al. 2008). The reason for the higher Fe^{3+}/Fe^{2+} in some of the North American microtektites is not known. Determining the water content should be a good way to distinguish between impact and volcanic spherules; however, Fe^{3+}/Fe^{2+} may not be as useful as we originally thought. Microkrystites and condensate microtektites may also have low water contents and low Fe^{3+}/Fe^{2+}, but to our knowledge this has not been demonstrated.

Impact-generated accretionary lapilli form close to the source crater and are rare in distal impact ejecta layers. By themselves, it might be difficult to distinguish impact-generated accretionary lapilli from volcanic accretionary lapilli (Table 3.5). However, it should be possible to identify impact-generated accretionary lapilli because of the lack of associated volcanic ejecta and presence of other impact spherules and/or impact ejecta exhibiting evidence of shock metamorphism. Some impact-produced accretionary lapilli contain shock metamorphosed grains – for

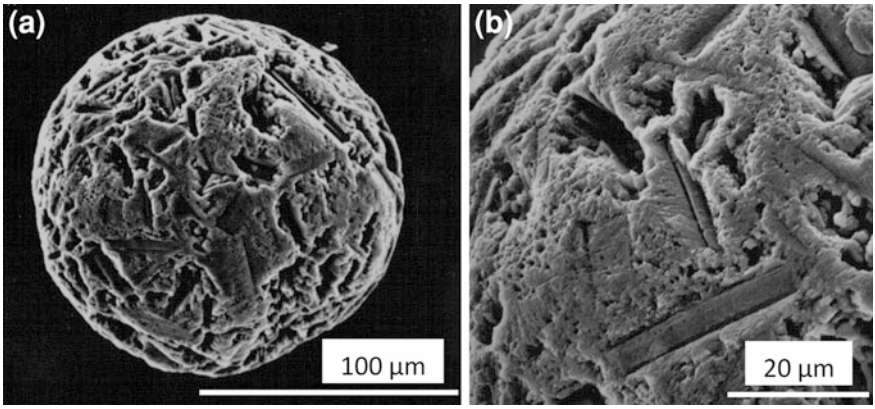

Fig. 3.24 Clinopyroxene-bearing spherules replaced by pyrite. **a** Clinopyroxene-bearing (cpx) spherule replaced by pyrite. Note that the crystalline texture of the cpx spherule has been preserved. Both lath-shaped and dendritic textures are present. **b** Close-up of a cpx spherule replaced by pyrite with lath-shaped crystal outlines preserved. Both **a** and **b** are from Ocean Drilling Program Site 709 in the northwest Atlantic off New Jersey, USA

example some accretionary lapilli found in the Sudbury ejecta layer contain shocked quartz grains with PDFs (Addison et al. 2005).

In summary, unaltered impact spherules should be easy to distinguish from most other naturally-occurring spherules, with the possible exception of volcanic spherules. Melt-drop microtektites can be identified by their characteristic splash forms including rotational shapes, absence of primary microlites/crystallites, presence of lechatelierite, and composition (especially their low water content and reduced iron; Table 3.5). However, as previously mentioned, individual microtektites may not contain lechatelierite and, depending on the nature of the target rock, it is theoretically possible that none of the microtektites in a given layer will contain lechatelierite. Microkrystites, which by definition contain primary microlites/crystallites, can be difficult to distinguish from volcanic spherules since both contain primary microlites/crystallites, but not lechatelierite. Furthermore, melt-drop microkrystites, like volcanic spherules, can have rotational as well as spherical shapes and can contain vesicles. However, the melt-drop microkrystites in a given layer should have a broader range in composition than do volcanic spherules and the compositional trends of melt-drop microkrystites would most likely not fall along igneous compositional trends. On the other hand, melt-drop microkrystites could have close to a basaltic composition depending on the nature of the target rock and percent meteoritic contamination. Although not distal, impact spherules found at the Lonar impact crater in India (Fig. 3.22) have basaltic compositions (Fredriksson et al. 1973; Fredriksson et al. 1978). The Lonar glass spherules can be distinguished from volcanic spherules by the presence of relict inclusions and schlieren and their generally lower water and, perhaps, higher FeO/Fe_2O_3 ratios (Fredriksson et al. 1973; Fredriksson et al. 1978). In addition, some of the spherules are slightly enriched in Ir (Morgan 1978). If present, Ni-rich spinels

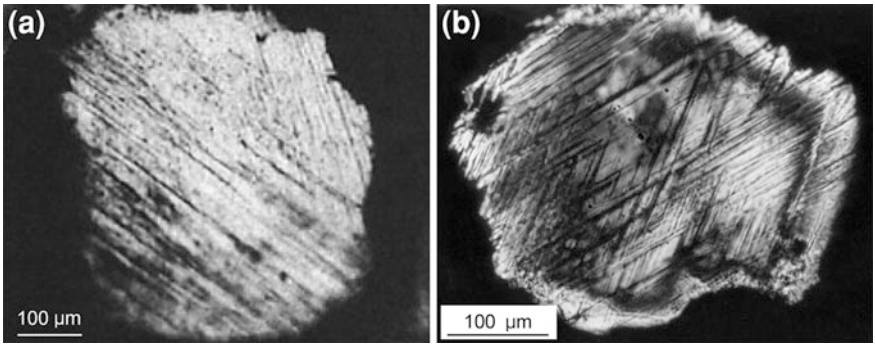

Fig. 3.25 Quartz grains with planar features. **a** Quartz grain from the Toba volcano, Sumatra, showing poorly to moderately well-defined lamellar features. These lamellae were probably produced by explosive volcanism. They lack sharpness and are generally discontinuous and do not meet the definition for planar deformation features (PDFs). From Alexopoulos et al. (1988), Fig. 1c. **b** Shocked quartz grain from the Ames impact structure, Okalahoma, USA, exhibiting two well-defined sets of PDFs, which are sharp and generally continuous. See Fig. 2.21 for other examples of shocked quartz with PDFs. This image was on the Dec. 1996 cover of AAPG Bulletin, vol. 12. Courtesy of Glen Izett

and/or compositional evidence of a meteoritic component in the spherules can be used to distinguish microkrystites from volcanic or most other types of spherules (Table 3.5). Glass spherules of impact and volcanic origin are common in most lunar fines and researchers have developed criteria for distinguishing between them (Delano 1986 and references therein), some of which are the same criteria as those discussed above.

Most impact spherules older than Cenozoic age have been diagenetically altered and the original phases (glass, silicate crystals) have been replaced by other phases such as: smectite, glauconite, K-feldspar, goyazite, calcite, pyrite, stilpnomelane, quartz, chlorite. This makes their identification difficult, especially in the absence of evidence for the presence of a meteoritical component and/or grains exhibiting evidence of shock metamorphism. However, it can be done, at least in some cases. If the shapes have been preserved, diagenetically-altered melt-drop microtektites can be distinguished from most other spherule types by the presence of rotational forms (i.e., teardrops, dumbbells, discs) as well as perfect spheres and oblate and prolate spheres. Depending on the nature of the alteration, evidence of internal vesicles may likewise be preserved (Simonson 2003a). However, volcanic lapilli can also occur as splash forms (i.e., spheres, teardrops, dumbbells) and contain vesicles. Thus, it may be difficult to distinguish between volcanic spherules and impact spherules, if they have been diagenetically altered. However, if the altered spherules contain preserved crystalline textures indicating rapid quenching, then they are not altered microtektites; rather they may be altered volcanic spherules or microkrystites. The presence of Ni-rich spinel microlites would indicate that the spherules are microkrystites. Fortunately, spinel is a stable phase and can generally withstand weathering, diagenesis, and low temperature

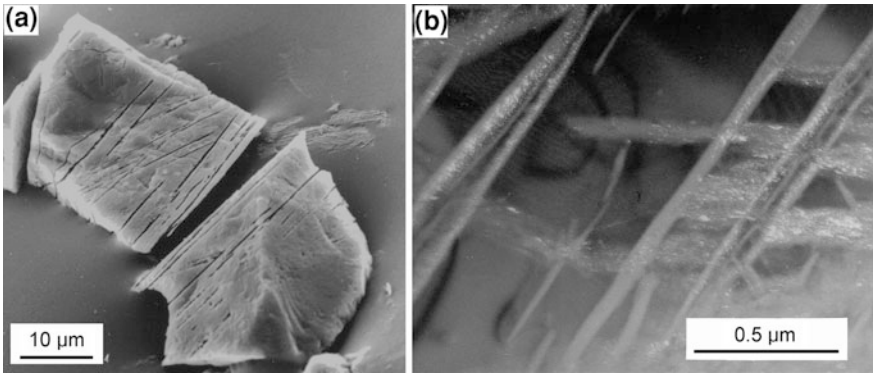

Fig. 3.26 Shocked quartz with planar deformation features (PDFs). **a** Scanning electron microscope image of a shocked quartz grain etched with HF. The grain is from the Cretaceous-Tertiary boundary at Deep Sea Drilling Project Site 596 in the South Pacific. Etching preferentially removed the glass in the lamellae to reveal two sets of PDFs. Courtesy of Bruce Bohor. **b** Transmission electron microscope image of PDF lamellae in shocked quartz from the late Eocene clinopyroxene-bearing spherule layer at Massignano, Italy. The amorphous lamellae are light-colored in this image. Bright spots in the lamellae originate from tiny crystallites reflecting under Bragg conditions. From Langenhorst (1996), Fig. 1d

metamorphism. This makes Ni-rich spinel especially useful in recognizing older, diagenetically-altered microkrystites.

Although more difficult than for unaltered spherules, the impact origin of diagenetically-altered spherules can be established. For instance, Late Eocene spherules found at Massignano, Italy, have been replaced by clay and flattened by the overburden. However, based on their stratigraphic age and the presence of Ni-rich spinels in the pancake-shaped spherules and on their surfaces (Fig. 3.23; Pierrard et al. 1998) these spherules were interpreted to be diagenetically-altered microkrystites belonging to the Late Eocene cpx spherule layer (Glass et al. 2004a). Likewise, pyrite spherules recovered from Late Eocene sediments in the NW Atlantic off New Jersey have been identified as diagenetically-altered cpx spherules (Glass et al. 1998). These spherules not only retained the shape of the cpx spherules, but they also preserved the crystalline structure of the cpx microlites and have, therefore, different surface features (compare Fig. 3.20d with Fig. 3.24) and internal structures than pyrite framboids. Numerous diagenetically-altered Precambrian spherule layers (>2.4 Ga old) have been identified as having a probable impact origin based on their character and geological context and on the nature of the spherules. The occurrence of a coarse spherule-bearing layer in an otherwise fine-grained, slowly deposited sedimentary sequence suggests a sudden catastrophic event (Hassler and Simonson 2001; Simonson 2003a) and a high abundance of spherules (>10 vol %) to the exclusion of formerly molten, irregularly-shaped (e.g., shard-like) particles is suggestive of impact, rather than volcanic, origin (Simonson 2003a). The spherules are generally spherical, but in most of the spherule layers rotational shapes are also present. Relict crystalline

textures in some indicate rapid cooling and some contain relict vesicles; and, as previously mentioned, spherules in one of the layers contain Ni-rich spinels. Shock metamorphosed grains are found in a few of these older Precambrian spherule layers, but are apparently absent from most. However, geochemical anomalies associated with these spherule layers indicate the presence of a meteoritic component and support an impact origin.

The identification of a spherule layer at just one site or location can be problematic, especially if the spherules have been diagenetically altered and the layer does not contain evidence of a meteoritic component or shock metamorphism. It is important to demonstrate that the spherule layer can be found in different environmental and diagenetic settings as well as at the same stratigraphic level over a large area, involving distances of hundreds or thousands of kilometers. This will help rule out other possible origins for the spherules and help support an impact origin for the spherule layer.

Manmade glass spherules put in paints used for highway markings and road signs can superficially resemble microtektites, but can be distinguished from them by their high Na_2O contents. Fly ash is a more widespread artificial contaminant. Because fly ash spheres are composed primarily of silicate glass and because of the presence of quench textures and Ni-rich spinels (e.g., trevorite), it is possible that these spherules could be mistaken for microkrystites. The generally high SO_3 content (average of $\sim$1.6 wt %) should be useful in distinguishing fly ash spheres from impact spherules. The best way to deal with artificial contaminants is to avoid them.

3.2.2 Shock Metamorphism

The most convincing evidence for an impact origin of a suspected distal impact ejecta layer is the confirmation of the presence of shock metamorphosed grains. Description and illustrations of most of the known shock metamorphic effects are found in Sect. 2.3. Many of these shock metamorphic effects have been observed in distal impact ejecta layers. The best diagnostic indicators of shock metamorphism are: PDFs (primarily in quartz, but also in feldspar), diaplectic glasses, high-pressure phases (especially coesite, stishovite, reidite, TiO_2II), and decomposition (e.g., breakdown of zircon to baddeleyite plus SiO_2). The most often recognized shocked grains are quartz grains with multiple sets of PDFs. An impact origin for the K-T boundary layer was proposed in 1980 based on elevated siderophile element contents (Alvarez et al. 1980), but the impact origin was highly controversial until 1984 when shocked quartz grains with multiple sets of PDFs were discovered in the K-T boundary layer at Brownie Butte, Montana (Bohor et al. 1984). These shocked quartz grains also contained traces of stishovite, which, along with coesite, is another commonly used indicator of shock metamorphism.

Care must be taken in identifying planar features in quartz as PDFs since they can be confused with non-impact planar microstructures formed by normal

geological processes (Fig. 3.25). These include deformation lamellae (Böhm lamellae), growth lines, extinction bands, deformation bands (kink bands), and sets of open or healed fractures (French and Koeberl 2010 and references therein). Shock-produced deformation lamellae (PDFs) are sharp, thin (<1 μm thick), parallel, closely spaced (1–4 μm in highly shocked grains), and tend to extend continuously across the entire grain (Alexopoulos et al. 1988). In addition, they generally occur in three or more sets per grain, they are confined to individual grains (i.e., they do not cross grain boundaries), and they consist of glass lamellae (when fresh) or arrays of small fluid inclusions (when decorated) (French and Koeberl 2010). They have specific orientations parallel to crystallographic planes within the crystal (Fig. 2.22). Tectonically-produced Böhm lamellae are generally less well-defined, slightly curved, sub-parallel, occur in only one or two sets or directions, commonly consist of bands that are >10 μm wide, and are usually spaced at distances of >10 μm (Alexopoulos et al. 1988; Stöffler and Langenhorst 1994). Because of their near-planar and near-parallel appearance, tectonically-produced Böhm lamellae are sometimes confused with shock-produced PDFs, especially by investigators unfamiliar with true PDFs. In order to avoid misidentification, the orientation of the planar features thought to be PDFs should be determined as discussed above and in Sect. 2.3.4.2.2. Unlike PDFs, the non-impact planar microstructures have relatively random orientations and form a broad bell-shaped distribution when plotted in a histogram of frequency versus angles between the quartz c-axis and the poles of the planar features (Fig. 2.22).

Measurements of the orientations of PDFs have generally been done using a universal stage on a petrographic microscope. Unfortunately most, if not all, microscope manufacturers no longer make universal stages and there are not many researchers left who know how to use them. PDF orientation can also be determined using a spindle stage; but these are also rare, and this method is less precise and more time-consuming than using a universal stage (Koeberl 2002). In addition, a spindle stage cannot be used to measure the orientation of PDFs in grains in thin sections. Some researchers believe that the combination of chemical etching and scanning electron microscopy (Fig. 3.26a) can be used to distinguish between true PDFs found in shock metamorphosed quartz and planar features produced by tectonic deformation (Gratz et al. 1996). Other researchers claim that PDFs are best identified using transmission electron microscopy or TEM (Fig. 3.26b; Langenhorst 1996; Grieve et al. 1996). However, TEM is very expensive and time consuming, especially sample preparation, which involves ion-beam thinning of the grains.

Other indicators of shock metamorphism that have been observed in distal ejecta layers are high-pressure polymorphs such as coesite, stishovite, reidite, and TiO_2II. Coesite and stishovite have been found in several distal impact ejecta layers including the Australasian and North American microtektite layers, the upper Eocene clinopyroxene-bearing (cpx) spherule layer, and the K-T boundary layer. These phases can be identified using X-ray diffraction (XRD), Raman spectroscopy, transmission electron microscopy, or nuclear magnetic resonance. Care should be taken when using XRD to identify coesite since barite has a similar pattern to that of coesite and has been misidentified as coesite on at least one

occasion (Fudali 1969). Reidite has been found in shocked zircons recovered from the North American microtektite layer (Glass and Liu 2001). TiO_2II, a high-pressure phase of rutile and anatase, has been found in the Australasian microtektite layer (Glass and Fries 2008) and in some Precambrian spherule layers in Western Australia and South Africa (Smith et al. 2010).

Shocked zircons exhibiting multiple sets of planar features and granular textures have been reported in the K-T boundary layer (e.g., Bohor et al. 1993). Under certain rare conditions, shocked zircons can be used to date the impact that produced the ejecta layer (e.g., the U–Pb method; see Sect. 3.3.2) and to help identify the target rock (e.g., Krogh et al. 1993a, b).

Both quartz and zircon are found in continental crust, but most of the Earth's crust is oceanic and, therefore, composed mostly of mafic minerals. The percent of mafic rock making up the Earth's crust was probably greater in the Precambrian, particularly during the Archean (Powell 2001; Taylor and McLennan 2009). Most impacts would, therefore, have been into mafic crust. Impacts into mafic crust are not likely to produce microtektites due to the low silica content of mafic rocks. Furthermore, quartz, and to a lesser extent zircon, will not be found in most of the ejecta layers produced by such impacts. This may be at least part of the explanation for why shocked quartz and zircon have not been reported in the older (>2.4 Ga) Precambrian spherule layers (a single quartz grain with PDFs was reported for the Jeerinah spherule layer by Rasmussen and Koeberl 2004). However, pyroxene and olivine, as well as feldspar, which are common in mafic rocks, can be converted to high-pressure polymorphs (see Sect. 2.3.3) and have been found in shocked meteorites. As of 2010, except for hollandite, these high-pressure polymorphs (e.g., majorite, akimotoite, ringwoodite) had not been observed in shocked terrestrial rocks; but the search for them should continue, particularly in the older Precambrian spherule layers. In the absence of shocked quartz, these high-pressure polymorphs may be the best bet for confirming the impact origin of the older Precambrian spherule layers. However, most mafic minerals (e.g., olivine, pyroxene) transform to metastable phases including glass when highly shocked, and are easily altered to secondary hydrous phases in sea water (Jones et al. 2003b).

3.3 Dating and Correlation of Distal Impact Ejecta Layers

Dating of distal impact ejecta layers is needed in order to correlate the layers and to help identify the source crater, which is discussed below.

3.3.1 Stratigraphy

Stratigraphic dating is a powerful tool for determining the age of distal impact ejecta layers. The absolute age precision of the chronostratigraphic timescale is continually being improved. Biostratigraphy is usually the first information used to

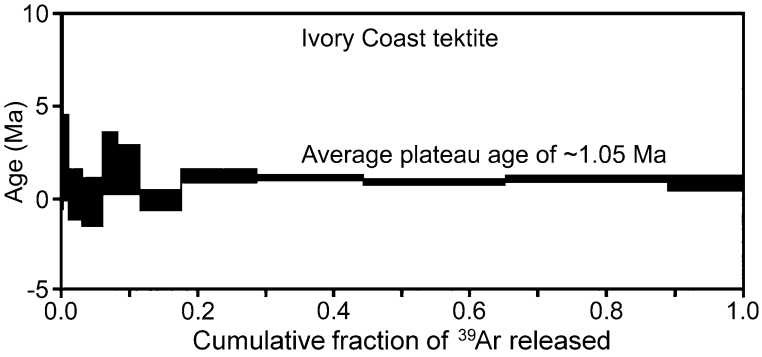

Fig. 3.27 Step-heating age spectra diagram (age versus fraction of ^{39}Ar released) for an Ivory Coast tektite indicating an ^{40}Ar-^{39}Ar plateau age of ~1.05 Ma. Modified after Koeberl et al. (1997b), Fig. 11a

determine the age of an ejecta layer. The North American microtektite layer has been correlated throughout the Gulf of Mexico, the Caribbean Sea, and NW Atlantic, and the late Eocene cpx spherule layer and the K-T boundary layer have been correlated around the globe using biostratigraphy; but not all sites have sufficient fossils for precise age dating. Unfortunately, as a general rule, the Precambrian spherule layers cannot be dated or correlated using biostratigraphy. An exception is the use of acritarchs to locate the Acraman impact ejecta layer at sites in the Officer Basin, South Australia (Hill et al. 2007).

There are definite limits to biostratigraphic dating and correlation. Based on high-resolution biostratigraphy (using mostly planktic foraminifera) it was proposed (Keller et al. 1987) that there are three upper Eocene spherule layers. Another investigator (Hazel 1989), using the graphic correlation method involving a wide range of microfossil and magnetopolarity data, concluded that there were six and possibly more upper Eocene spherule layers over a one million year period. Based on the composition and petrography of the spherules, other researchers argued for only two layers: a younger North American microtektite layer and an older clinopyroxene-bearing spherule layer (Glass and Burns 1987; Glass 1990b). The two-layer hypothesis was supported by Wei (1995) who concluded that it is consistent with the biostratigraphic data. The two-layer model also appears to be supported by Sr and Nd isotopic data (Whitehead et al. 2000; Liu et al. 2006; Liu et al. 2009). The argument over the number of upper Eocene spherule layers, for which there was an abundance of data, indicates the limits of biostratigraphy for high-resolution correlation.

Magnetostratigraphy has been used to correlate and date spherule layers of Cenozoic and, to a lesser extent Mesozoic age. Correlation of the Australasian microtektite layer at various sites was based primarily on the association of this layer with the Brunhes/Matuyama geomagnetic reversal (e.g., Glass 1972a; Glass et al. 1979) and correlation of the **Ivory Coast microtektite layer** was based on the occurrence of this layer just above the base of the Jaramillo subchron (Glass et al.

1991). In both cases the correlation of these layers from one core to the next was supported by the appearance and composition of the microtektites. The K-T boundary layer can also be correlated using magnetostratigraphy; it occurs in magnetochron C29R (Smit 1999). Earlier studies were not successful in attempts to correlate the North American microtektite and clinopyroxene-bearing spherule layers (e.g., Glass et al. 1985); however, more recent research suggests that these layers occur in magnetochron 16n.1n (Liu et al. 2009). Magnetostratigraphy cannot be easily used to correlate Paleozoic or Precambrian distal impact ejecta/spherule layers.

Another way to correlate ejecta layers is by use of geochemical anomalies such as Ir anomalies or carbon isotope anomalies. A positive Ir anomaly is associated with the late Eocene cpx spherule layer and the K-T boundary ejecta layer. In both cases researchers have taken advantage of this relationship to locate the late Eocene cpx spherule layer and the K-T boundary ejecta layer at new sites. This has been especially useful in locating the cpx spherule layer at new sites (e.g., Vonhof and Smit 1999; Liu et al. 2009), since the cpx spherule layer cannot be detected by visual observation of the sediments in which the layer has been found.

Large impacts can have global climatic effects which can then cause changes in the biota. Such changes can cause shifts in the marine carbon isotope ratios, which can be recorded in carbonate sediments. The late Eocene cpx spherule layer, the K-T boundary ejecta layer, and the Acraman ejecta layer have a carbon isotope shift or spike associated with them, which can be used to correlate these layers from site to site and to help locate new sites.

The above biostratigraphic, magneotostratigraphic, chemostratigraphic, and stable isotope stratigraphic methods can be used for correlation of spherule layers, but any ages assigned to spherule layers using these methods are based on calibration using radiometric dating.

3.3.2 Radiometric Dating

The most direct way to determine the chronological age of a distal ejecta layer is to date the layer using a radiometric dating method. If a layer contains impact-produced glass (e.g., microtektites), then it can be dated using the fission-track, K–Ar, and/or Ar–Ar methods. The fission-track method involves counting tracks produced during the spontaneous fission of ^{238}U. The sample (mineral grain or glass) is mounted, polished, and then etched to make the tracks visible. They can be counted at high magnification using an optical microscope. The number of tracks per unit area is related to the age of the sample and the uranium content of the sample. The uranium content can be determined by having the sample irradiated with a known flux of thermal neutrons and then counting the induced tracks formed by the radiation. For young samples (<1 Ma) and low U content, a large surface area is required. The tracks can be annealed over time, especially if the samples are exposed to even moderately high temperatures. The Australasian,

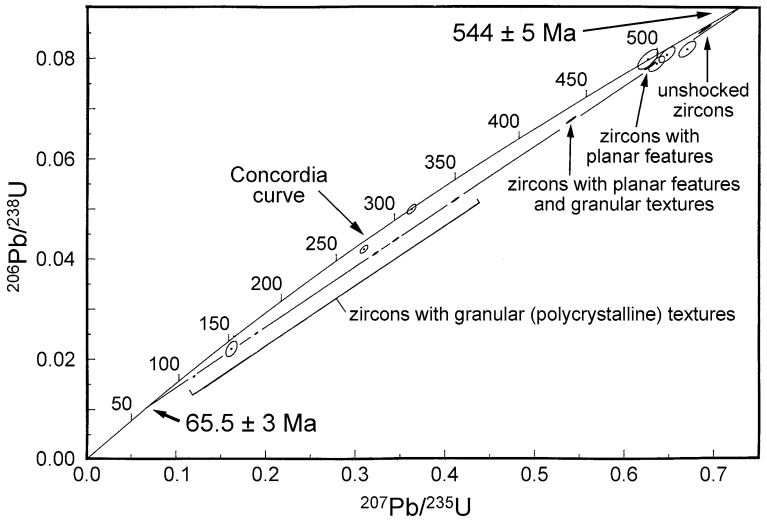

Fig. 3.28 U-Pb concordia diagram for single shocked zircons from the Cretaceous-Tertiary boundary layer, Berwind Canyon, Raton Basin, Colorado, USA. Shocked zircons suffered Pb loss. The most shocked zircons (granular grains with strawberry texture) lost the most Pb and the least shocked lost the least amount of Pb. The shocked zircons define a mixing line. The upper intercept of the mixing line defines the age of the source rocks for the zircons ($\sim$540 Ma) and the lower intercept indicates the time of shock metamorphism or impact (i.e., $\sim$65 Ma). Courtesy of Sandra Kamo

Ivory Coast, and North American microtektites were dated using the fission-track method (Gentner et al. 1970; Glass et al. 1973). In order to get enough surface area to obtain a statistically significant age, the microtektites were ground down, polished, etched, and after the tracks were counted the same microtektites were ground down, polished, re-etched and the tracks on the new surface were counted. This procedure was repeated until the microtektites were ground away. This method can be done with little expense as long as the researcher has a good optical microscope and access to a nuclear reactor where the samples can be exposed to a known flux of thermal neutrons. However, it requires skill to get a good polish on exposed cross sections and it can be time-consuming. This method is generally being replaced by the Ar–Ar method, but there may still be times when this method would be best (e.g., samples with young ages and very low potassium contents).

The K–Ar method has been used to date tektites from all the known tektite strewn fields (e.g., Zähringer 1963; Gentner et al. 1967). The K–Ar method is based on the decay of ^{40}K to ^{40}Ar with a half life of 1.27 Ga. In this method the ^{40}K and ^{40}Ar contents are determined using different subsamples. The K–Ar method requires relatively large samples depending on the amount of potassium present in the samples and the age of the samples. Individual Cenozoic microtektites, for example, could not be dated by this method because of their small size.

The most reliable isotope dating methods used to date impact products are the ^{40}Ar-^{39}Ar and U-Pb methods (Jourdan et al. 2009). The K–Ar method has generally been replaced by the ^{40}Ar-^{39}Ar method, which does not require large samples and which is more accurate than the K–Ar method. In the ^{40}Ar-^{39}Ar dating method, the ^{40}K and ^{40}Ar contents are determined for the same sample. The samples are bombarded with a known flux of neutrons in a nuclear reactor. This converts some of the ^{39}K to ^{39}Ar (the amount of conversion depends on the amount of neutron bombardment). The ^{39}Ar and ^{40}Ar contents are then determined in the samples using a mass spectrometer. The ^{39}Ar content indicates how much ^{39}K is present and, since the ^{40}K/^{39}K ratio is known, the ^{39}K content can be used to calculate the ^{40}K content of each sample.

Prior to ~1980, the ^{40}Ar and ^{39}Ar contents were determined by melting the sample in a single step. Now the samples are heated with a laser to successively higher temperatures in a series of steps. An age can be determined for each heating step. The argon released at lower temperatures comes from more open or leaky domains and the ages are considered to be unreliable. At higher temperatures, the Ar comes from less open domains resulting in better ages. In a plot of age versus cumulative fraction of ^{39}Ar release (or temperature steps), it is hoped that at higher temperatures a series of heating steps gives the same age, resulting in a plateau (Fig. 3.27). If a sample does not produce an age plateau, the ages obtained for the sample are considered to be unreliable.

The Cenozoic tektites have all been re-dated using the ^{40}Ar-^{39}Ar method (e.g., Izett and Obradovich 1992; Koeberl et al. 1997b; Yamei et al. 2000; Laurenzi et al. 2003). Tektite glass from the North American microtektite layer has been dated using the ^{40}Ar-^{39}Ar method with good results (Glass et al. 1986); however, single step heating of four Ivory Coast microtektites did not produce reliable ages because of a combination of young age, relatively low K contents, and small sample sizes (Koeberl et al. 1997b).

Although the K–Ar and ^{40}Ar-^{39}Ar methods can theoretically be used to date samples as old as the Earth, in practice older samples often give younger, unreliable ages due to Ar loss. Since Ar is a noble gas, it does not combine with other elements in crystalline structures and undergoes partial or complete loss if the sample is heated. The only component in a distal ejecta layer that can be dated by the K–Ar or ^{40}Ar-^{39}Ar method to give the age of the impact is impact-produced glass, generally in the form of microtektites. Individual microtektites are not large enough to date using the K–Ar method, but can be dated using the ^{40}Ar-^{39}Ar method if they are sufficiently old or contain enough potassium. However, the older the ejecta layer the more likely the glass has been heated or has been replaced by another phase resulting in Ar loss.

Some shock metamorphosed grains, found in distal impact ejecta layers, can be dated using the U–Pb or Pb–Pb method to determine not only the time of formation of the mineral grain, which gives information about the target rock, but also the age of the impact event that produced the ejecta layer. Uranium has two long-lived radioisotopes (^{235}U and ^{238}U) which decay to stable Pb isotopes. Uranium-235 decays to ^{207}Pb with a half life of 0.7 Ga and ^{238}U decays to ^{206}Pb with a half life

of 4.47 Ga. After correction for Pb present at the time of formation, the $^{206}Pb/^{238}U$ ratios can be plotted versus the $^{207}Pb/^{235}U$ ratios determined for the samples. If the measured parent-daughter ratios for the samples fall on the **concordia curve** (a hypothetical curve that shows how the parent-daughter ratios should evolve or change through time), it indicates a closed system and the ages should be correct. If the parent-daughter ratios plot below the concordia curve, then lead loss in indicated. If different grains experienced different amounts of lead loss during an event, then the parent-daughter ratios of the samples will fall below the concordia curve and they may define a linear array or mixing line with the upper intercept of the concordia curve indicating the original time of formation of the mineral grain (primary age) and the lower intercept indicating the time of lead loss or disturbance (e.g., time of impact) (Fig. 3.28). Co-linearity of the discordant grains indicates that the upper (primary) and (lower) secondary (or disturbance) ages are valid (Krogh et al. 1993a, b). The conventional way to determine the isotopic ratios for U–Pb dating is by using a mass spectrometer, such as a thermal ionization mass spectrometer (**TIMS**) or a multi-collector inductively-coupled plasma mass spectrometer (**MC-ICP-MS**). Relatively new analytical improvements in Pb–Pb zircon dating using thermal extraction TIMS allow age dating with a precision of $\sim$0.2 Ma for Precambrian zircons (Davis 2008).

Zircons are ideal for U–Pb dating of distal impact ejecta layers because they incorporate small amounts of U during crystallization, have a very high thermal blocking temperature, are resistant to weathering, and do not anneal under conditions that would recrystallize other phases (Krogh et al. 1993a). In addition, zircons exhibit a range of shock metamorphic effects which can be used to confirm that they are part of the impact ejecta and not just some detrital grains that got mixed in with the ejecta.

Shocked zircons (ranging in mass between 1 to 3 μg), from the K-T boundary layer, were dated with the U–Pb method using a mass spectrometer (Krogh et al. 1993a, b). The zircons exhibited a range in shock effects. Some of the zircons did not exhibit any visible shock effects, some had PDFs, some PDFs and granular textures, and some granular (polycrystalline) textures without PDFs. The zircons gave mostly discordant ages which defined a linear array with the least shocked zircons plotting near the upper intercept, indicating the primary ages of the zircons ($\sim$544 $\pm$ 5 Ma), and the most shocked zircons plotted down close to the lower intercept giving an age of 65.5 $\pm$ 3.0 Ma for the time of the impact (Fig. 3.28).

An attempt to date zircons in blocky (Muong Nong-type) Australasian tektites using an ion probe was unsuccessful (Deloule et al. 2001). All the zircons gave highly discordant ages which were probably the result of partial to complete resetting of the isotopic system during the impact. However, two spots on a shocked zircon from a Muong Nong-type Georgia tektite gave discordant results indicating a primary age of crystallization of 0.6 $\pm$ 0.1 Ga, which is in agreement with Sr and Nd model ages of North American tektites, i.e., the age of the precursor material that was melted to make the tektites (Shaw and Wasserburg 1982; see Sect. 3.4.2).

Uranium/Pb dating using a **sensitive high-resolution ion microprobe (SHRIMP)** can be used to measure the age of a grain at micrometer scale (Jourdan et al. 2009). Dating of zircons in volcanic ash layers or volcanic flow rocks above and/or below a spherule/ejecta layer can be used to put limits on or bracket the age of the layer. This has been done for some Precambrian spherule layers. SHRIMP dating of zircons from two tuff layers was used to put age constraints on three Precambrian spherule layers in the Hamersley region of the Pilbara craton in Western Australia (Rasmussen et al. 2005). The new age data suggested that two of the spherule layers (the Carawine and Jeerinah) were formed by the same impact event (see Sect. 8.4.1).

Rutile may also be useful for U–Pb dating of distal impact ejecta layers, as it too is fairly resistant to weathering and can exhibit shock metamorphic effects (i.e., high-pressure polymorphs). To our knowledge, rutile has not yet been used for dating ejecta layers, although Kohl et al. (2007) made a reconnaissance study of using rutile to date Precambrian spherule layers in the Barberton Greenstone Belt in South Africa. The dating was used to put an age constraint on a possible new Archean impact spherule layer.

The U–Pb method was used to date carbonate associated with two Precambrian impact spherule layers in the Hamersley Region in Western Australia (Woodhead et al. 1998). Two good isochron ages were obtained, but the relationship of these ages to the spherule layers is not clear. However, Woodhead et al. (1998) argued that the ages represent depositional or early diagenetic ages and can, therefore, be used to constrain the age of the spherule layers. These ages appear to be consistent with zircon ages from volcanic ash layers in this section.

Studies indicate that ~90 % of target rocks affected by an impact preserve their pre-impact ages because the shock conditions are insufficient to reset most isotopic dating systems (e.g., Deutsch and Schärer 1994). Because of this problem, it has been suggested that in some cases the (U-Th)/He method might be a better dating method than, for example ^{40}Ar-^{39}Ar and U–Pb, because the (U-Th)/He system is more likely to be completely reset during an impact (van Soest et al. 2009). This method is less precise than ^{40}Ar-^{39}Ar and U-Pb; however, initial results using this method to date three previously well-dated impact structures (van Soest et al. 2009) indicate that this method might provide a suitable alternative dating tool that can give accurate and fairly precise ages. Minerals that can be dated using this method include: apatite, zircon, monazite, titanite, xenotime, and magnetite.

3.4 Search for Source Craters of Distal Ejecta Layers

Correlating a distal ejecta layer with a specific impact crater allows for correlation between an impact structure and biologic and climatic changes recorded in the rock record. If an ejecta layer can be found at several widely spaced geographic locations, it should be possible to determine the general location and size of the

Table 3.6 Strontium and neodymium isotopic data and model ages for Cenozoic tektites (from Shaw and Wasserburg 1982)

Tektites[a]	ε_{Nd} (0)[b]	ε_{Sr}(0)[c]
Australasian (7)	−10.9 to −12.2	134.6 to 212.5
Ivory Coast (3)	−19.5 to −20.2	267.4 to 301.1
Central European (4)	−9.8	242.4 to 268.6
North American (6)	−6.1 to −6.7	114.3 to 129.3
	T_{Nd}^{CHUR} (Ga)	T_{Sr}^{UR} (Ga)
Australasian (7)	1.07 to 1.17	0.348 to 0.536
Ivory Coast (3)	1.84 to 1.91	2.12 to 2.44
Central European (4)	0.88 to 0.96	0.392 to 0.566
North American (6)	0.62 to 0.67	0.515 to 0.568

[a] Numbers in parentheses are the number of specimens analyzed
[b] Referenced to $(^{143}Nd/^{144}Nd)_{CHUR} = 0.511847$
[c] Referenced to $(^{87}Sr/^{86}Sr)_{UR} = 0.7045$

source crater. This was done successfully for the K-T boundary layer with the discovery of the Chicxulub impact structure on the Yucatan Peninsula in Mexico. Studies of distal impact ejecta layers can provide information regarding the age, location, and size of the source crater, and nature of the target rock.

3.4.1 Age of the Source Crater

Determining the age of the ejecta layer based on stratigraphic means or radiometric dating of the impact glass or shocked mineral grains such as zircon or rutile, as discussed above, will also indicate the time of formation or age of the source crater. Because of the errors involved in dating, the age of the ejecta layer will not be enough to prove that an ejecta layer was derived from a given crater, but it can narrow down the possible choices and could put limits on where the source crater might be located. As discussed above, U-Pb zircon ages from the K-T boundary ejecta layer were used to support Chicxulub as the source crater for this ejecta layer. Strontium and Nd model ages (see Sect. 3.4.2) for the North American tektites/microtektites narrowed down the possible location of the source crater to the Atlantic and Gulf coastal plains and adjacent continental shelf where the source crater (Chesapeake Bay structure) was eventually found (see Sect. 4.5.9).

3.4.2 Nature of the Target Rock

Distal impact ejecta can contain both melted (e.g., microtektites) and unmelted components. The unmelted components give direct information regarding the

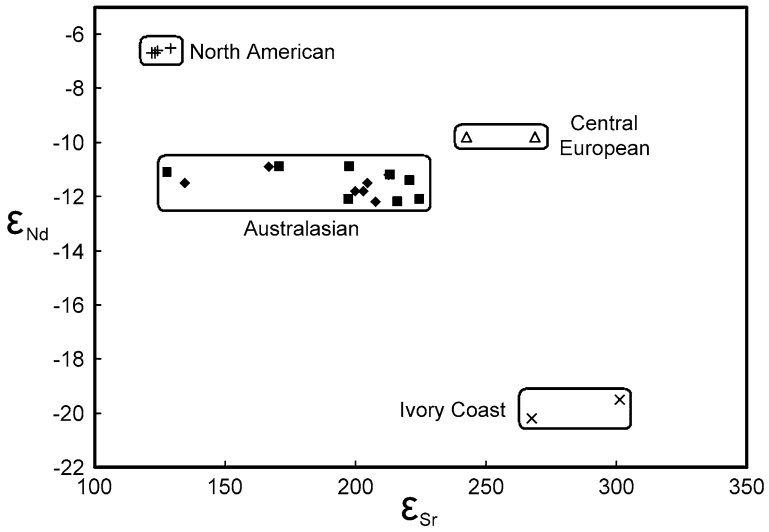

Fig. 3.29 Sr/Nd isotope plot for tektites showing the differences between the strewn fields. The Sr/Nd isotopic data also indicate the provenance of the source rocks. Data from North American, Central European, and Ivory Coast tektites are from Shaw and Wasserburg (1982). Australasian tektite data are from Shaw and Wasserburg (1982) (*diamonds*) and Blum et al. (1992) (*squares*)

petrography and composition of the target rocks. In 1983, a layer of fragmented red felsic volcanic rock was discovered in the late Neoproterozoic Bunyeroo Formation (a marine mudstone unit) in the Flinders Range in South Australia by Vic Gostin (Williams and Gostin 2005). Gostin et al. (1986) ruled out glacial-ice rafting, debris flow, and fluvial deposition as the origin of this fragmental layer. Radiometric dating of the volcanic rock making up the fragmental layer indicated an age of 1575 Ma, which is close to the age of the Gawler Range Volcanics to the west (Gostin et al. 1986). It was soon learned that a 90-km-diameter crater, the Acraman impact structure, had been discovered by George Williams (Williams 1986) ~250 km west of where the fragmental layer was found. Gostin and colleagues searched for and found PDFs in quartz grains in the felsic volcanic rocks from the fragmental layer and eventually concluded that the layer was impact ejecta from the Acraman impact structure (Gostin et al. 1986). Thus, the age and petrography of the fragmental rocks in the ejecta layer provided the evidence to correlate the ejecta with the Acraman impact structure.

In the absence of rock fragments, the size and kinds of shocked mineral grains in an ejecta layer can indicate the nature of the target rocks. In the absence of both shocked rock fragments and shocked mineral grains, the composition of impact glass in an ejecta layer can indicate the major oxide, trace element, and isotopic composition of the target rock, although some of the more volatile elements may have been lost during glass formation. If an impact structure is suspected of being the source of impact glass (e.g., microtektites) in an ejecta layer, mixing calculations can be used to determine if the glass composition can be matched by a

mixture of target rocks at the proposed crater site. For example, the major and minor element compositions of the Ivory Coast tektites and microtektites were matched to a mixture of target rocks at the Bosumtwi impact crater, Ghana, West Africa (Koeberl et al. 1998). Mixing calculations are important to define the indigenous contents of siderophile elements in the glass, which is important for the determination of the possible presence and identification of an extraterrestrial component in the glass (Koeberl 2007). An example of a mixing model is the harmonic least-squares (HMX) mixing calculation program of Stöckelmann and Reimold (1989) which allows the usage of any number of components (e.g., target rocks) and component or mixing parameters (e.g., element abundances), and can include the analytical uncertainties in the model computations.

Heavy mineral studies can be used to correlate an ejecta layer with its source crater (Thackrey et al. 2009). The heavy mineral assemblage can help define the nature of the target rocks and the heavy mineral assemblage in an ejecta layer can be compared with the heavy mineral assemblage at proposed source craters. In addition, some heavy minerals (e.g., zircon, rutile) can be radiometrically dated, which can provide information about the provenance of the target rocks, and, in some cases, can provide the age of the impact/ejecta layer. Of course, it is necessary to demonstrate that the heavy minerals are part of the ejecta layer and not just locally derived detrital grains. The most convincing way is to demonstrate that the heavy minerals show evidence of shock metamorphism. Additional evidence that the heavy minerals in the ejecta layer are part of the ejecta is to demonstrate that the heavy mineral assemblage of the ejecta layer is distinctly different from that in the layers above and below the ejecta layer. Once it is demonstrated that the heavy minerals are part of the ejecta, then selected heavy minerals can be dated using one or more of the methods discussed above. Most heavy minerals are relatively stable and this makes the heavy mineral assemblage a good choice for correlation purposes.

Another very important method that can be used to help determine the nature of the source rock involves Sm–Nd and Rb–Sr systematics. The Sm–Nd system is based on the α-decay of ^{147}Sm to ^{143}Nd with a half-life of 106 Ga, and the Rb–Sr system is based on the β-decay of ^{87}Rb to ^{87}Sr with a half-life of 48.8 Ga. Sm–Nd and Rb–Sr isotopic analyses of impact glasses (e.g., tektites, microkrystites) can be used to put constraints on the age and provenance of the target rocks which were melted to form them (Shaw and Wasserburg 1982). Sm–Nd and Rb–Sr isotopic data for impact glasses can be used to determine ε_{Nd} and ε_{Sr} values where

$$\varepsilon_{Nd} = \left[\left({}^{143}Nd/{}^{144}Nd \right)_{sample} / \left({}^{143}Nd/{}^{144}Nd \right)_{standard} - 1 \right] \text{ x } 1000 \qquad (3.2)$$

and

$$\varepsilon_{Sr} = \left[\left({}^{87}Sr/{}^{86}Sr \right)_{sample} / \left({}^{87}Sr/{}^{86}Sr \right)_{standard} - 1 \right] \text{ x } 1000 \qquad (3.3)$$

The ε_{Nd} and ε_{Sr} values can be used to characterize the glasses and to compare them with ε_{Nd} and ε_{Sr} values determined for target rocks at possible impact craters.

In addition, Sm–Nd and Rb–Sr isotopic data for impact glasses can be used to calculate model ages. Model ages are essentially based on a one point isochron with an assumed initial value. The Nd model age, T_{Nd}^{CHUR}, is interpreted as the time of formation of the source terrain that was weathered to produce the sediments which were melted to form the impact glasses (CHUR = Chondritic Uniform Reservoir, which has the $^{147}Sm/^{144}Nd$ and $^{143}Nd/^{144}Nd$ of chondrites and presumably the bulk Earth). Weathering does not disturb the Sm–Nd isotopic system. However, the Rb–Sr isotopic system can be severely disturbed during weathering and sedimentation, resulting in an increase in the Rb/Sr ratios (Koeberl 1994). The Sr model ages, T_{Sr}^{UR}, under the favorable conditions of very high Rb/Sr ratios, are close to the time of deposition of the sediment that was melted to produce the impact glass (UR = Uniform Reservoir and is the Rb/Sr equivalent of CHUR; Shaw and Wasserburg 1982). The Nd and Sr model ages of impact glasses can be used to help identify the source crater.

Shaw and Wasserburg (1982) found that Cenozoic tektites have distinct negative ε_{Nd} values and large variable ε_{Sr} values (Table 3.6), which are characteristic of old continental crust (Fig. 3.29). They also determined the Nd and Sr isotopic ages for Cenozoic tektites (Table 3.6). Based on Nd model ages for the North American tektites and microtektites, researchers concluded that the target rocks that were melted to produce the North American tektites and microtektites were derived from late Precambrian crust ($\sim$0.62–0.67 Ga old), which narrowed the location of the source crater to the Appalachian mountain belt and the adjacent coastal plains and continental shelf (Atlantic and eastern part of the Gulf Coast) (Shaw and Wasserburg 1982; Ngo et al. 1985; Stecher et al. 1989). This area is consistent with the location of the Chesapeake Bay impact structure, which was later discovered and is now believed to be the source crater for the North American tektites/microtektites (Poag et al. 1994; Koeberl et al. 1996).

The methodology of Rb-Sr and Sm–Nd isotopic analysis is fairly routine. It involves whole-rock powders or mineral separates which are spiked with an isotopic standard and dissolved. The various elements are separated, mostly by ion exchange, and the isolated elemental fractions are then subjected to thermal ionization mass spectrometry to determine the isotopic ratios (Papanastassiou and Wasserburg 1981; Koeberl 2007).

3.4.3 Size of and Distance to Source Crater

Various kinds of information about an ejecta layer can be used to estimate the size of and/or distance to its source crater. One method involves using the relationship between thickness of an ejecta layer and the distance from and size of the source crater. Other methods involve using spherule size or compositional data (e.g., Ir content) to estimate the size of the source crater. Another method uses some parameter/feature of the ejecta layer that varies radially away from the source crater to estimate the distance to the source crater.

As previously indicated (Sect. 2.6), the thickness of an ejecta layer decreases as a power function (with an exponent of approximately −3.3) with distance from the source crater. For example, the K-T boundary layer is about 45 cm thick at Haiti, which, at the time of impact, was only ~900 km from the Chicuxlub impact structure. At sites that vary between 2300 and 13,900 km from Chicxulub at the time of the impact the K-T boundary ejecta layer only varies between about 1 and 3 cm in thickness. The thickness of an ejecta layer by itself will not indicate how far the site is from the source crater. For example, a 10 cm thick ejecta layer could be ~40 km from a 10-km-diameter crater or ~650 km from a 100-km-diameter crater. However, if the thickness of an ejecta layer is known for three or more widely scattered locations, it should be possible to use equations that relate ejecta thickness to size of and distance to the source crater (as discussed in Sect. 2.6) to determine the location and size of the source crater (Hildebrand and Stansberry 1992).

If the thickness of an ejecta layer is known for several widely spaced sites, it may be possible to determine the size and location of the source crater by trial and error. A crater size can be assumed and then used to calculate the distance to the source crater for each ejecta site using the thickness of the ejecta layer at each site. Circles are then drawn around each site using the calculated distance to the source crater for each site as the radius. If there is a lot of overlap, then a smaller crater diameter is used to calculate the distance from each ejecta site to the source crater. If the circles based on this crater diameter do not all overlap, the chosen crater size is too small. This process is repeated until all the distance circles around the ejecta sites overlap or come into contact with each other at the same location. This is the predicted location for the source crater and the crater diameter used to get this fit is the predicted crater size. For ejecta layers older than ~10 Ma, plate reconstructions need to be done before doing the calculations. Hildebrand and Stansberry (1992) used the ejecta thickness at three different K-T boundary ejecta layer sites to calculate the size of and distance to the source crater. They found good agreement with the size and location of the Chicxulub impact structure, which is believed to be the source crater of the K-T boundary ejecta layer (see Sect. 5.2.6 for details).

Attempts to determine the geographic location and size of the source crater of an ejecta layer based on geographic variations in thickness of the ejecta layer provide at best a rough estimate. The thickness of an ejecta layer can be altered by a number of processes including slumping, erosion and redeposition, tectonic deformation, and compaction. In addition, calculations indicate that the Coriolis effect due to the Earth's rotation can significantly modify the distribution of ejecta (Wrobel and Schultz 2003). As a result, radial decay laws (e.g., Eqs. 2.2 and 2.3) will not always accurately predict the thickness of a distal ejecta layer. Conversely, the size of the impact crater may not be accurately predicted based on thickness of its distal ejecta layer at a given distance from the source crater. The degree and nature of the modification depends on the geographic latitude of the impact (Wrobel and Schultz 2003).

As discussed in Sect. 2.4, it has been suggested that the size of impact spherules formed as condensate droplets (O'Keefe and Ahrens 1982) or formed as melt droplets (Melosh and Vickery 1991) can be used to estimate the size of the impacting body and, therefore, the source crater. Some authors have used the equations that relate spherule size to projectile size to estimate the size of the projectiles for several of the Precambrian spherule layers. Melosh and Vickery (1991) used the maximum size of the spherules in the S3 spherule layer in South Africa to estimate a projectile diameter up to 160 km. However, Byerly and Lowe (1994) used a smaller spherule size for that layer and estimated the projectile diameter to be only 24 km. Glikson and Allen (2004) used O'Keefe and Ahrens' (1982) equation to estimate the size of the projectile responsible for the Dales Gorge Precambrian spherule layer in Western Australia and obtained a projectile diameter of 15–25 km. Glikson and Allen (2004) also used Melosh and Vickery's (1991) equation to calculate a projectile diameter of 16–30 km for the same spherule layer. Hassler et al. (2000) used a corrected version of Melosh and Vickery's (1991) equation (see Sect. 2.4) to calculate a projectile diameter of $\sim$4.9 km for the Bee Gorge spherule layer (Western Australia).

Alvarez et al. (1980) used the Ir content of the K-T boundary layer to estimate a projectile size of $\sim$10 km. A projectile this size could have produced a crater the size of the Chicxulub impact structure which was later discovered and identified as the source crater for that layer. Several investigators have used the Ir concentrations in South African Precambrian spherule layers to estimate the percent extraterrestrial components in the layers and then used that to calculate the size of the projectile for each layer. The calculations are based on the assumptions that the spherule layers were global in extent and that the Ir fluxes determined for one or two sites were close to the average flux for each layer. Based on the measured Ir concentration, Kyte et al. (2003) estimated that the Ir fluxes in the S2, S3, and S4 spherule layers were 162, 16,200, and 2700 ng/cm^2, respectively. This indicates projectile diameters that are just slightly larger, 7 times larger, and 3 times larger, respectively, than the Chicxulub projectile, or about 11, 70, and 30 km in diameter. If the diameters of the craters produced by these projectile were 18 times larger than the projectile diameters as is apparently the case for Chicxulub (i.e., 180 km/10 km = 18), then the crater sizes for the S2, S3, and S4 spherule layers would have been $\sim$200, 1260, and 540 km in diameter, respectively. Glikson and Allen (2004) made similar calculations for the S4 spherule layer (South Africa) and the Bee Gorge and Dales Gorge spherule layers (Western Australia) and obtained projectile diameters of 46, 16, and 28 km, respectively. The 46 km diameter for the S4 layer is larger than the 30-km-diameter size obtained by Kyte et al. (2003) and larger than the size estimated for this layer by Glikson and Allen (2004) using spherule size data as discussed above. Likewise, the 16 km diameter for the Bee Gorge projectile is much larger than the 4.9 km diameter obtained by Hassler et al. (2000) using spherule size.

In addition to the thickness of an ejecta layer, several other parameters/features exhibit systematic change with distance from the source crater. For example, Bohor and Izett (1986) determined the maximum size of shocked quartz grains in

11 K-T boundary layer sites around the globe and found that the largest shocked quartz grains occur in North America. From this they concluded that the source crater must be somewhere in or near North America. This helped focus the search for this crater. The Chicxulub crater, believed to be the source crater for the K-T boundary ejecta layer, was eventually found on the Yucatan Peninsula, Mexico. Other parameters/features of distal eject layers that vary systematically with distance from the source crater include: percent glass (impact spherules), percent broken spherules, abundance of impact pits on the surface of spherules, and percent alkali content of glassy spherules. With additional data about how these parameters/features vary with distance from the source crater it may be possible to use some or all of them to indicate the distance to the source crater for a given ejecta layer. Variations in distal impact ejecta with distance from the source crater are discussed in more detail in Chap. 10 (Sects. 10.1.2 and 10.2), after discussion of the known distal impact ejecta layers in Chaps. 4–9.

3.5 Examples of Spherules Misidentified as Impact Spherules

Dark-colored glassy spherules were recovered from Tertiary clays at Deep Sea Drilling Project Site 32 in the northeast Pacific (von der Borch 1970). The greatest number of spherules was recovered from lower to middle Tertiary sediments over a 20 m interval. They are dark brown to black in color and range from translucent to opaque. When broken, the thin edges are translucent greenish-brown. The spherules range between 0.3 and 1.2 mm in size and are mostly spherical, but teardrops are fairly abundant and dumbbells are also present (Fig. 3.15). The external surfaces range from smooth and highly glossy to rough and dull. Spherical bubble cavities are common and some spheres are essentially hollow. In the initial study of these spherules, it was concluded that they are microtektites or microlapilli of volcanic origin (von der Borch 1970). However, in retrospect, several lines of evidence suggested that they were of volcanic origin: 1) the spherules were scattered over 20 m of core instead of being confined to a single well-defined layer; 2) the spherules were associated with phillipsite and altered ash and scattered shards; 3) spherules with dull surfaces have a thin devitrified crust; 4) X-ray diffraction studies suggested the presence of possible microlites of calcic plagioclase and clinopyroxene; and 5) the mineralogy along with the high refractive index of the glass (1.60 to 1.61) suggested a composition equivalent to a basaltic glass. In a later study, von der Borch (1971) reported that the composition of the spherules was similar to that of oceanic tholeiite (i.e., basalt) and he concluded that they have a volcanic origin.

A researcher wrote to one of the authors (BPG) saying that he did not understand why there was so much excitement in finding microtektites since he was finding them all through the cores he was studying from the Antarctic Ocean. It later was discovered that a colleague of his was doing sedimentation experiments with artificial glass beads and some of the smaller beads were carried throughout

the core laboratory by the air conditioning system and deposited on all the exposed cores. The lack of lechatelierite inclusions and surface pits and grooves commonly found on microtektites, as well as, their soda lime compositions was an indication that the glass beads were manmade, rather than microtektites.

In 1970, Dieter Storzer and colleagues studied some spherules which had allegedly been recovered from Cretaceous deposits in Switzerland (Storzer 1992). Because of their chemical composition and virtually zero fission-track ages, it was concluded that these spherules were manmade contaminants. Storzer (1992) reported the discovery of numerous glass spherules in a drill core from Gabon, West Africa, in 1986. The spherules were splash forms (spheres, teardrops, dumbbells) ranging in size from 100 μm to 1 mm. No fission tracks were observed in the spherules, indicating an age of <10 ka, which is considerably less than the late Cretaceous stratigraphic age of the core. Their major oxide compositions were similar to those of blast furnace slag or mineral wool shot. Mineral wool shot refers to the non-fibrous particles produced during the manufacturing of glass wool. It was concluded that the Gabon glass spherules were artificial contaminants (Storzer 1992). In 1987, spherules interpreted as being of impact origin were found in Molino de Cobo, Spain (Keller et al. 1987). These spherules are similar in major oxide compositions to the Swiss spherules. Storzer (1992) concluded that both the Swiss and Molino de Cobo spherules are surface contaminants of modern industrial origin, probably mineral wool shot.

Keller (1986) also reported finding microtektites at a quarry in Cynthia, Mississippi, USA. Later work on splits of the same samples showed that the "microtektites" were probably glass beads from a nearby lightweight aggregate plant that produces aggregate by firing or sintering clay (Byerly et al. 1990). The glass spherules range between 75 and 250 μm in diameter. Many have smaller spheres down to 5–10 μm welded to their surfaces (Byerly et al. 1990). The smaller spherules are pale yellow to pale yellow–brown, but the larger ones are nearly black. Most of the larger spherules contain vesicles and those >200 μm in diameter generally contain a large central vesicle that makes up over half of the volume of the spherule. These spherules have much lower SiO_2 contents (down to 40 wt %) and higher Al_2O_3 (up to 24 wt %) and CaO (up to 38 wt %) than the typical Cenozoic microtektites (Byerly et al. 1990). They are generally holohyaline, but some contain small inclusions of lechatelierite and rare quenched microlites of aluminous pyroxene and magnetite. The spherules are associated with irregular glassy particles which are highly vesicular and which contain lechatelierite and partially fused mineral grains including zircon. Byerly et al. (1990) pointed out that production of this type of lightweight aggregate and its transport produces a contamination problem for samples collected from outcrops along railways, highways, or in developed areas.

It is clear from the above discussion that one must be careful when taking samples at an outcrop. The exposed surface rock should be removed before taking samples; but even this may not be sufficient in outcrops where root cavities from dead plants and cracks in the rocks can serve as conduits for surface contamination to make its way down into the subsurface deposits. Contamination can be a major

problem, especially near industrialized areas (Byerly et al. 1990; Storzer 1992); but contamination can also be a problem along roads and railroad tracks (see, e.g., Montanari 1986; Montanari and Koeberl 2000). It is equally important to avoid contamination of samples in the laboratory. Sieves, in particular, can be a major source of contamination and must be cleaned thoroughly and viewed with a microscope to make sure that no grains are caught in the mesh before re-using. It would be best to avoid using sieves whose past histories are not known.

Chapter 4
Cenozoic Microtektite/Ejecta Layers

4.1 Introduction

4.1.1 Background

The earliest recognized and some of the best studied distal impact ejecta layers are Cenozoic in age. The first to be discovered and one of the best defined Cenozoic distal ejecta layers is the Australasian microtektite layer. It was first reported in 1967 (Glass 1967). The Ivory Coast microtektite layer was reported a year later. Discovery of the North American microtektite layer was reported in 1973. Still later, it was recognized that clinopyroxene-bearing spherules found associated with the North American microtektites belonged to a slightly older impact event. When the Australasian and Ivory Coast microtektite layers were first reported, they were recognized as being part of the Australasian and Ivory Coast tektite strewn fields, respectively. The origin of tektites was not, at that time, unanimously agreed upon. A number of different origins had been suggested including: silica-rich meteorites, lunar volcanic glass, lunar impact debris, terrestrial volcanic bombs, terrestrial impact glass, glass objects formed by fusion of dust in the atmosphere by lightning, straw silica glass, and manmade glass (Baker 1963; Barnes 1939; Barnes and Barnes 1973, and references therein). By the time of the lunar Apollo Program, most researchers believed that tektites were formed by impact on the Moon or by impact on the Earth. With the return of the first lunar samples came the death of the lunar hypothesis for the origin of tektites (Schnetzler 1970). John A. O'Keefe attempted to resuscitate the lunar hypothesis by proposing that tektites were formed by lunar volcanism (see e.g., O'Keefe 1976), but most investigators continued to accept the terrestrial impact origin for tektites (e.g., Taylor and Koeberl 1994; Koeberl 1994).

The Cenozoic microtektite/microkrystite layers are discussed in this chapter. Because the microtektites are microscopic tektites found in marine deposits and because much of the evidence for an impact origin for these glasses has been derived from the study of tektites, tektites are briefly discussed in the next section

B. P. Glass and B. M. Simonson, *Distal Impact Ejecta Layers*, Impact Studies,
DOI: 10.1007/978-3-540-88262-6_4, © Springer-Verlag Berlin Heidelberg 2013

prior to discussion of the microtektite layers. Following the discussion of the Cenozoic microtektite/microkrystite layers, we discuss the **Darwin glass**, **Libyan Desert Glass**, and the impact glasses found in Argentina. The Darwin glass and Libyan Desert Glass are not found in situ in stratigraphic layers, but appear to be distal impact ejecta. The Argentina impact glasses range in age from Pleistocene to Miocene. Some of the glasses are found in stratigraphic context, but most, if not all, of these glasses appear to be proximal impact glasses. Except for the **Rio Cuarto glasses**, the source craters are not known.

After the discovery of the Cretaceous-Tertiary boundary impact ejecta layer and the proposal that the impact that produced that layer was responsible for the mass extinction at the end of the Cretaceous Period (Alvarez et al. 1980), more geologists became aware of impact ejecta layers and their importance. Many investigators began searching for additional impact ejecta layers associated with other mass extinctions. Several additional possible/probable Cenozoic distal impact ejecta layers have been described. However, most of these are based on a single outcrop and/or lack definitive proof of an impact origin. These possible/probable Cenozoic distal impact ejecta layers are discussed briefly at the end of this chapter. A list of the Cenozoic spherule and ejecta layers discussed in the chapter is given in Table 4.1.

4.1.2 Tektites and Tektite Strewn Fields

Tektites are silica-rich glass bodies formed by impact melting of terrestrial surface deposits (Koeberl 1994; Artemieva 2008). They are thrown away from the source crater and are found in the distal part of the ejecta. The geographical area over which they are found is called a **strewn field**. There are four well-known Cenozoic tektite strewn fields: Australasian, Ivory Coast, Central European, and North American (Fig. 4.1). The ages for these tektites range from 0.78 Ma for the Australasian to 35 Ma for the North American (Table 4.2).

There are three types or forms of tektites based on their shapes: Muong Nong-type (or layered), splash forms, and ablated or **flanged tektites** (Fig. 4.2). The Muong Nong-type tektites (named after a region in Laos) are blocky, layered tektites, some of which are larger than any of the splash-form or **ablated tektites**. The Muong Nong-type tektites are up to several tens of centimeters in size and can weigh as much as 24 kg (Koeberl 1992a). Petrographic and geochemical data indicate that they were not heated as intensely as the splash and ablated forms. For example, unlike the splash and ablated forms, they contain relict mineral grains (Fig. 4.3) and they have higher water contents compared to the splash-form and ablated tektites (Glass and Barlow 1979; Koeberl 1992b). Muong Nong-type tektites are believed to have been deposited closer to the source crater than were the ablated tektites and most of the splash-form tektites; and ^{10}Be data indicate that they came from a greater depth in the target deposits than did the splash-form and ablated tektites (Koeberl 1994; Ma et al. 2004).

Table 4.1 Cenozoic impact spherule/ejecta layers

Ejecta layer	Location	Impact evidence[a]	Age	Source crater	References
Well defined distal ejecta layers					
Australasian microtektite	Indian Ocean; western equatorial Pacific; Philippine, Sulu, Celebes, and South China Seas	L; SQ; SR with C, S and R; Ir (small)	780 ± 20 ka	Unknown (probably in Indochina)	Glass and Koeberl (2006)
Ivory Coast microtektite	Eastern equatorial Atlantic	L	~1.06 Ma	Bosumtwi	Koeberl et al. (1997b)
North American microtektite	Gulf of Mexico; Caribbean Sea; Barbados; western N. Atlantic	L, SQ with C, S, R, TiII	35.5 ± 0.3 Ma	Chesapeake Bay	Glass (2002)
Cpx spherule	Global?	SQ, C, Ir, HNi, NiSp, CrI	~35.5 Ma	Popigai	Liu et al. (2009)
Additional probable distal ejecta layers					
North Pacific microtektites	Core M14 (~8°N, 176°W) taken in the North Pacific	MOC, HNi, HCo, HIr	~2.14–2.30 Ma	Unknown	Peng (1994)
Tasman Rise microtektites	ODP Site 1169 on the western Tasman Rise, SE Indian Ocean	MOC	~4.6–12.1 Ma	Unknown	Kelly and Elkins-Tanton (2004)
Nuussuaq spherules	Nuussuaq, western Greenland	NiSp, HCo, HNi, HIr	~60 Ma	Unknown	Jones et al. (2005a)
Distal impact glasses not found in stratigraphic sections					
Tikal tektites	Tikal, Guatemala	NM, LW, RFe	800 ± 100 ka	Unknown	Hildebrand et al. (1994)
Darwin glass	Western Tasmania	L, C, HNi, HCo, HCr	816 ± 7 ka	Darwin	Howard (2008)
South-Ural glasses	Southern Urals, Western Siberia	LW, RFe	6.2 ± 0.3 Ma	Unknown	Koroteev et al. (1994)
High Na/K "australites"	Australia	L	10.2 ± 0.5 Ma	Unknown	Chapman and Scheiber (1969)
Central European tektites	Germany; Czech Republic; Austria	L, LW, RFe	14.7 ± 0.5 Ma	Ries	McCall (2001)

(continued)

Table 4.1 (continued)

Ejecta layer	Location	Impact evidence[a]	Age	Source crater	References
Libyan Desert Glass	Western Egypt	L; Zr > Bd; HCo, HNi, and HIr w/CR; OsI	~28–29.5 Ma	Unknown	de Michele (1997)
Urengoites	Northern West Siberia	L, LW, RFe	23.6 ± 1.6 Ma	Unknown	Masaitis et al. (1988)
Other proposed distal impact ejecta layers					
Younger Dryas	North America; Belgium	Ir, Fu(^{3}He), ND	~12.9 ka	?	Firestone et al. (2007)
Late Pliocene ejecta	Ross Sea, near Antarctica	?	~3–4 Ma?	?	Gerard-Little et al. (2006)
The Paleocene–Eocene Event	Global?	Ir (Italy& Slovenia)	~55 Ma	Unknown	Kent et al. (2003)
Miscellaneous					
Rio Cuarto glasses	Rio Cuarto, Argentina	L, DG, Zr > Bd	2–6 ka	Rio Cuarto	Schultz et al. (1994), Schultz et al. (2004)
Rio Cuarto glasses	Rio Cuarto, Argentina	L, DG, Zr > Bd	114 ± 26 ka	Unknown	Schultz et al. (1994), Schultz et al. (2004)
Lower Centinela del Mar	Centinela del Mar, Argentina	SM	230 ± 30 ka	Unknown	Schultz et al. (2004)
L1 meteoritic dust layer	EPICA-Dome C ice core, Antarctica	MD	434 ± 6 ka	Unknown	Narcisi et al. (2007)
Upper Centinela del Mar	Centinela del Mar, Argentina	SM	445 ± 21 ka	Unknown	Schultz et al. (2004)
L2 meteoritic dust layer	EPICA-Dome C ice core, Antarctica	MD	481 ± 6 ka	Unknown	Narcisi et al. (2007)
Rio Cuarto glasses	Rio Cuarto, Argentina	Unknown[b]	570 ± 100 ka[b]	Unknown	Bland et al. (2002)
Eltanin spherule layer	Bellingshausen Sea	MC	~2.15 Ma	No crater	Kyte (2002)

(continued)

Table 4.1 (continued)

Ejecta layer	Location	Impact evidence[a]	Age	Source crater	References
Mar del Plata glasses	Mar del Plata, Argentina	Zr > Bd	3.27 ± 0.08 Ma	Unknown	Schultz et al. (1998)
Bahia Blanca glasses	Bahia Blanca, Argentina	SQ, SF, DG	5.33 ± 0.5 Ma	Unknown	Schultz et al. (2006)
Chasicó glasses	Chasicó, Argentina	SQ, SF, DG	9.23 ± 0.09 Ma	Unknown	Schultz et al. (2006)

C coesite, *CR* chondritic ratios, *CrI* Cr isotope data, *DG* diaplectic glass, *Fu*(^{3} He) fullerenes containing ^{3} He, *HCo* high Co content, *HCr* high Cr content, *HIr* high Ir content, *HNi* high Ni content, *Ir* iridium anomaly, *L* lechatelierite in glass/spherules, *LW* low water in glass, *MC* meteoritic component, *MD* meteorite dust, *MOC* major oxide content of glass, *ND* nanodiamonds, *NiSp* Ni-rich spinel, *NM* no microlites in glass spherules, *OsI* osmium isotope data, *R* reidite, *RFe* reduced iron in glass, *S* stishovite, *SF* shocked feldspar with PDFs, *SM* shocked mineral grains, *SQ* shocked quartz with PDFs, *SR* shocked rocks, *TiII* the high-pressure phase TiO_2II, *Zr > Bd* zircon decomposed to baddeleyite and SiO_2

[a] Published evidence given in support of an impact origin; not all are unique to impact

[b] May be the same glasses from Rio Cuarto that were dated at 114 ka by Schultz et al. (2004). If so, then at least one of the dates is incorrect, but the glasses would have the same evidence for an impact origin as those described by Schultz et al. (2004)

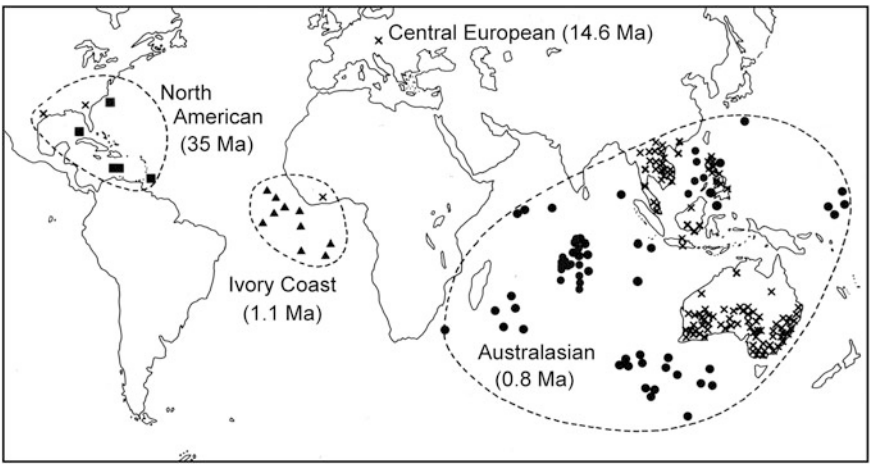

Fig. 4.1 Map showing the locations of the Cenozoic tektite/microtektite strewn fields. Formation ages of the tektites are shown in *parentheses*

Splash-form tektites occur as spheres, teardrops, dumbbells, and disc shapes. They are generally a few centimeters to 10 or more centimeters in size. The ablated tektites are splash-form tektites which were thrown up out of the atmosphere and were reheated and ablated as they came back down through the atmosphere. Some of the melted glass flowed back to form a flange around the periphery of these tektites (Fig. 4.2e, f). Flanged tektites are generally only a few centimeters in size. The best examples of ablated tektites are found in the Australasian strewn field where they are believed to be farther from the source crater than the splash-form tektites and, especially, the Muong Nong-type.

Tektites generally appear opaque black in reflected light, but the **Central European tektites** are transparent to translucent green. In transmitted light, a thin section of a tektite is generally transparent green. The surfaces are usually pitted and grooved due to solution while lying on the Earth's surface. Tektites contain lechatelierite particles (melted quartz grains) (Fig. 2.9), but are generally devoid of any crystalline material; the main exception being rare relict mineral grains, found in some Muong Nong-type tektites, which show evidence of shock metamorphism (Glass and Barlow 1979). Tektites can also contain vesicles, sometimes quite large, and schlieren or flow lines.

As previously mentioned, tektites are silica rich (Table 4.3). The silica content is generally between 66 and 83 wt %. The other major oxides vary inversely with the silica content (e.g., Fig. 4.4). Individual tektites are relatively homogeneous except at below about a 10 μm scale. However, plots of major oxides versus silica for a group of tektites from a given strewn field show well-defined compositional trends. The major and minor element and isotopic compositions are consistent with formation from sediments generally derived from post-Archean crust (Koeberl 1990, 1994).

Table 4.2 Tektite strewn fields

Strewn field	Location	Formation age[a] (Ma)	References	Sr model age (Ma)	Nd model age (Ga)	References	Source crater
Australasian	Southern China, Hainan Island, Indochina (Vietnam, Laos, Thailand, Cambodia), Malaysia, the Philippines, Brunei, Borneo, Belitung, Java, Flores, Australia, Tasmania	0.78 ± 0.02	Izett and Obradovich (1992), Kunz et al. (1995), Yamei et al. (2000)	175–250	1.04–1.19	Shaw and Wasserburg (1982), Blum et al. (1992)	Unknown (but probably in Indochina)
Ivory Coast	Ivory Coast, Africa	~1.1	Koeberl et al. (1997b)	950	1.9	Shaw and Wasserburg (1982)	Bosumtwi
Central European	Czech Republic, western Germany, northern Austria	~14.6	Storzer et al. (1995), Schwarz and Lippolt (2002), Laurenzi et al. (2003)	15	0.9	Shaw and Wasserburg (1982)	Ries
North American	U.S.A (Texas; Georgia; Martha's Vineyard, Massachusetts?), Cuba?	~35.4	Albin and Wampler (1996)	~400–490[d]	0.6–1.0	Shaw and Wasserburg (1982), Deutsch and Koeberl (2006)	Chesapeake Bay

[a] Age of tektites based on fission-track, K–Ar, and/or $^{40}Ar/^{39}Ar$ dating

[b] Time of weathering and major Rb/Sr fractionation (i.e., depositional age of the target rock)

[c] Age of source terrain which was eroded and deposited to produce the sedimentary target rock

[d] If Rb/Sr data for the tektite fragments from ODP Site 612 in the NW Atlantic off New Jersey are included, the range is between 316 and 742 Ma (Stecher et al. 1989)

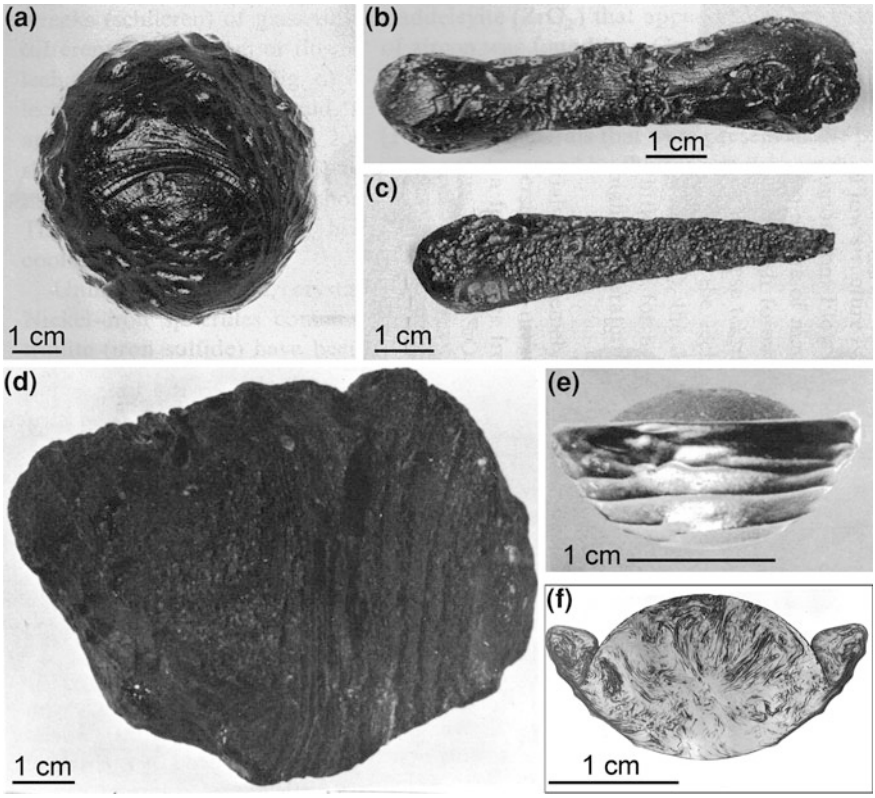

Fig. 4.2 Photographs of Australasian tektites showing the various types or forms. **a** Spherical-shaped indochinite (tektite from Indochina). Note pits and etched flow lines. **b** Dumbbell-shaped indochinite. Some pits and U-shaped grooves are present. **c** Teardrop-shaped indochinite with a pitted surface. **d** Muong Nong-type indochinite exhibiting some obvious layering. **e** Ablated australite. The anterior surface shows flow rings. The posterior surface, which is partially covered with the flange, is smooth and is a remnant of the original spherical surface. **f** Thin section of an ablated australite with the anterior surface at the *bottom* and posterior surface at the *top*. A section of the flange is evident on both sides. Flow lines or schlieren are evident throughout the tektite. **a**–**c**, **e**, and **f** are from Glass (1982). Reprinted with permission of Cambridge University Press

The water content of tektites is generally quite low ($\leq$0.02 wt %; Koeberl 1994; Beran and Koeberl 1997; Watt et al. 2011). The low water content may be due to "bubble stripping" (Melosh and Artemieva 2004). Vapor bubbles form in the shocked melt at relatively high pressures and when the melt is accelerated out of the crater at close to 50 g. Under these conditions vapor bubbles rapidly travel through the melt, carrying water vapor and other volatiles, and burst at the tektite surface (Melosh and Artemieva 2004). Tektite glass is relatively reduced as indicated by its low ferric to ferrous iron ratios (Fudali et al. 1987; Giuli et al. 2010). Sm–Nd isotopic data indicate that the source terrain for the sediments which were melted to produce the tektites ranges from 0.6 to 1.9 Ga (Table 4.2),

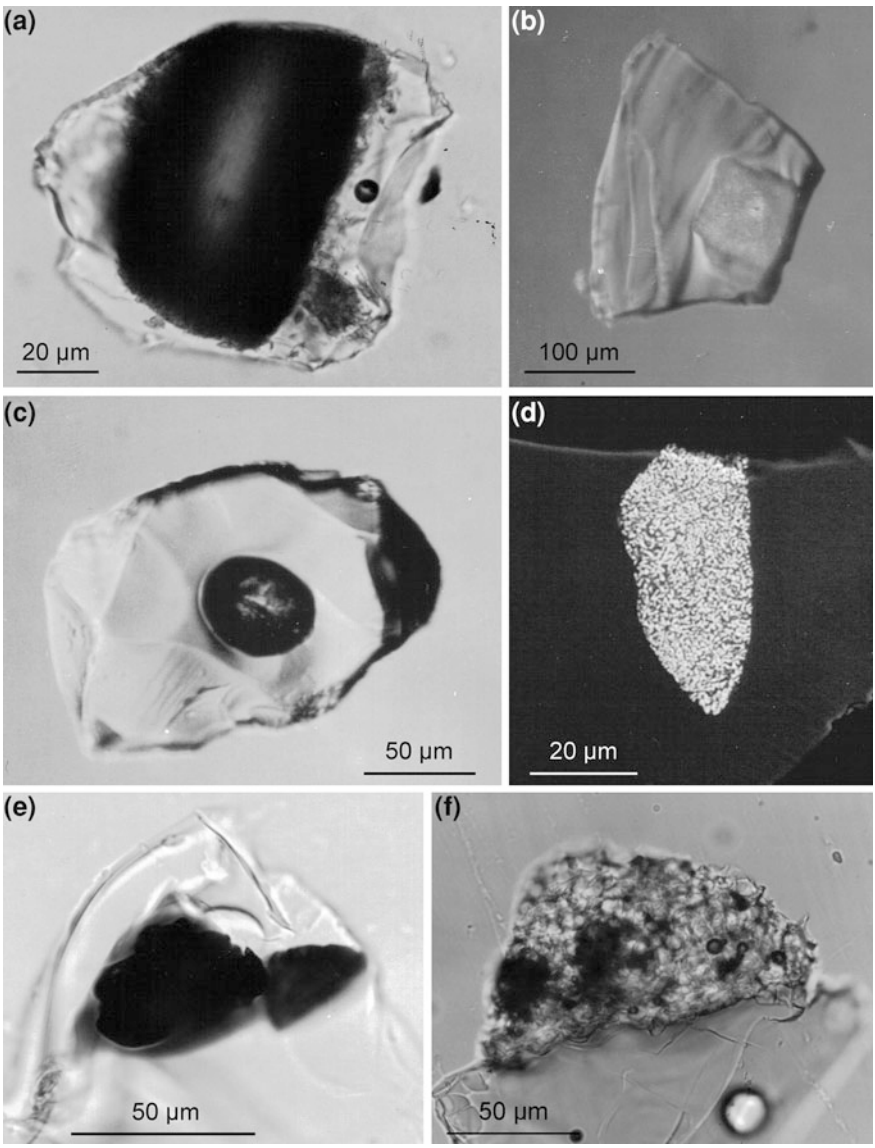

Fig. 4.3 Mineral inclusions recovered from Muong Nong-type indochinites. All are still at least partly enclosed in tektite glass. **a** Aluminum silicate (Al_2SiO_5) grain (dark with a translucent core) composed of submillimeter-sized corundum crystals (not obvious in this optical microscope image; see Fig. 2.11) in an SiO_2 glass matrix. **b** Octahedral chromite crystal ($\sim$80 µm across) in the *right side* of the glass fragment. **c** Rounded zircon crystal ($\sim 40 \times 50$ µm) in the center of a glass fragment. **d** Scanning electron microscope image of a polished section of a zircon (*light colored*), exhibiting a granular texture, in a glass matrix (*dark gray*). **e** Two rutile grains (*black*) in a glass fragment. Note that the glass is darker around the grains. This is due to the higher Ti content of the glass as a result of incipient melting of the rutile grains. **f** Quartz grain ($\sim 60 \times 120$ µm), with a few vesicles, attached to glass (at the *bottom*). **a**, **c**, **e**, and **f** are optical images taken in transmitted light. **b** was taken in reflected light. **d** is a scanning electron microscope image taken in backscattered electron mode. **a** and **e** are courtesy of Joy Deep Dass (Figs. 3c and 4c, respectively, in Dass 1999)

Table 4.3 Tektite compositions

	Australasian				Ivory
	Australites (17)	Philippinites (17)	High Mg (10)	Muong Nong (19)	Coast (11)
SiO_2	70.42–78.79	68.9–72.1	64.8–77.0	77.08–81.73	66.17–68.48
TiO_2	0.55–0.81	0.75–1.02	0.66–0.77	0.53–0.72	0.54–0.61
Al_2O_3	9.36–13.70	12.33–15.23	10.7–13.3	8.60–11.41	16.28–17.72
Fe_2O_3	0.23–1.01	0.50–1.20			
FeO	3.46–4.60	4.04–4.81	**3.85–8.63**	**3.18–4.15**	**5.84–6.45**
MgO	1.50–2.48	2.32–2.93	1.83–7.95	1.19–1.65	2.98–4.39
CaO	2.13–5.09	2.50–3.97	1.79–3.73	1.03–1.63	1.21–1.52
Na_2O	1.12–1.52	1.18–1.76	0.62–1.38	0.77–1.07	1.53–2.08
K_2O	2.08–2.55	2.17–2.56	1.34–2.56	2.24–2.55	1.73–2.13
	Central European			North American	
	Bohemia (43)	Germany (15)	Austria (7)	Bediasites (21)	Georgiaites (24)
SiO_2	71.9–81.0	77.2–81.1	77.8–85.1	71.89–80.17	78.9–83.4
TiO_2	0.23–0.50	0.26–0.42	0.24–0.35	0.59–1.05	0.42–0.57
Al_2O_3	8.96–12.7	8.94–11.8	8.10–10.6	11.19–17.56	10.3–12.3
Fe_2O_3				0.00–0.45	
FeO	**1.28–2.86**	**1.32–2.51**	**1.02–1.78**	2.29–5.26	**1.85–3.68**
MgO	1.52–3.73	1.06–2.73	1.25–2.10	0.37–0.95	0.49–0.76
CaO	2.05–4.48	0.93–3.85	1.46–3.30	0.49–0.96	0.40–0.53
Na_2O	0.25–0.60	0.28–0.70	0.19–0.49	1.20–1.84	0.78–1.06
K_2O	2.88–3.77	3.06–3.75	2.62–3.90	1.60–2.43	2.28–2.58

Note Australites are from Australia, philippinites are from the Philippines, indochinites are from Indochina, the high-Mg tektites are mostly from Java, Muong Nong-type tektites are blocky, layered tektites from Indochina, Bohemia is in the Czech Republic, bediasites are from Texas, and georgiaites are from Georgia, USA

Compositional data are from the following sources: australites, Taylor (1962); philippinites and indochinites, Schnetzler and Pinson (1963); high-Mg tektites, Chapman and Scheiber (1969); Muong Nong-type tektites, Koeberl (1992a); Ivory Coast tektites, Koeberl et al. (1997b); Central European tektites from Bohemia and Germany, Lange (1996); Central European tektites from Austria, Koeberl et al. (1988); bediasites, Chao (1963); georgiaites, Albin et al. (2000)

FeO values given in bold indicate that total iron is reported as FeO

Numbers in parentheses indicate the number of analyses

while Rb–Sr isotopic data indicate sedimentation ages for the target rocks that range from 15 to 950 Ma (Shaw and Wasserburg 1982; Blum et al. 1992). Surprisingly, meteoritic contamination is generally below detection limit; however, Koeberl and Shirey (1993) found up to 0.1 % meteoritic component in Ivory Coast tektites using the Os isotopic method.

At first glance, tektites, with the exception of the Central European tektites, can be mistaken for obsidian (volcanic glass), but they can be distinguished from obsidian by their petrography and composition (Table 4.4). Unlike volcanic glass, tektites do not contain microlites or crystallites, but they do contain lechatelierite particles. Tektites generally have lower alkali (Na_2O and K_2O) and higher MgO contents for a given silica content. More importantly, tektites can be distinguished from volcanic glass by their lower water content and lower Fe^{3+}/Fe^{2+} ratios.

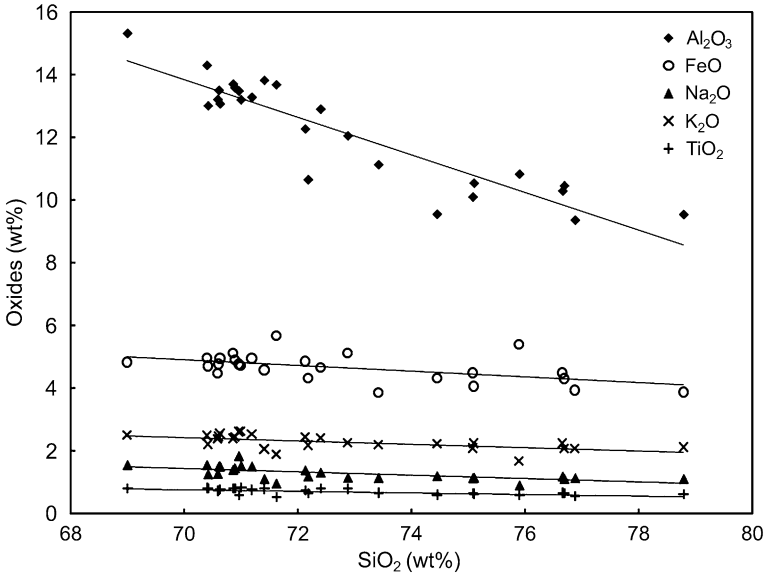

Fig. 4.4 Al_2O_3, FeO, Na_2O, K_2O, and TiO_2 contents versus SiO_2 contents for australites (tektites from Australia). Note that oxide contents vary inversely with SiO_2 contents. CaO and MgO contents also vary inversely with SiO_2, but were not included in the figure for the sake of clarity. Compositional data used in these plots are from Schnetzler and Pinson (1963) and Chapman and Scheiber (1969)

Table 4.4 Comparison between tektites and volcanic glass

	Tektites	Volcanic glass
Morphology		
Evidence of aerodynamic ablation	Sometimes	No
Splash forms (teardrops, dumbbells, etc.)	Common	Rare
Petrography		
Contain microlites/crystallites	No	Yes
Contain shocked relict mineral grains	Rarely	No
Contain lechatelierite	Yes	No
Chemistry		
Water content	<0.02 wt %	>0.1 wt %
Fe^{3+}/Fe^{2+} ratio	Low (generally <0.2)	High (generally >0.2)

The evidence for an impact origin for tektites includes the ubiquitous presence of lechatelierite particles, the presence of rare shock-metamorphosed mineral grains in some Australasian, Central European, and North American Muong Nong-type tektites, and the evidence for up to 0.1 % meteoritic component in some Ivory Coast tektites as mentioned above. Evidence of shock metamorphism in mineral grains recovered from some Muong Nong-type tektites includes X-ray asterism, breakdown of zircon to baddeleyite and silica glass, and breakdown of an Al_2SiO_5

phase to corundum plus silica glass (Glass and Barlow 1979; Glass et al. 1995; Dass 1999; Fig. 4.3). Furthermore, shocked quartz grains (exhibiting planar deformation features or partially converted to coesite and/or rarely stishovite) and shock-metamorphosed rock fragments have been found in the Australasian and North American microtektite layers (this is discussed in more detail in Sects. 4.2.7 and 4.5.7). In addition, to date source craters have been identified for three of the four Cenozoic tektite strewn fields.

The source crater for the Ivory Coast tektites is the Bosumtwi crater in Ghana, the Central European source crater is the **Ries crater** in Germany, and the North American source crater is the **Chesapeake Bay structure** on the east coast of the U.S.A. Identifications of the source craters are based on geographic location, age (Ar–Ar, Rb–Sr, Sm–Nd), and composition (Horn et al. 1985; Engelhardt et al. 1987; Poag et al. 1994; Koeberl et al. 1996, 1997b, 1998; Deutsch and Koeberl 2006). The source crater for the Australasian tektites has not been found, but most investigators believe that it is somewhere in the Indochina area (e.g., Schnetzler 1992; Koeberl 1994; Ma et al. 2004; Glass and Koeberl 2006). The evidence for identification of the source craters is discussed in more detail below.

Most tektite researchers agree that tektites are distal impact glasses (e.g., Koeberl 1994), and ^{10}Be concentrations measured in Australasian and Ivory Coast tektites suggest that tektites are derived from surface or near surface deposits (e.g., Ma et al. 2004; Serefiddin et al. 2007). However, the details of tektite/microtektite formation and how they are distributed from the source crater are unknown, or at least not agreed upon. Some authors have proposed that tektites formed by jetting (e.g., Vickery 1993); but, according to expectations from model calculations, melt produced by this process should be enriched in projectile (meteoritic) material, and tektites generally show no evidence of meteoritic contamination. Other authors have proposed that tektites (or a restricted population of tektites) might have been formed by melting of surface sediments and ejection of melt by the impact-heated and compressed atmosphere prior to the projectile making contact with the Earth's solid surface (Scott 1999). However, it does not seem likely that such a mechanism could explain the widespread geographic distribution of most tektite strewn fields.

It has been proposed that, if an impact is big enough, a vapor plume is formed that can accelerate molten blobs of impact melt into space where they solidify to form glass bodies (e.g., tektites and microtektites). These bodies can then travel above the atmosphere along ballistic trajectories before falling back to Earth forming tektite strewn fields that can extend thousands of kilometers across the Earth's surface. Numerical modeling indicates that high-velocity (35–40 km/s) impacts into a dry target with impact angles of 30 to 50° may provide the best conditions for tektite production (Artemieva 2001, 2008). Numerical simulations suggest that cm-sized melt masses can move in the post-impact flow with local gas velocity without appreciable drag and along ballistic-like trajectories.

Thousands of papers and several books have been written about tektites. For more information about these unusual glasses the reader is referred to one or more of the following books or review articles: O'Keefe (1963) (this book, edited by John A. O'Keefe, summarizes what was known about tektites up to the early

1960s), Barnes and Barnes (1973) (this is a collection of some of the most important papers on tektites up until the early 1970s), Glass (1990a) (this paper is a brief summary of what was known about tektites and microtektites as of the late 1980s), O'Keefe (1976) (this book, written by John A. O'Keefe, summarizes what is known about tektites, but with emphasis on supporting the lunar volcanic origin for tektites), Koeberl (1994) (this paper summarizes the geochemistry of tektites and what is known about the origin of tektites by hypervelocity impact), and McCall (2001) (this book summarizes much of what we know about the tektite strewn fields, with emphasis on the Australasian strewn field).

4.2 The Australasian Microtektite Layer

Australasian microtektites were discovered in deep-sea sediments in the mid 1960s (Glass 1967). As of 2007, Australasian microtektites had been identified in over 60 cores (Prasad et al. 2007). The Australasian strewn field is the largest of the Cenozoic tektite/microtektite strewn fields in terms of its known geographic extent. This microtektite layer is closely associated with the Brunhes–Matuyama geomagnetic polarity reversal boundary (Glass 1972a; Schneider et al. 1992). The Australasian microtektites are believed to be associated with the Australasian tektites based on their geographic proximity, age, and chemical compositions (Glass 1967, 1972a; Cassidy et al. 1969; Gentner et al. 1970). More recently, microtektites have been found in the Transantarctic Mountains in Antarctica. These microtektites appear to belong to the Australasian strewn field (Folco et al. 2008, 2009, 2010a).

4.2.1 Description of the Australasian Microtektites

Unbroken Australasian microtektites are generally spherical in shape, but other splash forms (teardrops, dumbbells, discs) are also present (Fig. 4.5a). Estimates of the percent abundance of spherical shaped microtektites ranges from 62 to 90 % (Smit et al. 1991; Prasad and Sudhakar 1996; Lee and Wei 2000). Rarely, irregular but rounded forms have also been observed. Glass fragments make up from <1 to ~40 % of the glass particles at a given site. It is generally the larger microtektites that are broken.

Most Australasian microtektites are less than a millimeter in diameter or length, but some splash forms are a millimeter or more in length. At one site in the central Indian Ocean, 29 microtektites with sizes ~1 mm were recovered from a box core with a cross section of 30 × 30 cm (Prasad and Sudhakar 1999). Sixteen of these minitektites were spherical with diameters up to 2.03 mm. The remainder were dumbbells, teardrops, disc, and oval shapes. The largest was an oval-shaped minitektite with a length of 3.75 mm (Prasad and Sudhakar 1999). The

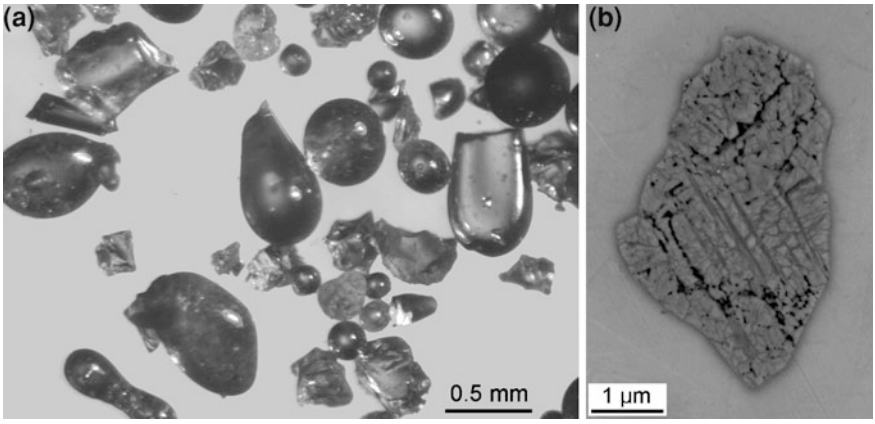

Fig. 4.5 Images of Australasian microtektites. **a** Optical microscope image of a group of Australasian microtektites from Deep-Sea Drilling Project Site 1144 in the northern South China Sea. Microtektites consist of splash forms and fragments. The splash forms are mostly spherical in shape, but teardrop and dumbbell shapes are also present. Vesicles can be seen in many of the microtektites. Most are transparent, but some are translucent. **b** A backscattered-electron image of a quartz inclusion in an Australasian microtektite from Core SO95-17957-2 taken in the South China Sea. The grain has presumably undergone incipient melting preferentially along planar features (perhaps planar deformation features). The melt was quenched to form lechatelierite lamellae (*darker gray*). **b** is courtesy of Luigi Folco

Australasian microtektites increase in abundance with decreasing size. In one core, the number of microtektites was determined to increase in abundance with decreasing size down to at least 38 μm, but most of the mass (over 90 wt %) was in the >125 μm size range (Cassidy et al. 1969).

The Australasian microtektites generally range from transparent colorless, to pale yellow, to greenish yellow, to dark brown in color (Smit et al. 1991; Prasad and Sudhakar 1996; Lee and Wei 2000; Glass and Koeberl 2006). The darker colored ones are generally translucent, but can be opaque. The transparent colorless microtektites are usually smaller than the darker ones. There are also some transparent bottle-green microtektites. The percent abundance of each color varies from site to site.

Most Australasian microtektites exhibit some surface sculpturing due to solution in the pore water in the sediment, although some have shiny smooth surfaces (Figs. 4.5a and 4.6a). The most common surface features are pits (Fig. 4.6b and c; Glass 1974, 1984a). In addition, circular features are observed protruding above the surface of some microtektites (Fig. 4.6d). These are believed to be silica-rich inclusions which were originally at the surface of the microtektites, but underwent solution at a much lower rate than the adjacent glass. Some microtektites have flow lines that have been etched out on the surface (Smit et al. 1991). The bottle-green microtektites generally have badly corroded surfaces (Fig. 4.6f). In addition to the surface features formed by solution, high velocity impact pits have been observed on the surface of some of the Australasian microtektites (Fig. 3.9f; Prasad and Sudhakar 1998).

Table 4.5 Composition of Australasian microtektites and tektitestektites

	Microtektites								Tektites
	Normal (30)		High Ni (7)		High Mg (4)		Transantarctic Mountain (53, 12)		Australites (17)
SiO_2	60.48–78.05		66.69–72.01		51.83–56.35		59.8–77.6		70.4–78.8
TiO_2	0.64–1.18		0.69–0.81		0.72–1.17		0.71–1.29		0.55–0.81
Al_2O_3	10.25–21.46		12.48–14.94		14.66–20.66		12.2–23.4		9.36–13.70
FeO	2.90–7.23		5.11–6.77		4.50–7.78		2.60–5.49		3.67–5.51
MgO	1.67–5.07		2.90–4.17		11.34–21.82		1.89–5.57		1.50–2.48
CaO	1.63–6.56		2.37–4.30		4.37–5.72		2.17–5.3		2.13–5.09
Na_2O	0.22–1.70		0.98–1.59		0.43–0.79		0.15–0.42		1.12–1.52
K_2O	0.67–3.21		2.22–2.86		0.04–0.17		0.38–1.49		2.08–2.55
	Average	S.D.	Average	S.D.	Average	S.D.	Average	S.D.	Range
Sc	14.3	3.7	12.9	1.1	21.7	4.5	18.4	2.5	8.2–13
Cr	128	105	215	100	962	374	72.5	19.8	58–145
Co	12	7	26	10	11.0	5.9	6.0	1.2	14–25
Ni	39	21	260	110	44.3	22.4	6.0	1.1	22–105
Zn	13	12	19	17	8	2	1.7	0.5	n.d.
Ga	38	34	76	49	59	49	n.d.	n.d.	4.5–12
Rb	76	46	122	14	4	2	36	8	75–106
Sr	200	78	161	35	235	66	212	19	150–250
Zr	315	81	280	67	358	172	320	18	238–326
Sb	0.26	0.25	0.87	1.13	0.25	0.38	n.d.	n.d.	n.d.
Cs	4.30	3.11	6.9	1.1	0.18	0.10	2.15	0.55	4.2–5.7
Ba	475	112	452	66	560	165	519	46	320–380
La	48.3	9.5	44.6	4.0	56.8	15.2	52.0	4.0	32.3–37.4
Ce	95.5	25.6	82.5	5.8	95.3	31.5	101	8	70.7–80.0
Nd	43.9	10.6	39.2	5.8	48.4	11.8	43.6	3.4	29.6–35.4
Sm	8.54	2.00	7.99	1.15	9.75	2.58	8.5	0.7	5.51–6.22

(continued)

Table 4.5 (continued)

	Microtektites								Tektites
	Normal (30)		High Ni (7)		High Mg (4)		Transantarctic Mountain (53, 12)		Australites (17)
	Average	S.D.	Average	S.D.	Average	S.D.	Average	S.D.	Range
Eu	1.56	0.43	1.42	0.20	1.89	0.49	1.62	0.13	0.97–1.17
Gd	7.20	1.52	6.59	0.39	8.86	2.44	n.d.	n.d.	4.48–5.99
Tb	1.19	0.32	1.02	0.09	1.46	0.42	1.04	0.08	0.70–0.10
Yb	3.87	0.83	3.58	0.54	4.39	1.06	3.90	0.32	2.43–2.80
Lu	0.57	0.13	0.52	0.11	0.65	0.15	n.d.	n.d.	n.d.
Hf	8.07	2.30	7.60	2.43	10.85	4.18	8.53	0.49	n.d.
Ta	1.57	0.35	1.48	0.08	1.96	0.60	1.81	0.15	n.d.
Th	16.0	4.3	13.5	2.3	20.1	5.5	19.4	1.6	12.6–15.0
U	1.76	1.34	2.57	0.76	0.58	0.14	0.49	0.12	2.02–2.60

Numbers in parentheses indicate number of analyses. Where there are two numbers the first number is for the major oxides and the second is for trace elements

Major oxides given as wt % and minor element contents are ppm

All iron reported as FeO

S.D. Standard deviation ($\pm 1\sigma$), *n.d.* no data

Compositional data for normal, high-Ni, and high-Mg Australasian microtektites are from Glass et al. (2004b); data for Transantarctic Mountain microtektites are from Folco et al. (2009); data for australites are from Taylor and Sachs (1964) and Taylor and McLennan (1979)

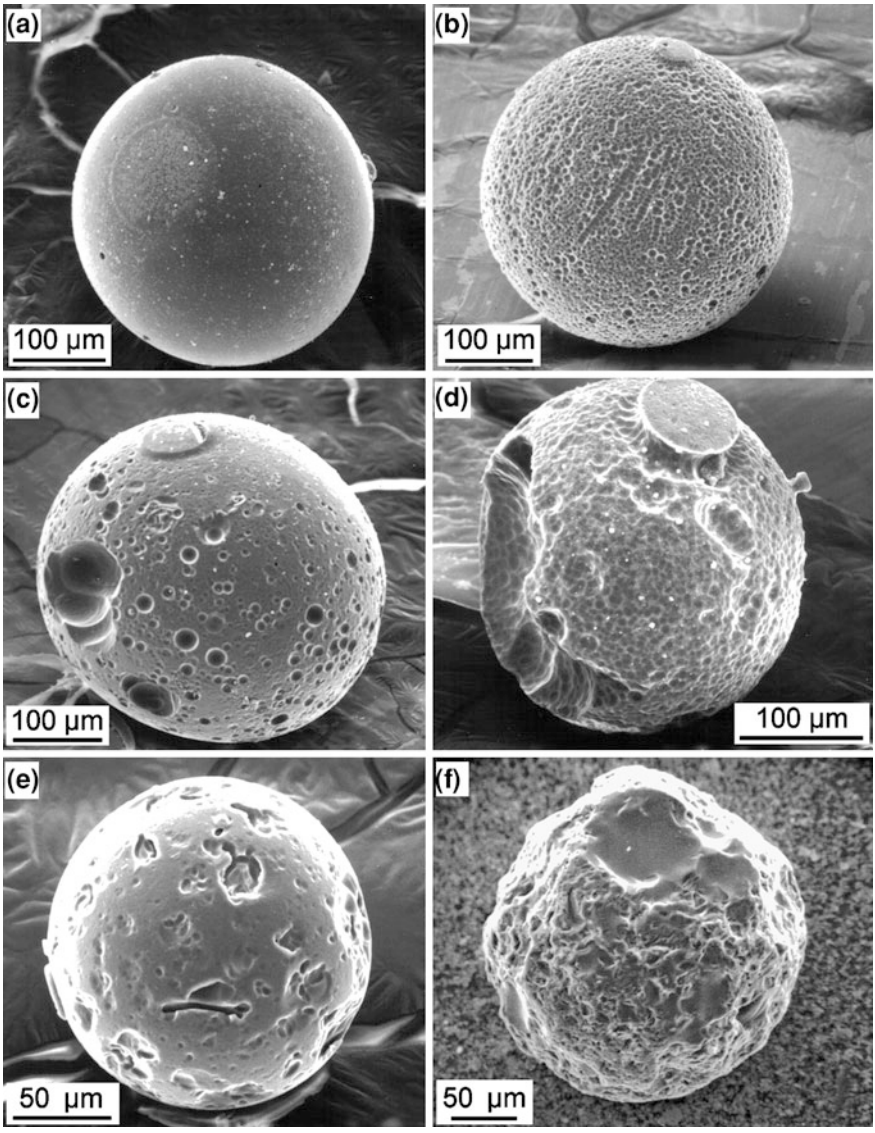

Australasian microtektites are generally holohyaline; however, some Australasian microtektites in the South China Sea region do contain rare quartz inclusions in addition to some sub-micrometer sized Fe-rich crystals and a Zr phase, probably zircon (Folco et al. 2010a). Bubble cavities are common and schlieren (flow lines) and lechatelierite particles have been observed in some Australasian microtektites (Cassidy et al. 1969; Smit et al. 1991; Glass and Koeberl 2006).

◀ **Fig. 4.6** Scanning electron microscope images of Australasian microtektites exhibiting a variety of surface features. **a** Image of a microtektite with a relatively smooth surface. This microtektite has a shiny smooth surface in reflected light. **b** Microtektite with numerous small pits scattered over most of the surface. Near the *top* and slightly to the *right* there is a smooth circular area (~50 μm in diameter) that is elevated above the surrounding surface. The elevated circular area is probably silica rich and is elevated due to solution of the surrounding glass. This microtektite has a frosted appearance in reflected light. **c** A microtektite with numerous moderately large (up to almost 100 μm diameter) pits scattered over its surface. An ~70 μm diameter elevated circular area (probably silica rich) is present near the *top* and slightly to the *left* in this image. Elevation of the circular area is likely due to differential solution between it and the surrounding glass. **d** A heavily pitted microtektite with a U-shaped groove (~25 μm across) and two elevated circular protrusions: one near the *top* (~80 μm diameter) and one protruding at the *upper right* (~10 μm). They are elevated ~10 μm above the adjacent surface. Elevation is presumably due to differential solution. **e** This microtektite has a large number of irregular pits and some narrow U-shaped grooves, and a raised circular area barely visible on the *lower left* (~30 μm diameter). Some of the pits appear to be micro-impact craters which have been modified by dissolution. **f** This is a high-Mg, bottle-green, microtektite. The corroded appearance is typical for the high-Mg microtektites. **a** and **b** are from Core RC12-328 and RC12-327, respectively, from the northwest Indian Ocean. **c** is from Core LSDH-23G-1 taken in the southwest Indian Ocean and **d** is from Core V16-70, which was also taken in the southwest Indian Ocean. **e** is from Core V20-138 taken in the Philippine Sea and **f** is from Core V19-153, taken in the eastern equatorial Indian Ocean south of Sumatra

4.2.2 Composition of the Australasian Microtektites

Based on their appearance and composition, the Australasian microtektites can be divided into two end-member groups: (1) normal microtektites, which are generally transparent pale yellow to brown in color, and (2) bottle-green, highly corroded, magnesium-rich (up to 24 wt % MgO) microtektites. The normal Australasian microtektites are the most abundant and have major and trace element compositions similar to the Australasian tektites; however, the microtektites have a broader range in composition than the tektites and extend down to lower SiO_2 contents (Table 4.5; Fig. 4.7; Cassidy et al. 1969; Frey et al. 1970; Glass 1972a, b; Glass et al. 2004b).Yellow-green Australasian microtektites have compositions that are intermediate between the normal and high-Mg, bottle-green microtektites (Cassidy et al. 1969). The normal Australasian microtektites have trace element contents similar to the average trace element content of the upper continental crust. Glass et al. (2004b) identified a high-Ni group of normal Australasian microtektites with higher Ni and Co and generally higher Cr contents than the other normal Australasian microtektites (Table 4.5). The Cr, Co, and Ni contents of the high-Ni Australasian microtektites are positively correlated with each other and with the FeO and MgO contents, and are negatively correlated with the other major oxides. This is suggestive of meteoritic contamination; but the ratios between Cr, Co, and Ni contents are closer to mantle ratios than to meteoritic.

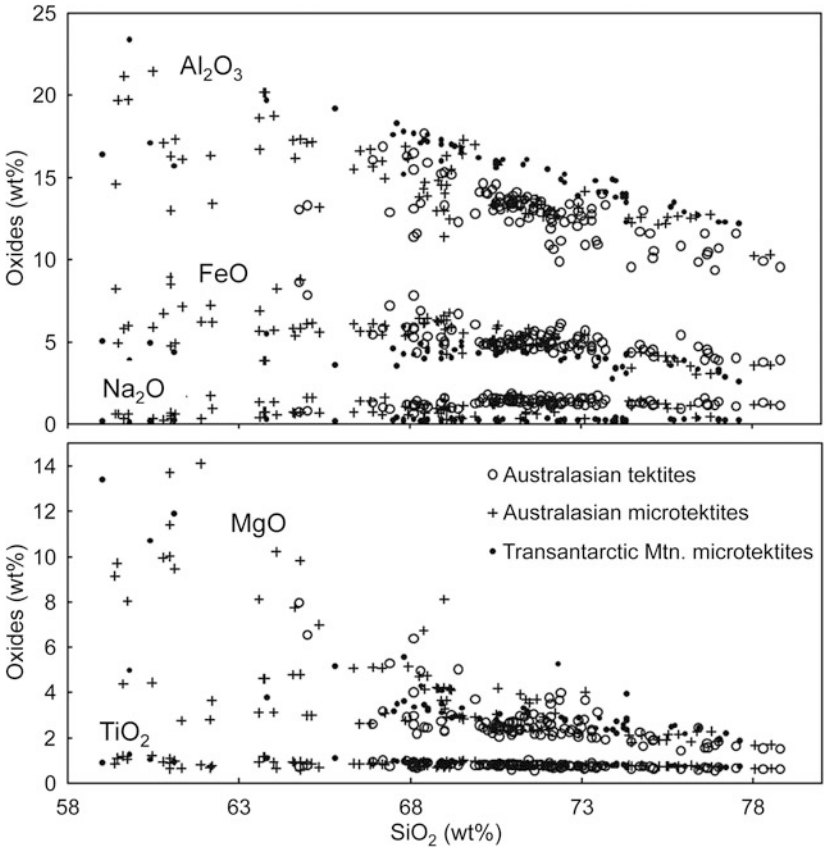

Fig. 4.7 Al_2O_3, FeO, Na_2O, MgO, and TiO_2 contents versus SiO_2 contents for Australasian tektites and microtektites and Transantarctic Mountain microtektites. Note that the tektites and microtektites (including the Transantarctic Mountain microtektites) fall along similar compositional trends. The same is true for CaO and K_2O versus SiO_2, which are not shown here. The microtektites extend the trends down to lower SiO_2 contents with corresponding increases in the other major oxides, with the exception of K_2O (not shown) and Na_2O. The Transantarctic Mountain microtektites generally have higher Al_2O_3 and lower Na_2O contents for a given SiO_2 content compared to the Australasian tektites and microtektites. Australasian tektite compositional data are from Schnetzler and Pinson (1963) and Chapman and Scheiber (1969). Australasian microtektite compositional data are from Glass (1972a) and Glass et al. (2004a). Transantarctic Mountain microtektite data are from Folco et al. (2009)

4.2.3 Age

The Australasian microtektite layer is closely associated with the Brunhes–Matuyama (B–M) geomagnetic polarity reversal boundary. In cores with low sediment accumulation rates (i.e., <1 cm/ka), the microtektite layer is generally on or

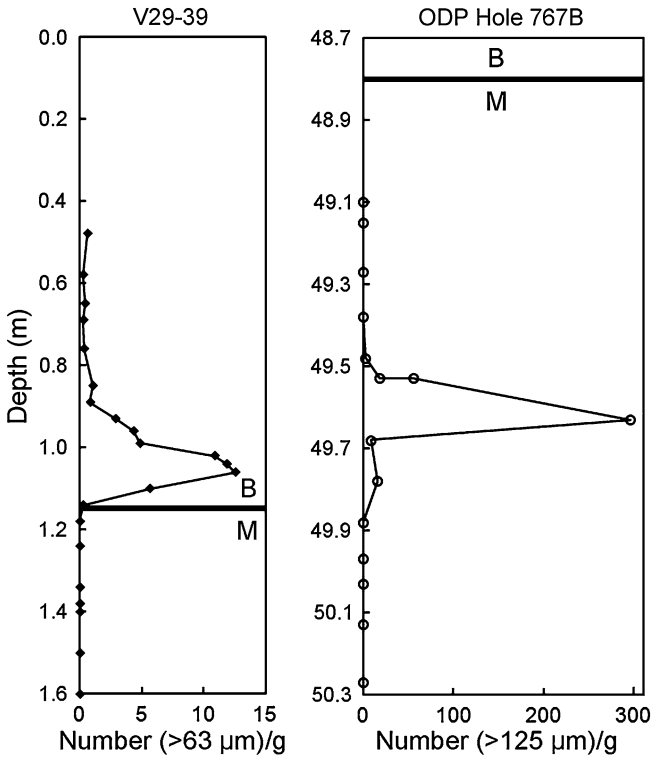

Fig. 4.8 Relationship between the Australasian microtektite layer and Brunhes–Matuyama (B–M) geomagnetic reversal boundary in Core V29-39 and Core 6H from Ocean Drilling Project Hole 767B. The microtektite layer in Core V29-39 is ~9 cm above the B–M boundary, but at Hole 767B the microtektite layer is ~80 cm below the B–M. The difference is apparently due to post-depositional remanent magnetization (see Sect. 11.2.2)

slightly above the B–M reversal boundary. However, in cores with high sediment accumulation rates, the microtektite layer is below the B–M reversal boundary (Fig. 4.8). This apparent inconsistency is probably due to post-depositional remanent magnetization (see Sect. 11.2.2). Detailed studies of the relationship indicate that the microtektites were deposited ~12 ka before the B–M reversal (Burns 1989; Schneider et al. 1992). The age of the B–M reversal boundary is estimated to be ~0.78 Ma (Izett and Obradovich 1994; Sarna-Wojcicki et al. 2000). This indicates a stratigraphic age of ~0.78 Ma for the Australasian microtektite layer. This is consistent with the formation age of 0.7 ± 0.1 Ma for the Australasian microtektites as determined by fission-track dating (Gentner et al. 1970) and it is consistent with the 0.78 ± 0.02 Ma formation age of the Australasian tektites determined by ^{40}Ar-^{39}Ar dating (Izett and Obradovich 1992; Kunz et al. 1995; Yamei et al. 2000). More recently, ^{40}Ar-^{39}Ar plateau ages for eight Australasian tektites indicate an age of 0.786 ± 0.013 Ma for the Australasian tektites (Trieloff et al. 2007).

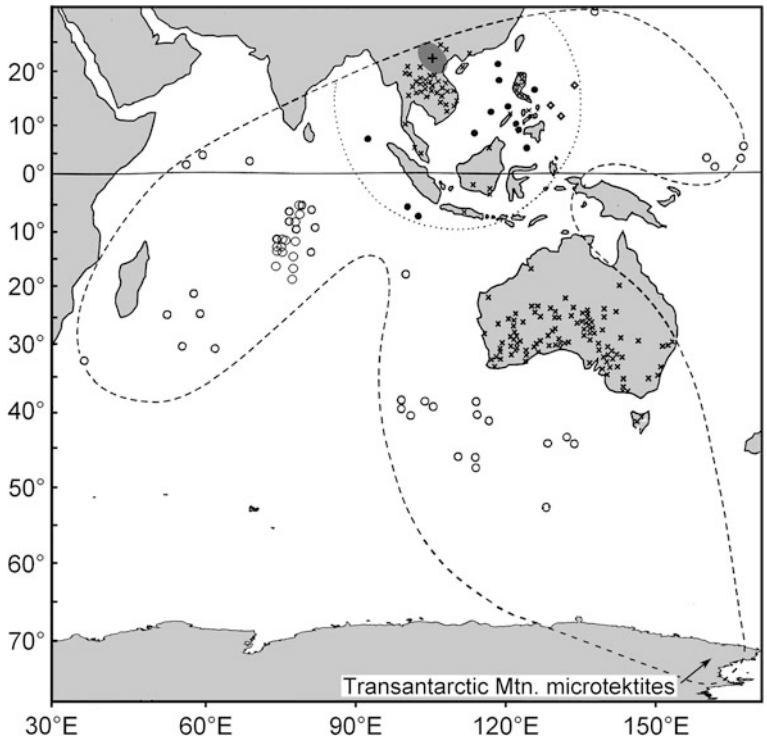

Fig. 4.9 Map of the Australasian tektite/microtektite strewn field. The *dashed line* encloses the area where Australasian tektites (Xs) and microtektites have been found. *Circles* indicate sites on the seafloor where cores have been taken that contain Australasian microtektites. Australasian microtektites have also been found in the Transantarctic Mountains (see Sect. 4.2.8). Core sites where both microtektites and unmelted ejecta (e.g., shocked quartz and coesite) have been found are indicated by *solid black circles*. Core sites where only microtektites were found are indicated by *open circles*. *Open diamond shapes* east of the Philippines indicate sites where only unmelted ejecta have been found at the same stratigraphic level as the microtektite layer at other sites. A *dotted line* separates the region where unmelted ejecta have been found in the microtektite layer from the sites where only microtektites have been found. The *shaded oval* (with a *plus sign* in its *center*) in northern Indochina marks the area where a source crater would best explain the distribution of the Australasian microtektites (see Fig. 4.16 and Sect. 4.2.10)

4.2.4 Geographic Occurrence

Australasian microtektites have been found mostly in the Indian Ocean, but they have also been found in the western equatorial Pacific Ocean, the Philippine, Sulu, Celebes, and, more recently, South China Seas (Fig. 4.9; Glass and Koeberl 2006; Prasad et al. 2007, and references therein). The strewn field may be divided into three lobes; one extending from the Indochina area into the southwest Indian Ocean towards the southern tip of Africa, one extending from Indochina down

through Australia toward Antarctica, and one extending from Indochina to the east out into the western Pacific. The boundary of the Australasian microtektite strewn field is based on where the number of microtektites falls below detection limit, which is generally less than $\sim 0.5/cm^2$. The shape of the strewn field shown in Fig. 4.9 is based on where Australasian tektites and microtektites have been found and not found; but the absence of tektite/microtektites at a given site can be due to a number of factors (e.g., erosion). Thus, the absence of microtektites in a core may or may not indicate that microtektites did not fall in that area. Microtektites believed to be Australasian microtektites have been found in the Transantarctic Mountains in Antarctica (see Sect. 4.2.8). In addition, glass spherules referred to as microtektites have been found in a loess layer in northwestern China.

Nineteen glass spherules, believed to be microtektites, were recovered from loess deposits in the Luochuan Province of northwest China (Li et al. 1993). The glass spherules were found in the L8 loess unit. According to Li et al. (1993), the layer containing the glass spherules lies 40–70 cm above the Brunhes–Matuyama (B–M) reversal boundary. The spherules range between 65 and 220 μm in size and are mostly spherical- to kidney-shaped, but some have a teardrop or elongated shape. They range from transparent to translucent and they range in color from green to amber and yellow. The surfaces of the spherules are etched and exhibit pits and grooves (Li et al. 1993). They contain spherical bubble cavities less than 10 μm in diameter. There is no mention of the presence or absence of microlites/crystallites or lechatelierite particles. Based on their geographic location, age of deposition, appearance, and chemical composition, Li et al. (1993) proposed that these spherules are microtektites and they might belong to the Australasian microtektite strewn field.

Based on their major oxide compositions, Li et al. (1993) divided the Chinese spherules into four chemical groups: normal, bottle-green, high aluminum, and silica-magnesium (Si–Mg). Li et al. (1993) referred to the spherules in the first three groups as microtektites and the spherules in the fourth group as glassy "Si–Mg microspherules." The composition of only one normal 'microtektite' was given and it had a silica content of ~ 85 wt %. The Australasian microtektites do not have a silica content that high (see Table 4.5). The average composition plus/minus one standard deviation for three bottle-green 'microtektites' is: $SiO_2 = 51.59 \pm 4.06$, $Al_2O_3 = 15.52 \pm 2.89$, $FeO = 9.75 \pm 0.85$, $MgO = 7.03 \pm 1.04$, $CaO = 0.52 \pm 0.45$, $Na_2O = 0.53 \pm 0.91$, $K_2O = 8.43 \pm 0.68$, $TiO_2 = 0.85 \pm 0.87$ (in wt %; Li et al. 1993). Compared with the composition of the high-Mg (bottle-green) Australasian microtektites (see Table 4.5), the bottle-green Chinese 'microtektites' have high FeO and very high K_2O (more than an order of magnitude) and very low MgO and CaO contents. The average composition plus/minus one standard deviation for seven high-Al_2O_3 'microtektites' is: $SiO_2 = 48.95 \pm 4.71$, $Al_2O_3 = 37.64 \pm 9.63$, $FeO = 2.58 \pm 1.73$, $MgO = 1.99 \pm 1.58$, $CaO = 0.27 \pm 0.29$, $Na_2O = 1.00 \pm 1.12$, $K_2O = 5.11 \pm 4.39$, $TiO_2 = 0.15 \pm 0.21$ (in wt %; Li et al. 1993). The high-Al_2O_3 Chinese 'microtektites' appear to be the most abundant, but they are very rare among the Australasian microtektites, making up less than 1 % by number. Compared with

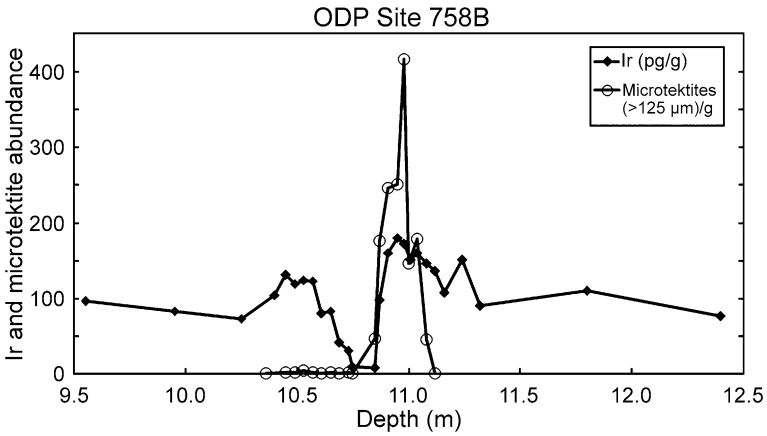

Fig. 4.10 Australasian microtektite and Ir distribution at Ocean Drilling Program Site 758 in the northeast Indian Ocean. Note that the peak Ir content correlates with the peak abundance of microtektites. Australasian microtektite data from Schneider et al. (1992) and Ir data from Schmidt et al. (1993)

the high-Al_2O_3 Australasian microtektites, the high-Al_2O_3 Chinese 'microtektites' have lower average MgO and very low CaO and TiO_2 (but with some overlap) and most have much higher (an order of magnitude) K_2O contents. The glassy Si–Mg microspherules are composed of approximately equal amounts of SiO_2 and MgO with less than 2.3 wt % FeO, less than 1.5 wt % Al_2O_3 and Na_2O, less than 0.5 wt % CaO, less than 0.2 wt % K_2O, and only a trace amount of TiO_2. None of the Australasian microtektites have compositions similar to these spherules. Li et al. (1993) proposed that these spherules might have formed as ablation droplets off of meteorites, but we are not aware of any meteorite types with this low FeO content.

In summary, there is not enough petrographic data to determine whether or not the Chinese glass spherules are microtektites; and, even if they are microtektites, the presently available compositional data do not support the proposal that they may be part of the Australasian strewn field.

4.2.5 Nature of the Australasian Microtektite Layer

Calling the Australasian microtektite layer a layer is technically incorrect, because there is not a discrete layer of microtektites in any of the cores studied up until 2010. It would be more correct, but more verbose, to refer to it as a microtektite-bearing layer. The layer is not generally evident in the cores, even if one knows where to look. There is no obvious change in lithology across the microtektite-bearing layer and the microtektites generally cannot be seen in the sediment, even with a hand lens. All of the Australasian microtektite-bearing sediments have been

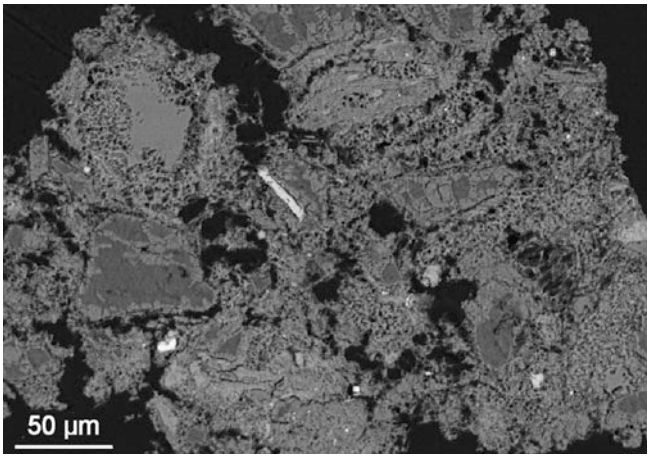

Fig. 4.11 Backscattered electron image of a shock-metamorphosed rock fragment, from the Australasian microtektite layer, containing a TiO_2 grain consisting primarily of the TiO_2II high-pressure polymorph (bright acicular grain $\sim 5 \times 40$ µm). The *rock fragment* shows evidence of partial melting and vesiculation. This specimen is from Ocean Drilling Program Site 1144 in the northern South China Sea

affected by bioturbation and the microtektites have been generally scattered over a vertical interval of at least 20 cm (Figs. 4.8 and 4.10). In the core with the greatest abundance of microtektites (Core 37x, Ocean Drilling Program Site 1144), microtektites make up <1 vol. % of the sediment, even in the part of the layer with the highest concentration. At this site, prior to bioturbation, the microtektite layer, including the unmelted ejecta, would have had a thickness of only about 2 mm (Glass and Koeberl 2006). At most of the sites, prior to bioturbation, the original "layer" would have consisted of microtektites scattered over the ocean floor with only a small fraction of the microtektites in contact with another microtektite.

4.2.6 Iridium Anomaly Associated with the Australasian Microtektite Layer

A small positive Ir anomaly has been found associated with the Australasian microtektite layer at Ocean Drilling Program (ODP) Site 758 on the Ninetyeast Ridge in the northeast Indian Ocean (Schmidt et al. 1993; Koeberl 1993a). The peak Ir concentration is $\sim 170 \pm 5$ ppt, which is only two times the background level (Fig. 4.10; Schmidt et al. 1993; Koeberl 1993a). The peak Ir abundance is associated with the peak abundance of Australasian microtektites. The best estimate of the net fluence is 1.3 ± 0.7 ng/cm^2 (Schmidt et al. 1993). A small, but significant, anomaly in the elemental abundances of Co and Ni was also found to be associated with the microtektite layer (Koeberl 1993a).

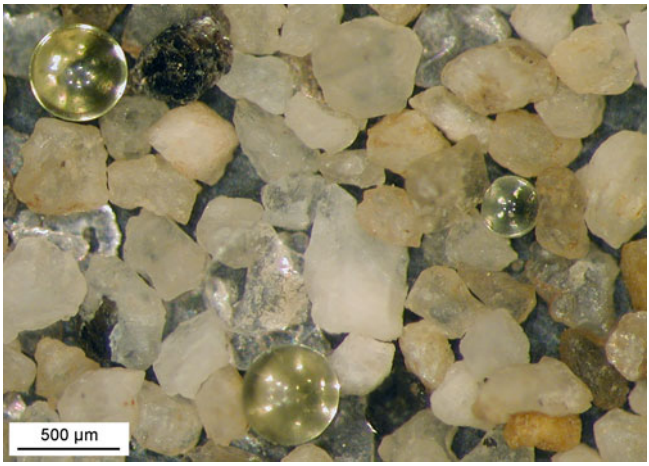

Fig. 4.12 Image of detritus, including three transparent *pale-yellow* microtektites ranging between ~300 and 500 µm in diameter, collected from a weathering pit or fracture on the top of the Victoria Land Transantarctic Mountains in Antarctica. Courtesy of Luigi Folco

4.2.7 Unmelted Ejecta in the Microtektite Layer

Shocked quartz with PDFs and/or coesite has been found associated with the Australasian microtektites at 12 sites (Glass and Wu 1993; Glass and Koeberl 2006). In addition, coesite and shocked quartz have been found at the same stratigraphic level as the Australasian microtektites at three sites that have no microtektites. All 15 of these sites are within ~3000 km of the Indochina area. Shock-metamorphosed rock fragments containing coesite and stishovite have been found at three of the 15 sites (Glass and Koeberl 2006); these three sites are in the South China Sea. The high-pressure phase TiO_2II (Fig. 4.11) was identified in several rock fragments from two of the South China Sea sites (Glass and Fries 2008). The shocked-rock fragments appear to have been derived from fine-grained sedimentary deposits. They have major and trace element compositions similar to those of the Australasian tektites and microtektites (except for generally higher volatile element contents), suggesting that they may be fragments of the source rocks which were melted to form the Australasian tektites and microtektites (Glass and Koeberl 2006).

4.2.8 Transantarctic Mountain Microtektites

Transparent, splash-form, silicate glass spherules found on the tops of the Transantarctic Mountains in Victoria Land, Antarctica, have been identified as Australasian microtektites (Folco et al. 2008, 2009). They, along with thousands of

micrometeorites/cosmic spherules, were found in fine-grained, local detritus trapped in weathering pits, joints, and fractures on glacially eroded summits of Miocene age. The glass spherules are mostly spherical in shape (~98 %) (Fig. 4.12), but oblate and prolate ellipsoid and rare lens shapes are also present (Folco et al. 2009). They range up to at least 800 μm in diameter, but the lower size range is not known at the present time. Most are transparent pale yellow in color; the rest are transparent pale green. The Transantarctic Mountain glass spherules have smooth surfaces without any pits or grooves or other evidence of solution. This is probably due to the cold, dry environment of Antarctica. Some of the Transantarctic Mountain spherules contain one or a few vesicles up to 20 μm in diameter. They do not contain any crystalline phases, but examination with an optical microscope indicates that several of the spherules contain what appear to be silica-rich inclusions. Electron microprobe analysis of one of these inclusions confirmed that it is silica rich (SiO_2 up to ~93 wt %). Like tektites and microtektites, the Transantarctic Mountain glass spherules have very low water contents (average ~0.0085 wt % or 85 μg/g; Folco et al. 2009). Identification of the Transantarctic Mountain glass spherules as microtektites is supported by their: (1) silicate glass nature; (2) splash-form shapes; (3) petrography (absence of crystalline phases and presence of silica-rich glass inclusions); (4) major oxide and trace element compositions, which are similar to those of previously known microtektites; (5) low water content; and (6) widespread geographic distribution (they are found over a region at least 500 km across) (Folco et al. 2008, 2009).

Several lines of evidence suggest that the **Transantarctic Mountain microtektites** are Australasian microtektites: age, major oxide and trace element compositions and Sr and Nd isotopic compositions. A ^{40}Ar-^{39}Ar total fusion analysis of 25 individual microtektites provided an isochron age of 1.4 ± 1.5 (2σ) Ma and a multi-grain stepwise heating ^{40}Ar-^{39}Ar analysis of eleven microtektites indicated a "plateau-isochron" age of 0.76 ± 0.98 (2σ) Ma (Folco et al. 2008). The large uncertainty in the ^{40}Ar-^{39}Ar age of the Transantarctic Mountain microtektites is due to the presence of excess argon, their low K content, and their young age. More recently, a fission-track age of 0.85 ± 0.17 Ma was determined for the Transantarctic Mountain microtektites (Folco et al. 2011). This age is better constrained than the ^{40}Ar-^{39}Ar ages and is consistent with the 0.78 Ma age for the Australasian tektites and microtektites.

Like Australasian microtektites, the Transantarctic Mountain microtektites can be divided into two groups based on color and composition: (1) pale yellow, or normal microtektites, with relatively high SiO_2 contents (usually >67 wt %) and low MgO contents (<6 wt %; Table 4.5), and (2) pale green microtektites with relatively low SiO_2 contents (<62 wt %) and high MgO contents (>10 wt %). Approximately 99 % of the Transantarctic Mountain microtektites are the normal type and only ~1 % are pale green or high-Mg microtektites. The normal Transantarctic Mountain microtektites have major oxide contents and compositional trends similar to those of the Australasian microtektites, except the normal Transantarctic Mountain microtektites appear to have a more restricted range in composition and lower average K_2O and especially Na_2O contents for a given

Table 4.6 Strontium and Nd Isotopic data for Australasian tektites and microtektites (including Transantarctic Mountain microtektites) Transantarctic Mountain microtektites

Sample	$^{87}Sr/^{86}Sr$	ϵ_{Sr}	$^{143}Nd/^{144}Nd$	ϵ_{Nd}	T_{Sr}^{UR} (Ga)	T_{Nd}^{CHUR} (Ga)	References
Australasian Tektites							
Thailand A	0.71894	204.4	0.511260	−11.5	0.371	1.12	Shaw and Wasserburg (1982)
Thailand B	0.71880	203.0	0.511246	−11.8	0.407	1.15	Shaw and Wasserburg (1982)
Cambodia A	0.71857	199.8	0.511241	−11.8	0.365	1.15	Shaw and Wasserburg (1982)
Cambodia B	0.71947	212.5	0.511271	−11.2	0.368	1.14	Shaw and Wasserburg (1982)
Cambodia C	0.71912	207.6	0.511224	−12.2	0.348	1.17	Shaw and Wasserburg (1982)
HCa australite	0.71398	134.6	0.511258	−11.5	0.536	1.13	Shaw and Wasserburg (1982)
HMg australite	0.71625	166.8	0.511290	−10.9	0.496	1.06	Shaw and Wasserburg (1982)
X-102[a]	0.718405	197.4	0.511227	−12.1	0.392	1.19	Blum et al. (1992)
X-103[a]	0.718426	197.7	0.511288	−10.9	0.395	1.08	Blum et al. (1992)
F-16[a]	0.719721	216.1	0.511225	−12.2	0.390	1.18	Blum et al. (1992)
8301[a]	0.720063	220.9	0.511262	−11.4	0.381	1.12	Blum et al. (1992)
319L[a]	0.720325	224.6	0.511227	−12.1	0.373	1.18	Blum et al. (1992)
319D[a]	0.719528	213.3	0.511273	−11.2	0.400	1.10	Blum et al. (1992)
2537[b]	0.716533	170.8	0.511292	−10.9	0.510	1.04	Blum et al. (1992)
4831[b]	0.713491	127.6	0.511279	−11.1	0.633	1.09	Blum et al. (1992)
NE Thailand[c]	0.7182–0.7203	n.d.	0.51206	n.d.	n.d.	n.d.	Wasson and Mezger (2007)
Australasian Microtektites							
BG-1	0.71680	174.6	n.d.	n.d.	0.590	n.d.	Shaw and Wasserburg (1982)
BG-2	0.71870	201.6	n.d.	n.d.	1.830	n.d.	Shaw and Wasserburg (1982)
Transantarctic Mountain Microtektites							
Sample A	0.716215	166	0.512086[d]	−10.8[d]	1.80	1.09[d]	Folco et al. (2009)
Sample B	0.716373	168			1.83		Folco et al. (2009)

Sr isotopic compositions normalized to $^{86}Sr/^{88}Sr = 0.1194$. Nd isotopic compositions normalized to $^{146}Nd/^{142}Nd = 0.636151$

[a] Muong Nong-type tektite from the Indochina region

[b] Australites

[c] Results of measurements made on nine tektites from this region

[d] Samples A and B were combined to get the Nd isotopic data

silica content compared to the Australasian microtektites (Table 4.5; Fig. 4.7; Folco et al. 2009).

The trace element contents of the Transantarctic Mountain microtektites are also similar to the trace element contents of the Australasian microtektites. The average trace element contents of the Transantarctic Mountain microtektites are generally within a factor of two of the average trace element contents of the Australasian microtektites and most Transantarctic Mountain microtektite trace element contents overlap those of the Australasian microtektites, except for Ni (Folco et al. 2009). Even though there is some overlap, the average Cr, Co, Zn, Rb, Cs, and U, in addition to Ni contents of the Transantarctic Mountain microtektites are lower, but within a factor of ten, of the average contents of the those elements in the Australasian microtektites.

Transantarctic Mountain microtektites have $^{87}Sr/^{86}Sr$ ratios and ε_{Sr} values within the range reported for Australasian tektites (Shaw and Wasserburg 1982; Blum et al. 1992; Ho and Chen 1996; Lee et al. 2004; Folco et al. 2009), but they have $^{87}Sr/^{86}Sr$ ratios and ε_{Sr} values that are slightly lower than those reported for Australasian microtektites (Shaw and Wasserburg 1982; Folco et al. 2009; Table 4.6). The ε_{Nd} values reported for the Transantarctic Mountain microtektites (Folco et al. 2009) are only slightly lower than the ε_{Nd} values reported for Australasian tektites (Shaw and Wasserburg 1982; Blum et al. 1992; Table 4.6). No ε_{Nd} values have been reported for the Australasian microtektites. The T_{Nd}^{CHUR} age of the Transantarctic Mountain microtektites is within the range of T_{Nd}^{CHUR} ages reported for the Australasian tektites, but the two T_{Sr}^{UR} model ages obtained for the Transantarctic Mountain microtektites are both much higher than T_{Sr}^{UR} ages determined for the Australasian tektites (Table 4.6). However, the T_{Sr}^{UR} ages obtained for the Transantarctic Mountain microtektites are within the range obtained for two Australasian microtektite measurements (Shaw and Wasserburg 1982; Folco et al. 2009; Table 4.6). No T_{Nd}^{CHUR} model ages have been reported for the Australasian microtektites. Thus, the present Sr and Nd isotopic data indicate that the Transantarctic Mountain microtektites were derived from the same, or very similar, target rock as the Australasian microtektites.

The lower average volatile element (Na, K, Zn, Rb, Cs) contents of the Transantarctic Mountain microtektites, compared to the volatile element contents in previously described Australasian microtektites, suggest that the Transantarctic Mountain microtektites were on average more intensely heated than the Australasian microtektites found closer to the proposed source crater location in Indochina (see Sect. 4.2.10). The Transantarctic Mountain and Australasian microtektites have $T_{Sr}^{UR} > T_{Nd}^{CHUR}$ suggesting a recent decrease in the $^{87}Rb/^{86}Sr$ ratio, which is consistent with volatile element loss (Papanastassiou and Wasserburg 1981; Folco et al. 2009). The lower average Cr, Ni, and Co contents of the Transantarctic Mountain microtektites compared with the abundances of Cr, Ni, and Co in the Australasian microtektites could indicate less meteoritic contamination in the Transantarctic Mountain microtektites compared to the average Australasian microtektite.

Assuming that the Transantarctic Mountain microtektites do belong to the Australasian strewn field, this means that the strewn field extends $\sim$3000 km

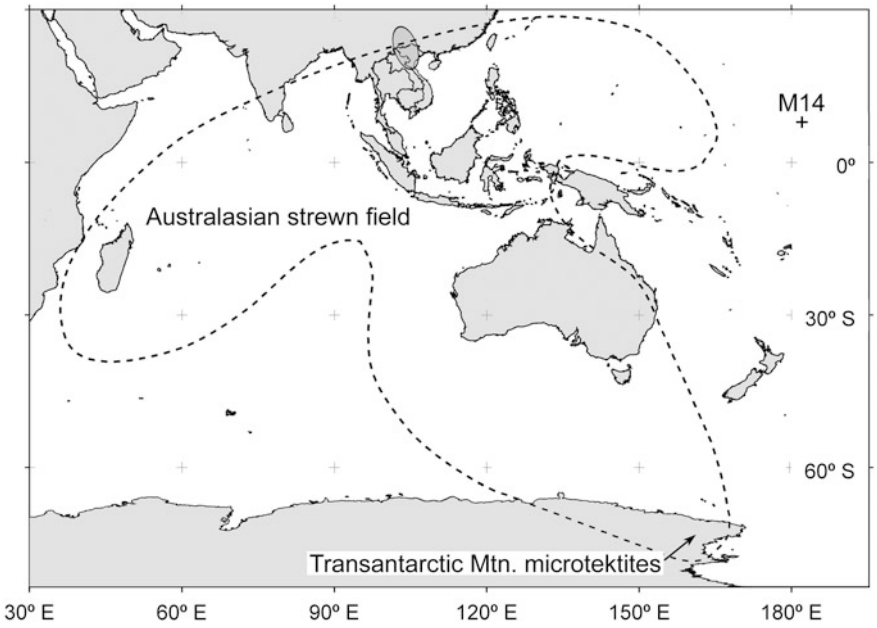

Fig. 4.13 Map showing the Transantarctic Mountain microtektite collection sites and the Australasian tektite/microtektite strewn field. Also shown is the M14 core site (*plus sign*) in the equatorial western North Pacific (~8° N, 176° W) where microtektites were found. The M14 microtektites were interpreted to be 2.14–2.3 Ma old (Peng 1994), but are similar to Australasian microtektites in appearance and composition (see Sect. 4.7.1). The oval-shaped region extending from the Gulf of Tonkin up through northern Vietnam and eastern Thailand into southern China is believed to be the general location of the Australasian tektite/microtektite source crater (see Fig. 4.16 for more detail). Modified after Folco et al. (2009), Fig. 1b

farther to the south southeast than was previously known (Folco et al. 2008, 2009; Fig. 4.13). The low volatile content of the Transantarctic Mountain microtektites compared to the volatile content of Australasian microtektites found closer to the proposed source area location in Indochina and the absence of teardrop- and dumbbell-shaped Transantarctic Mountain microtektites may indicate changes with distance from the source crater (Folco et al. 2009, 2010b).

4.2.9 Geographic Variations Within the Australasian Microtektite Strewn Field

The number of microtektites (>125 μm dia.)/cm^2 has been calculated for most of the Australasian microtektite-bearing sites (Glass and Pizzuto 1994; Glass et al. 1997; Lee and Wei 2000; Glass and Koeberl 2006; Prasad et al. 2007). Abundance (number/cm^2) of microtektites, percent microtektite fragments versus whole splash

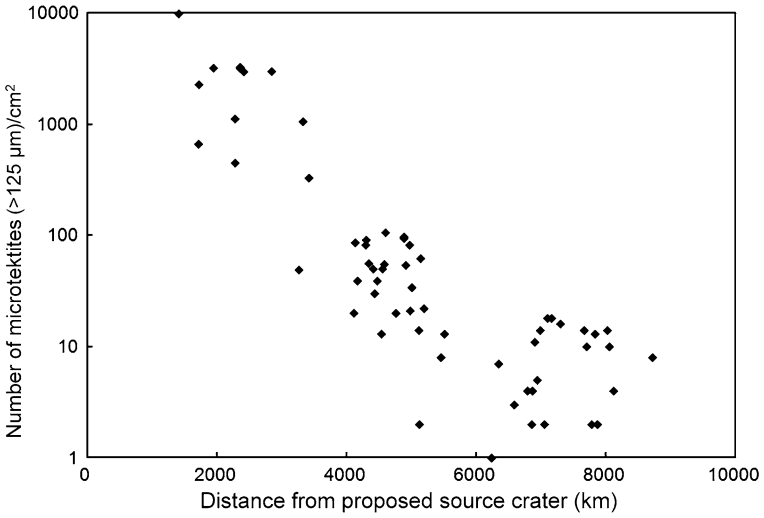

Fig. 4.14 Abundance (number >125 μm/cm^2) of Australasian microtektites versus distance (for ~60 core sites) from the proposed source area in Indochina. For this plot a hypothetical crater location at 22° North Latitude and 104° East Longitude was used. See Sect. 4.2.10 for discussion regarding the probable location of the Australasian tektite/microtektite source crater. This plot includes some data from Lee and Wei (2000) and Prasad et al. (2007)

forms, and the percent unmelted ejecta (shocked quartz and rock fragments) all decrease with distance from the Indochina area (Glass and Pizzuto 1994; Glass et al. 1997; Glass and Koeberl 2006; Figs. 4.14 and 4.15). In addition, the abundance of microtektites containing quartz inclusions also decreases with distance from the Indochina area. Furthermore, quartz inclusions have not been observed in microtektites found farther than ~3000 km from the Indochina area (Folco et al. 2010a). As previously mentioned, shocked quartz and shocked-rock fragments also occur within ~3000 km of the Indochina area in Australasian microtektite-bearing cores containing the greatest abundances of microtektites and the highest percent of fragmented microtektites.

As a result of a study of over 4,600 microtektites from 11 cores, taken in the Central Indian Ocean at distances between ~3,900 and 5,000 km from the suggested source crater location in Indochina, Prasad et al. (2010) found that the number of microimpact craters on the surfaces of the Australasian microtektites decreases with distance from the proposed source crater location in Indochina (see Sect. 10.1.2.4). In addition, at sites closer to the proposed source crater location the microcraters are small in diameter (generally less than ~30 μm) and were apparently formed by hypervelocity impacts, but those farther from the source crater are, on average, larger (generally greater than ~40 μm in diameter) and were formed by lower velocity impacts (Prasad et al. 2010).

Smit et al. (1991) suggested that the fragmentation of the larger microtektites may have been due to stress developed during cooling while the microtektites were

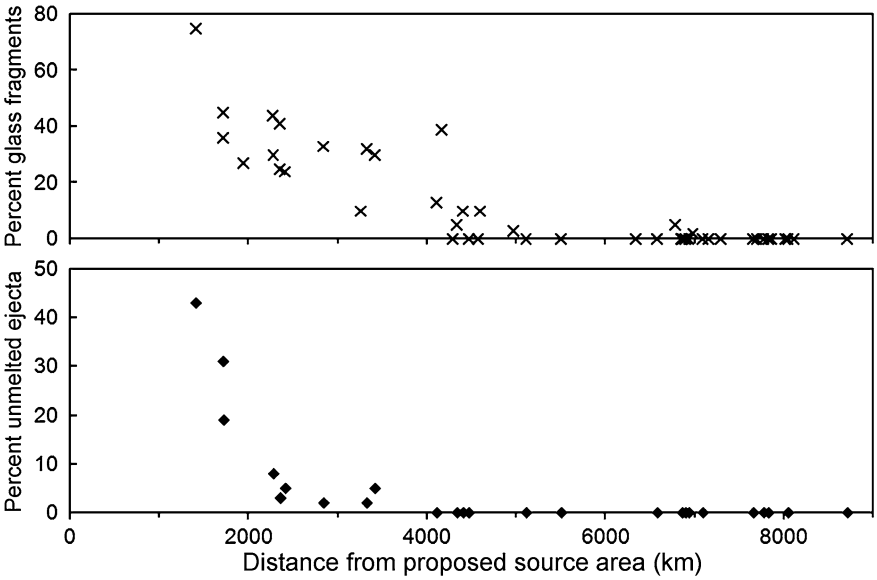

Fig. 4.15 Percent glass fragments and percent unmelted ejecta versus distance from a hypothetical source crater at 22° North Latitude and 104° East Longitude. The percent glass fragments is the percent of the total number of glass particles (fragments and splash forms) which are fragments. Data from two sites are from Schneider et al. (1992), data from two other sites are from Lee and Wei (2000), and data from one site are from Smit et al. (1991). Unmelted ejecta refer to shocked-rock fragments and shocked quartz grains containing planar deformation features or coesite. Note that both the percent glass that are fragments and the percent unmelted ejecta decrease with distance from the proposed source crater location

still in flight. This does not seem to explain why the larger tektites survived, nor does it seem to explain why there was higher fragmentation closer to the Indochina area. It may be that the larger microtektites were still hot when they landed in the ocean and the thermal shock caused some of them to fragment. (The ocean may have been cold relative to the atmosphere, which would have been heated by the impact and by ejection of melt and hot rock debris into the atmosphere.) Thus the larger microtektites that fell closest to the source crater would have been the hottest and would have experienced the greatest thermal stress and the most fragmentation (Glass et al. 1997). On the other hand, unfragmented tektites, which are much larger than the microtektites, have been recovered from the central Indian Ocean (Prasad and Rao 1990; Prasad and Sudhakar 1999). It appears that at least some of the fragmentation was due to high-velocity impacts as the microtektites reentered the atmosphere (Prasad and Khedekar 2003).

Assuming that the Transantarctic Mountain microtektites belong to the Australasian strewn field, Folco et al. (2010b) documented that the average alkali content of the Australasian microtektites decreases with distance from the proposed location of the source crater in Indochina (see Sect. 10.1.2.7).

4.2.10 Parent Rocks and Estimated Location and Size of the Source Crater

The source crater for the Australasian tektites/microtektites had not been found as of 2010, but the parent rock is believed to have been near-surface, fine-grained sedimentary deposits of, perhaps, Jurassic age. Most authors agree that the source crater must be somewhere in the Indochina area.

Geochemical studies of the Australasian tektites suggest that the parent (or source) rock was a sedimentary deposit or rock similar to a graywacke (Taylor and Kaye 1969). The size, shape, and mineral assemblage of the relict mineral inclusions found in some Muong Nong-type Australasian tektites are consistent with a sedimentary source, perhaps coarse silt or sand-sized (Glass and Barlow 1979). Beryllium-10 studies suggest that the Australasian tektites (and presumably microtektites) were derived from surface or near surface deposits, and that the ablated australites (found in Australia) come from closer to the surface than the large, blocky, layered (Muong Nong-type) tektites (Pal et al. 1982; Ma et al. 2004). Blum et al. (1992) interpreted Sr isotopic data (Table 4.6) as indicating that the source rock was a sedimentary deposit or rock of Jurassic age and suggested that the Australasian tektites may have been derived from Jurassic formations found in Indochina that consist of sandstone and conglomerate interlayered with micaceous shale and siltstone. Other authors have proposed loess or loess-like deposits as the source rock for the Australasian tektites based on Sr and Nd isotope data (Wasson and Heins 1993; Wasson and Mezger 2007).

Since the ablated tektites found in Australia must have been thrown out of the atmosphere before reentering and being ablated, they must have been thrown farther from the source crater than the unablated splash-form tektites. Furthermore, the higher volatile contents, greater chemical heterogeneity, and presence of relict mineral grains in the Muong Nong-type tektites indicate they were not heated as intensely as the splash-form and ablated tektites and, therefore, were probably deposited closer to the source crater. Thus, geographic variation in the types of tektites in the Australasian tektite strewn field indicates a source crater in or near Indochina. This is consistent with ^{10}Be data, which indicate that the australites were derived from shallower depths in the target rocks than were the Muong Nong-type tektites found in Indochina. Several source crater locations have been proposed based on tektite data (Stauffer 1978; Ford 1988; Schnetzler et al. 1988; Schnetzler 1992; Hartung and Koeberl 1994; Koeberl 1994; Ma et al. 2004), but none have so far resulted in discovery of the source crater.

The location of the source crater has been estimated based on the location that best explains the geographic variation in the abundance of the Australasian microtektites (Glass and Pizzuto 1994; Lee and Wei 2000; Glass and Koeberl 2006; Prasad et al. 2007). This is determined by selecting possible crater locations (for example using locations defined by the intersection of lines of latitude and longitude at some arbitrary interval, e.g., every 5°), determining the distance between a given location and every microtektite-bearing core location, and then

calculating R^2 values for each location by doing regression analysis (abundance versus distance) for each theoretical crater location. The R^2 values are then contoured to find the location that gives the highest R^2 value and thus explains the geographic distribution of microtektite abundance the best. Unfortunately, this method is not very sensitive and the location that best explains the geographic variation in abundance covers a fairly large area (Fig. 4.16). The most recent results indicate an area that includes eastern Thailand, most of Laos, north and central Vietnam, and the adjacent Gulf of Tonkin. These results are consistent with predicted source crater locations based on Muong Nong-type tektite distribution and geographic variations in composition of tektites in Indochina (Schnetzler 1992) and in ^{10}Be data (Ma et al. 2004).

The size of the Australasian tektite/microtektite source crater has been estimated using equations that relate crater size to thickness of the ejecta layer at a given distance from the source crater. Since the location of the Australasian tektite/microtektite source crater is not known for certain, it is necessary to assume a location in order to use one of the equations that relates thickness of an ejecta layer to the distance from (and size of) the source crater. The thickness of the ejecta layer is based on the volume of microtektites found in a column of sediment through the microtektite layer at each site. Since the equations that relate ejecta size to thickness of the ejecta layer at a given distance from the crater were derived for proximal ejecta, using the distal microtektite layers to estimate the size of the source crater involves a large extrapolation. Estimates for size of the Australasian source crater made using this method range from 32 to 120 km diameter (Glass and Pizzuto 1994; Lee and Wei 2000; Glass and Koeberl 2006; Prasad et al. 2007). However, the abundance of North American microtektites at a given distance from the 85-km-diameter Chesapeake Bay impact structure, which is believed to be the source crater of the North American tektite/microtektite strewn field, appears to be higher than the average abundance of Australasian microtektites at the same distance from the proposed source crater location for the Australasian tektite/microtektite strewn field (Fig. 4.17). This suggests that the source crater for the Australasian strewn field is probably smaller than 85 km in diameter. However, the target area of the Chesapeake Bay structure at the time of the impact consisted of three layers: a water layer $\sim$300 m deep, a middle layer $\sim$600–1000 m thick composed mostly of water-saturated unconsolidated sediments, and a basal layer composed of crystalline basement rock. The impact produced a 40-km-diameter crater in the basement rock and a much larger crater in the overlying weaker sediment layer. The flow of water as it rushed back into the crater may have enlarged it still further (Collins and Wünnermann 2005; see Sect. 4.5.9). This would suggest that the Australasian source crater could be much smaller than the Chesapeake Bay structure if, for example, the impact was into consolidated sediment, which is in agreement with estimates of a 33–43 km diameter for the Australasian source crater (Glass and Koeberl 2006; Prasad et al. 2007).

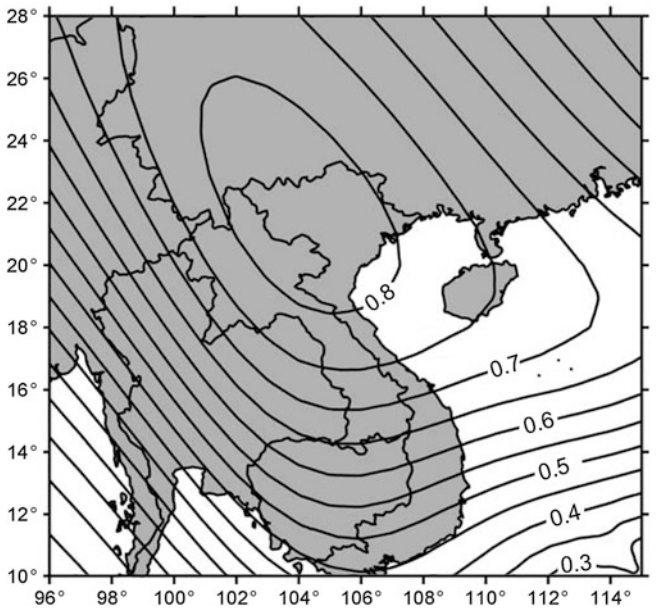

Fig. 4.16 Plot of contours of R^2 values obtained by regression analyses of the abundance of microtektites (>125 μm/cm^2) at hypothetical source crater sites versus distance from each site. Hypothetical crater sites were chosen at the intersection of lines of latitude and longitude. The R^2 value obtained for each hypothetical crater site indicates how well that site explains the geographic variation in abundance of microtektites. The R^2 values for each hypothetical crater site are plotted on a map and contoured. It is assumed that the location that gives the highest R^2 value should indicate the probable location of the source crater. The highest R^2 value (0.84) is for a location at 22°N, 104°E. However, the R^2 values in the oval region between 26°N, 102°E and 19°N, 107°E are all similar and any location within the oval could explain the geographic distribution in microtektite abundances equally well. Modified after Glass and Koeberl (2006), Fig. 10

4.3 The Ivory Coast Microtektite Layer

The Ivory Coast microtektites were discovered just 1 year after the Australasian microtektites (Glass 1968); however, as of 2010, the Ivory Coast microtektites had only been reported in deep-sea cores from 10 sites and they are not as abundant as the Australasian microtektites.

4.3.1 Description of the Ivory Coast Microtektites

The Ivory Coast microtektites are generally spherical in shape (~90 %), but oval, disc, dumbbell, and teardrop shapes are also present (Glass 1968). The spherical microtektites are generally less than 1 mm in diameter, but some dumbbell and

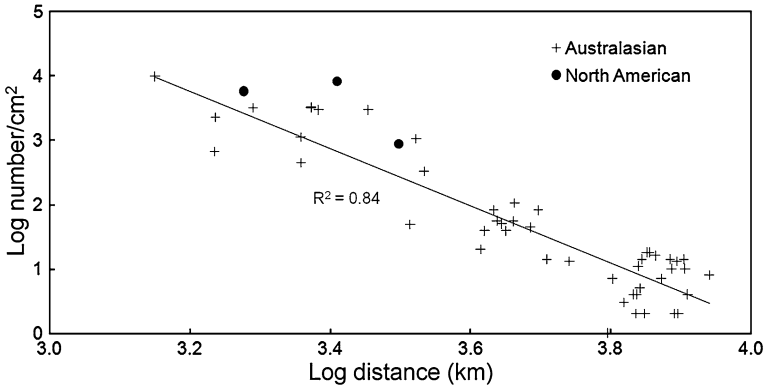

Fig. 4.17 Log number of microtektites (>125 μm)/cm^2 versus log distance from the source crater for the Australasian and North American strewn fields. The Australasian plot is based on a hypothetical source crater at 22°N, 104°E (see Fig. 4.16). The North American plot is based on the Chesapeake Bay structure being the source crater. Note that data for the North American strewn field plot above the best fit correlation line for the Australasian strewn field, suggesting that the Australasian source crater, if it is near the hypothetical location used, is probably slightly smaller than the Chesapeake Bay structure. The diameter of the Chesapeake Bay structure is usually given as 85 km, but may have been ~40 km prior to backwash

teardrops are up to 1.2 mm in length. Most of the Ivory Coast microtektites are transparent to translucent and in transmitted light have an olive brown to olive green color. The remainder are mostly transparent colorless to yellow green, and a few are bottle green. Some are translucent dark brown to opaque black. The Ivory Coast microtektites range from glassy smooth to very irregular and badly pitted. U-shaped grooves and pits are common surface features (Fig. 3.9b–e; Glass 1974). Overlapping shallow pits give many of the Ivory Coast microtektites a scalloped appearance (Fig. 4.18a). Some irregular shapes were formed by fusion of two or more microtektites and V-shaped grooves, presumably formed by solution, mark the surface expression of the plane where the forms were fused together (Fig. 3.9c). Some of the Ivory Coast microtektites have circular elevated regions (Fig. 4.18b). These protrusions were apparently formed by differential solution with the protrusions being more silica rich than the surrounding glass (Glass 1974, 1984a). As a group, the Ivory Coast microtektites appear to have undergone more solution than have the Australasian microtektites. Like the Australasian microtektites, some of the Ivory Coast microtektites contain bubble cavities and lechatelierite particles. The Ivory Coast microtektites are free of any crystalline phases.

4.3.2 Composition

Like Ivory Coast tektites, the Ivory Coast microtektites can generally be distinguished from the Australasian microtektites by their higher MgO/CaO ratio (>2)

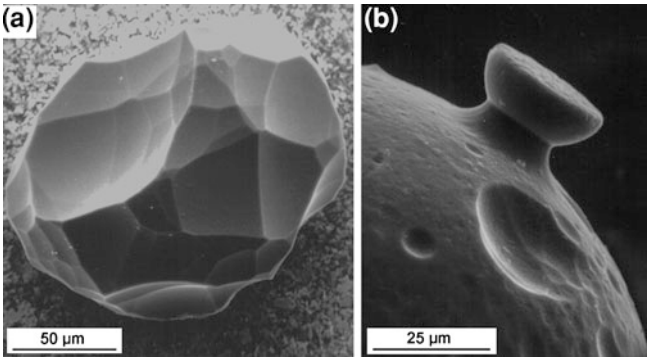

Fig. 4.18 Scanning electron microscope images of Ivory Coast microtektites (from Core K9-56) showing surface features. **a** This microtektite is covered with large, shallow overlapping pits which give it a scalloped appearance. **b** This microtektite shows some pitting and has a silica-rich hemisphere sitting on top of a pedestal. The flat surface of the hemisphere is ~15 µm above the adjacent microtektite surface and parallel to it. The difference in elevation between the top of the hemisphere and the adjacent microtektite surface is probably due to differential solution and the flat surface probably represents the original surface level of the microtektite. This suggests that the microtektite has experienced ~15 µm of solution. The small conical-shaped protrusion on the surface of the microtektite at the *top left* (just below the "B") is probably the remainder of a column that once supported a smaller silica-rich body

and a higher Na_2O/K_2O ratio (average > 1; Fig. 4.19). Like the Australasian microtektites, the Ivory Coast microtektites can be divided into two main groups: (1) normal microtektites with compositions similar to those of the Ivory Coast tektites (Fig. 4.20); and (2) bottle-green microtektites with low SiO_2 (as low as 49 wt %) and high MgO (up to 21 wt %; Glass 1969, 1972b).

The trace element contents of the Ivory Coast microtektites are also similar to those of the Ivory Coast tektites (Fig. 4.21); however, the Ivory Coast microtektites have slightly higher averages of refractory lithophile elements, except for Rb and U and slightly higher averages of the siderophile elements Cr, Co, Ni, and Ir compared with those of the Ivory Coast tektites (Koeberl et al. 1997b; Glass et al. 2004b). Compared to the Ivory Coast tektites, the Ivory Coast microtektites have lower average volatile elements, especially Zn, which is the most volatile of the volatile elements for which we have data. The higher refractory element abundances and lower volatile abundances in the Ivory Coast microtektites compared with the Ivory Coast tektites may be due to more intense heating of the microtektites.

The rare earth element (REE) contents are also slightly higher in the Ivory Coast microtektites compared to the REE contents of the Ivory Coast tektites (Fig. 4.22; Koeberl et al. 1997b; Glass et al. 2004b). In contrast to the chondrite-normalized REE patterns of the Australasian, Central European, and North American tektites, which have the shape, abundances, and a distinctive negative Eu anomaly like the post-Archean upper crust, the Ivory Coast tektites and microtektites do not have a negative Eu anomaly and the overall pattern is more similar to that of Archean rocks (Koeberl et al. 1997b).

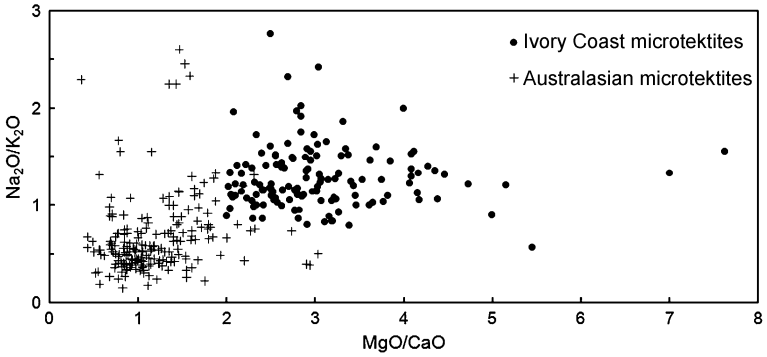

Fig. 4.19 Na_2O/K_2O versus MgO/CaO for Ivory Coast and Australasian microtektites. The plot shows that as a group Ivory Coast microtektites can be distinguished from Australasian microtektites. Data for the Ivory Coast microtektites is from Glass (1969) and Glass and Zwart (1979b). Australasian microtektite compositional data are from Cassidy et al. (1969), Glass (1972a, b), Burns (1990), Smit et al. (1991), Prasad and Sudhakar (1996, 1999)

4.3.3 Age

Ivory Coast microtektites have a fission-track age of 1.09 ± 0.20 Ma (Gentner et al. 1970). The Ivory Coast microtektites appear to have been deposited ~8 ka after the onset of the Jaramillo magnetostratigraphic normal subchron (Glass et al. 1991), which has been dated as 1.07 Ma. This indicates an age of ~1.06 Ma for the Ivory Coast microtektites. This age is indistinguishable from the ^{40}Ar-^{39}Ar age of 1.1 ± 0.05 Ma for the Ivory Coast tektites (Koeberl et al. 1997b). An attempt to date the Ivory Coast microtektites using the ^{40}Ar-^{39}Ar method was unsuccessful due to their small size and young age (Koeberl et al. 1997b).

4.3.4 The Ivory Coast Strewn Field

The Ivory Coast microtektites have been found at ten sites in the eastern equatorial Atlantic (Fig. 4.23; Glass et al. 1991). The Ivory Coast strewn field covers a relatively small area compared with the Australasian or North American strewn field. The highest abundance of microtektites in this strewn field, ~80 microtektites (>125 μm)/cm^2, is found at the V19-297 core site. The abundance drops off radially from that site down to <1 microtektite/cm^2. No shock-metamorphosed rock or mineral grains have been found in the Ivory Coast microtektite layer. No one to our knowledge has attempted to look for an Ir or other geochemical anomalies that might be associated with this layer. However, because of the small size of the proposed source crater (see below), and distance from the proposed source crater, an Ir anomaly would not be expected.

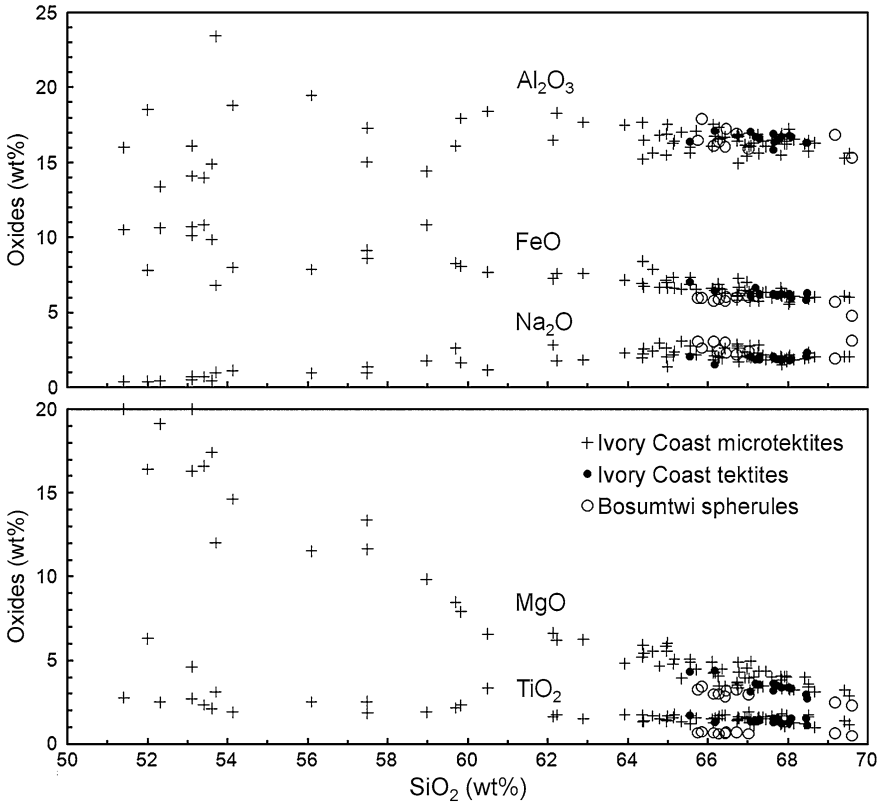

Fig. 4.20 Major oxides versus SiO_2 for Ivory Coast tektites and microtektites and Bosumtwi crater fallback spherules. The Bosumtwi crater fallback spherules have compositional trends similar to those of the Ivory Coast tektites. The Ivory Coast microtektites also have compositions quite similar to those of the Ivory Coast tektites, but extend the compositional trends down to much lower silica contents. Data for the Ivory Coast tektites are from Cuttitta et al. (1972) and Koeberl et al. (1997b). Data for the Ivory Coast microtektites are from Glass (1969) and Glass and Zwart (1979b). Data for the Bosumtwi fallback spherules are from Koeberl et al. (2007b)

4.3.5 The Source Crater: Bosumtwi

Several lines of evidence indicate that the source crater for the Ivory Coast tektite/microtektite strewn field is the 10.5-km-diameter Bosumtwi impact crater in Ghana (6° 30′ N, 1° 25′ E; for a discussion of the geology of this crater, see Koeberl and Reimold 2005). Cohen (1963) suggested that the Bosumtwi crater might be the source of the Ivory Coast tektites based on location (Fig. 4.23) and similarity in major oxide composition between the Ivory Coast tektites and impact glasses found at Bosumtwi crater. The age of the crater had not been determined by radiometric dating, but the crater was believed to be of Pleistocene age. Later, K–Ar and fission-tack studies indicated that the Ivory Coast tektites and Bosumtwi

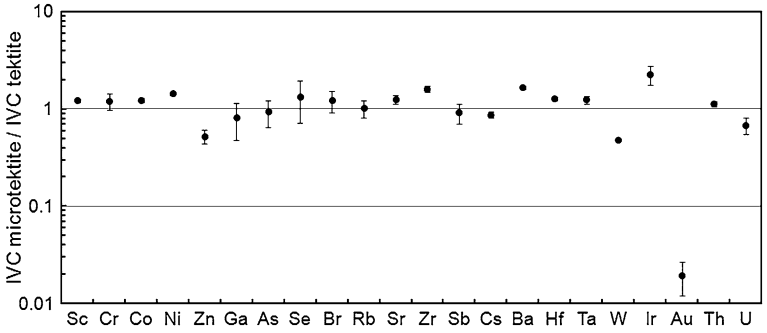

Fig. 4.21 Average trace element contents for Ivory Coast (IVC) microtektites normalized to the average Ivory Coast tektite contents. Note that in most cases the average Ivory Coast microtektite trace element contents are within a factor of two of the average trace element contents of the Ivory Coast tektites. A major exception seems to be the much lower Au content of the Ivory Coast microtektites compared to that of the Ivory Coast tektites. Trace element contents are from Koeberl et al. (1997b)

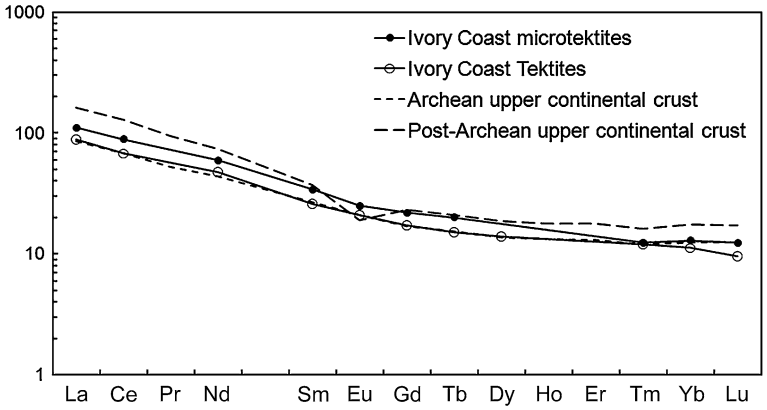

Fig. 4.22 Plot of CI chondrite normalized rare earth element (REE) contents for Ivory Coast tektites and microtektites and for the average Archean and post-Archean upper continental crust. Note that the REE pattern of the Ivory Coast microtektites is similar to that of the Ivory Coast tektites and that neither the Ivory Coast tektites nor microtektites have a negative europium anomaly and that both have REE patterns more similar to that of the Archean continental crust than to that of the post-Archean upper continental crust. CI chondrite data are from Lodders and Fegley (1998); upper continental crust data are from Taylor and McLennan (2009) and Ivory Coast tektite and microtektite data are from Koeberl et al. (1998) and Glass et al. (2004b), respectively

impact glasses have similar ages (e.g., Gentner et al. 1967; Storzer and Wagner 1977). More recently, the similarity in age between the Ivory Coast tektites and Bosumtwi crater glasses was supported by ^{40}Ar-^{39}Ar and fission-track dating of the Ivory Coast tektites (Koeberl et al. 1998). Schnetzler et al. (1966) found that the Ivory Coast tektites have Rb–Sr model ages similar to the Rb–Sr model ages of

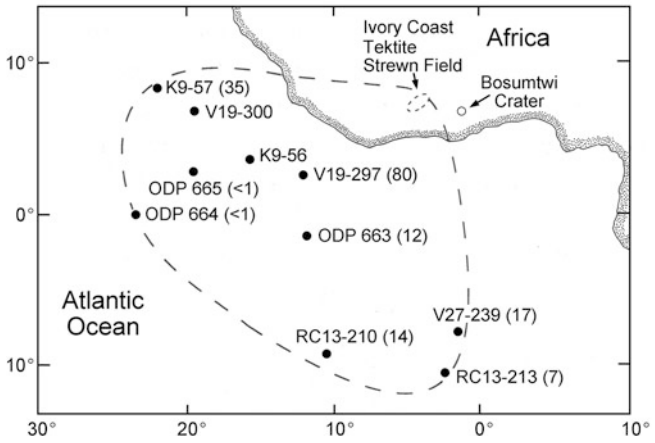

Fig. 4.23 Map of the Ivory Coast tektite/microtektite strewn field. Also shown is the location of Bosumtwi impact crater, which is believed to be the source crater for the Ivory Coast tektites and microtektites. The numbers in parentheses after the core numbers are the estimated number of microtektites (>125 μm)/cm^2 for that site

the Bosumtwi crater rocks. This similarity in Rb–Sr ages was confirmed by Shaw and Wasserburg (1982), who also demonstrated a similarity in Sm–Nd model ages.

The similarity in chemical composition between the Ivory Coast tektites and Bosumtwi crater glasses and target rock was supported by Schnetzler et al. (1967) and Jones (1985). In more detailed studies, Koeberl et al. (1997b, 1998) and Glass et al. (2004b) confirmed that the major and trace element compositions of the Ivory Coast tektites and microtektites are similar to the major and trace element compositions of the Bosumtwi crater glasses and rocks (Table 4.7). It has been shown that the composition of the Ivory Coast tektites and microtektites can be matched with a mixture of the major target rocks found at Bosumtwi crater (Table 4.8; Koeberl et al. 1998; Glass et al. 2004b).

The Ivory Coast microtektites appear to decrease in abundance with distance from Bosumtwi crater (Glass et al. 1991; Fig. 4.24), as would be expected if Bosumtwi is the source crater. However, there is a great deal of scatter, which is not surprising since the microtektite-bearing sites are between ~120 and 240 crater diameters from the Bosumtwi crater. The thickness of the Ivory Coast microtektite layer, estimated from the number of microtektites (>125 μm)/cm^2, was used to calculate the size of the source crater at Bosumtwi's location using an equation that relates the thickness of an ejecta layer to size and distance from the source crater. The crater size estimated this way is 12.6 ± 3.4 km, which is the same (within one standard deviation) as the diameter of the Bosumtwi crater. Thus, geographic variation in abundance of the Ivory Coast microtektites and estimated thickness of the microtektite layer is consistent with Bosumtwi being the source crater of the Ivory Coast microtektites.

Table 4.7 Major oxide and trace element compositions of Ivory Coast microtektites, Ivory Coast tektites, and Bosumtwi suevite and fallback spherules

	Microtektites (16)		Microtektites (4)		Tektites (11)		Suevite[a] (11)		Spherules[b](15)	
	Ave.	S.D.	Ave.	S.D.	Ave.	S.D.	Ave.	S.D.	Ave.	S.D.
SiO_2	66.4	2.0	67.4	1.2	67.58	0.59	69.46	3.29	67.10	2.53
TiO_2	0.55	0.04	0.59	0.02	0.56	0.02	0.70	0.08	0.64	0.11
Al_2O_3	16.9	0.5	17.1	0.2	16.74	0.37	17.02	1.26	15.30	1.48
FeO	6.65	0.58	6.40	0.23	6.16	0.15	6.47	2.45	5.90	0.76
MgO	4.27	1.25	3.70	0.86	3.46	0.35	1.56	0.59	3.33	1.39
CaO	1.73	0.37	1.22	0.30	1.38	0.11	1.52	0.67	2.88	0.79
Na_2O	1.92	0.23	1.63	0.29	1.90	0.16	1.89	0.58	2.55	0.47
K_2O	1.60	0.39	1.86	0.27	1.95	0.11	1.39	0.42	1.85	0.28
Sc	11.3	1.2	17.9	0.7	14.7	1.2	15.3	5.3	17.7	2.7
Cr	281	139	292	54	244	20	373	45	151	48
Co	23.3	4.0	32.7	1.7	26.7	2.5	19.9	12.7	48.2	10.8
Ni	122	51	224	63	157	52	106	108	373	204
Zn	6	2	12	2	23	18	73	16	n.d.	n.d.
Rb	51	15	66.7	13.2	66	10	51.4	17.7	80	49
Sr	256	60	325	31	260	70	301	56	n.d.	n.d.
Zr	131	25	215	15	134	27	122	19	312	174
Ba	533	85	620	0.27	374	94	563	83	545	221
La	19.4	3.5	25.9	2.3	20.7	2.4	18.9	5.1	18.8	1.6
Ce	41.7	6.9	55.1	5.9	41.9	4.0	38.8	8.5	41	4
Nd	19.8	3.1	27.3	3.3	21.8	2.9	18.2	4.8	23	3
Sm	3.76	0.65	5.10	0.41	3.95	0.57	3.53	0.74	3.76	0.36
Eu	1.17	0.23	1.43	0.12	1.20	0.07	1.07	0.18	1.42	0.24
Tb	0.50	0.09	0.74	0.04	0.56	0.09	0.47	0.10	0.5	0.2
Yb	1.69	0.27	2.07	0.18	1.79	0.23	1.57	0.28	2.1	0.4
Hf	3.19	0.47	4.28	0.14	3.38	0.29	3.22	0.24	4.31	1.12
Ta	0.34	0.07	0.42	0.04	0.34	0.06	0.30	0.08	0.5	0.1
Th	3.39	0.53	3.99	0.22	3.54	0.43	2.94	0.61	4.09	2.24
U	0.57	0.17	0.64	0.12	0.94	0.27	1.05	0.58	1.1	0.4

Note Numbers in parentheses are the number of analyses. Major oxides given in wt % and trace element contents are in ppm. Total iron given as FeO

Ave. average, *S.D.* Standard deviation (±1), *n.d.* not determined

Sources Microtektite data from Glass et al. (2004b; 16 analyses) and Koeberl et al. (1997b; four analyses) and tektite data from Koeberl et al. (1997b); suevite data from Boamah and Koeberl (2003); glass spherule data from Koeberl et al. (2007b)

[a] For these samples an average of 7.68 wt % was lost on ignition; thus, for comparison with the tektite and microtektite data the major oxide total was normalized to 100 wt %

[b] The glass spherules are from the uppermost fallback unit in Bosumtwi impact crater

Microtektite-like glass spherules (spheres, ovals, teardrops, dumbbells, discs) with compositions similar to the compositions of Ivory Coast tektite/microtektites (Table 4.7; Fig. 4.20), except for higher CaO contents, were found in the uppermost layer (~5 cm thick) of fallback ejecta inside the Bosumtwi crater (Koeberl et al. 2007b). Whole splash forms in this layer make up nearly 40 % by number of the particles in the 250–500 μm size fractions.

Table 4.8 Comparison of the average Ivory Coast microtektite composition with the composition of a mixture of Bosumtwi crater target rocks derived using mixing calculations

	Observed composition		Calculated composition	Observed minus calculated
	Average	S.D.		
SiO_2	66.4	2.0	66.78	−0.38
TiO_2	0.55	0.04	0.64	−0.09
Al_2O_3	16.9	0.5	17.0	−0.10
FeO	6.65	0.58	6.42	0.23
MgO	4.27	1.25	3.95	0.32
CaO	1.73	0.37	1.64	0.09
Na_2O	1.92	0.23	2.01	−0.09
K_2O	1.60	0.39	1.59	0.01
Sc	11.3	1.2	16.9	−5.6
Rb	51	15	46.9	4.1
Zr	131	25	128	3
La	19.4	3.5	23.1	−3.7
Yb	1.69	0.27	1.69	0.0
Hf	3.19	0.47	3.1	0.09
Th	3.39	0.53	2.90	0.49

Major oxides are in wt % and minor elements in ppm. All iron given as FeO. *S.D.* Standard deviation (±1)
The best match for the calculated composition was obtained for a mixture of 78.9 % average phyllite-graywacke and 21.1 % Pepiakese "granite" (Glass et al. 2004b)

In summary, the conclusion that the Ivory Coast tektites/microtektites were derived from the Bosumtwi crater is supported by similarity in age and composition (both major and trace element) between the tektites/microtektites and Bosumtwi crater glasses (including fallback spherules) and rocks. Also the geographic variation in abundance of Ivory Coast microtektites and calculated thickness of the Ivory Coast microtektite layer versus distance from Bosumtwi crater are consistent with Bosumtwi being the source crater.

4.4 The Central European Tektite Strewn Field

Central European tektites have been found in the Czech Republic, Austria, and Germany (Trnka and Houzar 2002; Fig. 4.25). These tektites were originally called **moldavites** after the Moldau River. Tektites found in the Czech Republic (Bohemia) were first mentioned in the scientific literature in 1788 by Joseph Mayer and tektites found in Slovakia (Moravia) were first mentioned in 1878 (Barnes 1963). More recently, tektites of the same composition and age have been found in Germany and Austria (Rost et al. 1979; Koeberl et al. 1988; Störr and Lange 1992; Fig. 4.25). The Central European tektites are generally transparent with a deep green color. They are considered semiprecious stones and are used in jewelry

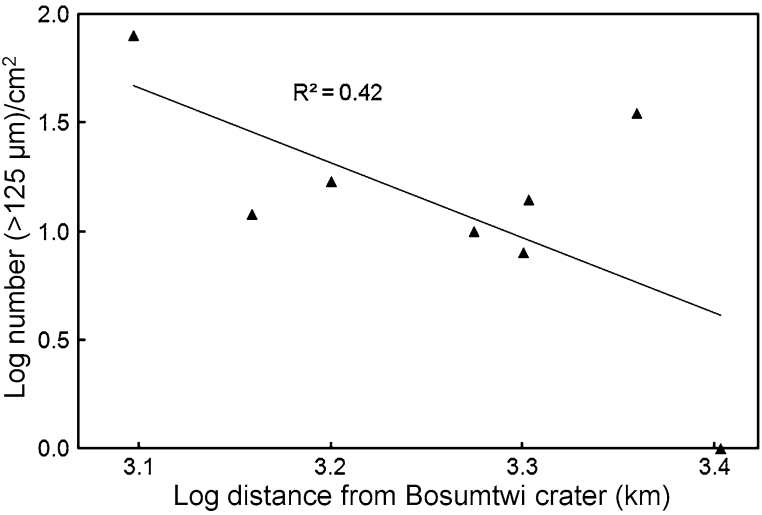

Fig. 4.24 Log number of microtektites (>125 μm)/cm^2 versus log distance from Bosumtwi impact crater. There is a great deal of scatter, but the general trend is that the microtektite abundance decreases with distance from Bosumtwi. Data are from Glass et al. (1991)

(Bouška et al. 1993). Compared with tektites from other strewn fields, the Central European tektites are silica rich; the SiO_2 contents range from 72 to 85 wt % (Table 4.3). Like most other tektite groups, the Central European tektites have rare earth element patterns consistent with post-Archean continental crust (Koeberl et al. 1988).

The Central European tektites have been dated using the fission-track, K–Ar, and ^{40}Ar-^{39}Ar methods. Published ages range from 14 to 15.3 Ma (Laurenzi et al. 2003). Storzer et al. (1995) determined the mean value of 17 age determinations published prior to 1995 using the K/Ar and ^{40}Ar-^{39}Ar methods and obtained an age of 14.82 ± 0.32 Ma. More recently determined ^{40}Ar-^{39}Ar ages for 12 specimens give a somewhat lower average age of 14.4 ± 0.2 Ma (Schwarz and Lippolt 2002; Laurenzi et al. 2003), but within the quoted errors the newer determinations are indistinguishable from the older ones.

The 24-km-diameter Ries impact crater, in Germany, has been suggested as the source crater for the Central European tektites based on its proximity to the strewn field, similarity in age (within experimental errors), and systematic changes in size and composition of tektites with distance from Ries (Cohen 1963). Strontium and Nd isotopic data support the conclusion that the Central European tektites were derived from the Ries crater (Shaw and Wasserburg 1982; Horn et al. 1985). The major and trace element compositions of the Central European tektites are similar to, but not exactly the same as, the composition of the Upper Freshwater-Molasse unit (referred to as the OSM unit based on the German name for the unit), which is the uppermost stratigraphic unit at Ries (Bouška et al. 1973; Delano and Lindsley 1982; Engelhardt et al. 1987).

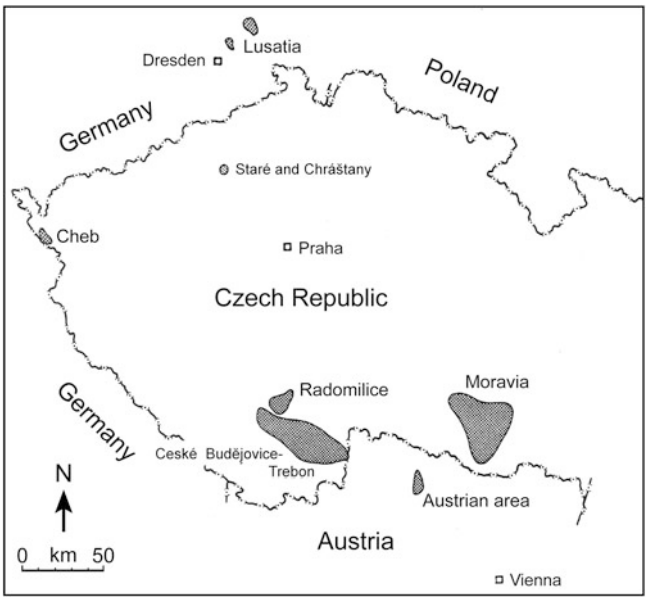

Fig. 4.25 Map of the Central European tektite strewn field. Crosshatched area (*gray*) indicates where the Central European tektites have been found. Ries Crater (not on this map), ~250 km east of the strewn field, is believed to be the source crater. Modified after Bouška (1998), Fig. 3. Reprinted with the permission of *Chemie der Erde*

Microtektites belonging to the Central European tektite strewn field have not been found and the tektites have not been found in situ. The Central European tektites are found as transported or reworked objects in sedimentary units ranging from Middle Miocene to Holocene (Bouška 1998; Trnka and Houzar 2002) and thus lack the stratigraphic control that has been useful for studying microtektite layers in marine sediments. Therefore, we do not know whether or not the Central European tektites are associated with unmelted ejecta and/or geochemical anomalies.

4.5 The North American Microtektite Layer

4.5.1 Introduction

The first North American microtektites were discovered in the core catcher of core 31 from Deep Sea Drilling Project (DSDP) Site 149 in the Caribbean Sea (Donnelly and Chao 1973). Donnelly and Chao (1973) recovered a few glass spherules which they suggested belonged to the North American strewn field based on their age, proximity to the North American strewn field, and similar major oxide

compositions. Shortly after that, Glass et al. (1973) reported the discovery of over 6,000 microtektites in Lamont Doherty Earth Observatory Core RC9-58, also from the Caribbean Sea. This core has been important in the study of the North American microtektite layer and the relationship between the North American microtektite layer and the slightly older clinopyroxene-bearing (cpx) spherule layer. North American microtektites were then found at DSDP Site 94 in the Gulf of Mexico (Glass and Zwart 1979a). They were later found on Barbados in the West Indies (Sanfilippo et al. 1985). As of 2010, Barbados is the only location where microtektites have been found on land. This is the only site where large samples can be recovered from a Cenozoic microtektite layer. Another very important find in the study of this microtektite layer was the discovery of a thick layer of North American microtektites and associated tektite fragments and shocked-rock and -mineral grains at DSDP Site 612 in the northwest Atlantic off New Jersey (Thein 1987). This is the first site where tektite fragments and shock-metamorphosed grains were found associated with a microtektite layer and the thickness of the layer (at least 8 cm) suggested that Site 612 is much closer to the source crater than any other North American microtektite-bearing site (Glass 1989).

4.5.2 Description of the North American Microtektites

Like the Australasian and Ivory Coast microtektites, the North American microtektites are generally less than a millimeter in size; however, at DSDP Site 612 in the northwest Atlantic, microtektites up to several millimeters in size have been recovered (Keller et al. 1987; Glass 1989). In addition, centimeter-sized tektite fragments have been reported from this site (Thein 1987). In Core RC9-58 from the Caribbean Sea, microtektites as small as 30 μm in diameter were observed (Glass et al. 1973). Most (>80 %) of the North American microtektites are spherical, but ellipsoid forms, usually oblate, are also common (∼15 %); the remainder are irregular forms plus teardrop and dumbbell shapes (Fig. 4.26; Glass and Zwart 1979a). Some fused forms (two or more microtektites fused together) were also observed. Most of the North American microtektites are transparent and range in color from pale yellow to brown; however, translucent dark brown to opaque black microtektites have also been recovered (e.g., Glass et al. 1973; Glass and Zwart 1979a). Thin edges of the larger tektite fragments recovered from Site 612 are transparent with a yellow green to dark olive green color.

The North American microtektites exhibit a wide range of surface textures, from smooth (shiny) to extremely rough with deep pits (Glass and Zwart 1979a). Most are fairly smooth with irregular pitting. A few are very finely pitted, which gives them a frosted appearance. Some have relatively large circular pits and some have raised circular areas that are enriched in silica compared to the adjacent glass (Fig. 4.27). Star-shaped pits were observed on several North American microtektites from the Caribbean Sea (Core RC9-58; Fig. 4.27). Grooves are not as

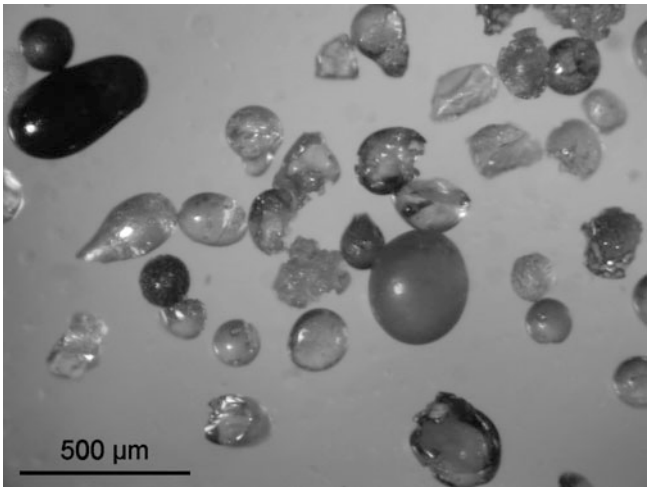

Fig. 4.26 Photomicrograph of North American microtektites from Core RC9-58 (see Fig. 4.29) from the Caribbean Sea. Note that fragments are abundant and that spheroids make up most of the splash forms. The microtektites range from transparent pale yellow–brown to opaque black

common on the surfaces of the North American microtektites as they are on the Ivory Coast microtektites (Glass 1974; Glass and Zwart 1979a).

Most of the North American microtektites are fairly uniform in color, but some have faint flow lines or schlieren. Spherical bubble cavities are common and many of the microtektites contain lechatelierite inclusions which are often sinuous or irregular in shape (Donnelly and Chao 1973; Glass and Zwart 1979a). White opaque inclusions of cristobalite were identified in some North American microtektites from the Gulf of Mexico and Caribbean Sea (Glass et al. 1973; Glass and Zwart 1979a). At Site 612 in the northwest Atlantic, some glass fragments and microtektites contain quartz grains, a few of which were partially melted to form lechatelierite (Glass 1989). Several of the glass fragments have fine-grained crystalline textures near the outer edges which may indicate diagenetic alteration following hydration (Thein 1987). In addition, many of the glass fragments and microtektites at Site 612 have pyrite coatings and a few even appear to have been partly replaced by pyrite (Glass 1989).

4.5.3 Composition

The North American microtektites have a wide range in major oxide compositions with silica ranging generally between 63 and 83 wt % (Table 4.9, Fig. 4.28; Glass et al. 1985, 1998, 2004b; D'Hondt et al. 1987; Koeberl and Glass 1988). The other major oxides, except for Na_2O, generally vary inversely with the silica content. Although the average silica content varies from one site to another, there is a great

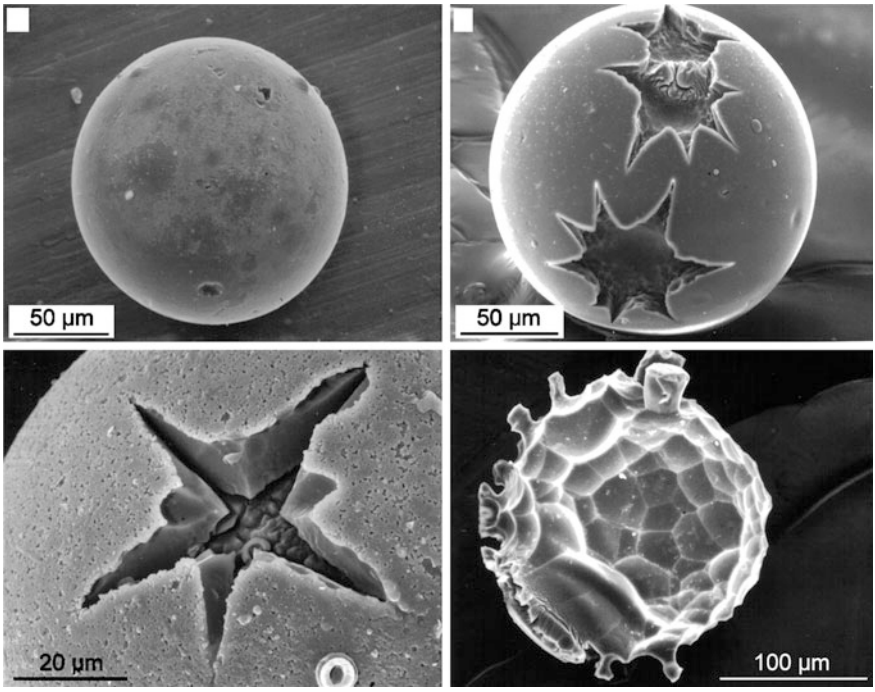

Fig. 4.27 Scanning electron microscope images of North American microtektites from Core RC9-58 taken in the Caribbean Sea. **a** A relatively smooth microtektite. **b** A microtektite with large star-shaped pits, but otherwise relatively featureless. These star-shaped pits have only been found on North American microtektites from the Caribbean Sea. Their origin is unknown. **c** Close-up view of a star-shaped pit. The sides of the pit look like they are vertical or almost so. There appears to be a thin (a few microns) outer layer (*light colored*). Below the outer layer is another layer (*dark gray*) that is ~10 µm thick. The ~8 µm diameter light-colored doughnut shaped object in the lower right is a calcareous nannofossil (coccolith). **d** A microtektite with shallow overlapping pits and numerous protrusions, most with circular caps with a larger diameter than the conical-shape pedestal on which they sit. All the caps are roughly the same height above the adjacent surface. The caps are silica-rich and less soluble than the rest of the microtektite. The difference in height between the top of the protrusions and the adjacent glass is due to differential solution and indicates that the microtektite has undergone ~29 µm of solution

deal of overlap and the microtektites from all the sites fall on the same compositional trends. There is a rough correlation between color and silica content of the North American microtektites, with the lighter-colored microtektites having higher silica contents. The North American microtektites with silica contents greater than ~70 wt % have compositions similar to the compositions of the North American tektites, although the microtektites have a greater range in oxide contents (Table 4.9, Fig. 4.28). Like North American tektites, the microtektites generally have low MgO and CaO contents for a given silica content compared with tektites in the other strewn fields (see Tables 4.3, 4.9).

4.5.4 Age

A fission-track age of 34.6 ± 4.2 Ma was determined for the North American microtektites from Core RC9-58 in the Caribbean Sea (Glass et al. 1973). North American tektite fragments recovered from the microtektite layer on Barbados were determined to have age an of 35.4 ± 0.6 Ma (2σ error) using ^{40}Ar-^{39}Ar laser-probe dating (Glass et al. 1986), and tektite fragments in the North American microtektite layer from Site 612 yielded an ^{40}Ar-^{39}Ar plateau age of 35.5 ± 0.3 Ma (Obradovich et al. 1989). These ages are in agreement with the 35.4 ± 0.2 Ma age obtained for North American tektites from Georgia, U.S.A. (Albin and Wampler 1996).

4.5.5 Geographic Occurrence

North American microtektites have been found in the Gulf of Mexico, in the Caribbean Sea, on Barbados, and in the northwest Atlantic off the coast of New Jersey (Fig. 4.29). Core E67-128 from the Gulf of Mexico contains only a few scattered microtektites (Keller et al. 1983, 1987; Glass et al. 1985) and Core 31 (DSDP Site 149) from the Caribbean Sea contains a large core gap that truncates the upper part of the microtektite layer (Glass and Zwart 1979a). North American microtektites were found at two sites on Barbados, both on the east coast: Bath Cliff, near Bathsheba, and Gay's Cove ~17 km north of Bath Cliff (Saunders et al. 1984; Sanfilippo et al. 1985). The layer has also been found at two sites in the northwest Atlantic: DSDP Site 612, which was mentioned above, and ODP Site 904 (McHugh et al. 1996), which is only a few kilometers north of Site 612. Harris et al. (2009) have reported finding shocked-quartz grains and microtektite fragments in a 3-cm thick gray clay layer of late Eocene age in the Bracewell Kaolin mine in eastern Jefferson County, Georgia. The major oxide composition of the glass shards is similar to that of the silica-poor (~64 %) North American microtektites, but with much higher Na_2O contents (~6 wt %). Without additional compositional data or any detailed petrographic information, it would be difficult to distinguish these glass fragments from volcanic ash.

4.5.6 Relationship to the Clinopyroxene-Bearing Spherule Layer

Crystal-bearing spherules are found associated with the North American microtektites in cores from the Gulf of Mexico and Caribbean Sea (John and Glass 1974; Glass and Zwart 1979a). The major crystalline phase in these spherules is clinopyroxene and, therefore, they are often referred to as clinopyroxene-bearing spherules or cpx spherules. Because they are impact spherules containing primary

Table 4.9 Major oxide (wt %) and trace element (ppm) of North American microtektites and tektites

	Microtektites[a] (25)		Microtektites Barbados[b] (30)		Tektite frags. Site 904[c] (28)		Bediasites[d] (35)		Georgiaites[e] (24)	
	Average	S.D.	Average	S.D.	Average	S.D.	Average	S.D.	Average	S.D.
SiO_2	73.4	4.8	78.0	3.1	74.6	2.2	76.36	2.42	81.8	1.0
TiO_2	0.73	0.15	0.62	0.12	0.71	0.08	0.77	0.13	0.51	0.04
Al_2O_3	14.1	2.0	12.9	1.7	13.9	1.2	13.77	1.56	11.2	0.5
FeO	4.37	1.30	2.84	1.11	4.03	0.62	4.01	0.84	2.64	0.40
MgO	1.73	0.87	0.88	0.24	1.12	0.18	0.69	0.21	0.61	0.07
CaO	1.64	0.80	1.11	0.66	1.00	0.21	0.56	0.20	0.45	0.03
Na_2O	1.06	0.23	0.89	0.23	0.65	0.26	1.51	0.20	0.94	0.07
K_2O	2.92	0.47	2.72	0.53	3.21	0.52	2.04	0.28	2.44	0.08
	(25)		(1)		(8)		(9–18)		(23)	
Sc	13.2	5.4	4.6	n/a	12.9	1.8	14	5	8.7	1.0
Cr	65	51	50	n/a	46.4	16.8	45	13	n.d.	n.d.
Co	17.5	9.3	20	n/a	13.6	6.0	12	2	7.5	1.1
Ni	58	57	n.d.	n/a	48	71	13	4	7.4	1.9
Ga	25	35	n.d.	n/a	12	5	13	2	n.d.	n.d.
Rb	116	49	n.d.	n/a	179	37	63	8	76	5
Sr	187	72	n.d.	n/a	149	45	102	34	163	8
Zr	213	86	n.d.	n/a	284	73	221	34	187	14
Sb	1.96	2.79	n.d.	n/a	0.72	0.74	n.d.	n.d	n.d.	n.d
Cs	5.70	3.37	6	n/a	14.3	6.5	2	0	1.74	0.22
Ba	554	164	n.d.	n/a	541	122	527	181	572	25
La	42.4	15.6	15	n/a	51	14.5	39	10	21.1	2.0
Ce	79.8	28.3	38	n/a	102.8	29.7	79	12	46.2	4.0
Nd	40.6	16.7	20	n/a	50.7	12.3	n.d.	n.d.	20.6	2.0
Sm	7.79	2.89	4.5	n/a	9.78	2.22	7.5	1.2	4.07	0.43
Eu	1.58	0.56	0.59	n/a	1.61	0.25	1.64	0.24	0.99	0.09
Gd	6.24	2.28	n.d.	n/a	8.49	1.82	n.d.	n.d.	3.44	0.40
Tb	1.01	0.33	0.8	n/a	1.30	0.19	1.02	0.17	n.d.	n.d.
Tm	0.51	0.19	n.d.	n/a	0.70	0.08	n.d.	n.d.	n.d.	n.d.
Yb	3.48	1.29	3.5	n/a	4.26	0.42	3.13	0.50	1.91	0.17
Lu	0.53	0.19	3	n/a	0.59	0.09	0.49	0.08	0.29	0.03
Hf	5.30	2.18	n.d.	n/a	7.39	1.05	6.9	0.8	4.64	0.39
Ta	1.30	0.43	n.d.	n/a	1.42	0.60	n.d	n.d.	0.57	0.05
Th	11.1	4.1	4	n/a	15.6	5.2	7.9	1.2	5.81	0.51
U	2.06	0.94	n.d.	n/a	3.36	0.85	2.1	0.5	1.46	0.15

Number in parentheses indicates number of analyses. Total iron reported as FeO

S.D. Standard deviation, *n.d.* no data, *n/a* not applicable

[a] Compositional data for microtektites from DSDP Sites 94 and 149 and Core RC9-58 (Glass et al. 2004b)

[b] Major oxide data from Burns (1985). Trace element data are for a composite of two microtektites (Koeberl and Glass 1988)

[c] Major oxide and trace element data from Glass et al. (1998)

[d] Major oxide data from Chao (1963). Trace element data from Cuttitta et al. (1967) and Haskin et al. (1982)

[e] Albin et al. (2000)

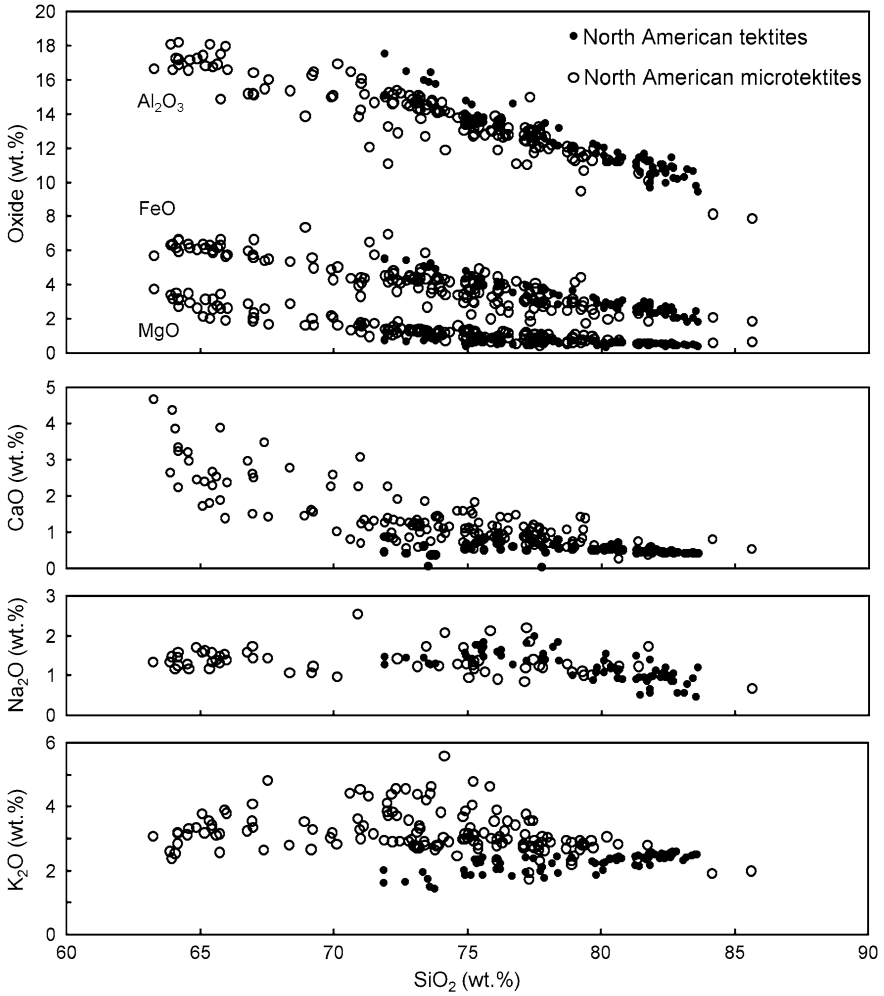

Fig. 4.28 Major oxide contents versus SiO_2 for North American tektites and North American microtektites. Except for K_2O versus SiO_2, the microtektites have compositional trends similar to the compositional trends of the North American tektites, but extend those trends down to lower SiO_2 contents. Tektite data are from Chao (1963), Schnetzler and Pinson (1963), King (1966), Cuttitta et al. (1967), Garlick et al. (1971), O'Reilly et al. (1983), Dod et al. (1985), and Glass (1989)

microlites/crystallites, they can also be called microkrystites. They were originally believed to belong to the North American microtektite layer and their occurrence in cores in the equatorial Pacific and eastern equatorial Indian Ocean were interpreted as indicating that the North American microtektite layer extended across the equatorial Pacific into the eastern Indian Ocean (Glass et al. 1979; Glass 1982). However, it was eventually shown that the cpx spherules belong to a different,

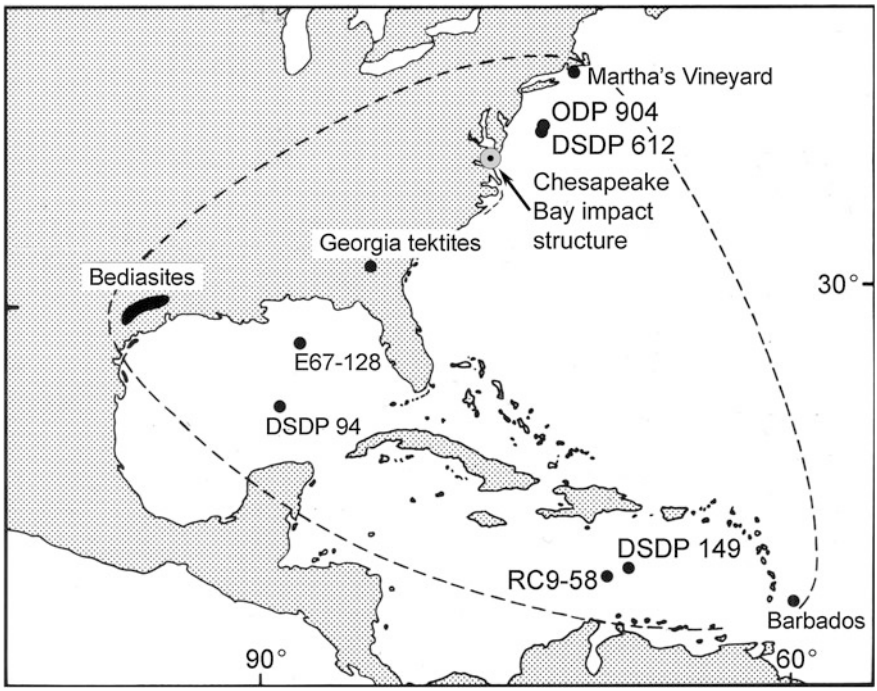

Fig. 4.29 Map of the North American tektite/microtektite strewn field. Only one tektite was found at Martha's Vineyard. Scattered microtektites, but no well-defined microtektite layer was found in Core E67-128. Also shown is the location of the Chesapeake Bay impact structure

slightly older (~10–15 ka) event (e.g., Glass 1986; Glass et al. 1998). The cpx spherule layer is discussed in Sect. 4.6.

4.5.7 Unmelted, Shock-Metamorphosed Ejecta Associated with the North American Microtektite Layer

Shock-metamorphosed grains were discovered in the North American microtektite layer at DSDP Site 612 on the upper continental slope off New Jersey (Thein 1987). This was the first time that unmelted shock-metamorphosed grains had been found associated with any microtektite layer and it provided further evidence of the impact origin of the microtektites. Thein (1987) described shocked quartz and feldspar grains that exhibit multiple sets of planar deformation features from the tektite/microtektite layer at this site. White opaque grains containing coesite and, sometimes, stishovite were also found to be common in this layer (Glass 1989). Many of the quartz, feldspar, and coesite-rich grains appear to be coated with a layer of glass (Bohor et al. 1988). In addition, there are also shock-metamorphosed,

fine-grained rock fragments that contain coesite and stishovite. The layer of tektite fragments and millimeter-sized splash forms are concentrated in an ~8 cm thick layer at this site. The shocked rock and mineral grains are most abundant in the upper 3 cm of the layer, where they make up ~42 % of the grains in the >250 μm size fraction.

Shocked quartz and coesite were later found in the North American microtektite layer on Barbados and at sites in the Gulf of Mexico and Caribbean Sea (Glass and Wu 1993) and at ODP Site 904 just north of DSDP Site 612 in the North Atlantic (Glass et al. 1998; Fig. 4.30a). In addition, a layer (~2 cm thick) of shocked quartz (Fig. 4.30b) and coesite was found at Site 903, close to Site 904 (Glass et al. 1998) and at Site 1073, approximately 62 km northeast of Site 612 (Liu et al. 2009). No tektite fragments or microtektites were found at either of these sites, but based on their geographic proximity and stratigraphic age the ejecta at these sites are believed to be from the same impact as the North American tektites/microtektites. Shocked zircons (Fig. 4.30c, d), some containing a high-pressure polymorph of $ZrSiO_4$, were found in the North American tektite/microtektite layer at Sites 612, 903, and 904 and on Barbados (Glass and Liu 2001). This was the first time this phase was found occurring naturally. It was named reidite after Alan F. Reid who produced this phase in laboratory experiments in 1969 (Glass et al. 2002).

4.5.8 Geographic Variation Within the North American Strewn Field

The abundance of tektites/microtektites varies greatly within the North American tektite/microtektite layer, with the highest abundance at DSDP/ODP Sites 612 and 904 in the northeast Atlantic and the lowest abundance found on Barbados. At Sites 612 and 904 the layer is 8 and 3 cm thick, respectively, and it consists almost entirely of tektite fragments, millimeter-sized splash forms, and unmelted shock-metamorphosed rock and mineral grains. On Barbados the tektite fragments and microtektites have an abundance of 877 (>125 μm)/cm^2 (Glass et al. 1998). This abundance is greater than that found in the Australasian strewn field except for a few sites within ~3000 km of the Indochina area where the source crater is believed to be. This suggests that even the site with the lowest abundance of microtektites in the North American strewn field is not close to the edge of the strewn field. The North American microtektite strewn field may be much larger than shown in Fig. 4.29.

Not only are the microtektites and tektite fragments more abundant at DSDP/ODP Sites 612 and 904, but the percent glass fragments and abundance of unmelted shock-metamorphosed ejecta is greater than at other sites in the strewn field (Glass and Wu 1993; Glass et al. 1997, 1998). These observations suggested that Sites 612 and 904 are close to the source crater (e.g., Glass 1989), and, as indicated in the next section, this appears to be the case.

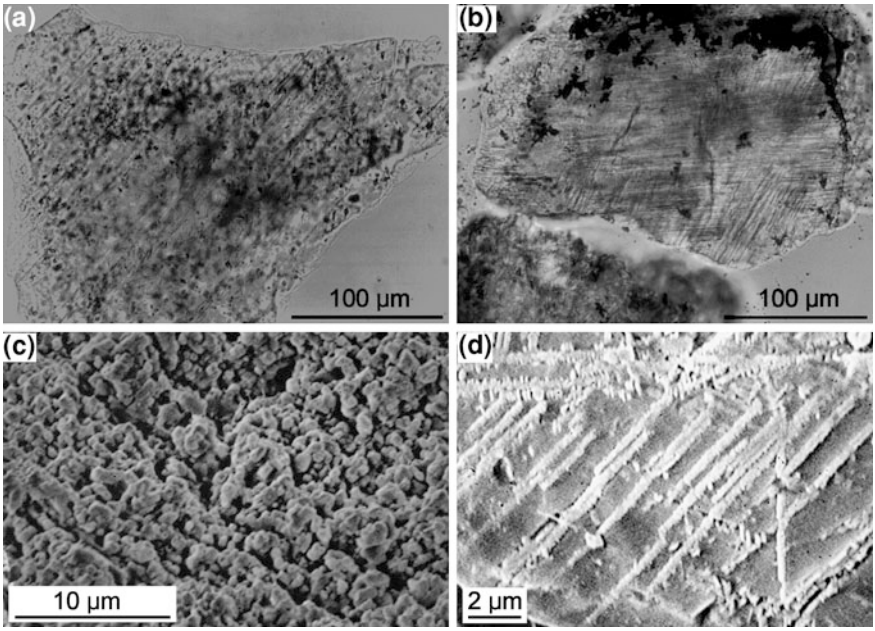

Fig. 4.30 Shocked quartz and zircon from the North American microtektite layer/Chesapeake Bay impact ejecta layer. **a** Quartz grain from the North American microtektite layer at Ocean Drilling Program (ODP) Site 904 in the northwest Atlantic off the coast of New Jersey, U.S.A. One set of NE-SW trending PDFs is present. **b** Quartz grain with two sets of PDFs from ODP Site 903 in the northwest Atlantic, ~8 km north-northwest of Site 904. The North American microtektite layer is not present at this site, but the shocked-quartz grain was found in an ejecta layer with the same stratigraphic age as the North American microtektite layer and is believed to be from the same impact (see Glass et al. 1998). **c** Scanning electron microscope (SEM) image of the surface of a shocked zircon with granular or strawberry texture from the North American microtektite layer at ODP Site 904. **d** SEM image of the surface of a shocked zircon containing lamellae of reidite (*white*) in zircon (*gray*) from ODP Site 904

4.5.9 The Source Crater: Chesapeake Bay

Based on Sm–Nd and Rb–Sr systematics, Shaw and Wasserburg (1982) suggested that the North American tektites were derived from relatively young (~0.6 Ga) crustal material, probably on the Appalachian orogenic belt or the Atlantic or Gulf Coastal Plains or adjacent continental shelves. Ngo et al. (1985) determined the Sm–Nd and Rb-Sr systematics for tektite fragments and microtektites from Barbados and obtained the same results as Shaw and Wasserburg (1982) obtained for the North American tektites (Fig. 4.31). This not only supported the conclusion that the tektite fragments and microtektites found on Barbados belong to the North American tektite strewn field, but it supported the proposed source area. On the other hand, Stecher et al. (1989) studied the tektite fragments found at Site 612 and obtained a much wider range in Sr and Nd isotopic values than previously obtained

for North American tektites and microtektites. The isotopic data obtained for the DSDP Site 612 tektite fragments indicate that they were derived from an older crustal source region (0.8–1.0 Ga) and target rocks were apparently deposited more recently (i.e., ~400 Ma ago). However, the isotopic data plot along a trend that, if extrapolated, goes through the values previously obtained for North American tektites (Fig. 4.31), and the isotopic values for the Site 612 tektites still indicate a source area along the eastern continental margin of North America.

The abundance of tektite fragments and shock-metamorphosed unmelted ejecta at Site 612 suggested that the source crater was close to that site; how close, depended on the size of the crater (Glass 1989). Glass (1989) further pointed out that the Paleogene sediments are carbonate rich in the southern part of the Atlantic Coastal Plain and adjacent continental shelf and, therefore, if the crater was south of Site 612 and on the coastal plain or adjacent continental shelf, it had to be fairly close, since the North American tektites/microtektites have low CaO contents.

The Chesapeake Bay impact structure (Fig. 4.32) was first reported in 1994 and was immediately recognized as a possible source of the North American tektites and microtektites (Poag et al. 1994; Poag and Aubrey 1995). The water depth at the time of impact was several hundred meters. The diameter of the crater is reported to be ~85 km (Poag et al. 2004), but it may have been smaller prior to backwash which filled in the crater and increased the diameter (Collins and Wünnermann 2005). Biostratigraphic data indicate that formation of the crater was coeval with the deposition of the North American microtektite layer (Poag et al. 1994; Poag and Aubry 1995). Major and trace element and Sr and Nd isotopic data for outcrop samples of target lithologies and crater-fill breccias from the Chesapeake Bay impact structure are generally consistent with derivation of the North American tektites and microtektites from this structure (Koeberl et al. 1996; Deutsch and Koeberl 2006); however, the exact target lithology or lithologies that were melted to produce the tektites and microtektites remained unknown as of 2010.

4.6 The Clinopyroxene-Bearing Spherule Layer

4.6.1 Introduction

As previously mentioned, the upper Eocene clinopyroxene-bearing spherules (cpx spherules) were originally thought to belong to the North American microtektite layer and their presence in the equatorial Pacific and eastern Indian Ocean was interpreted to indicate that the North American strewn field extended across the Pacific and into the Indian Ocean. After the identification of an Ir anomaly at the Cretaceous-Tertiary (K-T) boundary, which was interpreted to indicate a major impact event associated with a mass extinction event 65 Ma ago (Alvarez et al. 1980), several researchers began to search for additional Ir anomalies that might be

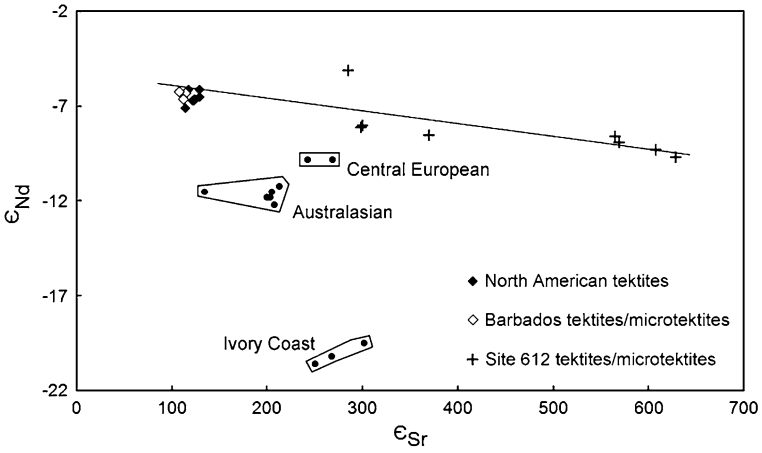

Fig. 4.31 A plot of ε_{Nd} versus ε_{Sr} for North American tektite fragments from the North American microtektite layer on Barbados, West Indies, and Deep Sea Drilling Project Site 612 in the Northwest Atlantic off New Jersey, U.S.A. Note that the Barbados tektite fragments plot with the other North American tektites (from Texas and Georgia), while the Site 612 tektite fragments/microtektites plot in a linear trend to the *right* in the diagram. However, an extrapolation of the best fit line through the Site 612 data intersects the data for the Texas, Georgia, and Barbados tektites. Neodymium and strontium isotopic data for the Central European, Ivory Coast, and Australasian tektites are plotted for comparison with the North American tektite/microtektite data. North American tektite data are from Shaw and Wasserburg (1982). Barbados and Site 612 data are from Ngo et al. (1985) and Stecher et al. (1989), respectively. Central European and Australasian tektite data are from Shaw and Wasserburg (1982). Ivory Coast tektite data are from Shaw and Wasserburg (1982) and Koeberl et al. (1998)

associated with other major impact events. Ganapathy (1982) reported a positive Ir anomaly about 30 cm below the peak abundance of North American microtektites in Core RC9-58 from the Caribbean Sea. In order to determine more precisely the relationship between the Ir anomaly and the North American microtektite layer, the samples that Ganapathy used for Ir studies were searched for microtektites. It was found that what was thought to be a single layer was actually two layers: an upper layer composed primarily of microtektites and a lower layer composed primarily of cpx spherules (Glass et al. 1982). The peak abundance of the cpx spherules was found about 25 cm below the peak abundance of the microtektites (Fig. 4.33), and the Ir anomaly was clearly associated with the cpx spherules. This result should have been interpreted to indicate that there were two impact events: one that produced the cpx spherules and associated Ir anomaly and a younger impact that produced the North American microtektite layer. Instead the authors proposed that there was only one impact and that the separation into two layers may have been produced by differential settling in the sediment due to density differences between the microtektites and the denser cpx spherules (Glass et al. 1982). However, laboratory experiments, done after the paper by Glass et al. (1982) was published, indicated that the larger, but lower density, microtektites

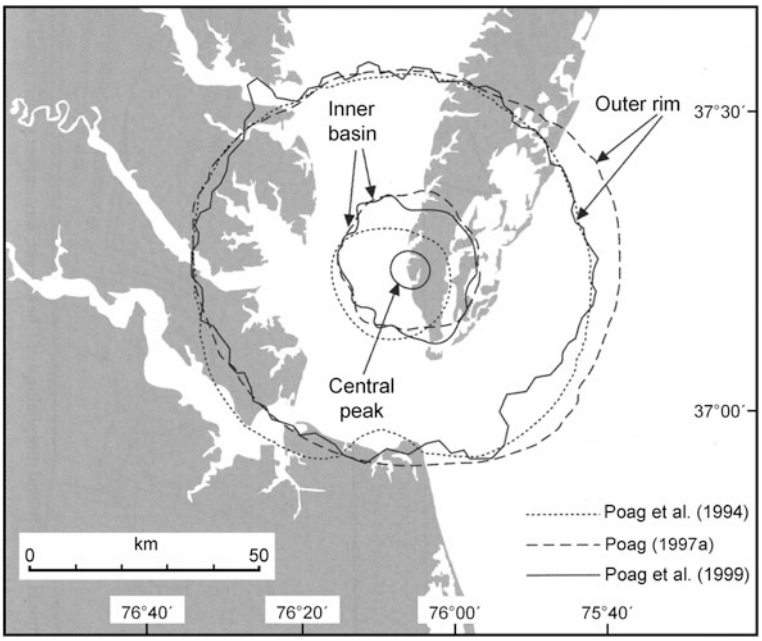

Fig. 4.32 Map showing the location of the outer rim, inner basin, and central peak of the Chesapeake Bay impact structure. Modified after Poag et al. (2004), Fig. 1.4

would settle deeper into unconsolidated sediment than would the smaller, but denser, cpx spherules (Burns 1985). In later publications, the cpx spherules were recognized as belonging to an older impact event, ~10–15 ka older than the North American microtektite event.

4.6.2 Description of Cpx Spherules

Cpx spherules are generally opaque, but translucent forms also occur (Fig. 4.34). The opaque cpx spherules have a wide range of colors including: white, tan, brown, or black. Many have a mottled appearance. The translucent cpx spherules are usually pale yellow in color and can sometimes have a yellow to bluish opalescent appearance (Fig. 4.34). The cpx spherules are generally <200 μm in diameter. Most whole cpx spherules are spherical in shape, but some are irregular in shape and fused forms consisting of two or more spheres fused together are also fairly common. Some have blebs or small spherules attached to their surfaces or embedded into them. Fragments of the translucent cpx spherules are common and some of the fragments are larger than the largest whole form (Fig. 4.34). Teardrop- and dumbbell-shaped cpx spherules have not been observed. The surfaces of the cpx spherules range from glassy smooth to rough with a dull luster (John and Glass

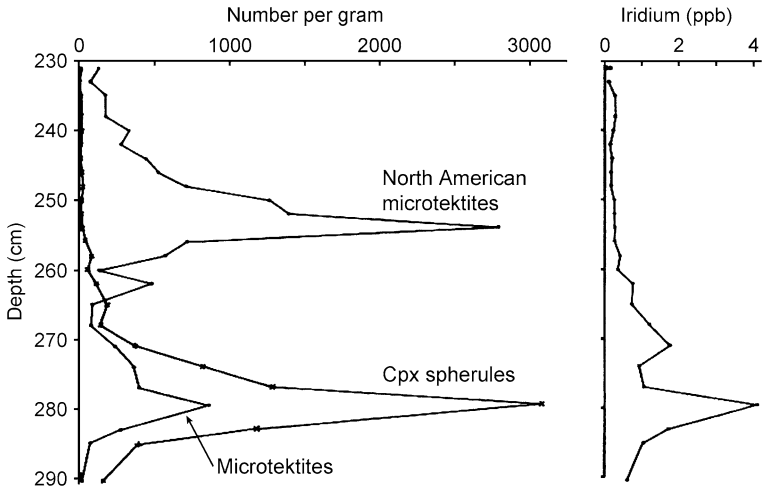

Fig. 4.33 Vertical distribution of North American microtektites, cpx spherules, and Ir in Core RC9-58 from the Caribbean Sea. The lower cpx spherule layer contains microtektites as well as cpx spherules. Most, if not all of the microtektites in the cpx layer are probably part of the cpx layer, but some may have come from the younger North American microtektite layer due to core disturbance and/or bioturbation. Note that the Ir anomaly is definitely associated with the older cpx spherule layer and not with the younger North American microtektite layer. The iridium data are from Ganapathy (1982)

1974; Glass and Zwart 1979a). Crystalline textures are present on the surfaces of some of the cpx spherules. In some spherules the crystalline phase has been removed, leaving voids or pits with crystalline outlines; but in other spherules the adjacent glass has been partially removed by solution, leaving the crystalline phase standing out in relief (Fig. 3.11).

Interior polished surfaces of the opaque cpx spherules reveal a wide variety of crystalline textures including: dendritic, feathery, bladed, skeletal, and equant (John and Glass 1974; Glass et al. 1985; Glass and Burns 1987; Fig. 4.35). The most common crystalline phase in the cpx spherules is clinopyroxene; however, skeletal and equant microlites of Fe-rich, Fe- and Cr-rich, Ni- and Fe-rich, and Ni-, Cr-, and Fe-rich spinels have also been identified (John and Glass 1974; Glass et al. 1985, Glass and Burns 1987; Fig. 4.36). The spinel microlites are usually scattered around the interior of the spherules, but in some spherules the spinel microlites are concentrated at the surface (Fig. 3.12). The translucent cpx spherules have a cryptocrystalline texture and are birefringent (Glass et al. 1985). Like the opaque cpx spherules, the major crystalline phase in the translucent, cryptocrystalline spherules is clinopyroxene. Unlike microtektites, the cpx spherules do not contain bubble cavities or lechatelierite particles. However, silica inclusions with crystal shapes are present in some of the cpx spherules (Fig. 4.35d). Based on the crystal shapes, the silica crystals may be cristobalite (Glass et al. 1985), but this could not be confirmed with micro-Raman spectrography.

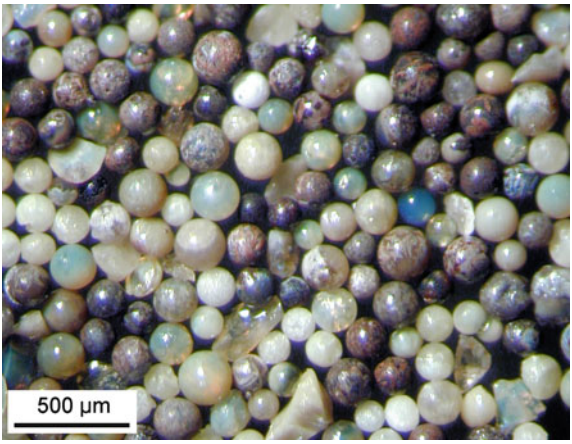

Fig. 4. 34 Photomicrograph of cpx spherules (late Eocene microkrystites) from Ocean Drilling Program Site 709 in the northwestern Indian Ocean. Note that all the spherules are spheres or fragments; no dumbbells or teardrops are present. The spherules range from translucent pale yellow to blue to opaque white, dark gray or tan; some have a mottled appearance. Note also that the largest cpx grains are fragments, which are usually white opaque and cryptocrystalline in nature. Image is from Liu (2006), Fig. 10, with permission

Some of the cpx spherules have voids with crystalline shapes (Fig. 4.35e and f). The voids generally have prismatic, hopper, chain, or dendritic shapes and were probably produced by dissolution of a more soluble phase or phases. Based on crystal habit, it has been proposed that the phase responsible for the prismatic, hopper, and chain-like voids was probably olivine (Glass et al. 1985). The voids with feathery or dendritic textures (Fig. 4.35f) may have been formed by dissolution of Fe-rich pyroxene skeletal microlites (Glass et al. 1985).

Glass spherules (microtektites) without any crystalline phases have been found associated with the cpx spherules (Fig. 4.37; Glass et al. 1985; Glass and Koeberl 1999; Liu et al. 2009). Microtektites in the cpx spherule layer are generally transparent to translucent and occur in a wide range of colors including colorless, pale brown, brown, and green. At some of the sites many of the microtektites are larger than any of the cpx spherules. Most of the microtektites are spherical, but disc, teardrop, and dumbbell shapes are also present, and fragments are common at many of the sites. Spherical microtektites up to 1.1 mm in diameter have been recovered from the cpx spherule layer. Most have shiny smooth surfaces, but many are pitted. Lechatelierite particles have not been identified in the microtektites from the cpx spherule layer, but during energy dispersive X-ray analysis, one of the microtektites was found to contain a silica-rich area that was probably lechatelierite (Glass and Koeberl 1999).

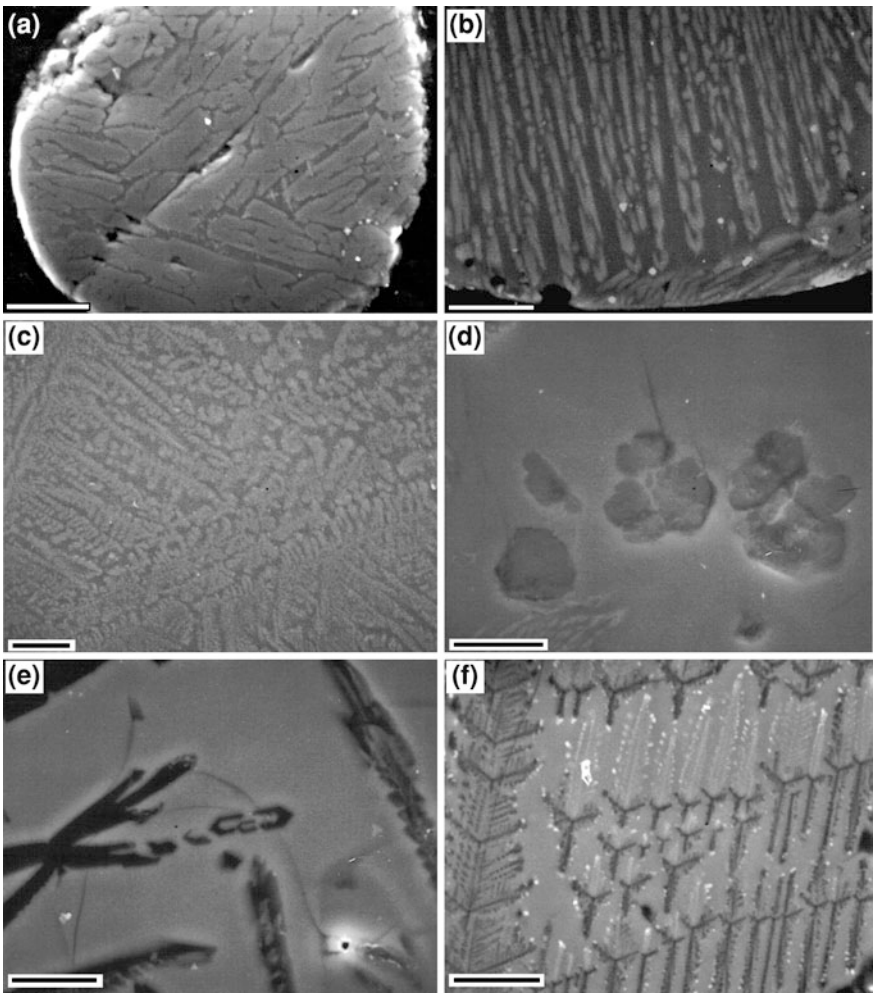

Fig. 4.35 Scanning electron microscope image of polished sections of cpx spherules showing internal crystalline textures. **a** Image of a cpx spherule, from Deep Sea Drilling Project (DSDP) Site 166 in the central equatorial North Pacific, showing lath-shaped clinopyroxene crystals (*light gray*) in a glass matrix (*dark gray*). Small white crystals in the glass matrix are spinels. **b** Chain-like clinopyroxene crystals (*light gray*) and small (<1 μm) spinel crystals (*white*) in a glass matrix (*dark gray*) in a cpx spherule from DSDP Site 216 in the northeast Indian Ocean. **c** Clinopyroxene (*light gray*) with a feathery texture in a glass matrix (*dark gray*). This spherule is from DSDP Site 69 in the central equatorial Pacific. **d** Silica crystals (*dark gray*) in a glass matrix (*gray*) in a cpx spherule from Site 216 in the northeast Indian Ocean. **e** Crystal-shaped voids (*black*) in a glass matrix (*gray*) in a cpx spherule from DSDP Site 94 in the Gulf of Mexico. **f** Missing crystalline phase (*black* Y-shape regions) in a glass matrix (*gray*). Trains of small («1 μm) crystallites (*white*) may be Fe-rich clinopyroxene. This spherule is from Site 94 in the Gulf of Mexico. All scale bars are 10 μm except for the one in **a**, which is 20 μm

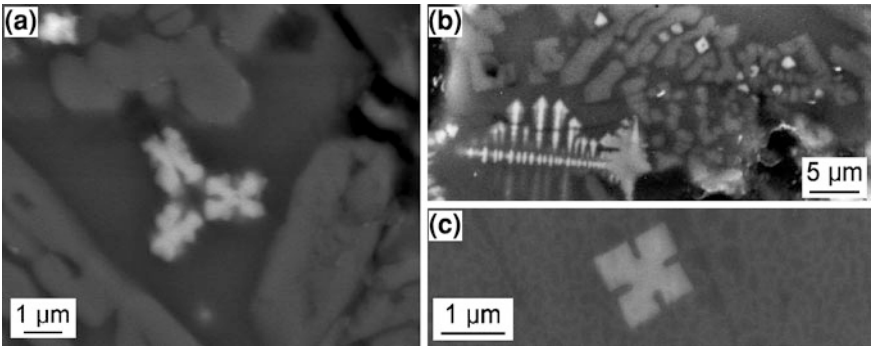

Fig. 4.36 Scanning electron microscope images of polished sections of cpx spherules showing spinel microlites. **a** Skeletal spinel crystals (*white*) and clinopyroxene crystals (*light gray*) in a glass matrix (*dark gray*) in a cpx spherule from Deep Sea Drilling Project (DSDP) Site 216 in the northeastern Indian Ocean. **b** Skeletal and octahedral spinel crystals (*white*) and clinopyroxene crystals (*light gray*) in a glass matrix (*dark gray*). *Black* regions are where a phase was removed by solution. This cpx spherule is from DSDP Site 166 in the equatorial Pacific. **c** Skeletal spinel crystal (*light gray*) in a glass matrix (*dark gray*) in a cpx spherule from DSDP Site 94 in the Gulf of Mexico

4.6.3 Composition

The cpx spherules have a wide range in major oxide compositions (Table 4.10; Fig. 4.38; Glass et al. 1985, 2004b; D'Hondt et al. 1987; Marchand and Whitehead 2002). The wide range in compositions may be due, at least in part, to the presence of a crystalline phase in a glass matrix which makes getting representative compositions of the spherules difficult. In addition, the missing phases in many of the cpx spherules mean that the original compositions of those spherules are unknown. However, there are some observed differences in major oxide compositions between the cpx spherules and the Cenozoic microtektites (particularly the North American microtektites) that appear to be real. Compared with the North American microtektites the cpx spherules generally have lower Al_2O_3 and TiO_2 and higher MgO and CaO contents for a given SiO_2 content (Tables 4.9, 4.10; Fig. 4.38; Glass et al. 1985, 2004b; D'Hondt et al. 1987; Marchand and Whitehead 2002; Liu et al. 2009). Generally, the FeO and/or CaO (and often MgO) contents are approximately equal to or higher than the Al_2O_3 contents (Glass et al. 2004b). The light-colored cpx spherules (including the translucent cryptocrystalline ones) generally have lower FeO and higher CaO contents than do the dark opaque cpx spherules (Table 4.10).

The trace element contents of cpx spherules are highly variable, especially Cr, Co, Ni, and the volatile elements (Table 4.10; Glass et al. 2004b). Compared with upper continental crust, the cpx spherules have high Cr, Ni, and Co contents (Fig. 4.39), with an average Cr content of $\sim 990 \pm 795$ ppm and an average Ni content of $\sim 1495 \pm 1249$ ppm (Glass et al. 2004b). Furthermore, the dark cpx

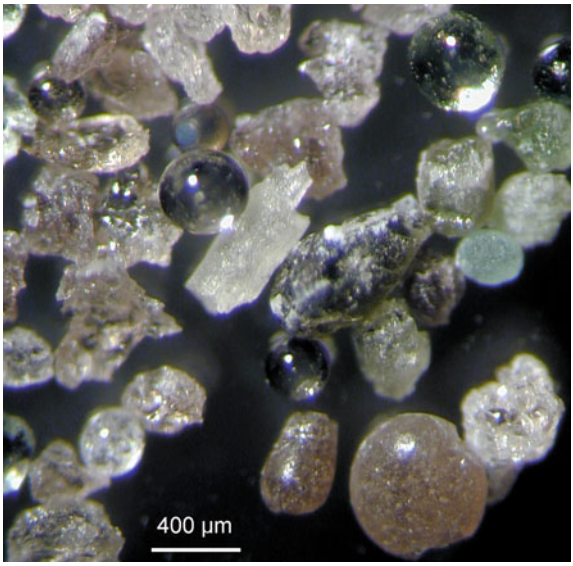

Fig. 4.37 Photomicrograph of microtektites recovered from the cpx spherule layer at Ocean Drilling Program Site 709 in the northwest Indian Ocean. Most are transparent, but there is a wide range in color from clear to *yellow–brown* to *green*. There are more glass fragments than whole splash forms. The splash forms are mostly spherical, but several elongate forms are also present. Image is from Liu (2006), Fig. 12, with permission

spherules generally have higher Cr, Ni, and Co contents compared with the light-colored cpx spherules (Table 4.10).

The microtektites found in the cpx spherule layer can be divided into two groups based on their appearance and composition: (1) transparent colorless to pale brown microtektites with high SiO_2 contents (>74 wt %), and (2) transparent to opaque microtektites with low SiO_2 contents (<75 wt %; Table 4.10; Fig. 4.38). The high-silica cpx microtektites have low MgO and CaO contents (generally <1 wt %). They have compositions similar to the North American microtektites, except for their very low Na_2O contents (generally <0.4 wt %) and generally higher Al_2O_3 contents for a given SiO_2 content (Vonhof and Smit 1999; Glass and Koeberl 1999; Glass et al. 2004b; Liu et al. 2009; Fig. 4.38). The colorless, silica-rich microtektites have low FeO contents (<2.5 wt %) and the pale brown, silica-rich microtektites have high FeO contents (>2.5 wt %). The low-silica microtektites generally have major oxide and trace element compositions similar to the cpx spherules, and like the cpx spherules they also have high Cr, Ni, and Co contents (Table 4.10, Fig. 4.39).

4.6.4 The Number of Upper Eocene Spherule Layers

There has been much controversy regarding the number of upper Eocene spherule layers (Keller et al. 1983, 1984, 1987; Glass 1984b, 1986, 1990b, 2002; Glass et al. 1985; D'Hondt et al. 1987; Glass and Burns 1987; Hazel 1989; Miller et al. 1991; Wei 1995; Whitehead et al. 2000; Marchand and Whitehead 2002; Liu et al. 2006, 2009). Glass et al. (1979) assumed that the crystal-bearing or cpx spherules were

Table 4.10 Major oxide (wt %) and trace element (ppm) composition of cpx spherules

	Cpx spherules[a] (71)		Dark cpx spherules[b] (10)		Light cpx spherules[b] (11)		Cpx-related microtektites			
							Low silica[c] (91)		High silica[c] (88)	
	Average	S.D.	Average	S.D.	Average	S.D.	Average	S.D.	Average	S.D.
SiO_2	64.8	4.6	67.7	6.6	68.7	1.8	65.4	4.78	79.4	4.1
TiO_2	0.31	0.08	0.30	0.09	0.28	0.05	0.40	0.21	0.46	0.16
Al_2O_3	7.42	1.45	6.90	1.14	6.83	1.00	9.35	3.23	12.59	3.38
FeO	7.18	2.90	7.59	2.36	3.69	0.68	6.50	2.55	2.70	2.32
MgO	7.37	2.56	6.38	2.86	6.83	0.66	6.75	3.24	0.70	0.64
CaO	9.91	3.12	7.95	3.81	11.4	2.1	7.15	4.20	0.52	0.70
Na_2O	0.89	0.33	0.90	0.24	0.57	0.13	1.56	1.15	0.36	0.53
K_2O	1.85	0.47	2.04	0.44	1.64	0.21	2.43	1.35	2.34	1.23
	(71)		(10)		(11)		(4)		(27)	
Sc	8.74	4.44	6.37	2.06	6.17	1.93	13.4	2.0	6.76	1.84
Cr	990	795	818	372	250	109	482	170	33	18
Co	89	56	92	32	32	13	72	21	8.4	4.8
Ni	1495	1249	1566	704	508	231	1082	622	26.3	23.2
Zn	42	29	40	17	22	8	79	50	18	13
Ga	47	59	18	32	70	71	21	18	38	54
As	1.5	2.0	0.6	0.4	1.1	1.0	0.6	0.5	2.1	2.0
Br	5.3	6.4	n.d.	n.d.	n.d.	n.d.	0.6	0.3	0.6	0.5
Rb	64	28	59.5	23.3	39.8	12.8	122	66	79	23
Sr	195	118	173	50	142	38	200	46	176	88
Zr	188	93	146	48	145	47	181	86	307	103
Sb	1.65	3.84	0.75	0.51	0.27	0.15	0.53	0.64	0.36	0.59
Cs	1.43	1.93	n.d.	n.d.	n.d.	n.d.	1.71	1.72	1.53	0.44
Ba	411	179	328	82	301	101	495	68	1167	449
La	31	12	26.9	6.8	25.9	8.5	51.1	9.6	45.3	11.4

(continued)

Table 4.10 (continued)

	Cpx spherules[a] (71)		Dark cpx spherules[b] (10)		Light cpx spherules[b] (11)		Cpx-related microtektites			
							Low silica[c] (91)		High silica[c] (88)	
	Average	S.D.	Average	S.D.	Average	S.D.	Average	S.D.	Average	S.D.
Ce	56.1	20.0	50.6	13.7	45.7	14.7	96.4	23.5	77.9	20.4
Nd	23.8	9.0	19.8	5.7	18.8	5.8	42.5	7.0	35.8	10.5
Sm	4.28	1.68	3.42	0.89	3.36	0.99	6.74	0.98	6.19	1.68
Eu	0.91	0.38	0.71	0.21	0.68	0.21	1.47	0.40	1.33	0.36
Gd	3.47	1.52	3.06	0.67	2.76	0.99	5.61	1.16	4.84	2.24
Tb	0.54	0.23	0.49	0.15	0.44	0.15	0.93	0.21	0.67	0.33
Tm	0.30	0.13	0.27	0.09	0.24	0.08	0.50	0.08	0.36	0.17
Yb	2.06	0.76	1.84	0.58	1.71	0.54	3.84	0.94	2.52	1.21
Lu	0.31	0.12	0.27	0.09	0.26	0.09	0.58	0.14	0.38	0.18
Hf	4.80	1.52	3.67	0.85	3.84	1.09	7.35	1.03	7.74	2.28
Ta	0.49	0.80	0.29	0.12	0.31	0.12	0.53	0.20	0.78	0.38
Th	7.19	2.52	2.10	7.31	7.31	2.61	9.07	1.26	8.13	1.96
U	2.06	0.91	0.77	1.95	1.95	0.69	1.19	0.62	1.91	0.83

Numbers in parentheses are the number of analyses, *n.d.* no data, *S.D.* one standard deviation

[a] Cpx spherules from the Caribbean Sea, Gulf of Mexico, equatorial Pacific and Indian Ocean sites (Glass et al. 2004b)

[b] Cpx spherules from Site 216 in the eastern equatorial Indian Ocean (Glass et al. 2004b)

[c] Major oxide data for microtektites from the cpx spherule layer in the Caribbean Sea, equatorial Pacific and Indian Oceans, and South Atlantic (DuBois 1983; Glass et al. 1985; Glass and Koeberl 1999; Liu et al. 2009; unpublished data); trace element data for low-silica microtektites from the equatorial Pacific (Glass et al. 2004b); trace element data for high-silica microtektites from the equatorial Pacific and Indian Oceans and S. Atlantic (Glass and Koeberl 1999; Glass et al. 2004b)

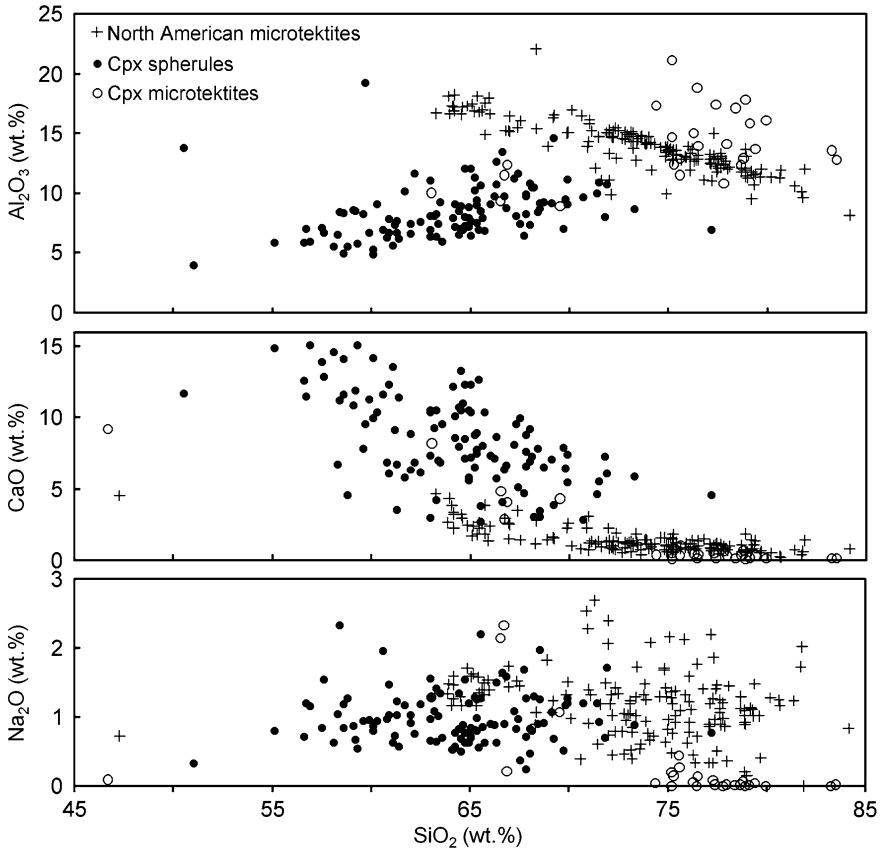

Fig. 4.38 Major oxide contents versus silica content for North American microtektites, cpx spherules, and microtektites from the cpx spherule layer. Note that the cpx spherules have different oxide contents and compositional trends compared with the North American microtektites. For example, the Al_2O_3 content for the cpx spherules is lower for a given SiO_2 content than that of the North American microtektites. Also the Al_2O_3 content of the cpx spherules decreases with decreasing SiO_2 content, but the Al_2O_3 content of the North American microtektites increases with decreasing SiO_2 content. The low-silica microtektites from the cpx layer generally have compositions similar to those of the cpx spherules. The high-SiO_2 cpx microtektites have compositions more similar to those of the North American microtektites, but can be distinguished from them by their generally higher Al_2O_3 content and much lower Na_2O content

part of the North American microtektite layer and thus only recognized one upper Eocene microtektite/spherule layer. Keller et al. (1983, 1984) proposed that there were at least three upper Eocene microtektite layers. By 1985, Glass and colleagues had recognized that the cpx spherules were not part of the North American microtektite layer, but belonged to a slightly older event (e.g., Glass et al. 1985). Keller et al. (1987) agreed that there was only one microtektite layer, correlated with the North American tektite strewn field; however, they argued that the cpx

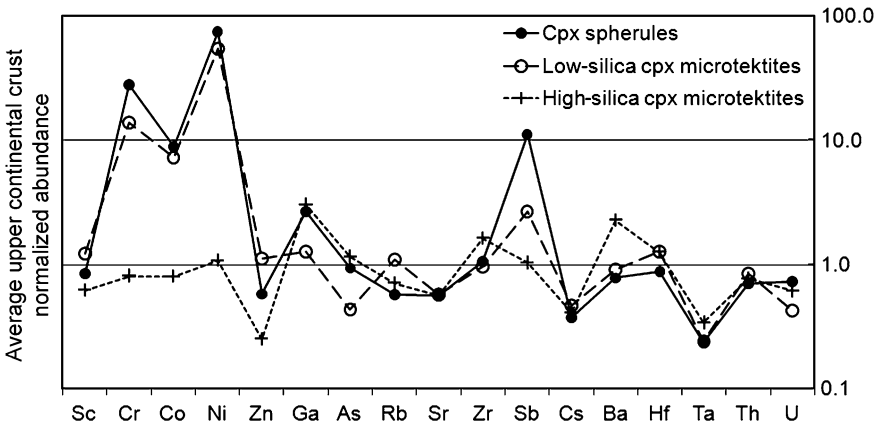

Fig. 4.39 Upper-continental-crust-normalized average trace element data for cpx spherules and microtektites from the cpx spherule layer. The high-SiO_2 microtektites from the cpx spherule layer generally have trace element contents within a factor of 2 or 3 of the average trace element contents of the upper continental crust. Note however, that both the cpx spherules and low-SiO_2 microtektites have 1–2 orders of magnitude higher Cr, Co, and Ni than that of the average upper continental crust. They also appear to have higher Sb contents than that of the average upper continental crust. The high average Cr, Co, and Ni contents appear to be the result of meteoritic contamination (see Sect. 4.6.10). Upper continental crust data are from Lodders and Fegley (1998). Cpx microtektite data are from Glass et al. (2004b)

spherules (which they called crystal-bearing microspherules) occurred in two closely spaced layers based on biostratigraphy and major oxide composition (Keller et al. 1987; D'Hondt et al. 1987). Glass and Burns (1987) continued to argue in favor of a single cpx spherule layer plus the North American microtektite layer. However, Miller et al. (1991) suggested that there are least three, maybe four, upper Eocene microtektite/spherule layers based on biostratigraphy and Sr isotope stratigraphy primarily at Site 612 on the upper continental slope off New Jersey.

Hazel (1989) studied the known upper Eocene spherule layer occurrences using the graphic correlation method and concluded that there must be at least six, possibly more, spherule layers. Glass (1990b) reviewed the petrographic and compositional data, as well as the biostratigraphic data, and again concluded that there were probably only two, four at most, upper Eocene microtektite/spherule layers. As late as 1993, Keller and colleagues still argued for three, possibly four, upper Eocene microtektite/spherule layers (Molina et al. 1993). Wei (1995) did a more in-depth study of the biostratigraphy of the upper Eocene microtektite/spherule layers and concluded that the available data are consistent with one couplet of microtektite-microkrystite (cpx spherule) layers in the upper Eocene; i.e., the North American microtektite layer and the slightly older cpx spherule (or microkrystite) layer. The two-layer model was further supported by Whitehead et al. (2000) and Liu et al. (2006, 2009) based on Sr–Nd isotopic data and by Marchand and Whitehead (2002) based on a statistical study of compositional data

for the upper Eocene spherules. Thus, the present data appear to indicate that there are only two widespread upper Eocene spherule layers: (1) the North American microtektite layer, and (2) the slightly older cpx spherule layer.

4.6.5 Age of the Cpx Spherule Layer

The cpx spherules have not been radiometrically dated. Biostratigraphic data indicate that the cpx spherule layer is late Eocene in age (e.g., Glass et al. 1985; Keller et al. 1987; Wei 1995). The cpx spherule layer occurs below the North American microtektite layer and various estimates suggest that it is 10–15 ka older (e.g., Sanfilippo et al. 1985; Glass 1986; Glass et al. 1998). Tektite fragments from the North American microtektite layer on Barbados and at DSDP Site 612 in the northwest Atlantic have been dated, using ^{40}Ar-^{39}Ar, at 35.4 ± 0.6 and 35.3 ± 0.3 Ma, respectively (Glass et al. 1986; Obradovich et al. 1989). North American tektites from Georgia have been dated at 35.4 ± 0.2 Ma using K–Ar (Albin and Wampler 1996). These data suggest an age of ~35.4 Ma for the North American microtektite layer and thus for the cpx spherule layer. The cpx spherule layer appears to occur within magnetochron 16n.1n (Jovane et al. 2006; Florindo and Roberts 2005; Liu et al. 2009), which ranges in age between 35.343 and 35.526 Ma (Cande and Kent 1995). This implies an age of ~35.4 ± 0.1 Ma for the cpx spherule layer in agreement with the age estimated from the radiometric age of the slightly younger North American tektites/microtektites.

4.6.6 Geographic Distribution of Cpx Spherules

Cpx spherules have been found below or overlapping the North American microtektite layer in the northwest Atlantic Ocean, Caribbean Sea, and Gulf of Mexico (Figs. 4.33 and 4.40). The cpx spherule layer has also been found along the equatorial Pacific and Indian Oceans, and in the South Atlantic (Fig. 4.4; Glass et al. 1985; Keller et al. 1987; Liu et al. 2009). At several sites in the northwest Atlantic (DSDP/ODP Sites 612, 903, and 904) and in a site in the Tasman Sea (DSDP Site 592), the cpx spherules have been partly or completely replaced by pyrite, preserving the crystalline textures (Fig. 3.23; Glass et al. 1998; Liu et al. 2009). Pancake-shaped clay spherules (Fig. 4.41), many containing or coated with Ni-rich spinel crystals (Fig. 3.14), have been found associated with an Ir anomaly in Massignano, Italy (Pierrard et al. 1998). These pancake spherules are believed to be diagenetically altered cpx spherules that have been flattened by the weight of the overlying rocks (Glass et al. 2004a). Silica-rich microtektites, but no cpx spherules, have been found at a site in the South Atlantic (ODP Site 699). The microtektites at Site 699 are associated with an Ir anomaly. Although no cpx spherules were found at this site, the microtektites are believed to belong to the

cpx spherule layer because of the stratigraphic age, association with an Ir anomaly, and similarity in appearance and major oxide composition to microtektites found associated with cpx spherules at other sites in the South Atlantic (Liu et al. 2009). Likewise, colorless glass spherules (probably microtektites) and an associated Ir anomaly, but no cpx spherules were found at ODP Site 738 in the Southern Indian Ocean (Liu et al. 2009).

At Bath Cliff on Barbados, an Ir anomaly is found below the North American microtektite layer. Cpx spherules are not found associated with the Ir anomaly at this site, but the Ir anomaly is believed to be the same Ir anomaly found associated with the cpx spherule layer at other sites. It has been suggested that the cpx spherules were dissolved by ground water at this site (Sanfilippo et al. 1985). At the Fuente Caldera section, Spain (Fig. 4.40), Ni-rich spinels are found at a level believed to be coeval with the Ir anomaly and pancake spherules with Ni-rch spinels at Massignano, Italy (Robin and Molina 2006). It is possible that the Ni-rich spinel crystals at this site are remnants of spinel-bearing cpx spherules which have been destroyed by diagenesis or ground water solution.

The cpx spherule layer has been observed at 29 sites around the globe (Fig. 4.40) if the following sites are included: Massignano, Italy; the sites where the cpx spherules have been replaced with pyrite; Site 699, where only silica-rich microtektites have been recovered; Site 738, where an Ir anomaly and glass spherules, but no cpx spherules, have been observed; Barbados, where there is only an Ir anomaly; and the Fuente Caldera section, Spain, where Ni-rich spinel crystals have been recovered. The widespread geographical distribution of the cpx spherules suggests that the layer may be global in extent. However, the presently known distribution can be inferred to indicate a ray-like pattern (see Sect. 4.6.11).

4.6.7 Associated Ir Anomaly and Shock-Metamorphosed Grains

An Ir anomaly appears to be a normal characteristic of the upper Eocene cpx spherule layer and has been identified at every site with the cpx spherule layer in which Ir has been measured (Liu et al. 2009). The peak Ir content generally coincides with the peak abundance of spherules at each site and ranges from as low as 40 pg/g at DSDP Site 292 in the western equatorial Pacific to as high as 4100 pg/g (4.1 ppb) at core site RC9-58 in the Caribbean Sea (Table 4.11; Fig. 4.33). A better indication of the amount of Ir in the spherule layer at each site is the estimated fluence which varies from 0.6 to 42 ng/cm^2 (Liu et al. 2009). Neither the peak abundance nor the fluence appears to exhibit any systematic geographic variation. Study of a large sample from the cpx spherule layer at ODP Site 709 in the northwest Indian Ocean indicates that the bulk of the iridium ($\sim$95 %) is in the silt- and clay-sized fractions (i.e., <63 μm; Liu et al. 2009). Only $\sim$5 % of the Ir is found in the spherules in the >63 μm size fraction.

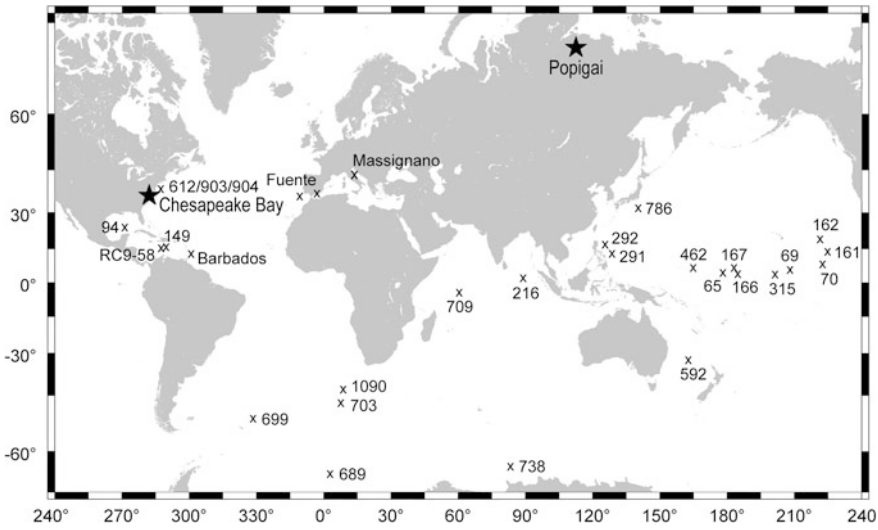

Fig. 4.40 Map showing the sites where the cpx spherule layer has been found. The layer was not found on Barbados, but an Ir anomaly was found below the North American microtektite layer on Barbados that is interpreted to indicate the former existence of the cpx spherules, prior to solution. At Massignano, Italy, flattened clay spherules containing, and sometimes coated with, Ni-rich spinel crystals are interpreted as being diagenetically altered cpx spherules. At Fuente Caldera, Spain, Ni-rich spinel crystals have been found at the appropriate stratigraphic level for the cpx spherule layer, but no spherules have been reported. No cpx spherules but microtektites and an associated Ir anomaly have been found at Ocean Drilling Program (ODP) Site 699 in the South Atlantic and at ODP Site 738 in the Indian Ocean sector of the Southern Ocean. These microtektites appear to be of the correct biostratigraphic age to belong to the cpx spherule layer. Locations of the Popigai and Chesapeake Bay impact structures are indicated with *black stars*. Modified after Liu et al. (2009), Fig. 1

As discussed above, pancake-shaped spherules containing, and sometimes coated with, Ni-rich spinel microlites have been found associated with an Ir anomaly at Massignano, Italy (Pierrard et al. 1998; Glass et al. 2004a). These spherules are believed to be diagenetically altered and compacted cpx spherules (Glass et al. 2004a). Shocked quartz with multiple sets of PDFs was discovered in the spherule layer at Massignano (Clymer et al. 1996; Fig. 4.42). Assuming that the spherules are diagenetically altered cpx spherules, this is the first time that shocked quartz has been recognized in the cpx spherule layer. More recently, coesite was found in the cpx spherule layer at DSDP Site 216 and coesite and shocked quartz were discovered in the cpx spherule layer at ODP Site 709 (Liu et al. 2009); both of these sites are in the equatorial Indian Ocean. No shock-metamorphic grains have been reported in the cpx spherule layer at any other site; but at most sites the cpx spherule layer has not been searched in detail for shocked mineral grains.

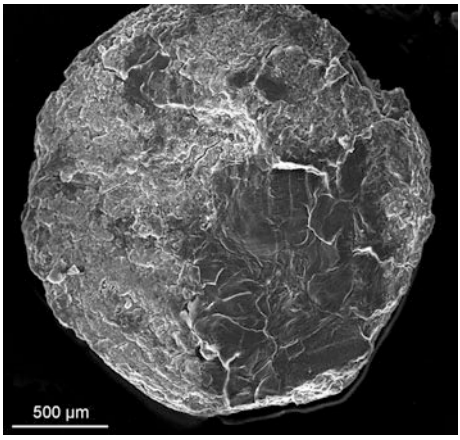

Fig. 4.41 Scanning electron microscope image of a pancake-shaped spherule from an upper Eocene section at Massignano, Italy. These spherules are often coated with Ni-rich spinel crystals (see Fig. 3.14). The spherule layer is associated with an Ir anomaly and shocked quartz with multiple sets of planar deformation features (see Fig. 4.42). The spherules are composed of an iron-rich clay (perhaps nontronite). They are interpreted to be diagenetically altered cpx spherules which have been flattened by the weight of the overburden

4.6.8 Nature of the Target Rock: Chemical Composition and Sr–Nd Isotopic Data

Langenhorst (1996) concluded that the characteristics of the shocked quartz found in the cpx spherule layer at Massignano, Italy, imply a nonporous, quartz-rich, near-surface rock as its source. However, the relative abundance of coesite compared with the abundance of shocked quartz in the cpx spherule layer in the northwestern Indian Ocean (ODP Site 709), indicates that the source rock was porous, i.e., probably sandstone (Liu et al. 2009).

Sr and Nd isotopic studies of the cpx spherules and associated microtektites from several sites indicate that they were derived from the same source rocks (Whitehead et al. 2000; Liu et al. 2006; Fig. 4.43a). The T_{UR} and T_{CHUR} model ages indicate that the cpx spherules and microtektites were formed from Proterozoic sedimentary deposits, mostly ranging in age between 0.9 and 1.5 Ga (T_{Sr}^{UR}), which were derived from source rocks, mostly ranging in age between 1.5 and 2.1 Ga (T_{Nd}^{CHUR}; Fig. 4.43b).

The wide range in major and trace element contents of the cpx spherules suggests that the target rock was heterogeneous. It must be kept in mind, however, that some of the variation in composition of the cpx spherules is due to a missing phase (or phases). In addition, there is evidence that many of the cpx spherules have a significant meteoritic component from the projectile (see Sect. 4.6.10). The light-colored cpx spherules have higher CaO and lower FeO contents than do the darker

Table 4.11 Iridium data for cpx spherule-bearing sites

Site/Hole	Location	Peak Ir (pg/g)	Ir fluence (ng/cm^2)
ODP Hole 1090B	Agulhas Ridge, S. Atlantic	1046	15
ODP Hole 699A	Georgia Rise, S. Atlantic	666	13
ODP Hole 689B	Maude Rise, S. Atlantic	156	2.5
ODP Hole 689D	Maude Rise, S. Atlantic	188	2.5
ODP Hole 709C	Mascarene Plateau, W. Indian Ocean	309	8.8
ODP Hole 738B	Kerguelen Plateau, S. Indian Ocean	157	1.2
Massignano	Italy	200	4.7
Gay's Cove	Barbados, Caribbean Sea	200	12
RC9-58	Venezuela Basin, Caribbean Sea	4100	42
DSDP Site 149	Caribbean Sea	>410	>4
DSDP Site 292	Equatorial Pacific	40	1.5
DSDP Site 315	Equatorial Pacific	250	7
DSDP Site 462	Equatorial Pacific	220	15
DSDP Site 612	Equatorial Pacific	104	0.6

Data from Liu et al. (2009)

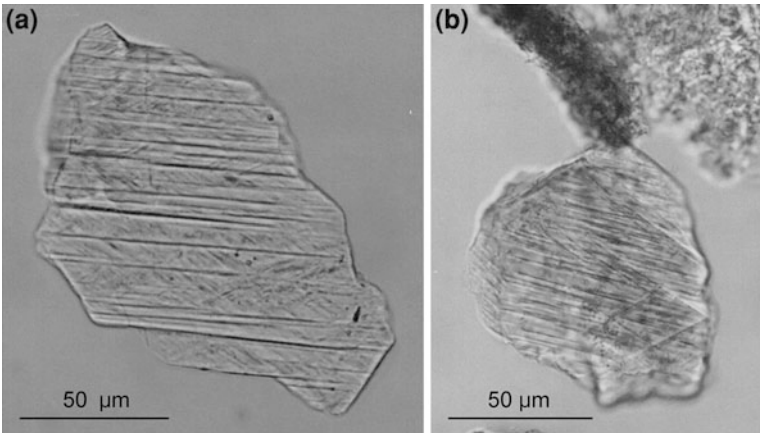

Fig. 4.42 Shocked-quartz grains from an upper Eocene section at Massignano, Italy. The shocked quartz is associated with an iridium anomaly and diagenetically altered cpx spherules containing and/or coated with Ni-rich spinel crystals (see Figs. 3.14 and 4.41)

cpx spherules. At ODP Site 786 in the northwestern Pacific the cpx spherules have CaO contents as high as 26 wt % (Liu et al. 2009). They also generally have higher MgO contents (up to 18 wt %), but the spherules with the higher MgO contents also have high Cr and Ni contents, which indicate a meteoritic component. If we only consider the spherules at this site with lower Ni and Cr contents, the MgO content is not quite as high, but still as high as ~14 wt %.

The composition of the source rocks for the low-CaO, dark cpx spherules was estimated by determining the average composition of the unetched to slightly

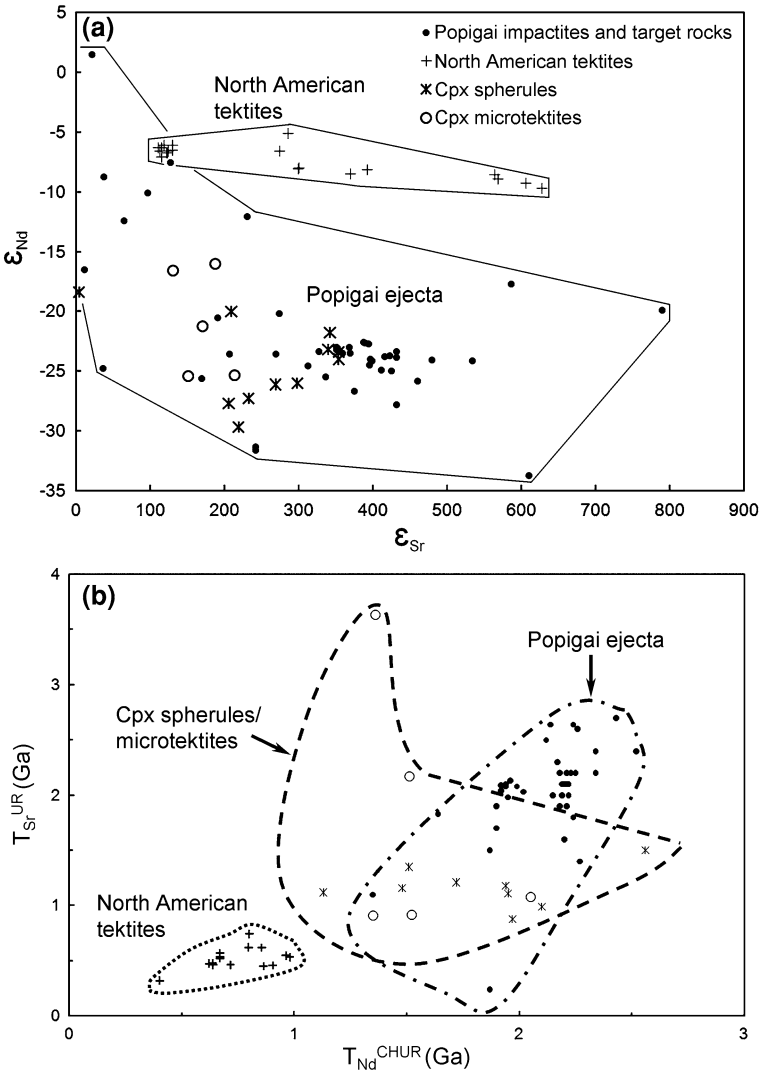

Fig. 4.43 Neodymium and Sr isotope data (**a**) and model ages (**b**) for cpx spherules and associated microtektites, Popigai impact crater impactites and target rocks, as well as, North American tektites. Cpx spherule data are from Whitehead et al. (2000) and Liu et al. (2006). Data for Popigai impactites and target rocks are from Hölker et al. (1997), Whitehead et al. (2000), and Kettrup et al. (2003). North American microtektite data are from Shaw and Wasserburg (1982), Ngo et al. (1985), Stecher et al. (1989), Glass et al. (1998), and Whitehead et al. (2000). **a** is modified after Liu et al. (2009), Fig. 8. **b** is modified after Liu (2006), Fig. 48

etched dark cpx spherules and using the average Ni content to correct for the supposed meteoritic component (see Sect. 4.6.10). This gave a composition of: 74 wt % SiO_2, 9.2 wt % Al_2O_3, 1.9 wt % FeO, 3.1 wt % MgO, 8.1 wt % CaO, 1.0 wt % Na_2O, 24 wt % K_2O, and 0.4 wt % TiO_2 (Glass et al. 2004b).

The low Al_2O_3 contents of both the dark- and light-colored spherules indicate that shale and graywacke can be ruled out as major source rocks for the cpx spherules. Arkoses and lithic arenites are possible source rocks. The high CaO and MgO contents of the light-colored cpx spherules suggest that some of the target rocks contained a carbonate component. The low SiO_2 contents of the cpx spherules indicate that quartz arenites were not a major source rock. However, the presence of silica-rich microtektites in the cpx spherule layer does suggest that a silica-rich rock, such as a quartz arenite, was at least a minor component of the target rock.

4.6.9 Popigai: The Source Crater

Several researchers have proposed that the 100-km-diameter **Popigai impact structure** in northern Siberia is the source of the cpx spherule layer (Langenhorst 1996; Poag 1997a; Vonhof and Smit 1999; Whitehead et al. 2000; Kettrup et al. 2003; Glass et al. 2004b; Liu et al. 2006). The main evidence in favor of this conclusion is the age, size, and Sr–Nd isotopic data. The Popigai impact crater has an ^{40}Ar-^{39}Ar age of 35.7 ± 0.8 Ma (Bottomley et al. 1997). Within the errors involved, this is the same age as the cpx spherule layer. Several late Eocene impact craters with similar ages are known, but Popigai is the largest and probably the only one large enough to spread ejecta around the globe. Furthermore, Sr and Nd isotopic data for the cpx spherules and associated microtektites fall within the range of values determined for Popigai impactites and target rocks (Fig. 4.43). In addition, the meteoritic component in the cpx spherules and microtektites appears to be the same as in Popigai impactites (see below) and the cpx spherule layer appears to show systematic changes with distance from Popigai (see Sect. 4.6.11).

4.6.10 Meteoritic Contamination and Projectile Identification

The cpx spherules have Cr, Ni, and Co contents ranging up to 3,250, 5,854, and 260 ppm, respectively, which are interpreted to indicate the presence of a meteoritic component (Glass et al. 2004b). Assuming that the source rock for the cpx spherules had close to the average Ni content of the upper continental crust, the high Ni contents imply a high percent contamination by the projectile, up to at least 50 wt % (depending on the composition of the projectile) for cpx spherules with the highest Ni contents. This would require much higher Ir and Au contents than were measured (Glass et al. 2004b). The low Ir and Au contents might be the result of fractionation of the meteoritic component prior to incorporation into the cpx spherules.

Compositional plots involving Cr, Ni, and Co exhibit a great deal of scatter, which is most likely due in part to the dissolution of a more soluble phase (or

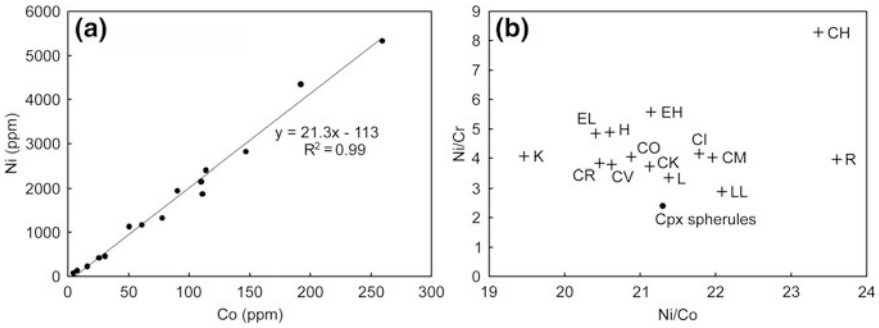

Fig. 4.44 Nickel versus Co (**a**) for relatively unaltered (i.e., no void regions where a soluble phase was removed by solution) cpx spherules and Ni/Cr versus Ni/Co (**b**) for relatively unaltered cpx spherules and various chondrite meteorite types. Note that the cpx spherules plot closer to the L chondrites than to other chondrite types. Cpx data are from Glass et al. (2004b) and meteorite data are from Lodders and Fegley (1998)

phases) in these spherules. The Ni contents of the cpx spherules and low-SiO_2 microtektites are positively correlated with FeO, MgO, Cr, and Co (Glass et al. 2004b). This correlation is best illustrated using only compositional data from cpx spherules which exhibit little or no evidence of dissolution as indicated by scanning electron microscopy. A plot of Ni versus Co contents for cpx spherules, that exhibit little or no dissolution, shows a strong positive correlation between these two elements (Fig. 4.44a). The slope of the correlation line ($\sim$21) is interpreted to indicate the Ni/Co ratio of the projectile (see Tagle and Hecht, 2006, for discussion of geochemical identification of projectile material in impactites). A similar plot of Ni versus Cr indicates a Ni/Cr ratio of 2.41. The Ni/Co and Ni/Cr ratios are closest to those of the L chondrites (Fig. 4.44b), suggesting that the projectile was an L chondrite.

The interpretation that the cpx spherules contain an L chondrite component is consistent with the identification of an ordinary chondrite, most likely an L chondrite, as the projectile that produced Popigai crater (Tagle and Claeys 2005). Initial Cr-isotopic measurements of a concentration of cpx spherules from ODP Site 709 in the northwestern Indian Ocean and a magnetic coarse fraction of the cpx spherule layer from Massignano, Italy, obtained ε^{53}Cr values of 0.39 $\pm$ 0.04 (2σ) and 0.26 $\pm$ 0.04 (2σ), respectively (Kyte et al. 2011). These values indicate a meteoritic component, and are consistent with an ordinary chondrite, but Kyte et al. (2011) favor an H chondrite because of an $\sim$35 Ma spike in cosmic-ray exposure ages for the H chondrites that indicates a major collision event in the asteroid belt at this time. Kyte et al. (2011) proposed that a large fragment from this collision could have produced the Popigai impact crater and dust from the impact may have produced an upper Eocene ^{3}He peak observed at Massignano, Italy (Farley et al. 1998; Farley 2009).

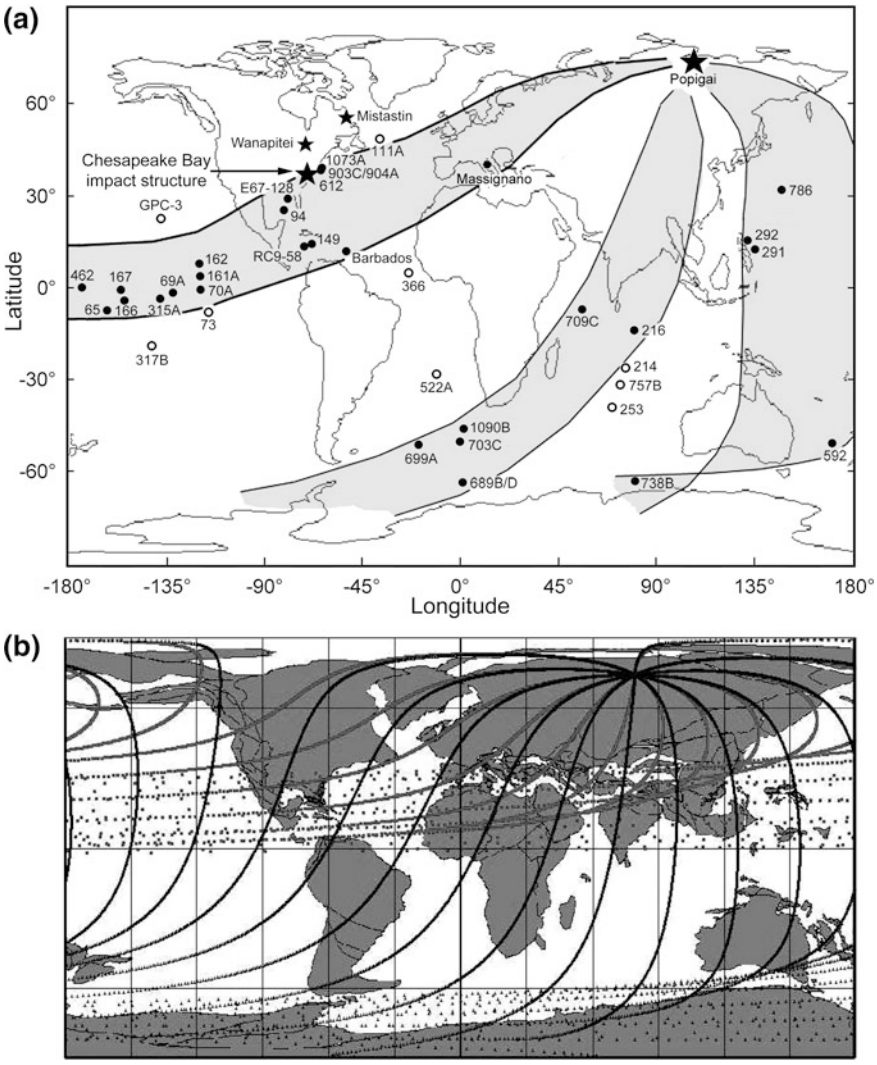

4.6.11 Geographic Variations Within and Ray-Like Nature of the Cpx Spherule Strewn Field

Liu et al. (2009) proposed that the cpx spherule strewn field may have a ray-like structure (Fig. 4.45a). Furthermore, they suggested that the rays appear to follow ejecta trajectories from Popigai as proposed by Wrobel and Schultz (2003) (Fig. 4.45b). Liu et al. (2009) proposed three rays: (1) a high angle ejecta ray that extends across Europe, the North Atlantic, through the Caribbean and Gulf of Mexico, and most of the way across the equatorial Pacific, (2) a nominal (45°)

◀ **Fig. 4.45** Geographic distribution of cpx spherules (**a**) and calculated trajectories for Popigai impact ejecta (**b**). **a** Presently available data can be interpreted as indicating that the cpx spherules fell along rays that originate from Popigai impact crater. *Black dots* indicate sites where the cpx spherule layer has been found (see also Fig. 4.40) and *open circles* indicate sites where cpx spherules were not found at what appears to be the appropriate stratigraphic level. Also shown in the figure are the locations of three other late Eocene impact structures. The Chesapeake Bay structure appears to be the source of the late Eocene North American tektites/microtektites. Wanapitei and Mistastin appear to be too small to be the source of the cpx spherules. **b** Calculated trajectories for Popigai impact ejecta. *Solid black lines* are low-angle (45°) ejecta trajectories and the *solid gray lines* are high-angle ejecta trajectories. Note that two of the rays in **a** (i.e., the ray that passes through the Indian Ocean and continues into the South Atlantic and the ray that goes down through the western Pacific) appear to follow low-angle trajectories and that one ray appears to follow high-angle trajectories through Europe, across the North Atlantic, and along the equatorial Pacific. **a** is modified after Liu et al. (2009), Fig. 3, with permission of the Geological Society of America; and **b** is from Wrobel (2008), Fig. 2

ejecta ray that extends through the western Indian Ocean and into the South Atlantic, and (3) a nominal ejecta ray that extends down through the western Pacific into the Indian Ocean sector of the Southern Ocean (Fig. 4.45a). Within the Indian Ocean/South Atlantic ray, the abundance of cpx spherules/microtektites decreases and the percent microtektites increases with distance from Popigai (Fig. 4.46). The western Pacific ray may show similar variations with distance from Popigai, but the data are not as reliable. Three of the closest sites to Popigai (Massignano and ODP/DSDP Sites 709 and 216 in the northern Indian Ocean) are the only sites where coesite and/or shocked quartz have been found in the cpx spherule layer.

The ray-like distribution pattern of the cpx spherules and variations in nature of the ejecta with distance from Popigai are consistent with the Popigai structure being the source crater for the cpx spherule layer.

4.6.12 Formation of Cpx Spherules

Ebel and Grossman (2005) concluded that the Ni-rich spinel-bearing spherules found in the Cretaceous-Tertiary (K-T) boundary layer were formed by condensation from the impact-generated vapor plume. By analogy, the cpx spherules were also probably produced by condensation from an impact-generated plume and would, therefore, be examples of condensate spherules as discussed in Sect. 3.2.1.1. The lack of vesicles and lechatelierite particles and the lack of teardrop, dumbbell, and disc shapes, seem to support such an origin. If so, this might have implications concerning the relationship between the compositions of the cpx spherules and the composition of the target rocks.

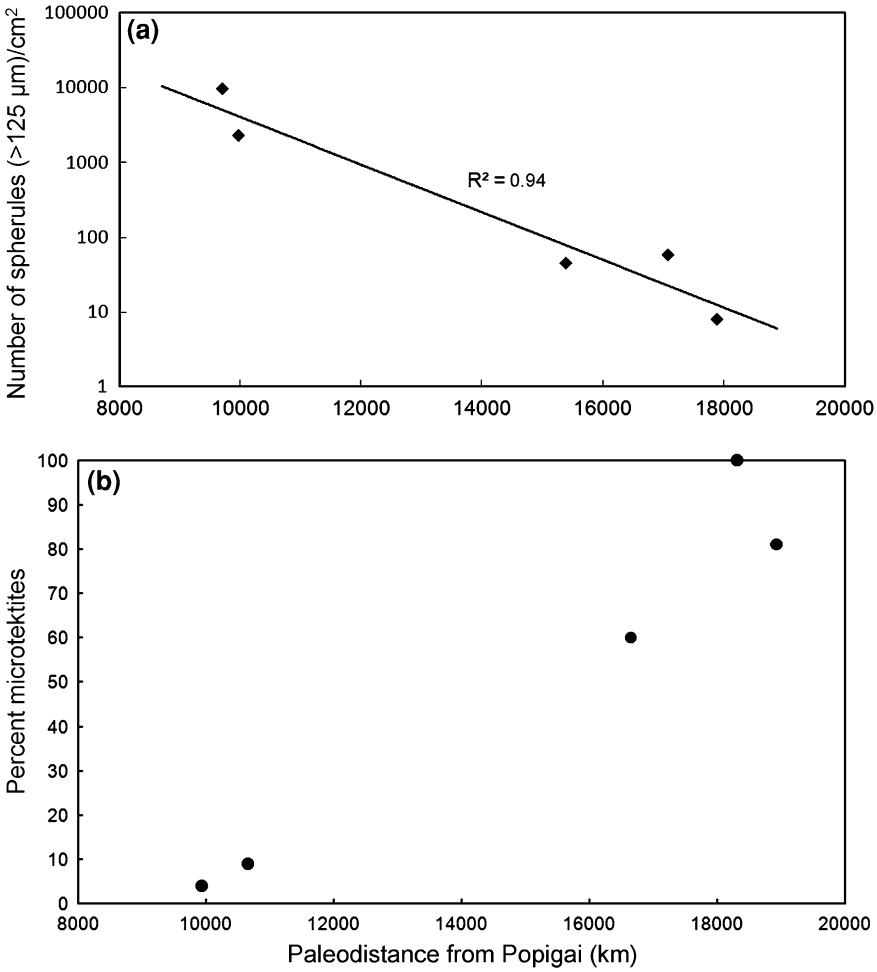

Fig. 4.46 Abundance of cpx spherules (**a**) and percent microtektites in the cpx spherule layer (**b**) versus paleodistance from Popigai along the proposed Indian Ocean/South Atlantic ray (see Fig. 4.45a). **a** Abundance is based on the number of cpx spherules >125 μm in size per cm^2 at each site. Paleodistance is based on plate reconstruction that indicates the location of the tectonic plates in the late Eocene, which is then used to estimate the distance between Popigai and each site at the time of the impact. **b** Percent abundance of microtektites in the cpx spherule layer is based on the number of microtektites in the cpx spherule layer at a given site versus the number of microtektites and cpx spherules. Data for these plots are from Liu et al. (2009)

4.6.13 Associated Climatic and Biological Changes

Alvarez et al. (1980) discovered an Ir anomaly at the K-T boundary which they attributed to a major impact event that may have been responsible for the mass extinction at the end of the Cretaceous Period ~65 Ma ago. Confirmation of an

impact event at the end of the Cretaceous Period was presented 4 years later when Bruce Bohor and colleagues announced the discovery of shocked quartz containing multiple sets of PDFs from the K-T boundary layer (Bohor et al. 1984). That same year, Raup and Sepkoski (1984) proposed that there have been periodic mass extinction events approximately every 26 Ma. They further stated that two of the mass extinction events, the terminal Cretaceous and late Eocene, have been linked to meteorite impacts. Later, Raup proposed a kill curve that related percent species extinction with the size of an impact as indicated by crater size (e.g., Raup 1992). According to Raup's impact-kill curve, a 100-km-diameter impact crater should correlate with the extinction of at least 50 % of the species. Poag (1997b) pointed out that the two large impacts during the late Eocene (i.e., the Popigai and Chesapeake Bay) are not associated with any apparent immediate extinction pulse. He proposed a revision of Raup's kill curve (see Sect. 11.3.2 for more detail) and suggested that the collective environmental effects of the two large late Eocene impacts may have either delayed the terminal Eocene-early Oligocene mass extinction event or produced the threshold conditions necessary for it to take place. Poag (1997b) pointed out that there is evidence of a warm pulse that briefly interrupted the Eocene–Oligocene cooling trend. He speculated that the warming pulse may have resulted from elevated CO_2 levels derived from degassing of carbonate target rocks as a result of one of the late Eocene impacts. However, more recent studies suggest that the cpx spherule layer may be closely associated with a sharp drop in surface water temperature (or increase in ice volume) and an increase in surface productivity.

Vonhof et al. (2000) interpreted oxygen- and carbon-isotope data across the cpx spherule layer at ODP Site 689 in the South Atlantic as indicating accelerated climatic cooling and an increase in surface-water productivity, respectively. A decrease of 0.4–0.5 ‰ in deep-water benthic foraminiferal $\delta^{13}C$ values was found to be coincident with the cpx spherule layer at three sites: DSDP Site 612 (NW Atlantic), Core RC9-58 (Caribbean Sea), and ODP Site 1090 (South Atlantic) (Pusz et al. 2009). However, Spezzaferri et al. (2002) interpreted changes in planktonic foraminiferal assemblages across the cpx spherule layer at Massignano, Italy, as indicating that cooling started immediately after the impact and was then interrupted by a warming episode due to a short-term, impact-induced, greenhouse episode. Liu et al. (2009) reported oxygen isotope data for ODP Site 738 in the southern Indian Ocean associated with the occurrence of glass spherules and an Ir anomaly, which they interpreted as indicating the cpx spherule layer (Fig. 4.47). The oxygen isotope data indicate a sharp drop in surface water temperature (or sharp increase in ice volume) coincident with the cpx spherule layer, similar to what was observed at Site 689 by Vonhof et al. (2000) in the South Atlantic. Neither Vonhof et al. (2000) nor Liu et al. (2009) reported evidence of a warming pulse following the cooling event. On the other hand, Pusz et al. (2009) state that their high-resolution bulk-carbonate and benthic foraminiferal $\delta^{18}O$ records for four sites (Core RC9-58, and DSDP/ODP Sites 612, 689 and 1090) show no global temperature change coincident with the cpx spherule layer.

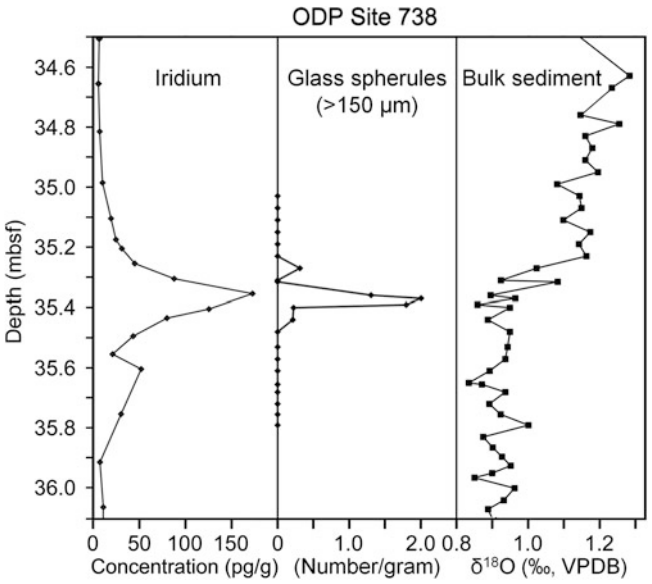

Fig. 4.47 Plot of $\delta^{18}O$, number of spherules per gram, and iridium concentration (pg/g) through a late Eocene section at Ocean Drilling Program Site 738 in the Indian Ocean sector of the Southern Ocean. No cpx spherules were observed at this site, but the biostratigraphy, Ir anomaly, and presence of glass spherules suggests that this layer is equivalent to the cpx spherule layer. Note the increase in $\delta^{18}O$ (going up section), which indicates a cooling event following the impact. *Mbsf* meters below sea floor and *VPDB* Vienna Pee Dee belemnite. Modified after Liu et al. (2009), Fig. 15

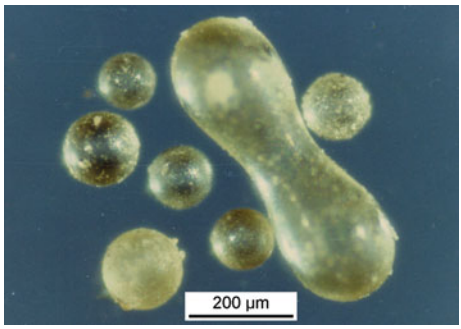

Fig. 4.48 Microtektites recovered from Core M14 taken in the North Pacific (8° 00.15′N, 176° 10.65′W). See Fig. 4.13 for core location and relationship to the Australasian strewn field. These microtektites have compositions similar to Australasian microtektites, but appear to be older. Courtesy of Hanchang Peng

4.7 Additional Probable Cenozoic Distal Ejecta Layers

Additional probable distal ejecta layers have been described. They are: (1) microtektites of Pleistocene age found in a single core from the North Pacific, (2) microtektites of Early Pliocene age recovered from the core catcher of a core taken on the Tasman Rise, and (3) a spherule bed of Paleocene age found in Nuussuaq on the western coast of Greenland. All of these spherule layers have been found in

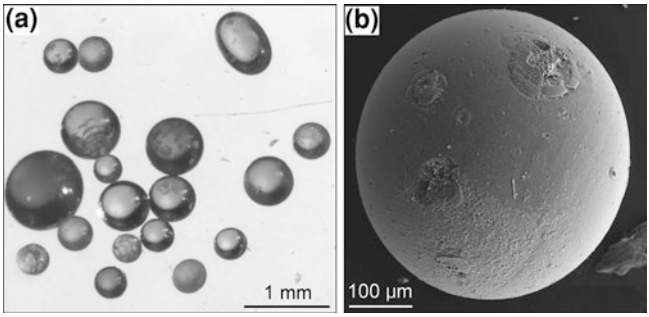

Fig. 4.49 Images of transparent green spherules found in the core catcher of Core 22X from Ocean Drilling Program Site 1169 on the Tasman Rise in the southeast Indian Ocean. **a** An optical microscope image of a group of spherules, showing that they are spheroids with shiny smooth surfaces. **b** A scanning electron microscope image of a Tasman Rise sphere showing what appear to be two or three high-velocity impact pits on the surface. **a** and **b** are courtesy of D. Clay Kelly (these images were published in Kelly and Elkins-Tanton, 2004, Figs. 3a and b, respectively)

only one location and no evidence of shock metamorphosed grains has been reported for any of these layers.

4.7.1 North Pacific Microtektites

Peng (1994) described glass spherules found in a core (M14) taken in the North Pacific (8° 00.15′ N, 176° 10.65′ W). The spherules are generally pale yellow-green. They are mostly spherical in shape, but dumbbell shapes also occur (Fig. 4.48). Most are ~200 µm in diameter and the largest has a diameter of ~340 µm. Their major oxide compositions are similar to the major oxide compositions of Australasian microtektites, except for their low Na_2O contents (0.11–0.18 wt %; Tables 4.5 and 4.12). Peng (1994) concluded that the glass spherules are microtektites. No petrographic data were given, but their appearance and major oxide compositions are consistent with this conclusion. Based on magnetostratigraphy and biostratigraphy, Peng (1994) concluded that this microtektite layer occurs at the Pliocene–Pleistocene boundary (2.14–2.30 Ma). Assuming that this is correct, the **North Pacific microtektites** must be ejecta from an older impact than the one which produced the Australasian tektites/microtektites. However, three lines of evidence suggest that they may belong to the Australasian tektite/microtektite strewn field: (1) proximity to the strewn field, (2) abundance of microtektites, and (3) similarity in composition between the North Pacific microtektites and the Australasian microtektites.

The M14 core site lies along an extension of the east–west lobe of the Australasian microtektite strewn field (Fig. 4.13). It is about 7,700 km from the proposed source area in Indochina (see, e.g., Glass and Koeberl 2006). At that

Table 4.12 Major oxide (wt %) and trace element (ppm) compositions of North Pacific microtektites, Tasman Rise microtektites, and Nuussuaq spherules

	North Pacific microtektites[a] (6)	Tasman Rise microtektites[b] (4)	Nuussuaq Spherules[c] (30)	
			Average	Standard deviation
SiO_2	68.49–70.54	56.43–60.61	48.6	0.3
TiO_2	1.06–1.34	0.71–0.81	1.1	0.1
Al_2O_3	15.89–18.95	17.40–19.97	14.3	0.2
Cr_2O_3	n.d.	n.d.	0.2	0.1
FeO	3.45–4.96	6.57–9.03	12.8	0.3
MnO	n.d.	0.12–0.14	<0.1	n.a.
MgO	2.33–3.62	4.81–8.35	6.4	0.3
CaO	1.93–5.06	5.01–5.81	8.1	0.1
Na_2O	0.11–0.18	0.85–1.09	2.0	0.5
K_2O	1.25–2.78	0.44–0.52	0.6	0.1
SO_3	n.d.	n.d.	0.3	0.1
Sc	13.3–27.9	29–34	28	4.1
Cr	84.3–225	152–512	1615	718
Co	<4.7–21.7	14–37	299	181
Ni	220–1380	n.d.	4269	2910
Rb	56.2–137	6–13	n.d.	
Sr	n.d.	420–520	n.d.	
Y	n.d.	19–21	n.d.	
Zr	n.d.	140–154	n.d.	
Nb	n.d.	5–6	n.d.	
Ba	n.d.	470–600	343	124
La	40.5–89.1	20–24	17.2	2.8
Ce	80.5–155	50–55	33.6	5.6
Nd	<61–97.9	24.8–29.5	17.4	2.3
Sm	6.15–13.7	5.1–6.2	3.9	0.6
Eu	<1.7–4.98	1.3–1.4	1.2	0.1
Yb	<0.9–5.24	1.8–2.9	2.6	0.4
Lu	0.62–1.53	0.2–0.4	0.25	0.04
Hf	<3.9–17.1	3.3–4.0	2.4	0.3
Ta	<1.6–1.8	0.4–0.5	n.d.	
Th	15.1–31.1	5.6–7.2	3.12	0.74
U	n.d.	0.0–0.8	0.66	0.30

Total iron reported as FeO; numbers in parentheses are number of analyses; *n.d.* no data

[a] H. Peng (personal communication, June 14, 1992)

[b] Kelly and Elkins-Tanton (2004)

[c] Trace element data are based on only 14 analyses. All iron originally reported as Fe_2O_3. Ir is 3.5 ± 1.7 ppb. Robin et al. (1996)

distance from the proposed source area at other sites within the Australasian microtektite strewn field the number of microtektites (>125 μm in size)/cm^2 is about 8 ± 7 (Fig. 4.14). Peng (1994) stated that the microtektites occur over a 30 cm interval and that the average number is 15 microtektites/100 g. This

suggests that the number of microtektites at this site is about 9/cm^2, which is in agreement with the number expected for this distance from the proposed Australasian strewn field source crater location (Fig. 4.14). The lower Na_2O contents of the North Pacific microtektites could be due to a greater degree of heating of microtektites which were thrown farther from the source crater, as has been suggested for the Transantarctic Mountain microtektites (see Sect. 4.2.8). Some of the North Pacific microtektites have high Ni, Co, and Ir contents compared with most Australasian microtektites; however, a group of Ni-rich Australasian microtektites has been identified (Glass et al. 2004b) which have Ni and Co contents that overlap the Ni and Co contents of the North Pacific microtektites.

Thus, it seems that there are a lot of coincidences or the age data are incorrect. In order to confirm that the North Pacific microtektites are part of an older strewn field and do not just represent an extension of the Australasian strewn field, it will be necessary to: (1) determine the abundance of the spherules (number/cm^2) more precisely, (2) describe the petrography of the spherules (e.g., do they contain lechatelierite particles?), and (3) determine their radiometric age and/or their stratigraphic age at other nearby sites.

4.7.2 Early Pliocene (4.6–12.1 Ma) Tasman Rise Microtektites

Forty-eight bottle-green glassy spherules were recovered from the core catcher of core 22x (202.14 m below the sea floor) at ODP Site 1169 along the western margin of the Tasman Rise in the southeastern Indian Ocean south of Tasmania (Kelly and Elkins-Tanton 2004). The spherules range in size from ~100 to 900 μm. They are generally spherical, but ellipsoidal forms were also recovered (Fig. 4.49a and b).

The surfaces are smooth and generally without pits or grooves, although one has what appear to be microimpact craters on its surface (Kelly and Elkins-Tanton 2004). The major oxide and trace element contents of four of the spherules indicate that the spherules have a small range in composition internally and from spherule to spherule (Table 4.12). Compared with most Cenozoic microtektites, the South Tasman Rise spherules have low SiO_2 (~56–60 wt %) and K_2O (~0.4–0.5 wt %) contents. Based on biostratigraphy, the age of the glass spherules appears to be late-middle Miocene to earliest Pliocene, ~4.6–12.1 Ma (Kelly and Elkins-Tanton 2004).

Based on the size, shape, and composition of the Tasman Rise glass spherules, their identification as microtektites seems reasonable. The apparent absence of lechatelierite particles makes this identification less certain, but the high-Mg, bottle-green Australasian microtektites also do not contain lechatelierite. The presence of what appear to be hypervelocity impact pits on one of the **Tasman Rise microtektites** is consistent with an impact origin and the homogeneity of the spherules and lack of any crystalline phases indicate that they must be distal ejecta.

Kelly and Elkins-Tanton (2004) point out that within the large uncertainty in the age of the Tasman Rise microtektites, they could be the same age as the HNa/K "australites" discussed below (Sect. 4.8.4). The composition of the Tasman Rise microtektites is similar in some respects to that of the HNa/K "australites," but there are a number of differences. The Tasman Rise microtektites have lower SiO_2, Na_2O, and K_2O and higher Al_2O_3, MgO, and TiO_2 and generally higher CaO and FeO contents compared to the HNa/K "australites" (Tables 4.12 and 4.13). However, with the exception of Na_2O, which is much too low, the HNa/K "australites" fall on or close to the extrapolated trends, major oxides versus SiO_2, of the Tasman Rise microtektites (Fig. 4.50). The low Na_2O content could be explained if the Tasman Rise microtektites were heated more intensely than the HNa/K "australites." This would explain the homogeneity of and lack of vesicles and lechatelierite particles in the Tasman Rise microtektites.

Before the Tasman Rise microtektites can be considered as belonging to a new strewn field or part of the HNa/K "australites," they need to be found at additional sites and their age needs to be better constrained, preferably by radiometric dating (e.g., using the ^{40}Ar-^{39}Ar method). Strontium and Nd isotopic studies also should be done.

4.7.3 Paleocene Nuussuaq Spherule Bed

Glassy spherules (Fig. 4.51a) have been found in several sandstone beds in the Abraham Member of the Agatdalen Formation in Nuussuaq on the western coast of Greenland (Margolis et al. 1991b). Volcanic deposits are common in this area. The **Nuussuaq spherules** are found in a 3-m-thick interval of dark green-gray marine shales and sandstones (Robin et al. 1996). They occur in 1–4 layers ranging in thickness from a few millimeters up to more than 10 cm (Jones et al. 2005a). They are abundant, nearly close-packed, and surrounded by delicate glass spherule fragments and altered glass (Jones et al. 2005a). The spherules can easily be seen in the field on weathered rock surfaces. The spherule-bearing Abraham Member at Nuussuaq has been correlated with the Asuk Member of the Vaigat Formation on Disko Island, which is ~50 km from Nuussuaq (Robin et al. 1996). The Asuk Member is highly unusual for its content of reduced iron (Nordenskiöld 1872); some of the blocks of Ni-Fe metal weigh up to several tons. The metal contains high contents of Ir and other siderophile elements (Klöck et al. 1986).

The Nuussuaq spherules are between 100 μm and 1 mm in diameter and mostly spherical, but a few are teardrop or dumbbell in shape (Robin et al. 1996). The glass spherules vary between colorless and light brown with yellow, gray, and reddish bands. Glass shards with irregular shape (some cuspate) and similar in size to the spherules are also relatively common. Microlites in the glass range from absent to abundant. Nearly all the spherules and glass shards contain vesicles ranging from 20 to 200 μm (Robin et al. 1996; Fig. 4.51a). Some of the vesicles are filled with secondary minerals (e.g., calcite, zeolite?). Many of the spherules

are partly altered to palagonite clay-like minerals and some are completely palagonatized (Jones et al. 2005a). Jones et al. (2005a) also described some carbonate spherules within the unaltered glass spherules. Some of these carbonate spherules appear to be completely enclosed within unfractured silicate glass and may be immiscible carbonate melts that were trapped as fine droplets within the silicate liquid (Jones et al. 2005a).

Flow banding, indicated by contorted brighter and darker zones and by trains of small inclusions (a few micrometers in diameter), is visible in back-scattered electron images. The inclusions are mostly spherical in shape, but octahedral and skeletal shapes were also observed. The inclusions are most abundant in the brown glass (which is Fe-rich) and they consist of iron oxide, iron sulphide (pyrite, pentlandite, chalcopyrite), and sometimes Ni-Fe metal (Robin et al. 1996). Inclusions of plagioclase, pyroxene, olivine, chromite, and spinel ($MgAl_2O_3$), some of which are partly dissolved in the glass matrix, have also been observed. Minute cruciform and skeletal Ni- and Cr-rich spinel crystals (Fig. 4.51b) with magnesioferrite compositions are also present (Margolis et al. 1991b). Some of the Ni-rich spinel crystals have almost pure native nickel at their centers (A.P. Jones, personal communication, 2009).

The average composition of the Nuussuaq spherules corresponds to that of a basalt or basaltic-andesite (Table 4.12). However, compared with basaltic glass the spherules are highly enriched in Fe, Ni, Cu, and Ir (Robin et al. 1996; Jones et al.2005a). Cobalt, Ni, Cu, and Ir contents are positively correlated with iron content (Robin et al. 1996). The spherules have a wide range in siderophile contents from one spherule to another and even within a given spherule (Robin et al. 1996).

Dinoflagellates from the Abraham Member place it in the NP5-6 Zone (Piasecki et al. 1992), which is approximately the Danian/Thanetian boundary (i.e., ~60 Ma). Nannofossil data and magnetostratigraphy indicate that the spherules fell close to the onset of the West Greenland flood lavas (~61–62 Ma ago; Jones et al. 2005a).

Margolis et al. (1991b) were the first to propose that the Nuussuaq spherules may have been produced by impact, based primarily on their exotic glass chemistry, presence of skeletal crystals of Ni- and Cr-rich magnesioferrite, and morphologies similar to tektites and to Cretaceous-Tertiary boundary spherules. In particular they suggested that the Nuussuaq spherules may have been produced by the impact of an extraterrestrial body into an active flood-basalt province. However, they also said that the Nuussuaq spherules might be due to an exotic type of volcanic eruption.

According to Robin et al. (1996) the high Cu content of the spherules and the nonmeteoritic Ir/Cu, Ir/Ni, and Ir/Co ratios of the spherules exclude a meteoritic origin for these elements. They state that the compositional characteristics of the spherules indicate a purely terrestrial origin, likely to be the result of contamination of a basaltic-andesitic melt with sulphide liquid formed by reduction of a magma which came into contact with carbon-bearing sediments. This mechanism was previously proposed to explain the Ni–Fe metal found on Disko Island.

Jones et al. (2005a) suggested that the Nuussuaq spherules should be reinterpreted as impact ejecta. Their main evidence is the presence of highly oxidized

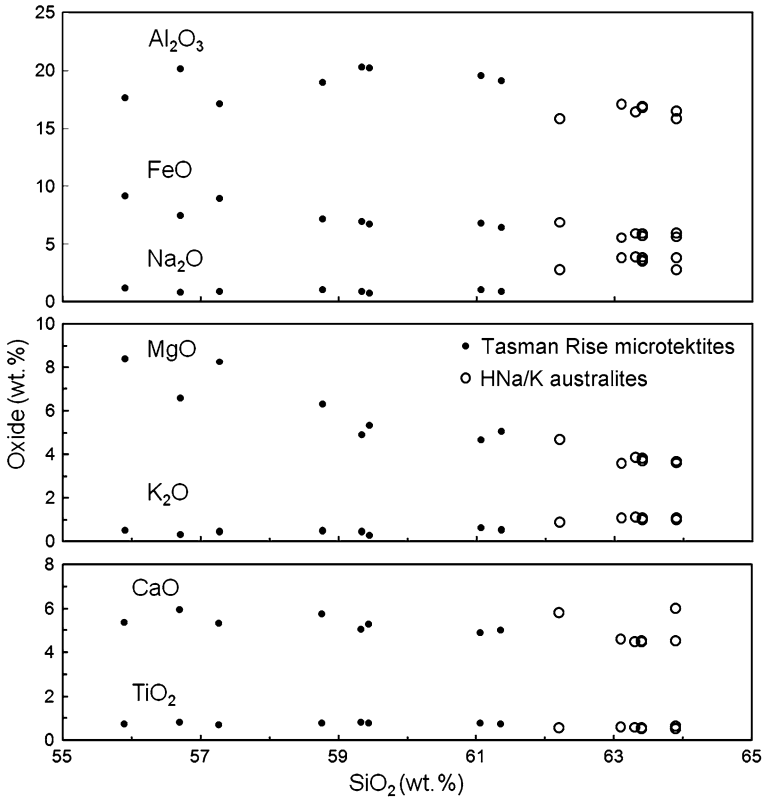

Fig. 4.50 Major oxides versus SiO_2 for Tasman Rise microtektites and HNa/K "australites." Note that with the possible exception of Na_2O, the Tasman Rise microtektites and HNa/K "australites" fall along the same or similar compositional trends. Data for the HNa/K "australites" are from Chapman and Scheiber (1969). Data for the Tasman Rise microtektites are from Kelly and Elkins-Tanton (2004)

Ni-rich spinel crystals in the spherules, which they state is a signature of meteorite impact. The Ni-rich spinel is comparable in morphology, size, and composition to Ni-rich spinel which has been found in some confirmed impact deposits. Jones et al. (2005a) described a few quartz grains that have unusual melt textures and anomalous isotropic and tartan-textured plagioclase that they believe is due to shock metamorphism; however, grains with diagnostic evidence of shock metamorphism have not been reported. French and Koeberl (2010) concluded, based on the texture, mineralogy, and chemistry of the Nuussuaq spherules (which they called Disko microspherules) presented by Jones et al. (2005a) and by the apparent differences between the Nuussuaq spherules and similar volcanic material, that the Nuussuaq spherules may have an impact origin. If the Nuussuaq spherules do have an impact origin, they may be examples of microkrystites produced as impact melt droplets (i.e., melt-drop microkrystites).

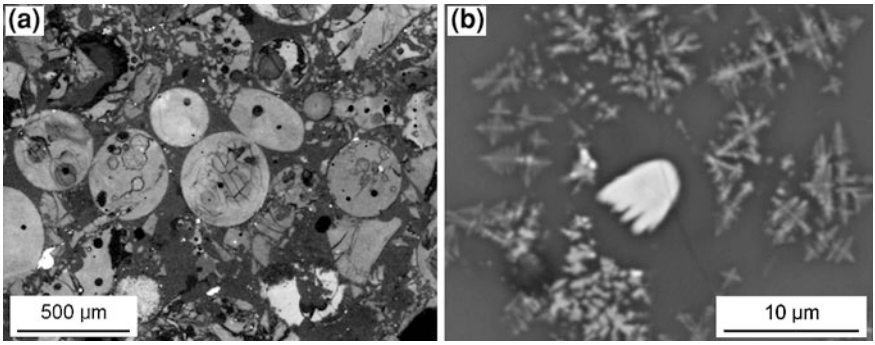

Fig. 4.51 Nuussuaq spherules from the Abraham Member of the Agatdalen Formation in Central Nuussuaq on the western coast of Greenland. **a** Group of spherules. **b** Scanning electron microscope image of a polished section of a Nuussuaq spherule showing numerous skeletal Ni-rich spinel crystals. Some of the Ni-rich spinels have almost pure native Ni at their centers. **a** is from Robin et al. (1996), Fig. 5a, with permission from Elsevier. **b** is courtesy of A. P. Jones

4.8 Distal Impact Glasses not Found in Stratigraphic Layers

Glasses believed to be of impact origin and ranging in age from ~0.8 to 24 Ma have been found at the Earth's surface in several different locations. These are: (1) Darwin glass found in Tasmania, (2) Libyan Desert Glass found in western Egypt, (3) tektites found at Tikal in Guatemala, (4) glasses (South-Ural glasses and urengoites) found in Siberia, and (5) high Na/K tektites found in Australia. All of these glasses are almost certainly impact glasses, but none have been found in stratigraphic context.

4.8.1 Guatemalan (Tikal) Tektites (0.8 Ma)

While sorting and classifying glass artifacts found during the excavation of Mayan ruins at Tikal, Guatemala, 11 glass bodies were separated, based on their shape, size (1.3–3 cm in longest dimension), and color (clear brownish-green), from the commonly found obsidian artifacts (Moholy-Nagy and Nelson 1990). Three of the glass bodies were studied and found to be free of phenocrysts, microlites, or schlieren (Essene et al. 1987; Hildebrand et al. 1994). However, spherical vesicles up to ~0.5 mm were observed.

The Tikal glasses are homogeneous, not only within a specimen, but from specimen to specimen (Essene et al. 1987). The major oxide composition closely resembles that of andesite (Table 4.13) with a SiO_2 content of ~63 wt % (Essene et al. 1987). However, the major oxide composition is also similar to that of the high-Na/K (HNa/K) "australites" (Table 4.13; see Sect. 4.8.4). In general, the

Table 4.13 Major oxide (wt %) and trace element (ppm) contents of Tikal tektites, South-Ural glass, urengoites, and high-Na/K "australites"

	Tikal tektites[a]	South-Ural glass[b] (1)	Urengoites[b] (3) Range	High Na/K "australites"[c] (8) Range
SiO_2	62.7	66.87	89.4–95.5	62.2–63.9
TiO_2	0.9	0.35	0.11–0.23	0.53–0.65
Al_2O_3	17.6	14.10	1.39–4.84	15.8–17.1
Cr_2O_3	n.d.	n.d	n.d.	n.d.
FeO	5.6	0.43	0.32–1.03	5.54–6.88
MnO	n.d.	0.02	<0.04–0.04	n.d.
MgO	1.8	3.75	0.69–1.38	3.57–4.68
NiO	n.d	n.d	n.d.	n.d.
CaO	5.1	12.08	1.00–2.50	4.49–6.00
Na_2O	3.7	1.96	0.04–0.16	2.75–3.91
K_2O	1.8	0.25	0.35–1.08	0.90–1.12
Sc	n.d.	n.d.	n.d.	n.d.
Cr	n.d.	n.d.	n.d.	220–385
Co	n.d.	n.d.	n.d.	41–68
Ni	n.d.	n.d.	n.d.	630–875
Y	n.d.	8.1	0.98–7.23	<15–18
Zr	n.d.	n.d.	n.d.	130–170
Ba	n.d.	64	26–209	300–395
La	n.d.	25.5	9.5–16.2	n.d.
Ce	n.d.	49.3	33.03–24.70	n.d.
Pr	n.d.	5.30	2.10–3.62	n.d.
Nd	n.d.	18.12	7.95–13.26	n.d.
Sm	n.d.	3.26	1.38–2.29	n.d.
Eu	n.d.	0.72	0.35–0.57	n.d.
Gd	n.d.	2.94	1.49–2.84	n.d.
Tb	n.d.	0.33	0.21–0.32	n.d.
Dy	n.d.	1.73	1.10–1.61	n.d.
Ho	n.d.	0.40	0.27–0.37	n.d.
Er	n.d.	0.92	0.72–0.94	n.d.
Tm	n.d.	0.11	0.10–0.14	n.d.
Yb	n.d.	1.01	0.84–1.05	n.d.
Lu	n.d.	0.12	0.12–0.14	n.d.

Number in parentheses is number of analyses. All iron given as FeO
[a] Essene et al. (1987)
[b] Deutsch et al. (1997)
[c] Chapman and Scheiber (1969)

lithophile-incompatible elements are low relative to their abundances in tektites from the four major Cenozoic tektite strewn fields; however, an upper crustal affinity is evident (Hildebrand et al. 1994). The water content was found to range from 0.006 to 0.008 wt %, which is within the range of water contents of tektites (Beran and Koeberl 1997). The magnetic properties are similar to those of Muong Nong-type tektites (Senftle et al. 2000).

The petrography and composition are consistent with the Tikal glass objects being tektites; however, lechatelierite was apparently not observed. It is assumed that the **Tikal tektites** were originally collected from unknown locations and transported by the Mayans to the city of Tikal. The age of these glasses has been determined by ^{40}Ar-^{39}Ar dating, but the experimental error is quite large (i.e., 800 ± 100 ka; Hildebrand et al. 1994). The age and composition appear to rule out association with any known tektite strewn field, but additional studies are needed.

4.8.2 Darwin Glass

Dawin glass (Fig. 4.52a) is an impact glass found in western Tasmania. It was traded by Tasmanian aborigines thousands of years before its discovery by Europeans in the middle of the 1800s (Storey 1987). The glass occurs as irregular fragments, twisted masses, or chunks up to 10 cm in size. The color ranges from white, translucent pale green, dark green, dark brown, gray, to black. The glasses are generally vesicular and often exhibit flow structure marked by bands of elliptical vesicles. Spherical bubbles and elliptical bubbles are about equally abundant (Barnes 1967). Some specimens of Darwin glass have a frothy appearance.

Splash-form Darwin glasses (mini Darwin glasses), <5 mm in size (Fig. 4.52b), have also been found scattered across the Darwin glass strewn field (Howard 2008). The splash forms consist of spheres and rotational forms such as teardrops and dumbbells. They range in color from transparent pale yellow, to translucent yellow–brown, to opaque dark brown. Their surfaces are rough due to pitting.

Darwin glass contains bubbly to frothy lechatelierite particles (Barnes 1967). Spencer (1933) reported finding metallic spherules in Darwin glass, but this has not been confirmed by later studies (O'Keefe 1976). Coesite and tourmaline were discovered in Darwin glass (Reid and Cohen 1962). The presence of lechatelierite and coesite confirms the impact origin of these glasses, while the presence of tourmaline suggests the material that was melted to produce the glass must have been terrestrial.

Darwin glass is silica rich; the silica content averages approximately 84–89 wt % (Table 4.14; Meisel et al. 1990). The splash-form, mini Darwin glasses have compositions similar to those of the larger Darwin glasses (Table 4.14). The major and trace element compositions indicate that these glasses were probably derived from terrestrial sediments similar to an argillaceous sandstone (Taylor and Solomon 1964). Some of the Darwin glasses are enriched in Cr, Co, and Ni, which is suggestive of meteoritic contamination (Meisel et al. 1990; Howard 2008). The Ir content is too low to indicate a meteoritic component (Meisel et al. 1990), but there may have been some fractionation of the siderophile elements.

Darwin glass is found associated with quartzite rubble and in many places underlies 9–18 cm of peat formed in glacial times (Barnes 1963). It has been

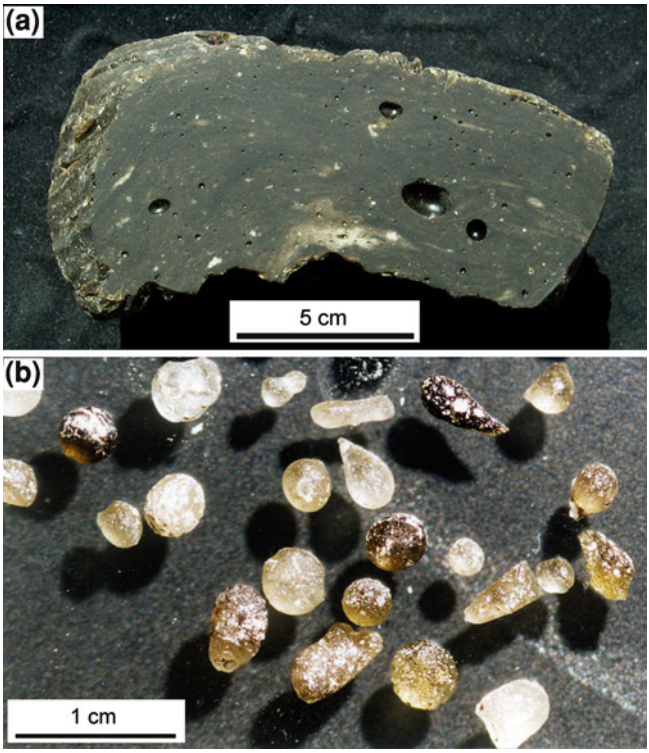

Fig. 4.52 Darwin glass. **a** Polished interior section of Darwin glass showing a few large (mostly elongate) vesicles. Variations in color and alignment of the long axes of the large vesicles indicate internal layering probably due to flow of the melt prior to solidification. **b** Mini Darwin glass or splash forms. Note that most are spherical, but elongate forms such as teardrops and dumbbells are common. Most are translucent *pale yellow–brown* to *brown*, but some are opaque *white* or *dark brown*. All show evidence of solution etching. Courtesy of Kieren T. Howard

proposed that the glass formed during a period of Pleistocene glaciation (Barnes 1963). Laser fusion ^{40}Ar-^{39}Ar ages indicate that the Darwin glass has an age of $\sim$816 $\pm$ 7 ka (i.e., mid-Pleistocene; Lo et al. 2002), which is similar to the age of the Australasian tektites, particularly the age of 803 $\pm$ 3 ka reported by Yamei et al. (2000). The similarity in age between the Australasian tektites and Darwin glass is intriguing. It may be a coincidence or it may indicate the breakup of the projectile and the simultaneous formation of at least two craters and associated strewn fields (Gentner et al. 1969; Lo et al. 2002).

Darwin crater has been suggested as the source of Darwin glass (Ford 1972; Fudali and Ford 1979; Howard and Haines 2007; Howard 2008). The crater is $\sim$1.2 km in diameter and is located at the southeast edge of the Darwin glass strewn field. As of 2011, no conclusive evidence of shock metamorphism has been found in the crater (Howard and Haines 2007; Howard 2008) and its impact origin, therefore, remains unconfirmed. However, the compositions (major and trace

Table 4.14 Major oxide (wt %) and trace element (ppm) compositions of Darwin glass and Libyan Desert Glass

	Darwin glass				Libyan Desert	
	Macro[a] (18)		Mini[b] (78)		Glass[c] (11)	
	Range	Average	Range	Average	Average	Standard deviation
SiO_2	84.0–89.3	86.1	75.2–93.2	84.4	98.37	0.89
TiO_2	0.52–0.62	0.56	0.13–0.70	0.56	0.12	0.06
Al_2O_3	5.79–8.47	7.25	1.98–10.7	7.37	1.19	0.69
FeO	1.06–3.78	2.51	0.74–6.20	2.87	0.12	0.09
MgO	0.61–2.51	0.85	0.19–3.67	1.56	0.01	0.00
CaO	0.03–0.23	0.09	0.00–0.22	0.09	0.01	0.00
Na_2O	0.02–0.06	0.04	0.02–0.19	0.08	0.005	0.001
K_2O	1.51–2.93	2.04	0.61–2.40	1.71	0.009	0.003
Sc	6.0–8.1	7.1	3.9–9.8	6.8	0.79	0.42
Cr	48–522	86	39.4–372	120	5.74	2.64
Mn	32–282	44	n.d.		13.2	3.62
Co	4.6–39.0	11	4.2–59.7	20.4	0.26	0.14
Ni	30–536	120	35–842	246	2.5	2.0
Ga	3–9	5	n.d.	n.d.	1.1	0.5
Rb	71–137	95	35–118	68	0.46	0.12
Sr	n.d.	n.d.	7.9–24.3	14.8	24	7
Zr	254–547	397	181–920	417	196	47
Nb	n.d.	n.d.	6.0–14.6	11.2	n.d.	
Sb	0.2–0.6	0.4	n.d.	n.d.	0.09	0.03
Cs	2.5–4.5	3.3	1.6–6.7	3.3	0.09	0.06
Ba	182–450	291	167–385	293	37.09	12.87
La	35.0–46.5	40.3	17.1–45.5	35.1	6.91	1.99
Ce	70.0–97.8	87.7	41.2–105	78.3	15.11	4.26
Nd	29–42	34.7	16.1–43.4	32.2	6.01	2.07
Sm	6.6–9.0	7.7	3.4–8.6	6.7	1.06	0.35
Eu	0.9–1.5	1.3	0.7–1.8	1.3	0.17	0.07
Yb	2.7–4.5	3.8	1.3–4.4	3.1	0.53	0.16
Lu	0.5–0.8	0.6	0.1–0.6	0.5	0.07	0.02
Hf	11–20	15	n.d.	n.d.	4.30	1.10
Ta	1.1–1.6	1.3	n.d.	n.d.	0.28	0.13
Th	12–19	16.3	6.6–19	14	2.59	0.83
U	1.9–5.4	2.8	0.4–3.6	1.5	0.96	0.28

Numbers in parentheses are number of analyses. All iron given as FeO

[a] Meisel et al. (1990)

[b] Howard (2008). Mini Darwin glass refers to splash forms <5 mm in size

[c] Koeberl (1997)

elements) of the Darwin glasses can be produced from a mixture of the target rocks at Darwin crater (Meisel et al. 1990; Howard and Haines 2007; Howard 2008). Furthermore, Sr and Nd isotopic data are consistent with Darwin crater being the source crater (Howard 2008), and glasses found in the crater have ages similar to the age of the Darwin glass (Gentner et al. 1973).

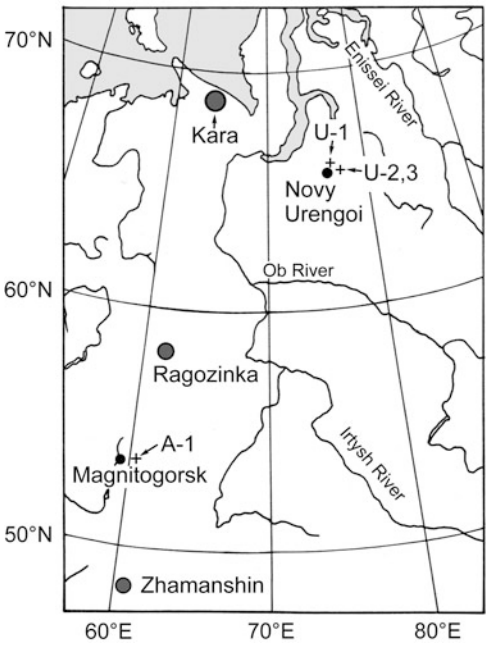

Fig. 4.53 Map of western Siberia showing where the urengoites and South-Ural glass were found. Kara, Ragozinka, and Zhamanshin are impact craters with ages of ~70 Ma, 55 ± 5 Ma, and 0.9 ± 0.1 Ma, respectively. After Deutsch et al. (1997), Fig. 1, with permission of Meteoritic & Planetary Science

4.8.3 South-Ural Glass

Koroteev et al. (1994) reported finding a tektite-like object in a placer deposit (Astaf Evskaya) in the Southern Urals near Magnitogorsk (Fig. 4.53). This specimen (A-1) is rounded, weighs ~90 g, and is pale green. It has a flow texture with small vesicles (Koroteev et al. 1994). The **South-Ural glass** contains ~67 wt % SiO_2, ~14 wt % Al_2O_3 and it has low iron (0.4 wt % total iron reported as FeO) and low K_2O (0.25 wt %) and unusually high CaO (~12 wt %; Table 4.13). The major oxide composition and the steeply negative CI-normalized REE distribution pattern indicate sediments of crustal origin as a precursor (Deutsch et al. 1997). Like tektites, the South-Ural glass has a low water content (< <0.09 wt %) and the iron is highly reduced (Koroteev et al. 1994). The South-Ural glass appears to be a tektite. It has an age of 6.2 ± 0.3 Ma, based on K–Ar dating (Koroteev et al. 1994). The age and composition indicate that it is not part of any previously known tektite strewn field.

4.8.4 High Na/K "Australites"

Chapman and Scheiber (1969) identified a group of australites from four different locations in Australia which have lower SiO_2 (~63 wt %) and higher Na_2O and

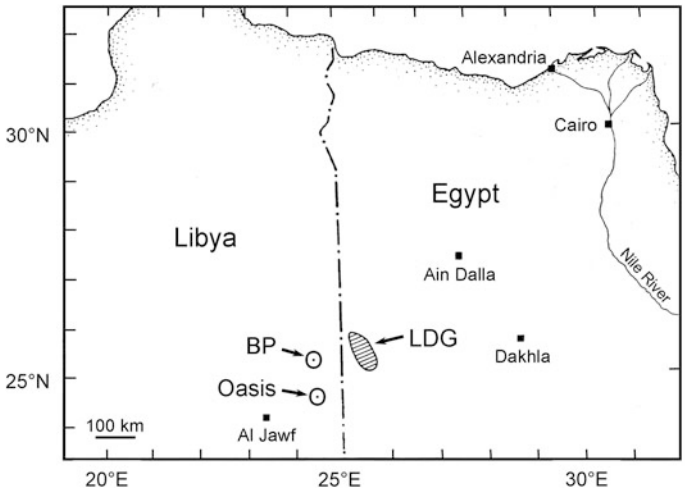

Fig. 4.54 Location of the Libyan Desert Glass (LDG) strewn field and the BP and Oasis craters. Modified after Koeberl (1997), Fig. 1

lower K_2O contents, and, thus, higher Na/K ratios than other australites or Australasian tektites (Tables 4.3 and 4.13). Their oxygen isotopic (Taylor and Epstein 1969) and strontium isotopic (Compston and Chapman 1969) compositions also clearly distinguish them from other australites. Like other tektites, the high Na/K (or HNa/K) tektites contain lechatelierite particles and exhibit flow structures (Chapman and Scheiber 1969). Earlier fission-track dating of the HNa/K "australites" gave an age of ~3–4 Ma and indicated that the HNa/K "australites" are older than the other australites. Storzer (1985) obtained a mean fission-track age of 8.35 ± 0.90 Ma for three HNa/K "australite" specimens and Storzer and Müller-Sohnius (1986) obtained a mean K–Ar age of 11.0 ± 0.7 Ma for the same three specimens. More recent ^{40}Ar-^{39}Ar dating indicates an age of 10.2 ± 0.5 Ma for the HNa/K "australites" (Bottomley and Koeberl 1999). It is clear that the HNa/K "australites" were formed in an older impact event than were the other australites and Australasian tektites. Within the quoted errors, the Tasman Rise microtektites have the same age as the HNa/K "australites" and may, therefore, belong to the same strewn field; however, additional studies are required (see Sect. 4.7.2).

4.8.5 Libyan Desert Glass

In 1932, during a routine survey of the Libyan Desert in western Egypt, P. A. Clayton found masses of silica glass strewn across the exposed surface of sandstone bedrock in the linear corridors between large N–S trending seif dunes (Clayton and Spencer 1934). The glass is found over an oval area ~130 km long

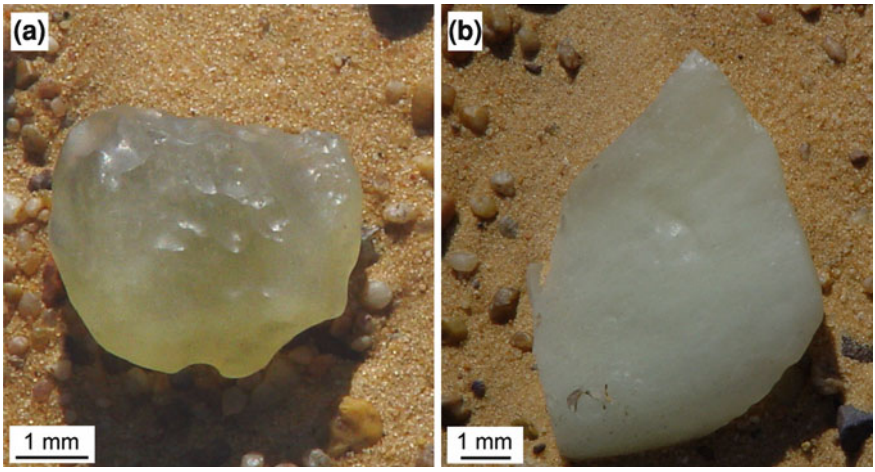

Fig. 4.55 Photographs of Libyan Desert Glass specimens in field where they were found. **a** Translucent pale yellow specimen. **b** Opaque white specimen. Courtesy of Christian Koeberl

by 50 km wide ($\sim$6500 km^2) (Fig. 4.54). In a 1981 expedition, it was estimated that the total mass of glass in the strewn field exceeds 1.4×10^9 g and that the original mass may have been 10,000 times greater (i.e., $>1.4 \times 10^{13}$ g or 14 million metric tons) (Weeks et al. 1984).

Libyan Desert Glass (Fig. 4.55) ranges in size from 30 cm down to <1 cm. The largest known piece weighs 26 kg (Diemer 1997). Most are transparent to translucent. They exhibit a range in color from almost colorless, to pale yellow, pale yellow-green, and gray. Some are milky white and almost opaque. A few contain dark brown layers or schlieren, and vesicles. In some cases the schlieren produce a layered appearance, probably due to flow. Vesicles often have an elongated shape parallel to the layering. The exposed surfaces are lustrous with a smooth polish, but the buried surfaces are dull, finely-textured, and rough, probably due to solution etching by water. Some of the pieces show evidence of working by prehistoric man.

Lechatelierite particles are abundant in Libyan Desert Glass (Barnes 1967). White spherulitic inclusions, observed in many specimens, have been identified as cristobalite (Kleinmann 1969; Barnes and Underwood 1976; Greshake et al. 2010). One possible tourmaline inclusion has also been reported (Barnes and Underwood 1976). Zircons that have partially decomposed to baddeleyite plus silica glass have been identified in some specimens (Kleinmann 1969; Storzer and Koeberl 1991). Rutile and decomposition products of titanomagnetite (Kleinmann 1969) and low-Ca, Al-rich orthopyroxene inclusions (Greshake et al. 2010) have also been identified in Libyan Desert Glass.

Libyan Desert Glass is extremely silica rich; the SiO_2 content generally varies between $\sim$97 and 99 wt %, with an average of $\sim$98 wt % (Table 4.14; Barnes and Underwood 1976; Fudali 1981; Koeberl 1997). Most lithophile major and

trace element contents vary inversely with the silica content and the rare earth element abundance pattern is typical of upper continental crustal rocks (Koeberl 1997). However, Co, Ni, and Ir are significantly enriched in the rare dark streaks or bands that occur in some Libyan Desert Glass specimens (Rocchia et al. 1997; Murali et al. 1989; Koeberl 1997). In addition, Ni content is positively correlated with the Fe and Mg contents. The enrichments in Co, Ni, and Ir contents and positive correlation with Fe and Mg content indicate the presence of a meteoritic component. Murali et al. (1997) suggested that the siderophile element ratios in the dark streaks indicate that the meteoritic component is chondritic. Barrat et al. (1997) found significant PGE concentrations in the dark streaks. The CI chondrite normalized PGE pattern indicates the presence of a chondritic component. Re–Os isotopic data for the dark bands confirms the presence of a meteoritic component (Koeberl 2000).

Lechatelierite together with cristobalite indicate that the quartz-dominated source rock was quickly heated to at least 1,550 °C. Rapid quenching of SiO_2 melt resulted in the crystallization of β-cristobalite, which reverted to α-cristobalite (Greshake et al. 2010). The breakdown of zircons to baddeleyite plus SiO_2 indicates that the glass experienced temperatures in excess of 1,676 °C. Thus, the petrography of the Libyan Desert Glass indicates that the glass was formed by melting and rapid quenching of a quartz-rich source rock during a hypervelocity impact.

Attempts to date the Libyan Desert Glass by K–Ar have failed (e.g., Zähringer 1963; Horn et al. 1997); however, the glasses have been dated using the fission-track method. Corrected fission-track ages for Libyan Desert Glass range from 28 to 29.5 Ma (e.g., Gentner et al. 1969; Storzer and Wagner 1977; Bigazzi and de Michele 1997; Horn et al. 1997).

Although petrographic and chemical data support an impact origin for the Libyan Desert Glass, no source crater has been confirmed. Two impact structures have been proposed as possible source craters: (1) the 3.2-km-diameter BP structure and (2) the 18-km-diameter Oasis impact structure (Martin 1969; Underwood and Fisk 1980; Murali et al. 1988; Koeberl 1997). These impact structures are $\sim$150 km west to southwest of the Libyan Desert Glass strewn field (Fig. 4.54). Petrographic and geochemical data indicate that the target rocks at both structures could be the parent material for the Libyan Desert Glass (Abate et al. 1999); however, Sr and Nd isotopic studies indicate that the Nubian rocks found at these craters are not a possible precursor for the Libyan Desert Glass (Schaaf and Müller-Sohnius 2002). Furthermore, the ages of these structures are not known well enough to determine if either could be the source crater.

Some researchers have proposed that Libyan Desert Glass was formed more locally. Indeed, sandstones from the Libyan Desert Glass strewn field exhibit evidence of shock metamorphism including undulatory extinction, mosaicism, partial isotropization, and multiple sets of planar deformation features (e.g., Kleinmann et al. 2001); however, no evidence of an impact crater has been found in this area. Wasson (2003) and Boslough and Crawford (2008) have proposed that the Libyan Desert Glass was formed by radiative melting from a low-altitude

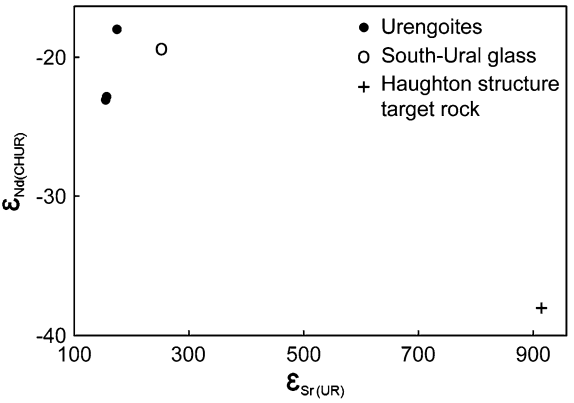

Fig. 4.56 Plot of ε_{Nd} versus ε_{Sr} values for urengoites, South-Ural glass, and Haughton crater target rocks. Neodymium and Sr isotope data support the hypothesis that the urengoites belong to a single strewn field. In addition, the Nd and Sr isotope data suggest that neither the urengoites nor South-Ural glass were derived from the Haughton impact structure. Data are from Deutsch et al. (1997)

airburst. However, a more recent oxygen isotope study of the Libyan Desert Glass and underlying sands and sandstones does not support this hypothesis. The $\delta^{18}O$ values measured for 25 Libyan Desert Glass specimens range from 9.0 to 11.9 ‰ (Vienna Standard Mean Ocean Water) and are clearly different from the sands and sandstone found in the same area which have $\delta^{18}O$ values ranging from 12.6 to 19.5 ‰ (Longinelli et al. 2011). Thus, the underlying sands and sandstones could not have been melted to form the Libyan Desert Glass. On the other hand, quartz grains separated from the underlying sands do have $\delta^{18}O$ values compatible with the Libyan Desert Glass values suggesting that the modern surface sand inherited quartz from the target rock. If the Libyan Desert Glass were formed locally, as suggested by some studies, then it is probably not distal ejecta.

4.8.6 Urengoites

Three glass bodies (U-1, U-2, U-3) were recovered from Late Pleistocene sandy fluvioglacial deposits in the northern part of West Siberia near Novy Urengoi (66° 07′ N, 78° 57′ E; Fig. 4.53; Masaitis et al. 1988; Deutsch et al. 1997). The largest specimen measured 3.5 × 2.7 × 1.6 cm and weighed 19.35 g. The other two smaller samples were found about 40 km from the largest specimen. The glasses are pale green to bottle-green in color and they exhibit flow structure. The larger sample contains vesicles up to 5 mm in diameter and lechatelierite (Masaitis et al. 1988). The glasses are silica rich with SiO_2 contents between ~89 and 96 wt % (Table 4.13; Deutsch et al. 1997). The average REE distribution patterns match that of the average upper crust (Deutsch et al. 1997). The iron in the glass appears to be highly reduced; all three contain only ferrous iron (Masaitis et al. 1988). The water content is quite low (0.008–0.024 wt %) and in the range observed for tektites (Beran and Koeberl 1997). Thus, these glasses are impact glasses with characteristics similar to those of known tektites, except for the very high silica contents. Masaitis et al. (1988) named the glasses **urengoites**.

The urengoites have a mean age of 23.6 ± 1.6 (2σ) Ma based on fission-track and K–Ar dating (Komarov et al. 1991; Koroteev et al. 1994; Deutsch et al. 1997). Rubidium-strontium and Sm–Nd systematics of the urengoites indicate that the precursor material was heterogeneous and was derived from Paleoproterozoic continental crust which underwent Rb/Sr fractionation and partial Sr homogenization in Jurassic time (Deutsch et al. 1997).

The age of the urengoites is, within errors, indistinguishable from the age of the ~24 km diameter Haughton impact structure in northern Canada, which has an age of ~23 Ma based on ^{40}Ar-^{39}Ar and fission-track dating (Jessberger 1988; Omar et al. 1987). However, the distinct difference in Nd–Sr isotope parameters between urengonites and Haughton impact structure target material (e.g., see Fig. 4.56) indicates that the Haughton impact structure is not likely to be the source crater for the urengoites.

4.9 Other Proposed Cenozoic Distal Ejecta Layers

Three other ejecta layers have been proposed: (1) the Younger Dryas "impact" layer, (2) a Late Pliocene "ejecta" layer in the Ross Sea near Antarctica, and (3) the Paleocene-Eocene event layer. No convincing evidence for an impact origin has been given for any of these layers.

4.9.1 Younger Dryas "Impact" Layer

Firestone et al. (2007) have proposed that ~12.9 ka ago one or more low-density extraterrestrial objects (probably comets) exploded over North America, partially destabilizing the Laurentide Ice Sheet and triggering the Younger Dryas cooling event, which in turn contributed to extinctions of Pleistocene megafauna and the termination of the Clovis culture. The authors also proposed that the impact event triggered wildfires, which caused continent-wide burning of the biomass. More recently, Marlon et al. (2009) used charcoal and pollen data from 35 sites to assess how fire regimes in North America changed through the last glacial-interglacial transition and concluded that their data did not support continent-wide wildfires at 12.9 ka ago.

According to Firestone et al. (2007), evidence for this Younger Dryas event is found just below a carbon-rich black layer ("black mat"), dating to ~12.9 ka. The "black mat," which was previously found at numerous Clovis-age sites across North America, appears to be contemporaneous with the abrupt onset of the Younger Dryas cooling. The evidence for impact includes: an Ir anomaly, magnetic spherules, fullerenes containing ^{3}He, and nanodiamonds. The Ir anomaly was found in the bulk sediment from just below the Younger Dryas boundary at five of these 12 sites. The peak abundance of Ir ranges from 0.5 up to 3.75 ppb (near the

detection limit of the method used; Firestone et al. 2007). The authors also reported that the Younger Dryas boundary is modestly enriched in Ni; however, there does not appear to be any correlation between Ni content and Ir content.

A peak abundance of magnetic spherules was found at or near the Younger Dryas boundary at eight of nine sites (Firestone et al. 2007). The spherules range between 10 and 250 μm in size. The average abundance was ~390/kg, with the highest abundances in the northern sites. Analyses of some of the spherules indicated that they are enriched in titanomagnetite. Several sites yielded what appear to be silicate spherules (Firestone et al. 2007), but no petrographic or compositional data were presented. In a more recent study, Surovell et al. (2009) were not able to confirm the presence of peaks in the content of magnetic spherules at or near the Younger Dryas boundary.

Fullerenes, containing ^{3}He, were found associated with the Younger Dryas boundary at three out of four sites (Firestone et al. 2007). Firestone et al. (2007) also described glass-like carbon up to several centimeters in diameter found in the Younger Dryas boundary sediments at most sites. They stated that nanodiamonds are found in the glass-like carbon at nine out of nine of the Younger Dryas boundary sites.

No crater of the appropriate age is known. Firestone et al. (2007) suggested that the lack of a crater may be due to fragmentation of an extraterrestrial body (probably a comet) in the atmosphere resulting in multiple airbursts or craters. They further suggested that if the impacts were at low angles (<30°) into the Laurentide Ice Sheet, they may have left negligible, if any, shock effects. Pinter and Ishman (2008a, b) argue that none of the evidence from the Younger Dryas boundary sediments requires an impact event and suggested that micrometeorite debris and associated Ir anomaly in the layer could have been concentrated by variation in clastic input and other terrestrial mechanisms.

The strongest evidence for an impact 12.9 ka ago is the occurrence of alleged nanodiamonds (Firestone et al. 2007). However, Pinter and Ishman (2008a) said of the reported nanodiamonds that "…this material was identified only obliquely and requires rigorous corroboration." More recently, Kennett et al. (2009) claimed that nanometer-sized diamonds, identified by selected area electron diffraction patterns, are abundant at multiple locations across North America at the lower Younger Dryas boundary dated at 12.9 ± 0.1 ka. French and Koeberl (2010) state that images of the "diamonds" published by Kennett et al. (2009) are not of "sufficient quality, magnification, and resolution to allow an easy comparison with meteoritic diamonds" and the reported X-ray d-spacings "are not uniquely characteristic of diamonds." Daulton et al. (2010) searched without success for nanodiamonds in two Younger Dryas deposits. They concluded that "previous studies misidentified graphene/graphene oxide aggregates as hexagonal diamond and likely misidentified graphene as cubic diamond."

In summary, none of the evidence given in support of an impact at ~12.9 ka ago requires an impact and no definitive proof of an impact has been given. The debate concerning a possible impact associated with the Younger Dryas event continued (see, e.g., Bunch et al. 2010; Paquay et al. 2010); but Pinter et al. (2011)

in a paper entitled "The Younger Dryas impact hypothesis: A requiem" concluded that none of the 12 proposed Younger Dryas impact signatures have been subsequently corroborated by independent tests (see also Pigati et al. 2012). They further stated that of the 12 original proposed lines of evidence for an impact, seven were found to be non-reproducible; and the remaining signatures appear to represent either non-catastrophic mechanisms and/or terrestrial rather than extraterrestrial or impact-related sources.

4.9.2 Late Pliocene "Ejecta" in the Ross Sea, Antarctica

Gerard-Little et al. (2006) reported finding what they interpreted to be impact ejecta in late Pliocene sediments from six cores taken in the Ross Sea near Antarctica. They reported finding dense, black, K-rich "impact" glasses that do not contain vesicles, and "microtektites" that are mostly spherical and are more abundant in the >150 μm size fraction. The "microtektites" are composed of silica and some of the "microtektites" exhibit exfoliation. No detailed petrographic or compositional data were given and no diagnostic evidence of shock metamorphism was reported.

4.9.3 The Paleocene-Eocene Event

The Paleocene-Eocene boundary (~55 Ma) is marked by an abrupt negative carbon isotope excursion (i.e., sharp decrease in $\delta^{13}C$ values) recorded in marine and terrestrial deposits (Kennett and Stott 1991; Koch et al. 1992). The negative carbon isotope excursion is coincident with a rapid oxygen isotope excursion referred to as the **Paleocene-Eocene thermal maximum** (Zachos et al. 1993). The largest deep-sea benthic extinction over the last 90 Ma (Thomas and Shackleton 1996) and a major radiation in mammals took place at about this time (Maas et al. 1995). The most widely accepted explanation for the carbon isotope excursion is the sudden dissociation of oceanic methane hydrate (e.g., Dickens et al. 1997). However, Kent et al. (2003) proposed that the negative carbon isotope excursion may have resulted from the impact of an ~10-km-diameter comet which would have introduced a significant amount of ^{12}C-enriched carbon.

Kent et al. (2003) proposed that the carbon released into the atmosphere from the comet would have oxidized to form CO_2, which would have caused a greenhouse warming. This could have caused corrosive and warmer (and therefore less oxygenated) bottom waters resulting in the extinction of benthic foraminifera coincident with the carbon isotope excursion. In addition, the warmer bottom water could have eventually resulted in thermal dissociation of methane hydrates, enhancing the thermal maximum and causing more extinctions.

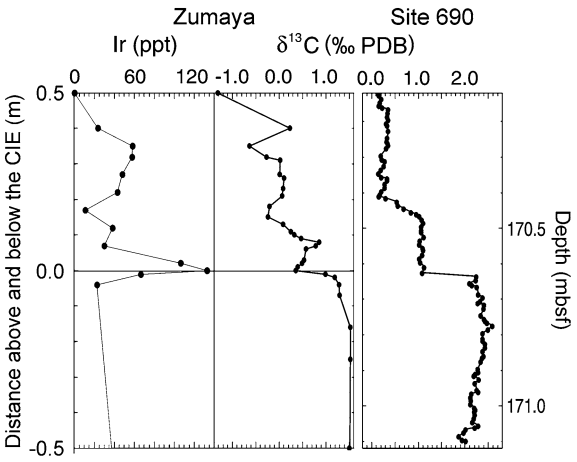

Fig. 4.57 Iridium distribution across the Paleocene/Eocene (P–E) boundary (0.0 m) at Zumaya and $\delta^{13}C$ values across the P–E boundary at Zumaya, Spain, and at Ocean Drilling Program Site 690 in the Southern Ocean. *msbs* meters below sea floor. After Kent et al. (2003), Fig. 6, with permission from Elsevier

Evidence for an impact at this time includes a small Ir anomaly at the Paleocene-Eocene boundary (Fig. 4.57) and an unusual abundance of magnetic nanoparticles that coincide with the onset of the carbon isotope excursion. A small, but reproducible, Ir anomaly was found associated with the carbon isotope excursion in an expanded bathyal section at Zumaya, Italy (Schmitz et al. 1997). Ir contents of 143 ± 22 ppt and 133 ± 15 ppt were reported. The background level at this site was ~38 ppt Ir. The Ir anomaly at this site occurs in a 1-cm-thick gray layer and is coincident with the onset of the carbon isotope excursion (Fig. 4.57). An Ir anomaly was also reported near the Paleocene-Eocene boundary in flysch deposits in Slovenia (Dolenec et al. 2001).

Kent et al. (2003) reported evidence of an unusual abundance of magnetic nanoparticles in kaolinite-rich shelf sediments that coincides with the onset of the carbon isotope excursion at three drill sites on the Atlantic Coastal Plain. After considering other possible sources for the magnetic nanoparticles (e.g., biogenic processes, erosion and redeposition from the K-T boundary), Kent et al. (2003) suggested, based on analogy with the K-T boundary magnetic nanoparticles (Wdowiak et al. 2001), that the magnetic nanoparticles associated with the carbon isotope excursion may have formed by condensation from an impact plume.

In a more recent study of the magnetic particles, Kopp et al. (2007) concluded that they were biogenetic magnetite and were, therefore, not produced by an impact. They concluded that the magnetic particles reflect environmental changes along the eastern margin of North America during the Paleocene-Eocene thermal maximum that led to enhanced production and/or preservation of the magnetofossils.

Although the Ir anomaly and magnetic nanoparticles are consistent with an impact origin, no diagnostic evidence of an impact (e.g., PDFs, high-pressure phases) has been reported to be associated with the Paleocene-Eocene thermal maximum and carbon isotope excursion.

Table 4.15 Localities, ages and references for Argentine glasses

Location	Stratigraphic age	Radiometric age	Reference
Rio Cuarto	Holocene	6 ± 2 ka	Schultz et al. (2004)
	Pleistocene	114 ± 26 ka	Schultz et al. (2004)
		570 ± 100 ka	Bland et al. (2002)
Centinela del Mar	Pleistocene		
Lower		230 ± 30 ka	Schultz et al. (2004)
Upper		445 ± 21 ka	Schultz et al. (2004)
Mar del Plata	Pliocene	3.3 ± 0.2 Ma	Schultz et al. (1998)
Bahia Blanca	Late Miocene	5.28 ± 0.04 Ma	Schultz et al. (2006)
Chasicó	Late Miocene	9.24 ± 0.09 Ma	Schultz et al. (2006)

4.10 Miscellaneous

Several additional ejecta and a few meteoritic layers are discussed in this section: (1) seven or eight occurrences of impact glasses with ages ranging between Holocene and late Miocene in Argentina, (2) two meteoritic dust layers of Pleistocene age in ice cores from Antarctica, and (3) meteoritic debris (including spherules) of Pliocene age from an ocean impact in the Bellingshausen Sea (the Eltanin event). The Argentine glasses are mostly, if not entirely, proximal in nature. The meteoritic layers in Antarctica were included because of a possible (but not probable) connection with one of the impact glass occurrences in Argentina. The ejecta from the Eltanin impact consist of unmelted and melted meteorite debris.

4.10.1 Argentine Impact Glasses

As of 2011, impact glasses representing at least seven impact events ranging in age from ~6 ka to ~9 Ma have been found in the Argentine Pampas (Table 4.15; Schultz et al. 2004, 2006). The two (or three) youngest groups of glasses are found associated with some elongated depressions found in a thick loess sequence just north of the Rio Cuarto River and the city of Rio Cuarto, Argentina. Schultz and Lianza (1992) proposed that the elongate depressions were formed by recent (<10,000 years) grazing impacts of a chondritic body originally 150–300 m in diameter. Two small fragments of an H4 chondrite were recovered as well as vesicular glass samples, which were interpreted to be impactites. Bland et al. (2002), however, argued that the elongate depressions are eolian features. Some of the glasses in this area are fresh looking and appear to be Holocene in age. Radiometric dating of these glasses indicates an age of 6 ± 2 ka (Table 4.15). The other glasses are dull in appearance and are apparently Pleistocene in age. According to Schultz et al. (2004), these glasses have a ^{40}Ar-^{39}Ar age of 114 ± 26 ka. However, Bland et al. (2002) obtained a ^{40}Ar-^{39}Ar age of 570 ± 100 ka for a glass from this area.

It is not clear if this represents another impact event or if one, or both, of the ages are incorrect.

The Rio Cuarto glasses (Table 4.15) are relatively homogeneous and have compositions (Table 4.16) similar to the local loess (Schultz and Lianza 1992; Koeberl and Schultz 1992). Shock-metamorphic effects, such as diaplectic glass, lechatelierite, rare quartz grains exhibiting planar deformation features, and thermal decomposition of zircon to baddeleyite and silica glass were observed (Schultz et al. 1994). In addition, the glasses show evidence of rapid quenching and low water content consistent with an impact origin. Furthermore, glasses with the lowest volatile content generally have the highest Cr, Ni, and Ir contents, which suggest meteoritic contamination from the projectile (Schultz et al. 1994).

Schultz et al. (2004) reported finding two layers of impact glasses in a paleosol sequence of Pleistocene age near Centinela del Mar (CdM) on the coast of Argentina south of Buenos Aires (Fig. 4.58). The glasses found in the lower layer have a ^{40}Ar-^{39}Ar age of 230 ± 30 ka, while the glasses in the upper layer have an older age (445 ± 21 ka). Schultz et al. (2004) proposed that the glasses in the upper layer have been eroded from an older layer and redeposited. The glasses from both of these layers exhibit evidence of shock metamorphism, including quartz grains with PDFs, diaplectic glass, and zircons decomposed to baddeleyite and silica. The Centinela del Mar glasses are fairly homogeneous (Table 4.16). Unlike the Rio Cuarto glasses which have compositions similar to that of the loess in the area where they were recovered, the compositions of the Centinela del Mar glasses do not closely match the compositions of the Pleistocene sediments at the location where they are found.

Pliocene-aged impact glasses were found in the Chapadmalal Formation at Mar del Plata (MdP), on the coast just north of the Centinela del Mar site (Schultz et al. 1998; Fig. 4.58). These glasses have a ^{40}Ar-^{39}Ar age of 3.3 ± 0.02 Ma. The best evidence of shock metamorphism is the presence in the glass of zircons that have broken down to baddeleyite and silica. The compositions of these glasses (Table 4.16) indicate that they could have been derived from the local loessoid deposits and perhaps from marine clays known to occur at depth nearby (Schultz et al. 1998).

Glasses of Late Miocene age were found at Bahia Blanca (BB) and Chasicó (Ch), which are also on the coast, but west of the Centinela del Mar and Mar del Plata sites (Fig. 4.58; Schultz et al. 2006). These glasses have ^{40}Ar-^{39}Ar ages of 5.28 ± 0.04 Ma and 9.24 ± 0.09 Ma, respectively (Table 4.15). Evidence of shock metamorphism in these glasses includes: quartz with PDFs, diaplectic glasses, and zircon that decomposed to baddeleyite plus silica (Schultz et al. 2006). Compared with the other Argentine glasses, the Bahia Blanca and Chasicó glasses contain fewer relict grains, but more quench crystals. Glasses found in upper Miocene deposits in a railroad cut ~90 km east of Bahia Blanca have compositions similar to the glasses at Bahia Blanca (RR in Table 4.16; Fig. 4.58). In one of their tables (Table 5) Schultz et al. (2006) refer to the glasses from the railroad cut as distal glasses probably related to the Bahia Blanca glasses, but no petrographic data are given in support of the distal nature of these glasses.

The major oxide compositions of the Chasicó glasses are similar to the composition of the host sediments (Table 4.16). However, the barium content of these glasses is much higher than that of the host sediments (Table 4.16), and, therefore, Schultz et al. (2006) suggested that the impact that produced these glasses probably excavated the marine sequences that are known to be at depth in this region. Schultz et al. (2006) pointed out that the Chasicó glasses have major oxide compositions similar to that of the HNa/K "australites," and like the HNa/K "australites" the glasses found at Chasicó have high alkali contents with the Na_2O content being higher than the K_2O. They further point out that the age of the Chasicó glasses is, within experimental error, the same age as the HNa/K "australites" (see Sect. 4.8.4). Schultz et al. (2006) speculated that the HNa/K "australites" may have originated as high-angle, distal ejecta from an impact in Argentina.

All of the Argentine glasses discussed above are probably proximal glasses, based on their high content of relict crystalline material and relatively high water contents (Schultz et al. 1994, 2004).

As previously stated, Bland et al. (2002) obtained a ^{40}Ar-^{39}Ar age of 570 ± 100 ka for a Rio Cuarto glass. They claimed that this age is similar to the age of glass from the upper layer at Centinela del Mar 800 km to the southeast near the coastal city of Necochea (Table 4.15; Schultz et al. 2000). Bland et al. (2002) also stated that the glass found at Necochea (Centinela del Mar) has similar major oxide compositions to the glasses found at Rio Cuarto and to glass found at Santa Rosa (SR; Fig. 4.58); but no age was given for the Santa Rosa glass. Bland et al. (2002) concluded that the glasses from Rio Cuarto, Necochea, and Santa Rosa were formed by the same impact about 0.48 Ma ago and that they may represent a new tektite strewn field. No petrographic data were given for the Santa Rosa glass, but the Rio Cuarto and Necochea (Centinela del Mar) glasses generally contain numerous crystalline inclusions, are generally highly vesicular, sometimes contain primary microlites/crystallites (quenched crystals), and have water content too high (Schultz et al. 1994, 2004) to be distal ejecta or tektites. Thus, present data do not appear to support the presence of a possible tektite strewn field in the Argentine Pampas as proposed by Bland et al. (2002).

Harris and Schultz (2006) have described two small (~2 mm) glass objects, from the vicinity of Bahia Blanca on the coast of Argentina, that they believe are tektites and have named them "**airesites**." One is described as a teardrop and the other as disk shaped. They are described as having grooved and pitted surfaces similar to surface sculpturing found on tektites. One lechatelierite particle was observed, but the glass objects contain many relict mineral grains including: chromite, Cr-spinel, zircon (one partly decomposed to baddeleyite), numerous remnants of shocked plagioclase, and merrillite containing submicron inclusions of Cu-bearing iron sulfide. Electron microprobe data (Harris and Schultz 2006) for one of the glass objects (which they called airesites) indicate that it has low SiO_2 content (~54 wt %) and high CaO and Na_2O contents (~9.4 and 9.3 wt %, respectively) compared with Cenozoic tektites (Tables 4.3 and 4.16). The measured water content for one of the glass bodies was found to range from 0.05 to

0.07 wt % (Harris and Schultz 2006). Although these glass objects are probably impact glasses, the composition and petrography are not consistent with them being tektites.

4.10.2 Meteoritic Dust Layers in Antarctic Ice

Two distinct dust layers in the EPICA-Dome C ice core (75° 06′ S, 123°21′ E, East Antarctic Plateau) were interpreted to be the result of meteoritic events (Narcisi et al. 2007). The upper layer, designated L1, lies at the end of marine isotope stage (MIS) 12 and has an age of 434 ± 6 ka. The lower (L2 layer) is in the upper part of MIS 13 and has an age of 481 ± 6 ka. The dust grains in these layers are coarser than eolian dust found in the ice at this location. Both layers contain angular olivine grains (some with metal inclusions) and spherical particles. Spherical particles are more abundant in L2; they are up to 25 μm in diameter and are mostly glassy with magnetite dendrites. L2 also contains pyroxene crystals with metal inclusions. The major oxide and Ni compositions of the dust layers are similar to the composition of chondrite meteorites (Narcisi et al. 2007). No shock-metamorphosed grains were mentioned by the authors. The abundance of unmelted meteoritic debris and apparent lack of shock-metamorphosed grains suggest that the dust is from a meteoritic body that broke up in the atmosphere. Similar meteoritic dust layers were found ~2000 km west of EPICA-Dome C in the Dome Fuji ice core (Misawa et al. 2010). Aggregates of spherules with a variety of textures and chondrite composition have been recovered from several locations in the Transantarctic Mountains (van Ginneken et al. 2010). These authors suggested that the spherules were correlative with the 481 ka-old meteoritic dust layer found in the EPICA-Dome C and Dome Fuji ice cores. They proposed that the meteoritic debris is from a Tunguska-like impact event. Assuming that the elongate depressions near Rio Cuarto, Argentina, were from the impact and ricochet of meteoritic bodies travelling to the southwest as proposed by Schultz and Lianza (1992), it is possible that a body in the cluster had a somewhat higher elevation and traveled to Antarctica where it broke up in the atmosphere. Bland et al. (2002) obtained an age of 570 ± 100 ka for an impact glass from the Rio Cuarto "crater field." Unfortunately the experimental error is very large, but the age could be concordant with one of the meteoritic dust layers (L1 or L2) found in the EPICA-Dome C and Dome Fugi ice cores. In order to determine the geographic distribution and to document geographic variations in thickness, these meteoritic dust layers should be searched for in other Antarctic ice cores; and the Rio Cuarto glasses should be more precisely dated.

Table 4.16 Major oxide (wt %) and selected trace element (ppm) compositions of Argentine impact glasses and host sediment

	Rio Cuarto glasses[a]		Upper CdM[b] (3)		Mar del Plata[b] (1)	Bahia Blanca[c] (1)	RR[c] (1)	"Aire-site"[d] (1)	Chasicó[c] (4)	Chasicó host sed.[c] (1)
	Vesicular (5) Range	Drop (1)	Average	S.D.					Range	
SiO_2	48.6–58.3	69.0	61.1	1.72	60.93	60.18	59.44	54.0	59.66–62.5	62.3
TiO_2	0.0–3.5	0.64	0.69	0.06	0.65	0.81	0.77	0.72	0.77–0.99	0.70
Al_2O_3	14.5–25.1	16.3	12.3	0.64	16.88	16.55	17.25	15.7	14.5–16.0	14.9
FeO	1.4–20.1	3.8	4.37	0.35	6.65	5.18	5.04	4.54	5.12–5.48	5.00
MgO	0.34–2.8	1.4	3.47	0.43	2.83	2.69	2.62	3.42	2.37–3.24	3.82
CaO	4.1–8.0	3.4	5.51	1.05	2.36	5.58	6.71	9.36	4.18–6.97	5.55
Na_2O	3.0–5.4	3.5	4.48	0.82	3.41	2.88	2.66	9.27	3.4–4.24	4.32
K_2O	1.8–3.2	2.6	3.17	0.91	2.19	3.69	3.14	2.44	2.80–3.51	2.08
LOI	n.d.	n.d.	2.87	0.46	2.78	2.20	5.17		3.28–4.79	11.52
	(1)	(1)	(3)		(1)	(1)	(1)	(1)	(4)	(1)
Sc	10.5	n.d.	11.3	0.6	12.7	14.8	13.6	n.d.	12.1–15.2	13.9
Cr	34.1	n.d.	31.9	2.8	34.8	46.6	88.3	n.d.	23.9–34.1	30.3
Mn	46	774	206	224	46	852	774	697	31–387	39
Co	8.86	n.d.	8.51	0.55	9.55	13.5	11.6	n.d.	7.58–10.1	8.42
Ni	9	n.d.	9	1	10	20	25	n.d.	5–10	9
Cu	<2	n.d.	<3.5	>0.7	<2	27	36	n.d.	<2–6	<2
Zn	38	n.d.	34	15	19	31	25	n.d.	22–49	60
Ga	12	n.d.	17	6	15	n.d.	n.d.	n.d.	5–60	20
As	3.61	n.d.	2.79	1.61	5.18	2.9	2.7	n.d.	3.48–8.43	7.57
Br	0.8	n.d.	4.4	3.1	8.9	0.4	8.5	n.d.	0.9–5.9	19.1
Rb	107	n.d.	58.8	6.5	61.7	58.1	54.8	n.d.	43.9–71.3	69.2
Sr	339	n.d.	401	58	438	430	546	n.d.	424–585	371
Zr	208	n.d.	192	16	184	164	178	n.d.	157–176	159
Nb	11	n.d.	10	0.6	9	12	11	n.d.	8–10	n.d.

(continued)

Table 4.16 (continued)

	Rio Cuarto glasses[a]		Upper CdM[b] (3)		Mar del Plata[b] (1)	Bahia Blanca[c] (1)	RR[c] (1)	"Aire-site"[d] (1)	Chasicó[c] (4)	Chasicó host sed.[c] (1)
	Vesicular (5) Range	Drop (1)	Average	S.D.					Range	
Sb	0.51	n.d.	0.28	0.15	0.32	0.37	0.31	n.d.	0.08–0.31	0.34
Cs	5.52	n.d.	2.37	0.25	3.29	3.29	3.10	n.d.	2.33–4.64	5.04
Ba	556	n.d.	446	13	484	562	445	n.d.	613–7693	374
La	28.1	n.d.	23.1	1.6	21.2	19.4	18.7	n.d.	18.8–20.5	21.5
Ce	54.9	n.d.	43.5	3.1	46.3	38.8	35.5	n.d.	39.7–50.2	48.2
Nd	26.8	n.d.	24.3	1.9	22.6	20.4	19.5	n.d.	21.1–26.1	25.1
Sm	5.65	n.d.	4.68	0.24	4.29	4.21	4.16	n.d.	4.17–5.44	4.81
Eu	1.11	n.d.	1.18	0.13	1.18	1.15	1.19	n.d.	1.08–1.41	1.35
Gd	5.3	n.d.	4.7	0.7	3.9	3.75	3.47	n.d.	4.2–5.2	5.5
Tb	0.79	n.d.	0.80	0.11	0.71	0.63	0.65	n.d.	0.67–0.92	0.74
Tm	0.47	n.d.	0.43	0.04	0.36	0.33	0.34	n.d.	0.38–0.47	0.48
Yb	2.81	n.d.	2.85	0.22	2.49	2.25	2.29	n.d.	2.39–2.94	3.17
Lu	0.41	n.d.	0.44	0.04	0.37	0.34	0.35	n.d.	0.35–0.41	0.48
Hf	6.31	n.d.	5.83	1.04	5.48	4.11	4.18	n.d.	4.35–4.82	4.69
Ta	0.79	n.d.	0.59	0.08	0.59	0.44	0.42	n.d.	0.33–0.55	0.65
Th	11.5	n.d.	7.72	0.48	7.43	6.12	5.75	n.d.	5.32–7.23	7.41
U	3.11	n.d.	1.21	0.22	1.75	1.65	1.39	n.d.	1.02–1.99	2.25

Numbers in parentheses are number of analyses; all iron given as FeO; *LOI* lost on ignition; *n.d.* no data; *S.D.* standard deviation

[a] Major oxide data for vesicular impactite and a vesicle-poor glass drop (Schultz and Lianza 1992); trace element data from Schultz et al. (2004)

[b] Glasses from the upper level at Centinela del Mar (CdM) and Mar del Plata. Schultz et al. (2004)

[c] Glass found in Miocene deposits at Bahia Blanca, at a railroad cut ~90 km east of Bahia Blanca, and Chasicó and Chasicó host sediments (Schultz et al. 2006)

[d] Glass object interpreted to be a tektite (Harris and Schultz 2006)

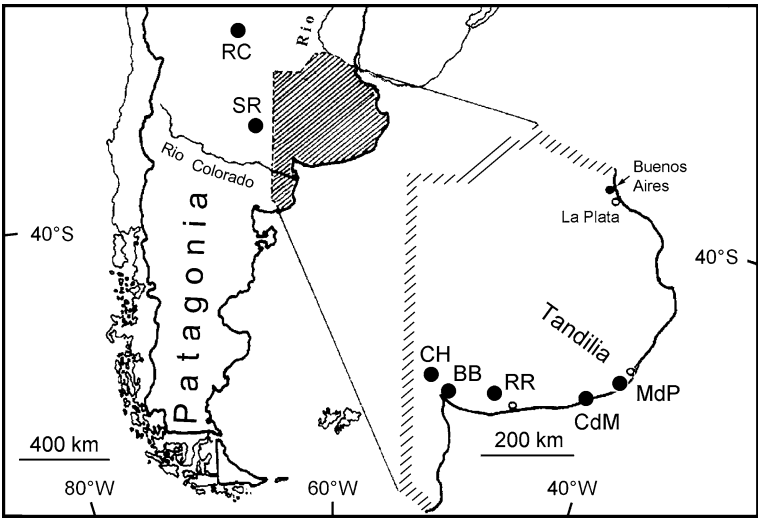

Fig. 4.58 Map showing locations of Argentine glass occurrences. *RC* Rio Cuarto, *SR* Santa Rosa, *CH* Chasicó, *BB* Bahia Blanca, *RR* Railroad cut near Bahia Blanca, *CdM* Centinella del Mar (Necochea), *MdP* Mar del Plata (Chapadmalal Formation). For age of the glasses see Table 4.15. Reprinted from Schultz et al. (2004), Fig. 1, with permission from Elsevier

4.10.3 The Eltanin Event

Unmelted and melted meteoritic debris has been associated with an Ir anomaly in late Pliocene sediments in the Bellingshausen Sea (eastern Pacific sector of the Southern Ocean) (Kyte et al. 1981, 1988; Kyte and Brownlee 1985; Gersonde et al. 1997). The projectile appears to have been a basaltic achondrite body (Kyte 2002), which has been named the Eltanin meteorite (Margolis et al. 1991a). The size of the impacting body responsible for the **Eltanin Event** was estimated to be between 1 and 4 km in diameter (Gersonde et al. 1997). Debris from this impact consists primarily of mm- to cm-sized vesicular impact melt-rock, but a few percent unmelted meteorite fragments and trace amounts of spinel-bearing spherules have also been observed. This debris has been found in sediments over a distance of $\sim$500 km (Gersonde et al. 1997). The age of the impact is estimated to be $\sim$2.15 Ma based on combined magnetostratigraphy and biostratigraphy of cores containing the debris layer (Gersonde et al. 1997). However, Frederichs et al. (2002) gave a revised age of 2.51 $\pm$ 0.07 Ma for the age of the impact.

Margolis et al. (1991a) reported finding glassy spherules (Fig. 4.59), which the title of their paper suggests are microtektites and microkrystites, in the debris layer. However, the spherules appear to be melted meteoritic material and thus are not microtektites or microkrystites, which are distal ejecta composed primarily of target material. Most of the spherules are between $\sim$50 and 200 μm in diameter. The spherules are shiny submetallic gray to dark black or reddish-brown. Their

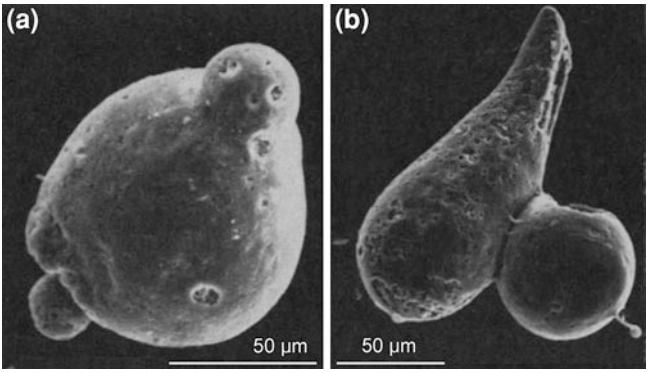

Fig. 4.59 Scanning electron microscope images of spherules from the Eltanin Event layer recovered from Cores E13-3 and E13-4 taken in the Southern Ocean (Bellingshausen Basin). Although they have been referred to as microtektites and microkrystites, they are melted meteoritic material. **a** A large sphere with at least two smaller spheres fused to it. **b** Teardrop form with a large sphere attached to it. The sphere has a delicate drop-shaped protrusion on the *lower right*. From Margolis et al. (1991a), Fig. 1a and e, reprinted with permission from AAAS

Table 4.17 Major oxide (wt %) and trace element composition of Eltanin spherules

Major oxide	Range for 144 spherules
SiO_2	41.11–49.88
TiO_2	0.3–0.61
Al_2O_3	7.6–17.61
FeO	9.84–18.03
MnO	0.24–0.53
MgO	9.86–18.55
CaO	7.62–15.20
Na_2O	1.11–9.10
K_2O	0.01–0.11
Trace element	Average of 5 spherules
Sc (ppm)	19
Cr (ppm)	2200
Co (ppm)	131
Ni (ppm)	2.4
La (ppm)	1.7
Ir (ppb)	5

Major oxide compositions determined by microprobe analysis. Trace element concentrations determined by NAA. All iron given as FeO. Margolis et al. (1991)

shapes range from spheres to teardrops, dumbbells, compound spherules (two or more fused together), and unusual shapes such as glassy stringers (Margolis et al. 1991a). Most of the spherules are glassy with minor amounts of Ni- and Cr-rich spinel (magnesioferrite) microlites with a variety of textures (dendritic, equant, skeletal). The glass content of the spherules is generally between 80 and 100 %.

These spherules have compositions (Table 4.17) similar to those of a basaltic achondrite and appear to be composed of melted projectile (Gersonde et al. 1997). There is no evidence of incorporation of ocean floor sediments or crust in the spherules, nor is there any evidence of shock-metamorphosed terrestrial material associated with this impact (Gersonde et al. 1997). Because the spherules were not formed by melting and ejection of target material, they are not microtektites or microkrystites by definition.

Chapter 5
Mesozoic Spherule/Impact Ejecta Layers

5.1 Introduction

The Cretaceous-Tertiary (K-T), or Cretaceous-Paleogene (K-Pg), boundary impact ejecta layer; the Late Cretaceous Manson crater ejecta layer; the Late Triassic spherule/ejecta layer; and a possible impact ejecta layer at the Triassic-Jurassic boundary are discussed in this chapter (Table 5.1). As previously mentioned, the K-T boundary ejecta layer is the most studied and best known distal impact ejecta layer. The Manson structure is a buried impact crater located in Iowa, USA, which at one time was thought to be the, or a, source crater for the K-T boundary layer. Distal impact ejecta from this structure have been found in South Dakota and Nebraska. An impact spherule layer containing shocked quartz has been found in Late Triassic deposits in southwestern England. Some researchers have reported finding evidence for an impact ejecta layer at the Triassic-Jurassic boundary, but others do not find the evidence convincing.

5.2 Cretaceous-Tertiary (K-T) Boundary Impact Ejecta Layer

5.2.1 Introduction

In this section, we summarize what is known about the K-T (or K-Pg) boundary ejecta layer. There are too many publications on this subject to cover all aspects of the K-T boundary layer. For additional details, the reader is referred to the review papers by Smit (1999), Claeys et al. (2002), Schulte et al. (2010), and papers in the proceedings of the Snowbird conferences (Silver and Schultz 1982; Sharpton and Ward 1990; Ryder et al. 1996; Koeberl and MacLeod 2002).

B. P. Glass and B. M. Simonson, *Distal Impact Ejecta Layers*, Impact Studies,
DOI: 10.1007/978-3-540-88262-6_5, © Springer-Verlag Berlin Heidelberg 2013

Table 5.1 Mesozoic impact ejecta/spherule layers

Layer	Location	Impact evidence[a]	Age (Ma)	Source crater	Ref[b]
Well-defined distal impact ejecta layers					
Cretaceous-Tertiary boundary	Global	Ir, Sph, SM, S	65	Chicxulub	1, 2
Manson crater ejecta	South Dakota and Nebraska, USA	SM	74	Manson	3
Late Triassic ejecta	Southwest England	Sph, SQ	~214	Manicouagan	4, 5
Possible distal impact ejecta					
Triassic-Jurassic boundary	Global (?)	Ir?, SQ?	~200	Unknown	6

[a] Ir = Ir anomaly, S = stishovite, SM = shocked mineral grains, Sph = impact spherules, SQ = shocked quartz with PDFs

[b] Selected references: 1) Smit (1999), 2) Schulte et al. (2010), 3) Izett et al. (1998), 4) Kirkham (2002), 5) Walkden et al. (2002), 6) Bice et al. (1992)

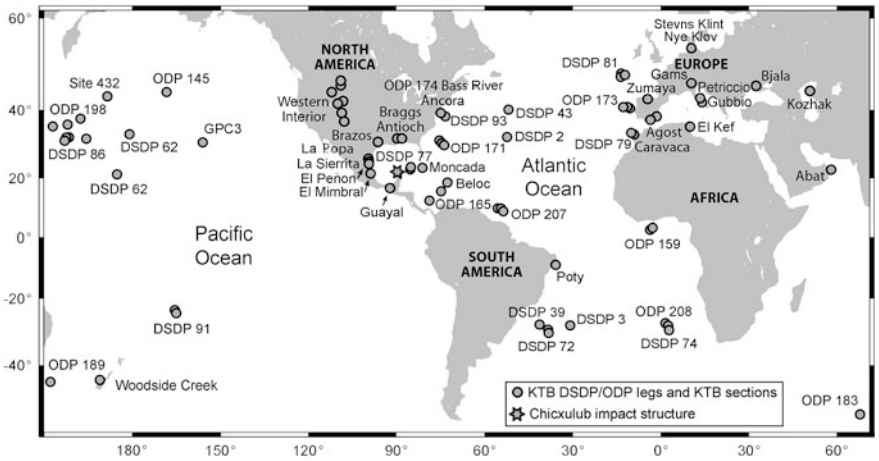

Fig. 5.1 Global map showing location of K-T boundary sites. DSDP = Deep Sea Drilling Project; ODP = Ocean Drilling Program; KTB = K-T boundary. Site 432 refers to a specific DSDP site rather than a leg. Sites 524, 577, and 596 were cored during DSDP legs 74, 86, and 91, respectively. Braggs = Braggs Creek. Modified after Fig. 5.1 in Schulte and Kontny (2005)

5.2.2 General Description of the K-T Boundary Layer

In 2002, about 101 K-T boundary sites containing impact ejecta debris were known (Fig. 5.1; Claeys et al. 2002). As of 2010, over 350 K-T boundary sites were known (Schulte et al. 2010). The K-T boundary ejecta layer is found over most of the globe and it varies greatly from one part of the globe to another; however, there appears to be a systematic variation in the thickness and character of the layer from the Gulf of Mexico outward (Table 5.2). At many of the K-T boundary sites around the Gulf of Mexico, in Haiti, the equatorial western Atlantic Ocean, and in the Western Interior

Table 5.2 General description of the Cretaceous-Tertiary (K-T) ejecta layer

Location[a]	Layer thickness		Spherules		Comments[f]
	Lower[b]	Upper[c]	Without crystalline textures[d]	With crystalline textures[e]	
Northeast Mexico; USA Gulf Coast	Up to a meter or more	Not well-defined	Abundant	Rare	Generally shows evidence of reworking; sometimes multiple spherule layers
Haiti	Up to 90 cm	A few centimeters	Abundant	Yes	Dual nature of the layer is clear; some reworking
Cuba	Unknown	Unknown	Yes	Unknown	Thick reworked sections
Western Interior, North America	Several centimeters	Several millimeters	Rare to abundant	Not mentioned	Dual nature very obvious; spherule layer overlain with an Ir-rich and shocked quartz-bearing layer
Western North Atlantic (Blake Nose)	Up to 17 cm	3–7 cm	Yes	Not mentioned	
W. equatorial Atlantic (Demerara Rise)	~2 cm	A few millimeters	Yes	Not mentioned	Undisturbed complete section
Pacific Ocean	Not well-defined	Not well-defined	Rare in W. Pacific	Yes	
Europe	A few millimeters[g]		No	Yes	A single layer

[a] Locations are listed according to increasing distance from the Gulf of Mexico region
[b] Spherule layer. Spherules are generally large (1 mm or more) and often hollow
[c] Fireball layer. Contains an Ir anomaly, shocked quartz, Ni-rich spinels, and spinel-bearing spherules (<400 μm in diameter)
[d] Large (up to 1 mm or more), often hollow
[e] Small (<1 mm) spherules often with Ni-rich spinels
[f] Most K-T boundary layers contain an Ir anomaly and shocked mineral grains
[g] No distinction is made between lower and upper layers at European sites

of North America, the K-T boundary ejecta layer consists of two layers: (1) a lower layer containing abundant splash-form, diagenetically-altered, millimeter-sized impact spherules (which may have originally been microtektites) and rare shocked mineral grains; and (2) an upper layer containing spherules with relict crystalline textures (microkrystites) and Ni-rich spinel crystals, an Ir-anomaly, and abundant shocked mineral grains. The upper layer is found globally. In many of the sites around the Gulf of Mexico, the two layers are separated by meters-thick sands, which were deposited by mass flows or high-energy currents. However, in the Western Interior of North America the upper layer lies directly on the lower layer. Over most of the rest of the globe, only the upper layer is present and it is merely centimeters to millimeters thick. In the following subsections, a general description of the K-T boundary sections at various sites around the globe is provided.

5.2.2.1 Gulf of Mexico Region and Cuba

In general, the K-T boundary layer is thicker and more complex (depending on water depth) in and around the Gulf of Mexico than at most other locations (Hildebrand and Boynton 1990; Smit et al. 1992a; Stinnesbeck et al. 1993; Montanari et al. 1994; Stinnesbeck et al. 1996; Smit 1999; Tada et al. 2002; Schulte et al. 2010). K-T boundary sites have been described at Shell Creek, Moscow Landing, Antioch Church, and Braggs in Alabama, and Brazos River, Texas, in the USA; at more than 30 sites in eastern and southern Mexico (e.g., Smit et al. 1992a; Stinnesbeck et al. 1993; Montanari et al. 1994; Stinnesbeck et al. 1996; Smit 1999; Lawton et al. 2005; Schulte and Kontny 2005; King and Petruny 2008); and on Cuba (e.g., Tada et al. 2002; Alegret et al. 2005) (Fig. 5.2). Many of the K-T boundary sites in or adjacent to the Gulf of Mexico contain a thick, coarse-grained, clastic complex, which was deposited by a high-energy event or events. These clastic layers, sometimes referred to as the clastic complex unit (CCU), contain a distinctive mixture of reworked microfossils of different ages, varying amounts of impact ejecta, and heterogeneous lithic fragments (Smit et al. 1996; Bralower et al. 1998; Arenillas et al. 2006). Bralower et al. (1998) referred to this mixture as the **K-T boundary "cocktail"** and they suggested that this mixture was deposited by giant gravity flows, triggered by the collapse of the continental margin around the Gulf of Mexico and adjacent region of the Caribbean (e.g., Cuba).

The K-T boundary section at Guayal in SE Mexico is one of the thicker K-T boundary sections (Fig. 5.2). The clastic complex at Guayal can be divided into four subunits (Grajales-Nishimura et al. 2003; Arenillas et al. 2006). The lowest subunit (subunit 1) is approximately 40 m thick and consists of very coarse-grained carbonate breccia at the base which grades into fine-grained carbonate breccia at the top. Limestone blocks up to 2 m across are common in the basal part. Subunit 2 ($\sim$5 m thick) consists of fine-grained carbonate breccia and coarse-grained calcareous sandstone containing some rare impact ejecta such as shocked quartz and altered impact spherules, and limestone clasts a few centimeters in diameter (Arenillas et al. 2006). Subunit 3 ($\sim$5 m thick) consists of very fine-

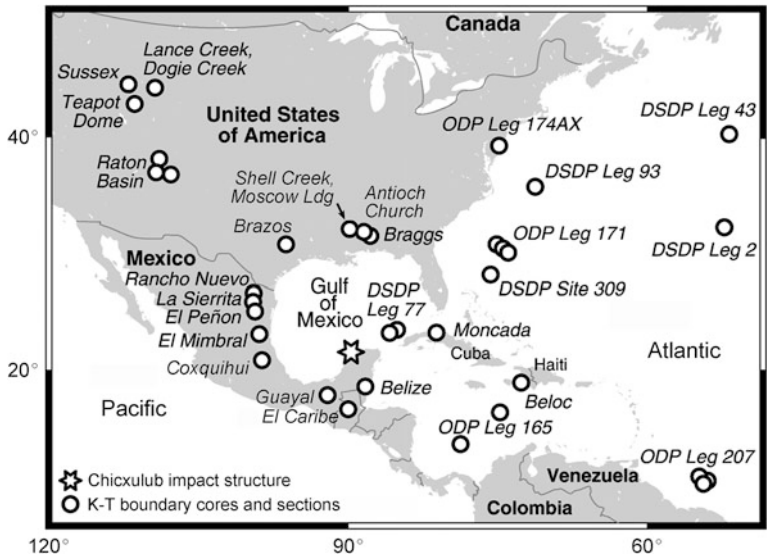

Fig. 5.2 K-T boundary sites in and around the Gulf of Mexico, the Western Interior of North America, western North Atlantic and adjacent North America, and the Caribbean Sea. DSDP = Deep Sea Drilling Project; ODP = Ocean Drilling Program; Ldg = Landing. After Fig. 1 in Schulte et al. (2006). Reprinted with permission of Elsevier

grained rippled sandstone and siltstone rich in impact ejecta such as shocked quartz and accretionary lapilli. The uppermost layer, subunit 4, is a thin ($\sim$1 cm) yellow to red shaly layer that represents the finest ejecta. This subunit contains an Ir anomaly (up to 0.8 ppb), altered spherules, shocked quartz, and Ni-rich spinels (Arenillas et al. 2006). Subunit 1 contains little if any impact ejecta and may be a slump or gravity deposit from the adjacent Chiapas-Tabasco carbonate platforms. Subunits 2 and 3 are a mixture of allochthonous carbonate and impact ejecta which were reworked by **impact-produced tsunami** waves or currents. The layer at the top (subunit 4) is primarily fine-grained ejecta that settled slowly out of the atmosphere and through the water column.

The K-T boundary layer in NE Mexico can generally be divided into three to four units (Fig. 5.3; Smit 1999). The lowermost unit (unit I or spherule layer) is characterized by channeled, poorly sorted, coarse-grained pebbly sandstone containing flat rip-up clasts, abundant spherules, and limestone particles interpreted as unmelted limestone ejecta (Smit et al. 1996). This unit displays low-angle cross bedding. The spherule layer varies greatly in thickness from zero up to over 1 m (Smit 1999).

Unit II (Fig. 5.3) is composed of a series of upward-thinning and-fining lenses or beds of finer-grained, well-sorted calcareous sandstone. Lithic clastic grains are more common than in unit I, and reworked planktonic foraminifera are present. Locally, plant debris occurs in layers. Rounded, armored mud balls are commonly found at the base; the armoring consists of spherules. At Mimbral, up to six

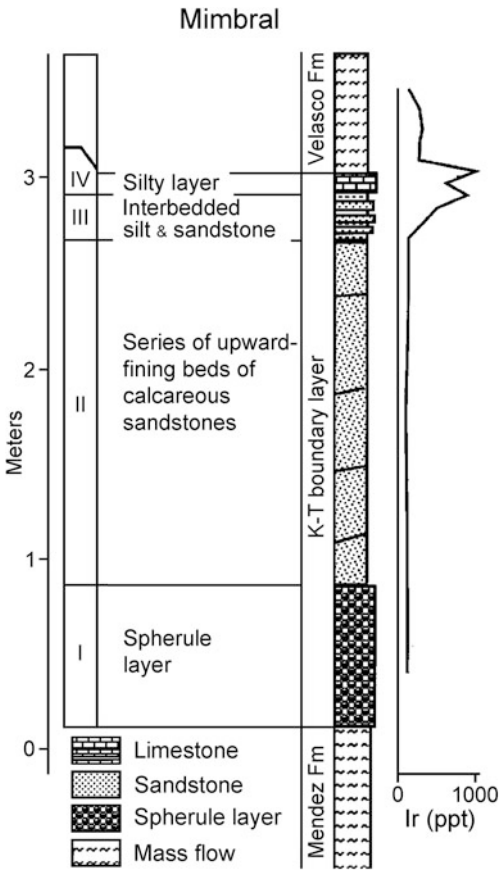

Fig. 5.3 K-T boundary section and iridium anomaly in Mimbral, northeast Mexico. Roman numerals I to IV indicate subdivisions of clastic beds which make up the K-T boundary layer at this site. The clastic units are interpreted to be the result of reworking due to impact-induced tsunami waves. The Mendez Formation is a pelagic marl of Maastrichtian age. The Velasco Formation is a pelagic marl of Danian age. Modified after Fig. 10 in Smit (1999)

stacked and imbricated lenticular sandstone layers are present. The basal part of each layer contains a few spherules, which are probably reworked from unit I (Smit 1999). Unit II displays numerous sedimentary structures including parallel laminations with current lineations, and lunate, linguoid, and climbing ripples. Paleocurrent measurements indicate bimodal current directions with the dominant directions differing by $\sim 180°$ (i.e., on and off shore; Smit et al. 1996).

Unit III consists of a series of alternating thin silt layers and thin, rippled, fine-grained sandstone layers. These layers are the lowermost layers enriched in iridium. Paleocurrent directions are variable, again often differing by $\sim 180°$ (Smit et al. 1996). The upper two to three sandstone layers contain diverse burrow traces, mostly confined to the surfaces of the sandstone layers.

Unit IV (Fig. 5.3), the highest unit, is only locally present. It is a silty layer of variable thickness on top of the last sandstone layer (Smit et al. 1996). This layer is often visible in outcrops because it forms a conspicuous orange-red micritic layer about 5–10 cm thick. In places in NE Mexico, it consists largely of reworked

material from the underlying Cretaceous Mendez Shale. Unit IV is size graded and contains the highest Ir concentrations in the Gulf of Mexico sites (Smit 1999).

The origin of the clastic layers in these Gulf of Mexico sites has been a matter of debate. Smit et al. (1996) proposed that the clastic layers were formed by tsunami waves produced by ejecta falling in the Gulf of Mexico and by impact-produced slumping along the Campeche escarpment. Bohor (1996) interpreted the clastic layers in NE Mexico as turbidite deposits produced by a gravity-flow event triggered by the impact. However, Smit (1999) stated that the interpretation of the clastic layers as being the result of a single turbidite flow does not explain the frequent hydrodynamic jumps indicated by the grain size shifts at each successive layer or the reversal in current direction interpreted from the sedimentary structures.

Stinnesbeck and Keller (1996) proposed that the upward-thinning and -fining clastic layers were formed at sea-level lowstand followed by transgression, or by repeated gravity flows related to eustatic sea-level changes that took place over thousands of years. Stinnesbeck and Keller (1996) suggested that the fine-grained material between the clastic layers are "normal hemipelagic layers" and they identified what they called burrow structures in units I and II. Stinnesbeck and Keller (1996) placed the K-T boundary above the clastic layers. See Sect. 5.2.5 for further discussion of the interpretation of these layers.

At the K-T boundary in the Moncada section (Fig. 5.4) in western Cuba, there is a ~2-m-thick complex (the Moncada Formation) characterized by repetition of calcareous sandstone units that exhibit overall upward fining and thinning (Tada et al. 2002). The Moncada Formation has ripple cross-laminations at several horizons that indicate north–south trending paleocurrent directions with reversals. The ripple cross-laminations may have been deposited by tsunami waves generated by a gravity-flow (or flows) triggered by seismic shocks from the impact (Tada et al. 2002; Goto 2008).

An Ir anomaly occurs at the top of the complex with a peak concentration of ~760 ppt in a layer ~15 cm thick (Fig. 5.4). Shocked quartz grains with multiple sets of PDFs are common throughout the formation (Tada et al. 2002). Angular, whitish, vesicular, smectite grains containing blade-like clinopyroxene crystals also occur in the Moncada Formation and are interpreted to be altered impact glass (Tada et al. 2002). Olive-green flattened and deformed grains consisting of chlorite and pumpellyite are also interpreted to represent altered impact glass (spherules?).

The K-T boundary layer at Loma Capiro, Cuba, consists of a 9.6 m fining-upward clastic complex (Alegret et al. 2005). At the base is a breccia layer overlain by microconglomerates and coarse- to fine-grained sandstones. The clastic complex contains reworked foraminifera of different ages and paleoenvironments. Spherules and shocked quartz occur near the top of the clastic unit (Alegret et al. 2005). There is no mention of an Ir anomaly at this site. Alegret et al. (2005) suggested that the clastic complex may have been produced by the collapse of the Cuban platform triggered by the impact.

The K-T boundary sections at Coxquihui, Mexico and at Deep Sea Drilling Project Site (DSDP) Sites 536 and 540 were formed in deeper water (600–3000 m

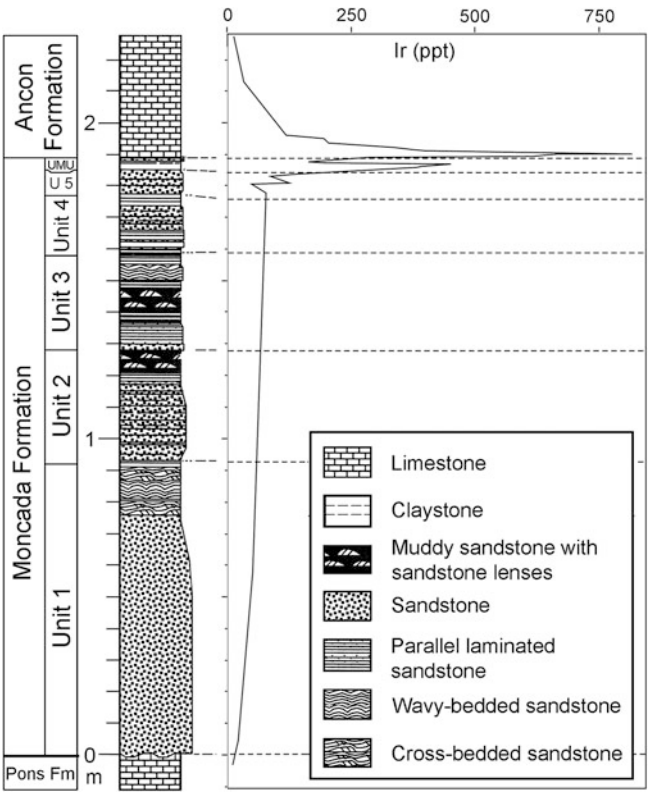

Fig. 5.4 K-T boundary section and iridium anomaly in the Moncada section in western Cuba. Cross-bedded standstones may have been deposited by tsunami waves. The uppermost unit (UMU) is a 3–5 cm-thick layer of alternating light-colored, calcareous claystone and dark, very fine, calcareous claystone. Modified after Fig. 6 in Tada et al. (2002)

depth; Smit 1999). The K-T boundary sediments at Coxquihui were deposited at a depth of >600 m. Here the K-T boundary layer consists of an ~90 cm thick layer of poorly graded vesicular calcite spherules. The 90-cm-thick layer is made up of three cross-bedded sublayers. The Ir content is elevated throughout the layer, but highest at the top.

The water depth at DSDP 540 (Leg 77) in the Gulf of Mexico (Fig. 5.2) is nearly 3000 m. The K-T boundary section at Site 540 can be divided into three units. The lower unit is ~45 m of matrix-supported pebbly mudstone, which unconformably overlies early Campanian limestone. This unit was probably formed by mass wasting from the Campeche platform margin to the south. The mass wasting may have been triggered by slope failure induced by seismic energy from the impact (Smit 1999). Above the pebbly mudstone is a normally-graded, cross-bedded, sandy unit, ~2.6 m thick, containing smectitic spherules (some with remnant glass), shocked mineral grains, and elevated Ir content (Alvarez et al. 1992). This unit is believed to be impact ejecta that were reworked by strong bottom currents (perhaps

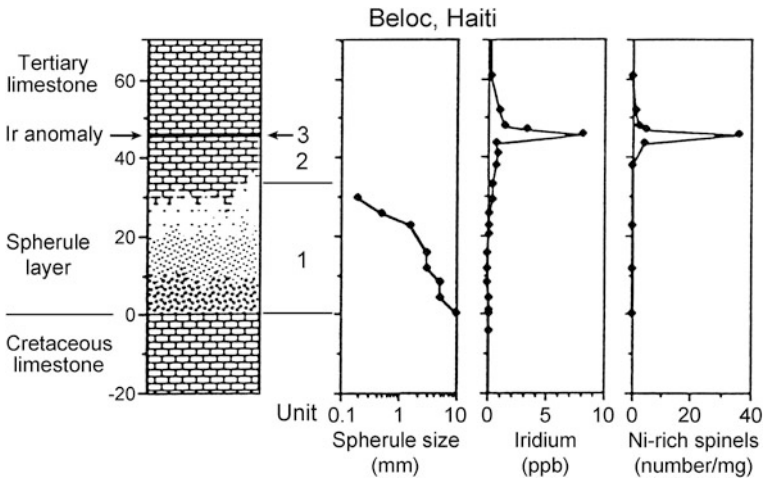

Fig. 5.5 K-T boundary section near Beloc, Haiti (Section A of Jéhanno et al. 1992). Unit 1 is the spherule layer sensu stricto. Unit 2 is a pelletoidal carbonate mudstone containing Cretaceous microfossils. The boundary between Unit 1 and Unit 2 is gradational. Unit 3 is a clay layer containing an Ir anomaly, Ni-rich spinel-bearing spherules, and shocked quartz. Modified after Fig. 1 in Jéhanno et al. (1992)

generated by an impact-produced tsunami). Above this unit is a 50-cm-thick layer of fine-grained sediment containing very small planktonic foraminifera. This upper unit is interpreted as fine-grained sediments that were suspended by coarser ejecta falling on the sea floor, nearby slumping, and/or wave action. The highest Ir content is found in this unit (Alvarez et al. 1992).

5.2.2.2 Beloc, Haiti

The K-T boundary sediments on Haiti were deposited at a depth of >2000 m (Smit 1999). The K-T boundary outcrops along an ~3 km stretch of road between Beloc and Jacmel in the southern peninsula of Haiti (Hildebrand and Boynton 1990; Maurrasse and Sen 1991; Jéhanno et al. 1992). The K-T boundary layer was originally described as a volcaniclastic turbidite (Maurrasse et al. 1979), but Hildebrand and Boynton (1990) reinterpreted it as an impact ejecta layer. Most of the sections show evidence of faulting and slumping. One of the most complete sections studied by Jéhanno et al. (1992) is their section A. They divided the section into three units (Fig. 5.5). The lower unit (Unit 1) is about 30–35 cm thick and consists of normally-graded clay spherules (some with silicate glass cores) in a slightly clayey calcareous matrix (Fig. 5.6). The lower 2 cm of this layer consists of ~60 % spherules and spherule fragments (Izett 1991b). Spherule fragments appear to make up ~85 % of the formerly-glassy component. The acid-insoluble residue of the spherule layer makes up ~0.006 % of the layer and consists primarily of quartz, of which ~75 % appears to be shocked (i.e., exhibit PDFs; Izett

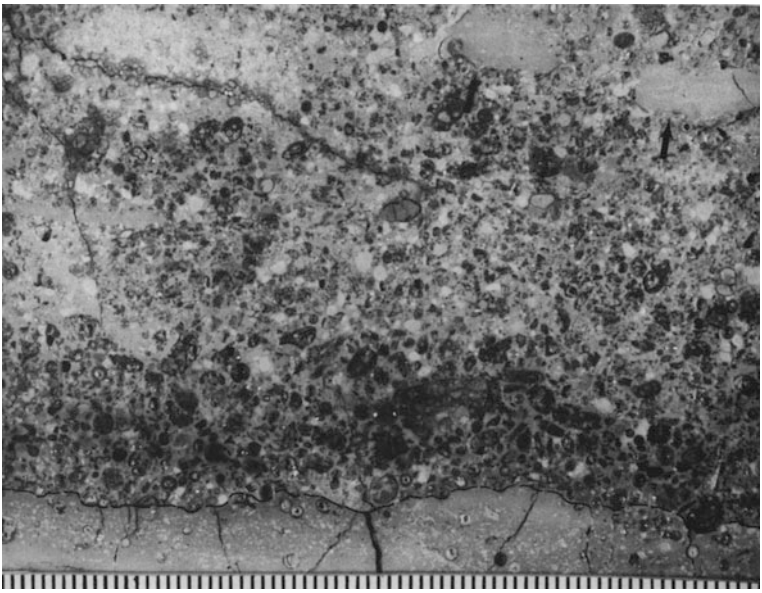

Fig. 5.6 Image of a polished slab of the K-T boundary spherule bed from near Beloc, Haiti. Smectite pseudomorphs of impact spherules are concentrated in the lower 1–2 cm of the K-T boundary layer which overlies a Cretaceous marl. The contact between the spherule layer and the underlying Cretaceous marl (emphasized with a dashed line) is sharp. Note centimeter-sized marl clasts in the upper portion of the slab. Scale divisions at the bottom are in millimeters. This image was previously published as Fig. 1 in Izett (1991b). Courtesy of Glen Izett

1991b). Unit 2 is a 10–15 cm-thick layer above the spherule layer (Unit 1). Unit 2 consists of pelletoidal mudstone containing poorly preserved Cretaceous microfossils. Bohor and Glass (1995) concluded that this unit was formed by fine-grained ejecta settling through the water column, plus deposition of detritus suspended by nearby slumping. Unit 3, the uppermost unit, is a thin (a few centimeters thick) grayish-green clay layer, which contains an Ir anomaly, shocked quartz, and **Ni-rich magnesioferrite** (spinel)-bearing spherules (Jéhanno et al. 1992; Bohor and Glass 1995). Tertiary fossils are found above Unit 3. Another fairly complete and un-deformed section on Haiti is section H (Jéhanno et al. 1992). At this section, the spherule layer (Unit 1) is 25 cm thick, Unit 2 is 25–35 cm thick, and the uppermost layer (Unit 3) is a few centimeters thick (Jéhanno et al. 1992; Leroux et al. 1995a). Here the clay layer (Unit 3) is sometimes barely visible and contains rust-colored lenses.

5.2.2.3 Western Interior, North America

In the Western Interior of North America, the K-T boundary layer has been found at numerous sites extending across >2000 km from New Mexico, USA, up to Alberta, Canada (Fig. 5.7; Bohor et al. 1987a; Izett 1990). The K-T boundary in

Fig. 5.7 Map showing locations of Western Interior, North America, K-T boundary sites. The Raton Basin sites include: Clear Creek, Berwind Canyon, Madrid, and Starkville in Colorado and Climax Canyon in New Mexico. Modified after Fig. 1 in Bohor et al. (1987a)

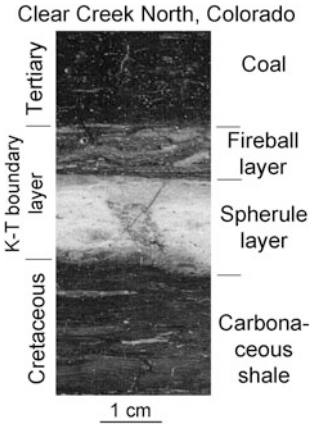

Fig. 5.8 A portion of a slab through the K-T boundary layer at Clear Creek North, Colorado. The fireball layer contains an iridium anomaly and abundant shocked mineral grains. Modified after a figure on the cover page of *Geological Society of America, Special Paper* 249 (Izett 1990)

the Western Interior is thinner than in and around the Gulf of Mexico and lacks a distinct intercalated clastic unit. In addition, in the Western Interior sites the layer is in a nonmarine (coal swamp environment), rather than a marine section, and is, therefore, generally less reworked. The K-T boundary layer in the Western Interior is composed of two layers (Fig. 5.8). The lower or basal layer is composed of kaolinitic claystone, which contains abundant diagenetically-altered spherules (often "hollow") and some shock metamorphosed mineral grains. This spherule layer is overlain by a thinner smectitic layer, which contains an Ir anomaly,

magnesioferrite (spinel) crystals, and shock metamorphosed minerals (Bohor et al. 1987a). The lower spherule layer has been referred to as the K-T boundary claystone (Izett 1990), ejecta layer (Hildebrand 1993), or the **melt-ejecta layer** (Bohor and Glass 1995) and the upper smectite layer has been referred to as the K-T boundary impact layer (Izett 1990), or **fireball layer** (Hildebrand 1993; Bohor and Glass 1995). In the Raton Basin of Colorado and New Mexico, USA, the spherule layer is ~3 cm thick and the overlying fireball layer, containing shocked mineral grains and an Ir anomaly, is 5–8 mm thick (Izett 1987, 1990). Farther north, at Dogie Creek, Wyoming, the basal spherule layer is up to 3 cm thick and the upper, fireball, layer is 2–3 mm thick (Bohor et al. 1987a). However, still farther north at Rock Creek West, southernmost Saskatchewan, Canada, Lerbekmo et al. (1999) describe the K-T boundary section as having a hackly claystone layer 1–2 cm thick overlain with satiny claystone and laminated shale layers which are both ~3–8 mm thick. The upper laminated shale layer contains elongated pellets (altered and deformed spherules?), shocked quartz, and a large Ir anomaly. The underlying satiny layer contains some shocked quartz and a moderate Ir anomaly. The lower hackly claystone contains microspherules and an Ir abundance that is marginally higher than the background values. Lerbekmo et al. (1999) imply that the satiny claystone and laminated shale units are equivalent to the fireball layer and the hackly claystone layer is equivalent to the lower spherule layer describe by other authors for sections to the south in the Western Interior, USA.

5.2.2.4 Western North Atlantic and East Coast of the USA

K-T boundary impact ejecta have been described at several sites in the northwestern Atlantic and along the east coast of the USA, such as: Ocean Drilling Program (ODP) Sites 1049, 1050, and 1052 on the Blake Nose in the western North Atlantic off the coast of South Carolina (Norris et al. 1999; Martínez-Ruiz et al. 2002); Deep Sea Drilling Project Site 603 located on the lower continental rise off the coast of North Carolina (Klaver et al. 1987; Bohor and Betterton 1989); and the Bass River borehole in New Jersey taken during ODP Leg 174X (Olsson et al. 1997, 2002). At these sites the K-T boundary consists of a spherule-bearing layer that ranges between 7 and 17 cm thick. In addition to spherules, the layer contains shocked quartz, usually more abundant in the upper part of the layer, and accretionary lapilli composed of micrometer-sized microspar of low-Mg calcite, which may have formed in the vapor plume (Yancey and Guillemette 2008). At the Blake Nose sites (ODP Leg 171: Sites 1049, 1050, and 1052) the spherule-bearing layer is capped by a 3-mm-thick orange limonitic layer (Norris et al. 1999). A sharp contact separates the dark spherule bed from the underlying Cretaceous nannofossil-foraminifera ooze (Norris et al. 1999). The limonitic layer is overlain with 2–7 cm of dark, burrow-mottled ooze, which contains an Ir anomaly. The spherule layer at Site 603 has a small Ir anomaly (Bohor and Betterton 1989). An Ir anomaly with a peak abundance of ~2.8 ppb was found at the Bass River section (Olsson et al. 2002).

5.2.2.5 Western Equatorial Atlantic

During Ocean Drilling Program Leg 207, holes were drilled at five sites on the northern slope of the Demerara Rise in the equatorial western North Atlantic. A well-preserved spherule bed and adjacent sediments were recovered in Holes 1258A, 1259B, 1259C, and 1260A (Erbacher et al. 2004). The spherule layer at these sites is ~2 cm thick and normally graded. The spherule layer shows no evidence of reworking and it lies directly on youngest Cretaceous sediments. The spherules range from 0.1–1 mm in size. They are composed of aluminous smectite; however, some relict Si–Al-rich hydrated glass is present (Schulte et al. 2009). The spherules range from hollow, to vesicle rich, to vesicle free. The spherule layer contains a positive Ir anomaly, with the highest concentration at the top of the layer (MacLeod et al. 2007). Shocked quartz was observed at the K-T boundary layer at these sites (Morgan et al. 2006). Along with shocked silicate minerals, abundant carbonate and rare gneissic clasts are present in the uppermost 0.5–0.7 mm of the layer (Schulte et al. 2009). The exotic textures of some of the carbonate clasts are very similar to textures observed in calcite spherules found in the Gulf of Mexico K-T boundary sites and are thought to be, at least in part, the result of shock metamorphism. The dual nature of the layer with the Ir and shocked mineral grains being concentrated at the top of the layer is similar to that observed in the Western Interior of North America (Schulte et al. 2009, 2010).

5.2.2.6 Pacific Ocean Sites

The K-T boundary layer has been identified and studied at several central to western Pacific Ocean sites including: Core LL44-GPC3 (Kyte and Wasson 1986); DSDP Sites 465 (Kyte et al. 1980; Thiede et al. 1981), 576 (Kyte et al. 1995), 577 (Michel et al. 1985; Heath et al. 1985), and 596 (Zhou et al. 1991); and ODP Sites 803 and 886 (Kyte et al. 1995). The thickness of the layer at each site is not well defined. At Site 465 there appears to be an ~3-cm-thick pyrite-rich black clay layer at the K-T boundary, but the core containing the boundary is badly disturbed by rotary coring (Kyte et al. 1996). In Core LL44-GPC3 there is a homogeneous clay layer (~57 cm thick) at the K-T boundary with laminated clay above and below the homogeneous layer (Kyte et al. 1996). An Ir anomaly occurs near the base of the homogeneous layer. Spherules and spinel crystals have been recovered from this core (Kyte and Smit 1986), but the vertical distribution of these components was not provided. At Site 577 there is a slight change in color across the K-T boundary (Heath et al. 1985). At the remainder of the sites, there is no K-T boundary clay or obvious lithologic change across the boundary. The K-T boundary at these sites was recognized by a combination of biostratigraphy and identification of an Ir anomaly. The impact nature was confirmed by the presence of shocked quartz. In addition, spherules were observed at all of the sites except Site 803, although millimeter-sized flat lenses at this site may be flattened

spherules (Kyte et al. 1996). Magnesioferrite (spinel) crystals were recovered from all of the sites except Site 465 (Zhou et al. 1991; Kyte et al. 1995; Kyte et al. 1996).

5.2.2.7 Europe and North Africa

The K-T boundary ejecta layer has been found in numerous carbonate marine sites in Europe, southwest Asia, and north Africa including: Caravaca and Agost, Spain; Stevns Klint and Nye Klov, Denmark; Petriccio, Pontedazzo, and Gubbio, Italy; Tetri-Tskaro, Republic of Georgia; and El Kef, Tunisia (Fig. 5.1). The El Kef section has been designated as the Global Boundary Stratotype Section and Point for the base of the Danian (Paleocene, Paleogene, "Tertiary", Cenozoic; Molina et al. 2006). In the benchmark paper by Alvarez et al. (1980), Stevns Klint and Gubbio are two of the sections where they found a positive Ir anomaly at the K-T boundary. In the European and North African area there is generally a **K-T boundary clay layer** (Fig. 5.9). The boundary clay has either almost zero carbonate, or significantly lower carbonate content than the underlying Cretaceous rock and the overlying Paleogene deposits. The boundary clay is usually between 3 and 20 cm thick and is characterized by very low calcareous nannofossil and planktonic foraminiferal abundance (Smit 1990; Smit 1999). The boundary clay layer apparently represents reduced carbonate content due to a brief decrease or collapse in marine productivity after the impact. At the base of the boundary clay is a layer (sometimes laminated), which contains an Ir anomaly, spherules (Fig. 5.10), shock metamorphosed mineral grains, and Ni-rich spinels. At sites with the most complete K-T boundary section, the highest sediment accumulation rate, and least amount of reworking (e.g., Caravaca and El Kef) the laminated layer containing the impact ejecta and Ir anomaly is only a few millimeters thick (Smit 1990; Smit 1999). At Caravaca, this impact or ejecta layer is 1–3 mm thick and it is usually ferruginous and contains orange-brown laminae (Izett 1987).

5.2.2.8 Indian Ocean

The K-T boundary has been found in ODP Hole 761C in the Indian Ocean off the northwest coast of Australia (Shipboard Scientific Party 1992). There is no distinctive K-T boundary clay layer at this site, but rather a slight color change. An Ir anomaly occurs in close coincidence with the color change. Abundant Ni-rich spinel crystals occur over a few centimeters just above the color change and preliminary observations indicate that shocked quartz grains are also present (Rocchia et al. 1992). Many of the spinel crystals occur clustered in flat pancakes or lenses believed to be diagenetically-altered and flattened impact spherules.

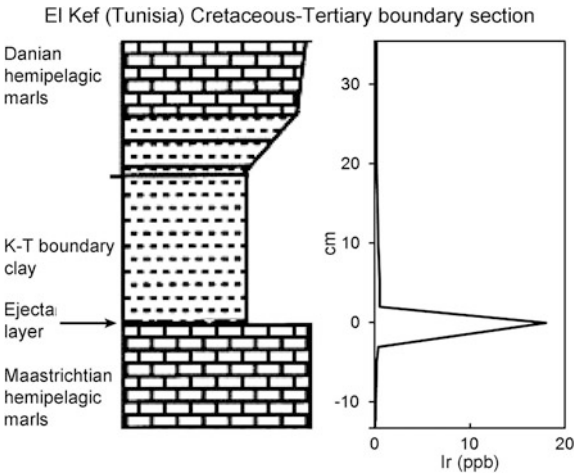

Fig. 5.9 The K-T boundary section and Ir anomaly at El Kef, Tunisia. The ejecta layer is a 1–3 mm-thick, rusty-looking layer containing an Ir anomaly, shocked quartz, Ni-rich spinels, and altered microkrystites. The K-T boundary clay contains little or no carbonate in contrast to the underlying Cretaceous (Maastrichtian) and overlying Tertiary (Danian) deposits. The stratigraphic section is based on Fig. 2 in Smit (1999). The Ir data are based on Fig. 1 in Rocchia et al. (1996)

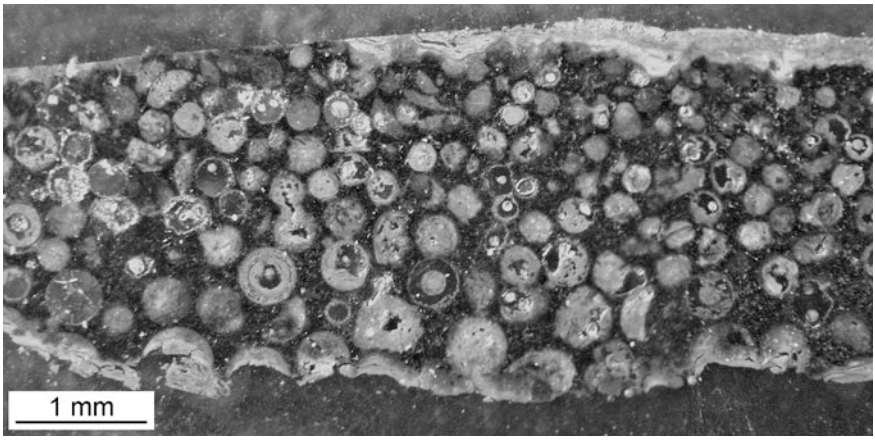

Fig. 5.10 Photograph of the polished surface of a thin section of a sample from the K-T boundary spherule layer at Tetri-Tskaro, near Tbilisi, Republic of Georgia. The spherule layer is normally graded and is highly enriched in iridium (up to 86 ppb). The spherules have been diagenetically altered to goethite. Courtesy of J. Smit

5.2.2.9 Woodside Creek, New Zealand

At the K-T boundary section at Woodside Creek (and Flaxbourne River) in the northern part of South Island, New Zealand, there is an 8-mm-thick shale unit (K-T boundary clay) between an upper Cretaceous carbonate and a lower Paleocene carbonate unit (Brooks et al. 1984). An Ir anomaly occurs in the shale unit with the peak concentration in the basal 2 mm. Shocked quartz was found in this layer (Bohor et al. 1987b; Morgan et al. 2006). Although spherules occur in the Ir-rich shale layer, Brooks et al. (1985) concluded that they were weathered diagenetic pyrite lumps.

5.2.3 Evidence for an Impact Origin

After Alvarez et al. (1980) concluded that there was a major impact at the end of the Cretaceous Period, other researchers began to search for evidence that would support/confirm or refute the impact hypothesis. Additional studies quickly showed that the Ir anomaly found at the K-T boundary by Alvarez et al. is global in extent. Ratios between platinum group elements and osmium isotope data provided further evidence of an extraterrestrial component in the K-T boundary layer. The discovery of spherules interpreted to be of impact origin at several K-T boundary sites was used to support the impact hypothesis. However, it was the discovery of shock metamorphosed mineral grains (especially quartz) in the K-T boundary layer at several sites around the globe that confirmed that a major impact did take place at the end of the Cretaceous. The evidence for an impact at K-T boundary time is discussed in more detail below.

5.2.3.1 Ir Anomaly, Platinum Group Elements (PGEs), and Osmium Isotope Data

The first indication that there might have been a major impact at the end of the Cretaceous was the discovery of a sharp increase in Ir, with the peak concentration at or very near the K-T boundary at three widely-spaced sites (i.e., in Denmark, Spain, and New Zealand; Alvarez et al. 1980). The presence of a positive Ir anomaly is probably the most characteristic feature of the K-T boundary. The early Ir analysis of the K-T boundary indicated that there was a single sharp peak (Fig. 5.9). Later studies found multiple smaller Ir peaks above and/or below the K-T boundary Ir anomaly at some sites around the Gulf of Mexico (e.g., Crocket et al. 1988; Graup et al. 1989; Keller et al. 2003). Some authors have suggested that the secondary peaks may indicate multiple impacts before and after the K-T boundary (see Sect. 5.2.5). However, it seems likely that the secondary peaks are the result of burrowing, sediment reworking, or erroneous measurements. Small Ir anomalies in lower Paleocene deposits can be attributed to redeposition of eroded

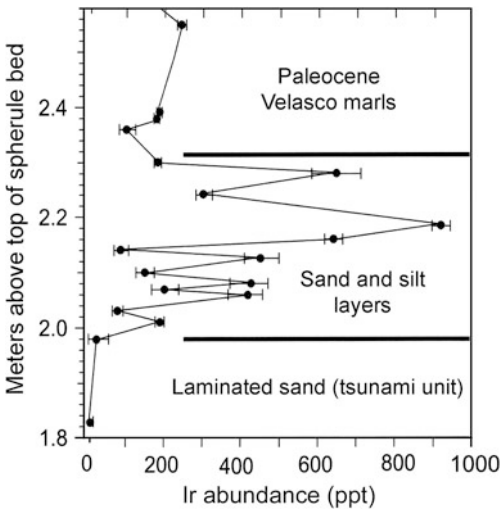

Fig. 5.11 Iridium anomaly across the alternating sand and silt layers (Units III and IV in Fig. 5.3) in the upper portion of the K-T boundary layer at Mimbral, northeastern Mexico. After Fig. 6 in Claeys et al. (2002), with permission of the Geological Society of America

Ir-rich K-T boundary sediments and are likely to be associated with reworked Cretaceous microfossils (Pospichal 1996). Until contemporaneous secondary Ir peaks are found at other K-T sites and associated with additional impact evidence (e.g., shocked minerals), there is no substantial evidence that they indicate additional impacts around the time of the K-T event. Therefore, in the following discussion, we assume that there is only one widespread or global Ir anomaly at or near the K-T boundary.

As of 2002, an Ir anomaly had been reported for 85 K-T boundary sites around the world (Claeys et al. 2002). The maximum concentration at a given site varies from 0.1 to >100 ppb (Claeys et al. 2002). Some of the lowest concentrations are found in the Gulf of Mexico region where the K-T boundary is marked by evidence of strong sediment reworking and the Ir is spread vertically over tens of centimeters or a meter or more, often with several secondary peaks (Fig. 5.11; Smit 1999; Claeys et al. 2002). However, if the Ir concentrations are integrated over the entire thickness of the Ir anomaly, the Ir flux in these sites is found to be comparable to the highest flux values found outside the Gulf of Mexico.

Outside the Gulf of Mexico region, there is no systematic geographic variation in maximum Ir concentration (Fig. 5.12). At some locations bioturbation, reworking, diagenesis, and chemical diffusions can cause the remobilization of Ir and spread it over up to several meters of section (Claeys et al. 2002).

The iridium fluence at a site can be determined by integrating the concentration of Ir in a column through the Ir anomaly and is generally given as mass/cm^2. Iridium fluences for 52 K-T boundary sites range from 3 to 580 ng/cm^2 and the mean global Ir fluence was determined to be 55 ± 3 ng/cm^2 (Donaldson and Hildebrand 2001). The mean global Ir fluence for the K-T boundary is about an order of magnitude higher than is the mean global Ir fluence for the late Eocene cpx spherule layer.

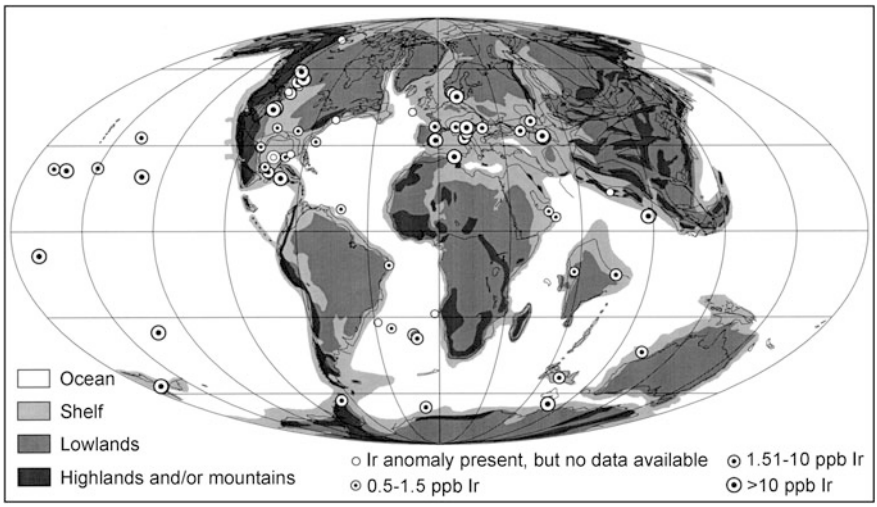

Fig. 5.12 Map showing K-T boundary sites where an iridium anomaly has been found and the approximate maximum Ir content at each site. No obvious geographic variation in Ir content is evident. After Fig. 5 in Claeys et al. (2002), with permission of the Geological Society of America

In addition to an iridium enrichment at the K-T boundary, other platinum group elements (e.g., osmium, platinum, rhenium, ruthenium, palladium) and nickel, cobalt, chromium, and gold also have high concentrations compared to the concentration of the these metals in the Earth's crust. At most K-T boundary sites, the PGE abundance exceeds that of the crust by more than a factor of 50–4000 or more (Lodders and Fegley 1998; Claeys et al. 2002). In general, ratios between the PGEs, Ni, Co, Cr, and Au support the conclusion that the high Ir content of the K-T boundary deposits is from an extraterrestrial body (Ganapathy 1980; Smit and Hertogen 1980; Kyte et al. 1980; Palme 1982; Evans et al. 1993). However, the noble metal ratios are variable, suggesting that some fractionation must have taken place (Palme 1982).

An extraterrestrial origin for the K-T boundary layer is also supported by the $^{187}Os/^{186}Os$ ratios of 1.65 and 1.29 found for K-T boundary deposits at Stevns Klint, Denmark, and Raton Basin, Colorado, respectively (Luck and Turekian 1983). These ratios are close to the ratio of ~ 1 for meteorites, compared to ~ 10 for the Earth's crust. More recent measurements of the $^{187}Os/^{186}Os$ ratios for the K-T boundary layer at Stevns Klint (Denmark), Raton Basin (USA), Woodside Creek (New Zealand), Sumbar (Turkmenistan), and DSDP Sites 577 and 596 (Pacific Ocean) (Meisel et al. 1995, and references therein) support Luck and Turekian's (1983) conclusion.

A negative excursion or sharp drop in $^{187}Os/^{188}Os$ (earlier studies normalized to ^{186}Os rather than ^{188}Os) has been observed at the K-T boundary in deep-sea sediments (Core LL44-GPC3) in the North Pacific (Pegram and Turekian 1999) and in ferromanganese crust from the central Pacific (Klemm et al. 2005). The

marine isotopic record for the last 80 Ma clearly shows a negative excursion in $^{187}Os/^{188}Os$ or $^{187}Os/^{186}Os$ at the K-T boundary (Fig. 3.5; Peucker-Ehrenbrinck 1996; Klemm et al. 2005). This is interpreted as indicating a meteoritic component in the K-T boundary layer. A more recent study indicates a somewhat more complicated $^{187}Os/^{188}Os$ record for the end of the Cretaceous and beginning of the Paleogene (Robinson et al. 2009). A decline in $^{187}Os/^{188}Os$ started well below the K-T boundary and lasted for ~200 ka. This period of low $^{187}Os/^{188}Os$ may be the result of diminished carbonate burial due to ocean acidification caused by Deccan volcanism (Robinson et al. 2009). A second more rapid decline in $^{187}Os/^{188}Os$ is associated with the K-T boundary and is accompanied by a significant increase in Os concentrations (Robinson et al. 2009). This negative excursion in $^{187}Os/^{188}Os$ is consistent with a major impact at the end of the Cretaceous. Paquay et al. (2008) used the marine osmium isotope record to estimate a diameter for the K-T boundary (Chicxulub) and late Eocene (Popigai) impactors of ~4.1–4.4 km and ~2.9 km, respectively. These estimates are based on total vaporization and dissolution of osmium in seawater. They are within ~50 % of the size estimates derived from Ir data.

Cr isotopic data have been used to support the evidence for a meteoritic component in the K-T boundary and to indicate the type of projectile responsible for the formation of the source crater and the K-T boundary impact ejecta layer (Shukolyukov and Lugmair 1998; see Sect. 5.2.8).

5.2.3.2 Spherules and Accretionary Lapilli

Impact spherules have been found in the K-T boundary layer at numerous sites around the Earth (Fig. 5.13, Fig. 5.14, Fig. 5.15). Unfortunately, all of the spherules have undergone various degrees of diagenetic alteration and their original petrography and compositions can generally only be inferred. However, relict glass cores have survived in a small percent of the spherules found in Haiti and northeastern Mexico and Ni-rich spinels have survived in some of the K-T boundary spherules found in Europe and the Pacific Ocean core sites.

K-T boundary spherules were first reported by Smit and Klaver (1981) in the K-T boundary section near Caravaca, Spain, where they are composed of K-feldspar. Smit and Klaver (1981) proposed that these "sanidine spherules" resulted from rapid cooling of a K-rich melt and suggested that they were analogous to microtektites or were derived from the impacting body or projectile. However, DePaolo et al. (1983) found that the Caravaca spherules have a $\delta^{18}O$ value of +24 ‰ (PDB), which indicates that the K-feldspar was formed authigenically at low temperatures and not by crystallization from a melt. At about the same time, Montanari et al. (1983) described spherules from the K-T boundary clay layer at Caravaca and Petriccio, Italy (Fig. 5.13b, d), and Deep Sea Drilling Project Site 465 in the central Pacific.

The spherules at Petriccio are about the same size and shape as those at Caravaca, but are mineralogically more diverse. They are composed of varying

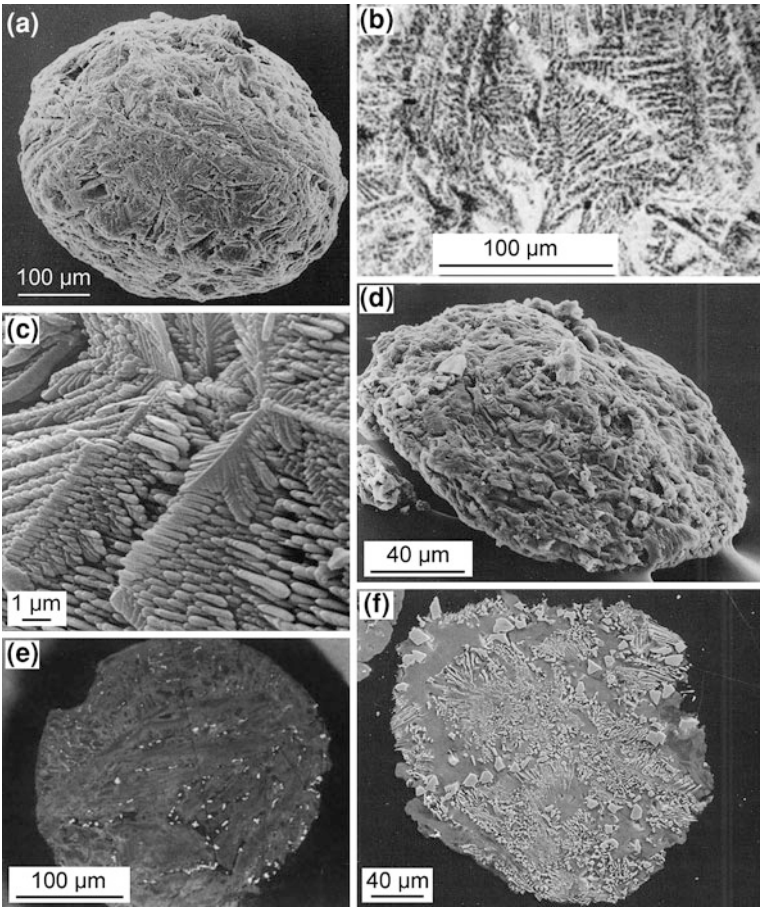

Fig. 5.13 Scanning electron microscope images of K-T boundary impact spherules. **a** A spherule replaced by sanidine from Gubbio, Italy. **b** Dendritic texture preserved in the interior of a sanidine spherule from Caravaca, Spain. **c** Relict clinopyroxene dendrites in a spherule (microkrystite) from the K-T boundary at Deep Sea Drilling Project Site 577 in the North Pacific. **d** Mafic spherule from Petriccio, Italy. Discoid shape is probably the result of compaction after diagenetic alteration. **e** Polished section of a mafic spherule containing Ni-rich spinel crystals (bright crystals) from Furlo, Italy. **f** Polished section of a mafic spherule from Petriccio, Italy, showing Ni-rich spinel (magnesioferrite) crystals in an amorphous Fe-oxide-rich matrix. **a**, **d**, and **f** are from Bohor and Glass (1995), Figs. 2a, 3a, and 3b, respectively, with permission of the Meteoritical Society © 1995. **b** is from Fig. 1a in Montanari et al. (1983). **c** is courtesy of J. Smit. **e** is from Fig. 1a in Smit and Kyte (1984), with permission of Macmillan Publishers Ltd. [*Nature*] copyright (1984)

proportions of K-feldspar, glauconite, and magnetite (Montanari et al. 1983). The spherules at Site 465 are composed of K-feldspar and pyrite. Montanari et al. (1983) interpreted the spherules as diagenetically-altered microcrystalline impact spherules of basaltic composition. This conclusion was supported by DePaolo et al. (1983) who stated that the compositional and oxygen isotopic data are most

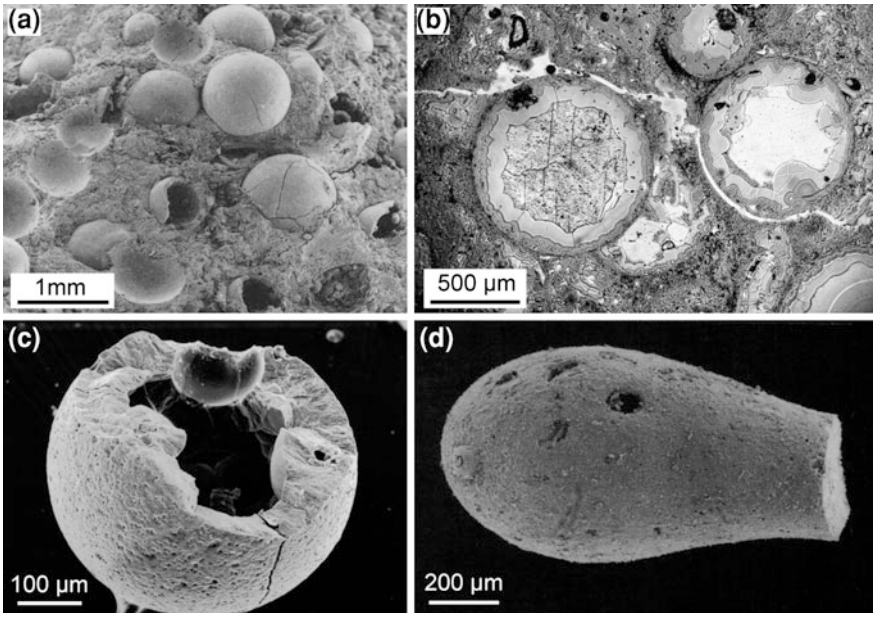

Fig. 5.14 Impact spherules from the Cretaceous-Tertiary boundary in the Western Interior USA. **a** Scanning electron microscope (SEM) image of a sample from the K-T boundary at Dogie Creek, Wyoming, showing numerous diagenetically-altered hollow spherules. The outer shells of these spherules have been replaced with goyazite. The smooth circular depressions are where spherules fell out during handling of the sample. **b** Optical microscope image (plane polarized light) of a thin section of a sample from the K-T boundary layer at Dogie Creek, Wyoming, showing several "hollow" goyazite spherules. The interior of the larger spherule is filled with gypsum. Other infilling minerals include calcite, barite, or kaolinite. Note the concentric layering in the goyazite shells and the inner mammillated surfaces of the shells. **c** SEM image of a broken goyazite spherule from Teapot Dome, Wyoming, showing the hollow interior and the inner mammillated surface. Note the smooth spherical depression in the shell, at the top of the image, which may be a remnant of a large (>150 µm) vesicle. A smaller ($\sim$20 µm) vesicle can be seen in the broken wall on the right side. **d** SEM image of a broken elongate goyazite spherule from Dogie Creek, Wyoming. This appears to have been a dumbbell-shaped spherule before it was broken. **a** is Fig. 1 from Bohor and Glass (1995), with permission of the Meteoritical Society © 1995. **b** and **c** are courtesy of Bruce Bohor. **d** is from Izett (1991b), Fig. 12d

easily explained if the impact took place on oceanic, rather than continental, crust. However, Bohor (1984) suggested that these spherules may be melt droplets of the impacting body rather than of the target rocks. By 1985, spherules had been found in the K-T boundary layer from at least 21 sites around the globe (Smit and Romein 1985). Smit and Romein (1985) referred to the spherules as microtektite-like and stated that they formed a worldwide strewn field.

The K-feldspar spherules contain relict dendritic textures (Fig. 5.13b). They consist of a porous meshwork of prismatic K-feldspar crystals usually arranged in bundles and sheaves (Izett 1987). A few spherules which contain quenched clino-pyroxene crystals with a dendritic texture were found in the K-T boundary layer at

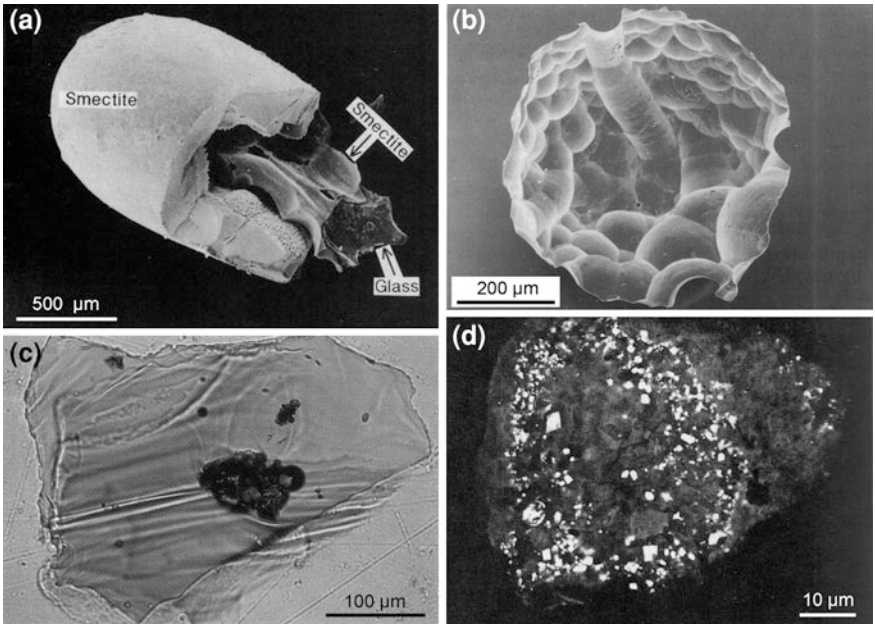

Fig. 5.15 Spherules and glass from the K-T boundary near Beloc, Haiti. **a** Scanning electron microscope (SEM) image of a fragment of a dumbbell or teardrop with a remnant black glass core. The shell is composed of smectite and there is a yellow smectite layer covering most of the glass core. **b** Black glass core from a spherical-shaped spherule (SEM image). Notice the scalloped appearance and U-shaped groove. Compare with the Ivory Coast microtektites in Fig. 3.9c, d. c) Optical microscope image (plane polarized light) of a fragment of yellow glass. The dark rounded inclusion ($\sim$100 µm long) is $CaSO_4$. d) An SEM image of a diagenetically-altered and deformed spherule from the top of the K-T boundary layer (Unit 3 of Jéhanno et al. 1992). The bright crystals are Ni-rich spinels. **a** is from Izett (1991b), Fig. 14b. **b** and **c** are from Bohor and Glass (1995), Fig. 7 and Plate Id, respectively, with permission of the Meteoritical Society © 1995. **d** is from Jéhanno et al. (1992), Plate 2f, with permission from Elsevier

DSDP Site 577 in the western Pacific (Smit 1990; Fig. 5.13c). According to Smit (1990) the clinopyroxene-dendritic textures are similar to the dendritic textures found in the K-feldspar spherules found in the K-T boundary layer sites in Europe. He, therefore, concluded that clinopyroxene dendrites are the precursor of the K-feldspar dendrites which formed pseudomorphically preserving the quench texture of the original clinopyroxene crystals.

Montanari et al. (1983) described black magnetic spherules, containing "magnetite" crystals, from the K-T boundary layer in Petriccio, Italy (Fig. 5.13d, f). They found that the magnetite-bearing spherules contain high Ir (69 $\pm$ 5 ppb). Smit and Kyte (1984) observed that the "magnetite" commonly occurs as skeletal crystals and less commonly as dendritic crystals in a translucent, brownish, Fe-rich groundmass, probably composed of hydrous Fe-oxides and clay minerals. They pointed out that these textures indicate rapid crystallization from a high-temperature melt. These authors also found high Ir contents in the magnetite-bearing spherules and they

observed that some had high Ni contents (up to 12 wt % NiO). Later it was recognized that the "magnetite" crystals found in the K-T boundary layer at Petriccio and other sites are spinels with a wide range in composition and textures. Most authors believe that the spinel crystals were derived primarily from the vaporized projectile (see Sect. 5.2.3.3). Thus, the occurrence of Ni-rich spinels in some K-T boundary spherules supports their impact origin.

Four compositional types of spherules are found at the K-T boundary in the Raton Basin, Colorado and New Mexico, USA: kaolinite, goyazite, layered goyazite/kaolinite, and jarosite (Izett 1987, 1990). The kaolinite spherules have a kaolinite core surrounded by a shell 5–10 μm thick composed of radially-oriented columnar kaolinite. Some of the goyazite spherules are solid and others are hollow with thick rims or outer shells (Izett 1987, 1990). The internal surface of the rims is mammillary. The third type of spherule has a kaolinite core surrounded by a thin ($\sim$10 μm) shell composed of translucent goyazite (Izett 1987, 1990). Again, the inner surface of the shell is mammillary. The fourth type of spherule is composed of jarosite (a hydrous iron sulfate mineral). These spherules are 10–50 μm in diameter and occur singly or in lenticular clusters (Izett 1987, 1990).

Bohor et al. (1987a) reported finding hollow spherules up to 1 mm diameter in a 3-cm-thick K-T boundary clay layer at Dogie Creek, Wyoming (Fig. 5.14). The walls of the spherules consist of goyazite (a hydrous alumino-phosphate mineral) and some are filled with gypsum (Fig. 5.14b). Similar large (up to 2.2 mm, average 1.24 mm) hollow splash-form spherules are found in the Gulf Coastal plain at Shell Creek, Alabama (Pitakpaivan et al. 1994; King and Petruny 2008). These spherules are composed of dark green (mostly smectite) clay with calcite cores. The spherules found at several Western Interior sites in North America, including the hollow spherules found at Dogie Creek, were interpreted as having an authigenic origin (Izett 1990).

Splash-form hollow spherules up to $\sim$10 mm in size are found in Beloc, Haiti (Izett 1991b). The shells of these spherules are composed of smectite. Some are filled with other phases, such as calcite. The Haitian spherules were originally interpreted as volcanic (Maurrasse et al. 1979), but were later reinterpreted as impact spherules by Hildebrand and Boynton (1990). An impact origin was supported by other researchers (e.g., Izett 1991b; Sigurdsson et al. 1991a; Bohor and Glass 1995). Some authors, however, continued to argue for a volcanic origin for these and other K-T boundary spherules (e.g., Jéhanno et al. 1992; Officer et al. 1992).

Sigurdsson et al. (1991a) reported that some of the spherules from Haiti contain relict glass cores (Fig. 5.15a, b). The relict glass cores in the Haitian spherules are generally black in reflected light. They are mostly spherical in shape, with diameters up to 6 mm; but ellipsoidal, teardrop, and dumbbell shapes are also present (Sigurdsson et al. 1991a). The black glass contains vesicles, but is devoid of microlites or crystals. However, yellow glass is also present and can be found as schlieren or streaks in the black glass, and the yellow glass does contain $CaSO_4$ inclusions (Fig. 5.15c) and microlites of melilite (Lyons and Officer 1992; Bohor and Glass 1995). The black glasses have andesitic to dacitic compositions and the yellow glasses are Ca-rich (with up to $\sim$28–30 wt % CaO; Table 5.3; Maurrasse and Sen

1991; Sigurdsson et al. 1991b; Izett 1991b; Jéhanno et al. 1992; Lyons and Officer 1992; Koeberl and Sigurdsson 1992; Bohor and Glass 1995).

Trace element studies (Koeberl and Sigurdsson 1992) indicate that the black glasses from Haiti have low Zn, As, Br, Cs, and U (Table 5.3) compared to the average composition of the upper continental crust, which has 52 ppm Zn, 1.3 ppm As, 1.6 ppm Br, 5.8 ppm Cs, and 2.5 ppm U (Wedepohl 1995). The yellow glasses not only have high CaO, MgO, and S contents compared with black glasses, they also have high Ni, As, Br, Sb, Au, and Ir contents. The high CaO and MgO contents are probably due to a carbonate component, while the sulfur probably came from evaporites (Sigurdsson et al. 1991b). The higher Ni, Au, and perhaps Ir contents, may be due to meteoritic contamination. The high variability in Ni, Ir, and Au could indicate variable amounts of meteoritic contamination, but at least part of the variability may be due to low precision because of small sample sizes (0.2–0.7 mg; Koeberl and Sigurdsson 1992). Both the black and yellow glasses have low Ga, As, Br, and Cs contents compared to those of the average upper continental crust. This may be attributed to volatilization due to the high temperature of formation.

Relict glass cores, with major oxide compositions similar to the major oxide compositions of the Haitian glasses, were found in some K-T boundary spherules from Mimbral in northeastern Mexico (Table 5.4; Smit et al. 1992a). Like the Haitian glasses, most of the Mimbral glasses are dark in color with andesitic to dacitic compositions, but CaO-rich glasses are also present. Glass fragments were also found at the K-T boundary in Deep Sea Drilling Project Sites 536 and 540 in the Gulf of Mexico. However, based on four analyses, these glasses appear to have higher Al_2O_3 and lower FeO, MgO, and CaO contents compared with the black Haitian and Mimbral glasses (Tables 5.3, 5.4; Sigurdsson et al. 1991a; Smit et al. 1992a; Alvarez et al. 1992; Koeberl and Sigurdsson 1992).

The age of the K-T boundary glasses and their major oxide, trace element, and isotopic compositions were important in identifying the source crater which is discussed below (Sect. 5.2.6).

Deutsch et al. (2010) have proposed that most of the calcite in K-T boundary spherules found at sites around the Gulf of Mexico is primary calcite from carbonate melt rather than secondary carbonate that replaced silicate glass after dissolution. Some spherules appear to be mixtures of primary calcite and silicate glass. Evidence for the calcite being primary rather than secondary includes, but is not limited to: the presence of very complicated spherule in spherule textures, the dull brick-red cathodoluminescence of the calcite, the occurrence of calcite blebs within silicate glass spherules, and feathery textures in calcite rims of silicate spherules.

Ni-rich spinel crystals do not occur in the hollow spherules found in the Western Interior of North America or other nearby locations. This and other differences indicate that there are two major kinds of K-T boundary spherules: 1) larger (up to 1 mm or more) splash-form spherules that are often hollow (Fig. 5.14) and do not contain Ni-rich spinel crystals, and 2) generally smaller (0.1–0.5 mm) oblate spheroid- to discoid- or lens-shaped spherules that often have crystalline textures

Table 5.3 Major and minor oxide contents (wt %) and trace element contents (ppm except where noted) of Haitian K-T boundary glasses

	Black[a]		Yellow[a]		Black[b]		Yellow[b]	
Oxide	Average (11)	S.D.	Average (7)	S.D.	Average (74)	S.D.	Average (13)	S.D.
SiO_2	63.29	1.09	48.73	0.71	64.29	2.1	46.76	1.7
TiO_2	0.68	0.03	0.64	0.01	0.65	0.07	0.61	0.07
Al_2O_3	15.33	0.20	13.25	0.41	15.21	0.30	12.50	0.81
FeO	5.27	0.17	4.98	0.06	4.79	0.34	4.42	0.19
MgO	2.55	0.16	4.02	0.14	2.67	0.21	4.27	0.15
CaO	7.21	0.82	24.71	1.10	6.52	1.2	27.00	2.7
Na_2O	3.72	0.33	2.54	0.20	3.56	0.29	2.36	0.30
K_2O	1.62	0.09	0.7	0.08	1.58	0.12	0.62	0.12
M_nO	0.17	0.01	0.15	0.00	n.d.		n.d.	
SO_3	<0.01		0.55	0.17	0.10	0.05	0.83	0.05
Sc	20.59	0.79	21.34	0.82				
Cr	27.63	2.48	29.7	10.9				
Co	14.77	0.97	22.74	3.53				
Ni	22	13	285	135				
Zn	27.1	11.5	74.3	14.2				
Ga	11.8	2.8	6.5	1.3				
As	0.13	0.05	0.65	0.22				
Br	0.12	0.06	1.40	0.58				
Rb	59.2	8.76	25.6	3.16				
Sr	401	147	704	325				
Zr	166	36	199	42				
Sb	0.28	0.07	2.6	0.82				
Cs	1.57	0.3	2.43	0.65				
Ba	503	263	974	1122				

(continued)

Table 5.3 (continued)

	Black[a]		Yellow[a]		Black[b]		Yellow[b]	
Oxide	Average (11)	S.D.	Average (7)	S.D.	Average (74)	S.D.	Average (13)	S.D.
La	22.41	1.78	17.81	1.11				
Ce	46.30	4.42	35.83	5.07				
Nd	24.47	2.49	19.95	7.28				
Sn	5.23	0.32	4.12	0.16				
Eu	1.52	0.12	1.17	0.22				
Gd	5.11	0.26	4.28	1.96				
Tb	0.89	0.06	0.78	0.05				
Dy	5.39	0.25	4.78	1.70				
Tm	0.47	0.03	0.46	0.21				
Yb	3.20	0.23	2.78	0.45				
Lu	0.45	0.04	0.36	0.05				
Ta	0.33	0.14	0.66	0.25				
Ir (ppb)	<2	0	2	1				
Au (ppb)	1.80	0.90	11.5	6.1				
Th	6.36	0.72	5.08	0.82				
U	1.10	0.27	1.24	0.26				

S.D. = standard deviation; n.d. = no data; numbers in parentheses are number of analyses; all iron given as FeO

[a] Major and minor oxide contents by electron microprobe and trace element contents by INAA analyses (Koeberl and Sigurdsson 1992)

[b] Electron microprobe analyses (Sigurdsson et al. 1991b)

Table 5.4 Major and minor oxide compositions (wt %) of K-T boundary glasses from Mimbral (NE Mexico) and DSDP Sites 536 and 540, clinopyroxene spherules, and Chicxulub melt rock

Oxide	Mimbral Glasses[a]				DSDP Sites 536 and 540 Glasses[b]	Clinopyroxene Spherules[c]		Chicxulub Melt Rock[d]	
	Black		Ca-rich Glass	K-rich Glass					
	Average	S.D.			(4)	Average (13)	S.D.	Average (4)	S.D.
SiO_2	62.99	1.55	52.2	66.20	60.41–70.40	46.3	0.7	61.3	0.93
TiO_2	0.7	0.09	0.56	0.02	0.01–0.13	0.35	0.06	0.41	0.05
Al_2O_3	15.73	0.63	12.4	18.73	19.32–21.58	4.91	0.97	15.0	0.8
FeO	5.32	1.48	4.73	5.67	0.09–0.79	9.79	0.92	4.01	0.64
MgO	3.01	0.58	3.9	2.64	0.05–0.19	11.68	0.29	3.03	0.26
CaO	6.88	1.87	22.96	0.84	0.26–4.97	23.13	0.26	8.36	1.42
Na_2O	3.32	0.32	2.02	0.84	0.84–4.32	0.66	0.23	5.32	0.53
K_2O	1.5	0.37	0.58	3.68	2.96–10.21	0.07	0.02	2.23	0.38
MnO	0.13	0.08	0.14	0.00	0.03–0.06	n.d.		0.10	0.02
P_2O_5	n.d.		n.d.		n.d.	0.49	0.33	0.09	0.02
Cr_2O_3	0.05	0.02	n.d.		n.d.	0.1	0.04	n.d.	
NiO	0.03	n.d.	0.02	n.d.	n.d.	0.59	0.08	n.d.	

S.D. = one standard deviation; numbers in parentheses are number of analyses; n.d. = no data
All iron reported as FeO

[a] Electron microprobe analyses (Smit et al. 1992a)

[b] Electron microprobe analyses (Alvarez et al. 1992)

[c] Average of 13 analyses for five clinopyroxene-bearing spherules from Site 577A in the North Pacific. Iron originally reported as Fe_2O_3 and FeO (Smit et al. 1992b)

[d] Electron microprobe analyses (Kettrup et al. 2000)

(Fig. 5.13) and/or contain Ni-rich spinel crystals (Figs. 5.13 and 5.15d; Bohor and Betterton 1990; Smit 1990; Bohor and Glass 1995). It has been proposed that the larger splash-form spherules are diagenetically-altered microtektites and that the smaller spherules, which often contain Ni-rich spinel crystals and have relict dendritic textures, are diagenetically-altered microkrystites (Smit 1999). The larger, splash-form spherules are most common in and adjacent to North America, whereas the smaller spherules with crystalline textures are more common outside of North America, but may be distributed globally (Kyte et al. 1996). Furthermore, the larger splash-form spherules occur in a thicker layer (up to a meter or more) below a clay layer which contains an Ir anomaly and more abundant shocked mineral grains.

The lower layer, containing the splash-form spherules, has been referred to as the melt ejecta layer (Pollastro and Bohor 1993; Bohor and Glass 1995) and the spherules are interpreted as originally being composed of glass quenched from melted target rock. The smaller spherules with crystalline textures occur in a thinner Ir-rich layer, which has been called the fireball layer (Hildebrand and Boynton 1990; Pollastro and Bohor 1993). These spherules may have formed by condensation of vaporized projectile and target rock (Smit et al. 1992b; Bohor and Glass 1995). Their compositions and corresponding textures were determined, at least in part, by the composition of the projectile as well as that of the target rocks.

The composition and texture of the microkrystites at any given site may also be controlled by the place of condensation within the ejecta vapor plume or cloud and oxygen fugacity (Smit et al. 1992b). Reheating on reentry into the atmosphere may also play a role in determining the final texture. The splash-form spherules are probably melt-drop microtektites and the crystalline spherules, many containing Ni-rich spinels, are probably condensate spherules as defined in Sect. 3.2.1.1.

The dual nature of the K-T boundary layer and segregation of the spherule types is well represented at the Beloc, Haiti, sites. On Haiti, the lower spherule layer contains splash-form spherules up to a centimeter or more in size and is up to at least 30 cm thick. Above this spherule layer, there is a grayish-green clay layer that contains high concentrations of Ir, Ni-rich spinels, and shocked quartz (Fig. 5.5; Hildebrand and Boynton 1990; Jéhanno et al. 1992). According to Jéhanno et al. (1992), the Ni-rich spinel crystals occur in spheroidal bodies (microkrystites) up to 200 μm in diameter (Fig. 5.15d).

Although the majority of researchers now accept the impact origin for most of the K-T boundary spherules, some researchers have proposed other origins for some K-T boundary spherules such as: biogenic (Hansen et al. 1986; Schmitz et al. 1988), authigenic/weathering (Brooks et al. 1985; Izett 1990), and volcanic (Naslund et al. 1986; Jéhanno et al. 1992; Officer and Lyons 1993). Nearly all the K-T boundary spherules have been diagenetically altered and most of the glass that might have been originally present has been dissolved or replaced by another phase. Thus, it is difficult to prove that they have an impact origin. Hansen et al. (1986) dissolved some K-feldspar spherules in hydrofluoric acid and recovered organic remains of prasinophyte algae. They concluded that the K-feldspar spherules were formed as authigenic infills of prasinophyte algae. However, Smit et al. (1992b) repeated their experiment and found no traces of organic remains. They concluded that the K-feldspar spherules had a strictly mineralogic origin and suggested that the organic structures reported by Hansen et al. (1986) were probably due to biological contamination of the shallow outcrop where the samples were obtained. On the other hand, many of the goethite spherules found at some K-T boundary sites may have formed by weathering/alteration and overgrowth of pyrite framboids, which are a common authigenic bacterial product found in sediments under anoxic conditions (Schmitz et al. 1988; Smit et al. 1992b; Brooks et al. 1985).

Although some authors have concluded that the Haitian spherules have a volcanic origin, studies of the glass cores found in some of the Haitian spherules support an impact origin for these spherules. In contrast to volcanic glass which generally contains several weight percent water, these Haitian glasses have low water contents (<0.05 wt % water) like impact glasses (Koeberl 1992b; Claeys et al. 1993; Oskarsson et al. 1996). Sigurdsson et al. (1991b) concluded from comparison with experimental glasses, that the Haitian glasses were quenched from temperatures much higher than is common for volcanic processes. Major oxide and sulfur contents and oxygen isotope ratios of the Haitian glasses indicate that they are a mixture of carbonate and silicate rocks and the data exclude a volcanic origin for these glasses (Blum and Chamberlain 1992). Furthermore,

osmium isotopic data for a sample of Haitian glass indicates the presence of a small meteoritic component (Koeberl et al. 1994). Thus, geochemical data support an impact origin for the Haitian glasses and spherules and, by analogy, for similar K-T boundary spherules found in northeastern Mexico, the Western Interior of North America, and elsewhere. In addition, the presence of Ni-rich spinel crystals in many K-T boundary spherules found almost worldwide, supports an impact origin for those spherules as well.

Many authors have referred to the K-T boundary spherules as a whole, or just the larger spherules without crystalline textures or Ni-rich spinels, as microtektites, microtektite-like, or even tektites (Smit and Romein 1985; Hildebrand and Boynton 1990; Izett 1991b; Alvarez et al. 1992; Smit et al. 1992a; Claeys et al. 1993; Smit 1999; Campbell et al. 2008; King and Petruny 2003). As most of the glass originally present has generally been removed by dissolution or replaced by a mineral phase or phases (e.g., K-feldspar, smectite, glauconite, calcite, goyazite, gypsum, chlorite), confirmation that spherules at a given site were originally microtektites is generally not possible. The smaller K-T boundary spherules with crystalline textures that most authors interpret as being preserved original textures, and which generally contain Ni-rich spinel crystals, cannot be microtektites and are generally agreed to be altered microkrystites. On the other hand, the generally larger (often hollow) spherules, without evidence of crystalline textures and which do not contain spinel crystals, could be altered microtektites.

Even for the spherules containing relict glass, there is disagreement about whether or not they are microtektites (or minitektites since they are often larger than a millimeter). Cenozoic tektites and microtektites are generally silica rich with SiO_2 contents >66 wt % and most contain abundant lechatelierite particles, whereas the relict glass particles found at Haiti and Mimbral generally have SiO_2 contents <68 wt % (Tables 5.3, 5.4) and none contain lechatelierite particles. However, there is overlap in silica content and some Cenozoic microtektites (e.g., the high-Mg or bottle-green Australasian microtektites) do not contain lechatelierite particles. If quartz grains are not present in the target rock, then lechatelierite particles cannot be formed; so the absence of lechatelierite, by itself, is not a reason to conclude that the Haitian and Mimbral spherules are not microtektites. The water content of the Haitian glass (determined by infrared spectroscopy) is 0.013–0.021 wt % (Koeberl 1992b; Koeberl and Sigurdsson 1992). This is within the range of water contents of tektites, which have water contents below 0.05 wt %. However, the Haitian glass is apparently much more oxidized than tektites (Oskarsson et al. 1996; Giuli et al. 2008). The iron oxidation state of the black glasses ranges from ~20 to 75 mol % Fe^{3+} (Giuli et al. 2005), and the yellow glasses have 75–100 mol % Fe^{3+}. Cenozoic tektites, on the other hand, generally have <15 mol % Fe^{3+}. In addition, some of the black glasses contain regions of yellow glass with low silica and high CaO contents (Table 5.3). The yellow glasses contain melilite crystals (Lyons and Officer 1992; Bohor and Glass 1995). By definition, tektites and microtektites do not contain primary crystals. Thus, it is probably better to refer to the K-T boundary spherules with glass cores as impact

spherules rather than as microtektites, although they are microtektite-like in many respects.

Smit (1999) estimated that the abundance of microkrystites ($\sim$250 μm in mean size) at Agost and Caravaca (Spain) and Tetri-Tskaro (Republic of Georgia) is approximately 20,000 microkrystites per square centimeter. The total number of microkrystites, assuming a global coverage of similar abundance, is 1×10^{23} or a volume of $\sim$850 km^3 deposited in distal sites alone (Smit 1999).

Smit et al. (1992b) pointed out that the smectite spherules found at DSDP Site 603 in the northwest Atlantic and the goyazite spherules found at Dogie Creek, Wyoming, have mammillary features, banding parallel to outer surfaces, and internal cracks resembling textures found in palagonite. Bohor and Glass (1995) proposed that the hollow nature of the large splash-form spherules was due to palagonitization of the outer layer of glass that occurred when the spherules landed in water while still hot. During later diagenesis the palagonite rims were altered to smectite, glauconite, chlorite, kaolinite, goyazite or some other phase, while the glass cores were generally removed by dissolution. The interiors remained hollow or were filled with another phase.

Accretionary lapilli have been reported from several K-T boundary sites including: Guayal, southeastern Mexico (Salge et al. 2000; Burns et al. 2003; Dubron et al. 2006; Salge 2007); northeastern Mexico (Schulte and Kontny 2005); Brazos River, Texas, and Bass River, New Jersey, USA (Yancey and Guillemette 2008); and central Cuba (Alegret et al. 2005). The K-T boundary deposit at Guayal contains a 9–10-m-thick fining-upward siltstone and very fine-grained sandstone unit that overlies a 35–40-m-thick fining-upward carbonate mega breccia unit. Approximately 2 m below the top of the upper 9–10-m-thick unit is a 50–90-cm-thick siltstone bed containing abundant accretionary lapilli associated with rare shocked mineral grains (Burns et al. 2003; Dubron et al. 2006; Salge 2007). The lapilli have a gray waxy appearance on sawed or broken surfaces. They are rounded to flattened in shape with the long axis lying parallel to bedding. The lapilli are the largest objects in the layer with average dimensions of $0.8 \times 1.1 \times 1.4$ cm based on measurements of 24 of the lapilli (Burns et al. 2003). They appear to largely have been replaced with diagenetic chert, but they still retain a concentric layered structure around a small core composed of quartz or a lithic fragment. The layers tend to alternate between finer and coarser textures.

Accretionary lapilli found in the K-T boundary layer in northeastern Mexico have rounded shapes and range from 0.5 to >2 mm in diameter (Fig. 5.16; Schulte and Kontny 2005). They exhibit concentric layers composed of fine-grained carbonate and clayey particles. Each layer can have a slightly different grain size and color than the other layers, which suggests multiple episodes of accretion (Schulte and Kontny 2005). Some of the accretionary lapilli contain distinct cores consisting of limestone fragments or calcite aggregates, or spherule fragments.

In addition to clay spherules believed to be altered microtektites/microkrystites, rounded particles with carbonate composition and aggregate-like accretionary fabric are found in the K-T boundary layer at Brazos River, Texas, and Bass River, New Jersey (Schulte et al. 2006; Yancey and Guillemette 2008). The accretionary

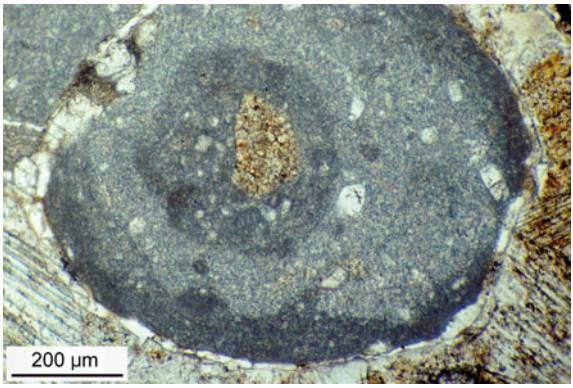

Fig. 5.16 Optical microscope photomicrograph (plane polarized light) of a thin section showing a spherule with an accretionary internal structure. This sample is from the K-T boundary layer at La Sierrita, northeast Mexico. Note the presence of a core ($\sim$200 μm long) and at least three concentric layers. Image provided by Peter Schulte and was published in Schulte and Kontny (2005), Fig. 6f

particles have a similar size range to the clay spherules. An impact origin for the carbonate particles is indicated by their co-occurrence with other impact ejecta and the fact that the occurrence is restricted to the K-T boundary layer. In addition, these particles have microgranular accretionary fabric comparable to that of large carbonate accretionary lapilli reported from ejecta deposits near the Chicxulub impact structure and in the Late Devonian Alamo impact deposit (Yancey and Guillemette 2008). At Brazos River, carbonate accretionary lapilli make up $\sim$25 % of the coarse fraction in the ejecta layer. They range in size from 0.5 to 3 mm in diameter; most have a diameter of 1–2 mm. Internally, the lapilli exhibit little zoning or banding other than a darker outer rim. Similar carbonate accretionary lapilli are found in the K-T boundary layer at Bass River. Both the Brazos River and Bass River accretionary lapilli are composed of micrometer-sized low-Mg calcite with an elevated sulfur content (Yancey and Guillemette 2008).

Alegret et al. (2005) stated that accretionary lapilli are found in the K-T boundary layer in Loma Capiro, central Cuba, but no description of the lapilli was given. They did show an image of one accretionary particle that is $\sim 1.2 \times 1.6$ mm in size and shows some concentric structure with a dark rim. According to Dubron et al. (2006), the accretionary lapilli at Loma Capiro are composed of pure carbonate.

5.2.3.3 Ni-Rich Spinel Crystals

Ni-rich spinel crystals appear to be globally distributed in K-T boundary sediments, where they generally occur in diagenetically-altered spherules (Kyte and Smit 1986; Bohor et al. 1986; Zhou et al. 1991). At some sites they have been recovered as individual crystals in the silt-sized fraction. However, the majority, if not all the spinel crystals in the silt-sized fraction were probably derived from spherules that were destroyed by diagenesis or sample processing. They were originally labeled magnetites (Montanari et al. 1983), then spinels (Kyte and Smit 1986), and magnesioferrites (Bohor et al. 1986). The spinels have a wide range in composition as discussed below. The Ni-rich spinels are generally confined to the

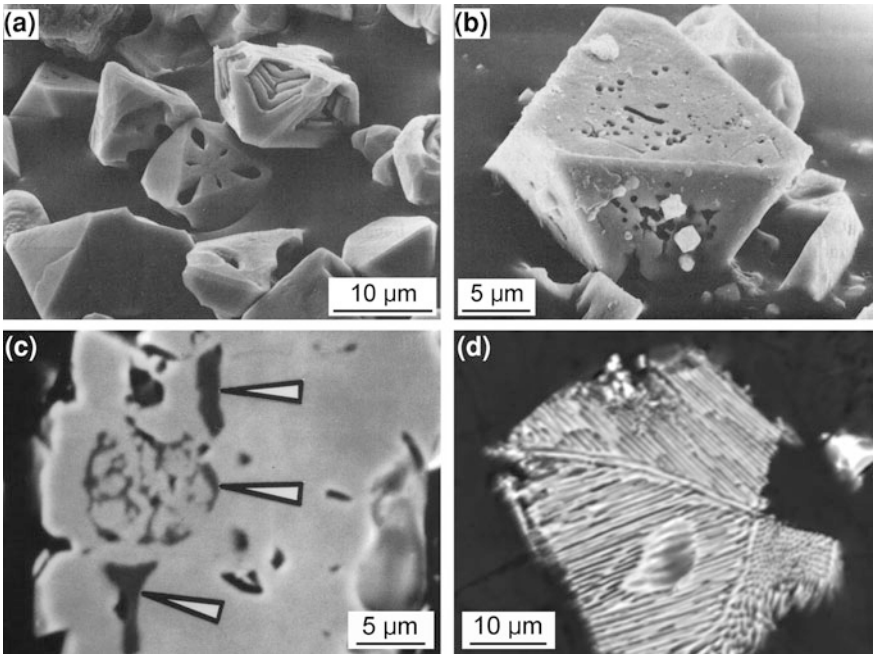

Fig. 5.17 Scanning electron microscope images of spinel crystals recovered from the K-T boundary layer or in polished sections of K-T boundary spherules. **a** Skeletal Ni-rich spinels (magnesioferrite) from the K-T boundary layer in Caravaca, Spain. **b** Ni-rich spinel (magnesioferrite), with octahedral morphology, from Caravaca, Spain. **c** Nickel-rich magnesiowüstite inclusions (indicated with *arrows*) in Ni-rich magnesioferrite (spinel) from DSDP Site 596 in the Pacific. **d** Ni-rich spinel with tube-shaped voids recovered from the K-T boundary layer at Ocean Drilling Program Site 596 in the South Pacific. **a** and **b** are from Bohor et al. (1986), Figs. 5b and d, respectively. **c** and **d** are courtesy of F. Kyte

Ir-rich layer at the K-T boundary, but often have a more restricted vertical distribution (Robin et al. 1991). They vary in size from <5 μm up to 50 μm (Bohor et al. 1986; Zhou et al. 1991; Jéhanno et al. 1992; Rocchia et al. 1992; Kyte et al. 1995). At DSDP Site 596 in the South Pacific Ni-rich spinel crystals are also found in clusters or aggregates up to 100 μm in size (Zhou et al. 1991). At this site, the number of spinel grains and clusters >30 μm is $\sim$1500/cm^2 (Zhou et al. 1991).

The K-T boundary Ni-rich spinels exhibit a wide range in crystal morphology (Fig. 5.17) and composition. They generally occur as subhedral to euhedral, frequently skeletal, octahedral crystals, but can also occur in dendritic form (Bohor et al. 1986; Kyte et al. 1996; Jéhanno et al. 1992). These morphologies indicate rapid crystallization and cooling from a high-temperature melt (Bohor et al. 1986; Kyte et al. 1995; Quitté et al. 2007). In the Pacific Ocean sites, the larger Ni-rich spinels often occur as irregular-shaped, porous grains in which the voids are sometimes elongate and tube-like (Fig. 5.17d; Kyte et al. 1996). These textures suggest myrmektic intergrowth of spinel with a preexisting phase that may have been magnesiowűstite (see below) (Kyte and Bostwick 1995).

Table 5.5 Major and minor oxide contents (wt %) and Fe^{3+}/Fe_T for Cretaceous-Tertiary spinels and magnesiowüstite inclusions

	Spinel					
	Furlo, Italy		Caravaca, Spain		S. Atlantic (Site 524)	
	(126)		(19)		(4)	
	Average	Range	Average	Range	Average	Range
SiO_2	0.01	0.00–0.07	0.09	0.05–0.16	0.02	0.01–0.03
TiO_2	0.51	0.18–3.56	0.35	0.25–0.82	0.40	0.26–0.58
Al_2O_3	3.40	0.43–10.21	6.62	4.17–9.02	2.25	0.82–4.08
Cr_2O_3	0.65	0.07–5.50	11.16	3.87–24.93	0.61	0.55–0.69
Fe_2O_3	68.50	58.72–72.10	55.23	38.82–63.07	67.41	66.91–67.86
FeO	9.78	2.05–31.98	9.41	2.38–20.09	12.97	7.15–16.66
MnO	1.15	0.24–2.55	0.27	0.16–0.52	1.64	1.01–2.16
MgO	9.94	0.01–17.92	12.52	5.32–17.67	7.40	4.35–11.13
NiO	5.50	0.82–10.17	3.67	2.92–5.84	4.56	3.42–6.11
CaO	0.32	0.00–0.72	0.10	0.05–0.18	0.49	0.35–0.64
Total	99.76		99.42		97.75	
Fe^{3+}/Fe_T	0.86		0.84		0.82	
	Spinel				Magnesiowüstite	
	Indian Ocean (ODP 761)		Pacific sites		DSDP 577 and 596	
	(13)		(432)		(4)	
	Average	Range	Average	Range	Average	Range
SiO_2	0.12	0.06–0.18	0.09	0.00–0.94	0.24	0.02–0.47
TiO_2	0.25	0.17–0.39	0.34	0.02–1.61	0.02	0.00–0.05
Al_2O_3	4.68	3.88–5.55	13.27	1.00–42.71	0.65	0.03–1.88
Cr_2O_3	1.46	0.67–2.62	0.69	0.00–6.63	0.20	0.07–0.28
Fe_2O_3	72.92	72.06–74.05	62.34	29.86–75.07	n.d.	
FeO	1.38	0.45–2.27	1.60	0.00–11.29	14.25	7.00–25.18
MnO	0.35	0.22–0.48	0.52	0.20–3.77	0.14	0.06–0.24
MgO	15.32	13.27–16.88	18.96	9.36–24.75	70.64	60.53–75.89
NiO	3.72	2.02–5.07	1.82	0.00–13.14	13.60	8.89–17.67
CaO	0.23	0.16–0.38	0.64	0.00–2.67	0.13	0.02–0.33
Total	100.43		100.27		99.87	
Fe^{3+}/Fe_T	0.98		0.97		n.d.	

Fe_T = total iron; n.d. = no data; numbers in parentheses are numbers of analyses
Pacific sites include: DSDP 576, 577, and 596; ODP 803 and 886, and Core LL44-GPC3
Data for spinels are from Kyte and Bostwick (1995) and data for magnesiowüstite are from Kyte and Bohor (1995). DSDP Sites 577 and 596 are in the Pacific Ocean

Compositional data indicate that the K-T boundary spinels have a wide range in major element composition (Table 5.5; Smit and Kyte 1984; Kyte and Smit 1986; Bohor et al. 1986; Jéhanno et al. 1992; Kyte and Bohor 1995; Kyte and Bostwick 1995). The Al_2O_3 contents range from <1 up to ~43 wt %, Fe_2O_3 varies from ~30 up to ~75 wt %, FeO varies between <1 up to ~32 wt %, MgO

Table 5.6 Normative compositions (mol %) of Cretaceous-Tertiary boundary spinels

Spinel end members	S. Atlantic Site 524 (7)	Caravaca, Spain (23)	Furlo, Italy (114)	Petriccio, Italy (10)	North Pacific GPC-3 (10)	North Pacific Site 577 (48)
Magnetite	38.0	17.8	25.4	19.1	2.9	0.0
Magnesioferrite	40.9	45.6	49.8	52.9	65.7	56.8
Trevorite	13.3	10.1	15.5	10.6	3.6	3.4
Ulvöspinel	1.1	1.1	1.4	0.0	1.8	0.7
Hercynite	2.8	3.8	2.4	3.6	1.1	0.0
Spinel	3.1	9.8	4.6	10.0	24.6	38.9
Chromite	0.4	3.3	0.3	1.0	0.0	0.0
Magnesiochromite[a]	0.4	8.5	0.6	2.8	0.3	0.2

Data from Robin et al. (1992). Number in parentheses is number of analyses. Sites 524 and 577 are Deep Sea Drilling Project sites. GPC-3 = LL44-GPC3 (giant piston core 3)
[a] Also called picochromite

varies between <1 up to 25 wt %, Cr_2O_3 varies from <0.1 up to ~25 wt %, and SiO_2, TiO_2, MnO, and CaO are generally all <1–2 wt %. Most of the K-T boundary spinel crystals, regardless of where they are found, have relatively high nickel contents (up to ~13 wt %; Kyte and Bostwick 1995). Bohor et al. (1986) reported 29 ± 11 ppb Ir in spinels from the K-T boundary at Caravaca, Spain.

The compositions of the K-T boundary layer spinels vary geographically. This variation in composition is reflected in their normative compositions (Table 5.6). The normative compositions of spinels from European and the South Atlantic K-T boundary sites indicate that magnesioferrite ($MgFe_2O_4$) is the most abundant spinel phase, followed by magnetite (Fe_3O_4). Magnesioferrite is also the most abundant spinel phase in the Pacific sites, but the second most abundant phase is $MgAl_2O_4$ spinel (Table 5.6; Robin et al. 1992). Other spinel phases present at most sites, in decreasing order of abundance, include: trevorite ($NiFe_2O_4$), hercynite ($FeAl_2O_4$), magnesiochromite ($MgCr_2O_4$), ulvöspinel (Fe_2TiO_4), and chromite ($FeCr_2O_4$) (Robin et al. 1992). At Caravaca, Spain, a trevorite-Ni chromite ($NiFe_2O_4$-$NiCr_2O_4$) component is also present (Bohor et al. 1986). K-T boundary magnesioferrites have high Fe_2O_3/FeO ratios, high concentrations of Ni, and low contents of Ti and Cr, which distinguish them from terrestrial spinels (Kyte et al. 1996). The Pacific K-T boundary spinels have generally higher average MgO and Al_2O_3 contents and higher average Fe_2O_3/FeO ratios than those from most other K-T boundary sites around the world (Kyte and Bohor 1995). This is reflected in the normative compositions and the Fe^{3+}/Fe_{total} (%) of the K-T boundary spinels (Tables 5.5, 5.6).

Ni-rich magnesiowüstite (Fig. 5.17c) occurs within some spinels recovered from the K-T boundary sediments at DSDP Sites 596 and 577 in the South Pacific and North Pacific, respectively (Kyte and Bohor 1995). This phase has a range in composition from $(Mg_{0.85}Ni_{0.11}Fe_{0.04})O$ to $(Mg_{0.74}Ni_{0.09}Fe_{0.17})O$. Coexisting magnesioferrite and magnesiowüstite can only crystallize from ultramafic, refractory, Mg-rich liquids with Mg/Si >2 (atom ratio). Such liquid compositions are

unknown to form in terrestrial igneous processes or during meteorite ablation (Kyte and Bohor 1995). Kyte and Bohor (1995) infer that the magnesiowüstite crystallized from liquid droplets that equilibrated with silicate vapor at high temperatures (probably >2300° C).

It is generally agreed that the K-T boundary Ni-rich spinels and, therefore, the spinel-bearing spherules were formed by an impact; however, the specific processes which formed the Ni-rich spinel crystals have been a matter of debate. The two main hypotheses are that the spinels crystallized in ablation melt debris from the projectile(s) or in silicate melt droplets condensed from the impact vapor cloud (Kyte and Smit 1986; Robin et al. 1993; Kyte and Bohor 1995; Kyte and Bostwick 1995; Gayraud et al. 1996). Based on the spinel textures and chemical compositions (e.g., Ni and Ir contents), Robin et al. (1992, 1993) concluded that the K-T boundary spherules are ablation debris. However, Kyte and Bohor (1995) pointed out that there is dissimilarity in spinel composition between known meteorite ablation debris and the Pacific K-T boundary spinels. They also pointed out that the meteorite ablation model is inconsistent with the observation that the composition and texture of the Pacific K-T boundary spinels represent a broad regional trend, rather than localized phenomenon. Furthermore, Kyte and Bohor (1995) stated that the formation of magnesiowüstite in the cores of some magnesioferrite crystals from two Pacific Ocean sites required a liquid composition that is not known to occur in meteoroid ablation melt.

5.2.3.4 Shock Metamorphosed and Shock Produced Mineral Grains

5.2.3.4.1 Shocked Quartz and Feldspar

Bohor et al. (1984) discovered shocked quartz and shocked K-feldspar grains with multiple sets of planar deformation features (Fig. 5.18) in sediments from the K-T boundary layer at Brownie Butte, Montana, USA. They also indicated that shocked quartz had been found in K-T boundary sediments in New Mexico, USA, and in Denmark and Italy. Bohor et al. (1984) demonstrated that the planar features are related to specific crystallographic planes in the quartz lattice (Fig. 5.19). In addition, they documented that the shocked quartz grains exhibit X-ray asterism and have low refractive index, which is further evidence that these grains have been shock metamorphosed. These data provided confirmation of an impact at the end of the Cretaceous Period as had been proposed by Alvarez et al. (1980) 4 years earlier. In addition, the shocked quartz and K-feldspar indicated that the impact probably took place on continental, rather than oceanic, crust as had previously been suggested by several researchers based on the relict textures of the spherules and their isotopic and trace element contents (e.g., Montanari et al. 1983; DePaolo et al. 1983). Later studies documented the worldwide distribution of shocked quartz in the K-T boundary layer and found that the largest shocked quartz grains occur in the North American Western Interior (Bohor and Izett 1986; Bohor et al.

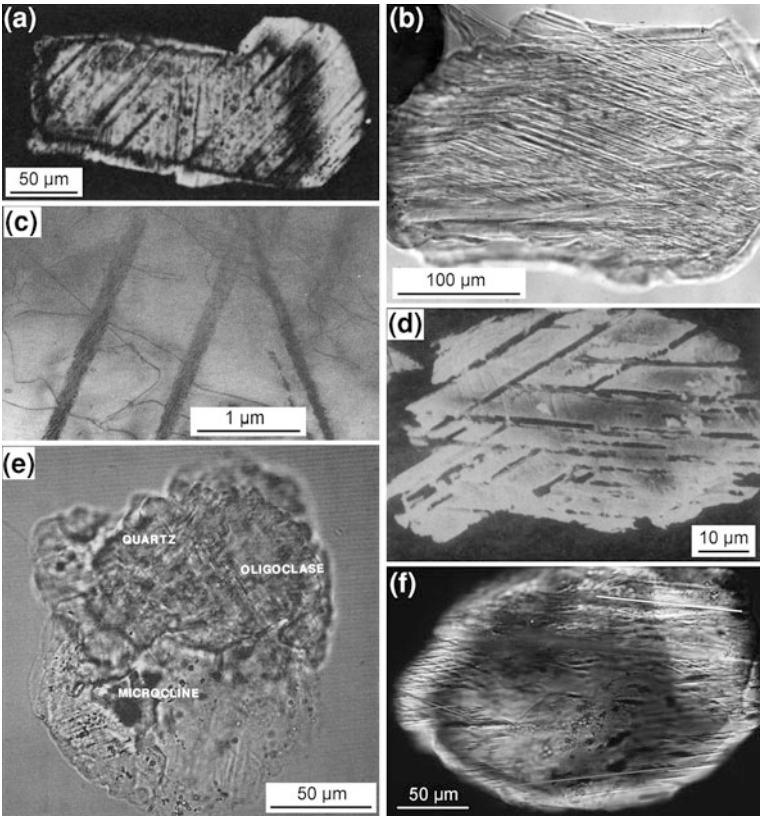

Fig. 5.18 Shocked mineral grains with multiple sets of planar deformation features (PDFs) from the K-T boundary layer. **a** Optical microscope image (polarized light) of shocked quartz grain, with two well-defined sets of PDFs, from near Beloc, Haiti. **b** Optical microscope image (polarized light) of shocked quartz, with three prominent sets of PDFs, from near Beloc, Haiti. **c** Transmission electron microscope image of shocked quartz grain, showing two sets of PDFs (dark bands <0.2 µm across), from near Beloc, Haiti. **d** Scanning electron microscope image of an HF-etched quartz grain, with two sets of PDFs (*dark bands*), from Brownie Butte, Montana. **e** Optical microscope image (plane polarized light) of a shocked rock fragment composed of quartz, oligoclase, and microcline. Faint PDFs can be seen in the quartz and oligoclase. This grain was found in the K-T boundary layer at Clear Creek North, ~10 km south of Trinidad, Colorado. **f** Optical microscope image (polarized light) of a shocked oligoclase grain, with two sets of PDFs, from Brownie Butte, Montana. The white line near the top shows the orientation of albite twins. Two gray lines at the extreme left and one near the bottom show the orientation of the PDFs. **a** is courtesy of G. Izett (this image was published in Hildebrand and Boynton, 1990, Fig. 2a). **b** is courtesy of G. Izett (it was published in Izett, 1991b, Fig. 2). **c** is from Leroux et al. (1995a), Fig. 1b, republished with permission of Elsevier. **d** is from Bohor et al. (1984), Fig. 1a. **e** is from Izett (1990), Fig. 36. **f** is from Izett (1990), Fig. 37a

1987b). By 2002, shocked quartz grains had been reported at ~40 K-T boundary sites around the world (Claeys et al. 2002, and references therein).

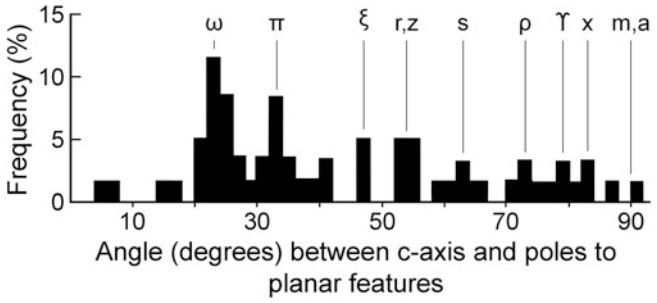

Fig. 5.19 Orientation of 61 sets of planar deformation features (PDFs) in 15 quartz grains from Brownie Butte, Montana. Some grains have as many as seven sets of PDFs. The plot demonstrates that the planar features are related to specific crystallographic directions in quartz and supports the conclusion that the planar features are shock lamellae or PDFs. Modified after Bohor et al. (1984), Fig. 2

Numerous researchers have mentioned the size of the largest shocked quartz grain found in the K-T boundary layer at a given site, but the most comprehensive studies have been by Bohor and Izett (1986), with a few additions by Izett (1990), and Morgan et al. (2006). Morgan et al. (2006) identified shocked quartz grains two different ways: 1) by optical microscopy and 2) by scanning electron microscopy. The samples used in the optical microscope studies involved large samples (50–400 g) from each K-T boundary site, but the samples used in the scanning electron microscope studies involved much smaller samples (0.5–8 g). In most cases, for a given site they found smaller maximum size for the shocked quartz in the smaller samples. This indicates that care must be taken in comparing the maximum size of shocked quartz grains between sites involving different sample sizes or number of quartz grains. With that caveat in mind, it appears that the largest shocked quartz grains are found in the Western Interior of North America where, according to Bohor and Izett (1986) and Izett (1990), the maximum size at different sites ranges between 480 and 560 μm.

In Europe the maximum size of shocked quartz grains is smaller, usually between 150 and 190 μm. Bohor and Izett (1986) studied only one Pacific Ocean site (Core LL44-GPC3) where they found the largest shocked grain to be 160 μm. This is smaller than the maximum sizes found for North American Western Interior sites, but comparable to the maximum sizes found for European sites. Bostwick and Kyte (1996) determined the maximum size of shocked quartz grains in the K-T boundary layer in six other sites from the Pacific and also found them to be smaller than the maximum size of shocked quartz in the Western Interior of North America, but comparable in size to the shocked quartz at the European sites. On the other hand, Morgan et al. (2006) reported maximum sizes of shocked quartz grains ranging from 40 to 120 μm for three Pacific sites. The site (ODP Site 1209) for which they reported a maximum size of 40 μm for the shocked quartz grains had not been studied previously, but the other two sites (LL44-GPC3 and

ODP 803) had been studied by Bostwick and Kyte (1996). In both cases, Morgan et al. (2006) reported smaller maximum sizes than did Bostwick and Kyte (1996).

There have been two quantitative studies of the abundance of shocked quartz grains with PDFs at a number of K-T boundary sites (Bostwick and Kyte 1996; Morgan et al. 2006). Bostwick and Kyte (1996) and Kyte et al. (1996) studied seven K-T boundary sites in the Pacific and determined the concentration (number/gram) of shocked quartz grains and found that the concentration varies between 95 and 892/g. A more recent and comprehensive study of the concentration of shocked quartz in the K-T boundary layer at numerous sites around the globe was made by Morgan et al. (2006). They processed the samples the same way that Bostwick and Kyte (1996) did. Morgan et al. (2006) identified one to two orders of magnitude more shocked quartz per gram using scanning electron microscopy than when using optical microscopy. However, concentrations obtained by Morgan et al. (2006) using scanning electron microscopy are one to two orders of magnitude lower than those obtained by Bostwick and Kyte (1996) using optical microscopy.

Morgan et al. (2006) concluded that Bostwick and Kyte's (1996) and their results were internally consistent and that both sets of data indicate a general decrease in the number of shocked quartz grains per gram westward across the Pacific. In their internally consistent and more comprehensive data set, Morgan et al. (2006) found concentrations of shocked quartz in the K-T boundary layer ranging from an average of $\sim$1600 grains/g in North America to $<$10 in the western Pacific and New Zealand sites, with intermediate values for sites in the equatorial Atlantic, Europe and eastern Pacific.

Because sediment reworking has spread ejecta above and below the K-T boundary at most sections, a better way to compare the amount of shocked quartz at each site is to estimate the fluence or number of shocked grains per unit area. This can be done by converting the number of shocked quartz grains per gram to number per cubic centimeter, using sediment density, and totaling the number per cubic centimeter every centimeter through the layer. This requires interpolation between samples, unless the layer containing the ejecta was sampled continuously through the layer [see Bostwick and Kyte (1996) and Morgan et al. (2006) for more detail]. Bostwick and Kyte (1996) and Kyte et al. (1996) obtained fluences for seven Pacific Ocean K-T boundary sites ranging from 1230 to 13,800 shocked quartz grains (>60 μm)/cm^2. Morgan et al. (2006) obtained much lower fluences (40–390 shocked grains/cm^2) for the Pacific Ocean sites that they studied. For example, Bostwick and Kyte (1996) obtained a fluence of 1230 grains/cm^2 for ODP Hole 803D, but Morgan et al. (2006) only obtained a fluence of 64 grains/cm^2 for this same core. Based on Morgan et al.'s (2006) data set, the fluence or number of shocked quartz grains per square centimeter follows the same trend as the number per gram with the highest fluences in North America and the lowest fluences in the western Pacific, southeastern South Atlantic, and New Zealand.

The reason for the difference between Morgan et al.'s (2006) results and those of Bostwick and Kyte (1996) are not known, but Morgan et al. (2006) suggested that it might be due to some aspect of sample handling, analytical techniques, and/

or mineral extraction procedures that lead to different absolute numbers of shocked quartz grains being recovered and recorded. Hydrofluoric acid (HF) was used during sample processing. As quartz, and even to a greater degree glass, are soluble in HF, if Morgan et al. (2006) had used a slightly stronger solution of HF, or higher temperatures, and/or longer etch times than other researchers, the glass lamellae in the PDFs may have dissolved more completely, allowing some pieces to break off some grains and some grains to break up altogether. This could explain both the smaller sizes and the lower abundances found by Morgan et al. (2006) when compared with those reported by other authors.

In addition to shocked quartz, shocked feldspar (both plagioclase and microcline) containing multiple sets of planar deformation features has been found in the K-T boundary layer in the Western Interior, USA, and at other K-T boundary sites (Fig. 5.18f; Izett 1990; Bohor 1990). Shocked feldspar grains have also been found in the K-T boundary layer in Turkmenistan (Badjukov et al. 1986) and in Austria (Preisinger et al. 1986). Shocked rock fragments consisting of two or more quartz grains (quartzite/metaquartzite), feldspar and quartz, quartz-sericite schist, and granite-like aggregates of quartz, oligoclase, and microcline (Fig. 5.18e) have been found in the K-T boundary layer in the Western Interior, USA (Izett 1987; Izett 1990; Sharpton et al. 1990). Shocked quartzite/metaquartzite fragments were also found in the K-T boundary layer in Haiti (Izett 1991b).

5.2.3.4.2 Stishovite

In the first report of shocked quartz grains in the K-T boundary layer, Bohor et al. (1984) stated that X-ray diffraction patterns of some of the shocked quartz grains from Brownie Butte, Montana, contained some very weak lines for stishovite, indicating the presence of trace amounts of stishovite in the shocked grains. They also treated several milligrams of clay-free sample from Brownie Butte with HF for 24 h to remove the quartz and obtained an X-ray pattern of the residue, which again had very faint lines for stishovite. In another study, McHone et al. (1989) found evidence of trace amounts of stishovite in a K-T boundary sample from Raton Basin, New Mexico, using solid state silicon-29 magic angle spinning nuclear magnetic resonance and X-ray diffraction.

5.2.3.4.3 Shocked Chromite and Zircon

Bohor et al. (1989, 1990) reported finding chromite crystals, in the K-T boundary layer, that exhibit multiple sets of planar features similar to PDFs. X-ray diffraction patterns of these chromite crystals display X-ray asterism. These chromites have a chromite-hercynite (picotite) composition, with the formula (Fe, Mg)(Cr, Al, Fe)$_2$O$_4$ (Bohor et al. 1990). These chromite crystals are larger than the Ni-rich spinels (magnesioferrites) which are also found in the K-T boundary layer

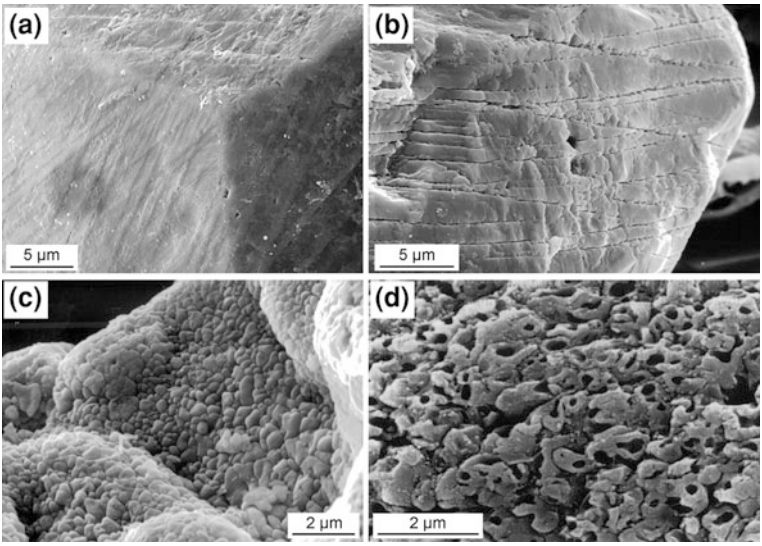

Fig. 5.20 Scanning electron microscope images of surface features on shocked zircons from the K-T boundary at Berwind Canyon, Raton Basin, Colorado. **a** Zircon with two directions of planar features. **b** Zircon with two sets of planar features. **c** Zircon with granular or strawberry texture. **d** Shocked zircon with rounded crystals, many with a centrally exposed vesicle, indicating incipient melting. **a**, **b**, and **c** are courtesy of Bruce Bohor. **d** is from Bohor et al. (1993), Fig. 2b

and they do not exhibit skeletal morphology or high nickel content characteristic of the Ni-rich spinels.

Bohor et al. (1990) found shocked zircon crystals in K-T boundary sediments that, after treatment with concentrated NaOH, exhibit multiple sets of planar features. A single crystal X-ray precession camera photograph of one of the zircon crystals with planar features showed extreme broadening and streaking (asterism) of the pattern indicating shock metamorphism. In a later study, Bohor et al. (1993) documented a series of textural changes in shocked zircons from the K-T boundary layer at Berwind Canyon, Colorado (Fig. 5.20). Dating of these zircons has been used to confirm the source crater for the K-T boundary layer (see Sect. 5.2.6).

5.2.3.4.4 Diamonds

Diamonds were first found in the K-T boundary layer in a sample from Alberta, Canada (Carlisle and Braman 1991). The diamonds were found in the acid residue from this sample. They were cubic diamonds 3–5 nm in size. Carlisle (1992) obtained a single $\delta\ ^{13}C$ value of −48 ‰ for these diamonds. Based on the carbon isotope composition and the small size, they proposed that the diamonds are meteoritic in origin (Carlisle and Braman 1991; Carlisle 1992).

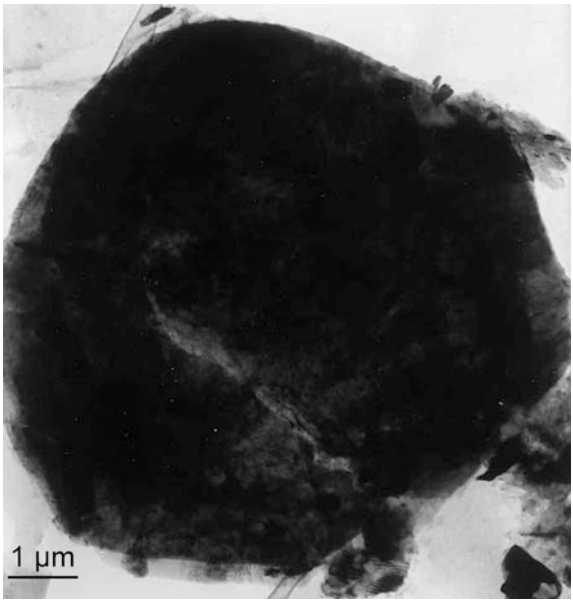

Fig. 5.21 Transmission electron microscope image of a polycrystalline diamond from the Ir-rich K-T boundary layer at El Mimbral, northeastern Mexico. Individual crystals range in size from 0.1 to 1 μm. The diamond has a pseudohexagonal morphology that may have been inherited from a precursor graphite crystal. From Hough et al. (1997), Fig. 2a

Gilmour et al. (1992) recovered diamonds from the K-T boundary layer at Brownie Butte (Montana, USA) and Berwind Canyon (New Mexico, USA), but did not find any in a sample from Petriccio (Italy). They obtained electron diffraction patterns of the diamonds and found that they are cubic diamonds. The diamonds occur in clumps, but individual crystals are $\sim$6 nm in size and vary in morphology from irregular to near-cubic. Gilmour et al. (1992) obtained carbon and nitrogen isotopic ratios of the diamonds. The diamonds have $\delta\ ^{13}C$ values between -14 and -19 ‰. Gilmour et al. (1992) stated that the isotopic signatures distinguish the K-T diamonds from known meteorite diamonds. They concluded that the K-T diamonds were most likely produced by shock metamorphism of target rock or in plasma resulting from the associated fireball.

Hough et al. (1997) recovered diamonds from the K-T boundary layer at El Mimbral (Fig. 5.21) and El Peñon in northeastern Mexico. Again electron diffraction patterns indicate that the diamonds have a cubic structure. No evidence of the hexagonal polymorph (lonsdaleite) was found. The diamonds from these sites are polycrystalline aggregates and up to 30 μm in size. The $\delta\ ^{13}C$ values are between -11 and -15 ‰, which is consistent with formation from terrestrial crustal rocks.

Table 5.7 Radiometric age of Cretaceous-Tertiary boundary impact glasses and Chicxulub impact melt rockmelt rock

Method	No. of measurements	Mean age			Reference
		Ma		S.D.	
Beloc, Haiti, glass					
$^{40}Ar/^{39}Ar$ plateau	4	64.75	±	0.08	Hall et al. (1991)
$^{40}Ar/^{39}Ar$ plateau	4	64.38	±	0.18	Izett et al. (1991)
$^{40}Ar/^{39}Ar$ total fusion	23	64.48	±	0.22	Izett et al. (1991)
$^{40}Ar/^{39}Ar$ plateau	5	65.01	±	0.08	Swisher et al. (1992)
$^{40}Ar/^{39}Ar$ total fusion[a]	3	65.07	±	0.19	Swisher et al. (1992)
Mimbral, Mexico, glass					
$^{40}Ar/^{39}Ar$ total fusion[a]	2	65.07	±	0.38	Swisher et al. (1992)
Chicxulub impact melt rock					
$^{40}Ar/^{39}Ar$ plateau	3	64.98	±	0.05	Swisher et al. (1992)
$^{40}Ar/^{39}Ar$ plateau	1	65.20	±	0.4	Sharpton et al. (1992)

S.D. = standard deviation

[a] The combined weighted mean age for the three Haitian and two Mimbral samples is 65.07 ± 0.10 Ma

5.2.4 *Radiometric Age of the Cretaceous-Tertiary (K-T) Boundary Layer*

Harland et al. (1990) obtained a radiometric age of 66 Ma for the K-T boundary using 20 age dates for the Maastrichtian and 15 for the Danian. The 66 Ma age estimate was supported by laser fusion ^{40}Ar-^{39}Ar dates of single sanidine crystals extracted from the lower Z coal (with a high Ir content) in Montana, which yielded an age of 66.1 Ma (C. Swisher, as cited by Berggren et al. 1992). However, these dates were later rejected by C. Swisher as being analytically suspect (Gradstein et al. 1995). In their 1995 calibration of the geomagnetic polarity timescale for the Mesozoic, Gradstein et al. (1995) combined the ^{40}Ar-^{39}Ar dates of 64.98 ± 0.05 (Swisher et al. 1992) and 65.2 ± 0.4 Ma (Sharpton et al. 1992) for the Chicxulub melt rock with the combined ages of 65.07 ± 0.10 (total fusion) for the Mimbral (Mexico) and Beloc (Haiti) K-T boundary impact glasses and 65.01 ± 0.08 Ma (plateau) for the Beloc K-T boundary impact glasses (see Table 5.7; Swisher et al. 1992) to obtain an age of 65.00 ± 0.04 Ma for the Cretaceous-Tertiary boundary. In their 1995 paper, Cande and Kent (1995) stated that a consensus was developing for an age of 65 Ma for the K-T boundary and they adopted this age for calibration of the geomagnetic polarity timescale for the Late Cretaceous and Cenozoic. However by 2002, a consensus was beginning to grow for a slightly older age for the K-T boundary.

Hicks et al. (2002) obtained a revised estimate for the K-T boundary of 65.51 ± 0.10 Ma by normalizing the most recently published Ar–Ar ages (at that time) for the K-T boundary (i.e., sanidine crystals from the Z coal layer and impact glasses) to a standard monitor age of 28.02 Ma for the Fish Canyon Tuff and 28.32 Ma for the Taylor Creek Rhyolite. Kuiper et al. (2008) compared astronomical and ^{40}Ar-^{39}Ar ages of tephra in marine deposits in Morocco to calibrate

the age of the Fish Canyon sanidine. According to Kuiper et al. (2008), this age results in a more precise age of 28.04 ± 0.046 Ma. These authors concluded that this calibration provides tight constraints on the astronomical tuning of the pre-Neogene successions, resulting in a mutually consistent age of ~65.95 Ma for the K-T boundary. In this book, we use 65 Ma for the age of the K-T boundary.

5.2.5 *Multiple Impact Ejecta Layers in Late Maastrichtian and Early Danian Deposits?*

Earlier petrographic and geochemical studies suggested that the K-T boundary spherules had a mafic source and some authors proposed that the target rock was oceanic crust (Montanari et al. 1983; DePaolo et al. 1983; Hildebrand and Boynton 1988a, b). However, the discovery of shocked quartz, K-feldspar, quartzite, and rock fragments composed of quartz, microcline, and oligoclase in the K-T boundary layer indicates a continental impact (Bohor and Izett 1986; Izett 1990; Sharpton et al. 1990). In addition, it was recognized that the K-T boundary layer in the Western Interior of the USA consists of two layers: 1) a lower spherule layer, and 2) an upper layer containing a positive Ir anomaly, Ni-rich spinel crystals, and abundant shocked mineral grains (Bohor et al. 1987a; Izett 1990). This led some authors to propose that there may have been more than one impact (Smit 1990; Sharpton et al. 1990; Izett 1991a; Shoemaker and Izett 1992). Eventually, most researchers concluded that the dual nature of the K-T boundary layer in the Western Interior, USA, was the result of a single impact (Bohor et al. 1987a; Hildebrand and Boynton 1990; Smit et al. 1992b; Bohor and Glass 1995).

Leroux et al. (1995a) determined the abundance of Ni-rich spinel and shocked quartz grains through section H near Beloc, Haiti. They found essentially the same Ni-rich spinel abundance up through this section as had previously been reported by Jéhanno et al. (1992). However, Leroux et al. (1995a) plotted the spinel abundance using a log scale which indicates a small peak in abundance in Unit 2 that was not as evident in Jéhanno et al.'s (1992) plot (see Sect. 5.2.2.2 and for a discussion of the units in the Haitian K-T boundary sections). There was complete overlap in the Cr content in the spinels from the two levels, but the average Cr content of the spinels in the lower part of the section (upper part of Unit 1 and lower part of Unit 2) is higher than in the spinels in the upper level (upper part of Unit 2 and Unit 3). Like the spinels, the shocked quartz grains were found to have a bimodal distribution. Shocked quartz grains are abundant in Units 1 and 2 with a peak abundance of ~500 shocked quartz grains per gram of sample within Unit 2. A smaller peak in abundance (~100 grains/g) occurs in Unit 3. Leroux et al. (1995a) reported a 4 cm interval with no shocked quartz at the top of Unit 2, just below Unit 3. They stated that the 4 cm interval without shocked quartz "might correspond to a long time interval". They interpreted this, plus the difference in composition of the spinels in the two layers, as indicating that the K-T boundary

sections in Haiti suggest two impact events. However, these observations might also be explained by a single impact. Because of the low abundance of spinels in the intermediate levels in the section, Leroux et al. (1995a) lumped together the compositional data into two groups: those between 28 and 50 cm and those between 53 and 63 cm. Thus, they do not have the resolution to determine if the two compositional groups are part of a continuous compositional variation through the section or if they represent two different populations of spinels separated by a sharp stratigraphic discontinuity. The 4 cm gap without any shocked quartz grains and with low numbers of spinels just below Unit 3 may simply be the result of deposition of fine-grained marine sediments that were put into suspension by the coarser ejecta falling on the sea floor. This material could have settled out fairly quickly before the arrival of the ejecta from the vapor plume.

As of 2000, some authors were still arguing for multiple impacts around the time of the K-T boundary (e.g., Stinnesbeck et al. 2000; Keller et al. 2001, 2003). In a number of papers Gerta Keller and colleagues pointed to the large errors in radiometric dating methods and argued that there were ~300 ka between formation of the Chicxulub crater and the K-T boundary (Keller et al. 2003; Keller et al. 2004a, b; Keller et al. 2007). Keller et al. (2003) proposed that there may be three impact ejecta layers in late Maastrichtian to early Danian deposits. According to these authors, the oldest of these ejecta layers is represented by the spherule layer (unit I) in the northeastern Mexico K-T boundary sites (Fig. 5.3). They proposed that this ejecta layer is from the nearby Chicxulub impact structure, which they concluded was formed ~300 ka before the K-T boundary impact and is represented by an Ir anomaly and associated shocked mineral grains found in unit IV in the northeastern Mexico sites and at most K-T boundary sites around the globe. Keller et al. (2003) tentatively identified a "…widespread Ir anomaly in the Early Danian subzone P1a(1)…" as record of a possible third impact event. However, Keller et al. (2004a, b) pointed out that, in the **Yaxcopoil-1 core**, which was drilled within the crater, there are ~50 cm of finely laminated dolomitic and micritic limestone of Late Maastrichtian age between impact breccia below and early Danian sediments above. They argued that this 50-cm-thick layer was deposited in a normal sedimentary environment, based on burrowing within the layer. They also concluded that sedimentation of the 50-cm-thick layer took place over a period of ~300 ka, based on biostratigraphy (Keller et al. 2004a, b). On the other hand, Smit et al. (2004) pointed out that the 50-cm-thick layer (they said 66 cm) is cross-bedded and suggests that it is crater infill deposits that were deposited by backwash. Smit et al. (2004) concluded that there is nothing in the biostratigraphy, geochemistry, or petrology that can be used to argue against synchroneity of the Chicxulub impact and K-T boundary ejecta layer and associated mass extinction.

Most authors agree that the lower spherule layer (unit I) was deposited by the Chicxulub impact, but they interpret the overlying clastic units (units II and III) as being deposited by impact-generated tsunami waves over a period of hours or days immediately following the Chicxulub impact (see, e.g., Schulte et al. 2010). They further proposed that unit IV represents deposition from the vapor plume from that

same impact. The early Danian Ir anomaly, where present, may be reworked from the K-T boundary Ir anomaly. On the other hand, Keller et al. (2003) argued that the siliciclastic units (units II and III in Fig. 5.3) were deposited over a period of nearly 300 ka, based on sediment accumulation rates. Keller et al. (2003) identified what they interpreted to be trace fossils (burrows) within units II and III. They proposed that the burrowed horizons indicate "…that sediment deposition occurred episodically with periods of erosion and rapid deposition alternating with periods of normal pelagic sedimentation and colonization of the ocean floor by bottom dwellers." They concluded, therefore that units II and III could not have been deposited by tsunami waves over a period of hours to days as concluded by other workers (e.g., Smit et al. 1996). Instead, Keller et al. (2003) proposed that the fining-upward calcareous sandstones and interbedded silt and sandstone may be related to sea-level changes and gravity flows. However, Smit (1999) proposed that the "burrow structures" might be flame structures formed by mud being squeezed into the bottom of the sand layer by loading and he pointed out that what Stinnesbeck and Keller (1996) referred to as "normal hemipelagic layers" were coarser grained than "undisputed upper Maastrichtian and Paleogene normal hemipelagic layers".

For additional discussion in favor of a single major impact at K-T boundary time see Schulte et al. (2008, 2010).

5.2.6 The K-T Boundary Source Crater: Chicxulub

After Alvarez et al. (1980) published their paper suggesting that a major impact took place at the end of the Cretaceous Period, the search began for the source crater. Some of the earlier searches were influenced by studies that suggested that the target rock was oceanic crust. If that were the case, then the chance of finding the source crater would be greatly reduced, since half of the oceanic crust present when the K-T boundary impact took place has been subducted. In spite of this, many researchers began to search for the source crater of the K-T boundary impact layer. Some of the potential sites for the K-T impact included: the Hawaiian hot spot (Smith and Smoluchowski 1981), northern Pacific-Bering Sea (Emiliani et al. 1981), Deccan Traps (India) or the Tagus Abyssal Plain in the northeast Atlantic (Alvarez et al. 1982), the British Tertiary igneous province (Cisowski and Housden 1982), the Nastapoka arc structure of Hudson Bay (Bohor and Izett 1986), and the Columbia Basin (Hildebrand and Boynton 1990). However, no evidence for impact was found at any of these sites.

Two structures that had already been identified as impact structures and that appeared to have close to the correct age were suggested as K-T boundary craters: 1) the 35-km-diameter **Manson impact structure** in Iowa, USA, and 2) the 65-km-diameter Kara impact structure in Russia. However, both were considered to be too small and later dating indicated that they were both too old. The Manson structure appears to be ~74 Ma old (Izett et al. 1993) and the Kara structure appears to

be ~70 Ma old (Koeberl et al. 1990; Trieloff et al. 1998). More recently, the 24-km-diameter Boltysh impact structure in the Ukraine was dated at 65.17 ± 0.64 Ma and, thus, within the quoted errors, could be the same age as the K-T boundary (Kelley and Gurov 2002). However, palynological and $\delta^{13}C$ data from the crater-fill sediments suggest that the Boltysh structure formed ~2–5 ka prior to the K-T boundary event (Jolley et al. 2010). Because of the small difference in ages, it would be difficult to distinguish between distal Boltysh ejecta and the K-T boundary ejecta layer stratigraphically; however, because of the relatively small size of the Boltysh structure, even if the Boltysh ejecta were mistaken as part of the K-T boundary ejecta, the combined thickness would be indistinguishable from the thickness of the K-T boundary alone, except locally–i.e., within ~1000 km.

Bohor and Izett (1986) and Izett (1990) found that the greatest abundance and maximum size of shocked quartz grains occur in the Western Interior of North America and concluded from this that the K-T boundary source crater must be in or adjacent to North America. High-energy K-T boundary deposits along the northern coast of the Gulf of Mexico (Smit 1999; Bourgeois et al. 1988) and a thick sequence of K-T boundary ejecta, including spherules and shocked quartz around the Gulf of Mexico (Hildebrand and Boynton 1990), suggested that the source crater was probably in the Gulf of Mexico or proto-Caribbean region. In 1990, Alan Hildebrand learned from a reporter that two geophysicists (Glen Penfield and Antonio Camargo), working for Petróleos Méxicanos, had described a large circular structure near Chicxulub Puerto on the Yucatan Peninsula, Mexico. Penfield and Camargo had suggested that the structure might be an impact crater. Hildebrand contacted Penfield and Camargo and they were able to find published gravity data for the structure and some pieces of cores drilled into the structure (Levi 1992).

Studies of the core samples indicated the presence of breccia and melt rocks containing quartz grains with multiple sets of PDFs (Hildebrand et al. 1991). Geophysical data indicated that the structure is ~180 km in diameter. The age was not well defined, but Hildebrand et al. (1991) concluded that it must be close to the age of the K-T boundary. Thus, the Chicxulub structure is in the right location, is large enough, and is approximately the right age to be the source crater for the K-T boundary layer. The impact origin of the Chicxulub structure was further supported by more recent coring of the structure and petrographic studies of the core (Yaxcopoil-1 core; see Meteoritics and Planetary Science 39 (6) June 2004). The trace element and rhenium-osmium isotope compositions of melt rocks and breccias from the Chicxulub structure, which exhibit shock metamorphic effects, have been determined (Koeberl et al. 1994). One melt rock sample has elevated Ir (15 ppb), an Os concentration of 25 ppb, and a low $^{187}Os/^{188}Os$ ratio of 0.113. The data from this study suggest the presence of a heterogeneously distributed meteoritic component in the Chicxulub melt and are consistent with the Chicxulub structure being an impact crater.

In addition to what has been mentioned above, several lines of evidence support the conclusion that Chicxulub is the source crater of the K-T boundary layer, including: 1) geographic variation in thickness of the K-T boundary ejecta layer;

2) radiometric age and major oxide and isotopic composition of the glass cores in impact spherules at Haiti and Mimbral; and 3) U–Pb dating of shocked zircons from the K-T boundary layer.

1) The thickness of the K-T boundary ejecta layer decreases exponentially with distance from Chicxulub (Hildebrand and Boynton 1990; Hildebrand et al. 1991; Vickery et al. 1992). Hildebrand et al. (1991) pointed out that Chicxulub is situated between the sites with the thickest known K-T boundary layer deposits: Haiti and northeastern Mexico. Hildebrand and Stansberry (1992) used McGetchin et al.'s (1973) equation that relates the thickness of an ejecta layer with crater size and distance from the crater to predict the location and size of the K-T boundary layer source crater (see Sect. 3.4.3 for methodology). Based on the thickness of the K-T boundary layer at three sites with the greatest known thickness, Hildebrand and Stansberry (1992) predicted that the source crater should be ~150 km north of the Chicxulub structure and have a diameter of ~178 km. They also compared the predicted thickness of the Chicxulub ejecta layer with the observed thickness of the K-T boundary layer for fifteen sites and found excellent agreement (see Sect. 5.2.7.3). Vickery et al. (1992) did a similar study and also found good agreement between predicted thickness of the Chicxulub ejecta layer and observed thickness of the K-T boundary layer. Thus, geographic variation in the thickness of the K-T boundary layer is consistent with a source crater with the size and location of the Chicxulub impact structure and, therefore, supports the conclusion that Chicxulub is the K-T boundary layer source crater.
2) Within dating errors, the glass cores found in the Haitian spherules have the same age as the Chicxulub crater, based on the age of the impact melt rock (Table 5.7; Hall et al. 1991; Izett et al. 1991; Swisher et al. 1992; Sharpton et al. 1992).

   Two kinds of glass particles have been found in the K-T boundary layer at Haiti and at Mimbral, Mexico: black glass with andesitic to dacitic compositions, and yellow glass with high CaO content (ave. ~26 wt %) and relatively high sulfur content (ave. ~0.7 wt %; Tables 5.3, 5.4; Sigurdsson et al. 1991a, b; Hildebrand et al. 1991; Kring and Boynton 1992; Jéhanno et al. 1992; Bohor and Glass 1995). The black glasses have compositions similar to the composition of the melt rock recovered from the Chicxulub impact structure (Tables 5.3; 5.4). Furthermore, the target rock at Chicxulub contained limestone, anhydrite, and gypsum which could be the source of the high CaO and sulfur observed in the yellow glasses (Sigurdsson et al. 1991b; Hildebrand et al. 1991; Kring and Boynton, 1992).

   Blum et al. (1993) and Blum and Chamberlain (1992) determined the oxygen, strontium, and neodymium isotopic ratios of the Chicxulub melt rocks and K-T boundary glasses from Haiti and concluded that the Haitian glasses are isotopically indistinguishable from those of the Chicxulub melt rocks. They further pointed out that the $\delta\ ^{18}O$ values vary inversely with SiO_2 content within the Haitian black glasses and between the black and yellow glasses (Fig. 5.22). Blum and Chamberlain (1992) state that such a trend can only result from mixing

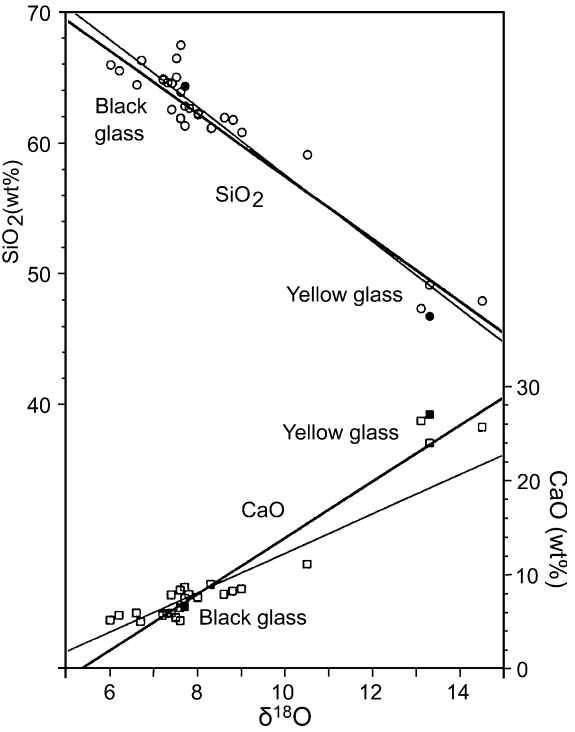

Fig. 5.22 Plots of SiO_2 and CaO versus $\delta^{18}O$ for black and yellow glasses from the K-T boundary layer near Beloc, Haiti. The thicker lines are linear regression analyses of both black and yellow glasses and the thinner lines are based on linear regression analyses of the black glasses only. The similarity in trends indicates that the variations within the glasses define similar trends whether or not the yellow glasses are included. These data indicate that the glasses were formed by melting a mixture of carbonate and silicate rocks similar to the target rocks found at the Chicxulub crater. From Blum and Chamberlain (1992), Fig. 2, reprinted with permission from AAAS

between silicate rocks and carbonates. Premo and Izett (1992) also found that the U-Th–Pb, Rb–Sr, and Sm–Nd isotopic signature of the Haitian black glasses are consistent with the target rocks at Chicxulub. The $\delta^{34}S$ values of two breccias and one evaporite sample from Chicxulub (Koeberl 1993b) are similar to the $\delta^{34}S$ value found by Sigurdsson et al. (1991b) for the Haitian yellow glasses.

Based on the boron and sulfur isotopic compositions of the yellow glass, Chaussidon et al. (1996) concluded that in addition to andesite and marine carbonates and evaporites, the source rock must have included some continental sediments or rocks. They suggested that the Todos Santos Formation, a red bed sequence, could explain the high boron content (>10 ppm) and low $\delta^{11}B$ value (<−10 ‰) of some of the yellow glasses. Chaussidon et al. (1996) found that mass balance mixing calculations (based on SiO_2, CaO, B contents and $\delta^{11}B$ values) show that the $\delta^{11}B$, $\delta^{34}S$, and $\delta^{18}O$ values of the yellow glasses can be explained by mixing of variable proportions of andesite (mean 49 %), sulfate (mean 30 %), red sandstone (mean 14 %), and carbonate (mean 7 %). Thus, the rock components indicated by the boron, sulfur, and oxygen isotopes support the conclusion that the Haitian glasses were derived from the Chicxulub impact structure.

3) Krogh et al. (1993a,b) and Kamo and Krogh (1995) did U–Pb isotopic dating of single zircon crystals from the K-T boundary ejecta layer at Raton Basin, Colorado (USA), Haiti, and the Rock Creek site in south-central Saskatchewan,

Canada. In the initial paper, Krogh et al. (1993a) demonstrated that the K-T boundary zircons from Raton Basin define a mixing line with the most heavily shocked zircons (see Sect. 5.2.3.4.3) exhibiting the most Pb loss. The upper intercept indicates an age of 544 ± 5 Ma for a component of the Pan-American target rocks and the lower intercept indicates an age of 65.5 ± 3 Ma for the time of impact. In another paper, Krogh et al. (1993b) obtained U–Pb data for 16 zircons from a polymict breccia recovered from a core drilled into the Chicxulub structure and for seven zircons from the K-T boundary layer at Haiti. They found that some of the Chicxulub and Haitian zircons are identical in age, texture, and lead loss pattern to the Colorado zircons. The results for 5 zircons from Chicxulub, 11 from Colorado, and 2 from Haiti define a line on the U–Pb concordia diagram with an upper intercept indicating a primary crystallization age of 544.5 ± 4.7 Ma (Fig. 3.28). U–Pb data for two other zircons from Haiti and three other zircons from Chicxulub define a primary crystallization age of 418 ± 6 Ma, suggesting that some of the Haitian zircons may have come from a different part of the target stratigraphy than did the Colorado zircons.

Kamo and Krogh (1995) reported U–Pb data for shocked zircons from the K-T boundary layer in Rock Creek in south-central Saskatchewan, Canada. These zircons were found to have a primary crystallization age of 548 ± 6 Ma, which is similar to the primary crystallization age for most of the Colorado zircons as well as some of the zircons from Haiti and Chicxulub. More recently, Kamo et al. (2011) dated shocked zircons from the K-T boundary at Caravaca, Spain, and Petriccio, Italy. The ages define a mixing line between a primary source age of ~549 Ma and the approximate time of the impact. The combined results of these studies strongly support the impact origin for the K-T boundary and indicate that the K-T boundary ejecta were derived from the Chicxulub impact structure (see also Schulte et al. 2010).

5.2.7 *Variations in Nature of the K-T Boundary Layer with Distance from Chicxulub*

Assuming that the Chicxulub impact structure is the source and only source (or at least the primary source) of the K-T boundary ejecta found around the globe, the study of the K-T boundary ejecta layer offers the opportunity to determine how impact ejecta vary with distance from a large impact structure and to test theoretical models for ejecta trajectories and distribution. However, since the Chicxulub impact took place in water on a continental shelf with a >3-km-thick carbonate- and evaporate-rich sedimentary cover, the lessons learned here may not apply to all impacts.

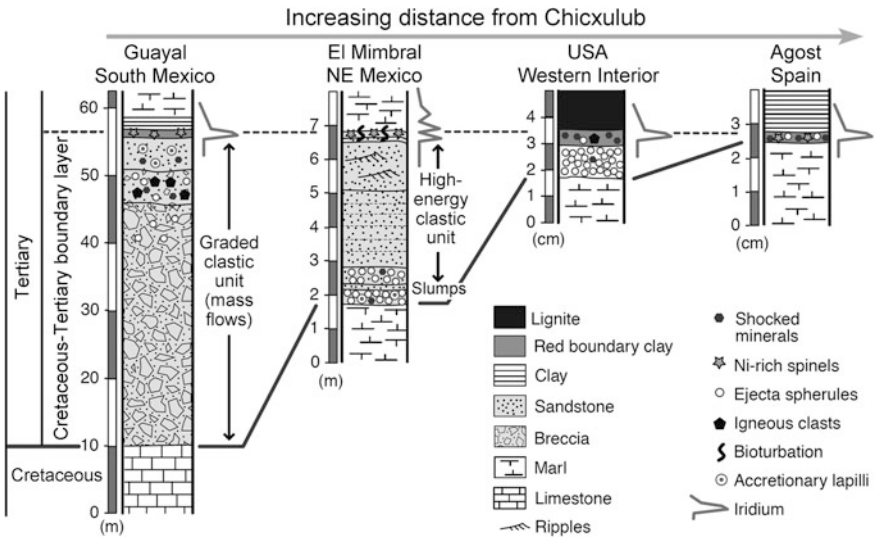

Fig. 5.23 Variations in the nature of the K-T boundary layer with distance from the Chicxulub impact structure. Guayal, El Mimbral, USA Western Interior, and Agost are typical of K-T boundary sections within 500, 500–1000, 1000–5000, and >5000 km of the Chicxulub impact structure, respectively. Note that the K-T boundary sections closer to Chicxulub are characterized by a thick, high-energy, clastic unit containing diagenetically-altered microtektite-like spherules. The thickness of the K-T boundary layer decreases with distance from the Chicxulub structure and abundant shocked minerals, Ni-rich spinels, and an Ir anomaly are always at the top of the layer. After Fig. 2a in Schulte et al. (2010), reprinted with permission of AAAS

5.2.7.1 General Nature of the K-T Boundary Ejecta Layer with Distance from Chicxulub

The thickness and nature of the K-T boundary ejecta layer changes systematically with distance from the Chicxulub impact structure (Fig. 5.23). In their review paper, Schulte et al. (2010), like Smit (1999) divided the K-T boundary sites into groups based on estimated paleodistance from Chicxulub: 1) "very proximal sites" within 500 km of Chicxulub, 2) "proximal sites" around the Gulf of Mexico located between 500 and 1000 km of Chicxulub, 3) "intermediate sites" between ~1000 km and ~5000 km of Chicxulub, and 4) "distal sites" >5000 km from Chicxulub. Based on the definition of distal ejecta used in this book, any ejecta farther than ~450 km from the 180-km-diameter Chicxulub impact structure would be considered distal. Thus, the "proximal sites", "intermediate sites", and "distal sites" are all distal by the definition used in this book.

At the "very proximal" sites in the Gulf of Mexico region (e.g., Guayal, south Mexico) the K-T boundary impact deposits are thick with clastic units (impact breccias) 10 s of meters thick (up to 100 or more meters thick at the more proximal sites; Fig. 5.23). These clastic units contain igneous clasts, shocked mineral grains, diagenetically-altered spherules, and agglutinated lapilli. The clastic units are overlain by a clay layer containing an Ir anomaly and Ni-rich spinel crystals.

At the "proximal sites" around the northwestern Gulf of Mexico (e.g., El Mimbral, NE Mexico), the K-T boundary is characterized by a series of cm- to m-thick ejecta spherule layers indicative of high energy sediment transport such as tsunami-induced currents (surges) and gravity flows (Fig. 5.23). At Haiti, the K-T boundary in the least disturbed section consists of a spherule layer about 25–35 cm thick (Fig. 5.5). This layer contains some shocked mineral grains in addition to diagenetically-altered spherules. Above the spherule layer is an ~15–35-cm-thick layer of fine-grained carbonate which is capped by a thin (one to a few centimeters) clay layer containing an Ir anomaly, shocked quartz, and Ni-rich spinel-bearing altered spherules.

At the "intermediate sites" in the Western Interior of North America, the K-T boundary layer consists of two layers (Figs. 5.8 and 5.23). The lower layer, 0.5–10 cm thick, contains altered impact spherules and the upper (fireball) 0.2–0.5-cm-thick smectitic layer is rich in PGEs (including Ir), shocked mineral grains, and Ni-rich spinels.

In distal marine sites, like Agost, Spain (Fig. 5.23), the K-T boundary layer usually consists of a reddish 2–5-mm-thick clay layer containing an Ir anomaly, altered Ni-rich spinel-bearing spherules, and shocked quartz. The layer at these more distal sites is equivalent to the upper (fireball) layer at the Western Interior, North American, sites.

5.2.7.2 Dual Nature of the K-T Boundary Layer and Its Cause

The dual nature of the K-T boundary is best seen in the Western Interior of North America, the western equatorial Atlantic (ODP Leg 207 sites) and at Haiti (Figs. 5.5, 5.8). Here we see a lower spherule or melt-ejecta layer and a thin upper layer enriched in Ir, Ni-rich spinel crystals, and shocked quartz grains. The melt-ejecta layer appears to contain relatively low-energy ejecta deposited from a ballistically emplaced ejecta curtain (Pollastro and Bohor 1993; Kring and Durda 2002). As previously mentioned, this layer contains spherules formed by quenching of droplets from melted target rocks. The spherules in the melt-ejecta layer appear to be altered microtektites (or microtektite-like spherules). In the Western Interior USA sites, this layer has been called the kaolinite or K-T boundary claystone layer (Bohor et al. 1987a; Izett 1990). In addition to the spherules, this layer contains rare shocked mineral grains and a subdued Ir anomaly (Pollastro and Bohor 1993). The upper Ir-rich layer containing Ni-rich spinel-bearing spherules (altered microkrystites) and abundant shocked mineral grains, consists of material that was entrained in, or condensed from, the vapor plume (Pollastro and Bohor 1993). This is the most highly shocked portion of the ejecta and it contains most of the vaporized projectile, which explains the Ir anomaly and spherules containing Ni-rich spinels (Vickery et al. 1992; Pollastro and Bohor 1993; Kring and Durda 2002). As previously mentioned, this upper, Ir-enriched layer is sometimes called the fireball layer and it appears to be global in extent. On the other hand, the melt-ejecta spherule layer is found only within 4000–6000 km of the Chicxulub impact structure.

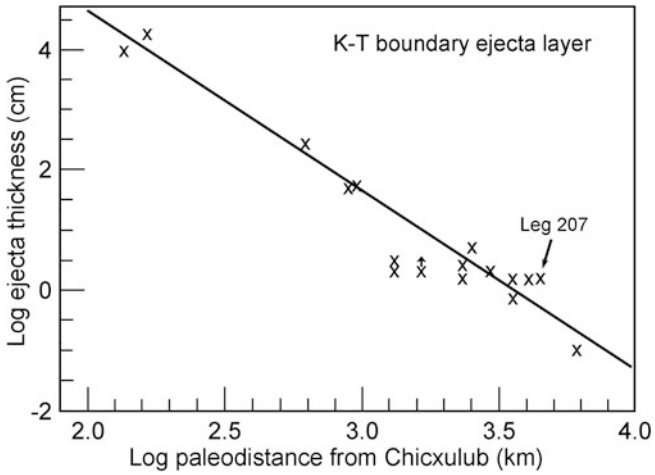

Fig. 5.24 Observed thickness of the K-T boundary layer versus paleodistance (Xs) from Chicxulub impact structure compared with predicted thickness (*solid line*) versus distance. The predicted thickness is based on the ejecta thickness scaling equation of McGetchin et al. (1973) (see Eq. 2.2 in Chap. 2). The ejecta layer thickness was accurately predicted over five orders of magnitude. Data for K-T boundary at ODP Leg 207 are from Schulte et al. (2009). Modified after Hildebrand and Stansberry (1992), Fig. 2

5.2.7.3 Variation in Thickness of the K-T Boundary Layer with Distance from Chicxulub

The thickness of the K-T boundary layer systematically decreases with distance from the Chicxulub impact structure at the time of the impact (Fig. 5.24; Hildebrand and Stansberry 1992; Vickery et al. 1992). The thickness of the Chicxulub ejecta layer with distance from the crater was predicted using McGetchin et al.'s (1973) equation that relates thickness of an ejecta layer to the size of the crater with distance from the crater (see Sect. 2.6). Comparison between the observed thickness of the K-T boundary layer (at 16 sites) and the predicted thickness showed agreement over five orders of magnitude.

5.2.7.4 Geographic Variation in Maximum Ir Content and Flux

As previously mentioned, the maximum Ir contents found at the K-T boundary layer do not vary systematically with distance from Chicxulub (see Sect. 5.2.3.1). Likewise, the Ir flux does not vary systematically with distance from Chicxulub. Since the K-T boundary layer at most of the sites has experienced some reworking, it is not surprising the maximum Ir content does not vary systematically with distance from the source crater. However, the lack of systematic variation in Ir fluence is more difficult to explain. One suggestion is that the carrier phase for the Ir is iron-rich nanophase particles (Wdowiak et al. 2001). Such small particles could stay in the

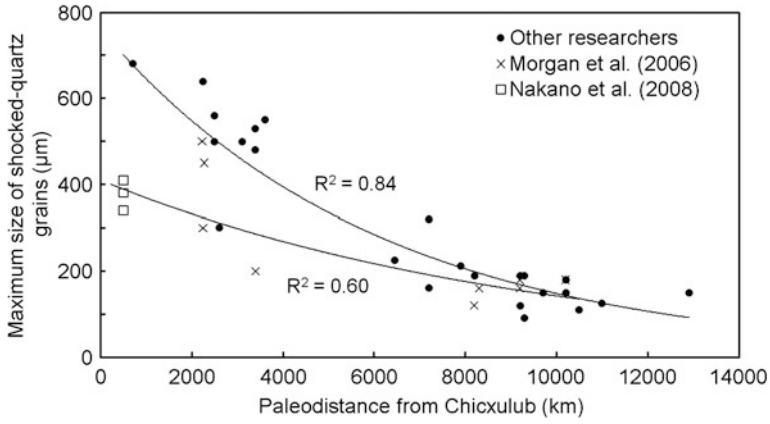

Fig. 5.25 Maximum size of shocked quartz in the K-T boundary layer versus paleodistance from Chicxulub impact crater. The upper curve is based on data from Bohor and Izett (1986), Bohor et al. (1987b), Izett (1990), Smit et al. (1992a), Kyte et al. (1996), and Bostwick and Kyte (1996), collectively called "Other researchers". The lower curve is based on data from Morgan et al. (2006). Both show an exponential decrease in maximum size of shocked quartz grains with distance from Chicxulub impact structure, but Morgan et al. (2006) generally reported smaller maximum sizes for a given distance from Chicxulub. Data from Nakano et al. (2008) were not used to calculate the best-fit curves, but they fall on the extrapolated curve based on Morgan et al.'s data

atmosphere long enough to be redistributed by atmospheric circulation (Wdowiak et al. 2001; de Niem et al. 2007).

5.2.7.5 Variation in Shocked Quartz Grains with Distance from Chicxulub

Earlier studies found global variations in the maximum size of shocked quartz grains from the K-T boundary layer (e.g., Bohor and Izett 1986; Bohor et al. 1987b; Izett 1990). These authors found that the largest shocked quartz grains were in the North American area and predicted that the source crater was somewhere on or close to the North American continent. After the Chicxulub impact structure was identified as the probable source crater for the K-T boundary ejecta layer, Morgan et al. (2006) found that the maximum size of shocked quartz grains in the K-T boundary layer does decrease exponentially with distance from the Chicxulub structure; however, for a given distance from Chicxulub, Morgan et al. (2006) generally reported smaller maximum sizes than did the previous authors (Fig. 5.25). In a still more recent study, Nakano et al. (2008) studied shocked quartz grains from three K-T boundary sites in Cuba and at DSDP Site 536 in the Gulf of Mexico. All four sites were about 500 km from Chicxulub at the time of the impact. The maximum size of shocked grains at these sites falls on the extrapolated trend for Morgan et al.'s (2006) data (Fig. 5.25). Morgan et al. (2006) found that the fluence (number of shocked quartz grains per square centimeter)

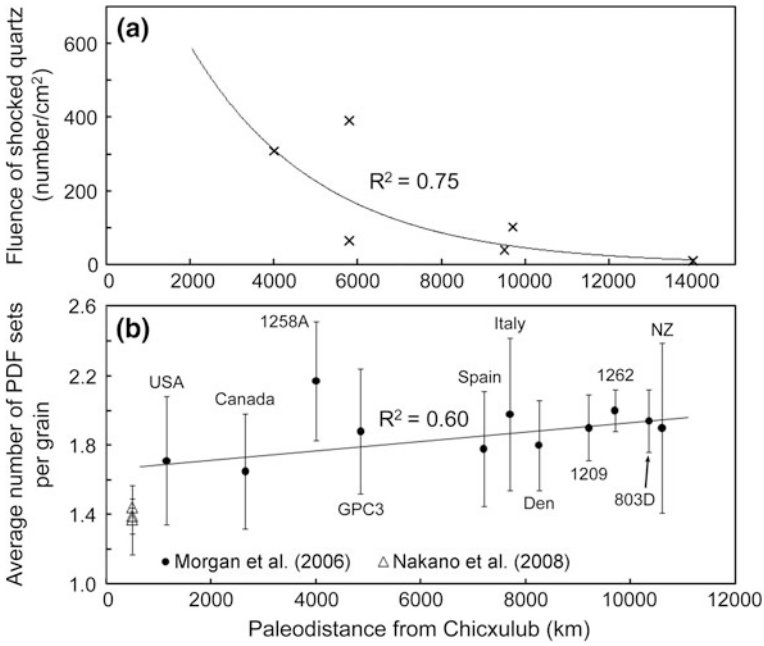

Fig. 5.26 Fluence (number/cm^2) of shocked quartz (**a**) and average number of PDF sets per grain (**b**) versus paleodistance from Chicxulub impact structure. Note that the fluence of shocked quartz grains decreases exponentially with distance from Chicxulub. The average number of PDF sets is used as a proxy for the degree of shock metamorphism; i.e., the higher the average number of sets of PDFs per grain, the higher the degree of shock metamorphism. Thus, the average degree of shock metamorphism appears to increase with distance from Chicxulub, but there are large error bars and the linear trend and r^2 value in B do not include data from Ocean Drilling Program Hole 1258A. Data used in A are from Morgan et al. (2006). The best-fit linear trend in B is based only on data from Morgan et al. (2006). "USA" includes Clear Creek East, New Mexico, and Berwind Canyon and Madrid East South, Colorado, USA. "Canada" includes Rock Creek East and Wood Mountain Creek, Saskatchewan. "1258A" is Ocean Drilling Program (ODP) Site 1258A in the western equatorial North Atlantic. "GPC3" is Core LL44-GPC3 taken in the eastern North Pacific. "Spain" is Caravaca, Spain. "Italy" includes Petriccio and Frontale. "Den" is Stevns Klint, Denmark. "1209" is ODP Site 1209 in the central North Pacific. "1262" is ODP Site 1262 in the eastern South Atlantic. "803D" is ODP Site 803D in the central South Pacific. "NZ" is Woodside Creek, New Zealand. Data from Nakano et al. (2008) are from Cuba

also decreases exponentially with distance from Chicxulub (Fig. 5.26a). Like the maximum sizes of shocked quartz grains, the fluences found by Morgan et al. (2006) are smaller than those found in earlier studies (e.g., Bohor and Izett 1986; Izett 1990; Bostwick and Kyte 1996) for the same K-T boundary sites, but are from a larger data set, which should be internally consistent. See Sect. 5.2.3.4.1 for a more detailed comparison between Morgan et al.'s (2006) shocked quartz studies and those of previous authors.

Croskell et al. (2002) proposed that the negative correlation between maximum size of shocked quartz grains and distance from Chicxulub is the result of annealing during atmospheric re-entry. The degree of heating of a grain increases with grain size and entry velocity. Since re-entry velocity increases with distance from the source crater, the maximum size of un-annealed quartz grains should decrease with distance from the source crater. Thus, the maximum size of shocked quartz grains exhibiting PDFs should decrease with distance from the source crater.

Morgan et al. (2006) also showed that the degree of shock metamorphism of the shocked quartz grains increases with distance from Chicxulub based on an increase in the average number of sets of PDFs observed on the quartz grains at each K-T boundary site (Fig. 5.26b). Nakano et al. (2008) also determined the average number of PDF sets in shocked quartz grains at three K-T boundary sites in Cuba and DSDP Site 536. The average number of PDF sets per grain observed for these sites falls below, but within the range, of the extrapolated trend based on Morgan et al.'s (2006) data.

5.2.8 Nature of the K-T Boundary (Chicxulub) Projectile

The high Ir and other siderophile contents in the K-T boundary layer are an indication of the presence of a meteoritic component. In an earlier study, good correlations were found among siderophile elements and Cr, in 23 samples from the K-T boundary layer at Stevns Klint, Denmark, suggesting that these elements are contained in a single component; however, the chondrite-normalized siderophile pattern did not match the chondrite siderophile element pattern (Palme 1982). Palme (1982) concluded that some fractionation may have modified the original pattern, making it difficult to identify the meteorite type. Osmium isotope data for a sample of impact glass (glass core from a spherule) from the K-T boundary section in Haiti also confirmed the presence of a small meteoritic component in the impact ejecta (Koeberl et al. 1994).

Kyte (1998) reported finding a fragment of a fossil meteorite ($\sim$2.5 mm in size) from the K-T boundary layer in a Deep Sea Drilling Project core (Site 576) from the North Pacific. The fragment is highly altered, but Kyte (1998) interpreted the petrographic and compositional data as indicating that the meteorite fragment may have been from a carbonaceous chondrite (Kyte 1998). Kyte (1998) suggested that it came from a relatively slow-moving asteroid rather than from a comet. However, Montanari and Koeberl (2000) questioned Kyte's (1998) interpretation stating that the severe alteration does not allow chemical data from the fragment to constrain the composition of the projectile. Measurements of extraterrestrial ^{3}He in the K-T boundary section from Gubbio and Monte Conero, Italy, and El Kef, Tunisia, indicate a near constant flux of extraterrestrial ^{3}He through the K-T boundary, which supports Kyte's (1998) conclusion that the K-T impact was asteroidal rather than cometary (Mukhopadhyay et al. 2001). In addition, the chromium isotopic composition of K-T boundary samples from Stevns Klint,

Denmark, and Caravaca, Spain, confirms the presence of a meteoritic component and is consistent with a carbonaceous chondrite-type projectile (Shukolyukov and Lugmair 1998). The tungsten and Cr isotopic compositions of Ni-rich spinels from the K-T boundary layer also indicate that the K-T projectile was chondritic in nature. In addition, the Cr isotopic data (ε^{53}Cr) indicate that more than 95 % of the chromium in the Ni-rich spinel is extraterrestrial in origin. Trinquier et al. (2006) state that ^{54}Cr is a better discriminator of meteorite type. In a study of K-T boundary samples using ^{54}Cr, they concluded that a CM2 carbonaceous chondrite explains the data best. Bottke et al. (2007) proposed that the carbonaceous chondrite-like asteroid Baptistina was broken up by a collision ~160 Ma ago and that the K-T boundary projectile was a fragment from this breakup. However, based on more detailed near-IR and thermal IR spectroscopic data, Reddy et al. (2009, 2011) concluded that the inferred mineralogy of Baptistina is inconsistent with a carbonaceous chondrite and more like that of an ordinary chondrite (possibly an LL type). Reddy et al. (2011) also stated that the albedo of the Baptistina family is much higher than the albedo used by Bottke et al. (2007) to date the breakup that formed the family. Reddy et al. (2011) concluded that at this time there is no reason to assume that the K-T impactor is related to Baptistina.

5.2.9 The K-T (Chicxulub) Impact as the Cause of the Terminal Cretaceous Mass Extinction

It is estimated that at the end of the Cretaceous Period, ~65 Ma ago, ~75–76 % of marine species and ~50 % of terrestrial species became extinct (Sheehan and Fastovsky 1992; Raup 1994; Jiang et al. 2010). The K-T boundary also marks the abrupt end to the age of the dinosaurs which lasted more than 180 Ma. In their 1980 paper, Alvarez and colleagues proposed that the impact of an ~10-km-diameter asteroid was responsible for the Cretaceous-Tertiary extinctions. They proposed that dust, thrown into the atmosphere by the impact, blocked out sunlight for several years, inhibiting photosynthesis and causing a collapse in the food chain, resulting in the mass extinction observed in the fossil record. This hypothesis is still being debated, but most researchers now accept the hypothesis that the impact played a role in the mass extinction, although not everyone agrees on the exact mechanism.

The size of an impact, its geographic location, the nature of the projectile and target rocks, and the ambient conditions on Earth at the time of the impact are all important in determining the environmental and biological consequences of an impact (Kring 2000). Thus, discovery of the Chicxulub impact structure helped researchers to better predict the environmental effects of the K-T impact. For example, the Chicxulub impact took place at low latitude on a partially submerged platform consisting of an ~3-km-thick sequence of carbonates and evaporites overlying continental crust. The carbonate/evaporite target rock probably played a

major role in climatic response to the impact. Computer models suggest that an impact of the size required to produce the Chicxulub structure would have produced an earthquake with a magnitude > 10, likely causing large-scale collapse of the continental shelf around the Yucatan platform and producing widespread tsunamis (Toon et al. 1997). Global environmental effects of the Chicxulub impact that have been proposed include: 1) choking dust, 2) global cooling, 3) cessation of photosynthesis, 4) wildfires, 5) acid rain, 6) ozone destruction, and 7) greenhouse warming.

5.2.9.1 Dust, Global Cooling, Cessation of Photosynthesis

Model calculations have suggested that dust and sulphate aerosols (vaporized anhydrite) from the K-T boundary (Chicxulub) impact, along with soot from wildfires ignited by the impact, blocked the sunlight, causing the temperature to drop globally and preventing photosynthesis (Alvarez et al. 1980; Toon et al. 1982; Pollack et al. 1983; Covy et al. 1994). Alvarez et al. (1980) proposed that enough dust would have been thrown into the atmosphere to block out most of the sunlight and stop photosynthesis for longer than a year. In their calculations of the climatic effect of the dust, Toon et al. (1997) estimated that $\sim 3 \times 10^{17}$ g of submicrometer-sized dust was lofted into the stratosphere by the Chicxulub impact. This "darkness at noon" scenario led to the well-known "nuclear winter" hypothesis (Crutzen and Birks 1982; Pierazzo et al. 2003).

More recently, Pope (2002) estimated that $<10^{14}$ g of submicrometer-sized dust was thrown into the stratosphere by the impact. This is more than two orders of magnitude less dust than proposed by Toon et al. (1997). Pope (2002) concluded that this amount of dust is too small to shut down photosynthesis. However, the large dust release in combination with sulfate aerosols from the target rocks and soot from wildfires are likely to have caused global cooling and to have shutdown photosynthesis. The fossil record shows that there is a drastic reduction in photosynthetic plankton at the K-T boundary (Kring 2007). In addition, the carbon isotope ($\delta\ ^{13}C$ values) gradient was reduced (Fig. 5.27) suggesting that surface productivity abruptly dropped at the K-T boundary (Perch-Nielsen et al. 1982; Hsü and McKenzie 1990; Hollander et al. 1993). This phenomenon has been called the **Strangelove Ocean**. In addition to the evidence of a drastic change in the marine biosphere at the K-T boundary, there is evidence for a major change in the terrestrial plant communities during which a diverse late Cretaceous flora assemblage was replaced by one dominated by a few species, especially ferns, in North America (Tschudy et al. 1984; Wolfe and Upchurch 1986; Nichols and Fleming 1990) and New Zealand (Vajda et al. 2001). This **fern spike** at the K-T boundary (Fig. 5.28) indicates widespread deforestation, which may have been global (Vajda et al. 2001).

It is difficult to model the exact temperature change caused by the Chicxulub impact. Several researchers agree that there must have been a significant drop in temperature (several degrees to a few tens of degrees centigrade) for a short period

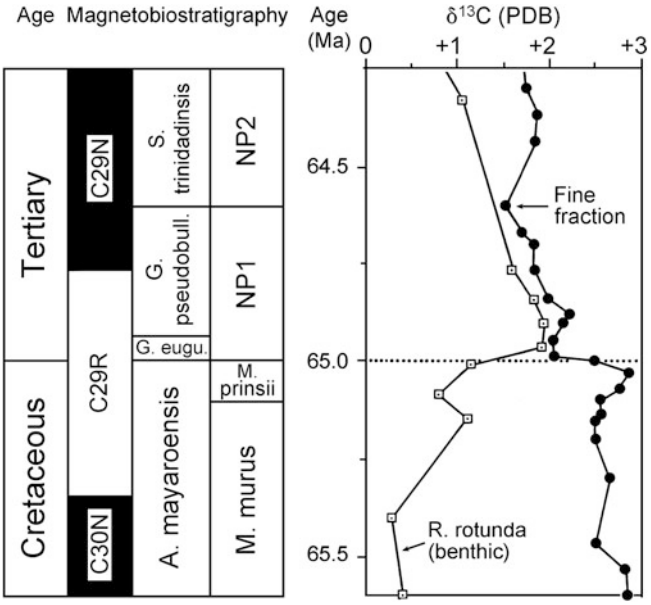

Fig. 5.27 Magnetostratigraphy, biostratigraphy, and carbon isotope stratigraphy across the Cretaceous-Tertiary (K-T) boundary at Deep Sea Drilling Project Site 577 in the North Pacific Ocean. Note that the fine fraction (primarily planktic calcareous nannofossils) $\delta^{13}C$ values decrease and the benthic foraminifera *R. Rotunda* $\delta^{13}C$ values increase converging to approximately the same value at the K-T boundary. This results in what has been referred to as a 'Strangelove' ocean and is interpreted to mean that the surface productivity of the ocean collapsed. PDB = Pee Dee belemnite. Modified after Fig. 1 in Hsü and McKenzie (1990)

of time (Gupta et al. 2001; Pierazzo et al. 2003). The δ ^{18}O marine record shows very little evidence for either warming or cooling associated with the K-T boundary suggesting that if any temperature change did take place at the time of the Chicxulub impact, it must have been short lived ($<10^4$ years; Pierazzo et al. 2003). As yet, the δ ^{18}O marine record does not provide the temporal resolution required to confirm the predicted temperature changes, although the sudden extinction of plankton is currently best explained by a brief period of severe darkening and cooling (e.g., Jiang et al. 2010; Schulte et al. 2010).

5.2.9.2 Wildfires

Evidence for impact-generated fires has been found in the K-T boundary layer in the form of soot (Fig. 5.29; Wolbach et al. 1985, 1990), pyrolitic polycyclic aromatic hydrocarbons (Venkatesan and Dahl 1989), carbonized plant debris (Smit et al. 1992a), and charcoal (Kruge et al. 1994). Earlier theoretical studies indicated that global fires would have been ignited by intense thermal radiation produced by

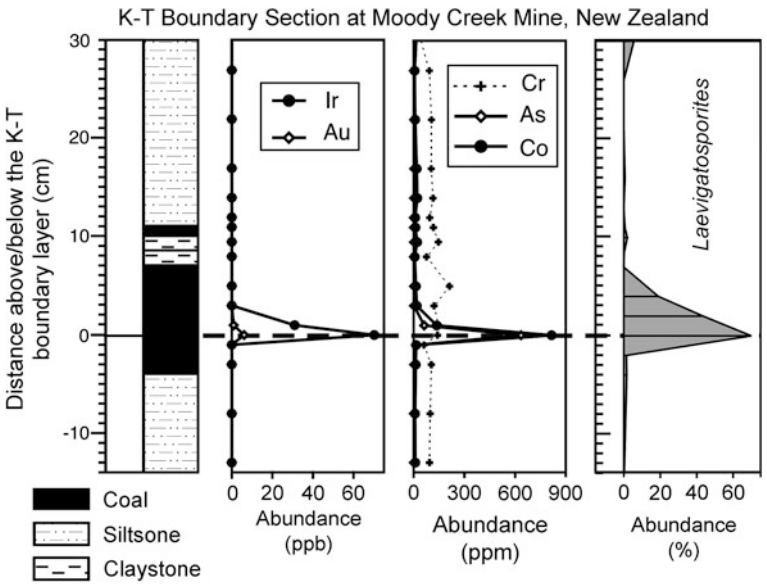

Fig. 5.28 Iridium, Au, Cr, As, and Co contents and *Laevigatosporites* (fern spores) abundance across the K-T boundary at Moody Creek Mine, New Zealand. Note that a fern spike is associated with the Ir anomaly at this site. After Vajda et al. (2001), Fig. 1, with permission of AAAS

ejecta reentering the atmosphere after the impact (Melosh et al. 1990). Robertson et al. (2004) suggested that for several hours after the impact, the Earth would have been bathed with intense infrared radiation that would have killed unsheltered organisms directly in addition to igniting fires where adequate fuel was present. However, Kring and Durda (2002) suggested that the fires may have had a more restricted geographic distribution than had previously been suggested. Furthermore, Goldin and Melosh (2009) pointed out that earlier models did not take into account that the early-arriving spherules would shield the Earth's surface from the thermal radiation produced by the later-arriving spherules. Such self-shielding may have prevented widespread wildfires, although the thermal pulse may have been sufficient to start localized fires.

5.2.9.3 Acid Rain

Theoretical studies suggest that intense heating of the atmosphere takes place during passage of a projectile, formation and expansion of a vapor plume (or fireball), and when hot ejecta rains back down through the atmosphere. Intense heating of the atmosphere can cause nitrogen to combine with oxygen to produce NO_x compounds and to form nitric acid (HNO_3) (Zahnle 1990). Since the Chicxulub impact took place in target rock containing anhydrite, sulfur vapor would

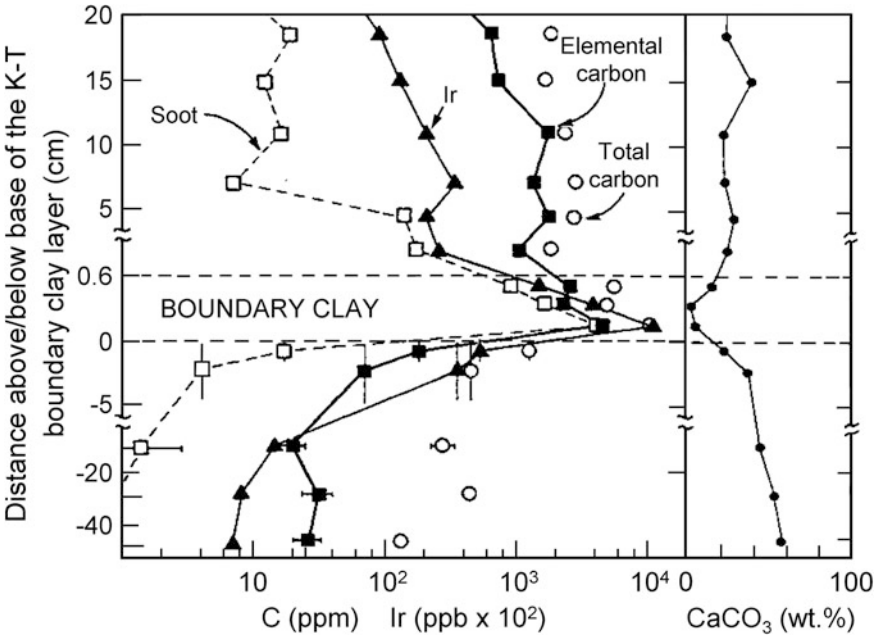

Fig. 5.29 Iridium, carbon, soot and $CaCO_3$ abundance across the K-T boundary at the Woodside Creek section in New Zealand. Note that the soot abundance increases by four orders of magnitude across the the K-T boundary and that the peak abundance of soot coincides with the peak abundance of Ir. After Wolbach et al. (1988), Fig. 2a. Reprinted with permission of Macmillan Publishers Ltd. [*Nature*] copyright (1988)

have been injected into the atmosphere forming sulphate aerosols which combined with water to form sulfuric acid. Thus, both nitric and sulfuric acids would have been produced by the impact. The resulting acid rain could have defoliated continental vegetation, enhanced continental weathering, and increased the acidity of oceanic surface waters.

Several researchers have found a spike, or a short term increase, in the $^{87}Sr/^{86}Sr$ ratio of marine carbonate at or just above the K-T boundary (Fig. 5.30; Hess et al. 1986; MacDougall 1988; Vonhof and Smit 1997; MacLeod et al. 2001), although other researchers did not find an increase (McArthur et al. 1998). Assuming that this increase is real, there are several possible sources/causes for this spike in the $^{87}Sr/^{86}Sr$ ratio at the K-T boundary: 1) vaporized projectile, 2) ejecta from Chicxulub, and/or 3) enhanced erosion and leaching of continental rock. Although both meteorites and continental rocks have relatively high $^{87}Sr/^{86}Sr$ ratios, Hess et al. (1986) concluded that neither the vaporized projectile nor ejecta from the impact could have supplied sufficient Sr to explain the observed increase in the $^{87}Sr/^{86}Sr$ ratio across the K-T boundary. Several researchers have concluded that the only possible mechanism for producing the increase in $^{87}Sr/^{86}Sr$ ratio is increased erosion and leaching of continental rock due to acid rain generated by the impact (MacDougall 1988; Vonhof and Smit 1997; MacLeod et al. 2001).

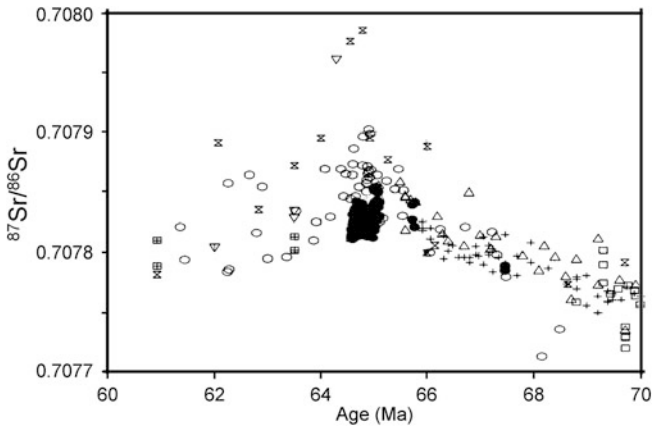

Fig. 5.30 Plot of $^{87}Sr/^{86}Sr$ values across the K-T boundary ($\sim$65 Ma). Note that the $^{87}Sr/^{86}Sr$ values increase across the K-T boundary. This increase has been interpreted as being caused by increased input of Sr from continental sources due to impact-generated wildfires and acid rains which resulted in increased weathering and erosion. The different symbols indicate data from different authors [see McArthur et al. (1998) for references]. After McArthur et al. (1998), Fig. 4b, reprinted with permission of Elsevier

Impact-produced wildfires also could have contributed to the increased erosion and exposure of rock to chemical weathering.

Strontium in sea water has two primary sources: runoff from continental land masses with an average $^{87}Sr/^{86}Sr$ ratio of 0.7119 and submarine hydrothermal activity which releases Sr with a $^{87}Sr/^{86}Sr$ ratio of 0.7033. A global increase in weathering of the continents would increase the amount of strontium introduced into the ocean from the continents causing an increase in the $^{87}Sr/^{86}Sr$ ratio of ocean water and thus in marine carbonates deposited at that time.

5.2.9.4 Ozone Destruction

Chlorine and bromine in sufficient concentrations in the atmosphere can destroy the ozone layer. Destruction of the ozone layer in the atmosphere allows lethal amounts of ultraviolet (UV) radiation from the sun to reach the Earth's surface. Chlorine and bromine can be produced from the vaporized projectile, vaporized target rocks, and biomass burning. Changes in the nitrogen chemistry of the atmosphere, as discussed above, can also destroy ozone. It has been estimated that over five orders of magnitude more chlorine was released into the stratosphere by the Chicxulub impact than is needed to destroy today's ozone layer. Thus, the amount of chlorine alone seems to have been sufficient to destroy the ozone layer after the K-T impact. However, initially, the dust, soot, and NO_2 may have absorbed the UV radiation and sulphate aerosols may have scattered the UV radiation (Kring 1999).

5.2.9.5 Greenhouse Warming

Significant quantities of greenhouse gases (water vapor, CO_2, and CH_4) were added to the atmosphere by the Chicxulub impact (O'Keefe and Ahrens 1989; Hildebrand et al. 1991; Pope et al. 1994; Pierazzo et al. 1998). Since the residence times of gases like CO_2 are greater than those of dust and sulphate aerosols, greenhouse warming may have occurred after a period of cooling (Kring 2007). Estimates of the increase in global mean temperature vary from 1° C to as high as ~7.5° C (Pierazzo et al. 1998; Beerling et al. 2002).

5.2.9.6 Other Possible Killing Mechanisms

Asphyxiation of animals by nitrous oxides and toxic poisoning by metals leached from the regolith by acid rains and from the projectile may have also played a role in the terminal Cretaceous mass extinction (Davenport et al. 1990; Prinn and Fegley 1987; Erickson and Dickson 1987).

5.2.9.7 Debate Regarding the Cause of the Terminal Cretaceous Mass Extinction

The cause of the terminal Cretaceous mass extinction is still being debated (Jiang et al. 2010; Schulte et al. 2010). It seems likely that some, if not all, of the mechanisms mentioned above may have played a role in the extinctions. Jiang et al. (2010) found that for nannoplankton the extinction rates were higher in the Northern Hemisphere oceans and the recovery slower than in the Southern Hemisphere. They proposed that an oblique impact coming from the southeast ejected more dust into the Northern Hemisphere, blocking sunlight and suppressing photosynthesis. They also speculated that metal poisoning from the fallout and soils leached by acid rain or wildfires may have exacerbated and extended the nannoplankton crisis in the Northern Hemisphere. However, other factors also may have played a role in the extinctions, such as a major regression of the sea (Keller et al. 2007) and extensive volcanism associated with the Deccan Traps in India (Officer and Drake 1985; McLean 1985; Morgan et al. 2004; Chenet et al. 2009). For additional discussion, see Schulte et al. (2010) and the corresponding discussion in *Science*, vol. 328, pages 973–976.

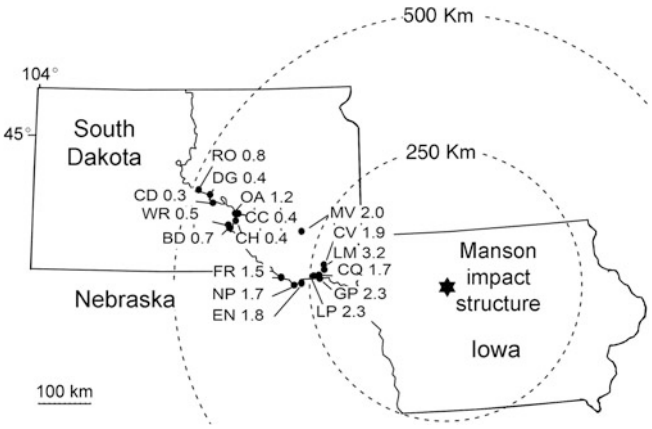

Fig. 5.31 Map showing location of the Manson impact structure and sites where Manson impact ejecta have been recovered. BD = Black Dog, CC = Crow Creek, CD = Cedar Creek, CH = Chamberlain, CQ = Cement Quarry, CV = Clay Valley, DG = DeGrey, EN = East of Niobrara, FR = Fort Randall Cemetery, GP = Gavins Point, LM = Lake Marindahl, LP = Lakeport, MV = Mount Vernon, NP = Niobrara State Park, OA = Oacoma, RO = Rousseau, and WR = White River. Number by each site is the maximum size of shocked quartz grains in millimeters. Modified after Fig. 4 in Izett et al. (1998)

5.3 Distal Impact Ejecta from the Manson Impact Structure

5.3.1 Manson Impact Structure

The Manson impact structure is located in northwestern Iowa (USA) about 30 km west of Fort Dodge near the town of Manson (Fig. 5.31). It has a diameter of ~35–37 km and is buried beneath 30–90 m of Pleistocene glacial till (Hartung and Anderson 1996; Earth Impact Database 2011 accessed 5 April 2011). Crystalline bedrock has been uplifted in the center of the structure (Kunk et al. 1989). The sedimentary rocks surrounding the uplift have been disrupted and are severely deformed. The Manson structure was originally interpreted as a cryptovolcanic structure (Hoppin and Dryden 1958), but was later recognized as an impact structure based on its overall morphology and by the discovery of shock metamorphosed quartz grains, with multiple sets of PDFs, recovered from the crystalline central uplift (Short 1966).

Early ^{40}Ar-^{39}Ar dating of the Manson structure indicated an age of 65.7 ± 1.0 Ma for the structure, an age that is indistinguishable from the K-T boundary layer. This led to a great deal of interest in the structure and several authors suggested that it was the K-T boundary source crater or at least one of the source craters (French 1984; Izett 1990; Shoemaker and Izett 1992). However, Izett et al. (1993) reported an ^{40}Ar-^{39}Ar age of 73.8 ± 0.3 Ma for the Manson structure and Izett et al. (1998) reported a weighted mean age of 74.1 ± 0.1 Ma for the Manson structure based on a set of 34 laser total-fusion ^{40}Ar-^{39}Ar analyses of sanidine from a

melt layer in the crater-fill deposits. Thus, the Manson structure is ~9 Ma older than the K-T boundary.

5.3.2 Distal Impact Ejecta from the Manson Impact Structure

5.3.2.1 Introduction

Shock metamorphosed grains have been discovered in the lower part of the Crow Creek Member of the Pierre Shale at numerous sites in South Dakota and Nebraska, approximately 215–475 km northwest of the Manson impact structure in Iowa (Fig. 5.31). The Pierre Shale is a widespread marine shale-dominated formation of Campanian and early Maastrichtian age found throughout the central and eastern part of the Cretaceous Western Interior of North America (Katongo et al. 2004). The Crow Creek Member (Fig. 5.32) consists of 2–3 m of marl with a 15–30 cm basal unit consisting of sandy siltstone that is commonly cross-bedded (Izett et al. 1998). It is the only bed of significant coarseness within the Pierre Shale and the basal contact is sharp and disconformable. Rip-up shale clasts are common in the lower part of the Crow Creek Member, especially in the southeastern exposures (Katongo et al. 2004).

5.3.2.2 Evidence of Shock Metamorphism

Shocked quartz and feldspar (microcline and plagioclase) with multiple sets of PDFs (Fig. 5.33) have been found in the lower part of the Crow Creek Member at 17 sites in South Dakota and Nebraska (Table 5.8; Fig. 5.31; Izett et al. 1993; Witzke et al. 1996; Izett et al. 1998; Katongo et al. 2004). Most shocked quartz grains display up to three sets of PDFs. The most common orientation is omega (ω), but pi (π), and sigma (σ) orientations are also present, indicating shock pressures of at least 15 GPa (Katongo et al. 2004). Although quartz grains with multiple sets of PDFs are most abundant in the lower part of the Crow Creek Member, they have also been found in the overlying marlstone (Izett et al. 1998). Some grains, especially potassium feldspar, exhibit pronounced mosaicism. Millimeter-size, well-rounded quartz grains with PDFs have been found, suggesting a sedimentary source. In addition, composite quartz and feldspar grains with PDFs are also present (Izett et al. 1998). Izett et al. (1998) stated that they recovered a few rounded, shock metamorphosed zircon crystals from the heavy-mineral fraction of the insoluble residue. However, no documentation of shock metamorphic features or high-pressure phases was presented. The highest concentration of shocked grains was found at the Lake Marindahl site (see Fig. 5.31 for location), where the clay-free HCl-insoluble residue contains ~20 % shocked quartz and feldspar grains. The lowest concentration of shocked grains is in the northwestern sites where the shocked grains make up much <1 % of the clay-free HCl-insoluble

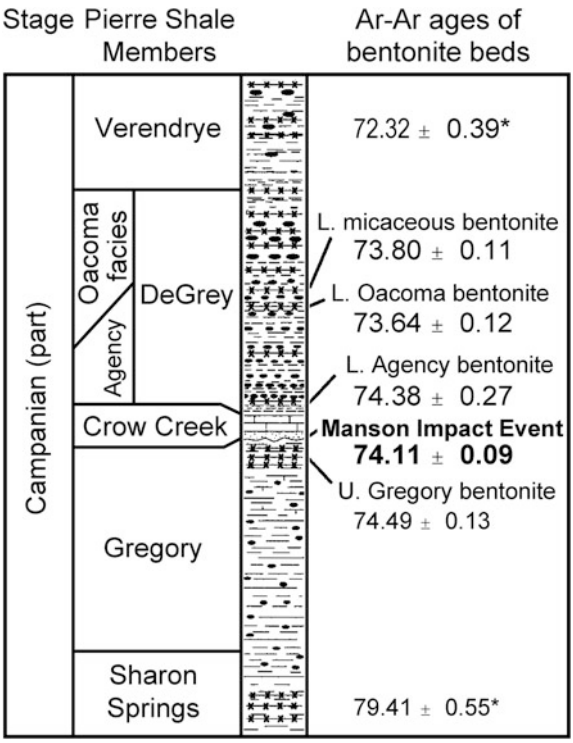

Fig. 5.32 Stratigraphy of a portion of the Campanian (Upper Cretaceous) rocks in eastern South Dakota and Nebraska where Manson impact ejecta have been found. The ejecta layer is found in the Crow Creek Member of the Pierre Shale. Ar–Ar ages of bentonite layers that bracket the Manson ejecta layer are also shown. L = lower and U = upper. Dates with asterisks after them are from J. D. Obradovich as reported by Izett et al. (1998). Modified after Fig. 5 in Izett et al. (1998)

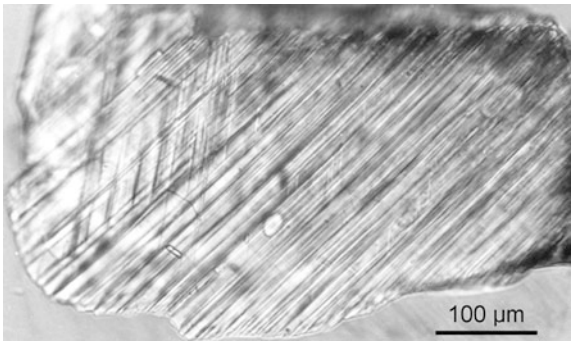

Fig. 5.33 Optical microscope image (plane polarized light) of a shocked quartz grain, from the Manson ejecta layer, with two obvious sets of PDFs. This grain was recovered from the basal part of the Crow Creek Member of the Pierre Shale near Gavins Point, South Dakota (see Fig. 5.31). Courtesy of Glen Izett

residue (Izett et al. 1998). The shocked quartz grains are up to 3.2 mm in size (Table 5.8; Fig. 5.34).

No spherules or Ir anomaly were reported for this layer. Somewhat elevated Cr, Co, and Ni abundances were found in the basal part of the Crow Creek Member at three sites, which might indicate the presence of a meteorite component; but low Ir contents do not allow unambiguous confirmation (Katongo et al. 2004).

Table 5.8 Maximum size of shocked quartz grains in the Crow Creek Member and distance from the Manson impact structure

State	County	Site	Distance from Manson (km)	Size (mm)
South Dakota	Yankton	Lake Marindahl	215	3.24
South Dakota	Yankton	Clay Valley	220	1.90
South Dakota	Yankton	Cement Quarry	235	1.72
Nebraska	Cedar	Gavins Point	245	2.28
South Dakota	Yankton	Lakeport	250	2.30
Nebraska	Knox	East of Niobrara	275	1.79
Nebraska	Knox	Niobrara State Park	285	1.70
South Dakota	Davidson	Mount Vernon	305	2.00
South Dakota	Gregory	Fort Randall Cemetery	315	1.50
South Dakota	Lyman	Chamberlain	410	0.45
South Dakota	Buffalo	Crow Creek	410	0.43
South Dakota	Lyman	Oacoma	415	1.20
South Dakota	Lyman	Black Dog	415	0.70
South Dakota	Lyman	White River	425	0.46
South Dakota	Lyman	Cedar Creek	455	0.26
South Dakota	Hughes	DeGrey	460	0.43
South Dakota	Hughes	Rousseau	475	0.80

Data from Izett et al. (1998)

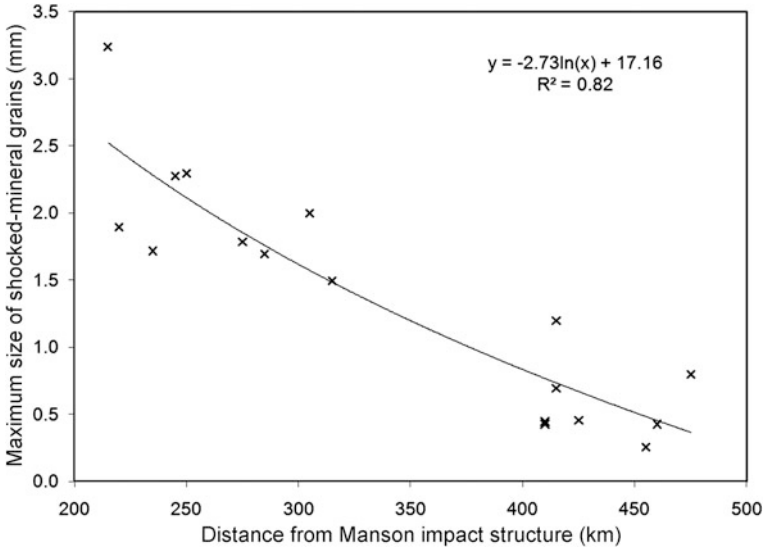

Fig. 5.34 Plot of maximum size of shocked quartz grains from the Manson ejecta layer versus distance from the Manson impact structure. Data from Izett et al. (1998)

5.3.2.3 Age of the Crow Creek Member Ejecta Layer

Argon-argon dating of bentonite layers above and below the Crow Creek Member indicates that the age of the Crow Creek Member is bracketed between 74.38 ± 0.27 and 74.49 ± 0.13 (Izett et al. 1998). Thus, within the quoted errors, the age of the Crow Creek Member ejecta layer is the same as the age of the Manson impact structure (i.e., ~74 Ma; see Fig. 5.32).

5.3.2.4 Evidence that the Manson Structure Is the Source of the Crow Creek Ejecta Layer

The geographic proximity of the Crow Creek ejecta layer to the Manson impact structure and the similarity in age suggest that the Crow Creek ejecta are from the Manson impact structure. The maximum size of shocked grains in the Crow Creek ejecta layer decreases with distance from the Manson structure (Table 5.8; Fig. 5.34; Izett et al. 1998), which is consistent with the Manson impact structure being the source crater. In addition, the thickness of the layer decreases with distance from the Manson structure; however, the observed thickness is greater than the calculated thickness (Katongo et al. 2004). The greater thickness may be due to the layer containing local sediment in addition to the ejecta. The presence of rip-up clasts and cross-bedding and the sharp unconformable lower contact are consistent with the proposal that ejecta from the Manson impact structure was reworked by an impact-triggered tsunami, which produced the Crow Creek Member (Izett et al. 1998).

5.4 Late Triassic Impact Ejecta Layer

A layer containing spherules and shocked quartz has been found in upper Triassic deposits near Bristol in southwestern England (Walkden et al. 2002). Unfortunately, these authors do not give the exact site location. Similar spherules were found in the Churchwood Quarry at Wickwar, ~20 km northeast of Bristol (Fig. 5.35; Kirkham 2002, 2003), but at this site the spherules have been reworked and redeposited. According to Walkden et al. (2002), the spherule layer at this site occurs ~1 m above the base of the 9-m-thick Mercia Mudstone within the upper part of the local Triassic succession, but well below the Triassic-Jurassic (Tr-J) boundary. The Mercia Mudstone unconformably overlies Lower Carboniferous (Dinantian) limestone. The spherule layer is between 0 and 15 cm thick over a 200-m-wide region, with an average of ~2.5 cm for eight sections. Spherules make up as much as ~50 % of the layer by volume. The spherule layer exhibits evidence of turbulent reworking such as convolute bedding, ripples, and mixing with local mud and lithoclasts (Walkden et al. 2002).

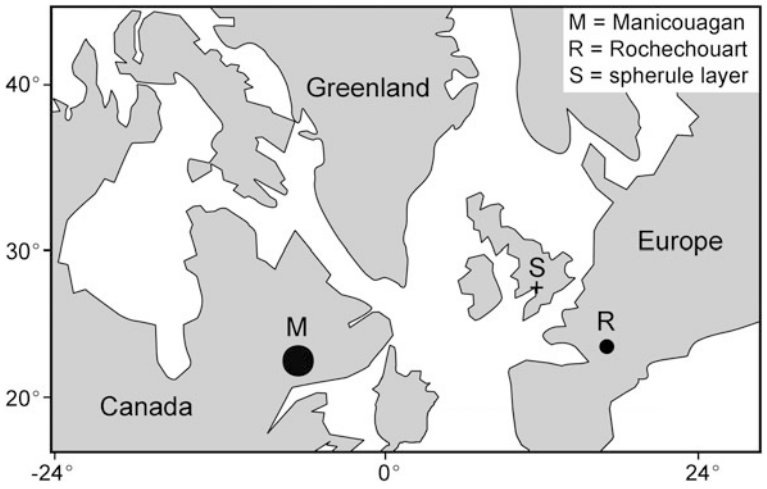

Fig. 5.35 Map showing the location of the late Triassic spherule layer in southwestern England described by Kirkham (2003). Also shown are the locations of the Rochechouart and Manicouagan impact structures. Modified after Kirkham (2003), Fig. 2

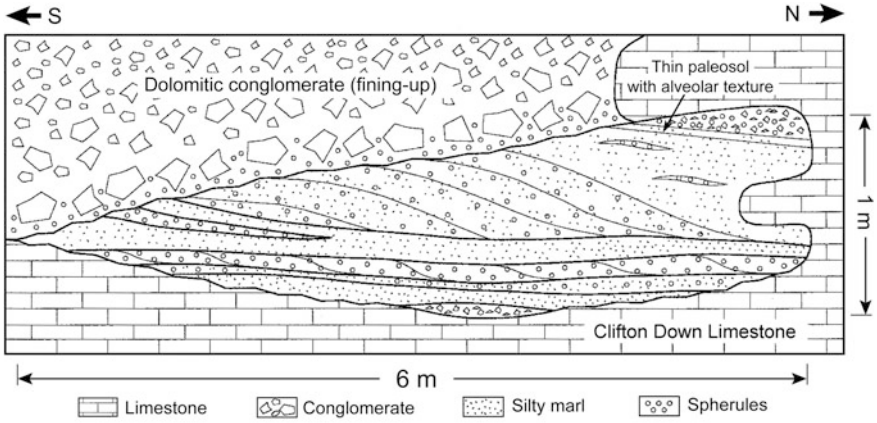

Fig. 5.36 Sketch of the spherule-bearing section in the Churchwood Quarry, Wickwar, England, as it was in 1976 (labeled *S* in Fig. 5.35). This exposure has since been removed by quarrying operations. Modified after Fig. 3 in Kirkham (2003), with permission from the Geologists' Association which holds the copyright

At the Wickwar site, the spherules are found within a partly cross-bedded deposit, ~6 m across and ~1 m thick, which unconformably overlies the Carboniferous (Dinantian) Clifton Down Limestone (Fig. 5.36; Kirkham 2003). The spherule deposit is unconformably overlain by what is probably the Dolomitic Conglomerate of Triassic age. Unfortunately, the outcrop has been destroyed by quarry operations (Kirkham 2003). The age of the spherule deposit appears to be

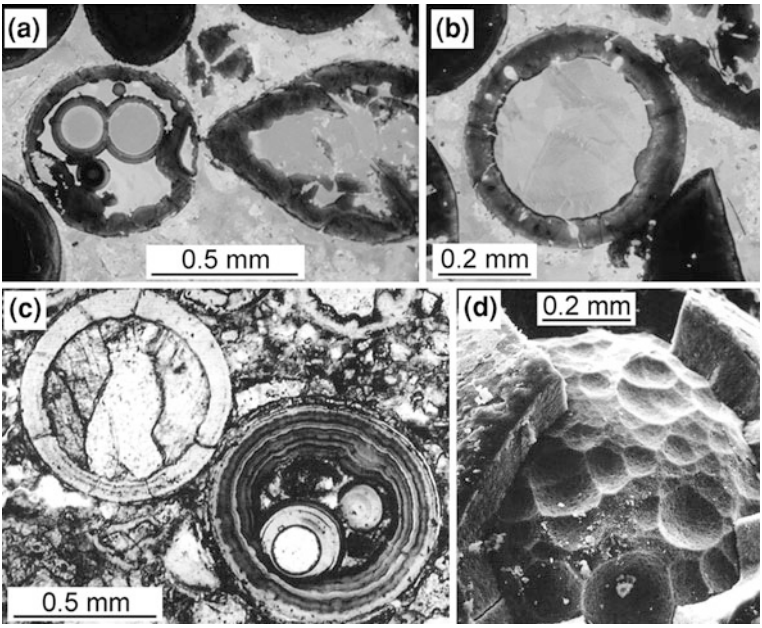

Fig. 5.37 Diagenetically-altered spherules recovered from the Late Triassic spherule/ejecta layer in southwest England. **a** Cathodoluminescence image of spherules in a calcite matrix. Clay and empty space is nonluminescent. Note the teardrop-shaped spherule and a circular spherule with two large circular areas inside. The circular areas are probably bubble cavities. (Polished standard optical thin section). **b** Cathodoluminescence image of a circular (in cross-section) spherule and parts of several other spherules. The circular spherule has an outer shell (~50–80 μm thick) with a botryoidal inner surface. **c** Optical microscope image (plane polarized light) showing two spherules and portions of several others. The wall of the larger spherule (lower right) exhibits concentric banding which may be related to Fe-oxidation state. The smaller spheres inside the large spherule may have been bubble cavities. The inner surface of the wall is slightly botryoidal. The other large spherule (upper left) has a thinner wall and a polycrystalline core of ferroan calcite cement. **d** Scanning electron microscope image of a spherule showing a broken outer shell composed of "glauconite" and a calcite cement core. Botryoidal protrusions on the inner surface of the shell produced depressions or dimples on the surface of the core. Compare A-D with the K-T boundary spherules from the Western Interior, USA, in Figs. 5.14 and 5.15. **a** and **b** are courtesy of G. Walkden. **c** and **d** are from Kirkham (2003), Figs. 4 and 6, respectively, with permission from the Geologists' Association which holds the copyright

between Late Carboniferous and Late Triassic, but Kirkham (2003) believes that a Triassic age is more likely. Based on their stratigraphic age, geographic location, and general appearance, it seems likely that the Wickwar spherules described by Kirkham (2002, 2003) belong to the same layer as the spherules described by Walkden et al. (2002).

The Late Triassic spherules (Fig. 5.37) are green within a clear calcite and/or pink potassium feldspar matrix. They are generally spherical to ovoid in shape, but teardrop and dumbbell shapes are also present. In addition, there are broken spherules and spherule fragments. The spherules are up to at least 1 mm in diameter

(Kirkham 2002, 2003). Many of the spherules are hollow, or were so before being filled with diagenetic minerals (Fig. 5.37; Walkden et al. 2002; Kirkham 2002, 2003). The Wickwar spherules have ferroan calcite cores (Kirkham 2002, 2003). The late Triassic spherules have disordered illitic clay (glauconite?) shells or outer layers with concentric layering and fibroradial textures. Concentric zonation within the spherule walls appears to be due to variations in iron oxidation (Fig. 5.37c; Kirkham 2003) or to variations in abundance of micrometer-sized titanium oxide crystals (Walkden et al. 2002). The exterior surfaces of the spherules are generally smooth, but the interior wall surfaces are botryoidal (Fig. 5.37b–d). Many of the spherules have one or more smaller spheres inside them (Fig. 5.37a), which have smooth inner surfaces and botryoidal (mammillary) outer surfaces. The smaller inner spheres are interpreted to be bubble cavities (Walkden et al. 2002; Kirkham 2002, 2003).

The hollow nature, concentric layering, and botryoidal inner surfaces of the Late Triassic spherules are similar to that of the hollow spherules in the K-T boundary layer at many of the Western Interior North American and Haitian sites and are believed to have been formed in the same way as proposed (Bohor and Glass 1995) for the K-T boundary spherules; i.e., by palagonitization of the outer layer of the impact-generated glass spherules, followed by solution of the remaining glass cores, diagenetic replacement of the palagonite, and, perhaps, later infill of the hollow spherules and vesicles with another diagenetic phase or phases.

The surmised impact origin of the Late Triassic spherules is based on their splash forms (especially rotational forms such as dumbbells and teardrops) and by their association with shocked quartz grains. The spherules are assumed to have been composed originally of glass which has undergone diagenetic alteration as described above. The spherules do not exhibit evidence of primary crystalline textures and Ni-rich spinel crystals have not been observed. Thus, there is no evidence to suggest that they were originally microkrystites. Kirkham (2003) proposed that they are diagenetically-altered microtektites. This is a reasonable interpretation, but it is probably better to refer to them as diagenetically-altered impact spherules.

Shocked quartz grains, some with multiple sets of PDFs, were recovered from the spherule layer (Fig. 5.38; Walkden et al. 2002; Kirkham 2003). Quartz grains are abundant in the spherule layer. They are mostly angular and between 50 and 300 μm in size. About 50 % exhibit multiple sets of PDFs (up to 5), which were observed by scanning electron microscopy after etching with hydrofluoric acid (Walkden et al. 2002). Approximately 42 % of the planar features fell along the omega (ω) direction and $\sim$26 % fell along the pi (π) direction.

Ar–Ar dating of authigenic K-feldspar in the spherule layer produced a low-precision plateau age of 214 $\pm$ 2.5 Ma (2σ errors). Because the feldspar is authigenic, it postdates the time of deposition of the spherules, but the age is consistent with the Norian age of the spherules based on the local stratigraphy (Walkden et al. 2002). Dating of the "glauconite" spherules, at Wickwar, using K–Ar yielded a wide range in ages with the oldest being 210 Ma, but the ages are considered to be unreliable due to argon loss (Kirkham 2003). Kirkham (2003)

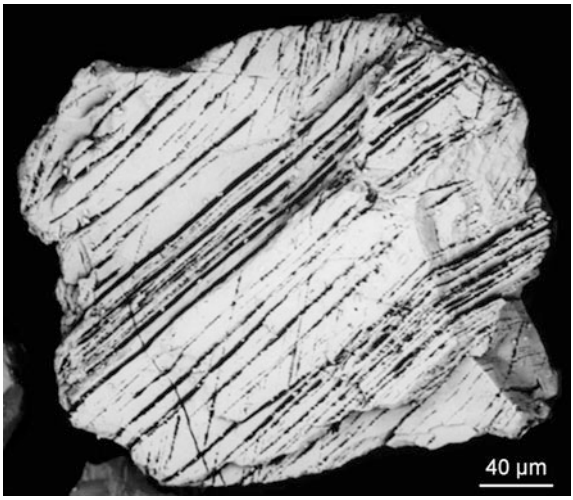

Fig. 5.38 Scanning electron microscope image of an etched shocked quartz grain with two sets of PDFs from the late Triassic spherule/ejecta layer in southwest England. From Walkden et al. (2002), Fig. 4, with permission from AAAS

stated that the real age is probably older than 210 Ma. This is consistent with the 214 ± 2.5 Ma age reported by Walkden et al. (2002).

Several Late Triassic impact structures are known, but the two largest with the best constrained ages are the 100-km-diameter **Manicouagan impact structure** in Quebec, Canada, and the 25-km-diameter **Rochechouart impact structure** in central France (Fig. 5.35). At the time that Walkden et al. (2002) published their paper on the Late Triassic spherule layer, the Manicouagan structure was believed to have an age of 214 ± 1 Ma (Hodych and Dunning 1992) and the Rochechouart structure was believed to have an age of 214 ± 8 Ma (Kelly and Spray 1997). More recently, Schmieder et al. (2010) obtained a ^{40}Ar-^{39}Ar plateau age of 201.4 ± 2.4 Ma for the Rochechouart structure. If this age is correct, this rules out the Rochechouart structure as a possible source crater for the Late Triassic spherule layer. However, based on age, size, and geographic location the Manicouagan structure could be the source of the Late Triassic spherule layer. Walkden et al. (2002) estimated the thickness of an ejecta layer from both of these craters based on crater size and distance from the spherule site 214 Ma ago using equations that relate thickness of an ejecta layer to crater size and distance from the crater (Table 5.9), and compared the calculated thicknesses with the observed thickness of ~2.5 cm. They concluded that Manicouagan gives the best match, but they stated that they could not rule out Rochechouart or both craters as the source of the spherules and shocked quartz. However, Walkden et al. (2002) used the rim-to-rim diameter of the craters to calculate the expected thickness of the ejecta layers from Rochechouart and Manicouagan rather than the estimated transient crater diameters on which the equations are based. If we use the estimated transient crater diameters of Manicouagan and Rochechouart to calculate the expected thickness, we find that the thicknesses are approximately one to nearly two orders of magnitude too thin, respectively, to explain the observed thickness of the spherule layer. However, as suggested by Walkden et al. (2002), Manicouagan

Table 5.9 Calculated thickness of Late Triassic ejecta layer near Bristol, southwestern England, assuming a source crater at Manicouagan or Rochechouart

Crater	Diameter (km)	Distance[a](km)	Calculated Thickness (cm)	Model[b]
Rochechouart	25	650	0.11	McGetchin et al. (1973)
Rochechouart	25	650	0.19	Stöffler et al. (1975)
Manicouagan	100	2000	0.65	McGetchin et al. (1973)
Manicouagan	100	2000	1.80	Stöffler et al. (1975)

Data mostly from Walkden et al. (2002)

[a] Estimated paleodistance between the respective impact craters and the Bristol spherule-bearing site ~214 Ma ago

[b] Equations used to estimate the thickness of an ejecta layer from the respective craters at the Bristol site are from the given references. See also Sect. 2.6

explains the observed thickness better than does Rochechouart. For additional discussion of the possible source crater of the Late Triassic spherule layer see Sect. 10.3.4.

Thackrey et al. (2009) studied the heavy mineral assemblage in the southwestern England Late Triassic spherule/ejecta layer and in target rocks from the Manicouagan impact structure in Quebec, Canada. They found that the heavy mineral assemblage, particularly the abundance of garnet types, in the ejecta layer is distinctive from the heavy mineral assemblage in the sediments beneath the ejecta layer, but similar to the heavy mineral assemblage in the target rocks at Manicouagan. In addition, they obtained whole grain fusion ^{40}Ar-^{39}Ar ages for "shocked" (kinked) biotite which are consistent with the Grenvillian age of the Manicouagan target rocks, but not with Rochechouart target rocks (Thackrey et al. 2009). They also dated zircons, using U–Pb, but the results were inconclusive.

5.5 Triassic-Jurassic Boundary Impact?

One of the five most severe marine extinction events in the Phanerozoic occurred at the **Triassic-Jurassic boundary** or **Tr-J boundary** (Raup and Sepkoski 1986; Sepkoski 1996). An abrupt turnover in both marine and terrestrial organisms appears to have taken place at the Tr-J boundary (Olsen et al. 2002a; Marzoli et al. 2004). The Tr-J extinctions may have involved ~22 % and ~53 % of marine families and genera, respectively (Sepkoski 1996), although some studies suggest that the extinctions took place in stages culminating in the boundary extinctions (Hallam 2002; Tanner et al. 2004). The age of the Tr-J boundary is estimated to be ~198–202 Ma (Hodych and Dunning 1992; Pálfy et al. 2002; Verati et al. 2007). Like the K-T boundary, the Tr-J boundary appears to be associated with a fern spike (Olsen et al. 2002a) and brief negative δ ^{13}C excursion (Ward et al. 2001; Pálfy et al. 2001; Hesselbo et al. 2002; Williford et al. 2007; and references

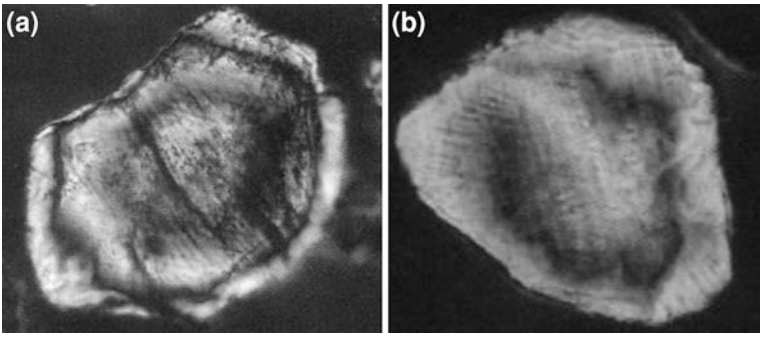

Fig. 5.39 Optical microscope images (plane polarized light) of quartz grains, with planar features, from near the Triassic-Jurassic boundary at the Il Fiume section, Italy. Although originally identified as planar deformation features, they may be Böhm lamellae. Compare with the shocked quartz grains in Figs. 2.21, 4.42, 5.18, and 5.33. From Bice et al. (1992), Figs. 3c and d. Reprinted with permission from AAAS

therein). However, unlike the K-T boundary, there is no globally distinct layer at the Tr-J boundary.

Badjukov et al. (1987) reported finding quartz grains with planar features at the Tr-J boundary in the Northern Limestone Alps, Austria. Most grains have only one set of planar features, but some have up to four sets. The grains with four sets of planar features also have reduced refractive indices (Badjukov et al. 1987). The maximum size of quartz grains with planar features is 80 μm. Bice et al. (1992) reported finding angular quartz grains with up to three sets of PDFs in three closely-spaced shale beds from the uppermost Triassic Calcare a Rhaetavicula in the Northern Alps of Italy (Fig. 5.39). They state that 32 % of the grains with PDFs from the boundary interval have two to three sets of PDFs and that most sets ($\sim$74 %) are approximately parallel to the basal, omega (ω), and pi (π) crystallographic planes.

Searches for shocked quartz grains in the Tr-J boundary interval in rift basins in Eastern North America have been negative (Mossman et al. 1998; Olsen et al. 2002a). Mossman et al. (1998) reported finding several quartz grains exhibiting planar features like PDFs that include one to as many as five intersecting, apparently straight, sets of internal parallel lamellae from the Tr-J boundary layer at Five Islands Provincial Park, near Parrsboro, Nova Scotia. The planar features appear to be oriented parallel to rhombohedral planes, which favors their impact origin (Mossman et al. 1998). However, transmission electron microscope observations indicate that the planar features observed by optical microscopy are subgrain boundaries and that the subgrains contain many perfect dislocations typical of a tectonic origin. Thus, Mossman et al. (1998) concluded that the structures are not the result of shock metamorphism, but were formed tectonically. Furthermore, these authors cast doubt on the conclusions of Badjukov et al. (1987) and Bice et al. (1992) who reported shocked quartz in the Tr-J boundary layer in the Northern Limestone Alps, Austria, and in the Northern Alps of Italy,

respectively, since these researchers did not use transmission electron microscopy to confirm the impact origin of the planar features. In addition, Hallam (1990) reported that Richard Grieve, an acknowledged impact expert, could not find any evidence of shock metamorphosed grains in Tr-J boundary samples (provided by Hallam) from the same section in Austria that was studied by Badjukov et al. (1987). More recently, Winslow et al. (2006) searched unsuccessfully for coesite, stishovite, and shocked zircons in several kilogram-sized samples from the Tr-J boundary in the Passaic Formation in the Newark rift basin (USA). In addition, Kring et al. (2007) searched for shocked quartz and soot in the Tr-J boundary interval at Muller Canyon, Nevada. No shocked quartz grains were identified and no increase in soot through the Tr-J boundary was observed.

Iridium has been searched for in the Tr-J boundary, but, as with shocked minerals, the results have been ambiguous. Smith et al. (1988) searched for an Ir anomaly in the Tr-J boundary layer in the Newark rift basin (Jacksonwald Syncline) without success, but the Ir amounts were below their detection limits. Mossman et al. (1998) looked for an Ir anomaly in the same section, again without success. Olsen et al. (1990) reported that Frank Asaro also was unable to find an Ir anomaly in the Tr-J boundary interval in the Newark basin (Jacksonwald Syncline). However, more recently a modest Ir anomaly has been found associated with the Tr-J boundary at four sites in the upper Passaic Formation in the Jacksonwald Syncline in the Newark rift basin in the USA (Olsen et al. 2002a,b) and in the Blomidon Formation in the Fundy rift basin in Canada (Tanner and Kyte 2005; Kyte et al. 2008). In the Newark basin, the Ir anomaly is associated with a fern spike (Fig. 5.40; Olsen et al. 2002a,b).

The maximum Ir contents were 285 and 449 ppt in the Newark and Fundy rift basins, respectively. However, comparison of the Ir contents with other siderophile element contents does not show strong correlations as would be expected if the siderophile elements were from a meteoritic source. On the other hand, there is no correlation between Ir and other elements (e.g., Cs, Al, Cu,V) that would indicate a volcanic source. Kyte et al. (2008) stated that attempts to demonstrate that an Ir anomaly at the Tr-J boundary occurs globally have failed, and that the occurrence of an Ir anomaly at the Tr-J boundary is restricted to the Fundy and Newark basins. They report multiple Ir anomalies near the palynological Tr-J boundary in the Fundy basin. Thus, as of 2008, the geochemical data do not unequivocally support or refute the hypothesis that a major impact took place at the end of the Triassic.

Some authors suggested that the Manicouagan impact may have been involved in the Tr-J extinctions (Olsen et al. 1987; McLaren and Goodfellow 1990; Olsen et al. 1990). The geologic time scale published by Harland et al. (1990) indicated an age of 208 ± 8 Ma for the Triassic-Jurassic boundary and in 1990 the age of the 100-km-diameter Manicouagan impact structure in Quebec, Canada, was thought to be 214 ± 5 Ma (Jahn et al. 1978). Thus, within the quoted errors, the Tr-J mass extinctions could have coincided with the Manicouagan impact. However, more recent dating indicates an age of ∼198–202 Ma for the Tr-J boundary (Hodych and Dunning 1992; Pálfy et al. 2002; Verati et al. 2007) and an age of 214 ± 1 Ma for the Manicouagan impact structure (Hodych and Dunning 1992).

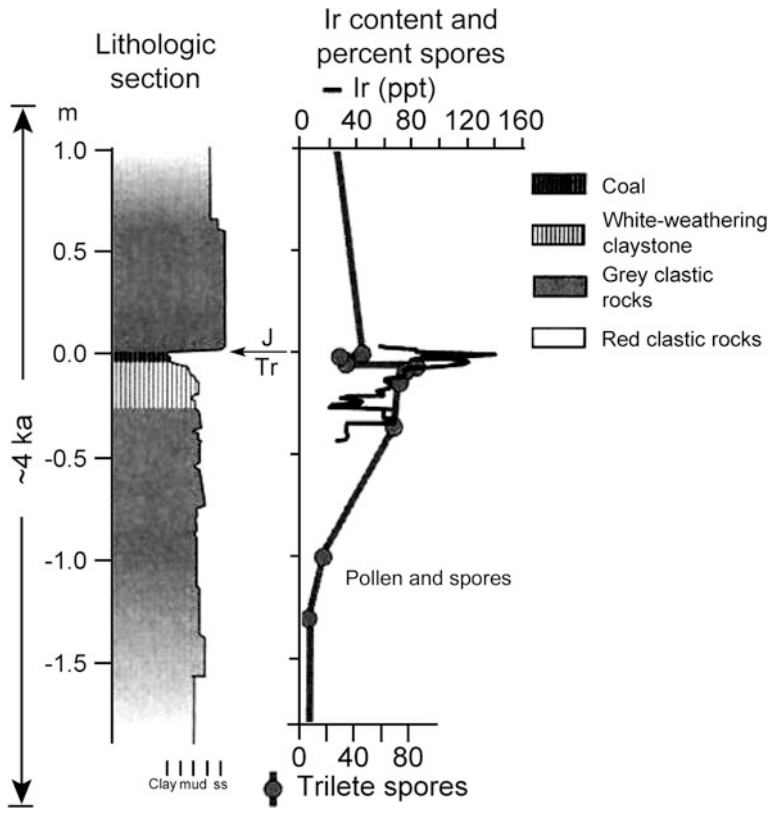

Fig. 5.40 Iridium (based on the average of data from four localities along strike) and fern spore content across the Triassic-Jurassic boundary in the Jacksonwald syncline section of the Newark basin in Pennsylvania, USA. Note that the maximum Ir content and fern spore abundance coincide with the Triassic-Jurassic (Tr-J) boundary. After Olsen et al. (2002b), Fig. 2. Reprinted with permission from AAAS

Likewise (U-Th)/He ages for nine zircons from a melt sheet sample from the Manicouagan impact structure yielded a weighted mean age of 213.2 ± 5.4 Ma (van Soest et al. 2011). Thus, the Manicouagan impact appears to have preceded the Tr-J boundary extinctions by ~13 Ma. However, the Manicouagan impact may have been responsible for a late Triassic spherule layer found in southwest England (see Sect. 5.4). Other known impact craters (Cloud Creek, Red Wing, Rochechouart, Saint Martin, Viewfield) of approximately the same age as the Tr-J boundary are not well dated and are probably too small (2.5–40 km diameter) to be responsible for the Tr-J extinctions.

Some researchers have suggested that the extinction event recorded at the Tr-J boundary may have been caused by the massive volcanic eruptions that produced the Central Atlantic magmatic province (CAMP) (Hesselbo et al. 2002; McHone 2003; Pálfy et al. 2002; Cohen and Coe 2002; Tanner et al. 2004; Marzoli et al.

2004; Kyte et al. 2008). Tanner and Kyte (2005) suggested that the Ir anomaly at the Tr-J boundary in the Fundy and Newark basins may have been related to the volcanism. Some authors have suggested that the Tr-J extinctions might have been caused by both volcanism and impact (White and Saunders 2005). On the other hand, Whiteside et al. (2007) concluded that there is no compelling evidence showing that any of the CAMP volcanism predated or was synchronous with the Tr-J extinctions.

Chapter 6
Paleozoic Impact Spherule/Ejecta Layers

6.1 Introduction

Although the Paleozoic Era lasted nearly five times longer than the Cenozoic, the number of Paleozoic distal impact ejecta layers that have been identified is much smaller (compare Table 6.1 with Table 4.1). Two probable Late Devonian distal impact ejecta layers have been reported. The youngest is a silicate glass spherule (microtektite?) layer and Ir anomaly found in Qidong (southern China) in Late Devonian deposits, about 1.5–2.0 Ma younger than the **Frasnian–Famennian boundary**. The second is an older layer of silicate glass spherules (microtektites) found just above the Frasnian–Famennian boundary at two sites (Senzeille and Hony) in Belgium. Four additional spherule occurrences of Frasnian to Famennian age have been reported in southern China: one above the Frasnian–Famennian boundary, one at the boundary, and two below the boundary. The most intensely studied Paleozoic 'ejecta' layer is at the **Permian–Triassic boundary**, but as of 2011, the impact origin of this boundary layer had not been established. Some researchers claim to have found evidence for an impact at the **Devonian–Carboniferous boundary** and at the **Eifelian–Givetian boundary**; however, the evidence is not yet convincing. Silicate glass spherules, interpreted as microtektites, have been found associated with the Devonian-Carboniferous boundary (also called the Devonian-Mississippian boundary) in southern China and shocked quartz has been reported from this boundary in northwestern Pennsylvania, USA. High concentrations of some siderophile elements, spherules, and shocked quartz in Middle Devonian (close to the Eifelian–Givetian boundary) deposits in Jebel Mech Irdane, Morocco, have been reported; but the presented evidence has been disputed by some researchers. At the end of the chapter, we have included a short section on the late Devonian (Frasnian Age) impact breccia (the Alamo Breccia) found in Nevada, USA. Some of the ejecta associated with this layer may be distal, but most of the Alamo Breccia appears to be proximal.

B. P. Glass and B. M. Simonson, *Distal Impact Ejecta Layers*, Impact Studies,
DOI: 10.1007/978-3-540-88262-6_6, © Springer-Verlag Berlin Heidelberg 2013

Table 6.1 Possible/probable Paleozoic impact spherule/ejecta layers

Layer[a]	Location	Impact evidence[b]	Age (Ma)	Possible source crater[c]	Selected references[d]
Well-established ejecta layers					
Base of Famennian	Senzeille and Hony, Belgium	Sph	~376	Siljan, Charlevoix, or Woodleigh	Claeys and Casier (1994)
Lower Frasnian Alamo Breccia	Southwest USA	SQ	~382	Alamo	Warme et al. (1991), Morrow et al. (2005)
Probable/possible distal ejecta layers					
Famennian	Qidong, South China	Sph	~374	Taihu Lake (?)	Wang (1992)
Near base of Famennian	Nandong and Xikuangshan, South China	Sph	~376	?	Ma and Bai (2002)
Frasnian–Famennian boundary	Nandong and Xikuangshan, South China	Sph	~376	?	Ma and Bai (2002)
Below Frasnian–Famennian boundary	Nandong and Xikuangshan, South China	Sph	~376	?	Ma and Bai (2002)

(continued)

Table 6.1 (continued)

Layer[a]	Location	Impact evidence[b]	Age(Ma)	Possible source crater[c]	Selected references[d]
Proposed, but not accepted distal ejecta layers					
Permian–Triassic boundary[d]	Antarctica	Ir, Sph, SQ, FwNG, NiFeP, MF, CrI	252.6 ± 0.1	Bedout (?)	For Ir references see Table 6.7 Jin et al. (2000), Yin et al. (1992), Petaev et al. (2004), Retallack et al. (1998), Becker et al. (2001), Basu et al. (2003), Shukolyukov et al. (2004)
	Southern China	Ir, PGEs, Sph, FwNG, NiFeP			
	Japan	Sph, FwNG			
	Australia	Ir, SQ			
Devonian-Carboniferous boundary	Huangmao and Muhua, South China	Sph, Ir(?)	~359	?	Bai (2001); Hill and Jimenez (2010),
	Northeastern Pennsylvania, USA	SQ(?)			
Middle Devonian	Morocco	SQ?	~388	?	Ellwood et al. (2003); Schmitz et al. (2006)

[a] The Famennian and Frasnian are Late Devonian stages

[b] Published evidence given in support of an impact origin; most are not unique to impact: *CrI* Chromium isotope data, *FwNG* Fullerenes containing extraterrestrial noble gases, *Ir* Iridium anomaly, *MF* Meteorite fragments, *NiFeP* Ni-Fe-rich particles, *PGEs* Platinum group elements with chondritic ratios, *Sph* Spherules, *SQ* Shocked quartz with PDFs

[c] The Bedout and Taihu Lake structures have not been accepted by the impact community as impact structures as of 2011

[d] Except for the Cr isotope data, all the evidence for an impact ejecta layer at the Permian–Triassic boundary has been refuted or at least questioned

6.2 Late Devonian Spherule/Ejecta Layers

6.2.1 Introduction

The Late Devonian is marked by numerous sea-level changes, mass extinction events, and several major impacts (Sandberg et al. 2002). The most prominent mass extinction event in the Late Devonian occurred at or near the Frasnian–Famennian boundary. The Frasnian–Famennian extinction event has been designated as one of the five largest mass extinction events known (Sepkoski 1982; McGhee 1996). In Europe, this mass extinction event corresponds to the geographically widespread Kellwasser black shale and bituminous limestone deposits and is known as the "Kellwasser Event" (McGhee et al. 1986). The major marine extinction event at this time may have been very abrupt, perhaps less than 20,000 yrs (Sandberg et al. 2002); however, some researchers suggest that the extinctions took place in steps or pulses over a period of $\sim$1 Ma (Walliser 1996; McGhee 2001, and references therein).

The accepted age of the Frasnian–Famennian boundary according to the Geologic Time Scale approved by the International Commission on Stratigraphy is 374.5 $\pm$ 2.6 Ma (Gradstein et al. 2004). However, based on U–Pb dating of volcanic zircon and monazite, Kaufmann (2006) obtained an interpolated age of 376.1 $\pm$ 3.6 Ma, and more recently Turgeon et al. (2007) obtained an interpolated age of 372.4 $\pm$ 3.8 Ma based on Re–Os depositional ages of four organic-rich shale intervals spanning the Frasnian–Famennian boundary in western New York. Within the dating errors, all these ages agree with each other.

6.2.2 The Qidong Silicate Glass Spherule Layer

Silicate glass spherules have been found in deposits of the Late Devonian Famennian Stage in Qidong, Hunan Province, southern China (Fig. 6.1; Wang 1992; Wang et al. 1994). **Qidong spherules** were recovered from the conodont Lower *Palmatolepis crepida* Zone (Fig. 6.2). Twenty-five samples were collected over a 20-m section (i.e., average of one sample per $\sim$0.8 m). The spherules were found in a single sample from a 3-cm-thick claystone between two carbonate formations (Shetianqiao and Xikuangshan); no spherules were found in any of the other samples (Wang 1992). Approximately 60 spherules were recovered. Petrographic and compositional data indicate that these spherules are impact spherules, perhaps microtektites. The following description is based on Wang (1992).

The spherules range from 80 to 160 μm in diameter, but most are $\sim$100 μm across. Most are spherical, but a few are pear- to teardrop-shaped (Fig. 6.3). A few are composed of two or more spheres welded together. The spherules range from opaque white, to translucent dark brown, to transparent colorless to yellowish brown. The surfaces vary from smooth with a glassy luster to pitted and corroded

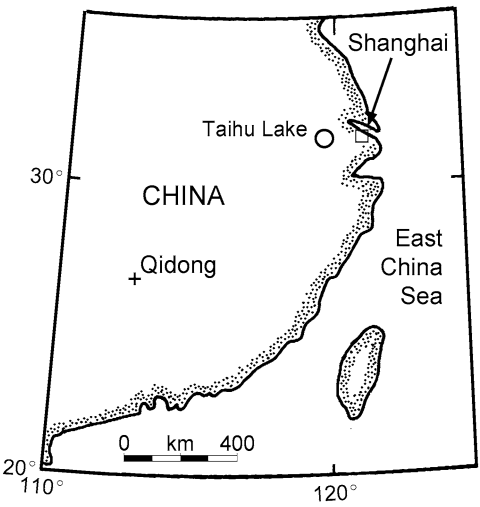

Fig. 6.1 Map of southern China, showing the location of Qidong and Taihu Lake. Modified after Wang (1992), Fig. 1

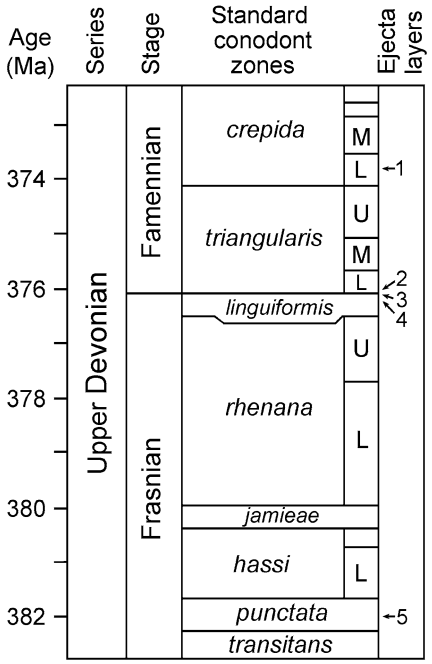

Fig. 6.2 Probable/possible Late Devonian spherule/ejecta layers tied to the standard conodont zones. Five spherule/ejecta layers are indicated: (*1*) The Qidong spherule layer in the *Palmatolepis crepida* Zone; (*2*) the Senzeille and Hony spherule (microtektite) layer in Belgium and a possible spherule layer in the Xikuangshan and Nandong sections in southern China in the Lower *triangularis* Zone near the Frasnian–Famennian boundary (FFB); (*3*) a possible spherule layer at the FFB in the Xikuangshan and Nandong sections in southern China; (*4*) a possible spherule layer below the FFB in the *linguiformis* Zone; and (*5*) the Alamo Breccia layer in the *punctata* Zone. *L* Lower; *M* Middle; *U* Upper. Ages of the conodont zones are based on Kaufmann (2006)

with a dull or frosted appearance (Fig. 6.3). Some have small circular raised areas or caps on their surfaces.

The spherules are isotropic except for a few relict (?) quartz inclusions in some of them (3 out of the 17 spherules studied). X-ray diffraction studies indicate that the spherules are amorphous except for the presence of quartz in some of them. No primary microlites/crystallites were observed; however, spherical vesicles are present. Energy-dispersive X-ray analysis indicates the presence of silica inclusions (>99 wt % SiO_2). In addition to the quartz, some of the silica inclusions are isotropic and are probably lechatelierite.

The matrix glass in the Qidong spherules has silica contents ranging from ~58 to 67 wt % and Al_2O_3 contents ranging between ~21 and 24 wt % (Table 6.2). In addition to the silica inclusions already mentioned, there are isolated regions of silica-rich glass in some of the spherules. The silica-rich glass regions have silica contents between ~80 and 93 wt %. The iron content of the spherules is relatively low (< 3 wt % FeO) and the CaO content is as high as 6.8 wt %. The Al_2O_3, FeO, MgO, CaO, and TiO_2 contents all decrease with increasing SiO_2 contents. Like most Cenozoic tektites and microtektites, the Qidong spherules have K_2O contents that are higher than the Na_2O contents (i.e., K_2O/Na_2O >1). The linear compositional trends (major oxides vs. silica) are similar to those observed for the Cenozoic microtektites, especially the North American microtektites (Fig. 6.4). The water content of these spherules was not determined, but Wang (1992) pointed out that the oxide totals are high (average of 99.48 wt % for 50 analyses of the matrix glass) and he concluded that the spherules must be volatile poor.

The occurrence of the spherules in the Lower *crepida* conodont Zone indicates that the spherule layer is ~2 Ma younger than the Frasnian–Famennian boundary, which has an age of ~376 Ma (Fig. 6.2; Kaufmann 2006). This suggests that the Qidong spherules were deposited ~374 Ma ago. There was an attempt to date three of the spherules using the laser step-heating $^{40}Ar - {}^{39}Ar$ method. Unfortunately, two of the spherules were too small to date and the third only gave a minimum age of ~160 Ma for the highest temperature fraction (Wang et al. 1994).

Preservation of glass for several hundred million years is most unusual. Wang (1992) suggested that the preservation of the glass spherules may have been aided by inclusion in a diagenetic limestone with low permeability.

The claystone layer containing the spherules has anomalously high Ir, Fe, Co Cr, Se, Sb, and As contents compared with the overlying and underlying deposits (Fig. 6.5; Wang et al. 1994). However, the peak Ir abundance is only 30 ppt. Because the overlying and underlying deposits are carbonates, the "anomalies" may simply be due to a change in the lithology (and lower sediment accumulation rate). An Ir anomaly of similar age has been found in the Canning Basin in Western Australia (Playford et al. 1984; Nicoll and Playford 1993). Here the Ir anomaly is associated with a microstromatolitic deposit composed of the cyanobacterium *Frutexites* which is known to concentrate noble metals (Playford et al. 1984; Nicoll and Playford 1993). Wallace et al. (1991) stated that the platinum group elements do not have chondritic ratios and there is no evidence that the

Table 6.2 Major oxide compositions (wt %) of the Qidong spherules from southern China (data from Wang 1992)

	Matrix glass (50)		High-silica glass (10)		Silica inclusions (20)	
	Average	Range	Average	Range	Average	Range
SiO_2	61.77	58.19–67.16	86.33	79.79–93.04	99.68	99.30–100.45
Al_2O_3	21.82	20.58–24.01	7.38	3.53–9.96	0.19	0.00–0.39
FeO	1.48	0.46–2.80	0.56	0.33–1.15	0.02	0.00–0.04
MgO	2.91	1.15–4.14	0.71	0.31–1.65	0.01	0.00–0.03
CaO	5.15	3.37–6.83	1.45	0.56–3.54	0.02	0.00–0.04
K_2O	3.23	2.66–4.45	1.97	1.29–2.71	0.05	0.00–0.11
Na_2O	2.48	2.31–2.70	1.08	0.59–1.41	0.00	0.00–0.01
TiO_2	0.55	0.20–0.70	0.24	0.14–0.55	0.07	0.00–0.33
MnO	0.04	0.00–0.09	0.02	0.00–0.07	0.01	0.00–0.05
Cr_2O_3	0.05	0.00–0.14	0.05	0.00–0.15	0.00	0.00–0.00
Total	99.48		99.79		100.05	

Compositional data obtained by electron microprobe. Numbers in parentheses are number of analyses. All iron reported as FeO
Silica inclusions are mostly isotropic (probably lechatelierite), but some are partially crystalline (probably quartz)

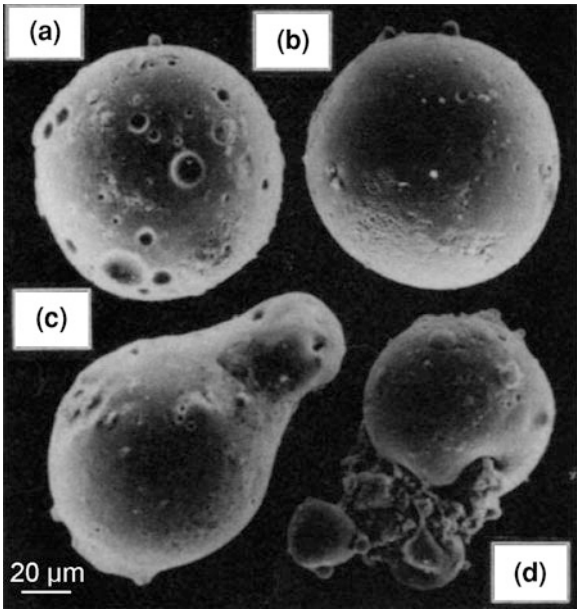

Fig. 6.3 Scanning electron microscope images of silicate glass spherules recovered from the Upper Devonian *Palmatolepis crepida* conodont Zone at Qidong, China. **a** A pitted spherule with protrusions or raised silica-rich caps. **b** A relatively smooth spherule with a couple of silica-rich caps. **c** Pear-shaped spherule with a few silica-rich caps. This spherule may have formed when two spherules of unequal size fused together. **d** This was described as a welded spherule with some silica-rich caps. From Wang (1992), Fig. 3. Reprinted with permission from AAAS

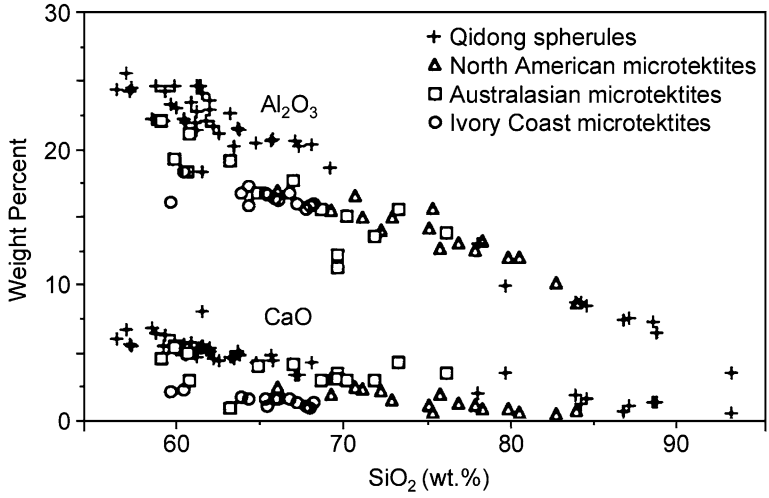

Fig. 6.4 Plot of Al_2O_3 and CaO versus SiO_2 for Qidong spherules and North American, Australasian, and Ivory Coast microtektites for comparison. North American microtektite data from Glass et al. (1985). Australasian microtektite data from Cassidy et al. (1969). Ivory Coast microtektite data from Glass and Zwart (1979b). From Wang (1992), Fig. 6. Reprinted with permission from AAAS

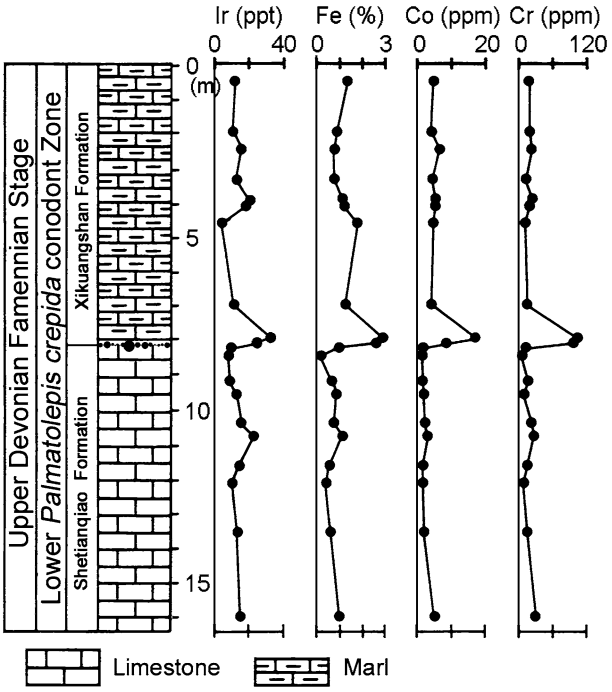

Fig. 6.5 Stratigraphy, lithology, and vertical distribution of Ir, Fe, Co, and Cr contents across the spherule layer at Qidong, southern China. Black dots in the lithology column indicate where the spherules were found in a 3-cm-thick claystone layer between the Shetianqiao and Xikuangshan Formations. The spherule layer occurs just below an increase in Ir, Fe, Co, and Cr content in the section. Modified after Fig. 2 in Wang (1992)

non-chondritic ratios are the result of low-Eh diagenetic alteration. In addition to the absence of a convincing Ir anomaly, no other evidence of an impact event (e.g., shock metamorphosed grains) has been reported in the spherule-bearing layer.

The petrography and major oxide composition of the Qidong spherules, especially the presence of lechatelierite, the absence of microlites/crystallites, the compositional trends, and the apparent low volatile content, are consistent with an impact origin. Wang (1992) concluded that the spherules are microtektites. The low abundance of the spherules, the presence of relict quartz grains, and the high vesicularity and heterogeneous nature of some of the spherules suggest that the source crater is nearby and not very large. On the other hand, if the source crater is nearby, there should be shock metamorphosed rock and mineral grains in the spherule layer.

Wang (1992) suggested that the source crater may be an impact crater (Taihu Lake) about 900 km northeast of Qidong (Fig. 6.1). However, this structure has not yet been recognized by the impact community as an impact crater. Other larger impact structures that could have the appropriate age to be the source crater for the Qidong spherules include: Siljan, Charlevoix, and Woodleigh (see Sect. 6.2.3.3.5).

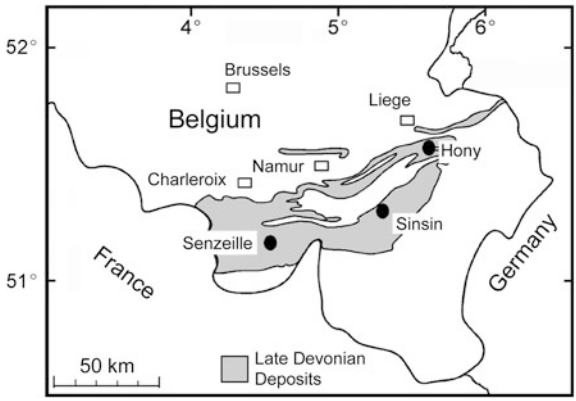

Fig. 6.6 Map showing the distribution of Late Devonian outcrops in Belgium and the location of the spherule-bearing sites (Senzeille and Hony) and another Frasnian–Famennian boundary site (Sinsin) mentioned in the text. Modified after Fig. 1 in Claeys and Casier (1994)

6.2.3 Evidence for an Impact Ejecta Layer Near the Frasnian–Famennian Boundary

6.2.3.1 Introduction

McLaren (1970) was probably the first to propose that the Frasnian–Famennian mass extinction event might be due to an impact. He reiterated this possibility (McLaren 1982) after Alvarez et al. (1980) published their benchmark paper suggesting that an impact was the cause of the mass extinction at the Cretaceous-Tertiary boundary. Numerous researchers have searched for evidence of an impact at the Frasnian–Famennian boundary with mixed results. The age of the Frasnian–Famennian boundary is 376.1 ± 3.6 Ma (Kaufmann 2006).

6.2.3.2 Ir and Other Platinum Group Element Data

Since 1984, there has been a series of attempts to find an Ir anomaly at the Frasnian–Famennian Boundary (**FFB**). In 1984, McGhee et al. reported searching for an Ir anomaly at the FFB at three sites in northwestern New York, USA, and at the Sinsin FFB section in Belgium (Fig. 6.6). No Ir anomaly was found at any of the four sites. The highest Ir concentration was ~120 ppt; the average was ~50 ppt. McGhee et al. (1984) concluded that the Frasnian–Famennianmass extinction "…does not appear to be associated with a large-body impact, unless it were an ice-rich (stone-poor) comet or a highly fractionated (Ir poor) body (eucrite, howardite, angrite, or nakhlite)."

Over et al. (l997) also studied the FFB in western New York (USA). They measured Ir, Pd, Pt, and Ru contents of samples taken across the FFB at the Irish Gulf and Perry Farm Creek sections in western New York. They reported Ir concentrations at the FFB of 0.11–0.24 ppb, two to five times the background levels of < 0.05 ppb. In addition, they determined that the Pt/Pd and Ru/Ir ratios at

the FFB are close to chondritic ratios. However, they found other Ir enrichments within 50 cm of the FFB. Over et al. (1997) concluded, "Multiple Ir anomalies and no definite PGE peak through the boundary interval in the absence of microtektites and shocked mineral grains are not consistent with a single impact." Turgeon et al. (2007) used Re–Os to date the FFB in a drillcore from western New York. Based on the low Os and Re abundances at the FFB, they concluded that their data were inconsistent with long-term volcanism or the impact of an extraterrestrial object as a potential mass extinction mechanism at the FFB. In a more recent paper, Gordon et al. (2009) reported Os isotope data for the FFB in the Irish Gulf section in western New York and concluded that the data were inconsistent with a large meteoritic component.

McGhee et al. (1986) reported that they were not able to find an Ir anomaly associated with the Frasnian–Famennianmass extinction event (or "Kellwasser Event") across the *Palmatolepis gigas*/*P. triangularis* conodont zonal boundary in a section near Bad Wildungen in Germany.

Claeys et al. (1996) searched for an Ir anomaly associated with a spherule layer just above the FFB in the Hony section in Belgium (see below). The Hony section is ~45 km north-northeast of Sinsin where McGhee et al. (1984) failed to find an Ir anomaly at the FFB (Fig. 6.6). Claeys et al. (1996) found a small Ir anomaly (one sample was 83 ppt above the background level of ~40 ppt) at the spherule layer. A similar spot excursion was found 18 cm above the spherule layer. Claeys et al. (1996) stated that the interpretation of the anomaly is not clear, but, considering the analytical uncertainties, the anomaly is probably not significant at the 2 sigma level. They, thus, concluded that no significant Ir anomaly was detected at the FFB or spherule layer in the Hony section.

Girard et al. (1997) searched for an Ir anomaly, microtektites, and Ni-rich spinels at the FFB (Kellwasser bed) in the stratotype area in southern France. No significant Ir anomaly, Ni-rich spinels, or microtektites were found. Likewise, no Ir anomaly was found at the FFB in the Long Rapids Formation in northern Ontario, Canada (Levman and von Bitter 2002).

6.2.3.3 Impact Spherules (Microtektites?) at Senzeille and Hony, Belgium

6.2.3.3.1 Introduction

Silicate glass spherules have been found in Upper Devonian deposits at Senzeille (Senzeilles) and Hony, Belgium (Fig. 6.6) (Claeys et al. 1992; Claeys and Casier 1994). At Senzeille, where the spherules were first found, the layer appears to be in the Lower *triangularis* conodont Zone ~7 m above the Frasnian–Famennian boundary (FFB) (Fig. 6.7); however, the conodont stratigraphy is poorly known at this site. At Hony, 90 km east-northeast of Senzeille, there is a 150-cm-thick shale unit that contains no identifiable conodonts. This shale unit is found between the Frasnian *linguiformis* conodont Zone below and the Famennian Lower *triangularis* conondont Zone above. The upper 40 cm of this unit consists of finer and more

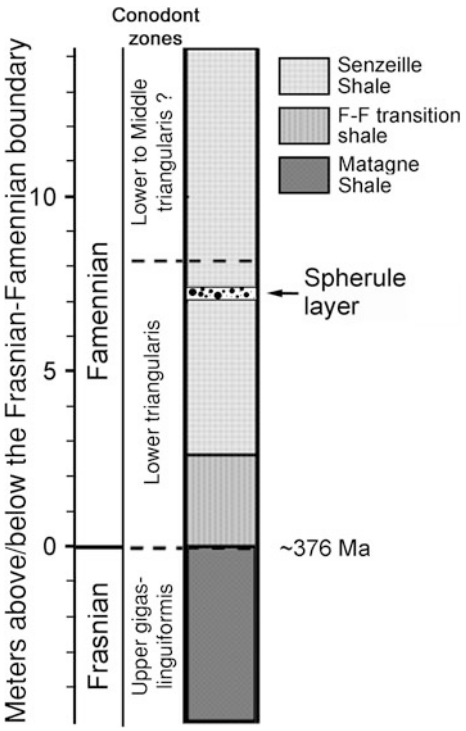

Fig. 6.7 Conodont zonation and lithology of the Senzeille section, Belgium, showing location of the spherule (microtektite) layer. Placement of the Frasnian–Famennian boundary is based on Casier (1992). See Sect. 6.2.1 for discussion of the age of the Frasnian–Famennian boundary. Modified after Fig. 1 in Claeys et al. (1992)

fissile dark gray shale. The FFB has been placed at the base of the dark gray shale bed (Sandberg et al. 1988; as quoted by Claeys and Casier 1994). At Hony, the spherules are concentrated in a 2-cm-thick layer at or just above the FFB with some scattered ones found in decreasing number up to ~25 cm above the layer. Where they are concentrated, the spherules at Senzeille and Hony make up about 0.0003 and 0.00005 wt % of the sediment, respectively. The following description of Senzeille and Hony spherules is taken from Claeys et al. (1992) and Claeys and Casier (1994).

6.2.3.3.2 Description

The **Senzeille spherules** range from 50 μm up to >1 mm in diameter, but most average ~300 μm in size. At Hony they are between 50 and 500 μm in diameter, with an average size of ~250 μm. At both sections, the spherules are primarily spherical in shape (Fig. 6.8), with some elongate and teardrop shapes. At Senzeille, some were also described as dumbbell shaped, but the only dumbbell form illustrated looks more like two spherules fused together (Fig. 6.8b) than like a dumbbell formed by rotation. Fused forms are present at both sites.

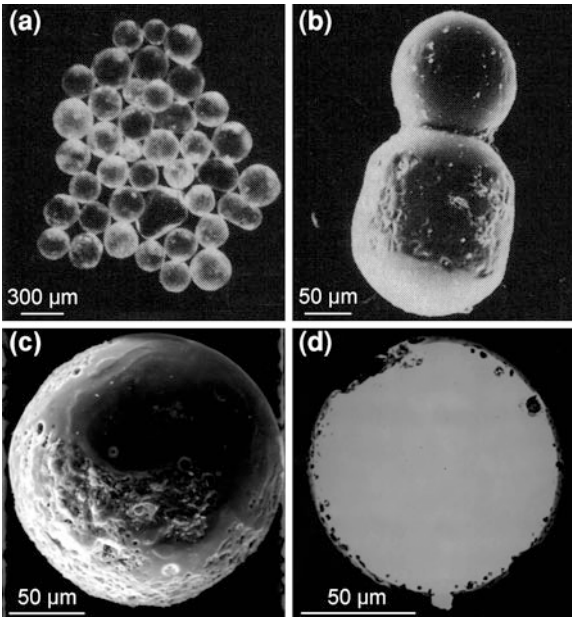

Fig. 6.8 Spherules (microtektites) found near the Frasnian–Famennian boundary at Senzeille, Belgium. **a** Reflected light photomicrograph of a group of spherules showing morphology. **b** Scanning electron microscope (SEM) photomicrograph of two Ca-rich spherules fused together. Note the V-shaped groove where they join. This feature has been observed in compound Cenozoic microtektites (Glass 1974). **c** SEM image of a spherule with exposed vesicles and evidence of surface sculpturing from solution. **d** Back scattered electron image of a polished section of a Fe-rich black spherule showing lack of microlites and numerous small vesicles around the margins. **a** and **b** are from Claeys et al. (1992), Figs. 2a and c, reprinted with permission of AAAS; **c** and **d** are courtesy of P. Claeys

The spherules at Senzeille are mostly transparent yellowish as are most of the spherules at Hony. A few of the Senzeille spherules are dark with a metallic luster. However at Hony, $\sim$30 % are described as transparent white and $\sim$20 % are described as black, with a few having a more reddish color. At both sections, the surfaces of the spherules range from smooth glassy to finely pitted with a frosted appearance to deeply etched with pitted surfaces. The pitting is often restricted to one side. Unlike the Cenozoic microtektites, the Belgian FFB spherules do not have grooves on their surfaces and none have a scalloped appearance. Some of the **Hony spherules** exhibit fine lines or striations on their surfaces and some have silica-rich protrusions or caps on their surfaces. Similar silica-rich protrusions have been observed on Cenozoic microtektites (Glass 1974).

At both sites, some of the spherules contain a few large vesicles and at the Hony site, at least, they are usually concentrated towards the surface. None of the Belgian spherules show evidence of devitrification or alteration. The spherules are isotropic in polarized light and generally lack microlites/crystallites. One Hony

Table 6.3 Major oxide and sulfur contents (wt %) of Late Devonian spherules from Senzeille and Hony, Belgium (data from Claeys and Casier 1994)

	Senzeille spherules											
	K-rich (27)			Al-rich (11)			Ca-rich (5)			Fe-rich (6)		
	Ave.		S.D	Ave.		S.D.	Ave.		S.D.	Ave		S.D.
SiO_2	63.5	±	2.9	51.70	±	3.3	44.8	±	1.9	42.30	±	2.0
Al_2O_3	22.8	±	2.2	29.30	±	2.1	20.2	±	1.7	19.40	±	1.9
FeO	1.58	±	2.0	7.31	±	2.9	5.40	±	1.3	28.62	±	1.8
MgO	2.12	±	0.4	2.41	±	0.4	2.10	±	0.4	2.18	±	0.7
CaO	3.26	±	0.8	4.09	±	0.3	23.11	±	2.9	1.54	±	0.2
K_2O	4.71	±	0.7	2.84	±	0.5	2.16	±	0.4	2.25	±	0.5
Na_2O	1.01	±	0.4	0.81	±	0.1	0.55	±	0.1	0.80	±	0.2
TiO_2	0.60	±	0.1	1.01	±	0.1	0.60	±	0.3	0.72	±	0.1
MnO	0.16	±	0.04	0.10	±	0	0.15	±	0	1.20	±	0.1
S		<DL			<DL			<DL		0.30	±	0.01
Total	99.7			99.6			99.1			99.3		
	Hony spherules											
	K-rich			Al-rich			Ca-rich			Si-rich		
SiO_2	59.44	±	3.3	47.00	±	0.6	63.39	±	2.7	85.10	±	2.2
Al_2O_3	25.05	±	2.6	28.90	±	0.5	20.73	±	2.0	6.89	±	1.9
FeO	4.55	±	1.7	13.06	±	0.7	1.62	±	0.7	0.90	±	0.3
MgO	1.05	±	0.1	1.28	±	0.1	1.00	±	0.2	0.40	±	0.1
CaO	0.43	±	0.1	4.95	±	0.1	8.94	±	1.5	0.04	±	0
K_2O	6.94	±	0.7	2.70	±	0.1	2.83	±	0.5	3.63	±	0.7
Na_2O	0.62	±	0.1	0.96	±	0.1	0.61	±	0.1	0.16	±	0.1
TiO_2	1.59	±	0.4	1.27	±	0.1	0.81	±	0.3	2.31	±	0.2
MnO		<DL		0.13	±	0		<DL			<DL	
S		<DL			<DL		0.14	±	0.1		<DL	
Total	99.7			100.25			100.07			99.4		

Numbers in parentheses are number of analyses; *Ave*. average; *S.D.* Standard deviation; all iron given as FeO; < *DL* Below detection limit
See text for the composition of the Si-rich Senzeille spherules.

spherule contains almost pure SiO_2 inclusions that are less than 10 μm in size. Most are probably lechatelierite particles, but some are locally crystalline and probably represent partially melted quartz. Partially melted quartz grains have been observed in some North American and Australasian microtektites that are close to the source crater (Glass and Zwart 1979a; Glass 1989; Folco et al. 2010a). Small (<10 μm) Al-rich rounded grains or inclusions are also present in the Hony spherules and are locally abundant.

6.2.3.3.3 Composition

Both the Senzeille and Hony spherules have a wide range in composition, although most of the Hony spherules are internally homogeneous at a 10 μm scale. Others are

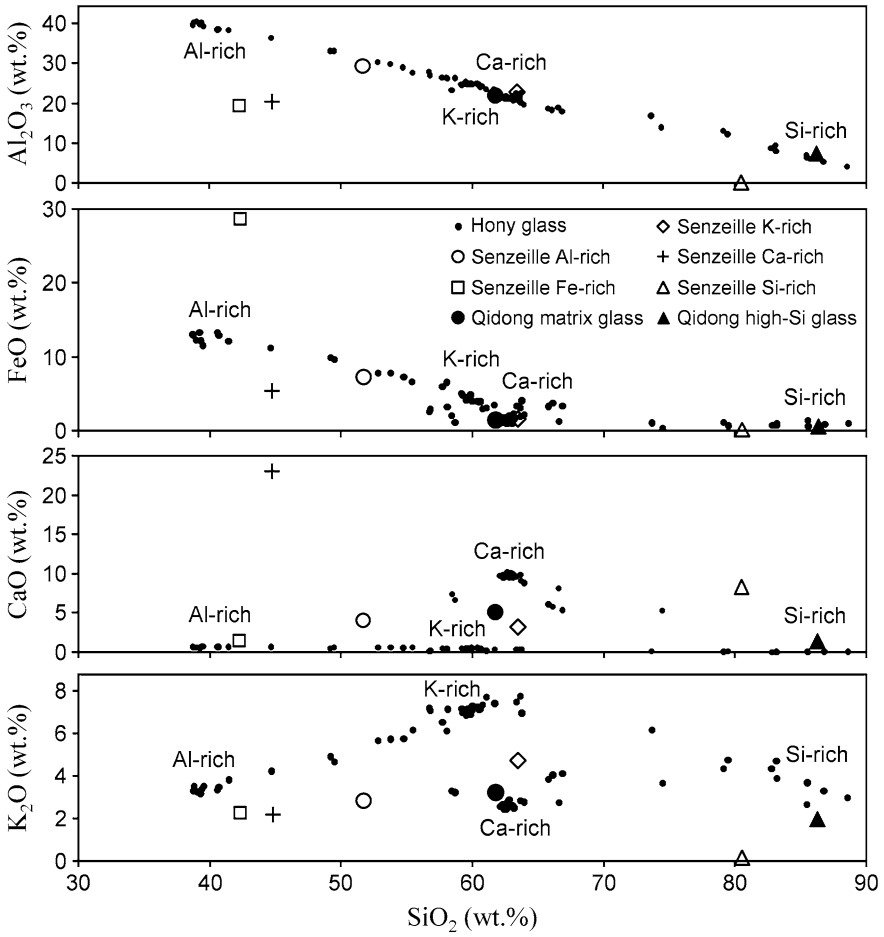

Fig. 6.9 Al_2O_3, FeO, CaO, and K_2O versus SiO_2 for Hony, Senzeille and Qidong spherules. The Hony data (black dots) are multiple analyses of approximately a half dozen spherules (80 analyses total). The labels "Al-rich", "K-rich", "Ca-rich", and "Si-rich" indicate the end-member compositions for the Hony glasses. In the Al_2O_3 versus SiO_2 plot, all the Hony data fall on a single well-defined linear trend extending from ~39 up to ~89 wt % SiO_2. A similar trend is seen in the FeO versus SiO_2 plot, but with a change in slope at a SiO_2 content of ~62 wt %. Note that the average compositions of the Al-, Fe-, Ca-, and Si-rich Senzeille glasses generally do not fall on the compositional trends of the Hony glasses. On the other hand, the average compositions of the Qidong matrix and high-silica glasses (HSi) do fall on or close to the compositional trend of the Hony glasses. The Hony compositional data are courtesy of P. Claeys. The Senzeille and Qidong compositional data are from Claeys et al. (1992) and Wang (1992), respectively

heterogeneous with regions of silica-rich and silica-poor glass. Five compositional end members were recognized at the Senzeille section: (1) K-rich, (2) Al-rich, (3) Fe-rich, (4) Ca-rich (Table 6.3), and (5) Si-rich (Fig. 6.9). The most common

Table 6.4 Average major oxide compositions (± 1 standard deviation) of Al-rich Senzeille and Hony spherules (Belgium) and Al-rich (HAl) Australasian microtektites

	Senzeille Spherules			Hony Spherules			Australasian Microtektites		
SiO_2	51.70	±	3.3	47.00	±	0.6	47.83	±	4.8
Al_2O_3	29.30	±	2.1	28.90	±	0.5	30.95	±	3.6
FeO	7.31	±	2.9	13.06	±	0.7	3.99	±	1.5
MgO	2.41	±	0.4	1.28	±	0.1	7.35	±	3.3
CaO	4.09	±	0.3	4.95	±	0.1	7.22	±	2.8
Na_2O	0.81	±	0.1	0.96	±	0.1	0.48	±	0.2
K_2O	2.84	±	0.5	2.70	±	0.1	0.27	±	0.3
TiO_2	1.01	±	0.1	1.27	±	0.1	1.54	±	0.4

All iron reported as FeO

Senzeille and Hony compositional data from Claeys and Casier (1994); Australasian microtektite composition is the average of one microtektite from Glass et al. (2004b) and six unpublished analyses

types are the K-, Al-, and Fe-rich glasses. In addition to their high K_2O contents, the K-rich glasses have high SiO_2 contents compared with those of the Al-rich, Fe-rich, and Ca-rich glasses. Spherules in the Fe-rich group have low average SiO_2 (~42 wt %) and high average FeO (~29 wt %) contents. Glasses in the Ca-rich group also have low SiO_2 content (average of ~45 wt %) in addition to high CaO contents (average ~23 wt %). The Al-rich glasses have an average of ~29 wt % Al_2O_3 and intermediate SiO_2 contents compared with the other Senzeille glasses.

Si-rich Senzeille glasses have unusual compositions. The silica-rich glasses have the following average composition based on 35 analyses: 80.5 wt % SiO_2, 0.46 wt % Al_2O_3, 0.18 wt % FeO, 3.86 wt % MgO, 8.30 wt % CaO, 0.16 wt % K_2O, and 7.28 wt % Na_2O. TiO_2, MnO, and S were all below detection limits. Claeys et al. (1992) refer to the Si-rich spherules as having anomalous compositions which are different from those of any tektite, microtektite, or volcanic glass reported in the literature. In fact, the compositions of Si-rich Senzeille glass spherules are close to that of common artificial soda-lime glass. Soda-lime glass generally has an SiO_2 content in the range of 70–75 wt %, with 5–10 wt % CaO, 13–17 wt % Na_2O, and other oxides (e.g., Al_2O_3, FeO, MgO) between 1 and 5 wt % (Jones 1956). Claeys et al. (1992) state, however, that the in situ occurrence of the Si-rich spherules rules out contamination.

Like the Senzeille spherules, the Hony spherules have a broad range in major oxide composition and the glass can be divided into K-rich, Al-rich, Ca-rich, and Si-rich groups (Table 6.3; Fig. 6.9). However, there are no Fe-rich Hony glasses and the Ca-rich Hony glasses have much lower CaO contents (average 8.94 ± 1.5 wt %) compared to the Ca-rich Senzeille glasses (average 23.1 ± 2.9 wt %; Table 6.3). The K-rich Hony glasses have lower CaO and higher K_2O contents compared to those of the K-rich Senzeille glasses (e.g., Fig. 6.9). The Si-rich Hony spherules have higher SiO_2 and much higher Al_2O_3 and K_2O and much lower CaO (Table 6.3; Fig. 6.9) and Na_2O contents compared to those of the Si-rich Senzeille

glasses. The Al-rich Hony spherules have lower SiO_2 and MgO and much higher FeO contents compared to those of the Al-rich Senzeille spherules (e.g., Table 6.3). Claeys et al. (1992) and Claeys and Casier (1994) pointed out that the Al-rich Senzeille and Hony spherules have higher Al_2O_3 contents (up to 30 wt %) than previously reported for any tektite or microtektite. Although true at the time, Australasian microtektites with high Al_2O_3 contents (up to at least 35 wt %) have now been described (e.g., Glass et al. 2004b; Table 6.4).

Plots of the major oxides versus silica content (Harker diagrams) for the Hony glasses show well-defined linear compositional trends between the Si-rich glasses, K-rich glasses, and the Al-rich glasses (Fig. 6.9). In the Al_2O_3 versus SiO_2 plot, all the Hony glass analyses fall along a trend of decreasing Al_2O_3 with increasing SiO_2 content from ~39 to 89 wt % SiO_2 (Fig. 6.9). In the FeO and K_2O versus SiO_2 plots, there is a change in slope at ~62 wt % SiO_2. Note, however, that the Hony Ca-rich glasses do not fall along the compositional trends of the Al-rich, K-rich, and Si-rich Hony glasses in the CaO and K_2O versus SiO_2 compositional plots (Fig. 6.9). Linear compositional trends similar to those of the Hony glasses are evident in Harker diagrams for the Cenozoic microtektites (Figs. 4.7, 4.20, 4.28), but the silica ranges are not as great.

The water contents of four of the Belgian FFB spherules were determined by Fourier transform infrared spectroscopy. The water content was found to range from 0.009 to 0.012 wt % (Claeys et al. 1992; Claeys and Casier 1994). This water content is in the range measured for tektites, but much lower than that found in volcanic glasses.

6.2.3.3.4 Comparison with the Qidong Spherules

Based on conodont biostratigraphy, the Qidong spherules are perhaps 1.5–2 Ma younger than the Belgian (Senzeille and Hony) spherules. There are some similarities between the Qidong and Belgian spherules (e.g., shape, surface textures, petrography, overlap in major oxide composition), but there are also a number of differences (Table 6.5). The Qidong spherules are, on average, smaller than the Senzeille and Hony spherules; maximum size of 160 μm, compared with the Senzeille and Hony spherules which have maximum sizes of >1 mm and 500 μm, respectively. The Qidong spherules appear to be in general more vesicular and heterogeneous than the Senzeille and Hony spherules. The matrix glass in the Qidong spherules is similar in composition to the K-rich Belgian glasses, except for apparently somewhat higher Na_2O contents (Tables 6.2, 6.3). However, there are no Al-rich, Fe-rich, or Ca-rich Qidong spherules.

6.2.3.3.5 Nature of the Source Rock and Possible Source Crater

The broad range in composition of the Senzeille and Hony spherules suggests that the source rock was heterogeneous. The high K_2O/Na_2O ratio of the spherules is

Table 6.5 Comparison between Belgian (Senzeille/Hony) and Qidong, China, spherules

	Qidong spherules	Senzeille spherules	Hony spherules
Size	80–160 μm; Ave. ~100 μm	50–>1000 μm; Ave. ~300 μm	50–500 μm; Ave. ~250
Shape	Mostly spherical; a few pear to teardrop shapes	Mostly spherical; some teardrop and dumbell (?) shapes	Mostly spherical; some teardrop shapes
Compound forms	Yes	Yes	Yes
Surface features	Smooth, finely pitted, pitted, corroded; Si-rich circular raised caps	Smooth, finely pitted, deeply etched; Si-rich protrusions or caps	Smooth, finely pitted, deeply etched; Si-rich protrusions or caps
Color and transparency	Opaque white, translucent dark brown, transparent colorless to yellowish brown	Mostly transparent yellowish; a few are dark with a metallic luster	Mostly transparent yellowish; ~30 % transparent white; ~20 % black; a few are more reddish
Vesicles	Spherical vesicles are present	A few large vesicles concentrated near the surface	A few large vesicles concentrated near the surface
Lechatelierite	Probably	No (?)	Probably in one spherule
Inclusions	Yes, probably quartz	No (?)	Probably quartz and Al-rich (< 10 μm) inclusions in one spherule
Major oxide composition	One group with SiO_2 between 58–67 wt % with Si-rich (80–93 wt %) regions	Five groups: K-rich, Al-rich, Ca-rich, Fe-rich, and Si-rich; K-rich group similar to the Qidong spherules	Four groups: K-rich, Al-rich, Ca-rich, Si-rich; K-rich group similar to the Qidong spherules
Heterogeneity	Rather heterogeneous	Mostly homogenous (?)	Mostly homogenous at a 10 μm scale; a few are more heterogenous
Water content	Low (?)	0.009 wt %	0.011–0.012 wt %

Source Wang (1992), Claeys et al.(1992), and Claeys and Casier (1994)

consistent with a sedimentary, rather than an igneous, source rock. The high Al_2O_3 content of some of the spherules suggests a pelitic or clay-rich component and the high CaO content of other spherules indicates a possible carbonate component. The high Fe content of some of the spherules might indicate a ferruginous sandstone component and the high SiO_2 content of a small number of the spherules could have been derived from a quartz arenite. Claeys and Casier (1994) pointed out that paleoclimatic studies suggest the presence of laterite deposits in the Late Devonian of Western Europe and proposed that laterite may be the source of the high Al_2O_3 content of some of the spherules.

Claeys and Casier (1994) suggested two possible source craters for the Belgian spherule layer based on the size and age of the craters: (1) the Siljan (Siljan Ring) impact structure in Sweden, and (2) the Charlevoix impact structure in Quebec,

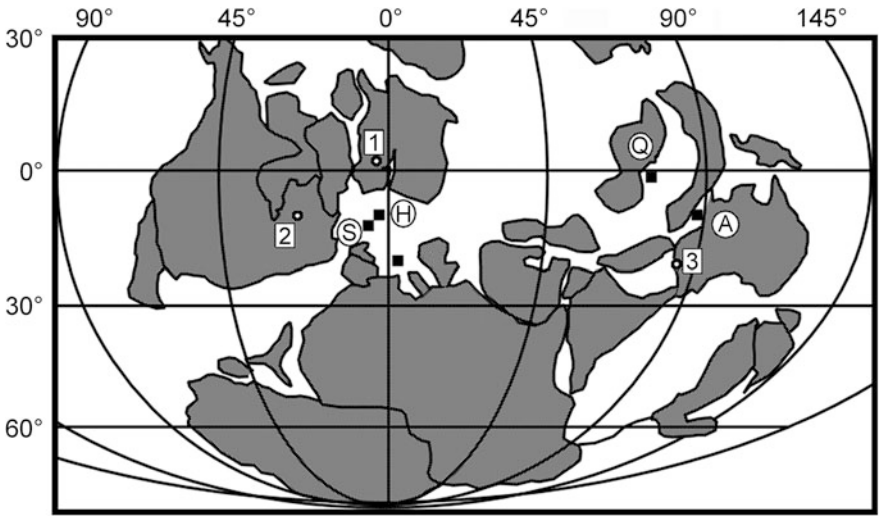

Fig. 6.10 Late Devonian paleogeographic map with location of the Qidong spherules (*Q*) in southern China, Senzeille (*S*) and Hony (*H*) spherules in Belgium, and the Canning Basin (*A*) in Australia. Also shown are the locations of possible source craters for the Senzeille and Hony spherules: Siljan structure (*1*) in Sweden; Charlevoix structure (*2*) in Quebec, Canada; and the Woodleigh structure (*3*) in Western Australia. Modified after Claeys and Casier (1994), Fig. 7

Canada (Fig. 6.10). The Siljan and the Charlevoix impact structures were approximately 1400 and 2300 km, respectively, from the spherule sites in Belgium at the time of the impact. Claeys and Casier (1994) proposed that the Siljan impact structure might be the source crater for the Belgian spherules since the pre-impact stratigraphy in the Siljan area consisted of a mixture of Precambrian granites and Upper Silurian sandstones, shales, and limestones. They used the ejecta thickness scaling relationship of McGetchin et al. (1973; see Sect. 2.6) to estimate the thickness of the ejecta layer from the Siljan impact structure (assuming a diameter of 52 km) at Hony's distance from Siljan. They obtained an estimated thickness of 2–3 mm, which they concluded was compatible with finding the spherules at Hony concentrated over a thickness of sediments $\sim$2 cm thick. For a more detailed discussion of the possible source crater for the Belgian spherule layer see Sect. 10.3.6.

6.2.3.3.6 Discussion

The petrography and composition of the Senzeille and Hony spherules indicate that they are impact spherules and the low water content is consistent with impact glasses including microtektites. The presence of partially melted quartz grains in one of the Hony spherules suggests that the Hony site was relatively close to the source crater. However, the absence of associated shocked mineral grains (e.g.,

Table 6.6 Compositions of spherules from above and below the Frasnian–Famennian boundary at the Xikuangshan section in southern China and of fly ash produced by burning subbituminous coal for comparison

Sample number	SiO_2	Al_2O_3	FeO	MgO	CaO	Na_2O	K_2O	TiO_2	Cr	MnO	Ni	Total
Upper layer												
3-3	55.09	33.10	3.17	0.77	3.93	0.56	1.91	0.89	0.01	0.14	0.11	99.68
m003	50.76	20.03	5.43	2.02	19.11	0.41	0.48	0.96	0.04	0.00	0.07	99.31
Lower layer												
4-4	55.25	26.22	2.17	1.19	9.78	1.62	2.40	0.65	0.08	0.14	0.05	99.55
11-1	46.65	31.93	1.01	0.47	17.54	0.93	0.26	0.03	0.21	0.08	0.00	99.11
11-2	60.31	21.28	3.66	1.87	6.87	1.47	2.89	0.95	0.03	0.06	0.01	99.40
m65	81.55	10.18	1.60	0.28	2.59	1.18	2.30	0.00	0.00	0.00	0.00	99.68
m004	63.34	18.14	3.45	1.44	6.67	1.64	3.43	1.38	0.00	0.00	0.06	99.55
m007	64.34	13.34	2.88	0.82	13.86	0.95	2.61	0.82	0.02	0.00	0.00	99.64
Fly ash (from burning subbituminous coal)												
	40–60	20–30	4–9	1–6	5–30	0–2	0–4	N.D.	N.D.	N.D.	N.D.	

Compositions of the Xikuangshan section spherules are from Ma and Bai (2002) and compositions of fly ash are from the US Department of Transportation Federal Highway Administration Publication Number: FHWA-RD-97-148 <http://www.fhwa.dot.gov/publications/research/infrastructures/97148/cfa51.cfm>

An 'm' in front of the sample number means the analysis was made on the outer surface of the spherule. N.D. = no data. Sample 11–1 has a composition similar to anorthite

Fly ash also has 0–2 wt % SO_3 and 1–3 wt % lost on ignition

shocked quartz with PDFs) suggests that the Senzeille and Hony sites are not close to the source crater. The latter hypothesis is supported by the apparently low abundance of spherules at these two sites.

It is surprising that the Senzeille and Hony spherules, like the Qidong spherules, have survived for several hundred million years. Preservation of the Senzeille and Hony spherules may be attributed to a number of factors including their low water content, rapid burial, the abundance of fine-grained silica in the sediment, and the low porosity and permeability of the enclosing rock (Claeys et al. 1992). In addition, the Hony spherules were coated with a thin layer of carbonates and/or clay minerals, which may have formed a protective sheath.

6.2.3.4 Other Possible Spherule Layers of Frasnian/Famennian Age

Ma and Bai (2002) described spherules from several different layers within rocks of Frasnian–Famennian age in the Xikuangshan section of southern China (Table 6.1). The upper layer is in the Lower *triangularis* conodont Zone a little over a meter above the FFB. Below that is a layer that straddles the FFB. A third layer is ~2 m below the FFB in the *linguiformis* Zone. Ma and Bai (2002) also show a layer about 24 m below the FFB in the Upper *rhenana* Zone, but this lower layer is shown with dotted lines and is not discussed by Ma and Bai. The three upper layers occur over a thickness of 4 m and they were defined by samples taken at an average interval of ~40 cm. Thus, the layers and peak abundances are not well defined. Several types of spherules were identified, but only those believed to be microtektites were discussed in any detail. The peak abundance of spherules (believed by the authors to be microtektites) are ~3, 5, and 22 per 100 g of sample in the upper, middle, and lower of these three layers, respectively. Spherules believed by Ma and Bai (2002) to be microtektites were also found in three layers in the Nandong section (~480 km SSW of Xikuangshan), but were not discussed.

According Ma and Bai (2002), the microtektite-like spherules, from the Xikuangshan section, range from 50 to 300 μm, with most being around 100 μm in diameter. They range in color from milky white to light brown and some are transparent and colorless. Most are spherical, but a few are agglutinated forms made up of two or more spherules fused together. Some have numerous smaller spherules or lumps on their surfaces. The authors do not mention rotational forms (teardrops, dumbbells, discs) being present and no images of rotational forms were shown in the publication. The spherules range from solid to vesicular and some are described as being partly hollow.

Major oxide compositions plus Cr, Mn, and Ni contents were given for 8 spherules (Table 6.6; Ma and Bai 2002). The compositions were determined using energy dispersive X-ray analyses using standards supplied by SPI. Two of the spherules are from the layer above the FFB and six are from the layer below the FFB. None of the analyzed spherules were from the FFB. Half of the analyses were made on polished interior sections and the other half were made on the surface of

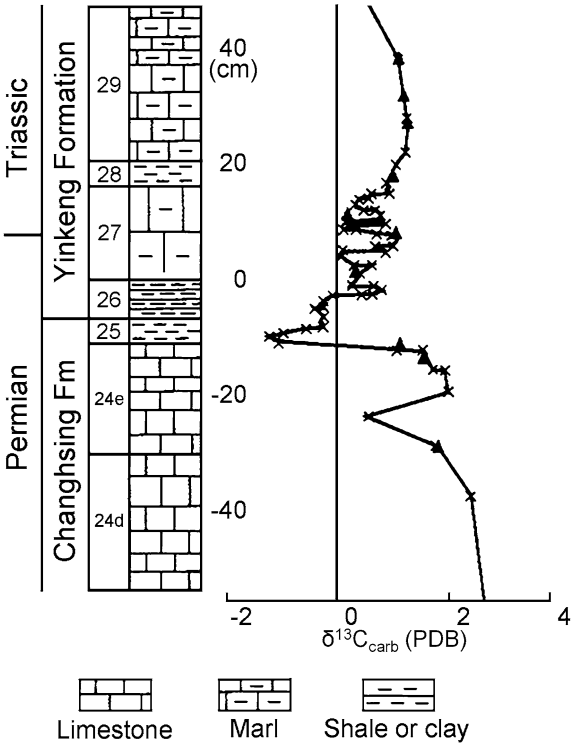

Fig. 6.11 Stratigraphy and carbonate carbon isotope profile across the Permian–Triassic boundary at the Meishan section, southern China. *Fm* Formation. PDB is Pee Dee belemnite used as a carbon isotope standard. Modified after Jin et al. (2000), Fig. 4. Reprinted with permission from AAAS

the spherules. The number of analyses made on a spherule ranges from two to four. The compositions of the two spherules from above the FFB are indistinguishable from the compositions of the six spherules from below the FFB, suggesting that they have the same source and mode of formation. Like the Hony and Senzeille spherules, these spherules can be divided into Al-rich, Ca-rich, and Si-rich groups; however, the overall compositions differ from the published compositions of the Hony and Senzeille spherules (compare Table 6.3 and Table 6.6) and, in contrast to the Hony and Senzeille spherules, K-rich and Fe-rich spherules do not appear to be present.

Ma and Bai (2002) do not mention searching for evidence of shock metamorphosed mineral grains or looking for evidence of an Ir anomaly associated with any of the spherule layers. They did report some element data, including some trace element contents (such as Ni and Co), for the rocks in the Xikuangshan section and they reported some horizons with anomalously high contents of Ni and some other trace elements. However, Ma and Bai (2002) concluded that the anomalies were probably due to hydrothermal activity. Thus, there are no data (e.g., evidence of shocked mineral grains or geochemical evidence of a meteoritic component) to support the proposed impact origin of the spherules. Ma and Bai (2002) did not give much petrographic data for the spherules other than indicating that some contain vesicles and stating that X-ray elemental mapping shows that most spherules are

Table 6.7 Peak abundance of iridium at or near the Permian–Triassic boundary (PTB) at various sites

Reference[a]	PTB section	Location[b]	Peak Ir Content (ppb)	Interpretation[c]
Asaro et al. (1982)	Meishan	South China	<0.4	No anomaly
	Wachapo Mtn	South China	<0.5	No anomaly
Alekseev et al. (1983)	Sovetashan	South Armenia	0.039	No anomaly
Sun et al. (1984)	Meishan	South China	8	Impact
Xu et al. (1985)	Shangsi	South China	2	Impact
Clark et al. (1986)	Meishan	South China	0.002-0.034	No anomaly
	Lichuan	South China	0.001	No anomaly
Brandner et al. (1986)	San Antonio	S. Alps, Italy	3	?
Oddone and Vanucci (1986)	Casera Federata	S. Alps, Italy	0.145	No evidence of impact
	Sass de Putia	S. Alps, Italy	0.020	
	Tesero	S. Alps, Italy	0.135	
	Butterloch	S. Alps, Italy	0.095	
Chai et al. (1987)	Meishan	South China	0.092	Impact
Gao et al. (1987)	Shangsi	South China	0.2	Possible impact
Zhou and Kyte (1988)	Meishan & Shangsi	South China	0.024	No anomaly
Holser et al. (1989)	Gartnerkofel core	Carnic Alps, Austria	0.165	Anoxia, algae
Orth et al. (1990)	Meishan	South China	0.025	No anomaly
	Shangsi	South China	0.035	No anomaly
Chai et al. (1992)	Meishan	South China	0.150	?
	Nammal	South China	0.366	Volcanic & impact
Yin et al. (1992)	Ermen	South China	<0.05	No anomaly
Xu and Yan (1993)	Meishan	South China	2.02	Probable impact
Retallack et al. (1998)	Mount Crean	Antarctica	0.080	No anomaly
	Graphite Peak	Antarctica	0.134	Impact (?)
	Wybung Head	Australia	0.120	Impact (?)
Hancox et al. (2002)	NW Karoo Basin	South Africa	0.32	No anomaly
Koeberl et al. (2004b)	Gartnerkofel core	Carnic Alps, Austria	0.17	Anoxia
	Val Bedia	Northeast Italy	0.242	Anoxia
Xu et al. (2007)	Meishan	South China	0.03	Volcanic

[a] Data for Brandner et al. (1986) and Oddone and Vannucci (1986) were obtained from Chai et al. (1992)

[b] S. Alps = Southern Alps

[c] Question marks in the 'Interpretation' column mean that we have no information regarding the authors' interpretation of the Ir data

isotropic (we assume that means homogenous). They also found some areas in the spherules that are highly enriched in Ca and suggested that there may be some inclusions of $CaSO_4$. They do not mention relict mineral grains or lechatelierite.

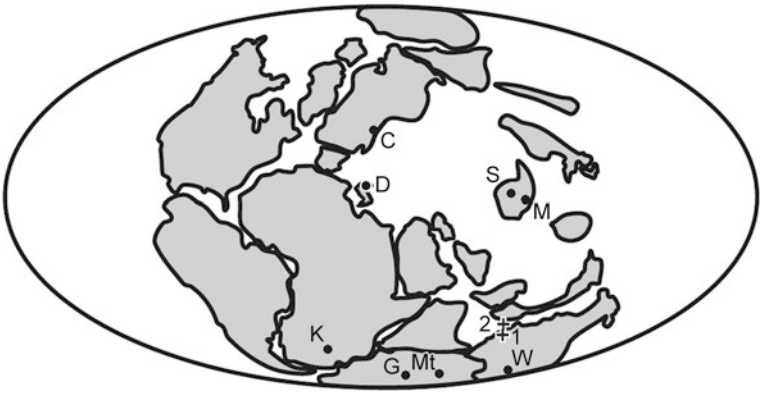

Fig. 6.12 Permian–Triassic paleogeographic map showing location of some Permian–Triassic boundary sections and possible source craters. Permian–Triassic boundary sections (*black* dots) include: *C* Carnic Alps (Gartnerkofel core/section), Austria; *D* Dolomites, Northern Italy; *G* Graphite Peak, Antarctica; *K* Karoo Basin, South Africa; *M* Meishan, Zheijiang Province, southern China; *Mt* Mount Crean, Antarctica; *S* Shangsi, Sichuan Province, southern China; *W* Wybung Head, Australia. Proposed source crater locations (plus signs) are: *1* Woodleigh impact structure; *2* Bedout High structure. Modified after insert in Fig. 2 in Xie et al. (2007)

The fact that the spherules are rather rare, scattered over the lower part of the section, are relatively small (ave. 100 μm in diameter), and that spherules from different "layers" are compositionally similar to each other suggests that they may be some kind of artificial contaminant. One possibility is that, if the site is close to a coal burning power station, the spherules might be fly ash (see Sect. 3.2.1.3). Fly ash spherules are mostly <100 μm in diameter, but can be up to 200 μm or more. The larger ones are generally hollow or mostly so. The composition of fly ash depends on the type of coal being burned in the power plant. Most of the Xikuangshan spherules have major oxides similar to fly ash produced by burning sub-bituminous coal (Table 6.6). Furthermore, fly ash often contains sulfur and can contain $CaSO_4$ phases, which, as pointed out by Ma and Bai (2002) may be present in the Xikuangshan spherules. Additionally, analysis of one of the spherules (11-1 in Table 6.6) indicates a composition similar to that of anorthite, another phase commonly found in fly ash.

More details on the abundance and stratigraphic distribution of the spherules and their petrography and chemical compositions are needed in order to determine their origin. Based on the presently available data it would be premature to conclude at this time that the spherules recovered from the Xikuangshan section are microtektites and therefore are evidence of an impact or impacts during late Frasnian to early Famennian time.

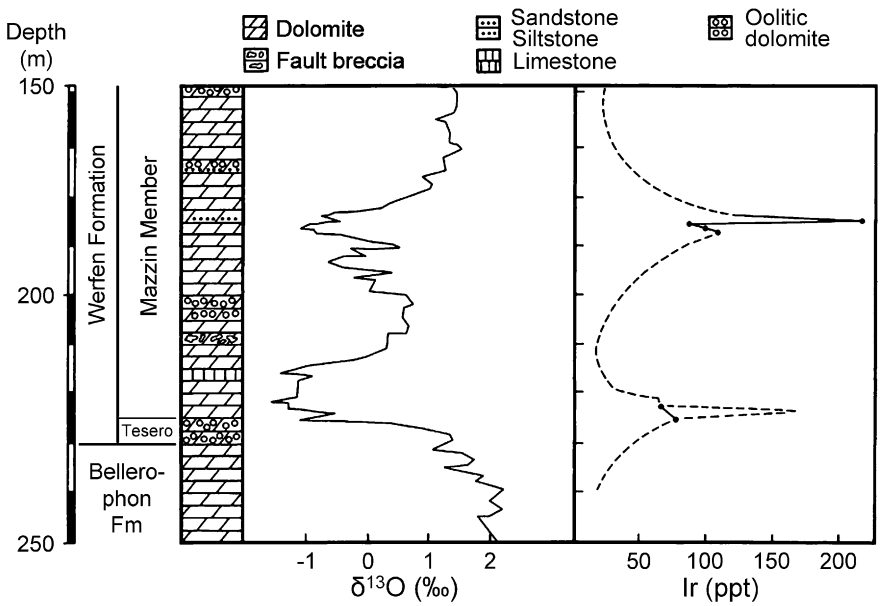

Fig. 6.13 Stratigraphy, lithology, carbon isotope data, and Ir abundance (dashed lines are after Holser et al. 1989) for the Gartnerkofel Permian–Triassic boundary (PTB) section, Austria. The Tesero oolite horizon is the lowermost unit of the Werfen Formation. Historically, the contact between the Bellerophon and Werfen Formations has been used to indicate the PTB in this region. However, the first appearance of the conodont *H. Parvus*, which defines the PTB, occurs at the base of the Mazzin Member of the Werfen Formation in this region. The Pee Dee Belemnite was used as a standard. Modified after Koeberl et al. (2004b), Fig. 2

6.3 Proposed, but Not Accepted Distal Ejecta Layers

6.3.1 Permian–Triassic Boundary (PTB)

6.3.1.1 Introduction

The most severe mass extinction in the Earth's history is recorded in uppermost Permian strata. It occurred prior to the breakup of the supercontinent Pangea. At that time up to 90–96 % of marine species and ~70 % of terrestrial vertebrate species became extinct (Raup 1979; Jin et al. 2000; White 2002; Benton and Twitchett 2003; Erwin 2006). Although generally referred to as the Permian–Triassic boundary (**P–Tr boundary** or **PTB**) mass extinction, the PTB (defined by the first appearance of the conodont *Hindeodus parvus*) actually occurs ~12 cm above the extinction event in the global stratotype section at Meishan, southern China (Yin et al. 2001; Erwin 2006). The late Permian extinction event has been dated at 252.6 ± 0.1 Ma based on U/Pb dating of zircons from nine volcanic ash layers within the Meishan and Shangsi (or Shangshi) PTB sections in southern

Table 6.8 Compositional data for spherules recovered from the Permian–Triassic boundary

	Shangsi Section, S. China[a]		Graphite Peak, Antarctica[b]	
Oxide	Ferruginous	Glassy	Bulk	Glass
SiO_2	29.5–48.0	34.6–54.9	0.06–49.46	43.23–59.29
Al_2O_3	15.8–22.7	4.9–17.8	1.97–30.97	17.98–27.74
Fe_2O_3	–	–	3.00–48.39	0.00–8.59
FeO	40.9–80.3	4.8–11.0	18.97–46.82	4.40–28.87
MgO	1.2–3.1	0.5–3.0	0.36–0.85	0.85–2.15
CaO	0.7–2.7	11.5–36.1	0.10–1.16	0.61–2.34
Na_2O	N.D.	N.D.	0.00–0.41	0.05–1.00
K_2O	0.0–0.0	0.0–0.0	0.00–2.17	1.11–3.43
TiO_2	N.D.	N.D.	0.07–1.08	0.77–1.72
Cr_2O_3	<0.1	<0.1	0.00–0.01	0.00–0.04
SO_3	<0.1	<0.1	N.D.	N.D.
NiO	<0.1	<0.1	n.d.	n.d.

N.D. No data; *n.d.* none detected
[a] Data are from endnote 23 in Jin et al. (2000)
[b] Data are from Michail I. Petaev (personal communication, January 2009)

China (Mundil et al. 2004; Crowley et al. 2006). The start of the Siberian Flood Basalt volcanism appears to be synchronous with the PTB and associated mass extinction (Renne and Basu 1991; Campbell et al. 1992; Erwin et al. 2002; Reichow et al. 2002; Mundil et al. 2004; Grard et al. 2005; Xu et al. 2007). More recently, Grasby et al. (2011) reported finding char in rocks from the PTB layer in the Canadian High Arctic, which they concluded was formed by combustion of coal and organic-rich sediments by the Siberian Flood Basalt volcanism. They posited that the global distribution of char, which is similar to modern fly ash, could have created toxic marine conditions resulting in anoxia. Studies of PTB sections indicate that there is a negative shift or excursion in $\delta^{13}C$, which is approximately synchronous with the mass extinction event just below the PTB (Fig. 6.11; Holser et al. 1989; Xu and Yan 1993; Jin et al. 2000; Krull et al. 2004; Twitchett 2007; Xie et al. 2007). This negative shift in $\delta^{13}C$ appears to be global and may be followed by at least two other negative excursions in lower Triassic deposits. The $\delta^{13}C$ shift at the PTB is found in both marine carbonates and in organic matter in continental deposits (Sephton et al. 2002). The marine carbonate $\delta^{13}C$ drops $\sim$4–6 ‰, which is much larger than the negative shift found at the K–T boundary.

Because the end-Permian mass extinction is the most severe mass extinction event known, there has been a great deal of interest in determining the cause. Numerous triggers/causes have been proposed including: regression (sea-level drop), anoxia, ocean overturn, release of methane from gas hydrates, and volcanism (Erwin 2006). After publication of Alvarez et al.'s (1980) proposal that a major impact at the end of the Cretaceous was responsible for the K–T boundary mass extinction and an Ir anomaly, one of the first places that researchers looked

for another Ir anomaly associated with a mass extinction was the Permian–Triassic boundary (Asaro et al. 1982; Xu et al. 1985; Clark et al. 1986). The search for an Ir anomaly brought mixed results, but the search for an Ir anomaly and other evidence for a major impact at the PTB continues.

6.3.1.2 Ir, Other PGE, and Osmium Isotope Data

An iridium anomaly has been searched for in many PTB sections around the globe (Table 6.7). Probably the most studied Permian–Triassic marine boundary is in the Meishan section, Changxing County in Zhejiang Province of southern China (Fig. 6.12), which has been designated the Global Stratotype Section and Point (GSSP) for the PTB (Yin et al. 2001). At least two research groups reported finding an Ir anomaly (>2 ppb) in the Meishan section (Sun et al. 1984; Xu and Yan 1993); however, several other research groups were not able to find an Ir anomaly in this section (Table 6.7; Asaro et al. 1982; Clark et al. 1986; Zhou and Kyte 1988; Orth et al. 1990). Furthermore, Xu et al. (2007) stated that at the Meishan section the platinum group element (PGE) patterns normalized to chondrites are highly fractionated, but are similar to PGE patterns of Siberian flood basalts. Asaro et al. (1982) were not able to find an Ir anomaly at the PTB in the Wachapo Mountain section near Guiyang in Guizhou Province, China. Xu et al. (1985) reported an Ir anomaly (~2 ppb) at the PTB at Shangsi, Guangyuan County, Sichuan Province in southern China and they stated that the Ni/Ir ratio at the PTB in Shangsi and Meishan is similar to the meteoritic (or cosmic) ratio (i.e., ~25,000). On the other hand, Zhou and Kyte (1988) were not able to find an Ir anomaly in the Shangsi section.

Oddone and Vannucci (1986) determined the concentration of Ir and several other PGEs across the PTB layer at four sites in the Southern Alps in Italy. They found peak concentrations of Ir within 2 m of the boundary that ranged between 0.02 and 0.14 ppb. Oddone and Vannucci (1986) suggested that the PGE abundances and distribution indicate multiple diagenetic remobilization and weathering processes. However, Chai et al. (1992) pointed out that the Ir/Au ratios at these four sites range between 3.5 and 3.8, which is close to the Ir/Au ratio of 3.2 for CI chondrites.

Holser et al. (1989) reported a small Ir anomaly (165 ppt) across the PTB in a core taken through the Gartnerkofel section in the Carnic Alps in Austria. Koeberl et al. (2004b) reported finding two Ir anomalies at the PTB section of the Gartnerkofel core (the peak abundance of the largest is 216 ppt; Fig. 6.13) and in the Val Badia section in northeast Italy (peak abundance of 242 ppt). In addition, Koeberl et al. (2004b) determined the $^{187}Os/^{188}Os$ ratios as well as Re, Os, Ru, Pd, and Pt concentrations. They proposed that the elevated Ir and other platinum group elements were due to anoxic conditions, as documented by high cerium to lanthanum ratios and the presence of pyrite framboids. They concluded that the geochemical data reveal no evidence of an impact of an extraterrestrial body and pointed instead to a terrestrial origin for the PGE anomaly.

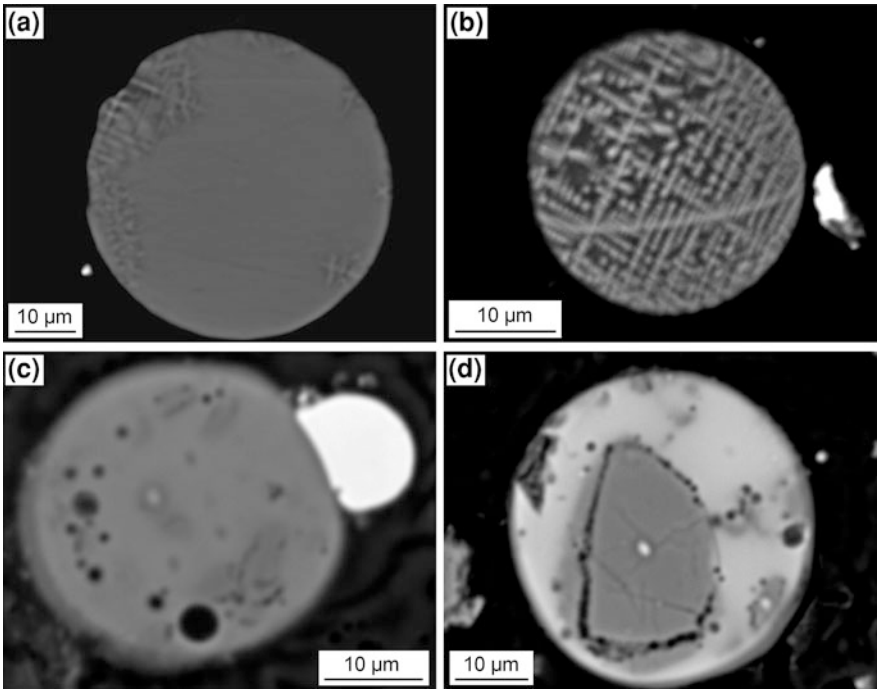

Fig. 6.14 Back-scattered electron images of spherules from the Permian–Triassic boundary layer at Graphite Peak, Antarctica. **a** Mostly glassy sphere with some skeletal magnetite around the margin. **b** Iron-rich spherule with abundant skeletal magnetite microlites. **c** Vesicle-rich spherule without magnetite microlites. **d** Spherule with a large silica grain (*gray*), probably quartz. Courtesy of A. I. Petaev (**b–d** were previously published in Petaev et al. 2004)

Retallack et al. (1998) reported a small Ir anomaly, associated with what they claimed was shocked quartz (see Sect. 6.3.1.4), between ~1.5 and 2 m below the PTB at Wybung Head (Australia) and at Graphite Peak (Antarctica); but neither Hancox et al. (2002) nor Coney et al. (2007) could find an Ir anomaly at the PTB in the Karoo Basin in South Africa.

Thus, there is no clear evidence of a global Ir anomaly at the PTB; and local minor Ir anomalies may have local causes such as anoxia and/or volcanism.

6.3.1.3 Spherules

Spherules (generally referred to as microspherules in the PTB literature) have been found at or close to the PTB in the Shangsi and Meishan sections in southern China (Gao et al. 1987; Xu and Yan 1993), in the Sasayama section in southwestern Japan (Miono et al. 1996), and at Graphite Peak, Antarctica (Petaev et al. 2003, 2004).

At Shangsi the peak abundance of the spherules appears to be 3–4 cm above the PTB where ~18,700 spherules were recovered (Gao et al. 1987). Spherule abundance is positively correlated with the Ir content of the sediment at this site. Most of the spherules are between 30 and 50 μm in diameter. Based on compositional data for 200 spherules, Gao et al. (1987) divided them into three groups: (1) Fe-rich, (2) Si-rich, and (3) Ca-rich (calcareous) spherules, which make up 85, 10, and 4 % of the spherules, respectively. According to Jin et al. (2000), the spherules from this site range in size from 50 to 300 μm in diameter and 95 % are spherical with a few being oval or teardrop shaped or consisting of two spherules fused together. The iron-rich spherules are black, with a metallic luster, and strongly magnetic. According to Jin et al. (2000), X-ray data suggest that the spherules "…are possibly composed of magnesioferrite and hematite, but one spherule is chromespinel." Jin et al. (2000) state that 10 % of the spherules from this site are glassy. Presumably, these are the silica-rich spherules of Gao et al. (1987). According to Jin et al. (2000), the glassy spherules "…range from colorless to yellowish, brownish, or semitransparent." The glassy spherules are isotropic in polarized light. They have smooth, reticulated, or pitted surfaces. No phenocrysts or microliths of high-temperature minerals were observed in the glass spherules. Both the Fe-rich and glassy spherules may contain vesicles.

Gao et al. (1987) provided compositional data for five of the ferruginous (Fe-rich) spherules from Shangsi. The FeO contents of these five spherules are between 83.2 and 93.4 wt %. The silica content of these spherules is as high as 11.5 wt %, and Al_2O_3 content is as high as 2.1 wt %. The K_2O, CaO, and Cr_2O_3 contents are generally <1 wt %. Unfortunately, the nickel contents are not given. According to Jin et al. (2000; footnote 23), microprobe analysis indicates that the iron-rich spherules contain up to 80 wt % FeO and as much a 48 wt % SiO_2 and that the glass spherules contain <12 wt % FeO, but up to 36 wt % CaO (Table 6.8). Both kinds of spherules contain less than 0.1 wt % Cr_2O_3, SO_3, and NiO (Jin et al. 2000). Jin et al. (2000; footnote 23) stated that the Fe-rich spherules have lower SiO_2 content than do the glassy spherules; however, according to them, the highest SiO_2 content in the Fe-rich spherules is 48 wt % and the lowest SiO_2 content of the glassy spherules is 34.6 wt % (Table 6.8). Thus, there must be overlap in the SiO_2 contents. Furthermore, if the highest FeO content of the Fe-rich spherules is ~80 wt %, then the lowest SiO_2 content would have to be less than the 29.5 wt % reported, especially since the lowest Al_2O_3 content reported is 15.8 wt %.

At the Meishan section, the peak abundance of the spherules is ~20 cm above the PTB and is coincident with an Ir anomaly and a negative shift in $\delta^{13}C$ (Xu and Yan 1993). In this section, a variety of spherules are found which range in size from 5 to 50 μm in diameter. The spherules are described as being globular in shape. According to Xu and Yan (1993), the most abundant elements in the spherules are Si or Si and Al, while Fe-rich spherules are very rare. Xu and Yan (1993) state, "…He (1987) discovered that several microspherules are similar to cosmic dust." Xu and Yan (1993) believed that the spherules found at Meishan probably have multiple origins.

Chai et al. (1992) stated that spherules from the PTB in southern China contain chrome ceylonite [ceylonite is a Fe-rich spinel; $(Mg, Fe^{2+})Al_2O_4$], diopside, and apatite. Chai et al. (1992) quote Xu et al. (1988) as saying that the chrome ceylonite and diopside spherules were probably related to an impact event, and they quote Yin et al. (1988) as concluding that the apatite spherules are probably biogenic in origin.

Yin et al. (1992) stated that they recovered several thousand spherules from PTB claystone at 16 localities in southern China. Magnetic spherules found in the Pingdingshan section, Caoxian, Anhui Province, and in the Meishan section are mostly spherical, but some are drop shaped. A few of the spherules are compound with two spherules fused together. According to Yin et al. (1992), some of the spherules have contraction wrinkles, spiral filaments, and/or impact pits on the surface. Some spherules contain vesicles, which in some cases are exposed at the surface. More than 1000 spherules were recovered from the Ermen section, Huangshi, Hubei Province. Some of these spherules contain vesicles and spiral filaments. These spherules were divided into two main groups; (1) lithic-ferruginous spherules and (2) siliceous spherules (Yin et al. 1992). Yin et al. (1992) state that the siliceous spherules have forms and compositions comparable to volcanic silicate spherules similar to those recovered from Mt. Etna ejecta. Apatite spherules found at Guangde and Meishan, southern China, probably have a biogenic origin (perhaps conodont 'pearls').

French and Koeberl (2010) state that many of the PTB Chinese spherules exhibit textures consistent with formation from melt droplets, but that so far none of the data provide any convincing evidence for an impact origin. They further point out that many of the PTB sites are close to active coal-fired power plants so that contamination of surface samples by fly ash is a concern (see Sect. 3.2.1.3 for a discussion of fly ash spherules).

Spherules were extracted from bedded cherts collected at the Sasayama section in southwestern Japan (Miono et al. 1993). The peak abundance of spherules (several hundred) occurs at or close to the PTB (Miono et al. 1996). Most of the spherules are less than 100 μm in diameter. The spherules are generally hollow and exhibit crystalline textures suggestive of rapid cooling. Miono et al. (1996) state that the relative elemental concentrations of the spherules are closely comparable to those in carbonaceous chondrites; but no concentrations are given, only elemental ratios. The average Ti/Fe and Ni/Fe ratios are close to that of the average CI chondrite and the Cr/Fe, Mn/Fe, and Co/Fe ratios are within a factor of ~6, 2, and 3, respectively. These spherules may be cosmic spherules and the hollow interiors could be where the metallic core rusted out. They do not appear to be impact-generated spherules.

Petaev et al. (2003, 2004) found numerous spherules associated with chondrite meteorite fragments (see Sect. 6.3.1.6) in samples from ~23 cm above the PTB at Graphite Peak, Antarctica. The spherules range from 18 to 53 μm in diameter. Most of the spherules are spherical in shape (Petaev et al. 2004). There are several specimens consisting of two spherules fused together. The spherules have a wide range in composition (Table 6.8), but they lie along compositional trends with two

end members: Fe-rich (up to ~95 wt % FeO plus Fe_2O_3) and Si-rich (up to ~59 wt %) with low iron (as low as ~4 wt %). The Fe-rich spherules often contain skeletal magnetite crystals (Fig. 6.14b). The Si-rich spherules (with low magnetite content) contain blocky or rounded silica grains (probably quartz) and a high abundance of rounded vesicles (Fig. 6.14c, d; Petaev et al. 2003; 2004). Some spherules have a magnetite-rich core surrounded by a silica-rich mantle.

The skeletal magnetite crystals in the Antarctic spherules indicate high cooling rates for the spherules and the heterogeneity of the spherules and presence of rounded remnants of silica grains indicate incomplete melting of the source rocks (Petaev et al. 2004). The high TiO_2 and Al_2O_3 contents, along with very low Cr_2O_3 and NiO contents indicate that the spherules are not extraterrestrial material (i.e., cosmic spherules). The low MgO, CaO, Na_2O, and K_2O contents of most of the spherules indicate that they are not volcanic in origin (Petaev et al. 2004). Thus, Petaev et al. (2004) concluded that the spherules must have an impact origin. The generally high TiO_2 and Al_2O_3 contents, along with very low Cr_2O_3, MnO, and NiO contents indicate that the source rock was continental crust (Petaev et al. 2004). Petaev et al. (2004) stated that the compositional trends among the spherules are very close to those of laterites, except for their somewhat higher MgO, CaO, and K_2O contents. They proposed that the impact responsible for the spherules may have occurred somewhere in the tropical region of the Pangea supercontinent.

The spherules found just above the PTB at Graphite Peak, Antarctica, are, in some respects, similar to the spherules found just above the PTB in Shangsi, southern China (Petaev et al. 2004). The Antarctic spherules have a size range comparable to the Chinese spherules. The spherules from both sites are vesicular, magnetic, and include some composite forms with two spherules fused together. The Antarctic spherules appear to have a broader range in composition, but like the Chinese spherules, the Antarctic spherules range from iron-rich to iron-poor (silica-rich) and both the Chinese and Antarctic spherules have very low Cr_2O_3 and NiO contents (Table 6.8). The biggest difference is that the Antarctic spherules generally have much lower CaO contents than do the Chinese spherules, although there is some overlap. Jin et al. (2000) suggested that at least some of the PTB spherules in southern China may be of volcanic origin; but the very low silica of many of the spherules, and the very high FeO content and low MgO for a given SiO_2 content would seem to rule out the possibility that these spherules had a volcanic origin. The similarity between the Chinese and Antarctic PTB spherules suggests a common origin and argues against a volcanic origin, but is consistent with an impact origin. If these spherules are impact spherules, then it is likely that they were produced by the same impact and the great abundance of spherules and the geographic separation between the two sites (Fig. 6.12) indicates that the impact must have been large.

In contrast to the above reports, Retallack et al. (1998) were not able to find spherules at the PTB layer at Graphite Peak and Mount Crean, Antarctica, or at Wybung, Australia; and Zhang et al. (2006b) reported that there are no spherules in the PTB layer at the Chahe section, western Guizhou, in southern China. Zhang

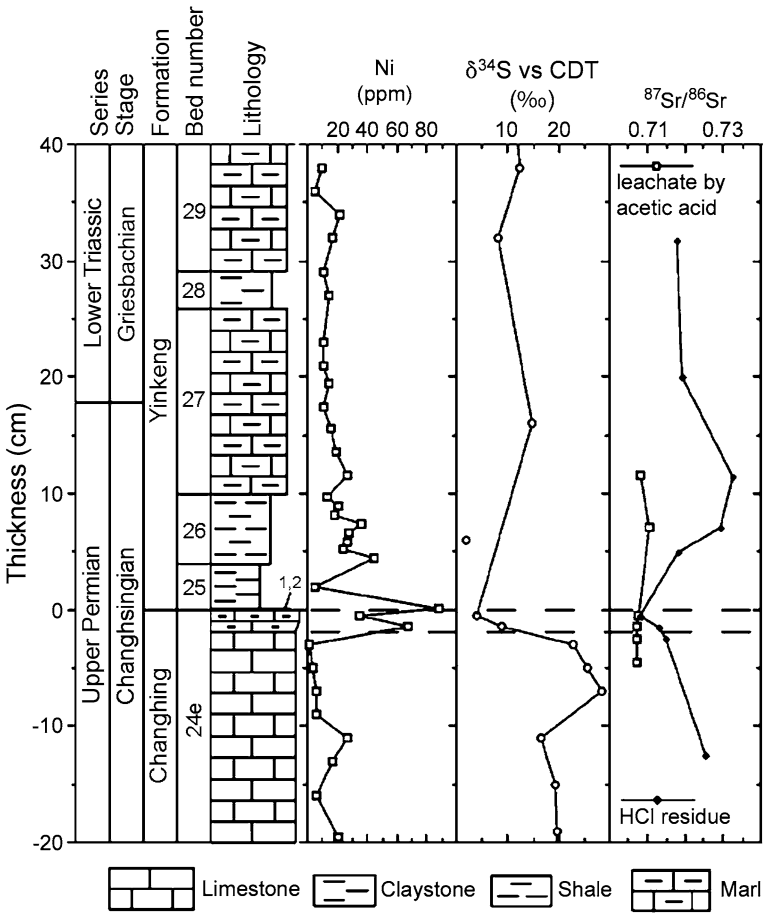

Fig. 6.15 Stratigraphy, lithology, nickel concentration, $\delta^{34}S$, and $^{87}Sr/^{86}Sr$ across the Permian–Triassic boundary in the Meishan section, southern China. 1,2 refers to beds 25-1 and 25-2 which are an Fe-rich basal layer and a gypsum layer, respectively. Base of the iron-rich black shale layer is defined as zero centimeters. Positive and negative numbers correspond to distances above and below the 0-cm horizon. CDT = Canyon Diablo triolite. Modified after Kaiho et al. (2001), Fig. 1

et al. (2006b) concluded that the PTB layer in the Chahe section contains a mineral assemblage indicative of a volcanic origin.

6.3.1.4 Shocked Quartz?

Retallack et al. (1998) reported finding rare shocked quartz grains with multiple sets of planar features, which they interpreted to be PDFs, in the PTB layer (6–15 cm of claystone breccia) at Graphite Peak and Mount Crean, Antarctica,

Table 6.9 Elemental compositions (wt %) of magnetic Fe–Si-Ni grains from the PTB layer in southern China and Graphite Peak, Antarctica

	Meishan section, southern China						Graphite Peak
	Kaiho et al. (2001)					Basu et al. (2003)	
	25-1,D	25-1,D	25-1,A	24-3,A	24-3,A		
Fe	73.2	90.8	89.6	85.2	67.7	99–100	Up to 100
Si	20.2	6.6	7.8	2.0	1.9	Up to 0.39	Up to 2.62
Ni	1.5	2.0	2.2	9.2	8.6	Up to 0.20	Up to 0.16
Al	4.2	0.0	0.0	2.8	2.4	n.d.	n.d.
K	1.0	0.0	0.4	0.1	0.0	n.d.	n.d.
Ca	0.0	0.6	0.0	0.0	0.0	n.d.	n.d.
Cr	0.0	0.0	0.0	0.0	16.1	Up to 0.60	Up to 12.48
Mn	0.0	0.0	0.0	0.8	1.9	n.d.	n.d.
Cu	0.0	0.0	0.0	0.0	0.3	n.d.	n.d.
Co	0.0	0.0	0.0	0.0	1.1	n.d.	n.d.

n.d. no data

and at Wybung Head, Australia. In the peak abundance at Graphite Peak, the percent of quartz grains that they identified as having PDFs is 0.2 vol %. They stated that no shocked quartz grains were found below the boundary layer. However, they did observe some shocked quartz grains up to a meter above the layer. The maximum observed diameters of the shocked quartz were 176, 168, and 150 μm at Mount Crean, Graphite Peak, and Wybung Head, respectively. The planar features are 1 μm thick and spaced 1–20 μm apart. Some of the grains were etched in HF and observed using scanning electron microscopy. Numerous intersecting grooves were observed where the "shock" lamellae had partially dissolved (Retallack et al. 1998). Orientations of the planar features were determined using a spindle stage. The features were oriented preferentially at 23° and 32° to the c-axis, which are the most common orientations for shocked quartz grains (i.e., ω and π, respectively). Becker et al. (2004a) reported finding shocked quartz ranging from 150 to 550 μm in size in the PTB layer at Fraser Park, adjacent to Wybung Head, in Australia, but no details were given.

Langenhorst et al. (2005) reexamined, using transmission electron microscopy, some of the grains from Graphite Peak that Retallack et al. (1998) used to determine the orientation of the planar features. They found that the optically visible deformation features are decorated subgrain walls and not shock-induced PDFs as concluded by Retallack et al. (1998). Hancox et al. (2002) searched for, but could not find any evidence of shocked quartz with PDFs at the PTB layer in the northwest Karoo Basin in South Africa.

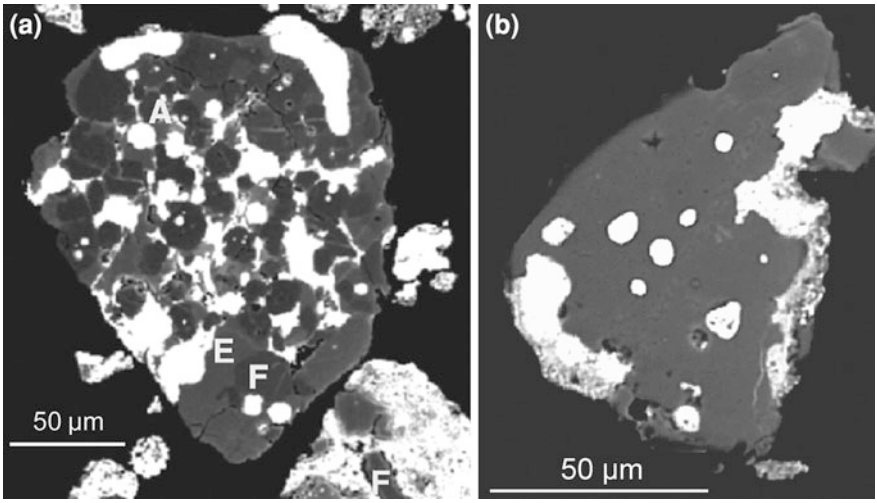

Fig. 6.16 Back-scattered electron image of meteorite fragments from the Permian–Triassic boundary at Graphite Peak, Antarctica. **a** The larger fragment consists of forsterite crystals "F" enclosed in enstatite "E" with interstitial Ca-bearing pyroxene "A". Globular or irregular masses of Fe,Ni,P-bearing oxides (*white*) are interstitial to the silicates. **b** A homogeneous enstatite grain (*gray*) containing euhedral to subhedral grains of primary Ni, Fe metal (*white*). From Basu et al. (2003), Fig. 3b and c, respectively. Reprinted with permission from AAAS

6.3.1.5 Fullerenes Containing Trapped Extraterrestrial Noble Gases

Chijiwa et al. (1999) were the first to report the discovery of fullerenes in the PTB layer. They extracted the fullerenes from deep-sea claystones from the PTB sections in the Inuyama area, central Japan. Their data indicate 10-20 ppt of C_{60} only in dark-colored rock from the PTB layer. Chijiwa et al. (1999) proposed that the fullerenes were produced by wildfire, although no evidence of soot has been reported from the PTB layer.

Becker et al. (2001) searched for fullerenes (C_{60} to C_{200}) in the PTB layer from three sites: Meishan section, southern China; Sasayama section, southwest Japan; and Bálvány section, northern Hungary. Fullerenes were found in the Meishan and Sasayama sections. According to Becker et al. (2001), the fullerenes contain trapped helium and argon with isotopic ratios similar to the planetary component of carbonaceous chondrites. They interpreted the results as indicating that an impact accompanied the PTB mass extinction. Based on the measured ^{3}He content for the PTB, Becker et al. (2001) estimated that the size of the impacting body was 9 ± 3 km; i.e., comparable in size to the K-T boundary impactor.

In contrast to Becker et al. (2001), Farley and Mukhopadhyay (2001) were not able to detect fullerene-hosted extraterrestrial ^{3}He in aliquots of the same samples from Meishan (Bed 25) that were analyzed by Becker et al. (2001); nor could they find fullerene-hosted extraterrestrial ^{3}He in six samples from the stratigraphically equivalent PTB bed at Shangsi, China. Farley and Mukhopadhyay (2001)

Table 6.10 Element concentrations in the magnetic fines from the Permian–Triassic boundary at Graphite Peak, Antarctica, and in CI and CM chondrites

	Magnetic fines	CI chondrites	CM chondrites
Fe (wt %)	20.1	18.2	21.3
Mg (wt %)	10.2	9.70	11.5
Al (wt %)	1.04	0.86	1.13
Ca (wt %)	0.73	0.93	1.29
Ni (wt %)	1.11	1.10	1.23
Co (ppm)	550	505	560
Cr (ppm)	2750	2650	3050
Mn (ppm)	1570	1940	1650
Ti (ppm)	610	440	550
V (ppm)	~70	55	75
K (ppm)	~570	550	370

Data for magnetic fines from Graphite Peak from Shukolyukov et al. (2004) and data for CI and CM chondrites from Lodders and Fegley (1998)

concluded that without confirmation of ^{3}He in Bed 25, the occurrence of an impact at the PTB must remain an open question. Becker and Poreda (2001) pointed out that they found the fullerene-hosted extraterrestrial component in carbon-rich basal material in Bed 25 and argued that the sample analyzed by Farley and Mukhopadhyay (2001) was a 150-g sample of volcanic ash, which was homogenized prior to being analyzed. Becker and Poreda (2001) suggested that homogenization may have severely diluted the already weak ^{3}He signal present in the bulk ash.

Isozaki (2001) argued that the sample from the Sasayama section, in which Becker et al. (2001) found a "^{3}He-enrichment", came from the late Permian, at least 0.8 m below the PTB. Becker and Poreda (2001) countered that because the PTB cannot be precisely defined in the Sasayama section because of poor stratigraphic control, they believed that the best interpretation for the boundary is the siliceous claystone where fullerenes and other extraterrestrial components have been found. Such a conclusion appears to involve circular reasoning.

In a later paper, Poreda and Becker (2003) reported new evidence for fullerenes with extraterrestrial noble gases in the PTB at Graphite Peak, similar to the PTB fullerenes from Meishan, China, and Sasayama, Japan. In addition, they isolated a ^{3}He-rich magnetic carrier phase from the Graphite Peak section. They stated that the noble gases in the magnetic fraction were similar to the noble gas fraction in deep-sea **interplanetary dust particles** (**IDPs**) and some magnetic grains isolated from the Cretaceous-Tertiary boundary. Poreda and Becker (2003) concluded that at Graphite Peak, "…two separate tracers are present (direct flux of IDPs for ^{3}He vs. giant impact for fullerenes)."

Table 6.11 Chromium isotopic compositions of the magnetic fines from the Permian-Triassic boundary at Graphite Peak, Antarctica, and for CI and CM carbonaceous chondrites for comparison (from Shukolyukov et al. 2004)

	$\varepsilon(^{53}Cr)_{corr.}$	$\varepsilon(^{53}Cr)_{raw}$	$\varepsilon(^{54}Cr)_{raw}$
Graphite Peak (MF)			
Bulk	−0.13 ± 0.04	n.d.	n.d.
Soluble phases	0.71 ± 0.03	0.29 ± 0.14	−0.85 ± 0.25
Acid residue	−4.69 ± 0.03	−0.37 ± 0.49	8.10 ± 0.78
Ivuna (CI chondrite)			
Bulk	−0.44 ± 0.03	0.41 ± 0.11	1.59 ± 0.24
Soluble phases	1.12 ± 0.03	0.57 ± 0.18	−0.66 ± 0.32
Acid residue	−7.95 ± 0.02	−0.90 ± 0.09	13.2 ± 0.20
Murray (CM chondrite)			
Bulk	−0.31 ± 0.03	0.27 ± 0.09	1.13 ± 0.21
Acid residue	−3.23 ± 0.03	0.34 ± 0.17	5.35 ± 0.29

The uncertainties are 2 σ_{mean}; *n.d.* Not determined; *raw* Raw ratios; *corr.* Second order correction; *MF* Magnetic fines

More recently, Farley et al. (2005) searched for extraterrestrial ^{3}He in a suite of samples across the PTB at Opal Creek, Canada. They concluded that no extraterrestrial ^{3}He was detected at this site.

6.3.1.6 Chondritic Meteorite Fragments and Osmium and Chromium Isotopic Data

Kaiho et al. (2001) reported finding numerous magnetic grains (2–50 μm in diameter) in a Ni-rich layer (close to 90 ppm Ni) approximately 18 cm below the internationally accepted PTB in the Meishan section, southern China (Fig. 6.15). The magnetic grains are composed primarily of iron, with relatively high contents of Si and Ni, although some also have up to 4.2 wt % Al and one has high Cr (16.1 wt %; Table 6.9). They proposed that the Fe and Ni came primarily from an extraterrestrial body that was vaporized on impact and the Si came from the target rock. In the conclusion of their paper, Kaiho et al. (2001) referred to high concentrations of impact-metamorphosed grains in the Ni-rich layer, but they did not document any shock metamorphic effects in the paper. These authors also pointed out that the Ni-rich layer is coincident with a negative shift in $\delta^{34}S$ (Fig. 6.15), which they proposed was due to massive release of sulfur from the mantle caused by a large impact into the ocean crust.

Koeberl et al. (2002b) were critical of Kaiho et al.'s (2001) conclusions. They stated that Kaiho et al. did not provide the data to support the interpretation that the Fe–Si-Ni-rich grains are impact-metamorphosed particles. Koeberl et al. (2002b) further stated that "the presence or absence of very small grains of badly known

composition does not constitute evidence for or against an impact event." Koeberl et al. also challenged Kaiho et al.'s (2001) suggestion that the negative shift in $\delta^{34}S$ was due to massive release of sulfur from the mantle. Koeberl et al. (2002b) pointed out that there is substantial evidence for anoxic conditions in many PTB sections, and they suggested that the $\delta^{34}S$ values observed by Kaiho et al. (2001) may have been the result of fractionation via bacterial sulfate reduction and reoxidation of isotopically light H_2S. Koeberl et al. (2002b) concluded that none of the arguments presented by Kaiho et al. (2001) provide evidence for an impact at the end of the Permian.

Basu et al. (2003) reported finding magnetic grains from the PTB in Meishan, China, that are compositionally similar to the Fe–Si-Ni-rich grains reported by Kaiho et al. (2001). However, Basu et al. (2003) stated that the grains are almost pure iron (99–100 wt %) with only trace amounts of Ni, Cr, and Si, whereas Kaiho et al. (2001) reported that the Fe–Si-Ni-rich grains they analyzed have <91 wt % Fe (Table 6.9). Basu et al. (2003) also found abundant Fe-rich metal nuggets near the PTB at Graphite Peak, Antarctica, which have compositions similar to the compositions of the Fe–Si-Ni grains at Meishan (Table 6.9). In addition, Basu et al. (2003) recovered less abundant Fe,Ni,P,S-bearing oxide grains and rare Fe,Ni–sulfide grains than did Kaiho et al. (2001). Furthermore, Basu et al. (2003) recovered >50 magnetic silicate aggregates (up to at least 300 μm in maximum length) in a claystone breccia at the PTB ~23 cm above the base. These polycrystalline fragments (Fig. 6.16) contain Ni–Fe metal grains, olivine, pyroxene, and Fe,Ni,P,S-bearing oxides. The Ni/Fe, Co/Ni, and P/Fe ratios of the metal grains, the Fe/Mg and Mn/Fe ratios in the olivine and pyroxene, and the composition of the Fe,Ni,P,S-bearing oxides indicate that the aggregates are meteorite fragments and that the best match is with a CM-type chondrite. Basu et al. (2003) realized that survival of meteoritic material in a terrestrial environment over millions of years is unprecedented, but maintained that it was not possible that the meteoritic fragments are contaminants. They proposed that preservation of these fragments for 250 Ma was due to rapid burial in a reducing environment and the unique Antarctic conditions.

Koeberl et al. (2004b) were skeptical that meteorite fragments could survive unaltered for ~250 Ma. Furthermore, several groups, e.g., U Reimold (University of Witwatersrand), P Claeys (Vrije Universiteit Brussels), and C Koeberl (University of Vienna), searched for meteorite fragments in the Graphite Peak sample that G J Retallack had provided to L Becker and M I Petaev and none of these researchers found any meteoritic fragments in that sample (C Koeberl, personal communication, 2012). Koeberl et al. (2004b) also searched without success for evidence of an impact in PTB deposits in Austria and Italy. They looked at samples from the drill core through the PTB Gartnerkofel section in the Carnic Alps, southern Austria, and from the Val Badia section in the western Dolomites, northern Italy. The samples from both locations were analyzed for Ir and platinum group elements (PGEs) and for Os isotope composition. In addition, they measured the He concentrations and isotope compositions across the PTB in the Gartnerkofel core. Although Koeberl et al. (2004b) found Ir anomalies at both of the sites, the

Os isotope and the PGE ratios did not support a meteoritic impact origin for the Ir anomalies. In addition, they found no evidence of extraterrestrial ^{3}He in the Gartnerkofel section.

In another search for an extraterrestrial component in the PTB layer at Graphite Peak, Antarctica, Shukolyukov et al. (2004) determined the Cr isotopic composition of magnetic separates recovered from a sample of the PTB layer. The concentrations of major and minor elements in the bulk magnetic fraction are similar to the concentrations of major and minor elements in chondritic meteorites (Table 6.10), suggesting that the magnetic residue was most likely pure meteoritic material. Chromium isotopic data were determined for the bulk magnetic fraction, a magnetic acid (HF/HNO_3) soluble fraction, and a magnetic acid residue fraction. The data clearly indicate that the Cr has a carbonaceous chondrite isotopic signature (Table 6.11; Fig. 3.6); however, Shukolyukov et al. (2004) could not match it to a particular carbonaceous chondrite type. The most striking finding was a large excess in ^{54}Cr in the magnetic acid residue fraction: $(\varepsilon^{54}Cr)_{raw} = +\ 8.10 \pm 0.78$ ‰ (the subscript "raw" indicates that the second order fractionation correction was not made). Similar ^{54}Cr excesses have been noted in the acid residues of CI and CM chondrites, but the Graphite Peak ^{54}Cr excess is intermediate between that of the CI chondrite Ivuna and that of the CM chondrite Murchison (Shukolyukov et al. 2004).

In a more recent study, Petaev et al. (2006) confirmed the presence of meteoritic fragments in a PTB sample from Graphite Peak, Antarctica.

6.3.1.7 Proposed Source Crater

Some authors have proposed that the impact that produced the Woodleigh structure in the Carnarvon Basin, Western Australia (Fig. 6.12), may have occurred at the time of the mass extinction that took place at PTB time about 253 Ma ago (Mory et al. 2000a). The diameter was originally proposed to be $\sim$120 km, which would have made it the fourth largest known terrestrial impact structure (Mory et al. 2000a). A more recent study suggests that the Woodleigh impact structure is probably Late Devonian (359 $\pm$ 4 Ma) and, therefore, much older than the PTB (Uysal et al. 2001). Furthermore, several authors have concluded that the structure is probably only 40–60 km in diameter (Reimold and Koeberl 2000; Renne et al. 2002; Hough et al. 2003). Thus, the impact that produced this structure was probably too small to be responsible for a mass extinction.

Based on a single seismic line, Gorter (1996) suggested that a structural high, Bedout High, offshore of northwestern Australia (Fig. 6.12) might be the central uplift of a large Permian impact crater. Becker et al. (2004a) studied samples from cores taken on top of the Bedout structure and identified what they called "impact breccias" and what they referred to as "nearly pure silica glass (SiO_2), fractured and shocked melted plagioclase, and spherulitic glass". Becker et al. (2004a) suggested that the structure may be $\sim$200 km in diameter. They made $^{40}Ar-^{39}Ar$ age measurements on feldspar concentrates from a breccia sample from one of the cores and obtained a plateau age of 250.1 $\pm$ 4.5 Ma. Thus, Becker et al. (2004a)

concluded that the Bedout structure is an ~200-km-diameter impact structure with an age that is indistinguishable from the PTB and associated mass extinction. However, several authors have been critical of Becker et al.'s (2004a) conclusions.

Wignall et al. (2004) pointed out that the proposal that the Bedout High is the central uplift of a large impact structure is readily testable, since nearby sedimentary deposits containing the PTB should contain a thick ejecta layer. They examined core material from a borehole (Hovea-3) located approximately 1000 km from the **Bedout structure** and found no evidence of an impact ejecta layer at the PTB. They also examined mudlog data and wireline logs from boreholes as close as 400–500 km from Bedout and concluded that they did not provide evidence of an ejecta layer at the PTB. Wignall et al. (2004) concluded, therefore, that either Bedout is not an impact structure or that it did not form in late Permian to early Triassic time. Becker et al. (2004b) agreed that the study of cores from the PTB sections in Western Australia could potentially provide a valuable test of the hypothesis that Bedout is an impact structure; however, they were not convinced that the cores or well logs contain a complete record across the PTB.

Renne et al. (2004) stated that the geophysical data do not define a crater, only a noncircular high, which Becker et al. (2004a) claimed to be a "central uplift". Furthermore, Renne et al. (2004) and Glikson (2004a) stated that the highly altered rocks described by Becker et al. (2004a) as impact breccias strongly resemble volcanic breccias and lack textures diagnostic of impact. In addition, Renne et al. (2004) criticized Becker et al.'s (2004a) age data for the Bedout structure saying that the 250 Ma age is from only one sample of unknown lithologic and stratigraphic relationship to the Bedout geophysical feature. They also stated the $^{40}Ar-^{39}Ar$ data do not define a plateau. Becker et al. (2004c) responded by saying that Renne et al. (2004) ignored the petrographic and chemical evidence provided in the Supporting Online Material in their paper. Becker et al. (2004c) conceded that they would have been better served not to have used the term "plateau", but stood by their age data.

Müller et al. (2005) made a geophysical evaluation of the Bedout structure and stated that the available geophysical and geological data provide no unequivocal evidence supporting the hypothesis that Bedout is an impact structure. They concluded instead, that the Bedout structure is a Paleozoic basement high formed by consecutive episodes of rifting, roughly orthogonal to each other, and capped by end-Permian igneous extrusives. However, Becker et al. (2006) determined the chromium isotopic composition of a sample of what they referred to as "Bedout impact melt breccia". The preliminary results indicate an extraterrestrial Cr isotopic composition ($\varepsilon^{53}Cr$ = approximately -0.25 ‰; Fig. 3.6). The apparent ^{53}Cr deficiency in the Bedout breccia indicates a carbonaceous chondrite projectile and is consistent with the chromium isotopic data obtained for the Graphite Peak, Antarctica, PTB sediments.

Brown (2002) suggested that the west coast of North Africa, the north coast of Africa, and the Great African Rift (East African Rift Zone) define 225° of arc curvature of a circle centered off the coast of Cameroon. Brown speculated that this circle defines a mega impact structure (basin) that formed at the time of the

mass extinction at the end of the Permian. He further speculated that the impact caused the breakup of Pangea. However, other than the proposed circularity, no evidence is given in support of this hypothesis.

6.3.1.8 Summary

Several research groups have claimed to have found evidence of an impact at or near the PTB. The proposed evidence includes: an Ir anomaly, spherules, shocked quartz with PDFs, fullerenes containing trapped extraterrestrial noble gases, chondritic meteorite fragments, Fe-rich metal nuggets, and chromium isotopic data indicating a chondritic component. Except for the Cr isotope data, all the evidence for impact in the PTB layer has been questioned or disputed; but, even if the data were not being questioned, the Ir anomaly, fullerenes with trapped extraterrestrial noble gases, chondritic meteorite fragments, Fe-rich metal nuggets, and chromium data simply indicate that there may be a minor meteoritic component at or near the PTB layer at some locations. Although the presence of a meteoritic component is consistent with an impact, it is not proof of an impact. On the other hand, if a meteoritic component were present globally at the PTB, then it would be hard to explain except as the result of a major impact event. However, there is presently no evidence that a meteoritic component is present globally at the PTB.

Most of the spherules described from the PTB layer appear to be meteoritic debris. However, some of the silicate spherules, with silica inclusions, described by Petaev et al. (2004) could be impact-generated spherules; but, again, they have not been found globally. Shocked quartz with PDFs would be evidence of an impact, but the identification of shocked quartz at the PTB has been questioned by some researchers. French and Koeberl (2010) summed it up well when they stated, "Studies to date have generated a large amount of ambiguity, controversy, and publicity…", but "…have not yet produced any convincing evidence for a large meteorite impact at the P-Tr boundary."

The impact that produced the Woodleigh impact structure in Western Australia has been proposed as being responsible for the mass extinction near the PTB and the source of what has been identified as evidence of an impact observed at some PTB sections. However, this structure is probably too small ($\sim$40–60 km) and, more importantly, much too old to be related to the PTB. More recently the Bedout High off northwestern Australia has been proposed as the central uplift of a PTB-age impact structure with a diameter of as much 200 km. The identification of this feature as an impact structure and its size and age have been questioned; but a recent study has found evidence for a meteoritic component in the breccias recovered from the structure. Thus, the evidence for an impact at PTB time remains ambiguous and the search for impact evidence continues.

6.3.2 Possible Devonian-Carboniferous Boundary Distal Ejecta Layer

Silicate glass spherules were found in sediments across the Devonian-Carboniferous boundary (in the *Siphonodella praesulcata* and basal *S. duplicate* conodont Zones) at Huangmao and Muhua in southern China (Bai 2001). Their distribution through the sections and abundances were not given. The spherules are described as being "…generally transparent to gray, brown, and black in color." According to Bai (2001) they have a mean diameter of 180 μm and they have splash forms similar to microtektites. However, there was no mention of rotational forms such as teardrops, dumbbells, or discs. Photographs of eight of the spherules suggest that they are mostly spherical and several have smaller spherules attached to their surfaces. No petrographic data were given; so we do not know if they contain vesicles, relict mineral grains, schlieren, primary microlites, or lechatelierite.

Major oxide compositions (Table 6.12) and Cr and Ni data were given for eight Devonian-Carboniferous boundary layer spherules (Bai 2001; 6 from Huangmao and 2 from Muhua). The compositional data were obtained using energy dispersive X-ray analysis. Compositionally, the Muhua spherules are indistinguishable from the Huangmao spherules, which supports the conclusion that they have the same source and origin. The silica contents of the spherules range between ~49 and 70 wt %, but most have silica contents between 58 and 60 wt %. Except for slightly higher Al_2O_3 contents, most of the spherules have compositions similar to the average composition of the Earth's crust (Table 6.12). Most Ni and Cr values were below the detection limit of 150 μg/g, but Bai (2001) reported Ni contents of 550 μg/g and 650 μg/g in two spherules and a Cr content of 780 μg/g in the spherule with 650 μg/g Ni.

Bai (2001) does not mention searching for or finding shocked mineral grains. The spherule layer is associated with positive Ni and Ir anomalies (peak content ~480 ppm and 250 ppt, respectively); but the occurrence of the spherules in a shale layer interbedded between limestone layers probably explains the higher contents of these elements compared to that of the underlying and overlying limestones. On the other hand, Bai (2001) pointed out that the Ni and Ir contents are higher than those of the average shale, but based on inter-element ratios and mineralogy of the shale, he concluded that the high Ni and Ir are the result of hydrothermal processes rather than meteoritic contamination. Wang et al. (1993) suggested that a positive Ir anomaly is found globally in the Devonian-Carboniferous boundary layer. They attributed the Ir anomaly to a sudden change in the redox conditions during deposition and/or early diagenesis. Without additional data (stratigraphic distribution of spherule abundance and petrographic data for the spherules) it is premature to conclude that the Huangmao and Muhua spherules are microtektites.

Hill and Jimenez (2010) reported finding shocked quartz at the Devonian-Carboniferous boundary (they called it the Devonian-Mississippian boundary) in the Upper Huntley Mountain Formation in NE Pennsylvania. The shocked quartz

Table 6.12 Major oxide compositions of spherules from the Devonian-Carboniferous boundary in southern China and the average continental crust for comparison

Sample number	SiO_2	Al_2O_3	FeO	MgO	CaO	Na_2O	K_2O	TiO_2
Spherules from the Devonian–Carboniferous boundary								
129	69.6	11.9	2.62	4.17	8.69	0.80	1.37	0.31
130	49.4	32.2	4.55	1.93	6.14	1.04	1.81	2.31
128	59.1	18.8	7.19	2.38	6.51	2.11	2.73	0.70
131	63.8	14.6	3.39	2.06	3.36	3.75	4.01	4.44
132	60.2	20.4	8.28	0.72	7.32	0.58	1.46	0.59
133	58.5	19.6	8.32	1.50	5.72	2.12	2.92	0.84
134	59.6	20.7	4.82	2.13	8.26	0.96	1.76	1.23
135	57.8	19.4	5.93	3.70	7.64	0.89	2.18	1.82
Ave.	59.8	18.9	6.32	2.08	6.47	1.74	2.51	1.60
S.D.	2.1	2.2	1.98	0.99	1.76	1.18	0.92	1.46
Average continental crust composition								
	61.9	16.7	6.9	3.5	3.4	2.2	4.2	1.1
	63.9	15.4	6.1	3.1	4.2	3.4	3.0	0.8
	60.2	15.6	7.1	3.9	5.8	3.2	2.5	1.0
	57.8	15.2	7.6	5.6	7.5	3.0	2.0	1.2
	61.9	15.6	6.2	3.1	5.7	3.1	2.9	0.8
	62.5	15.6	5.5	3.2	6.0	3.4	2.3	0.7
	63.8	16.0	5.3	2.8	4.7	4.0	2.7	0.7
	64.8	16.1	4.8	2.7	4.6	4.4	2.0	0.5
	58.0	18.0	7.5	3.5	7.5	3.5	1.5	0.8
	57.3	15.9	9.1	5.3	7.4	3.1	1.1	0.9
Ave.	61.2	16.0	6.6	3.7	5.7	3.3	2.4	0.9
S.D.	2.7	0.8	1.3	1.0	1.5	0.6	0.9	0.2

Ave. Average. *S.D.* Standard Deviation

The average and standard deviation for the Devonian–Carboniferous spherules are for samples 128 and 131–135. Spherules 133 and 134 are from Muhua and the rest are from the Huangmao section

Compositions of the Devonian–Carboniferous boundary spherules are from Bai (2001) and average compositions of the continental crust are from various sources in the literature published in Taylor and McLennan (1985)

occurs in the "Haystacks" sandstone which is a massively-bedded, thin, but laterally persistent sandstone within the fluvial sandstones of the Upper Huntley Mountain Formation. Hill and Jimenez (2010) found 82 sets of PDFs in ~30 quartz grains (i.e., an average of ~2.7 sets per grain). Individual grains contain one to five sets of PDFs. The most common orientations are $\omega\{10\overline{1}3\}$, $\xi\{11\overline{2}2\}$, and $\{10\overline{1}4\}$. If these are true PDFs, then this would be the first convincing evidence of a distal impact ejecta layer at the Devonian-Carboniferous boundary.

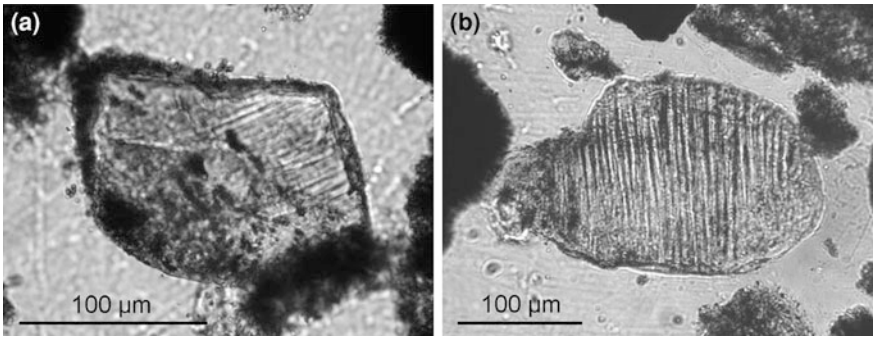

Fig. 6.17 Photomicrographs of quartz grains from the Middle Devonian Eifelian–Givetian boundary layer at Jebel Mech Irdane in the Anti Atlas desert near Rissani, Morocco. **a** Quartz grain exhibiting one set (NE-SW trend on the right side) of planar features. **b** Quartz grain with one set of quasi-planar features (N–S trend). Courtesy of B. Ellwood

6.3.3 Middle Devonian (Eifelian–Givetian Boundary) Ejecta Layer?

The late Eifelian Stage was a time of global anoxia resulting in the deposition of black shale. There was an extinction event at this time known as the Kačák Event (or *otomari* Event) (van Hengstum and Gröcke 2008). The Kačák Event was first described as an ammonoid extinction event correlated with eustatic sea-level and paleotemperature change (House 1985). It is now associated with the extinction of 15 % of marine genera (Sepkoski 1996), just preceding the Eifelian–Givetian Boundary. The age of the Eifelian–Givetian boundary is given as 388.1 ± 2.6 Ma (Kaufmann 2006). Evidence of an impact event associated with the Eifelian–Givetian boundary or Kačák/*otomari* Event has been controversial.

Ellwood et al. (2003) reported finding a high concentration of shocked quartz; positive Ni, Cr, As, V, and Co anomalies; microspherules and microcrysts; and a negative carbon isotope shift associated with the Kačák/*otomari* Event ~34 cm below the Eifelian–Givetian boundary. This section is located 25 km northeast of Jebel Mech Irdane in the Anti Atlas desert near Rissani, Morocco. The bed in which the impact evidence was reported is a gray shale-marl ~25 cm thick. Although it was reported that there was a high concentration of shocked quartz grains, little quantitative data were given. Ellwood et al. (2003) stated that they recovered 52 quartz grains with planar features that they interpreted as PDFs (Fig. 6.17). However, they did not give sample sizes, nor did they indicate the vertical distribution of "shocked quartz" grains through the section, although they reported that all were associated with the Kačák/*otomari* Event ~34 cm below the Eifelian–Givetian boundary. Ellwood et al. (2003) stated that they observed 54 sets of planar features in the 52 quartz grains, but that only 16 of the sets of planar features had orientations (determined by universal stage) similar to PDFs. In addition, only two grains exhibited multiple directions and both had only two sets

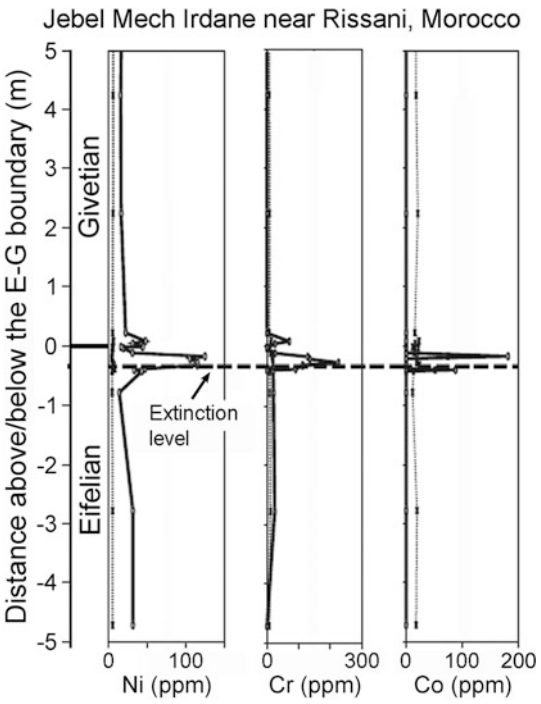

Fig. 6.18 Nickel, Cr, and Co content (determined using PIXE) across the Eifelian–Givetian boundary layer at Jebel Mech Irdane in the Anti Atlas desert near Rissani, Morocco. The dotted vertical lines represent instrumental limit of detection. The dashed horizontal line is the level at which the proposed impact evidence is centered and it coincides with the global Kacák/*otomari* mass extinction event. Zero on the vertical scale marks the base of the Givetian Stage. Modified after Ellwood et al. (2003), Fig. 1b

of planar features. One of these two grains was partially isotropic and Ellwood et al. (2003) suggested that the isotropic region may be diaplectic glass.

Racki and Koeberl (2004) stated that the images of grains identified as shocked quartz grains with PDFs by Ellwood et al. (2003) were not convincing and that the orientation measurements of the planar features suffer from an insufficient number of observations. Ellwood et al. (2004) replied by stating that the black color of the conodonts in the section indicate heating to a temperature of at least ~300 °C, which would have had annealing effects on quartz PDFs in rocks that old. They went on to say that they have now found two levels of shocked quartz with PDFs, suggesting the possibility of two impacts. However, the peaks are defined by peak abundances of only 2–4 quartz grains with planar features. A photomicrograph of one of the quartz grains shows what Ellwood et al. (2004) suggested are three sets of PDFs, but the resolution of the image is not sufficient to allow the readers to make their own determination.

The interval 12–40 cm below the Eifelian–Givetian boundary has high concentrations of Ni, Cr, As, V, and Co (Fig. 6.18; Ellwood et al. 2003). The Ni/Co ratio at the peak anomaly appears to be ~0.7. This is close to the average Ni/Co ratio of the upper continental crust, which is ~1.6 (Wedepohl 1995), but is much smaller than the Ni/Co ratio of CI chondrites of ~22. Racki and Koeberl (2004) pointed out that the As and V anomalies are not indicative of a meteoritic component and that Ir data, which would be better for indicating a meteoritic

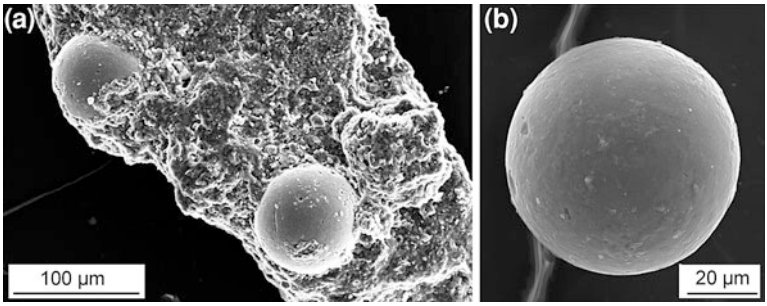

Fig. 6.19 Scanning electron microscope images of diagenetically-altered spherules from the Eifelian–Givetian boundary layer near Rissani, Morocco. **a** Spherules embedded in Devonian shale-marl matrix from Jebel Mech Irdane in the Anti Atlas desert. **b** Spherule with a relatively smooth surface. Courtesy of B. Ellwood

component, are absent. Furthermore, Racki and Koeberl (2004) stated that the sulfide-forming and redox-sensitive trace metals, reported by Ellwood et al. (2003) as evidence of an impact, could alternatively be thought of as a geochemical signature of oxygen deficiency. Ellwood et al. (2004) replied that they have not observed sulfides in the Eifelian–Givetian impact levels.

Spherules (Fig. 6.19; Ellwood et al. 2004 referred to them as microspherules), found below the Eifelian–Givetian boundary at Morocco, range in diameter between 10 and 150 μm. They were described as having a variety of morphologies that included some with equatorial bulges and "dimpling" that Ellwood et al. (2003) claimed resembled microtektite morphologies. Unless Ellwood et al. (2003) mean oblate spheres when they said equatorial bulges, we are not aware of microtektites with equatorial bulges. We assume that the "dimpling" refers to large shallow pits. Polished sections of the interior of a spherule show banding presumably due to diagenetic alteration.

The iron content of the Moroccan spherules ranges between 59 and 74 wt % FeO, and the Al_2O_3 and SiO_2 range between 0.9–11.4 and 2.8–6.1 wt %, respectively (Ellwood et al. 2003). The spherules are probably composed of a hydrated iron oxide, like goethite (Ellwood et al. 2003). Four spherules have NiO contents between 0.13 and 0.22 wt % and CoO contents between 0.07 and 0.35 wt %. One of the four spherules has a Cr_2O_3 content of 0.4 wt % (Cr contents of the other three spherules are below detection limits). None of the data for the Moroccan spherules require an impact origin.

Very little data are given for the microcrysts (microcrystals?). They are described as being from 10 to 150 μm in size and having compositions similar to the spherules, but no compositional data are given (Ellwood et al. 2003). Photomicrographs of two microcrysts indicate that at least one has an octahedral shape and they are described in the figure caption as being pseudomorphs (Ellwood et al. 2003).

Claeys (2004) searched for evidence of an impact across seven shale or clay beds at the Eifelian–Givetian boundary in the Dinant Synclinorium, Southern

Belgium. Some of the Eifelian–Givetian boundary layers exhibited enrichments in chalcophile elements (As, V) in agreement with those reported in the Moroccan site by Ellwood et al. (2003). However, Claeys (2004) interpreted the anomalies as the result of low oxygen conditions. Claeys (2004) also observed iron grains that he said could be equivalent to the spherules described by Ellwood et al. (2003), but he concluded that they clearly were not of impact origin. In this preliminary report, Claeys stated that so far none of the seven layers yielded any clear evidence of an impact origin. Claeys (2004) concluded that if the Moroccan (Jebel Mech Irdane) layer is indeed of impact origin as proposed by Ellwood et al. (2003), it must be a local event and too small to trigger a mass extinction.

In another search for a meteoritic component in the Kačák/*otomari* Event layer near Jebel Mech Irdane in Morocco, Schmitz et al. (2006) determined platinum group element (PGE) contents and osmium isotopic contents across the event layer at Jebel Mech Irdane and at Rich Haroun nearby. At the two sites, they found Ir contents of 0.13–0.28 ppm, but the Ir/Al ratios are only a factor of 1.5–2 higher than the background level. On an Al-normalized basis Pd and Pt show weak enrichments, only 2–4 times above the background level. According to Schmitz et al. (2006), such small anomalies can easily be explained by terrestrial processes and do not require a meteoritic component. A terrestrial origin is supported by non-chondritic ratios between the PGEs. Likewise, high $^{187}Os/^{188}Os$ ratios (1.1–3.8) found in the boundary layer are not consistent with a meteoritic component. Schmitz et al. (2006) concluded that if a meteoritic component is present in the beds, it represents less than 0.2 % by weight.

Based on the Earth Impact Database (2011), five known impact craters/structures have ages which appear to be close to the age of the Kačák/*otomari* Event: (1) Elbow crater in Saskatchewan, Canada; (2) Brent crater in Ontario, Canada; (3) Kaluga crater in Russia, (4) Crooked Creek crater in Missouri, USA, and (5) La Moinerie in Quebec, Canada. Except for Kaluga, all have large errors associated with their ages (i.e., $\geq \pm$ 20 Ma) and, except for the 15-km-diameter Kaluga structure, they are all $\leq$ 8 km in diameter. None appear to have been large enough or close enough to be responsible for an ejecta layer in Morocco, much less a mass extinction event.

6.4 Alamo Breccia Deposits

6.4.1 Introduction

The **Alamo Breccia** is a widespread carbonate unit of Late Devonian age that is found over much of south-central Nevada, USA. It is exposed in about 25 ranges in the Basin and Range Province, where it covers an area of $\sim$10,000 km^2 (Warme et al. 2002). It varies in thickness from $<$ 1 to more than 100 m, with an average of 50 m. The Alamo Breccia was recognized during field work in 1990 as an unusual unit within the Guilmette Formation (Warme et al. 1991). The Alamo Breccia is a

thick mass-flow deposit that strongly contrasts with the depositional style of the shallow water carbonate deposits that make up the rest of the Guilmette Formation (Warme et al. 2002). It has been formally designated as the middle member of the Guilmette Formation. Numerous authors have documented its impact-related origin due to the presence of: shocked quartz (e.g., Warme and Sandberg 1995, 1996; Leroux et al. 1995b; Morrow et al. 2005), clasts of carbonate accretionary lapilli (Warme et al. 2002), and a minor Ir anomaly (Warme and Sandberg 1995; Koeberl et al. 2003;). This impact ejecta layer occurs within the early Frasnian *punctata* conodont Zone (Fig. 6.2), indicating that this event is ~6 Ma older than the Frasnian–Famennian boundary and suggesting an age of ~382 Ma for the Alamo Breccia (Morrow et al. 2009).

The Alamo Breccia has been divided into three zones based on the nature of the breccia (Warme and Kuehner 1998; Morrow et al. 2005). Zone 1 is comprised of breccia fragments generally smaller than 2 m in size. These fragments spilled downslope and off the edge of the carbonate platform to form deposits at least 100 m thick. Zone 2 is composed of megablocks averaging ~80 m in thickness. Zone 3 is composed of tsunami uprush deposits between <1 and 10 m thick deposited across the inner platform and peritidal areas. These zones form partial rings around the proposed impact site (Fig. 6.20;Warme and Kuehner 1998; Morrow et al. 2005).

6.4.2 Crater Size and Location

The Alamo impact crater is obscured by post-Devonian geological and tectonic processes that probably include fault-dismemberment, eastward tectonic transport, post-Cretaceous extension, and burial beneath younger sedimentary and volcanic rocks (Morrow et al. 2005). Biostratigraphic and paleogeographic data obtained from the ejecta suggest that the crater penetrated the western edge of the early Devonian carbonate platform. Morrow et al. (2005) suggested that the present-day location of the crater, or at least its upper part, is between the west end of the Timpahute Range and the southern Hot Creek Range (e.g., RMW; Fig. 6.20). A sliver of the crater rim may be present at Tempiute Mountain South, Nevada (TMS; Fig. 6.20; Morrow et al. 2005).

Based on conodont biostratigraphic data and lithology of the ejecta, Morrow et al. (2005) concluded that the Alamo impact must have excavated to at least a depth of 1.7 km and maybe as deep as 2.5 km beneath the Late Devonian seafloor. Using crater scaling relationships, they calculated that the crater probably had a diameter between 44 and 65 km (Morrow et al. 2005).

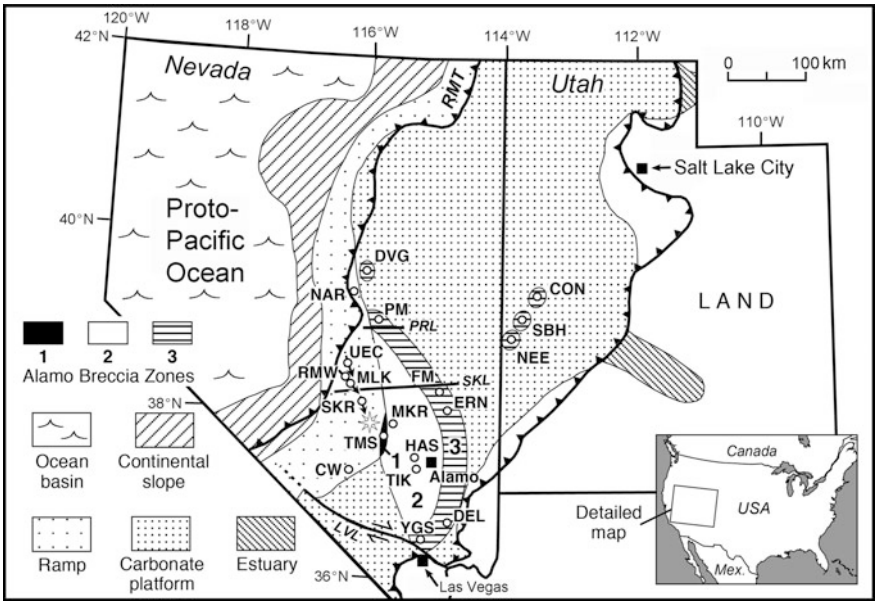

Fig. 6.20 Paleotectonic map (partly restored) of Nevada and Utah, USA, during the early Frasnian *punctata* conodont Zone showing the possible site of the eastward-transported Alamo impact crater (star symbol) and distribution of the Alamo impact ejecta. Alamo impact breccia zones 1, 2, and 3 form a semicircular pattern around the proposed crater site. Distal ejecta occur at Devils Gate (DVG) and Northern Antelope Range (NAR) in Nevada, and Confusion Range (CON), South Burbank Hills (SBH), and Needle Range (NEE) in western Utah. From Morrow et al. (2009), Fig. 2, with permission from Elsevier

6.4.3 Distal Ejecta Deposits

Distal ejecta from the Alamo impact have been found as far north as Devils Gate (DVG), northern Nevada, and as far northeast as the Confusion Range (CON), western Utah (Fig. 6.20; Morrow et al. 2005). These sites are located ~200 and ~270 km, respectively, from the inferred present-day location of the Alamo crater. Based on the upper limit of estimated crater size, the ejecta at these sites was deposited at least 3 crater diameters from the crater and are, therefore, distal ejecta.

At Devils Gate, the Alamo ejecta occurs in a 29-cm-thick layer of slightly sandy, graded, calcareous diamictite which is present ~120 m below the top of the lower member of the Devils Gate Limestone (Morrow et al. 2005). In the Confusion Range, the distal Alamo breccia consists of a 6-m-thick interval of thin-bedded, medium- to coarse-grained carbonate turbidite and breccia deposits, occurring ~170 m above the base of the Guilmette Formation. Identification of these layers as Alamo ejecta was based on conodont biostratigraphy (*punctata* Zone) and the presence of abundant quartz grains studded with hematite

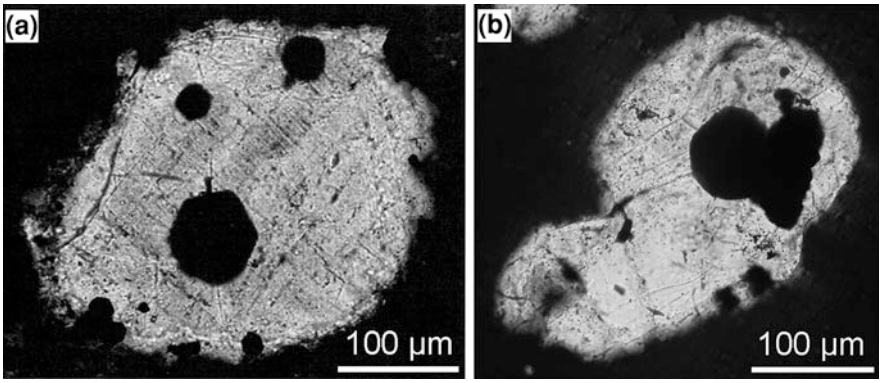

Fig. 6.21 Thin-section photomicrographs (cross polarized light) of hematite-bearing quartz grains from the Alamo breccia ejecta layer. **a** A studded quartz grain from Tikaboo Peak (TIK) containing hematite pseudomorphs after pyrite with three sets of partially decorated planar deformation features. **b** Quartz grain from Northern Antelope Range (NAR) with hematite pseudomorphs after pyrite (*black*). NAR is probably a distal site based on the proposed size and location of the Alamo Breccia impact structure. See Fig. 6.20 for locations of TIK and NAR. From Morrow et al. (2005), Figs. 4a and e, respectively, with permission from the Geological Society of America

pseudomorphs after pyrite pyritohedrons (Fig. 6.21), as well as geographic proximity to the main occurrence of the Alamo breccia (Morrow et al. 2005; Sandberg and Morrow 2007). An Ir anomaly is associated with the Alamo ejecta layer at Devils Gate and rare quartz grains exhibiting planar fractures and PDFs have been reported at the Confusion Range site (Sandberg and Morrow 2007).

Distal Alamo ejecta have been reported in South Burbank Hills (SBH) and Needle Range (NEE), western Utah (Fig. 6.20; Sandberg and Morrow 2007). These sites are located as far as 200–300 km from the proposed crater site. At both sites the ejecta occur in two thin beds separated by 1–2 m of carbonate-platform rocks representing a significant time separation. One interpretation is that the lower bed is a channel-deposited megatsunami backwash deposit, and the upper bed represents a later torrential rainfall runoff deposit in the same channel (Sandberg and Morrow 2007). Another, but probably less likely, possibility is that one of the deposits is from a second Alamo-like impact (Sandberg and Morrow 2007).

Morrow et al. (2005) proposed that a charcoal-bearing, early Frasnian estuarine deposit in the Bighorn Mountains, Wyoming, may be evidence of an Alamo impact fallout-generated forest fire.

The proposed distal Alamo Breccia ejecta deposits just barely meet the requirements for "distal ejecta" based on present knowledge regarding the size of and probable location of the source crater. If additional studies indicate a larger crater and/or a different crater location, some or all of the sites now assumed to be distal could be re-classified as proximal.

Chapter 7
Proterozoic Impact Spherule/Ejecta Layers Younger Than 2.4 Ga

7.1 Introduction

7.1.1 Stratigraphic Subdivision of the Precambrian

The Precambrian has been more difficult to subdivide stratigraphically than the Phanerozoic. It extends from the beginning of the Solar System at 4566 Ma (Allègre et al. 1995) to the start of the Cambrian Period around 542 Ma (Grotzinger et al. 1995). This represents ~88 % of Earth's history so Precambrian subdivisions generally cover vast stretches of time. Subdivision of the Phanerozoic Eon was also facilitated by the relatively rapid evolution of many different groups of organisms that produced skeletal remains (shells, teeth, etc.). Even though life appeared surprisingly early in Earth's history (Wacey 2009), the Precambrian was, until almost the very end, a time of unicellular organisms that did not produce skeletal remains (Knoll 2003). Macroscopic body fossils appeared as early as 2 Ga (Han and Runnegar 1992) and microbial communities formed macroscopic structures known as stromatolites throughout most of the Precambrian, but neither one rivals skeletal fossils as a basis for detailed stratigraphic subdivision. Moreover, sedimentary rocks and the information they contain are increasingly likely to be affected by tectonic deformation or eroded away altogether as they get progressively older. Therefore distal ejecta layers should become progressively harder to recognize back through time.

The Precambrian itself is not a formal stratigraphic unit, it simply encompasses all rocks predating the Cambrian (the oldest Period of the Phanerozoic Eon), yet it has been formally subdivided into two Eons: the Archean and Proterozoic (Van Kranendonk et al. 2008). The boundary between the two, i.e., the **Archean-Proterozoic boundary**, was defined chronometrically as 2.5 Ga; older rocks are Archean whereas rocks younger than 2.5 Ga but older than Cambrian are Proterozoic. The Archean-Proterozoic boundary coincides in a general way with a number of major shifts in Earth's systems, e.g., a change in global tectonic style

B. P. Glass and B. M. Simonson, *Distal Impact Ejecta Layers*, Impact Studies,
DOI: 10.1007/978-3-540-88262-6_7, © Springer-Verlag Berlin Heidelberg 2013

signaled by the disappearance of Greenstone Belts (see Chaps. 8 and 9 and Sect. 11.3.4 for further discussion of the Archean).

The International Union of Geological Sciences (IUGS) approved the subdivision of the Proterozoic Eon into three Eras with chronologically defined boundaries (Fig. 7.1) that have gained wide acceptance (e.g., Walker and Geissman 2009). These Eras are the Neoproterozoic from 0.542 to 1.0 Ga, the Mesoproterozoic from 1.0 to1.6 Ga, and the Paleoproterozoic from 1.6 to 2.5 Ga (Robb et al. 2004; Van Kranendonk et al. 2008). Even though these subdivisions are referred to as Eras, all three rival or exceed the entire Phanerozoic Eon in terms of duration. The Precambrian Eras have been subdivided into Periods (Fig. 7.1), but these names are not in wide use save for one, the Ediacaran Period (Knoll et al. 2006). The Ediacaran Period is at the end of the Precambrian and takes its name from an enigmatic but distinctive biota that appeared worldwide during this Period (Narbonne 2005; Vickers-Rich and Komarower 2007). It is the only time in the Precambrian when strata can be correlated globally on the basis of macroscopic fossils. The start of the Ediacaran Period is formally defined as a Global Boundary Stratotype Section and Point (GSSP) in South Australia dating to around 630 Ma (Knoll et al. 2006). The GSSP was placed near the top of a succession rich in glacial deposits (Williams et al. 2008) that some refer to as the "Snowball Earth" (Hoffman et al. 1998). Specifically, the GSSP for the start of the Ediacaran Period was placed at the contact between the Elatina and Nuccaleena Formations (Fig. 7.2). The GSSP for the end of the Ediacaran Period, which is also the end of the Precambrian and the start of the Cambrian period, is located in Newfoundland. Older boundaries, such as the Archean-Proterozoic boundary, are defined by reference to a fixed date known as a Global Standard Stratigraphic Age.

7.1.2 Secular Variation in Precambrian Ejecta Layers

The distal impact ejecta layers in this Chapter (Table 7.1) are described in reverse chronological order, but Precambrian distal ejecta layers are distributed very unevenly in time. One of the ejecta layers is Ediacaran in age and the other two are mid-Paleoproterozoic. Separating them is an interval of > 1.2 billion years of Earth history from which distal ejecta layers have yet to be reported (Fig. 7.1). The only ejecta occurrence described from this interval, a ~ 1.2 Ga layer in the Torridonian Supergroup of Scotland, appears to be proximal rather than distal (Amor et al. 2008), so it is not described here. Known impact structures outnumber known distal impact ejecta layers in Proterozoic rocks younger than ~ 2.4 Ga by a wide margin, as they do in the Phanerozoic. In contrast to 3 known distal ejecta layers, there are currently 7 impact structures formed in the Neoproterozoic, 1 in the Mesoproterozoic, 7 in the Paleoproterozoic, and ~ 11 more that formed at some unspecified time in the Precambrian (Earth Impact Database 2011; accessed 06/17/2011). The oldest impact structure currently recognized on Earth is the Suavjärvi Structure of Russia; it formed at ~ 2400 Ma and has a diameter of only 16 km (Earth Impact Database 2011;

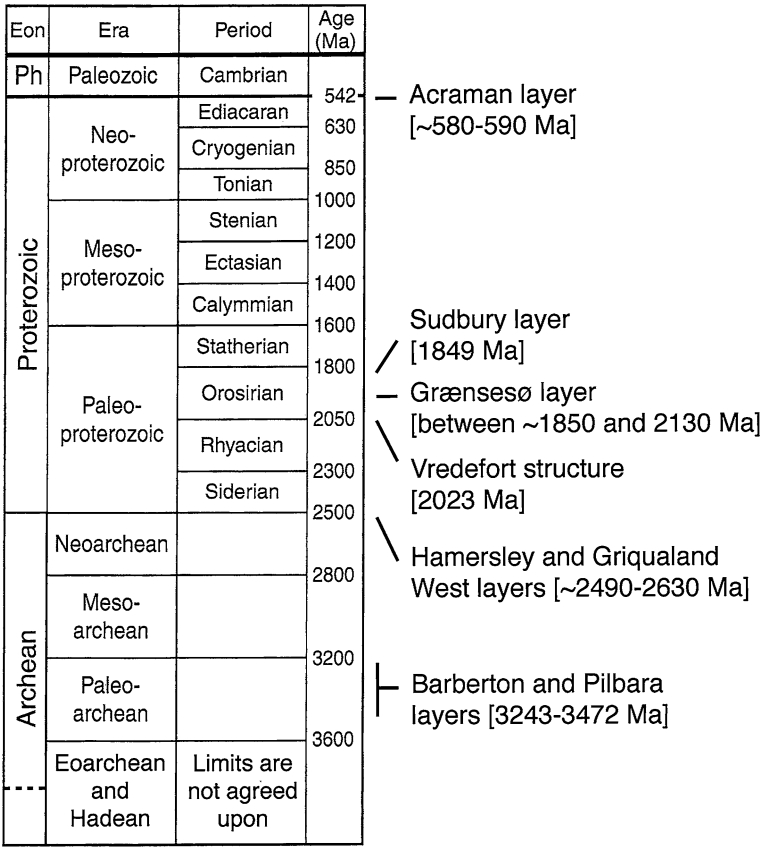

Fig. 7.1 Stratigraphic column of most of the Precambrian showing subdivisions and times at which the distal ejecta and spherule layers described in Chaps. 7, 8 and 9 and the Vredefort impact structure formed. Ph = Phanerozoic Eon. Modified after Fig. 9.1 in Robb et al. (2004) and reprinted with the permission of Cambridge University Press

accessed 06/17/2011). The second oldest impact structure recognized on Earth, the Vredefort Structure of South Africa, formed at 2023 Ma (Kamo et al. 1996). Although it ranks as Earth's largest impact structure with its diameter of 300 km, Vredefort's distal ejecta layer has yet to be positively identified.

In addition to being rare, distal Precambrian ejecta layers younger than 2.4 Ga generally resemble those of the Phanerozoic in having a mix of different types of unmelted and melted ejecta, e.g., shocked mineral grains and (replaced) impact spherules. The only exception is the **Grænsesø spherule layer** in Greenland (described in Sect. 7.4), which is probably the oldest layer in this group. In contrast, distal ejecta layers formed in the Archean and earliest Paleoproterozoic are different in character from most if not all of the younger layers. Specifically, the older layers have spherules in great abundance, many with textures rarely seen in younger layers

Table 7.1 Definite or probable Precambrian impact spherule/ejecta layers younger than 2.4 Ga

Layer	Location	Impact	Age	Source crater	Refs.
		Evidence[a]	(Ma)		
Acraman	South Australia	Ir, OsI, PGEs, SM, Sph	~580–590	Acraman	Gostin et al. (1986), Wallace et al. (1990a, b), Williams and Gostin (2005)
Sudbury	Lake Superior region, North America	Ir, PGEs?, SM, Sph	~1,849	Sudbury	Addison et al. (2005), Pufahl et al. (2007), Cannon et al. (2010)
Grænsesø	South Greenland	Sph	$> \sim 1{,}850, < \sim 2{,}130$	?	Chadwick et al. (2001), Smith et al. (2006)

[a] *Ir* Iridium anomaly, *OsI* Osmium isotope data, *PGEs* Platinum group elements with chondritic ratios, *SM* Shock-metamorphosed rock and mineral grains, *Sph* Spherules

(Simonson and Harnik 2000), and have almost no unmelted ejecta. Moreover, none of the older distal ejecta layers can be tied to a source crater because no impact structures that old have been recognized. The youngest of the well-documented "different" layers formed ~2.49 Ga (Sect. 8.2.2), whereas the oldest impact structure dates to ~2.4 Ga (described above) and the oldest of the "conventional" distal ejecta layers formed at 1.85 Ga (the **Sudbury ejecta layer**, described in Sect. 7.3). One distal ejecta layer has been recognized in strata deposited between 2.49 and 1.85 Ga, the Grænsesø spherule layer, but it differs in character from both older and younger layers (see Sect. 7.4). The older, spherule-rich layers are not evenly distributed in time either (Fig. 7.1). They are clustered in two groups that formed from ~2.49 to 2.63 Ga (Simonson et al. 2009a,b) and 3.24 to 3.47 Ga (Lowe and Byerly 2010); these are described in Chaps. 8 and 9 respectively. No impact layers or structures have been reported from strata formed during the intervening time, which lasted ~600 million years. The possible significance of the uneven distribution of the known Precambrian spherule layers is discussed in Chap. 11.

7.2 Acraman Ejecta Layer (Neoproterozoic, South Australia)

7.2.1 Description of Layer

The **Acraman ejecta layer** was initially identified in the Adelaide Fold Belt, an unusually thick and well-preserved sedimentary succession in South Australia (Fig. 7.3). Strata in the Adelaide Fold Belt range in age from mid-Neoproterozoic to Middle Cambrian and preserve a record of at least five major rift cycles as well as multiple major glaciations (Preiss 2000). The Acraman layer was subsequently recognized in the Officer Basin as well (Fig. 7.3), which extends for ~1400 km across South and Western Australia. The Adelaide Fold Belt and the Officer Basin lie on opposite sides of the Gawler Craton, a block of older Precambrian basement rocks that is circular in plan and occupies the center of South Australia (Fanning et al. 1988). The southern part of the Gawler Craton is covered by the Mesoproterozoic Gawler Range Volcanics. Part of the eastern edge of the Gawler Craton is covered by a thin package of shallow-water strata known as the Stuart Shelf that is stratigraphically equivalent to the upper part of the Adelaide Fold Belt succession. Despite their relatively close proximity and the fact that they show numerous similarities in age and stratigraphy (Grey and Calver 2007), the Adelaide Fold Belt and Officer Basin apparently developed more or less independently (Preiss 2000).

In the Adelaide Fold Belt, the ejecta layer is hosted by the Ediacaran Period Bunyeroo Formation (Fig. 7.2), which was deposited below wave base during one of multiple marine transgressions. It is probably the first Proterozoic distal ejecta layer to be recognized as such and also one of the best examples of any age of distal ejecta confidently correlated to a source impact structure. The layer consists largely of fragments of pinkish, porphyritic, felsic volcanic rock (Figs. 7.4, 7.5; Gostin et al. 1986)

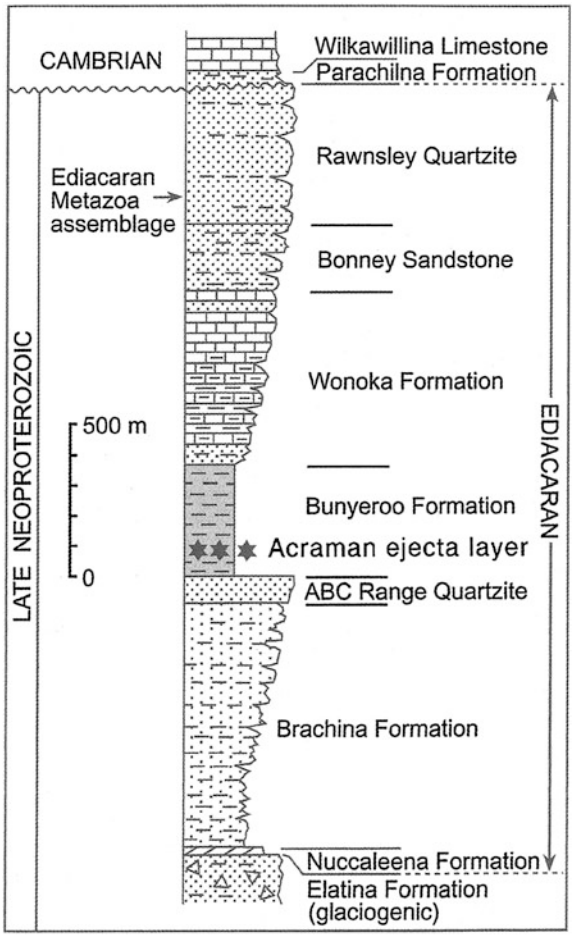

Fig. 7.2 Generalized stratigraphic succession of the Ediacaran Period formations in the Adelaide Fold Belt. The stratigraphic position of the Acraman ejecta layer in the Bunyeroo Formation is indicated with stars. From Williams and Gostin (2005), Fig. 3, with permission from the Geological Society of Australia

and was thought to be an unusual tuff until shock features were recognized (described in Sect. 7.2.3). The ejecta layer is stratigraphically ~40–80 m above the base of the Bunyeroo Formation; the formation consists largely of monotonously uniform, red to greenish-gray shale and rarely contains detritus coarser than siltstone laminae a few millimeters thick (Wallace et al. 1996). The ejecta layer stands out because it is anomalously thick and coarse (Fig. 7.5) and the shales next to the layer have an unusual greenish color (Figs. 3.1 and 7.5). The greenish color has been attributed to the layer's coarse grain size allowing it to serve as a high-permeability conduit for diagenetic fluids that preferentially reduced the adjacent shales (Wallace et al. 1990b).

The Acraman layer is a regionally persistent marker bed and ranges from 0 to 40 cm in thickness in the Bunyeroo Formation. Initially, Gostin et al. (1986) described the layer in terms of 4 subunits now known as the Type 1 Sequence (Fig. 7.6). The internal organization of the layer is different at some sites, as

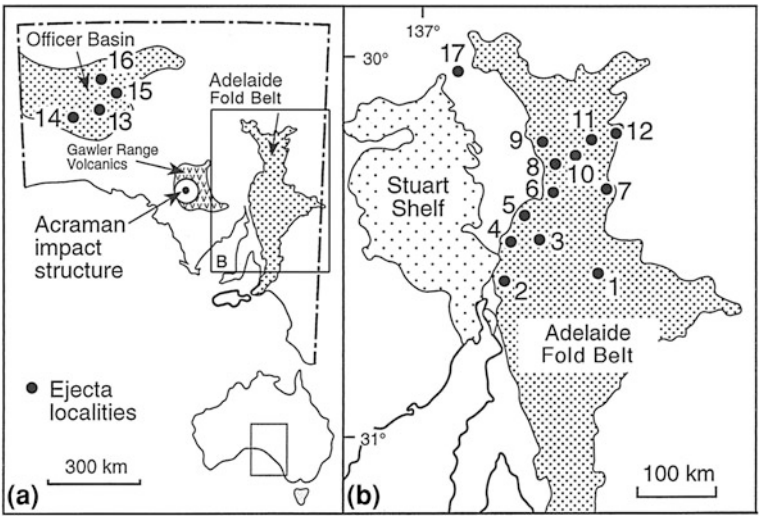

Fig. 7.3 Maps showing locations where the Acraman ejecta layer has been recognized. **a** Map of South Australia showing outlines of Adelaide Fold Belt and Officer Basin and the location of the Acraman impact structure. The numbered locations are drill cores in the Officer Basin containing the Acraman ejecta layer as follows: 13 = both Observatory Hill 1 and Murnaroo 1, 14 = Lake Maurice West 1, 15 = Giles 1, and 16 = Munta 1. **b** Map showing the outlines of the Adelaide Fold Belt and the equivalent Stuart Shelf and the locations of occurrences of the Acraman ejecta layer. Site 6 is Bunyeroo Gorge, site 12 is Wearing Hills, and all of the occurrences are surface outcrops except for 17, which is a drill core in strata of the Stuart Shelf. Modified after Fig. 1 in Wallace et al. (1996)

described in Sect. 7.2.4. In the Type 1 Sequence, the lowest and coarsest subunit (Layer 1) consists of lenses of coarse, angular sand that contain significant amounts of gravel (Fig. 7.5B). The latter may include clasts of extrabasinal rocks up to 30 cm in diameter that typically occur in isolation (as "lonestones") (Fig. 7.5A). Beds above and below the large clasts are bent after the manner of dropstones in ancient glacial varvites, reflecting compaction and possibly impact of the lonestones on the seafloor. Most of the sand and all of the large blocks in the basal subunit consist of rock fragments (Fig. 7.4) of pink to red volcanic rock that are generally dacitic to rhyodacitic in composition. In addition, most of the crystals (both individual sand grains and phenocrysts within the porphyries) are fractured (Fig. 7.7A). The basal subunit is overlain by a thin green shale containing scattered sand (Layer 2) that in turn is overlain by a normally graded layer of fine sand (Layer 3). These three subunits are capped by a lenticular sandy layer (Layer 4) with multiple graded beds and some cross-stratification indicating paleoflow was to the east and northeast down the paleoslope. Subsequent studies revealed more details about the lateral variability of the layer (described in Sect. 7.2.4).

In addition to unmelted ejecta, the ejecta layer in the Bunyeroo Formation locally contains replaced bodies whose shapes suggest they were originally spherules, most likely microtektites (Wallace et al. 1990a). This is based entirely on their external

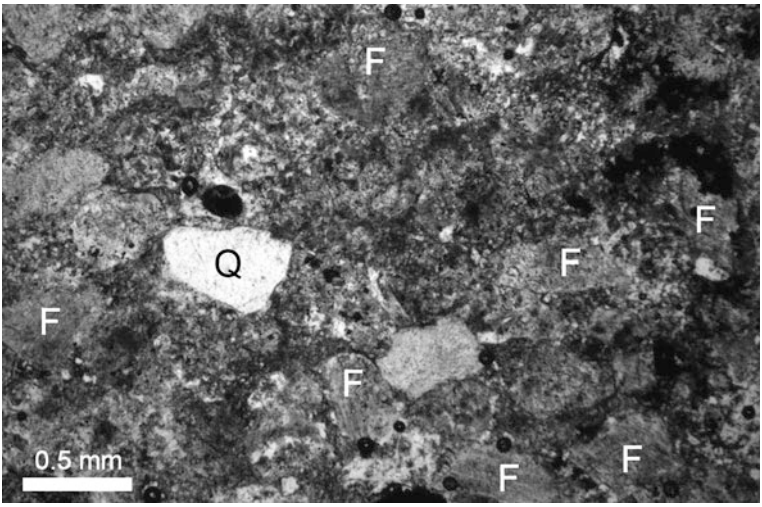

Fig. 7.4 Photomicrograph in plane polarized light of sand-rich sample from the Acraman ejecta layer at Bunyeroo Gorge near the exposures shown in Figs. 3.1 and 7.5. The medium to coarse sand is well-sorted but highly compacted and consists of finely crystalline lithic clasts with lesser numbers of feldspar grains (labeled 'F') and quartz grains (labeled 'Q')

shapes as no glass, primary phases, or pseudomorphs of internal textures were observed in them. The spherules are mostly spherical based on the dominance of circular cross-sections (Fig. 7.8), but a few have dumbbell-shaped cross-sections. They now consist of coarsely crystalline calcite or, less commonly, other diagenetic phases including microcrystalline quartz, albite, and barite. The bodies range in size from ~0.15 to 1 mm across and have only been reported from 3 localities in the northern part of the Adelaide Fold Belt. The spherules are accompanied by more angular particles described as "shard-like" that are replaced by the same minerals as the spherules, so their origins appear to be linked. These particles are likely to be replaced fragments of impact melt spherules in view of the fact they appear to be restricted to the known ejecta layer, but little more can be said about them.

7.2.2 Radiometric Age

The only ages from the Acraman ejecta layer are SHRIMP dates of zircons isolated from porphyritic clasts; they yielded an age of 1577 ± 11 Ma (Compston et al. 1987). This is clearly not the depositional age of the layer as it predates the Ediacaran Period by ~950 million years. Whole-rock Rb–Sr isochrons on shales either from the Bunyeroo Formation or correlated with it lithostratigraphically, e.g., the Yarloo Shale on the Stuart Shelf, yielded ages of 590–600 Ma, but with large error bars (summarized in Compston et al. 1987; Schmidt and Williams 1996). Schmidt

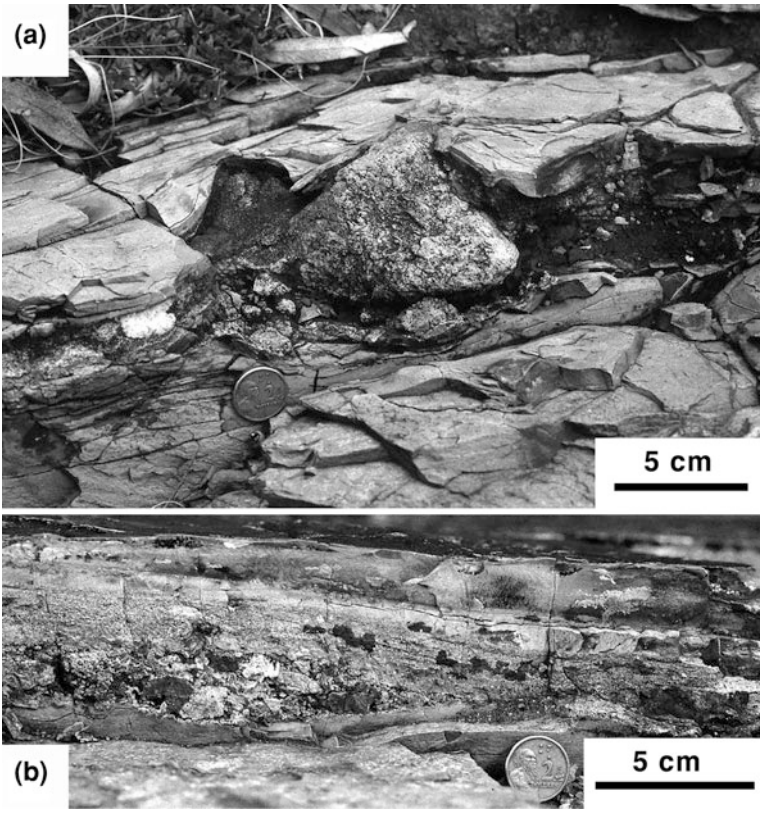

Fig. 7.5 Surface exposures of the Acraman ejecta layer in Bunyeroo Gorge. **a** Exposure of entire thickness of layer where it consists mainly of breccia (Layer 1 of Wallace et al. 1996) and contains a single outsized clast or "lonestone" of felsic volcanic rock (*center*). **b** Exposure of the layer close to spot shown in **a** where Layer 1 is tapering out (above coin) and is overlain by Layers 2 and 3 of Wallace et al. (1996); Layers 2 and 3 are finer and more continuous than Layer 1, even in the small area of this exposure (see Fig. 7.6 and text for further discussion)

and Williams (1991) noted that the paleomagnetic poles obtained for the Bunyeroo redbeds were typical of Late Proterozoic to Middle Cambrian poles but could not bracket their age more precisely than that. Schmidt and Williams (1996) were able to strengthen the paleomagnetic case for correlation by obtaining data from impact melt rock in the Acraman structure (the probable source crater of the Acraman ejecta layer) as well as higher quality data from the strata of the Bunyeroo Formation. More recently, Walter et al. (2000) synthesized chemostratigraphic data from Australia and Canada for most of the Neoproterozoic Era (from 840 to 544 Ma) and attempted to link it to both the glacial deposits of the so-called "Snowball Earth" and isotopically dated markers. They arrived at an age of about 578 Ma for the Acraman layer using this approach. Williams and Gostin (2005) suggested it was a bit younger based on ages of 582–575 Ma reported for rocks in Tasmania correlated

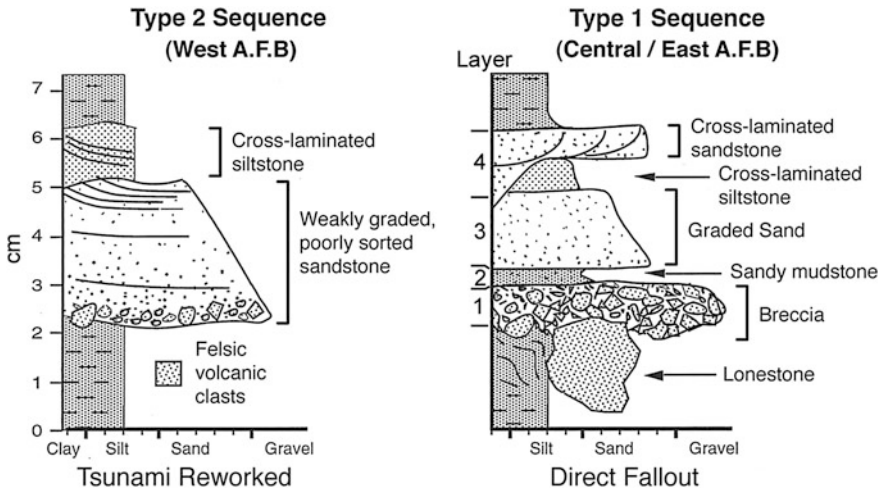

Fig. 7.6 Generalized diagrams of the two most common sedimentary sequences observed in the Acraman ejecta layer in the Adelaide Fold Belt (A.F.B). The Acraman layer generally shows the Type 1 Sequence in the central to eastern parts of the A.F.B. where the water was deeper compared to the Type 2 Sequence in the western part of the A.F.B. where the water was shallower (see text for fuller discussion). Modified after Fig. 5 in Wallace et al. (1996)

with the Elatina Formation, but subsequent work indicated the rocks in Tasmania are much older than that (G. Williams, personal communication, 2010). Therefore, the generally accepted age for the Acraman layer is ~580–590 Ma.

7.2.3 Evidence of Impact Origin and Extraterrestrial Component

One of the key criteria for recognizing the Acraman layer is an abundance of fractured crystals, especially quartz and feldspar, both in rock fragments and as individual crystals. In the Adelaide Fold Belt, the larger volcanic rock fragments in the ejecta layer contain ~40 % phenocrysts by volume, which are mostly plagioclase with rare quartz. Most of the phenocrysts in the larger clasts are fractured to some degree (Fig. 7.7a) and up to 90 % of the quartz crystals have multiple sets of PDFs (Fig. 7.7b) in some specimens (Gostin et al. 1986). Based on detailed study of one quartz-rich clast, the most common orientation for PDFs in quartz was $\omega\{10\bar{1}3\}$, but some with $\xi\{11\bar{2}2\}$ and $\{22\bar{4}1\}$ orientations were also present, indicating shock pressures of ~15 GPa (Gostin et al. 1986). Finely crystalline quartz in the groundmass of large clasts shows similar fracturing, indicating the shock deformation took place after devitrification. In contrast to the primary quartz crystals, the many fractured and presumably shocked feldspar crystals have been replaced by authigenic phases; they now have virtually pure end-member compositions of either Na- or K-feldspar (Gostin and Zbik 1999).

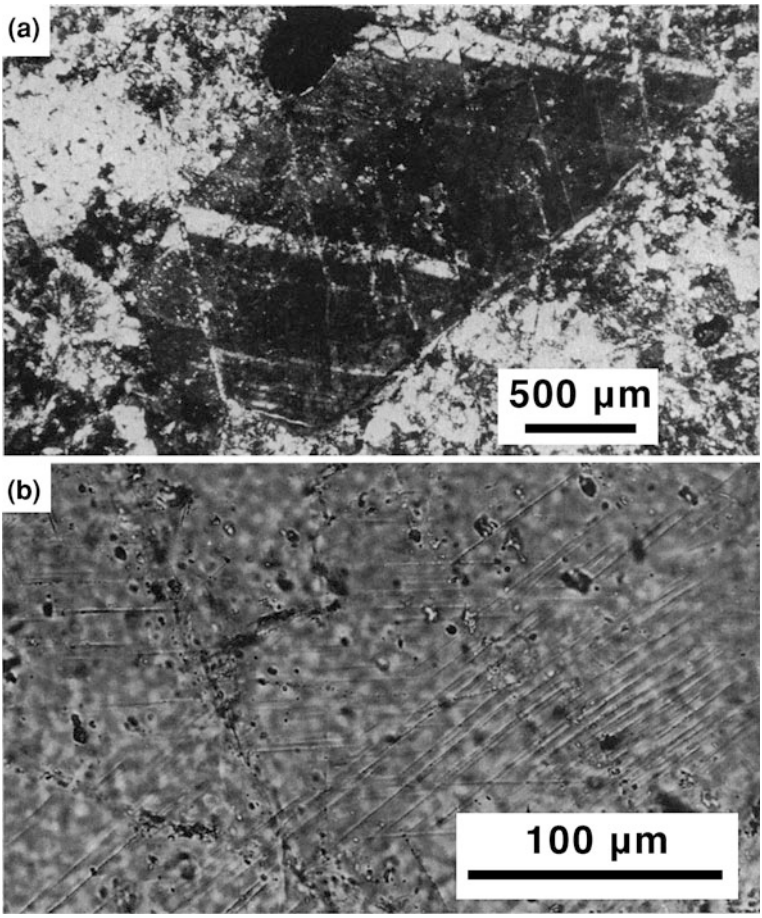

Fig. 7.7 Photomicrographs in plane polarized light of probable shock features in crystals in coarse impact debris from the Acraman ejecta layer. **a** A feldspar crystal with twin lamellae offset along multiple fractures. **b** A quartz crystal with two sets of lamellae, both parallel to $\omega\{10\bar{1}3\}$. From Gostin et al. (1986), Fig. 4, reprinted with permission of AAAS

Other types of minerals also appear to show shock features, most notably planar features in zircon crystals extracted from a single large clast (Fig. 7.9) that Gostin and Zbik (1999) interpreted as probable PDFs by using the method of Bohor et al. (1993). To our knowledge, no measurements of crystallographic orientations of planar features in any phases other than quartz have been published for this layer. Finally, probable shatter cones are present in a few of the larger ejecta clasts of dacite in the Adelaide Fold Belt (Fig. 7.10), but many of the rock fragments less than a few centimeters in diameter in the layer appear to be unshocked (Gostin and Zbik 1999).

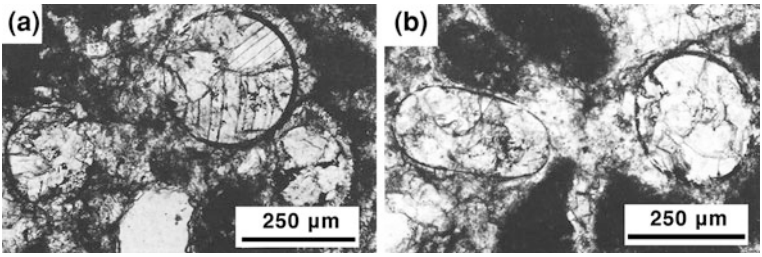

Fig. 7.8 Photomicrographs in plane polarized light of carbonate-replaced spherules from the Acraman ejecta layer occurrence at Wearing Hills. **a** Spherules with circular cross-sections plus interstitial calcite cement. **b** Spherules (*white*) together with volcanic rock fragments (*dark*) that are similar to the volcanic rocks in the Acraman impact structure. From Wallace et al. (1990a), Figs. 2a and b, respectively, with permission from the Meteoritical Society

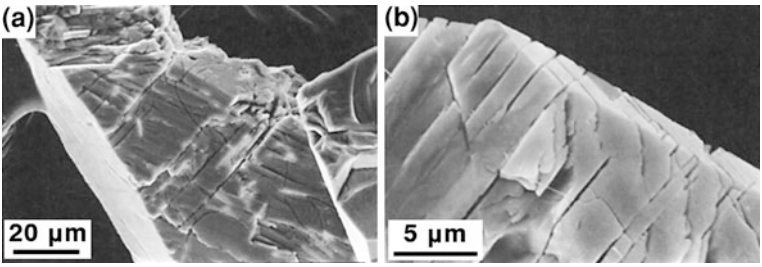

Fig. 7.9 Scanning electron photomicrographs of acid-etched zircon crystals from the Acraman ejecta layer showing multiple sets of planar features interpreted as PDFs by Gostin and Zbik (1999). From Gostin and Zbik (1999), Fig. 10, with permission from the Meteoritical Society

In the ejecta layer in cores taken in the Officer Basin, probable PDFs occur in quartz phenocrysts in volcanic rock fragments (Wallace et al. 1989, 1996), as well as in some individual quartz crystals (Hill et al. 2004). To our knowledge, no measurements of their crystallographic orientations have been published. There are also some unexplained variations in the distribution of shocked minerals and ejecta in general in cores from the Officer Basin (discussed in Sect. 7.2.4).

In addition to physical evidence of deformation by a hypervelocity impact, geochemical anomalies associated with the Acraman layer indicate extraterrestrial material is present. Specifically, concentrations of Ir, Au, Pt, Pd, Ru, and Cr in the ejecta layer at 9 localities in the Adelaide Fold Belt are 20–50 times greater than background concentrations in the associated ejecta-free shales of the Bunyeroo Formation (Gostin et al. 1989). Samples from the Yardea Dacite, the likely source of the bulk of the ejecta (see Sect. 7.2.5), likewise have low concentrations of these elements. Therefore, Gostin et al. (1989) believed the PGEs in the ejecta layer were largely derived from an extraterrestrial impactor. However, the Ir and associated anomalies differ from those of other distal ejecta layers in several regards. First, they are not as high as those observed in a number of other distal ejecta layers. The maximum concentration of Ir reported from the Acraman layer

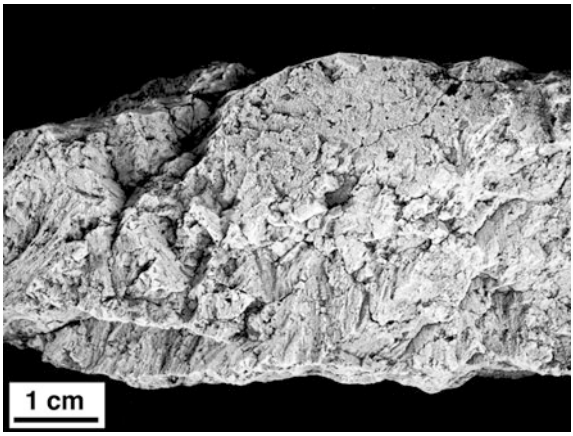

Fig. 7.10 Close-up of fractured surface of a 12-cm dacite fragment from the base of the impact ejecta layer near Bunyeroo Gorge showing features interpreted as small shatter cones by Gostin et al. (1986) in lower part of sample. Because of the coarse nature of the sample the striations are not well developed. Courtesy of Peter Haines

is 2 ppb, which is much lower than most of those reported for the K-T boundary layer (Chap. 5) or most of the Archean layers (Chap. 9). However, maximum Ir concentrations at sites at about the same distance, in crater diameters, from the Chicxulub structure are comparably low (<1 ppb) due to reworking and incorporation of local sediment (see Fig. 5.11). Gostin et al. (1989) estimated the Ir fluence for the Acraman layer to be 9–11 ng/cm^2 compared to an average of 55 ± 3 ng/cm^2 for the K-T boundary layer (Chap. 5) and 9.7 ± 11.1 ng/cm^2 for the cpx spherule layer from the 100-km-diameter Popigai structure (Sect. 4.6). Secondly, higher concentrations of Ir are consistently observed in the coarse basal part of the layer, which is rich in unmelted ejecta. Gostin et al. (1989) noted that even individual ejecta clasts are enriched in Ir (1 ppb). In contrast, the highest concentrations of Ir and other PGEs in the K-T boundary layer typically reside in the finer material at the top of the layer (e.g., MacLeod et al. 2007). Finally, the interelement ratios of the PGEs depart from chondritic values at some localities, although the majority fall in the range of 0.6–6 times chondritic, i.e., within one order of magnitude. Cr values for the ejecta samples are an order of magnitude higher than those of chondritic meteorites or the K-T boundary layer (Gostin et al. 1989).

At least some of these differences were ascribed to diagenetic mobilization and differential migration of some PGEs and other siderophile elements (Wallace et al. 1990b). The reduction halo of green shale around the ejecta layer (Fig. 3.1) shows moderate enrichments in Ir, as well as enrichments in Au, Cu, V, and Ni. These enrichments extend up to a few decimeters above and below the ejecta layer and are symmetrical (Fig. 7.11), so they are not likely to be products of either multiple impacts or resedimentation. A more plausible interpretation is that they reflect some mobility of Ir and other siderophiles and PGEs after burial. Wallace et al. (1990b) also noted that, where the ejecta layer is enriched in Cu, it is likely to be highly enriched in Au, Pt, and Pd relative to Ir and Ru, suggesting differential migration. In support of this, they noted that interelement ratios are closer to chondritic where the ejecta layer is low in Cu. Wallace et al. (1990b) also noted

there are layers with reduction haloes of green shale in the Bunyeroo Formation other than the ejecta layer. Most of these layers are fine silty laminae and their haloes show small PGE anomalies with Ir concentrations up to 0.25 ppb versus values no greater than 0.025 ppb in ambient red shales. The question of whether the elevated Ir in the non-ejecta layers is derived from the ejecta layer or not is still open. If it were, the scale of the migration is greater than has been reported for any other distal ejecta layer because some of the reduction haloes and minor Ir enrichments are over 100 m above the ejecta layer stratigraphically.

Wallace et al. (1989) found anomalously high concentrations of Ir of 0.80 and 0.16 ppb in the Acraman ejecta layer in 2 cores from the Officer Basin but provided no additional details. Keays et al. (2004) reported that ejecta from the Bunyeroo Formation had an initial $^{187}Os/^{188}Os$ ratio of 0.10. This is meteoritic in character and implies that the bulk of the Os in the ejecta layer is of extraterrestrial origin (Williams and Gostin 2005). Although the ejecta layer is commonly enriched in Cr, isotopic analyses to determine whether or not the Cr contains an extraterrestrial component have yet to be done.

7.2.4 Geographic Distribution and Variation

The Acraman layer has been recognized in at least 13 surface exposures and 1 drill core in the Adelaide Fold Belt and coeval Stuart Shelf area at sites currently located 238–385 km from the center of the Acraman structure (Fig. 7.3). These are probably less than the original distances because of tectonic deformation, but shortening may have only been on the order of 10 % (Williams and Wallace 2003). Assuming the structure was originally 90 km in diameter (Earth Impact Database 2011; accessed 06/17/2011), the sites in the Adelaide Fold Belt are ~5.3–8.5 crater radii from the point of impact so they just barely qualify as distal ejecta. All of these sites are believed to be much closer to the point of impact than any of the older layers described in Chaps. 8 and 9.

According to Wallace et al. (1996), the ejecta layer in the Adelaide Fold Belt can be characterized in terms of two main depositional styles (Fig. 7.6). The first style, the Type 1 Sequence, is essentially what Gostin et al. (1986) described (summarized in Sect. 7.2.1). The second style, the Type 2 Sequence, differs from Type 1 in being more weakly graded, more poorly sorted, commonly displaying cross-lamination throughout, and containing rounded quartz sand grains in higher abundance. Where it displays the Type 1 Sequence, Wallace et al. (1996) interpreted the layer as a primary fallout deposit save for the cross-laminated layer on top which they attributed to post-depositional reworking. The Type 2 Sequence they attributed entirely to reworking, most likely by impact-induced tsunami-type waves and currents. This interpretation is consistent with the fact that the Type 2 Sequence is only observed on or near the western margin of the Adelaide Fold Belt, which

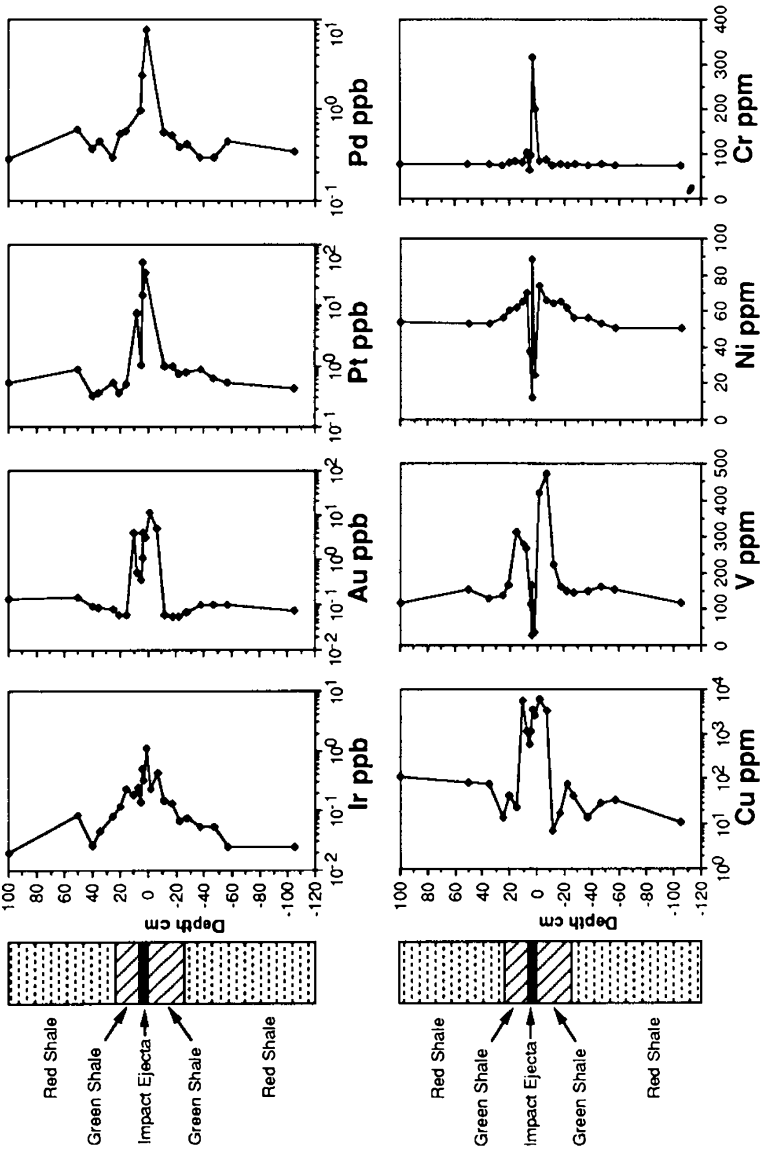

Fig. 7.11 Vertical profiles showing variations in the concentrations of Ir, Au, Pt, Pd, Cu, V, Ni, and Cr across the Acraman ejecta layer in Bunyeroo Gorge. Columns on left side indicate positions of both the layer *per se* and the green reduction halo around it. From Wallace et al. (1990b), Fig. 3, with permission from the Geological Society of America

would be the shallowest part of the basin preserved. In contrast, the Type 1 Sequence is widespread in the central to eastern portions of the Adelaide Fold Belt where paleodepths were greater so post-depositional reworking was less likely.

Neoproterozoic sediments are known from a string of basins across central Australia that are probably remnants of what was originally a single supracratonic sag basin. Walter et al. (1995) called this the Centralian Superbasin and said it was disrupted by orogenies at the end of the Neoproterozoic and the mid-Carboniferous into the isolated basins of today. The Officer Basin is the southernmost and largest of these. The current distances between the sites in the Officer Basin and the center of the Acraman structure range from 473 to 541 km, possibly shortened some by tectonic deformation (Williams and Wallace 2003). Again assuming the Acraman structure was originally 90 km in diameter, these sites are roughly 8.5–10.5 crater radii from the point of impact and clearly distal ejecta. In contrast to the decimeter- to centimeter-scale thickness of the layer in the Adelaide Fold Belt, its thickness in the Officer Basin is measured in millimeters.

The Acraman layer in the Officer Basin was initially found in 2 cores from the Dey Dey Mudstone (then known as the Rodda Beds) in the eastern part of the Officer Basin (Wallace et al. 1989). The layer is 7 mm thick in Lake Maurice West 1 and only one grain thick, i.e. <1 mm, in Observatory Hill 1 (Wallace et al. 1989). In both cores, the layer mainly consists of angular, medium to coarse sand-size clasts of reddish felsic volcanic rocks with probable PDFs in some quartz phenocrysts. As in the Adelaide Fold Belt, the ejecta layer sits amidst a greenish reduction halo in the surrounding shales; but like the layer itself, the halo is thinner in the Officer Basin, ~20 mm thick total. Many other layers of fine sand and silt are present in the strata associated with the layer in these two cores. None of the associated layers contain the volcanic clasts diagnostic of Acraman ejecta, but many have reduction haloes similar to the ejecta layer.

The Acraman layer was subsequently recognized in 4 more cores (Arouri et al. 2000; Hill et al. 2004), 3 in the Officer Basin and 1 in the Stuart Shelf (No. 17 in Fig. 7.3b), a shallow westward extension of the Adelaide Fold Belt, but there are some unexplained anomalies in its nature and distribution, particularly in the Munta core. In core Giles 1, the layer looks much as it does in previously described occurrences; it consists of a single lamina ~0.5 mm thick with angular clasts (mainly felsic volcanics) plus scattered clasts at a level ~1 mm higher. Hill et al. (2004) interpret the lower lamina as a primary fallout layer. In the Murnaroo 1 core, the layer is ~6 mm thick (Hill et al. 2004; Willman et al. 2006), but it differs in composition from other occurrences in that it consists largely of well-sorted quartz and feldspar with only a percent or so of the typical volcanic rock fragments. Probable PDFs were noted in the quartz crystals, but they are rare. The virtual absence of the volcanic detritus so dominant in other occurrences of the ejecta layer remains a mystery. In the Munta 1 core, scattered fine sand grains of pink volcanic rock fragments and feldspars with no definite PDFs (Hill et al. 2007) occur at the stratigraphic level of the Acraman layer predicted on the basis of isotopic and other criteria (as described in Sect. 7.2.6). However, ejecta including fragments of suevite were also reported through a stratigraphic interval of ~108 m above that level, and they get coarser and more abundant moving upsection (Arouri et al. 2000). This stratigraphic distribution was attributed to eolian reworking in the lower part of this interval versus "conspicuous concentrations of mass-flow-emplaced sand- and

gravel-sized microtectites and clasts of suevite" in the uppermost occurrence (Arouri et al. 2000, p. 252), but the authors gave no further description.

Cores drilled in the Amadeus Basin, another component of the Centralia Superbasin directly north of the Officer Basin, provide additional constraints on the ejecta layer. Two cores from the Amadeus Basin intersected well-preserved shales containing the stratigraphic level where the ejecta layer should be present based on isotopic and palynological correlations (described in Sect. 7.2.6). A search in these cores turned up neither the distinctive reddish volcanic fragments nor the quartz crystals with PDFs diagnostic of the Acraman layer (Grey et al. 2003). These cores were drilled roughly 750 km or 16.7 crater radii from the center of the Acraman structure. The absence of any detectable ejecta either means the layer was getting exceedingly thin at this distance or the ejecta were altered beyond recognition during diagenesis. The latter seems quite plausible given the total replacement of the spherules (Fig. 7.8) closer to the point of impact (Wallace et al. 1990a). No other occurrences of the Acraman layer have been reported from any other basins in Australia or any other continents.

Assuming the layer was dispersed equally in all directions, ejecta would have been deposited over an area of at least 10^6 km^2 (Williams and Gostin 2005). Throughout its area of occurrence, the thickness and maximum clast size of the ejecta layer decreases fairly systematically away from the Acraman impact structure in a radial direction (Fig. 7.12). Within the Adelaide Fold Belt, unmelted ejecta clasts up to 50 cm occur in the western part (i.e., nearest the Acraman structure) whereas few clasts coarser than 2 mm have been observed in the easternmost sites, the largest one being a single clast 2 cm across (Wallace et al. 1996). Likewise the layer thins from a maximum of 40 cm in the west to just a few centimeters in the east. As noted above, this includes sites from ~240–385 km away from the point of impact, ignoring any tectonic shortening (Williams and Wallace 2003). In contrast, the Officer Basin sites are further from the point of impact and the layer is accordingly finer and thinner, as noted above. The **aggregate thickness** of ejecta, corrected for 30 % compaction, is in reasonable agreement with the decrease as a function of distance predicted by McGetchin et al.'s (1973) equation (Williams and Wallace 2003; Williams and Gostin 2005).

7.2.5 Evidence that the Acraman Impact Structure is the Source Crater

The Adelaide Fold Belt and the Officer Basin are located on opposite sides of the 90-km-diameter Acraman impact structure (Fig. 7.3), which is one of the largest Proterozoic impact structures known in Australia (Haines 2005). The impact origins of the Acraman structure and the ejecta layer in the Bunyeroo Formation were established independently (as described in Williams and Gostin 2005) and the two have been linked since the simultaneous publication of Williams (1986) and Gostin et al. (1986). Although the Acraman structure is deeply eroded and the

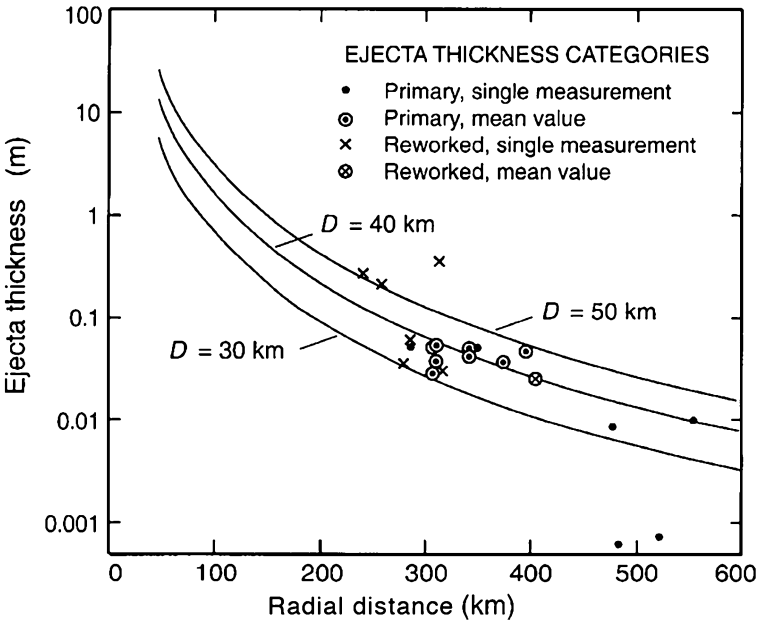

Fig. 7.12 Graph of the variation in the measured thickness of the Acraman ejecta layer (vertical axis) as a function of radial distance from the center of the Acraman impact structure (horizontal axis). The values for layer thickness were increased 30 % to compensate for compaction and some of the radial distances were increased slightly to partially compensate for tectonic shortening. The 3 curves show the predicted thickness of ejecta as a function of distance from the center of the Acraman structure based on the formula of McGetchin et al. (1973) for transient crater diameters (D) of 30 km, 40 km and 50 km. Modified after Fig. 10 in Williams and Wallace (2003), published with the permission of the Geology Society of London

ejecta layer is separated from it everywhere by erosional and/or tectonic gaps, the linkage is convincing. Before discussing the evidence supporting this linkage, pertinent characteristics of the Acraman structure are described below.

The center of the Acraman structure coincides with a near-circular depression ~30 km in diameter as well as a prominent circular magnetic low that reflect preferential erosion and decreased susceptibility, respectively, related to the impact (Williams et al. 1996). The target rocks included a thick, extensive succession of flat-lying, Mesoproterozoic volcanic rocks known as the Gawler Range Volcanics that are predominantly felsic pyroclastic rocks (Allen et al. 2003). One of the most widespread units in the Acraman depression is the Yardea Dacite (Creaser and White 1991). Although it is not widely exposed, where present the dacite is extensively fractured, contains shatter cones up to 15 cm long, and has multiple sets of decorated planar features with crystallographic orientations typical of shock lamellae in up to 90 % of the quartz crystals as well as some feldspar crystals according to Williams (1986, 1994a,b). The Yardea Dacite was extruded 1592 $\pm$ 3 Ma based on individual zircon crystal separates dated using the U–Pb

method with a SHRIMP (Fanning et al. 1988). The age of the impact *per se* is not well constrained from data inside the structure. A dike containing shocked quartz inclusions is present in the central area and interpreted as impact melt injected below the original crater floor, but no vestiges of an impact melt pool have been detected (Williams 1994a). K/Ar and $^{40}Ar/^{39}Ar$ analyses of samples from the dike yielded an age of ~450 Ma (Late Ordovician), but the K-bearing minerals were interpreted as diagenetic phases rather than primary crystals (Baldwin et al. 1991). The best constraints on the age of the impact are now believed to be those that establish the age of the distal ejecta layer (described in Sect. 7.2.2).

Several lines of evidence indicate the Acraman structure was the source of the ejecta layer in the Bunyeroo Formation and Dey Dey Mudstone. First, the ejecta layer is full of clasts that bear a close petrographic resemblance to the Yardea Dacite in its coarsest phases (Gostin et al. 1986). The rocks in the ejecta layer appear to be slightly more felsic than the Yardea Dacite on average (Williams and Gostin 2005), but they could have come from a higher level of slightly different composition than those exposed at the current erosion level. Second, zircons from clasts in the ejecta layer yielded an age of 1577 $\pm$ 11 Ma (described in Sect. 7.2.2). While this is slightly younger than the ages of the zircons from the Yardea Dacite, derivation of the ejecta from rocks at stratigraphic levels higher than the current level of erosion might also explain this discrepancy (Compston et al. 1987). Alternatively, some lead may have been lost via shock reheating (Williams 1994b). Finally, the thickness (Fig. 7.12) and grain size of the ejecta layer decrease away from the Acraman structure in a manner consistent with theoretical predictions for distal ejecta (see also Chap. 10).

The linkage between the Acraman structure and ejecta layer is also consistent with several additional lines of evidence. For example, paleocurrent data from the layer in the Adelaide Fold Belt indicate the ejecta were being transported eastward away from the Acraman structure. In addition, shock features in the Yardea Dacite in the central part of the Acraman structure (including shatter cones, fractured quartz crystals, and planar features in zircons described in Sect. 7.2.3) are very similar to those in the ejecta layer (Williams 1986, 1994a). However, Gostin and Zbik (1999, p. 590) described the shock features in zircon crystals from the Acraman structure as "relatively weak" compared to those in the ejecta layer. This is consistent with the derivation of the ejecta from higher levels in the Yardea Dacite that attained higher degrees of shock deformation and have since been eroded from the Acraman structure. Finally, the remanant magnetization of Bunyeroo redbeds and melt rock in the Acraman structure have paleomagnetic poles that are statistically indistinguishable (Schmidt and Williams 1991, 1996).

7.2.6 Possible Links to Biologic Changes

Large biologic shifts such as mass extinctions are most easily recognized in successions with extensive shelly fauna, but the Precambrian has its own record of

life, especially in the later part of the Neoproterozoic. In addition to the enigmatic Ediacaran biota (Narbonne 2005; Vickers-Rich and Komarower 2007), organic-walled microfossils known as acritarchs are widely preserved in shales deposited before, during, and after the Acraman impact took place (Grey and Willman 2009). The affinities of acritarchs are largely unknown, but most are probably preserved soft parts of unicellular marine phytoplankton. The Neoproterozoic shales of the Adelaide Fold Belt and Centralian Superbasin have been particularly prolific sources of acritarchs and have recently been studied in detail with an eye to detecting major changes in the microbiota during the Neoproterozoic. Grey et al. (2003) detected a major expansion in the diversity of acritarch assemblages not at, but soon after, the deposition of the Acraman ejecta layer. At that time, a low diversity assemblage of simple spheroids that appeared to have changed little since the Mesoproterozoic gave way to a much more diverse assemblage of morphologically complex acritarchs made up of a variety of short-ranging species. Samples from immediately above the ejecta layer are mostly barren, but close above that is evidence for a rapid radiation in a number of different cores. Williams and Wallace (2003) estimated the radiation took place $\sim$15 million years after the end of the final pulse of the Elatina glaciation (Williams et al. 2008). The ejecta layer also coincides with or is close to a large, short-lived negative $\delta^{13}C_{organic}$ excursion, so even where the ejecta layer is not present in a given core, its stratigraphic level can be inferred. Similar decreases in carbon isotope ratios are associated with most Phanerozoic mass extinction events and ascribed to declines in primary productivity and sudden biomass depletion on a large scale (Grey et al. 2003). The initial increase in $\delta^{13}C$ after the minimum value coincides with the initial increase in the abundance and diversification of the acritarchs. McKirdy et al. (2006) also noted a dramatic shift in sterane biomarkers at the same time, signaling a sharp decline in marine algal productivity for a time span they estimated to be roughly 20 million years. Finally, Hallmann et al. (2010) found enhanced concentrations of coronene, a polycyclic aromatic hydrocarbon (PAH) commonly produced by the combustion of organic matter. They noted that its appearance coincided with the negative $\delta^{13}C$ excursion and attributed it to the generation and dispersal of pyrogenic compounds over a broad area by the Acraman impact.

The Ediacaran Period is a uniquely important time in the evolution of life on Earth. It is when the first macroscopic, globally correlatable organic body fossils appeared, yet they are a "biological puzzle" whose "affinities are completely uncertain" (Antcliffe and Brasier 2007, p. 377). Moreover, more familiar animal phyla emerged for the first time by the end of the Ediacaran Period. Previously, researchers had focused on the widespread glaciations as a possible driver of change in the biosphere (Hoffman et al. 1998), but as noted above, the first major radiation of the acritarchs occurs well above the last of the glacial deposits in the Adelaide Fold Belt. Grey et al. (2003) make a point of noting that the radiation does not coincide with any obvious break in lithology in either the Adelaide Fold Belt or the Officer Basin, suggesting no major climate shift took place at the time of the radiation. This led them to suggest the Acraman impact resulted in a global

extinction that paved the way for a subsequent radiation. It also led Wallace et al. (1996) to conclude that the Acraman impact had little if any long-term effect on the deep-shelf environments in which the layer was preserved. Williams and Wallace (2003) pointed out that the Acraman impact was large enough to cause a global catastrophe based on the data and classifications in Toon et al. (1997), but they did not discuss any specific evidence that one happened beyond what was outlined above. The paleomagnetic data suggest the impact happened within roughly 12 degrees of the equator (Williams and Wallace 2003), in which case it may have been more disruptive than impacts at higher latitudes, e.g., the Popigai and Chesapeake Bay impacts. The most convincing evidence to support that would be the discovery of synchronous isotopic excursions and acritrach radiations in Ediacaran successions on other continents, but those have not been reported to our knowledge.

7.3 Sudbury Ejecta Layer (Paleoproterozoic, Lake Superior Region, North America)

7.3.1 Introduction

The Sudbury structure in Ontario (Canada) is one of the first impact structures on Earth to be recognized as such, thanks in part to the presence of diagnostic shock features such as shatter cones (Dietz 1964) and PDFs in quartz and feldspar crystals (French 1967). The impact origin of the Sudbury Igneous Complex and related features is now almost universally accepted (e.g., Naldrett 2003; Ames et al. 2008). Because the Sudbury structure is larger than the Chixculub structure (Grieve and Therriault 2000) it should have given rise to a global ejecta layer. Paleoproterozoic sedimentary basins in the Lake Superior area are potential repositories for a distal ejecta layer, but for years they were believed to be older than the Sudbury impact. For example, Morey and Southwick (1995, p. 1983) stated that "sedimentation … was essentially over by 1850 Ma" in the Lake Superior area and the Sudbury impact happened about 1.85 Ga (see Sect. 7.3.3). Nevertheless, the search went on until Addison et al. (2005) discovered an ejecta layer near the tops of the Gunflint and Biwabik Iron Formations in Ontario and Minnesota, respectively. Layers interpreted as Sudbury ejecta have now been recognized at more than 15 sites in the Lake Superior area (Fig. 7.13). A brief introduction to the geology of iron formations and the Lake Superior region is necessary to put the ejecta layer in context.

Iron formations are a type of chemical sedimentary rock that were deposited in a variety of environments in early Precambrian basins but rarely formed after about 1.8 Ga (Klein 2005). They consist largely of iron-rich minerals and chert and their exit from the stratigraphic record has been linked to major changes in the chemistry of Earth's oceans (e.g., Canfield 1998). Iron formations can be divided

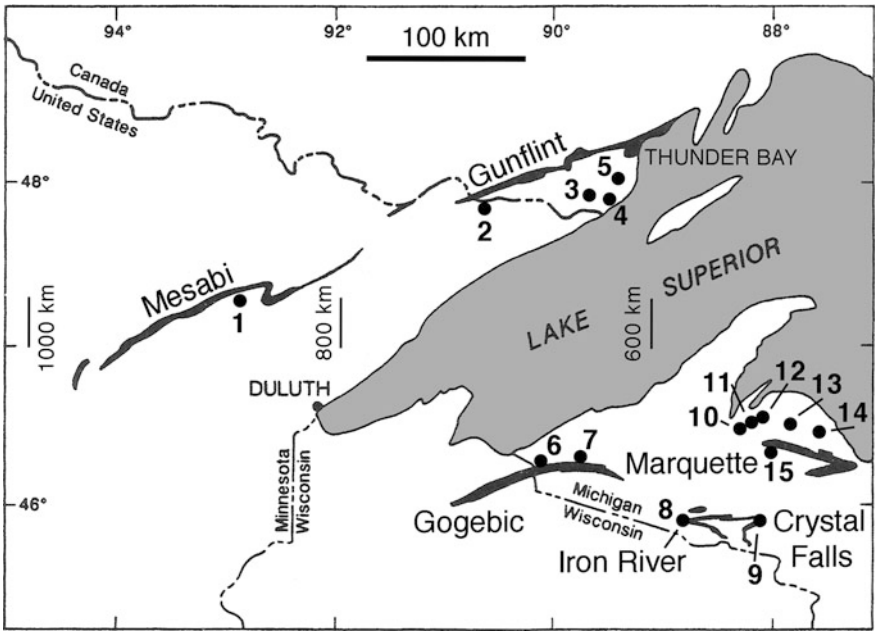

Fig. 7.13 Map showing the approximate locations of most of the iron ranges (*dark gray ribbons*) in the Lake Superior area and sites where the Sudbury ejecta layer has been positively or tentatively identified (*black dots*). In addition to the iron ranges, sites 10, 11 and 12 are in the Baraga Basin and sites 13 and 14 are in the Dead River Basin. Sites mentioned in the text and/or in the figure captions are as follows: 6 = Puritan, 9 = Crystal Falls, 12 = Huron River, and 13 = Connors Creek. An additional 8 outcrops of the layer have been reported in Thunder Bay, Ontario. The short vertical lines across the center of the map show the approximate distance to the center of the Sudbury structure with no correction for tectonic deformation. The locations are from Addison et al. (2005) and Cannon et al. (2010) and the distances to the Sudbury structure are from Cannon et al. (2010). Geological map modified after Fig. 1 in Morey and Southwick (1995) with the permission of the Society of Economic Geologists

into two broad categories based on the size of their original sedimentary constituents (e.g., Simonson 1985; Bekker et al. 2010). Granular iron formations (GIFs) largely consist of well-sorted, coarse sand-sized intraclasts and oolites and were deposited in water that was rarely deeper than a few tens of meters. In contrast, banded iron formations (BIFs) originally consisted of chemical muds and accumulated below wave base in deeper water than GIFs based on their fine grain size, the ubiquity of laterally persistent thin lamination, and the characteristics of the units associated with them (Simonson and Hassler 1996). BIFs are more abundant than GIFs so most researchers use BIF as a blanket acronym for all iron formations, but few GIFs have well-developed banding, i.e., thin lamination.

The iron formations in the Lake Superior region generally occur in strike belts informally known as "iron ranges" (Fig. 7.13) and consist of a combination of GIFs and BIFs. Each iron range has one dominant iron formation that gave rise to economic iron ore deposits (Morey 1983; Ojakangas et al. 2001a). Both the iron

formations and the stratigraphic units associated with them are marine deposits that accumulated on the south-facing (= current orientation) margin of an early continent (Addison et al. 2005; Pufahl et al. 2007). Iron formation deposition was focused in a broad shallow sea in the northern part of the Lake Superior area (i.e., the iron ranges of Ontario, northern Minnesota, and northern Wisconsin) versus volcanic grabens to the south (i.e., the iron ranges of northern Michigan). Therefore, GIFs are more prominent in the northern parts of the Lake Superior region, where they show tidally influenced cross-beds and stromatolites (Ojakangas 1983; Simonson 1985; Fralick and Barrett 1995). In contrast, BIFs are more prominent in the southern iron ranges where water was deeper on average, but paleoenvironments were generally more variable (Cannon et al. 2010). Iron formation deposition waned around 1.85 Ga as strong subsidence led to the deposition of a thick pile of deep-water shales and arc-derived turbidites throughout the region (Ojakangas et al. 2001a; Schulz and Cannon 2007). This reflects the fact that the Sudbury impact took place in an active tectonic belt (Cannon et al. 2010) formed during the Penokean Orogeny. The Orogeny began ~1875 Ma (Schneider et al. 2002) and involved northward-accreting island-arc terranes now located in Wisconsin (Schulz and Cannon 2007). It was extensive enough to deform the Sudbury impact structure itself (Spray et al. 2004) as well as most of the Paleoproterozoic strata around Lake Superior including the ejecta layer. With a few notable exceptions (Fig. 7.14), the Sudbury ejecta layer is located at or near the top of a large iron formation in a given iron range and more or less coincides with a shift in deposition from iron formation to shale (see Sects. 7.3.5 and 7.3.6 for more discussion).

Around 1.1 Ga, the iron ranges were disrupted by a major extensional episode that gave rise to the Midcontinent Rift System (Hinze et al. 1997; Ojakangas et al. 2001b). This rifting is largely responsible for the topographic basin now occupied by Lake Superior and it separated the Paleoproterozoic successions into two separate areas with no physical connection (Fig. 7.13). One area is now in Minnesota and Ontario and the other is in Michigan and Wisconsin. For convenience, these areas will be referred to as the northern and southern regions, respectively, in the descriptions that follow. However, the current limits of these regions do not necessarily coincide with original paleoenvironmental boundaries. Most notably, the westernmost iron formation in the southern region (the Ironwood Iron Formation in the Gogebic iron range) is more like those of the northern region than the others in the southern region. Specifically, it is a shallow-water, GIF-type iron formation (Pufahl and Fralick 2004), whereas most of the iron formations in the southern region are pure BIFs. In addition, the intensity of the tectonic deformation and metamorphism generally increases from northwest to southeast; most strata in the northern region are weakly metamorphosed and only tilted a few degrees, whereas those in the southern region are more likely to be folded, have foliation, and be metamorphosed. The distances between the iron ranges and the Sudbury impact structure were extended by no more than a few tens of kilometers during rifting (Cannon et al. 2010), so no attempt has been made to correct for tectonic changes in these distances.

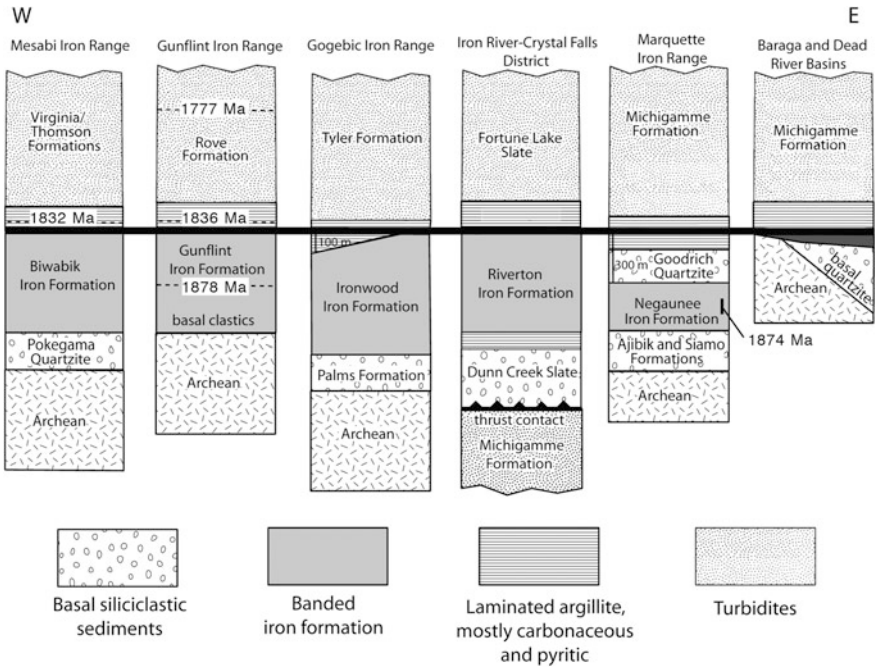

Fig. 7.14 Generalized stratigraphic columns for iron ranges in the Lake Superior region where the Sudbury ejecta horizon (*black line*) has been recognized. The stratigraphic positions and ages of radiometrically dated tuff beds are also indicated (see text for details). The Archean consists of granitic and gneissic basement rocks. The locations of these iron ranges and basins are indicated in Fig. 7.13. The Sudbury structure is located ~500 km east (*right*) of the easternmost column shown here. Modified after Fig. 2 in Cannon et al. (2010), with permission from the Geological Society of America

7.3.2 Description of Impact Ejecta

The Sudbury ejecta layer is quite variable in thickness and character throughout its known area, but most of the sections thought to be the layer contain one or more of a few distinctive components. These components are described here and their geographic variation and the sediments with which they occur are described more extensively in Sect. 7.3.5.

The component of the ejecta layer that is most easily recognized in outcrops and hand samples (Fig. 7.15a) in both the northern and southern regions is comprised of accretionary lapilli. Accretionary lapilli appear to be restricted to the layer in Paleoproterozoic strata in Michigan (Cannon et al. 2010), but some volcanic ones occur in tuffs ~100 m below the ejecta layer stratigraphically in Ontario (Hassler and Simonson 1989; Fralick et al. 2002). Most of the accretionary lapilli in the ejecta layer are ovoid and 0.5–1.0 cm in diameter, but they range up to 2.5 cm across. Internally, the lapilli are aggregates of fine particles with significant amounts of coarser material admixed (Fig. 7.15b). The latter includes numerous

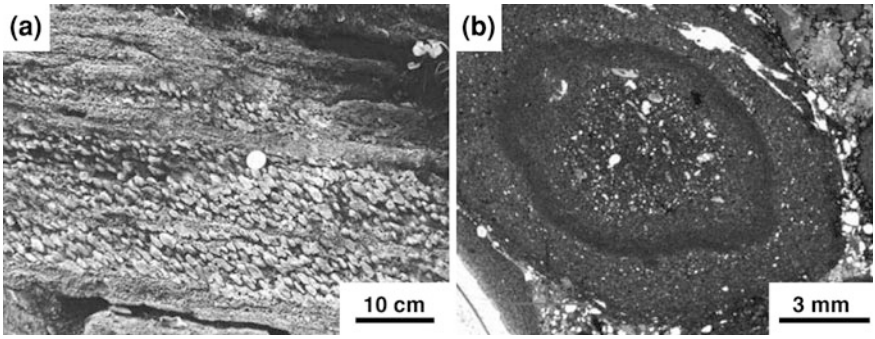

Fig. 7.15 Accretionary lapilli in the Sudbury ejecta layer at the Connors Creek, Michigan, locality. **a** Surface exposure of layer with zone rich in accretionary lapilli that have been tectonically elongated (the foliation runs diagonally from upper left to lower right). The finer layers consist of a combination of clastic quartz grains and devitrified glassy ejecta. **b** Photomicrograph in plane polarized light of an accretionary lapillus with typical growth banding surrounded by finer interstitial sediment. From Cannon et al. (2010), Figs. 4a and b respectively, with permission from the Geological Society of America

crystals of quartz and some feldspar up to the fine to medium sand size range; Addison et al. (2005) reported crystals as big as 0.8 mm across. Many of the quartz and feldspar crystals contained in the accretionary lapilli display shock metamorphic features (described in Sect. 7.3.4). In fact, most or all of the crystals in which shock features were detected occur inside accretionary lapilli at many sites rather than being dispersed as solitary clasts.

Where best developed, the accretionary lapilli consist of massive, unstructured cores coated by one or more layers of contrasting (and generally finer) material forming a rim (Fig. 7.15b). In contrast, some lapilli are cored by lithic fragments rather than dust clots; such particles are more correctly termed **armored lapilli** rather than accretionary lapilli (Fisher and Schmincke 1984). Accretionary and armored lapilli with textures like those in the Sudbury layer can be formed by both volcanic eruptions and large impacts and consist of either silicate or carbonate minerals (Warme et al. 2002; Brown et al. 2010; and references therein). Volcanic armored lapilli have only been described from base surge deposits formed by hydrovolcanic eruptions (e.g., Waters and Fisher 1971) and not from airfall deposits. In addition to particles with definite accretionary mantles, Addison et al. (2005) described "accreted grain clusters" in the Sudbury layer with textures similar to the cores of accretionary lapilli but lacking layered coatings. These clusters range in size from 0.3 to 4 mm and were interpreted as aggregates deposited before they had time to grow into normal accretionary lapilli. Alternatively, they may include fragments of accretionary lapilli broken during transport since they are smaller than accretionary lapilli. In addition, Cannon et al. (2010) described some particles at one site that were probably glass fragments originally but have partial coatings that resemble the rims of accretionary lapilli. Currently, all of these accretionary particles consist of a range of minerals, even where they

are not metamorphosed. Excluding obvious primary crystals, they consist largely of quartz, dolomite, feldspar, muscovite, and/or chlorite interpreted as secondary replacements after original phases. By analogy to volcanic accretionary lapilli, most of the fine particles presumably originated as tiny fragments of glass, in which case they (like the spherules and shards described below) have devitrified over time.

A second distinctive component of the layer consists of clasts with textures indicating they are devitrified glassy melt particles rather than physically accreted aggregates. The fact that these clasts were originally molten can only be inferred from pseudomorphic textures because all of the glass appears to have been replaced by secondary phases. The most unequivocal examples show vesicular textures internally, as either circular or oval features (Fig. 7.16a, b). In addition, some particles show flow banding, in which case the vesicles are elongated parallel to same. Most of the altered glass particles described to date appear to have irregular to angular outlines (Fig. 7.16c) and resemble fragments of volcanic pumice or impact melt in proximal deposits such as suevite breccias. The altered glass particles currently consist of a variety of secondary minerals, generally carbonate, quartz (as chert and chalcedony), chlorite, and sericite. In addition, in the northern region some of the vesicles are outlined by rims of smectite or illite–smectite (Addison et al. 2005, 2010), consistent with its low metamorphic grade. Similar textures have been described from spherules in both the K-T boundary layer and Archean spherule layers (Kohl et al. 2006).

In addition to the angular clasts, some of the devitrified particles are referred to as "tektites" (Pufahl et al. 2007) or "microtektites" (Addison et al. 2005) and have fluidal shapes typical of splash forms, e.g. teardrops and spheroids (Fig. 7.16a, b). Most are on the order of 1 mm across, but some are up to 5 cm long (Addison et al. 2010). Addison et al. (2005) described vesicular spherules as having "sphere-within-sphere features" in that they that have circular cross-sections overall and contain circular vesicles (Fig. 7.16a). Such spherules closely resemble the highly vesicular spherules in the Australasian microtektite layer and the K-T boundary layer (e.g., Fig. 6 of Smit et al. 1992b) and, in the case of some K-T spherules, are extensively replaced by carbonate in a very similar fashion. Other spherules have isopachous fibrous rims that closely resemble replaced and flattened spherules in some Archean layers (Kohl et al. 2006). Published reports give the impression that fluidal forms are less common than the more angular particles in the Sudbury layer, e.g., Pufahl et al. (2007) emphasized the presence of "shards" or even "vesicle wall fragments" in the layer. This may reflect the fact that described occurrences of Sudbury ejecta are more proximal than most of the other layers described in this book. Cannon et al. (2010, p. 55) state that "spherules and shards of devitrified glass" are both common and form from a few to 50 % of the layer. Both shard shapes and wall fragments suggest disruption by vesicle expansion, which is highly unlikely to happen in distal ejecta. Another possibility is in situ disruption of spherule rims during diagenesis as documented by Addison et al. (2010). Whether they are splash forms or angular particles, the altered glass fragments generally range in size up to a few millimeters across in the more distal

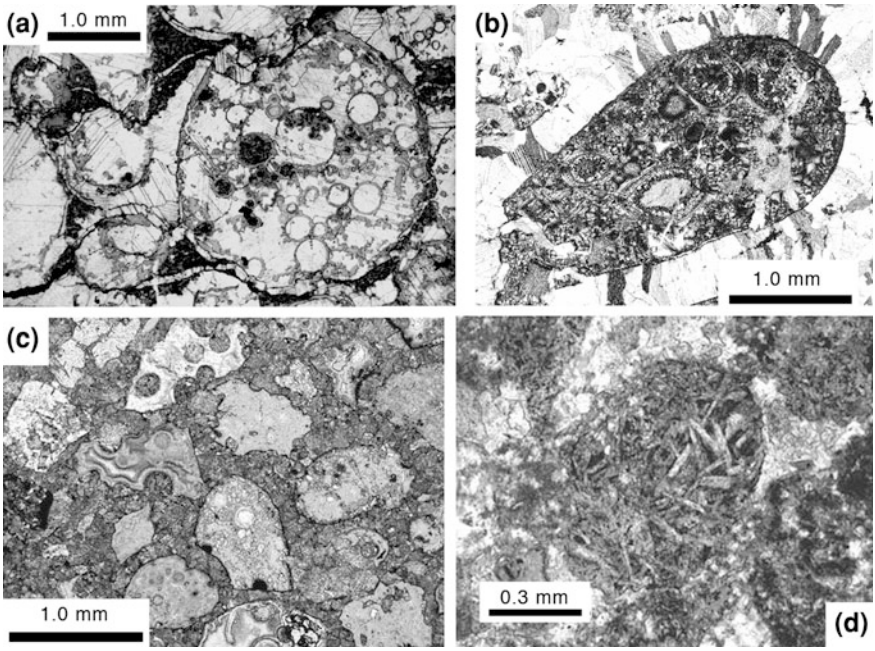

Fig. 7.16 Photomicrographs of spherules and other formerly molten particles from the Sudbury ejecta layer. **a** Large spherule with internal vesicles and smaller spherules (plane polarized light). Carbonate largely replaces the spherules and fills the interstices, but some finer sediment is also present. The sample is from a core drilled on the Biwabik iron range. From Addison et al. (2005), Fig. 3f. **b** Large particle surrounded by sparry carbonate in cross polarized light that appears to be a broken teardrop, has internal vesicles, and contains spherulitic growths of one or more phases that both line vesicles and replace intervening glass. The sample is from an outcrop in Thunder Bay, Ontario. From Addison et al. (2010), Fig. 7b. **c** Well-sorted sand-size particles (*plane polarized light*) consisting of a mixture of intact spherules, broken spherules and teardrops, and more angular (broken?) pieces. Most or all of these particles probably consisted of glass originally. The sample is from Thunder Bay, Ontario. From Addison et al. (2010), Fig. 7d. **d** Spherule (plane polarized light) with numerous randomly oriented feldspar laths, possibly a replaced microkrystite. The sample is from a layer at the Puritan locality that was originally described as a tuff but is now suspected to be the Sudbury impact ejecta layer. From Cannon et al. (2010), Fig. 12b. All four images used with permission from the Geological Society of America

sites versus ~20 mm across in some of the more proximal sites (described below). Typically, no distinction is made between splash forms and angular particles in terms of size and no dimensions at all are given in some reports.

In addition to the definite examples of altered glass described above, Pufahl et al. (2007) described rare, rounded carbonate bodies they interpreted as melt spherules in two cores from the ejecta layer in Michigan. Said bodies are oval rather than circular in cross-section, about 0.6 mm long, and apparently show no internal textures indicative of a molten origin. They suggest some of these carbonate bodies are dumbbell-shaped, but the imaged example is ambiguous. Pufahl et al. (2007) interpreted the carbonate bodies as splash-form impact spherules by

analogy to spherules in the Grænsesø layer (Chadwick et al. 2001; described in Sect. 7.4), but the Grænsesø spherules (like normal microtektites) have cross-sections that are more consistently circular. The carbonate bodies Pufahl et al. (2007) described currently consist of dolomite, but the Sudbury layer is unlikely to contain primary carbonate melt droplets because the sedimentary rocks in the target area (the Huronian Supergroup) are clastic units with very little carbonate (Young et al. 2001). Therefore, the bodies in the Sudbury layer are probably replaced, if indeed they were ejecta particles originally. No similar particles have been described in other accounts of the ejecta layer.

Lastly and perhaps most importantly, many but not all of the purported occurrences of the Sudbury ejecta layer contain sand-size crystals with features attributed to shock deformation (Fig. 7.17; see Sect. 7.3.4 for full description). As noted above, most of them are incorporated into accretionary lapilli, but some are isolated crystals and/or mixed with detrital grains introduced by reworking either during or after the impact event. Most of the reported examples are in quartz crystals, but feldspars with shock features also occur at a few sites. Relatively few details on the shocked crystals and their distribution have been published to date.

As noted above, the composition and thickness of the Sudbury layer varies considerably from site to site. Generally it consists of ejecta admixed with greater amounts of sediment derived more locally, although at some sites the layer is thought to consist of relatively undiluted ejecta. The types of sediment that are most commonly mixed with the ejecta are sand-size grains of chert and/or epiclastic quartz and larger intraformational clasts of chert. The general nature of these other sediments and the regional variation of the Sudbury layer are described in Sect. 7.3.5, focusing mainly on the occurrences that have the most in common with the other distal ejecta layers described in this book.

7.3.3 Radiometric Age

Dates from stratigraphic units in fairly close stratigraphic proximity to the ejecta layer constrain its age to some degree (Fig. 7.14). Fralick et al. (2002) obtained a date of 1878.3 ± 1.3 Ma from tuffs in the middle of the Gunflint Formation. Although these tuffs are reworked (Hassler and Simonson 1989), Fralick et al. (2002) analyzed a population of euhedral zircons that appear to be synchronous with deposition. The dated tuffs are ~105 m below the ejecta layer stratigraphically (Addison et al. 2005) and set a maximum age limit. Schneider et al. (2002) obtained a roughly comparable age of 1874 ± 9 Ma from a rhyolite in the Hemlock Formation believed to be laterally equivalent to the Negaunee Iron Formation, which is ~550 m below the ejecta layer stratigraphically (Cannon et al. 2010). Schneider et al. (2002) also reported an age of 1833 ± 6 Ma from a pluton cutting across a lateral equivalent of the Hemlock Formation believed to be younger than the ejecta layer. Collectively, these dates constrain the age of the

layer to a span of some 40 million years that straddles the age of the Sudbury structure as discussed below.

More recently, dates have been obtained in and around the ejecta layer itself. Addison et al. (2005) obtained a U/Pb zircon age from two tuffs ~5–6 m above the ejecta layer. A tuff above the layer in the Gunflint Iron Formation yielded a date of 1836 ± 5 Ma and one above the ejecta layer in the Biwabik Iron Formation 260 km to the southwest yielded a date of 1832 ± 3 Ma. Then Addison et al. (2010) obtained an age of 1856 ± 2 Ma from 6 euhedral zircon crystals separated from the layer itself and believed to be derived from subjacent tuffs in the Gunflint Iron Formation. These dates constrain the age of the ejecta layer more tightly.

Krogh et al. (1984) made a convincing case that the Sudbury Igneous Complex (SIC), found only inside the Sudbury impact structure, formed very close to 1850 Ma. They did this by compiling multiple high-precision U/Pb dates of zircons from the norite that forms the lower part of the main mass of the SIC and determining that the dates overlapped one another within statistical error. They then averaged these dates to arrive at a probable age of 1850 ± 1 Ma for the crystallization of the norite. They also cited a U/Pb date from zircons from granophyre in the upper part of the main mass which yielded an overlapping date of 1850.5 ± 3 Ma. The SIC is now believed to be a melt sheet (Therriault et al. 2002; Grieve 2006) that formed within "a few minutes" of impact (Zieg and Marsh 2005). Because all indications are that the ejecta layer is a product of the Sudbury impact (see Sect. 7.3.4), the age of the SIC is thought to be the same as the age of the ejecta layer. Subsequent isotopic work (summarized in Table 2 of Ames et al. 2008) has mostly served to confirm Krogh et al.'s (1984) conclusions, but Davis (2008) used more advanced techniques to obtain distinct dates from zircons from different parts of the norite. Specifically, one sample near the base of the norite layer yielded an age of 1849.53 ± 0.21 Ma whereas another from several hundred meters higher yielded an age of 1849.11 ± 0.19 Ma. Davis (2008) stated that the implied duration of cooling on the order of 400,000 years is consistent with thermal modeling of such an enormous, superheated melt sheet. In summary, it is highly likely that the Sudbury ejecta layer formed within a million years of 1849 Ma.

7.3.4 Evidence of Impact Origin and Sudbury as the Source Crater

The key evidence that some of the material in the ejecta layer formed by hypervelocity impact is the presence of quartz and feldspar crystals with textures indicative of shock metamorphism (Fig. 7.17). As noted in Sect. 7.3.2, most of the grains with shock features are in accretionary lapilli. The size of the quartz crystals showing shock features are not specified in most cases, but they do not appear to get systematically smaller with increasing distance from the Sudbury structure in the known occurrences. Most of the documented shock features are in fine to

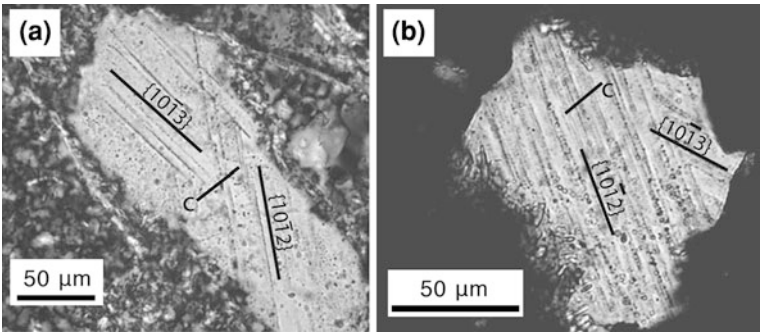

Fig. 7.17 Photomicrographs in cross polarized light of quartz crystals from the Sudbury ejecta layer with multiple sets of decorated PDFs. **a** Quartz crystal from the Huron River locality in the Baraga Basin, Michigan. **b** Quartz crystal with two sets of decorated PDFs from a core in the Hiawatha Graywacke drilled near Crystal Falls, Michigan. From Cannon et al. (2010), Figs. 3a and e, respectively, with permission from the Geological Society of America

medium sand-sized crystals. However, Pufahl et al. (2007) observed silt-sized grains with shock features in some of the most proximal sites, whereas the largest crystals with shock features reported (0.8 mm across) are in the Gunflint Iron Formation approximately halfway across the known geographic range of the layer (Addison et al. 2005). The shock features consist of one or more sets of parallel planes defined by fluid inclusions rather than true shock lamellae as the originally amorphous material has been recrystallized over time (Pufahl et al. 2007; Cannon et al. 2010). These are decorated PDFs (see Sect. 2.3.4.2.2; Fig. 2.21c, d), and some of the first examples ever described came from shocked quartz crystals in the Onaping Formation of the Sudbury impact structure (French 1967).

In the ejecta layer in the southern region, the most common crystallographic orientations of the planar features are parallel to the low-index rhombohedral planes $\omega\{10\bar{1}3\}$ and $\pi\{10\bar{1}2\}$ with most of the remaining sets at higher angles, suggesting relatively high shock levels (Cannon et al. 2010). Orientations have yet to be published for planar features in crystals from the northern region, but Addison et al. (2010) reported up to three intersecting sets of PDFs in quartz crystals from the easternmost site. PDFs and planar fractures may actually be more abundant in crystals in the northern region as the strata are less deformed (as described above) and because they are farther from the Sudbury structure (the average degree of shock metamorphism increases with distance from the source crater; see Sect. 2.6). Shocked quartz crystals are widely distributed, but they have only been identified at about half of the sites reported to date and are rarely if ever abundant. This may be due to their proximity to the source crater, but may in part reflect poor preservation, particularly in the southern region where the level of deformation and metamorphic grade is generally higher (Cannon et al. 2010). Dispersal of accretionary lapilli may also be a contributing factor as they are absent from a number of sites (Cannon et al. 2010).

Addison et al. (2005) also noted the presence of "laddered PDFs" in feldspar crystals and planar fractures in unspecified crystals. Shocked feldspar crystals appear to be restricted to sites in the northern region. This too could be an artifact of the higher level of deformation and metamorphism in the southern region (as noted above) because feldspars are much more prone to alteration than is quartz. The presence of shocked feldspars in the layer in the Gunflint Iron Formation may be particularly telling because it has the lowest grade of metamorphism of any iron formation in the Lake Superior region (Floran and Papike 1975). This helps account for its uniquely well-preserved suite of microfossils (Planavsky et al. 2009, and references therein).

In support of the presence of extraterrestrial material, Pufahl et al. (2007) determined that the concentrations of Ir, Ru and Rh in 10 bulk samples of the ejecta layer were anomalously high compared to 20 bulk samples of strata adjacent to the layer in 2 cores from Michigan. However, the anomalies they reported are not particularly high. The highest Ir concentrations they found are 0.73 and 0.74 ppb, about one order of magnitude higher than the surrounding strata and one order of magnitude less than in the K-T boundary layer. However, as noted in Sect. 7.2.3, in a few cases the Ir anomalies at K-T boundaries are below 1 ppb (see Fig. 5.11) where there has been a great deal of reworking, but in most cases the Ir content in the K-T boundary layer is much higher. The greatest enrichments in Rh and Ru are even lower, 3 and 8 times the background values, respectively. However, the Rh/Ir and Ru/Ir mass ratios both decrease upwards through the layer in both cores, attaining near-chondritic values near the top of the layer. In contrast, Au, Pt, and Pd concentrations exhibit no discernible trends and Ni appears to have been mobilized during metamorphism according to Pufahl et al. (2007), who gave no further explanation. Interestingly, the least altered formerly molten material in the Onaping Formation in the Sudbury structure have Ir concentrations of roughly the same order of magnitude as the ejecta layer, namely 0.11–0.35 ppb (Mungall et al. 2004).

Cannon et al. (2010) analyzed the major and trace elements (including rare earth elements or REEs) of 12 samples from 11 sites in the southern region and 1 site in the northern region. These samples were selected from the least altered and most ejecta-rich parts of the layer. Their key finding was that the chemistry of the samples they analyzed from the ejecta layer is more like the Onaping melts (as given in Mungall et al. 2004) than the felsic volcanic rocks closest to the impact layer in the Lake Superior region. Specifically, the major element compositions of samples from the ejecta layer and the Onaping resemble those of andesites whereas the felsic volcanic rocks in question are rhyolitic. Moreover, REE abundances are significantly lower in samples from the ejecta layer than samples from the volcanics but overlap those of the Onaping Formation and have similar chondrite-normalized patterns. Cannon et al. (2010) attributed the unusual composition of the layer mainly to the derivation of much of the ejecta from highly weathered clastic sediments in the target area. This is consistent with the large sedimentary component Mungall et al. (2004) proposed for the Onaping Formation, as well as the presence of a thick succession of clastic rocks in the Sudbury region at the time of

impact (Young et al. 2001). These geochemical similarities strengthen the case that the ejecta layer in the Lake Superior area is derived from the Sudbury impact structure.

Finally, the fact that the Sudbury impact happened during the time interval when the successions in the iron ranges were accumulating means that the ejecta layer is probably present somewhere in the stack. As Addison et al. (2005, p. 196) noted, if the ejecta layer described here is not from the Sudbury impact, there must be a second major ejecta layer in the iron ranges and a second large impact structure nearby, neither of which has been detected. Moreover, the thicker sections of the ejecta layer are in the eastern part of the Lake Superior area (as described in Sect. 7.3.5), consistent with its derivation from a source to the east (Cannon et al. 2010). The correlation of the ejecta layer and the Sudbury impact structure is also permitted by the radiometric dates described in Sect. 7.3.3.

7.3.5 Geographic Distribution and Variation

About two-thirds of the sites where candidates for the Sudbury ejecta layer have been identified are located in the southern region versus one-third in the northern region as defined in Sect. 7.3.1 (Fig. 7.13). All sites are currently located between 480 and 875 km from the center of the Sudbury impact structure. Using 260 km for the diameter of the Sudbury structure (Spray et al. 2004), these sites fall between 3.7 and 6.7 crater radii from the center of the Sudbury structure and are about evenly divided between proximal and distal sites. Although proximal and distal sites occur in both regions, the northern region sites are farther from the Sudbury structure on average so a higher percentage are distal. The layer ranges in thickness from 0 to 150 m; varies in composition from pure impact ejecta to layers consisting largely of iron-rich sediment, sandstone, or chert breccia; and has depositional features ranging from normal grading and cross-bedding to wholesale brecciation. The characteristics of the layer do not seem to vary systematically from site to site in a way that relates simply to whether they are proximal or distal, but there are some general trends (see Sect. 7.3.4 and discussion below). The descriptions that follow focus on the distal sites to facilitate comparisons with the other layers described in this book. A full description of the proximal ejecta is beyond the scope of this book, but given their intermingling with distal sites in the Lake Superior area, some description of them is in order.

As summarized in Sect. 7.3.1, the Sudbury ejecta layer was deposited in shallower, more uniform paleoenvironments in the northern region versus more variable paleoenvironments in the southern region. The latter were deeper on average, but even there the layer was deposited in peritidal shoals and possibly subaerial settings locally (described below). Despite this variability, all the known sites where the layer exceeds 10 m in thickness are in the southern region. The thickest sections of all are in the iron range connecting Iron River and Crystal Falls (Fig. 7.13) where a stratigraphic unit known as the Hiawatha Graywacke has been

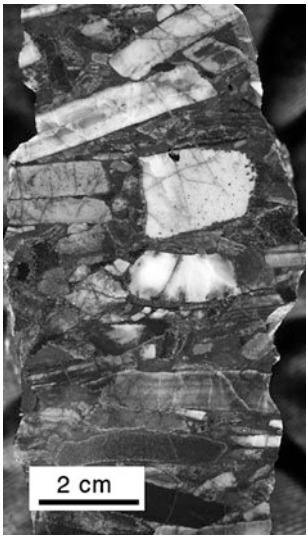

Fig. 7.18 Sawn slab of a breccia sample from the Hiawatha Graywacke from a surface exposure at Crystal Falls, Michigan, where it consists of tabular, cherty intraclasts (light to medium *gray*) in a fine ferruginous matrix (*dark*) that was originally rich in sideritic mud, but has weathered to ferric hydroxides

reinterpreted as the ejecta layer (Cannon et al. 2010). This unit is up to 150 m thick, consists partly of intraformational breccia with slabs of chert and iron-rich mud up to 0.7 m long (Fig. 7.18), and was attributed by James et al. 1968 (p. 62) to deep-water slope movement triggered by a "structural disturbance". Cannon et al. (2010) recognized shock features in a few quartz sand grains and suggested the mass movement was triggered seismically by the Sudbury impact. They also suggested that comparable intraformational breccias at other sites in the southern region have a similar origin. One of the breccias thus interpreted is located at the top of the iron formation in the Gogebic range, but it has yet to yield any impact ejecta. In contrast, other locations where the Sudbury layer consists of breccia have been interpreted as products of a ground surge (see discussion below).

The Sudbury ejecta layer was first recognized in drill cores from the northern region where it is typically less than a meter thick and consists of a mixture of sandy detritus and impact ejecta (Addison et al. 2005). The impact ejecta in these cores are comprised of accretionary lapilli, spherules, shards, and quartz and feldspar crystals with shock features (described in Sect. 7.3.2 and 7.3.4). Stratigraphically, the layer is located near the top of a laterally persistent iron formation that is interrupted by a large intrusion related to the 1.1 Ga rifting. This iron formation is known as the Biwabik in the Mesabi iron range west of the intrusion and the Gunflint east of the intrusion (Fig. 7.13). Accretionary lapilli are present in the Gunflint, but none have been noted in the Biwabik, consistent with the latter being more distal. Addison et al. (2005) noted that smaller accreted clusters (described in Sect. 7.3.2) are present in the layer in both iron formations, but they did not quantify the size distributions or abundances of the ejecta at any sites. Larger, more irregular particles of former glass are also present in the Gunflint but not the Biwabik whereas "sphere-in-sphere" bodies like vesicular microtektites

(Fig. 7.16A) occur in both. Quartz and feldspar crystals with shock features are also present in both iron formations but scarcer in the Biwabik. Addison et al. (2005) did not describe any sediment in the layer in the cores other than ejecta beyond the mention of "carbonate-replaced" material, and at least some of that is ejecta. The only interpretation for how the layer in these cores was deposited is a statement that the lapilli "probably fell from [a] debris cloud" (Addison et al. 2005, p. 194).

In contrast to the sites just described, some sites in the northern region are more proximal in character. Definite occurrences of the Sudbury layer in the vicinity of Thunder Bay, Ontario (the easternmost site in the northern region), contain boulder-size rip-up clasts and all of the different types of ejecta described in Sect. 7.3.2. Addison et al. (2010) described 8 surface exposures around Thunder Bay and noted that coarser clasts are normally graded but the layer is otherwise chaotic. It also contains the largest splash forms yet reported from the layer; some are up to 5 cm long (see Sect. 7.3.2). Addison et al. (2010) interpreted the layer at these sites as a product of base surge-type debris flows or possibly impact-induced tsunami-type activity. Another possible occurrence of the layer is a 7-meter-thick layer of breccia atop the Gunflint Iron Formation in Minnesota. It contains tabular clasts up to 3 m long that appear to have formed via disaggregation of the uppermost layers of the subjacent iron formation (Jirsa et al. 2008). No shocked grains or formerly molten particles have been identified from this site, but the layer is in the right stratigraphic position and intermittently capped by a layer rich in accretionary lapilli that Jirsa et al. (2008) suggested were impact lapilli even though no shocked grains have been detected as yet.

The occurrences in the southern region are more proximal on average. The Hiawatha Graywacke (described above), the thickest occurrence of all, was deposited in deep water, but at a more proximal site (Huron River) the layer consists of silicified chert breccia and has been interpreted as the deposit of a ground surge in a peritidal paleoenvironment because locally it rests on stromatolitic chert (Cannon et al. 2010). Likewise, Pufahl et al. (2007) attributed the deposition of the ejecta layer in two cores from the Michigamme Formation (Fig. 7.14) to impact-induced tsunami-type waves and currents in peritidal to subaerial paleoenvironments. In these two cores, the ejecta layer consists of 1 or 2 sandstone layers 0.8–4.4 m thick that contain cobble-size rip-up clasts. Accretionary lapilli and particles interpreted as splash-form tektites are abundant in one core; the accretionary lapilli (0.5–1.0 cm across) are smaller than the purported tektites (1.0–2.0 cm long). Pufahl et al. (2007) also reported the presence of very fine sand- to silt-size subrounded quartz grains with planar microstructures that are probably decorated PDFs (described in Sect. 7.3.4).

In contrast to the sites just described, the Sudbury layer seems distal in character at some sites in the southern region. Foremost among the latter is a possible occurrence of the layer in the Tyler Formation roughly 100 m stratigraphically above the top of the Ironwood Iron Formation (Fig. 7.14). Schmidt (1980, p. 73) described the candidate as "a layer of lithic tuff containing fragments 2–3 mm … in diameter." No samples or outcrops of this layer are known, but Cannon et al. (2010)

examined thin sections and found it to be rich in replaced glass fragments, including a number of spherules containing either vesicles or lath-shaped feldspar crystals internally (Fig. 7.16d). The latter are the best candidates for microkrystites reported from the Sudbury layer to date. In these same thin sections, accretionary lapilli and candidates for incipient armored lapilli are probably present, but no shock features were detected by Cannon et al. (2010). Overall, Cannon et al. (2010) attributed the deposition of the ejecta layer in the southern region to a combination of four different processes: 1) airfall from the ejecta plume, 2) passage of an ejecta curtain resulting in both ballistic deposition and high-velocity ground surges, 3) large tsunamis generated by the impact, and 4) submarine debris flows generated by strong impact-related earthquakes.

The most distinctive component of the ejecta layer, the accretionary lapilli (see Sect. 7.3.2), vary in abundance and mode of occurrence from site to site. Even in the small Thunder Bay area described by Addison et al. (2010), lapilli were present at some sites but absent from most of them. Most commonly, the accretionary lapilli are dispersed in finer sediment in zones one to several decimeters thick and/or concentrated in lapilli-rich beds located above the base of the layer (Fig. 7.15A). For example, they are concentrated in a zone 11 cm thick in the middle of an ~55 cm thick layer at one distal site (Addison et al. 2005) and concentrated in two 70-cm-thick beds separated by 12 m stratigraphically in one proximal site (Cannon et al. 2010). The lapilli can be admixed with rip-up clasts, particularly where the layer is thicker and more proximal in character. The widespread presence of armored lapilli suggests they originated in a manner more analogous to base surges than as fallout from airborne ejecta clouds.

No definite occurrences of the Sudbury ejecta layer have been reported outside of the Lake Superior area, although Chadwick et al. (2001) suggested a spherule layer in Greenland might be ejecta from Sudbury (see Sect. 7.4.6). The next logical place to look for Sudbury ejecta would be in the Paleoproterozoic succession known as the Labrador Trough. This succession is located ~1200 km northeast of Sudbury and contains a large iron formation, the Sokoman, that has been correlated with the iron formations of the Lake Superior area (Gross and Zajac 1983). The Sokoman Iron Formation is of the shallow-water GIF type and is abruptly overlain by a thick pile of shales and turbidites (Zajac 1974; Simonson 1985). By analogy, the Sudbury ejecta layer could occur at or above the top of the Sokoman, but to date no one has reported finding it.

7.3.6 Possible Links to Biologic and Environmental Changes

Although the study of the Sudbury ejecta layer has only just begun, suggestions are already being made about possible changes in Earth's hydrosphere and biosphere induced by the Sudbury impact. In the first report of the layer, Addison et al. (2005) speculated about whether the impact could have caused a mass extinction since the underlying Gunflint Iron Formation has long been famous for its

exquisitely preserved microfossils (e.g., Barghoorn and Tyler 1965), whereas none have been reported from the shales of the overlying Rove Formation. However, as they correctly noted later in the article, the excellent microfossil preservation in the Gunflint owes much to the early silificification that is common in iron formations (Simonson 1987) but rare in shales. The fact that the Rove Formation is typically carbonaceous suggests there was no shortage of microorganisms living in the local seas after the impact, and Slack and Cannon (2009) used this to make exactly the opposite proposal. They suggested organic productivity increased in the aftermath of the impact, similar to Grey et al.'s (2003) suggestion that the Acraman impact was followed by a radiation of marine protozoa. Whether or not the Sudbury impact event had any effect on the biosphere is difficult to judge given the relative simplicity of early Precambrian organisms and their generally poor state of preservation.

More easily tested is the possibility of a connection between the Sudbury impact and the nature of sedimentation in the Lake Superior area. The large iron formations of the Lake Superior iron ranges have long been correlated on the basis of many similarities in their stratigraphic successions and were perceived as being coeval (Morey and Southwick 1995; Ojakangas et al. 2001a). This vision of a single period of widespread iron sedimentation was consistent with radiometric age dates that were available at the time, but these data left considerable leeway in terms of what was being deposited where and when. The discovery of the Sudbury ejecta layer at the top of most of these iron formations largely confirmed that many of the iron formations were accumulating simultaneously in an unexpectedly unequivocal way; as Cannon and Addison (2007) put it, the ejecta layer is "a timeline from the heavens."

The fact that the ejecta layer coincides closely with the end of the deposition of large iron formations in most of the iron ranges of the Lake Superior area immediately suggests the possibility of a causal connection. Slack and Cannon (2009) proposed an elegantly simple model for how the impact could have "switched off" the iron formations. The deposition of large iron formations is widely attributed to precipitation of iron-rich phases along a chemocline in a world ocean with a surface layer too oxidized to contain appreciable dissolved iron and a deep anoxic layer that allowed iron to be transported in solution from distant hydrothermal sources (e.g., Beukes and Gutzmer 2008; Bekker et al. 2010). Slack and Cannon (2009) suggested the Sudbury impact homogenized these two layers to produce an unstratified, suboxic global ocean, after which dissolved iron precipitated close to its hydrothermal sources in the deep sea instead of migrating to distant depocenters. They cite a shift from sulfides to oxides in deep-water exhalative sediments around 1.85 Ga to support their interpretation. However, there are problems with this model. One is the position of the ejecta layer; it does not always coincide with the end of iron sedimentation. For example, $\sim$100 m and 500–600 m of shale accumulated in the Gogebic and Marquette iron ranges, respectively, after iron formation deposition ended and before the ejecta arrived (Cannon et al. 2010). On the other hand, smaller but significant iron formations are locally present above the ejecta layer. Slack and Cannon (2009) attributed these

discrepancies to local conditions without specifying what those were. Their interpretation also runs counter to the widely accepted theory that the deep ocean became anoxic and sulfidic about the time the Sudbury impact happened (Canfield 1998; Anbar and Knoll 2002). Poulton et al. (2004) explicitly attributed the termination of iron formation deposition in the Lake Superior area to the development of sulfidic deep waters, but changes in one region may not be a faithful record of global conditions (Johnston et al. 2006; Pufahl et al. 2010). In any event, there were fundamental changes in the nature of chemical sedimentation about the time of the Sudbury impact that will surely stimulate researchers for years to come. The fact that two things coincide closely in time does not, or course, prove a cause-and-effect relationship. For example, the Sudbury structure was undergoing compressional tectonic deformation within 2.5 million years of the impact according to Cowan and Schwerdtner (1994, cited in Grieve 2006), but it is unlikely the impact caused the Penokean Orogeny.

7.4 Grænsesø Spherule Layer (Paleoproterozoic, South Greenland)

7.4.1 Introduction

The least well known of the Proterozoic ejecta layers younger than 2.4 Ga is located in South Greenland (Fig. 7.19). Spherules are restricted to a single dolomitic layer in the Grænsesø Formation, which is the uppermost unit of the Vallen Group. This unit is in the Border Zone along the northern edge of the Ketilidian orogen, which was formed by oblique convergence ~1.8 Ga (Chadwick and Garde 1996). The Vallen Group is ~1.2 km thick, consists mainly of clastic strata, and shifts upsection from shallow marine to deeper marine deposits (Garde et al. 2002). Where the layer has been recognized, the Vallen Group experienced low-grade metamorphism, rests unconformably on Archean gneisses, and was overthrust by rocks of the Sortis Group (Bondesen 1970; Higgins 1970). The Sortis Group is ~4 km thick, consists largely of mafic volcanic rocks, and may be a lateral equivalent of the Vallen Group. In part because the Grænsesø layer contains carbonaceous matter and a variety of organic compounds (Lam and Raunsgaard Pedersen 1968), its spherules were interpreted as microfossils by the original discoverers and given the name *Vallenia erlingi* (Bondesen et al. 1967). Chadwick et al. (2001) subsequently suggested the spherules originated as impact melt droplets, but unequivocal evidence of an impact origin has yet to be found in this layer (as discussed in Sect. 7.4.5).

Despite being metamorphosed, strata of the Vallen Group are well enough preserved in two areas at the northern edge of the Ketilidian Border Zone to show primary depositional features. These areas are known as Midternæs and Grænseland (Fig. 7.19c) and are currently separated by ~26 km (Garde et al. 1998, 2002).

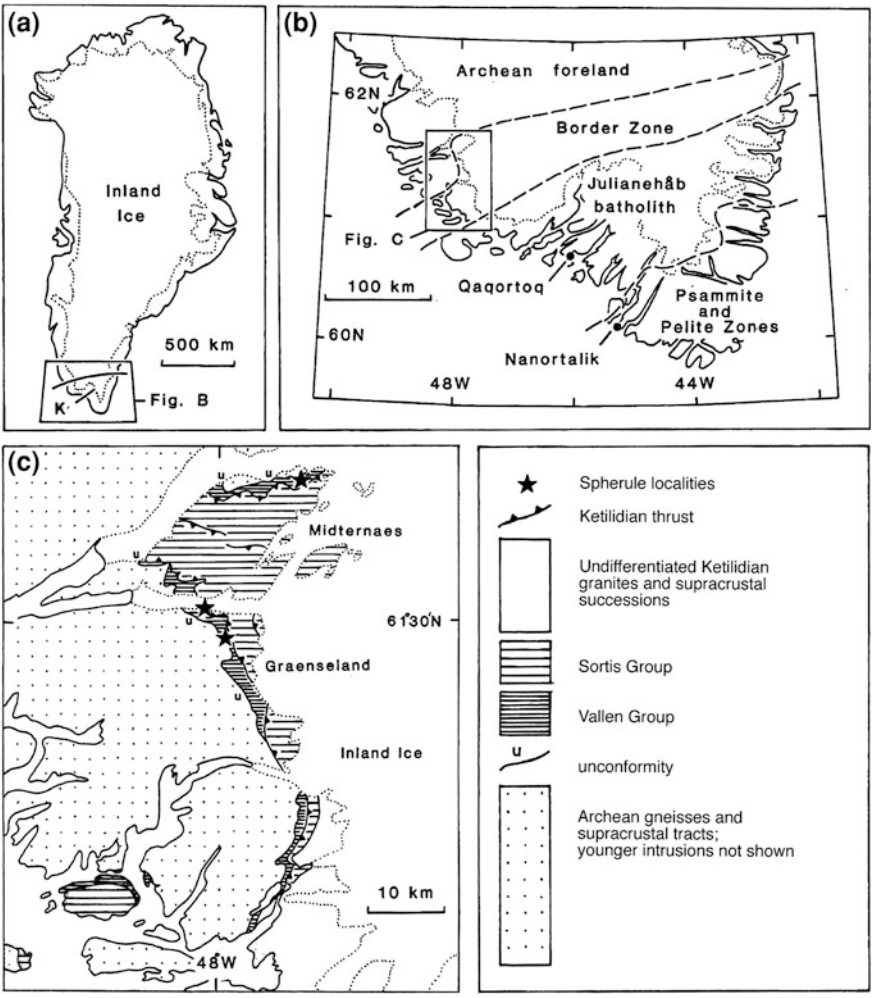

Fig. 7.19 Maps of locations and geology associated with the Grænsesø spherule layer. **a** Map of Greenland showing outline of study area. **b** Map of tectonic zones in South Greenland. **c** Map of generalized geology and locations where Grænsesø spherule layer has been recognized. Modified after Fig. 1 in Chadwick et al. (2001), published with the permission of the Geology Society of London

Although equivalent strata are present further south, their sedimentary features are obscured by a higher level of deformation (Garde et al. 2002). In the Midternæs area, the Grænsesø spherule layer is part of a ~30-m-thick succession of dolomites and shales with some cherts (Higgins 1970). The layer was probably deposited below wave base in this area based on the even bedding and an apparent lack of current structures. In the Grænseland area, the Grænsesø spherule layer is part of a heterolithic succession ~50–100 m thick consisting of dolomites, carbonaceous shales, and cherts that were intruded by sills (Bondesen 1970). The strata in this area

were probably deposited below wave base also, but not too deep (deep shelf?). This is inferred from the fact that the Grænsesø Formation conformably overlies a turbidite-rich flysch-type unit (Bondesen 1970), but modern glacial erratics thought to be of "very local origin" contain purported stromatolites (Plate 11 of Bondesen et al. 1967). The descriptions that follow are mostly based on hand samples of the layer collected in the Midternæs area in the 1960's.

7.4.2 Description of Layer and Spherules

In the few localities where it has been studied (see Sect. 7.4.4), the Grænsesø spherule layer is on the order of 1 m thick and consists largely of coarsely crystalline dolomitic carbonate (Chadwick et al. 2001). The carbonate crystals are diagenetic because they form an equigranular mosaic, lack detrital outlines, and show euhedrally zoned cores in cathodoluminescence images. Floating in the carbonate are three types of non-carbonate clasts: spherules, chert clasts, and epiclastic sand grains. Spherules in the coarse sand size range (described below) are the most abundant of the three types, making up roughly 15 % of the layer by volume. The spherules and chert clasts typically stand out as dark bodies uniformly dispersed in a light background (Fig. 7.20). The chert clasts are slightly less abundant than the spherules, and the epiclastic sand forms no more than a few percent of the layer by volume (Chadwick et al. 2001; Smith et al. 2006). The chert clasts appear to be intraclasts as they range in size from sand to tabular pebbles; they are also texturally diverse and contain traces of quartzose silt to very fine sand. Hand samples contain patches of pure carbonate that are more finely crystalline than the ambient carbonate and also appear to be tabular intraclasts. Smith et al. (2006) observed chert intraclasts up to 10 cm long and dolomite intraclasts up to 110 cm long in one outcrop of the layer (Fig. 7.21). The epiclastic detritus is well-sorted very fine to fine sand. It consists largely of monocrystalline quartz, but detrital grains of feldspar (both microcline and albite), mica, chlorite, and zircon are also present. The epiclastic sand grains have internal textures typical of basement-derived detritus and no shock features were detected in any of the quartz grains (Chadwick et al. 2001). Like the spherules, both the chert clasts and epiclastic grains are dispersed in a surprisingly uniform fashion rather than being concentrated in particular zones or layers.

Smith et al. (2006) described one outcrop of the spherule layer $\sim$4 m long in the Midternæs area that is 145 cm thick and consists of calcitic dolomite with admixed detritus. The layer appears to be homogeneous and does not exhibit either grading or current structures (Fig. 7.21). Spherules and chert grains each make up 15–20 % of the rock and epiclastic sand forms 1–2 % by volume at this site. The spherules are 0.4–1.8 mm across, most chert grains are in the coarse sand to granule size range, and epiclastic quartz is in the very fine to coarse sand size range. The strata enclosing the layer are uniformly fine-grained dolomites and shales typical of the Grænsesø Formation. Neither spherules nor intraclasts of

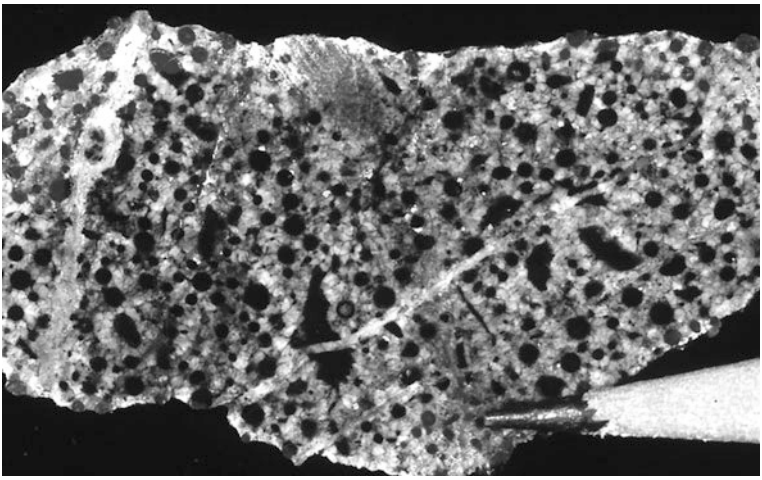

Fig. 7.20 Sawn slab of sample from the Grænsesø spherule layer at the Midternæs location consisting of a mixture of sparry carbonate (*white* to light *gray*), spherules (*black* circles), and chert intraclasts that are generally larger and more angular (also *black*). The largest *gray* patch (in middle of upper edge) is a carbonate intraclast with saw marks (parallel lines). The fine quartzose sand is not evident at this scale. The white strips crossing the sample are tectonic veinlets. Pencil point in lower *right* for scale

either chert or carbonate were detected in close stratigraphic proximity in the strata above and below the layer. The only published mention of potentially higher energy deposits in the unit hosting the layer comprises several meters of dolomite breccia at the base of the local succession (Higgins 1970).

Although it has not been studied extensively, enough is known about the Grænsesø layer to indicate that its spherules were not deposited by direct fallout. The most telling evidence is the presence of epiclastic sand and intraclasts of carbonate and chert throughout the layer. The lack of normal grading also argues against direct fallout. The fact that the spherules are significantly larger than the epiclastic sand suggests they were brought to the depositional site by different processes; they should be closer in size if they had been transported by the same waves and/or currents. The epiclastic detritus was clearly derived from a continental source, whereas the spherules could have arrived independently if they are impact-related (see discussion in Sect. 7.4.5). As the Grænsesø layer contains by far the largest clasts amongst local strata, it clearly represents an event of unusually high energy. The nature of this event is hard to interpret, in part because the original grain size of the carbonate is not known. Based on the well-sorted nature of the non-carbonate sand it contains and its similarity to dolomitic breccias in the better-studied Carawine spherule layer of the Hamersley Basin (described in Sect. 8.2.5), the Grænsesø layer may have originated as a mixture of carbonate and silicate detritus that was deposited as a sand-rich debris flow. This could account for the presence of large intraclasts and the uniform way the spherules and epiclastic sand are dispersed throughout the layer. Available data are inadequate

Fig. 7.21 Surface exposure of the Grænsesø spherule layer at the Midternæs location showing a high abundance of large chert intraclasts (dark *gray*) in dolomite (light *gray*) and the homogeneous nature of the layer. The scale in lower right is 10 cm long and the white strip in the center is a ruler. Courtesy of Frank C. Smith

for determining whether the energy for this event was provided by an impact or some other process, but the apparent restriction of the spherules to the highest-energy layer in a given succession certainly suggests it may have been impact-related. Further research is needed to pinpoint the paleoenvironments and processes involved in forming the Grænsesø layer.

The spherules in the Grænsesø layer are mainly coarse sand size, i.e., 0.5–1.0 mm in diameter. The largest spherules reported are 1.5–1.8 mm across (Bondesen et al. 1967; Smith et al. 2006). Individual spherules liberated from the layer by Hansen (1978, Figs. 1–3) are spherical to ovoid, consistent with the dominance of circular to oval cross-sections in thin section (Fig. 7.22). A few are highly elongated rotational forms and have cross-sections like the dumbbell to teardrop shapes (Fig. 7.23) observed among splash form melt-drop impact spherules (Fig. 3.8). The spherules' original shapes are largely unmodified because most of them are isolated in dolomite. Exceptions occur where spherules that touch silicate grains or stylolites are indented by pressure solution or where spherules are cross-cut by tectonic veinlets.

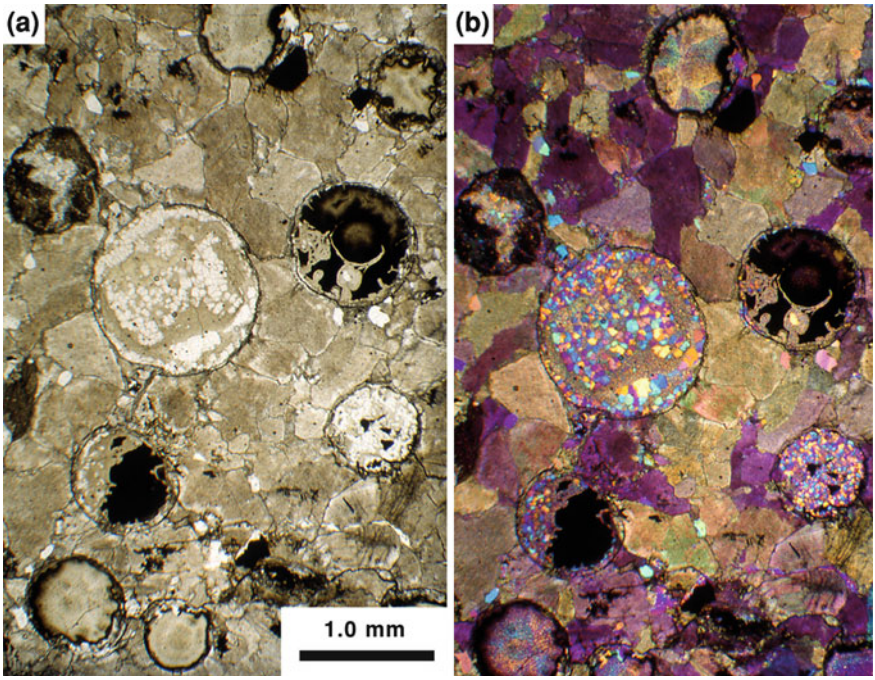

Fig. 7.22 Photomicrographs of sample from the Grænsesø spherule layer at the Midternæs location. **a** Spherules (*circular*), sparry dolomite (*tan*), and finer quartzose sand grains (*white*) in plane polarized light. Some but not all of the black material inside the spherules is organic matter. **b** Same area in cross polarized light with gypsum plate inserted. The spherules, composed of equant mosaics of blue and yellow crystals (near *center* and *right* edge), consist largely of quartz whereas the spherules near top and bottom edges consist largely of inward-directed radial-fibrous aggregates of chalcedony and sericite

Internally, the spherules show diverse textures but two components are dominant: 1) radial-fibrous aggregates of chalcedony, sheet silicate, and/or K-feldspar and 2) mosaics of blocky quartz crystals $\sim$100 μm across associated with felted to locally radial-fibrous sheet silicates (Fig. 7.22a, b). The chert intraclasts also show mosaics of randomly oriented quartz crystals, but they differ from those in the spherules in being more finely crystalline and lacking radial-fibrous textures. Some sheet silicates in the spherules have the composition of Mg-rich phlogopite (Hansen 1978), but for convenience they are collectively referred to here as sericite, which they resemble optically. The radial-fibrous aggregates generally radiate inwards towards the centers of spherules and meet along planar to smoothly curved interfaces suggesting competitive growth of botryoids. This is consistent with Hansen's (1978) report that some central regions were layered in a way that resembled agate. The sericite crystals associated with the blocky mosaics are larger and more randomly oriented on average than the sericite associated with the radial-fibrous aggregates. The relative proportions of the two main textural

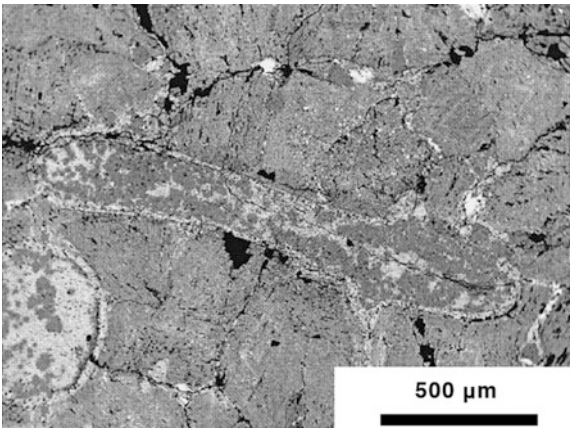

Fig. 7.23 Backscattered scanning electron micrograph of sample from the Grænsesø spherule layer at the Midternæs location showing a highly elongated particle interpreted as a dumbbell-type splash form in center plus part of a typical spherule with a circular cross-section in lower left. Both particles consist of a combination of quartz and dolomite (*gray*) plus sericite and possibly K-feldspar (white) and are surrounded by coarsely crystalline dolomite (also *gray*). From Chadwick et al. (2001), Fig. 4a, published with the permission of the Geology Society of London

components vary widely from one spherule to another, but blocky quartz and felted sericite consistently post-date the radial-fibrous aggregates. This is based on cross-cutting relationships and the presence of relict radial-fibrous extinction patterns in some quartz mosaics. Dark material is present in many spherules, especially in their central regions (Fig. 7.22a), but it appears to be less common and more irregular than Bondesen et al. (1967) described.

Irrespective of their internal textures, many spherules are replaced by coarsely crystalline carbonate, most commonly in a thin marginal zone of uneven thickness. In many cases, a dark line or selvedge is found along the contact between the invading carbonate and the silicates in the cores of the spherules or along the outer edges of spherules that the carbonates did not invade. Bondesen et al. (1967) suggested these selvages were relicts of external cell walls (see Sect. 7.4.5), but Hansen (1978) found the selvages were a mixture of quartz and phlogopite rather than carbonaceous in composition.

In addition to the textures described above, a minority of the spherules contain unusual textures relevant to their interpretation as impact ejecta. One such texture consists of families of dark parallel lines ranging from orthogonal grids to feathery or cruciform patterns (Fig. 7.24). These patterns occur in roughly 5 % of the spherules, which generally consist of finely polygonal quartz and sericite. The patterns are strikingly similar to skeletal spinels grown from natural (Fig. 4 d in Byerly and Lowe 1994) and synthetic (Fig. 3d in Gayraud et al. 1996) silicate melts, as well as skeletal spinels in spherules from the K-T boundary layer (Fig. 5d in Chadwick et al. 2001). The patterns fill the interiors of some spherules completely (Fig. 7.24a) but are confined to the edges of others. Chadwick et al. (2001)

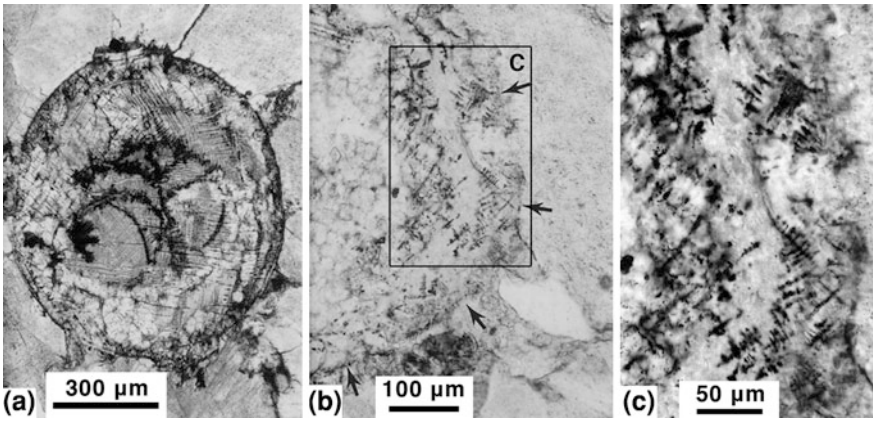

Fig. 7.24 Photomicrographs (plane polarized light) of spherules from the Grænsesø layer with spinel-like patterns in sample from the Midternæs location. **a** Spherule consisting of a combination of coarser quartz-sericite (*lighter areas*) and fibrous chalcedony and sericite (*darker areas*) with orthogonal networks that resemble skeletal spinel crystals spread across most of its cross-section. **b** Part of another spherule consisting of coarse quartz-sericite with discrete dark inclusions resembling skeletal (cruciform) spinel crystals. The arrows indicate the original margin of the spherule, which is embayed by dolomite. The elongated white grain below box to the right is a quartz sand grain. **c** Enlargement of part of the spherule in **b** showing the dark inclusions that resemble skeletal spinel crystals at higher magnification. **a** and **b** are from Chadwick et al. (2001), Figs. 5a and b, respectively, and published with the permission of the Geology Society of London

were unable to detect any of the elements typical of spinels along the dark lines so they suggested they were pseudomorphs of spinel. Chadwick et al. (2001) also reported dark arcuate lines resembling perlitic cracks in a few spherules. Perlitic cracks have been reported from tektite glass (Thein 1987), but such reports are rare. Even rarer are spherules showing what appear to be sprays of pseudomorphed acicular crystals radiating inwards from their margins resembling spherulites grown in devitrified glass. Smith et al. (2006) also reported a few blocky particles with possible flow banding defined by minute sericite laths. Only one candidate for an infilled vesicle has been reported to date (Smith et al. 2006).

The original composition of the Grænsesø spherules is uncertain because all of their primary phases were replaced during diagenesis. Available evidence is scanty but suggests they had a wide range of compositions. On the one hand, the possible presence of perlitic cracks suggests some were originally high-silica melts. On the other hand, the possible pseudomorphs of skeletal spinels suggest some were low-silica melts. Spherules in Paleoarchean layers (described in Chap. 9) are almost entirely replaced by secondary phases, yet careful petrographic and geochemical analyses (Lowe et al. 2003; Krull-Davatzes et al. 2006; and references therein) have demonstrated that they originally had a wide range of compositions. The same may be true in the Grænsesø layer, but further work is needed to determine this.

7.4.3 Radiometric Age

The age of the Grænsesø layer is not well constrained. A minimum age is provided by U/Pb zircon ages of 1845 and 1848 Ma for an intrusion cutting across the deformed extension of the Vallen Group south of Grænseland (Garde et al. 2002). A maximum age is indirectly indicated by dikes in the basement beneath the Vallen Group thought to have intruded about 2130 $\pm$ 65 Ma based on regional correlations (Chadwick et al. 2001). The most that can be said at present is that the spherule layer was probably deposited after $\sim$2130 Ma but before $\sim$1850 Ma.

7.4.4 Geographic Distribution and Variation

As noted above, the Grænsesø layer has only been observed in two areas in South Greenland. According to Higgins (1970), the layer has been identified at four sites in the Grænseland area but only one in the Midternæs area. The site in Midternæs is separated from the most distant one in Grænseland by a distance of $\sim$26 km; that is the total known extent of the layer at present. Locally, it is traceable along strike for at least 100 m. The layer looks about the same wherever it has been observed (as described above) and occurs at the same stratigraphic position. Bondesen (1970, p. 94) viewed this as an example of biostratigraphic correlation in Precambrian strata, but it may be an example of correlation using a distal impact ejecta layer instead. Existing data are insufficient to determine whether or not the layer shows lateral variations within its known area of occurrence. However, possible impact spherules have been reported from several cores drilled in roughly contemporaneous strata in Karelia, Russia, that could be equivalent (Huber et al. 2011, 2012), but they have yet to be described in detail.

7.4.5 Evidence of Impact Origin

The Grænsesø layer contains a few percent by volume of very fine to fine quartzose sand, but no definite evidence of shock deformation has been observed in any of these crystals (Chadwick et al. 2001). Smith et al. (2006) detected possible shock features in 5 zircon grains. A single sample from the layer was analyzed in bulk for platinum group elements and found to contain 0.02 ppb iridium and low levels of other PGEs (Chadwick et al. 2001). The absence of an anomalously large enrichment in iridium does not advance the case that they are impact spherules, but it does not rule it out either. Glassy impact spherules, such as Cenozoic microtektites (Glass 1990a) and spherules in Late Devonian strata (Claeys et al. 1996), show little or no enrichment in iridium or other PGEs.

Despite the lack of any definitive proof of an impact origin, the characteristics of the spherules in the Grænsesø layer fit an origin as distal impact ejecta better than any known alternative. First of all, the external shapes of the spherules indicate they were once molten, especially the rare particles that are highly elongated (Fig. 7.23). In addition, some of the textures inside the Grænsesø spherules are typical, and possibly diagnostic, of crystallization from a melt and/or devitrification (described in Sect. 7.4.2), leaving two possible origins: as impact ejecta or via volcanic eruption. All of the shapes seen in the Grænsesø spherules have been reported from both microtektites (see Chap. 4; Glass 1990a) and droplets of magma quenched during volcanic eruptions (Heiken and Wohletz 1985), but there is a big difference in the relative proportions of different shapes between impact and volcanic droplets. On the one hand, spheroidal to ovoid shapes with lesser numbers of highly elongated particles are the norm for impact spherules. In contrast, highly elongated shapes dominate and true spherules are rare among volcanic melt droplets (see discussion in Simonson 2003a), although there may be exceptions (see Sect. 3.5). The only common volcaniclastic deposits in which spheroidal shapes dominate are layers of accretionary lapilli which, like those described in Sect. 7.3.2, are physical aggregates rather than melt droplets. Moreover, the Grænsesø spherules lack accretionary textures internally (Fig. 7.22), whereas well-preserved volcanic accretionary lapilli occur in adjacent units, as do examples of devitrified shards (Higgins 1970). Another argument in favor of an impact origin for the spherules is their restriction to a single layer. Lam and Raunsgaard Pedersen (1968, p. 7) reported that "the Grænsesø Formation has many other dolomitic layers, but in spite of exhaustive searching *Vallenia* has only been found in this [one] uppermost layer." Where volcaniclasts are present, they are generally more widely distributed stratigraphically. Similar textural arguments as well as their silicate composition make it highly unlikely the Grænsesø spherules are replaced oolites. Finally, the Grænsesø spherules do not appear to change size over a distance of 26 km; this is consistent with dispersal by a large impact but not a volcanic eruption, particularly a fire fountain. In summary, interpreting the Grænsesø spherules as reworked impact ejecta provides the best explanation of their known characteristics, but the paucity of unmelted ejecta is puzzling.

Lastly, let us revisit the original interpretation of the Grænsesø spherules as microfossils (Bondesen et al. 1967). This was based on their spherical shapes, the presence of carbonaceous matter, and internal features interpreted as cellular structures. The latter included double-layered outer walls and internal thickenings. $\delta^{13}C$ values obtained from carbonaceous matter extracted from spherule-bearing samples were also close to those of freshwater green algae. Hansen (1978) subsequently studied some Grænsesø spherules with an electron microscope and detected some carbon, but he found that the dark material in the center of the spherules, which Bondesen et al. (1967) interpreted as relict cell structures, consisted largely of phlogopite-type silicates. He also disagreed on other key points. Specifically, he suggested the double-layered walls were the result of diagenetic shrinkage and the internal thickenings were an optical effect related to phlogopite twinning rather than biogenic features. Perhaps the carbonaceous matter in the

Grænsesø layer was introduced during diagenesis. Black shales that are potential source rocks are in close stratigraphic proximity lower in the Grænsesø Formation and in the underlying Blåis Formation (Bondesen 1970) and clear evidence of hydrocarbon migration has been found in other early Precambrian strata (e.g., Dutkiewicz et al. 1999). Finally, spherical shapes are no longer a compelling argument for a biogenic origin for spherules this old and this large. Many organic-walled Precambrian microfossils are spheroidal (commonly known as sphaeromorphs), but the diameters of the largest ones older than ~1.65 Ga are around 0.3 mm (Javaux et al. 2010) whereas Grænsesø spherules can exceed 1 mm in diameter. For such reasons, Mendelson and Schopf (1992, p. 870) interpreted the Grænsesø spherules as "recrystallized ooliths or spherulites" and placed them in a table of "micropseudofossils." The rare spherules that are highly elongated (Fig. 7.23) are particularly problematic for the biogenic interpretation.

7.4.6 Constraints on Potential Source Crater

If they were produced by an impact, the volume of spherules in the Grænsesø spherule layer indicates it was a large impact. The spherules make up ~15–20 % of a layer about 1 m thick, so their aggregate thickness is 15–20 cm. This is on a par with the thickest accumulations of impact spherules reported from any Phanerozoic layer, namely those of the K-T boundary layer where their aggregate thickness can be that high or even higher due to local reworking (e.g., Schulte et al. 2003). Therefore, it seems likely that the impact responsible for creating the Grænsesø layer was roughly commensurate in size to the end-Cretaceous impact, depending on the distance to the source crater. This is also suggested by the fact that the total thickness of spherules in the Grænsesø layer equals or exceeds the thickest accumulations of spherules in many or most of the older Precambrian spherule layers (described in Chap. 8 and 9).

The two terrestrial impact structures closest in age to the Grænsesø spherule layer are the two largest ones known. One is the Vredefort structure formed around 2023 Ma (Kamo et al. 1996) and the other is the Sudbury structure dated to 1849 Ma (see Sect. 7.3.3). Both of these structures presumably gave rise to global ejecta layers as they are both larger than the Chicxulub structure. As the Grænsesø layer was probably deposited between 2.13 and 1.848 Ga (see Sect. 7.4.3), it could potentially contain distal ejecta from either one of these impact structures. However, the Ketilidian orogeny was in full swing by ~1845 Ma and possibly by 1848 Ma (Garde et al. 2002), so it seems unlikely the Grænsesø layer could have been deposited in undisturbed sediment at the time of the Sudbury impact. Moreover, the spherules do not seem to have much in common with the ejecta in the layer west of the Sudbury structure (described in Sect. 7.3.2; see also Sect. 10.3.9 for further discussion). Geochemical work is currently in progress on the potentially correlative spherules in Karelia, Russia, to see if they may be ejecta from the Vredefort impact structure (Huber et al. 2012). If the Grænsesø spherules

are ejecta, but are not from either the Vredefort or Sudbury structures, there is probably another large Paleoproterozoic impact structure yet to be found.

7.4.7 Possible Links to Biologic and Climatic Changes

The Grænsesø spherule layer does not appear to coincide with any marked change in the lithology of the host formation, nor have any claims been made that it coincides with any major change in the biosphere, hydrosphere, and/or atmosphere. However, it took years of study before the dramatic change in acritarch diversity in close stratigraphic proximity to the Acraman layer was detected (Grey et al. 2003; described in Sect. 7.2.6). Therefore, no firm conclusions should be drawn without much additional investigation.

Chapter 8
Spherule Layers Near the Archean-Proterozoic Boundary

8.1 Introduction

As noted in Chap. 7, strata deposited during a relatively short period of time straddling the Archean-Proterozoic boundary contain an unusually high concentration of spherule layers. At least 4 bodies roughly the size of the end-Cretaceous impactor or larger hit the Earth in a span of some 140 million years (Table 8.1). To date, spherule layers from these impacts have only been found in two limited geographic areas where sedimentary strata are unusually well preserved: the Hamersley Basin of Western Australia and the Griqualand West Basin of South Africa. These two successions are thought to be largely contemporaneous and host some of the largest banded iron formations (BIFs) and iron mines in the world (Fig. 8.1; Beukes and Gutzmer 2008; de Kock et al. 2009). Spherule layers are hosted by both BIFs and associated strata and it appears that most can be correlated between the two basins (Simonson et al. 2009a; Hassler et al. 2011; see Sect. 8.4). The Hamersley layers are described first, then those in the Griqualand West Basin, and finally their correlations are discussed.

8.2 Archean-Proterozoic Boundary Spherule Layers in Australia

8.2.1 Introduction

Trendall (1983) defined the Hamersley Basin as the basin in which, from oldest to youngest, the Fortescue, Hamersley, and Wyloo Groups were deposited. Together these three Groups comprise the Mt. Bruce Supergroup, a succession of sedimentary and volcanic rocks 5–9 km thick that rests unconformably on the Pilbara Craton (Myers 1993). The latter is one of the two oldest continental blocks in Australia and contains greenstone belt successions that host the Paleoarchean

B. P. Glass and B. M. Simonson, *Distal Impact Ejecta Layers*, Impact Studies,
DOI: 10.1007/978-3-540-88262-6_8, © Springer-Verlag Berlin Heidelberg 2013

Table 8.1 Impact spherule layers close to the Archean-Proterozoic boundary

Spherule layer	Location	Impact evidence[a]	Age (Ma)	References
Dales Gorge[b]	Hamersley Basin, Western Australia	Cr, Ir, NiP, PGEs, Sph	~2490	Glikson and Allen (2004), Sweeney and Simonson (2008), Simonson et al. (2009b)
Kuruman[b]	Griqualand West Basin, South Africa	Sph	> ~2460, < ~2520	Simonson et al. (2009a)
Bee Gorge	Hamersley Basin, Western Australia	Ir, PGEs, Sph, TiII	~2540	Simonson et al. (2009b), Smith et al. (2010)
Paraburdoo[c]	Hamersley Basin, Western Australia	Ir, PGEs, Sph	~2570	Hassler et al. (2011), Goderis et al. (2012)
Reivilo[c]	Griqualand West Basin, South Africa	Ir, PGEs, Sph	> ~2550, < ~2590	Simonson et al. (2009a), Simonson et al. (2009b)
Monteville[d]	Griqualand West Basin, South Africa	Ir, PGEs, Sph, TiII	> ~2590, < ~2650	Simonson et al. (2009b), Smith et al. (2010)
Carawine[d]	Hamersley Basin, Western Australia	Cr, Ir, PGEs, Sph, TiII	~2630	Simonson et al. (2009b), Smith et al. (2010)
Jeerinah[d]	Hamersley Basin, Western Australia	Cr, Ir, PGEs, Sph, SQ?, TiII	~2630	Simonson et al. (2009b), Rasmussen and Koeberl (2004), Smith et al. (2010)

[a] *Cr* chromium isotope data, *Ir* iridium anomaly, *NiP* Ni-Fe-rich phase, *PGEs* platinum group elements with chondritic ratios, *Sph* spherules, *SQ* shocked quartz with planar deformation features, *TiII* TiO_2II.

[b] These two layers were probably formed by the same impact around 2.49 Ga

[c] These two layers were probably formed by the same impact around 2.57 Ga

[d] These three layers were probably formed by the same impact around 2.63 Ga

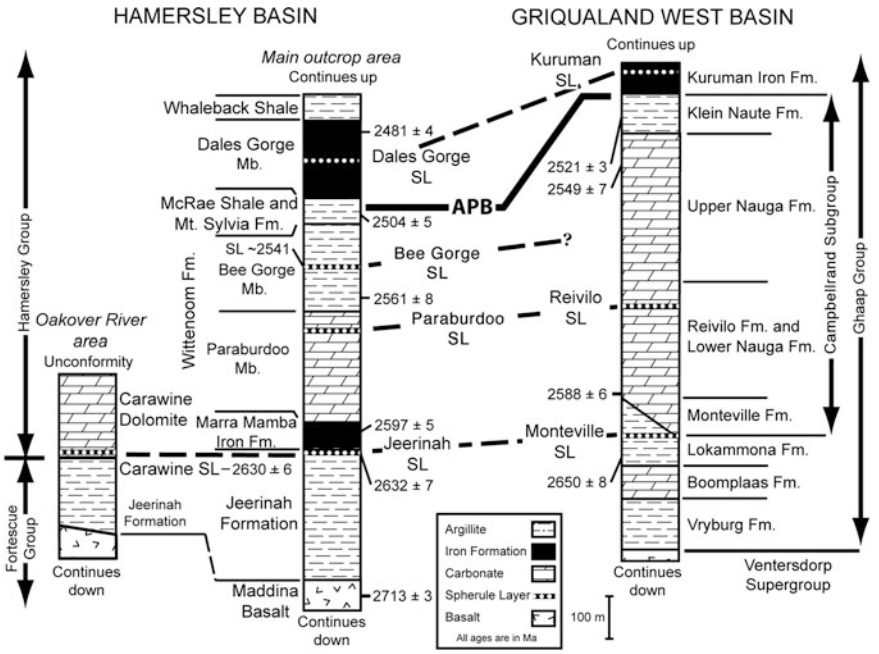

Fig. 8.1 Schematic columns showing the stratigraphic units and principal lithologies for the parts of the Hamersley Basin (Western Australia) and Griqualand West Basin (South Africa) successions that host known spherule layers. Rows of white dots indicate the stratigraphic positions of the spherule layers. The thick *black line* (labeled APB) indicates the approximate stratigraphic position of the Archean-Proterozoic boundary. The Roy Hill Shale is always the uppermost member of the Jeerinah Formation where present. The Klein Naute Formation is a lateral equivalent of the Gamohaan Formation and is restricted to the southwest part of the Griqualand West Basin. The *dashed lines* connect layers that may have been formed by a single impact. Numbers on sides of columns are radiometric ages in Ma (see text for details). *Fm* formation, *Mb* member, *SL* spherule layer. Modified after Hassler et al. (2011), Fig. 1, with permission from Elsevier

spherule layer(s) described in Chap. 9. In the Hamersley Basin, spherule layers have only been identified among some 800 m of strata in the middle of the Mt. Bruce Supergroup. The oldest spherule layer is very near the top of the Fortescue Group in the Jeerinah Formation, whereas the youngest spherule layer is in the Dales Gorge Member in the middle of the overlying Hamersley Group (Fig. 8.1). Spherule layers have been identified in 5 different stratigraphic units in the Hamersley Basin (Table 8.1). Strata of the Hamersley Group occur in two geographic areas currently separated by a wide alluvial valley. Within the Hamersley Basin, these two areas are informally known as the main outcrop area and the smaller Oakover River area. Three of the five layers (the Dales Gorge, Bee Gorge, and Paraburdoo) are in units that are restricted to the main outcrop area, one of the layers (the Carawine) is in a formation that is restricted to the Oakover River area, and one layer (the Jeerinah) is in a formation that occurs in both areas (Fig. 8.2), but the layer is restricted to the

main outcrop area. Based on stratigraphic correlations between the two areas (Fig. 8.1; Rasmussen et al. 2005; Hassler et al. 2005, 2011), these five occurrences were probably produced by 4 impacts of large extraterrestrial bodies (as discussed in Sect. 8.4.1). As in previous chapters, the layers are described below in descending chronological order Tables 8.2 and 8.3.

8.2.2 Dales Gorge Spherule Layer

8.2.2.1 Description of Layer

The youngest spherule layer reported from the Hamersley Basin is in the Dales Gorge Member of the Brockman Iron Formation, one of eight formations that make up the Hamersley Group throughout the main outcrop area of the Hamersley Basin. The Brockman itself is divided into four members. From oldest to youngest, these Members are named the Dales Gorge BIF, Whaleback Shale, Joffre BIF, and Yandicoogina Shale (Trendall and Blockley 1970; Trendall 1983). The Dales Gorge BIF is sandwiched between a pair of shaly units inasmuch as it is underlain by the Mt. McRae Shale and overlain by the Whaleback Shale (Fig. 8.1). Within the Dales Gorge Member, BIFs alternate with shaly interbeds to form 16 distinctive couplets that persist throughout most of the Hamersley Basin (Trendall and Blockley 1970; Ewers and Morris 1981). Individual BIF and shaly layers are both on the order of a few meters thick, referred to as macrobands, and numbered sequentially from bottom to top as S1, BIF1, S2, BIF2, etc. To distinguish them from similar shaly interbeds in other Hamersley BIFs, the shaly macrobands in the Dales Gorge Member are designated DS1, DS2, etc. The **Dales Gorge spherule layer** is in macroband DS4, i.e., the fourth shaly interbed from the base of the Dales Gorge Member. DS4 is about 4 m thick on average and the Dales Gorge spherule layer is the only definite occurrence of spherules reported from the Dales Gorge Member, save for a possibly reworked second layer with spherules close above the Dales Gorge spherule layer at one location of DS4 (Pickard et al. 2004).

The Dales Gorge spherule layer ranges in thickness from $\sim$14 to 110 cm with an average between 25 and 75 cm, but only a fraction of that normally consists of spherules. The layer varies in character throughout its known area of occurrence, but nowhere does it appear to be an undisturbed product of direct fallout. Spherules in the spherule layer are associated with boulder-size intraclasts at sites located higher on the paleoslope versus symmetric bedforms of probable wave origin deeper in the Hamersley Basin. At some sites, the Dales Gorge spherule layer contains well-sorted layers or lenses of spherules up to $\sim$10 cm thick whereas at other sites the spherules are sparsely distributed in the layer. The original characteristics of the spherules, especially their shapes, are best preserved where the layer contains abundant intergranular cement (Fig. 8.3). The cement consists of fibrous stilpnomelane, an unusual iron-rich sheet silicate, and was emplaced early enough in diagenesis to protect many spherules from compaction

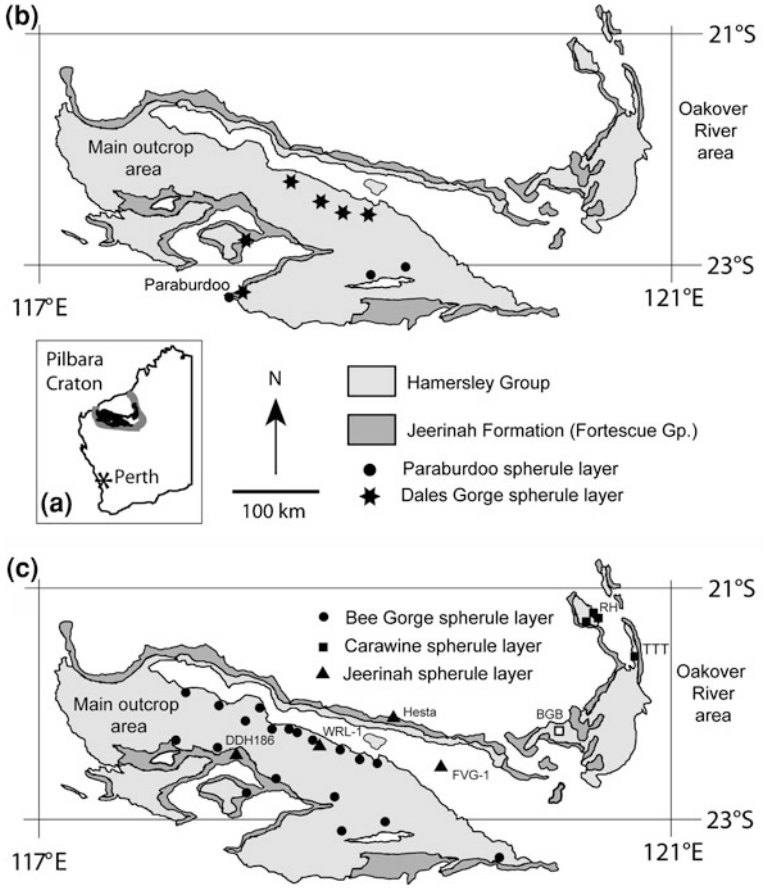

Fig. 8.2 Generalized geological map of the Hamersley Basin. **a** Index map showing the location of the Pilbara Craton (inside *gray line*) in the state of Western Australia and where strata of the Hamersley Basin are preserved (*black*). **b** Generalized map of the areas of occurrence of the Jeerinah Formation (the uppermost unit of the Fortescue Group) and the Hamersley Group showing the principal sites where the Dales Gorge and Paraburdoo spherule layers have been identified. The Oakover River area lies east of ~120° E and is separated from the main outcrop area of the Hamersley Basin by a broad alluvial valley. **c** Same map as **b** showing the principal sites where the Bee Gorge, Carawine, and Jeerinah spherule layers have been identified. Labeled outcrops are *RH* Ripon Hills, *TTT* Tarra Tarra turnoff, and Hesta. Labeled coresites are *BGB* Billygoat bore, FVG-1, WRL-1, and DDH186. Modified after Simonson et al. (2009a), Fig. 1a, with permission from Elsevier

(Sweeney and Simonson 2008). Throughout its area of occurrence, the layer is capped by decimeter-scale, sandy layers of normally graded shaly intraclasts that are probably turbidites and generally lack spherules (see Sect. 8.2.2.4). The average aggregate thickness of spherules in the Dales Gorge spherule layer throughout its area of occurrence is hard to estimate because of this variability, but it is believed to be on the order of 6 cm.

Table 8.2 Averages of selected elements' concentrations in samples from Archean-Proterozoic boundary spherule layers in Hamersley Basin (Western Australia) and Griqualand West Basin (South Africa)

	Hamersley Basin				Griqualand West Basin	
	Dales Gorge spherule layer[a](5)	Bee Gorge spherule layer[a](3)	Carawine spherule layer[b] (5)	Jeerinah spherule layer[a] (4)	Reivilo spherule layer[a] (1)	Monteville spherule layer[a] (8)
SiO_2 (wt %)	37.65	30.04	n.d.	49.95	54.23	40.15
Fe_2O_3 (wt %)	6.64	7.23	n.d.	12.32	14.79	14.43
Al_2O_3 (wt %)	22.81	3.85	n.d.	22.49	0.53	3.83
K_2O (wt %)	3.93	4.20	n.d.	7.52	9.10	6.48
Cr (ppm)	218	86	n.d.	297	830	227
Co (ppm)	35.7	8.9	n.d.	21.9	189	14.3
Ni (ppm)	297	31.0	n.d.	178	3931	40
Ir (ppb)—ave.	11.5	0.49	0.60	10.4[c]	176	2.78
Ir (ppb)—max.	~18	~0.68	1.54	15.5	176	6.4
Ru (ppb)	18.9	0.70	1.12	14.0	262	3.25[d]
Pt (ppb)	24.1	1.47	5.82	17.4	380	4.45[d]
Rh (ppb)	4.03	0.18	n.d.	3.08	61.0	0.70[d]
Pd (ppb)	11.37	3.55	3.73	9.66	59.4	4.09[d]
Au (ppb)	1.86	1.26	0.82	5.99[c]	7.0	2.3

n.d. no data. Numbers in parentheses indicate number of analyses
[a] Data are from Simonson et al. (2009b)
[b] Data are from Simonson et al. (1998)
[c] Average includes 2 additional analyses from Rasmussen and Koeberl (2004)
[d] Only 4 samples analyzed for this element

Based on their sedimentary textures and structures, both the Dales Gorge spherule layer and the strata that enclose it were deposited under generally quiet, low-energy conditions. This is typically the case for BIFs, which are fine-grained, thinly laminated chemical sediments consisting of chert and various iron-rich minerals (Simonson 2003b; Bekker et al. 2010). Various lines of evidence indicate the Dales Gorge Member was deposited beneath several hundred meters of seawater in deep shelf to upper slope paleoenvironments (Simonson et al. 1993a; Krapež et al. 2003). This evidence includes the presence of thin layers that persist laterally for hundreds of kilometers in the BIFs (Trendall and Blockley 1970; Ewers and Morris 1981), as well as carbonate and volcaniclastic turbidites and thin normally graded tuffs in both DS (shale) macrobands in the Dales Gorge Member and in associated units, such as the Mt. McRae Shale (Simonson et al. 1993b; Hassler 1993; Pickard 2002; Pickard et al. 2004). The fact that the sediments of the Dales Gorge Member accumulated below wave base aided in the preservation of the spherule layer. It also indicates that unusually large waves were involved in creating the bedforms in the Dales Gorge spherule layer, as no wave structures have been reported from any other layer in the Dales Gorge Member.

Table 8.3 Chromium isotopic compositions of samples from selected Archean-Proterozoic boundary layers (from Simonson et al. 2009b)

	$\varepsilon(^{53}Cr)_{corr.}$
Dales Gorge spherule layer	
96466, HCl leach	0.28 ± 0.03
96466, residue	0.35 ± 0.04
Carawine spherule layer	
46-2, fraction 1	0.16 ± 0.03
Jeerinah spherule layer	
W-94-1Q, fraction 1	0.12 ± 0.03
W-94-1Q, fraction 2	0.01 ± 0.04
Monteville spherule layer	
P11-1, bulk	−0.02 ± 0.03
P11-1, spherules	−0.04 ± 0.04

The uncertainties are 2 σ_{mean}

8.2.2.2 Description of Spherules

Spherules in all of the layers deposited close to the Archean-Proterozoic boundary show very similar textures, so the Dales Gorge spherule layer spherules are described in detail to serve as a template. Spherules and related particles in this layer are generally equant and in the coarse to very coarse sand-size range, the largest ones observed being ~1.8 mm across. Roughly 80 % of the particles by volume are splash forms whereas the rest are similar compositionally but more angular in outline; there is relatively little intergradation between the two different types (Sweeney and Simonson 2008). Most unbroken splash forms have circular to oval cross-sections (Fig. 8.3a) with larger particles generally more elongated than smaller ones, but a few are shaped like dumbbells or teardrops (Fig. 8.3b,c). Some of the splash forms have truncated outlines indicating they are fragments of larger spherules that were broken prior to deposition (described below). Some spherules have two markedly different textures internally where discrete particles appear to have collided in flight and agglutinated to form a single particle (Fig. 8.3d). Mineralogically, the spherules and related particles consist of oxidized stilpnomelane with lesser amounts of K-feldspar, calcite, and opaque phases in samples from surface outcrops versus unoxidized stilpnomelane with minor opaque phases in unweathered core samples (Pickard et al. 2004). Most opaque phases are either very finely crystalline or highly elongated and conform to shapes defined by non-opaque phases (notably the K-feldspar described below). Some of the opaque phases may represent skeletal growth forms, but none of the shapes typical of spinel (e.g., Fig. 9.11) have been reported from the Dales Gorge spherule layer. Some opaques are rich in nickel and may represent original, unreplaced crystals grown from melt (Glikson and Allen 2004). Glikson and Allen (2004) also noted ilmenite needles on the order of 10 μm long in K-feldspar microlites and attributed them to exsolution. Where present, calcite and other carbonate phases tend to be coarsely crystalline and obscure primary textures (Fig. 8.3a).

Internally, the spherules in the Dales Gorge spherule layer have relatively few textural components, but they occur in a variety of combinations. Perhaps the most distinctive element of these spherules, as in most Archean-Proterozoic boundary spherule layers, comprises highly elongated microlites of K-feldspar. Many of these microlites are lath-shaped, have a dark central stripe, and in some instances have pronged terminations or occur in "bowtie" or rosette-type clusters. Such skeletal morphologies match the shapes of plagioclase microlites formed by rapid cooling in natural and experimental basaltic rocks (Gélinas and Brooks 1974; Bryan 1972; Pearce 1974; Lofgren and Donaldson 1975; Lofgren 1977, 1980, 1983). The lath-shaped microlites are randomly oriented in some spherules (Fig. 8.4a) and create textures identical to those of finely crystalline basalts. Other K-feldspar microlites are acicular or needle shaped; these are generally organized into radial-fibrous aggregates known as spherulites (Lofgren 1971a). The radial-fibrous and to a lesser extent lath-shaped K-feldspar microlites form thin to thick rims on the edges of a majority of the spherules (Fig. 8.3a,e; Sweeney and Simonson 2008). Lath-shaped microlites look similar whether they are in rims or inside spherules. The formation of the K-feldspar by replacement of original plagioclase is consistent with its near-stoichiometric $KAlSi_3O_8$ composition; this is typical (if not diagnostic) of K-feldspar crystallized at low-temperatures and found in all the Archean-Proterozoic boundary spherule layers (Simonson 1992; Simonson et al. 2009a). The textural retention during the replacement of plagioclase is impressive and has also been observed in basaltic tuffs in the Hamersley and other iron formation basins (Hassler and Simonson 1989; Hassler 1993; Simonson et al. 1993b).

As noted above, stilpnomelane is the most abundant mineral in the Dales Gorge spherule layer spherules, generally in the form of fibrous microlites that fill much of the interiors of most spherules (Fig. 8.3). Given its central position and the local presence of infilled vesicles (e.g., Fig. 8.3b), the stilpnomelane inside appears to have replaced original glass volume for volume during diagenesis. The fibrous stilpnomelane looks similar whether it replaces glass or fills either vesicles or intergranular pores, although it tends to be lighter in pores. Stilpnomelane is common in iron formations (Klein 2005) where it usually signals the presence of aluminous impurities, such as silicate clays or volcanic ash. In the Dales Gorge spherule layer, it signals the arrival of aluminous glass from an extraterrestrial impact instead (Sweeney and Simonson 2008).

About 13 % of the splash forms have truncated outlines indicating they were broken prior to deposition (Sweeney and Simonson 2008). Internally, broken spherules show the same textures as unbroken ones, most commonly massive stilpnomelane with a thin rim of K-feldspar on what was originally the external surface (Fig. 8.3f). Breakage must have happened before deposition because, had the spherules broken in situ, multiple smaller fragments would be grouped together, as seen where hollow spherules were crushed, for example, in the Monteville spherule layer (described in Sect. 8.3.4.2) and the K-T boundary layer (Kohl et al. 2006). The fact that the vast majority of the K-feldspar rims are restricted to what would have originally been the external surface of a given spherule indicates the rims mostly formed in flight. However, K-feldspar rims do occur on broken

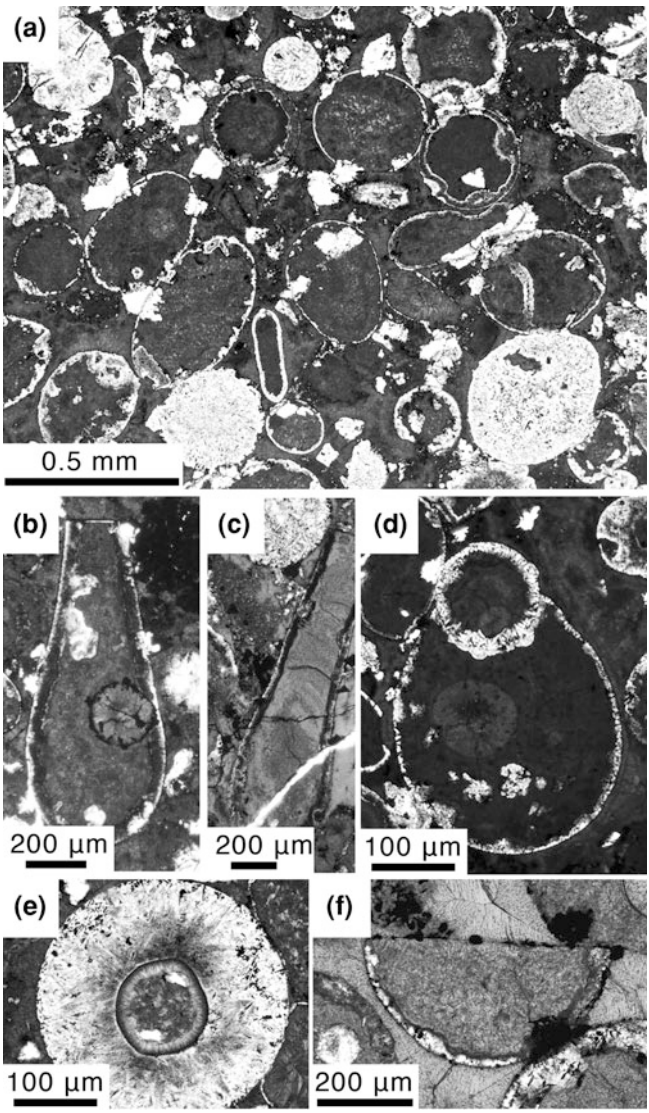

surfaces in a few spherules, although they are typically thinner than rims on original external surfaces (e.g., Fig. 8.3b). Moreover, some splash forms have internal septae consisting of back-to-back selvages of K-feldspar microlites (Fig. 8.3a) that appear to be hairline cracks along which crystals nucleated. These textures suggest some rims grew after deposition. Breakage could have been caused by collisions either in the ejecta cloud during flight or during transport by high-energy waves and/or currents. Alternatively, cracking could have resulted

◀**Fig. 8.3** Photomicrographs in plane polarized light of spherules from the Dales Gorge spherule layer in samples with abundant stilpnomelane cement. **a** General view of spherules including a few dumbbells. Most spherules consist largely of stilpnomelane (*dark gray*, probably replaced glass) and have rims of K-feldspar (*white*). Note septum similar to a rim inside one spherule (*center right*) and thin lines of opaque inclusions in another spherule that may be crystal pseudomorphs (*upper left corner*). Some spherules consist largely of K-feldspar and have basaltic textures, e.g., in lower right and at right end of scale bar. Interstitial voids are filled with stilpnomelane interpreted as cement. Polygonal white patches are carbonate crystals that replace both spherules and cement. From Simonson (2003a), Fig. 2a. **b** Teardrop-shaped spherule consisting largely of stilpnomelane with a rim of K-feldspar (*white* to *dark gray*) except at top where the tip of the droplet was broken. The particle has an internal circle that is probably a vesicle filled with stilpnomelane and some opaque phase(s). **c** Another teardrop with a K-feldspar rim and a broken tip at top. The spherule at top is mostly K-feldspar and has a basaltic texture. *White diagonal line* in lower part is a glue-filled crack. **d** Agglutinated particle where a small spherule that already had a rim of inward-directed lath-shaped microlites collided and fused with a larger, hotter particle with a thinner rim. **e** Perfectly circular spherule with a thick rim of lath- to needle-shaped microlites of K-feldspar that radiate in from the outer edge. The concentrically banded circle in the center is probably a vesicle filled by several different generations of stilpnomelane cement. **f** Half a spherule with a thin K-feldspar rim that must have been broken in half before burial. The central stilpnomelane (*mottled gray*) presumably replaced an original glass core whereas the lighter stilpnomelane in the adjacent pores shows competing-growth textures typical of void-filling fibrous cement

from thermal stresses when hot particles hit cold seawater as in Cenozoic Australasian microtektite strewn fields (Glass et al. 1997 and Sect. 4.2.9).

In contrast to normal splash forms, ~20 % of the presumed ejecta particles in the Dales Gorge spherule layer are more angular in cross-section (Fig. 8.4b). The angular particles have about the same aspect ratio and size range as the splash forms, but they are smaller on average. Like the splash forms, they consist mainly of elongated K-feldspar microlites and stilpnomelane, but rims are rarely present, random textures are more common, and K-feldspar is more abundant overall in the angular particles. Some appear to show flow banding internally (Fig. 8.4b) and what appear to be vesicles are present in a higher percentage of the angular particles than in the splash forms, although they are less likely to have perfectly circular cross-sections. A few angular particles contain polygonal bodies that could be phenocryst pseudomorphs (e.g., Fig. 10 in Sweeney and Simonson 2008). As in the splash forms, the K-feldspar and stilpnomelane in the angular particles probably replaced plagioclase and glass, respectively, but retained the original textures. The close association of the splash forms and angular particles and their textural similarities suggest they both originated as molten material in a single large impact. This is consistent with what appear to be rare angular particles agglutinated to splash forms. The angular particles may have originated as fragments of larger melt droplets broken in transit, although few if any appear to have rounded edges like the broken splash forms. Alternatively, they could be solid fragments of target rocks, in which case shock deformation features could have been present at the time of deposition, but were masked by diagenetic replacement. The lack of any quartzose detritus in the Dales Gorge spherule layer analogous to the epiclastic sediment present in other Archean-Proterozoic boundary spherule layers

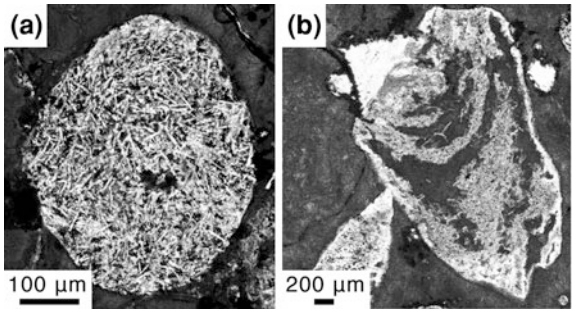

Fig. 8.4 Photomicrographs in plane polarized light of formerly molten particles from the Dales Gorge spherule layer in samples with abundant stilpnomelane cement. **a** Spherule with a basaltic texture consisting of randomly oriented microlites of K-feldspar with a mesostasis of stilpnomelane and opaque phases that probably replaced original glass. **b** Large angular particle with internal banding consisting of alternating layers rich in K-feldspar microlites (*light gray*) and stilpnomelane (*dark gray*). Large carbonate crystals (*white spots*) locally replace both particles and stilpnomelane cement. Note smaller triangular particle with fine basaltic texture (*lower left*) and spherule that consists of stilpnomelane (*left edge*) that probably originated as a microtektite. **a** is from Simonson (2003a), Fig. 8d. **b** is from Sweeney and Simonson (2008), Fig. 9, with permission from the Meteoritical Society

(Simonson 1992; Simonson et al. 2000b; Jones-Zimberlin et al. 2006) makes it highly unlikely that the angular particles are epiclastic detritus brought in by impact-induced waves or currents. Furthermore, the angular particles do not bear a close textural resemblance to lithic clasts in tuffs in the same stratigraphic succession (Hassler 1993; Simonson et al. 1993b; Pickard 2002).

Based on their textures and geochemical data (discussed in Sect. 8.2.2.5), the splash forms and angular particles in the Dales Gorge spherule layer were probably originally basaltic in composition. As noted above, it appears most of the rims formed in flight and the plagioclase microlites formed before the spherules entered the water in the Hamersley Basin. Lofgren (1971b) suggested similar textures in lunar impact spherules formed in flight via a combination of direct growth from melt and thermal devitrification. One alternative for forming the rims is aqueous devitrification during diagenesis; this is deemed unlikely because the rims vary considerably from one spherule to the next whereas the stilpnomelane is relatively homogenous. Bohor and Glass (1995) attributed rims on K-T impact spherules to rapid hydration and palagonitization when hot spherules hit water, followed by devitrification and diagenesis. The rims of the Dales Gorge spherule layer spherules are unlikely to have formed this way because a nucleus-rich material like palagonite is much more likely to foster crystal growth in random directions rather than highly directed fibers (Gary Lofgren, personal communication, 2008). In contrast, inward-directed crystal growth in flight seems reasonable; microlites could nucleate readily on molten spherule margins via cooling effects and as dust strikes their outside surfaces (Connolly and Hewins 1995). If the rims formed in flight and thermal devitrification was responsible, it would require complex trajectories along which spherules were cooled and reheated, unless they were

reheated during reentry. Some rare spherules in the suevite breccia of the Ries crater with rims of plagioclase microlites are very similar to Dales Gorge spherule layer spherules with K-feldspar rims (Figs. 3 and 7 of Graup 1981) indicating impact spherules can crystallize rapidly. Rare spherules from the Eltanin impact also have acicular crystals growing inward from their margins (Margolis et al. 1991a). The Eltanin spherules are mafic (Kyte and Brownlee 1985) and deposited in seawater relatively close to the point of impact (Gersonde et al. 1997), again indicating rapid crystallization. In addition, very similar rims composed of quench crystals occur on basaltic spherules in Miocene deep-sea sediments that probably formed during fire fountaining nearby (Melson et al. 1988, esp. their Fig. 4e).

The distance traveled by the Dales Gorge spherule layer spherules cannot be determined because, as with all early Precambrian layers, no source crater has been identified. The fact that the spherules do not show any significant change in size over a distance of ~200 km suggests they were deposited in a relatively distal location.

8.2.2.3 Radiometric Age

The Dales Gorge spherule layer has not been dated directly, but tuffs are widespread in the shaly macrobands of the Dales Gorge Member and the enclosing shaly units (LaBerge 1966; Trendall and Blockley 1970; Pickard 2002; Pickard et al. 2004). The U–Pb ages of zircon crystals separated from some of these tuffs have been determined using a SHRIMP (Fig. 8.1). Dates of 2495 ± 16 and 2504 ± 5 Ma were obtained from older tuffs in the DS2 macroband (Trendall et al. 2004) and the Mt. McRae Shale (Rasmussen et al. 2005), respectively; they are ~10 and 60 m below the Dales Gorge spherule layer stratigraphically. Younger tuffs yielded dates of 2481 ± 4 and 2461 ± 6 Ma from the DS9 and DS13 macrobands, respectively, and 2463 ± 5 Ma from the overlying Whaleback Shale Member (Trendall et al. 2004). Stratigraphically, these three tuffs are ~30, 65, and 110 m above the spherule layer, respectively. Given the uncertainties involved and the reversed order of the younger dates, great accuracy is not to be expected. Proportioning between the two closest dates yields a depositional age for the Dales Gorge spherule layer around 2.49 Ga, whereas proportioning between the dates next closest yields an age of 2.48 Ga. In summary, the Dales Gorge spherule layer formed soon after 2.50 Ga, the assigned age of the Archean-Proterozoic boundary (see Chap. 7).

8.2.2.4 Geographic Distribution and Variation

The Dales Gorge spherule layer has been identified at more than 6 sites in an area of ~17,000 km^2 in the main part of the Hamersley Basin (Fig. 8.2b; Hassler and Simonson 2001). The most widely separated sites are over 200 km apart in a WNW-ESE direction, which is the approximate strike of the paleoslope. The greatest separation down the paleoslope, which is towards the SSW, is

Fig. 8.5 Images of the Dales Gorge spherule layer. **a** Outcrop showing most of the lower, coarser-grained part of the Dales Gorge spherule layer in DS4 consisting of tabular intraclasts of cherty BIF (*arrows* indicate the two largest ones) and spherule-rich sand (similar to the sample shown in **b**) that weathers more readily. The upper, finer-grained part consisting of thin graded beds is present but only a few centimeters thick here. The basal contact is covered but the resistant layers at the *top* are the basal strata of the overlying cherty BIF5. Modified from Hassler and Simonson (2001), Fig. 7e. **b** Polished slab of Dales Gorge spherule layer that largely consists of well-sorted spherules with K-feldspar rims (*white to light gray*) and cement in a background of stilpnomelane (*medium to dark gray*) similar to Fig. 8.3a

only ~80 km. The Dales Gorge spherules change little in size or texture throughout their area of occurrence, but the depositional structures of the spherule layer change significantly. The depositional features of the Dales Gorge spherule layer fall into three categories, as follows: those restricted to upslope sites, those restricted to downslope sites, and those present in both.

Only at the upslope sites does the lower part of the Dales Gorge spherule layer consist of two decimeter-scale beds with large clasts overlain by a series of partial Bouma sequences (Hassler and Simonson 2001). These two beds both have erosional basal contacts and consist of a mixture of intraclasts and spherules. In the lower layer, the spherules make up ~20 % by volume and the intraclasts are matrix supported and show weak coarse tail grading upward from flat pebbles to very fine sand. The upper layer is massive and mainly composed of pebble-sized argillite and cherty BIF intraclasts with few spherules. The intraclasts in the upper bed include cobble- to boulder-sized slabs (Fig. 8.5a) that are concentrated at the top and form a continuum with the smaller intraclasts, which support them. The intraclasts typically have rounded ends, but some are frayed and brecciated locally. The largest intraclast is cherty, 234 cm long, and oriented vertically. The cherty BIF clasts were presumably produced by erosion higher on the paleoslope because the Dales Gorge spherule layer is separated from the subjacent BIF3 by about a meter of shaly strata in its known occurrences.

Only at the downslope sites does the lower portion of the Dales Gorge spherule layer consist entirely of spherules and appear to lack large rip-up clasts. The

spherules are organized into symmetrical, dune-like bedforms whose wavelengths and heights (= thicknesses) range from 39–50 cm and 2–9 cm, respectively. The spherule layer is underlain by chert in this area and its basal contact is sharp, planar and nonerosive.

At both upslope and downslope sites, i.e., throughout its area of occurrence, the Dales Gorge spherule layer is capped by decimeter-scale, normally graded beds that show partial Bouma sequences. These beds are composed mainly of fine sand to silt-sized clasts of argillite and contain rare intraclasts of chert, BIF, and carbonate but lack spherules. At the upslope sites, these beds either truncate against or drape over boulder-sized intraclasts whereas they drape the bedforms nonerosively in the downslope area.

As previously noted, the Dales Gorge Member was deposited below wave base in deep shelf to upper slope paleoenvironments. The boulder-size intraclasts in the Dales Gorge spherule layer are probably the coarsest detritus in the entire Member, so the spherule layer was clearly the product of an unusually high-energy event (Hassler and Simonson 2001; Pickard et al. 2004). Since it also contains the only known impact spherules in the Dales Gorge Member, the spherules and high-energy waves and currents were probably all produced by a single oceanic impact. Despite the high energy, no unambiguously extrabasinal detritus coarser than mud has been detected in the Dales Gorge spherule layer, even though sand-size volcaniclasts (e.g., shards) are present in other DS macrobands (LaBerge 1966; Trendall and Blockley 1970). The absence of terrigenous sand may reflect the deposition of the spherule layer during a sea level highstand when craton-derived sands were unlikely to reach deep paleoenvironments (Simonson and Hassler 1996). The characteristics of this layer require multiple episodes of deposition involving both sediment gravity flows and probable wave action. Once the spherules arrived and started to settle out, deposition in three phases could account for the features of the Dales Gorge spherule layer, as follows (from Hassler et al. 2005): (1) unusually large waves reworked the spherules into symmetrical bedforms throughout much of the Hamersley Basin; (2) a series of sediment gravity flows reworked the wave bedforms and generated intraclasts in the shallower areas but deposited sediment without eroding the substrate deeper on the paleoslope; and (3) fine-grained material was deposited throughout the Hamersley Basin by waning turbidity currents and/or more dilute suspension settle-out. Both phases one and two may have been products of bottom return flow set up by an impact-induced tsunami. The sharp contacts and the lack of intervening sediment suggest all three subunits were deposited in rapid succession.

8.2.2.5 Extraterrestrial Component and Target Material

Several different geochemical lines of evidence indicate the Dales Gorge spherule layer contains extraterrestrial material. One line of evidence is the fact that spherule-rich samples from this layer have concentrations of Ir about two orders of magnitude higher than associated strata. Specifically, Ir concentrations in 5

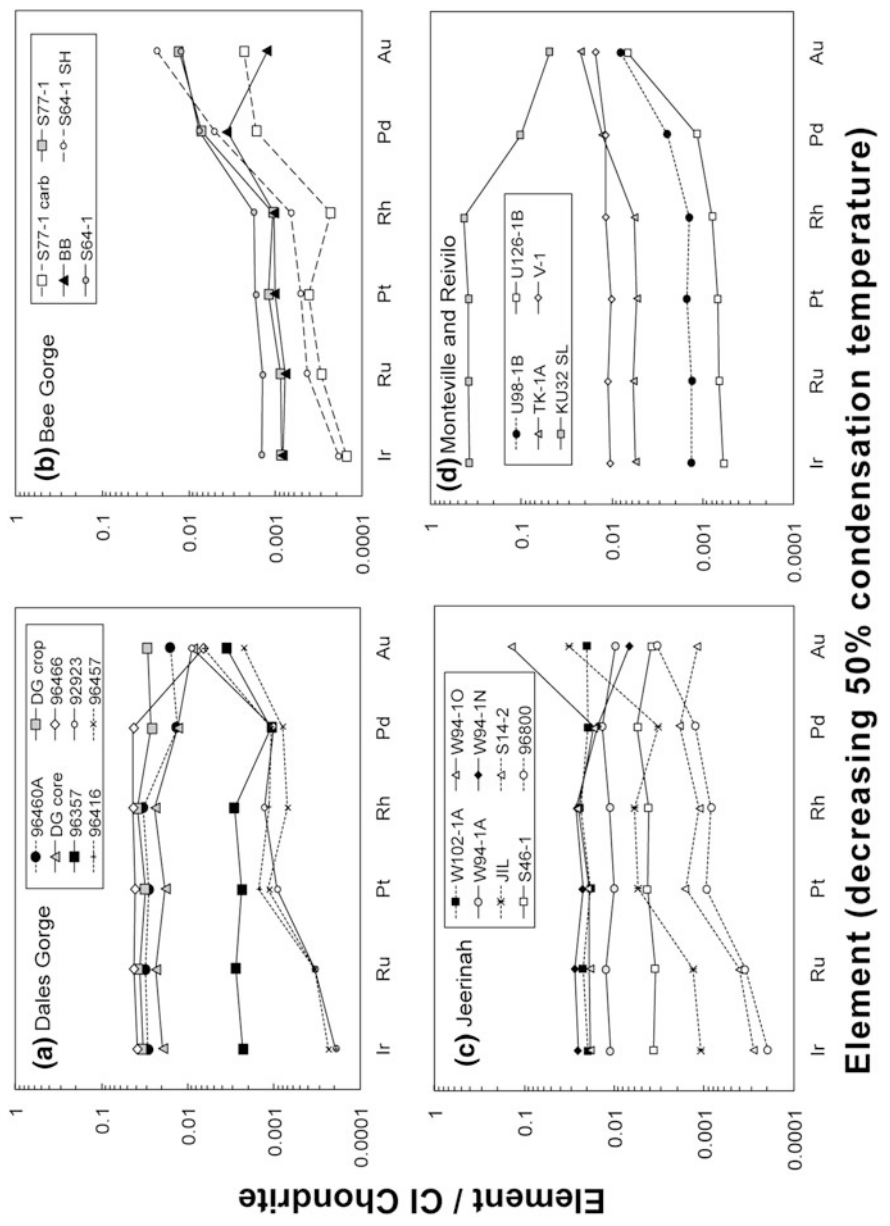

Fig. 8.6 CI-chondrite-normalized PGE plots of samples from or associated with five of the Archean-Proterozoic boundary spherule layers. Chondrite normalization values are taken from Lodders (2003). **a** Samples 96357, 96460A, 96466, DG crop, and DG core are from the Dales Gorge spherule layer; the other 3 are from associated limestone, shale, and BIF. **b** Samples BB, S64-1, and S77-1 SL are from the Bee Gorge spherule layer; S64-1 SH and S77-1 carb are from associated shale and carbonate, respectively. **c** Samples W94-1A, W94-1 N, W94-1O, and W102-1A are from the Jeerinah spherule layer; the other four are from associated shales and tuffs. **d** Sample KU32 SL is from the Reivilo spherule layer; the remaining samples are from the Monteville spherule layer. Modified after Simonson et al. (2009b), Fig. 8

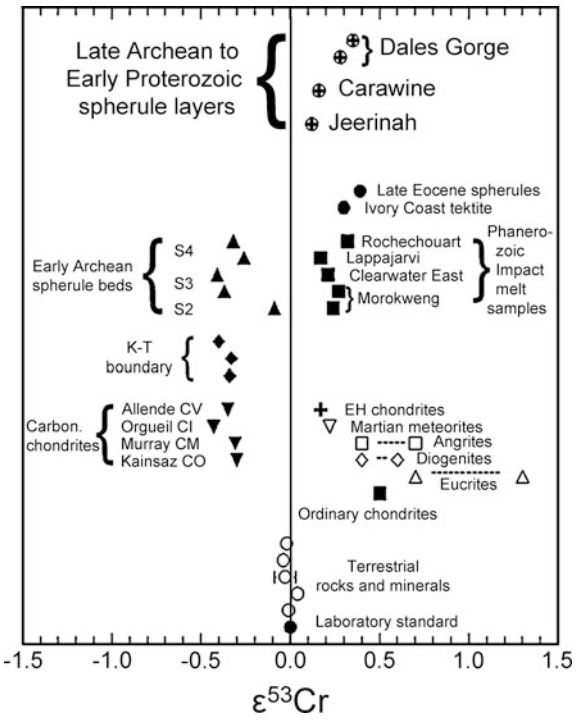

Fig. 8.7 Plot of normalized ε^{53}Cr values of samples from the Dales Gorge, Carawine, and Jeerinah spherule layers (*uppermost* in *right* half) and Paleoarchean spherule layers S2, S3, and S4 (*uppermost* in *left* half—described in Chap. 9) compared to values typical of meteorites, other impact-related materials, and normal terrestrial rocks and minerals. From Simonson et al. (2009b), Fig. 11

spherule-rich samples (like the one in Fig. 8.5b) from the Dales Gorge spherule layer ranged from 1.1 to 17.8 ppb Ir and averaged 12.1 ppb, whereas 3 samples from ambient shale, chert, and carbonate that were free of spherules had between 0.09 and 0.11 ppb Ir (Simonson et al. 2009b). Two samples of the layer analyzed by Glikson and Allen (2004) likewise contained 13.1 ppb Ir on average. When normalized to chondritic abundances, the PGE interelement ratios for the Dales Gorge spherule layer are essentially flat from Ir to Rh (Fig. 8.6) suggesting they were derived from an extraterrestrial object. That would also explain high concentrations of Ni observed in bulk samples rich in spherules (Simonson et al. 2009b), as well as in certain phases inside individual spherules (Glikson and Allen 2004). In contrast, the elements Pd and Au depart somewhat from chondritic ratios relative to the PGEs. Glikson and Allen (2004) and Glikson (2005) argued these and other volatile metals were systematically depleted relative to refractory ones via condensation in an impact vapor cloud. While this would result in systematic fractionation, Simonson et al. (2009b) found Pd and Au concentrations were variable in the samples they analyzed. Kyte et al. (1992) noted similar non-systematic variations in Pd and Au concentrations in Paleoarchean spherule layers and suggested they probably reflect local diagenetic conditions.

Extraterrestrial material can also be detected by analyzing the isotopic composition of Cr if it has not been too diluted by terrestrial sources (Chap. 3; Shukolyukov and Lugmair 1998). Given the absence of coarse terrigenous detritus,

the Dales Gorge spherule layer is well suited for this type of analysis. The isotopic composition of Cr in one sample from this layer has been analyzed and two fractions extracted from this sample yielded positive ε^{53}Cr values of 0.28 ± 0.03 and 0.35 ± 0.04 (Fig. 8.7), indicating they each contained about 65 wt % extraterrestrial Cr. Taking into account the total mass of the sample, the extraterrestrial component of the sample as a whole is estimated to be about 4.5 wt %. This is similar to an extraterrestrial component of 2–3 wt % calculated from an Ir concentration of 11.5 ppb in the same sample (Glikson and Allen 2004; Simonson et al. 2009b).

Given the clear presence of an extraterrestrial component in the Dales Gorge spherule layer samples, constraints can also be placed on the composition of the impactor. The presence of a positive ^{53}Cr anomaly in impact-related materials indicates the extraterrestrial object responsible for generating the spherules did not have the composition of a carbonaceous chondrite. Moreover, the ε value is too large to be an enstatite chondrite, indicating that the projectile had the composition of an ordinary chondrite (Simonson et al. 2009b). Certain PGE ratios can also be used to constrain impactor compositions. A regression run on all analyzed samples from the Dales Gorge spherule layer was clearly inconsistent with a carbonaceous chondritic impactor, but resolution between ordinary versus enstatite chondrites was not possible at the two sigma confidence interval (Fig. 10a, b in Simonson et al. 2009b). Given the Cr isotope results, the impactor that generated this layer probably had the composition of an ordinary chondrite.

As with most impact melts, the bulk of the mass in the Dales Gorge spherule layer spherules was probably derived from terrestrial target materials. As described above, the textures of some spherules strongly suggest they originally consisted of mafic or low-silica melts, but few if any original phases survived diagenesis. Glikson and Allen (2004) cited high Ni/Cr and Ni/Co ratios as evidence the target materials had a mafic to ultramafic composition. In contrast, Simonson et al. (2009b) found moderate to strong light rare earth element (LREE) enrichment in all of the samples analyzed from the Dales Gorge spherule layer and associated strata. This suggests the target did not consist exclusively of LREE-depleted material, such as mid-ocean ridge basalt, but may have included some higher-silica rocks (e.g., continental crust) as well. Additional work focused specifically on this issue will be necessary to clarify the nature of the target materials.

8.2.3 Bee Gorge Spherule Layer, Wittenoom Formation

8.2.3.1 Description of Layer

The next oldest spherule layer is hosted by the Bee Gorge Member of the Wittenoom Formation (Fig. 8.1). Stratigraphically, the Wittenoom Formation is directly above the Marra Mamba BIF, the oldest of the five major BIFs in the Hamersley Group. Internally, the Wittenoom Formation is divided into three

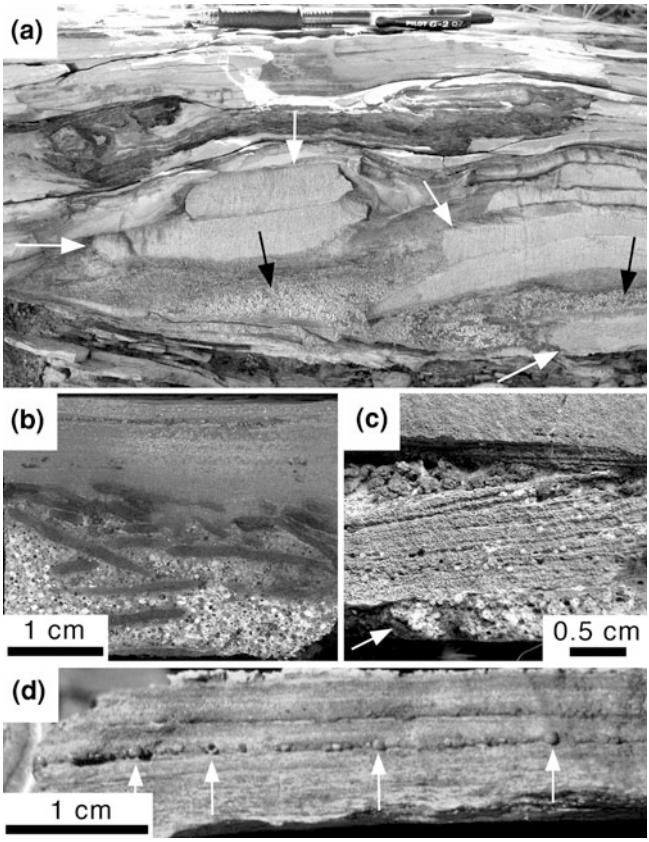

Fig. 8.8 Images of the Bee Gorge spherule layer. **a** Outcrop in zone A (zones are described in text) showing most of the lowest of 3 subunits with large tabular intraclasts of carbonate mud (e.g., *white arrows*) and pockets of spherule-rich sand (e.g., *black arrows*) with smaller intraclasts of pyrite and shale (*darker bodies*). The intraclast-rich zone is underlain by shale (e.g., *lower left*) and overlain by sands rich in compacted silicate peloids that contain round hollows (near *left edge*) formed by soft-sediment deformation. Pen at top is ~14 cm long. **b** Polished sample from zone B with basal ~1.5 cm rich in spherules and tabular intraclasts of iron hydroxides (*dark gray*) that are early diagenetic concretions of pyrite eroded locally and oxidized by modern weathering. This is overlain by weathered carbonate-rich fine sand with horizontal lamination (*medium gray* at *top*). **c** *Lower part* of the Bee Gorge spherule layer in outcrop where the sample in **b** was collected showing 4 mm of almost pure spherules (*white arrow*) overlain by current cross-laminated fine carbonate-rich sand with stray spherules; paleoflow was to the south (*left*) and the dark objects are probably weathered pyrite intraclasts and/or secondary crystals. At top is finer carbonate-rich sand similar to the upper part in **b**. **d** Outcrop in zone C where it locally dwindles to a train of isolated spherules (e.g., *at white arrows*) enclosed in weathered shale

members, the Bee Gorge Member being the uppermost. The Bee Gorge Member is heterolithic and consists of shale with subordinate amounts of dolomite, limestone, banded iron-formation, chert, and volcaniclastic strata (Simonson et al. 1993a, b). In previous publications, the **Bee Gorge spherule layer** has been referred to as

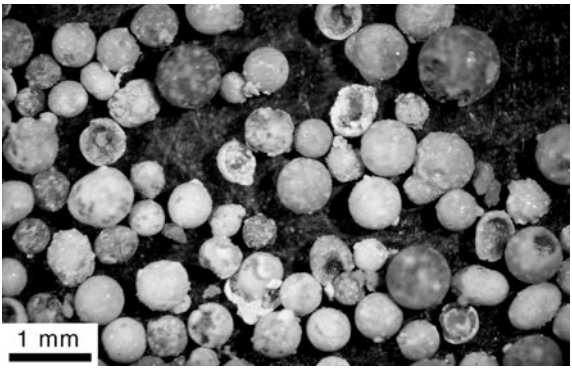

Fig. 8.9 Photomicrograph of K-feldspar spherules hand picked from HCl-insoluble residue of a carbonate cement-rich sample of the Bee Gorge spherule layer. Spherical shapes dominate, but some ovoids and probable agglutinated particles (e.g., *middle right*) are present. The hollow spherules probably had glass cores or vesicles that were replaced or infilled, respectively, by carbonate that dissolved in the HCl

both the Spherule Marker Bed (Simonson 1992) and the Wittenoom spherule layer (Simonson et al. 2009a). We refer to it here as the Bee Gorge spherule layer because another spherule layer was recently discovered in the Wittenoom Formation (Hasser et al. 2011) in the subjacent Paraburdoo Member (described in Sect. 8.2.4).

The Bee Gorge spherule layer is a sand-rich layer that was shaped largely by high-energy currents and waves. Like the Dales Gorge spherule layer, it thins and fines dramatically down the paleoslope, i.e., from northeast to southwest. It is up to 350 cm thick and contains large tabular rip-up clasts in its northeasternmost occurrences (Fig. 8.8a,b), but it is only a few centimeters thick on average in its southern- and westernmost occurrences and locally dwindles to a single stringer of discontinuous spherules (Fig. 8.8c,d). Throughout its area of occurrence, the abundance of spherules as a fraction of the total thickness of the Bee Gorge spherule layer varies widely from a few to virtually 100 %; however, the aggregate thickness of the spherules remains fairly consistent at around 1 cm (Simonson 1992). Despite the variability in the thickness of the Bee Gorge spherule layer and related shifts in the coarseness of its other components, the spherules are similar in size and show similar textures throughout its area of occurrence (Scally and Simonson 2005). More details of its depositional characteristics are given in Sect. 8.2.3.4.

8.2.3.2 Description of Spherules

The spherules in the Bee Gorge spherule layer are mostly medium to coarse sand size; they average about 0.6 mm in diameter, the largest being ~1.7 mm in diameter. In contrast to most Precambrian layers, the three dimensional shapes of some spherules can be readily determined because carbonate cement is locally

abundant in the Bee Gorge spherule layer and individual spherules can be liberated by dissolving such samples in HCl (Fig. 8.9). Most of these particles are spheres or ovoids, like splash forms in Cenozoic ejecta layers. Spherule fragments liberated from such samples are generally products of differential carbonate replacement rather than fracturing prior to deposition. Carbonate replacement is widespread in the Bee Gorge spherule layer, as is replacement by iron oxides and quartz, all of which tend to obscure rather than preserve primary textures.

Internally, Bee Gorge spherule layer spherules show textures similar to those of the Dales Gorge spherule layer spherules (described in Sect. 8.2.2.2), the principal difference being the absence of stilpnomelane. The most distinctive component is again K-feldspar, mostly ranging in shape from fibers to laths. Most fibrous crystals occur in radial aggregates forming botryoidal rims or randomly nucleated inside spherules (Fig. 8.10). Laths likewise can radiate inwards from spherules' margins or occur randomly in spherule interiors (Fig. 8.10b). The laths are from 5–50 μm long and 1–5 μm thick and many have skeletal morphologies extremely similar to those of plagioclase microlites in basaltic melts (described in Sect. 8.2.2.2). Laths and fibers generally form a bimodal population in a given spherule with laths more common in spherule interiors and fans more common on spherule edges (Scally and Simonson 2005).

Blocky K-feldspar crystals also occur in spherule interiors in two contexts; some fill former vesicles in ~15 % of the spherules, as evidenced by circular cross-sections with sharp boundaries (Fig. 8.10c, e). In other spherules, blocky K-feldspar forms central spots with irregular shapes that lack a well-defined boundary or have a sharp boundary dictated by the scalloped terminations of a botryoidal rim. Such spots are interpreted as residual glass cores replaced during diagenesis (Simonson 2003a; Scally and Simonson 2005) analogous to glass cores in K-T spherules (Sigurdsson et al. 1991a,b; Bohor and Glass 1995). Some of the K-feldspar filling vesicles and/or replacing glass cores is radial-fibrous instead of blocky, but such K-feldspar is clear in plane polarized light whereas the K-feldspar forming rims or random laths have fine inclusions that are tan in transmitted light (Fig. 8.10). The inclusions are probably titanium-bearing oxides (Scally and Simonson 2005) and are also present in the K-feldspar in the Dales Gorge spherule layer, but less obvious because of the strong color of stilpnomelane. Clear and tan fibrous K-feldspar crystals are commonly in optical continuity, suggesting the rims and laths served as nucleation sites during diagenetic replacement of the glass cores. At least some of the clear K-feldspar must have replaced glass directly rather than filling voids after glass dissolution based on the fact that the shapes of vesicles are often preserved. In addition to K-feldspar, both vesicles and replaced glass cores also contain blocky crystals of quartz and carbonate, whereas other central spots consist of matted masses of fine, more randomly oriented crystals. Some spherules are completely clear in plane polarized light; they are presumably replaced microtektites. As in the Dales Gorge spherule layer, the K-feldspar in the Bee Gorge spherule layer is believed to be authigenic in origin, formed via replacement of plagioclase microlites and glass and, to a lesser extent, void-filling cementation.

In addition to cementation and replacement, spherules in the Bee Gorge spherule layer were extensively modified by compaction based on the widespread occurrence of tight packing, long and sutured contacts between grains, and spherules with shapes modified by pressure solution (Fig. 8.10a; Scally and Simonson 2005). A few spherules were broken in situ and must have been hollow; they are analogous to the crushing of partially dissolved carbonate ooids during compaction that Wilkinson and Landing (1978) called "eggshell diagenesis." Despite these modifications, a small population of particles that were not originally spheroidal is recognizable in the Bee Gorge spherule layer. Some of these are pairs of spherules that agglutinated in flight (Fig. 8.10b). Other particles have truncated circular cross-sections indicating they are fragments of spherules broken prior to deposition; they are comparable to the spherule fragments in the Dales Gorge spherule layer but harder to recognize due to the compaction. Other non-spheroidal particles that were formerly molten make up less than 2 % of the spherule population, lack the smooth external morphology of splash forms, and are generally holocrystalline with many randomly oriented laths. They could be analogous to the angular particles in the Dales Gorge spherule layer and have originated as either fragments of spherules larger than any of the intact ones in the Bee Gorge spherule layer or possibly as solid, unmelted ejecta. They could also be analogous to irregular melt particles in the Carawine and Jeerinah spherule layers (described in Sects. 8.2.5.2 and 8.2.6.2; Simonson et al. 2000b; Jones-Zimberlin et al. 2006). They do not appear to show flow banding or abundant fine vesicles like the irregular particles in the older layers, but they are smaller on average so such textures would be harder to recognize.

Given their many similarities, several of the interpretations of the Dales Gorge spherule layer spherules can be extended to the Bee Gorge spherule layer spherules. For example, the internal textures of some of the Bee Gorge spherule layer spherules strongly suggest they were originally basaltic in composition and that some of the K-feldspar pseudomorphed plagioclase microlites whereas the rest formed via a combination of glass replacement and void-filling cementation. It also appears that the rims and lath-shaped crystals mostly formed in flight rather than after deposition based again on the diversity of textures seen in the spherules and the textures in spherule fragments broken before deposition. Finally, the Bee Gorge spherule layer spherules are probably relatively distal ejecta from a large impact. As with the Dales Gorge spherule layer (see Sect. 8.2.2.2), this follows mainly from the great abundance of spherules and the paucity of candidates for broken spherule fragments and unmelted solid ejecta. While the more highly compacted nature of the layer makes it difficult to quantify such characteristics, the fact that the sizes and aggregate thickness of the Bee Gorge spherule layer spherules are close to constant for 300 + km is further evidence of a distal position. This is also consistent with the fact that the spherules in the Bee Gorge spherule layer are a bit smaller than those in the Dales Gorge spherule layer on average (Simonson 1992) and the rims are more abundant and thicker in the Bee Gorge spherule layer spherules, suggesting they had more time to crystallize. The most dramatic difference between the Bee Gorge spherule layer and the Dales

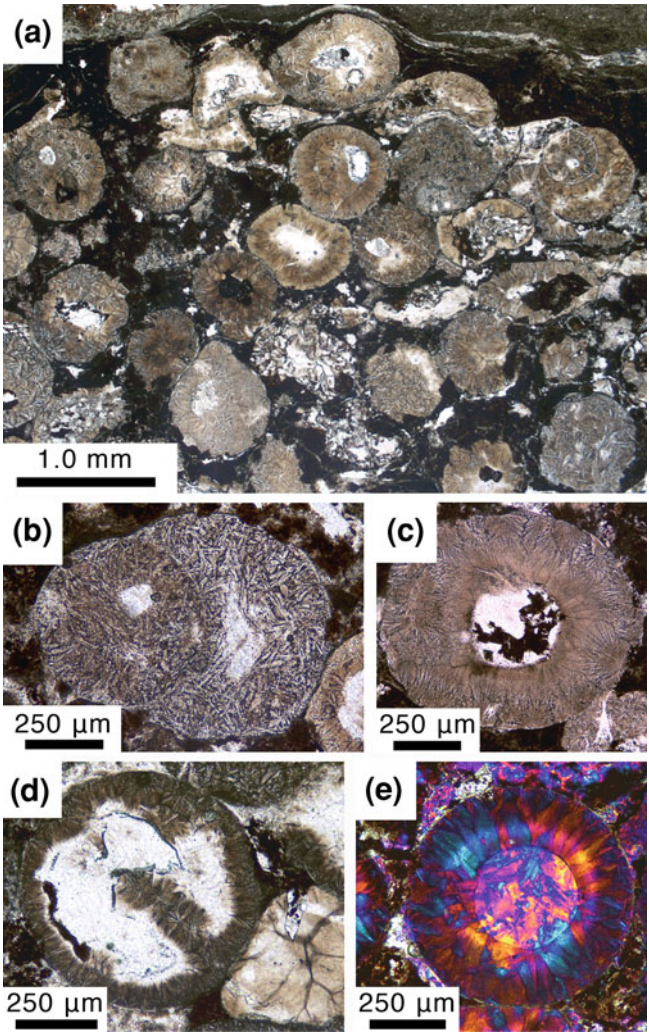

Gorge spherule layer is the lack of stilpnomelane in the Bee Gorge spherule layer, but this is to be expected since stilpnomelane requires an iron-rich diagenetic environment (Sweeney and Simonson 2008).

8.2.3.3 Radiometric Age

The approximate age of the Bee Gorge spherule layer can be interpolated using U–Pb ages determined via SHRIMP analysis of zircon crystals from tuffaceous interbeds above and below the layer itself (Fig. 8.1). A marker bed informally known as the crystal-rich tuff ~75 m below the Bee Gorge spherule layer stratigraphically (Simonson et al. 1993b) yielded an age of 2561 ± 8 Ma (Trendall

◀ **Fig. 8.10** Photomicrographs, taken in plane polarized light (except for E), of spherules from the Bee Gorge spherule layer. **a** Spherule-rich sample showing some compaction; the long and sutured contacts between spherules, as well as the distorted shapes of some spherules, indicate they have been affected by a combination of pressure solution and ductile deformation. Both the tan rims and the clear central spots (probably a combination of replaced glass cores and infilled vesicles) consist largely of K-feldspar. The dark material is a combination of shale (at top where it is compacted over spherules) and oxidized ferroan carbonate (e.g., dark rhombic shape in spherule in middle right). **b** Composite particle in which it appears that two highly-crystallized spherules collided in flight and fused to form an agglutinated spherule. **c** Nearly circular spherule with a thick rim of K-feldspar in radial-fibrous fans diverging inward from the outer edge. The central clear spot consists of coarse crystals of quartz and oxidized carbonate and is probably a filled-in vesicle. **d** Circular spherule with a thin rim of fibrous K-feldspar (*dark tan*) plus an internal septum from which fibrous K-feldspar radiates outward in opposite directions. The clear material around the septum consists of K-feldspar and is probably replaced glass. **e** Perfectly circular K-feldspar spherule, photographed with crossed polarizers using a gypsum plate. The spherule has an outer rim of radial-fibrous fans (*dark outer zone*) and a central circle defined by traces of dark impurities (interpreted as a filled-in vesicle due to its perfectly circular cross-section). Between the two is a clear zone consisting of fibrous K-feldspar in optical continuity with the rim (interpreted as glass replaced by radial-fibrous crystals nucleated on the outer rim). **a** and **d** are from Simonson (2003a), Figs. 2c and 7a, respectively

et al. 1998). The next closest date below that is 2597 ± 5 Ma, but it comes from a tuff that is hundreds of meters lower stratigraphically in the subjacent Marra Mamba BIF. The closest date from a younger tuff is 2504 ± 5 Ma; it comes from about 135 m stratigraphically above the Bee Gorge spherule layer in the Mt. McRae Shale (Rasmussen et al. 2005). Proportioning between the two closest dates yields a depositional age of ~2.54 Ga for the Bee Gorge spherule layer.

Direct dating of the Bee Gorge spherule layer has been attempted by two different methods. Using a Pb–Pb method on carbonates of the Bee Gorge spherule layer, Woodhead et al. (1998) obtained a date of 2541 + 18/−15 Ma consistent with the date interpolated from the nearest tuffs stratigraphically. Zircon crystals were also extracted from the Bee Gorge spherule layer and yielded a SHRIMP date of 2565 ± 9 Ma (Trendall et al. 2004). The zircon grains analyzed were relatively small, few in number, and gave diverse results, so this age is thought to be older than the depositional age of the Bee Gorge spherule layer. The layer contains fine quartzose epiclastic detritus (Simonson 1992; Simonson et al. 1998), so the zircons analyzed were probably reworked from older tuffs and/or basement rocks. In summary, the Bee Gorge spherule layer was probably deposited ~2.54 Ga or about 40 million years before the Archean-Proterozoic boundary.

8.2.3.4 Geographic Distribution and Variation

The Bee Gorge spherule layer is exposed throughout most of the main outcrop area of the Hamersley Basin, but it has yet to be recognized in the southwestern or extreme western parts of the Hamersley Basin or in the Oakover River area (Fig. 8.2c). At present, the most widely separated sites known are some 330 km

away from one another along a northwest-southeast line. Simonson (1992) recognized three different paleogeographic zones moving down the paleoslope in the Bee Gorge spherule layer. Specifically, it is thickest and coarsest in the northeast (zone A) and thinnest and finest to the south and west (zone C) with zone B intermediate. The characteristics of the layer in each zone are summarized below.

In zone A, the Bee Gorge spherule layer consists mostly of intraclastic peloids of carbonate and shale in the fine to medium sand size grades (0.125–0.5 mm across). It also contains tabular intraclasts of carbonate up to 62 cm long (Fig. 8.8a), spherules (described above), and traces of fine to very fine sand-size quartzo-feldspathic detritus (Simonson 1992). The latter appears to be normal epiclastic sediment derived from the Pilbara shield rather than solid impact ejecta (Simonson et al. 1998). The large intraclastic slabs were presumably formed by substrate erosion and transported relatively short distances, as were smaller pebble-size intraclasts of shale and oxidized pyrite. The layer in zone A consists of one to three beds showing normal grading, planar lamination, and/or climbing current ripple cross stratification whose contacts are generally horizontal with scours up to ~10 cm deep (Hassler and Simonson 2001). All three beds have stratification typical of low-density turbidites and commonly show liquefaction structures. Spherules are present in the lower two beds but not in the uppermost, and they are generally highly concentrated within a centimeter of the base of a given bed. The paleocurrents that deposited the Bee Gorge spherule layer in zone A generally flowed towards the south and southwest based on the dip of the cross-stratification (Fig. 8.8c), the direction of imbrication of the large intraclasts, and the asymmetry of the larger scours (Simonson et al. 1993a). The maximum thickness of the layer in published descriptions is 130 cm (Simonson 1992), but locally it ranges up to 350 cm.

In zone B, the Bee Gorge spherule layer shows the same depositional features as in zone A and was deposited by paleocurrents moving in the same directions, south to southwest. The principal difference is that large carbonate intraclasts are absent but oxidized pyritic intraclasts are locally abundant (Fig. 8.8b). The latter are commonly disc-shaped, up to ~2 cm long, and closely resemble early diagenetic pyritic concretions in associated black shales. They tend to rest on ripple foresets and are therefore generally imbricated to the south and west. As noted at the outset, neither the sizes, the textures, nor the aggregate thickness of the spherules in zone B differ significantly from those in zones A or C (Scally and Simonson 2005).

Zone C comprises just a few sites deeper on the paleoslope, but the Bee Gorge spherule layer differs from zones A and B in that it is split into two parts. The lower part is a zone up to several centimeters thick rich in spherules and the upper part is a spherule-free current-deposited dolomite bed ~10 cm thick. The two are separated by shale ~0.5 to 7 cm thick that appears to be free of spherules. The spherule-rich zone consists of multiple layers or lenses ranging from stringers one spherule thick (Fig. 8.8d) to symmetrical lenses 1–3.5 cm thick. Most commonly, spherules are concentrated into a single train of lenses averaging 32 cm crest to crest by 1.5 cm in maximum thickness. Hassler et al. (2000) interpreted these

lenses as anorbital wave ripples and attributed them to an impact-induced tsunami (discussed below). The current-deposited dolomite bed is thought to be a downslope equivalent of the turbidites of zones A and B; the absence of spherules has been attributed to the fact that the turbidity currents were less energetic further downslope and therefore did not erode the substrate (Hassler and Simonson 2001).

The Bee Gorge spherule layer was deposited below wave base as it is enclosed by fine-grained sediments largely deposited by suspension settle-out within which calcarenites and tuffs with features typical of turbidites are widespread (Simonson et al. 1993a,b; Hassler 1993). The deposition of the layer in zones A and B has been attributed to low-density turbidites coming in pulses rather than a single event (Hassler and Simonson 2001; Hassler et al. 2005). Many turbidites in the Bee Gorge Member (including the Bee Gorge spherule layer) thin and fine rapidly towards the south and west and have structures indicating paleoflows in the same directions (Simonson et al. 1993a). The Bee Gorge spherule layer closely resembles other thick carbonate turbidites in zones A or B, but is neither the thickest in the Bee Gorge Member nor the only one with large rip-up clasts. Glikson (2004b) attributed the multiple beds to multiple impacts; this is unlikely given the textural consistency of the spherules throughout the layer (Scally and Simonson 2005). Moreover, similar composite layers are present in both the K-T boundary layer (Yancey 1996; Chap. 5) and the Acraman ejecta layer (Gostin et al. 1986; Chap. 7). In contrast, the spherules in zone C were probably deposited under the influence of unusually large impact-induced waves. Hassler et al. (2000) based this conclusion largely on the fact that no other wave-generated structures have been reported from the Bee Gorge Member and C was the deepest of the three zones (Simonson et al. 1993a). Hassler et al.'s (2000) calculations suggest the site of the impact was roughly 1,650–2,000 km away from the Hamersley Basin (see Sect. 10.3.11 for further discussion). The turbidity currents that deposited the Bee Gorge spherule layer may represent bottom return flow produced by onshore surges of impact-generated tsunamis (Hassler and Simonson 2001), but the spherule-free shale between the spherules and the carbonate turbidite in zone C runs counter to this interpretation. If the carbonate turbidite is indeed a downslope continuation of those in zones A and B, the interposed shale suggests significant time elapsed between the events that deposited them. Whatever processes deposited the Bee Gorge spherule layer, the fact that the spherules are the same size in all three zones and larger than other types of sand suggests they were dispersed as impact ejecta rather than transported down the paleoslope by normal (albeit high energy) currents and waves.

8.2.3.5 Extraterrestrial Component and Shock Metamorphism

Based on PGE analyses of 12 samples, spherule-rich portions of the Bee Gorge spherule layer contain up to 1.5 % by weight of extraterrestrial material (Simonson et al. 2009b). The concentration of Ir in spherule-rich samples from the layer is consistently about one order of magnitude higher than it is in associated shales,

cherts, and carbonates of the Wittenoom Formation. Specifically, 9 spherule-rich samples from the base of the Bee Gorge spherule layer averaged 0.32 ppb Ir whereas 13 samples from associated strata free of spherules contained 0.04 ppb Ir on average (Simonson et al. 1998, 2009b). The concentration of Ir in 3 samples from the upper part of the layer also averaged 0.04 ppb, indicating spherules and other ejecta were highly diluted by the intraclastic material forming most of the layer. Simonson et al. (1998) reported Ir values as high as 1.69 ppb from samples then correlated with the Bee Gorge spherule layer, but these samples came from the Billygoat Bore core (described in Simonson and Hassler 1997) and were subsequently recorrelated with the Jeerinah spherule layer (Hassler et al. 2005; see Sect. 8.4.1 for more discussion).

The presence of extraterrestrial material in the Bee Gorge spherule layer is also reflected in the interelement ratios of the PGEs. When normalized to chondritic abundances (Fig. 8.6), the PGE ratios for the Bee Gorge spherule layer are essentially flat from Ir to Rh, i.e., unfractionated relative to CI chondrites (Simonson et al. 1998, 2009b). The concentrations of Pd and Au are more variable in the layer, suggesting some differential remobilization after deposition (Simonson et al. 1998, 2009b). Samples from the Bee Gorge spherule layer have yet to be analyzed for extraterrestrial Cr via the isotopic method because of the low abundance of extraterrestrial material. The low level and narrow range of PGE concentrations likewise prevented Simonson et al. (2009b) from shedding any light on the composition of the impactor.

Given the low level of extraterrestrial material in the Bee Gorge spherule layer spherules, they must have originally consisted largely of mass derived from terrestrial target materials. Although the spherules' primary phases were replaced wholesale during diagenesis, analyses of rare earth elements (REEs) place some constraints on the nature of the target material. Despite the fact that the internal textures of some spherules (described in Sect. 8.2.3.2) suggest they were originally mafic or low-silica melts, the fact that spherule-rich samples are enriched in light REEs relative to chondritic materials (Fig. 7 in Simonson et al. 2009b) suggests the target did not consist exclusively of LREE-depleted material such as mid-ocean ridge basalt. The presence of some continental crust in the target area would help explain the observed REE patterns, assuming they have not been disturbed during diagenesis. In contrast, the Jeerinah spherule layer has relatively flat REE patterns when normalized to chondritic values (see Sect. 8.2.6.5 for discussion).

Smith et al. (2010) identified particles of an α-PbO_2-structured TiO_2 phase (TiO_2II) among heavy minerals isolated from a sample of the Bee Gorge spherule layer. A total of 23 similar particles have been isolated from the Bee Gorge spherule layer, as well as the Jeerinah, Carawine, and Monteville spherule layers (described below). These particles appear to be the first shock-induced, high-pressure polymorphs recognized from spherule layers formed around the Archean-Proterozoic boundary or earlier. None were found in seven samples of ambient carbonate that were collected close to these spherule layers stratigraphically and analyzed for control. No other evidence of shock metamorphism has been found in the Bee Gorge spherule layer.

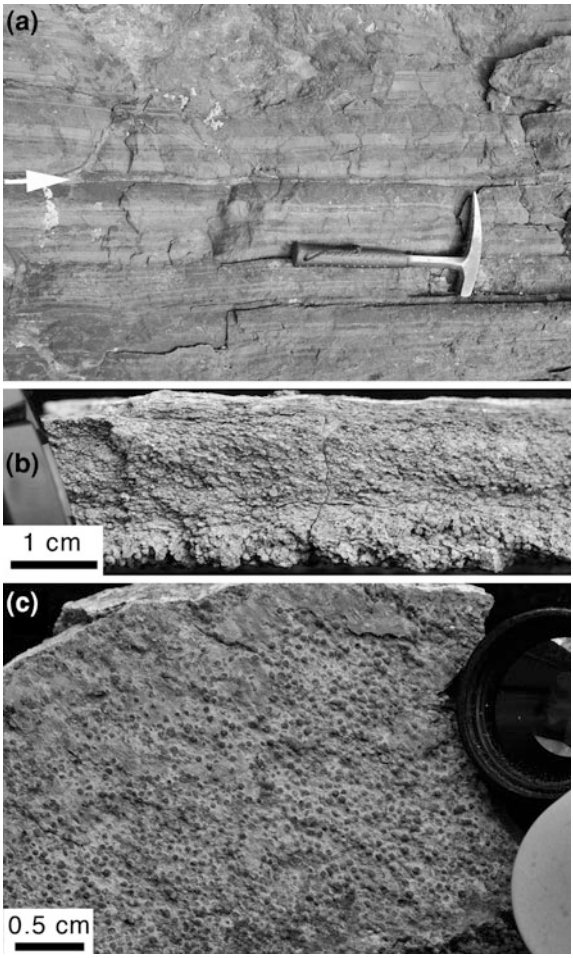

Fig. 8.11 Images of the Paraburdoo spherule layer. **a** Outcrop of the Paraburdoo spherule layer (*at level of arrow*) with thinly laminated, basinal dolomite typical of the Paraburdoo Member directly above and below it. Rock hammer is ~32 cm long. **b** Close-up of weathered surface of entire Paraburdoo spherule layer showing normal grading plus a little shale on *top*. **c** Underside of the Paraburdoo spherule layer showing dominance of spherules. **a** and **b** are from Hassler et al. (2011), Figs. 2a and b, respectively, with permission from the Geological Society of America

8.2.4 Paraburdoo Spherule Layer, Wittenoom Formation

8.2.4.1 Description of Layer

Stratigraphically, the Paraburdoo Member lies beneath the Bee Gorge Member within the Wittenoom Formation (Fig. 8.1) The Paraburdoo Member consists of dolomite with minor shale and chert and shows sedimentary structures typical of muds deposited below wave base in basinal paleoenvironments (Fig. 8.11a; Simonson et al. 1993a; Simonson and Carney 1999). It is restricted to the main outcrop area of the Hamersley Basin where it is either the basal unit in the Wittenoom Formation or underlain by shale of the West Angela Member (Blockley et al. 1993). Most of the carbonate mud that became the Paraburdoo Member was probably derived from a shallow-water carbonate platform to the

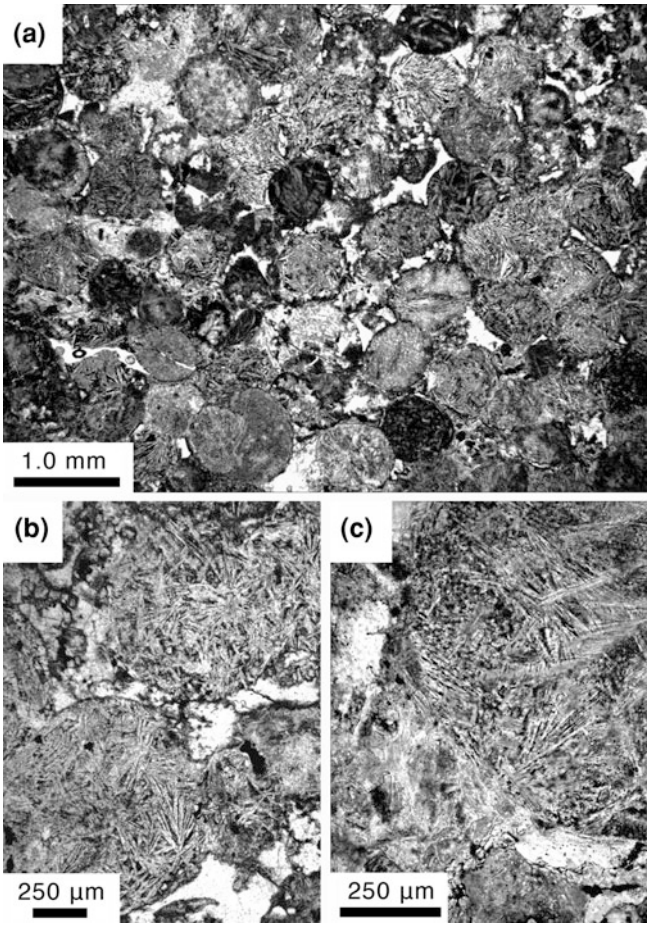

Fig. 8.12 Photomicrographs, taken in plane polarized light, of spherules from the Paraburdoo spherule layer. **a** Typical spherules that consist largely of K-feldspar and are both highly crystallized and texturally heterogeneous. The shard-shaped patches of carbonate (*white*) are interstitial cement, but most pores were compacted out of existence. **b** Two circular spherules with an abundance of lath- to needle-shaped K-feldspar microlites radiating fairly randomly. The circular edges of the spherules are well-displayed where sparry carbonate cement is present but not elsewhere. **c** Part of one spherule (*upper right side*) containing both thin K-feldspar microlites and darker, broader pseudomorphs of phlogopite, some with faceted terminations (probably replaced olivine). The mesostasis is a combination of K-feldspar, phlogopite, and finely disseminated opaques. The material in the *lower left* is more highly compacted spherules and matrix

north and east, part of which survived as the Carawine Dolomite (see Sect. 8.2.5; Simonson et al. 1993a; Simonson and Hassler 1996; Beukes and Gutzmer 2008). As noted in Sect. 8.2.3.1, the Bee Gorge spherule layer was referred to as the Wittenoom spherule layer in earlier publications; this had to be changed after the

Paraburdoo spherule layer was discovered ~170 m lower stratigraphically in the same formation.

In contrast to other Hamersley layers found to date, the Paraburdoo spherule layer consists almost entirely of spherules and lacks any signs that high energy processes were involved in its deposition (Hassler et al. 2011). Specifically, there are no structures indicative of current or wave reworking, it contains no obvious intrabasinal (e.g., rip-up clasts) or extrabasinal (e.g., quartzose detritus) sediment, and the base of the layer is not erosive. The Paraburdoo spherule layer is ~2 cm thick and generally normally graded (Fig. 8.11b). These features suggest the spherules in the layer settled to the seafloor with little or no reworking. Direct deposition of spherules without reworking is exceptional among Precambrian layers but has been reported from Paleoarchean spherule layers in the Barberton Greenstone Belt (Lowe et al. 2003; Chap. 9). The fact that the dolomite enclosing the Paraburdoo spherule layer looks the same above and below the layer (Fig. 8.11a) suggests there were no long-term environmental changes caused by this impact. Spherules appear to be absent from the layers around the Paraburdoo spherule layer.

8.2.4.2 Description of Spherules

The spherules in the Paraburdoo spherule layer are medium to coarse sand size and average about 0.5 mm in diameter. In the normally graded occurrences mentioned in Sect. 8.2.4.1, the spherules range in maximum diameter from 0.8 mm at the base to 0.4 mm at the top of the layer. Most were originally spheroids to ovoids (Figs. 8.11c, 8.12a), but many had their shapes modified by compaction. This is evidenced by a high number of contacts per grain and a high incidence of long and concavo-convex intergranular contacts in the layer (Fig. 8.12a). Generally, little cement is in evidence in the Paraburdoo spherule layer, but small shard-like pockets of sparry carbonate are present locally (Fig. 8.12a). As in the Bee Gorge spherule layer and Dales Gorge spherule layer, sparry carbonate crystals replace Paraburdoo spherule layer spherules locally and generally obscure or obliterate internal textures.

Internally, the Paraburdoo spherule layer spherules show an abundance of fibrous to lath-shaped K-feldspar microlites that, like those in the Dales Gorge and Bee Gorge spherule layers, appear to be pseudomorphs of plagioclase (Fig. 8.12b). However, the Paraburdoo spherule layer spherules are crystallized to a greater degree than those of the Dales Gorge spherule layer and Bee Gorge spherule layer. Laths are particularly abundant in spherules from the Paraburdoo spherule layer whereas radial-fibrous rims are rare (Fig. 8.12). In addition, the Paraburdoo spherule layer spherules have pseudomorphs consisting of finely crystalline phlogopite with shapes not seen in any of the other Hamersley layers. Specifically, approximately one-third of the spherules in the layer contain patches of phlogopite in elongated strips and/or more polygonal shapes that appear to be pseudomorphs of larger skeletal crystals (Figs. 8.12c, 8.13). The elongated strips are broader and

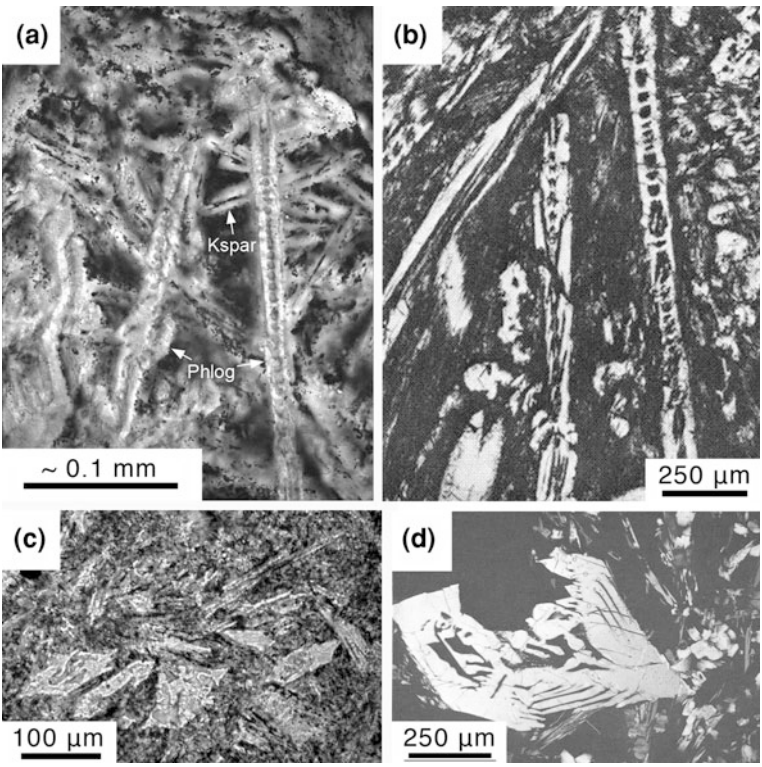

Fig. 8.13 Photomicrographs, taken in plane polarized light, of phlogopite pseudomorphs in spherules from the Paraburdoo spherule layer and analogous textures in basalts. **a** Interior of a spherule containing phlogopite pseudomorphs (Phlog) of highly elongated crystals with trains of small internal cavities that appear to have crystallized before the crystallization of the crystals pseudomorphed by K-feldspar (Kspar), which are smaller, slimmer, and tend to have central *dark lines* (probably replaced plagioclase). The mesostasis is rich in opaque material. **b** Chain pigeonite formed experimentally by rapid cooling of a basaltic melt; chain olivines are similar but generally smaller (Lofgren 1980). **c** Interior of a spherule containing phlogopite pseudomorphs of skeletal, doubly terminated crystals in a mesostasis consisting of phlogopite, K-feldspar, and finely disseminated opaques. **d** Skeletal, doubly terminated or hopper crystal of olivine in a lunar basalt. **b** is from Lofgren (1980), Fig. 11c; **c** is from Hassler et al. (2011), Fig. 4a, with permission from the Geological Society of America; and **d** is from Donaldson (1976), Fig. 9b

longer than the K-feldspar laths and many resemble ladders or chains due to small internal cavities (Fig. 8.13a). In contrast, the more polygonal pseudomorphs have larger, more irregular internal cavities and some have faceted terminations (Fig. 8.13c). These appear to be pseudomorphs of skeletal clinopyroxene and/or olivine crystals, respectively, as their shapes are identical to skeletal crystals grown experimentally (Fig. 8.13b,d) and naturally, e.g., in komatiites and chondrules (Hassler et al. 2011). In keeping with their high degree of crystallization, few candidates for vesicles or large patches of replaced glass have been observed in Paraburdoo spherule layer spherules. However, small areas of finely

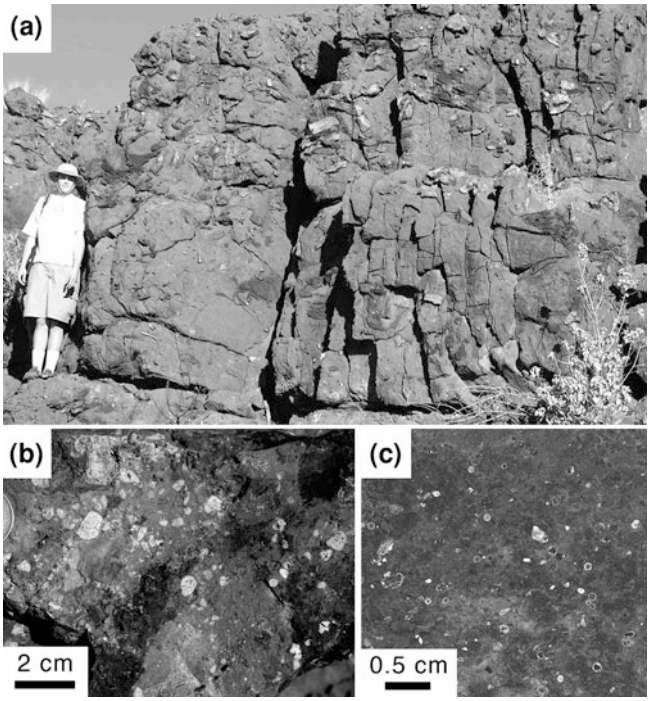

Fig. 8.14 Images of the Carawine spherule layer. **a** Weathered outcrop of a small part of the full thickness of the Carawine spherule layer showing its dolomite-rich composition and dispersed chert intraclasts that are resistant to weathering. Most of the dolomite is incorporated into intraclasts larger than the chert ones and bedding is chaotic. Geologist is ~2 m tall. **b** Close-up of weathered face near the base of the Carawine spherule layer where it is unusually rich in irregular particles of former silicate melt (the *lighter gray*, *pebble*-like particles; like those in Fig. 8.16). The dolomite matrix is discolored by manganese and iron oxides and/or hydroxides (*dark gray*); spherules are present but not visible at this distance. **c** Polished slab typical of the Carawine spherule layer with spherules (*light*) dispersed in sparry dolomite discolored by weathering (*dark*)

crystalline material between the crystal pseudomorphs presumably represent glassy mesostasis that was replaced during diagenesis.

8.2.4.3 Radiometric Age

The age of the Paraburdoo spherule layer is not well constrained. The closest control point is the aforementioned date of 2561 ± 8 Ma from a tuff near the base of the overlying Bee Gorge Member (Trendall et al. 1998). Stratigraphically, this tuff is about 100 m above the Paraburdoo spherule layer (Fig. 8.1). The closest control point stratigraphically beneath the layer is the aforementioned date of 2597 ± 5 Ma from a tuff in the Marra Mamba BIF (Trendall et al. 1998). The total thickness of the Paraburdoo Member is roughly 300 m (Simonson et al. 1993b)

and the Paraburdoo spherule layer is approximately 70 m below its top. The Marra Mamba BIF is about 180 m thick on average (Trendall 1983) and the dated tuff is located about one-fourth of the way below its top stratigraphically. Therefore, the stratigraphic separation of the dated Marra Mamba tuff and the Paraburdoo spherule layer is roughly 275 m. Accepting these thicknesses and dates at face value and proportioning between them yields a depositional age of ~2.57 Ga for the layer. Tuffs are rare in the Paraburdoo Member so it may be difficult to constrain the age of the Paraburdoo spherule layer with greater accuracy.

8.2.4.4 Geographic Distribution and Variation

To date, the Paraburdoo spherule layer has only been identified at 3 sites in surface exposures. Each of these exposures is limited in extent; for example, the layer is only exposed for a strike length of ~6 m at the discovery site. The 3 sites all lie in a straight line ~150 km long in the south-central part of the Hamersley Basin (Fig. 8.2b). The sizes and aggregate thicknesses of the spherules are essentially the same at all 3 sites. Likewise the depositional structures in the Paraburdoo spherule layer do not seem to change significantly from one site to the next. Simonson et al. (1993a,b) measured multiple sections of the Paraburdoo Member throughout its area of occurrence but failed to recognize the spherule layer in either core or outcrop. Several possibilities could explain this oversight, as follows: (1) the layer may have been overlooked due to its thinness; (2) the Paraburdoo spherule layer may have been eroded in shallower paleoenvironments north of the sites where it was ultimately discovered; and/or (3) the stratigraphic interval in which the spherule layer occurs may have been removed during diagenesis. Option 3 is a serious possibility as there was significant dissolution of carbonates in the upper Paraburdoo Member, particularly in close proximity to large iron ore deposits (Simonson et al. 1993a). As with the Dales Gorge spherule layer and Bee Gorge spherule layer, the characteristics of the Paraburdoo spherule layer suggest it is probably relatively distal ejecta from a large impact.

8.2.4.5 Extraterrestrial Component

Six samples from the Paraburdoo spherule layer that were analyzed for their PGE content yielded Ir concentrations ranging from 131 to 357 ppb; they also display a chondrite-normalized pattern that is essentially flat from Ir to Rh, whereas Pd and Au are strongly depleted (Goderis et al. 2012). These are the highest concentrations of Ir found to date in any samples from an Archean-Proterozoic boundary spherule layer. The highest concentration of Ir in the Paraburdoo spherule layer is equivalent to a content of ~70 wt % chondritic material in the sample, which consists almost entirely of spherules. This composition is consistent with the textures described in Sect. 8.2.4.2, particularly the presence of pseudomorphs of ferromagnesian silicate minerals that suggests the spherules were originally mafic,

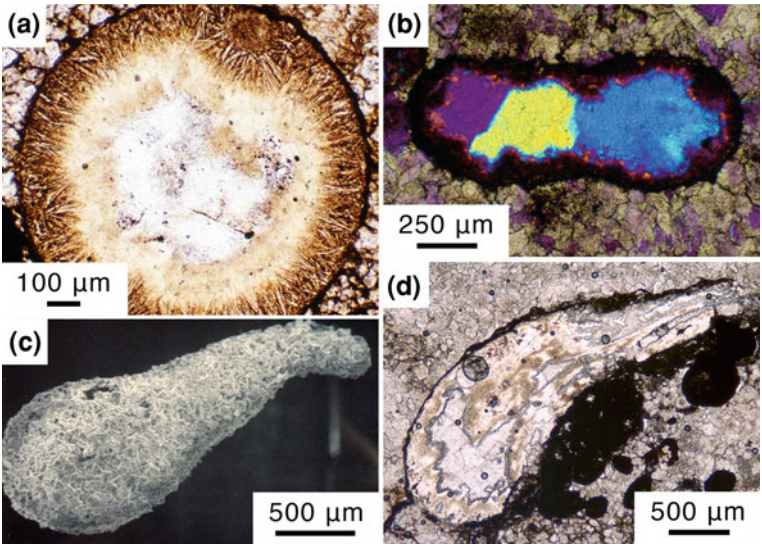

Fig. 8.15 Photomicrographs of splash form particles from the Carawine spherule layer. **a** Perfectly circular spherule, taken in plane polarized light, with tan rim of K-feldspar microlites projecting inward from the outer edge. The central spot consists of a combination of K-feldspar crystals that are optically continuous with the rim (*pale tan*) and coarse quartz crystals (*clear center*). Spherule is surrounded by a mosaic of dolomite crystals that is typical of the Carawine spherule layer. **b** Spherule, taken with crossed polarizers using a gypsum plate, that is like the one in **a** except it has a dumbbell shape and the center consists of a few quartz crystals (probably a replaced glass core). The surrounding mosaic of dolomite crystals is again typical of the Carawine spherule layer. **c** SEM image of a *teardrop*-shaped particle with a bent tip (*upper right*) that was liberated by dissolving a sample in HCl. Its pitted surface is due to many small rhombic impressions from dolomite crystals that replaced the edge of the particle. **d** Another teardrop-shaped particle, taken in plane polarized light, with faint longitudinal flow banding in middle. It consists of K-feldspar (*mottled tan areas*) except where it was replaced by coarse carbonate crystals (clear patches with jagged edges). The opaque bodies in the surrounding dolomite are probably oxidized pyrite (possibly intraclasts)

if not ultramafic, in composition. This in turn suggests the spherule layer is the product of an impact into a target that was more mafic than the other Hamersley layers and/or it contains significant amounts of chondritic material. The high levels of Ir and other PGEs in the Paraburdoo spherule layer favor the latter of these two possibilities. We are not aware of any attempts to perform Cr isotope analyses on the Paraburdoo spherule layer.

The Paraburdoo spherule layer has been correlated with the Reivilo spherule layer in the Griqualand West Basin based on textural and stratigraphic similarities (discussed in Sect. 8.3.3; Hassler et al. 2011). Like the Paraburdoo spherule layer, the Reivilo spherule layer has higher Ir concentrations than any of the other Archean-Proterozoic boundary spherule layers analyzed to date (Simonson et al. 2009b). Moreover, the relative proportions of the PGEs analyzed in the Paraburdoo spherule layer are very similar to those in the Reivilo spherule layer (Goderis

et al. 2012). The relative proportions of the PGEs analyzed in these two layers also show a pattern similar to those in the S4 spherule layer of the Barberton Greenstone Belt (Fig. 9 in Simonson et al. 2009b—see Sect. 8.3.3.5 for further discussion).

8.2.5 Carawine Spherule Layer

8.2.5.1 Description of Layer

The oldest spherule layer in the Hamersley Group, the **Carawine spherule layer**, is located near the base of the Carawine Dolomite stratigraphically (Fig. 8.1). It has only been identified in the Oakover River area where it crops out in two places separated by ~70 km (Fig. 8.2c); one is a strike belt ~10 km long on the southern edge of the Ripon Hills and the other is a smaller area to the southeast known informally as the Tara Tara Turnoff or TTT (Hassler et al. 2005) (see Sect. 8.2.5.4 for further description of these sites). Originally called the "dolomixtite" (Simonson 1992), the Carawine spherule layer ranges from ~7 to 25 m thick in its known occurrences (Fig. 8.14a), making it the thickest of any early Precambrian spherule layer. Like the other layers near the Archean-Proterozoic boundary, it is the only layer known to contain spherules in its host formation or member. Spherules and related particles combined make up ~2 % of this layer by volume (Fig. 8.14a,b) so their aggregate thickness is ~30 cm. The Carawine spherule layer also contains the coarsest formerly molten impact ejecta in any Archean layer, with particles up to at least 2 cm across (Fig. 8.14b).

The Carawine Dolomite overall is >500 m thick and also restricted to the Oakover River area (Fig. 8.2c). None of the other formations of the Hamersley Group extend into the Oakover River area except for the Marra Mamba BIF, which pinches out to the northeast and is absent at the Carawine spherule layer sites. However, the uppermost unit of the underlying Fortescue Group, known as the Jeerinah Formation, extends throughout the entire Hamersley Basin. The Carawine Dolomite rests directly and conformably on the Jeerinah Formation at the Carawine spherule layer sites. Most of the Carawine Dolomite was deposited in platformal, i.e. shallow-water, paleoenvironments, but some intervals (particularly low in the formation stratigraphically) accumulated in basinal paleoenvironments where Simonson et al. (1993a) estimated the water was at least 200 m deep. The Carawine spherule layer is enclosed by basinal strata, but platformal features typical of most of the Carawine Dolomite begin to appear a few tens of meters above this layer stratigraphically (Dawn Sumner, personal communication, 2007). The basinal Carawine strata are very similar to those of the Paraburdoo Member of the Wittenoom Formation, which has been correlated with the Carawine Dolomite as a whole (Rasmussen et al. 2005; Hassler et al. 2005). As with the Paraburdoo spherule layer, the strata directly above and below the Carawine spherule layer do not appear to contain any spherules or show any changes in sedimentary features,

suggesting there was little long-term environmental change at the time of the impact.

In all its occurrences, the Carawine spherule layer is a thick, coarse-grained, poorly sorted layer dominated by dolomitic sediment (Fig. 8.14a). It is ~25 m thick in the Ripon Hills area versus ~7 m thick at the TTT site, but it is a composite of three amalgamated subunits at both sites (Hassler and Simonson 2001; Hassler et al. 2005). Each subunit has a lower part rich in pebble- to boulder-sized clasts and a finer-grained upper part. The larger clasts are mostly laminated carbonate slabs (like the enclosing strata) that range up to 2.2 m in length and formed by scour and redeposition (Simonson et al. 1993a). This is consistent with the fact that the basal contact of the Carawine spherule layer is erosive with local relief of at least 25 cm. This layer also contains lesser amounts of smaller chert intraclasts and scattered platformal carbonate clasts such as cross-bedded oolites up to 20 cm across (Simonson et al. 1993a). The three subunits were probably deposited in rapid succession by three debris flows. This event may have been triggered directly by the impact which formed the spherules; in fact, the coarser Carawine spherule layer breccias resemble some of the more proximal K-T ejecta in Belize (Smit et al. 2002). Alternatively, the debris flows that formed this layer may have been triggered by subsequent, potentially unrelated events. Carbonate debris flows occur elsewhere in the Hamersley Group (e.g., Kepert 2001), but few are as thick or as coarse-grained as the Carawine spherule layer. No spherules have been reported from any other layer in the Carawine Dolomite or from any other carbonate debris flow in the Hamersley Basin.

Spherules are present in both the upper and lower parts of each subunit within the Carawine spherule layer, but they are more abundant in the upper parts of the subunits. The larger, more irregular melt particles (described in Sect. 8.2.5.2) mainly occur within 2.5 m of the base of the layer as a whole (Fig. 8.14b). At the TTT site, the Carawine spherule layer is capped by a carbonate layer 30 cm thick that displays climbing current ripple cross-lamination, so it must have been deposited as well-sorted sand. This layer contains rare spherules and irregular particles in its lower third and was probably deposited by a low-density turbidity current.

Terrigenous sand makes up about 2 % by volume of the Carawine spherule layer (Simonson et al. 2000b; Jones-Zimberlin et al. 2006). It consists largely of subrounded to very well-rounded quartz grains of medium to coarse sand size, which is the coarsest terrigenous sand reported from any of the Hamersley spherule layers. The quartz grains display textures typical of basement rocks in Precambrian shields (Simonson et al. 1998); the layer also contains minor amounts of microcline and zircon. The terriginous sand in this layer at the TTT site may have a slightly different provenance than the sand in the Ripon Hills area (see Sect. 8.2.5.4).

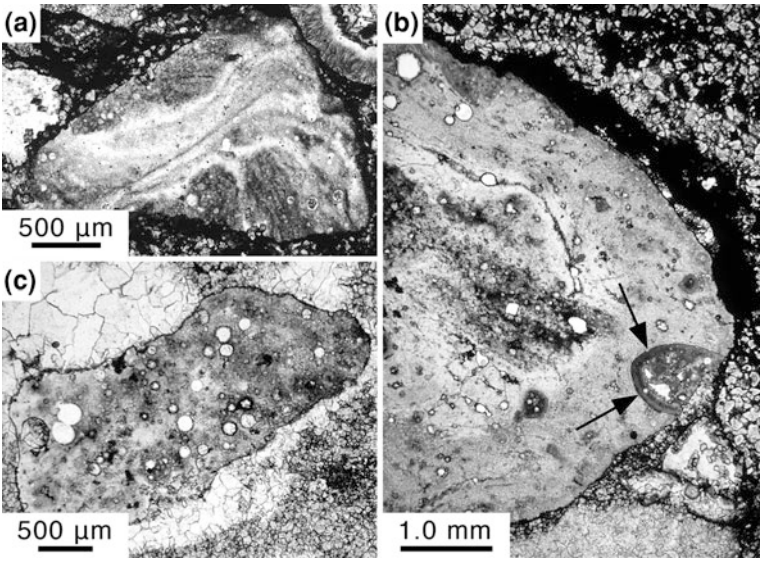

Fig. 8.16 Photomicrographs, taken in plane polarized light, of irregular particles consisting of almost pure K-feldspar from the Carawine spherule layer. **a** Angular particle with prominent internal flow banding that could be relict schlieren and small vesicles (*white*) filled with sparry carbonate and quartz crystals. The flow banding is sharply truncated at the edges of the particle and no fibrous rim is developed on same, in contrast to splash form spherules such as the one in the upper right corner. **b** Part of a larger ovoid particle like those in Fig. 8.14b that contains what appears to be a truncated spherule embedded in its side (*black arrows*). The dolomite along the bottom is a combination of recrystallized pebble-size carbonate intraclasts and formerly molten particles almost entirely replaced by carbonate; the dolomite in upper right is probably another intraclast that contains weathered pyrite. **c** A more rounded particle similar to the one in **a** but lacking banding and showing prominent circular vesicles (*white*) instead.

8.2.5.2 Description of Spherules and Related Particles

About half of the former melt particles in the Carawine spherule layer are typical millimeter-scale splash forms, i.e., spherical to rotational shapes (Fig. 8.15). However, unlike in the Dales Gorge and Bee Gorge spherule layers, the rest of the formerly molten particles have more irregular shapes and show different textures internally (Figs. 8.14b, 8.16; Simonson et al. 2000b). The spherules *per se* and irregular particles each make up ~1 vol % of the Carawine spherule layer (Fig. 8.14c), although locally they occur in much greater abundance. They are described separately below, although some particles are transitional in character. The irregular particles are described in more detail because they differ in character from most of the formerly molten particles described above.

Spherules *per se* range from 0.25 to over 2 mm in diameter, averaging about 1 mm. They are dominantly circular to oval in cross-section with a mean axial ratio (= minor axis ÷ major axis) of 0.84. About 13 % by number of the spherules are more elongated and shaped like dumbbells, peanuts, or teardrops

(Fig. 8.15b,c,d). Others show composite internal textures and were presumably fused in flight via agglutination. Internally, the most common textures in the spherules not replaced by carbonate are a combination of elongated K-feldspar microlites and areas (often central spots) that are clear in plane polarized light. The K-feldspar microlites tend to form radial-fibrous rims (Fig. 8.15a), although some are randomly oriented laths that resemble basaltic textures. The clear spots consist of sparry K-feldspar, carbonate and/or quartz crystals or finely felted chlorite or sericite. As in the Dales Gorge spherule layer and Bee Gorge spherule layer, these spots are interpreted as a combination of cement-filled vesicles and replaced glass cores (Simonson et al. 2000b; Simonson 2003a).

On average, the more irregular particles are larger, more angular, and more elongated than the spherules. The largest irregular particles observed to date are 20 mm across. The mean axial ratio of the irregular particles is 0.65 (Simonson et al. 2000b); none show the perfectly circular to oval cross-sections observed in many spherules. However, a few of the smoother and more rounded "irregular" particles have shapes like splash forms, e.g., teardrops. Internally, the irregular particles consist largely of K-feldspar, but few show the radial-fibrous rims or fans seen in many spherules. Instead, many irregular particles contain planar to swirling lines that resemble flow banding or schlieren (Fig. 8.16). The K-feldspar in such particles tends to be sub-microscopic but optically aligned parallel to the banding. However, many irregular particles contain thin lath-shaped microlites of K-feldspar like those in the Carawine spherule layer spherules *per se* as well as in other Archean-Proterozoic boundary spherule layers. These microlites vary in abundance from rare to widespread and in orientation from crudely aligned parallel to flow banding (where present) to randomly oriented. In addition, a minority of the irregular particles contain local pockets or layers rich in sprays of minute lath-shaped crystals that closely resemble some of the fabrics in the spherules.

About 95 % of the irregular particles contain vesicles, but they generally take the form of disseminated small vesicles (Fig. 8.16b) instead of the larger single vesicles present in some spherules (e.g., Fig. 8.10c,e). The vesicles are generally filled with secondary sparry quartz or carbonate and/or sericite. Larger vesicles tend to be elongated parallel to the long axes of the irregular particles, particularly those with pronounced banding. The vesicles only make up $\sim$14 % by volume of the most vesicle-rich irregular particles.

Many of the larger irregular particles show considerable heterogeneity; some even consist of composites with sharp internal boundaries separating areas with very different textures. Some of these particles appear to be agglutinates formed by collisions of smaller particles in flight, including what appear to be solitary spherules (Fig. 8.16b). The latter have teardrop or oval shapes in cross-section and range from 0.36 mm to 0.68 mm across. Such particles indicate the spherules and irregular particles in the Carawine spherule layer are products of the same impact.

A few irregular particles (especially the more strongly banded and vesiculated ones) contain cloudy patches or lenses up to $\sim$0.6 mm long that resemble augen in deformed rocks. Such lenses consist mainly of clusters of quartz crystals up to $\sim$50 μm across, a few of which show parallel lines of minute inclusions that

resemble PDFs (Fig. 7b in Simonson et al. 2000b). Isolated quartz crystals ~40 μm across also occur as inclusions in some of the irregular particles, especially those that are more strongly banded and vesiculated. The irregular particles resemble Muong Nong-type tektites in their irregular blocky shapes, layering, and the possible presence of relict mineral inclusions. However, they differ from Muong Nong-type tektites in that they are smaller, more rounded, and probably were partially crystallized in flight.

Spherules and irregular particles in the Carawine spherule layer were both extensively modified during diagenesis; the nature of the modification was similar in some ways to that experienced by the spherules in the Dales Gorge and Bee Gorge spherule layers but different in others. One similarity is K-feldspar replacement; the laths and radial-fibrous fans are believed to be pseudomorphs of plagioclase (as explained in Sects. 8.2.2.2 and 8.2.3.2). On the other hand, the submicroscopic K-feldspar crystals replacing many of the flow-banded irregular particles have few analogs in the Dales Gorge spherule layer or Bee Gorge spherule layer. The K-feldspar probably formed via the replacement of glass. The greatest contrasts between the Carawine spherule layer and most younger layers are the higher abundance of spherules replaced by carbonate and the scarcity of shape modification by compaction in the Carawine spherule layer. Both are consistent with the fact that most of the spherules and irregular particles are isolated in sparry dolomite (Figs. 8.15, 8.16). As in other Archean-Proterozoic boundary layers, the replacive carbonate in the Carawine spherule layer obscures primary textures in spherules and irregular particles (e.g., Fig. 8.15d); some spherules survive only as circular "ghosts" in a mosaic of sparry dolomite. Other replacive phases are present locally, mainly chlorite and opaques such as pyrite (Simonson et al. 2000b). Despite the generally unmodified shapes of the spherules, stylolites are widespread in this layer. Spherules and irregular particles are more abundant close to some stylolites; they were concentrated there during diagenesis given the fact that silicates are much less susceptible to pressure solution than carbonate (Trurnit 1968). At least local cementation is indicated by the presence of rare spherules that disintegrated into small piles of rim fragments like the "eggshell diagenesis" described in the Bee Gorge spherule layer (Sect. 8.2.3.2).

8.2.5.3 Radiometric Age

Rasmussen et al. (2005) analyzed zircon crystals from a tuff ~30 m above the base of the Carawine Dolomite stratigraphically in its type area using a SHRIMP. They obtained an age of 2630 ± 6 Ma (Fig. 8.1). The Carawine spherule layer has not been identified in this area (see next section), but it is ~60 m above the base of the formation stratigraphically in the Ripon Hills area ~50 km to the northwest (Simonson and Hassler 1997). The only other published dates from the Carawine Dolomite were obtained via direct dating of carbonate. Using Pb–Pb isotopic analysis, Jahn and Simonson (1995) obtained a date of 2541 ± 32 Ma from 16 carbonate samples and Woodhead et al. (1998) obtained a date of 2548 +26/−29 Ma

from 12 carbonate samples. These dates do not constrain the deposition of the Carawine spherule layer tightly because the samples came from a broad range of stratigraphic levels. Given the fact that the average stratigraphic position of Woodhead et al.'s (1998) samples was ~190 m above the layer, at best they constrain the minimum age of the Carawine spherule layer. Because of its great thickness and the presence of a profound erosional unconformity at its top (Blake et al. 2011), no formations above the Carawine Dolomite can provide meaningful constraints on the age of the Carawine spherule layer. Likewise, no strata close beneath this spherule layer stratigraphically have been dated to our knowledge. Therefore the most that can be said at present is that the Carawine spherule layer was deposited before 2.63 Ga, possibly slightly earlier, and is Neoarchean in age. This interpretation is supported by the correlation of the Carawine spherule layer and the Jeerinah spherule layer discussed below.

8.2.5.4 Geographic Distribution and Variation

As noted above, the Carawine spherule layer is a coarse, poorly sorted layer deposited by three large carbonate debris flows at the two main sites where it has been described to date. However, thickness and certain other characteristics of this spherule layer change between the two sites. This layer is up to ~25 m thick in the Ripon Hills area versus ~7 m thick at the TTT site some 70 km to the southeast. The type area of the Carawine Dolomite lies about midway between these two sites, yet no trace of the Carawine spherule layer has been found there despite good exposures and extensive searching (Simonson 1992; Rasmussen et al. 2005). This suggests the layer is laterally discontinuous; possible causes could include (1) channelization of the debris flows, (2) postdepositional erosion of the layer, or (3) restriction of the original ejecta to lobes or rays. The second option seems unlikely given the thickness of the layer. Some differences in the make-up of the Carawine spherule layer at the two sites suggest the first option is a possibility. As noted above, this spherule layer at the TTT site is capped by a carbonate turbidite not seen in the Ripon Hills area. The latter contains the only known paleocurrent indicators in the Carawine spherule layer and they show paleoflow was towards the south-southwest, i.e., at right angles to the line connecting the Ripon Hills and TTT sites. Moreover, the large intraclasts at the TTT site are more diverse lithologically and shale and chert intraclasts are larger and more abundant on average compared to this layer in the Ripon Hills area (Hassler et al. 2005). These differences are consistent with, but do not prove, a different provenance for the Carawine spherule layer in these two areas. Additional localities have been reported along the western edge of the Ripon Hills (Fig. 8 of Glikson 2004b), but descriptions of the layer at these sites have not been published.

Several lines of evidence indicate the Carawine spherule layer was deposited in deeper water at the TTT locality than it was in the Ripon Hills area. First, the fact that this layer is much thicker in the Ripon Hills area suggests the TTT locality is farther from the carbonate platform. Secondly, the Carawine spherule layer lies

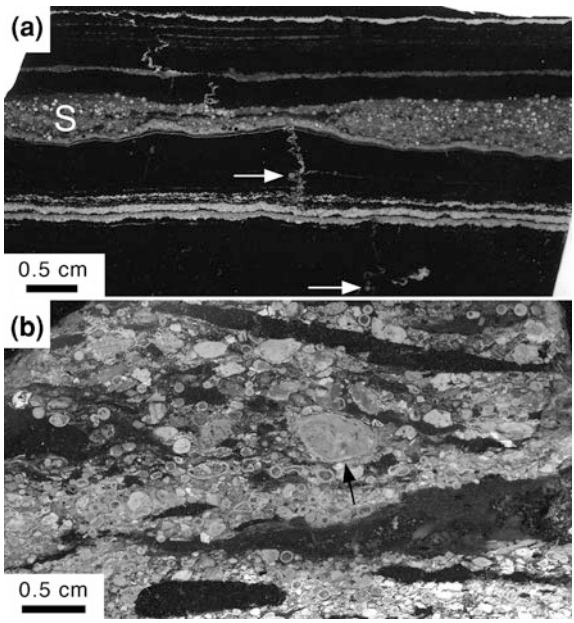

Fig. 8.17 Images of the Jeerinah spherule layer. **a** Scan of a large thin section from core FVG-1 showing the spherule layer (S) pinching and swelling laterally. It is encased in carbonaceous shale (*black*) with thin laminations of fine tuffaceous material (*light to medium gray*). Minute micro-folded soft sediment injection dikes cut across the shale above and below the spherule layer; but only those below the layer contain spherules (e.g., *at white arrows*). **b** Polished slab from the coarse basal zone at Hesta where larger, more irregular particles (e.g. *at black arrow*) and spherules are both abundant but cement is absent. Compacted rip-up clasts of local muds (probably weathered ferruginous shales and/or carbonates) form thin strips and lozenge-shaped bodies (generally *dark gray*). Many spherules also contain secondary quartz thought to be a product of weathering

above a thicker pile of carbonate sediments in the Ripon Hills area than at the TTT site. The Carawine Dolomite overlies the Jeerinah Formation conformably in both areas, but the Carawine spherule layer is $\sim$60 m above the Jeerinah stratigraphically in the Ripon Hills area (Simonson and Hassler 1997) versus $\sim$4 m above it at TTT (Hassler et al. 2005). Lastly, the stratigraphically lowest platformal features in the Carawine Dolomite appear in strata a few tens of meters above the Carawine spherule layer in the Ripon Hills area whereas none are that close to this layer stratigraphically in the TTT area. A more distal position could help explain the greater abundance of non-carbonate intraclasts at TTT since this site was farther from the shallow-water carbonate paleoenvironment.

As for the ejecta, the largest irregular particles observed in the Carawine spherule layer are in the Ripon Hills area and irregular particles are smaller on average at the TTT site. Average spherule size is also lower at TTT, but spherules and irregular particles make up a slightly higher percentage of the Carawine spherule layer samples from the TTT site (each about 1–4 vol % of the rock) compared to the 1

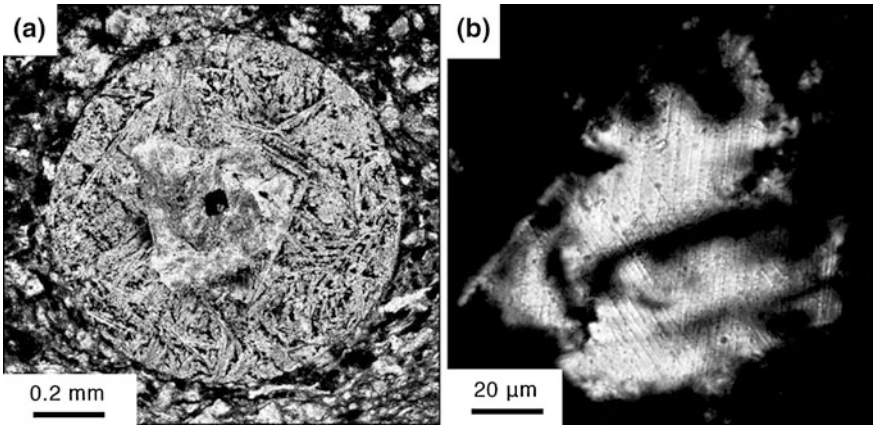

Fig. 8.18 Photomicrographs, taken in plane polarized light, of particles from the Jeerinah spherule layer. **a** Circular spherule from core WRL-1 that consists largely of lath-shaped, randomly oriented microlites of K-feldspar, but it also has a central area with a polygonal outline that may be a crystal pseudomorph. **b** A single quartz crystal from the Jeerinah spherule layer in core WRL-1 with two sets of *parallel lines* interpreted as PDFs. From Rasmussen and Koeberl (2004), Figs. 2c and d, respectively, with permission from the Geological Society of America

vol % of each in the Ripon Hills area (Jones-Zimberlin et al. 2006). Despite the variation in thickness of the layer, the aggregate thickness of spherules and irregular particles is about the same at both sites. No significant differences have been noted in the shapes, internal textures, or relative abundance of the spherules and/or irregular particles between the two sites, although irregular particles are slightly more abundant relative to spherules at the TTT site (Jones-Zimberlin et al. 2006).

8.2.5.5 Extraterrestrial Component, Target Material, Shock Metamorphism

Despite the fact that it consists largely of dolomite and contains the coarsest terrigenous detritus of any of the Archean-Proterozoic boundary layers, the Carawine spherule layer has a measurable component of extraterrestrial material. For example, 5 samples from this layer averaged 0.60 ppb Ir, whereas 11 samples from ambient shales, cherts, and carbonates that were free of spherules contained 0.033 ppb Ir on average (Simonson et al. 1998). The highest Ir concentration they obtained was 1.54 ppb. While this is low compared to some samples from the K-T boundary layer (see Chap. 5) and Paleoarchean spherule layers (see Chap. 9), all of the Carawine spherule layer samples analyzed consisted of dolomite with spherules and irregular particles much in the minority. One core sample analyzed had at best a few percent of spherule material yet still showed some Ir enrichment. It seems likely that a sample rich in spherules would produce a much higher Ir concentration.

Except for Ru, none of the other siderophile elements (Pd, Pt, Au, Cr, Co, and Ni) in the Carawine spherule layer samples analyzed by Simonson et al. (1998)

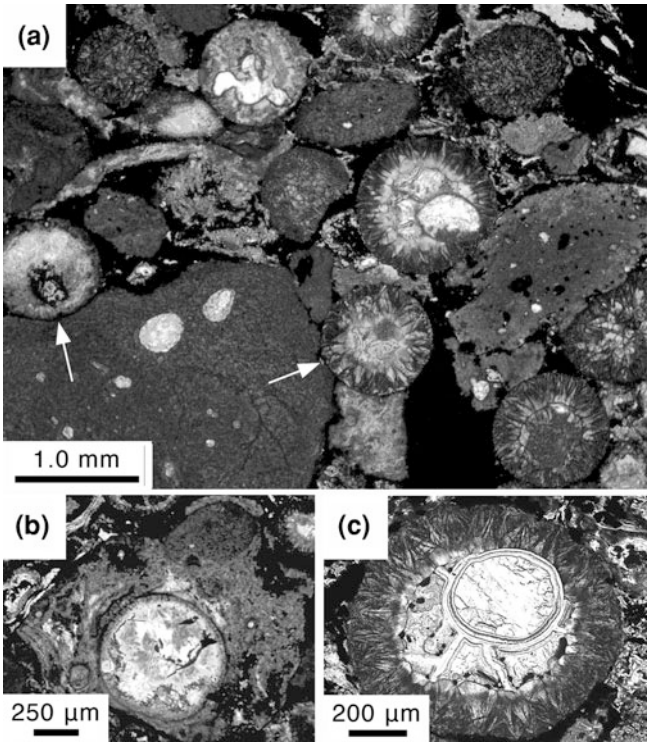

Fig. 8.19 Photomicrographs, taken in plane polarized light, of particles from the Jeerinah spherule layer. **a** Mixture of spherules (circular cross-sections, most having rims) and more irregular particles (mostly massive with small clear spots that are probably infilled vesicles) from the Hesta outcrop. Gray particles all consist largely of K-feldspar whereas dark gray to black areas are mostly intraclasts rich in iron hydroxides (probably weathered pyrite) with some sericite. No cement is present and many grains show evidence of compaction (e.g., contacts at arrows were modified by pressure solution). **b** An irregular composite particle from the Hesta oucrop that is locally flow-banded and appears to have a spherule with a thin rim and a darker ovoid irregular particle (*uppermost part*) embedded in it. **c** A spherule with a botryoidal rim of inward-radiating fibrous K-feldspar (*dark gray*) and a complex central spot consisting of sparry K-feldspar (clear) and isopachous ribbons of fibrous sericite (probably lining a former vesicle and following former cracks in a glass core). **a** and **b** are from Jones-Zimberlin et al. (2006), Figs. 3a and 6a, respectively. **c** is from Simonson et al. (2009a), Fig. 8c, with permission from the Geological Society of America

displayed significant anomalies relative to the background sediments. However, the interelement ratios of Ir, Ru, and Ni were close to chondritic. In addition, the Co content displayed a correlation with that of Ir, but the interelement relationship was not chondritic. Simonson et al. (1998) argued that these data lent support to the presence of extraterrestrial material in the Carawine spherule layer because the Acraman ejecta layer has a very similar PGE signature (see Sect. 7.2.3). Because it is clearly rich in impact ejecta, the non-chondritic ratios of Ir and other platinoids in the Acraman layer were ascribed to differential mobilization during low-

temperature diagenesis under reducing conditions (Wallace et al. 1990b). A similar response would be reasonable in the Hamersley Basin since the enclosing shales are pyritic and carbonaceous.

The clearest evidence that the Carawine spherule layer contains some extraterrestrial material comes from a chromium isotopic analysis of one sample from the basal zone collected close to and very similar to the sample that had the highest Ir concentration. Because of its relatively low Ir concentration, a differential dissolution procedure was used to yield phases that would be enriched in any extraterrestrial component. As described in Simonson et al. (2009b), one fraction had a ε^{53}Cr value of 0.16 ± 0.03, clearly signaling the presence of extraterrestrial material (Fig. 8.7). Mass balance calculations indicate a cosmic Cr concentration between 11 and 24 ppm for the bulk sample. This is equivalent to 0.3 to 0.6 wt % chondritic extraterrestrial material in the sample as a whole. A similar range of 0.2 to 0.4 wt % extraterrestrial material in the bulk sample is suggested by the Ir content. The positive Cr isotopic signature also distinguishes it from carbonaceous chondritic material and indicates an affinity for ordinary chondritic rather than enstatite chondritic material (Simonson et al. 2009b).

Neither the Cr isotope data nor the PGE analyses shed light on the composition of the target material. Some of the spherules in the Carawine spherule layer have internal textures suggesting they were basaltic in composition, but such textures are not nearly as abundant in the Carawine spherule layer as they are in the Dales Gorge spherule layer or Bee Gorge spherule layer (Scally and Simonson 2005; Jones-Zimberlin et al. 2006; Sweeney and Simonson 2008).

No PDFs or any other textures indicative of shock metamorphism have been detected in quartz grains from the Carawine spherule layer, but Smith et al. (2010) identified a high-pressure TiO_2 polymorph (TiO_2II) among heavy minerals isolated from a sample of this layer (as noted in Sect. 8.2.3.5).

8.2.6 Jeerinah Spherule Layer

8.2.6.1 Description of Layer

The **Jeerinah spherule layer** has been identified at one surface site (known as Hesta) and in three drill cores (DDH-186, FVG-1, and WRL-1) (Fig. 8.2c; Simonson et al. 2000a; Rasmussen et al. 2005; Hassler et al. 2005). Stratigraphically, the Jeerinah spherule layer is very near the top of the Roy Hill Shale, the uppermost Member of the Jeerinah Formation, which in turn is uppermost in the Fortescue Group (Fig. 8.1). The Roy Hill Shale is a carbonaceous and pyritic unit that was deposited during a major marine transgression after a prolonged period dominated by flood basalt volcanism (Thorne and Trendall 2001). In the drill cores, the Jeerinah spherule layer is a centimeter-scale bed consisting almost entirely of spherules sandwiched between thinly laminated shales typical of the Roy Hill Shale (Fig. 8.17a). In contrast, the layer is 1.6 m thick and enclosed by

weathered shale at Hesta. The aggregate thickness of spherules at Hesta is ~18 cm thanks to a coarse basal zone 50 cm thick with large rip-up clasts that is rich in spherules and irregular particles (Fig. 8.17b) like those in the Carawine spherule layer (described in Sect. 8.2.5.2). The Jeerinah spherule layer is ~2.5 m below the base of the Marra Mamba BIF stratigraphically at Hesta (Hassler et al. 2005) and ~2.7 m below it in core FVG-1 (Simonson et al. 2000a). It is located in a similar stratigraphic position in the other two drill cores. Further details of the Jeerinah spherule layer at all of these sites are given in Sect. 8.2.6.4.

Another drill core, the Billygoat Bore (BGB) core, contains a single spherule layer that has been variously described as either the Jeerinah spherule layer (Hassler et al. 2005) or the Carawine spherule layer (Rasmussen et al. 2005). The BGB core was drilled in the western part of the Oakover River area midway between the Jeerinah spherule layer and Carawine spherule layer occurrences described above (Fig. 8.2c). The layer is intermediate in thickness between the Jeerinah spherule layer as described below and the Carawine spherule layer as described in Sect. 8.2.5 and more or less transitional in sedimentary character as well. In brief, it is a 2.8-m-thick layer that originally consisted mostly of carbonate sand but contains both spherules and irregular particles like those in the Jeerinah spherule layer at Hesta and the Carawine spherule layer. The aggregate thickness of spherules in the layer in the BGB core is roughly 2 cm as they are highly diluted by carbonate sand. According to the original drilling report, the spherule layer in the Billygoat Bore core is ~22 m below the contact between the Jeerinah Formation and Carawine Dolomite stratigraphically, although they are also separated by an additional 70 m of intrusive dolerite (Simonson and Hassler 1997).

Like the Carawine spherule layer, the Jeerinah spherule layer at Hesta contains detrital grains of quartz and feldspar, each around 1 % by volume. Most of the quartz grains are fine sand size, subrounded, and have internal textures typical of basement-derived crystals. A few partially faceted quartz crystals are present suggesting a minor component of volcanic quartz. Detrital quartz is also present in the Jeerinah spherule layer in the Billygoat Bore core that is like the quartz at Hesta petrographically but appears to be finer on average. As in the Carawine spherule layer, the detrital quartz grains in the Jeerinah spherule layer constitute the coarsest quartz observed in their immediate stratigraphic vicinity and possibly over a much thicker interval. Rasmussen and Koeberl (2004) also found unusually coarse feldspathic fine sand-sized grains in the Jeerinah spherule layer in cores DDH-186 and WRL-1. One quartz crystal among them appears to have shock lamellae (Fig. 8.18b), but no other candidates for shock features have been detected in any quartz grains from the Hesta or Billygoat Bore core occurrences (Jones-Zimberlin et al. 2006). In contrast to other occurrences, none of the detrital quartz in this spherule layer in the FVG-1 core is coarser than the ambient silt found in the surrounding shales.

The feldspar grains in the Jeerinah spherule layer at Hesta are coarser (medium to coarse sand size) and more angular than the associated quartz grains on average. Moreover, many of the feldspar grains have angular facets and some appear to be euhedral, suggesting they are volcanic crystals that have been transported short

distances (Jones-Zimberlin et al. 2006). In contrast, few if any of the feldspars in this layer in the Billygoat Bore core are faceted and a few are microclines, indicating they were eroded from basement rocks. Most of the feldspar crystals at the Hesta site were probably replaced by K-feldspar during diagenesis; they are similar to replaced feldspar crystals in basaltic tuffs in the Hamersley (Simonson et al. 1993b; Hassler 1993) and other iron formation basins (Hassler and Simonson 1989).

8.2.6.2 Description of Spherules and Related Particles

In both the Hesta and Billygoat Bore core occurrences, the Jeerinah spherule layer contains a combination of spherules *per se* and more irregular melt particles. Both of these resemble their counterparts in the Carawine spherule layer closely so the descriptions below focus on ways in which the particles in the Jeerinah spherule layer differ from those described in Sect. 8.2.5.2.

As in all of the Archean-Proterozoic boundary layers, the spherules in the Jeerinah spherule layer generally have circular to oval cross-sections (Figs. 8.17, 8.19a), but a small minority have other shapes including rotational forms like teardrops and dumbbells. The spherules range in diameter from around 0.4 to 1.4 mm and average ~0.9 mm, closer in size to the spherules in the Carawine spherule layer than to those in the Bee Gorge spherule layer (Table 1 of Simonson 1992). A few fragments of spherules broken prior to deposition were observed, but they are rare. Internally, most spherules display the usual abundance of elongated microlites of K-feldspar. Some microlites take the form of radial-fibrous sprays, typically nucleated on spherule margins (Fig. 8.19c), whereas others have lath shapes typical of rapidly grown plagioclase microlites in basaltic melts (Fig. 8.18a). As in the Carawine spherule layer, spherules with random laths form a much smaller fraction of the population than they do in the Dales Gorge and Bee Gorge spherule layers, with the exception of the FVG-1 core (discussed below). The abundance of spherules in the Jeerinah spherule layer with central clear spots thought to be cement-filled vesicles and replaced glass cores is similar to most other Archean-Proterozoic boundary layers, e.g., the Dales Gorge spherule layer and Bee Gorge spherule layer.

Although K-feldspar is the dominant mineral, the Jeerinah spherule layer spherules contain other minerals as well; these differ significantly from site to site. At Hesta, many spherules contain secondary quartz, iron hydroxides (probably a weathering product of pyrite) or more rarely carbonate (Fig. 8.17b), all of which typically obscure primary textures. Some spherules also contain sericite, generally as vesicle linings and/or septarian networks that probably formed along micro-fractures in glass cores (Fig. 8.19c). Sericite showing similar textures has not been reported in any other Hamersley spherule layer, but spherules in the Monteville layer in South Africa show very similar textures (Kohl et al. 2006). In the Billygoat Bore core, spherules in the Jeerinah spherule layer have been extensively replaced by coarsely crystalline carbonate, similar to those in the Carawine spherule layer. The Jeerinah spherules in the FVG-1 core differ again in that they

are extensively replaced by coarsely crystalline quartz, which can be common in weathered samples of the Archean-Proterozoic boundary layers, but is rarely seen in cores. The Jeerinah spherule layer in the FVG-1 core also has a much higher abundance of spherules with basaltic textures compared to the occurrences at Hesta, the Billygoat Bore core, or the Carawine spherule layer; it is more in keeping with the Bee Gorge spherule layer (Jones-Zimberlin et al. 2006). No detailed descriptions of the Jeerinah spherule layer in the core occurrences further west have been published, but the spherules appear to be similar in the photomicrographs of Rasmussen and Koeberl (2004).

Irregular particles of former melt are best known from the Jeerinah spherule layer at Hesta and range up to 1 cm across. They closely resemble those in the Carawine spherule layer in that they are more angular, elongated, and larger on average (Figs. 8.17b, 8.19a) than the associated spherules. The original external shapes of irregular particles in the Jeerinah spherule layer cannot be readily quantified because they were widely modified by compaction (Fig. 8.19a; Jones-Zimberlin et al. 2006). Internally, the irregular particles in the Jeerinah spherule layer resemble those in the Carawine spherule layer; they mostly consist of K-feldspar ranging from submicroscopic to elongated needle- to lath-shaped crystals and many have small vesicles (Fig. 8.19a) and/or textures that resemble flow banding or schlieren. The radial-fibrous rims and internal aggregates commonly present in spherules are rarely present in the irregular particles in either the Jeerinah spherule layer or Carawine spherule layer. The only consistent difference noted between the irregular particles in these two spherule layers is that vesicles are more likely to be filled with sericite in the Jeerinah spherule layer. As in the Carawine spherule layer, some irregular particles, particularly larger ones, are texturally very heterogeneous and a few appear to have spherules embedded in them (Fig. 8.19b) or vice versa. These composite particles are presumably products of collisions between partially molten bodies in the ejecta cloud (Jones-Zimberlin et al. 2006). Similar irregular particles accompany the spherules in the Jeerinah spherule layer in the Billygoat Bore core, but irregular particles are either rare or absent in this spherule layer in the FVG-1 core (Jones-Zimberlin et al. 2006). It is not known whether irregular particles are present in the Jeerinah spherule layer core occurrences further to the west. Possible implications of the differences between this spherule layer in the FVG-1 and other occurrences are discussed in Sect. 8.4.1.

8.2.6.3 Radiometric Age

The age of the Jeerinah spherule layer is currently the best constrained of any of the Hamersley spherule layers. Rasmussen and Fletcher (2010) used a SHRIMP to determine the ages of zircon crystals in situ in tuffaceous layers < 1 mm thick in cores from the Jeerinah Formation. One tuff which was 15 mm above the Jeerinah spherule layer stratigraphically yielded an age of 2632 ± 7 Ma (Fig. 8.1). Other tuffs lower in the formation yielded ages up to $\sim$2680 Ma, all of which were

appropriate for their stratigraphic positions. In addition, Trendall et al. (2004) analyzed zircon crystals from a tuffaceous interbed a few meters below the stratigraphic top of the Jeerinah Formation using a SHRIMP and obtained an age of 2629 ± 5 Ma. Because the Jeerinah spherule layer is within a few meters of the top of the Jeerinah Formation, the dated tuff and the spherule layer should be essentially coeval. These ages are also consistent with the aforementioned date of 2597 ± 5 Ma from the overlying Marra Mamba Iron Formation (Trendall et al. 2004) and dates of 2715 ± 2 and 2713 ± 3 Ma in the upper part of the subjacent Maddina Basalt (Blake et al. 2004). In summary, the depositional age of the Jeerinah spherule layer is very close to 2.63 Ga and statistically indistinguishable from the age of the Carawine spherule layer. This supports their proposed correlation, as discussed in Sect. 8.4.1.

8.2.6.4 Geographic Distribution and Variation

Dramatic changes take place in the Jeerinah spherule layer in a north–south direction over a relatively short distance in the main part of the Hamersley Basin, similar to the Dales Gorge spherule layer and Bee Gorge spherule layer. This implies a relatively rapid increase in paleodepth to the south. The characteristics of the Jeerinah spherule layer at Hesta are described first as it is the northernmost site and was presumably deposited in the shallowest water. Next the characteristics of the spherule layer in the 3 core occurrences to the south and west are described as they are all similar in character and were deposited in deeper water. Finally, the spherule layer in the Billygoat Bore core is described, as it has been assigned to both the Carawine spherule layer and Jeerinah spherule layer. Despite inferred differences in paleodepth, the Jeerinah spherule layer was deposited below wave base in low energy paleoenvironments in all its known occurrences.

At the Hesta locality, the Jeerinah spherule layer is 1.57 m thick and consists of three subunits, as follows: (1) a basal zone, which is 50 cm thick and rich in large intraclasts; (2) a middle zone, which is 95 cm thick and consists of cobble-sized chert intraclasts with a fine matrix; and (3) a fine argillaceous capping zone, which is up to 22 cm thick and lacks spherules or other sand-size detritus (Hassler et al. 2005). The basal zone largely consists of sand- to granule-sized detritus (Fig. 8.17b), but cobble-sized intraclasts are scattered throughout, the largest being tabular ferruginous clasts up to 50 cm long. Spherules and irregular melt particles make up about 35 vol % of the basal zone overall. Due to compaction, the original grain size of much of the material is unclear, but it contains abundant clay- to sand-sized material that probably represents shale intraclasts eroded from the substrate. In contrast, the large clasts in the middle zone are essentially monomictic chert intraclasts that vary in orientation from horizontal to vertical and range up to 30 by 10 cm in cross-section. Some of the intraclasts are ellipsoidal, suggesting they are early diagenetic concretions exhumed by erosion. The chert intraclasts make up ~65 vol % of this subunit; the finer-grained material between the intraclasts is composed of the same materials as the finer fraction of the lower

subunit, other than having a much lower abundance of spherules and irregular particles. Finally, the capping zone is highly weathered and totally lacks coarser particles; however, ripple cross-stratification may be present in its lowest 5 cm, suggesting it originally consisted of sand-size detritus. Hassler et al. (2005) interpreted the basal zone as the product of a high density turbidity current, the middle zone as a debris flow deposit, and the capping zone as a turbidite deposited from a dilute sediment plume trailing the debris flow. Whatever processes were responsible, the Jeerinah spherule layer at Hesta represents one of the highest energy events during the deposition of the Roy Hill Shale.

In the FVG-1 core, the Jeerinah spherule layer ranges from 2 to 6 mm in thickness, yet it is still a composite of several different subunits internally (Simonson et al. 2000a). Most of the spherules are incorporated into lenses that thicken and thin laterally (Fig. 8.17a) and are admixed with a fine-grained matrix of uncertain origin. Faint cross-lamination suggests the lenses originally consisted of well-sorted sand. The lenses are underlain by a continuous, finer-grained lamination that is $\sim$700 μm thick and rich in angular, very fine sand-size feldspar crystals. Petrographically, the feldspar crystals are like those in thin tuffaceous laminations in the shales that enclose the Jeerinah spherule layer (Fig. 8.17a), but the lamination at the base of the spherule layer contains sparse spherules. The layer is capped by a thin zone that is rich in coarse silt to very fine sand but poor in recognizable spherule material, although a few spherules occur in it or are perched on top of it. These characteristics indicate the Jeerinah spherule layer in the FVG-1 core was reworked, possibly by impact-induced tsunami-type waves, rather than a product of direct ejecta fallout. As noted in Sect. 8.2.6.1, the Jeerinah spherule layer in the FVG-1 core contains little if any detrital quartz coarser than the silt present in ambient shales, unlike other occurrences of this layer, so the feldspar was probably derived locally from tuffaceous interbeds. Finally, a few spherules are present 18 mm or more below the base of the Jeerinah spherule layer in small, ptygmatically folded soft-sediment injection dikes (Fig. 8.17a). Similar dikes that lack spherules extend upward from the spherule layer, indicating they are not impact-induced structures.

The Jeerinah spherule layer in the two cores west of FVG-1 has not been described in detail, but it appears to be similar to the layer in FVG-1. According to Rasmussen and Koeberl (2004), the spherule layer in these cores is 1–5 mm thick and has a composite structure in both cores consisting of a thin lamination of finer, tectosilicate-rich material overlain by a somewhat thicker spherule-rich layer that in turn is overlain by a bit of finer sediment with less spherule-related material. The Jeerinah spherule layer in these cores appears to differ from FVG-1 in that the spherule-rich part of the layer does not look as lenticular and some quartz sand grains are present, the latter including the single shocked quartz crystal mentioned previously (Fig. 8.18b).

As noted in Sect. 8.2.6.1, a spherule layer 2.8 m thick variously described as either the Carawine spherule layer or the Jeerinah spherule layer occurs in the Billygoat Bore core. It consists largely of a crystalline mosaic of diagenetic dolomite, but it contains minor amounts of several additional types of detritus. The

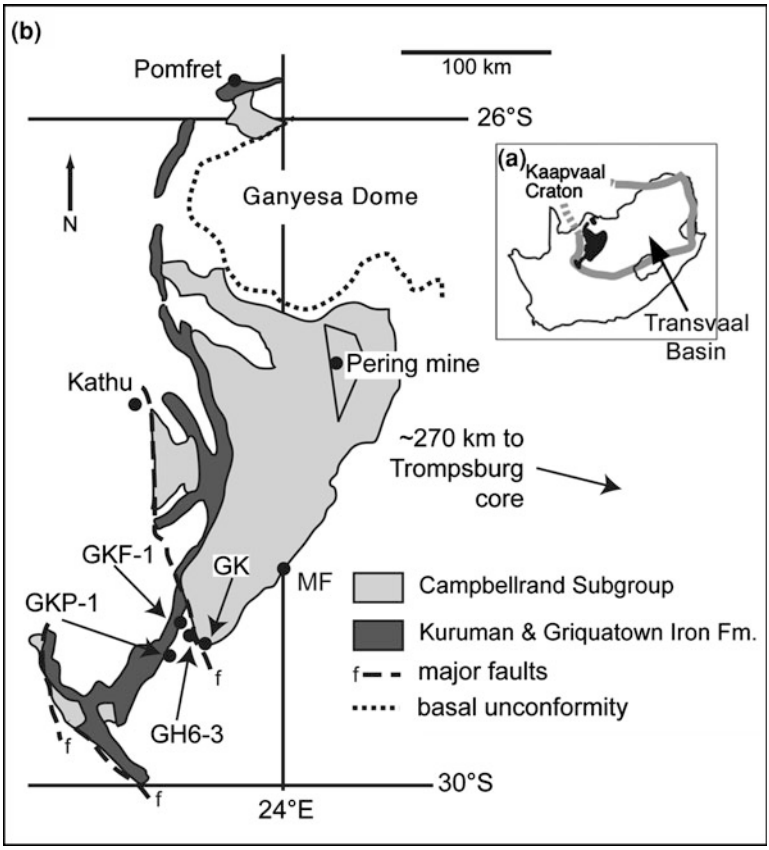

Fig. 8.20 Generalized geological map of the Griqualand West Basin (South Africa). **a** Index map showing the location of the Kaapvaal Craton (*inside gray line*), where strata of the Griqualand West Basin are preserved (*black*), and the general vicinity of the largely coeval Transvaal Basin. **b** Generalized map of the areas of occurrence of the carbonate-rich Campbellrand Subgroup and the iron formation-rich Asbesheuwels Subgroup showing the sites where Archean-Proterozoic boundary spherule layers have been identified. GKF-1 and GKP-1 are Agouron Institute cores; the Kuruman, Reivilo, and Monteville spherule layers have all been identified in both cores. The Reivilo and Monteville spherule layers have both been identified in the Kathu core, an exploration drill core drilled near the town of Kathu (Altermann and Siegfried 1997). The Kuruman spherule layer has also been identified in one exploration core drilled by an asbestos mining company near Pomfret. The Reivilo spherule layer was initially identified in core GH6-3, also drilled for exploration purposes. The Monteville spherule layer has also been identified in 10 cores drilled in and around the Pering Mine area (indicated by a trapezoid - see Fig. 8.28 for a more detailed map of this area) and another exploration core drilled in the vicinity of the town of Trompsburg ~108 km south of Bloemfontein. Outcrops where the Monteville spherule layer has been identified are GK (Goudkop) and MF (Monteville farm). Modified after Simonson et al. (2009a), Fig. 1b, with permission from Elsevier

latter consists of coarse sand- to pebble-sized tabular intraclasts of carbonaceous shale and early diagenetic pyrite, spherules and irregular particles, and lesser

amounts of fine to medium quartzose sand (Simonson and Hassler 1997; Hassler et al. 2005). The quartz and feldspar sand grains are similar to those in the Jeerinah spherule layer at Hesta (described in Sect. 8.2.6.1). Although all detrital textures in the carbonate have been eradicated by diagenetic recrystallization, the basal concentrations of spherules, irregular melt particles, and other coarse clasts indicate this layer is normally graded. Nevertheless, it consists of several distinctive subunits internally and isolated spherules occur as high as 1.8 m above the base. Most of the layer displays planar lamination, but ripple cross-stratification up to 3 cm thick is present near the top of the layer. Simonson and Hassler (1997) interpreted the layer in the Billygoat Bore core as the product of two to three high-density turbidity currents deposited in relatively rapid succession.

8.2.6.5 Extraterrestrial Component, Shock Metamorphism, and Target Material

The Jeerinah spherule layer has a definite component of extraterrestrial material based on two lines of geochemical evidence. In the first analyses reported, Rasmussen and Koeberl (2004) found Ir concentrations of 13.8 ppb on average in 2 samples of this spherule layer from cores DDH-186 and WRL-1 in the Hamersley Basin. In contrast, 6 shale samples from within 10 m of the spherule layer stratigraphically in the same 2 cores all had Ir concentrations <1.5 ppb (Rasmussen and Koeberl 2004). The high Ir content relative to the Carawine and Bee Gorge spherule layers may reflect the fact that the samples analyzed were richer in spherules than previously reported samples from other Archean-Proterozoic boundary layers and/or contained finer ejecta. The Jeerinah spherule layer is only 1-5 mm thick in these cores (as described in Sect. 8.2.6.4), so the samples Rasmussen and Koeberl (2004) analyzed are probably from the lowest-energy Archean-Proterozoic boundary spherule layer analyzed to date, and therefore the finest-grained and least diluted. They also noted high abundances of Cr, Co, Ni, and Au in the Jeerinah spherule layer samples, Ir/Au values that were "close to chondritic," and estimated the extraterrestrial content of their samples to be about 2–3 wt %.

Simonson et al. (2009b) found Ir concentrations that ranged from about 5.18 to 11.8 ppb and averaged ~8.7 ppb in 4 samples from the surface exposure of the Jeerinah spherule layer at Hesta. All of the CI chondrite-normalized patterns are essentially flat from Ir to Rh, i.e., unfractionated relative to CI chondrites, although concentrations of Pd and Au are more variable (Fig. 8.6). This provides strong evidence for an extraterrestrial component on the order of 1 wt % in the Jeerinah spherule layer at Hesta. As described above, this layer is much thicker and contains a much higher proportion of non-spherule sediment at Hesta relative to the core occurrences analyzed, so a lower content of extraterrestrial material is to be expected. For comparison, 4 samples from tuffs and shales in the Jeerinah Formation but not from the Hesta locality had Ir concentrations that ranged from 0.09 to 1.66 ppb and averaged ~0.6 ppb. One of the shale samples collected within

centimeters stratigraphically of the Jeerinah spherule layer in core FVG-1 is enriched in Ir, Ru, Pt, and Rh relative to typical crustal shales (e.g., McDonald et al. 2006), yet it still contains only 5–10 wt % of the Ir and Ru observed in the spherule layer. As with the Carawine spherule layer, the most likely explanation is via the mobilization of some PGE out of the spherule layer into adjacent strata as shown for modern marine sediments (Colodner et al. 1992) as well as the Neoproterozoic ejecta layer from the Acraman impact structure (Wallace et al. 1990b). Simonson et al. (2009b) did not attempt to determine the type of projectile responsible for the Jeerinah spherule layer on the basis of PGE ratios because of large uncertainties associated with these ratios.

The clearest evidence that the Jeerinah spherule layer contains extraterrestrial material again comes from a chromium isotopic analysis of one sample which was from Hesta (Fig. 8.7). Like the Carawine spherule layer, the spherules in this layer are diluted with other material including coarse terrigenous detritus, so the sample was analyzed using a differential dissolution procedure described in Simonson et al. (2009b). Unlike in the Carawine spherule layer, siliciclastics rather than carbonates form the bulk of the non-spherule detritus in the Jeerinah spherule layer, but one fraction has a ε^{53}Cr value of 0.12 ± 0.03, confirming the presence of an extraterrestrial component. Mass balance calculations indicate the spherule layer sample analyzed contains ~ 1 % by mass extraterrestrial material, similar to the values mentioned above based on the Ir content. The positive Cr isotopic anomaly indicates the extraterrestrial material is similar in composition to either an ordinary chondrite or an enstatite chondrite rather than carbonaceous chondrites (Simonson et al. 2009b).

Rasmussen and Koeberl (2004) identified a single angular quartz crystal ~ 90 μm across with 2 well-developed sets of planes, and possibly a third, that appear to be shock lamellae (PDFs) in the Jeerinah spherule layer in core WRL-1 (Fig. 8.18b). Universal stage work was mentioned but no orientations were given. This is the only quartz crystal with likely shock features reported to date from any early Precambrian spherule layer or any rock older than the Vredefort structure. Like in the Bee Gorge and Carawine spherule layers, grains containing the high-pressure polymorph TiO_2II were found in the Jeerinah spherule layer (Smith et al. 2010).

The textures of the spherules in the Jeerinah spherule layer again suggest they were generally basaltic in nature (Jones-Zimberlin et al. 2006), and there is some geochemical evidence to support this interpretation. Specifically, the REE patterns in this spherule layer are quite distinct from the associated sedimentary strata in that the latter show enrichment of all the LREE and markedly higher absolute REE concentrations (Simonson et al. 2009b). The relative amounts of these immobile elements are unlikely to have been significantly altered by post-depositional processes, so these patterns probably reflect a component of foreign crustal material significantly different from local sedimentary materials. Most sediments, sedimentary rocks, and continental crustal rocks show REE fractionation characterized by pronounced LREE enrichment on chondrite-normalized plots. One way to explain the flat patterns in the Jeerinah spherule layer is the addition of a component depleted in the LREEs, such as mid-ocean ridge basalt that combined with crustal rocks to produce a generally flat pattern.

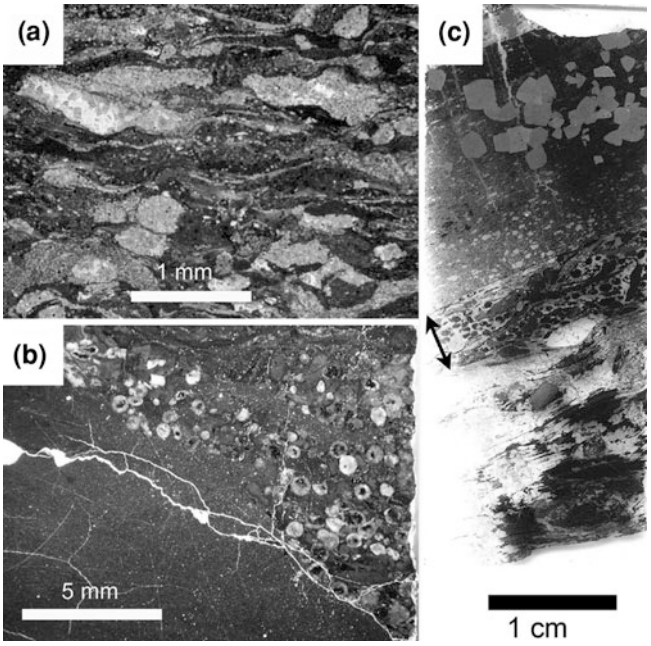

Fig. 8.21 Images of the Kuruman spherule layer in the two Agouron Institute cores. **a** Cut slab from the middle of the Kuruman spherule layer in core GKP-1 which, like most of the layer, is highly compacted and consists of tabular rip-up clasts rich in either chert with carbonate (*light gray*) or stilpnomelane (*dark gray*). No spherules are apparent. **b** Cut slab of most of an infilled scour at the base of the layer in core GKP-1 which contains most of the spherules detected to date in the Kuruman spherule layer. The spherules consist largely of K-feldspar and/or carbonate (*white to light gray*); the remaining sediment is a mix of sand-size to tabular fine pebble-size intraclasts (and possibly cement) made of stilpnomelane. The squiggly *white lines* in the stilpnomelane-rich mud below the scour are glue-filled cracks. **c** A large thin section, taken in reflected light, from the Kuruman spherule layer in core GKF-1. Most of the clear material is carbonate and the *darker gray* material is stilpnomelane. The double-headed arrow indicates the only part of the core where spherules are present; they are most obvious next to the arrow where the thin section is thinnest and mixed with tabular rip-up clasts made of stilpnomelane throughout. Immediately above this layer is an anomalous carbonate-rich layer which contains numerous coarse crystals of diagenetic pyrite (*medium gray*) in its *upper part*. **a**, **b**, and **c** from Simonson et al. (2009a), Figs. 6a, 6b, and 5c, respectively, with permission from Elsevier

8.3 Archean-Proterozoic Boundary Spherule Layers in South Africa

8.3.1 Introduction

All of the South African spherule layers deposited near the Archean-Proterozoic boundary that have been reported so far are hosted by strata of the Transvaal Supergroup or Sequence. This succession was deposited on top of the Kaapvaal

Craton from roughly 2.7 to 2.0 Ga. The Kaapvaal is one of the most stable continental nuclei on Earth, having been a thick stable plate for over 3 billion years (Moser et al. 2001). On its eastern margin, it contains the Barberton Greenstone Belt, which hosts most of the Paleoarchean spherule layers described in Chap. 9. The Transvaal Sequence has an aggregate thickness of ~15 km of relatively unmetamorphosed clastic, chemical, and volcanic rocks (Eriksson et al. 1993); although most of them have been eroded, two large tracts survive. The largest tract covers most of the eastern half of the Kaapvaal Craton and is known as the Transvaal Basin, but spherule layers have only been detected on the southwestern margin of the Craton in the second and smaller area of preserved strata known as the Griqualand West Basin (Fig. 8.20a) with one exception (see below). The Transvaal and Griqualand West Basins are geographically separated at present because equivalent strata were eroded from the intervening Vryberg Rise (Eriksson et al. 1993). The failure to detect spherule layers in the Transvaal Basin could reflect the fact that these strata were generally deposited in higher energy paleoenvironments and are more highly metamorphosed than those of the Griqualand West Basin. In any event, spherule layers from 3 distinct impacts have been recognized in the Griqualand West Basin (Fig. 8.1). The only occurrence of an Archean-Proterozoic boundary layer outside this Basin is in an isolated core drilled ~270 km southeast of the Basin (Fig. 8.20b; Simonson et al. 2009c; described in Sect. 8.3.4.4).

Well-preserved chemical sedimentary rocks are abundant in the Griqualand West Basin in what is known as the Ghaap Group (Fig. 8.1). The Ghaap Group is divided into several subgroups, one being the Campbellrand Subgroup. This Subgroup is dominated by carbonate, most of which accumulated in platformal or shallow-water paleoenvironments (Beukes 1987). This carbonate-rich succession has an aggregate thickness of up to ~2.4 km and contains two of the Archean-Proterozoic boundary spherule layers (Reivilo and Monteville; described in Sects. 8.3.3 and 8.3.4). The Campbellrand Subgroup is overlain by the Asbesheuwels Subgroup; it consists of two large iron formations, the older one being the Kuruman Iron Formation (Beukes 1983). The Kuruman Iron Formation is a regionally extensive unit that was deposited in the course of a major marine transgression (Beukes and Gutzmer 2008). The youngest of the Archean-Proterozoic boundary spherule layers (Kuruman; described in Sect. 8.3.2) is located low in the Kuruman Iron Formation stratigraphically.

The strata of the Campbellrand Subgroup thin dramatically across a fault zone (Fig. 8.20b) so the succession in the southwestern part of the Griqualand West Basin consists of ~0.5 km of basinal or deeper-water strata (Beukes and Gutzmer 2008). The Campbellrand Subgroup in this area is a monotonous pile of basinal shales, carbonates, and volcaniclastics that is known as the Nauga Formation (Fig. 8.1). The platformal carbonates to the north are thicker and more diverse, so the succession there is divided into eight different formations, the two lowermost stratigraphically being the Monteville and Reivilo Formations. A research consortium supported by the Agouron Institute of Pasadena, California, USA, drilled two long cores, GKF-1 and GKP-1, at carefully chosen sites in an area of intermediate water depth where the transition from the platformal to basinal strata takes

place (Knoll and Beukes 2009). Core GKP-1 was drilled ~30 km southsouthwest of core GKF-1 in a direction that was more or less directly down the paleoslope. All three of the spherule layers have each been identified in both of these cores (Fig. 8.20b; Schröder et al. 2006; Simonson et al. 2009a), and they provide most of our current data about two of the three layers.

8.3.2 Kuruman Spherule Layer

8.3.2.1 Description of Layer

The youngest spherule layer reported from the Griqualand West Basin (the Kuruman) is in the lower part of the Kuruman Iron Formation (Fig. 8.1) that has been correlated with the Dales Gorge Member in the Hamersley Basin (Beukes and Gutzmer 2008). The Kuruman Iron Formation has distinctive alternations of BIF and shaly layers that are regionally extensive and like those in the Dales Gorge Member (see Sect. 8.4.2 for further discussion). Spherules have been positively identified at only one stratigraphic level in a few drill cores (described below) in the Kuruman Iron Formation. Limited searching for the **Kuruman spherule layer** at the appropriate stratigraphic level in surface exposures failed to reveal any potential occurrences, but this may simply reflect the highly weathered state of most outcrops of the shaly interbeds of the Kuruman Iron Formation.

The Kuruman spherule layer is best known in two of the Agouron Institute research drill cores, but it is very different in these two cores. In Agouron Institute core GKP-1, the spherule layer is ~98 cm thick and mainly consists of discoidal rip-up clasts of carbonate, chert, and/or stilpnomelane (Fig. 8.21a). The layer is normally graded with rip-up clasts up to several centimeters long near the base versus up to only a few millimeters long near the top, but maximum clast size varies some in between. The only place where spherules are concentrated is in a scour pocket 9 mm deep at the base of the layer eroded into the underlying massive stilpnomelane mudstone. The pocket is filled with sand-size intraclasts as well as spherules (Fig. 8.21b). Spherules are quite scarce within the layer but present locally, especially in a thin zone ~45 cm above the base. In the other Agouron Institute core, GKF-1, spherules are still associated with tabular rip-up clasts, up to at least 7 mm long. consisting of stilpnomelane and carbonate, but the Kuruman spherule layer is only 6 mm thick and has a much higher ratio of spherules to rip-up clasts (Fig. 8.21c). The spherule-rich layer in GKF-1 is overlain by an anomalous carbonate-rich layer 17 mm thick that may represent finer sediment deposited in the waning stages of the formation of the spherule layer.

A third possible occurrence of the Kuruman spherule layer is in a core drilled in connection with asbestos mining in the vicinity of Pomfret ~370 km north of the Agouron Institute sites (Fig. 8.20b). No samples are available from this core, only images in a masters' thesis (Van Wyk 1987), but these images show a thin layer rich in stilpnomelane ovoids at the same stratigraphic level as the Kuruman

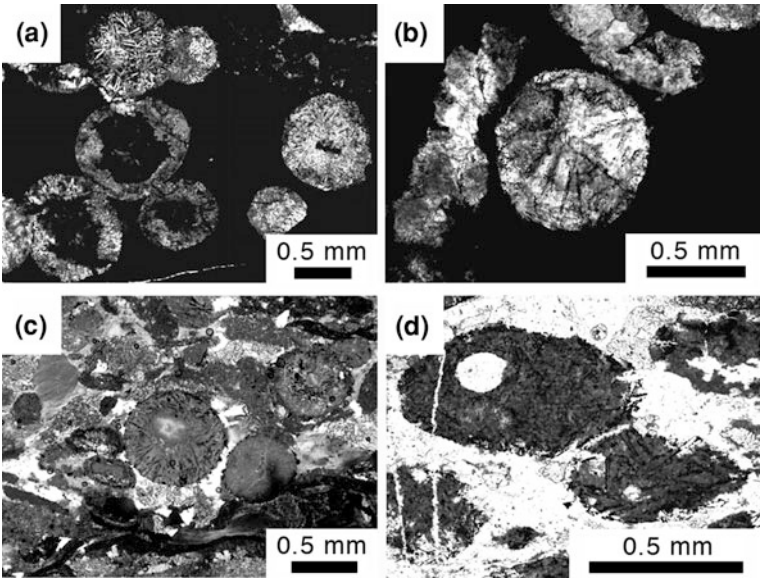

Fig. 8.22 Photomicrographs, taken in plane polarized light, of spherules from the Kuruman spherule layer. **a** Spherules and associated sediment in the scour filling in core GKP-1 shown in Fig. 8.21b. The spherules consist of stilpnomelane (*dark*) and some carbonate and K-feldspar (*both light to medium gray*); much of the latter is in lath-shaped microlites. Some spherules have basaltic textures (e.g., *in upper left*). The dark matrix is also stilpnomelane. **b** A spherule in the scour filling in core GKP-1 shown in Fig. 8.21b that is replaced by coarsely crystalline carbonate and has opaque inclusions in thin trains that might be crystal pseudomorphs. **c** Well-sorted sand consisting of stilpnomelane-rich intraclasts and spherules ~45 cm above the base of the Kuruman spherule layer in core GKP-1. The spherule in the middle has thin trains of opaque inclusions like those in B and a light off-center spot that is either an infilled vesicle or a replaced glass core that is concentrically layered with two generations of stilpnomelane. The clear material between clasts is carbonate cement. **d** Spherules in GKF-1 elongated parallel to bedding; clear material is mainly carbonate cement, although it replaces spherules along their edges. One spherule (*upper left*) contains a clear carbonate oval that is probably an infilled vesicle. Several spherules contain thin trains of opaque inclusions like those in **b** and **c**. From Simonson et al. (2009a), Fig. 7, with permission from Elsevier

spherule layer in the Agouron Institute cores. It is a thin layer with possible replaced spherules that appear to be mixed with larger, tabular rip-up clasts as in the spherule layer in core GKF-1. Little more can be said about this occurrence.

It is clear from its placement within a regionally extensive BIF that the Kuruman spherule layer was deposited below wave base in a deep shelf to slope environment (Beukes and Gutzmer 2008). The Kuruman spherule layer is anomalously thick and coarse-grained relative to surrounding layers in both Agouron Institute cores, indicating it is the product of an unusually high-energy event. The processes responsible for depositing this spherule layer cannot be analyzed in detail given the limited data available, but it is similar to many other layers deposited near the Archean-Proterozoic boundary. Specifically, the pebble-rich

nature of the spherule layer in core GKP-1 suggests it was deposited by debris flows, whereas its sandy and spherule-rich nature in the other two cores suggests it was deposited via waves and/or currents. More sites must be identified before the Kuruman spherule layer's mode of emplacement can be interpreted with confidence. No regional trends in depositional processes are evident (as discussed in Sect. 8.3.2.4). Despite the variable thickness of the layer as a whole, the aggregate thickness of spherules in the Kuruman spherule layer appears to be a few millimeters at most in all three occurrences.

8.3.2.2 Description of Spherules

In the few occurrences of the Kuruman spherule layer known to date, spherules are not nearly as abundant as they are in other layers near the Archean-Proterozoic boundary, nor have they been studied in as much detail. The spherules in all of the occurrences are in the coarse sand size range, averaging about 0.8 mm in diameter with a maximum of $\sim$1.0 mm (Fig. 8.22). Spherules of three main compositions occur in the Kuruman spherule layer in the GKP-1 core: some consist almost entirely of stilpnomelane, others consist of stilpnomelane and K-feldspar combined, and yet others consist largely of coarsely crystalline carbonate (Simonson et al. 2009a). All of these minerals are interpreted as secondary phases replacing original constituents. As in other layers formed near the Archean-Proterozoic boundary, the K-feldspar tends to occur in highly elongated, needle- to lath-shaped microlites that are believed to be pseudomorphs of rapidly grown plagioclase crystals. K-feldspar microlites range from randomly oriented laths to radial-fibrous fans in rims like those of other Archean-Proterozoic boundary spherule layers; spherules rich in laths have textures closely resembling basalts (Fig. 8.22a). K-feldspar was only observed in spherules at the base of the Kuruman spherule layer. As in the Dales Gorge spherule layer (Sect. 8.2.2.2), stilpnomelane tends to replace spherules wholesale and preserve both external shapes and vesicles (Fig. 8.22c), but no other internal textures are apparent. It is likely that most of the stilpnomelane replaced original glass, but texturally similar stilpnomelane fills vesicles and more rarely interstitial pores as a cement. As in other layers near the Archean-Proterozoic boundary, coarsely crystalline carbonate tends to obscure primary textures where it replaces spherules (Fig. 8.22b). Many spherules that consist almost entirely of stilpnomelane or carbonate contain opaque inclusions in strips resembling long, narrow microlites (Fig. 8.22b,c). Spherules in the Dales Gorge spherule layer show similar textures (Fig. 8.3a). In the only place they are abundant, the scour pocket at the base of the Kuruman spherule layer in drill core GKP-1, most of the spherules have circular cross-sections (Fig. 8.21b). Oval and other non-spherical shapes also occur including one spherule that appears to have the shape of a broken dumbbell. However, many of the original shapes have been modified by compaction so it is uncertain whether or not rotational shapes were present.

The spherules in the other two occurrences show a more restricted range of composition. In Agouron Institute core GKF-1, the spherules consist largely of

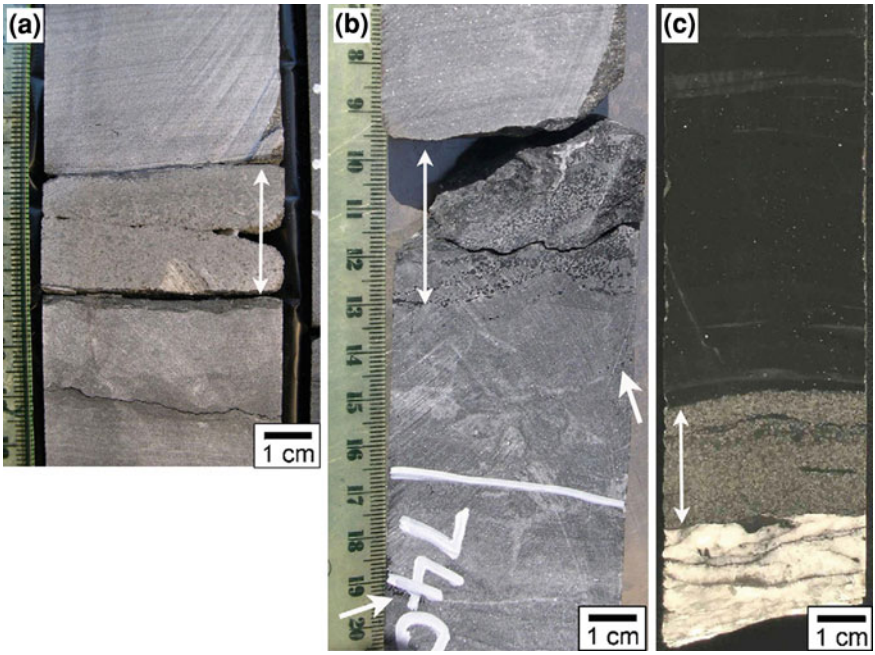

Fig. 8.23 Images of the Reivilo spherule layer in 3 cores. The double-headed arrow in each core indicates the part of the core where spherules are abundant. **a** Reivilo spherule layer in core GKF-1 where it consists of pure light-gray spherules and is under- and overlain by thinly laminated, spherule-free, basinal carbonate. **b** Reivilo spherule layer in core GKP-1 where darker spherules are abundant and mixed with larger carbonate intraclasts in one zone but also occur in isolated pockets lower down (*short single-headed arrows*) that are thought to be interstitial to large carbonate intraclasts. The carbonates at top and bottom are thinly laminated basinal deposits free of spherules. **c** Reivilo spherule layer in the Kathu core where it consists of a spherule-rich layer with thin shale rip-up clasts (*black*), is underlain by a thick vein of quartz and carbonate (*white*), and is overlain by thinly laminated dark carbonate with stray spherules and local cross-lamination (*in slightly lighter gray lens near top*) indicating it was deposited as sand. From Simonson et al. (2009a), Fig. 3, with permission from Elsevier

stilpnomelane and carbonate and no K-feldspar was observed. Some of the spherules in GKF-1 contain vesicles and/or elongated opaque inclusions like spherules in the GKP-1 core. However, most of the spherules in GKF-1 have oval cross-sections elongated parallel to bedding (Fig. 8.22d), suggesting they were flattened during compaction. Although ductile deformation of spherules during diagenesis is unusual in the Archean-Proterozoic boundary spherule layers, it has been documented locally, e.g., in the Monteville spherule layer (Kohl et al. 2006 and Sect. 8.3.4.2). In the Pomfret core, the candidates for Kuruman spherule layer spherules appear to be even more restricted in composition. The photomicrograph in Van Wyk (1987) shows nothing but ovoids of stilpnomelane aligned parallel to bedding. However, they do contain elongated opaque inclusions like those in the spherule layer in the Agouron Institute cores. In general, the spherules in the

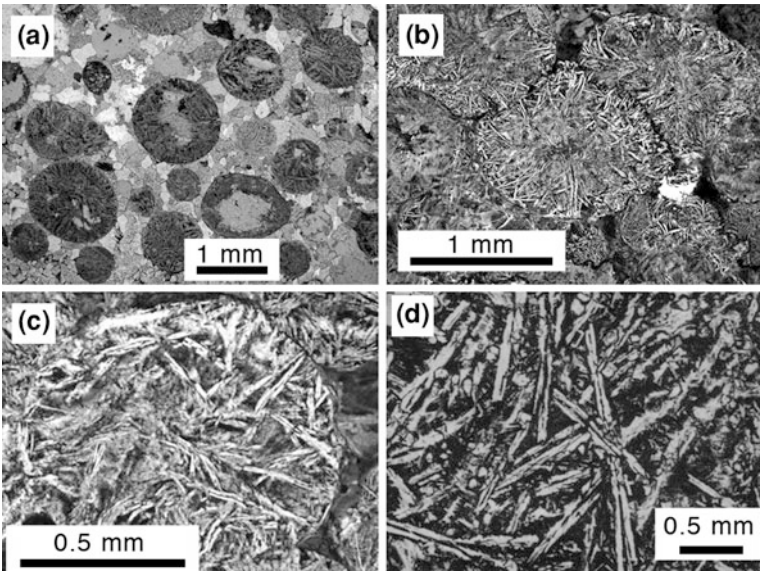

Fig. 8.24 Photomicrographs, taken in plane polarized light, of spherules from the Reivilo spherule layer and an analogous texture in an experimentally crystallized basalt. **a** Uncompacted spherules in core GKP-1 that are isolated in and locally replaced by sparry carbonate. **b** Spherules in core GH6-3 with diverse textures featuring abundant laths and some radial-fibrous aggregates of K-feldspar. The central spherule was probably flattened by a combination of both physical and chemical compaction. **c** A single spherule in core GH6-3 that is rich in K-feldspar laths with central lines of dark inclusions. Some of the laths appear to be bent, presumably from physical compaction. **d** Plagioclase laths in an experimentally crystallized basalt with central *dark lines* like the laths in **c**. **a**, **b**, and **c** from Simonson et al. (2009a), Figs. 4a, c, and e, respectively, with permission from Elsevier. **d** from Lofgren (1983), Plate 6f, with the permission of Oxford University Press

Pomfret core appear to be more highly compacted and perhaps less regular in shape than those in the Agouron Institute cores.

8.3.2.3 Radiometric Age

Zircon crystals from a number of tuffaceous interbeds in the Griqualand West Basin have been dated via SHRIMP (Fig. 8.1). None of the dated tuffs are in close stratigraphic proximity to the Kuruman spherule layer. The closest dates stratigraphically below the spherule layer are in the underlying Gamohaan Formation; they are 2521 ± 3 Ma (Sumner and Bowring 1996) and 2516 ± 4 Ma (Altermann and Nelson 1998). The Gamohaan Formation overlies the platformal carbonates that extend through most of the Griqualand West Basin; the Klein Naute Formation (Fig. 8.1), its lateral equivalent, is restricted to the southwest part of the Basin. The closest date above the spherule layer stratigraphically is 2460 ± 5 Ma from a tuff higher in the Kuruman Iron Formation (Pickard 2003). Thus the

Kuruman spherule layer was deposited between about 2.52 and 2.46 Ga, which means it could be, but is not necessarily, contemporaneous with the Dales Gorge spherule layer at 2.49 Ga. Deposition of the spherule layer close to 2.49 Ga is also supported by an age of 2480 ± 6 Ma obtained from a tuff in the middle of the Penge BIF (Nelson et al. 1999); the Penge is the stratigraphic equivalent of the Kuruman Iron Formation in the Transvaal Basin hundreds of kilometers northeast of the Griqualand West Basin.

8.3.2.4 Geographic Distribution and Variation

As noted in Sect. 8.3.2.1, possible occurrences of the Kuruman spherule layer are restricted to three cores. In two of the cores, the spherule layer is less than a centimeter thick, whereas in the third core it is about 1 m thick. However, this contrast provides no evidence of consistent paleogeographic variation because the two cores drilled closest to one another show the greatest variation. Surprisingly, the Kuruman spherule layer in Agouron Institute core GKF-1 is a much better match for the layer in the distant Pomfret core than it is for the thick, high-energy Kuruman spherule layer in nearby Agouron Institute core GKP-1. Sumner and Beukes (2006) documented a number of stratigraphic discrepancies between the successions in the two Agouron Institute cores and attributed much of this variability to post-depositional disturbance; apparently the cores were drilled on a paleoslope that was prone to slumping. At a minimum, no simple regional gradients can be detected in the Kuruman spherule layer given the limited data available, but provided the Pomfret layer is actually the Kuruman spherule layer, the size, aggregate thickness, and nature of the spherules remain impressively similar over distances on the order of hundreds of kilometers.

8.3.2.5 Extraterrestrial Component

No geochemical or isotopic data have been reported for the Kuruman spherule layer as yet. Given its similarity to and proposed correlation with the Dales Gorge spherule layer, it seems reasonable to expect that it will show levels of PGEs and extraterrestrial Cr similar to the Dales Gorge spherule layer once it is analyzed.

8.3.3 Reivilo Spherule Layer

8.3.3.1 Description of Layer

The **Reivilo spherule layer** is ~100 m stratigraphically below the top of the Reivilo Formation (Fig. 8.1). The Reivilo Formation consists of carbonates deposited in shallow subtidal paleoenvironments and extends throughout most of

the Griqualand West Basin, but as explained in Sect. 8.3.1, equivalent strata of the Nauga Formation were deposited in deeper water to the southwest (Beukes 1987). The Reivilo spherule layer has been identified in the same two Agouron Institute cores in which the Kuruman spherule layer was identified (GKF-1 and GKP-1). Although the spherule layer was also recognized in core GH6-3 drilled nearby (Fig. 8.20b), it was not described or sampled systematically in this core. These 3 cores are located in the transition zone where the Reivilo spherule layer is hosted by shales and carbonates of the Nauga Formation that were deposited below wave base in slope paleoenvironments (Schröder et al. 2006). The spherule layer has also been identified in a fourth core drilled ~100 km to the north near the town of Kathu (Fig. 8.20b). In contrast to the other occurrences, the Reivilo spherule layer in this core is hosted by platformal carbonates (Altermann and Siegfried 1997); it is the only Archean-Proterozoic boundary spherule layer known to date that was preserved in a shallow-water paleoenvironment.

The character of the Reivilo spherule layer differs in each of the 3 cores where it has been fully recovered, as follows. In core GKF-1, it consists of 2 cm of pure, well-sorted, gray spherules showing little or no grading (Fig. 8.23a). The spherule layer is underlain by a black shale lamination 1–2 mm thick but otherwise enclosed between typical deeper-water laminated carbonates that lack spherules. In core GKP-1, the spherules are much darker and concentrated in several pockets distributed through a stratigraphic thickness of 9 cm (Fig. 8.23b). Spherules are most abundant in the upper few centimeters where they are associated with carbonate rip-up clasts several centimeters long. The pockets lower in the core probably occupy interstices between carbonate rip-up clasts that could be on the order of half a meter long. The aggregate thickness of spherules in the Reivilo spherule layer in core GKP-1 again seems to be around 2 cm. Finally, the spherule layer in the Kathu core is ~20 cm thick and consists of 2.5 cm of nearly pure spherules overlain by 17.5 cm of almost pure carbonate (Fig. 8.23c). The basal bed in the Kathu core spherule layer contains a few rip-up clasts of black shale up to at least 4 cm long. Like those in the GKF-1 core, the spherules in the Kathu core are gray, very well sorted and show little or no grading. The upper carbonate in the Reivilo spherule layer in the Kathu core shows faint horizontal lamination plus thin cross-stratified lenses locally; it only contains a few spherules near the base. The differences outlined above may reflect the fact that the Agouron Institute and other cores in which the spherule layer was recognized were drilled in what were originally contrasting paleoenvironments as described in Sect. 8.3.2.4. Despite the high energy with which it was deposited, the layer appears to be devoid of siliciclastic sand, although some samples contain minor amounts of feldspathic silt that may be siliciclastic and/or volcaniclastic.

8.3.3.2 Description of Spherules

Originally the spherules in the Reivilo spherule layer were probably well-sorted spherical grains in the coarse sand size range. This is clearest in GKP-1 where the

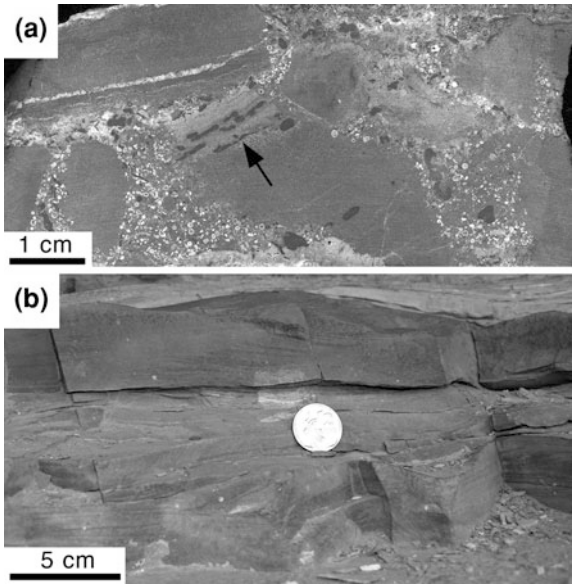

Fig. 8.25 Images of the Monteville spherule layer. **a** Polished slab from the basal zone of the Monteville spherule layer at the Goudkop outcrop where it largely consists of large carbonate intraclasts (*solid gray masses*) with interstitial sand pockets rich in spherules (*white circles and ovals*) and oxidized pyrite intraclasts (*dark bodies*). Intraclasts of weathered black shale that contain oxidized early diagenetic pyrite concretions (e.g., *one indicated by arrow*) are also present. **b** Outcrop of the entire Monteville spherule layer in a cliff exposure at Monteville farm where the coarser basal zone is locally absent and spherules are rare. It consists almost entirely of fine carbonate-rich sand with cross-lamination (probably of the hummocky type). The basal contact of the spherule layer is at level of the bottom of the coin, below which is thinly laminated basinal dolomite that is undisturbed

spherules were locally shielded from compaction by carbonate (Fig. 8.24a). They are generally 0.8–0.9 mm across but range up to about 1.3 mm across. As in other layers near the Archean-Proterozoic boundary, a minority has oval cross-sections and a few have possible teardrop shapes or appear to be composites that agglutinated in flight (Simonson et al. 2009a). A few of the spherules have jagged outlines and appear to have been broken before burial, as in other Archean-Proterozoic boundary layers. The original sizes and shapes of most of the Reivilo spherule layer spherules have been modified by compaction including truncations along edges by pressure solution and/or overall ductile flattening (Fig. 8.24b,c).

The textural components of the spherules in the Reivilo spherule layer are the same as those in other Archean-Proterozoic boundary layers. The most abundant phase in these spherules is K-feldspar in forms ranging from laths to acicular microlites. The laths are up to $\sim$0.7 mm long and many have skeletal shapes with a "racing stripe" of dark inclusions down their center (Fig. 8.24b,c). Some of the laths also have pronged terminations or branch out from a single stem, but the

branches all have the same optical orientation. Such shapes are typical of plagioclase microlites grown in basaltic melts (Fig. 8.24d) and suggest the K-feldspar replaced primary plagioclase; this would be consistent with its purity, especially its low sodium content (Simonson et al. 2009a). Acicular microlites also range up to 0.7 mm in length, but they are never more than 5 μm thick and generally have a radial-fibrous growth habit. Some fans nucleate on the outer edges of spherules whereas others appear to have nucleated in the interiors of spherules. However, the fibrous rims so common in the Dales Gorge (Fig. 8.3e), Bee Gorge (Fig. 8.10), Carawine (Fig. 8.15), and Jeerinah spherule layers (Fig. 8.19) are rare in the Reivilo spherule layer. This is in keeping with the fact that spherules in the Reivilo spherule layer are more highly crystallized than spherules in any of the other Archean-Proterozoic boundary layers except for those of the Paraburdoo spherule layer (as described in Sect. 8.2.4.2), which they closely resemble. K-feldspar microlites with shapes intermediate between acicular and lath-shaped are present, but not abundant.

In addition to K-feldspar, some spherules in the Reivilo spherule layer contain variable amounts of phlogopite, pyrite, carbonate, and/or sericite. As in other Archean-Proterozoic boundary layers, carbonate and pyrite tend to be coarsely crystalline and obscure primary textures. In contrast, some of the phlogopite gives definition to pseudomorphs of skeletal crystals of olivine and possibly clinopyroxene like those in the Paraburdoo spherule layer (Fig. 8.13). In addition, some of the phlogopite forms a fine-grained matrix interstitial to these pseudomorphs and the K-feldspar microlites and presumably represents replaced glass. Some spherules in the Reivilo spherule layer contain clear internal spots (Fig. 8.24a); they vary in cross-section from circular (rare) to more irregular, range in size from 0.06 to 1 mm across, and mostly consist of carbonate, K-feldspar, and/or phlogopite. As in other Archean-Proterozoic boundary layers, these spots are probably a combination of cement-filled vesicles and relict glass cores replaced later during diagenesis; but in keeping with their more highly crystallized nature, such spots are much rarer in the Reivilo spherule layer than they are in other Archean-Proterozoic boundary layers with the exception of the Paraburdoo spherule layer. Another difference is that the sericite in the Reivilo spherule layer spherules tends to follow spherule edges and form thin bands that appear more tectonic than sedimentary in origin instead of pseudomorphing internal textures as they do in the Jeerinah spherule layer (Fig. 8.19c) and Monteville spherule layer (see Sect. 8.3.4.2).

8.3.3.3 Radiometric Age

The age of the Reivilo spherule layer is even more poorly constrained than that of the Kuruman spherule layer. No dates have been reported in close stratigraphic vicinity to the Reivilo spherule layer, but existing dates from tuffs elsewhere in the Griqualand West Basin succession and sequence stratigraphic correlations to the Hamersley succession suggest the lowest sequence in the Reivilo Formation dates to ~2585 Ma (Sumner and Beukes 2006). Using average sequence durations

(Sumner and Beukes 2006) and assuming constant rates of sediment deposition yields an age of ~2560 Ma for the Reivilo spherule layer. This is consistent with SHRIMP ages from zircons in tuffs of 2549 ± 7 Ma (Altermann and Nelson 1998) and 2552 ± 11 Ma (Barton et al. 1994) several hundred meters above the spherule layer and 2588 ± 6 Ma ~200 m below the layer stratigraphically (Martin et al. 1998). However, the Reivilo spherule layer would appear to be slightly older than 2.56 Ga if one assumes a linear change in age for the strata between these dates since it is closer to the older tuff stratigraphically (Fig. 8.1). Given the uncertainties involved, the Reivilo and Paraburdoo spherule layers could have formed contemporaneously around 2.57 Ga (see Sect. 8.4.2 for more discussion).

8.3.3.4 Geographic Distribution and Variation

As with the Kuruman spherule layer, the number of known occurrences is so small that no firm conclusions can be drawn about possible paleogeographic gradients in the Reivilo spherule layer, but variations in its character between cores may reflect contrasts in the paleoenvironmental settings in which it was preserved. In core GKP-1, the Reivilo spherule layer spherules were deposited in conjunction with large carbonate intraclasts, similar to spherules in parts of the Bee Gorge spherule layer (Fig. 8.8a) and Monteville spherule layer (see Fig. 8.25a and Sects. 8.3.4.1 and 8.3.4.4). By analogy to these two better-studied layers, the Reivilo spherule layer at this site could have been produced by high-energy waves and/or currents with significant bottom scour and local transport of large rip-up clasts of mud. However, the spherule layer in core GKF-1 consisted entirely of spherules when deposited and it is under- and overlain by laminated carbonate mud with no evidence of high-energy processes beyond the spherules themselves. They may have accumulated by direct fallout at this site, although no grading is apparent. More troublesome is the fact (noted in Sect. 8.3.1) that GKF-1 was drilled in a shallower part of the paleoenviroment than GKP-1; if high-energy processes were involved in depositing the Reivilo spherule layer at GKP-1, it is reasonable to expect there to be signs of equally (if not greater) energy where the layer was deposited in shallower water. This supports the alternative interpretation that the large intraclasts in GKP-1 are products of mass movement on a slope, consistent with the evidence of slope movement from surrounding strata (Sumner and Beukes 2006; see also Sect. 8.3.2.4). Perhaps the Reivilo spherule layer in core GKP-1 is a debris flow deposit, although it is much thinner than the Carawine spherule layer (see Sect. 8.2.5.1). The differences between the occurrences of the Reivilo spherule layer in the two Agouron Institute cores are in fact no greater than those observed within one ~45-m-long surface exposure of the Monteville spherule layer (described in Sect. 8.3.4.1). All that can be said without additional data is that the Reivilo spherule layer was deposited by an anomalously high-energy event with significant seafloor scour, at least in some places.

In the Kathu core, the Reivilo spherule layer is different from either of the Agouron Institute cores. Specifically, it consists of a basal sand bed consisting

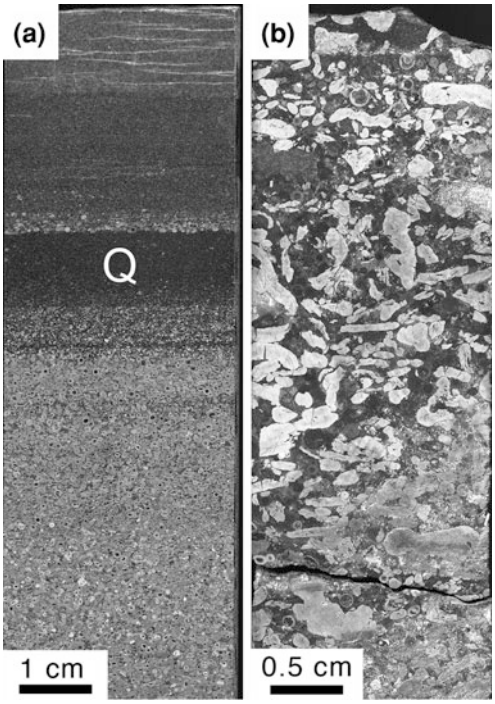

Fig. 8.26 Images of polished slabs from the Monteville spherule layer in 2 drillcores. **a** Monteville spherule layer in core TK1 showing its composite nature. The basal zone (*medium gray*) consists of both flattened and unflattened spherules with ~10 % interstitial sericite (probably cement) and ~3 % quartzose sand. In contrast, the dark band labeled 'Q' is ~70 % quartzose sand with admixed spherules and derived detritus and the lighter gray layer at the top is ~95 % carbonate. Thin zones just above and below band Q are also rich in spherules (white to very light gray grains). **b** Monteville spherule layer in Agouron Institute core GKF-1 where it is rich in pyrite intraclasts (*light to medium gray*), most of which are locally reworked early diagenetic concretions. Most of the spherules appear as circles with white rims (made of K-feldspar) with dark centers (mostly sparry carbonate). Most of the dark gray material is sparry carbonate

almost entirely of spherules overlain by a fine carbonate sand layer with very few spherules (Fig. 8.23c). The presence of shale rip-up clasts in the basal bed proves it was formed by waves and/or currents rather than as a direct fallout deposit. The upper carbonate-rich part of the Reivilo spherule layer in the Kathu core is also anomalous relative to the surrounding carbonate strata, most of which display microbial structures such as stromatolites. The fact that it is one of the few physically deposited layers in the local succession coupled with its position directly atop the spherules suggests this upper layer is fine carbonate sand deposited by bottom return flow or backwash from an onshore-directed, tsunami-style surge induced by the impact that created the spherules (Simonson et al. 2009a). This is not as clear a case as the backwash bed in the Monteville spherule

layer (described in Sect. 8.3.4.4), but it seems like a good fit to available data. Whatever processes were involved in depositing the Reivilo spherule layer found in the Kathu and Agouron Institute cores, the size and nature of the spherules do not change significantly over a distance of ~100 km.

8.3.3.5 Extraterrestrial Component and Target Material

Only one sample from the Reivilo spherule layer has been analyzed for its PGE content. The sample is from the spherule-rich basal bed in the Kathu core; it yielded an Ir concentration of 176 ppb and displays a chondrite-normalized pattern from Ir to Rh that is essentially flat, whereas Pd and Au show strong depletion (Fig. 8.6). The high levels of PGEs are equivalent to a content of about 40 wt % chondritic material in the Reivilo spherule layer sample, which consists almost entirely of spherules. Because only one sample was analyzed, it is not known whether such high levels of chondritic material are typical of this layer or just a local anomaly, but samples from the Paraburdoo spherule layer yielded even higher values of Ir (see Sect. 8.2.4.5). The Reivilo spherule layer has been correlated with the Paraburdoo spherule layer in the Hamersley Basin based on textural and stratigraphic similarities (Hassler et al. 2011). The relative proportions of the PGEs analyzed in the Paraburdoo and Reivilo spherule layers support this correlation (Goderis et al. 2012; see Sect. 8.4.2 for further discussion). In addition to the Paraburdoo spherule layer, selected samples from the Paleoarchean S3 and S4 spherule layers in the Barberton Greenstone Belt have levels of Ir (described in Sects. 9.2.2.5 and 9.2.1.5, respectively; see also Kyte et al. 1992; Reimold et al. 2000) that are higher than the single value reported from the Reivilo spherule layer. However, the relative proportions of the PGEs analyzed in the Reivilo spherule layer are very similar to those in the S4 spherule layer (Fig. 9 in Simonson et al. 2009b). We are not aware of any attempts to perform Cr isotope analyses on the Reivilo spherule layer.

8.3.4 Monteville Spherule Layer

8.3.4.1 Description of Layer

The **Monteville spherule layer** is hosted by the Monteville Formation, the lowest unit of the Campbellrand Subgroup stratigraphically. The Monteville extends throughout the Griqualand West Basin and marks a transition from the dominantly siliciclastic sedimentation that went before to the carbonate sedimentation that followed. It consists of a mixture of carbonate, shale, and several minor lithologies and the ratio of carbonate to shale increases upsection, as does the relative abundance of shallow-water depositional structures (Beukes 1987). However, most of the Monteville was deposited in deeper water paleoenvironments (Sumner and

Beukes 2006; Schröder et al. 2006) and the Monteville spherule layer is located in the lower part of the Monteville Formation among strata deposited below wave base. The Monteville Formation is capped by a thin but regionally extensive layer of quartzarenite known as the Motiton Member (Beukes 1987; Sumner and Beukes 2006); it and the Monteville spherule layer contain the only quartzose sand in the formation (see Sect. 8.3.4.4 for further discussion).

The Monteville spherule layer was originally recognized in multiple outcrops and cores bracketing a triangular area of $\sim$15,000 km^2 (Fig. 8.20b) in the central Griqualand West Basin (Simonson et al. 1999). It was subsequently identified in two Agouron Institute cores and another drilled $\sim$270 km southeast of the Griqualand West Basin near Trompsburg (Simonson et al. 2009c), expanding its minimum preserved area to $\sim$46,000 km^2. The size and abundance of spherules in the Monteville spherule layer do not appear to change systematically throughout this entire area, but the nature of the spherule layer varies significantly from place to place. At least some of these changes appear to be related to differences in the paleodepth of water and/or proximity to land. The main features of the Monteville spherule layer are summarized here briefly with an emphasis on the characteristics that indicate it is the product of an unusually high-energy event. More details of how these features vary laterally are given in Sect. 8.3.4.4.

In many locations, the Monteville spherule layer consists of a coarser lower part rich in large intraclasts and a finer upper sandy part (Fig. 8.25). In the type section of the Monteville Formation where it is exposed for $\sim$45 m on a cliff face, the two parts of the spherule layer are both $\sim$25 cm thick on average. However, they pinch and swell laterally and independently; locally they both dwindle to almost nothing (Simonson et al. 1999). The lower part of the Monteville spherule layer at the type section contains abundant spherules as well as tabular rip-up clasts of carbonate up to 1.8 m long eroded from underlying and/or nearby strata (Hassler and Simonson 2001). Equally large slabs may also be present in this spherule layer in some cores, e.g., Agouron Institute core GKF-1 (Schröder et al. 2006), but such large clasts are difficult to confirm in narrow cores. The layer also contains smaller rip-up clasts of shale and pyrite, the latter being derived from early diagenetic concretions in underlying shales and locally quite abundant. The shale rip-up clasts are thin and generally intermediate in size between the carbonate and pyrite intraclasts.

The upper part of the Monteville spherule layer varies in character throughout its area of occurrence. It consists of a combination of spherules and sands of other compositions (most typically carbonate), but the ratio of spherules to non-spherule sands varies dramatically. Commonly, the upper part of the spherule layer contains a basal zone up to $\sim$5 cm thick that consisted almost entirely of spherules when it was originally deposited (Fig. 8.26a). In its northeasternmost occurrences, the layer contains abundant quartzose sand presumably derived from the Kaapvaal Craton to the northeast (see Sect. 8.3.4.4 for more discussion). As in the Carawine spherule layer and Jeerinah spherule layer (described in Sects. 8.2.5.1 and 8.2.6.1, respectively), the quartz grains in the Monteville spherule layer show textures typical of continental basement rocks and no candidates for PDFs or other shock

features have been detected. The only other coarse quartz sand in the Monteville Formation is in the Motiton Member, ~38 m stratigraphically above the Monteville spherule layer. The strata between the spherule layer and Motiton show evidence of continued sedimentation below wave base under low-energy conditions. Hassler and Simonson (2001) attributed the coarse quartz sand in this layer to offshore bottom-return flow induced by a pile-up of water in coastal areas triggered by an oceanic impact (see Sect. 8.3.4.4 for further discussion). One common feature of the upper sandy part is cross-stratification (Fig. 8.25b) that varies from cm-scale current cross-laminae to decimeter-scale hummocky cross-stratification. In addition, smaller intraclasts of pyrite, shale, and carbonate occur near the base of the upper part. The Monteville spherule layer was apparently deposited by a combination of both waves and currents during one of the highest-energy events to take place during the deposition of the Monteville Formation (Simonson et al. 1999; Hassler and Simonson 2001).

8.3.4.2 Description of Spherules and Related Particles

The spherules in the Monteville spherule layer closely resemble those in most of the Archean-Proterozoic boundary layers described above, particularly those of the Jeerinah spherule layer (Sect. 8.2.6.2). The following descriptions focus on the ways in which spherules in the Monteville spherule layer differ from those already described for other Archean-Proterozoic boundary layers.

The best preserved spherules in the Monteville spherule layer are found in cores drilled near the Pering mine (Fig. 8.20b; Wheatley et al. 1986) where they average 0.65 mm in diameter and range up to 1.6 mm (Simonson et al. 1999). Most of the spherules are coarse sand size in both surface exposures and cores throughout the spherule layer's area of occurrence, including the Trompsburg core (Simonson et al. 2009c). The spherules in this layer are generally circular to oval in cross-section (Fig. 8.27a,b,d), although most have been moderately to strongly compacted (Kohl et al. 2006; described below). Also present are a few solitary fragments of spherules broken prior to deposition as well as fragments of rims where hollow spherules cracked in situ à la Wilkinson and Landing's (1978) "eggshell diagenesis" (Fig. 8.27e).

Internally, acicular to lath-shaped K-feldspar microlites are the dominant constituent of the Monteville spherule layer spherules; rims of inward-directed radial-fibrous aggregates are common (Fig. 8.27a,d,e). Spherules with randomly oriented laths whose textures resemble basalts are present (Fig. 8.27b), but as in the Jeerinah spherule layer and Carawine spherule layer, they form a smaller fraction of the spherule population than they do in the Dales Gorge and Bee Gorge spherule layers. In addition to K-feldspar, the Monteville spherule layer spherules contain carbonate (locally in great abundance), pyrite, sericite, quartz (relatively rare), and disseminated iron hydroxides. As in other layers near the Archean-Proterozoic boundary, the carbonate, pyrite, and quartz tend to be coarsely crystalline and typically obscure primary textures, as do the finely crystalline iron

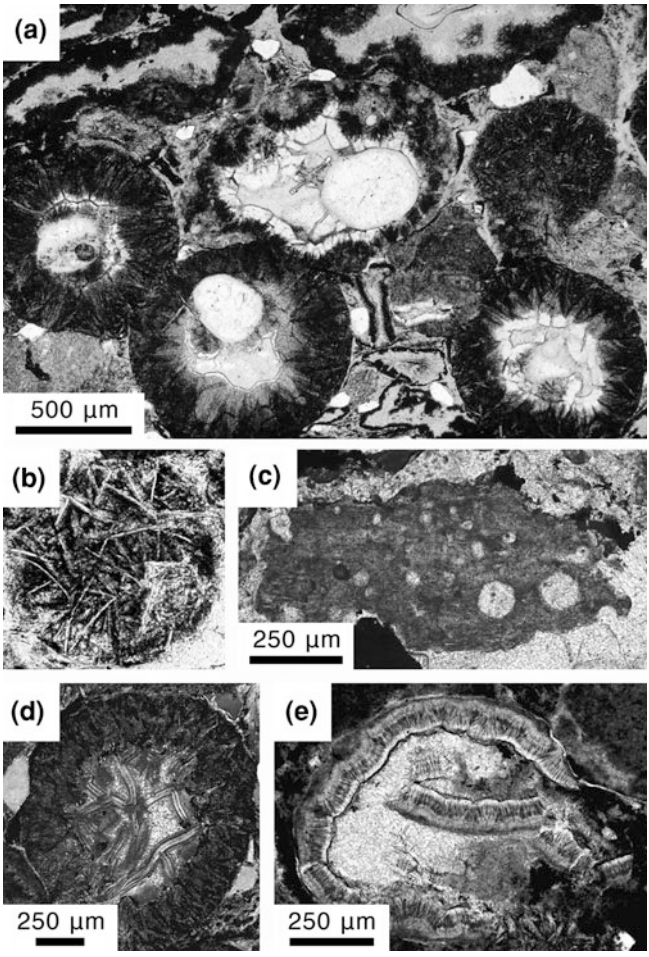

hydroxides. Some of the sparry K-feldspar, carbonate, and/or quartz form clear spots interpreted as cement-filled vesicles and replaced glass cores (Fig. 8.27a). As in the Jeerinah spherule layer spherules (described in Sect. 8.2.6.2), thin ribbons of pure sericite criss-cross central spots in septarian networks (Fig. 8.27d) that probably originated along microfractures in glass cores. Sericite ribbons also line some vesicles like those in the Jeerinah spherule layer (Fig. 8.19c). In addition, some of the clear central spots consist entirely of felted masses of sericite.

The Monteville spherule layer also contains particles of former melt whose shapes are more angular, elongated, and larger on average than the spherules *per se* (Fig. 8.27c). These irregular particles also differ from spherules internally; specifically, they are more likely to have relict flow banding or schlieren as well as multiple small vesicles instead of larger solitary ones. These particles are very similar to but generally not as abundant as the irregular particles in the Carawine

◀ **Fig. 8.27** Photomicrographs, taken in plane polarized light with the exception of **d**, of particles from the Monteville spherule layer. **a** Compacted spherule-rich sand from core P11 similar to lower part of core in Fig. 8.26a. Most spherules have rims of inward-radiating fibrous K-feldspar and central clear spots with composite textures. Both spherules in the middle have circular to oval areas of sericite (*light gray*) that are probably infilled vesicles; otherwise the central spots consist largely of K-feldspar (*pale tan*, probably replaced glass). Most of the rest of the sample also consists of K-feldspar. Small clear spots between spherules are detrital quartz grains. Interstitial cement is scarce; evidence of compaction includes a ductilely flattened spherule (*upper left* corner). **b** A perfectly circular spherule with randomly oriented laths of K-feldspar that texturally resembles a basalt. The mesostasis is rich in opaque material. **c** An irregular melt particle that consists almost entirely of K-feldspar, contains clear circles of sericite that are probably infilled vesicles, shows faint longitudinal flow banding, and contains small K-feldspar microlites aligned with same. **d** Spherule from core TL1, taken with crossed polarizers, that has a botryoidal rim of inward-radiating fibrous K-feldspar (*dark gray*) and a clearer central spot consisting largely of sericite. Some of the sericite is in the form of fibrous isopachous ribbons that probably follow former cracks in a glass core. The small light gray bodies around the spherule are detritial grains of monocrystalline quartz. **e** A formerly hollow spherule (probably due to dissolution of glass core) with a thin botryoidal rim of K-feldspar which was broken during compaction. Some of the rim pieces fell into the central void before it was filled with sericite (clear). **e** is from Simonson (2003a), Fig. 7d

spherule layer and Jeerinah spherule layer (described in Sects. 8.2.5.2 and 8.2.6.2, respectively). Few if any irregular particles are present in the other layers in the Griqualand West Basin (the Kuruman and Reivilo spherule layers).

Both the spherules and irregular particles have been widely modified by compaction, although its effects are more obvious on the spherules because of their regular geometric shapes. Both the external shapes and internal textures of many spherules were modified by both brittle and ductile physical compaction as well as by pressure solution (Kohl et al. 2006). This is evidenced by an abundance of concavo-convex to sutured grain-to-grain contacts and subtle to extreme flattening of internal textures. Spherules in carbonate-rich samples are typically the least affected by compaction, suggesting they were the ones cemented the earliest.

Finally, the mineral compositions of samples from cores versus outcrops tend to differ, presumably reflecting the effects of surface weathering. Specifically, spherules in cores consist largely of K-feldspar, whereas in samples from surface exposures carbonates and iron hydroxides (probably a weathering product of pyrite) are much more abundant. In addition, fresh sericite is much more scarce in samples from outcrops than in those from cores. That said, the spherules in some cores are also extensively replaced by carbonate, e.g., in the Trompsburg core.

Given their similarities, many of the interpretations of the spherules in other Archean-Proterozoic boundary layers apply to those in the Monteville spherule layer as well. To recapitulate, the K-feldspar microlites are probably pseudomorphs of plagioclase and most of the rest of the minerals as well as the sparry K-feldspar formed via glass replacement and void-filling cementation. It again appears that the rims and lath-shaped crystals mostly formed in flight and that the spherules in this layer are probably relatively distal ejecta from a large impact. Finally, some of the spherules in the Monteville spherule layer show basaltic textures, but fewer than in some of the other Archean-Proterozoic boundary layers.

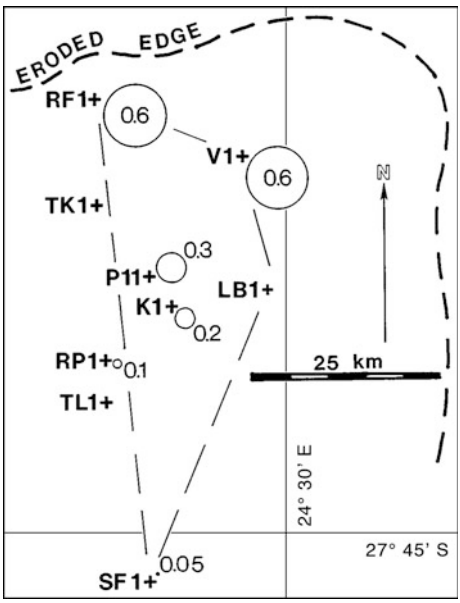

Fig. 8.28 Map showing the relative sizes of the coarsest terrigenous quartz sand (represented by *circles*) in the Monteville spherule layer in cores drilled near the Pering mine. The numbers inside or next to the circles give the diameter of the largest detrital quartz grains in millimeters. Each plus symbol represents a location where the spherule layer was identified in a drillcore. Core P11 was drilled at the Pering Mine. The curving *dashed line* labeled "eroded edge" is the northern to eastern limit of preservation of the Monteville Formation; crystalline basement rocks of the Kaapvaal Craton lie further to the northeast. The trapezoidal *dashed line* on this map outlines the same area as the solid trapezoid in Fig. 8.20. From Simonson et al. (1999), Fig. 8, with permission from the Geological Society of America

8.3.4.3 Radiometric Age

None of the tuffaceous layers in the Griqualand West Basin that have been dated via SHRIMP using the zircon crystals they contain are in close stratigraphic proximity to the Monteville spherule layer (Fig. 8.1). Strata correlated with the Monteville Formation have been dated to 2.55 Ga (as summarized in Simonson et al. 2000a), but this correlation is disputed. As noted above, the Reivilo spherule layer probably formed around 2.57 Ga and it is ~200 to 300 m above the Monteville spherule layer stratigraphically. The closest date to the Monteville spherule layer is from a tuff roughly 50 m below it stratigraphically in the Lokammona Formation. This tuff yielded a date of 2650 ± 8 Ma (Gutzmer and Beukes 1998). This means the Monteville spherule layer could be contemporaneous with the Jeerinah spherule layer and Carawine spherule layer at around 2.63 Ga, but it could also be significantly different in age.

8.3.4.4 Geographic Distribution and Variation

The Monteville spherule layer has been preserved over a minimum area of ~46,000 km^2 (Fig. 8.20b; Simonson et al. 2009c). As noted above, the size and abundance of spherules in the Monteville spherule layer do not appear to change systematically throughout this area. The thickness and coarseness of this spherule layer as a whole do vary from site to site, but few systematic trends that could be related to paleoslope or other paleoenvironmental controls are apparent. As described in Sect. 8.3.4.1, the Monteville spherule layer contains a lower part with large carbonate intraclasts and a sand-rich upper part in most of its known occurrences. However, large carbonate intraclasts are not always present. In Agouron Institute core GKP-1 for example, the entire spherule layer is only 1.5 cm thick and consists largely of fine carbonate sand with only a few spherules and spherule fragments. In contrast, this spherule layer in Agouron Institute core GKF-1 drilled ~30 km away and higher on the paleoslope is 90 cm thick and does contain large carbonate intraclasts. In the Trompsburg core drilled ~270 km further east, the Monteville spherule layer is again different; here it lacks large carbonate intraclasts and is sandy throughout, but it is almost a meter thick. Diagenetic pyrite intraclasts are also common in this layer and locally quite abundant (Fig. 8.26b); in the Trompsburg core for example, pyrite intraclasts make up ~50 vol % of the basal 40 cm of the layer (Simonson et al. 2009c). The sandy upper part of the Monteville spherule layer is likewise highly variable; it ranges from a layer ~3 cm thick that consisted almost entirely of intact spherules when deposited (Fig. 9a of Simonson et al. 1999) to a cross-bedded fine sand ~10 cm thick with very little spherule material (Fig. 8.25b) to a mixture of spherules and other types of sand (Fig. 8.26a) that can be up to ~2 m thick (Fig. 5 of Simonson et al. 1999). The Monteville spherule layer shows almost the full range of variability in its thickness and spherule and large intraclast content within a single cliff exposure ~45 m long at the Monteville farm. In short, it appears that the Monteville spherule layer was deposited during an anomalously high-energy event that resulted in meter-scale thickness variations even in local areas.

The only feature of the Monteville spherule layer that appears to vary systematically as a function of palogeographic position is its content of quartzose sand. As noted in Sect. 8.3.4.1, this sand was eroded from continental basement rocks. Its derivation from the Kaapvaal Craton to the northeast is clearly signaled by the fact that the quartzose sand gets coarser and thicker rapidly moving northeast towards the Craton (Fig. 8.28). The maximum size of the quartzose sand in the spherule layer decreases from ~0.6 mm (coarse sand) to 0.05 mm (silt) in a horizontal distance of less than 65 km (Fig. 8.28). Quartzose silt is common in ambient shales throughout the Monteville Formation, but no other coarse quartz sand is found in the Monteville Formation save for the Motiton Member. The thickness of the quartz sand-rich part of the Monteville spherule layer also decreases from ~200 to 0.5 cm in the same distance, whereas the size and aggregate thickness of the spherules remain essentially constant. Detecting this trend was made possible by the fact that an unusually large number of drillcores

intersected this layer in the vicinity of the Pering Mine (Fig. 8.28). The fact that this was not just an anomalous local influx is indicated by the presence of coarse quartzose sand in the Monteville spherule layer in the Trompsburg core (Simonson et al. 2009c). The Trompsburg core was drilled ~250 km to the southeast, but it and the northeastern corner of the Griqualand West Basin are in equivalent positions relative to the paleo-shelf break (Knoll and Beukes 2009; de Kock et al. 2009).

In summary, the primary sedimentary structures and areal variability in the Monteville spherule layer indicate it was deposited by several different but related processes. The most important processes were the delivery of an abundance of spherules to the Griqualand West Basin, their reworking by strong waves and currents as well as sediment gravity flows locally (the latter described in Hassler and Simonson 2001), and extensive substrate erosion in a variety of water depths during the reworking of the spherules. All of these processes could have been caused by an oceanic impact with the attendant tsunami-like waves that would inevitably result. The co-deposition of impact spherules and anomalously coarse terriginous sand supports this interpretation.

8.3.4.5 Extraterrestrial Component, Target Material, and Shock Metamorphism

Like all of the Archean-Proterozoic boundary layers analyzed to date, the Monteville spherule layer has anomalously high concentrations of PGEs relative to the surrounding strata, but the concentration of extraterrestrial material appears to be smaller than in other Archean-Proterozoic boundary layers analyzed to date. Clear enrichment is only observed in samples from spherule-rich parts of the spherule layer (Simonson et al. 2000c, 2009b). Specifically, the Ir concentration in 5 spherule-rich samples averages 4.5 ppb with a maximum of 6.4 ppb, even though 3 of the 5 samples analyzed contain quartzose detritus. In contrast, the concentration of Ir only averages 0.35 ppb in 3 samples from carbonate-rich parts of the layer, the latter including samples from both the basal part rich in carbonate rip-up clasts and the upper part rich in finer carbonates. The Ir concentrations in associated strata were 0.2 ppb in one of the 15 associated samples analyzed and below detection limits that ranged from 0.2 to 1.1 ppb in the other 14. These samples encompassed a broad range of lithologies that included pyritic shales, cherts, carbonates, and tuffs.

As in other Archean-Proterozoic boundary layers, the interelement ratios of the PGEs in the Monteville spherule layer are consistent with an extraterrestrial origin (Simonson et al. 2000c, 2009b). When normalized to CI chondrite abundances (Fig. 8.6), the PGE ratios for this spherule layer are essentially flat i.e., unfractionated relative to chondrites, although most samples show enrichment of Pd and Au relative to the other PGEs. As in the Bee Gorge spherule layer (described in Sect. 8.2.3.5), the latter suggests some differential remobilization of PGEs after deposition. The relative abundance of the PGEs do not shed much light on the

nature of the impactor. At the 2 sigma confidence level, PGE data from the Monteville spherule layer overlap with those of ordinary, enstatite, and CI-type carbonaceous chondrites (Simonson et al. 2009b). However, REE contents of the Monteville spherule layer suggest something about the nature of the target material. Two carbonate-poor samples from the layer display flat middle and heavy rare earth element patterns consistent with a basaltic component (and an oceanic impact), albeit mixed with more continental material than in other layers such as the Jeerinah spherule layer (described in Sect. 8.2.6.5).

One sample from the Monteville spherule layer was analyzed for extraterrestrial Cr via the isotopic method, but no isotopic anomaly was detected. This is not surprising in view of the fact that the sample that was analyzed contains appreciable quantities of fine quartzose sand and other detrital contaminants (Simonson et al. 2000b). The latter could be masking any signal associated with low levels of extraterrestrial material in the spherules.

Like from the Bee Gorge, Carawine, and Jeerinah spherule layers, grains containing the high-pressure TiO_2II phase were recovered from the Monteville spherule layer (Smith et al. 2010). Otherwise, no evidence of shock metamorphic effects has been found in this spherule layer.

8.4 Correlations among Archean-Proterozoic Boundary Spherule Layers

8.4.1 Correlations within the Hamersley Basin

The stratigraphic succession within the main part of the Hamersley Basin is very well known (Trendall and Blockley 1970; Trendall 1983) and, at least in the interval where the spherule layers have been identified, it approximates a "layer cake" of laterally extensive units. Given the positions of the spherule layers in this succession (Fig. 8.1), four large impacts ranging in age from 2.63 to ~2.49 Ga are required to account for the Dales Gorge (Sect. 8.2.2), Bee Gorge (Sect. 8.2.3), Paraburdoo (Sect. 8.2.4), and Jeerinah (Sect. 8.2.6) spherule layers. A fifth layer in the Oakover River area, the Carawine spherule layer (Sect. 8.2.5), is geographically isolated from the others (Fig. 8.2) in a stratigraphic succession that is somewhat different (Simonson et al. 1993a), so it could either represent a fifth impact or correlate to one of the four layers in the main outcrop area of the Hamersley Basin. Simonson (1992) and Simonson and Hassler (1997) originally correlated the Carawine spherule layer with the Bee Gorge spherule layer, but this hypothesis was falsified when it was determined that the Carawine and Jeerinah spherule layers were both deposited ~2.63 Ga (see Sects. 8.2.5.3 and 8.2.6.3) whereas the Bee Gorge spherule layer was deposited ~2.54 Ga (see Sect. 8.2.3.3). Closer study of the Jeerinah spherule layer also revealed the presence of irregular particles that were formerly molten (Fig. 8.17b, 8.19a,b) very much like those in

the Carawine spherule layer (Fig. 8.16). Similar particles are rare in the other spherule layers in the Hamersley Basin. Therefore, it seems possible, if not likely, that the Jeerinah and Carawine spherule layers are both ejecta from the same impact.

One concern about correlating the Jeerinah and Carawine spherule layers is that they are hosted by different formations. The Jeerinah spherule layer is restricted to the main outcrop area where it is just below the top of the Jeerinah Formation stratigraphically whereas the Carawine spherule layer occurs low in the Carawine Dolomite but close above the top of the Jeerinah Formation in the Oakover River area. Therefore these two layers could have been deposited simultaneously, provided the lowest strata in the Carawine Dolomite are equivalent to the upper part of the Jeerinah Formation in the main outcrop area (Fig. 8.1). This would require the contact between the Hamersley and Fortescue Groups to be time-transgressive and get older from southwest to northeast. Given the facies relationships and paleogeography of the upper Fortescue and lower Hamersley Groups (outlined in Sects. 8.2.5 and 8.2.6; see Simonson et al. 1993a; Thorne and Trendall 2001), this may well be the case. Therefore, the fact that the Jeerinah and Carawine spherule layers are hosted by different formations does not preclude their having been formed by a single impact.

Even if the Jeerinah and Carawine spherule layers were formed in the same event, there are important differences between these two layers. The most obvious difference is in thickness; the Carawine spherule layer is ~7 to 25 m thick whereas the Jeerinah spherule layer is at most 1.6 m thick (at Hesta). One possibility is that both layers were produced by a sediment gravity flow moving south and west across the Hamersley Basin; one could reasonably expect a shift from deposition by debris flows such as the Carawine spherule layer to deposition from turbidity currents such as the Jeerinah spherule layer from a sediment gravity flow moving down the paleoslope away from the carbonate platform (Hassler et al. 2005). This interpretation is also consistent with the fact that a layer at a site intermediate between the Hesta and Carawine spherule layer occurrences geographically (the Billygoat Bore core, described in Sects. 8.2.6.1 and 8.2.6.4) has an intermediate thickness (2.8 m). One problem with a simple sedimentological interpretation of the westward change in thickness of the Jeerinah spherule layer is that it dwindles to just a few millimeters in thickness (Fig. 8.17a) in all of the occurrences south and west of the Hesta exposure.

The aggregate thickness of spherules and related particles also differs from ~30 cm in the Carawine spherule layer to ~18 cm in the Jeerinah spherule layer at Hesta. One possibility is that this change represents ejecta thinning away from a source crater northeast of the Oakover River area (current coordinates), which would be consistent with the fact that the largest ejecta, irregular particles up to 2 cm across (Fig. 8.14b), occur in the northeasternmost occurrences of the Carawine spherule layer. However, the spherules in the Jeerinah spherule layer south and west of Hesta dwindle to a discontinuous stringer that is only one spherule thick (Rasmussen and Koeberl 2004). As explained in Chap. 10, based on well-characterized Phanerozoic layers, the aggregate thickness of distal ejecta

should not change so dramatically in such a short distance unless the sites are close to the source crater. Several extenuating factors might be responsible for this dramatic change in thickness. One is the possibility that the aggregate thickness of spherules and related particles is anomalously thick in the Oakover River area as a result of reworking. Secondly, ejecta may not have been dispersed equally in all directions, as suggested by thickness variations in the Carawine spherule layer within the Oakover River area (see Sect. 8.2.5.4). Finally, reworked spherule layers can vary in thickness from millimeters to a meter or more even in a small area, as documented for the Monteville spherule layer (described in Sect. 8.3.4.1), so the aggregate thickness of spherules in a single core is not necessarily representative of its average thickness throughout a given area.

There are more subtle differences between the Jeerinah spherule layer at Hesta and the Carawine spherule layer as well. For example, the quartzose detritus is similar in size and abundance and appears to be derived from continental basement rocks in both layers, but the feldspar at Hesta differs from the feldspar in the Carawine spherule layer in being coarser, more abundant, and including many broken euhedral crystals probably derived locally from tuffaceous layers. There are also subtle differences in the textures of the spherules. A higher proportion of the spherules at Hesta have well-developed radial-fibrous rims compared to those in the Carawine spherule layer (Jones-Zimberlin et al. 2006) and the Carawine spherule layer spherules lack sericite ribbons like those in the Jeerinah spherule layer. The latter could reflect different diagenetic histories in different areas, but the differences in the crystallization textures are more worrisome. The small amount of geochemical work that has been done on the Carawine and Jeerinah spherule layers does not prove they were produced by the same impact, but it provides data consistent with this correlation. Samples from both of these spherule layers have positive Cr isotopic anomalies (Fig. 8.7), indicating they were both produced by ordinary chondritic impactors. Both layers have also yielded anomalously high concentrations of Ir (Simonson et al. 1998, 2009b), although the maximum concentrations in the Carawine spherule layer are about an order of magnitude lower than they are in the Jeerinah spherule layer (see Sects. 8.2.5.5 and 8.2.6.5). In addition, the Carawine and Jeerinah spherule layers both contain shocked rutile containing the high-pressure polymorph TiO_2II. Additional work is clearly required to test the correlation of the Jeerinah and Carawine spherule layers.

The most problematic occurrence is in FVG-1, the core in which the Jeerinah spherule layer was originally discovered (Simonson et al. 2000a); neither irregular particles of former melt like those in the Carawine spherule layer nor quartzose detritus like that in the Carawine spherule layer, the Jeerinah spherule layer at Hesta, and the Billygoat Bore core appear to be present in the layer in this core. The Jeerinah spherule layer in cores DDH-186 and WRL-1 west of Hesta contains detrital quartz grains (Rasmussen and Koeberl 2004) but it is not known whether irregular particles are present. In addition, the internal textures of the spherules in the layer in FVG-1 appear to be more like those in the Bee Gorge spherule layer

than those in the Carawine spherule layer or the Jeerinah spherule layer at Hesta (Scally and Simonson 2005). The correlation of the spherule layer in the FVG-1 core is complicated by the fact that the shale hosting the layer in this core is overlain by an anomalous stratigraphy; specifically, the Marra Mamba BIF is anomalously thin and overlain by a thick succession of enigmatic carbonate breccias instead of the usual thinly layered Paraburdoo Member dolomites. Therefore, the possibility that the spherule layer in FVG-1 is the product of a different impact from any of the other Hamersley layers cannot be ruled out.

No equivalents for the Dales Gorge, Bee Gorge, or Paraburdoo spherule layers have been reported from the Oakover River area of the Hamersley Basin. However, given its apparent stratigraphic equivalence with at least part of the Wittenoom Formation (Fig. 8.1), the Paraburdoo spherule layer and possibly the Bee Gorge spherule layer could be present in the Carawine Dolomite. It is unlikely the Dales Gorge spherule layer will be found in the Oakover River area because the Carawine Dolomite is capped by a major erosional unconformity (Blake et al. 2011); any strata equivalent to or younger than the Dales Gorge iron formation have been eroded, if they were ever deposited in the Oakover River area.

8.4.2 Correlations between the Hamersley and Griqualand West Basins

As in the Hamersley Basin (Western Australia), the stratigraphic succession within the Griqualand West Basin (South Africa) is very well known (Beukes 1983, 1987). Three spherule layers have been found to date, each one at a different stratigraphic level (Fig. 8.1) and therefore the product of a different impact. The layer in the Trompsburg core is clearly at the lowest of these three levels (Simonson et al. 2009c) even though it is well outside the Griqualand West Basin (Fig. 8.20b). Unfortunately, the ages of the Kuruman (Sect. 8.3.2.3), Reivilo (Sect. 8.3.3.3), and Monteville (Sect. 8.3.4.3) spherule layers are not as well constrained as the layers in the Hamersley Basin. Therefore, it is possible that the three impacts that produced the Archean-Proterozoic boundary spherule layers in South Africa took place between 2.63 and 2.49 Ga, but there is more uncertainty involved. Equivalents of the layers in the Griqualand West Basin may also be present in the Transvaal Basin further east, but none have been reported as yet (as noted in Sect. 8.3.1).

The stratigraphic successions and other geologic features of the Hamersley and Griqualand West Basins are remarkably similar in many ways, as originally noted by Button (1976). The similarities are so numerous that Cheney (1996) suggested the two successions were deposited jointly on the trailing edge of a single continental block for which he proposed the name Vaalbara, a hybrid derived from the names Transvaal and Pilbara. Subsequent geochronological work has demonstrated that the two successions are in large part contemporaneous (Fig. 8.1). Detailed sedimentological studies have also revealed numerous paleoenvironmental

similarities between the formations that host the spherule layers (Beukes and Gutzmer 2008: Knoll and Beukes 2009). Although objections to the Vaalbara hypothesis were raised on the basis of paleomagnetic studies, de Kock et al. (2009) recently published paleomagnetic data consistent with the two basins being in close geographic proximity around the time of the Archean-Proterozoic boundary. If the two basins were side by side in a global context at that time, any distal ejecta they contained would be roughly the same distance from a given source crater and therefore any layers that correlate should be similar in character.

The most obvious correlation is between the Dales Gorge and Kuruman spherule layers (Rasmussen et al. 2005; Simonson et al. 2009a). The Dales Gorge Member and Kuruman Iron Formation have already been correlated because they are contemporaneous (Pickard 2002, 2003) and show numerous points of lithologic similarity (see Sect. 8.3.2.1). The Dales Gorge and Kuruman spherule layers appear to be at comparable stratigraphic levels within their respective host BIFs. Both the Dales Gorge Member and Kuruman Iron Formation consist of alternating BIF and shaly layers internally. There are 16 named alternations in the Dales Gorge Member and there are also 16 alternations in the Kuruman Iron Formation in its type section (Beukes and Gutzmer 2008); the Kuruman spherule layer occurs in the fourth shale layer, which would be equivalent to the DS4 shale layer that hosts the Dales Gorge spherule layer. The Kuruman and Dales Gorge spherule layers also consist of the same types of minerals (stilpnomelane, K-feldspar, carbonates, and opaques) and show similar textures, provided allowances are made for the surface weathering that has affected most of the Dales Gorge spherule layer occurrences but not the Kuruman spherule layer cores. However, this correlation has yet to be tested by in-depth geochemical analyses of both layers.

Hassler et al. (2011) also suggested the Paraburdoo and Reivilo spherule layers were formed by a single impact. Based on the sequence stratigraphic correlation between the Hamersley and Griqualand West Basins of Sumner and Beukes (2006), the Paraburdoo and Reivilo spherule layers are located at equivalent stratigraphic positions. In fact, Sumner predicated the stratigraphic level at which the Paraburdoo spherule layer should occur on the basis of the position of the Reivilo spherule layer and her correlations to the Hamersley strata, and the layer was discovered the following year during a search initiated on the basis of that prediction. The formation of the Paraburdoo and Reivilo spherule layers by a single impact is also consistent with a number of their characteristics, including the aggregate thickness and sizes of the spherules as well as the internal textures they display. As described in Sects. 8.2.4.2 and 8.3.3.2, the spherules in the Paraburdoo and Reivilo spherule layers represent on average the mostly highly crystallized spherules in their respective basins (Figs. 8.12, 8.24). Moreover, the Paraburdoo and Reivilo spherule layers both contain phlogopite pseudomorphs of skeletal olivine and possibly clinopyroxene crystals (e.g., Fig. 8.13a,c) not reported from other Archean-Proterozoic boundary layers. These pseudomorphs were not recognized in the Reivilo spherule layer spherules at first because they are not as well preserved as the spherules in the Paraburdoo spherule layer. The Paraburdoo spherule layer also differs from the other Hamersley layers in that it appears to be a

direct fallout deposit that was not reworked. While the spherules in the Reivilo spherule layer were reworked at most localities, they look very similar to the Paraburdoo spherule layer in core GKF-1, which may be a direct fallout deposit. Most recently, samples from the Paraburdoo spherule layer have been analyzed, and like the Reivilo layer, yielded Ir concentrations much higher than other Archean-Proterozoic boundary layers (see Sects. 8.2.4.5 and 8.3.3.5). In addition, these two layers display a similar chondrite-normalized pattern that is flat from Ir to Rh, and depleted in Pd and Au (Goderis et al. 2012). The concentrations of PGEs in the Paraburdoo and Reivilo spherule layers suggest roughly half the mass of the spherules in both of these layers consists of chondritic material, which is much higher than any of the other layers. In summary, the limited amount of geochemical data now available on these two layers supports the proposed correlation of the Paraburdoo and Reivilo layers.

Finally, the oldest of the layers in the Griqualand West Basin, the Monteville spherule layer, is a good candidate for correlation with the Carawine and Jeerinah spherule layers. Not only do they all have approximately the same stratigraphic positions (Fig. 8.1), the spherules in these layers all show similar textures. Specifically, the ratios of spherules with botryoidal rims to those with randomly oriented laths are similar in the Carawine, Jeerinah, and Monteville spherule layers (but not the Bee Gorge spherule layer) and all three have relatively high abundances of irregular melt particles (Figs. 8.16, 8.17b, 8.19a,b, 8.27c). Similar irregular particles (described in Sects. 8.2.5.2, 8.2.6.2, and 8.3.4.2) are rare in other Archean-Proterozoic boundary layers. In addition, the spherules and irregular melt particles in the Jeerinah and Monteville layers had similar diagenetic histories, including the formation of distinctive sericite ribbons (Figs. 8.19c, 8.27d) that are rarely present in other Archean-Proterozoic boundary spherule layers. Similar diagenetic histories lend support to the idea that the Hamersley and Griqualand West successions were part of a single basin at the time the impacts occurred and for a prolonged time thereafter rather than having been deposited on separate continents that were widely separated and experienced different geologic histories. The ages of the Carawine and Jeerinah spherule layers are fairly well constrained at $\sim$2.63 Ga. Unfortunately, the age of the Monteville spherule layer is not well constrained, but existing dates would allow it to be $\sim$2.63 Ga (Fig. 8.1).

Unlike the correlations of the Dales Gorge spherule layer with the Kuruman spherule layer and the Paraburdoo spherule layer with the Reivilo spherule layer discussed above, at least some geochemical work has been done on all three layers in the case of the Carawine, Jeerinah, and Monteville spherule layers. The data available are not extensive enough to establish the correlation beyond a doubt, but they do not invalidate the correlation. For example, the PGE patterns in the Monteville and Jeerinah spherule layers are similar in being unfractionated with little evidence of Pd depletion, although the Jeerinah spherule layer has a larger meteoritic component (Simonson et al. 2009b). Likewise, crust-normalized spidergrams for the Monteville and Jeerinah spherule layers are similar with strong enrichments in Ti and Cr. These two layers differ slightly in that the Monteville spherule layer shows moderate LREE enrichment over the Jeerinah spherule layer,

but the concentrations of the LREEs in the Monteville spherule layer are still low compared to the younger Archean-Proterozoic boundary layers that have been analyzed. As noted in Sect. 8.4.1, the Carawine and Jeerinah spherule layers both have positive Cr isotope anomalies, but extraterrestrial Cr has yet to be detected in the Monteville spherule layer. Despite these encouraging results, more in-depth geochemical studies of all three layers are needed to test the proposed correlations more rigorously.

Chapter 9
Paleoarchean Spherule Layers

9.1 Introduction: The Archean Stratigraphic Record

The Archean marks the earliest time in Earth history for which there is a decipherable record of surface events. As noted in Chap. 7, the end of the Archean Eon is formally defined chronologically as 2,500 Ma. The International Union of Geological Sciences (IUGS) provisionally recommended dividing the Archean into four Eras named the Neoarchean, Mesoarchean, Paleoarchean, and Eoarchean (Robb et al. 2004). They also suggested placing the Mesoarchean-Neoarchean boundary at 2,800 Ma, the Paleoarchean-Mesoarchean boundary at 3,200 Ma, and the Eoarchean-Paleoarchean boundary at 3,600 Ma (Fig. 7.1). The time period from the start of Earth history to the beginning of the Archean is widely referred to as the Hadean (Cloud 1972), but there is no universal agreement on where to place the Hadean-Eoarchean boundary. Robb et al. (2004) say the age of the Hadean-Eoarchean boundary is "undetermined," whereas Van Kranendonk et al. (2008) gave an age of ~4,000 Ma for the boundary but other values (e.g., 4,030 Ma) are under consideration. Cawood et al. (2006) put the boundary at 3.8 Ga, whereas Tanaka and Hartmann (2008) avoid the term Hadean altogether and extend the Eoarchean from 3,600 Ma back to the start of Earth history. In terms of the IUGS-recommended subdivision, the spherule layers described in this chapter are all Paleoarchean in age. More significantly, they are ~600 million years or more older than the Neoarchean layers described in Chap. 8, and no distal ejecta or spherule layers of intermediate ages have been reported.

Every continental landmass is built around at least one more or less centrally located block of ancient rock known as a Precambrian shield or craton. Our entire record of Archean history comes from cratons, all of which consist of rocks buried to great depth, then exhumed tectonically and/or by prolonged erosion. Most Archean rocks are highly metamorphosed and contain few features that can tell us what surface conditions were like on the early Earth. Individual zircon crystals as old as ~4.4 Ga have oxygen isotopic compositions suggesting oceans already existed at that time (Cavosie et al. 2005), but no rocks that old have been found

B. P. Glass and B. M. Simonson, *Distal Impact Ejecta Layers*, Impact Studies,
DOI: 10.1007/978-3-540-88262-6_9, © Springer-Verlag Berlin Heidelberg 2013

whose metamorphic grade is low enough for primary depositional textures and structures to have survived. The oldest rocks showing primary features are the Isua and Akilia successions of West Greenland (Nutman et al. 1997; Nutman and Friend 2009). These successions formed around 3.8–3.7 Ga and consist of metavolcanic and metasedimentary rocks. Although primary features like pillows in lavas and graded beds are locally recognizable (Nutman et al. 1984; Appel et al. 1998), the ambient level of deformation is so high that the textures needed to recognize distal ejecta layers are unlikely to be preserved in these rocks. It is, however, possible that geochemical signals of extraterrestrial material could have survived the deformation.

Because of the high level of alteration, distal impact ejecta have not and perhaps never will be recognized in the field among the supracrustal rocks of West Greenland. Despite this fact, multiple attempts have been made to detect evidence of impacts and/or extraterrestrial material in this region. Appel (1979) suggested tiny chromite grains in Isua BIFs were extraterrestrial in origin, but the Cr isotopic ratios of Isua samples are indistinguishable from terrestrial values according to Frei and Rosing (2005). Koeberl et al. (2000) found extensive fracturing in zircon crystals from Isua, but none show patterns diagnostic of shock metamorphism. Koeberl et al. (2000) also rejected an extraterrestrial origin for up to 0.2 ppb of Ir in Isua samples because the PGEs in general were highly fractionated and non-chondritic. Jørgensen et al. (2009) did ascribe a similar small enrichment in Ir in Isua rocks to an input from impacts of the **Late Heavy Bombardment**, but they did not report the data for other siderophile elements needed to demonstrate a chondritic signature. Finally, some researchers have attempted to use tungsten isotopic ratios to detect extraterrestrial material in Isua rocks. Schoenberg et al. (2002) detected negative tungsten isotopic anomalies in samples from Isua and closely related rocks from Labrador that they attributed to the presence of extraterrestrial material, However, Moynier et al. (2009) were unable to obtain similar anomalies in distal ejecta and other materials formed by Phanerozoic impacts and Willbold et al. (2011) obtained positive isotopic anomalies that they attributed to the survival of crustal values acquired prior to, not during, the "terminal" bombardment. In summary, an unambiguous signal of impact ejecta has yet to emerge from the Eoarchean strata of West Greenland, despite the fact that they were deposited shortly after the Late Heavy Bombardment.

The oldest supracrustal rocks yet found that are not highly metamorphosed and retain a wealth of paleoenvironmental information in the form of depositional textures and structures are located in two relatively small areas in South Africa and Western Australia. These areas are in the Kaapvaal and Pilbara Cratons, respectively, and the oldest well-preserved strata in both cases date to around 3.49 Ga (Van Kranendonk et al. 2008). Another commonality is that the successions are dominated by volcanic rocks. Such successions are known as Greenstone Belts (de Wit and Ashwal 1997) and typical of Archean supracrustal successions. As the name suggests, the dominant supracrustal rocks in these belts are mafic volcanic rocks metamorphosed to low or medium grades. Greenstone Belts tend to form narrow arcs sandwiched between or wrapped around domal bodies of granitic and

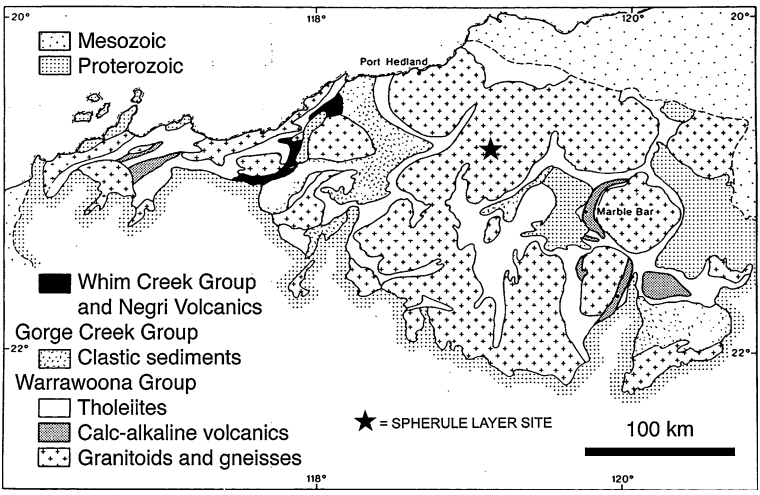

Fig. 9.1 Regional map of Pilbara Craton (Western Australia). Organization of Archean crust into domal masses of gneiss and granitoids separated by narrow greenstone belts (shown primarily as tholeiites) is typical of Archean crust. Star indicates the only area where Paleoarchean spherules have been recognized to date. Modified after Nisbet (1987), Fig. 3.19

gneissic rocks. This is well illustrated by both the Kaapvaal Craton (de Wit et al. 1992) and the Pilbara Craton (Fig. 9.1; Van Kranendonk et al. 2007a). Because this architecture is typical of many Archean cratons and rare in terranes formed since the Archean, many researchers believe Archean tectonics operated differently in some way from the plate tectonics of today. One key difference is scale; Archean successions rarely persist laterally for more than 100 km whereas many depositional basins on modern continent and plate margins persist for distances on the order of 1,000 km. This has fueled a lively debate about when modern plate tectonics started (Condie and Pease 2008), but the older terranes may be smaller simply because they are more highly deformed as a consequence of their great age. Few would dispute that something akin to modern plate tectonics was at work by the beginning of the Proterozoic Eon. Some have suggested that large impacts played a role in changing Earth's tectonic style regionally or even globally during the Archean (see Chap. 11).

Whatever their tectonic setting was, Greenstone Belts host the oldest known distal impact ejecta layers on Earth. This includes the first Precambrian spherule layers to be recognized as products of impacts, Paleoarchean layers that still constitute the oldest terrestrial evidence of impacts (Lowe and Byerly 1986; Shukolyukov et al. 2000). Almost all of the Paleoarchean spherule layers described to date are located in the west-central part of the Barberton Greenstone Belt (BGB) of the Kaapvaal Craton of South Africa (Table 9.1; Fig. 9.2). Despite the fact that it is structurally complex and virtually all its strata are tightly folded and faulted (Lowe et al. 1999), the BGB contains one of the best-preserved records of paleoenvironments from early Earth history, including evidence of early

Table 9.1 Paleoarchean impact spherule layers

Layer	Location	Impact evidence	Age (Ma)
S5	Barberton Greenstone Belt, South Africa	Sph	~3,230[a]
S4	Barberton Greenstone Belt, South Africa	Cr, Ir, Sph	<3,243[b]
S3	Barberton Greenstone Belt, South Africa	Cr, Ir, NiSp, Sph	3,243[b]
S2	Barberton Greenstone Belt, South Africa	Cr, Ir?, Sph	3,260[b]
S6	Barberton Greenstone Belt, South Africa	Sph	~3,330[a]
S7	Barberton Greenstone Belt, South Africa	Sph	~3,410[a]
S1[c]	Barberton Greenstone Belt, South Africa	Ir?, Sph	3,470[d]
Warrawoona (Apex Basalt)[c]	Pilbara Craton, Western Australia	Sph	3,470[d]

Cr chromium isotope data, *Ir* iridium anomaly, *NiSp* Ni-rich spinel, *Sph* spherules
[a] Lowe and Byerly (2010)
[b] Lowe et al. (2003)
[c] These two layers were probably formed by the same impact
[d] Byerly et al. (2002)

ecosystems (Tice and Lowe 2004). The BGB evolved over time from a basin dominated by volcanic inputs to one of a sedimentary character. This is reflected in its stratigraphic subdivision into three main units, as follows (Fig. 9.3). The lowest unit, the Onverwacht Group, is up to 10 km thick and consists mainly of mafic to ultramafic lavas with minor volcaniclastic interbeds. Above it is the Fig Tree Group, from 0.5 to 1.5 km thick, which consists of detritus eroded from Onverwacht-type rocks combined with felsic volcaniclastic rocks and cherty strata. The youngest unit of the BGB triad, the Moodies Group, is up to 3 km thick and composed largely of sandstone and conglomerate. Lowe and Byerly (2010) stated that there are spherule layers from seven (and perhaps more) impacts in the BGB, but to date they have only published detailed descriptions on four of these layers (Lowe et al. 2003). In terms of stratigraphic position, these layers range from the middle of the Onverwacht Group up into the lower part of the Fig Tree Group (Table 9.1; Fig. 9.3). The four spherule layers, for which detailed accounts are available, are described in reverse chronological order in Sect. 9.2. Any additional layers cannot be described at present.

The BGB is rivaled by the supracrustal successions of the Pilbara Craton, which also contain a wealth of information on early life and surface conditions (e.g., Allwood et al. 2007; Van Kranendonk 2006). However, spherule layers have only been reported from one small area in the East Pilbara Terrane (Fig. 9.1), one of five structural-stratigraphic units recognized in the older parts of the Pilbara Craton (Van Kranendonk et al. 2007a, b). At least one Paleoarchean spherule layer is

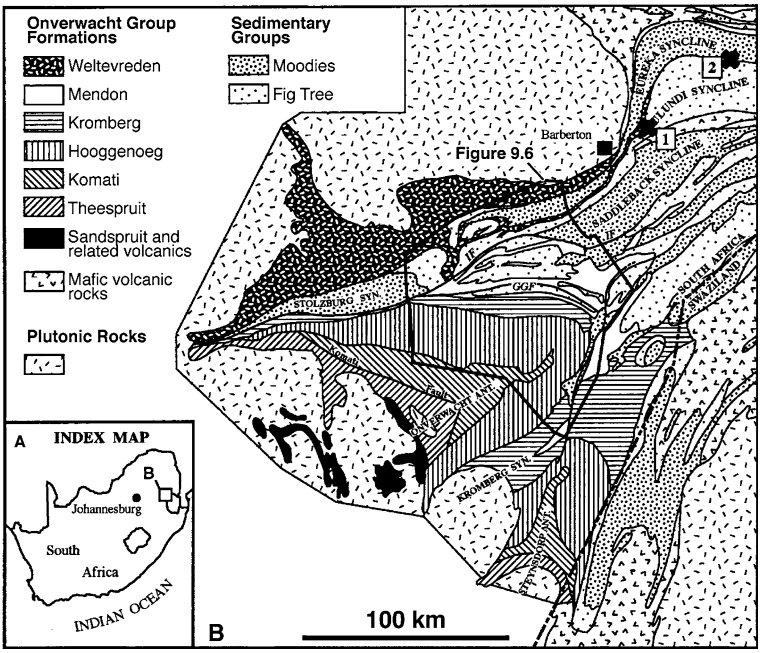

Fig. 9.2 Generalized geological map of western Barberton Greenstone Belt. Outlying occurrences of the S3 layer are indicated by X's numbered 1 and 2 (in *upper right*). The rest of the sites where Paleoarchean spherule layers have been recognized occur within outlined area shown in Fig. 9.6. Major structural boundaries include Granville Grove Fault (GGF) and Inyoka Fault (IF). Modified after Lowe et al. (2003), Fig. 1, with permission from Mary Ann Liebert, Inc.

present and possibly more, but they have not been described in as much detail as the BGB layers so the description here is necessarily brief. Even though they are remarkably well preserved for their great age, the Paleoarchean spherule layers are more highly metamorphosed than younger distal ejecta layers so primary textures such as crystal pseudomorphs are not as well preserved as they are in most of the younger layers.

9.2 Spherule Layers in the Barberton Greenstone Belt

9.2.1 The S4 Layer

9.2.1.1 Description of Layer

The S4 layer is the youngest of the spherule layers in the Barberton Greenstone Belt (BGB) for which detailed descriptions are currently available. Lowe and Byerly (2010) mentioned one younger layer, but details have yet to be published.

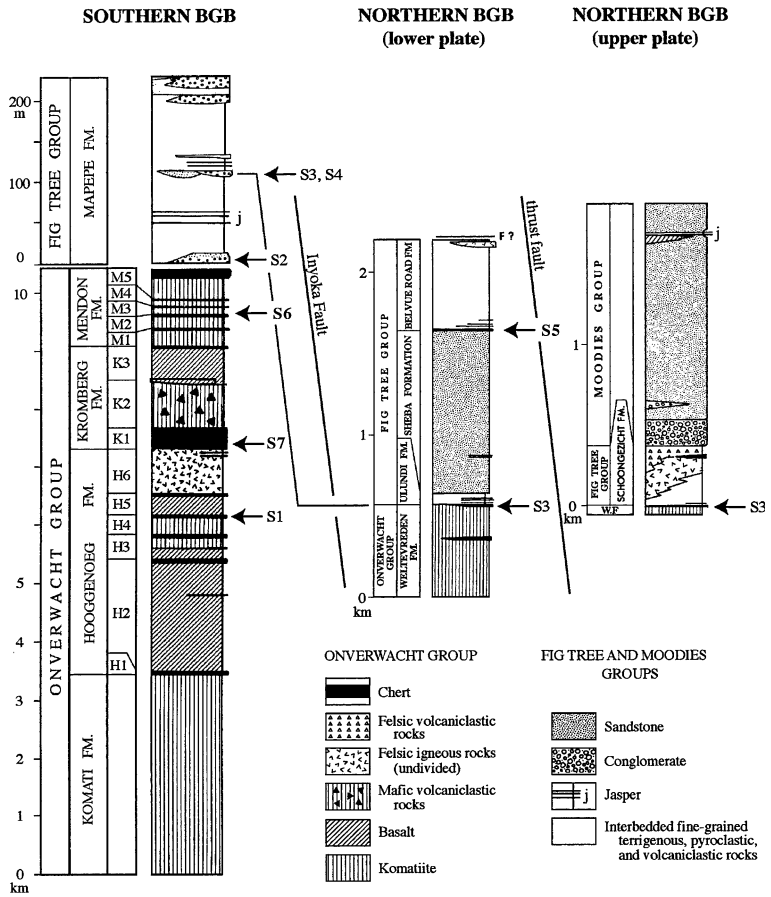

Fig. 9.3 Schematic stratigraphic columns of supracrustal units in western BGB, showing stratigraphic positions of seven spherule layers reported to date. From Lowe et al. (2003), Fig. 2, with stratigraphic positions of the S5, S6, and S7 layers added from Lowe and Byerly (2010), Fig. 1, with permission from Mary Ann Liebert, Inc.

Stratigraphically, the S4 layer is located in the Mapepe Formation of the Fig Tree Group (Fig. 9.3). The Mapepe is a heterogeneous unit that consists of a combination of volcaniclastic, terrigenous, and chemical sedimentary rocks deposited in diverse paleoenvironments ranging from low-energy deep-water to high-energy shallow-water settings (Lowe and Nocita 1986). The S4 layer has only been recognized at one site where it is in the midst of sandstone and conglomerate deposited on a fan-delta and in close proximity to the S3 layer (described in Sect. 9.2.2). Like many of the volcanic and sedimentary rocks of the Onverwacht and Fig Tree Groups, the strata hosting the S4 layer were extensively silicified very early (Lowe 1999a), despite their clastic origin. This helped to shield the spherules from subsequent compaction and alteration and led to the naming of the unit

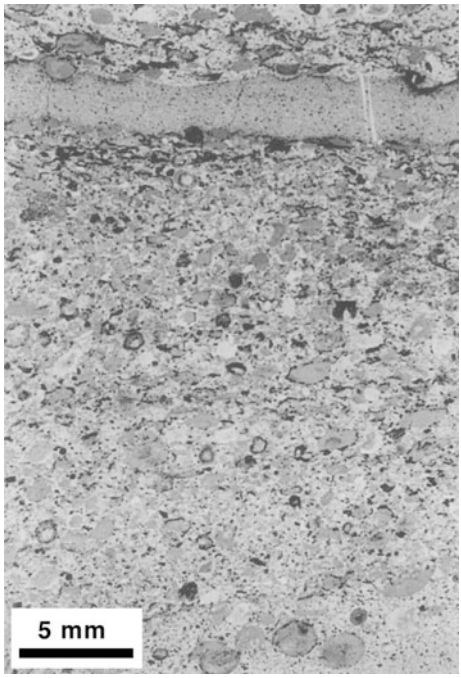

Fig. 9.4 Sample of part of the S4 layer showing normal grading. The layer also contains locally derived volcanogenic and carbonaceous chert clasts. From Shukolyukov et al. (2000), Fig. 1

hosting the S4 layer as "Jay's chert." The S4 layer has been studied relatively intensively despite its limited occurrence (e.g., Kyte et al. 1992; Shukolyukov et al. 2000). Based on geochemical indicators (described in Sect. 9.2.1.5), it has a high content of extraterrestrial material. Apparently the amount of reworking even in this high-energy, subaerial setting was insufficient to substantially dilute the impact ejecta.

In its only outcrop, the S4 layer is a dark greenish-gray sandy layer $\sim$15 cm thick that contains up to 50 % by volume of intact spherules (Shukolyukov et al. 2000). The rest of S4 consists largely of crushed spherules, irregular chlorite-rich grains, and fine chloritic matrix. In the sample they analyzed, Kyte et al. (1992) estimated that 25–40 % consisted of intact spherules and <20 % consisted of material that was not impact ejecta or derived from same. The non-impact material is largely volcanic and carbonaceous chert detritus and locally makes up from <5 to >90 % by volume of the layer. The latter are mostly comprised of angular to subangular particles of chert, but coarsely crystalline quartz grains constitute up to 5 % of the detritus (Lowe et al. 2003). Most of the latter originated as phenocrysts in volcanic rocks, especially tuffs (Lowe and Nocita 1986). The only other primary (i.e., unaltered) phases in the layer are some heavy minerals. With the exception of the aforementioned quartz and heavy minerals, all of the constituents of S4 have been heavily altered (see the following section). At least part of the layer shows normal grading (Fig. 9.4), but this is not a result of ballistic settling because S4 contains some ambient sediment and shows some current structures (Lowe et al. 2003).

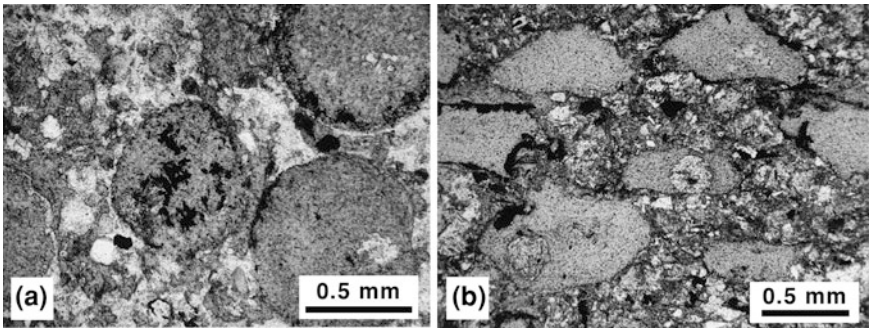

Fig. 9.5 Photomicrographs in plane polarized light of spherules from the S4 layer. **a** Uncompacted chlorite spherules; opaque (*black*) material is rutile. **b** Chlorite spherules flattened by physical and/or chemical compaction; some contain circular bodies of microquartz and chlorite that are probably infilled vesicles. The chlorite-rich matrix probably consists mostly of spherule debris but contains a few detrital quartz grains (*clear*). From Lowe et al. (2003), Figs. 18b and a, respectively, with permission from Mary Ann Liebert, Inc.

9.2.1.2 Description of Spherules

Intact spherules in the S4 layer range from 0.2 to 2.8 mm in diameter (Shukolyukov et al. 2000; Lowe et al. 2003). They are relatively homogeneous in terms of size, more so than the older BGB spherule layers (described below). Many have circular cross-sections suggesting they were originally spherical (Fig. 9.5a), but most are flattened parallel to bedding, presumably reflecting diagenetic and/or tectonic modification (Fig. 9.5b; Lowe et al. 2003). Lowe et al. (2003) do not state whether or not they detected any rotational forms such as teardrops and dumbbells in the S4 layer. Internally, the spherules in the S4 layer are probably the simplest texturally of any of the BGB spherules because they are composed largely of very finely crystalline chlorite and rarely show pseudomorphed crystallization textures (Fig. 9.5). This suggests the S4 spherules largely originated as microtekites, i.e. pure glass, rather than as microkrystites, although it may also reflect a higher degree of metamorphic alteration. Many of the spherules contain small amounts of rutile either as thin rims or disseminated in irregular patches internally. Both the rutile and the chlorite are rich in Cr. A few spherules show more heterogeneity internally in the form of possible crystallization textures or concentric layers of different minerals, the latter suggesting devitrified margins. Some spherules also contain clear spots of phases other than chlorite suggestive of infilled vesicles. Spherules that consist almost entirely of quartz are present but quite rare. In addition to chlorite, quartz, and rutile, some of the spherules in S4 also contain up to 50 % by volume apatite, up to 50 % siderite, and minor amounts of pyrite, chalcopyrite, and iron oxides (Kyte et al. 1992).

9.2.1.3 Radiometric Age

S4 is very close to the S3 layer stratigraphically (see Sect. 9.2.1.4). Individual zircon crystals separated from a dacitic tuff directly overlain by the S3 layer yielded a $^{207}Pb/^{206}Pb$ evaporation age of 3,243 ± 4 Ma (Kröner et al. 1991). This was taken as the age of S3, and given that they are part of a relatively coarse-grained, high-energy succession, the S3 and S4 layers must be very close in age. The fact that the impact ejecta in the S4 layer are relatively undiluted suggests there was little reworking after they arrived in the depositional environment. Therefore the age of the S4 layer is thought to be very close to but slightly less than 3,243 Ma.

9.2.1.4 Geographic Distribution and Variation

The S4 layer is only known from a single surface outcrop on the northwest limb of the Onverwacht Anticline where it is closely associated with layer S3 (Fig. 9.6). In fact, the S4 layer is only 6.5 m stratigraphically above bed S3 (Lowe et al. 2003), but the two contain spherules that are texturally and mineralogically distinct, so they are thought by Lowe et al. (2003) to represent two different impacts that were closely spaced in time. The full lateral extent of the S4 layer is only on the order of 1 m because it is erosionally truncated at both ends along scour surfaces in the coarse clastic sediments that host it (Fig. 9.7). Lowe et al. (2003) noted that rocks of the Fig Tree Group weather deeply and therefore are poorly exposed, which may help account for the lack of additional sites of the S4 layer. However, this is puzzling in light of the fact it is closely associated with S3 which has been recognized at numerous sites throughout the west-central BGB (Figs. 9.2 and 9.6).

9.2.1.5 Extraterrestrial Component

Iridium concentrations in 17 subsamples of a slab from the S4 layer analyzed by Kyte et al. (1992) ranged from 8 to 450 ppb with an average of 116 ppb. In contrast, samples from ambient beds lacking spherules within a few meters of the S4 layer stratigraphically all yielded Ir concentrations that fell in a range from 0.12 to 0.31 ppb. The highest of the values obtained from the S4 layer approaches the average concentration of Ir in chondritic meteorites, but the average concentration of all the samples combined is substantially lower than the average of CI chondrites. This is consistent with the dilution of both the projectile by the target rocks during the impact and the ejecta by non-impact sediment during deposition. Kyte et al. (1992) also analyzed the contents of Pd, Os, Pt, and Au in the S4 layer. Os/Ir and Pt/Ir ratios showed values that are ~80 % of those of CI chondrites. In contrast, Pd/Ir and Au/Ir are 40 and 2 % of CI chondritic values, respectively. In addition to the dilution with sediment noted above, the fractionation implied by the non-chondritic ratios of these elements, particularly the last two, is probably a reflection of their differential migration during regional hydrothermal and/or

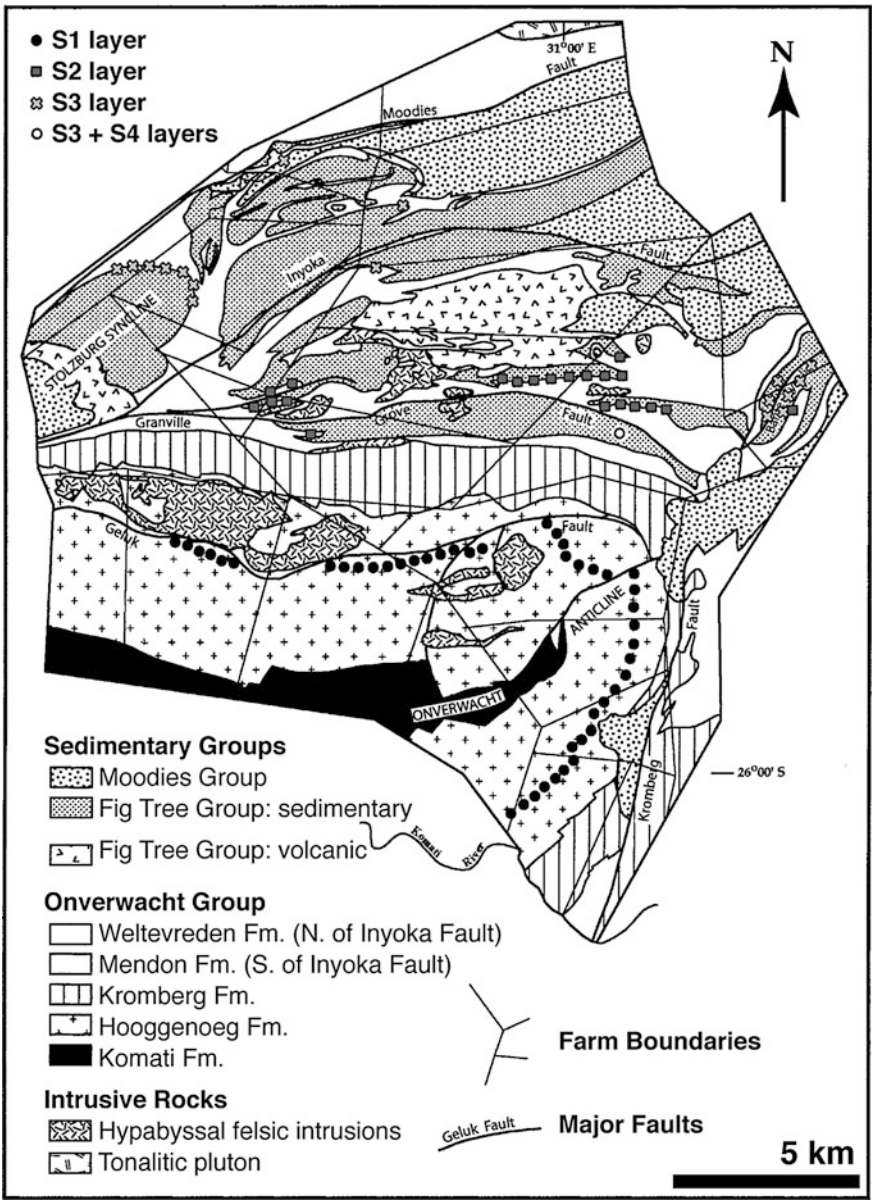

Fig. 9.6 Generalized geologic map of area in western Barberton Greenstone Belt outlined in Fig. 9.2, where most known occurrences of Paleoarchean spherule layers are located. Trains of closely spaced symbols for a given spherule layer, e.g., the black dots for the S1 layer around the Onverwacht Anticline, are schematic indicators of strike belts within which layers have been repeatedly identified rather than actual sites where the layers are exposed. Modified after Lowe et al. (2003), Figs. 3 and 7, with permission from Mary Ann Liebert, Inc.

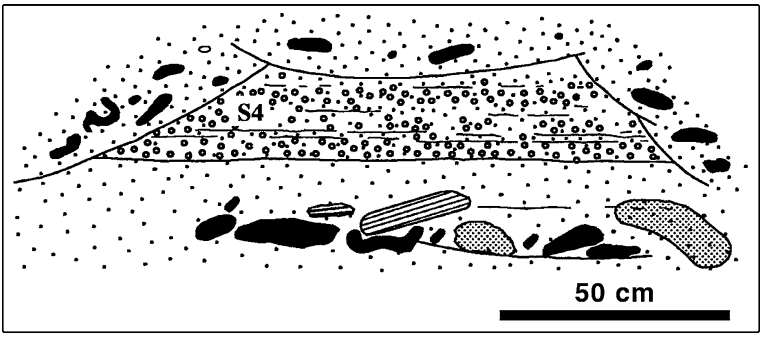

Fig. 9.7 Sketch of the only known occurrence of the S4 layer; note erosional truncations along top and both sides. From Lowe et al. (2003), Fig. 17, with permission from Mary Ann Liebert, Inc.

Table 9.2 Chromium isotopic compositions and Cr and Ir concentrations of selected samples from Barberton Greenstone Belt spherule layers (from Kyte et al. 2003)

	$\varepsilon(^{53}Cr)_{normalized}$	$\varepsilon(^{53}Cr)_{raw}$	$\varepsilon(^{54}Cr)_{raw}$	Cr (mg/g)	Ir (ng/g)
Bed S2					
SAF-275-4C	-0.09 ± 0.03	n.d.	n.d.	0.16	6
Bed S3					
SAF-380-5B	-0.41 ± 0.10	n.d.	n.d.	2.45	519
SAF-381-10B	-0.37 ± 0.07	n.d.	n.d.	0.98	104
SAF-381-10G	-0.41 ± 0.08	0.08 ± 0.18	0.89 ± 0.23	3.67	725
Bed S4					
SAF-349-3, C	-0.26 ± 0.11			1.36	154
SAF-349-3, D4	-0.32 ± 0.06			1.63	240
C + D4		-0.1 ± 0.2	0.4 ± 0.3		

n.d not determined

metasomatic alteration (Kyte et al. 1992). The recent discovery that PGEs in the Paraburdoo and Reivilo layers show similar fractionations (see Sects. 8.2.4.5 and 8.3.3.5, respectively) suggests this may represent a consistent response to diagenetic conditions. It is not known what phases contain the PGEs in the S4 layer (Kyte et al. 1992).

In addition, Shukolyukov et al. (2000) analyzed the Cr isotopic compositions of two of the same subsamples from the S4 layer that Kyte et al. (1992) analyzed. The ε^{53}Cr values they obtained were -0.32 ± 0.06 and -0.26 ± 0.11 (Table 9.2). As explained in Sect. 3.1.2.3, any ε^{53}Cr values that depart from zero in either the positive or negative direction indicates extraterrestrial material is present because terrestrial rocks consistently yield values very close to zero (Fig. 8.7; Shukolyukov and Lugmair 1998). This is demonstrated by several analyses of chert and sandstones lacking spherules from the Barberton Greenstone Belt, some close to the S4 layer stratigraphically, that yielded ε^{53}Cr values statistically indistinguishable from zero (Kyte et al. 2003). The Cr isotopic anomaly both confirms the presence of extraterrestrial material in the S4 layer and suggests the impactor was similar in

composition to a carbonaceous chondrite. The magnitudes of both the Cr anomaly and the Ir concentrations (Table 9.2) suggest ~20 % of the mass in the S4 layer was derived from an extraterrestrial body, assuming it had the average composition of a carbonaceous chondrite (Shukolyukov et al. 2000).

9.2.2 The S3 Layer

9.2.2.1 Description of Layer

In contrast to the S4 layer, which is only known from a single outcrop, occurrences of the S3 layer have been reported from numerous sites throughout the west-central BGB (Figs. 9.2 and 9.6). Regional correlations across the BGB are complicated by the fact that it consists of several fault-bounded tectono-stratigraphic units that structurally duplicate sections of the uppermost Onverwacht volcanic rocks and overlying Fig Tree strata (Lowe et al. 1999). In the description that follows, this geologic complexity is drastically simplified by referring to just two broadly different areas separated by the Inyoka Fault (Figs. 9.2, 9.3 and 9.6) informally referred to here as the southern and northern regions (after Lowe et al. 2003). Based on close similarities in age, spherule types, and geochemistry (described below), Lowe et al. (2003) have made a persuasive case that most or all of the occurrences they ascribe to the S3 layer are products of a single impact. According to their correlations, S3 is the only spherule layer described in detail from the northern region and it has been recognized over a wider area than any other Paleoarchean distal ejecta layer (see Sect. 9.2.2.4). However, the reader should be aware that it is difficult to correlate spherule layers unambiguously across major tectonic discontinuities such as the Granville Grove and Inyoka Faults (Fig. 9.6). Lowe, Byerly and coworkers have revised some of their proposed correlations as work has continued (as described in the next paragraph) and there may still be problems with correlations to specific sites (e.g., Hofmann et al. 2006), especially given the existence of additional spherule layers (Lowe and Byerly 2010).

The type locality of the S3 layer is in the southern region of the BGB ~100 m stratigraphically above the upper contact of the Onverwacht Group. This is the same as the type locality of the S4 layer (described above), which is in close stratigraphic proximity. The Onverwacht Group in the southern region is a volcanic package on the order of 10 km thick, but in the northern region it is only on the order of 1 km thick. The only spherule layer described in detail to date in the northern region is at the contact between the Onverwacht and overlying Fig Tree Groups (Fig. 9.3). Because the S2 layer (described in Sect. 9.2.3) is located at the contact between the Onverwacht and Fig Tree Groups in the southern region, Lowe et al. (1989) initially interpreted all spherule layers near the Onverwacht/Fig Tree contact as products of a single impact. However, subsequent investigations indicated the Onverwacht/Fig Tree contact was diachronous across the BGB (Kröner et al. 1991; Byerly et al. 1996) and also revealed significant differences

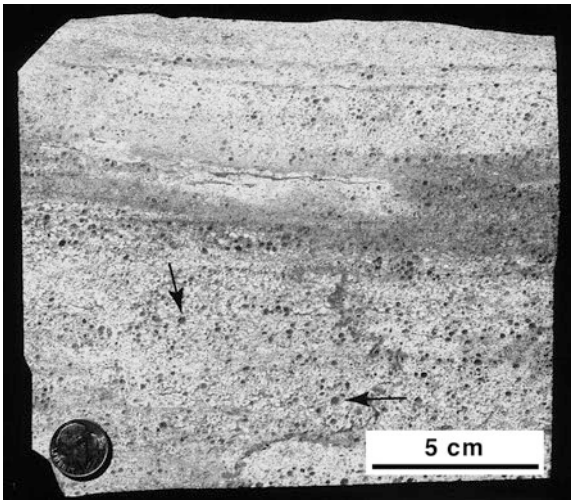

Fig. 9.8 Sample from the S3 layer at an unspecified location where the detritus consists almost entirely of spherules or debris derived from them. The spherules range from silica-rich (*dark*, examples at *arrows*) to sericite-rich (*light*) types. This sample is interpreted as a fallout deposit despite the presence of weak horizontal stratification. From Lowe et al. (2003), Fig. 13, with permission from Mary Ann Liebert, Inc.

between what they were calling the S2 layer in the northern and southern regions. Byerly and Lowe (1994) signaled this uncertainty by labeling the layer near the Onverwacht/Fig Tree contact in the northern region as "S2?". Eventually they correlated the S3 layer in the southern region with the layer at the Onverwacht/Fig Tree contact in the northern region based on similarities in ages, spinel contents, Ir contents, and spherule types (described below) (Lowe et al. 2003). The descriptions that follow are based on this correlation, but as investigations continue, additional recorrelations are a possibility.

In general, the strata in the southern region of the BGB were deposited in shallower water under higher-energy conditions whereas the strata in the northern region were deposited in deeper water under lower-energy conditions. This is reflected in the nature of the S3 layer. In the southern region, it occurs in the middle of the Mapepe Formation of the Fig Tree Group amidst terrigenous and tuffaceous strata that were deposited in paleoenvironments ranging from subaerial fan deltas to tidally influenced shallow seafloors. The S3 layer in the southern region therefore tends to be thicker and shows more evidence of redeposition in the form of current structures and greater dilution by non-impact detritus. In the northern region, the S3 layer directly overlies cherts and komatiites of the Weltevreden Formation (the uppermost unit of the Onverwacht Group) and marks the base of the Ulundi Formation of the overlying Fig Tree Group (Fig. 9.3). The Ulundi Formation consists of ferruginous sediments and cherts deposited below wave base in waters that grew progressively deeper northward. According to Lowe et al. (2003), in some locations, particularly in the northern region, the S3 layer consists almost entirely of spherules (Fig. 9.8) in a normally graded bed $\sim$30 cm thick that appears to be a direct fallout deposit (Krull-Davatzes et al. 2006). Despite the deeper water, in some areas in the northern region the deposition of the S3 layer involved the erosion of preexisting sediments from the top of the Onverwacht Group thereby exposing komatiitic volcanic rocks. At such sites, the S3

layer consists of a lower graded zone with clasts up to 1.5 m thick overlain by conglomeratic sandstone with only a few spherules (Lowe et al. 2003). Throughout the BGB, the thickness of the S3 layer varies from as little as 15 cm in sections affected by tectonic shearing to 3 m in locations where it was redeposited by currents and/or waves. Like the S4 layer, the S3 layer is part of an extensively silicified unit known as "Jay's chert."

In addition to the stratabound S3 layer *per se*, spherules are also found locally in black chert dikes that cut down into underlying altered komatiitic volcanic rocks (Lowe et al. 2003; Hofmann et al. 2006). Some of these spherules occur at least 10 m beneath the S3 layer stratigraphically and must have been moved or injected downward. Lowe et al. (2003) suggested the dikes formed penecontemporaneously with deposition of the S3 layer as a consequence of crustal stresses associated with a large impact. One piece of evidence they cite in support of this interpretation is that the spherules occur as loose, individual grains, indicating the S3 layer was unlithified when injection occurred. However, Hofmann et al. (2006) describe the spherules as "more tightly packed" in the dikes than the layer *per se*, raising questions about this interpretation.

9.2.2.2 Description of Spherules

Since the S3 layer is the most laterally extensive of any of the BGB spherule layers, its spherules have been described in the greatest detail (Lowe et al. 2003; Krull-Davatzes et al. 2006). Intact spherules range in diameter from ~0.1 to 4 mm, but broken or deformed spherules are widespread in many locations (Lowe et al. 2003). Lowe et al. (2003) do not state whether or not they detected any rotational forms such as teardrops and dumbbells in the S3 layer. Where there is little evidence of reworking, the S3 layer consists essentially of spherules and spherule fragments. The intact spherules comprise a bimodal assemblage of two types: (1) larger silica-rich spherules with internal crystal pseudomorphs and thin rims of greenish Cr-rich sericite, and (2) smaller, more homogeneous spherules consisting of Cr-rich sericite or, more rarely, chlorite (Fig. 9.9a). Both types commonly have rutile-rich rims <0.1 mm thick. In contrast, where it shows more evidence of reworking, the S3 layer contains a more diverse suite of spherules (e.g., Fig. 9.9a, c). The more notable varieties are pure silica spherules that are generally smaller, sheet silicate-rich spherules that are generally larger, spherules with concentric bands rich in either quartz or sheet silicates (either an outer rim of silica and a core of sheet silicates or vice versa), and spherules showing various types of crystallization textures internally. The latter include spherules with parallel lines that Lowe et al. (2003) interpret as replaced olivine crystals with barred habits similar to those in chondrules, as well as radial-fibrous to lath-shaped crystals similar to those described in Chap. 8 from spherules in the APB layers. The pseudomorphs probably replaced a combination of primary and secondary phases, i.e., crystals grown directly from melt and others formed via devitrification of impact glass. Most likely they are replaced feldspars and ferromagnesian phases

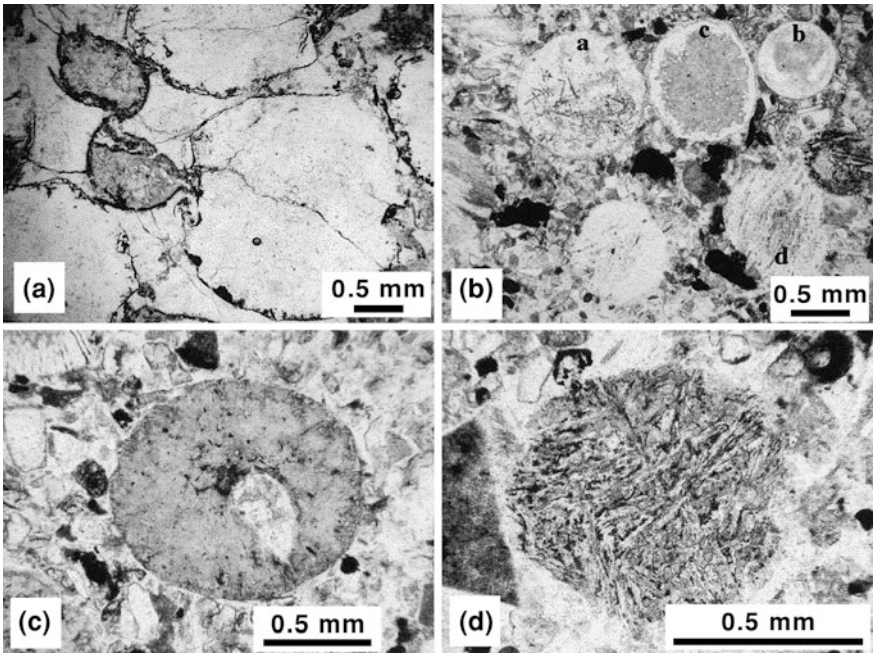

Fig. 9.9 Photomicrographs in plane polarized light of spherules from the S3 layer. **a** Bimodal mixture of large silica-rich spherules (*white*) with thin rims of Cr-rich sericite and small spherules consisting almost entirely of Cr-rich sericite (*dark*); both types of spherules commonly have thin opaque rutile-rich rims and the shapes of the sericite-rich spherules were clearly modified during compaction. **b** Well-sorted coarse sand-size spherules with diverse textures including spherule with fine dendritic spinels (a), spherule rich in silica (b), spherule with chlorite-rich center and silica-rich edge (c), and a spherule that may contain pseudomorphs of olivine crystals with barred habits similar to those in chondrules (d). **c** Well-preserved chlorite-rich spherule with possible quartz-filled vesicle (*white*). **d** Well-preserved spherule (presumably a replaced microkrystite) consisting of chlorite, quartz, and rutile with abundant microlite pseudomorphs. From Lowe et al. (2003), Figs. 15b, a, c, and h, respectively, with permission from Mary Ann Liebert, Inc. **a** was collected at 25° 54.52' S, 31° 03.36' E; **b**, **c** and **d** were collected at 25° 54.9' S, 31° 01.13' E

such as olivines and/or clinopyroxenes. In addition to crystal pseudomorphs, many spherules contain pure quartz masses with circular cross-sections that are thought to be infilled vesicles (Fig. 9.9c). In two sites studied in detail by Krull-Davatzes et al. (2006) where it is normally graded and appears to be a direct fall-out deposit, the S3 layer shows a progressive upward change in spherule textures (Fig. 9.10) believed to reflect a progressive condensation sequence in the impact plume. Although rarely organized this coherently, the diversity of the spherules clearly indicates they were heterogeneous both compositionally and texturally when they were originally deposited (Lowe et al. 2003).

Minerals other than quartz and sheet silicates are also found in the spherules in the S3 layer, locally in great abundance. Apatite is a consistent accessory mineral in the spherules and locally makes up as much as 60 % of the spherules by volume

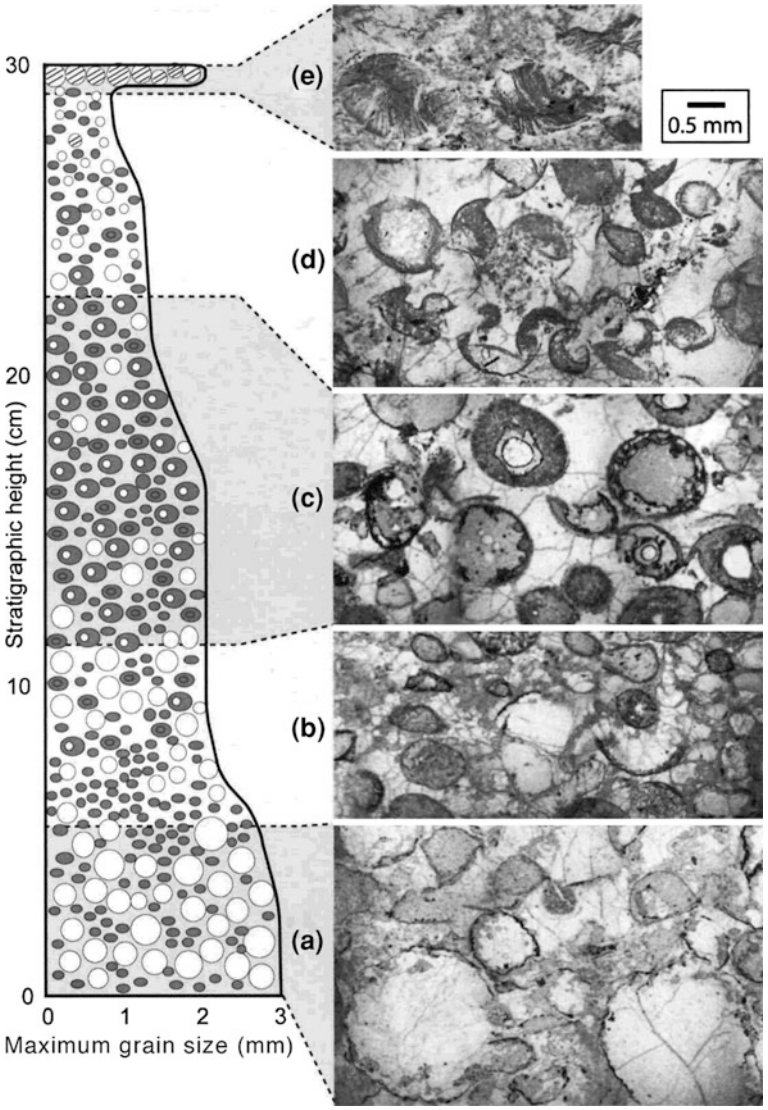

Fig. 9.10 Diagram with photomicrographs, taken in plane polarized light, showing vertical changes in the S3 layer at 25 ° 54.52' S, 31 ° 03.36' E where it is 30 cm thick, normally graded, and interpreted as a direct fallout deposit. Solid white circles represent silica-rich spherules, solid gray circles and ovals represent phyllosilicate-rich spherules, gray ovals that contain either white circles or gray ovals internally are compositionally zoned (see photomicrographs), and circles with parallel lines represent spherules with relict barred texture. Krull-Davatzes et al. (2006) divided the layer into five zones as follows: **a** Contains large microcrystalline quartz-rich spherules and small aluminous spherules; **b** contains smaller microcrystalline quartz-rich and phyllosilicate-rich spherules; **c** contains mainly zoned spherules; **d** contains small silica and phyllosilicate-rich spherules; and **e** contains spherules with relict barred textures. The compactive crushing of spherules is particularly prominent in zones b, c. and d. Courtesy of Alexandra Davatzes, from Krull-Davatzes et al. (2006), Fig. 3

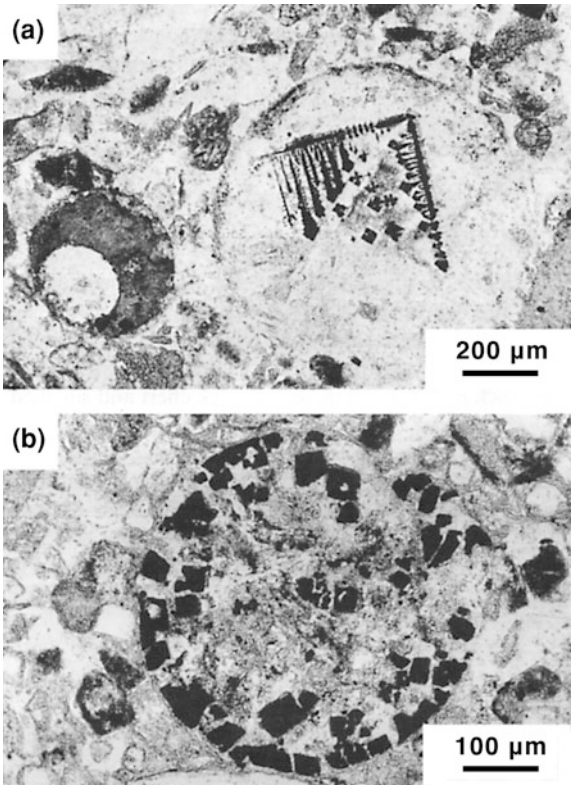

Fig. 9.11 Photomicrographs, in plane polarized light, of spinels in spherules from the S3 layer at 25 ° 54.9′ S, 31 ° 01.13′ E. **a** Larger silica-rich spherule on right with dendritic spinel (*black*) and chlorite-rich spherule on left with internal circular region (*white*) that could be an infilled vesicle or a droplet of an immiscible liquid. **b** Chlorite-chert spherule with abundant chromite octahedra (*black*), presumably Ni-rich. Many of the octahedra are hollow, especially near the outer margin. From Byerly and Lowe (1994), Figs. 3a and c, respectively, with permission from Elsevier

(Lowe et al. 2003). Barite is also widespread and replaces the spherules extensively at some sites. Additional phases recorded include siderite, sulfides, and feldspars, but the most intriguing accessory phase comprises crystals of spinel with unusual compositions (Byerly and Lowe 1994). These spinel crystals are the only primary or unreplaced phases reported in the S3 layer or in any Archean spherule layer. Byerly and Lowe (1994) reported examples of what they originally thought were the S2 layer in the northern region, but all of the localities from which they analyzed samples were subsequently recorrelated with the S3 layer (as explained in Sect. 9.2.2.1). The similarity of the spinels in samples from the southern and northern regions of the BGB is a key piece of evidence supporting the preferred correlation. The abundance of spinel-bearing spherules in the S3 layer ranges up to $\sim$10 % by volume at one site, but values of 1 to 3 % are more typical and no spinels at all were observed at some sites, particularly those showing evidence of reworking. Spinel can form up to 40 % of the cross-section of a given spherule by area and it often appears to be the only primary phase crystallized within a given spherule (i.e., no pseudomorphs of other phases are present). Morphologically, the larger spinels tend to be finely dendritic whereas the smaller ones are typically hollow octahedra (Fig. 9.11). These habits are typical of spinels grown rapidly from high temperature melts. In addition, the spinels tend to appear in sericite-rich rather than sericite-

poor, silica-rich spherules. The latter are much more likely to show pseudomorphs of microlites (Fig. 9.9d), some of which strongly resemble basaltic textures.

Like those found in distal Cenozoic impact ejecta, the spinel crystals in the S3 layer have very high Ni and ferric iron contents, but they differ in other ways (Byerly and Lowe 1994). The spinels mainly consist of Fe, Ni, Cr, and V and two main types were recognized: (1) chalcophile spinels with low MgO, Al_2O_3, and TiO_2, and (2) lithophile spinels with up to 5 wt % Al_2O_3 and MgO. Both types of spinel occur in the S3 layer in both the northern and southern regions. Byerly and Lowe (1994) stated that they are unlike spinels in either fresh or highly altered komatiitic volcanic rocks nearby, but Koeberl and Reimold (1995) found they had some compositional features in common. To arrive at these unusual compositions, Byerly and Lowe (1994) suggested a complex series of events during the condensation and reentry of particles formed in a large impact-produced vapor cloud. Specifically, they postulated that initial reduction at high temperatures generated immiscible silicate-metal/sulfide melt droplets, some of which subsequently evolved independently and formed spherules with highly variable chalcophile element contents. Oxidation during atmospheric reentry increased the Ni/Fe and Fe^{+3}/Fe^{+2} in the chalcophile-siderophile melts. The Archean spinels have higher Ni/Fe but distinctly lower Fe^{+3}/Fe^{+2} than Cenozoic impact spinels. Byerly and Lowe (1994) attributed these differences to the Paleoarchean atmosphere having low oxygen content relative to the Cenozoic.

Broken or deformed spherules are widespread in the S3 layer and originated in two distinctly different ways. Some have truncated cross-sections like those described in the Archean-Paleoproterozoic boundary spherule layers (e.g., Fig. 8.3f); these were clearly broken before deposition, e.g., as they fell to Earth and/or were transported by waves or currents. More commonly, spherules were deformed either by compaction during diagenesis or by tectonic processes (Fig. 9.9a). The former includes both physical and chemical compaction, i.e., ductile deformation and pressure solution respectively. The sericitic spherules are more commonly physically deformed, whereas the siliceous spherules are more likely to be modified by pressure solution. This reflects the fact that quartz is more readily dissolved during pressure solution than aluminous sheet silicates (Trurnit 1968). In addition to stylolites, pressure solution gave rise to spherules with characteristic prongs and hooks creating unusual shard-like shapes. Similar shapes occur in oolitic limestones (Conley 1977) and intraclastic iron formations (Simonson 1987) where clasts are more susceptible to pressure solution than the early cements that filled the pores between them. In contrast, ductilely deformed spherules are primarily flattened in either the plane of bedding (for compaction) or cleavage (for tectonic deformation).

9.2.2.3 Radiometric Age

As noted in Sect. 9.2.1.3, zircons from a tuff immediately underlying the S3 layer yielded a $^{207}Pb/^{206}Pb$ age of 3,243 ± 4 Ma (Kröner et al. 1991). Therefore, it appears the S3 layer was deposited right around 3,243 Ma (Lowe et al. 2003).

Table 9.3 Iridium and chromium concentrations reported from samples that are probably from the S3 spherule layer in the Barberton Greenstone Belt

	Koeberl and Reimold (1995)	Reimold et al. (2000)	Lowe et al. (2003)[g]
Ir (ppb)-maximum	2,730[a,b]	1,518[d,e]	725
Ir (ppb)—average of all samples reported	~253	~283	~149
Ir (ppb)—average excluding the highest value	~88	~218	~137
Ir (ppb)-minimum	2.4	2.88	~1
Cr (ppm)-maximum	16,400[a,c]	8,531[d,f]	3,665
Cr (ppm)—average of all samples reported	~1,735	~1,676	~1,505
Cr (ppm)—average excluding the highest value	~757	~1,316	~1,391
Cr (ppm)-minimum	183	48.2	204
Total number of samples	~8	~3	~38
Total number of analyses	23	20	50

[a] Highest values of Ir and Cr are both from the same "altered spherule layer" sample
[b] Second highest value reported is 437 ppb
[c] Second highest value reported is 2,065 ppm
[d] Highest values of Ir and Cr are both from the same sample
[e] Second highest value reported is 849 ppb
[f] Second highest value reported is 4,364 ppm
[g] Only 20 analyses of Cr were reported in Lowe et al. (2003)

9.2.2.4 Geographic Distribution and Variation

All of the occurrences currently correlated with the S3 layer (as explained in Sect. 9.2.2.1) currently lie in an area whose dimensions are on the order of tens of kilometers both parallel to and across the structural grain of the BGB (Figs. 9.2 and 9.6). Because the area is traversed by several major faults trending east–west, the current 40 km separation of the most distant locations in a north–south direction may have been shortened tectonically from as much as 100 km (Krull-Davatzes et al. 2006). As outlined in Sect. 9.2.2.1, the S3 layer was generally deposited in shallower water under higher-energy conditions in the southern region of the BGB and therefore likelier to be thinner and have a higher proportion of spherules than in the northern region.

9.2.2.5 Extraterrestrial Component

The Ir concentrations of samples from the S3 layer that have been analyzed are highly variable. They range from ~1 ppb to a reported high of 2,730 ppb (Table 9.3). Hofmann et al. (2006) likewise obtained variable Ir concentrations in 5 samples that probably came from the S3 layer, as correlated by Lowe et al. (2003);

they ranged from <1 to ~100 ppb. In contrast, most Archean spherule layers analyzed to date have maximum Ir concentrations that are low and rarely exceed ~20 ppb, with some notable exceptions. Specifically, some samples from the S4 spherule layer contain 100's of ppb Ir (see Sect. 9.2.1.5), as do the Neoarchean Paraburdoo and Reivilo spherule layers (see Sects. 8.2.4.5 and 8.3.3.5, respectively). At one site where the S3 layer consists almost entirely of spherule material (but is thinned tectonically), seven samples taken at centimeter intervals yielded Ir concentrations ranging from 104 to 725 ppb (Table 2 of Lowe et al. 2003). Krull-Davatzes et al. (2006) found a positive correlation between higher concentrations of Ir and the abundance of Cr-rich spinels in samples from an unusual site where the spherules in the S3 layer were deposited by direct fallout from the impact plume without subsequent reworking. At most sites, the spherules were redeposited by waves and/or currents and diluted with non-impact detritus (see Sect. 9.2.2.1); some of the lower Ir values surely reflect this dilution. For example, Lowe et al. (2003) noted that the Ir abundances measured at two sites where the spherules in the S3 layer were reworked and diluted by non-impact detritus were generally <5 ppb. However, not all low values reflect dilution. Samples from the S3 layer at one site where the spherules were nearly undiluted yielded Ir concentrations of only 1.1 to 12.6 ppb, the highest values coming from samples in the upper part of the layer where cross-stratification is present (Lowe et al. 2003). Some low values probably reflect diagenetic removal of Ir and other siderophile elements. For example, Krull-Davatzes et al. (2006) found Cr-bearing spinels were absent from samples of the S3 layer from one site and attributed their absence to dissolution early in diagenesis during microbial sulfate reduction of organic matter.

At the opposite extreme, surprisingly high concentrations of Ir have been reported from selected samples that are definitely or probably from the S3 layer. At one site where spherules make up as little as 10 vol % of the S3 layer, three samples yielded Ir concentrations ranging from 426 to 519 ppb (Lowe et al. 2003). Koeberl et al. (1993) reported an Ir concentration of 2,730 ppb in a single sample from a layer that is probably equivalent to the S3. The latter is well in excess of the average concentration of Ir in a chondritic meteorite, but this particular sample was characterized as an "altered spherule layer" from a mylonitic zone. Moreover, this and most of the other samples discussed in Reimold et al. (2000) were collected in or around gold mines. Ir and presumably other PGEs had clearly been remobilized in rocks they analyzed as Reimold et al. (2000) reported Ir concentrations above the chondritic average from samples close to, but not part of, spherule layers, the highest being 1,051 ppb Ir in a sample of sheared BIF and mylonitic graphite. Secondary enrichment related to metamorphism and/or ore formation is the likeliest explanation for such high values. Post-depositional remobilization is also likely to be a factor in explaining the fact that the abundances of some volatile (and non-meteoritic) elements like Zn, Sb, and As are closely correlated to Ir in some samples (Reimold et al. 2000; Hofmann et al. 2006). The fact of the matter is that even the best preserved Paleoarchean layers are more highly altered and

deformed than most of the occurrences of younger layers. Even those Paleoarchean spherule layers that still exhibit primary sedimentary and igneous textures have undergone a more extensive series of diagenetic and low-grade metamorphic alterations (e.g., Krull-Davatzes et al. 2012) than well-preserved Neoarchean spherule layers (see Chap. 8).

Given the more highly altered states of the Paleoarchean spherule layers, the interpretation of their geochemical compositions is bound to be subject to more uncertainty than similar analyses of younger spherule layers, other than those located in orogenic zones. Determining if Ir and other PGEs are present in chondritic ratios is one way to test whether or not high concentrations of Ir have an extraterrestrial provenance. Relatively few samples from the S3 layer have been extensively analyzed, but Reimold et al. (2000) reported analyses of 6 samples that are probably from the S3 layer. In these samples, the ratios of the PGEs other than Pd and Au are close to CI chondritic, despite the fact that their absolute concentrations vary greatly. This is consistent with the presence of extraterrestrial material in the S3 layer diluted by varying amounts of terrestrial sediment. In contrast, Reimold et al. (2000) found PGE ratios in non-spherule samples that are more consistent with a terrestrial and possibly komatiitic source. The presence of extraterrestrial material in the S3 layer is also supported by isotopic analyses of the Cr (see discussion in next paragraph). The mode of occurrence of the spherules in the S3 layer and the types of textures they display are also more in keeping with an origin as distal ejecta analogous to spherule layers found in younger successions than with any type of volcaniclastic deposit described to date. The origin of the S3 layer as a volcanic tuff, specifically one of komatiitic composition, seems unlikely in light of recent work by Thompson Stiegler et al. (2008, 2010, 2011). Such tuffs do occur in the Barberton succession and contain spheroidal volcaniclasts, but their detailed studies indicate their petrographic and geochemical characteristics are consistently different from those of the impact spherule layers. In summary, there appears to be a consensus that the S3 layer contains extraterrestrial material and represents distal impact ejecta, but the details of how many of the samples acquired their present compositions are still unclear.

Cr isotopic analyses by Kyte et al. (2003) also indicated the S3 layer contains a high percentage of extraterrestrial material. They analyzed three samples from two localities (Table 9.2) and obtained normalized ε^{53}Cr values of -0.37 ± 0.07, -0.41 ± 0.08, and -0.41 ± 0.10 compared to -0.01 ± 0.08 in a closely associated chert lacking spherules. As explained in Sect. 3.1.2.3, this confirms the presence of extraterrestrial material in the S3 layer that is similar in composition to a carbonaceous chondrite, most likely a CV-type body. Based on the isotopic ratios obtained, Kyte et al. (2003) concluded that virtually all of the Cr in the S3 layer was extraterrestrial in origin and around 50–60 wt % of the total mass in this layer was derived from an extraterrestrial body.

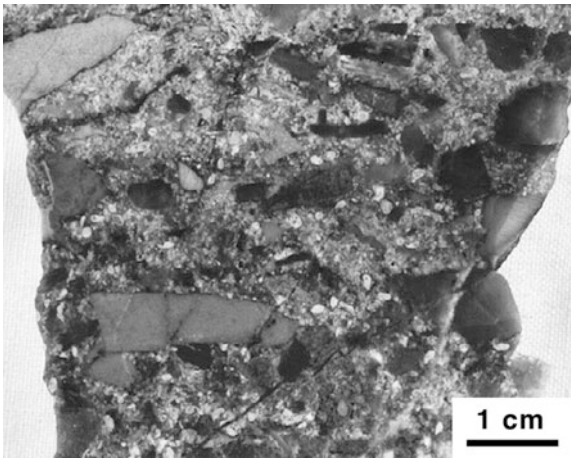

Fig. 9.12 Sawn slab from the S2 layer from an unspecified location where it contains an abundance of intraclastic flat cherty pebbles in addition to spherules (*light circles*) as well as other finer detritus. From Simonson et al. (2004), Fig. 1.3–4c, with permission from Elsevier

9.2.3 The S2 Layer

9.2.3.1 Description of Layer

The S2 layer was the first Archean distal ejecta layer recognized as such. In their initial description, Lowe and Byerly (1986) simply designated the layer with an "S" because there were no other firmly established spherule layers in the Barberton Greenstone Belt (BGB) at that point. By the time Lowe et al. (1989) was published, three more layers had been recognized and they were numbered sequentially from oldest to youngest. The S2 layer received its name because it was the second oldest. Initially, Lowe and Byerly (1986, p. 83) described the stratigraphic position of the S2 layer as "near the base of the largely sedimentary Fig Tree Group," i.e., within the Fig Tree succession. More recently they have described it as at "the contact between black cherts at the top of the Onverwacht Group and fine ferruginous, cherty, and volcaniclastic sediments of the Fig Tree Group," i.e., right at the contact between the Onverwacht and Fig Tree Groups (Lowe et al. 2003, p. 17) or they show it below the Onverwacht/Fig Tree contact in cherts assigned to the former (e.g., Fig. 3 in Lowe et al. 1999). All known occurrences of the S2 layer are in the southern region of the BGB according to current correlations (Figs. 9.3 and 9.6).

The S2 layer ranges in thickness from 0.2 cm to at least 3.1 m at different sites and generally contains less than 10 % spherules by volume. The bulk of the layer consists of cherty detritus ranging in size from silt to cobbles eroded from underlying volcanic and sedimentary rocks (Fig. 9.12). In most sections, the S2 layer is a compound unit consisting of at least two distinct layers separated by an erosional surface or a thin layer of finer sediment. At the locality Lowe et al. (2003) designated as the type section, the S2 layer is unusually thick and rich in spherules, being 3.1 m thick in total and consisting of 2 or more normally graded subunits. The lower subunit contains clasts of chert up to 30 cm long and $\sim$30 to 50 % spherules by volume in its

lower part overlain by medium- to coarse-grained sand (with current structures) that contains ~10 % spherules by volume. This in turn is capped by silicified fine-grained sediment lacking spherules and deposited under lower energy conditions. The upper subunit in the S2 layer at the type locality is also graded, consists mainly of coarse to very coarse chert sand, and contains abundant chert clasts 2–4 cm long and ~30 % spherules by volume. Internally, the upper subunit displays numerous current structures and contains several thin interbeds of silicified fine-grained sediments. At this site, the S2 layer is directly overlain by finely laminated ferruginous chert assigned to the Fig Tree Group (Lowe et al. 2003). At another site to the south across two or more major faults, the S2 layer is 1.5 m thick and still a sandy unit that includes two graded subunits with up to ~10 % spherules by volume in some zones. At this site, the S2 layer is immediately overlain by a layer of conglomerate consisting largely of chert cobbles. Occurrences of the S2 layer have been observed at many sites (Fig. 9.6) but few details have been published from other sites.

Based on the characteristics outlined above and other data they collected during years of fieldwork in the BGB, Lowe et al. (2003, p. 24) interpreted the S2 layer as the product of an abrupt, short-lived, high-energy event within otherwise quiet, low-energy, possibly deep-water environments. The latter is indicated by the fine-grained nature of the strata above and below the S2 layer. The multiple graded sandy beds with wave and/or current structures indicate the S2 "layer" itself was deposited by an anomalously high-energy event, but the presence of fine-grained interbeds between them requires low-energy interludes that would allow finer suspended sediment to settle out. Consequently, it appears the S2 layer was deposited by waves and/or currents in two high-energy pulses separated by low-energy conditions. Other than the spherules, the detritus in the S2 layer could have been derived locally from materials in the underlying Onverwacht cherts and komatiitic volcanic units. Lowe et al. (2003) suggested this detritus was stripped off of adjacent, more exposed areas by the high-energy events that created the S2 layer.

9.2.3.2 Description of Spherules

Spherules in the S2 layer range from 0.15 to 2.5 mm in diameter and in mineralogy from nearly pure sericite to nearly pure quartz with all intergradations between these two end members (Fig. 9.13a). Silica-rich spherules commonly have thin sericite rims with fine rutile inclusions. Some of the sericite-rich spherules, which make up about half of all the spherules, also have rutile-rich rims (Fig. 9.13b). The interiors of silica-rich spherules are made up of coarse, blocky to lath-shaped quartz crystals, whereas sericitic spherules are composed of very finely crystalline sericite containing variable amounts of microquartz. Internally, some spherules show randomly oriented pseudomorphs of needle-like crystals or radial-fibrous textures in their rims. Some show pseudomorphs of fine needle- or lath-shaped and possibly barred microlites internally as indicated by variations in the abundance of rutile inclusions. A few spherules are composed largely of apatite (Lowe et al. 2003).

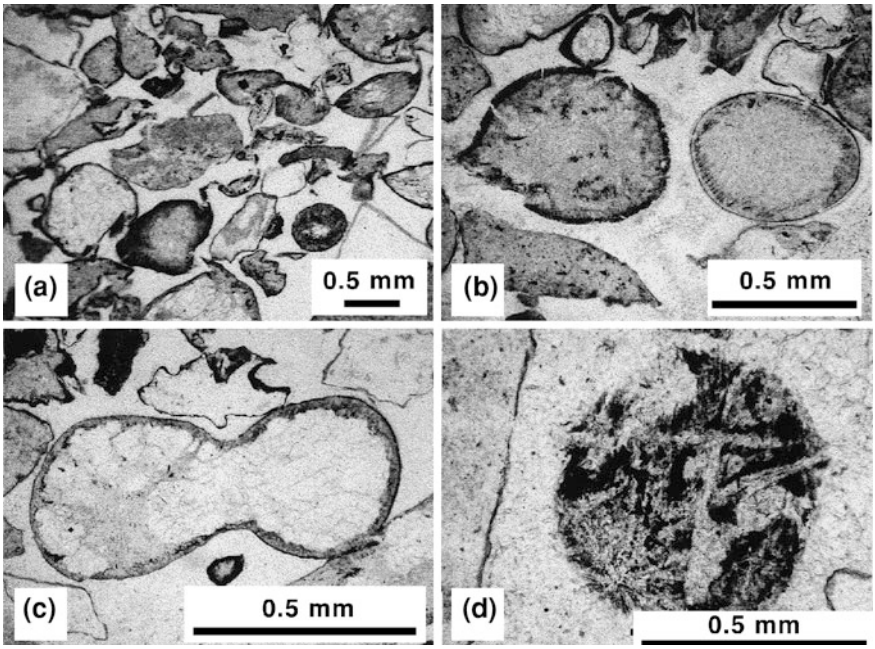

Fig. 9.13 Photomicrographs, taken in plane polarized light, of spherules from the S2 layer at 25 ° 53.78' S, 31 ° 01.09' E. **a** Well-sorted coarse sand-size detritus that is strongly modified by compaction locally, resulting in hook-shaped particles (e.g., in center) similar to distorted ooids described by Conley (1977). The detritus includes abundant sericite-rich spherules associated with other detritus that is generally more angular and cherty and produced by local erosion. Former pores contain siliceous cement, but cementation was not as early or pervasive as in sample shown in Fig. 9.14a. **b** Two sericite-rich spherules with differing concentrations of rutile (*black*) in their rims; spherule on left has thicker rutile rim that is broken off on lower left side of spherule. **c** "Dumbbell-shaped" spherule with a thin sericitic rim; spherule consists largely of quartz but left half contains patches of sericite (darker material). **d** Spherule with randomly oriented pseudomorphs of microlites of an unspecified composition, perhaps quartz. From Lowe et al. (2003), Figs. 11a, d, c, and f, respectively, with permission from Mary Ann Liebert, Inc.

Presumably most of these spherules were truly spheroidal at the time of deposition. Circular to oval cross-sections are common where pore-filling silica cement is abundant (Fig. 9.13a, b, d). Lowe et al. (2003) stated that rare spherules with cross-sections like dumbbells are present (Fig. 9.13c); however, the published image may be two spherules fused together rather than a dumbbell formed by rotation. Lowe et al. (2003) also stated that there may be some teardrops present; whereas Krull-Davatzes et al. (2006) stated that no teardrop-shaped particles are present in any of the Paleoarchean spherule layers. In any case, the shapes of many or most spherules have been modified to at least some extent by compaction and/or tectonic deformation. One process whose effects are widespread is pressure solution, which gave rise to textures ranging from stylolites to individual clasts that were partially dissolved at the expense of the cements. The latter have hook-

like extensions and unusual shard-like shapes (Fig. 9.13a) like those described in the S3 layer (see Sect. 9.2.2.2) and by Krull-Davatzes et al. (2006). However, the degree of contrast between chert clasts and chert cement varies from one area to another. At the site Lowe et al. (2003) designated as the type locality of the S2 layer, the interstitial chert is easily distinguished from spherules and detrital chert clasts, but the silica in the S2 layer at some other sites is so uniform that distinguishing clasts from cement is much more subjective.

9.2.3.3 Radiometric Age

The S2 layer is believed to have formed at about 3,260 Ma. This is based on a mean age of 3,258 ± 3 Ma obtained from 6 zircon crystals from a felsic tuff located 20 m above the Onverwacht/Fig Tree contact stratigraphically (Byerly et al. 1996). Zircons from a dacitic tuff 3 m above the Onverwacht/Fig Tree contact stratigraphically at a different site yielded a mean age of 3,243 ± 2 Ma which led Byerly et al. (1996) to suggest the contact was diachronous across the BGB. The older of the two dates is closer to the "oldest ages" reported from the Fig Tree in Kröner et al. (1991) and appears to be closer in age to the S2 layer as well.

9.2.3.4 Geographic Distribution and Variation

In their initial paper, Lowe and Byerly (1986, p. 959) stated that the S2 layer was "present across virtually the entire greenstone belt." As explained in Sect. 9.2.2.1, additional study convinced them to correlate the layer near the Onverwacht/Fig Tree contact in the northern region of the BGB with the S3 layer in the southern region instead of the S2 layer. Accepting this revised correlation, the S2 layer is restricted to the southern part of the BGB, but occurs in at least two different structural belts and can be correlated across at least two major faults on the northwest limb of the Onverwacht Anticline. Overall, the occurrences of the S2 layer can be followed along strike for about 15 km versus only a few kilometers across the structure in a north–south direction (Fig. 9.6). However, given the extensive thrust faulting in this area (Lowe et al. 1999), the original extent of the layer in the north–south direction was presumably significantly greater. Multiple sections of the S2 layer measured throughout its entire area of occurrence indicate there is considerable lateral variability, but to our knowledge no systematic description of how it varies spatially has been published.

9.2.3.5 Extraterrestrial Component

Ir concentrations have been measured in over 20 samples from the S2 layer. They range from below detection limits to a maximum of 6.1 ppb with an average of ~1.4 ppb (Table 2 of Lowe et al. 2003). This is anomalously high because

adjacent beds that do not contain spherules and are probably silicified tuffs have Ir concentrations on the order of 0.1 ppb (Fig. 10 and Table 3 of Lowe et al. 2003). However, the S2 layer shows little or no Ir anomaly relative to adjacent beds in some sections. Locally, elevated Ir levels in the S2 layer may reflect the presence of reworked komatiitic debris. Ni-rich spinels have not been detected in any samples from the S2 layer as currently defined (Lowe et al. 2003). Some samples originally thought to be from the S2 layer contain spinel crystals with unusual compositions (Byerly and Lowe 1994), but those samples were from sites that are now correlated with the S3 layer.

Kyte et al. (2003) analyzed the Cr isotopic composition of one sample from the upper ~20 cm of the S2 layer where it is 120 cm thick. The ε^{53}Cr value they obtained was -0.09 ± 0.03 (Table 9.2). Since it is statistically distinguishable from zero, this indicates the sample contains a small extraterrestrial component. A smaller Cr isotopic anomaly than either the S3 or S4 layer is to be expected as the spherules in the S2 layer are more highly diluted by ambient sediment than those in the other layers. The fact that the anomaly is negative suggests the impactor responsible for the S2 layer again had a composition like that of a carbonaceous chondrite. Assuming that is the case, the magnitudes of both the Cr anomaly and the Ir concentrations (Table 9.2) suggest that the total content of extraterrestrial material in the S2 layer is on the order of only 1 % (Kyte et al. 2003).

9.2.4 The S1 Layer

9.2.4.1 Description of Layer

The S1 layer is the oldest spherule layer found to date in the BGB and, combined with an equivalent layer in Western Australia (described in Sect. 9.3.1), comprises the oldest evidence of an impact by an extraterrestrial object found to date on Earth. Despite this, less has been published about the S1 layer than other layers in the BGB. Stratigraphically, the S1 layer is located in the upper part of the Hooggenoeg Formation, one of the medial units in the dominantly volcanic Onverwacht Group (Fig. 9.3). The S1 layer occurs in an interval of chert and silicified fine-grained tuff in the midst of komatiitic to basaltic lava flows that range from 0.3 to 3 m in total thickness.

At the site Lowe et al. (2003) designated as the type locality, the S1 layer is generally both underlain and overlain by cherts representing silicified fine-grained pyroclastic, carbonaceous, and chemical sediments (Lowe 1999; Walsh and Lowe 1999) each of which is on the order of 1 m thick. Spherules at this site occur in a pair of closely spaced layers. The lower layer is a coarse- to medium-grained sandstone 10–15 cm thick that contains 10–30 % by volume spherules. Substrate erosion prior to deposition is indicated by scours into the underlying chert and the presence of rip-up chert clasts in the layer. This layer shows normal grading as well as cross-lamination in its upper part. It is followed closely by an upper

layer ~20 cm thick that is also a well-sorted, medium-grained sandstone with normal grading. The upper layer contains 10–20 % spherules by volume and shows large-scale low-angle cross-stratification. More commonly, the S1 layer is a single bed of medium- to coarse-grained current-deposited sandstone, 10–35 cm thick. In sections where the cherty interval that contains it is <100 cm thick, the S1 layer generally rests directly on the underlying lava or is separated from it by just a few centimeters of sediment. Where the S1 layer rests directly on volcanic rocks instead of sediment, it contains 1–10 % spherules by volume and clasts of altered basaltic rock as well as chert.

Lowe et al. (2003) interpreted the S1 layer as the product of an unusually high energy event during an interlude of low-energy, quiet-water sedimentation. The latter coincided with a widespread period of magmatic quiescence between the major eruptive events that created the underlying basalts and komatiites and the overlying basalts (Lowe and Byerly 1999). In support of their interpretation, Lowe et al. (2003) noted that the S1 layer is the only layer that displays large-scale cross-stratification, scour, and coarse detritus in an interval of fine-grained sediments that rarely show any cross-lamination or other current structures. Based on the persistence of these characteristics throughout its known outcrop, the unit hosting the S1 layer was probably deposited below wave base in water that was at least moderately deep rather than in a high-energy environment.

9.2.4.2 Description of Spherules

Most of the spherules in the S1 layer consist of micromosaics of microquartz and sericite, but they range in composition from virtually pure fine-grained quartz to nearly pure sericite (Lowe et al. 2003). Their diameters range from 0.10 to 1.2 mm, but most have long axes between 0.30 and 0.60 mm. They range in shape from spheres to ovoids but rare dumbbell-shaped spherules that Lowe et al. (2003) interpret as spherules fused together are present and broken segments of spherules are common (Fig. 9.14a). From 40 to 60 % of the spherules by number have dark rims composed of microcrystalline rutile and some of the rims show faint radial-fibrous textures (Fig. 9.14b). Some of the rims appear clotted and many of the spherules with rims have bumpy external surfaces. Some spherules have fine rutile crystals disseminated throughout. The largest spherules consisting entirely of silica also tend to be somewhat blocky in shape rather than smooth spheroids or ovoids. A few of the pure-silica spherules consist of one to several coarse quartz crystals internally instead of microquartz. Whatever their composition, most of the spherules are homogeneous internally although a small minority show textural heterogeneity. Foremost among the latter are spherules with circular bodies of coarse quartz or sericite that are probably infilled vesicles, spherules that have concentric layers or zones, and rare spherules with randomly oriented, needle- or lath-shaped pseudomorphs that resemble microlites in mafic volcanic rocks. No pseudomorphs resembling olivine crystals with barred habits similar to those in chondrules (as mentioned in Sects. 9.2.2.2 and 9.2.3.2) or inclusions of spinel,

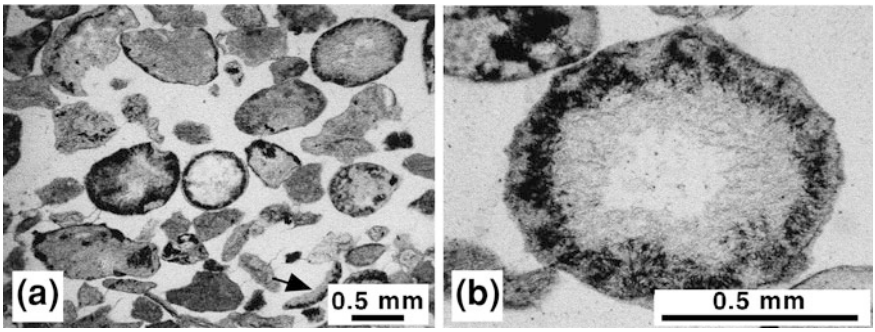

Fig. 9.14 Photomicrographs in plane polarized light of spherules from the S1 layer at 25 ° 56.4' S, 30 ° 52.94' E. **a** Well-sorted coarse sand-size spherules and associated detritus including fragments of spherule rims (e.g. at *arrow* near *bottom*). Former pores were filled with silica cement before significant compaction. **b** Well-preserved spherule with an outer rim (*dark*) of intergrown rutile, mica, and quartz with discontinuous pockets of sericite (*gray*) on the outer edge. The central spot consists of nearly pure quartz surrounded by intergrown quartz and sericite (*gray band*). From Lowe et al. (2003), Figs. 6a and g, respectively, with permission from Mary Ann Liebert, Inc.

barite, or apatite have been seen in the S1 layer, but tourmaline is relatively common. No differences were noted between the spherules in the upper and lower layers at the type section of the S1 layer. Based on these textures, it appears the spherules in the S1 layer originally consisted largely of glass, i.e., were like microtektites, but a small number of microkrystites were probably present as well.

The nonspherical clasts mixed with the obvious spherules in the S1 layer are well sorted and also composed largely of microquartz and sericite (Fig. 9.14a). Some of these nonspherical particles have internal textures similar to those in the spherules and may be impact ejecta, but most appear to be altered detrital fragments of the underlying volcanic or sedimentary rocks (Lowe et al. 2003).

As in the S2 layer, no spinels have been detected in the S1 layer.

9.2.4.3 Radiometric Age

Byerly et al. (2002) inferred an age of 3,470 ± 2 Ma for the impact by separating about 50 zircons out of the S1 layer and obtaining single-zircon U–Pb ages from 19 of them. Of the 19 zircons, they excluded 4, interpreted 2 with ages of about 3,510 Ma as older xenocrysts, and averaged the rest to obtain the age. No shock features were observed in any of the zircons so they do not appear to be unmelted impact ejecta. In addition, no cores were recognized in any of the zircons, suggesting they are juvenile magmatic crystals rather than recycled detrital grains. Byerly et al. (2002) interpreted these zircon crystals as detrital grains, but given the fact they are mostly euhedral, they could not have been transported very far. Byerly et al. (2002) viewed them as detritus from nearby felsic igneous rocks that were coeval or only slightly older than the S1 impact and most likely incorporated

into the S1 layer by the high-energy waves and/or currents generated by the same impact as the spherules. The age of 3,470 ± 2 Ma is consistent with dates obtained from zircons from tuffs in the Hooggenoeg Formation and adjacent stratigraphic units (Armstrong et al. 1990; Kröner et al. 1991; Byerly et al. 1996; Dann 2000), but the latter only bracket the age of the S1 layer between ~3,481 and 3,445 Ma. This age is statistically indistinguishable from an age derived from a spherule layer in the Pilbara Craton of Western Australia (Byerly et al. 2002; see Sect. 9.3.1.3 for further discussion).

9.2.4.4 Geographic Distribution and Variation

All of the occurrences of the S1 layer are restricted to essentially one strike belt of the thin cherty interval that hosts it. This interval can be traced for roughly 25 km around the nose of the Onverwacht Anticline (Fig. 9.6). No rocks this old have been recognized in the northern region or anywhere else in the BGB (Lowe et al. 2003), so no occurrences of the S1 layer are known outside of this strike belt. To our knowledge, no systematic descriptions of how the S1 layer varies along strike have been published.

9.2.4.5 Extraterrestrial Component

Iridium concentrations have been measured in four samples from the S1 layer. They were found to range from below detection limits to a maximum of 3 ppb (Table 2 of Lowe et al. 2003). This is slightly anomalous as most sedimentary and volcanic units in the BGB tend to have Ir concentrations on the order of 0.5 ppb (Table 3 of Lowe et al. 2003). However, some samples of komatiitic volcanics, including one close to the S1 layer, have Ir concentrations as high as 2.1 ppb. Chromium concentrations in the S1 layer samples are on the order of 500 ppm, but no Cr isotopic analyses of the S1 layer have been attempted to date.

9.3 Spherule Layer(s) in East Pilbara Terrane

9.3.1 Warrawoona Spherule Layer

9.3.1.1 Description of Layer

In their seminal paper, Lowe and Byerly (1986) briefly described one spherule layer in the Warrawoona Group of the East Pilbara Terrane. The Warrawoona Group is the oldest of four autochthonous volcano-sedimentary groups deposited on the Pilbara Craton between ~3.53 and 3.17 Ga (Van Kranendonk et al. 2007a).

The bulk of the Group consists of mafic to ultramafic volcanic rocks, most of which were deposited subaqueously, but thinner, generally tuffaceous intervals of felsic volcanics are present. The volcanic rocks erupted in cycles capped by thin sedimentary rock units silicified by hydrothermal fluids (Van Kranendonk 2006). The spherule layer reported by Lowe and Byerly (1986) occurs in one such silicified unit. Byerly et al. (2002, p. 1325) simply described the host as "a 10 m-thick chert" whereas Glikson et al. (2004) reported a diverse suite of silicified lithologies associated with the layer including well-sorted arenites that contained clasts showing pseudomorphed volcanic textures. Glikson et al. (2004) also reported that "dispersed spherules" were present at multiple levels in a zone ~14 m thick but did not provide details on their distribution (see Sect. 9.3.2 for further discussion). The proper stratigraphic name for the cherty unit hosting the spherule layer is unclear from published reports. Byerly et al. (2002) placed the layer in an unnamed chert member in the midst of the Apex Basalt, Glikson et al. (2004) placed it in the Antarctic Chert Member at the base of the Apex Basalt, and Van Kranendonk et al. (2007b) placed it in the Antarctic Creek Member in the middle of the Mount Ada Basalt, which underlies the Apex Basalt. Whatever its name is, the spherule layer is hosted by a chert interval ~10 m thick that, like the cherts in the BGB, represents an unusual episode of sedimentation in a succession constructed largely by volcanic eruptions (Fig. 9.15).

The spherule layer itself is described by Lowe and Byerly (1986) as a 15–50 cm thick bed rich in medium to coarse sand with some current structures. The non-impact detritus in the layer consists mainly of sand-size aggregates of homogeneous microcrystalline chert, sericite, and to a lesser extent chlorite, although some primary crystals of quartz and biotite are present. The former probably represent a mix of intraclasts and replaced lithic fragments, whereas the latter are essentially euhedral and probably juvenile crystals eroded from local felsic volcanic rocks. Lowe and Byerly (1986) said shards, pumiceous grains, and other recognizably volcanic detritus are absent from the layer. Spherules generally make up <10 % of the layer by volume, but locally increase to nearly 100 % of the silt to sand size detritus (Fig. 9.16a). No detailed descriptions of its depositional structures have been published to our knowledge.

9.3.1.2 Description of Spherules

As described in Lowe and Byerly (1986), the spherules are 0.10–0.75 mm in diameter and mostly circular in cross-section, but non-circular cross-sections and broken fragments of spherules are common. Non-circular spherules include compound spherules and dumbbell-shaped particles that Lowe and Byerly (1986) attributed to agglutination of multiple droplets rather than rapid spin of single, larger droplets as in normal splash forms. Around 60 % by number of the spherules show pseudomorphs of crystallization textures internally, and these include a range of morphologies from radial-fibrous to lath-shaped or acicular microlites (Fig. 9.16b). The original phases were most likely plagioclase,

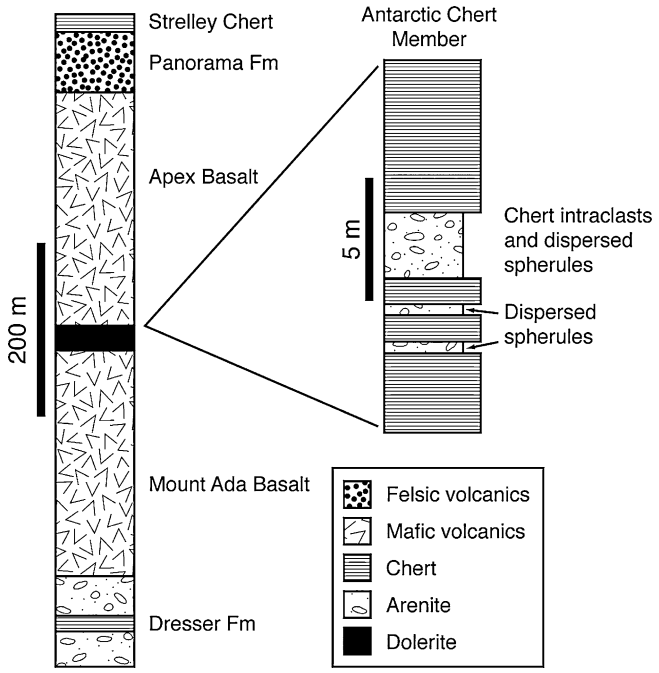

Fig. 9.15 Schematic stratigraphic columns of rock types and stratigraphic names of units in upper Warrawoona Group that contain one or more Paleoarchean spherule layers in the North Pole area of the Pilbara Craton (see Fig. 9.1 for geographic location). Based on data in Glikson et al. (2004), Fig. 2

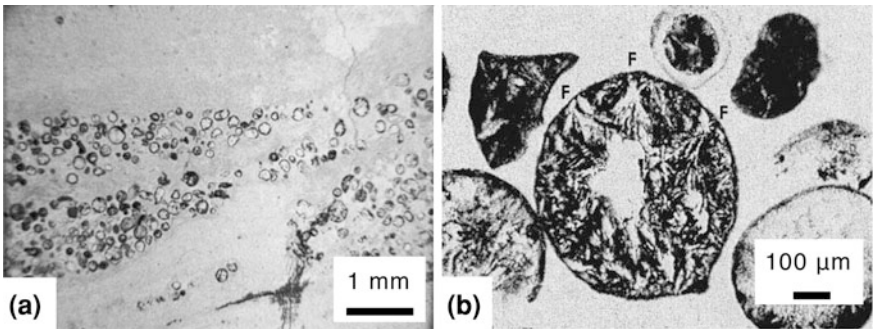

Fig. 9.16 Photomicrographs of spherules in plane polarized light from the Warrawoona layer. **a** Spherule-rich lenses interbedded with chert. **b** Single sericitic spherule with central quartz spot (*clear*) and pseudomorphs of both microlites and inward-radiating fans (F). In both a and b, the pores were filled with silica cement before any significant compaction. From Glikson et al. (2004), Figs. 4a and c, respectively, with permission from Elsevier

pyroxene, and/or olivine and formed via a combination of spinifex-like crystallization from the original melt and subsequent devitrification of glass. Lowe and Byerly (1986) also reported parallel lines resembling barred olivine pseudormophs are present in ~5 % of the spherules. At present, the spherules consist of a combination of quartz (in the form of chert), sheet silicates (mainly sericite), and iron oxide. The spherules described by Glikson et al. (2004) show similar features.

9.3.1.3 Radiometric Age

Byerly et al. (2002) inferred an age of 3,470 ± 2 Ma for the impact by separating about 30 zircons out of a 2 kg sample from the Warrawoona layer and obtaining single-zircon U–Pb ages from 20 of them. Of the 20 zircons, they excluded 3, interpreted 2 with ages of about 3,510 Ma as older xenocrysts, and averaged the rest to obtain the age. This is statistically indistinguishable from the date they obtained from the S1 layer in the BGB (see Sect. 9.2.4.3). The ages from the Warrawoona layer are consistent with a date of 3,457 ± 3 Ma obtained from a felsic volcanic rock ~2–3 km higher stratigraphically and an age of at least 3,471 Ma for rocks correlated with those beneath the spherule layer (Byerly et al. 2002). The age of the Warrawoona layer is also consistent with ages of 3,467 ± 4 Ma from underlying felsic volcanics and 3,458–3,454 Ma from overlying felsic volcanics reported in Glikson et al. (2004). Like those from the S1 layer of the BGB (see Sect. 9.2.4.3), the zircons from the Warrawoona layer do not show any shock features or cores and appear to be juvenile magmatic crystals reworked detritally rather than unmelted impact ejecta. As in the S1 layer, Byerly et al. (2002) interpreted the zircon crystals as detritus from nearby felsic igneous rocks coeval with or slightly older than the impact and probably redeposited by high-energy waves and/or currents generated by the impact that formed the spherules.

9.3.1.4 Geographic Distribution and Variation

In the first description, Lowe and Byerly (1986) noted that the spherule layer persisted along strike for at least 1 km. Glikson et al. (2004) extended this to a minimum extent of ~8 km. Van Kranendonk (2010) showed the spherule layer is part of a small circular dome and no correlative layers have been reported from anywhere else in the Pilbara Craton. However, as noted in Sect. 9.3.1.3, the Warrawoona layer and the S1 layer of the BGB yield identical ages within analytical error. This raises the question of whether these two layers are different parts of a single distal ejecta blanket. In addition to the similarities in their ages, their zircon populations are similar in other ways as well, including their habits and lack of inclusions. Byerly et al. (2002) also pointed out the S1 layer in the BGB and the proposed equivalent in the Warrawoona Group (both of which they called the S1 layer in their article) are close to features suggesting local effects of a major

impact. In the case of the Warrawoona layer, they point to a "major unconformity" in the general geographic and stratigraphic vicinity of the spherule layer and suggest it "may be the result of the S1 impact and tsunami." While no unconformity has been recognized in the BGB in close proximity to the S1 layer, it was the product of "a high-energy depositional event produced by multiple tsunami waves" (as described in Sect. 9.2.4.1) that Byerly et al. (2002) attributed to the same impact. Simonson and Hassler (2002) suggested that these and the other similarities Byerly et al. (2002) documented so well were most easily explained if the spherule layers in the Pilbara and Kaapvaal cratons were in close physical proximity to one another at the time of impact, but Byerly and Lowe (2002) argued that this was not necessarily the case.

9.3.1.5 Geochemistry

No geochemical data were published by Lowe and Byerly (1986) or Byerly et al. (2002) other than those directly pertaining to the zircons and outlined above. Glikson et al. (2004) published some geochemical data on spherules from the Warrawoona Group, but they only analyzed major and selected minor and trace elements. They noted that sericite-rich spherules are somewhat enriched in Ni and Cr relative to associated lavas, but not by much. Moreover, they do not specify exactly what stratigraphic level the spherules they analyzed came from, so it is unclear if the samples they analyzed were from the same layer described by Lowe and Byerly (1986) or possibly a different one (see Sect. 9.3.2). Neither PGE nor Cr isotopic data from the Warrawoona spherules have been published to our knowledge.

9.3.2 Possible Additional Layer(s)

Glikson et al. (2004) revisited the type exposure of the layer originally described by Lowe and Byerly (1986) and claimed to have identified spherules from one or more additional impacts in the associated strata. The second spherule layer is purported to be older and separated from the layer described in Sect. 9.3.1.1 by $\sim$230 m of rock, but most if not all of the intervening rock is intrusive in origin (mainly dolerite). Glikson et al. (2004) conceded that what they describe as a second spherule layer may have originally been close to the one already described and also mentioned that correlations are complicated by numerous closely spaced faults. These circumstances raise questions about whether or not there are spherule layers from two different impacts. Glikson et al. (2004) described the second layer as a spherule-bearing conglomerate 0.6–0.8 m thick with clasts of chert up to $\sim$40 cm long and cited the lack of pebbles in the original layer as evidence it and the newly described occurrence are not one and the same layer. Glikson et al. (2004) cited concentrations of spherules in "streaks and lenses within chert," as

well as scattered in associated arenites and conglomerates as "somewhat inconsistent" with post-impact redeposition of spherules from a single layer but provide no detailed descriptions to support this assertion. Glikson et al. (2004) descriptions of the spherules themselves are very similar to those of Lowe and Byerly (1986) and they are presented en masse with no distinctions made between spherules from different levels. In summary, additional data are needed before it can be confidently concluded that more than one large impact is needed to account for the known spherule occurrences in the Warrawoona Group. However, given the rich record of spherule layers in the BGB, it would not be surprising if more spherule layers were found in the East Pilbara Terrane.

Chapter 10
Modeling Variations in Distal Impact Ejecta/Spherule Layers through Space and Time

10.1 Variation in Distal Ejecta with Distance from the Source Crater

In this section, we summarize theoretical and experimental studies of how impact ejecta should vary with distance from the source crater. We then summarize what has been learned from studies of distal impact ejecta layers and compare these observational data with the theoretical and experimental results. In Sect. 10.2 we present a preliminary model for how distal ejecta vary with distance from the source crater based primarily on younger (Cenozoic and K-T boundary) ejecta layers whose source craters, with one exception, have been identified. We then discuss how well this model conforms to observations of older layers where the source craters are known with less certainty or altogether unknown (and possibly unknowable, especially in the case of Archean layers); and, where possible, we try to use the model to predict the size of and distance to the source crater.

10.1.1 Summary of Theoretical, Experimental, and Observational Studies

Theoretical and model studies of the impact cratering process, laboratory and field experiments, and studies of ejecta blankets around impact craters indicate that the ejecta blanket is thickest adjacent to the crater and thins exponentially away from the crater (McGetchin et al. 1973; Stöffler et al. 1975; Melosh 1989, and references therein). Ejecta thickness (t) is a function of crater radius (R) and distance or range (r) from the crater center. The crater radius refers to the transient crater radius. For simple craters the transient crater radius is slightly smaller than the radius based on the final rim-to-rim diameter, but for complex craters the transient crater radius can be much smaller than the radius based on the final rim-to-rim diameter (Turtle et al. 2005; Collins et al. 2005). For simple terrestrial craters the transient crater size is

B. P. Glass and B. M. Simonson, *Distal Impact Ejecta Layers*, Impact Studies,
DOI: 10.1007/978-3-540-88262-6_10,

$\sim$80 % of the final rim-to-rim size. For complex craters the discrepancy between transient crater size and final rim-to-rim size increases with crater size. For example, the transient crater size of a 100-km-diameter crater is estimated to have been only about 60 % of the final rim-to-rim diameter. Thickness of an ejecta layer is indicated by the general equation: $t = aR^b(r/R)^{-c}$. The numerical values of the coefficient "a" and exponents "b" and "c" vary from one investigator to another, but "c" is generally given as 3 ± 1. Two of the most widely used equations are from McGetchin et al. (1973) and Stöffler et al. (1975) (see Eqs. 2.2 and 2.3, respectively). Note that if the distance from the center of the crater is equal to the crater radius, then "$(r/R)^{-c}$" equals 1 and, therefore, "aR^b" is the thickness of the ejecta blanket at the crater rim. These equations are intended for proximal ejecta. Furthermore, they apply to vertical impacts, since oblique impacts lead to asymmetric distribution of the ejecta (Gault and Wedekind 1978; Melosh 1989). However, the most common impact angle is about 45° and the asymmetry is not significant except for impact angles of $\sim$30° or less (Kring and Durda 2002).

Another factor complicating the way impact ejecta are distributed across the Earth's surface is the generation of vapor plumes during large impacts, which can blow out the top of the atmosphere. Large vapor plumes entrain melt and solid ejecta shocked to various degrees (Kring and Durda 2002). Although it seems counterintuitive that shocked mineral grains, such as quartz with PDFs, could survive the intense heat, thermal heterogeneities in the plume as well as brief interaction times apparently allow some shocked mineral grains to survive. Above the atmosphere, these ejecta particles travel along ballistic trajectories until they reenter the atmosphere. In larger impacts, unmelted, as well as melted, ejecta can be distributed around the globe. In general, ejecta deposited more that $\sim$400 km from the source crater were carried above the atmosphere (Kring and Durda 2002).

Computer models suggest that in large impacts, distal ejecta are concentrated at the antipodal region (Argyle 1989; Melosh et al. 1990; Kring and Durda 2002). Furthermore, the Earth's rotation can affect the distribution of ejecta, especially in large impacts where the ejecta are distributed globally. For example, because the Earth is rotating eastward, particles ejected at high velocity and at high angles (e.g., greater than 60°) to the east would land closer to the source crater than particles ejected at the same velocity and angle to the west (Alvarez et al. 1995). In addition, computer models suggest that deposition can be greatly enhanced in equatorial regions in the opposite hemisphere (relative to what would be expected from simple exponential decay) when ejecta is launched at 45° in low latitudes (Wrobel and Schultz 2003). On the other hand, some authors have proposed models suggesting that interactions between the ejecta and the atmosphere during reentry may result in a more even distribution of the distal ejecta than predicted by simple exponential decay (see Sect. 2.7.1; Goldin and Melosh 2008; Atemieva and Morgan 2009). Thus, even though ejecta falling into the upper atmosphere from a large expanding impact plume may be asymmetrically distributed, this may not be faithfully reflected in depositional patterns on the Earth's surface.

In spite of the above limitations, some authors have used equations that relate ejecta thickness to the size of, and distance from, the source crater to determine

where a source crater might be located or which known crater of the appropriate age might be the source crater for a given ejecta layer (e.g., Hildebrand and Stansberry 1992; Walkden et al. 2002). Some older ejecta layers may have been deeply buried and compacted before being exhumed by erosion (Williams and Wallace 2003). The thickness of these layers will, therefore, be thinner than that predicted from the exponential decay equations. The amount of compaction varies with the nature of the ejecta layer (e.g., grain size and shape, composition), depth of burial, diagenetic conditions, and age.

Cratering models and field studies of impact craters indicate that the material nearest the surface in the target area is ejected first and is thrown the farthest (Melosh 1989). Deep-seated rock is ejected last and at a slower velocity than surface material. In addition, the surface material that is thrown the farthest is, on average, shocked to a higher degree than ejecta derived from greater depths in the target rock. Thus the percent melt, represented by impact glass in the form of spherules (e.g., microtektites) should increase with distance from the source crater (e.g., Vickery et al. 1992; Fig. 2.35). The percent of unmelted ejecta should decrease with distance from the source crater, but the average degree of shock metamorphism should increase. In quartz grains, for example, an increase in the degree of shock metamorphism can be indicated by an increase in the average number of sets of PDFs.

It appears that there are four types of impact-generated spherules: (1) microtektites produced as melt droplets, (2) microtektites formed as condensate droplets, (3) microkrystites formed as condensate droplets, and (4) microkrystites formed as melt droplets. Melt droplets in an impact plume can be quenched to form glass spherules (microtektites), and condensation within the plume can form droplets which can partially crystallize to produce microkrystites. The melt-drop microtektites generally have compositions reflecting that of the target rocks, with little or no contamination from the projectile. However, some low silica microtektites found in the cpx spherule layer are enriched in Cr, Ni, and Co (Glass et al. 2004b) and it seems possible that these microtektites may have formed by condensation from the impact vapor plume (see Sect. 3.2.1.1). The microkrystites formed as condensate droplets can be highly contaminated by the projectile and often contain Ni-rich spinel crystals. On the other hand, although they have been diagenetically altered, some Precambrian spherules with relict crystalline textures have teardrop and dumbbell shapes and/or contain relict vesicles but not Ni-rich spinels. It seems possible that these spherules were formed as melt droplets rather than as vapor condensate droplets (see Sect. 10.4).

Many of the spherules from larger impacts (e.g., K-T boundary ejecta layer and Archean-Proterozoic boundary and Paleoarchean spherule layers) have crystallized rims. Rims on the K-T boundary spherules have been explained as a possible result of palagonitization when the hot spherules landed in water (Bohor and Glass 1995). However, by the time the spherules landed, they may not have been hot enough for palagonitization to occur (NA Artemieva, personal communication, 2012). The crystallized rims on the Precambrian spherules have been explained as the result of thermal devitrification due to intensive heating during re-entry into the

atmosphere (Artemieva and Simonson 2012). What should we call impact spherules with crystallized rims? Should they be called microkrystites because of the crystalline phases present in the rims? We believe that the presence of crystalline phases produced by thermal devitrification does not meet the definition for microkrystites; that is, the crystalline phases produced by devitrification are not primary phases. Does this mean that they should be called microtektites? Not necessarily. We must look at the entire spherule. If the core (i.e., all of the interior below the rim) contains microlites interpreted as having formed from the melt during cooling, then the spherule is a microkrystite. If the core is still glassy and free of microlites, then it is a microtektite with a crystalline rim formed by devitrification. However, if a spherule has undergone diagenesis and the core was replaced by another phase or phases, then one could not ascertain if the original spherule was a microkrystite or a microtektite. If it is not possible to determine whether or not the core originally contained primary microlites, then it should simply be called an impact spherule.

10.1.2 Spatial Variations in Phanerozoic Distal Ejecta Layers

Only a handful of Phanerozoic distal impact ejecta layers, for which the source crater is known or for which the source region is believed to be known, have been observed at numerous sites (Table 10.1). The best known and most studied are the Cretaceous-Tertiary (K-T) boundary ejecta layer and the Australasian microtektite layer. Unfortunately, the Australasian microtektite source crater is not yet known; however, most investigators believe that it is in the Indochina area (see Sect. 4.2.10). In the following subsections, we have used a predicted source crater location at 17° N latitude and 107° E longitude in the Gulf of Tonkin (off the coast of Vietnam) as suggested by Ma et al. (2004) based on ^{10}Be data from Australasian tektites. We have used a crater diameter of 38 km which is intermediate between the crater sizes proposed by Glass and Koeberl (2006) and Prasad et al. (2007) of 43 and 33 km, respectively. Additional well-studied Phanerozoic distal ejecta layers with known source craters include the Ivory Coast and North American microtektite layers, the late Eocene clinopyroxene-bearing (cpx) spherule layer, and the Manson ejecta layer. In this section, we summarize how the ejecta layers mentioned above vary with distance from their proposed source craters and compare observed data with theoretical data where possible. We note that the melt-drop microtektites and microtektite layers vary systematically with distance from the source craters, but condensate spherules, exemplified by the Late Eocene cpx spherules, do not appear to vary with distance from the source crater in the same way as the melt-drop microtektites, nor does the cpx spherule layer exhibit a clear systematic variation from the source crater.

Table 10.1 Phanerozoic ejecta layers used to develop a model for how distal ejecta varies with distance from the source crater

Ejecta layer	Age (Ma)	Number of cores/sites	Source crater	Diameter (km)	Transient diameter (km)[a]
Australasian microtektite	0.8	>70	Unknown[b]	60[c]	38
Ivory Coast microtektite	1.1	10	Bosumtwi	10.5	9
North American microtektite	35	7	Chesapeake Bay	85	40
Cpx spherule	35	28	Popigai	100	60
K-T boundary ejecta	65	>100	Chicxulub	180	100
Manson ejecta	74	20	Manson	35–37	21

[a] Transient crater size for the Australasian source crater is an average of 33 and 43 from Prasad et al. (2007) and Glass and Koeberl (2006), respectively, based on McGetchin et al.'s (1973) equation (see Sect. 2.6) that relates ejecta thickness to distance from and transient crater size of the source crater. Transient crater sizes of the Bosumtwi and Chesapeake Bay impact structures are from Artemieva (2002) and Poag et al. (2004), respectively. Transient crater sizes for the Popigai and Chicxulub impact structures are from Grieve and Cintala (1992). Transient crater size for the Manson impact structure was calculated from the following equation: $D_{fr} = 1.17(D_{tc}^{1.13}/D_{c}^{0.13})$, where D_{fr} is final rim-to-rim crater diameter, D_{tc} is the transient crater diameter, D_c is the diameter at which the transient crater changes from simple to complex (i.e., ~3.2 km on Earth; Collins et al. 2005)

[b] The Australasian source crater is not known, but several different lines of evidence indicate that the source crater is in the Indochina area. We use the estimate of 17° N and 107° E from Ma et al. (2004) in this chapter

[c] This estimate is derived from the transient crater diameter using the equation in footnote "a" from Collins et al. (2005)

10.1.2.1 Fluence of Impact Ejecta

Most Phanerozoic marine sediments have been reworked by bottom currents and/or bioturbation. These bottom processes disperse sediment components, including ejecta, horizontally and vertically through the sediment column (Figs. 4.8, 4.10, 4.33, 4.47). Bottom currents are generally localized and too weak to rework bottom sediments. Bioturbation is fairly ubiquitous and can move recently deposited sediment downward and bring older sediment up to the sediment–water interface (see, e.g., Ruddiman et al. 1980). The peak abundance of ejecta found in a deep-sea core will depend on sediment accumulation rate and the amount of reworking, as well as, the number (or volume) of ejecta particles that fell per unit area on the ocean floor at the core site. Thus, in order to compare the abundance of ejecta particles from one site to another it is necessary to determine the total number of ejecta particles through a vertical column with a given cross-sectional area (see, e.g., Glass and Pizzuto 1994). For unconsolidated sediments, this can be done by sieving and then counting the number of ejecta particles, larger than a given size, in a series of closely-spaced samples of known size (or weight) through the ejecta layer. If the sampling is not continuous, then the number of ejecta particles in unsampled sections can be estimated by interpolation. The number of ejecta particles in the column is then totaled to give the number per unit area. For the Cenozoic microtektite and/or microkrystite layers, the abundance is given as the number of microtektites and/or microkrystites and/or ejecta particles (>125 μm)/cm^2 (see Table 10.2). Using a smaller grain size than 125 μm for the lower cutoff size would be preferable, especially for the cpx spherules, but at some sites the microtektites, microkrystites and/or other ejecta particles in the smaller size fractions are too numerous to be counted easily, especially since other sediment components are usually much more abundant in the smaller size ranges.

Determining spherule abundance is more difficult when dealing with consolidated sediment or rock. Spherule abundances cannot be determined via the methods used for unconsolidated sediment, so various approximations have to be made on a case by case basis. It is difficult to translate measurements on a 2-dimensional surface (e.g., thin or polished section) into abundances, even if the particles are generally spherical. Thus, care must be taken in comparing spherule abundances and size distributions in unconsolidated sediments with estimated spherule abundances and size distributions in lithified sediments.

10.1.2.1.1 Microtektite/Impact Spherule Fluence

As of 2011, the abundance of Australasian microtektites was estimated to vary between <1 and ~9800 (>125 μm)/cm^2 and the highest abundance in the Ivory Coast strewn field was ~80 (>125 μm)/cm^2 (Table 10.2). The abundances of North American microtektites (>125 μm) at Barbados and in the Caribbean Sea and Gulf of Mexico vary between ~880 and 8100/cm^2, but formerly molten ejecta particles are much more abundant at two sites (DSDP 612, ODP 904) off the coast of New

Table 10.2 Cenozoic microtektite/spherule/ejecta layer core/site location, distance from source crater, abundance, and percent fragments and unmelted ejecta

Core/Site	Latitude (degrees)	Longitude (degrees)	Distance (km)[a]	Number (>125 μm)/square cm[b]	Percent fragments[c]	Percent unmelted ejecta[d]
Australasian Microtektite Strewn Field						
ODP 1143A	9.362 N	113.285 E	1085	973	36	32
SO95-17959	11.138 N	115.287 E	1105	n.d.	n.d.	n.d.
SO95-17957-2	10.90 N	115.31 E	1123	2819	45	19
ODP 772A	16.65 N	117.70 E	1141	n.d.	n.d.	n.d.
ODP 1144A	20.05 N	117.42 E	1151	17161	75	43
MD972142	12.69 N	119.56 E	1433	3199	27	n.d.
ODP 769A	8.79 N	121.22 E	1791	3307	25	3
ODP 768B	8.00 N	121.22 E	1839	3107	24	5
MD972143	15.87 N	124.65 E	1889	1117	44	n.d.
DSDP 292	15.82 N	124.65 E	1890	489	30	8
ODP 758B	5.38 N	90.36 E	2226	3339	41	3
ODP 767B	4.79 N	123.50 E	2253	3056	33	2
RC14-46	7.82 S	100.00 E	2852	1082	32	2
V19-153	8.85 S	102.12 E	2909	348	30	5
V20-138	28.87 N	135.55 E	3210	49	10	0
DSDP 213	10.21 S	93.90 E	3342	160	n.d.	0
V19-171	7.07 S	80.77 E	3943	20	13	0
V19-158	18.18 S	99.40 E	3981	39	0	0
RC14-24	6.62 S	79.44 E	4020	39	4	0
AAS38/1	4.98 S	78.029 E	4024	86	n.d.	n.d.
V19-169	10.22 S	81.62 E	4125	56	5	0
AAS22/8	7.09 S	78.128 E	4165	91	n.d.	n.d.
V29-39	7.70 S	77.38 E	4273	50	10	0
AAS38/2	8.50 S	77.996 E	4280	30	n.d.	n.d.

(continued)

Table 10.2 (continued)

Core/Site	Latitude (degrees)	Longitude (degrees)	Distance (km)[a]	Number (>125 μm)/square cm[b]	Percent fragments[c]	Percent unmelted ejecta[d]
RC12-331	2.50 N	69.87 E	4378	82	0	0
AAS22/7	10.016 S	78.150 E	4382	50	n.d.	n.d.
SK69/001	8.981 S	77.117 E	4389	13	10	n.d.
V29-40	10.48 S	78.05 E	4426	106	10	0
RC14-23	9.18 S	76.76 E	4434	55	0	0
AAS4/6	12.616 S	78.513 E	4557	20	n.d.	n.d.
AAS4/5A	12.508 S	76.516 E	4706	94	n.d.	n.d.
AAS4/1	11.261 S	75.012 E	4734	97	n.d.	n.d.
AAS4/2	12.002 S	75.499 E	4749	54	n.d.	n.d.
AAS22/5	15.109 S	78.196 E	4784	34	n.d.	n.d.
V29-43	12.33 S	75.08 E	4809	82	3	0
AAS38/3	12.581 S	75.256 E	4813	21	n.d.	n.d.
AAS38/4	14.004 S	75.001 E	4943	2	n.d.	n.d.
AAS22/3	16.999 S	77.997 E	4955	22	n.d.	n.d.
SK16/176	14.050 S	74.767 E	4965	62	n.d.	n.d.
AAS38/5	17.053 S	74.044 E	5257	8	n.d.	n.d.
RC12-328	3.95 N	60.60 E	5281	14	0	0
RC12-327	1.73 N	57.83 E	5659	13	0	0
E48-6	34.00 S	97.54 E	5736	<1	n.d.	n.d.
V28-239	3.25 N	159.18 E	5918	7	0	0
V28-238	1.02 N	160.48 E	6140	3	0	0
RC8-53	39.38 S	104.37 E	6243	4	5	0
ODP 804C	1.005 N	161.594 E	6258	(13)	0	n.d.
E50-2	39.96 S	104.93 E	6305	2	0	n.d.
E45-89	39.52 S	114.47 E	6305	11	0	0

(continued)

Table 10.2 (continued)

Core/Site	Latitude (degrees)	Longitude (degrees)	Distance (km)[a]	Number (>125 μm)/square cm[b]	Percent fragments[c]	Percent unmelted ejecta[d]
E49-51	39.93 S	99.94 E	6344	4	0	0
E49-50	40.61 S	99.91 E	6419	5	0	0
RC8-52	41.10 S	101.42 E	6456	14	2	0
RC9-143	41.36 S	114.13 E	6502	18	0	0
RC9-142	42.72 S	116.89 E	6693	16	0	0
V16-75	22.22 S	58.38 E	6931	2	n.d.	0
V16-76	25.15 S	59.90 E	7005	18	0	0
E49-4	46.99 S	110.13 E	7088	14	0	0
E45-74	47.55 S	114.44 E	7187	2	0	0
E35-9	45.05 S	128.02 E	7231	2	0	0
E45-71	48.02 S	114.49 E	7239	13	0	0
RC9-137	45.02 S	132.75 E	7404	10	0	0
E39-45	45.16 S	133.02 E	7468	4	0	0
V20-184	25.80 S	53.68 E	7578	10	0	0
V16-70	32.10 S	55.85 E	7833	14	0	0
E35-6	53.21 S	128.10 E	8085	8	0	0
V21-125[e]	13.68 N	128.48 E	2336	26	n.a	100
V19-116[e]	11.23 N	130.17 E	2582	29	n.a	100
V20-142[e]	17.18 N	133.27 E	2796	6	n.a	100
Ivory Coast Microtektite Strewn Field						
V19-297	2.62 N	12.00 W	1250	80	44	0
ODP 663	1.02 S	11.88 W	1441	12	48	0
V27-239	7.83 S	1.52 W	1585	17	3	n.d.
K9-56[f]	8.38 N	15.50 W	1613	n.a.	7	0
RC13-213	10.48 S	2.40 W	1881	10	7	n.d.

(continued)

Table 10.2 (continued)

Core/Site	Latitude (degrees)	Longitude (degrees)	Distance (km)[a]	Number (>125 μm)/square cm[b]	Percent fragments[c]	Percent unmelted ejecta[d]
V19-300	6.88 N	19.47 W	1996	8	0	n.d.
RC13-210	9.13 N	10.62 W	2009	14	0	n.d.
K9-57	8.63 N	22.03 W	2287	35	6	n.d.
ODP 664	0.10 N	23.27 W	2529	1	0	n.d.
North American Microtektite Strewn Field						
DSDP 612	38.82 N	72.78 W	332	(544,000)	99	35
ODP 904	38.863 N	72.768 W	335	(242,857)	>98	44
ODP 903C	38.938 N	72.817 W	338	0	n.a.	100
DSDP 94	24.53 N	88.47 W	2246	5750	37	<1
DSDP 149	24.53 N	88.47 W	2449	n.a.	17	<1
RC9-58	14.56 N	70.81 W	2511	8100	24	<1
Barbados	13.20 N	59.51 W	2855	877	52	<1
Clinopyroxene-Bearing Spherule Strewn Field						
ODP 786A	31.875 N	141.226 E	5084	(8)	n.d.	n.d.
Massignano[g]	43.54 N	13.59 E	5732	(46)	n.d.	n.d.
DSDP 292	15.818 N	124.484 E	6501	213	n.d.	17
DSDP 291	12.807 N	127.832 E	6662	<1	n.d.	n.d.
ODP 903C[h]	38.938 N	72.817 W	7531	n.d.	n.d.	n.d.
ODP 904A[h]	38.863 N	72.768 W	7542	(206)	n.d.	n.d.
DSDP 612 [h]	38.820 N	72.779 W	7543	(123)	26	n.d.
DSDP 94	24.527 N	88.469 W	9217	(84)	n.d.	n.d.
ODP 709C	3.915 N	60.552 E	9486	9574	16	4
DSDP 216	1.462 N	90.208 E	9682	2274	n.d.	9
DSDP 162	14.870 N	140.044 W	9804	244	n.d.	9
DSDP 149	15.104 N	69.364 W	10457	n.d.	n.d.	n.d.

(continued)

Table 10.2 (continued)

Core/Site	Latitude (degrees)	Longitude (degrees)	Distance (km)[a]	Number (>125 μm)/square cm[b]	Percent fragments[c]	Percent unmelted ejecta[d]
DSDP 462	7.238 N	165.030 E	10685	n.d.	n.d.	n.d.
RC9-58	14.557 N	70.810 W	10686	891	n.d.	2
DSDP 70A	6.335 N	140.362 W	10762	5	n.d.	(25)
DSDP 167	7.068 N	176.825 W	10779	40	n.d.	<8
DSDP 166	3.762 N	175.080 W	10804	854	n.d.	10
DSDP 161A	10.238 N	139.954 W	10939	NWDL	n.d.	n.d.
DSDP 315A	4.171 N	158.526 W	11038	n.a.	n.d.	n.d.
DSDP 69A	6.000 N	152.866 W	11252	926	n.d.	4
DSDP 65	4.353 N	176.986 W	11476	NWDL	n.d.	n.d.
ODP 738B[i]	62.709 S	82.788 E	15222	(11)	n.d.	(100)
ODP 699A[i]	51.542 S	30.677 W	15551	8	n.d.	100
ODP 1090B	42.914 S	8.900 E	15636	45	n.d.	60
ODP 703A	47.051 S	7.895 E	15810	<1	n.d.	n.d.
ODP 689 B,D	64.517 S	3.100 E	17048	57	n.d.	81

n.a. = not applicable; n.d. = no data; NWDL = no well-defined layer; values in parentheses are questionable

[a] Distance between source crater and core/site. Distances for the North American and cpx strewn field have been corrected for tectonic plate movement

[b] Number of microtektites/spherules plus unmelted ejecta where present. The percent unmelted ejecta (in the last column) can be used to determine the number of ejecta particles in this column that are microtektites/spherules

[c] Percent fragments of microtektites/tektites as opposed to whole, or nearly so, specimens

[d] Percent of ejecta (>125 μm) that is unmelted (e.g., shocked quartz with PDFs, coesite) at each site, except in the cpx spherule strewn field. For the cpx strewn field the percent microtektites, as opposed to unmelted ejecta, is given

[e] Only unmelted ejecta are found at these sites, but the ejecta occur at the same stratigraphic level as Australasian microtektites

[f] A few microtektites were found at the bottom of the core; i.e., the layer was not penetrated

[g] Pancake-shaped clay "spherules" coated with Ni-rich spinel crystallites are interpreted as diagenetically altered cpx spherules

[h] Cpx spherules at these core sites are partly or completely replaced with pyrite

[i] No cpx spherules were found at these sites, but microtektites found at these sites are believed to belong to the cpx strewn field

Australasian data are from Smit et al. (1991), Wu (1995), Glass et al. (1997), Prasad and Sudhakar (1999), Wang et al. (2000), Lee and Wei (2000), Glass and Koeberl (2006), Prasad et al. (2007); Ivory Coast and North American data are from Glass et al. (1997); and cpx spherule data are from Liu et al. (2009)

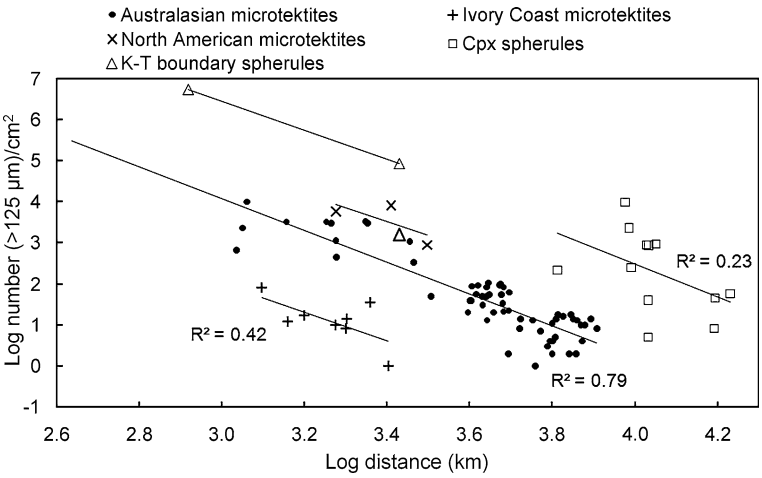

Fig. 10.1 Log number of microtektites/spherules per square centimeter versus log distance from the source crater in kilometers. The source crater for the Australasian strewn field is not known, but most investigators believe it is in the Indochina area. A location at 17° N and 107° E in the Gulf of Tonkin off the coast of Vietnam as proposed by Ma et al. (2004) was used to plot the Australasian microtektite data. Two estimates of the number of spherules/cm^2 in the K-T boundary layer at Dogie Creek, Wyoming (USA), are included. The smaller estimate of ~1570 spherules/cm^2 (*bold triangle*) is based on an average spherule diameter of 900 μm as given in Izett (1990). The larger estimate of ~82,900 spherules/cm^2 is based on an average diameter of 270 μm which is an average size for the Cenozoic microtektites. In spite of the scatter in the data as indicated by low r^2 values for the cpx spherule layer and the Ivory Coast spherule layer, the best-fit linear trends are all more or less parallel to each other. See Table 10.2 for the Cenozoic microtektite and cpx spherule data used in this figure

Jersey (USA). At these two sites, millimeter-sized splash forms (minitektites) are common and tektite fragments are abundant but microtektites <1 mm in diameter are rare. Tektite fragments make up the bulk of the glass particles at these sites and are too numerous to count in a reasonable period of time. We estimate that the combined number (>125 μm)/cm^2 of tektite fragments, millimeter-sized splash forms, and microtektites are ~243,000 and 544,000 for Sites 904 and 612, respectively; but these numbers are only approximations.

A graph of log number of microtektites (>125 μm)/cm^2 versus log distance from the source crater shows that the abundance of microtektites decreases systematically with distance from the source crater (Fig. 10.1), but there is a great deal of scatter. The Australasian microtektite data show a reasonably well-defined linear trend ($r^2 = 0.79$) with decreasing abundance away from the predicted source crater location in the Gulf of Tonkin. A source crater location near the border between northern Vietnam and China at 22° N and 104° E explains the geographic variation in abundance better. This site gives a linear trend with a somewhat steeper slope and with less scatter ($r^2 = 0.85$). However, as no relatively large, young impact crater has been identified at this site, we used the predicted location given by Ma et al. (2004).

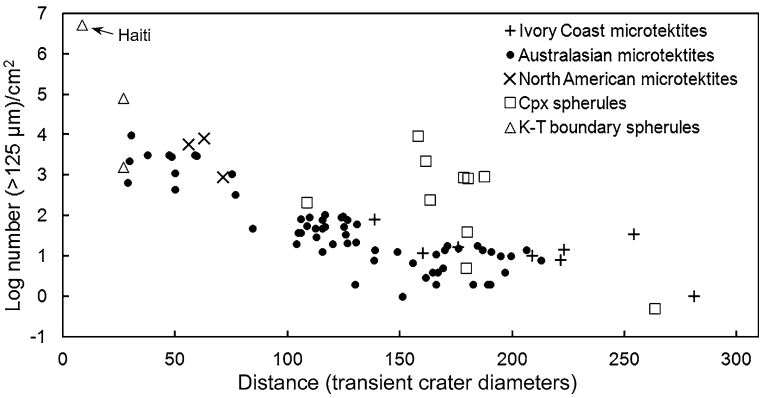

Fig. 10.2 Log number of microtektites/spherules (>125 μm)/cm^2 versus distance from all source crater in crater diameters. Note that data from all Cenozoic microtektites plot along the same trend. However, the cpx spherule abundances mostly plot above the Cenozoic microtektite trend. Abundance of K-T boundary spherules at Haiti appears to plot above the extrapolated Cenozoic microtektite abundance trend. Two abundances are plotted for the K-T boundary layer spherules at Dogie Creek (*unlabeled triangles*) based on calculations using different average spherule sizes (see caption for Fig. 10.1 for details). Transient crater diameters used to plot the distances to the source craters in crater diameters can be found in Table 10.1. See Table 10.2 for distances to the source craters and abundances of microtektites/spherules used in this figure. For the Australasian microtektite layer, distances in crater diameters were calculated using a proposed source crater location in the Gulf of Tonkin (17° N and 107° E) as proposed by Ma et al. (2004)

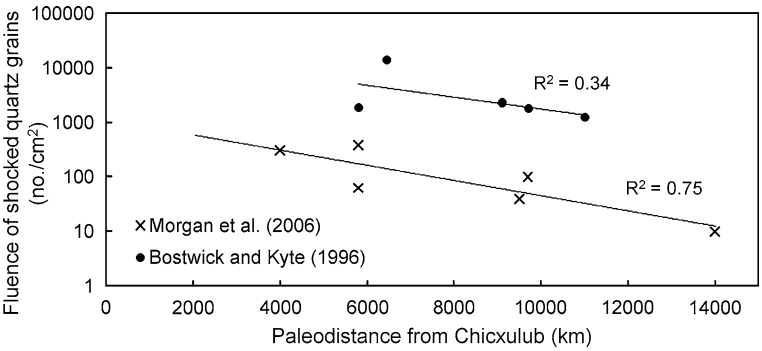

Fig. 10.3 Fluence (number/cm^2) for shocked quartz in the K-T boundary layer versus paleodistance (in kilometers) from the source crater, Chicxulub. For a given distance, the fluences reported by Morgan et al. (2006) are generally lower by more than an order of magnitude than the fluences given by Bostwick and Kyte (1996). However, both sets of data show a decrease in fluence of shocked quartz with increasing distance from Chicxulub

For a given distance from the source crater, the Ivory Coast microtektites are much less abundant, so fluence data from those sites plot below data for the Australasian sites (Fig. 10.1). This presumably reflects the smaller size of the Ivory Coast microtektite source crater. The data for the Ivory Coast strewn field

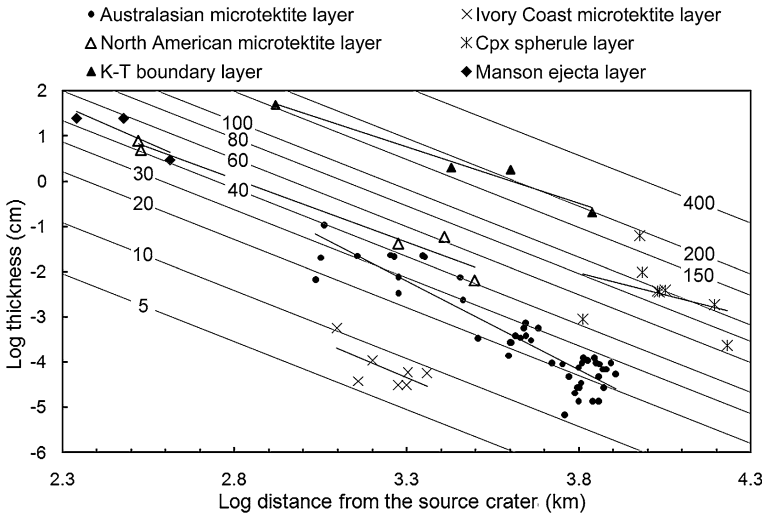

Fig. 10.4 Log thickness of the microtektite/spherule layer versus log distance from the source crater for the Australasian, Ivory Coast, and North American microtektite layers, the cpx spherule layer, and the Chicxulub (K-T boundary) and Manson impact ejecta layers. Best-fit linear trend lines are indicated for each microtektite/spherule/ejecta layer. As expected, they all (with the possible exception of the cpx spherule layer) show a trend of decreasing thickness away from the source crater. Also shown are the hypothetical ejecta thicknesses for craters with transient crater diameters of 5 up to 400 km. Thicknesses of the microtektite and cpx spherule layers are estimated from the microtektite/spherule abundance and average size at each site (see Table 10.2 and Fig. 10.1 for abundances). See the figure caption for Fig. 10.2 for the proposed Australasian source crater location used in this graph. The hypothetical ejecta thickness trend lines were calculated using the equation by McGetchin et al. (1973) (see Eq. 2.2 in Sect. 2.6). Transient crater diameters for the proposed source craters are given in Table 10.1. K-T boundary data are from Izett (1990), Jéhanno et al. (1992), Smit (1999), and MacLeod et al. (2007). Manson ejecta data are from Katongo et al. (2004). For source of data for the Cenozoic microtektites and Late Eocene cpx spherules see footnote to Table 10.2

are scattered ($r^2 = 0.42$), but the slope of the linear trend is similar to that for the Australasian strewn field.

The best-fit linear trend for North American microtektites is based on spherule abundances for only three sites ($r^2 = 0.50$), but it also has a slope similar to that of the Australasian strewn field (Fig. 10.1). If we include data for the two sites off New Jersey (i.e., DSDP 612 and ODP 904), the slope of the best-fit linear trend would be much shallower. We did not use the abundance data from these two sites because of the uncertainty in estimating the number of microtektites per square centimeter as discussed above. The North American microtektite abundances plot above the best-fit linear trend for the Australasian strewn field suggesting that the source crater for the North American strewn field is larger than the estimated size of the source crater for the Australasian strewn field.

Although the late Eocene cpx spherule layer (see Sect. 4.6) contains microtektites, it consists mostly of cpx spherules. Unlike microtektites, these spherules

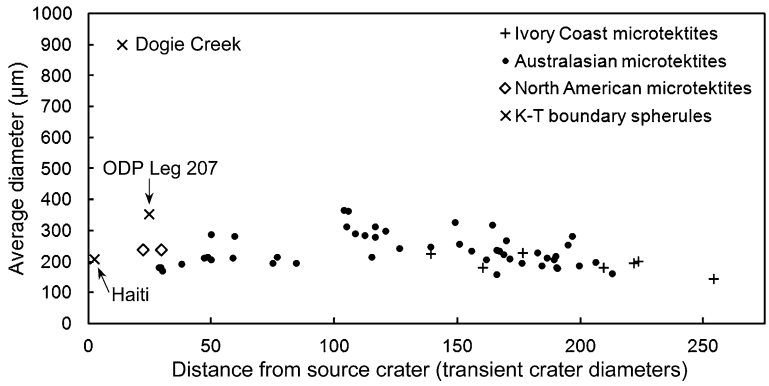

Fig. 10.5 Average diameter of microtektites/spherules (>125 μm diameter) versus distance from the source crater in transient crater diameters. See the figure caption for Fig. 10.2 for the proposed Australasian source crater location and Table 10.1 for estimated transient crater diameters of the source craters. The average diameters of the K-T boundary spherules at Haiti appear to fall on the extrapolated trend of the Australasian and North American microtektites, but the average sizes of the K-T boundary spherules at Ocean Drilling Program Leg 207 (western equatorial Atlantic) and at Dogie Creek, Wyoming (USA), are much larger. Australasian microtektite data are from Burns (1990). North American microtektite data are from Glass and Zwart (1979a). K-T boundary spherule size data from Dogie Creek, Haiti, and ODP Leg 207 are from Izett (1990), Jéhanno et al. (1992), and MacLeod et al. (2007), respectively

appear to contain a high proportion of projectile material in addition to target rock, and some authors have proposed that they are formed by condensation from a vapor plume; i.e., they are condensate spherules rather than melt drop spherules formed from melted drops of target rock. A plot of the log number of cpx spherules/cm^2 versus the shortest (i.e., great circle) paleodistance from the proposed source crater (Popigai) has a best-fit linear trend with a slope similar to the slope of the best-fit linear trend for the Cenozoic microtektites; however, this may just be a coincidence since there is a great deal more scatter ($r^2 = 0.23$; Fig. 10.1). A plot of log number of spherules/cm^2 versus paleodistance from Popigai along the proposed Indian Ocean/South Atlantic ray (Fig. 4.45a) has much less scatter ($r^2 = 0.71$), but the slope is much greater than the slopes for the Cenozoic microtektite linear trends (Fig. 10.1). The scatter in the cpx spherule layer data may be due to the large size of this impact, which resulted in ejecta being thrown around the globe and the ejecta distribution pattern being affected by the Earth's rotation. Furthermore, the cpx spherules may have been deposited along rays (see Sect. 4.6.11; Fig. 4.45a).

Quantitative abundance data in terms of number of spherules/cm^2 is difficult to obtain for the K-T boundary layer. Like the late Eocene cpx spherule layer, both microtektites (or microtektite-like spherules) and microkrystites are found in the K-T boundary layer; however, nearly all the glass in the K-T boundary spherules has been altered to other phases. Furthermore, no researchers reported the abundance of the spherules in terms of number per unit area and most did not give

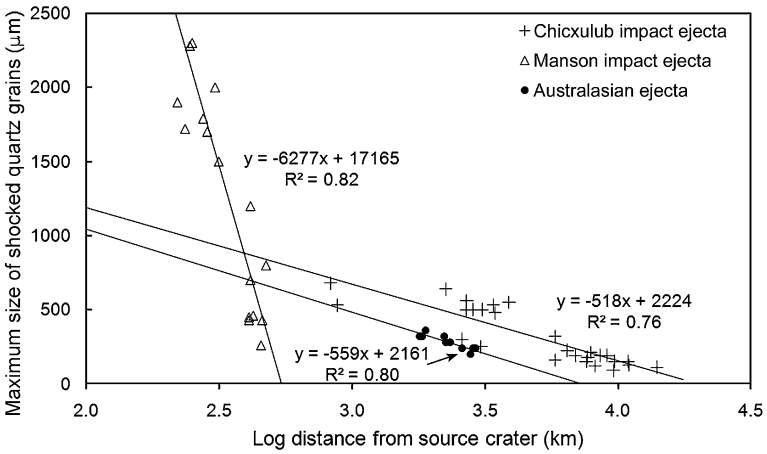

Fig. 10.6 Maximum size of shocked quartz in the K-T boundary (Chicxulub impact ejecta), Manson, and Australasian ejecta/microtektite layers versus log distance from their respective source craters. See the figure caption for Fig. 10.1 for the location used for the Australasian microtektite source crater. Shocked quartz grains were identified by the presence of planar deformation features. K-T boundary data are from Bohor and Izett (1986), Bohor et al. (1987b), Izett (1990), Smit et al. (1992a), Kyte et al. (1996), and Bostwick and Kyte (1996); Manson data are from Izett et al. (1998); Australasian data are from Wu (1995)

enough information to accurately estimate the abundance per unit area. In spite of the problems, we were able to find enough data in the literature to make estimates for two sites: Beloc, Haiti, and Dogie Creek, Wyoming. We estimated the number of spherules (microtektites?)/cm^2 at Haiti based on data in Izett (1991b) and Jéhanno et al. (1992). Izett (1991b) stated that the basal 2 cm of the spherule layer at Beloc contains ~60 % spherules. Using this as a starting point and then using variation in the carbonate content of the spherule layer, given by Jéhanno et al. (1992), we estimated the percent spherules up through the section. The carbonate content of the rock below the spherule layer is ~60 %. At the bottom of the spherule layer it is only ~5 %. The carbonate content increases up through the section to ~40 % near the top of the spherule layer. From these data we estimated the percent spherules or volume of spherules in 5-cm intervals up through the layer. We used the maximum size of the spherules in each 5-cm interval as given by Jéhanno et al. (1992) to estimate the average size based on data from the Australasian microtektite layer where the average size is approximately 1/3 of the maximum size. We then divided the volume of spherules in each 5-cm interval by the volume of the average size spherule in each 5-cm-thick section to estimate the number of spherules in each 5-cm-thick section (with a cross section of 1 cm^2). The number of spherules in each 5-cm-thick interval was totaled to give a total number of spherules (greater than ~125 μm) at this site of ~5.4 million/cm^2.

At Dogie Creek, Wyoming, the K-T boundary layer is ~2 cm thick and it contains ~30 % impact spherules (replaced by goyazite) with an average diameter

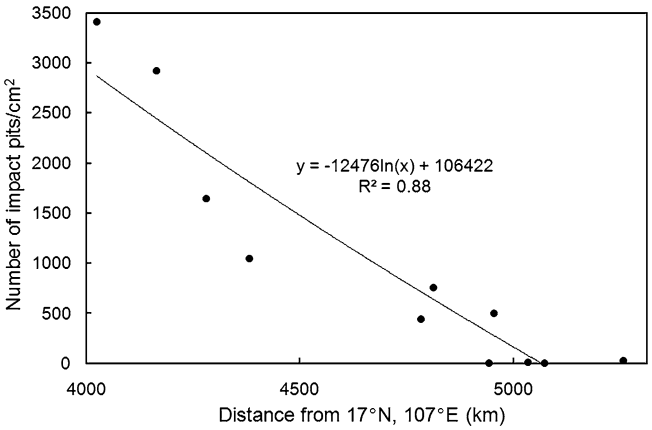

Fig. 10.7 Impact pits per surface area on Australasian microtektites versus distance from the proposed source crater location at 17° N and 107° E as proposed by Ma et al. (2004). Prasad et al. (2010) used a proposed source crater location at 12° N and 104° E, but the results were similar. Data are from Prasad et al. (2010)

of 0.9 mm (Sect. 5.2.2.3; Izett 1990). Using these data, we estimate that the K-T boundary layer at Dogie Creek contains ~1572 spherules/cm^2; this is represented by the lower triangle (in bold) at a log distance of 3.43 in Fig. 10.1. This is less than the number of North American microtektites/cm^2 at the same distance from their source crater (i.e., Chesapeake Bay); however, the total volume of spherules per unit area is much greater than the volume of North American microtektites per unit area, which have an average size of only ~238 μm. Thus, in order to compare the abundance of spherules at Dogie Creek with the abundance of spherules at Haiti and the abundance of Cenozoic microtektites found at the same distance from their respective source crater, we recalculated the number of spherules at Dogie Creek using a diameter of 240 μm, which is slightly larger than the average for the Cenozoic microtektites and the K-T boundary spherules at Haiti. This yielded an abundance of ~82,900/cm^2. A trend line based on this value for Dogie Creek and 5.4 million/cm^2 for Haiti is parallel to, but higher than the best-fit trend lines for the Cenozoic microtektite layers (Fig. 10.1). Thus, as expected, for a given distance from the respective source craters, the number of microtektites/spherules per unit area increases with increasing diameter of the source crater in the following order: Ivory Coast (10.5 km), Australasian (estimated to be between 33 and 43 km), North American (generally given as 85 km, but may be as small as 40 km), cpx spherules (100 km), and K-T boundary (180 km).

In a plot of the log number of microtektites (>125 μm)/cm^2 versus the distance (in transient crater diameters) from the proposed source crater locations for the Australasian, Ivory Coast, and North American strewn fields, we find that the data from all three strewn fields plot along the same trend (Fig. 10.2). Distances in crater diameters are based on the estimated transient crater sizes given in

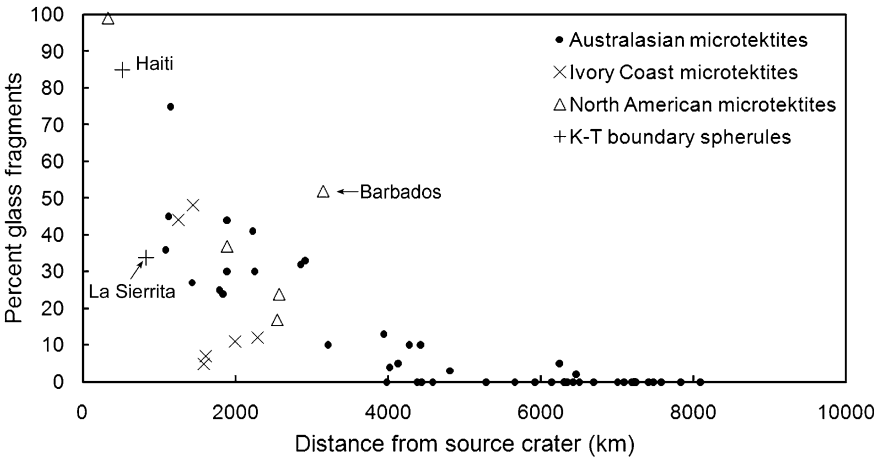

Fig. 10.8 Percent glass that occurs as fragments (as opposed to whole microtektites and spherules) versus distance from the source crater for the Australasian, Ivory Coast, and North American microtektites and the K-T boundary spherules. In the case of the K-T boundary spherules and fragments, most of the glass has been replaced by other phases. Microtektite data used in this graph are in Table 10.2. K-T boundary data for Haiti are from Izett (1991b) and data from La Sierrita, northeastern Mexico, are from Schulte et al. (2003)

Table 10.1. As previously stated, we assumed a source location at 17° N and 107° E as proposed by Ma et al. (2004) and a source crater diameter of 38 km for the Australasian microtektite strewn field. Using 22° N and 104° E as the source crater location (as proposed by Glass and Koeberl 2006) or a transient crater size of 33 or 43 km as proposed by Glass and Koeberl (2006) and Prasad et al. (2007), respectively, does not appreciably change the results. Note that the abundance (number >125 μm/cm^2) decreases with distance from the source crater up to a distance of ~150 crater diameters; beyond ~150 crater diameters, there appears to be little or no significant change in the microtektite abundance with distance from the source crater. Abundances of the K-T boundary spherules at Dogie Creek (based on an average size of 0.9 mm) is within the range expected for the Cenozoic microtektites at the same distance in crater diameters. However, the abundance of K-T boundary layer spherules at Dogie Creek (based on an average size of 240 μm) and at Beloc, Haiti, are both above the trend for Cenozoic microtektites (Fig. 10.2).

Data for most of the cpx spherule layer sites plot above the trend for the Cenozoic microtektites whether the data are plotted using great circle paleodistances from Popigai (Fig. 10.2) or distances along the Indian Ocean/South Atlantic ray (see Sect. 4.6.11). This may be due to the larger size of the impact and/or to a different mode of formation and distribution for the cpx spherules than for the microtektites.

10.1.2.1.2 Fluence of Shocked Quartz

Determining the fluence of shocked mineral grains is time consuming and tedious; thus, not many investigators have undertaken such an arduous task. Bostwick and Kyte (1996) determined the number of K-T boundary quartz grains with PDFs (>30 μm)/cm^2 at seven Pacific Ocean sites. The fluence at these sites ranges from 1230 to 18,820/cm^2. Morgan et al. (2006) provided shocked quartz fluence data for six more sites with a wider geographic range. Fluences determined by Morgan et al. (2006) range from 10 to 390/cm^2 and are over an order of magnitude smaller for a given distance from the proposed source crater (i.e., Chicxulub) than the results of Bostwick and Kyte (1996). However, both sets of data show a decrease in fluence with distance from Chicxulub (Fig. 10.3).

10.1.2.2 Thickness of the Ejecta Layer

The aggregate thicknesses of the North American (except for two sites, see below), Australasian, and Ivory Coast microtektite layers and the cpx spherule layer were calculated from the average size of the microtektites/spherules and the number/cm^2 at each site. Distances for the Australasian sites are from a source area in the Gulf of Tonkin predicted using ^{10}Be data from Australasian tektites (Ma et al. 2004). In contrast, the plotted thicknesses of the North American layer at the two sites closest to the source crater (DSDP Site 612 and ODP Site 904) and at four K-T boundary sites (Beloc, Haiti; Dogie Creek, Wyoming, USA; Ocean Drilling Program Leg 207 sites in the western equatorial Atlantic; Caravaca, Spain) are measured stratigraphic thicknesses, rather than aggregate thickness estimates based on the number of microtektites/spherules present. The best-fit trend lines through the microtektite/spherule data are similar to trends of the variation in thickness of ejecta layers from different transient crater diameters as calculated using the equation of McGetchin et al. (1973) (Fig. 10.4). The cpx spherule data show more scatter than do the data for the microtektite and K-T boundary ejecta layers and the trend line is less steep. The measured (as opposed to estimated) thicknesses of the Manson ejecta layer at three sites are also plotted (Fig. 10.4).

For a given distance from a source crater, the thickness of a spherule/ejecta layer increases as a function of the transient crater diameter (see Table 10.1) in the following order: the Ivory Coast microtektite layer (Bosumtwi crater), the Australasian microtektite layer (source crater estimated to have a transient crater diameter of ~38 km), the Manson crater ejecta layer (Manson impact structure), the North American microtektite layer (Chesapeake Bay impact structure), the cpx spherule layer (Popigai structure), and the K-T boundary ejecta layer (Chicxulub structure) (Fig. 10.4). The trend line for the Ivory Coast microtektite layer lies close to the thickness trend line for a 9-km-diameter transient crater in agreement with the proposed transient crater size of the Bosumtwi crater. The trend line for the Australasian microtektite layer is steeper than the hypothetical trend lines based on McGetchin et al.'s (1973) equation, suggesting a transient crater size

between 20 and 40 km in diameter. The steeper slope may indicate that the chosen source crater location is incorrect or that McGetchin et al.'s (1973) equation doesn't work that well for distal ejecta layers.

Of the five sites plotted for the North American microtektite layer, two lie on and two just above the hypothetical ejecta thickness line for a crater with a transient crater diameter of 40 km, which is in agreement with a proposed transient crater diameter of 40 km for this structure (Poag et al. 2004). However, Collins and Wünnemann (2005) proposed that the transient crater size of the Chesapeake Bay structure may have been as small as 25 km. Data for three Manson ejecta layer sites plot between the hypothetical ejecta thickness lines for craters with transient crater diameters between 40 and 60 km. These sizes are much greater than the proposed transient crater diameter of 21 km for the Manson impact structure (see Table 10.1). Likewise, the four K-T boundary layer sites plotted in Fig. 10.4 indicate a transient crater diameter (between 150 and 200 km) that is much greater than the proposed transient crater size of 100 km for Chicxulub, the proposed source crater. It may be that the Manson and K-T boundary ejecta layers contain a significant amount of local material reworked into the ejecta layer. Finally, we note that the cpx spherule layer data plot between ejecta thicknesses for craters with hypothetical transient crater diameters between 40 and 200 km, with most of the data suggesting a transient crater size of about 100 km, which is larger than the proposed transient crater size for the Popigai impact structure which is $\sim$60 km. In this case, the difference between predicted and observed may be due to the cpx spherules having formed as condensate droplets and/or due to the possibility that the cpx spherules were distributed along rays (see Sect. 4.6.11).

10.1.2.3 Size of Spherules/Microtektites and Shocked Quartz

The average size of Australasian microtektites (>125 μm in diameter) increases with increasing distance from the proposed source crater location (17° N, 107° E) out to about 100 crater diameters (Fig. 10.5). In Fig. 10.5 the distances in crater diameters are based on the estimated transient crater diameters in Table 10.1. Farther than $\sim$100 crater diameters the average diameter of the Australasian microtektites appears to decrease with increasing distance. The average size of the Ivory Coast microtektites also decreases with increasing distance from $\sim$140 to at least 250 crater diameters; but trends closer to Bosumtwi impact crater cannot be determined because none of the Ivory Coast microtektite sites are closer than $\sim$140 crater diameters to the source crater (Fig. 10.5). The decrease in size of microtektites within 100 crater diameters of the source crater may be related to an increase in the percent fragments closer to the crater (see Sect. 10.1.2.5).

The average Ivory Coast microtektite diameters are generally on the small end of the size range of the average Australasian microtektite diameters for a given distance (in transient crater diameters) from their respective source craters. North American microtektites at two sites (DSDP Sites 94 and 149 in the Gulf of Mexico and Caribbean Sea, respectively) appear to have larger average diameters than

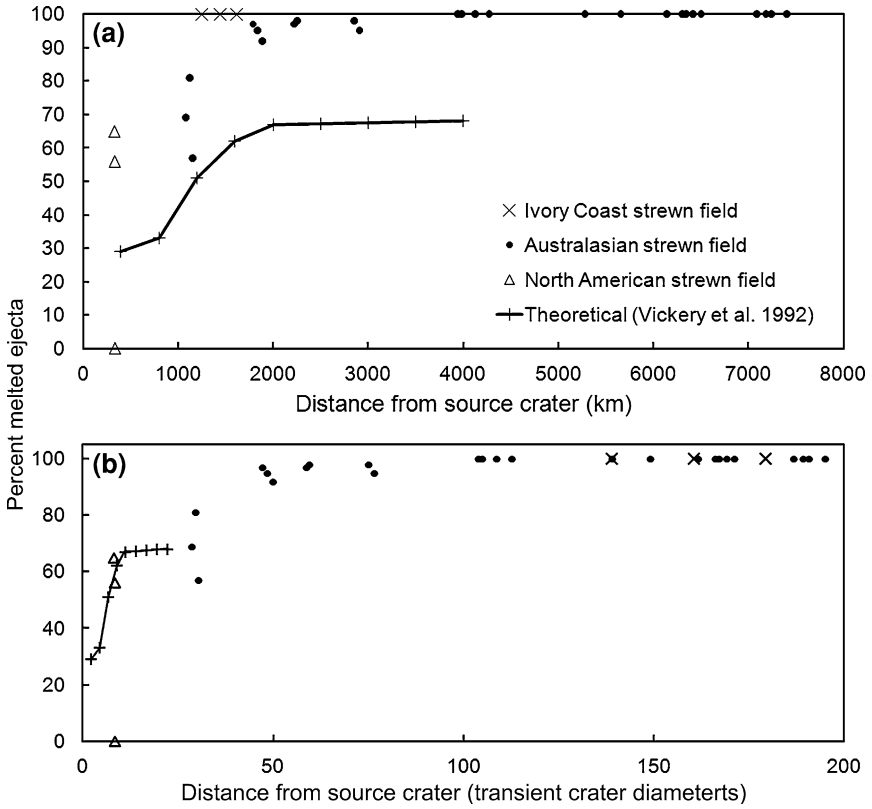

Fig. 10.9 Number percent of ejecta that were melted (i.e., microtektites) in the Australasian, Ivory Coast, and North American microtektite layers versus distance from the respective source craters. Also shown is the theoretical percent melt in a hypothetical ejecta layer from a 180-km-diameter crater based on data from Vickery et al. (1992). **a** Percent melt versus distance in kilometers. **b** Percent melt versus distance in crater diameters. Transient crater diameters (of the source craters) used to calculate the distances in crater diameters are given in Table 10.1. Distance (in kilometers) to each site from the source crater and percent unmelted ejecta in the microtektite layers are given in Table 10.2. Percent melt can be determined for each site by subtracting the percent unmelted ejecta from 100 %

Australasian microtektites at the same distance from the source crater (in crater diameters; Fig. 10.5). In summary, the average diameter of microtektites appears to increase with increasing source crater size for a given distance (in crater diameters) from the source crater. However, the accuracy of this trend is difficult to quantify precisely because the location and diameter of the Australasian microtektite source crater is unknown.

The maximum sizes of shocked quartz grains with PDFs in the Chicxulub (K-T boundary) impact ejecta, Manson impact ejecta, and the Australasian microtektite layers decrease away from their respective source crater (Figs. 5.25, 5.34 and 10.6). The Manson crater is much smaller than the Chicxulub impact structure, and

the rate of decrease in the maximum size of shocked quartz grains with distance from the 35-km-diameter Manson structure is much greater than it is for the 180-km-diameter Chicxulub structure (Fig. 10.6). Extrapolation of the increase in maximum size of the shocked quartz grains back to the source crater indicates that the quartz grains in the Manson target rocks must have been larger than the quartz grains in the Chicxulub target rocks (see Sect. 10.2 for more discussion of this subject). The rate of decrease in the maximum size of the shocked quartz grains in the Australasian microtektite layer is similar to that of the Chicxulub (K-T boundary) ejecta layer even though the proposed size of the Australasian source crater is about the same size as Manson and much smaller than the Chicxulub structure (Fig. 10.6).

10.1.2.4 Impact Pits on the Surface of Microtektites

Impact pits, including hypervelocity micro-craters, have been observed on the surfaces of numerous Australasian microtektites (Fig. 3.9f; Prasad and Sudhakar 1996; Prasad and Sudhakar 1998). The impacts that produced these micro-craters are believed to have been between microtektites while they were in flight. Some microtektites have registered multiple impacts on their surfaces (Prasad and Sudhakar 1996; Prasad and Sudhakar 1998). A more recent study has shown that the number of microtektites with impact pits and the number of impact pits per unit surface area decreases with distance from a proposed source crater site in Indochina (Fig. 10.7; Prasad et al. 2010). These authors suggested that impacts between microtektites while in flight caused fragmentation of some of the microtektites.

10.1.2.5 Percent Spherule Fragments Versus Whole Spherules

The percent microtektite fragments increases toward the source crater in the Australasian and North American microtektite strewn fields (Table 10.2; Fig. 10.8). The percent of microtektite fragments is anomalously high in the North American microtektite layer at the sites on Barbados. The North American microtektite layer on Barbados differs from the layer at other known occurrences in that it is within sediments that were deformed and uplifted above sea level whereas at the other sites the layer is still on the seafloor and relatively undisturbed. The greater fragmentation of microtektites at the Barbados sites compared with microtektites at other sites at roughly the same distance from the source crater may be the result of ground water solution and, perhaps, tectonic deformation. In contrast, the percent of microtektite fragments at a few of the Ivory Coast microtektite sites is anomalously low. This may be related to the small size of the source crater (i.e., only 10.5 km diameter). We only have data for the abundance of spherule fragments at two K-T boundary sites: Beloc (Haiti) and La Sierrita (northeastern Mexico), both of which appear to fall on the trend defined by the

Australasian and North American microtektites (Fig. 10.8). The percent fragments in the K-T boundary layer at Haiti is based on Izett's (1991b) description of the spherules as being 15 % spherical and 85 % irregular. The irregular particles are described as being subrounded to angular. As a photomicrograph of a portion of the spherule layer shows that many of the irregular particles are angular, we interpret the irregular particles as being mostly spherule fragments. The percent fragments actually is probably less than 85 % since the subrounded particles may be irregular spherules rather than fragments of spherules. At La Sierrita, fragments on average are about half as abundant as the spherules (Schulte et al. 2003) and thus make up about 33 % of the diagenetically altered glass particles.

At some of the Australasian strewn field sites, the largest glass fragments are larger in at least one dimension than the diameter of the largest intact spherical microtektite (Glass et al. 1997; Glass and Koeberl 2006). This is consistent with the hypothesis that the microtektites may have fragmented due to thermal stresses generated when the hot microtektites fell into the relatively cold ocean because the larger microtektites would have remained hot longer and would be more likely to fragment (Glass et al. 1997). However, the microtektites may not have been hot enough to fragment due to thermal stress (NA Artemieva, personal communication, 2012). Another possible cause of fragmentation is high velocity impacts between microtektites/tektites during their descent back down through the atmosphere. Because microtektites increase in abundance toward the source crater (Fig. 10.1), it seems likely that more interparticle collisions would occur in closer proximity to the source crater. This is confirmed by a scanning electron microscope study of impact pits on the surfaces of the microtektites (Sect. 10.1.2.4; Prasad et al. 2010). Thus, fragmentation of microtektites by high-velocity interparticle collisions should lead to an increase in percentage of fragments versus whole microtektites closer to the source crater.

The Late Eocene cpx spherule sites are more than 5000 km from their source crater (Popigai). Based on analogy with microtektites, we would expect to find <1 % fragments at these distances (see Fig. 10.8). Unfortunately, we only have quantitative data for two sites: DSDP Site 216 in the northeast Indian Ocean and ODP Site 709 in the northwest Indian Ocean. Both sites were about 9600 km from Popigai at the time of the impact (See Table 10.2). At both of the sites there is a significant number of broken cpx spherules. The percent of cpx spherules that are fragments is estimated to be 26 and 16 % for Sites 216 and 709, respectively. However, as discussed in Sect. 4.6.2, the cpx spherules can be divided into two groups: light-colored cryptocrystalline cpx spherules and dark-colored cpx spherules. The darker spherules are generally brown, tan, or gray in color and generally opaque. They have microlites/crystallites scattered throughout a glass matrix. The light-colored cpx spherules are very finely crystalline with very little glass matrix. It is these spherules that are often fragmented and many, if not most, of the fragments have at least one dimension that is longer that the maximum diameter of the unbroken spherules. It is clear that the ratio of fragments to whole spherules versus distance from the source crater does not follow the same trend as for the Cenozoic microtektites. We do not have quantitative data for the dark cpx

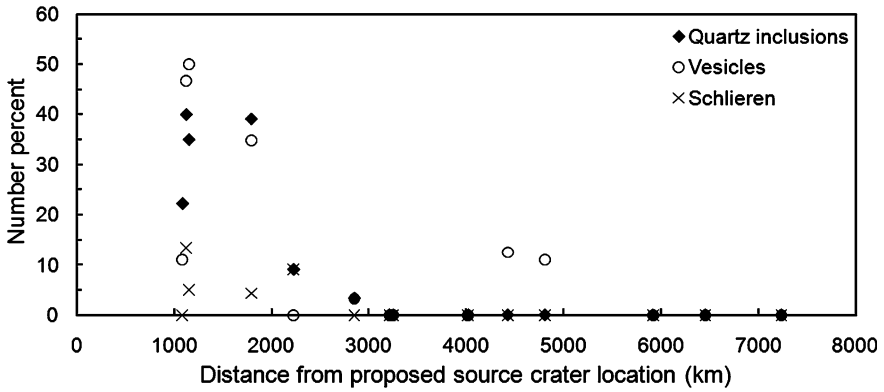

Fig. 10.10 Abundance of relict quartz inclusions, vesicles, and schlieren in Australasian microtektites versus distance from the proposed source crater location at 17° N and 107° E in the Gulf of Tonkin. Microtektites with abundant inclusions were defined as containing >5 quartz inclusions. Microtektites with abundant vesicles were defined as containing more than 10 vesicles >5 μm in diameter. Based on data in Folco et al. (2010a)

spherules, but it appears that the ratio between fragments and whole spherules may be similar to that of the Cenozoic microtektites.

10.1.2.6 Degree of Shock Metamorphism of Impact Ejecta

The average degree of shock metamorphism of distal impact ejecta can be quantified in a number of ways, including: (1) average number of sets of PDFs in shocked quartz; (2) percent of the ejecta that has been melted (i.e., ratio between spherules and unmelted shocked mineral/rock grains); (3) petrographic and chemical homogeneity of impact spherules (e.g., microtektites); and (4) alkali content of microtektites/spherules. The first three indicators are discussed under this heading. The alkali contents of microtektites/spherules are discussed in Sect. 10.1.2.7.

10.1.2.6.1 Average Number of PDF Sets in Shocked Quartz

The mean number of PDF sets in quartz grains from eleven K-T boundary sites increases with distance from the Chicxulub impact structure (Fig. 5.26b; Morgan et al. 2006). This is consistent with the degree of shock metamorphism increasing with distance from the source crater. Unfortunately there are no comparable data for any other ejecta/spherule layers and the errors are so large (Fig. 5.26b) in the present data set that the number of PDF sets does not provide a useful parameter for estimating paleodistance from the source crater.

10.1.2.6.2 Percent Glass in the Ejecta Layer

Theoretical studies indicate that as the thickness of an ejecta layer thins away from the source crater, the percent melt (i.e., glass) increases (e.g., Vickery et al. 1992; Fig. 2.35). Vickery et al.'s (1992) calculations were for a 180-km-diameter crater like Chicxulub (K-T boundary ejecta layer). Unfortunately, nearly all the silicate glass melt component (spherules) in the K-T boundary layer has been diagenetically altered to other phases. Moreover, the glass and unmelted components were largely partitioned into separate layers at the time of deposition. Furthermore, since the upper 3 km or so of the target rock at Chicxulub was carbonate, much of the melt in the distal ejecta should have been carbonate rather than silicate. Indeed, carbonate melt has recently been recognized in some K-T boundary sections (Deutsch et al. 2010). Thus, there are very few, if any, reliable estimates of the original percent glass in the K-T boundary layer. There are, however, some quantitative data for the percent glass versus unmelted ejecta in the Cenozoic microtektite layers (Table 10.2). This includes data for three North American sites (Glass 1989; Glass et al. 1998), three Ivory Coast sites (Glass and Wu 1993), and 26 Australasian sites (Wu 1995).

The three North American sites are all ~330 km from the presumed source crater. Glass (microtektites, minitektites, and tektite fragments) at two of these sites, DSDP 612 and ODP 904 (see Fig. 4.29 for location), make up 56 and 65 % by number of the ejecta layer, but the layer at the third site (ODP 903; close to ODP 904) does not contain any glass (Fig. 10.9). It is not likely that microtektites fell at Site 903 and were later removed by dissolution since all three sites are within ~12 km of each other and were at approximately the same water depth (~ 1000 m) at the time of deposition. Furthermore, the presence of rare siliceous spicules in the Site 903 ejecta layer appears to be consistent with the conclusion that the lack of microtektites in the layer is not due to solution since biogenic silica should have been dissolved long before millimeter-sized silicate glass particles. Glass et al. (1998) suggested that the lack of glass at Site 903 may be the result of the glass component being ejected along rays and Site 903 lying beyond the edge of a ray. The percent glass in four other North American microtektite sites between ~2250 and ~2850 km from the Chesapeake Bay structure is not known quantitatively, but is probably close to or greater than 99 % since only trace amounts of shocked mineral grains have been recovered from these sites. This agrees with percent glass (microtektites) in the Australasian microtektite layer at this distance from the proposed source crater location (see below).

All of the Ivory Coast microtektite sites are more than ~1250 km from the source crater (Bosumtwi). Unmelted ejecta have not been found in samples from any of these sites, but we only have quantitative data for ejecta content for three core sites (V19-297, K9-56, and ODP 663; Table 10.2; see Fig. 4.23 for location of core sites). Like two of the three North American sites, these three sites have higher glass contents for their distance from the source crater than Vickery et al.'s (1992) theoretical prediction (Fig. 10.9a).

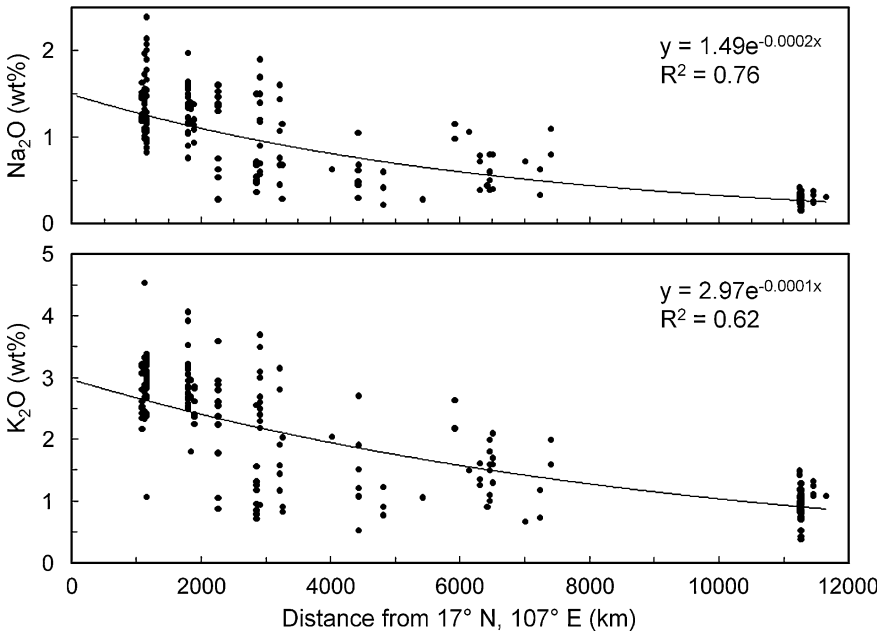

Fig. 10.11 Na_2O and K_2O contents (wt %) of Australasian microtektites versus distance from the proposed Australasian microtektite source crater location at 17° N and 107° E in the Gulf of Tonkin. Data from Folco et al. (2010b)

Table 10.3 Variation in Na_2O and K_2O contents in Australasian microtektites with distance from the proposed source crater location at 17° N latitude and 107° E longitude

Range in Distance (km)	Number of analyses	Na_2O			K_2O		
		Wt %		S.D.	Wt %		S.D.
1123–1151	60	1.32	±	0.34	2.89	±	0.43
1791–2852	51	1.16	±	0.39	2.46	±	0.82
2909–7404	58	0.81	±	0.40	1.81	±	0.80
11239–11653[a]	54	0.27	±	0.06	0.98	±	0.21

S.D. = standard deviation
[a] Transantarctic Mountains microtektites.
Data from Folco et al. (2010b)

More is known about the geographic variations in glass content of the Australasian microtektite layer than for any other impact ejecta layer. Unfortunately, there are no sites for this layer closer than ~1100 km from the proposed source crater location at 17° N and 107° E, but we do have quantitative data for sites at distances from ~1100 to 8100 km (Table 10.2). At the three sites closest to the proposed source crater location, the abundance of melt particles (>125 μm in size) varies from 57 to 81 % by number. The melt content of the ejecta layer increases to ~95 % at ~2900 km. There is a data gap between 2900 and

3900 km, but from 3900 out to 8100 km the percent melt is always 100 % (Fig. 10.9a). Thus, the Australasian microtektite layer shows a clear increase in the percent melt (microtektites) with increasing distance from the proposed target area. However, like the North American and Ivory Coast microtektite layers, the Australasian microtektite layer always has a higher glass content for a given distance from the source crater than is predicted using Vickery et al.'s (1992) model. This is unexpected since theoretical studies suggest that, everything else being equal, the percent of the displaced mass that is melt increases with crater size (see Sect. 7.10 in Melosh 1989). Thus for a given distance from the source crater, we would have expected that the percent melt from a hypothetical 180-km-diameter structure would have been greater than the percent melt in an ejecta layer from a 60-km-diameter crater, which in turn would be greater than the percent melt in an ejecta layer from a 10.5-km diameter crater; but that does not appear to be the case.

There are several possible causes for the difference between observed and predicted amounts of melt (glass) in an ejecta layer for a given distance from the source crater. First, we used estimated size and location for the Australasian microtektite layer source crater since the source crater had not yet been found. Second, although not explicitly stated, the predicted melt amounts calculated by Vickery et al. (1992) are probably in terms of mass or volume, while the observed percents in the Cenozoic microtektite layers are based on numbers. However, the unmelted grains are generally smaller than the microtektites at a given site; therefore, converting the numbers to volume would increase the discrepancy. Third, the theoretical melt percents are for the total amount of ejecta at a given distance, but the observed melt (microtektite) and unmelted ejecta percents are based on the coarser size fraction (i.e., >125 μm). Both the microtektites and the unmelted grains increase in number with decreasing grain size; but depending on the rate of increase in number of microtektites versus unmelted grains with decreasing size, it is possible that the finer size fractions may contain a higher percentage of unmelted ejecta grains than the coarser fractions. This appears to be the case for the North American microtektite layer at DSDP Site 612 as discussed in the next paragraph. It is possible that impact ejecta occur in the finer fraction (<125 μm) at some of the sites where no ejecta were observed in the coarser fraction. Fourth, in determining the number of grains of unmelted ejecta at each site, only the grains that exhibited obvious evidence of shock metamorphism were counted. The amount of unshocked or weakly shocked ejecta at each site is unknown, but probably underestimated in most cases. Thus, the exact or total percent unmelted ejecta at most (all?) sites is unknown. On the other hand, at many of the sites, even if all the rock and mineral grains in the coarse fraction were counted as impact ejecta, it would not make much difference in the percent glass. It might, however, make a significant difference in the finer fractions, especially in the <63 μm size fraction.

The North American microtektite layer at DSDP Site 612 off the coast of New Jersey is approximately 8 cm thick. Whole microtektites are relatively rare in the layer, but fragments of microtektites and tektites make up as much as 82 % (by

number) of the ejecta grains in the >250 μm size fractions. Rock and mineral grains are concentrated in the upper part of the layer, where they make up as much as 41 % (by number) of the >250 μm size fractions. Quartz and feldspar grains with PDFs are common as are shocked rock fragments and white opaque grains containing coesite and sometimes stishovite. It is assumed that at least in the coarser size fractions (>250 μm) all the rock and mineral grains are part of the ejecta, because no rock and mineral grains are found in the >250 μm size fractions above or below the layer.

Throughout the upper part of the layer at DSDP Site 612, where the rock and mineral grains (unmelted ejecta) are most abundant, the percent ejecta composed of rock and mineral grains increases with decreasing size down to at least 125 μm. Near the top of the layer, rock and mineral grains make up 6.7, 26.1, 45.0, and 53.7 % (by number) of the impact ejecta in the >1 mm, 0.5–1 mm, 250–500 μm, and 125–250 μm size fractions, respectively. If this trend extends down into the finer size fractions and because the finer size fractions (<125 μm) make up >70 wt % of the sediment in this ejecta layer, it is probable that, at least at this site and the nearby ODP Site 904, the unmelted portion of the ejecta is more abundant and, therefore, the melted portion is less abundant than the values plotted in Fig. 10.9 based on the number percents in the >250 μm size fractions. Therefore, the glass contents at these two sites are probably closer to the theoretical percent melt than is indicated in Fig. 10.9a.

In spite of the reasons given above for why the observational data might not agree with the theoretical estimates of percent melt with distance from the source crater, we find that there is fairly good agreement when the percent melt is plotted versus distance normalized to transient crater size (Fig. 10.9b).

In summary, we don't have enough data at present to predict accurately how the percent melt (spherules) in an ejecta layer varies with distance from the source crater for different size craters.

10.1.2.6.3 Shocked Rock Fragments (Lithic Clasts) and Mineral Grains

Shocked rock (lithic) fragments that are part of the ejecta have been found as far as ~1150 km from the proposed source crater location (17° N and 107° E) of the Australasian microtektite strewn field. This is ~30 transient crater diameters assuming the source crater had a transient crater diameter of ~38 km. Shocked rock fragments have been found in the North American microtektite layer as far as 330 km (~ 8 transient crater diameters, assuming that the Chesapeake Bay impact structure had a transient crater diameter of ~40 km) from the source crater, but not at sites in Barbados, the Caribbean Sea, and Gulf of Mexico, which are ~2250 and 2850 km (>56 transient crater diameters; see Table 10.1 for transient crater diameters) from the Chesapeake Bay structure. Unfortunately, no sites have been found between 8 and 56 crater diameters from the source crater. Lithic fragments thought to be part of the ejecta from the Chicxulub impact structure have been found up to ~5000 km or ~50 crater diameters (paleodistance) at the ODP Leg

207 sites in the western Atlantic (Schulte et al. 2009). In all the above examples, the clasts are generally smaller than the spherules. It appears that clasts larger than sand size only occur within about 10 transient crater diameters of the source crater.

Unmelted ejecta have been searched for in the Ivory Coast microtektite layer at only three sites. These three sites are three of the four sites closest to the source crater, Bosumtwi. The layer at these three sites does not contain unmelted ejecta suggesting that unmelted ejecta (>125 μm) are not found as far as 139 transient crater diameters from Bosumtwi. However, shocked mineral grains have been found in the North American microtektite layer at all the sites where this layer has been found. The most distant known site from the Chesapeake Bay structure is about 71 transient crater diameters from the Chesapeake Bay structure. Assuming that the Australasian microtektite source crater is located near 17° N and 107° E and has a transient crater diameter of 38 km, unmelted ejecta have been found as far as 77 transient crater diameters but not as far as 104 transient crater diameters from the source crater. Sand-sized, shocked mineral grains have been found in the cpx spherule layer as far as ~9680 km (paleodistance), or at least 161 transient crater diameters, from the 100-km-diameter Popigai crater, and in the K-T boundary layer at least ~11,000 km (paleodistance), or ~110 transient crater diameters, from the 180-km-diameter Chicxulub structure. If shocked mineral grains were deposited globally at the K-T boundary as has been proposed, then they would have been deposited at least 200 transient crater diameters from the source crater. Thus, it appears that the distance (in transient crater diameters) shocked mineral grains (>125 μm in size) can be found from the source crater increases with increasing crater size.

10.1.2.6.4 Petrographic and Chemical Homogeneity of Impact Spherules

Proximal impact glasses are generally vesicular, frequently contain relict mineral grains or unmelted clasts, and are often chemically heterogeneous (Fig. 2.8). Microtektites, on the other hand, were originally described as microscopic (<1 mm) silicate glass bodies which are free of crystalline inclusions (e.g., Glass 1967, 1968; Cassidy et al. 1969); however, as more studies were made it was realized that some North American microtektites contain relatively small inclusions of quartz and cristobalite (e.g., Glass and Zwart 1979a). More recently, inclusions of relict quartz have been reported in some Australasian microtektites (Folco et al. 2010a). Based on a study of 161 microtektites from fourteen core sites, Folco et al. (2010a) concluded that the percent microtektites containing relict quartz inclusions decreases with increasing distance from the proposed source crater location in Indochina (Fig. 10.10). There is some scatter in the data, but the highest percentages of microtektites containing quartz inclusions are found at the four sites closest to the proposed source crater location and no quartz inclusions have been found in microtektites from sites greater than ~3000 km from the proposed source crater location.

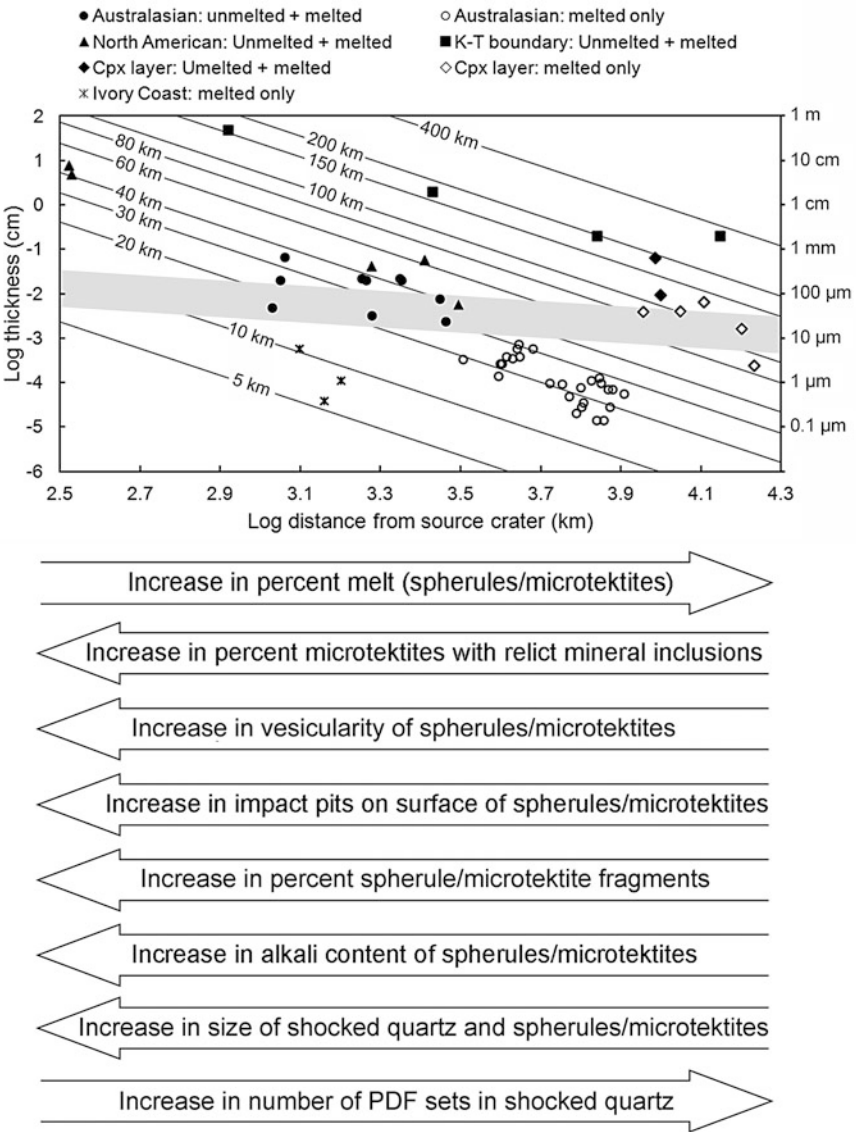

Although there is more scatter than for the inclusion data, the percent microtektites containing abundant vesicles may also decrease with increasing distance from the proposed source crater location (Fig. 10.10; Folco et al. 2010a). In addition, the percent abundance of microtektites containing schlieren may also decrease away from the proposed source crater location (Fig. 10.10). Since schlieren are streaks of glass with different colors and refractive indices due to

◀**Fig. 10.12** Model for how distal impact ejecta changes with distance from the source crater. The microtektite, spherule, and ejecta data in the graph are the same as in Fig. 10.4; however, in this figure, sites where the ejecta layer contains both melted (spherules and/or microtektites) and unmelted ejecta are indicated with solid symbols and sites where the ejecta consist only of melted ejecta (microtektites/spherules) are indicated with *open symbols*. Hypothetical ejecta thicknesses, based on McGetchin et al.'s (1973) equation (see Eq. 2.2 in Sect. 2.6), are shown for craters with transient crater diameters between 5 and 400 km. The gray band separates sites containing both melted ejecta (e.g., impact spherules) and unmelted ejecta (above the gray band) from sites where only melted ejecta are found in the >125 μm size range. Below the graph, *arrows* indicate the direction of increase in various characteristics of the spherules/unmelted ejecta or spherule/ejecta layers. *Arrows* pointing to the *right* indicate an increase with increasing distance from the source crater and *arrows* pointing to the *left* indicate an increase toward the crater. For example, the percent melt in the ejecta layer increases away from the source crater and percent spherules/microtektites with relict mineral inclusions increases toward the source crater

differences in chemical composition, their presence indicates internal variation in composition or chemical heterogeneity of the glass. Microtektites containing relict mineral inclusions, abundant vesicles, and schlieren are more petrographically and chemically heterogeneous than those without them. The increase in chemical and petrographic homogeneity with increasing distance from the source crater reflects the expected increase in the average degree of shock metamorphism with increasing distance from the source crater.

10.1.2.7 Alkali Element Content

Folco et al. (2010b) found that the average alkali contents of Australasian microtektites decrease with increasing distance from the proposed source crater location of 18° N, 106° E. We obtained a similar trend using a source crater location of 17° N, 107° E (Fig. 10.11). The average Na_2O and K_2O contents of the microtektites decrease from 1.32 and 2.89 wt %, respectively, at sites between 1123 and 1151 km from the proposed crater location to only 0.27 and 0.98 wt %, respectively, at the Transantarctic Mountain sites, which are ~11,000 to 12,000 km from the proposed crater location (Table 10.3). The range in alkali contents from one microtektite to another at each site also decreases with distance from the source crater. This probably indicates that microtektites found closer to the source crater experienced a greater range of heating conditions whereas those thrown farther from the crater experienced more uniform and more intense heating (higher temperature and/or heating for a longer period of time). The decrease in alkali contents of the Australasian microtektites away from the proposed source crater location is consistent with theoretical and observational data that indicate that the average degree of shock metamorphism of distal ejecta increases away from the source crater. Geographic variations in alkali content of impact spherules may thus provide another tool for searching for the source crater of a distal ejecta layer and for determining how far the ejecta may be from the source crater. However, using the alkali content to determine the distance to a source crater requires making assumptions about the alkali content of the target rock.

Plots of Na_2O and K_2O contents of the Australasian microtektites (excluding the Transantarctic Mountain microtektites) versus distance from the proposed source crater location are similar to those that include the Transantarctic Mountain microtektites, but the fit is not as good (r^2 is only 0.36 and 0.39 for the Na_2O and K_2O plots, respectively). However, the extrapolated trend lines for both the Na_2O and K_2O plots intersect the Transantarctic Mountain microtektite values. This is consistent with the conclusion that the Transantarctic Mountain microtektites belong to the Australasian strewn field.

10.1.2.8 Melt-Drop and Condensate Spherules

In Chap. 3 we discussed the possibility that there may be four types of impact spherules: melt-drop and condensate microtektites and condensate and melt-drop microkrystites (Sect. 3.2.1.1). The most common types are the melt-drop microtektites and the condensate microkrystites as exemplified by the Australasian, Ivory Coast, and North American microtektites and Late Eocene cpx spherules, respectively. The Late Eocene cpx spherule layer and the K-T boundary layer contain examples of both types of spherules, but most of the glass and mineral phases in the K-T boundary layer spherules have been replaced by other phases. The cpx spherules have undergone some alteration and at some sites have been partially to completely replaced by pyrite or clay.

Melt-drop microtektites have been found as far as 280 crater diameters (based on transient crater size) from their source crater (Fig. 10.2); however, at that distance the microtektites would not have been in a layer, but would have been scattered over the ocean floor. Even at the closest sites ($\sim$30 transient crater diameters) to the proposed source crater location (17° N, 107° E), the Australasian microtektite layer would have been <1 mm thick (based on estimated aggregate thickness) and would have contained abundant unmelted ejecta (up to 43 % by number in the >125 μm size fraction; Fig. 10.12; Table 10.2). At the closest site ($\sim$8 transient crater diameters) to the source crater (Chesapeake Bay structure), the North American microtektite layer is about 8 cm thick, but consists mostly of tektite and microtektite fragments ($\sim$65 % by number) and contains $\sim$35 % (by number) unmelted ejecta, which are concentrated in the upper half of the layer. At $\sim$8 transient crater diameters distance, the K-T boundary layer at Haiti has an estimated aggregate thickness of $\sim$12 cm, or $\sim$30 cm if the spherule layer originally had a porosity of 40 %. The spherules here are diagenetically altered melt-drop microtektite-like spherules. Very few shocked mineral grains (<0.0006 % by weight; Izett 1991b) have been found in the spherule layer here, but shocked mineral grains are common in the overlying Ir-rich layer, which is a few centimeters thick. The overlying layer also contains altered spherules (probably microkrystites) containing Ni-rich spinel crystals (see Sect. 5.2.2.2; Jéhanno et al. 1992). So the K-T boundary layer at Haiti appears to have been a $\sim$30-cm-thick layer composed primarily of microtektite-like spherules with very little unmelted shock-metamorphosed ejecta, except immediately above the main spherule layer. Thus, the apparent low abundance of unmelted

shocked silicate ejecta in the main spherule layer at Haiti is not in agreement with the high content of unmelted shocked mineral grains and rock fragments found at the same distance (in transient crater diameters) in the North American microtektite layer. Perhaps this is the result of the upper layer of target rocks at Chicxulub (the source crater of the K-T boundary layer) being carbonates.

Unlike the Late Eocene cpx spherule and K-T boundary ejecta layers, no condensate spherules have been found in the Ivory Coast, Australasian, or North American microtektite layers. Therefore, it appears that condensate spherules do not form in impacts that produce transient craters less than ~40 km in diameter. We suspect that impacts of this size are too small to form a vapor cloud dense enough for condensation droplets to be produced, or the condensate droplets produced would be too small to occur in the >63 μm size fraction. The latter appears to be supported by a theoretical study by Johnson and Melosh (2012a) in which they calculate the average diameters of condensate spherules for different size projectiles (and impact velocities). Assuming that the impact of a projectile ~2 km in diameter would produce a 40-km-diameter crater, we estimate, using Fig. 13 in Johnson and Melosh (2012a), that such an impact would produce spherules with an average diameter of only ~20 μm (assuming an impact velocity of ~20 km/s). Such small spherules, because of their more mafic compositions compared with most Cenozoic microtektites, most likely would not survive in the marine environment. Australasian microtektites have been recognized in the <63 μm size fraction, but no obvious condensate spherules were observed. However, to our knowledge, there has been no concerted effort to search for condensate spherules in the <63 μm size fractions of any of the Cenozoic microtektite layers.

Condensate microkrystites are widespread in the K-T boundary ejecta layer and at sites >8000 km from Chicxulub the major component of the layer is Ni-rich-spinel-bearing microkrystites. The layer appears to be fairly uniform in thickness, generally a few millimeters. It is usually assumed that the K-T boundary layer is global in extent and that, therefore, the microkrystites have a global distribution; however, the farthest sites from Chicxulub where the K-T layer has been found (and where microkrystites have been observed) are ODP Sites 803 and 807 in the equatorial west Pacific (see the Supporting Online Material for Schulte et al. 2010). At the time of the impact, these sites were ~11,000 km from Chicxulub. Thus, we have no direct observation of microkrystites being found at the K-T boundary sites between 11,000 and 20,000 km from Chicxulub. Likewise, it is assumed that the Late Eocene cpx spherule layer is global in extent, but the farthest that cpx spherules have been found from their assumed source crater (Popigai) is ~17,000 km (Table 10.2). Geographic variations in abundance of cpx spherules with distance from Popigai do not show any clear trend and even at the site with the greatest abundance of cpx spherules, the calculated aggregate thickness of the layer is only a few hundred microns (i.e., about one spherule thick). However, the closest known site to Popigai was nearly 5100 km (~86 transient crater diameters) away at the time of the impact.

In summary, melt-drop spherules can form in impacts where the transient crater size is as small as 9 km, but condensate spherules (>63 μm in size) appear to form only in impacts where the transient crater diameter is >40 km and may have global distribution when the transient crater diameter is greater than 60 to 100 km.

10.2 Variation in Distal Ejecta with Distance from the Source Crater: A Preliminary Model

A model for how impact ejecta vary with distance from the source crater is shown in Fig. 10.12. This is a working model based primarily on observations of the Cenozoic microtektite layers, the late Eocene cpx spherule layer, and the K-T boundary impact ejecta layer. Unfortunately, we have found that most authors do not quantify much of the basic information about the distal ejecta layers such as the ratio between melted (spherules) and unmelted (e.g., shocked quartz) ejecta or spherule shape and size distribution. This has severely limited our ability to construct a comprehensive model of how distal ejecta layers vary with distance from the source crater. We have, therefore, added a table which lists information that we urge all authors who describe distal ejecta/spherule layers to provide in their published descriptions (Table 11.2).

The graph in the upper part of Fig. 10.12 is similar to the one in Fig. 10.4, but in this figure we used solid symbols for sites where both unmelted and melted (microtektites and/or microkrystites) ejecta are found and open symbols where only melted ejecta have been found (see Sect. 10.1.2.2 for how thicknesses were estimated). As discussed in Sect. 10.1.2.2, the estimated ejecta layer thicknesses are close to the theoretical thicknesses expected from transient craters the size assumed for the proposed source craters of the Ivory Coast and North American microtektite layers (i.e., Bosumtwi and Chesapeake Bay, respectively); but the measured thicknesses are thicker than the theoretical thicknesses expected from transient craters the size assumed for the proposed source craters of the Manson and K-T boundary ejecta layers (i.e., Manson and Chicxulub, respectively). Thickness versus distance for the cpx spherule layer shows a lot of scatter, but most of the thicknesses indicate a transient crater of between 80 and 100 km, which is much larger than the estimated 60 km transient crater diameter for the Popigai impact structure.

The wide gray band in Fig. 10.12 separates sites containing both unmelted and melted ejecta (above the band) from sites where only melted ejecta has been reported (below the band). Specifically, unmelted grains have not been observed in the Ivory Coast microtektite layer, but have been found in a few cpx spherule layer sites, several Australasian microtektite sites, all the known North American microtektite layer sites, and up to at least 11,000 km and perhaps globally from the Chicxulub structure (believed to be the source of the K-T boundary ejecta layer). Based on ejecta grains >125 μm in size, the distance at which unmelted plus

melted ejecta (above the gray line) changes to melted ejecta only (below the band) varies from a distance of ~90 transient crater diameters from a source crater with a transient crater diameter of ~40 km to between 110 and 200 transient crater diameters for source craters with transient crater diameters of ~100 km. At the present time, the position of this band is not well defined, as the best data come the Australasian microtektite layer whose source crater is still unknown and from the K-T boundary layer where we assume that unmelted ejecta occurs globally, but for which we only have data for sites out to 11,000 km from the proposed source crater, Chicxulub.

The proposed changes in impact ejecta layers that occur as a function of distance from their source craters are shown qualitatively by the arrows below the graph in Fig. 10.12. The arrows only show general trends; the degree of change with distance from a given source crater depends, in addition to other factors, on the size of the source crater. The arrows point in the direction of increase, which is toward the source crater in some cases and away in others. Many of the changes are related to an increase in the average degree of shock metamorphism away from the source crater. This results, for example, in an increase in the ratio of melted to unmelted ejecta away from the source crater. However, it must be emphasized that, on average, the amount or abundance of ejecta, both melted and unmelted, decreases away from the source crater as indicated by the decrease in thickness of ejecta layers with distance from the source crater. If the percent melted ejecta (spherules) at several distances from the source crater for several different ejecta layers were known, then lines showing the percent melted ejecta could be added to the ejecta thickness versus distance plot. The aggregate thickness and percent melted ejecta of a newly discovered, relatively undisturbed, ejecta layer could be plotted on such a diagram to determine the size of and distance to the source crater. See Sect. 11.4 (question 5) for additional discussion of this subject.

Microtektites close to the source crater in the Australasian and North American microtektite layers contain relict mineral inclusions. The percent microtektites containing relict mineral inclusions and the vesicularity of the microtektites increases toward the source crater (Fig. 10.12). The average alkali contents of the Australasian microtektites decrease away from the source crater over a distance from ~30 to 294 transient crater diameters (assuming a transient crater diameter of 38 km and a location for the source crater at 17° N and 107° E). The decrease in vesicularity and abundance of relict mineral grains in the microtektites, as well as alkali content of the microtektites are all related to the increase in degree of shock metamorphism with distance away from the source crater.

There is a general increase in size of impact spherules and microtektites toward the source crater, but close to the source crater (<100 crater diameters) the size of the spherules/microtektites decreases, probably as a result of increased fragmentation. The fragmentation appears to be the result of interparticle collisions between spherules while still in the atmosphere. These impacts are recorded on the surfaces of the microtektites as impact pits (or microcraters) which increase in number toward the source crater.

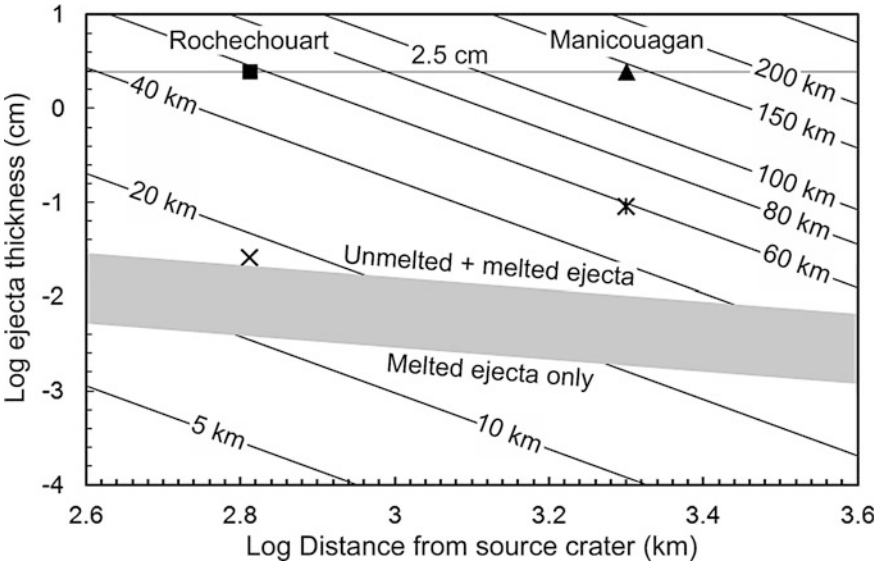

Fig. 10.13 Log thickness of the Late Triassic spherule layer (horizontal *gray line* labeled 2.5 cm) in southwestern England versus log paleodistances of 650 km (the distance to the 25-km-diameter Rochechouart structure) and 2000 km (the distance to the 100-km-diameter Manicouagan structure). The estimated thickness of the spherule layer (~2.5 cm; Walkden et al. 2002) is plotted versus the paleodistance from the Rochechouart (*solid black square*) and Manicouagan (*solid black triangle*) impact structures. Also plotted are the calculated thicknesses of ejecta layers at those distances based on the estimated transient crater diameters for Rochechouart (X) and Manicouagan (*asterisk*) (17 and 59 km, respectively) derived from McGetchin et al.'s (1973) equation relating ejecta thickness with size of and distance to the source crater. Note that at 650 km, the thickness of the spherule layer lies close to the thickness of an ejecta layer expected from an impact structure with a transient diameter of 60 km. Thus, at this distance, the spherule layer appears to be nearly two orders of magnitude too thick to have been derived from a crater with a transient crater the size proposed for the Rochechouart structure. At the estimated paleodistance (2000 km) to Manicouagan, the measured thickness of the Late Triassic spherule layer plots just below the thickness line for a crater with a transient crater diameter of 150 km, and is more than an order of magnitude too thick compared with the calculated thickness of an ejecta layer from a crater with a transient crater diameter the size proposed for the Manicouagan. Transient crater diameters were calculated using an equation from Collins et al. (2005) (see footnote "a" for Table 10.1 for the equation)

The maximum size of shocked quartz grains with PDFs also increases toward the source crater (see Fig. 10.6). We propose that equations for the best-fit trend line for a plot of maximum size of shocked quartz grains versus the log of the distance from the source crater can be used to estimate the maximum size of quartz crystals in the source crater target rocks. Extrapolation of the best-fit line back to the crater rim suggests that the maximum size of quartz grains at the Manson and Chicxulub impact structures is 0.9 cm and 1.2 mm, respectively. The maximum sizes of shocked quartz grains in the Australasian microtektite layer (Wu 1995)

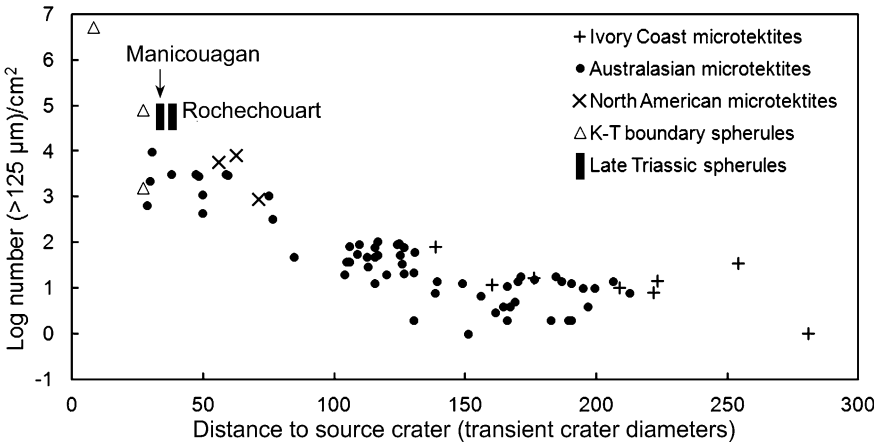

Fig. 10.14 Log number of Late Triassic spherules (>125 μm)/cm^2 versus distance (in transient crater diameters) from the proposed source craters. The proposed source craters are the Rochechouart impact structure in France and the Manicouagan impact structure in Canada. The transient crater diameters of these structures are about 17 and 59 km, respectively (transient crater diameters were estimated using an equation given in footnote "a" for Table 10.1). At the time of the impact, Rochechouart was ~650 km (38 crater diameters) from the Late Triassic spherule layer location in southwest England and Manicouagan was ~2000 km (34 crater diameters) from the spherule layer site. See Table 10.2 for source of data for the microtektite layers and Fig. 10.1 caption for K-T boundary layer data. Calculations of the number of spherules/cm^2 for the Late Triassic spherule layers were based on data in Walkden et al. (2002)

plot below the best-fit trend line for the Chicxulub data (Fig. 10.6); however, extrapolation to the proposed source crater location indicates a similar grain size in the target rock for the Australasian ejecta layer; i.e., ~1.1 mm.

The maximum size of shocked quartz in an ejecta layer and the rate at which the maximum size of shocked quartz grains decreases with distance from the source crater both appear to be related to the maximum size of the quartz grains in the target rock, but not to crater size. If two or more craters have been suggested as a possible source crater for an ejecta layer, geographic variations in the maximum size of shocked quartz in the ejecta layer may be useful in determining which of the craters is more likely to be the source.

Shocked quartz up to 125 μm in size has been found as far as 14,000 km from the Chicxulub impact structure (Fig. 10.6). Extrapolation of the best-fit trend lines for the Manson and Australasian shocked quartz data (Fig. 10.6), suggests that shocked quartz ~125 μm in size should be present as far as ~510 km from the Manson impact structure and up to ~4400 km from the hypothetical Australasian source crater location at 17° N and 107° E. No shocked quartz grains have been identified in the Australasian layer at core sites farther than ~2900 km from this proposed source crater site; however, there is a gap between ~2900 and 3900 km

for which we have no data, so unmelted ejecta (>125 μm) could extend as far as ~3900 km from the proposed source crater location. The apparent lack of shocked quartz in cores taken more than 2900 to 3900 km from the proposed source crater location may be the result of the small sample sizes (generally less than 10 g) and the low abundance of shocked quartz grains at these distances from the proposed source crater location. Although the average size of shocked quartz grains decreases with distance from the source crater, the average number of PDF sets in the shocked quartz increases with increasing distance from the source crater (Fig. 5.26b), which is in agreement with other data indicating that the average degree of shock metamorphism increases with distance from the source crater.

10.3 Using the Model to Study Other Distal Impact Ejecta Layers

The model proposed above for how distal impact ejecta vary with distance from the source crater is based mainly on observation of Cenozoic and the K-T boundary ejecta layers; primarily melt-drop microtektites. No quantitative data are available for melt-drop microkrystites or condensate microtektites. The distance (in transient crater diameters) where the percent unmelted ejecta falls to zero may be similar for condensate and melt-drop spherules, but variations in characteristics of melt-drop spherules with distance from the source crater do not apply to the condensate spherules (see Sect. 3.2.1.1 for definition and discussion of spherule types). Of course the nature of the projectile, its velocity, angle of impact, and nature of the target are all factors that control the nature and thickness of a distal ejecta layer for a given distance from the source crater. However, for large impacts forming craters greater than 100 km in diameter, most projectiles are chondritic, the average impact velocity is about 20 km/s, most impact angles are close to 45°, and the target rock is generally felsic or mafic (mostly mafic, especially in the Archean). We do not yet have much quantitative data for how various ejecta parameters change with distance from different sized source craters.

In this section, we discuss whether or not some (mostly older) distal ejecta layers, which were not used to develop the above model but with known (or suspected) source craters, fit the present model (Fig. 10.12). We also use the model to say what we can about the size and location of the source craters of some of the older ejecta layers whose source craters have not yet been identified and may never be. We find that most of the Phanerozoic and late Precambrian (2 Ga or younger) ejecta/spherule layers seem to fit the proposed model, but most of the older Precambrian (>2 Ga) spherule layers do not appear to fit the model.

10.3.1 The Middle Paleocene Nuussuaq Spherule Bed

Unlike most Phanerozoic ejecta/spherule layers, the Middle Paleocene Nuussuaq spherule bed does not fit the model for distal impact ejecta layers discussed above; it appears to have more in common with the Paleoarchean spherule layers. Like the distal K-T boundary (Chicxulub) layer at the more proximal sites and many of the older Precambrian spherule layers, the Nuussuaq spherules occur in several layers separated by finer-grained deposits. Insufficient detail is given in published descriptions of this layer to estimate its aggregate thickness, but it appears to be at least a few centimeters but <10 cm thick. Similar to well-documented impact spherules, the Nuussuaq spherules are mostly spherical, but teardrops and dumbbells are also said to be present (although not shown in published images). Images of the spherules suggest they are fairly vesicular, although it has been suggested that at least some of the calcite-filled spherical areas in the glass spherules are due to liquid immiscibility rather than vesicles which were later filled with calcite (Robin et al. 1996; Jones et al. 2005b). The presence of primary microlites, vesicles, and rotational shapes indicates that the spherules are melt-drop microkrystites. The apparent vesicularity and compositional and petrographic heterogeneity of the spherules suggest that, if they are impact spherules, the layer must be fairly close to the source crater, probably less than 25 transient crater diameters and maybe <10. Broken spherules and spherule fragments appear to be abundant, but no quantitative data are given. A crater with a transient diameter of 60 km could have an ejecta layer a few centimeters thick at a distance of 10 crater diameters; however, the ejecta layer should contain abundant shocked mineral grains and shocked lithic clasts (Fig. 10.12). No definitive evidence of shocked mineral or shocked rock fragments have been reported for this spherule layer. An impact into a basaltic target could explain the absence of shocked quartz and if the impact occurred in an active flood-basalt province (Margolis et al. 1991b) this might explain the absence of any unmelted ejecta, although we regard this as unlikely. Impact into basaltic (oceanic) crust has also been used to explain why none of the Paleoarchean spherule layers contain shock-metamorphosed mineral grains (see Sect. 10.4).

The Middle Paleocene Nuussuaq spherules in Western Greenland contain vesicles, as well as primary microlites, and some may have rotational shapes (Sect. 4.7.3). Thus, if the Nuussuaq spherules are really impact spherules, then they may be a Phanerozoic example of microkrystites formed as melt droplets (melt-drop microkrystites).

10.3.2 The K-T Boundary Layer

Spherules are the most abundant component in the K-T boundary layer at all the distal sites around the globe. Unfortunately, at most K-T boundary sites the glass

and silicate phases in the spherules have been replaced by other phases and many spherules have been deformed by compaction, making detailed studies of the original composition and petrography of the spherules difficult. However, spherules believed to be diagenetically altered microtektites (or at least microtektite-like) have been found at most distal sites out to a distance of ~6000 km from the Chicxulub impact structure. This conclusion is supported by the presence of remnant glass cores in some of the K-T boundary spherules at Haiti and NE Mexico. At more distal sites (>8000 km from Chicxulub) most K-T boundary spherules have relict crystalline textures and many of these contain primary Ni-rich spinel microlites. These spherules are believed to be diagenetically altered microkrystites formed as condensate droplets.

Data from the Cenozoic microtektite layers indicate that microtektites can be found out to 280 transient crater diameters (see Fig. 10.2). Since half way around the globe from Chicxulub is ~200 transient crater diameters (20,000 km/100 km = 200), microtektites should be found in the K-T boundary layer globally. Diagenetic alteration has made identification of spherule type difficult, but some authors have reported finding diagenetically altered microtektites in the K-T boundary layer at sites in the North Pacific (ODP Site 886, Core LL44-GPC-3; Smit et al. 1992b; Kyte et al. 1996) and in Europe and southwest Asia (Agost and Caravaca, Spain; Tetri-Tskaro, Republic of Georgia; Martínez-Ruiz et al. 1997; Smit 1999) at paleodistances between ~6450 and 9500 km (or between ~64 and 95 crater diameters) from Chicxulub. In addition to the microkrystites, Cenozoic melt-drop microtektite data suggest that at these more distal K-T boundary sites there should be between 100 and 1000 melt-drop microtektites/cm^2 (see Fig. 10.2). Smit (1999) estimated that the abundance of spherules at Agost, Caravaca and Tetri-Tskaro is ~20,000/cm^2. If, as suggested above, there are as many as 1000 microtektites/cm^2 in the layer at these sites, then melt-drop microtektites could make up as much as 5 % of the spherules by number, but if the abundance is as low 100/cm^2, the microtektites would only make up 0.5 % and could be easily missed among the abundant microkrystites. At even more distal sites, microtektites would probably be less abundant, but we suggest that they should be present. On the other hand, silicate melt-drop spherules may not have been thrown globally since the upper 3 km or more of the target rocks were carbonates and ^{10}Be studies indicate that melt-drop tektites (and presumably microtektites) come from the surface or near surface target rocks.

10.3.3 The Manson Impact Ejecta Layer

Distal impact ejecta from the ~35- to 37-km-diameter Late Cretaceous Manson impact structure in northwestern Iowa (USA) have been found in the lower part of the Crow Creek Member of the Pierre Shale at numerous sites in South Dakota and Nebraska (see Sect. 5.3). The ejecta layer has been found at 20 sites between 215 and 475 km from the Manson structure. That would be ~10 to 23 transient crater

diameters based on a transient crater diameter of 21 km (Table 10.1). Shocked quartz and feldspar with multiple sets of planar deformation features have been reported in the ejecta layer, but there is no mention of impact spherules (Izett et al. 1998; Katongo et al. 2004).

The thickness of the ejecta layer decreases with distance from the Manson structure. Katongo et al. (2004) gave the thickness of the layer at three sites: Wakonda lime quarry, Iroquois core, and Gregory 84–21 core which are 219, 300, and 409 km from the Manson impact structure, respectively. The thickness of the ejecta layer at these sites is 12.2, 4.7, and 1.9 cm. The best-fit line for these data, on a log thickness versus log distance graph, indicates a transient crater size closer to 45 km than to the estimated transient crater diameter of 21 km (Witzke and Anderson 1996; Fig. 10.4).

At distances, between 219 and 409 km from the source crater, the melt content of the ejecta layer is expected to be low, but still should be at least 20 % by volume (Fig. 10.9a). Twenty percent of a column (with a cross-sectional area of 1 cm^2) through a 1.9-cm-thick layer is 0.38 cm^3. If the melt consisted of spherules with an average diameter of 400 μm, then the layer should contain ~11,300 spherules/cm^2. This agrees with extrapolation based on data from the Cenozoic microtektite/spherule layers which suggests that an impact layer should contain between ~2000 and 100,000 spherules/cm^2 at a distance of 6 to 13 crater diameters (Fig. 10.2). So, where is the melt? Why are there no spherules? Katongo et al. (2004) concluded that the Crow Creek basal unit containing the ejecta layer has been subjected to high degrees of alteration and weathering. Perhaps dissolution of the spherules, if they were ever present, during weathering explains the absence of impact spherules in the Manson impact ejecta layer.

10.3.4 The Late Triassic Spherule Layer

A layer containing diagenetically altered spherules (up to ~1 mm in diameter) and shocked quartz grains occurs in upper Triassic deposits near Bristol in southwestern England (see Sect. 5.4; Walkden et al. 2002; Kirkham 2002, 2003). According to Walkden et al. (2002) the spherule layer averages ~2.5 cm in thickness. Spherules make up as much as ~50 % of the layer by volume. Quartz grains are abundant in the spherule layer. They are mostly angular and 50 to 300 μm in size. About 85 % exhibit multiple (up to 5) sets of PDFs with an average of 2.3 sets of PDFs per grain (Fig. 5.38; Walkden et al. 2002; Kirkham 2003). The absence of evidence for primary microlites and the presence of vesicles and rotational shapes suggest that the spherules are diagenetically altered melt-drop microtektites.

Walkden et al. (2002) suggested that the 25-km-diameter Rochechouart impact structure in France or the 100-km-diameter Manicouagan impact structure in Canada might be the source crater for this spherule layer. At the time of formation of the SW England spherules, Rochechouart was ~650 km and Manicouagan was

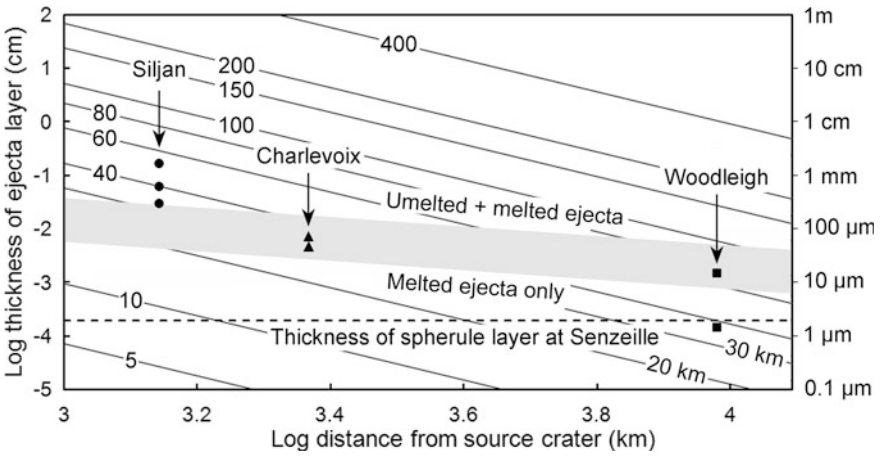

Fig. 10.15 Log thickness of impact ejecta from Siljan (*black circles*), Charlevoix (*black triangles*), and Woodleigh (*black squares*) impact structures versus log distance (km) from the Late Devonian spherule layer at Senzeille, Belgium, at the time of the impact. The thicknesses were calculated using the equation from McGetchin et al. (1973; Eq. 2.2 in Sect. 2.6). Calculations were made for three estimated diameters for the Siljan structure of 52, 65, and 85 km, two estimated diameters for the Charlevoix structure of 46 and 54 km, and two estimated diameters for the Woodleigh structure of 60 and 120 km. The corresponding transient crater diameters for Siljan (33, 40, and 51 km), Charlevoix (30 and 34 km), and Woodleigh (37 and 69 km) were calculated using the equation in footnote "a" in Table 10.1. The estimated original thickness of 2 µm for the spherule layer at Senzeille is indicated by the horizontal *dashed line*. The estimated original thickness for the Hony site is only 0.1 µm and it plots off the graph at the bottom. Calculations of the thicknesses of the spherule layer at Senzeille and Hony are based on data from Claeys and Casier (1994). See the text (Sect. 10.3.6) for information on how the thicknesses were estimated

~2000 km from the location of the spherule layer in SW England. Based on the distances of these impact structures from the spherule site and the thickness of the spherule layer, Walkden et al. (2002) concluded that the most likely source crater was the Manicouagan impact structure. This conclusion was later supported by the similarity between the heavy mineral assemblage (including garnet varieties) in the ejecta layer and the Manicouagan target rocks (Thackrey et al. 2009). In addition, a more recent attempt to date the Rochechouart structure yielded an age of 201.4 ± 2.4 Ma (Schmieder et al. 2010). This is too young to be the source crater for the spherule/ejecta layer in SW England, which has an age of 214 ± 2.5 Ma (Walkden et al. 2002).

We have plotted the data for the late Triassic spherule layer site in SW England on a log–log graph of thickness versus distance, using the thickness and distances cited above (Fig. 10.13). At distances of 650 and 2000 km, 2.5 cm plots just above the ejecta thickness for a crater with a transient crater diameter of 60 and 140 km, respectively; however, Rochechouart and Manicouagan have estimated transient crater diameters of 17 and 60 km, respectively. Thus the reported thickness is much too thick for craters the size of Rochechouart and Manicouagan at the

estimated paleodistances. However, the spherule layer shows evidence of re-working and the spherules generally make up less than 50 % of the layer. Thus the un-reworked spherule layer would probably have been much thinner. We find, in agreement with Walkden et al. (2002), that the thickness of the spherule layer in SW England is more consistent with derivation from the Manicouagan impact structure than from the Rochechouart impact structure; however, neither structure explains the thickness of the spherule layer very well. On the other hand, at these distances, ejecta from either impact structure plot well within the region where we expect to find both unmelted and melted ejecta (Fig. 10.13). This is consistent with the presence of abundant shocked quartz within the spherule layer

Assuming that the spherule layer is 2.5 cm thick and that the spherules make up as much as 50 % (by volume) of the spherule layer as stated by Walkden et al. (2002), we calculate that the volume of spherules in a column, with a 1 cm^2 cross-sectional area, would be $\sim$1.25 cm^3. Unfortunately, neither Walkden et al. (2002) nor Kirkham (2003) give any detailed information regarding the size distribution of the Late Triassic spherules. However, assuming an average diameter of 300 to 400 μm for the spherules (based on photomicrographs of the spherules in thin sections), we estimate that the number of spherules (>125 μm)/cm^2 is between $\sim$37,000 and 88,000. For both Manicouagan and Rochechouart, the estimated number of spherules is somewhat higher than the number estimated from the Cenozoic microtektite and K-T boundary spherule layers at these distances (in transient crater diameters) from the source craters (i.e., 33 for Manicouagan and 38 for Rochechouart; Fig. 10.14). Based only on this abundance data, we cannot rule out Rochechouart as the source crater, but the Manicouagan impact structure appears to be a marginally better match.

The percent spherule fragments in the Late Triassic spherule layer also appears to be more consistent with the more distant source crater. Both Walkden et al. (2002) and Kirkham (2003) mentioned the presence of broken spherules and fragments (shards), but they do not indicate their abundance relative to whole splash forms. Based on published photomicrographs of the spherules in thin sections, we estimate that fragments make up $\sim$10 % of the "glass" component in this spherule layer. Even though this abundance is somewhat low for a spherule layer $\sim$2000 km from the source crater (Fig. 10.8), it is much too low for a source crater only 650 km away.

Unfortunately, since the spherules have been diagenetically altered, there are no compositional data and very little petrographic data. However, interior "spheres" are present in many of the spherules which are interpreted as outlines of vesicles preserved during diagenetic alteration (Kirkham 2002; Walkden et al. 2002). This is consistent with the spherule layer being $\sim$2000 km away from the source crater.

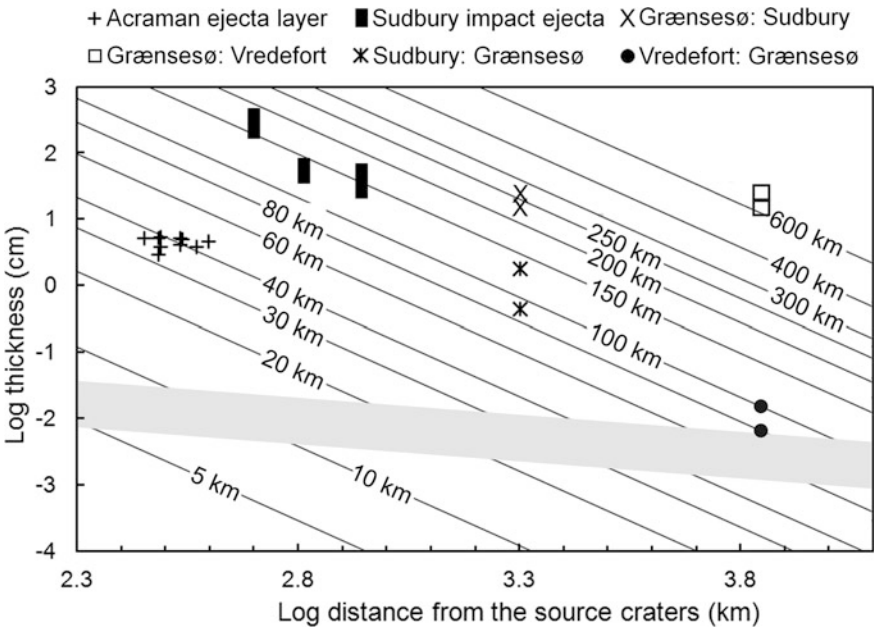

10.3.5 Late Devonian Qidong Spherule Layer

Silicate glass spherules have been found in deposits of the Late Devonian Famennian Stage in Qidong, Hunan Province, South China (see Sect. 6.2.2; Wang 1992; Wang et al. 1994). However, the thickness of the spherule layer and abundance of spherules is not well documented. The apparent low abundance of the spherules, the presence of relict quartz grains in some spherules, and the high vesicularity and heterogeneous nature of some of the spherules suggest that the source crater is nearby and not very large. The matrix glass in the spherules contains an average of 3.23 and 2.48 wt % K_2O and Na_2O, respectively, which is similar to the contents of these oxides in the average continental crust (see Table 6.2). This suggests that the alkali contents of the spherules have not been much affected by vapor fractionation and that, therefore, the spherules were found relatively close to the source crater. However, if the source crater is nearby, shock metamorphosed rock and mineral grains should be relatively abundant in the spherule layer. Wang (1992) and Wang et al. (1994) did not mention shocked mineral grains in the spherule layer, but they did not state whether or not they searched for them. Additional studies of this spherule layer at Qidong and other sites are needed in order to be able to better define limits on the size and location of the source crater.

◀**Fig. 10.16** Log thickness versus log distance for the Acraman and Sudbury ejecta layers and the Grænsesø spherule layer. Most of the Acraman data plot close to the ejecta thickness line for a crater with a transient diameter of 40 km, which is the estimated transient crater diameter for that structure (see Williams and Wallace 2003). The range in thickness of Sudbury ejecta is plotted for three locations: northern Michigan, southwestern Ontario, northeastern Minnesota (*black bars*). Also shown in this figure is the estimated aggregate thickness of the Grænsesø spherule layer (15–25 cm; log 1.2–1.4) at the estimated distance the spherule layer site was from Sudbury (~2000 km) at the time of the impact (Xs). Note that at that distance the estimated thickness of the spherule layer plots close to that of the thickness of an ejecta layer expected from an impact crater with a transient diameter of ~250 km. We also plotted the calculated thickness of an ejecta layer 2000 km (log 3.3) from Sudbury (the paleodistance between Sudbury and Grænsesø) based on two estimates of the transient crater diameter for the Sudbury structure of 90 and 130 km (asterisks). It is obvious that the expected thickness of an ejecta layer at the Grænsesø spherule layer site is over an order of magnitude thinner than the estimated aggregate thickness of the Grænsesø spherule layer. The estimated aggregate thickness of the Grænsesø spherule layer (*open squares*) at the distance the spherule layer site was from Vredefort (~7000 km) at the time of the impact is also shown. The paleodistance between the Grænsesø spherule layer site and the Vredefort impact structure ~2 Ga ago was estimated from the proposed position of the continental landmasses at that time based on paleomagnetic data (see Pesonen et al. 2003). At 7000 km (log 3.85) the estimated aggregate thickness of the Grænsesø spherule layer plots close to the thickness of an ejecta layer expected from an impact crater with a transient diameter of >600 km! We also plotted the calculated thickness of an ejecta layer 7000 km from Vredefort based on two estimates (Turtle et al. 2005) of the transient crater diameter for that structure of 80 and 100 km (*solid black circles*). Note that the expected thickness of an ejecta layer at the Grænsesø spherule layer site is several orders of magnitude thinner than the estimated thickness of the Grænsesø spherule layer. The Acraman ejecta thickness data are from Williams and Wallace (2003). We only used the thicknesses for sites where the ejecta layer was said by Williams and Wallace (2003) to be primary rather than reworked. The Sudbury ejecta layer thicknesses are from Addison et al. (2005) and Pufahl et al. (2007). The estimated aggregate thickness estimate for the Grænsesø spherule layer is based on data from Chadwick et al. (2001) and Smith et al. (2006)

10.3.6 Late Devonian Belgian Spherule Layer

Silicate glass spherules have been found in Upper Devonian deposits at Senzeille and Hony, Belgium (see Sect. 6.2.3.3; Claeys et al. 1992; Claeys and Casier 1994). The two sites are about 90 km apart (Fig. 6.6). The spherule layer occurs at or just above the Frasnian-Famennian boundary (FFB). Variations in the published (Claeys and Casier 1994) thickness of the spherule layer (5-10 cm at Senzeille and <2 cm at Hony), glass content (0.03 mg/g at Senzeille and 0.005 mg/g at Hony), and average size of the spherules (~ 300 μm at Senzeille and ~250 μm at Hony) suggest that Senzeille may have been closer to the source crater than was Hony. Based on the reported layer thicknesses, glass concentrations, and average spherule sizes at these two sites, we estimate that the abundance of spherules at Senzeille and Hony is ~14 and ~1 spherules/cm^2, respectively. This suggests that these sites are probably more than ~130 crater diameters from the source crater. However, since the samples were crushed and sieved in order to extract the spherules, we are not sure how accurate the glass concentrations are. According to Claeys and Casier (1994) no

shocked mineral grains were found in the spherule layer. In the absence of reported evidence for the presence of unmelted ejecta in the spherule layer, we have calculated the original thickness of the spherule layer at Senzeille and Hony using the reported glass content at the two sites. The calculated original spherule layer thickness is 2 and 0.1 μm at Senzeille and Hony, respectively. Thus, if the reported glass content is an accurate reflection of spherule abundance at the two sites and if no unmelted ejecta are present, then it appears that there was never a continuous ejecta layer at these two sites, just spherules scattered over the surface.

Claeys and Casier (1994) suggested two possible source craters for the spherule "layer" based on the age and size of the craters: (1) the Siljan (Siljan Ring) impact structure in Sweden, and (2) the Charlevoix impact structure in Quebec, Canada. At the time of the impact, the Siljan and the Charlevoix impact structures were approximately 1390 and 2330 km, respectively, from the spherule sites in Belgium. Since the publication by Claeys and Casier (1994) another impact structure has been discovered that may have the correct age; i.e., the Woodleigh impact structure in Western Australia (Mory et al. 2000a,b; Reimold et al. 2003). We estimate that the distance between the Woodleigh structure and the Belgian spherule sites at the time of the impact was ~10,700 km. None of the three craters is well dated, but their estimated ages overlap the proposed age for the FFB (~ 376 ± 4 Ma), and, thus within dating errors any of them may have the correct age to be the source crater of the Belgian spherule layer.

The Siljan (or Siljan Ring) impact structure is in the Dalarna region of south-central Sweden (Fig. 6.10; Svensson 1971; Henkel and Aaro 2005). Its diameter was originally estimated to be ~52 km (Grieve 1988), but Kenkmann and Von Dalwigk (2000) suggested that it may have a diameter of at least 65 km and Henkel and Aaro (2005) estimated that the pre-erosional diameter may have been as large as 85 km. Some previously quoted ages for the Siljan structure range between 342 and 368 Ma (Bottomley et al. 1978; Åberg and Bollmark 1985; Bottomley et al. 1990). More recently, Reimold et al. (2005b) dated several impact melt breccia samples from the Siljan structure using Ar–Ar laser spot and laser step heating techniques. They obtained an age of 377 ± 2 Ma (95 % confidence level) for Siljan.

The Charlevoix impact structure in Quebec, Canada, has a diameter of 54 km (Trepmann and Spray 2005). Claeys and Casier (1994) stated that the target rocks at Charlevoix consist of a mixture of Precambrian granite, gneiss, migmatite, charnockite, gabbro, and anorthosite; however, Middle-Late Ordovician arkoses, quartzites, silstones, and limestones probably formed a continuous cover above the basement rock at the time of the impact (Trepmann and Spray 2005, and references therein) and may have made suitable source rocks for the Senzeille and Hony spherules. The age of the Charlevoix structure is not well defined: Grieve and Pesonen (1992) gave an age of 357 ± 15, Claeys and Casier (1994) quoted an age of 360 ± 20 Ma, and the Earth Impact Database (2011; accessed 5 April 2011) gave an age of 342 ± 15 Ma for this structure. The age given in the Earth Impact Database is, within the quoted errors, younger than the age of the FFB and, therefore, the Senzeille and Hony spherule layers. However, field data suggest that

Table 10.4 Impact ejecta/spherule layers

Spherule Layer	Location	Age (Ma)	Aggregate Thickness[1] (cm)	Proposed source crater
Australasian microtektite	Indian Ocean; S. China, Philippine, Sulu, Celebes Seas; W. equatorial Pacific; Antarctica	~0.8	<0.0001–0.17	Unknown; but probably in Indochina
Ivory Coast microtektite	E. equatorial Atlantic	1.1	<0.001	Bosumtwi
North American microtektite	Gulf of Mexico, Caribbean, Barbados, NW Atlantic	35	<0.01–8	Chesapeake Bay
Cpx spherule	Global	35	<0.0001–0.06	Popigai
Nuussuaq spherule bed[2]	Western Greenland	~60	~30–60	Unknown
K-T boundary	Global	65	~0.2–25	Chicxulub
Late Triassic spherule	SW England, near Bristol	~214	~1.6	Manicouagan
Qidong spherule	Qidong, South China	~372	Unknown	Unknown
Senzeille/Hony microtektite	Belgium	~374	<0.001	Unknown
Acraman	South Australia	~578	0.5–3.5	Acraman
Sudbury	Lake Superior region, USA	1850	~25	Sudbury
Grænsesø	South Greenland	~1990	15–25	Unknown
Dales Gorge[3]	Western Australia	~2490	~6	Unknown
Kuruman[3]	South Africa	~2490	0.5	Unknown
Bee Gorge	Western Australia	~2540	~1–3	Unknown
Reivilo[4]	South Africa	~2560	2–2.5	Unknown
Paraburdoo[4]	Western Australia	~2570	2	Unknown
Jeerinah[5]	Western Australia	2630	0.4–20	Unknown
Carawine[5]	Western Australia	2630	~30	Unknown
Monteville[5]	South Africa	<2650	~6	Unknown
S5	South Africa	~3230	?	Unknown
S4	South Africa	<3243	12	Unknown
S3	South Africa	3243	~30	Unknown

(continued)

Table 10.4 (continued)

Spherule Layer	Location	Age (Ma)	Aggregate Thickness[1] (cm)	Proposed source crater
S2	South Africa	3260	~10–70	Unknown
S6	South Africa	~3330	?	Unknown
S7	South Africa	~3410	?	Unknown
S1[6]	South Africa	3470	~6	Unknown
Warrawoona[6]	Western Australia	3470	~5	Unknown

[1] Aggregate thicknesses estimated from layer thickness and percent spherules
[2] Also referred to as Disco spherules
[3] These two spherule layers may be from the same impact
[4] These two spherule layers may be from the same impact
[5] These three spherule layers may be from the same impact
[6] These two spherule layers may be from the same impact. The Warrawoona layer is also known as the Apex Basalt layer

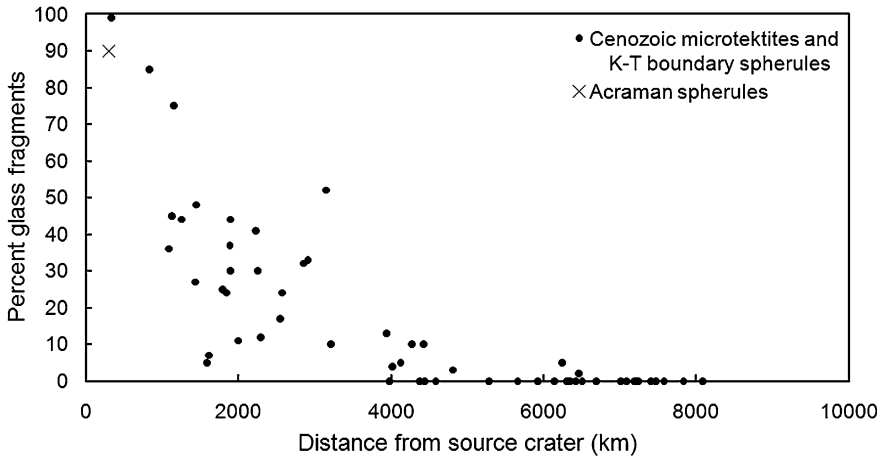

Fig. 10.17 Percent glass fragments in distal impact ejecta layers versus distance (km) from the source crater. The percent of glass fragments refers to the percent glass that occurs as fragments rather than whole microtektites or spherules. In the case of the K-T boundary and Acraman ejecta layers, the glass has been replaced by other phases. See Table 10.2 for the Cenozoic microtektite data and Fig. 10.8 caption for K-T boundary spherule data. The percent of glass fragments in the Acraman ejecta is based on data in Wallace et al. (1990a)

the crater was formed during Ordovician to early Silurian time, an age that is supported by more recent Ar–Ar ages (Whitehead et al. 2003). If this is correct, then the Charlevoix structure is too old to be the source of the Belgian spherule layer.

The Woodleigh impact structure is located on the western coast of Australia (Mory et al. 2000a,b; Reimold et al. 2003; Glikson et al. 2005). One research group supports a diameter of 120 km for the structure (Mory et al. 2000a,b), but others believe the diameter is closer to 60 km (Hough et al. 2003; Reimold et al. 2003). The age of the structure is even less well known than that of the Charlevoix structure. The stratigraphic age is constrained by overlying Lower Jurassic deposits of lacustrine origin and by seismic evidence of deformed Devonian strata on the northern and western flanks of the structure (Iasky et al. 2001). Mory et al. (2000a) proposed that the large size of the crater suggests that it might correlate with a mass extinction event, perhaps at the Permian–Triassic boundary or possibly in the late Triassic.

Uysal et al. (2001) dated the Woodleigh structure using K–Ar dating of authigenic illitic clay minerals considered by them to be impact-induced hydrothermal alteration products. However, other researchers were critical of Uysal et al.'s (2001) proposed age (Renne et al. 2002; Reimold et al. 2003). Uysal et al. (2001) obtained 25 K–Ar ages ranging between 110 and 801 Ma. Twelve of the ages cluster between 308 and 364 Ma and Uysal et al. (2001) used the weighted average of the mean of the twelve to obtain an age of 359 ± 4 Ma for the Woodleigh structure. Renne et al. (2002) argued that the range in ages between

308 and 364 Ma does not convincingly indicate a discrete event. In addition, Renne et al. (2002) argued that there is no valid statistical, geological, or geochronological justification for the selection of the ages used to define an age for the Woodleigh structure. Furthermore, Renne et al. (2002) claim that Uysal et al. (2001) did not provide evidence linking the dated clays to the impact event. More recently, Uysal et al. (2005) provided Rb–Sr data and additional K–Ar data in support of an age of ~360 Ma for the Woodleigh impact structure, and they discussed the evidence that indicates that the illite ages reflect the time of formation of the Woodleigh crater.

Whether or not the Woodleigh structure has the correct age to be the source crater of the Senzeille and Hony spherules, it appears likely that the target rocks may have been an appropriate source for the spherules. The Kopke Sandstone appears to have been near the surface at the time of the impact (Mory et al. 2000a; Glikson et al. 2005), and this sandstone deposit is a redbed unit, which contains minor amounts of carbonate and siltstone (Mory et al. 2003). In addition to shock metamorphosed basement rock (consisting of gneiss, granite, and amphibolites), sandstone and siltstone clasts have been observed in a core recovered from the Woodleigh structure (Glikson et al. 2005; Uysal et al. 2005).

The estimated thicknesses of ejecta layers from the Siljan, Charlevoix, and Woodleigh structures (using the equation by McGetchin et al. 1973) are plotted on a graph of log thickness versus log distance using the estimated transient crater diameters for the proposed source craters and estimated paleodistances to the Hony and Senzeille sites (Fig. 10.15). Also plotted on this graph is the estimated original thickness of the spherule "layer" at Senzeille; the estimated thickness of the spherule "layer" at Hony plots off the bottom of the graph. If the thickness of the Belgian spherule layers is between ~2 and 10 cm as reported by Claeys et al. (1992) and Claeys and Casier (1994), then the best match in terms of thickness of the layer would be the Siljan impact structure as pointed out by Claeys and Casier (1994). Nevertheless, the estimated thickness of an ejecta layer from a crater the size of Siljan at its distance from the spherule site at the time of the impact (i.e., 1390 km) would be one to two orders of magnitude thinner than the quoted thickness of ~2 to 10 cm (Fig. 10.15). However, based on the estimated spherule abundances of 1 to 14/cm^2 and absence of shocked mineral grains, we calculate that the original aggregate thickness of the layer at the two sites was only 2 μm or less. If this estimate is correct, the estimated thickness of an ejecta layer from the Siljan structure would be 2 to 3 orders of magnitude too thick (Fig. 10.15). Likewise, ejecta from the Charlevoix structure would be too thick by more than an order of magnitude. If the Woodleigh impact structure is 120 km in diameter, then the transient crater diameter would have been ~69 km and the ejecta layer should have been an order of magnitude thicker than the calculated thickness of the spherule layer at Senzeille. However, if the diameter is ~60 km as proposed by Reimold et al. (2003) and Hough et al. (2003), then the transient crater diameter for a 60-km-diameter impact structure would have been ~37 km and the expected thickness would be close to the estimated thickness of the spherule layer at Senzeille (Fig. 10.15). Furthermore at a distance of 10,700 km (or ~290 transient

crater diameters) we would not expect the layer to contain any unmelted ejecta, such as shocked quartz, at least in the >125 μm size range (see Sect. 10.2; Fig. 10.15). In addition, at a distance of 290 crater diameters, we would expect the microtektite abundance to fall between ~1 and 10/cm^2 (Table 10.2; Fig. 10.2), which is agreement with the estimated abundances.

According to Claeys et al. (1992), most of the Senzeille spherules lack crystallites and vesicles, although some contain a few large vesicles. Most of the Hony spherules are homogenous at the 10 μm scale (Claeys and Casier 1994). Only one Hony spherule was described as containing inclusions of partly melted quartz. No quantitative data are given, but it appears that relict quartz grains are found in less than 10 % of the spherules, maybe less than 1 %. In the Australasian strewn field, microtektites containing relict quartz inclusions are not found beyond ~3200 km (Fig. 10.10) or about 84 transient crater diameters (assuming the source crater location is near 17° N and 107° E and the transient source crater diameter was ~38 km). If Woodleigh has a diameter of ~60 km (with a transient crater diameter of ~37 km) and was about 10,700 km from the Belgian spherule sites at the time of the impact, the spherule sites would have been about 290 transient crater diameters from Woodleigh. At this distance we would not expect any of the spherules to contain relict quartz grains. If on the other hand, the diameter of Woodleigh is 120 km, then the transient crater diameter would have been ~69 km and the Belgian spherule sites would have been only 155 transient crater diameters away. But even at this distance we would not expect there to be any relict quartz grains in the spherules.

At 10,700 km from the source crater, we would expect the alkali content of the spherules to be quite low. Indeed the Na_2O contents are generally less than 1 wt % (except for the Si-rich spherules with an average of ~7.2 wt % Na_2O). However, some of the Hony spherules have up to 7 or more wt % K_2O (Table 6.3). At that distance from the proposed source crater location, Australasian microtektites had lost on average about 2/3 of their K_2O (Fig. 10.11). If the Belgian spherules with 7 wt % K_2O had lost 2/3 of their K_2O, then the target rock would have had ~21 wt % K_2O. It is difficult enough trying to find a target rock with 7 wt % K_2O; a target rock with 21 wt % K_2O does not seem to be realistic.

Thus, the Woodleigh impact structure would appear to explain the Belgian spherule "layer" better than does the Siljan or Charlevoix impact structures except for the presence of relict quartz grains in one spherule and high K_2O content of some of the spherules. Unless some of the Woodleigh target rocks contain unusually high K_2O contents, it does not seem likely that this structure is the source crater. In addition, as previously mentioned, some data suggest that the source crater should be closer to Senzeille than to Hony and thus was probably west of the Belgian sites. This does not agree with Woodleigh being the source crater; but, because of the low abundance of spherules, it may be that the observed differences in glass content and spherule size are not statistically important. For example, at a distance >155 transient crater diameters there is 2 orders of magnitude difference in number of microtektites/cm^2 (Fig. 10.2) and more than

100 μm difference in the average diameter of microtektites (Fig. 10.5) in the Cenozoic strewn fields.

10.3.7 Acraman Impact Ejecta

Ejecta from the Acraman impact structure in South Australia have been found at numerous sites to the east and northwest at distances between ~240 and 540 km (Gostin et al. 1986; Wallace et al. 1996; Williams and Gostin 2005). The ejecta consist primarily of sand- to boulder-sized clasts of fractured and shock metamorphosed felsic volcanic rock. Diagenetically altered spherules are present at some sites (Wallace et al. 1990a). Williams and Wallace (2003) found that the unfolded distance between the ejecta sites and the Acraman impact structure versus uncompacted thicknesses of the ejecta layer suggest an original transient crater diameter of ~40 km. We have plotted their data using log thickness versus log distance (Fig. 10.16) and we agree with their conclusion. The Acraman data plot well above the line separating unmelted plus melted ejecta from melted only ejecta. This is consistent with the presence of both shock-metamorphosed quartz grains and rare spherules in the layer.

The Acraman ejecta layer has undergone extensive diagenetic alteration and the original glassy components have been replaced with other phases (Wallace et al. 1990a). Obvious spherules have been found only at three sites (Bunyeroo Gorge, Bunyeroo Gorge North, and Wearing Hills). In addition to the spherules, diagenetically replaced angular to subrounded grains are also present, some of which have shard-like morphologies. The angular fragments may be fragments of what were originally larger glass bodies. Modal analysis of 600 clasts in the 0.5 to 1 mm size range indicates that 0.5, 1.5, and 5 % by volume are spherules, shard-like particles, and angular particles, respectively (Wallace et al. 1990a). At Bunyeroo Gorge, well-defined spherules most commonly occur within a 0.5-cm-thick sandy mudstone layer which directly overlies the basal ejecta breccia (Wallace et al. 1990a). This layer is described as containing scattered sand-sized fragments (clasts). If the clasts make up 10 % of this layer and 0.5 % of the clasts are spherules, the spherules would make up 0.05 % of the sandy mudstone layer. A column with a cross-sectional area of 1 cm^2 through the 0.5-cm-thick laminae layer would have a volume of 0.5 cm^3. The volume of spherules in the column would be 0.5×0.0005 or 2.5×10^{-4} cm^3. The spherules range in size from 150 μm to 1 mm in diameter. Assuming that the average size is 1/3 of the maximum size, as is the case for the Cenozoic microtektites, the average diameter of the spherules would be ~300 μm. A 300-μm-diameter sphere has a volume of 1.41×10^{-5} cm^3. Thus, there would be ~18 spherules/cm^2 in the column $[(2.5 \times 10^{-4}\ cm^3)/(1.41 \times 10^{-5} cm^3) = 17.7]$. However, in the Australasian microtektite layer there are 19 times more microtektites in the 125–500 μm size range than in the 0.5–1 mm size range. If this is true for the Acraman spherules, then this indicates an abundance of ~340 spherules (>125 μm in diameter) per

cm^2 in the Acraman layer. At this distance from the source crater ($\sim$ 8 transient crater diameters, assuming a transient diameter of $\sim$40 km for Acraman) we would expect at least 10 thousand spherules (>125 μm in diameter) per cm^2 (see Fig. 10.2). However, if all the shard-like fragments and half the irregular fragments are broken or irregular spherules, then there would be about 8 times more spherules (including fragments) in the column or $\sim$2700 spherules (>125 μm in diameter) per cm^2 which is still lower than the predicted abundance. On the other hand, the proportion of spherules that are fragments would be close to 90 %, which is in agreement with what would be expected at that distance from the source crater (Fig. 10.17). The absence of spherules in the Acraman ejecta layer at most of the sites may be the result of solution of the glass during diagenesis.

In summary, the Acraman ejecta layer appears to fit the distal ejecta layer model discussed in Sect. 10.2 fairly well except for the low apparent abundance of spherules which may be the result of the old age of the layers and subsequent diagenesis.

10.3.8 Sudbury Impact Ejecta

Impact ejecta believed to be from the Sudbury impact structure in Ontario, Canada, have been found in northern Michigan, southwestern Ontario, and northeastern Minnesota (see Sect. 7.3). The Michigan, Ontario, and Minnesota sites are $\sim$500, 655, and 875 km, respectively, from the Sudbury structure. The ejecta layer is 2.4 to 4.4 m, 43 to 70 cm, and 25 to 58 cm thick at the Michigan, Ontario, and Minnesota sites, respectively (Addison et al. 2005; Pufahl et al. 2007). The ejecta layer contains shock-metamorphosed quartz and feldspar grains with PDFs, accretionary lapilli, spherules, and angular shards (Addison et al. 2005; Pufahl et al. 2007). Platinum group element (including Ir) anomalies are associated with the layer at the Michigan site (Pufahl et al. 2007). Cannon et al. (2010) reported finding the Sudbury ejecta layer in northern Michigan in the Lake Superior region at 10 sites which are between 480 and 660 km from the Sudbury structure. At these sites, the ejecta layer is between $\sim$1 and 150 m thick. Cannon et al. (2010) concluded that at these sites the "…local settings for deposition and preservation were more important than distance from Sudbury in determining the thickness of the layer."

A plot of thickness versus distance, including the thickness of the Sudbury ejecta layer is shown in Fig. 10.16. The thicknesses of the layer are plotted for three sites based on data from Addison et al. (2005) and Pufahl et al. (2007). The best fit for the three sites is for a transient crater size of $\sim$150 km. This is close to the transient crater size of $\sim$130 km for the Sudbury structure as proposed by Spray et al. (2004). The thicknesses used in Fig. 10.16 have not been corrected for compaction. If the layers had been compacted by 50 %, then the best fit would be for a crater with a transient diameter of $\sim$175 km. Layer thicknesses reported by Cannon et al. (2010) are on average thicker for the same distance from Sudbury and are consistent with a transient crater diameter of between $\sim$200 and 300 km.

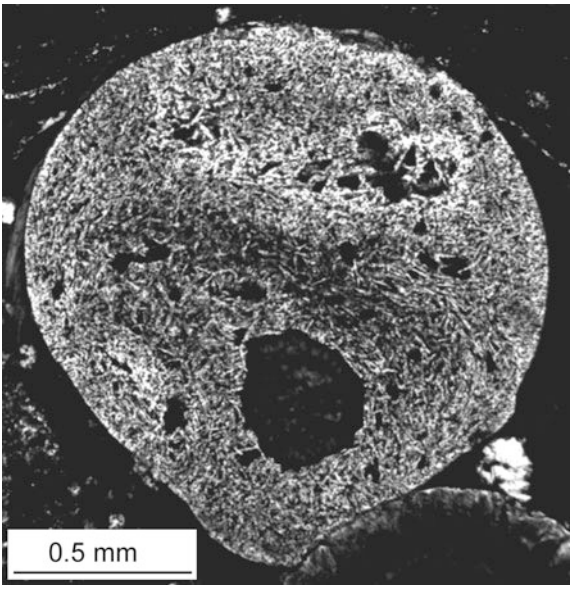

Fig. 10.18 Photomicrograph (plane polarized light) of a spherule from the Dales Gorge spherule layer. The spherule contains numerous randomly oriented lath-shaped K-feldspar microlites (*gray*). The *dark* polygonal to circular areas within the spherule are believed to be vesicles filled with stilpnomelane cement which also fills in the interstices around the spherule. The spherule has been slightly deformed especially where it is in contact with a smaller spherule (with a crystalline rim) to the *lower right*

However, many, if not most, of these sites may contain a high proportion of local material in addition to the ejecta. The Sudbury data plot on the part of the diagram where we expect to find both melted and unmelted ejecta in agreement with the published observations.

If we use a transient crater diameter of 130 km for the Sudbury structure, then the ejecta locations are between $\sim$4 and 7 transient crater diameters away. At a distance of $\sim$7 transient crater diameters, we would expect the percent glass to have been comparable to that found in the North American microtektite layer off the coast of New Jersey, i.e., $\sim$60 % or less by number (see Fig. 10.9). Unfortunately, the ejecta in the Michigan site have been subjected to greenschist metamorphism and are mostly altered to a mixture of dolomite, actinolite, and tremolite whereas ejecta at the Ontario and Minnesota sites have undergone recrystallization and silicification. Thus, any glass originally present has been altered to another phase. Spherules have been identified at all three locations and at the Michigan site centimeter-sized clasts have been interpreted as altered tektites (Addison et al. 2005; Pufahl et al. 2007). No detailed information on the percent spherules/'tektites' or their size distribution has been reported. There is no mention of spherule fragments at the Ontario and Minnesota sites, but melt-like shards with vesicle walls are present at the Michigan site (Pufahl et al. 2007). No information

regarding the ratio between whole spherules/'tektites' and spherule fragments was given; but the vesicular nature of the spherules and angular fragments is consistent with observations that the Cenozoic melt-drop microtektites are more vesicular close to their source craters (e.g., Fig. 10.10).

10.3.9 The Grænsesø (Greenland) Spherule/Ejecta Layer

The Grænsesø spherule layer is found in the low-grade Paleoproterozoic metasedimentary rocks of the Vallen Group in southwest Greenland (see Sect. 7.4). Estimates of the aggregate thickness of the Grænsesø spherule layer range between 15 and 25 cm (Table 10.4). No unmelted shock-metamorphosed mineral grains have been observed in this layer (Smith et al. 2006). The age of the Grænsesø spherule layer is not well known, but is apparently between 1.85 and 2.13 Ga. Thus, either the 1.849-Ga Sudbury impact structure or the 2.023-Ga Vredefort impact structure could be a possible source crater for the spherule layer. The distance from these craters to the location of the spherule layer at the time of the impact is not known, but position of continental landmasses for 2 Ga ago based on paleomagnetic data (Pesonen et al. 2003) suggests that Greenland was next to North America with the Grænsesø spherule layer site at about 15° N and the Vredefort structure in South Africa was about 45° S. This indicates that Sudbury was ~2000 km and Vredefort was ~7000 km from the Grænsesø spherule layer site at the time the spherule layer was formed.

The Sudbury structure is highly deformed, but probably about 250 km in diameter and may have had a transient crater diameter of between 90 and 130 km (Turtle et al. 2005). The thickness of an ejecta layer at 2000 km from Sudbury should be about 2 cm. Thus the aggregate thickness of the Grænsesø spherule layer is much thicker than the ejecta thickness expected from a 250-km-diameter crater (with an estimated transient crater diameter of 90 to 130 km) at a distance of 2000 km (Fig. 10.16). At this distance from the source crater (i.e., about 15 crater diameters), spherules should make up at ~60 % of the layer (Fig. 10.9b), and the aggregate thickness of spherules should be only ~1 cm. Thus the estimated aggregate thickness (15-25 cm) of the Grænsesø spherule layer is more than 15 times the expected thickness at 2000 km from Sudbury. At 7000 km the 300-km-diameter Vredefort structure with a transient crater diameter of 80 to 100 km (Turtle et al. 2005) should have produced a spherule-rich ejecta layer <0.2 mm thick (Fig. 10.16). Thus, neither crater would explain the observed thickness of the Grænsesø spherule layer very well, but the expected thickness of an ejecta layer from Sudbury fits better. However, at that distance from Sudbury we would expect abundant unmelted shock-metamorphosed ejecta (Fig. 10.16). On the other hand, the Grænsesø site would have been ~70 transient crater diameters from Vredefort and at that distance, we would expect very little (a few percent or less) unmelted shock-metamorphosed ejecta. Thus, if Vredefort were the source crater for the

Grænsesø spherule layer, this could explain the apparent lack of shocked mineral grains in the layer better than if the spherules came from Sudbury.

Unfortunately, neither the size distribution of the Grænsesø spherules nor the ratio between spherules and spherule fragments has been documented. The maximum diameter of the spherules is ~1.8 mm (Sect. 7.4.2). If the ratio between average size and maximum size is the same as for the Cenozoic microtektites, then the average size of Grænsesø spherules >125 μm in diameter should be ~600 μm (1800 μm/3) which is consistent with a large source crater (i.e., ~200 km in diameter or larger). If the layer were from Sudbury, we would expect that spherule fragments would make up ~10 to 40 % of the glass (spherules plus fragments), but if the layer were from Vredefort we would expect the spherule fragments to be very rare, making up less than 5 % and probably <1 %. According to Chadwick et al. (2001), the spherules have mostly circular cross-sections, but a minority has ovoid to pear-shaped cross-sections and a few are highly elongated with bilobate shapes. Although not specifically mentioned, no spherule fragments were observed. We believe that, at most, spherule fragments couldn't make up more than a few percent of the "glass" in the coarse sand size fraction. Thus, the lack (or nearly so) of spherule fragments is more consistent with the Vredefort structure being the source crater of the Grænsesø spherules (see Fig. 10.8).

In summary, neither Sudbury nor Vredefort appears to explain the estimated thickness of the Grænsesø spherule layer. Vredefort as the source crater would explain the apparent absence of unmelted shock metamorphosed grains and apparent lack, or nearly so, of spherule fragments in the layer better than would Sudbury. However, either the thickness estimates for the Grænsesø spherule layer are too high, or the suggested source craters were much closer than proposed, or the estimated transient crater diameters are too small. Alternatively, our distal impact ejecta model is incorrect, the spherules do not have an impact origin, or neither Sudbury nor Vredefort is the source crater for the Grænsesø spherule layer and there must be another large crater that was formed ~2 Ga ago.

10.3.10 The Early Paleoproterozoic Dales Gorge Spherule Layer

Ejecta make up about 65 % of the Dales Gorge spherule layer (Sweeney and Simonson 2008). We estimate that the aggregate thickness of this layer is ~6 cm. It is difficult to accurately determine the percent spherule fragments versus whole (or nearly so) spherules in spherule layers near the Archean-Proterozoic boundary (APB) because the shapes are generally modified due to compaction. However, in the Dales Gorge spherule layer, there are places where the interstitial cement is abundant. At these sites the shapes of the ejecta particles are well preserved (Fig. 8.3). The ejecta component of the spherule layer at these sites consists of spherules (70 %), fragments of spherules (11 %) and angular fragments (19 %) (Sweeney and Simonson 2008). No unambiguous shock-metamorphosed grains

have been reported for this layer, despite the fact that any shocked silicate grains should be unusually easy to recognize. Most Precambrian spherule layers show widespread evidence of reworking during deposition including an abundance of siliciclastic and/or volcaniclastic detritus admixed with the spherules by waves and currents. The Dales Gorge spherule layer was deposited by a high energy event that transported large intraclasts, but because it is a fine-grained chemical sediment, there is no significant admixture of quartz sand or other extrabasinal silicate detritus.

The angular fragments have been interpreted as lithic clasts and/or spherule fragments; however, both the spherules (including spherule fragments) and angular fragments have been replaced by other phases; no original phases are present. Our best estimate, based on textural features, is that at least $\sim$16 % of the angular fragments are spherule fragments and the remainder is probably a mixture of spherule fragments and lithic clasts. This indicates that the ejecta consist of 70 % spherules, a minimum of 14 % spherule fragments, and 16 % angular fragments, which could include both spherule fragments and lithic clasts (i.e., unmelted ejecta). If none of the angular fragments are fragments of spherules, this would indicate that $\sim$17 % of the "glass" particles are fragments. The textures of the Dales Gorge spherules appear to be similar to that of the dark cpx spherules rather than to that of the light-colored cpx spherules. It seems possible, therefore that the percent fragments versus distance from the source crater may follow the same, or very nearly so, trend as the Cenozoic microtektites. If so, this would indicate that the Dales Gorge site was $\sim 3000 \pm 1000$ km from the source crater at the time of the impact (see Fig. 10.8). At a distance of 3000 km, it would take an impact crater with a transient crater diameter of 250 km to produce a layer 6 cm thick and the layer would have been $\sim$12 transient crater diameters from the source crater. At this distance (in transient crater diameters) from the Chicxulub impact structure, the Chicxulub ejecta layer (K-T boundary) contains recognizable lithic clasts about the same size as the spherules (Schulte et al. 2003). Thus, we would expect some lithic clasts in the Dales Gorge layer. At the other extreme, if all of the angular fragments in the Dales Gorge ejecta are spherule fragments, then the percent of the glass that would have been fragments would be 30 % and the distance from the source crater would be $\sim 2000 \pm 1000$ km (Fig. 10.8). At a distance of 2000 km the transient crater size required to produce a 6-cm-thick ejecta layer would have been $\sim$180 km. In either of the scenarios proposed above, we would expect the Dales Gorge layer to contain shock metamorphosed mineral grains, as well as, lithic clasts. The apparent lack of any evidence of shock metamorphosed grains in the layer is not consistent with the model for Phanerozoic distal ejecta discussed above in Sect. 10.2. Possible reasons for the dearth of shocked grains in this and other APB spherule layers are discussed in Sects. 10.4 and 11.4.

10.3.11 The Neoarchean Bee Gorge Spherule Layer

The Bee Gorge spherule layer occurs near the APB and is found in the Bee Gorge Member of the Wittenoom Formation in the Hamersley Basin, Western Australia. The Bee Gorge spherule layer has been mapped over a larger area than any other Archean to early Paleoproterozoic spherule layer and has been traced over a distance of 330 km. The thickness and nature of the spherule layer changes systematically from the northwest to the southeast (see Sect. 8.2.3.4), but the size of the spherules and the aggregate thickness of the spherule layer remain about the same. The aggregate thickness of the spherules in this layer is ~1–3 cm (Table 10.4). Except for trace amounts of shocked rutile containing the high-pressure polymorph TiO_2II (Smith et al. 2010), no unmelted ejecta (lithic clasts, shocked mineral grains) have been found in the Bee Gorge spherule layer. However, shocked minerals would be harder to isolate in the Bee Gorge spherule layer than in the Dales Gorge layer because of the introduction of considerable quartzose siliciclastic detritus during the high-energy event that deposited the layer. It has been estimated that the projectile responsible for the impact that produced the Bee Gorge spherule layer was ~4.9 km in diameter (Hassler et al. 2000). A 4.9-km-diameter projectile would produce a crater ~90 km in diameter (assuming that the crater diameter is ~18 times the diameter of the projectile as for the Chicxulub impact). Such a crater would have had a transient crater diameter of ~54 km (see footnote "a" to Table 10.1 for the equation used to calculate the transient crater size). Hassler et al. (2000) estimated that the Bee Gorge spherule site was between 2000 and 8000 km from the source crater at the time of the impact based on sedimentary structures that they attributed to tsunami waves generated by the impact. However, based on McGetchin et al.'s (1973) equation that relates ejecta thickness to size and distance from the source crater, we calculate that at a distance of 2000 km a crater with a transient crater diameter of 54 km would only produce an ejecta layer ~0.7 mm thick and at 8000 km distance the layer would only be ~10 μm thick. An ejecta layer from a transient crater this size would be ~2 cm thick at a distance of ~640 km or ~12 transient crater diameters. Furthermore, based on the aggregate thickness of the spherule layer and the average size of the spherules (~ 600 μm), we calculate that the there are ~18,000 spherules/cm^2 which indicates a distance from the source crater of no more than ~10 transient crater diameters (Fig. 10.2). If the source crater had a transient diameter of ~54 km as suggested above, that would be a distance of ~540 km which is in good agreement with a distance of ~640 km based on the thickness of the layer. However, the distance derived from the estimated number of spherules/cm^2 is based on data from microtektites and the Bee Gorge spherules are believed to be primarily altered microkrystites rather than microtektites. At this distance the ejecta layer should contain lithic clasts as well as mineral grains, but the clasts should generally be smaller than the spherules and may be difficult to recognize in these ancient deposits where the original phases have been replaced.

10.3.12 Paleoarchean Spherule Layers

The Paleoarchean spherule layers are more difficult to explain and little can be said about the size of, or distance to, the source crater for these spherule layers using the Phanerozoic model for distal ejecta layers. The aggregate thicknesses of the Paleoarchean spherule layers are generally ≥ 5 cm (Table 10.4; Lowe et al. 2003; Simonson and Glass 2004). No unmelted ejecta (e.g., shocked quartz with PDFs, high-pressure phases) have been found in any of the Paleoarchean spherule layers. Since no impact structures this old have been identified, none of these older impact ejecta layers have been associated with an impact structure. Like the rest of the Precambrian spherule layers, the Paleoarchean layers have generally been reworked by waves and currents so that the thickness of each varies by more than an order of magnitude locally and the layers contain variable amounts of admixed detritus (Lowe and Byerly 1986; Lowe et al. 1989, 2003). In addition, most of these layers have been subjected to regional metamorphism of at least greenschist level. Furthermore, it is not possible to trace the Paleoarchean spherule layers over great distances because of the high degree of tectonic deformation. The fact that these layers appear to be composed primarily of spherules coupled with the estimated aggregate thicknesses of these layers (Table 10.4) suggest that these spherule layers are distal impact ejecta layers from large impact craters rather than proximal layers from small craters. However, the apparent absence of shock-metamorphosed grains in the Paleoarchean spherule layers is difficult to explain in either case.

Based on data from Phanerozoic spherule layers, unmelted, shocked ejecta should be found globally in ejecta layers from craters with transient crater diameters ≥ 100 km and half-way around the globe the ejecta layer from a crater with a transient diameter of 100 km should be less than 20 μm thick (Fig. 10.12). Thus, a spherule layer ≥ 5 cm should contain unmelted, shock-metamorphosed ejecta no matter how far it is from the source crater. The occurrence of thick spherule layers without any unmelted ejecta is therefore not possible based on data from Phanerozoic impact ejecta/spherule layers. Perhaps a combination of their great age and metasomatism, which resulted in the replacement of most silicate minerals, with the notable exception of quartz crystals, destroyed shock metamorphic effects in the layers. However, high-pressure phases and shocked quartz with PDFs have survived greenschist metamorphism in impact structures as old as 2 Ga. Some authors have proposed that the lack of shocked quartz grains in the Paleoarchean spherule layers may be due to the impacts taking place in oceanic crust (e.g., Lowe et al. 1989). However, none of the heavy minerals in the Paleoarchean S4 spherule layer, including those indicative of a mafic source (e.g., anatase, chromite, rutile), exhibit conclusive evidence of shock metamorphism (Zullo et al. 2010). The problem of the lack of shocked mineral grains in the Paleoarchean spherule layers is discussed in more detail in Sect. 11.4, question 4.

10.4 Secular Variations in Distal Impact Ejecta Layers: Implications

Precambrian distal impact ejecta layers are similar to Phanerozoic distal impact ejecta layers in many respects. The more distal portions of both Precambrian and Phanerozoic ejecta layers are dominated by impact spherules (microtektites, microkrystites) and in both cases the spherules are predominantly sand and silt sized. Spherical shaped spherules are the most common, but rotational shapes (e.g., teardrops, dumbbells), indicative of melt-drop spherules, often occur.

The main differences between Precambrian and Phanerozoic spherule layers are: (1) the generally greater thickness of the Precambrian spherule layers (Table 10.4); (2) internal textures of many of the Precambrian spherules that suggest mafic compositions (although some of the Late Eocene cpx spherules have mafic textures); (3) lack of unmelted shock-metamorphosed grains in the older (>3 Ga) Precambrian spherule layers (Simonson and Harnik 2000); (4) the presence of altered microkrystites with infilled vesicles and teardrop and dumbbell shapes in the Precambrian spherule layers (i.e., condensate spherules); and (5) geochemical anomalies, indicating the presence of a meteoritic component, associated with most of the Precambrian distal spherule/ejecta layers, but with less than half of the Phanerozoic spherule/ejecta layers. The Phanerozoic spherule layers rarely exceed 1 cm in aggregate thickness, whereas the aggregate thickness of many Precambrian spherule layers is 5 cm or more (Simonson and Glass 2004). The greater thickness of most of the Precambrian spherule layers suggests that they are the result of large impacts which would have produced craters larger than any that are known of Phanerozoic age.

Some investigators have used the size of the Paleoarchean spherules or the aggregate thickness and geochemistry of the Paleoarchean S2, S3, and S4 spherule layers to estimate the size of the impacting bodies that formed the spherule layers. Estimates of the diameters of the projectiles responsible for these Paleoarchean spherule layers range from 12 to 160 km (Byerly and Lowe 1994; Melosh and Vickery 1991; Shukolyukov et al. 2000; Kyte et al. 2003). All of these proposed projectile diameters are larger than the proposed size for the Chicxulub projectile and the estimated crater sizes are also proportionately larger. Based on a ratio of 18 between the crater size and projectile size, the same as for the Chicxulub impact (i.e., 180 km/10 km = 18), the estimated diameters of the S2, S3, and S4 source craters would range between ~220 and 2900 km.

All the Precambrian spherules have been altered and the glass and any crystalline phases that were originally present have been replaced with the exception of spinel microlites found in some of the spherules in one Paleoarchean spherule layer. Fortunately, in most cases what is interpreted as the original crystalline texture has been preserved. Most impact spherules of Neoarchean to early Paleoproterozoic age contain fibrous to lath-shaped microlites that have been replaced with K-feldspar. These microlites typically radiate inward from the surface of the spherule in confocal aggregates (Fig. 8.3e). Less commonly the

lath-shaped microlites are randomly oriented and have hollow centers and split ends (Figs. 8.12b,c and 8.13a). The radiating microlites may have formed by devitrification, whereas the random microlites probably formed during cooling. The spherules with randomly oriented laths have textures similar to basaltic glasses. Recently, phlogopite pseudomorphs of skeletal ferromagnesian crystals such as pyroxene and olivine have been recognized in spherules in two layers in the Hamersley (Western Australia) and Griqualand West (South Africa) successions that may have been formed by the same impact (Hassler et al. 2011). These textures suggest the spherules were mafic or possibly ultramafic in composition.

In addition to shocked mineral grains, shocked rock fragments (lithic clasts) have been found in almost all of the Phanerozoic impact ejecta/spherule layers. Clasts have been reported in most early Precambrian spherule layers, but generally they have been interpreted as rip-up clasts, rather than impact ejecta. Since their discovery in the mid 1980's only one shocked quartz grain with PDFs has been reported in any of the Precambrian spherule layers older than 2.4 Ga, and it was found in a Neoarchean layer (Jeerinah; Sect. 8.2.6.1). Some planar features, which might be relict PDFs, have been found in a few quartz grains from the Carawine spherule layer, but their identification as PDFs has not been confirmed (Glass et al. 2007). Other than the single shocked quartz grain mentioned above, the only other shock metamorphosed grains found in the spherule layers older than 2.4 Ga are trace amounts of rutile containing the high-pressure polymorph TiO_2II found in three Neoarchean spherule layers in Western Australia (the Carawine, Jeerinah, and Bee Gorge) and one spherule layer from South Africa (the Monteville) (Smith et al. 2010). However, three of these spherule layers may have been formed by the same impact $\sim$2.63 Ga ago: the Jeerinah, Carawine, and Monteville. No shock-metamorphosed grains have been identified in any of the Paleoarchean spherule layers.

If the Precambrian spherule layers older than 2.4 Ga are found within about 30 crater diameters of their source craters, then unmelted ejecta (mineral grains, lithic clasts) exhibiting evidence of shock metamorphism should make up a significant fraction (i.e., greater than $\sim$20 %) of the ejecta layer (see Sect. 10.1.2.6.3). If the spherule layers represent distal ejecta layers >30 crater diameters from the source crater, then the thickness of the spherule layers indicates that the impacts must have been energetic enough to form craters >200 km in diameter and shocked mineral grains should be present as they are in the K-T boundary ejecta layer. Thus, the almost complete absence of shocked mineral grains in the spherule layers older than $\sim$2.4 Ga is not easily explained.

The absence of shocked quartz in nearly all the spherule layers >2.4 Ga old could be explained if the impacts were into mafic crust. It seems likely that continental crust was less abundant more than 2.4 Ga ago (Powell 2001; Taylor and McLennan 2009) and thus most impacts would have been into basaltic crust containing little, if any, quartz. Additional possible explanations for the lack of shocked mineral grains in the Paleoarchean spherule layers include: (1) age, (2) metamorphism/diagenesis, (3) thin lithosphere, and (4) atmospheric heating. See Sect. 11.4, question 4, for discussion of these possibilities.

Precambrian spherules with relict quench textures have been interpreted as diagenetically altered microkrystites (Simonson et al. 1998; Sweeney and Simonson 2008). These spherules fall into two main groups: 1) spherules with randomly oriented scattered lath-like crystals (basaltic texture), and 2) those with crystallized margins or rims. The spherules with basaltic textures are generally spherical in shape, but, unlike the Late Eocene cpx spherules and perhaps the K-T boundary layer microkrystites, some contain features interpreted to be relict vesicles (Fig. 10.18). The spherules with crystallized rims are also mostly spherical in shape, but, in contrast to the cpx spherules, teardrop and dumbbell shapes have also been observed and some appear to have relict vesicles (Fig. 8.3). If the crystallized rims originally formed by crystallization in flight as proposed by Artemieva and Simonson (2012) and/or were formed after deposition (e.g., by palagonitization and later crystallization), then they could be either altered microtektites or microkrystites. The rotational shapes, presence of vesicles, and general lack of Ni-rich spinel crystals suggest that they formed as melt ejecta from a mafic crust, rather than by condensation from an impact plume of vaporized target and projectile as has been suggested for the Late Eocene cpx spherules and the K-T boundary microkrystites.

Most Precambrian spherule layers are associated with a Cr isotope anomaly and/or a strong Ir anomaly indicating the presence of a meteoritic component from the impacting body; but, less than half of the Phanerozoic spherule/ejecta layers are known to be associated with a strong geochemical anomaly indicative of a meteoritic component (see Table 11.1). However, not all the layers have been analyzed for the presence of a meteoritic component.

In summary, the Precambrian distal impact ejecta/spherule layers differ from most Phanerozoic distal ejecta/spherule layers by being on average thicker, having few or no mineral grains showing evidence of shock metamorphism, and by containing many spherules with relict crystalline textures suggestive of a basaltic composition. The relict quench textures indicate that these spherules were microkrystites rather than microtektites. Some of the spherules with relict textures have dumbbell and teardrop shapes and some contain relict vesicles. This suggests that they were formed as melt droplets rather than as condensation droplets. The relict textures of the spherules and apparent lack of shocked quartz, except for a single shocked quartz grain, in the Precambrian spherule layers older than $\sim$2.4 Ga could be explained if the impacts were into oceanic crust (i.e., basaltic rock).

Chapter 11
Distal Impact Ejecta Layers and Earth History

11.1 Known Distal Impact Ejecta Layers

As of the beginning of 2012, at least 23 probable or confirmed occurrences of distal impact ejecta or distal impact ejecta layers had been reported in the literature, including: five in the Cenozoic, three in the Mesozoic, three or possibly four in the Paleozoic, and twelve in the Precambrian (Table 11.1). In addition to the five well-defined distal ejecta layers, there are at least nineteen other possible/probable or proposed Cenozoic ejecta layers or occurrences (Table 11.1). Many of the Cenozoic ejecta are tektites or impact glasses not found in situ in stratigraphic sections (e.g., Tikal tektites, Darwin glass, South-Ural glasses, High Na/K "australites", Central European tektites, urengoites, Libyan Desert Glass), or are probably proximal ejecta (Rio Cuarto glasses, Centinela del Mar glasses, Mar del Plata glasses, Chasicó glasses). The Eltanin spherule layer in the South Pacific (Bellingshausen Sea) was produced by an ocean impact, but the spherules are just melted meteoritic material. The North Pacific microtektites, Tasman Rise microtektites, and Nuussuaq spherules may belong to distal impact ejecta layers, but identification as such would be more convincing if they were found at additional sites. Furthermore, their stratigraphic ages need to be better defined. There is no definitive evidence for a distal impact ejecta layer at the Younger Dryas or associated with the Paleocene-Eocene event. Thus, the only well-defined Cenozoic distal ejecta layers found in situ in stratigraphic sections are the Australasian, Ivory Coast, and North American microtektite layers, the cpx spherule layer, and perhaps the Darwin glasses. Only Darwin glasses, the Ivory Coast and North American microtektite layers, the cpx spherule layer, and the Central European tektites have been linked to known or suspected impact craters/structures.

The three Mesozoic distal impact ejecta layers reported in the literature are: the Cretaceous-Tertiary boundary layer (Chicxulub ejecta), Manson crater ejecta layer, and the Late Triassic spherule/ejecta layer. Several authors have suggested the presence of an impact ejecta layer associated with the Triassic-Jurassic

B. P. Glass and B. M. Simonson, *Distal Impact Ejecta Layers*, Impact Studies,
DOI: 10.1007/978-3-540-88262-6_11, © Springer-Verlag Berlin Heidelberg 2013

boundary; however, evidence of impact ejecta at the Triassic-Jurassic boundary is in dispute.

The four Paleozoic distal ejecta layers are: the Qidong spherule layer, the Senzeille/Hony (Belgium) spherule layer, the Alamo Breccia deposits, and possibly a layer at the Devonian–Carboniferous boundary. The Qidong and Senzeille/Hony spherules are probably microtektites, but they need to be found at additional sites in order to estimate the size and location of their source crater. The Alamo Breccia layer is confirmed as an impact ejecta layer, but most of the occurrences are probably proximal. A few apparently distal sites have been described, but shock-metamorphic data are weak or missing. Numerous researchers have proposed that there may be evidence of an impact at the Permian–Triassic boundary. It appears that there is a meteoritic component in the boundary layer, but evidence of shocked quartz grains has been disputed. Shocked quartz grains have been reported in Middle Devonian deposits in Morocco, but identification of the PDFs has been questioned by some researchers. Except for perhaps the Alamo Breccia ejecta, none of the Paleozoic ejecta layers have been convincingly linked to a known impact crater/structure, although some possibilities have been proposed.

Of the 20 Precambrian ejecta/spherule layers, four are <2.2 Ga old and two of these are associated with known impact craters: the Acraman ejecta in South Australia and the Sudbury ejecta found in the Lake Superior area of North America. Many of the Sudbury ejecta sites are proximal, the remainder are the most proximal part of the distal ejecta. The Acraman ejecta sites are also the more proximal part of the distal ejecta. The other two layers are the Grænsesø spherule layer in western Greenland and the Karelian spherule layer near Karelia, Russia. The Grænsesø spherule layer could represent ejecta from either the Sudbury or the Vredefort impact structure. The Karelian spherule layer may be from the Vredefort impact structure in South Africa. No evidence of shock metamorphism has been found in either layer. Eight of the Precambrian ejecta layers are found close to the Archean-Proterozoic boundary. These layers are composed of sand sized spherules with only a trace of shock-metamorphosed grains in four of the layers. The eight Archean–Proterozoic boundary spherule layers may be the result of only four impacts. There are probably eight Paleoarchean spherule layers, which may represent seven impacts. No shock-metamorphosed grains have been identified in any of the Paleoarchean spherule layers. Furthermore, no large impact structures with a well-determined age >2.1 Ga are known on Earth at this time and thus none of the Archean–Proterozoic boundary or Paleoarchean spherules have been linked to any known impact craters/structures.

11.1.1 Preservation of Distal Impact Ejecta Layers

As previously pointed out, distal impact ejecta layers cover much larger areas than do their source craters and on that basis alone are more likely to be preserved at

Table 11.1 Distal impact ejecta layers (italics), distal ejecta, and probable/possible and proposed distal impact layers or occurrences

Ejecta or ejecta layer	Age (Ma)	Evidence of impact origin[a]	Aggregate thickness (cm)[b]	Source crater	Projectile type[c]	Section[d]
Cenozoic						
Rio Cuarto glasses	<0.006	L, DG, Zr > Bd	n/a	Rio Cuarto crater field?	Chondrite(?)	4.10.1
Younger Dryas	~0.013	Ir, Fu, ND	Unknown	Unknown	Unknown	4.9.1
Rio Cuarto glasses	~0.11	L, DG, Zr > Bd	n/a	Unknown	Unknown	4.10.1
Lower Centinela del Mar	~0.23	SMG	Unknown	Unknown	Unknown	4.10.1
Upper Centinela del Mar	~0.44	SMG	Unknown	Unknown	Unknown	4.10.1
Rio Cuarto glasses	~0.57	?	Unknown	Unknown	Unknown	4.10.1
Australasian microtektite	~0.78	SMG, Ir, Tek	<0.001−0.2	Unknown	Unknown	4.2
Darwin glass	~0.8	L, Coe, HNi	Unknown	Darwin	Unknown	4.8.2
Tikal tektites	~0.8	NM, LW, RFe	Unknown	Unknown	Unknown	4.8.1
Ivory Coast microtektite	~1.1	L, Tek	<0.001	Bosumtwi	Chondrite	4.3
North Pacific microtektites	~2.2	MOC, HNi, HCo, HIr	4×10^{-4}	Unknown	Unknown	4.7.1
Mar del Plata glasses	~3.8	Zr > Bd	?	Unknown	Unknown	4.10.1
Tasman Rise microtektites	5 to 12	MOC	(9×10^{-5})	Unknown	Unknown	4.7.2
Bahia Blanca glasses	~5	SMG, DG	?	Unknown	Unknown	4.10.1
South Ural glasses	~6	MOC, LW, RFe	Unknown	Unknown	Unknown	4.8.3
Chasicó glasses	~9	SMG, DG	?	Unknown	Unknown	4.10.1
High Na/K "australites"	~10	MOC, L	n/a	Unknown	Unknown	4.8.4
Central European tektites	~15	L, LW, RFe	n/a	Ries	Unknown	4.4
Urengoites	~24	L, LW, RFe	n/a	Unknown	Unknown	4.8.6

(continued)

Table 11.1 (continued)

Ejecta or ejecta layer	Age (Ma)	Evidence of impact origin[a]	Aggregate thickness (cm)[b]	Source crater	Projectile type[c]	Section[d]
Libyan Desert Glass	~29	L; Zr > Bd; HCo, HNi, HIr w/CR; OsI	n/a	Unknown	Unknown	4.8.5
North American microtektite	~35	L, SMG, Tek	<0.01–8	Chesapeake Bay	Unknown	4.5
Cpx spherule	~35	SMG, Ir, CrI, NiSp	<0.001–0.06	Popigai	Chondrite (LL?)	4.6
Paleocene-Eocene event	~55	Ir	Unknown	Unknown	Unknown	4.9.3
Nuussuaq spherule	~60	NiSp, Ir	~30–60	Unknown	Unknown	4.7.3
Mesozoic						
K-T boundary	~65	SMG, Ir, CrI, NiSp	0.3–25+	Chicxulub	Carbonaceous chondrite	5.2
Manson ejecta	~74	SMG	3–25	Manson	Chondrite	5.3
Triassic-Jurassic boundary	~200	SMG (?), Ir	Unknown	Unknown	Unknown	5.5
Late Triassic spherule	~214	SMG	~1.6	Manicouagan?	Unknown	5.4
Paleozoic						
Permian–Triassic boundary	~253	SMG(?), Ir, CrI, Met, Sph	Unknown	Unknown	Unknown	6.3.1
Devonian-Carboniferous boundary	~359	SMG	Unknown	Unknown	Unknown	6.3.2
Qidong spherule	~372	L?, Ir?	Unknown	Unknown	Unknown	6.2.2
Senzeille/Hony sph.	~374	L, LW	<0.001	Unknown	Unknown	6.2.3.3

(continued)

Table 11.1 (continued)

Ejecta or ejecta layer	Age (Ma)	Evidence of impact origin[a]	Aggregate thickness (cm)[b]	Source crater	Projectile type[c]	Section[d]
Frasnian-Famennian boundary	~376	Sph	Unknown	Unknown	Unknown	6.2.3.4
Alamo breccia	~377	SMG, Ir	Unknown	Unknown	Achrondrite?	6.4
Middle Devonian	~388	SMG(?)	Unknown	Unknown	Unknown	6.3.3
Proterozoic						
Acraman ejecta	~578	SMG, Ir, OsI	0.5–3.5	Acraman	Chondrite	7.2
Sudbury ejecta	1850	SMG, Ir	~25	Sudbury	Unknown	7.3
Grænsesø spherule	~1990		~25	Sudbury?	Unknown	7.4
Karelian spherule	1980–2060	Ir	~12[j]	Vredefort?	Unknown	
Neoarchean to Early Paleoproterozoic						
Dales Gorge spherule[e]	~2490	Ir, CrI	~6	Unknown	Chondrite	8.2.2
Kuruman spherule[e]	~2490		0.5	Unknown	Unknown	8.3.2
Bee Gorge spherule	2540	SMG, Ir	~1–3	Unknown	Chondrite	8.2.3
Paraburdoo spherule[f]	~2570	Ir	2	Unknown	Unknown	8.2.4
Reivilo spherule[f]	~2560	Ir	2–2.5	Unknown	Chondrite	8.3.3
Carawine spherule[g]	2630?	SMG	~30	Unknown	Chondrite	8.2.5
Jeerinah spherule[g]	2630	SMG, Ir, CrI	0.4–20	Unknown	Ordinary or enstatite chond.	8.2.6
Monteville spherule[g]	~2600	SMG, Ir	~6	Unknown	Chondrite	8.3.4
Paleoarchean						

(continued)

Table 11.1 (continued)

Ejecta or ejecta layer	Age (Ma)	Evidence of impact origin[a]	Aggregate thickness (cm)[b]	Source crater	Projectile type[c]	Section[d]
S5 spherule	~3230		<50	Unknown	Unknown	
S4 spherule	<3243	Ir, CrI	12	Unknown	Carbon. chond.	9.2.1
S3 spherule	3243	Ir, CrI, NiSp	~30	Unknown	Carbon. chond.	9.2.2
S2 spherule	3260	Ir, CrI	~10–70	Unknown	Carbon. chond.	9.2.3
S6 spherule	~3300		<50	Unknown	Unknown	
S7 spherule	3400		<50	Unknown	Unknown	
S1 spherule[h]	3470	Ir	~6	Unknown	Unknown	9.2.4
Warrawoona sph.[h, i]	3470		~5	Unknown	Unknown	9.3.1

The spherule layers (S5, S6, and S7) in italics were newly discovered at the time of this writing and very little has been published about them. *n/a* not applicable

[a] The Cenozoic microtektite layers are associated with known tektite strewn fields of impact origin. The spherules in the other spherule layers are believed to have an impact origin based on their size, shape, petrography, and in some cases composition, in addition to the other information given in this column. *Coe* coesite, *CR* chondritic ratios, *CrI* chromium isotope data, *DG* diaplectic glass, *Fu* fullerenes containing ^{3}He, *HCo* high Co content, *HNi* high Ni content, *HIr* high Ir content, *Ir* Ir anomaly, *L* lechatelierite, *LW* low water content, *Met* meteorite fragments, *MOC* major oxide content, *ND* nanodiamonds, *NiSp* Ni-rich spinel, *NM* no microlites, *OsI* osmium isotope data, *RFe* reduced iron, *SMG* shock-metamorphosed grains, *Sph* spherules, *Tek* associated with a tektite strewn field, *Zr* > *Bd* zircon decomposed to baddeleyite plus SiO_2

[b] The aggregate thickness is thickness of just the ejecta in the ejecta layer at a given site. It can be estimated by multiplying the volume percent ejecta in an ejecta layer by the thickness of the ejecta layer. For example, if an ejecta layer is 20 cm thick and contains 40 % impact spherules and 5 % unmelted ejecta by volume, the aggregate thickness would be 20 cm × 0.45 = 9 cm

[c] Chondrite is usually an ordinary chondrite unless otherwise stated. *Carbon. chond.* carbonaceous chondrite

[d] Section refers to the section in the book where the layer is discussed

[e] The Dales Gorge and Kuruman spherule layers may have been formed by the same impact

[f] The Paraburdoo and Reivilo spherule layers may have been formed by the same impact

[g] The Carawine, Jeerinah, and Monteville spherule layers may have been formed by the same impact

[h] The S1 and Warrawoona spherule layers may have been formed by the same impact

[i] Also known as the Apex Basalt spherule layer

[j] Aggregate thickness is based on an average spherule diameter of 850 μm and a layer thickness of 1.23 m with 5068 spherules in an area 2.5 by 123 cm, which suggests a spherule abundance of ~9 vol%. Data from Huber et al. (2012)

least locally. However, distal ejecta layers are generally thin unless they have been reworked, in which case they can be highly diluted. In either case, they can be easily overlooked, and often have been, unless one is looking for them, and even then they can be difficult to find and identify. Large impacts in ocean basins can generate tsunamis which can rework the ejecta locally and even in the shallow marine environments on the other side of the ocean basin.

Distal ejecta more than $\sim$30 crater diameters away from the source crater are composed primarily of spherules consisting entirely of glass (microtektites) or mixtures of glass and primary crystallites (microkrystites) with only traces of shocked mineral grains. Spherules are much easier to recognize in the field than are shocked mineral grains. However, since glass is unstable, the spherules are more easily destroyed or altered to other phases than are the shocked mineral grains. The Australasian, Ivory Coast, and North American microtektites are unaltered except for some dissolution. However, many of the late Eocene cpx spherules have a missing crystalline phase (or phases) and some, in reducing environments (e.g., upper continental slope), have been partly or completely replaced by pyrite. At Massignano, Italy, the cpx spherules have been replaced with clay (nontronite). Nearly all of the K–T boundary spherules (microtektites and microkrystites) have been replaced by a wide variety of phases (e.g., kaolinite, smectite, goyazite, calcite, K-feldspar, jarosite, glauconite) depending on the composition of the spherules and the environment of deposition. The outer layer of the microtektite-like spherules in K–T boundary deposits appears to have undergone palagonitization or devitrification by some other process (e.g., see Sect. 11.3, question 4). This outer layer was then replaced with another phase and the glass core underwent dissolution to produce a hollow spherule which was frequently filled by another phase. The Late Triassic spherules found near Bristol, England, appear to have also undergone a similar alteration process with the outer layer being replaced with clay (glauconite?) and the core being filled with calcite. All of the Precambrian spherules have been replaced by other phases. On the other hand, microtektites from the late Devonian spherule layers near Qidong, China, and in Belgium are still composed of silicate glass. Preservation of the Belgian microtektites has been attributed to their low water content and rapid burial in an impervious clay/shale layer with a high content of fine-grained silica.

The Cenozoic microtektite/microkrystite layers are best preserved in deep-sea environments. However, all but the thickest part of the layers close to the source craters have been extensively bioturbated so that a layer that was originally $<$1 mm in thickness is usually spread vertically over an interval of tens of centimeters or even a meter or more. Precambrian spherule layers likewise are preserved primarily in marine successions and most were deposited below wave base on continental margins. The lack of bioturbation in Precambrian sediments means that in theory the Precambrian spherule layers should be better preserved and less diluted by local sediments than their Phanerozoic counterparts. However, in most cases the Precambrian spherule layers occur in anomalously coarse beds indicating a high-energy event in an otherwise low-energy environment. The high-energy processes could involve impact-produced tsunamis, impact-induced bottom

return flow and/or turbidity currents directed downslope, or sedimentary gravity flows initiated by failure of impact-weakened basin margin slopes (Simonson et al. 1999; Hassler et al. 2000; Hassler and Simonson 2001; Lowe et al. 2003). A few of the Precambrian spherule layers that have been recognized to date were deposited ballistically into ambient low-energy environments without subsequent reworking.

11.2 Distal Impact Ejecta Layers: Some Geological Applications

11.2.1 Bioturbation Studies

Deposition of microtektites after an impact is a geologically instantaneous event and the microtektites should have been deposited in discrete layers on the ocean floor. However, Phanerozoic microtektites are found dispersed vertically over an interval of tens of centimeters or more. This vertical dispersion is believed to be due primarily to bioturbation. Guinasso and Schink (1975) developed a model to describe biological mixing of sediments (bioturbation). They used the vertical distribution of microtektites to estimate some mixing parameters. They concluded that the maximum mixing depth was between 17 and 40 cm. During bioturbation the microtektites were spread vertically and the peak abundance was shifted downward. They proposed that the original depth of sedimentation of the microtektites could be found by calculating the weighted mean depth of the microtektites. They found that the peak abundance was shifted down between 0 and 15 cm, but in most cores the shift was less than 9 cm. Ruddiman et al. (1980) studied size and shape dependency in deep-sea sediments using the vertical distributions of different size fractions of volcanic ash and microtektites in the same cores. They found similar amounts of reworking for the different size fractions and for volcanic ash (angular shard-like particles) and microtektites (smooth rounded particles). From this they concluded that significant lead/lag offsets in various paleoclimatic signals do not result from size- or shape-selective mixing.

11.2.2 The Australasian Microtektite Layer, the B-M Reversal, and PDRM

The Australasian microtektite layer is found throughout most of the Indian Ocean, the South China, Philippine, Sulu, and Celebes Seas, and western equatorial Pacific, an area equivalent to ~ 10 % of the Earth's surface. The layer is generally found in close proximity to the Brunhes–Matuyama (B–M) reversal boundary. Geomagnetic reversal boundaries are widely used for time-stratigraphic correlation. However, in the 1960s it was recognized that the peak abundance of

Australasian microtektites often occurred above the B–M reversal boundary, sometimes right on it, and rarely below it. Both the Australasian microtektite layer and the B–M reversal boundary were supposed to be time-stratigraphic horizons. However, because the sediments near the sediment–water interface are highly porous and poorly compacted, during a reversal of the Earth's magnetic field magnetic particles in the uppermost sediment column can be oriented in the direction of the new field; thus the reversal boundary is shifted down in the sediment to a depth where the magnetic particles are too compacted to be realigned with the new field direction. This is referred to as post-depositional remanent magnetization (PDRM) and the depth below which the magnetic particles cannot be realigned to the new field direction is the lock-in depth or depth of acquisition. Burns (1989) used microtektite data from 20 Australasian microtektite-bearing cores to show that the average depth of acquisition was 34 ± 7 cm. He was also able to show that the Australasian microtektite event occurred $\sim 12 \pm 6$ ka before the B-M reversal. Whether or not the Australasian microtektite layer occurred above, on, or below the B-M reversal boundary depends on the depth of acquisition and sedimentation rate.

11.2.3 Time-Stratigraphic Correlation

Like volcanic ash layers, distal impact ejecta layers record an instantaneous event and can thus be used for chronostratigraphic correlation. Like ash layers they can occur over large areas of the Earth's surface and can be preserved in a wide range of depositional environments, but are best preserved in low-energy environments. However, they are better than ash layers in several respects. Large impacts can produce global ejecta layers, whereas ash layers are useful only for local or regional correlation. Each impact only produces a single ejecta layer, but volcanic eruptions can produce numerous ash layers over an extended period of time, which can make correlation difficult.

We already mentioned the relationship between the Australasian microtektite layer and the Brunhes-Matuyama reversal boundary. The North American microtektites are found in upper Eocene sediments well below the Eocene–Oligocene (E–O) boundary. In the early 1980s, the age of the E-O boundary was given as 37.5 Ma. At that time, the North American microtektites were thought to have an age of ~ 34 Ma and Glass and Crosbie (1982) estimated that there is about 1.9 Ma between the microtektite layer and the E-O boundary. This suggested an age of 32 ± 1 Ma for the E-O boundary, which is close to the presently accepted age of 33.9 Ma (the 2009 Geologic Time Scale; Walker and Geissman 2009). However, if we use the most recently published age of ~ 35.5 Ma (Obradovich et al. 1989; Albin and Wampler 1996) for the North American tektites (and presumably microtektites), this indicates an age of ~ 33.6 Ma for the E–O boundary, which is even closer to the presently accepted age.

Precambrian rocks are generally devoid of fossils that can be used for correlation. However, several spherule layers have been correlated between South Africa and Western Australia (Byerly et al. 2002; Simonson et al. 1999, 2009b; Goderis et al. 2012). If confirmed, these correlations should allow researchers to compare the timing of events between these two continents. Correlations using sperule layers within Precambrian basins have already led to the realization that major stratigraphic boundaries generally thought of as time planes are in fact time-transgressive. The best examples are the contacts between the Onverwacht and Fig Tree Groups in the Barberton Greenstone Belt (Fig. 9.3; Lowe et al. 2003) and the Fortescue and Hamersley Groups in the Hamersley Basin of Western Australia (Fig. 8.1; Rasmussen et al. 2005: Hassler et al. 2005).

11.2.4 Cratering Mechanics and Plume Conditions

Tektites and microtektites are homogeneous, dense, silicate glass bodies with low water contents and reduced iron. Geochemical (^{10}Be) studies indicate that the Cenozoic tektites were formed from surface sedimentary deposits (Koeberl 1994; Serefiddin et al. 2007). Folco et al. (2010b) have shown that the average alkali contents of the Australasian microtektites decrease with distance from the source crater. In addition, Herzog et al. (2008) found significant variations in potassium isotope ratios in some Australasian microtektites, which suggest evaporation of isotopically light K and condensation of potassium during the cratering process and/or in the vapor plume. Prasad et al. (2010) have shown that the percent Australasian microtektites with impact microcraters, and the spatial density of impact pits/microcraters on the surfaces of the microtektites, decrease with distance from the source crater. The microcraters are small close to the predicted source crater location in Indochina, but are larger at greater distances. Prasad et al. (2010) proposed that the smaller microcraters were formed by hypervelocity impacts of small objects, but the large microcraters were formed at relatively low velocities by larger objects. The impacts that produced the microcraters appear to have taken place as the particles fell back to Earth and they indicate the frequency and velocity of interparticle collisions during the descent stage. A few researchers have modeled tektite formation during an impact in order to explain some of these observations (e.g., O'Keefe and Ahrens 1982; Artemieva 2008).

Several observations of the nature of the K–T boundary distal ejecta layer have resulted in attempts by researchers to model them. For example, it has been observed that within several 1000 km of Chicxulub, the K–T boundary ejecta occur as a couplet with a thick lower microtektite layer overlain by a thin layer containing microkrystites with Ni-rich spinel, shocked quartz, and a positive Ir anomaly. Vickery et al. (1992) have modeled large impacts to show that they can produce such a couplet. Another observation is that beyond about 4000–6000 km the K–T boundary ejecta layer has a fairly uniform thickness (Smit 1999) rather than continuing to decrease exponentially as would be expected.

Goldin and Melosh (2008) modeled the ejection and transport of the distal ejecta particles (spherules) and found that as the spherules come back down through the atmosphere the base of the spherule layer becomes unstable and density currents form, some of which transport the spherules horizontally, producing a more uniform distribution of spherules over the Earth's surface. Artemieva and Morgan (2009) proposed a similar model to explain why the ejecta layer is apparently uniform in thickness beyond 4000–6000 km. As the spherules reenter the atmosphere, the atmosphere is heated and undergoes expansion causing ejecta to move horizontally as well as downward. They call this process "floating of impact debris in the atmosphere". They proposed that this process can carry shocked mineral grains farther from the source crater than is possible by simple ballistic transport. Finally, we note that Krull-Davatzes et al. (2006) have interpreted vertical variations in spherule textures and compositions within the 30-cm-thick Precambrian S3 spherule layer as representing large-scale compositional and thermal layering in the impact plume. They propose that the S3 spherule layer provides a unique record of the dynamics and evolution of the impact plume.

11.3 Distal Impact Ejecta Layers and Earth History

Study of distal impact ejecta layers in sedimentary sections can provide a direct link between large impacts and other Earth events (climate change, mass extinctions, tectonics) recorded in the same sedimentary sequence. Impacts producing craters >125 km in diameter involve energies in excess of 10^8 megatons of TNT. Impacts large enough to produce basin-sized craters (>200–300 km in diameter) involve energies in excess of a billion megatons of TNT. It is not unrealistic to imagine that such energetic events could have devastating effects on the solid Earth, atmosphere, climate, and life. In the following sections we consider what we have learned and can learn from the study of distal impact ejecta layers.

11.3.1 Terrestrial Cratering History

Lunar studies indicate that the impact cratering rate was orders of magnitude greater prior to 4.4 Ga ago (the early heavy bombardment period) and that it declined very rapidly between $\sim$ 3.8 and $\sim$ 3.1 Ga (e.g., Hartmann 1972). Some authors argue for a substantial peak in large lunar basin-forming impacts $\sim$ 3.9 Ga ago, sometimes called the lunar cataclysmic event or Late Heavy Bombardment (e.g., Ryder 2002). Unfortunately, there is no terrestrial cratering record (impact craters or ejecta layers) for this time period. Most models indicate that the Earth–Moon cratering rate has been relatively constant, within a factor of 2, for the last 3 Ga. However, Hartmann et al. (2007) proposed that the cratering rate slowly declined after 2.3 Ga ago, dropping by a factor of $\sim$ 3 from about $\sim$ 2.3 Ga ago until the present.

All the known Precambrian spherule layers were formed within two relatively narrow windows; one between ~2.49 and 2.64 and one between ~3.23 and 3.47 Ga. A realistic understanding of the terrestrial impact environment during the Earth's early history is needed in order to place constraints on when and where life may have originated. Some authors have argued that life may have originated several times only to be removed or adversely affected by impacts large enough to cause evaporation and sterilization of the ocean (see Chyba 1993). At the present time at least seven spherule layers ranging in age from 3.23 to 3.47 Ga have been reported (Lowe and Byerly 2010). It is estimated that most of the projectiles responsible for forming these spherule layers were between 20 and 100 km in diameter (Melosh and Vickery 1991; Kyte et al. 1992; Lowe et al. 2003; Johnson and Melosh 2012b). Projectiles this size would have formed craters between ~360 and 1800 km in diameter. Thus, a crater >100 km diameter would have formed on average every 33 Ma. There is only evidence for three impact structures of Phanerozoic age ≥100 km in diameter. Since the Phanerozoic lasted for 542 Ma, this indicates an average of one structure that large every 180 Ma. This suggests that between 3.24 and 3.47 Ga the production rate for impact structures ≥100 km in diameter was ~5 times the Phanerozoic rate. If the estimates of projectile sizes are within a factor of two of being correct, then most, if not all, of these impacts were larger than any of the known Phanerozoic impacts.

At least eight spherule layers have been identified with ages between 2.49 and 2.64 Ga. These eight layers must represent at least four impact events. The aggregate thicknesses of these spherule layers are generally less than those of the Paleoarchean spherule layers, but are still thicker than most Phanerozoic spherule layers (Table 11.1). Most, if not all, of these Precambrian spherule layers are from craters that are at least 100 km in diameter (see below and Sect. 10.4; Hassler et al. 2000; Glikson 2005). This indicates a cratering rate (for impacts producing craters ≥100 km in diameter) of ~4/150 Ma or one every 38 Ma on average between 2.49 and 2.64 Ga ago, which is approximately five times the Phanerozoic rate. This appears to be consistent with Hartmann et al. (2007) proposal that the cratering rate dropped by a factor of ~3 from about ~2.3 Ga ago until the present.

As indicated above, the older Precambrian impact spherule layers occur in two relatively narrow time periods of time (2.49–2.64 Ga and 3.24–3.47 Ga) separated by ~600 Ma. This could reflect a variation in the flux of large impactors over time with the two short intervals of spherule layer occurrence representing spikes in the cratering rate separated by a long period of relative quiescence with no large impacts. However, the fact that the two periods of spherule occurrences were found in the most pristine early Precambrian successions on Earth suggests this may simply be a preservational bias.

With the exception of the K–T boundary (Chicxulub) ejecta layer, which was formed by a carbonaceous chondrite projectile, the Phanerozoic, Proterozoic, and Neoarchean ejecta/spherule layers (for which we have enough data) appear to have been formed by ordinary chondritic projectiles (Table 11.1). On the other hand, all of the Paleoarchean spherule layers for which we have data (three) appear to have been formed by carbonaceous chondrites. If it is found that the other Paleoarchean

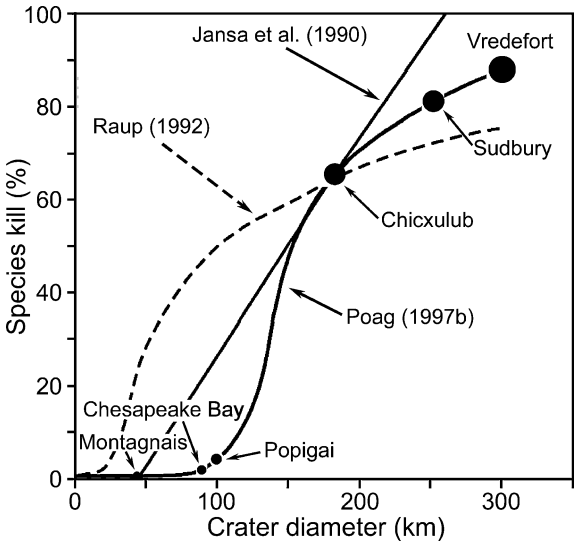

Fig. 11.1 Impact kill-curve. The original impact-kill curve proposed by David Raup (Raup 1992) is shown with a dashed line. Jansa et al. (1990) revised kill-curve (straight solid line) as well as Poag's (1997b) revised kill-curve (sigmoid solid line) are also shown. Poag (1997b) plotted the Sudbury and Vredefort impact structures on the curve based only on their diameters. There are no data that indicate that either of these impact structures are associated with a mass extinction. Modified after Poag (1997b), Fig. 4

spherule layers were also produced by the impact of carbonaceous chondrite bodies, then it would appear that the type of projectiles producing large terrestrial impact structures (> 100 km in diameter) has changed over time.

Johnson and Melosh (2012b) pointed out that the total mass of spherules in a global spherule layer is related to the mass of the projectile. They stated that for typical asteroid impact velocities on Earth, the mass of the vapor plume is made up of material primarily from the isobaric core. The isobaric core is the most highly shocked region of the impacted target rock. It is derived from a spherical region beneath the impact and has a volume comparable to the impact but with twice the mass of the projectile (Johnson and Melosh 2012b). Some of the material is ejected into space at a velocity greater than the Earth escape velocity ($\sim$25 % for a typical impact velocity of $\sim$20 km/s) and only a fraction ($\sim$50 %) of the vapor condenses into spherules. They assume that the thickness of a global spherule layer (consisting of condensate spherules) is roughly the same thickness globally. They use the thickness of the global spherule layer to calculate the mass of spherules in the ejecta layer using the following equation:

$$M_{sp} = 4\pi R_e^2 \rho_{sp} (t_r/2) \tag{11.1}$$

where M_{sp} is the mass of the spherules, R_e is the Earth's radius, ρ_{sp} is the spherule density, and t_r is the reduced layer thickness. The reduced layer thickness can be determined from the following equation, $t_r = 2 f_{sp} t$, where f_{sp} is the spherule volume fraction of the layer and t is the measured layer thickness. From the above relationships Johnson and Melosh (2012b) derived an equation that can be used to calculate the diameter of the projectile or impacting body (D_{imp}) as follows:

$$D_{imp} = 17(t_r/\check{\xi})^{1/3} \tag{11.2}$$

where D_{imp} is in kilometers and t_r is in centimeters and ξ is an efficiency factor that relates the mass of the spherules in an ejecta layer to the mass of the projectile. It ranges between 0.5 and 2. This equation is also based on the assumption that the density of the spherules is similar to the density of the projectile.

Johnson and Melosh (2012b) used Eq. 11.2 to estimate the projectile diameters for 12 Precambrian spherule layers with unknown source craters, and for the K–T boundary ejecta layer and the Late Eocene cpx spherule layer. They obtained projectile diameters of 29–70 km for the S1, S2, S3, and S4 spherule layers; 6.3–90 km for the Jeerinah, Monteville, and Carawine spherule layers, which are probably from the same impact event about 2.63 Ga (Table 10.4; Sect. 8.4); projectile diameters of 17–27 km for both the Reivilo and Paraburdoo spherule layers, which appear to be from the same impact about 2.57 Ga (Sects. 10.4, 8.4.2); and projectile diameters of ~6–21, 31–49, and 46–73 km for the Bee Gorge, Dales Gorge, and Grænsesø spherule layers, respectively. They obtained projectile diameters of 9–14 km and 4.6–7.3 km for the K–T boundary and cpx spherule layers, respectively. Johnson and Melosh (2012b) then used the estimated projectile diameters and average spherule sizes for each layer to estimate the projectile impact velocity using the model of Johnson and Melosh (2012a) (see Sect. 2.4). They found an average impact velocity for the spherule layers of 21.8 ± 2.3 km/s, which is close to the expected average of ~20 km/s for asteroids impacting the Earth as given in Minton and Malhotra (2010). Johnson and Melosh (2012b) concluded that the average projectile flux over the last 3.5 Ga is higher than the present-day flux, which they said is consistent with a slow decrease in post late heavy bombardment projectile flux.

Based on modeling of the early evolution of the asteroid belt, Bottke et al. (2012) concluded that the late heavy bombardment lasted much longer than previously thought with most projectiles (impactors) coming from the E-belt, which is now a largely empty extension of the asteroid belt between 1.7 and 2.1 astronomical units from the Sun that was destabilized by a late giant planet migration. Bottke et al. (2012) proposed that some of the asteroids ejected from the E-belt impacted the Earth and produced ~15 Archean-age basins between 2.5 and 3.7 Ga ago as well as ~60 Chicxulub-sized or larger craters between 1.7 and 3.7 Ga ago. They concluded that the number of large impacts indicated by their model could easily explain the number of spherule layers that have been documented during that time period.

11.3.2 Impacts, Climate, and Life

As previously mentioned, large impacts involve the release of a tremendous amount of energy and can cause local or regional destruction. Larger impacts (producing craters >100 km in diameter) have the potential to change the climate and adversely affect life globally. However, the environmental and biological

effects depend on a number of variables including: composition, density, size, and velocity of the projectile; location (ocean versus continent, latitude) and angle of impact; nature of the target rock (porous versus dense, felsic versus mafic); and the nature of the biota, environment, and atmosphere at the time of the impact.

During a major impact, the incoming projectile heats the adjacent atmosphere, the impact sends a hot plume of vaporized and melted projectile and target rock up and outward through the atmosphere, and the ejecta falling back down through the atmosphere around the globe heats the atmosphere (e.g., Toon et al. 1997; Kring 2000). If the impact is large enough, the incoming ejecta could ignite wildfires all around the globe and heat the surface water of the ocean to the point of boiling. Dust and aerosols ejected into the atmosphere could be carried around the globe and stay in the atmosphere for months after the impact causing global cooling equivalent to a "nuclear winter". Such impacts can release a large amount of greenhouse gases (e.g., water vapor, carbon dioxide, and/or methane, depending on the nature of the target rock) into the atmosphere causing a greenhouse warming that can last for years or decades or more after the cold period. The absence of sunlight for a period of time can kill off life that is dependent on photosynthesis, which, in effect, destroys the base of the food chain. The dust and aerosols can have adverse effects on both plants and animals. Nitrous oxides and sulfate aerosols (if, for example, the target rocks contain anhydrite) can combine with water vapor to form nitric acid and sulfuric acid, respectively. The resulting acid rains can kill vegetation and increase the acidity of ocean water. Another possibility is destruction of the ozone layer by chlorine and bromine released into the atmosphere, which could result in lethal amounts of ultra violet radiation reaching the Earth's surface. All of these processes/mechanisms have been used to explain the mass extinction at the end of the Cretaceous by the impact that produced the Chicxulub impact structure (see Sect. 5.2.9). Several Geological Society of America Special Papers have dealt with impacts and mass extinctions including: Silver and Schultz (1982), Sharpton and Ward (1990), Ryder et al. (1996), and Koeberl and MacLeod (2002). In addition, several books cover this subject including: Bobrowsky and Rickman (2007) and Adushkin and Nemchinov (2008). A good summary of impacts and their effects on life is in Kring (2000).

After it was generally accepted that the Chicxulub impact was probably responsible for the mass extinction at the end of the Cretaceous, numerous researchers began looking for evidence that other mass extinctions might have been caused by impacts; but as of early 2012, the K–T boundary mass extinction remains the only event for which there is convincing evidence of a causal relationship between an impact and a mass extinction (see Sects. 5.5, 6.2.3, 6.3.1). The combined effects of the Popigai and Chesapeake impacts should have had some global environmental consequences. In fact, some microfossil and stable isotope changes across the cpx spherule layer suggest that a drop in temperature and/or increase in ice volume and change in ocean productivity coincided with the impacts (Vonhof et al. 2000; Coccioni et al. 2000; Spezzaferi et al. 2002; Poag et al. 2004; Bodiselitsch et al. 2004; Liu et al. 2009); however, these impacts do not correlate with a mass extinction event. On the other hand, there is evidence for

diversification of large complex acritarchs (probably phytoplanktonic green algae) just above the Acraman ejecta layer (Grey et al. 2003; Willman et al. 2006). Hill et al. (2007) stated that palynological, biomarker, and carbon isotope anomalies correlate with the Acraman ejecta layer in two drill cores (one from the Stuart Shelf and one from the Officer Basin). They suggested that "… the Acraman impact may have had far reaching influences on the rapidly evolving Ediacaran biological and geochemical cycles". The large sizes proposed for the Paleoarchean impacts that produced the spherule layers between 3.23 and 3.47 Ga ago, although not large enough to sterilize the planet, may have had significant effects on life in the early Archean. They may, for example, have heated the atmosphere and boiled off the upper layer of the ocean (Lowe and Byerly 2010).

Raup (1991, 1992) combined extinction data and impact flux to produce a hypothetical impact-kill curve (Fig. 11.1). According to this kill-curve a 45-km-diameter crater would be associated with the extinction of ~25 % of the species present at the time of the impact. However, Jansa et al. (1990) pointed out that the 45-km-diameter Montagnais impact structure (NW Atlantic) is not associated with any extinctions and revised the impact-kill curve to require a minimum crater diameter of >45 km to cause substantial extinctions. They also changed the shape of the curve from a sigmoid shape to a straight line. Furthermore, they used the Chicxulub crater and an approximately 40 % extinction for the K–T boundary to define their curve. Poag (1997b) revised Jansa et al. (1990) curve by using 180 km for the diameter of the Chicxulub crater and 65 % extinction (Fig. 11.1). However, as Poag (1997b) pointed out, such a curve implies 100 % extinction for both the Sudbury and Vredefort structures. Poag further revised the impact-kill curve using the 85-km-diameter Chesapeake Bay structure and the 100-km-diameter Popigai structure, which are associated with little, if any, species extinctions (Fig. 11.1). Poag (1997b) placed the Sudbury and Vredefort structures on the curve based on their diameters; there is no evidence for extinctions associated with these impact events, but the data available are not very amenable for recognizing one.

11.3.3 Oceanic/Continental Crust

In spite of the fact that ~60 % of the Earth's crust is oceanic, no distal ejecta layers from an oceanic impact have been identified in the Phanerozoic record. On the other hand, based on the textures and compositions of Archean spherule layers, it has been proposed that most of them were produced by impacts into oceanic crust (see also Chaps. 8 and 9; e.g., Lowe et al. 1989; Simonson et al. 1998; Simonson and Harnik 2000; Glikson 2005; Sweeny and Simonson 2008). The conclusion that the target rocks for the Archean spherule layers are mostly, if not entirely, basaltic has been used to explain the absence of shocked quartz in nearly all of these layers (e.g., Lowe et al. 1989; Simonson and Harnik 2000). In addition, this observation has been used to support the idea that the continents have grown in size over time (Simonson and Harnik 2000) and is consistent with the estimates

that continental crust probably covered less than 10 % of the Earth's surface >3 Ga ago and maybe only ~25–29 % by the end of the Archean (Taylor and McLennan 2009).

The deep ocean floor is shielded from smaller impacts; the diameter of the projectile has to be greater than 20 % of the water depth in order for a crater to be excavated on the sea floor (Artemieva and Shuvalov 2002). Interaction between the projectile and water column causes loss of the projectile's kinetic energy through oceanic drag and through mass loss as a result of hydrodynamic heating (Artemieva and Shuvalov 2002; Wünnemann and Lange 2002). For example, for an impact into a water depth five times the projectile diameter, the velocity of the projectile will be reduced to ~ 30 % of its original velocity. The impact of a Chicxulub-size projectile into the deep-ocean basin would result in a thinner ejecta layer than the observed Chicxulub ejecta layer (i.e., the K–T boundary layer), probably < 2 mm over much of the Earth's surface, and would have produced little or no shocked quartz. Diagnostic shock-metamorphic features are rarely produced in mafic minerals during terrestrial impacts and mafic minerals are relatively easily destroyed by weathering and diagenesis (see Sects. 2.3.3 and 11.4, questions 3 and 4). Spherules produced by such an impact would be mafic in composition and, like mafic minerals, would be more easily destroyed by diagenesis and/or weathering than felsic minerals. Thus, such a layer would be difficult to find and recognize. Smaller impacts would only produce regional ejecta layers at best. Thus, the dearth of known ejecta layers from oceanic impacts in the Phanerozoic, as indicated by the ejecta/spherule record, may be due, at least in part, to the smaller size of the impacting bodies rather than due to an increase in the percent of the Earth's surface covered by continental crust.

11.3.4 Impacts and Volcanism/Tectonics

Numerous researchers have discussed the possibility that mega-impacts might trigger volcanic and/or tectonic activity either directly or indirectly (e.g., Green 1972; Rogers 1982; Rampino 1987; Glikson 1999; Jones et al. 2003a; Ingle and Coffin 2004; Jones et al. 2005b; Glikson 2008, and references therein; Sankaran 2010). For example, it has been suggested that such a mega-impact might trigger a mantle plume that could potentially resemble a mantle hotspot (e.g., Jones et al. 2003a; Ingle and Coffin 2004). Jones et al. (2003a) proposed that the impact of a 20-km-diameter iron projectile traveling at 10 km/s into the younger (hot) oceanic lithosphere could produce a volume of melt comparable to that of a large igneous province (i.e., $\sim 10^6$ km^3). These authors proposed that the ~120 Ma Ontong Java plateau and the ~250 Ma (end-Permian) Siberian Traps might have been produced by mega-impacts. Jones et al. (2003a) suggested that auto-obliteration by impact-generated volcanism could explain the absence of all craters larger than ~200 km on the Earth. In addition, any impact crater produced on the deep-ocean floor older than ~160 Ma would have been destroyed by subduction. However,

mega-impacts on the ocean floor (or anywhere else on the Earth) would have produced thick global distal ejecta (spherule) layers. Such layers might be difficult to find and identify due to the lack of shocked quartz and possible alteration/destruction of shocked mafic phases and glassy spherules with mafic compositions. However, preservation of such spherule layers has occurred, e.g., the Paleocene Nuussuaq spherule bed and the Archean spherule layers. With the possible exception of the Nuussuaq spherule bed, the apparent absence of such impact spherule layers in the Phanerozoic suggests that such impacts did not take place.

Numerous authors have searched for evidence of an impact near the Permian–Triassic boundary. The results have been controversial and no one has reported finding a thick global spherule layer of that age, which should have been formed if a mega-impact were responsible for triggering the Siberian Traps. Furthermore, Ivanov and Melosh (2003) did numerical simulations of large impacts and concluded that impacts do not initiate volcanic eruptions. They also stated that statistical considerations suggest that impacts cannot be the common initiator of larger igneous provinces. However, they qualified their conclusion by stating that the role of large impacts triggering volcanism has been small, if not negligible, for the last 3–3.3 Ga. They went on to allow that volcanism could be triggered by a large impact, if it happened to occur just above a young hot-spot or mantle plume just as it was about to erupt.

Glikson (2008) noted a similar age for the Bee Gorge spherule layer (or as Glikson referred to it, the spherule marker bed) in Western Australia and the Great Dike in Zimbabwe, Africa, and suggested that there might be a causal relationship between the impact that produced the spherule layer and the Great Dike. However with the errors involved in the ages, the two events could have been separated by as much as 46 Ma. Glikson also pointed out the similarity in age between the impact that produced the $\sim$2.49 Ga-old Dales Gorge-Kuruman spherule layer and global dike events with ages between 2.42 and 2.48 Ga. He suggested that the impact that produced this spherule layer caused crustal fracturing that lead to dike formation.

Lowe et al. (1989, 2003) noted that the S2 and S3 spherule layers in South Africa mark the transition from the 300-Ma-long Onverwacht stage of predominantly basaltic and komatiitic volcanism to the late orogenic stage of greenstone belt evolution involving the sedimentation of interbedded fine-grained terrigenous, pyroclastic, and volcaniclastic rocks, sandstones, and conglomerates of the Fig Tree Group. They proposed that regional and possibly global tectonic reorganization resulted from the large impacts that produced these spherule layers. Glikson (2008) suggested that the tectonic reorganization may have been the result of impact-generated rearrangement of mantle convection patterns.

Green (1972) pointed out that the lower portions of the volcanic sequence of some greenstone belts include komatiites that crystallized from ultramafic liquids extruded at the Earth's surface at a temperature of 1600–1650° C. Green (1972) proposed that major (basin forming) impacts were responsible for the conditions that produced partial melting of mantle rocks which resulted in the extrusion of the komatiites. He further speculated that some greenstone belts are very large impact

scars which were initially filled with impact-triggered melts of ultramafic to mafic compositions (komatiites and basalts) and thereafter evolved with further magmatism, deformation, and metamorphism to produce the present greenstone belts. We note that if both Green (1972) and Lowe et al. (1989, 2003) are correct, then the komatiitic and basaltic volcanism in the Barberton Greenstone Belt below the S2 and S3 spherule layers was triggered by a mega-impact and the change to primarily sedimentation above the spherule layers was triggered by another impact or impacts.

11.3.5 Ocean Composition and Atmospheric Oxygen Content

In the Lake Superior region, North America, ejecta from the Sudbury impact directly overlie banded iron formations (BIFs) (Cannon et al. 2010, and references therein). Slack and Cannon (2009) have proposed a causal relationship between the abrupt end of BIF formation in this region and the Sudbury impact. They proposed that the impact produced global mixing of the shallow oxic and deep anoxic waters of the ocean, creating a suboxic redox state in the deep ocean. This suboxic state prevented transport of hydrothermally produced Fe^{+2} from the deep ocean to the continental-margin environments, which ended the $\sim$1.1 Ga-long period of episodic BIF formation in the Lake Superior region. Slack and Cannon (2009) stated that this model is supported by change in the nature of Paleoproterozoic hydrothermal vent deposits in the deep ocean which changed from predominantly sulfide facies prior to the impact 1.85 Ga ago to mainly oxide facies thereafter.

It has been claimed that many of the Archean spherule layers are overlain by ferruginous deposits, including BIFs (Lowe et al. 1989; Lowe et al. 2003; Glikson 2006; Glikson and Vickers 2010). Glikson (2006) and Glikson and Vickers (2010) suggested that the ferruginous deposits may have formed in response to an enrichment of soluble iron in the seawater under low-oxygen atmosphere/hydrosphere conditions due to enhanced denudation of mafic volcanic terranes uplifted and exposed by impact-induced tectonic movements and/or by impact-triggered mafic volcanic and hydrothermal activity. Low oxygen content of the atmosphere is supported by the Fe oxidation level of the Ni-rich chrome spinels found in the 3.24-Ga-old S3 spherules (Byerly and Lowe 1994).

Spinel crystallites found in impact spherules in the K–T boundary and cpx spherule layers can be distinguished from normal terrestrial spinels by their higher Ni/Fe and higher Fe^{+3}/Fe^{+2}, which are the results of crystallization in silicate melt droplets in an oxygen-rich atmosphere (Robin et al. 1992). Byerly and Lowe (1994) pointed out that the Ni-rich chrome spinels in spherules in the S3 spherule layer have higher Ni/Fe and distinctly lower Fe^{+3}/Fe^{+2} than impact-produced spinels in the cpx and K–T boundary spherules. They proposed that the differences were due to a less oxidizing atmosphere during the Paleoarchean. This conclusion was supported by Krull-Davatzes et al. (2010), who suggested that the

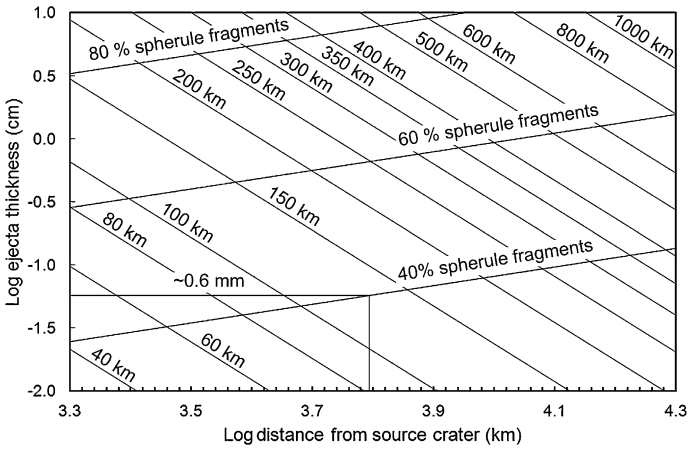

Fig. 11.2 Log ejecta thickness versus log distance from the source crater. The diagonal lines slanted down to the right indicate ejecta thickness versus distance for craters with transient diameters ranging from 40 up to 1000 km based on McGetchin et al.'s (1973) equation (Eq. 2.2 in Sect. 6). The *diagonal lines* slanting from the *upper right down* to the *lower left* are lines of equal percent spherule fragments (i.e., percent of spherule fragments versus whole spherules). The position of the percent fragments is based on data from the Cenozoic microtektites (Fig. 10.8) and is extrapolated to other crater sizes assuming that a specific percent fragments occurs at the same distance (in transient crater diameters) for each crater size. The horizontal line indicates the distance from each size crater where the ejecta would be 0.06 cm (0.6 mm) thick. As an example, an ejecta layer ~0.6 mm thick in which the percent fragments versus whole spherules is ~40 % could be produced by a crater with a transient crater diameter of ~130 km at a log distance of ~3.79 or ~6200 km from the crater

Paleoarchean spinels were formed at oxygen fugacities below 10^{-4} bars (based on experimental studies), which is consistent with a much lower oxygen level in the Paleoarchean atmosphere 3.24 Ga ago.

11.4 Unanswered Questions and Future Studies

The study of distal impact ejecta layers is relatively new. The first studies of distal impact ejecta layers were the discovery and description of the Australasian, Ivory Coast, and North American microtektite layers in the late 1960s and early 1970s. At that time, it was not generally accepted that the microtektites were of impact origin. After the K–T boundary layer was confirmed as an impact ejecta layer associated with the mass extinction at that time, the search for and study of additional distal impact ejecta layers took on greater importance and more geoscientists began to search for them. However, there are still a lot of unanswered questions and things we do not understand about distal impact ejecta layers. We mention a few here in hopes that we can stimulate more research in this field. We hope that field geologists, sedimentologists, stratigraphers, and

micropaleontologists will keep an eye out for any layers that look out of place or that contain spherules of unknown origin. The following is a partial list of questions that need to be resolved.

1. Are there systematic differences between Phanerozoic and Archean distal impact/spherule layers that reflect secular changes in projectiles and/or the Earth's surface through geologic time? Some possible differences were noted above, but more data are needed.
2. Why do some distal ejecta layers have spherules containing Ni-rich spinels, but others do not? The K–T boundary layer consists of Ni-rich spinel-bearing microkrystites as well as microtektites. Where they are found together in the more proximal of the distal sites, the Ni-rich spinel-bearing microkrystites are above the microtektites and appear to be far less abundant. In the Late Eocene cpx spherule layer the microtektites and Ni-rich spinel-bearing microkrystites do not appear to be partitioned into separate layers and the microkrystites are more abundant than the microtektites except, perhaps, in some of the more distal parts of the strewn field. There are no microkrystites (spinel-bearing or otherwise) in the Australasian, Ivory Coast, or North American microtektite layers. Why? Is it because these microtektite layers were formed by smaller impacts than were the cpx and K–T boundary ejecta/spherule layers? It does not appear to be dependent on the type of projectile. Both the K–T boundary and cpx spherule layers appear to have been produced by a chondritic projectile (Table 11.1). The Ivory Coast microtektites also appear to have been formed by the impact of a chondrite, but no microkrystites containing Ni-rich spinels have been found in that strewn field. Furthermore, at least seven of the Archean spherule layers were produced by chondritic projectiles and only one contains Ni-rich spinel-bearing microkrystites. Thus, the present data suggest that only large impacts, producing craters $\geq$100 km in diameter, produce spherules containing Ni-rich spinels. However, not all large impacts produce spherules with Ni-rich spinels.
3. The type of projectiles responsible for the Australasian and North American microtektite layers has not been determined. This could be because the projectile in both cases was an achondrite. Why have no Phanerozoic distal ejecta/spherule layers from an oceanic impact been found? At least two Phanerozoic global ejecta layers have been found that were produced by impacts on continental crust (i.e., the K–T boundary and the Late Eocene cpx spherule layer). Since $\sim$60 % of the Earth's crust is oceanic, one would expect that there should have been at least three impacts into ocean crust during the Phanerozoic that produced global, or almost so, ejecta layers. Why have none been found? An impact on land or the shallow marine environment that produces a global spherule layer might only produce a regional spherule layer if the impact were in a deep-ocean basin. Even if the spherule layer were global it might be very thin (<1 mm thick). In addition, such an impact would produce little, if any, shocked quartz. Most shocked phases, including impact-generated spherules, would have a mafic composition and would be easily destroyed by diagenesis and/or weathering. Such an ejecta/spherule layer would be difficult to find and

Table 11.2 Data required for description of a distal ejecta/spherule layer

Ejecta/Spherule Layer
Thickness and **aggregate thickness**[a]
Nature of bottom and top contacts
Petrography:
Grain size, shape, mineralogy/phases (including **glass content**); sorting
Percent spherules versus percent unmelted ejecta
Sedimentary structures: massive, laminae, cross-bedding, graded bedding
Lateral variation in thickness, contents, percent spherules, etc.
Spherules
Size: size range and size distribution
Shape: Percent spheroids, dumbbells[b]*, teardrops, discs*; **percent spherule fragments**[c]
Petrography:
Phases present (glass, lechatelierite, crystallites, relict grains, Ni-rich spinels)
Texture/structure:
Massive, outer layer with botryoidal inner layer, hollow
Crystalline phases: abundance, size, shape (*evidence of quench texture?*), mineralogy
Vesicularity: **abundance, size, and shape of vesicles**
Composition:
Glass: *major and trace elements, Fe oxidation state, water content*, Sr and Nd isotopic data
Crystalline phases: especially *Ni-rich spinel*s
Unmelted Ejecta
Size: size range and size distribution
Shape
Petrography:
Mineralogy: major phases, heavy minerals[d]
Shock metamorphism: PDFs, high-pressure phases (e.g., coesite, stishovite, reidite, TiO_2II)

Information in bold is needed for putting together a model of how distal ejecta varies with distance from the source crater or to determine the size of and distance to the source crater if it is not known. Information in italics is needed in order to determine if the layer is an impact ejecta layer

[a] See Table 11.1, footnote b, for discussion of aggregate thickness

[b] Dumbbells are not just two spherules stuck together. See Sect. 3.2.1.1 and Figs. 3.8c, 4.2b, 4.48

[c] In previous publications, the total number/volume of microtektites/spherules includes whole or chipped spherules plus fragments of spherules that are less than half the size of the original spherule but similar in size to the spherules (the general cut-off size is 125 μm). The percent fragments are the number of fragments of spherules divided by the total population of spherules plus spherule fragments multiplied by 100. The percent spherule fragments decreases with distance from the source crater (see Fig. 10.8)

[d] The mineralogy of the unmelted ejecta as well as the composition of the glass spherules can be used to indicate the nature of the source rock and therefore be used to help in identification of the source crater. In addition, the heavy mineral assemblage can not only be used to help identify the source crater but XRD and microRaman spectroscopy can be used to search for shock-produced high-pressure polymorphs (e.g., coesite, stishovite, reidite, etc.). Furthermore, some heavy minerals, like zircon, can be dated to determine the age of the parent rocks as well as the time of the impact

recognize. Thus, it is possible such deep-ocean impacts have taken place, but have not yet been discovered or recognized.

4. Why are there no evidence of shock-metamorphosed grains in the Paleoarchean spherule layers and very little evidence of shocked grains in Neoarchean spherule layers? The thicknesses of the Archean spherule layers indicate that they are either close to a relatively small crater or they are far way from a really big crater. In either case, there should be unmelted ejecta present, especially if a layer is close to a relatively small crater. Since traces of shocked mineral grains, such as quartz with multiple sets of PDFs and the high-pressure TiO_2II phase, have been reported for some of the Neoarchean spherule layers, it appears that shocked mineral grains can survive for at least 2.63 Ga.
   Several researchers have suggested that all the impacts that produced the Archean spherule layers were into oceanic crust and that is the reason why no shocked quartz has been found in any of the Paleoarchean layers and only one of the Archean-Proterozoic boundary spherule layers. But this does not explain what appears to be the complete absence of shocked mineral grains in some of the Archean–Proterozoic boundary spherule layers and all the Paleoarchean spherule layers. High-pressure polymorphs of mafic minerals, such as olivine, pyroxene, and feldspar, can be produced by shock metamorphism (see Sect. 2.3.3), but have not yet been observed in any terrestrial impactites. If high-pressure polymorphs of mafic minerals were formed during the impacts that produced the Archean-Proterozoic boundary and Paleoarchean spherule layers they may not be easy to recover and recognize. Mafic minerals are more unstable at the Earth's surface than are felsic minerals. Unless mafic minerals were converted entirely to a high-pressure polymorph, the remaining mafic phases could have been destroyed leaving very small (perhaps <10 μm) crystallites of the high-pressure phase in a clay or iron oxide/hydroxide matrix, making recovery and identification difficult.
   The older Precambrian spherule layers have experienced at least low grade metamorphism and many have been deformed tectonically. Maybe shocked grains were present originally, but the shock-metamorphic effects were destroyed over time. Most, if not all, high-pressure polymorphs recrystallize to an amorphous phase or a low-pressure polymorph at moderately high temperatures. For example, stishovite reverts to an amorphous phase at a temperature as low as 300 °C, and TiO_2II quickly reverts back to rutile when heated to 500 °C. These temperatures are both in the temperature range of greenschist metamorphism, which is particularly problematic in the case of the Paleoarchean spherule layers. The impacts that produced the Archean spherule layers appear to be bigger than any known to have taken place in the Phanerozoic and the abundance of spherules coming back down through the atmosphere after these mega-impacts may have heated the atmosphere to high enough temperature to anneal PDFs in quartz (see, e.g., Croskell et al. 2002) and perhaps in other minerals and to destroy most high-pressure polymorphs. As previously mentioned, Artemieva and Simonson (2012) have pointed out that since large impacts produce more spherules than do small impacts the spherules produced by large impacts experience much more heating

during re-entry. This results in the spherules produced by large impacts being more extensively crystallized by thermal devitrification than spherules from smaller impacts. This would seem to support the proposal that thermal annealing during large impacts could destroy shock-metamorphic effects in the impact ejecta grains. This subject warrants additional study.

5. Can a model be produced that can be used to tell the size of and distance to the source crater for a given ejecta/spherule layer? Some authors have used the Ir content of a distal impact ejecta layer to estimate the size of the impacting body (e.g., Alvarez et al. 1980; Kyte et al. 2003) and some have used the size of impact spherules in an ejecta layer to estimate the size of the impacting body (e.g., Melosh and Vickery 1991; Byerly and Lowe 1994). These methods are based on the assumption that the layers are global in extent and uniform in thickness and meteoritic content. Based on the projectile size, the size of the crater can be estimated and then the distance to the source crater can be calculated using the radial decay of ejecta thickness equations (Sect. 2.6). However, if the thicknesses of the distal ejecta layers are uniform over much of their geographic extent as assumed above, they would not follow the radial decay relationship, and therefore the radial decay equations would not work. We propose that variations in properties of the ejecta layer and spherules within the ejecta layer (Sects. 10.1.2 and 10.2) could theoretically be used to estimate the distance to and size of the source crater as discussed below.
   Variations in distal ejecta layers with distance from the source crater are summarized in Fig. 10.12. The changes in an ejecta layer with distance from the source crater are generalized in this diagram. The changes need to be quantified. If they were quantified then we could, for example, use the percent melted (spherules) versus unmelted ejecta (Fig. 10.9) or the percent spherule fragments versus whole spherules (Fig. 10.8) to estimate how far a spherule layer site is from the source crater. The thickness of the ejecta layer combined with the estimated distance to the source crater could then be used to calculate the size of the source crater using one of the equations that relate thickness of an ejecta layer to size of and distance from the source crater (e.g., Eqs. 2.2 and 2.3). For example, information on how the percent spherule fragments vary with distance from a source crater could be added to a plot of ejecta thickness versus distance as in Fig. 11.2. If a spherule layer were found that is 0.6 mm thick and fragments of spherules were 40 % of fragments plus whole spherules, then the combination of layer thickness plus percent spherule fragments would, in this hypothetical example, indicate that the source crater had a transient crater diameter of $\sim$130 km and was 6200 km away from the spherule layer location (Fig. 11.2). Unfortunately, we do not yet have the data needed to construct such a diagram. This became painfully clear as we put together Fig. 10.12. We found that in nearly every published description of distal ejecta layers, some, or even most, of the basic data were missing. In Table 11.2 we list the basic data that we believe is required to describe a distal ejecta layer. In some, or even most, cases it will be difficult to acquire all the basic information needed to fully describe an ejecta layer. However, if all researchers studying distal ejecta layers report as much of

the basic information about the spherule layer as possible, it should eventually be feasible to construct at least a semi-quantitative model for how distal impact ejecta layers vary with distance from the source crater and to be able to use that model to predict the size of and distance to the source crater when a new ejecta/spherule layer is discovered. We realize that every impact is different and that variations in ejecta with distance from the source crater may not be exactly the same. But, if we can collect enough information for different sized craters we should be able to put some limits on variations in different parameters with distance from the source crater.

6. Where is the source crater for the Australasian tektite/microtektite strewn field? The best studied distal impact ejecta layer, in many respects, is not the K–T boundary layer but the Australasian microtektite layer. More is known about how the ejecta in that layer vary geographically than for any other impact ejecta layer, but the impact crater responsible for the Australasian tektites/microtektites has not yet been discovered. Numerous researchers agree that the crater is probably in the Indochina region and most agree on the general area within Indochina. However, searches for the crater in the predicted region have failed (Hartung and Koeberl 1994; Schnetzler and McHone 1996). When this crater is found it will be possible to quantify for the first time how various parameters of an ejecta layer vary with distance from the source crater.

11.5 Synopsis

The impact of a large extraterrestrial body at a velocity greater than the speed of sound in the target rock (hypervelocity impact) produces shock waves that travel radially away from the point of impact producing a more or less hemispherical wave front that passes through the surrounding target rock subjecting it to transient high pressures and temperatures (contact and compression stage of crater formation; Sect. 2.2.2.1). A shock wave is also produced that travels back through the impacting body (or projectile). Near the point of impact, the high pressure and temperature vaporizes and melts the target rock, but the peak pressure and temperature drop off rapidly away from the point of impact. A large volume of rock around the region that is vaporized and melted is subjected to sufficiently high pressure and temperature to undergo permanent changes; that is the rock is subjected to shock metamorphism (Sect. 2.3). Shock- metamorphic effects, some of which are unique to high velocity impacts, can be used to identify rock and mineral grains that have undergone shock metamorphism. Examples include planar deformation features (PDFs) and high pressure polymorphs (e.g., coesite, stishovite, reidite, TiO_2II).

A rarefaction wave follows behind the shock or compression wave and decompresses the rock and sets it in motion up and out from the point of impact (excavation stage; Sect. 2.2.2.2). The combined effect of the compression and rarefaction waves forms a depression in the Earth's surface called a hypervelocity impact crater. An impact crater at the instant that excavation has ceased is called a transient crater. The transient crater size is used in most theoretical studies of impact craters. Almost immediately after excavation stops, crater modification begins and the crater diameter is increased by slumping of the crater walls and other processes (modification stage; Sect. 2.2.2.3).

Material that is thrown out of the expanding crater is called ejecta (Sect. 2.4). The ejecta blanket or layer thins away from the crater in a more or less predictable manner (radial decay law). Ejecta that land more than 5 crater radii (2.5 crater diameters) from the crater are called distal impact ejecta. Ejecta that land more than $\sim$400 km from the source crater were carried above the atmosphere before falling back to Earth. During impacts producing craters $\geq$100 km in diameter, ejecta can be thrown all the way around the globe. Radial decay laws can be used to estimate the thickness of an ejecta layer radially away from the source crater. However, the Earth's rotation and interactions between the ejecta falling back to Earth and the atmosphere can cause variations in the thickness of the ejecta layer away from the source crater that deviate from the thickness predicted by radial decay laws (Sect. 2.7). Computer models suggest that the average degree of shock metamorphism experienced by ejecta increases with distance from the source crater. Most distal ejecta consist of impact spherules which are generally composed of silicate glass formed from melt droplets or condensate droplets (Sect. 2.6 and 3.2.1).

We propose that there are four groups of impact-generated spherules based on petrography and mode of formation: (1) microtektites formed from melt droplets (melt-drop microtektites), (2) microtektites formed from condensate droplets (condensate microtektites), (3) microkrystites formed from condensate droplets (condensate microkrystites), and (4) microkrystites formed from melt droplets (melt-drop microkrystites) (Sect. 3.2.1.1). Microtektites are impact spherules consisting of glass without any primary crystals and microkrystites contain primary crystals. We propose that spherules formed from melt droplets occur as rotational forms (e.g., teardrops and dumbbells) in addition to the more common spherical to oval shapes and that they can contain vesicles, lechatelierite particles, and rare relict mineral grains. On the other hand, spherules that form from condensate droplets occur only as spherical forms, do not contain vesicles, lechatelierite particles, or relict mineral grains, but can contain Ni-rich spinel crystals and a significant projectile (meteorite) component. Most microtektites appear to have formed as melt droplets and most microkrystites appear to have formed as condensate droplets.

It is not always easy to confirm that a layer suspected of being an impact ejecta layer is, indeed, an impact ejecta layer (Chap. 3). The most convincing evidence that a layer is an impact layer is the presence of shock-metamorphosed rock and/or mineral grains. Unfortunately, shocked rock and/or mineral grains are not always present. In the Cenozoic microtektite layers, shocked grains have not been found

beyond about 80 transient crater diameters. Beyond ~80 transient crater diameters, the 'layer' consists only of scattered microtektites. However, for impacts large enough to produce global impact ejecta layers (e.g., the K–T boundary layer from Chicxulub), shocked mineral grains appear to be present globally, although the most distal part of the layer may be only a few millimeters thick. In still larger impacts, that produce spherule layers tens of centimeters thick, shock-metamorphosed ejecta grains appear to be very sparse or nonexistent (e.g., most of the Archean spherule layers). This may be due, at least in part, to thermal annealing as the greater number (compared to the number in a smaller impact) of ejecta particles re-enter the atmosphere.

In a large impact, most of the projectile is vaporized and melted. The vapor from the target rock and projectile produces a vapor plume that rises up through the atmosphere and can accelerate melt and shocked rock and mineral grains up and out of the atmosphere. The ejecta then travel along ballistic trajectories above the atmosphere before re-entering the atmosphere and falling to Earth. Since the vapor plume contains vaporized projectile in addition to vaporized target rock, a distal impact ejecta layer can often be identified based on geochemical data that indicate the presence of a meteoritic component (i.e., the impacting body; Sect. 3.1.2).

The presence of impact spherules can also be used to identify an impact ejecta layer. However, not all spherules have an impact origin and care must be taken in identifying spherules as impact spherules. Melt-drop microtektites can be identified by the presence of rotational forms such as dumbbells and teardrops. Note that true dumbbells formed by rotation are not just two spheres fused together (Sect. 3.2.1.4). However, shape is not sufficient to identify spherules as having an impact origin, as volcanic spherules can also have rotational forms. Thus, it must be demonstrated that the spherules are not volcanic in origin. If the microtektites are still composed of glass, this can be done using chemical compositional and petrographic data (e.g., the microtektites have low water content and can contain lechatelierite particles). Microkrystites can be identified by the presence of Ni-rich spinel crystals. However, Ni-rich spinels have been observed only in spherules from large impacts (producing craters >100 km in diameter), but not even all the large impacts produced Ni-rich spinel-bearing spherules. Unfortunately, glass is not very stable and is often dissolved or replaced by other phases. This makes identification difficult. Diagenesis and metamorphism can even affect the geochemical data and make shock metamorphic effects difficult to identify.

At least 42 distal ejecta layers have been proposed; however, several of those probably belong to the same impact event, making the total number of impacts they represent about 37 (Table 11.1; Chaps. 4–9). Several have been found at only one site and/or need more study before being accepted as distal impact layers, and several more have been discredited; so the total number of reasonably well-defined distinct distal ejecta layers is only about 23 (11 Phanerozoic and 12 Precambrian in age). The best defined Phanerozoic distal ejecta layers are the: Australasian, Ivory Coast, and North American microtektite layers; the late Eocene cpx spherule layer; the K-T boundary and Manson ejecta layers; and the Late Triassic spherule layer

(Chaps. 4 and 5). Except for the Australasian microtektite layer, all of these well-defined Phanerozoic distal ejecta layers have been linked with a known impact structure (Table 11.1) and all but the Manson ejecta layer are spherule layers. The Australasian microtektite layer is one of the best studied distal impact ejecta layers (Sect. 4.2). Unfortunately, the source crater for this layer has not yet been identified; however, most authors agree that it is likely in the Indochina area and is probably a few tens of kilometers in diameter. Other probable distal ejecta layers include the Late Devonian Qidong spherule (Southern China) and the Senzeille/Hony spherule layers (Belgium). In addition to the distal ejecta layers, at least six occurrences of impact glasses not found in stratigraphic context have been described: Tikal tektites (Guatemala), South Ural glasses (Western Siberia), high Na/K tektites (Australia), Central European tektites (Czech Republic, Germany, Austria), urengoites (northern West Siberia), and Libyan Desert Glass (Western Egypt). All of these are Cenozoic in age.

The youngest Precambrian distal ejecta layer ($\sim$578 Ma) is associated with the Acraman impact structure (South Australia). Ejecta from this structure have been found up to 385 and 540 km east and northwest of the structure, respectively. Although the Precambrian is $\sim$4 Ga long, the remaining distal impact ejecta layers have been found only in three narrow time intervals: $\sim$1.85–2.06 Ga, $\sim$2.49–2.63 Ga, and $\sim$3.23–3.47 Ga. Three ejecta layers are known in the youngest group: the Sudbury ejecta layer (1.85 Ga) found in the Lake Superior region (USA), the Grænsesø spherule layer ($\sim$1.99 Ga) found in West Greenland, and the Karelian spherule layer (between 1.98 and 2.06 Ga) found in Karelia, Russia (Chap. 7). The Sudbury ejecta are believed to be from the Sudbury impact structure (Ontario, Canada). The ejecta sites range from proximal to distal and the ejecta consist mostly of accretionary lapilli, devitrified glassy melt particles, spherules, and shocked mineral grains. Based on its age, the Grænsesø spherule layer may be from either the Sudbury or Vredefort (South Africa) impact structure. The Karelian spherules were found in two cores and, based on their probable age they could represent ejecta from the Vredefort impact structure. The older Precambrian distal ejecta layers are all spherule layers. Eight spherule layers have ages ranging from 2.49 to 2.63 Ga (Archean–Proterozoic boundary spherule layers) and represent ejecta from at least four impacts (Chap. 7). Three of the spherule layers were found in South Africa and the remainder in Western Australia. Seven spherule layers all thought to be from separate impacts have ages ranging from 3.24 to 3.47 Ga (Paleoarchean spherule layers) (Chap. 9). No ejecta layers have been found in the $\sim$600 Ma interval between the Paleoarchean spherule layers and the Archean-Proterozoic boundary spherule layers.

Based on data from the best studied distal ejecta layers (Table 10.1) with known source craters (with the exception of the Australasian microtektite layer) the following observations have been made (Sects. 10.1 and 10.2):

1. In agreement with computer models, the average degree of shock metamorphism of ejecta particles increases with distance from the source crater. Many of the following observations are manifestations of this conclusion.

2. The ratio of melted ejecta (spherules) to unmelted ejecta increases with distance from the source crater and at distances greater than ~10 crater diameters, distal ejecta consist primarily of impact spherules (Fig. 10.9b). Thus, distal impact ejecta layers are essentially impact spherule layers.
3. Unmelted ejecta can be found as far as 200 transient crater diameters from the source crater. This means that for craters with transient crater diameters of 100 km, unmelted ejecta can be found globally, although it is usually only found in trace amounts.
4. Spherules formed from condensate droplets have been found associated only with impact craters with transient crater diameters of 60 km or greater.
5. The percent fragmented spherules increases towards the source crater (Fig. 10.8). This may be the result of a higher percent of collisions between spherules (as they came back down through the atmosphere) nearer the source crater. This is supported by the increased number of impact pits on the surfaces of Australasian microtektites with decreasing distance from the proposed source crater location (Fig. 10.7; Prasad et al. 2010).
6. The homogeneity of melt-drop microtektites increases with distance from the source crater. This is indicated by a decrease in percent Australasian microtektites with relict mineral inclusions, vesicles, and schlieren with distance from the source crater (Fig. 10.10; Folco et al. 2010a).
7. The increase in homogeneity of melt-drop microtektites with distance from the source crater is also indicated by a decrease in alkali content as well as a decrease in the range of alkali contents of Australasian microtektites with distance from the proposed source crater location (Fig. 10.11; Folco et al. 2010b).
8. Unmelted ejecta also show systematic changes with distance from the source crater. For example, the size of shocked quartz grains with PDFs decreases (Fig. 10.6) as the average number of PDF sets increases with distance from the source crater (Fig. 5.26b).

The discovery and study of distal impact ejecta layers is important for several reasons (Sects. 11.2 and 11.3). Since distal ejecta layers cover much larger areas than their source craters, the chance of finding them is proportionately greater. Thus, finding distal impact ejecta layers can help fill in the incomplete terrestrial impact cratering record. The discovery of distal impact ejecta layers that can be linked to known impact structures can be used to test possible correlations between large impacts and other geological events (e.g., mass extinctions, climatic changes). Because they are deposited instantaneously (geologically speaking) over large areas of the Earth's surface, they can be used for regional or even global time-stratigraphic correlation. Studies of distal ejecta layers can be used as 'ground truth' for computer cratering models of ejection and distribution of impact ejecta, as well as changes in the flux of impactors over geologic time (e.g., Bottke et al. 2012). Comparison between Precambrian and Phanerozoic distal impact ejecta layers may give us information about changes in the nature of bodies impacting the Earth,

variation in atmospheric and oceanic composition, and nature of the Earth's crust over time.

Finally we note that there must be many more distal impact ejecta layers that have yet to be discovered and there are a number of major problems that need to be resolved (Sect. 11.4). We have more detailed information about the Australasian microtektite layer than any other distal impact ejecta layer, with the possible exception of the K–T boundary layer, but we still have not found the source crater. If that crater can be found, we will be able to quantify how that distal ejecta layer varies with distance from the source crater. Many of the Archean–Proterozoic boundary spherule layers but none of the Paleoarchean spherule layers contain recognizable shocked rock or mineral grains. Based on observations of the Phanerozoic distal ejecta layers, any distal ejecta layer as thick as the Precambrian spherule layers should contain abundant shock-metamorphosed grains. Where are they? Have the shock-metamorphic effects been destroyed by diagenesis or metamorphism or were they destroyed prior to deposition? Can a model be developed that will allow a researcher to use two or more parameters from an impact ejecta layer to determine the size of and distance to the source crater? We believe that it can, but, in general, researchers who find distal ejecta layers need to describe the layers in more detail and more quantitatively than has been done in the past (see Table 11.2 for a guide to the kinds of information that should be provided when describing an impact ejecta layer).

Appendix A
Recovery of Ejecta Material from Confirmed, Probable, or Possible Distal Ejecta Layers

A.1 Introduction

In this appendix we discuss the methods that we have used to recover and study ejecta found in various types of sediment and rock. The processes used to recover ejecta material vary with the degree of lithification. We thus discuss sample processing for unconsolidated, semiconsolidated, and consolidated material separately. The type of sediment or rock is also important as, for example, carbonate sediment or rock is processed differently from siliciclastic sediment or rock. The methods used to take and process samples will also vary according to the objectives of the study and the background of the investigator. We summarize below the methods that we have found useful in our studies of distal impact ejecta layers for those who are just beginning such studies. One of the authors (BPG) was trained as a marine geologist and the other (BMS) as a hard rock geologist. Our approaches to processing and studying impact ejecta differ accordingly. The methods used to recover ejecta from unconsolidated sediments have been successfully employed by BPG for more than 40 years.

A.2 Taking and Handling Samples

A.2.1 Introduction

The size, number, and type of samples will depend on the objective of the study and nature of the sediment/rock, but there a few guidelines that should be followed regardless of the objective or rock type. All outcrops, especially those near industrialized areas or transportation routes (e.g., highways, train tracks) need to be cleaned off (i.e., the surface layer removed) prior to sampling. The researcher should remove any objects (e.g., rings, necklaces, watches) that contain gold or

B. P. Glass and B. M. Simonson, *Distal Impact Ejecta Layers*, Impact Studies,
DOI: 10.1007/978-3-540-88262-6, © Springer-Verlag Berlin Heidelberg 2013

platinum if there is any chance that the samples might be used for PGE studies as this can cause a contamination problem.

A.2.2 Sample Interval and Size

If the researcher is doing a reconnaissance study to determine if a particular layer has an impact origin and the sampling site is easily accessible, then one large sample (at least 100 g) from the suspected ejecta layer and at least one similar sized sample from below and one from above the layer should be taken. If it is already known that the layer is a distal ejecta layer, then it would be best to take a series of small samples (the size will depend on the thickness of the layer) continuously through the layer as well as a large sample ($\sim$1 kg) from the layer. Furthermore, a series of samples should be taken above and below the layer over a distance of at least a meter in addition to one or more large samples from and adjacent to (above and below) the layer. At a minimum, the lower, middle, and upper part of the layer should be sampled separately. If the sampling location is difficult to access, it is best to take more and larger samples than you think you will need. We have never found that we took too many or too large samples, but we have often wished that we had taken more and/or larger samples. If the layer was previously unknown or not well studied, other researchers will often request samples so they can make additional studies of the layer/ejecta. If the samples are from a core, then, prior to processing, the outer surface of the core samples should be thoroughly cleaned or trimmed off. Trimming off of the outer layer (a few millimeters) is especially important if the core is unconsolidated sediment. If the sample is dry and coherent enough, a band saw can be used to trim off the outer layer. If the sample is still damp and clay rich, a knife with a serrated blade can be used.

A.3 Processing the Samples

After cleaning off the samples or trimming off the outer surface of the core samples, the samples should be thoroughly dried and weighed.

A.3.1 Unconsolidated Samples

Each sample should be put into a beaker filled with water and allowed to break up. We usually use a 250 ml beaker for a 10 g sized sample. Distilled water is best and it should be filtered prior to putting it in the beaker in order to avoid contamination. If the sample does not readily breakup, then it might be best to let it sit in water overnight. Gentle stirring with a stirring rod (polyethylene,

Teflon, or glass) may help to break up the sample. After it has broken up as much as it is going to, we then use ultrasonics to disaggregate the clay fraction.

A.3.1.1 Sieving

Prior to sieving we put the sieves in water in an ultrasonic bath to clean them. We then dry them and examine them using a binocular microscope to make sure that there are no grains caught in the mesh. If grains are caught in the mesh we try to remove them gently with a stiff brush. If that is not successful, we try to push them out with a sharp pick pushing from the underside of the sieve; but this must be done with great care so as not to damage the mesh. Once the sieves are cleaned, we then begin the sieving process. We have always used 3″ (~7.5 cm) diameter sieves. Larger sieves would take less time, but are harder to keep clean and more grains are lost due to being caught in the mesh. We usually use brass sieves (occasionally stainless steel), but we experimented using plastic sieves with replaceable nylon mesh. The mesh for the plastic sieves can be removed and discarded after sieving and replaced with a new mesh. This saves time in cleaning the mesh and avoids cross contamination. However, the design of these sieves results in numerous grains being trapped between the mesh and the walls of the sieves, resulting in more grains being lost than when using the brass sieves. Furthermore, electrostatic charges can build up when trying to brush the grains out of the plastic sieves and make it difficult to get the grains out of the sieve, especially the finer grains (<125 μm). We generally use a 63 μm and a 125 μm sieve, but if the layer is known to be very coarse grained, it might be useful to use a 250 μm and a 500 μm, and maybe even a 1 mm mesh sieve as well. However, the 63 and 125 μm sieves are generally sufficient for the more distal portions of distal ejecta layers.

The beaker containing the sample in water is put into an ultrasonic bath. We only leave the sample in the ultrasonic bath long enough to make the water as cloudy as it will get. For some samples this may take only ~30 s. We stir the sample briefly while it is in the ultrasonic bath. We take the beaker out of the ultrasonic bath and allow the coarse fraction to settle and then pour off the cloudy water through the nested sieves making sure that the 63 μm sieve is beneath the 125 μm sieve. If there is a lot of clay- and silt-sized material, the 63 μm sieve may clog and begin to overflow. If this happens, the 125 μm sieve can be removed and, using a spray of filtered water from a squeeze bottle, clear a small area on the 63 μm sieve, which will allow the water to go through. This may happen repeatedly with some samples. We then add more water to the beaker, ultrasonify for another 30 s or so, and then pour the cloudy water through the sieve set. We continue this process until the water does not get cloudy during ultrasonification. At that point we wash the coarse material out of the beaker into the sieve set using filtered water from a squeeze bottle. We then gently wash (with a squeeze bottle of filtered water) the grains in the top sieve to make sure the fine material has been washed through. We take the top sieve off and set it under a heat lamp to dry. We then gently wash the grains in the lower sieve and put this sieve under a heat lamp to dry. If there is even a remote possibility that the finer

fraction will be searched, a beaker can be put under the sieve set, before beginning to sieve, to collect the <63 μm size material. We generally use a 500 ml or 1 l sized beaker for a 10-g size sample. For larger sample sizes, several large beakers may be required to collect all the water that goes through the sieves, particularly if the sample requires repeated ultrasonifications to break up all of the clay material.

Do not put the heat lamp too close to the sieves when drying them. If you burn your fingers when you try to pick up the sieve, the lamp is too close to the sieve. Alternatively, the sieves could be put into an oven, set at about 40 °C, to dry or, even better, let them air dry. Air drying can take several hours or even overnight, depending on the humidity in the room. Unless several sieve sets are being used, air drying may take too long. However, if there is a chance that glass in the sample will be dated using fission-tracks, then the samples should be air dried as heating under heat lamps or in an oven might partially anneal the fission tracks.

We generally use at least two sets of sieves so that while one set is drying we can sieve the next sample. Remember to clean the sieves before reusing them.

A.3.1.2 Weighing and Storage

After the sieves containing the various size fractions have dried, we restack the sieves and gently tap on the rims to sieve the grains while dry. It may be necessary to brush down the sides of the sieves with a clean dry brush. A pan should be put under the sieve set to collect the material that goes through the finest sieve (i.e., the <63 μm size fraction). After dry sieving, the grains from each sieve should be weighed and stored until the samples are to be studied. We work over a $\sim$15 cm diameter shallow ($\sim$1.5 cm deep) pan with a flat bottom so that if we spill some of the sample we can recover it. We use weighing paper (105 $\times$ 105 mm) to collect each size fraction and weigh it. The weighing paper has a smooth surface which does not trap the grains and does not absorb moisture. We fold the paper down the middle to put a crease in it and weigh it. We then put the paper in the pan and pour the contents of one of the sieves into the center of the weighing paper. We gently tap on the sieve and then gently brush the backside of the mesh with a stiff brush to make sure all the grains go onto the weighing paper. If any of the grains miss the weighing paper, we take the paper out of the pan and put it into another pan and then brush the grains that were spilled in the first pan onto the weighing paper. We then weigh the paper with the grains on it. The weight of the grains is the weight of the paper plus the grains minus the weight of the paper.

If there are not many grains, we sometimes pour the grains into a glass cavity slide after weighing, but generally we pour the grains into a small glass vial with 1/2 to 1 or more dram capacity depending on the sample size (a dram equals 3.7 ml). We work over a pan so that if we spill some of the grains we can we catch them in the pan and can pour them back onto the weighing paper and from there into the cavity slide or glass vial. Once the grains are safely in the cavity slide we put a cover slide on it and an aluminum slide holder to keep the cover slide in place. If the sample is put in a glass vial, then we put the cap on. And of course, we put labels on the slides and glass vials indicating the sample number and size

fraction. The samples are then stored until we are ready to study them or do additional processing.

A.3.1.3 Concentrating the Ejecta Grains

In some cases the impact ejecta (e.g., spherules, shocked mineral grains) are by far the most abundant coarse components in the unconsolidated sediment, especially in the >125 μm size fraction. In that case, no further processing should be necessary. However, if the sediment is rich in biogenic components such as foraminfera or radiolaria, then further processing to concentrate the impact components may be useful and may save time in recovery of the ejecta components for further study. The methods include: acid solution to remove carbonate and magnetic or "heavy" liquid separation to remove biogenic silica (e.g., radiolaria, diatoms).

A.3.1.3.1 Removing Carbonate

If the biogenic component is composed of carbonate minerals (e.g., foraminifera), it can be removed using acetic acid or a dilute solution of hydrochloric acid (e.g., a 5 vol% solution). However, if the biostratigraphy of the section is not well known, then it may be best not to remove all of the carbonate component. One way would be to take a split of each sample and use one split from each sample for biostratigraphic studies and the other to recover and study the impact ejecta. The sample to be dissolved should be placed in a beaker that is much larger than the sample. Acetic or dilute hydrochloric (5 vol %) acid is then slowly added. If the acid is added too quickly, it may react violently and the froth produced by the reaction can fill up and overflow the beaker carrying small fragments of the sample. After the sample stops fizzing, gently stir the contents of the beaker; it may then continue to react. After it stops fizzing, even when stirred, add some additional acid (some of the liquid in the beaker may have to be decanted off first). Continue this process until the sample no longer fizzes when additional acid is added. Remove the acid by dilution and careful decanting until the solution is no longer acidic (the acidicity can be tested using litmus paper). Once the acid is removed by dilution and decanting, the samples can be processed in the same way as discussed above, beginning with ultrasonification and wet sieving. The work should be done in a hood and, of course, protective clothing and a face guard should be worn in case some acid is splashed or spilled.

A.3.1.3.2 Magnetic Separation

It is particularly difficult to remove or concentrate impact ejecta particles in a sample containing abundant biogenic silica (e.g., radiolaria, diatoms). This is especially true when working with the 63–125 μm sized grains. We have used two different methods for separating the biogenic silica from the rest of the grains, including the impact ejecta particles: (1) magnetic separation and (2) heavy liquid separation. Most unaltered impact spherules contain enough iron that they can be removed from the biogenic silica fraction using a Frantz isodynamic magnetic

separator. However, if the sample appears to contain any magnetic grains, pour out the grains a little at a time and hold a magnet (covered with plastic wrap) just above the sample to pull out any magnetic grains (such as magnetite) which could clog the magnetic separator. If it appears that iron-rich grains (e.g., numerous dark brown microtektites, pyroxene) are abundant, start with low amperage so as not to clog the chute. Then take the non-magnetic fraction and run it back through at higher amperage. Continue this process until no more spherules are being pulled out. The percent of spherules that can be separated from the biogenic silica depends on the amperage used, the vibration intensity, the size of the opening into the funnel that feeds into the chute, and the forward and side slopes of the chute. Experimentation can be used to see which settings give the best separation in the shortest amount of time. Subsequent samples can be done in two runs: one with relatively low amperage and then one at the highest amperage required to remove the remaining spherules.

It has been our experience that some of the more silica-rich spherules will stay in the non-magnetic fraction with biogenic silica. After the grains have stopped coming down the chute into the magnetic and nonmagnetic buckets, turn the amperage all the way down and set the vibration to the highest setting to get the remaining grains out; however, the grains recovered in this manner may not be separated very well into magnetic and nonmagnetic fractions. After all the grains have passed through the magnetic separator, the nonmagnetic fraction can be run through the magnetic separator again to see if any additional magnetic fraction is recovered. If the sample is fed through the chute too fast, the grains can bunch up and the separation will not be clean (i.e., some magnetic grains will be mixed with the nonmagnetic fraction and vice versa). If this happens, the funnel opening, or the forward angle of the chute, or the vibration or some combination, thereof, can be decreased in order to slow down the process and obtain a better separation. Once the best combination to give the cleanest separation in the shortest amount of time is found, the remaining samples can be run under the same conditions. This method is time-consuming, but other things can be done while each sample is going through the separator. Some of the finer fraction may stay in the chute due to electrostatic charges built up as the grains slide down the chute. It may help to spray the chute with an antistatic spray before starting each run. After each run is completed, the chute, funnel, and buckets should be removed, cleaned, and thoroughly dried before processing the next sample.

A.3.1.3.3 "Heavy" Liquid Separation

As the biogenic silica has a lower specific gravity ($\sim$2.2) than the distal ejecta grains (e.g., shocked quartz, spherules), heavy liquids adjusted to a specific gravity of 2.3 can be used to separate the biogenic component from the ejecta grains. Heavy liquid (e.g., 1,1,2,2-tetrabromoethane or bromoform) can be mixed with methanol, for example, in the appropriate proportion to produce a "heavy" liquid with a specific gravity of 2.3. We have put the word heavy in quotes because the heavy liquid has been diluted and has a lower specific gravity than what is generally called a heavy liquid. Both tetrabromoethane and bromoform are **highly toxic** and

you should not breathe the fumes or get any on your skin. Thus, the separations and drying of the heavy and light fractions **must be done in a hood** and a face guard, gloves, and protective clothing should be worn while working with the heavy liquid. An alternative heavy liquid that is less toxic can be prepared from sodium polytungstate powder; see end of section for further discussion.

The "heavy" liquid with a specific gravity of 2.3 is put into a separatory funnel and then the 63–125 or 125–250 μm size fraction of a sample is poured in. We use a 250 or 500 ml separatory funnel for a size fraction weighing a few grams; but for larger samples, we use separatory funnels with a capacity of 1,000–2,000 ml. A funnel with filter paper in it is put under the separatory funnel to collect the grains and a beaker is put under the funnel to collect the "heavy" liquid. The filter paper should be labeled with the sample name, size fraction, and an indication that it will contain the heavy fraction (i.e., specific gravity of >2.3). The label should be written in pencil as the "heavy" liquid will dissolve ink and may make the label illegible. If the sample is too large for the size of separatory funnel being used, a clean separation may not occur—i.e., some of the heavy grains may be held up by the light grains and some light grains may be dragged down with the heavy grains. You can experiment by running the light fraction back through again to see if you get a significant amount of grains with higher specific gravities than that of the "heavy" liquid. The "heavy" liquid can be stirred with a glass stirring rod to wet the sample and mix it in with the "heavy" liquid. After stirring, the rod should be washed down using "heavy" liquid with the same specific gravity as the liquid in the separatory funnel. Instead of using a stirring rod, we put the stopper cap on the separatory funnel and take it out of the stand and, being careful to hold the cap so it would not come off, turn the separatory funnel upside down and shake vigorously, turn it right side up and put it back in the stand. We then remove the cap and wash down the sides with "heavy" liquid with the same specific gravity using a large syringe. The cap is put back on the separatory funnel and the heavy grains are allowed to settle while the biogenic silica floats to the top. This will probably take at least several hours. The finer fractions, of course, will take longer to separate than will the coarser fractions. It may be necessary to let them sit overnight in the hood.

After it appears that the light material is all at the top and the heavy grains have all settled to the bottom, take the top off the separatory funnel and slowly open the valve (stopcock) in the stem at the bottom of the separatory funnel to let out enough "heavy" liquid to wash out the heavy grains that sank to the bottom. **Note**: if the cap is not removed first, when the valve is opened air bubbles will go up into the separatory funnel and vigorously mix the light grains and heavy grains together. Also, if the stopcock is opened too quickly or the funnel is too far below the separatory funnel, some of the "heavy" liquid, and the grains in it, can splash out of the filter paper. The stopcock needs to be opened all the way to make sure all the grains pass through. After all the heavy grains have been washed into the filter paper, close the valve and put the top back on the separatory funnel. The filter paper catches the grains and allows the "heavy" liquid to go through and into a beaker under the funnel. After all the "heavy" liquid has gone through the filter paper and into the beaker, the funnel with the filter paper and heavy grains can be

removed and put over another beaker. The filter paper and grains should then be gently but thoroughly washed with acetone to remove all the residue of the heavy liquid and then allowed to dry. This may have to be repeated several times before all the heavy liquid is removed from the filter paper. After all the heavy liquid has been rinsed from the filter paper and grains, leave the beaker with acetone and "heavy" liquid in the hood until all the acetone has evaporated. Once the acetone has evaporated the heavy liquid will be left and can be reused later.

While the heavy fraction is drying in the filter paper, another funnel is put under the separatory funnel with a filter paper in it that has been labeled with the sample number, size fraction, and a notation that indicates that it will contain the light fraction (e.g., specific gravity < 2.3). The rest of the "heavy" liquid can be let out (after the separatory cap is removed) into a new funnel carrying with it the light fraction (i.e., the biogenic silica). After all the "heavy" liquid has gone through the filter paper, the funnel with the filter paper containing the light fraction can be moved over another beaker and thoroughly washed with acetone and left to dry. The "heavy" liquid in the beaker can be used to do another "heavy" liquid separation. However, since the lighter liquid, methanol, evaporates easily, it is necessary to check the specific gravity of the liquid before using it in another separation. This can be done using a pycnometer or by using small glass blocks with densities that closely bracket that of the specific gravity of the "heavy" liquid being used. If both of the glass blocks float in the liquid, the specific gravity is too high, and methanol should be added, while stirring vigorously, until the higher density glass block sinks. If both sink, the specific gravity of the liquid is too low and heavy liquid should be added until the lower density glass floats to the top. In both cases the liquid needs to be stirred vigorously as the two liquids are being mixed.

The remaining "heavy" liquid can be washed out of the separatory funnel using acetone from a squeeze bottle and washed through a fresh filter paper into another beaker. This beaker can be left in the hood until the acetone has evaporated. The remaining heavy liquid can then be used in another heavy liquid separation.

Note that if the samples contain microtektites with large vesicles or numerous small vesicles, some of the microtektites may come out in the light fraction. Thus, some of the light fractions should be looked at to determine if this is the case. Some of the microtektites without vesicles may also be found in the light fraction; this would indicate a poor separation and if they are abundant enough, it may be worthwhile to run the light fractions back through the "heavy" liquid separation. Another possibility would be to use magnetic separation (discussed above) which will not be affected by the presence of vesicles in the microtektites.

Since each separation takes at least several hours, it is best to set up several separatory funnels and do several separations at the same time. One way that worked well in our lab was to start several separations in the afternoon and then let the heavy grains settle out overnight. The next morning the heavy grains could be recovered, washed with acetone, and put aside to dry. In the late afternoon, the next separations can be set up so they can settle overnight. However, before setting up for the next separation, the separatory funnel, including the cap and stopcock (which can be taken apart), should be thoroughly rinsed with acetone and allowed

to dry. Note that stopcocks with rubber gaskets should not be used, nor should grease be used to prevent leaking as the "heavy" liquid can interact with the rubber and grease and contaminate the "heavy" liquid and/or can cause the stopcock to leak. While waiting for the funnels to dry, the heavy and light fractions from the previous separation can be checked. If they still smell like heavy liquid, put them back in the hood and rinse again with acetone. When they are dry and free of heavy liquid, they can be transferred from the filter paper to appropriately labeled glass vials for further study. Again, work over a pan in case some grains are spilled (which often happens) while trying to put them in a glass vial.

Because the heavy liquids, methanol, and acetone are all toxic and should not be breathed or get on your skin, it might be better to use sodium polytungstate for the separations. The sodium polytungstate comes as a powder and is soluble in water. By adding the sodium polytungstate powder to water the specific gravity of the water mixture can be increased up to as high as ~ 3. Once the mixture has the appropriate specific gravity it can then be used for separations as described above, except that the heavy and light fractions should be rinsed with water rather than with acetone and the work does not need to be done in a hood, except perhaps when mixing the sodium polytungstate powder with the water. Sodium polytungstate is described as being nontoxic. We have not used sodium polytungstate for heavy liquid separations and thus cannot give any specific advice about using it.

A.3.2 Semiconsolidated Samples

Some semiconsolidated sediments can be disaggregated and sieved depending on lithology. Sediments held together by carbonate cement can be gently broken up and put into a beaker that is much larger than the sample. Acetic or dilute hydrochloric acid (5 vol%) is slowly added to the beaker. The methodology and precautions are the same as for unconsolidated sediments (see Sect. A.3.1.3.1); however, the process will take longer for semiconsolidated sediments because the sample fragments will be coarser grained.

Semiconsolidated sediments that are being held together by clay can sometimes be broken up by putting them into a beaker with water and then putting the beaker on a hot plate and boiling the water. This requires attention to prevent all the water from being boiled away, which could make the samples even harder to disaggregate. On the other hand, we have found that in some cases repeated wetting and oven drying (at ~ 70 °C) of a sample may cause the sample to break up. If boiling or repeated wetting and drying does not break up a sample, then Na pyrophosphate can be added to the water to aid in breaking the chemical bonds in the clay. We generally use approximately 5 g of Na pyrophosphate per liter of water. More would probably work faster and better; but if too much is added, crystallization can be more of a problem (see below). After the sample is disaggregated, carefully decant off as much of the Na pyrophosphate solution as possible and add more hot water and decant until all the Na pyrophosphate has

been removed. Then continue as before with ultrasonification and sieving. **Note:** If the solution is not diluted, when the Na pyrophosphate solution cools, crystals may form that will be difficult to get rid of and will make searching for the ejecta components more difficult.

For layers that are only 10 cm thick or less and which consist of sediment or rock that is friable or tends to break easily along bedding or cleavage planes, it might be best to take a large sample of the layer that is at least 10–20 cm across and deep and extends at least 10 cm above and below the layer. The top of the sample should be marked and it should be carefully wrapped and taped so that it can be transported back to the lab in one piece. At the lab, it should be carefully unwrapped and put into a plastic container that is just big enough to hold it. Make sure that it is still clearly marked so that the top (stratigraphically) of the sample is obvious. Pour epoxy into the container up to a level that is just above the sample. A low viscosity epoxy should be used and it should be poured in slowly so that it fills in the cracks without trapping too much air. After it hardens, the excess epoxy can be trimmed off with a rock saw, but keep the sample in the shape of a block with right angles and with the top and bottom parallel to the bedding planes or stratigraphic top and bottom of the sample. The front and back of the block should be trimmed down with the saw to remove all the epoxy and the outer layer of rock so that no epoxy is present except around the edges and in cracks if present. At least one column (but two or more is better) a few square centimeters in cross section or larger can be cut perpendicular to the bedding. Each column can then be sliced into a series of subsamples from top to bottom. These samples can then be processed like other samples, except the weight of any epoxy that might be present in a given sample needs to be subtracted. See Glass et al. (2004a) for an example of the above method.

A.3.3 Consolidated Samples

Consolidated samples can be processed or prepared for study in a number of ways depending on lithology, abundance of the ejecta component, and the goals of the study. Carbonate-rich samples can be treated in the same way as semiconsolidated sediments as discussed above. Petrographic slides can be made from both carbonate and noncarbonate samples or the noncarbonate samples can be crushed and sieved and then processed liked unconsolidated samples.

A.3.3.1 Carbonate Samples

Put each sample into a beaker that is much larger than the sample and add acetic or dilute hydrochloric (5 vol%) acid to dissolve the sample. As in the case of semiconsolidated samples, the acid should be added slowly. Do not fill up the beaker in case the acid reacts violently. A foam can form that can quickly fill up and overflow the beaker carrying small pieces of the sample with it. When the acid

stops reacting (i.e., the sample is no longer fizzing) more acid can be added. This process should be continued until the sample stops fizzing even when fresh acid is added and the contents of the beaker are stirred. The acid solution should be diluted and decanted repeatedly until the solution is no longer acidic (see Sect. A.3.1.3.1 for more details and precautions). The insoluble fraction can then be treated like an unconsolidated sample beginning with ultrasonification and sieving.

A.3.3.2 Thin Sections

One common method employed in the study of ejecta layers is to make thin sections which can be studied with a petrographic microscope. This method has some advantages over the method discussed below which involves crushing and sieving. First, the grains can be studied in context with other grains in the sample. Second, the distribution of grains over short distances (mm scale) can be observed. Third, some of the more fragile grains have a better chance of surviving than when the samples are crushed. However, there are some drawbacks with this method when studying the most distal part of an ejecta layer where the ejecta grains are rare (e.g., only a few ejecta particles per cubic centimeter of sample). A typical thin section is only 30 μm thick and $\sim 2 \times 4.4$ cm in surface area and thus the volume of rock in the thin section is <0.03 cm^3. If there are only a couple of ejecta grains per cubic centimeter, on average about 19 petrographic slides would have to be made to find one ejecta particle. If polished thin sections are made, which take more time to make and are more expensive, additional studies of the grains that are exposed at the surface of the thin section can be made, using methods such as: energy-dispersive X-ray analysis, wave-length X-ray analysis (i.e., microprobe), micro-Raman spectroscopy, or ion probe analysis. Our experience has been that if there is one or two grains in a thin section that we would like to study with other methods (other than by microscope), at least one of them will not be exposed at the surface. However, many of the Precambrian distal ejecta layers have spherule-rich zones 1 cm or more thick. Thin sections filled with spherules can be prepared from samples of such zones and the spherules are commonly ~ 500 μm in diameter. In such cases, roughly 3,000 spherules may be present in a thin section with the area specified above. Larger spherules and other ejecta particles can be counted in thin sections by point-counting via the same methods used to quantify the amounts and compositions of sedimentary constituents such as sand grains, cement, etc. It is generally not practical to optically identify or quantify the abundance of particles less than about 125 μm across; they are also likely to have been altered, sometimes beyond recognition, by diagenetic processes.

A.3.3 Crushing and Sieving

One way to recover ejecta particles for further study, when dealing with noncarbonate consolidated rocks, is to crush and sieve them and then treat them like unconsolidated sediments for additional processing. If no thick and/or pure accumulations of spherules or other types of ejecta particles are present, this

method allows one to look at grains dispersed in a larger volume of rock than could be done by making thin sections, unless, of course, hundreds or thousands of thin sections were made. Even if half of the >63 μm sized grains were crushed to <63 μm during processing of a 100 g (~40 cm^3) sample, it would require making ~780 thin sections to study the same number of grains and it is likely that many of these grains will not be exposed at the surface. However, it is unlikely that intact spherules would be recovered during crushing and it would be difficult, therefore, to determine certain parameters, such as, what fraction of the spherules were broken before burial.

We crush the samples using a stainless steel mortar and pestle as porcelain mortar and pestles can be broken when crushing some of the more indurated samples. A sample is coarsely crushed and then dry sieved using a nested set of sieves (63, 125, and 250 μm) with a pan underneath to collect the <63 μm size fraction. The 250 μm sieve is used to collect grains >250 μm that then will be returned to the mortar for additional crushing. Again the fragments are only coarsely crushed and then dry sieved and the >250 μm fraction is returned to the mortar for additional crushing. This is done numerous times until all of the material passes through the 250 μm sieve. If the sample is pulverized so that all the grains pass through the 250 μm sieve the first time, very little material will be recovered in the 63 and 125 μm sieves. It is best only to coarsely crush the sample each time, sieve, and then put the 250 μm fraction back in the mortar for further crushing and sieving. If done correctly, the amount of material in the 63 and 125 μm sieves can be maximized, but this is a very time-consuming process.

Because the crushed grains will have fine dust on them, after all the sample has gone through the 250 μm sieve, the 63–125 μm and 125–250 μm size fractions can be combined and wet sieved as described in Sect. A.3.1.1. The 63 μm and 125 μm sieves containing the 63–125 μm and 125–250 μm size fractions should then be dried. After drying, the sieves should be nested again (with a pan underneath them to collect the <63 μm size fraction) and dry sieved by gently tapping on the sieves. A clean brush can be used to loosen grains sticking on the inside walls of the sieves. After dry sieving, the grains should be weighed and put into labeled containers for storage until they can be processed further or studied (see Sect. A.3.1.1 for more detail).

A.4 Heavy Mineral Separation

In addition to using diluted heavy liquids to remove biogenic silica from a sample and thus concentrate the ejecta material, heavy liquid can be used undiluted to recover heavy minerals (i.e., minerals with densities >2.8 g/cm^3). Some of the heavy minerals are relatively stable both physically and chemically (e.g., zircon, rutile, spinel, diamond). Diamond can be produced by shock metamorphism and both zircon and rutile have high-pressure polymorphs that can be produced by shock metamorphism (see Sect. 2.3.3). In addition, zircon and rutile can be dated by the

U–Pb or Pb–Pb methods (see Sect. 3.2.2). Furthermore, the heavy mineral assemblage as a whole can indicate the nature of the source rock (provenance) and help in identification of the source crater. The heavy minerals are more likely to be concentrated in the finer size fraction (i.e., the 63–125 μm size fraction). The separation process is the same as that described in Sect. A.3.1.3.3) except that the heavy liquid is used at full strength and has, therefore, a specific gravity of 2.8. If the heavy minerals are numerous up to 125 μm in size, then it might be useful to recover heavy minerals from the 125–250 μm size fractions using the procedure outlined above.

Heavy minerals are generally trace minerals that make up <1 % of a rock, thus relatively large samples are generally required in order to adequately define the heavy mineral assemblage and to recover enough to look for high-pressure phases using, for example, X-ray diffraction or micro-Raman spectroscopy. Chemical compositional data for the heavy minerals can be useful in provenance studies and source crater identification (see Thackrey et al. 2009). Note that care must be taken in using heavy mineral assemblages to infer target rock compositions for Precambrian spherule layers because many of them were reworked and contain siliciclastic and/or volcanic components that were not part of the original ejecta.

A.5 Searching for Ejecta Particles

We identify and count particles separated from samples using a binocular microscope with up to 50x magnification and polarizing capabilities. We generally start with the coarsest size fraction. This is usually the >125 μm size fraction or, in the case of crushed and sieved samples, the 125–250 μm size fraction. We pour a small amount of the coarsest size fraction of a sample into a small (~8 cm diameter) watch glass. The watch glass is inside a small shallow pan so that if we spill some of the sample, we can recover it. We use a watch glass because the concave surface prevents spherical grains from rolling away and helps concentrate them in the center, making the search easier. If we are looking for evidence of impact ejecta at a new site, we will look at all the grains in the watch glass and pick out interesting grains for further study. Grains of interest would include spherules, glass, silicate grains that are translucent to white opaque, or opaque phases that are dull rather than shiny. We usually put the grains of interest in a cavity slide (either glass or cardboard) and label the slide accordingly. When we have looked at all the grains and picked out the interesting ones, we set the watch glass aside and put a cover over it, generally a larger watch glass turned upside down. Then we pour a few more grains in another watch glass and look at them with the microscope. After looking at those grains and picking out any interesting ones, we then pour the grains into the first watch glass, as always working in a pan in case some are spilled. We then pour some additional grains into the second watch glass and look at them. This process is repeated until we have looked at all the grains in the vial and picked out any grains of interest for further study.

We then pour all the grains in the watch glasses onto a piece of weighing paper that has been folded down the middle to make a trough and then pour the grains from the weighing paper back into the container they came from. This process can be repeated for several samples from the layer and the grains of interest can be studied for evidence of shock metamorphism or other evidence that the layer contains impact ejecta (see below). If none is found, then the process can be continued using the coarse fractions of other samples from the layer or using grains from the next (smaller) size fraction. The process can be repeated until all the grains >63 μm from selected (or all) samples have been searched for grains of interest. Note each progressively smaller size fraction will take roughly an order of magnitude longer than the preceding larger size fraction. The grains of interest can be searched for evidence that they are impact ejecta as outlined below.

If glass spherules are present, we mount a few on a one inch diameter (~2.54 cm) glass disc using thin-section epoxy and make a polished grain mount. The spherules can then be studied with a petrographic microscope. We look for features that indicate the origin of the spherules, such as vesicles, schlieren, mineral inclusions, and lechatelierite particles (see Sect. 3.2.1.4). Diagenetically altered spherules can also be mounted on glass discs and ground down and polished to make polished grain mounts that can be studied using a petrographic microscope, if they are sufficiently transparent, or a reflected light microscope if they are opaque. If a spherule contains crystalline phases that cannot be identified using a petrographic or a reflected light microscope and if they are exposed, they may be identified using micro-Raman spectroscopy. A variety of other techniques, such as back-scattered X-ray imaging or energy-dispersive or wavelength dispersive X-ray analysis, can be used to study spherules in the polished grain mounts.

If inclusions can be seen in unmounted spherules using crossed polarizers on the binocular microscope, then the crystalline phases can possibly be identified using synchrotron X-ray diffraction (see Folco et al. 2010a).

Translucent to white opaque grains are of interest because transparent silicate minerals, like quartz or feldspars, become translucent and then white opaque with increasing degree of shock metamorphism. The translucent grains can be covered with index oil and a cover slip or mounted on a glass disc and ground down and polished to make a grain mount and then studied with a petrographic microscope to search for indications of shock metamorphism such as PDFs. The white opaque grains can be studied using X-ray diffraction to identify high-pressure phases that may be present, such as coesite or stishovite (see Glass and Wu 1993). Shiny black opaque phases become dull gray when shocked, thus dull gray mineral grains should also be studied to search for evidence of shock metamorphism such as high-pressure phases (see Sect. 2.3.3). Both the white opaque and dull gray phases can be studied by micro-Raman spectroscopy to search for high-pressure phases. It should be noted that most translucent and white opaque silicate phases and dull gray minerals are not the result of shock metamorphism, but if such grains are in an impact ejecta layer, then that is certainly a possibility.

A.6 Abundance and Vertical Distribution of Ejecta Components

Once the impact origin of a layer has been established, it then is important to determine the abundance and vertical distribution of the various ejecta components through the ejecta layer. Such information is critical in developing models for how ejecta vary with distance from the source crater and could be used to indicate distance to the source crater. Alternatively, it may reflect reworking by high-energy events including, but not limited to, impact-induced tsunami-like waves and currents (e.g., Smit et al. 1992a; Hasser and Simonson 2001). In such cases, the lateral and vertical distribution of the ejecta components is critical to understanding the nature and timing of the reworking.

The two main types of ejecta components are melt versus solid ejecta: i.e., spherules versus shocked rock and mineral grains. Spherules can be subdivided into microtektites and microkrystites, but this may be difficult to do if the spherules have been diagenetically altered. The solid component can be divided, as indicated above, into shocked mineral grains and shocked rock fragments. The way that we determine the abundance and vertical distribution of the various ejecta components is similar to the method described in Sect. A.5. As before, we start with the coarsest size fraction first. We take a vial containing the coarsest size fraction of one of the samples and pour a few (no more than a hundred) into a watch glass as before; but this time we segregate the different components in the watch glass. It is better to line up the components in each group for easier counting. The spherules are generally put in the center of the watch glass because spherical particles tend to roll to the center anyway. We also separate spherule fragments from whole spherules and count them separately. It is also useful to separate the spherules according to shape—spheres, teardrops, dumbbells, discs, and others (e.g., irregular shapes or agglutinated forms). Other components may include translucent and white opaque grains, opaque mineral grains (it might be useful to separate shiny from dull grains), rock fragments, biogenic components (e.g., foraminifera, radiolaria) and others (e.g., manganese micronodules, authigenic pyrite). The number of each component is determined and the watch glass set aside and covered. Additional grains are poured into another watch glass, segregated into the various components, and counted. The contents of that watch glass are then poured/brushed into the first watch glass and more grains are then poured into the now empty watch glass and they are segregated into the various components and counted. This process is continued until all the grains from the sample have been examined and tallied. If this takes more than a few hours, it might be better to use a micro-splitter on the next sample if it looks like it has roughly the same amount of grains in the vial. The micro-splitter will divide the sample roughly into two parts. It should then be possible to make the counts in about half the time. After you have done a few samples and have gotten the technique down pat, the sample weights can be used to determine which samples might need splitting into halves or even quarters in order to go through all the samples in a reasonable amount of time. After all the samples have been counted, the data can be used to determine the percent (by number) of the

different components down through the ejecta layer and the percent melted versus unmelted ejecta down through the layer. However, remember to correct the final counts to 100 % for each sample that has been split; i.e., if, for example, the counts were made on only half of a sample, then multiply the number of each component by 2 and if the counts were made on a quarter of a sample, multiply by 4. The impact origin of the grains can be determined as discussed above. The abundance of components through the layer can be determined for the next largest size fraction in the same manner as described for the coarsest size fraction, but this may take an order of magnitude more time. Prior to processing, a portion of several of the samples should probably be used to make thin sections. This will allow the more common ejecta components to be seen in context and allow some of the more fragile components, which could be destroyed by crushing, to be seen.

Alternatively, thin sections can be made from the samples rather than crushing them. Ideally, thin sections should be made of samples taken every centimeter or so through the layer and point counts of the grains made to determine the abundance of the various components, although more selective sampling is probably in order for layers that are many meters thick, as is the case in some Precambrian layers. The thin section approach has the advantage of allowing one to search for shock metamorphic features such as PDFs at the same time the components are being counted. If the ejecta particles are abundant, this may be the best method; however, if the ejecta components are rare, the abundances obtained in this manner may not be very accurate and some of the rarer components might be missed altogether (see Sects. A.3.3.2 and A.3.3.3). In addition, it would be difficult to identify grains containing high-pressure polymorphs in the thin sections unless they were polished thin sections without cover slips, which are more expensive and more time-consuming to make.

Regardless of the method used, samples from at least a meter above and below the layer of interest should be searched. Any components (e.g., spherules, mineral phases, rock fragments) should be studied for evidence of shock metamorphism. If, however, rock fragments are present in the layer, but not above or below the layer, and several of the rock fragments from the layer are found to show evidence of shock metamorphism, then it is probably safe to assume that all the rock fragments are part of the ejecta, especially if all the rock particles are similar in size and petrography. However, such an assumption is predicated on the layer being a direct fallout unit and not, for example, a tsunamiite or gravity flow unit containing particles brought in from shallower water closer to land as well as reworked ejecta.

Whether the grains are counted in a watch glass or in thin sections, it is useful to recover the heavy minerals to look for high-pressure polymorphs and to determine the heavy mineral assemblage. The heavy minerals can be recovered from the 63–125 μm size fractions prior to counting the grains and determining the distribution of the various components through the layer. If thin sections are used to determine the distribution of the various components through the layer, then splits of the samples used to make the thin sections can be crushed and sieved and the 63–125 μm size fractions put through heavy liquid separation in order to recover the heavy minerals as described in Sect. A.4.

References

Åberg G, Bollmark B (1985) Retention of U and Pb in zircons from shocked granite in the Siljan impact structure, Sweden. Earth Planet Sci Lett 74:347–349

Abate B, Koeberl C, Kruger FJ, Underwood JR Jr (1999) BP and Oasis impact structures, Libya, and their relation to Libyan Desert Glass. In: Dressler BO, Sharpton VL (eds) Large meteorite impacts and planetary evolution II. Geological Society of America, Special Paper 339, pp 177–192

Addison WD, Brumpton GR, Vallini DA, McNaughton NJ, Davis DW, Kissin SA, Fralick PW, Hammond AL (2005) Discovery of distal ejecta from the 1850 Ma Sudbury impact event. Geology 33:193–196

Addison WD, Brumpton GR, Davis DW, Fralick PW, Kissin SA (2010) Debrisites from the Sudbury impact event in Ontario, north of Lake Superior, and a new age constraint: are they base-surge deposits or tsunami deposits? In: Gibson RL, Reimold WU (eds) Large meteorite impacts and planetary evolution IV. Geological Society of America, Special Paper 465, pp 245–268

Adushkin V, Nemchinov I (eds) (2008) Catastrophic events caused by cosmic objects. Springer, Dordrecht, 358 pp

Agee CB, Li J, Shannon C, Circone S (1995) Pressure-temperature phase diagram for the Allende meteorite. J Geophys Res 100:17725–17740

Ahrens TJ, O'Keefe JD (1977) Equations of state and impact-induced shock-wave attenuation on the moon. In: Roddy DJ, Pepin RO, Merrill RB (eds) Impact and explosion cratering. Pergamon Press, New York, pp 639–656

Albin E, Wampler JM (1996) New potassium-argon ages for georgiaites and the upper Eocene Dry Branch Formation (Twiggs Clay Member): inferences about tektite stratigraphic occurrence [abs]. Lunar Planet Sci 27:5–6

Albin EF, Norman MD, Roden M (2000) Major and trace element compositions of georgiaites: clues to the source of North American tektites. Meteorit Planet Sci 35:795–806

Alegret L, Arenillas I, José AA, Meléndez A, Molina E, Rojas R, Soria AR (2005) Cretaceous-Paleogene boundary deposits at Loma Capiro, central Cuba: evidence for the Chicxulub impact. Geology 33:721–724

Alekseev AS, Barsukova LD, Kolesov GM, Nazarov MS, Grigoryan AG (1983) The Permian-Triassic boundary event: geochemical investigation of the Transcaucasia section [abs]. Lunar Planet Sci 14:3–4

Alexopoulos JS, Grieve RAF, Robertson PB (1988) Microscopic lamellar deformation features in quartz: discriminative characteristics of shock-generated varieties. Geology 16:796–799

Allègre CJ, Manhès G, Göpel C (1995) The age of the Earth. Geochim Cosmochim Acta 59:1445–1456

B. P. Glass and B. M. Simonson, *Distal Impact Ejecta Layers*, Impact Studies,
DOI: 10.1007/978-3-540-88262-6, © Springer-Verlag Berlin Heidelberg 2013

Allen SR, Simpson CJ, McPhie J, Daly SJ (2003) Stratigraphy, distribution and geochemistry of widespread felsic volcanic units in the Mesoproterozoic Gawler Range Volcanics, South Australia. Aust J Earth Sci 50:97–112

Allwood AC, Walter MR, Burch IW, Kamber BS (2007) 3.43 billion-year-old stromatolite reef from the Pilbara Craton of Western Australia: ecosystem-scale insights to early life on Earth. Precambr Res 158:198–227

Altermann W, Nelson DR (1998) Sedimentation rates, basin analysis and regional correlations of three Neoarchean and Paleoproterozoic sub-basins of the Kaapvaal craton as inferred from precise U-Pb zircon ages from volcaniclastic sediment. Sediment Geol 120:225–256

Altermann W, Siegfried HP (1997) Sedimentology and facies development of an Archaean shelf: carbonate platform transition in the Kaapvaal Craton, as deduced from a deep borehole at Kathu, South Africa. J Afr Earth Sci 24:391–410

Alvarez LW, Alvarez W, Asaro F, Michel HV (1980) Extraterrestrial cause for the Cretaceous-Tertiary extinction. Science 208:1095–1108

Alvarez W, Alvarez LW, Asaro F, Michel HV (1982) Current status of the impact theory for the terminal extinction. In: Silver LT, Schultz PH (eds) Geological implications of impacts of large asteroids and comets on earth. Geological Society of America, Special Paper 190, pp 305–315

Alvarez W, Smit J, Lowrie W, Asaro F, Margolis SV, Claeys P, Kastner M, Hildebrand AR (1992) Proximal impact deposits at the Cretaceous-Tertiary boundary in the Gulf of Mexico: a restudy of DSDP Leg 77 Sites 536 and 540. Geology 20:697–700

Alvarez W, Claeys P, Kieffer SW (1995) Emplacement of Cretaceous-Tertiary boundary shocked quartz from Chicxulub crater. Science 269:930–935

Ames DE, Davidson A, Wodicka N (2008) Geology of the giant Sudbury polymetallic mining camp, Ontario, Canada. Econ Geol 103:1057–1077

Amor K, Hesselbo SP, Porcelli D, Thackrey S, Parnell J (2008) A Precambrian proximal ejecta blanket from Scotland. Geology 36:303–306

Anbar AD, Knoll AH (2002) Proterozoic ocean chemistry and evolution: a bioinorganic bridge? Science 297:1137–1142

Anderson CE Jr (1987) An overview of the theory of hydrocodes. Int J Impact Eng 5:33–59

Antcliffe JD, Brasier MD (2007) Towards a morphospace for the Ediacaran biota. In: Vickers-Rich P, Komarower P (eds) The rise and fall of the Ediacaran Biota. Geological Society of London, Special Publication 286, pp 377–386

Appel PWU (1979) Cosmic grains in an iron-formation from the early Precambrian Isua supracrustal belt, West Greenland. J Geol 87:573–578

Appel PWU, Fedo CM, Moorbath S, Myers JS (1998) Recognizable primary volcanic and sedimentary features in a low-strain domain of the highly deformed, oldest known ($\sim$3.7–3.8 Gyr) Greenstone Belt, Isua, West Greenland. Terra Nova 10:57–62

Arenillas I, Arz JA, Grajales-Nishimura JM, Murillo-Muñetón G, Alvarez W, Camargo-Zanoguera A, Molina E, Rosales-Dominguez C (2006) Chicxulub impact event is Cretaceous/Paleogene boundary in age: new micropaleontological evidence. Earth Planet Sci Lett 249:241–257

Argyle E (1989) The global fallout signature of the K-T boundary impact. Icarus 77:220–222

Armstrong RA, Compston W, de Wit MJ, Williams IS (1990) The stratigraphy of the 3.5–3.2 Ga Barberton Greenstone Belt revisited: a single-zircon microprobe study. Earth Planet Sci Lett 220:247–264

Arouri K, Conaghan PJ, Walter MR, Bischoff GCO, Grey K (2000) Reconnaissance sedimentology and hydrocarbon biomarkers of Ediacarian microbial mats and acritarchs, lower Ungoolya Group, Officer Basin. Precambr Res 100:235–280

Artemieva NA (2001) Tektite production in oblique impacts [abs]. Lunar Planet Sci 32: abstract no. 1216.pdf

Artemieva N (2002) Tektite origin in oblique impacts: numerical modeling of the initial stage. In: Plado J, Pesonen LJ (eds) Impacts in Precambrian shields. Springer, Berlin, pp 257–276

Artemieva N (2008) High-velocity impact ejecta: tektites and Martian meteorites. In: Adushkin VV, Nemchinov IV (eds) Catastrophic events caused by cosmic objects. Springer, Berlin, pp 267–289
Artemieva N, Morgan J (2009) Modeling of the formation of the K-Pg boundary layer. Icarus 201:768–780
Artemieva NA, Shuvalov VV (2002) Shock metamorphism on the ocean floor (numerical simulations). Deep-Sea Res II 49:959–968
Artemieva N, Simonson BM (2012) Elucidating the formation of Archean-Proterozoic boundary spherule layers [abs]. Lunar Planet Sci 43: abstract no. 1372.pdf
Artemieva NA, Wünnemann K, Meyer C, Reimold WU, Stöffler D (2009) Ries crater and suevite revisited: Part II modeling [abs]. Lunar Planet Sci 40: abstract no. 1526.pdf
Asahara Y, Kubo T, Kondo T (2004) Phase relation of a carbonaceous chondrite at lower mantle conditions. Phys Earth Planet Inter 143–144:421–432
Asaro F, Alvarez LW, Alvarez W, Michel HV (1982) Geochemical anomalies near the Eocene/Oligocene and Permian/Triassic boundaries. In: Silver LT, Schultz PH (eds) Geological Implications of Impacts of Large Asteroids and Comets on the Earth. Geological Society of America, Special Paper 190, pp 517–528
ASTM Standard C618 (2008) Standard specification for coal fly ash and raw or calcined natural pozzolan for use in concrete. ASTM International, West Conshohocken, Pennsylvania. doi:10.1520/C0618–08
Badjukov DD, Nazarov MA, Suponeva IV (1986) Shocked quartz grains from K/T boundary sediments [abs]. Lunar Planet Sci 17:18–19
Badjukov DD, Lobitzer H, Nazarov MA (1987) Quartz grains with planar features in the Triassic-Jurassic boundary sediments from Northern Limestone Alps, Austria [abs]. Lunar Planet Sci 18:38–39
Bai S-L (2001) Ni-Ir anomaly, microtektites, and the biotic crisis across the Devonian-Carboniferous boundary, southern China. Int Geol J 43:265–275
Baker G (1963) Form and sculpture of tektites. In: O'Keefe JA (ed) Tektites. University of Chicago Press, Chicago, pp 1–24
Baldwin SL, McDougall I, Williams GE (1991) K/Ar and $^{40}Ar/^{39}Ar$ analyses of meltrock from the Acraman impact structure, Gawler Ranges, South Australia. Aust J Earth Sci 38:291–298
Barnes VE (1939) North American tektites. Uni Texas Publ 3945:477–583
Barnes VE (1963) Tektite strewn-fields. In: O'Keefe JA (ed) Tektites. University of Chicago Press, Chicago, pp 25–50
Barnes VE (1967) Tektites. In: Runcorn K (ed) International dictionary of geophysics, vol 2. Pergamon Press, Oxford, pp 1507–1518
Barnes VE, Barnes MA (eds) (1973) Tektites. Benchmark papers in geology. Dowden, Hutchinson and Ross, Stroudsburg, Pennsylvania, USA, 445 pp
Barnes VE, Underwood JR Jr (1976) New investigations of the strewn field of Libyan Desert Glass and its petrography. Earth Planet Sci Lett 30:117–122
Barghoorn ES, Tyler SA (1965) Microorganisms from the Gunflint chert. Science 147:563–577
Barrat JA, Jahn BM, Amossé J, Rocchia R, Keller F, Poupeau GR, Diemer E (1997) Geochemistry and origin of Libyan Desert glasses. Geochim Cosmochim Acta 61:1953–1959
Barringer DM (1905) Coon mountain and its crater. Proc Acad Nat Sci Philidelphia 57:861–886
Barringer DM Jr (1928) A new meteor crater. Proc Acad Nat Sci Philadelphia 80:307–311
Barton ES, Altermann W, Williams IS, Smith CB (1994) U-Pb zircon age for a tuff in the Campbell Group, Griqualand West Sequence, South Africa: implications for Early Proterozoic rock accumulation rates. Geology 22:343–346
Basu AR, Petaev MI, Poreda RJ, Jacobsen SB, Becker L (2003) Chondritic meteorite fragments associated with the Permian-Triassic boundary in Antarctica. Science 302:1388–1392
Becker L, Poreda RJ (2001) An extraterrestrial impact at the Permian-Triassic boundary: response. Science 293:2343a

Becker L, Poreda RJ, Bada JL (1996) Extraterrestrial helium trapped in fullerenes in the Sudbury impact structure. Science 272:249–252

Becker L, Poreda RJ, Hunt AG, Bunch TE, Rampino M (2001) Impact event at the Permian-Triassic boundary: evidence from extraterrestrial noble gases in fullerenes. Science 291:1530–1533

Becker L, Poreda RJ, Basu AR, Pope KO, Harrison TM, Nicholson C, Iasky R (2004a) Bedout: a possible end-Permian crater offshore of northwestern Australia. Science 304:1469–1476

Becker L, Poreda RJ, Pope KO (2004b) Is Bedout an impact crater? Take 1: response. Science 306:609–610

Becker L, Poreda RJ, Basu AR, Pope KO, Harrison TM, Nicholson C, Iasky R (2004c) Is Bedout an impact crater? Take 2: response. Science 306:611–612

Becker L, Shukolyukov A, Macassic C, Lugmair G, Poreda R (2006) ET extraterrestrial chromium at the Graphite Peak P/Tr boundary and in the Bedout impact melt breccias [abs]. Lunar Planet Sci 37: abstract no. 2321.pdf

Beerling DJ, Lomax BH, Royer DL, Upchurch GR Jr, Kump LR (2002) An atmospheric pCO_2 reconstruction across the Cretaceous-Tertiary boundary from leaf megafossils. Proc Natl Acad Sci U S A 99:7836–7840

Bekker A, Slack JF, Planavsky N, Krapež B, Hofmann A, Konhauser KO, Rouxel OJ (2010) Iron formation: the sedimentary product of a complex interplay among mantle, tectonic, oceanic, and biospheric processes. Econ Geol 105:467–508

Bendeliany NA, Popova SV, Vereschagin LF (1966) A new modification of titanium dioxide stable at high pressure. Geokhimiya (No. 5): 499–502

Benton MJ, Twitchett RJ (2003) How to kill (almost) all life: the end-Permian extinction event. Trends Ecol Evol 18:358–365

Beran A, Koeberl C (1997) Water in tektites and impact glasses by FTIR spectrometry. Meteorit Planet Sci 32:211–216

Berggren WA, Kent DV, Obradovich JD, Swisher CC III (1992) Toward a revised Paleogene geochronology. In: Prothero DR, Berggren WA (eds) Eocene-Oligocene climatic and biotic evolution. Princeton University Press, Princeton, pp 29–45

Beukes NJ (1983) Palaeoenvironmental setting of iron-formations in the depositional basin of the Transvaal Supergroup, South Africa. In: Trendall AF, Morris RC (eds) Iron-formations: facts and problems. Elsevier, Amsterdam, pp 131–209

Beukes NJ (1987) Facies relations, depositional environments and diagenesis in a major early Proterozoic stromatolitic carbonate platform to basinal sequence, Campbellrand Subgroup, Transvaal Supergroup, southern Africa. Sediment Geol 54:1–46

Beukes NJ, Gutzmer J (2008) Origin and paleoenvironmental significance of major iron formations at the Archean-Paleoproterozoic boundary. In: Hagemann S, Rosiere C, Gutzmer J, Beukes NJ (eds) Banded iron formation-related high-grade iron ore, vol 15. Society of Economic Geologists, Reviews in Economic Geology, pp 5–47

Bice DM, Newton CR, McCauley S, Reiners PW, McRoberts CA (1992) Shocked quartz at the Triassic-Jurassic boundary in Italy. Science 255:443–446

Bigazzi G, de Michele V (1997) New fission-tack ages of Libyan Desert Glass. In: de Michele V (ed) «Silica '96››. Pyramids, Milano, Italy, pp 49–57

Binns RA, Davis RJ, Reed SJB (1969) Ringwoodite, natural $(Mg, Fe)_2SiO_4$ spinel in the Tenham Meteorite. Nature 221:943–944

Bischoff A, Stöffler D (1984) Chemical and structural changes induced by thermal annealing of shocked feldspar inclusions in impact melt rocks from Lappajärvi crater, Finland. In: Proceedings of the 14th lunar and planetary science conference, Part 2, vol 89(Suppl). Journal of Geophysical Research, pp B645–B656

Blake TS, Buick R, Brown SJA, Barley ME (2004) Geochronology of a Late Archean flood basalt province in the Pilbara Craton, Australia: constraints on basin evolution, volcanic and sedimentary accumulation, and continental drift rates. Precambr Res 133:143–173

Blake TS, Rothery E, Muhling JR, Drake-Brockman JAP, Sprigg LC, Ho SE, Rasmussen B, Fletcher IR (2011) Two episodes of regional-scale Precambrian hydrothermal alteration in the eastern Pilbara, Western Australia. Precambr Res 188:73–103

Bland PA, de Souza Filho CR, Jull AJT, Kelley SP, Hough RM, Artemieva NA, Pierazzo E, Coniglio J, Pinotti L, Evers V, Kearsley AT (2002) A possible tektite strewn field in the Argentinian Pampa. Science 296:1109–1111

Blockley JG, Tehnas IJ, Mandyczewsky A, Morris RC (1993) Proposed stratigraphic subdivisions of the Marra Mamba Iron Formation and the lower Wittenoom Dolomite, Hamersley Group, Western Australia. Geological Survey of Western Australia, Report 34, Professional Papers, pp 47–63

Blum JD, Chamberlain CP (1992) Oxygen isotope constraints on the origin of impact glasses from the Cretaceous-Tertiary boundary. Science 257:1104–1107

Blum JD, Papanastassiou DA, Koeberl C, Wasserburg GJ (1992) Nd and Sr isotopic study of Australasian tektites: new constraints on the provenance and age of target materials. Geochim Cosmochim Acta 56:483–492

Blum JD, Chamberlain CP, Hingston MP, Koeberl C, Narin LE, Schuraytz BC, Sharpton VL (1993) Isotopic comparison of K/T boundary impact glass with melt rock from the Chicxulub and Manson impact structures. Nature 364:325–327

Boamah D, Koeberl C (2003) Geology and geochemistry of shallow drill cores from the Bosumtwi impact structure, Ghana. Meteorit Planet Sci 38:1137–1159

Bobrowsky P, Rickman H (eds) (2007) Comet/asteroid impacts and human society. Springer, Berlin, 546 pp

Bodiselitsch B, Montanari A, Koeberl C, Coccioni R (2004) Delayed climate cooling in the late Eocene caused by multiple impacts: high-resolution geochemical studies at Massignano, Italy. Earth Planet Sci Lett 223:283–302

Bohor BF (1984) Comment on "Spheroids at the Cretaceous-Tertiary boundary are altered impact droplets of basaltic composition". Geology 12:695–696

Bohor BF (1990) Shocked quartz and more; impact signatures in the Cretaceous-Tertiary boundary clays. In: Sharpton VL, Ward PD (eds) Global catastrophes in Earth history: an interdisciplinary conference on impacts, volcanism, and mass mortality. Geological Society of America, Special Paper 247, pp 335–342

Bohor BF (1996) A sediment gravity flow hypothesis for siliciclastic units at the K/T boundary, northwestern Mexico. In: Ryder G, Fastovsky D, Gartner S (eds) The Cretaceous-Tertiary event and other catastrophes in Earth history. Geological Society of America, Special Paper 307, pp 183–195

Bohor BF, Betterton WJ (1989) Glauconite spherules and shocked quartz at the K-T boundary in DSDP Site 603 [abs]. Lunar Planet Sci 20:92–93

Bohor BF, Betterton WJ (1990) K/T spherules—clarifying the concept [abs]. Lunar Planet Sci 21:107–108

Bohor BF, Glass BP (1995) Origin and diagenesis of K/T impact spherules—from Haiti to Wyoming and beyond. Meteoritics 30:182–198

Bohor BF, Izett GA (1986) Worldwide size distribution of shocked quartz at the K/T boundary: evidence for a North American impact site [abs]. Lunar Planet Sci 17:68–69

Bohor BF, Foord EE, Modreski PJ, Triplehorn DM (1984) Mineralogic evidence for an impact event at the Cretaceous/Tertiary boundary. Science 224:867–869

Bohor BF, Foord EE, Ganapathy R (1986) Magnesioferrite from the Cretaceous-Tertiary boundary, Caravaca, Spain. Earth Planet Sci Lett 81:57–66

Bohor BF, Triplehorn DM, Nichols DJ, Millard HT Jr (1987a) Dinosaurs, spherules, and the "magic" layer: a new K-T boundary clay site in Wyoming. Geology 15:896–899

Bohor BF, Modreski PJ, Foord EE (1987b) Shocked quartz in the Cretaceous-Tertiary boundary clays: evidence for a global distribution. Science 236:705–709

Bohor BF, Betterton WJ, Foord EE (1988) Coesite, glass, and shocked quartz and feldspar at DSDP Site 612: evidence for nearby impact in the late Eocene [abs]. Lunar Planet Sci 19:114–115

Bohor BF, Foord EE, Betterton WJ (1989) Trace minerals in the K-T boundary clays [abs]. Meteoritics 24:253

Bohor BF, Betterton WJ, Foord EE (1990) Shocked zircons and chromite in K/T boundary claystones [abs]. Meteoritics 25:350

Bohor BF, Betterton WJ, Krogh TE (1993) Impact-shocked zircons: discovery of shock-induced textures reflecting increasing degrees of shock metamorphism. Earth Planet Sci Lett 119:419–424

Bondesen E (1970) The stratigraphy and deformation of the Precambrian rocks of the Grænseland area, South-West Greenland. Grønlands Geologiske Undersøgelse Bulletin 86, 210 pp

Bondesen E, Raunsgaard Pedersen K, Jørgensen O (1967) Precambrian organisms and the isotopic composition of organic remains in the Ketilidian of South-West Greenland. Grønlands Geologiske Undersøgelse Bulletin 67, 41 pp

Boslough MB, Crawford DA (2008) Low altitude airbursts and the impact threat. Int J Impact Eng 35:1441–1448

Boslough MB, Crawford DA, Robinson AC, Trucano TG (1994) Watching for fireballs on Jupiter: EOS. Trans Am Geophys Union 75(27):305–310

Bostwick JA, Kyte FT (1996) The size and abundance of shocked quartz in the Cretaceous-Tertiary boundary sediments from the Pacific. In: Ryder G, Fastovsky D, Gartner S (eds) The Cretaceous-Tertiary event and other catastrophes in Earth history. Geological Society of America, Special Paper 307, pp 403–415

Bottke WF, Vokrouhlicky D, Nesvorny D (2007) An asteroid breakup 160 Myr ago as the probable source of the K/T impactor. Nature 449:48–53

Bottke WF, Vokrouhlicky D, Minton D, Nesvorny D, Morbidelli A, Brasser R, Simonson B, Levison HF (2012) An Archean heavy bombardment from a destabilized extension of the asteroid belt. Nature 485:78–81

Bottomley RJ, Koeberl C (1999) The age of a separate Australian tektite event. Meteorit Planet Sci 34:A15–A16

Bottomley RJ, York D, Grieve RAF (1978) ^{40}Ar-^{39}Ar ages of Scandinavian impact structures: I. Mien and Siljan. Contrib Miner Petrol 68:79–84

Bottomley RJ, York D, Grieve RAF (1990) ^{40}Argon-^{39}Argon dating of impact craters. In: Proceedings of the 20th lunar and planetary science conference. Lunar and Planetary Institute, Houston, pp 421–431

Bottomley RJ, Grieve RAF, York D, Masaitis V (1997) The age of the Popigai impact event and its relation to events at the Eocene-Oligocene boundary. Nature 388:365–368

Bourgeois J, Hansen TA, Wiberg PL, Kauffman EG (1988) A tsunami deposit at the Cretaceous-Tertiary boundary in Texas. Science 241:567–569

Bouška V (1998) The moldavite strewn field. Chemie der Erde 58:321–343

Bouška V, Benada J, Rnada Z, Kuncir J (1973) Geochemical evidence for the origin of moldavites. Geochim Cosmochim Acta 37:121–132

Bouška V, Borovec Z, Cimbálniková A, Kraus I, Lajčáková A, Pačesová M (1993) Natural glasses. Academia Praha, Ellis Horwood Ltd., Chichester, 354 pp

Bralower TJ, Paull CK, Leckie RM (1998) The Cretaceous-Tertiary boundary cocktail: Chicxulub impact triggers margin collapse and extensive sediment gravity flow. Geology 26:331–334

Brandner R, Donofrio DA, Krainer L, Mostler H, Nazarov MA, Resch W, Stingl V, Weissert H (1986) Events at the Permian-Triassic boundary in the Southern and Northern Alps [abs]. In: Field conference on Permian and permian-triassic boundary in the south-alpine segment of the western tethys, and additional regional reports, Abstract volume, Pavia. Societa Geologica Italiana and International Geological Correlation Program Project 203, pp 15–16

Brooks RR, Reeves RD, Yang X-H, Ryan DE, Holzbecher J, Collen JD, Neall VE, Lee J (1984) Elemental anomalies at the Cretaceous-Tertiary boundary, Woodside Creek, New Zealand. Science 226:539–542

Brooks RR, Hoek PL, Reeves RD, Wallace RC, Johnston JH, Ryan DE, Holzbecher J, Collen JD (1985) Weathered spheroids in a Cretaceous/Tertiary boundary shale at Woodside Creek, New Zealand. Geology 13:738–740

Brown RD (2002) An impact centered near Cameroon at the time of the Permian extinction caused the fragmentation of Pangaea [abs]. EOS Trans Am Geophys Union 83(19): Abstract T22A-08

Brown RJ, Branney MF, Maher C, Dávilla-Harris P (2010) Origin of accretionary lapilli within ground-hugging density currents: evidence from pyroclastic couplets on Tenerife. Geol Soc Am Bull 122:305–320

Brownfield, ME, Affolter RH, Cathcart JD, O'Conner JT, Brownfield IK (1999) Characterization of feed coal and combustion products from power plants in Indiana and Kentucky. In: Proceedings of the 24th international technical conference on coal utilization and fuel systems, Clearwater, Florida, pp 989–1000

Bryan W (1972) Morphology of quench crystals in submarine basalts. J Geophys Res 77:5812–5819

Buchanan PC, Reimold WU (2002) Planar deformation features and impact glass in inclusions from Vredefort Granophyre, South Africa. Meteorit Planet Sci 37:807–822

Bucher W (1963) Cryptoexplosion structures caused from without or from within the Earth? ("Astroblemes" or "Geoblemes"). Am J Sci 261:597–649

Bunch TE, West A, Firestone RB, Kennett JP, Wittke JH, Kinzie CR, Wolbach WS (2010) Geochemistry data reported by Paquay et al. do not refute Younger Dryas impact event. Proc Natl Acad Sci U S A 107:E58. www.pnas.org/cgi/doi/10.1073/pnas.1001156107

Bundy FP, Kasper JS (1967) Hexagonal diamond–a new form of carbon. J Chem Phys 46:3437–3446

Bundy FP, Hall HT, Strong HM, Wentorf RH (1955) Man-made diamonds. Nature 176:51–54

Burns CA (1985) A study of North American microtektites from Barbados, West Indies. M.Sc. thesis, University of Delaware, Newark, Delaware, USA, 120 pp

Burns CA (1989) Timing between a large impact and a geomagnetic reversal and the depth of NRM acquisition in deep-sea sediments. In: Lowes FJ et al (eds) Geomagnetism and paleomagnetism. Kluwer Academic Publishers, Dordrecht, pp 253–261

Burns CA (1990) The Australasian microtektite layer: implications concerning its source area and its relationship to the Brunhes/Matuyama geomagnetic reversal. Ph.D. dissertation, University of Delaware, Newark, Delaware, USA, 210 pp

Burns E, Sigurdsson H, Carey S, D'Hondt S (2003) Geochemistry of accretionary lapilli from a Cretaceous-Tertiary impact breccia, Guayal, Mexico [abs]. Third International Conference on Large Meteorite Impacts; Nördlingen, Germay; August 5–7, 2003. Lunar and Planetary Institute, Houston, abstract no. 4113.pdf

Button A (1976) Transvaal and Hamersley Basins—review of basin development and mineral deposits. Miner Sci Eng 8:262–293

Byerly GR, Lowe DR (1994) Spinel from Archean impact spherules. Geochim Cosmochim Acta 58:3469–3486

Byerly GR, Lowe DR (2002) Revisiting an Archean impact layer (response). Science 298:750–751

Byerly GR, Hazel JE, McCabe C (1990) Discrediting the late Eocene microspherule layer at Cynthia, Mississippi. Meteoritics 25:89–92

Byerly GR, Kröner A, Lowe DR, Todt W, Walsh MW (1996) Prolonged magmatism and time constraints for sediment deposition in the early Archean Barberton Greenstone Belt: evidence from the upper Onverwacht and Fig Tree Groups. Precambr Res 78:125–138

Byerly GR, Lowe DR, Wooden JL, Xie X (2002) An Archean impact layer from the Pilbara and Kaapvaal cratons. Science 297:1325–1327

Campbell C, Oboh-Ikuenobe FE, Eifert TL (2008) Megatsunami deposit in Cretaceous-Paleogene boundary interval of southeastern Missouri. In: Evans KR, Horton JW Jr, King DT Jr, Morrow JR (eds) The Sedimentary Record of Meteorite Impact. Geological Society of America, Special Paper 437, pp 189–198

Campbell IH, Czamanske GK, Fedorenko VA, Hill RI, Stepanov V (1992) Synchronism of Siberian Traps and the Permian-Triassic boundary. Science 258:1760–1763

Cande SC, Kent DV (1995) A geomagnetic polarity timescale for the Late Cretaceous and Cenozoic. J Geophys Res 100:6093–6095

Canfield DE (1998) A new model for Proterozoic ocean chemistry. Nature 396:450–453

Cannon WF, Addison WD (2007) The Sudbury impact layer in the Lake Superior iron ranges: a time-line from the heavens [abs]. In: Woodruff L (ed). Proceedings and abstracts, 53rd annual meeting. Institute of Lake Superior Geology, Lusten, Minnesota, USA, pp 20–21

Cannon WF, Schulz KJ, Horton JW Jr, Kring DA (2010) The Sudbury impact layer in the Paleoproterozoic iron ranges of northern Michigan, USA. Geol Soc Am Bull 122:50–75

Carlisle DB (1992) Diamonds at the K/T boundary. Nature 357:119–120

Carlisle DB, Braman DR (1991) Nanometre-size diamonds in the Cretaceous/Tertiary boundary clay of Alberta. Nature 352:708–709

Carter NL, Friedman M (1965) Dynamic analysis of deformed quartz and calcite from the Dry Creek Ridge Anticline, Montana. Am J Sci 263:747–785

Cassidy WA, Glass BP, Heezen BC (1969) Physical and chemical properties of Australasian microtektites. J Geophys Res 74:1008–1025

Casier J-G (1992) Description and study of ostracods from two cross sections of the historic Frasnian-Famennian stratigraphic boundary at the type section. Bulletin de I'Institut Royal des Sciences Naturelles de Belgique Science de la Terre 62:109–119

Cavosie AJ, Valley JW, Wilde SA, E.I.M.F (2005) Magmatic $\delta^{18}O$ in 4400–3900 Ma detrital zircons: A record of the alteration and recycling of crust in the Early Archean. Earth Planet Sci Lett 235:663–681

Cawood PA, Kröner A, Pisarevsky S (2006) Precambrian plate tectonics: criteria and evidence. GSA Today 16(7):4–11

Chadwick B, Garde AA (1996) Palaeoproterozoic oblique plate convergence in South Greenland: a reappraisal of the Ketilidian orogen. In: Brewer TS (ed) Precambrian crustal evolution in the North Atlantic Region. Geological Society of London, Special Publication 112, pp 179–196

Chadwick B, Claeys P, Simonson BM (2001) New evidence for a large Paleoproterozoic impact: spherules in a dolomite layer in the Ketilidian orogen, South Greenland. J Geol Soc Lond 158:331–340

Chai CF, Ma SL, Mao XY, Zhou YQ, Sun YY, Xu DY, Zhang QW, Yang ZZ (1987) Neutron activation studies of refractory siderophile element anomaly and other trace element patterns in boundary clay between Permian/Triassic, Changxing, China. J Radioanal Nucl Chem 114(2):293–301

Chai C, Zhou Y, Mao X, Ma S, Ma J, Kong P, He J (1992) Geochemical constraints on the Permo-Triassic boundary event in South China. In: Sweet WC, Yang Z, Dickins JM, Yin H (eds) Permo-Triassic events in the eastern Tethys: stratigraphy, classification, and relations with the western Tethys. Cambridge University Press, Cambridge, pp 158–168

Chalmers RO, Henderson EP, Mason B (1976) Occurrence, distribution, and age of Australasian tektites. Smithson Contrib Earth Sci 17:1–46

Chao ECT (1963) The petrographic and chemical characteristics of tektites. In: O'Keefe JA (ed) Tektites. University of Chicago Press, Chicago, pp 51–94

Chao ECT (1967) Impact metamorphism. In: Abelson PH (ed) Researches in geochemistry, vol 2. Wiley, New York, pp 204–233

Chao ECT (1968) Pressure and temperature histories of impact metamorphosed rock—based on petrographic observations. In: French BM, Short NM (eds) Shock metamorphism of natural materials. Mono Book Corp, Baltimore, pp 135–158

Chao ECT, Shoemaker EM, Madsen BM (1960) First natural occurrence of coesite. Science 132:220–222

Chao ECT, Fahey JJ, Littler J, Milton DJ (1962) Stishovite, SiO_2, a very high pressure new mineral from Meteor Crater, Arizona. J Geophys Res 67:419–421

Chapman CR (2004) The hazard of near-Earth asteroid impacts on Earth. Earth Planet Sci Lett 222:1–15

Chapman DR, Scheiber LC (1969) Chemical investigation of Australasian tektites. J Geophys Res 74:6737–6776

Chaussidon M, Sigurdsson H, Métrich N (1996) Sulfur and boron isotope study of high-Ca impact glasses from the K/T boundary: Constraints on source rocks. In: Ryder G, Fastovsky D, Gartner S (eds) The Cretaceous-Tertiary event and other catastrophes in Earth history. Geological Society of America, Special Paper 307, pp 253–262

Chen J, Weidner DJ, Vaughan MT (2002) The strength of $Mg_{0.9}Fe_{0.1}SiO_3$ perovskite at high pressure and temperature. Nature 419:824–826

Chen M, Sharp TG, El Goresy A, Wopenka B, Xie X (1996) The majorite-pyrope + magnesiowüstite assemblage: constraints on the history of shock veins in chondrites. Science 271:1570–1573

Chen M, Shu J, Xie X, Mao HK (2003a) Natural $CaTi_2O_4$-structured $FeCr_2O_4$ polymorph in the Suizhou meteorite and its significance in mantle mineralogy. Geochim Cosmochim Acta 67:3937–3942

Chen M, Shu J, Mao HK, Xie X, Hemley RJ (2003b) Natural occurrence and synthesis of two new postspinel polymorphs of chromite. Proc Natl Acad Sci U S A 100:14651–14654

Chen M, Shu J, Mao HK (2008) Xieite, a new mineral of high-pressure $FeCr_2O_4$ polymorph. Chin Sci Bull 53:3341–3345

Chenet A-L, Coutillot V, Fluteau F, Gérard M, Quidelleur X, Khadri SFR, Subbarao KV, Thordarson T (2009) Determination of rapid Deccan eruptions across the Cretaceous-Tertiary boundary using paleomagnetic secular variation: 2. Constraints from analysis of eight new sections and synthesis for a 3500-m-thick composite section. J Geophys Res 114:B06103. doi:10.1029/2008JB005644

Cheney ES (1996) Sequence stratigraphy and plate tectonic significance of the Transvaal succession of southern Africa and its equivalent in Western Australia. Precambr Res 79:3–24

Chijiwa T, Arai T, Sugai T, Shinohara H, Kumazawa M, Takano M, Kawakami S (1999) Fullerenes found in the Permo-Triassic mass extinction period. Geophys Res Lett 26:767–770

Chyba CF (1993) The violent environment of the origin of life: progress and uncertainties. Geochim Cosmochim Acta 57:3351–3358

Chyba CF, Thomas PJ, Zahnle KJ (1993) The 1908 Tunguska explosion: atmospheric disruption of a stony asteroid. Nature 361:40–44

Cisowski SM, Housden J (1982) Was the emplacement of the British Tertiary Igneous Province initiated by an event 65 M.Y. ago? [abs]. EOS Trans Am Geophys Union 63(18):309

Claeys P (1995) When the sky fell on our heads: identification and interpretation of impact products in the sedimentary record. U.S. National Report to IUGG, 1991–1994. Rev Geophys 33(Suppl):95–100

Claeys P (2004) Searching for impact fragments across the Eifelian-Givetian boundary [abs]. Geol Soc Am Abstr Prog 36(5):265

Claeys P, Casier J-G (1994) Microtektite-like impact glass associated with the Frasnian-Famennian boundary mass extinction. Earth Planet Sci Lett 122:303–315

Claeys P, Casier J-G, Margolis S (1992) Microtektites and mass extinctions: evidence for a late Devonian asteroid impact. Science 257:1102–1104

Claeys P, Alvarez W, Smit J, Hildebrand AR, Montanari A (1993) KT boundary impact glasses from the Gulf of Mexico region [abs]. Lunar Planet Sci 24:297–298

Claeys P, Kyte FT, Herbosch A, Casier J-G (1996) Geochemistry of the Frasnian-Famennian boundary in Belgium: mass extinction, anoxic oceans and microtektite layer, but not much iridium. In: Ryder G, Fastovsky D, Gartner S (eds) The Cretaceous-Tertiary event and other

catastrophes in Earth history. Geological Society of America, Special Paper 307, pp 491–504
Claeys P, Kiessling W, Alvarez W (2002) Distribution of Chicxulub ejecta at the Cretaceous-Tertiary boundary. In: Koeberl C, MacLeod KG (eds) Catastrophic events and mass extinctions: impacts and beyond. Geological Society of America, Special Paper 356, pp 55–68
Clark DL, Wang C-Y, Orth CJ, Gilmore JS (1986) Conodont survival and low iridium abundances across the Permian-Triassic boundary in South China. Science 233:984–986
Clayton PA, Spencer LJ (1934) Silica glasses from the Libyan Desert. Mineral Mag 23:501–508
Cloud P (1972) A working model of the primitive earth. Am J Sci 272:537–548
Clymer AK, Bice DM, Montanari A (1996) Shocked quartz from the late Eocene: impact evidence from Massignano, Italy. Geology 24:483–486
Coccioni R, Basso D, Brinkhuis H, Galeotti S, Gardin S, Monechi S, Spezzaferri S (2000) Marine biotic signal across a late Eocene impact layer at Massignano, Italy: evidence for long-term environmental perturbation? Terra Nova 12:258–263
Coes L Jr (1953) A new dense crystalline silica. Science 118:131–132
Cohen AJ (1963) Asteroid- or comet-impact hypothesis of tektite origin: the moldavite strewn-fields. In: O'Keefe JA (ed) Tektites. University of Chicago Press, Chicago, pp 189–211
Cohen AS, Coe AL (2002) New geochemical evidence for the onset of volcanism in the Central Atlantic magmatic province and environmental change at the Triassic-Jurassic boundary. Geology 30:267–270
Colgate SA, Petschek AG (1985) Cometary impacts and global distribution of resulting debris by floating. LA-UR-84-3911. Los Alamos National Laboratory, Los Alamos, New Mexico, USA
Collins GS, Wünnemann K (2005) How big was the Chesapeake Bay impact? Insight from numerical modeling. Geology 33:925–928
Collins GS, Melosh HJ, Marcus RA (2005) Earth impact effects program: a web-based computer program for calculating the regional environmental consequences of a meteoroid impact on Earth. Meteorit Planet Sci 40:817–840
Colodner DC, Boyle EA, Edmond JM, Thomson J (1992) Post-depositional mobility of platinum, iridium and rhenium in marine sediments. Nature 358:402–404
Compston W, Chapman DR (1969) Sr isotope patterns within the Southeast Australasian strewn-field. Geochim Cosmochim Acta 33:1023–1036
Compston W, Williams I, Jenkins RJF, Gostin VA, Haines PW (1987) Zircon age evidence for the Late Precambrian Acraman ejecta blanket. Aust J Earth Sci 34:435–445
Condie KC, Pease V (eds) (2008) When did plate tectonics begin on planet Earth? Geological Society of America, Special Paper 440, 294 pp
Coney L, Reimold WU, Hancox PJ, Mader D, Koeberl C, McDonald I, Struck U, Vajda V, Kamo SL (2007) Geochemical and mineralogical investigation of the Permian boundary in the continental realm of the southern Karoo Basin, South Africa. Paleoworld 16:67–104
Conley CD (1977) Origin of distorted ooliths and pisoliths. J Sediment Petrol 47:554–564
Connolly HC Jr, Hewins RH (1995) Chondrules as products of dust collisions with totally molten droplets within a dust-rich nebular environment: an experimental investigation. Geochim Cosmochim Acta 59:3231–3246
Covey C, Thompson SL, Weissman PR, MacCraken MC (1994) Global climatic effects of atmospheric dust from an asteroid or comet impact on Earth. Global Planet Change 9:263–273
Cowan EJ, Schwerdtner WM (1994) Fold origin of the Sudbury Basin. In: Lightfoot PC, Naldrett AJ (eds) In: Proceedings of the Sudbury-Noril'sk symposium. Ontario Geological Survey, Special volume 5, pp 45–55
Creaser RA, White AJR (1991) Yardea Dacite—large-volume, high-temperature felsic volcanism from the Middle Proterozoic of South Australia. Geology 19:48–51
Creaser RA, Papanastassiou DA, Wasserburg GJ (1991) Negative thermal ion mass spectrometry of osmium, rhenium and iridium. Geochim Cosmochim Acta 55:397–401
Crocket JH, Officer CB, Wezel FC, Johnson GD (1988) Distribution of noble metals across the Cretaceous/Tertiary boundary at Gubbio, Italy: Iridium variation as a constraint on the duration and the nature of Cretaceous/Tertiary boundary events. Geology 16:77–80

Croskell M, Warner M, Morgan J (2002) Annealing of shocked quartz during atmospheric re-entry. Geophys Res Lett 29(20). doi:10.10291GL014382
Crowley JL, Bowring SA, Shen SZ, Wang J, Cao C, Jin YG (2006) U–Pb zircon geochronology of the end-Permian mass extinction [abs]. Geochim Cosmochim Acta 70(18) Suppl 1:A119
Crutzen PJ, Birks JW (1982) The atmosphere after a nuclear war: twilight at noon. Ambio 11:114–125
Currie KL, Shafiqullah M (1967) Carbonatite and alkaline igneous rocks in the Brent crater, Ontario. Nature 215:725–726
Cuttitta F, Clarke RS Jr, Carron MK, Annell CS (1967) Martha's Vineyard and selected Georgia tektites: new chemical data. J Geophys Res 72:1343–1349
Cuttitta F, Carron MK, Annell CS (1972) New data on selected Ivory Coast tektites. Geochim Cosmochim Acta 36:1297–1300
Dachille F, Zeto RJ, Roy R (1963) Coesite and stishovite: stepwise reversal transformations. Science 140:991–993
Dann JC (2000) The 3.5 Ga Komati Formation, Barberton Greenstone Belt, South Africa, Part I: New maps and magmatic architecture. S Afr J Geol 103:47–68
Dass JD (1999) Geographical variations in the abundance and nature of mineral inclusions in Muong Nong-type tektites from the Indochina area: implications for the location of the source crater for the Australasian strewn field. M.Sc. thesis, University of Delaware, Newark, Delaware, USA, 215 pp
Daulton TL, Pinter N, Scott A (2010) No evidence of nanodiamonds (and an impact event) in Younger-Dryas sediments. Proc Natl Acad Sci U S A 107:16043–16047
Davenport SA, Wdowiak TJ, Jones DD, Wdowiak P (1990) Chondritic metal toxicity as a seed stock kill mechanism in impact-caused mass extinctions. In: Sharpton VL, Ward PD (eds) Global Catastrophes in Earth history; an interdisciplinary conference on impacts, volcanism, and mass mortality. Geological Society of America, Special Paper 247, pp 71–76
Davis DW (2008) Sub-million-year age resolution of Precambrian igneous events by thermal extraction—thermal ionization mass spectrometer Pb dating of zircon: application to crystallization of the Sudbury impact melt sheet. Geology 36:383–386
DeCarli PS (1998) Direct synthesis of diamond in the laboratory and impact craters [abs]. Meteorit Planet Sci 33:A39
de Kock MO, Evans DAD, Beukes NJ (2009) Validating the existence of Vaalbara in the Neoarchean. Precambr Res 174:145–154
Delano JW (1986) Pristine lunar glasses: criteria, data, implications. In: Proceedings of the 16th lunar and planetary science conference, part 2, vol 91(B4). Journal of Geophysical Research, pp D201–D213
Delano JW, Lindsley DH (1982) Chemical systematics among the moldavite tektites. Geochim Cosmochim Acta 46:2447–2452
Deloule E, Chaussidon M, Glass BP, Koeberl C (2001) U-Pb isotopic study of relict zircon inclusions recovered from Muong Nong-type tektites. Geochim Cosmochim Acta 65:1833–1838
de Michele V (ed) (1997) «Silica '96›› Proceedings of the meeting on Libyan Desert Glass and related desert events. Pyramids, Milano, Italy, 158 pp
de Niem D, Kührt E, Motschmann U (2007) Ejecta range: a simulation study of terrestrial impacts. Planet Space Sci 55:900–914
DePaolo DJ, Kyte FT, Marshall BD, O'Neil JR, Smit J (1983) Rb-Sr, Sm-Nd, K-Ca, O, and H isotopic study of Cretaceous-Tertiary boundary sediments, Caravaca, Spain: evidence for an oceanic impact. Earth Planet Sci Lett 64:365–373
de Pater I, Lissauer JJ (2001) Planetary sciences. Cambridge University Press, Cambridge, 528 pp
Deutsch A, Koeberl C (2006) Establishing a link between the Chesapeake Bay impact structure and the North American tektite strewn field: the Sr-Nd isotopic evidence. Meteorit Planet Sci 41:689–703
Deutsch A, Schärer U (1994) Dating terrestrial impact events. Meteoritics 29:301–322

Deutsch A, Ostermann M, Masaitis VL (1997) Geochemistry and neodymium-strontium isotope signature of tektite-like objects from Siberia (urengoites, South Ural glass). Meteorit Planet Sci 32:679–686

Deutsch A, Masaitis VL, Langenhorst F, Grieve RAF (2000) Popigai, Siberia—well preserved giant impact structure, national treasury, and world's geological heritage. Episode 23:3–11

Deutsch A, Schulte P, Salge T (2010) Carbonate spherules in the K-Pg event deposit are Chicxulub ejecta [abs]. Meteorit Planet Sci 45 (Suppl):A45

de Wit MJ, Ashwal LD (eds) (1997) Greenstone belts. Oxford University Press, Oxford, 809 pp

de Wit MJ, Roering C, Hart RJ, Armstrong RA, de Ronde CEJ, Green RWE, Tredoux M, Peberdy E, Hart RA (1992) Formation of an Archaean continent. Nature 357:553–562

D'Hondt S, Keller G, Stallard RF (1987) Major element compositional variation within and between different Late Eocene microtektite strewn fields. Meteoritics 22:61–79

Dickens GR, Castillo MM, Walker JCG (1997) A blast of gas in the latest Paleocene: simulating first-order effects of massive dissociation of oceanic methane hydrate. Geology 25:259–262

Diemer E (1997) Libyan Desert Glass: an impactite. State of the art in July 1996. In: de Michele V (ed) «Silica '96››. Pyramids, Milano, Italy, pp 95–109

Dietz RS (1963) Cryptoexplosion structures. Am J Sci 261:650–664

Dietz RS (1964) Sudbury structure as an astrobleme. J Geol 72:412–434

Dietz RS (1968) Shatter cones in cryptoexplosion structures. In: French BM, Short NM (eds) Shock metamorphism of natural materials. Mono Book Corp, Baltimore, pp 267–285

Dod BD, Sipiera PP, Povenmire H (1985) Electron microprobe and INAA analysis of major and trace element content of six georgiaites [abs]. Lunar Planet Sci 16:187–188

Dodd RT (1986) Thunderstones and shooting stars. Harvard University Press, Cambridge, 196 pp

Dolenec T, Pavsic J, Lojen S (2001) Ir anomalies and other elemental markers near the Paleocene-Eocene boundary in a flysch sequence for the western Tethys (Slovenia). Terra Nova 12:199–204

Donaldson CH (1976) An experimental investigation of olivine morphology. Contrib Miner Petrol 57:187–213

Donaldson S, Hildebrand AR (2001) The global fluence of iridium at the Cretaceous-Tertiary boundary [abs]. Meteorit Planet Sci 36(Suppl):A50

Donnelly TW, Chao ECT (1973) Microtektites of late Eocene age from the eastern Caribbean Sea. Init Rep Deep Sea Drilling Proj 13:1031–1037

Dressler B (1990) Shock metamorphic features and their zoning and orientation in the Precambrian rocks of the Manicouagan Structure, Quebec, Canada. Tectonophysics 171:229–245

DuBois DL (1983) The spatial and temporal relationships of the North American microtektite layer. M.Sc. thesis, University of Delaware, Newark, Delaware, USA, 170 pp

Dubron L, Grajales-Nishimura JM, Alvarez W, Fouke B, Claeys P (2006) Breccia and fall-out suevite in the Guayal KT section (Tabasco, Mexico) [abs]. Geol Soc Am Abstr Prog 38(7):297

Dubrovinskaia NA, Dubrovinsky LS, Saxena SK, Tutti F, Rekhi S, LeBihan T (2000) Direct transition from cristobalite to post-stishovite α-PbO_2-like silica phase. Eur J Mineral 13:479–483

Dubrovinsky LS, Saxena SK, Lazor P, Ahuja R, Eriksson O, Wills JM, Johansson B (1997) Experimental and theoretical identification of a new high-pressure phase of silica. Nature 388:362–365

Dubrovinsky LS, El Goresy A, Gillet P, Wu X, Simionivici A (2009) A novel natural shock-induced high-pressure polymorph of $FeTiO_3$ with the Li-niobate structure from the Ries crater, Germany. Meteorit Planet Sci 44(Suppl):A64

Dutkiewicz A, Rasmussen B, Buick R (1999) Oil preserved in fluid inclusions in Archaean sandstones. Nature 395:885–888

Earth Impact Database (2011) http://www.passc.net/EarthImpactDatabase/

Ebel DS, Grossman L (2005) Spinel-bearing spherules condensed from the Chicxulub impact-vapor plume. Geology 33:293–296

El Goresy A, Fechtig H, Ottemann T (1968) The opaque minerals in impactite glasses. In: French BM, Short NM (eds) Shock metamorphism of natural materials. Mono Book Corp, Baltimore, pp 531–554

El Goresy A, Dubrovinsky L, Sharp TG, Saxena SK, Chen M (2000) A monoclinic post-stishovite polymorph of silica in the Shergotty meteorite. Science 288:1632–1634

El Goresy A, Chen M, Gillet P, Dubrovinsky L, Graup G, Ahuja R (2001a) A natural shock-induced dense polymorph of rutile with α-PbO_2 structure in the suevite from the Ries crater in Germany. Earth Planet Sci Lett 192:485–495

El Goresy A, Chen M, Dubrovinsky L, Gillet P, Graup G (2001b) An ultradense polymorph of rutile with seven-coordinated titanium from the Ries crater. Science 293:1467–1469

El Goresy A, Dubrovinsky LS, Gillet P, Mostefaoui S, Graup G, Drakopoulos M, Simionovici AS, Swamy V, Masaitis VL (2003) A novel cubic, transparent and super-hard polymorph of carbon from the Ries and Popigai craters: implications to understanding dynamic-induced natural high-pressure phase transitions in the carbon system [abs]. Lunar Planet Sci 34: abstract no. 1016.pdf

El Goresy A, Dera P, Sharp TG, Prewitt CT, Chen M, Dubrovinsky L, Wopenka B, Boctor NZ, Hemley RJ (2008) Seifertite, a dense orthorhombic polymorph of silica from the Martian meteorites Shergotty and Zagami. Eur J Mineral 20:523–528

Ellwood BB, Benoist ST, El Hassani A, Wheeler C, Crick RE (2003) Impact ejecta layer from the Mid-Devonian: possible connection to global mass extinction. Science 300:1734–1737

Ellwood BB, Benoist ST, El Hassani A, Wheeler C, Crick RE (2004) Response to comment on "Impact ejecta layer from the Mid-Devonian: possible connection to global mass extinction". Science 303:471c

Elsila JE, de Leon NP, Plows FL, Buseck PR, Zare RN (2005) Extracts of impact breccia samples from Sudbury, Gardnos, and Ries impact craters and the effects of aggregation on C_{60} detection. Geochim Cosmochim Acta 69:2891–2899

Emiliani C, Kraus EB, Shoemaker EM (1981) Sudden death at the end of the Mesozoic. Earth Planet Sci Lett 55:317–334

Engelhardt Wv, Bertsch W (1969) Shock induced planar deformation structures in quartz from the Ries Crater, Germany. Contrib Miner Petrol 20:203–234

Engelhardt Wv, Luft E, Arndt J, Schock H, Weiskirchner W (1987) Origin of moldavites. Geochim Cosmochim Acta 51:1425–1443

Erbacher J, Mosher DC, Malone MJ et al (2004) In: Proceedings of the ocean drilling program 207, Initial Reports. Ocean drilling program, College Station, Texas. doi: 10.2973/odp.proc.ir.207.2004

Erickson DJ, Dickson SM (1987) Global trace element biogeochemistry at the K/T boundary: oceanic and biotic response to a hypothetical meteorite impact. Geology 15:1014–1017

Eriksson PG, Schweitzer JK, Bosch PJA, Schereiber UM, Van Deventer JL, Hatton CJ (1993) The Transvaal sequence: an overview. J Afr Earth Sci 16:25–51

Erwin DH (2006) Extinction: how life on Earth nearly ended 250 million years ago. Princeton University Press, Princeton, 296 pp

Erwin DH, Bowing SA, Jin Y (2002) End-Permian mass extinction: a review. In: Koeberl C, MacLeod KG (eds) Catastrophic events and mass extinctions: impacts and beyond. Geological Society of America, Special Paper 356, pp 363–383

Essene EJ, Moholy-Nagy H, Nelson FW (1987) Crystal-free andesitic glasses from Tikal, Guatemala: possible impactites? [abs]. EOS Trans Am Geophys Union 68(16):462

Evans NJ, Gregoire DC, Grieve RAF, Goodfellow WD, Veizer J (1993) Use of platinum-group elements for impactor identification: terrestrial impact craters and Cretaceous-Tertiary boundary. Geochim Cosmochim Acta 57:3737–3748

Ewers WE, Morris RC (1981) Studies of the Dales Gorge Member of the Brockman Iron Formation, Western Australia. Econ Geol 76:1929–1953

Fanning CM, Flint RB, Parker AJ, Ludwig KR, Blissett AH (1988) Refined Proterozoic evolution of the Gawler Craton, South Australia, through U-Pb geochronology. Precambr Res 40(41):363–386

Farley KA (2009) Late Eocene and late Miocene cosmic dust events: Comet showers, asteroid collisions, or lunar impacts? In: Koeberl C, Montanari A (eds) The late Eocene Earth—hothouse, icehouse, and impacts. Geological Society of America, Special Paper 452, pp 27–35

Farley KA, Mukhopadhyay S (2001) An extraterrestrial impact at the Permian-Triassic boundary? Science 293:2343a

Farley KA, Montanari A, Shoemaker EM, Shoemaker CS (1998) Geochemical evidence for a comet shower in the late Eocene. Science 280:1250–1253

Farley KA, Ward P, Garrison G, Mukhopadhyay S (2005) Absence of extraterrestrial ^{3}He in Permian-Triassic age sedimentary rocks. Earth Planet Sci Lett 240:265–275

Farley KA, Vokrouhlicky D, Bottke WF, Nesvorny D (2006) A late Miocene dust shower from the break-up of an asteroid in the asteroid belt. Nature 439:295–297

Fehn U, Teng R, Elmore D, Kubik PW (1986) Isotopic composition of osmium in terrestrial samples determined by accelerator mass spectrometry. Nature 323:707–710

Feldman VI (1994) The conditions of shock metamorphism. In: Dressler BO, Grieve RAF, Sharpton VL (eds) Large meteorite impacts and planetary evolution. Geological Society of America, Special Paper 293, pp 121–132

Ferrière L, Morrow JR, Amgaa T, Koeberl C (2009a) Systematic study of universal-stage measurements of planar deformation features in shocked quartz: implications for statistical significance and representation of results. Meteorit Planet Sci 44:925–940

Ferrière L, Koeberl C, Reimold WU (2009b) Characterization of ballen quartz and cristobalite in impact breccias: new observations and constraints on ballen formation. Eur J Mineral 21:203–217

Ferrière L, Koeberl C, Reimold WU, Hecht L, Bartosova K (2009c) The origin of "toasted" quartz in impactites revisited [abs]. Lunar Planet Sci 40: abstract no. 1751.pdf

Ferroir T, Dubrovinsky L, El Goresy A, Simionovici A, Nakamura T, Gillet PC (2010) Carbon polymorphism in shocked meteorites: evidence for new natural ultrahard phases. Earth Planet Sci Lett 290:150–154

Fettes D, Desmons J (eds) Metamorphic rocks, a classification and glossary of terms. Cambridge University Press, Cambridge, 244 pp

Firestone EB, West A, Kennett JP, Becker L, Bunch TE, Revay ZS, Schultz PH, Belgya T, Kennett DJ, Erlandson JM, Dickenson OJ, Goodyear AC, Harris RS, Howard GA, Kloosterman JB, Lechier P, Mayewski PA, Montgomery J, Poreda R, Darrah T, Que Hee SS, Smith AR, Stich A, Topping W, Wittke JH, Wolbach WS (2007) Evidence for an extraterrestrial impact 12,900 years ago that contributed to the megafaunal extinctions and the Younger Dryas cooling. Proc Natl Acad Sci U S A 104:16016–16021

Fisher RV, Schmincke H-U (1984) Pyroclastic rocks. Springer, Berlin, 472 pp

Fisher RV, Schmincke H-U (1994) Volcaniclastic sediment transport and deposition. In: Pye K (ed) Sediment transport and depositional processes. Blackwell Scientific, Edinburgh, pp 351–388

Fiske PS, Nellis WJ, Sinha AK (1994) Shock-induced phase transitions of $ZrSiO_4$, reversion kinetics, and implications for terrestrial impact craters [abs]. EOS Trans Am Geophys Union 75(44):416–417

Floran RJ, Papike JJ (1975) Petrology of the low-grade rocks of the Gunflint Iron-Formation, Ontario-Minnesota. Geol Soc Am Bull 86:1169–1190

Florindo F, Roberts AP (2005) Eocene-Oligocene magnetobiochronology of ODP Sites 689 and 690, Maud Rise, Weddell Sea, Antarctica. Geol Soc Am Bull 117:46–66

Folco L, Rochette P, Perchiazzi N, D'Orazio M, Laurenzi M, Tiepolo M (2008) Microtektites from northern Victoria Land Transantarctic Mountains. Geology 36:291–294

Folco L, D'Orazio M, Tiepolo M, Tonarini S, Ottolini L, Perchiazzi N, Rochette P, Glass BP (2009) Transantarctic Mountain microtektites: geochemical affinity with Australasian microtektites. Geochim Cosmochim Acta 73:3694–3722

Folco L, Perchiazzi N, D'Orazio M, Frezzotti ML, Glass BP, Rochette P (2010a) Shocked quartz and other mineral inclusions in Australasian microtektites. Geology 38:211–214

Folco L, Glass BP, D'Orazio M, Rochette P (2010b) A common volatilization trend in Transantarctic Mountain and Australasian microtektites: implications for their formation model and parent crater location. Earth Planet Sci Lett 293:135–139

Folco L, Bigazzi G, D'Orazio M, Balestrieri ML (2011) Fission track age of the Transantarctic Mountain microtektites. Geochim Cosmochim Acta 75:2356–2360

Folger DW (1970) Wind transport of land derived mineral, biogenic and industrial matter over the North Atlantic. Deep-Sea Res 17:337–352

Ford RJ (1972) A possible impact crater associated with Darwin glass. Earth Planet Sci Lett 16:228–230

Ford RJ (1988) An empirical model for the Australasian tektite strewn field. Aust J Earth Sci 35:483–490

Fralick P, Barrett TJ (1995) Depositional controls on iron formation associations in Canada. In: Plint AG (ed) Sedimentary facies analysis. International Association of Sedimentologists, Special Publication 22, pp 137–156

Fralick P, Davis DW, Kissin SA (2002) The age of the Gunflint Formation, Ontario, Canada: single zircon U-Pb age determinations from reworked volcanic ash. Can J Earth Sci 39:1085–1091

Frederichs T, Bleil U, Gersonde R, Kuhn G (2002) Revised age of the Eltanin impact in Southern Ocean [abs]. EOS Trans Am Geophys Union 83 (47): Abstract OS22C-0286

Fredriksson K, Noonan A, Nelen J (1973) Meteoritic, lunar and Lonar impact chondrules. The Moon 7:475–482

Fredriksson K, Brenner P, Dube A, Milton D, Mooring C, Nelen JA (1978) Petrology, mineralogy, and distribution of Lonar (India) and lunar impact breccias and glasses. Smithson Contrib Earth Sci 22:1–13

Frei R, Rosing MT (2005) Search for traces of the late heavy bombardment on the Earth—results from high precision chromium isotopes. Earth Planet Sci Lett 236:28–40

French BM (1967) Sudbury structure, Ontario: Some petrographic evidence for origin by meteorite impact. Science 156:1094–1098

French BM (1968) Sudbury structure, Ontario: some petrographic evidence for an origin by meteorite impact. In: French BM, Short NM (eds) Shock metamorphism of natural materials. Mono Book Corp, Baltimore, pp 383–412

French BM (1984) Impact event at the Cretaceous-Tertiary boundary: a possible site. Science 226:353

French BM (1998) Traces of catastrophe: A handbook of shock-metamorphic effects in terrestrial meteorite impact structures. Lunar and Planetary Institute Contribution Number 954, Lunar and Planetary Institute, Houston, 120 pp

French BM, Koeberl C (2010) The convincing identification of terrestrial impact structures: what works, what doesn't, and why. Earth-Sci Rev 98:123–170

French BM, Short NM (eds) (1968) Shock metamorphism of natural materials. Mono Book Corp, Baltimore, 644 pp

French BM, Koeberl C, Gilmour I, Shirey SB, Dons JA, Naterstad J (1997) The Gardnos impact structure, Norway: petrology and geochemistry of target rocks and impactites. Geochim Cosmochim Acta 61:873–904

Frey FA, Spooner CM, Baedecker PA (1970) Microtektites and tektites: a chemical comparison. Science 170:845–847

Fudali RF (1969) Coesite from the Richat Dome, Mauritania: a misidentification. Science 166:228–230

Fudali RF (1981) The major element chemistry of Libyan Desert Glass and the mineralogy of its precursor. Meteoritics 16:247–259
Fudali RF, Ford RJ (1979) Darwin glass and Darwin crater: a progress report. Meteoritics 14:283–296
Fudali RF, Dyar MD, Griscom DL, Schreiber HD (1987) The oxidation state of iron in tektite glass. Geochim Cosmochim Acta 51:2749–2756
Ganapathy R (1980) A major meteorite impact on the Earth 65 million years ago: evidence from the Cretaceous-Tertiary boundary clay. Science 209:921–923
Ganapathy R (1982) Evidence for a major meteorite impact on the earth 34 million years ago: implication on the origin of the North American tektites and Eocene extinctions. In: Silver LT, Schultz PH (eds) Geological implications of impacts of larger asteroids and comets on the Earth. Geological Society of America, Special Paper 190, pp 513–516
Gao ZG, Xu DY, Zhang QW, Sun YY (1987) Discovery and study of microspherules at the Permian-Triassic boundary of the Shangi section, Guangyuan, Szchwan. Geol Rev 33:203–211
Garde AA, Chadwick B, McCaffrey KJW, Curtis M (1998) Reassessment of the north-western border zone of the Palaeoproterozoic Ketilidian orogen, South Greenland. Geol Greenl Surv Bull 180:111–118
Garde AA, Hamilton MA, Chadwick B, Grocott J, McCaffrey KJW (2002) The Ketilidian orogen of South Greenland: geochronology, tectonics, magmatism, and fore-arc accretion during Palaeoproterozoic oblique convergence. Can J Earth Sci 39:765–793
Garlick GD, Naeser CW, O'Neil JR (1971) A Cuban tektite. Geochim Cosmochim Acta 35:731–734
Gary M, McAfee R Jr, Wolf CL (eds) (1972) Glossary of geology. American Geological Institute, Washington, p 855
Gasparik T (1992) Melting experiments on the enstatite-pyrope join at 80–152 kbar. J Geophys Res 97:15181–15188
Gasperini L, Cocchi L, Stanghellini C, Stanghellini G, Del Bianco F, Serrazanetti M, Carmisciano C (2012) Magnetic and seismic reflection study of Lake Cheko, a possible impact crater for the 1908 Tuguska Event. Geochem Geophy Geosyst 13:Q05008. doi: 10.1029/2012GC004054
Gault DE, Wedekind JA (1978) Experimental studies of oblique impact. In: Proceedings of the 9th lunar and planetary science conference. Geochimica et Cosmochimica Acta, Suppl 10, pp 3843–3875
Gault DE, Quaide WL, Oberbeck VR (1968) Impact cratering mechanics and structures. In: French BM, Short NM (eds) Shock metamorphism of natural materials. Mono Book Corp, Baltimore, pp 87–99
Gayraud J, Robin E, Rocchia R, Froget L (1996) Formation conditions of oxidized Ni-rich spinel and their relevance to the K/T boundary event. In: Ryder G, Fastovsky D, Gartner S (eds) New developments regarding the K/T event and other catastrophes in Earth history. Geological Society of America, Special Paper 307, pp 425–443
Gélinas L, Brooks C (1974) Archean quench-texture tholeiites. Can J Earth Sci 11:324–340
Gentner W, Kleinmann B, Wagner GA (1967) New K-Ar and fission track ages of impact glasses and tektites. Earth Planet Sci Lett 2:83–86
Gentner W, Storzer D, Wagner GA (1969) New fission track ages of tektites and related glasses. Geochim Cosmochim Acta 33:1075–1081
Gentner W, Glass BP, Storzer D, Wagner GA (1970) Fission track ages and ages of deposition of deep-sea microtektites. Science 168:359–361
Gentner W, Kirsten T, Storzer D, Wagner GA (1973) K-Ar and fission-track dating of Darwin glass. Earth Planet Sci Lett 20:204–210
Gerard-Little P, Abbott D, Breger D, Burckle L (2006) Evidence for a possible late Pliocene impact in the Ross Sea [abs]. Lunar Planet Sci 37: abstract no. 1399.pdf

German VN, Podurets MA, Trunin RF (1973) Shock compression of quartz to 90 GPa. J Exp Theor Phys 37:107–115

Gersonde R, Kyte FT, Bleil U, Diekmann B, Flores JA, Gohl K, Hagen G, Hagen R, Kuhn G, Sierro FJ, Völker D, Abelmann A, Bostwick JA (1997) Geological record and reconstruction of the late Pliocene impact of the Eltanin asteroid in the Southern Ocean. Nature 390:357–363

Gibson RL, Reimold WU (2000) Deeply exhumed impact structures: A case study of the Vredefort structure, South Africa. In: Gilmour I, Koeberl C (eds) Impacts and the early Earth. Springer, Berlin, pp 249–277

Gilbert GK (1893) The Moon's face, a study of the origins of its features. Bull Philos Soc Wash 12:241–292

Gilbert GK (1896) The origin of hypotheses, illustrated by the discussion of a topographic problem. Science 3:1–13

Gillet P, Chen M, Dubrovinsky L, El Goresy A (2000) Natural $NaAlSi_3O_8$-hollandite in the shocked Sixiangkou meteorite. Science 287:1633–1636

Gilmour I (1998) Geochemistry of carbon in terrestrial impact processes. In: Grady MM, Hutchison R, McCall GJH, Rothery DA (eds) Meteorites: flux with time and impact effects. Geological Society London, Special Publication 140, pp 205–216

Gilmour I, Koeberl C (eds) (2000) Impacts and the Early Earth. Springer, Berlin, 445 pp

Gilmour I, Russell SS, Arden JW, Lee MR, Franchi IA, Pillinger CT (1992) Terrestrial carbon and nitrogen isotopic ratios from Cretaceous-Tertiary boundary nanodiamonds. Science 258:1624–1626

Girard C, Robin E, Rocchia R, Froget L, Feist R (1997) Search for impact remains at the Frasnian-Famennian boundary in the stratotype area, southern France. Palaeogeogr Palaeoclimatol Palaeoecol 132:391–397

Giuli G, Eeckhout SG, Paris E, Koeberl C, Pratesi G (2005) Iron oxidation state in impact glass from the K/T boundary at Beloc, Haiti, by high-resolution XANES spectroscopy. Meteorit Planet Sci 40:1575–1580

Giuli G, Eeckhout SG, Koeberl C, Pratesi G, Paris E (2008) Yellow impact glass from the K/T boundary at Beloc (Haiti): XANES determination of the Fe oxidation state and implications for formation conditions. Meteorit Planet Sci 43:981–986

Giuli G, Eeckhout SG, Cicconi MR, Koeberl C, Pratesi G, Paris E (2010) Iron oxidation state and local structure in North American tektites. In: Gibson RL, Reimold WU (eds) Large meteorite impacts and planetary evolution IV. Geological Society of America, Special Paper 465, pp 645–651

Glass B (1967) Microtektites in deep-sea sediments. Nature 214:372–374

Glass BP (1968) Glass objects (microtektites?) from deep-sea sediments near the Ivory Coast. Science 161:891–893

Glass BP (1969) Chemical composition of Ivory Coast microtektites. Geochim Cosmochim Acta 33:1135–1147

Glass BP (1972a) Australasian microtektites in deep-sea sediments. In: Hayes DE (ed) Antarctic oceanology II: the Australian–New Zealand sector. American Geophysical Union, Antarctic Research Series, vol 19, pp 335–348

Glass BP (1972b) Bottle-green microtektites. J Geophys Res 77:7057–7064

Glass BP (1974) Microtektite surface sculpturing. Geol Soc Am Bull 85:1305–1314

Glass BP (1982) Possible correlations between tektite events and climatic change? In: Silver LT, Schultz PH (eds) Geological implications of impact of large asteroids and comets on Earth. Geological Society of America, Special Paper 190, pp 251–256

Glass BP (1984a) Solution of naturally-occurring glasses in the geological environment. In: Pye LD, O'Keefe JA, Fréchette VD (eds) Natural glasses, vol 67. Journal of Non-Crystalline Solids, pp 265–286

Glass BP (1984b) Multiple microtektite horizons in upper Eocene marine sediments? Science 224:309

Glass BP (1986) Late Eocene microtektites and clinopyroxene-bearing spherules. In: Pomerol C, Premoli-Silva I (eds) Terminal Eocene Events. Elsevier, Amsterdam, pp 395–401
Glass BP (1989) North American tektite debris and impact ejecta from DSDP Site 612. Meteoritics 24:209-218
Glass BP (1990a) Tektites and microtektites: Key facts and inferences. In: Nicolaysen LO, Reimold WU (eds) Proceedings of the workshop on cryptoexplosions and catastrophes in the geological record, vol 171. Tectonophysics, pp 393–404
Glass BP (1990b) Chronostratigraphy of upper Eocene microspherules. Comment. Palaios 5:387–390
Glass BP (2002) Upper Eocene impact ejecta/spherule layers in marine sediments. Chemie der Erde 62:173–196
Glass BP, Barlow RA (1979) Mineral inclusions in Muong Nong-type indochinites: implications concerning parent material and process of formation. Meteoritics 14:55–67
Glass BP, Burns CA (1987) Late Eocene crystal-bearing spherule layers: two layers or one? Meteoritics 22:265–279
Glass BP, Burns CA (1988) Microkrystites: a new term for impact-produced glassy spherules containing primary crystallites. In: Ryder G (ed) Proceedings of the 18th lunar and planetary science conference. Cambridge University Press, Cambridge, pp 455–458
Glass BP, Crosbie JR (1982) Age of the Eocene/Oligocene boundary based on extrapolation from the North American microtektite layer. The American Association of Petroleum Geologists Bulletin 66:471–476
Glass BP, Fries M (2008) Micro-Raman spectroscopic study of fine-grained shock-metamorphosed rock fragments recovered from the Australasian microtektite layer. Meteorit Planet Sci 43:1487–1496
Glass BP, Koeberl C (1999) Ocean Drilling Program Hole 689B spherules and upper Eocene microtektite and clinopyroxene-bearing spherule strewn fields. Meteorit Planet Sci 34:197–208
Glass BP, Koeberl C (2006) Australasian microtektites and associated impact ejecta in the South China Sea and the Middle Pleistocene supereruption of Toba. Meteorit Planet Sci 41:305–326
Glass BP, Liu S (2001) Discovery of high-pressure $ZrSiO_4$ polymorph in naturally occurring shock-metamorphosed zircons. Geology 29:371–373
Glass BP, Pizzuto JE (1994) Geographic variation in Australasian microtektite concentrations: implications concerning the location and size of the source crater. J Geophys Res 99:19075–19081
Glass BP, Wu J (1993) Coesite and shocked quartz discovered in the Australasian and North American microtektite layers. Geology 21:432–438
Glass BP, Zwart MJ (1979a) North American microtektites in deep-sea drilling project cores from the Caribbean Sea and Gulf of Mexico. Geol Soc Am Bull, Part 1(90):595–602
Glass BP, Zwart PA (1979b) The Ivory Coast microtektite strewnfield: New Data. Earth Planet Sci Lett 43:336–342
Glass BP, Baker RN, Storzer D, Wagner GA (1973) North American microtektites from the Caribbean Sea and their fission track ages. Earth Planet Sci Lett 19:184–192
Glass BP, Swincki MB, Zwart PA (1979) Australasian, Ivory Coast and North American tektite strewn fields: Size, mass and correlation with geomagnetic reversals and other Earth events. In: Proceedings of the 10th lunar and planetary science conference. Geochimica et Cosmochimic Acta, Suppl 11, Pergamon Press, New York, pp 2535–2545
Glass BP, DuBois DL, Ganapathy R (1982) Relationship between an Ir anomaly and the North American microtektite layer in Core RC9-58 from the Caribbean Sea. In: Proceedings of the 13th lunar and planetary science conference, vol 87(Suppl). Journal of Geophysical Research, pp A425–A428
Glass BP, Burns CA, Crosbie JR, DuBois DL (1985) Late Eocene North American microtektites and clinopyroxene-bearing spherules. In: Proceedings of the 16th Lunar and Planetary Science Conference, Part 1, vol 90 (Suppl). Journal of Geophysical Research, pp D175–D196

Glass BP, Hall CM, York D (1986) $^{40}Ar/^{39}Ar$ laser-probe dating of North American tektite fragments from Barbados and the age of the Eocene-Oligocene boundary. Chemical Geology (Isotope Geology Section) 59:181–186

Glass BP, Kent DV, Schneider DA, Tauxe L (1991) Ivory Coast microtektite strewn field: Description and relation to the Jaramillo geomagnetic event. Earth Planet Sci Lett 107: 182–196

Glass BP, Koeberl C, Blum JD, Senftle F, Izett GA, Evans BJ, Thorpe AN, Povenmire H, Strange RL (1995) A Muong Nong-type Georgia tektite. Geochim Cosmochim Acta 59:4071–4082

Glass BP, Muenow DW, Bohor BF, Meeker GP (1997) Fragmentation and hydration of tektites and microtektites. Meteorit Planet Sci 32:333–341

Glass BP, Koeberl C, Blum JD, McHugh CMG (1998) Upper Eocene tektite and impact ejecta layer on the continental slope off New Jersey. Meteorit Planet Sci 33:229–241

Glass BP, Liu S, Leavens PB (2002) Reidite: an impact-produced high-pressure polymorph of zircon found in marine sediments. Am Miner 87:562–565

Glass BP, Liu S, Montanari A (2004a) Impact ejecta in upper Eocene deposits at Massignano, Italy. Meteorit Planet Sci 39:589–597

Glass BP, Huber H, Koeberl C (2004b) Geochemistry of Cenozoic microtektites and clinopyroxene-bearing spherules. Geochim Cosmochim Acta 68:3971–4006

Glass BP, Smith FC, Zullo JB, Simonson BM (2007) Possible shock-metamorphosed grains from the Precambrian Carawine spherule layer, Ripon Hills, Western Australia [abs]. Meteorit Planet Sci 42:A157

Glikson AY (1999) Oceanic mega-impacts and crustal evolution. Geology 27:387–390

Glikson A (2001) The astronomical connection of terrestrial evolution: crustal effects of post-3.8 Ga mega-impact clusters and evidence for major 3.2±0.1 Ga bombardment of the Earth-Moon system. J Geodyn 32:205–229

Glikson A (2004a) Comment on "Bedout: A possible end-Permian impact crater offshore of northwestern Australia". Science 306:613b. doi: 10.1126/science.1100404

Glikson AY (2004b) Early Precambrian asteroid impact-triggered tsunami: Excavated seabed, debris flows, exotic boulders, and turbulence features associated with 3.47–2.47 Ga-old asteroid impact fallout units, Pilbara Craton, Western Australia. Astrobiology 4:1–32

Glikson AY (2005) Geochemical and isotopic signatures of Archean to Paleoproterozoic extraterrestrial impact ejecta/fallout units. Aust J Earth Sci 52:785–798

Glikson A (2006) Asteroid impact ejecta units overlain by iron-rich sediments in the 3.5–2.4 Ga terrains, Pilbara and Kaapvaal cratons: accidental or cause-effect relationships? Earth Planet Sci Lett 246:149–160

Glikson AY (2008) Field evidence of Eros-scale asteroids and impact-forcing of Precambrian geodynamic episodes, Kaapvaal (South Africa) and Pilbara (Western Australia) cratons. Earth Planet Sci Lett 267:558–570

Glikson A, Allen C (2004) Iridium anomalies and fractionated siderophile element patterns, Brockman Iron Formation, Hamersley Basin, Western Australia: evidence for a major asteroid impact in somatic crustal regions of the early Proterozoic earth. Earth Planet Sci Lett 220:247–264

Glikson AY, Vickers J (2010) Asteroid impact connections of crustal evolution. Aust J Earth Sci 57:79–95

Glikson AY, Allen C, Vickers J (2004) Multiple 3.47-Ga-old asteroid impact fallout units, Pilbara Craton, Western Australia. Earth Planet Sci Lett 221:383–396

Glikson AY, Mory AJ, Iasky RP, Pirajno F, Golding SD, Uysal IT (2005) Woodleigh, southern Carnarvon Basin, Western Australia: history of discovery, Late Devonian age, and geophysical and morphometric evidence for a 120 km-diameter impact structure. Aust J Earth Sci 52:545–553

Goderis S, Simonson BM, McDonald I, Hassler SW, Izmer A, Vanhaecke F, Claeys P (2012) Geochemical correlation of two late Archean impact spherule layers between South Africa and Western Australia: the Paraburdoo-Reivilo link [abs]. Lunar Planet Sci 43: abstract no. 1882.pdf

Gohn GS, Koeberl C, Miller KG, Reimold WU, Browning JV, Cockell CS, Horton JW Jr, Kenkmann T, Kulpecz AA, Powars DS, Sanford WE, Voytek MA (2008) Deep drilling into the Chesapeake Bay impact structure. Science 320:1740–1745

Goldin TJ, Melosh HJ (2008) Chicxulub ejecta distribution: patchy or continuous? [abs]. Lunar Planet Sci 39: abstract no. 2469.pdf

Goldin TJ, Melosh HJ (2009) Self-shielding of thermal radiation by Chicxulub impact ejecta: firestorm or fizzle? Geology 37:1135–1138

Goldin TJ, Koeberl C, Melosh HJ (2010) The fate of ejecta rays in the Earth's atmosphere: from Popigai to Chicxulub [abs]. Meteorit Planet Sci 45(Suppl):A65

Goltrant O, Leroux H, Doukhan J-K, Cordier P (1992) Formation mechanism of planar deformation features in naturally shocked quartz. Phys Earth Planet Inter 74:219–240

Gordon GW, Rockman M, Turekian KK, Over J (2009) Osmium isotopic evidence against an impact at the Frasnian-Famennian boundary. Am J Sci 309:420–430

Gorter J (1996) Speculations on the origin of the Bedout High—a large circular structure of pre-Mesozoic age in the offshore Canning Basin, Western Australia. Petroleum Exploration Society of Australia News, pp 32–33

Gostin VA, Zbik M (1999) Petrology and microstructure of distal impact ejecta from the Flinders Range. Meteorit Planet Sci 34:587–592

Gostin VA, Haines PW, Jenkins RJF, Compston W, Williams IS (1986) Impact ejecta horizon within late Precambrian shales, Adelaide Geosyncline, South Australia. Science 233:198–200

Gostin VA, Keays RR, Wallace MW (1989) Iridium anomaly from the Acraman impact ejecta horizon: Impacts can produce sedimentary iridium peaks. Nature 340:542–544

Goto K (2008) The genesis of oceanic impact craters and impact-generated tsunami deposits. In: Shiki T, Tsuji Y, Yamazaki T, Minoura K (eds) Tsunamiites: features and implications. Elsevier, Amsterdam, pp 277–297

Gradstein FM, Agterberg FP, Ogg JG, Hardenbol J, van Veen P, Thierry J, Huang Z (1995) A Triassic, Jurassic and Cretaceous time scale. In: Berggren WA, Kent DV, Aubry M-P, Hardenbol J (eds) Geochronology, time scales and global stratigraphic correlation. Society for Sedimentary Geology, Special Publication 54, pp 95–126

Gradstein FM, Ogg JG, Smith AG, Bleeker W, Lourens LJ (2004) New geologic time scale, with special reference to Precambrian and Neogene. Episodes 27:83–100

Grajales-Nishimura JM, Murillo-Muñetón G, Rosales-Dominguez C, Cedillo-Pardo E, García-Hernández J (2003) Heterogeneity of lithoclast composition in the deep-water carbonate breccias of the K/T boundary sedimentary succession, southeastern Mexico and offshore Campeche. Am Assoc Pet Geol Mem 79:312–329

Grard A, François LM, Dessert C, Dupré B, Goddéris Y (2005) Basaltic volcanism and mass extinction at the Permo-Triassic boundary: environmental impact and modeling of the global carbon cycle. Earth Planet Sci Lett 234:207–221

Grasby SE, Sanei H, Beauchamp B (2011) Catastrophic dispersion of coal fly ash into oceans during the latest Permian extinction. Nat Geosci 4:104–107

Gratz AJ, Fisler DK, Bohor BF (1996) Distinguishing shocked from tectonically deformed quartz by the use of the SEM and chemical etching. Earth Planet Sci Lett 142:513–521

Graup G (1978) Das Kristallin im Nördlinger Ries. Petrographische Zusammensetzung und Auswurfmechanismus der kristallinen Trümmermassen, Struktur des kristallinen Untergrundes und Beziehung zum Modanubikum. Ferdinand Enke Verlag, Stuttgart, 190 pp

Graup G (1981) Terrestrial chondrules, glass spherules and accretionary lapilli from the suevite, Ries Crater, Germany. Earth Planet Sci Lett 55:407–418

Graup G, Spettel B, Hern D, Weidich KF (1989) Mineralogy and phase-chemistry of Ir-enriched pre-K/T layer from the Lattengebirge, Bavarian Alps, and significance for the KTB problem. Earth Planet Sci Lett 95:271–290

Green DH (1972) Archean greenstone belts may include terrestrial equivalents of lunar maria? Earth Planet Sci Lett 15:263–270

Greshake A, Lingemann CM, Schmitt RT, Kenkmann T, Stöffler D (2000) Pressure-temperature-time conditions for shock-produced high-pressure phases [abs]. Meteorit Planet Sci 33: A65–A66

Greshake A, Koeberl C, Fritz J, Reimold WU (2010) Brownish inclusions and dark streaks in Libyan Desert Glass: evidence for high-temperature melting of target rock. Meteorit Planet Sci 45:973–989

Grey K, Calver CR (2007) Correlating the Ediacaran of Australia. In: Vickers-Rich P, Komarower P (eds) The rise and fall of the Ediacaran Biota. Geological Society of London, Special Publication 286, pp 115–135

Grey K, Willman S (2009) Taphonomy of Ediacaran acritarchs from Australia: significance for taxonomy and biostratigraphy. Palaios 24:239–256

Grey K, Walter MR, Calver CR (2003) Neoproterozoic biotic diversification: snowball Earth or aftermath of the Acraman impact? Geology 31:459–462

Grieve RAF (1987) Terrestrial impact structures. Annu Rev Earth Planet Sci 15:245–270

Grieve RAF (1988) The formation of large impact structures and constraints on the nature of Siljan. In: Bodén A, Eriksson KG (eds) Deep drilling in crystalline bedrock, vol I., The deep gas drilling of Siljan impact structure, Sweden and astroblemes. Springer, Berlin, pp 328–348

Grieve RAF (1991) Terrestrial impact: the record in the rocks. Meteoritics 26:175–194

Grieve RAF (2006) Impact structures in Canada. Geological Association of Canada, GEOtext 5, St. John's, Newfoundland, Canada, 210 pp

Grieve RAF, Cintala MJ (1992) An analysis of differential impact melt-crater scaling and implications for the terrestrial impact record. Meteoritics 27:526–538

Grieve RAF, Masaitis VL (1994) The economic potential of terrestrial impact craters. Int Geol Rev 36:105–151

Grieve RAF, Pesonen LJ (1992) The terrestrial impact cratering record. Tectonophysics 216:1–30

Grieve RAF, Robertson PB (1976) Variations in shock deformation at the Slate Island impact structure, Lake Superior, Canada. Contrib Miner Petrol 58:37–49

Grieve RAF, Therriault AM (1995) Planar deformation features in quartz: target effects [abs]. Lunar Planet Sci 26:515–516

Grieve RAF, Therriault A (2000) Vredefort, Sudbury, Chicxulub: three of a kind? Annu Rev Earth Planet Sci 28:305–338

Grieve RAF, Sharpton VL, Stöffler D (1990) Shocked minerals and the K/T controversy. EOS Trans Am Geophys Union 71:1792–1793

Grieve RAF, Langenhorst F, Stöffler D (1996) Shock metamorphism in nature and experiment: II. Significance in geoscience. Meteorit Planet Sci 31:6–35

Gross GA, Zajac IS (1983) Iron formations marginal to the Ungava Craton. In: Trendall AF, Morris RC (eds) Iron-formations: facts and problems. Elsevier, Amsterdam, pp 253–294

Grotzinger JP, Bowring SA, Saylor BZ, Kaufman AJ (1995) Biostratigraphic and geochronologic constraints on early animal evolution. Science 270:598–604

Gucsik A, Zhang M, Koeberl C, Salje EKH, Redfern SAT, Pruneda JM (2004a) Infrared and Raman spectra of $ZrSiO_4$ experimentally shocked at high pressures. Miner Mag 68:801–811

Gucsik A, Koeberl C, Brandstätter F, Libowitzky F, Reimold WU (2004b) Cathodoluminescence, elctronmicroscopy, and Raman spectroscopy of experimentally shocked zircon crystals and naturally shocked zircon from the Ries impact crater. In: Dypvik H, Burchell M, Claeys P (eds) Cratering in marine environments and on ice. Springer, Heidelberg, pp 281–322

Guillemette RN, Yancey TE (2006) Microaccretionary and accretionary carbonate spherules of the Chicxulub impact event from the Brazos River, Texas, and Bass River, New Jersey [abs]. Lunar Planet Sci 37: abstract no. 1779.pdf

Guinasso NL Jr, Schink DR (1975) Quantitative estimates of biological mixing rates in abyssal sediments. J Geophys Res 80:3032–3043

Gupta SC, Ahrens TJ, Yang W (2001) Shock-induced vaporization of anhydrite and global cooling from the K/T impact. Earth Planet Sci Lett 188:399–412

Gutzmer J, Beukes NJ (1998) High-grade manganese ores in the Kalahari manganese field: characterization and dating of ore-forming events (final report to SAMANCOR, Johannesburg) 241 pp

Haines PW (2005) Impact cratering and distal ejecta: the Australian record. Aust J Earth Sci 52:773–783

Hall CM, York D, Sigurdsson H (1991) Laser $^{40}Ar/^{39}Ar$ step-heating ages from single Cretaceous-Tertiary boundary glass spherules [abs]. EOS Trans Am Geophys Union 72, Fall Meeting, Program & Abstracts, Suppl 531

Hallam A (1990) The end-Triassic mass extinction event. In: Sharpton VL, Ward PD (eds) Global catastrophes in earth history; an interdisciplinary conference on impacts, volcanism, and mass mortality. Geological Society of America, Special Paper 247, pp 577–583

Hallam A (2002) How catastrophic was the end-Triassic mass extinction? Lethaia 35:147–157

Hallmann C, Grey K, Webster LJ, McKirdy DM, Grice K (2010) Molecular signature of the Neoproterozoic Acraman impact event. Org Geochem 41:111–115

Han T-M, Runnegar B (1992) Megascopic eukaryotic algae from the 2.1-billion-year-old Negaunee Iron-Formation, Michigan. Science 257:232–235

Hancox PJ, Brandt D, Reimold WU, Koeberl C, Neveling J (2002) Permian-Triassic boundary in the northwest Karoo basin: current stratigraphic placement, implications for basin development models, and the search for evidence of impact. In: Koeberl C, MacLeod KG (eds) Catastrophic events and mass extinctions: impact and beyond. Geological Society of America, Special Paper 356, pp 429–444

Hanneman RE, Strong HM, Bundy FP (1967) Hexagonal diamonds in meteorites: implications. Science 155:995–997

Hansen HJ (1978) Electron microscopy of Precambrian *Vallenia* from Greenland. Bull Geol Soc Den 27 (Special Issue):55–61

Hansen HJ, Gwozdz R, Bromley RG, Rasmussen KL, Vogensen EW, Pedersen KR (1986) Cretaceous-Tertiary boundary spherules from Denmark, New Zealand and Spain. Bull Geol Soc Den 35:75–82

Harland WB, Armstrong RL, Cox AV, Smith LE, Smith AG (1990) A geologic time scale 1989. Cambridge University Press, Cambridge, 320 pp

Harris RS, Schultz PH (2006) Airesites: a new class of late Miocene tektites from Argentina [abs]. Lunar Planet Sci 37: abstract no. 2272.pdf

Harris RS, Duncan MS, Roden MF, Schroeder PA (2009) Discovery of *in situ* impact glass in upper Eocene Coastal Plain strata, Jefferson County, Georgia [abs]. Lunar Planet Sci 40: abstract no. 2502.pdf

Hartmann WK (1972) Paleocratering on the Moon: review of post-Apollo data. Astrophys Space Sci 17:48–64

Hartmann WK, Quantin C, Mangold N (2007) Possible long-term decline in impact rates 2. Lunar impact-melt data regarding impact history. Icarus 186:11–23

Hartung JB, Anderson RR (1996) A brief history of investigation of the Manson impact structure. In: Koeberl C, Anderson RR (eds) The Manson impact structure, Iowa: anatomy of an impact crater. Geological Society of America, Special Paper 302, pp 31–43

Hartung JB, Koeberl C (1994) In search of the Australasian tektite source crater: the Tonle Sap hypothesis. Meteoritics 29:411–416

Haskin LA, Braverman M, King EA (1982) Trace element analyses of some North American tektites [abs]. Lunar Planet Sci 13:302–303

Hassler SW (1993) Depositional history of the Main Tuff Interval of the Wittenoom Formation, late Archean-early Proterozoic Hamersley Group, Western Australia. Precambr Res 60:337–359

Hassler SW, Simonson BM (1989) Deposition and alteration of volcaniclastic strata in two large early Proterozoic iron-formations in Canada. Can J Earth Sci 26:1574–1585

Hassler SW, Simonson BM (2001) The sedimentary record of extraterrestrial impacts in deep shelf environments—evidence from the early Precambrian. J Geol 109:1–19

Hassler SW, Robey HF, Simonson BM (2000) Bedforms produced by impact-generated tsunami, ~2.6 Ga Hamersley basin, Western Australia. Sediment Geol 135:283–294
Hassler SW, Simonson BM, Sumner DY, Murphy M (2005) Neoarchean impact spherule layers in the Fortescue and Hamersley group, Western Australia: stratigraphic and depositional implications of re-correlation. Aust J Earth Sci 52:759–771
Hassler SW, Simonson BM, Sumner DY, Bodin L (2011) Paraburdoo spherule layer (Hamersley Basin, Western Australia): Distal ejecta from a fourth large impact near the Archean-Proterozoic boundary. Geology 39:307–310
Hattori Y, Suzuki K, Honda M, Shimizu H (2003) Re-Os systematics of the Taklimakan Desert sands, moraines and river sediments around the Taklimakan Desert, and Tibetan soils. Geochim Cosmochim Acta 67:1195–1205
Hazel JE (1989) Chronostratigraphy of upper Eocene microspherules. Palaios 4:318–329
Hazen RM (1999) The diamond makers. Cambridge University Press, New York, 244 pp
He JW (1987) Restudy of the Permian-Triassic boundary claystone in Meishan, Changxing, Zhejiang, China [abs]. In: Abstracts of the international geological correlation project 199 meeting, March 3–4, 1987, Beijing, China, pp 29–30
Heath GR, Burckle LH et al (1985) Initial reports of the deep sea drilling project 86. U.S. Government Printing Office, Washington, 804 pp
Heiken G (1972) Morphology and petrology of volcanic ashes. Geol Soc Am Bull 83:1961–1987
Heiken G, Wohletz K (1985) Volcanic ash. University of California Press, Berkeley, 246 pp
Henkel H, Aaro S (2005) Geophysical investigation of the Siljan impact structure—a short review. In: Koeberl C, Henkel H (eds) Impact tectonics. Springer, Berlin, pp 247–283
Herrick RR, Forsberg-Taylor NK (2003) The shape and appearance of craters formed by oblique impact on the Moon and Venus. Meteorit Planet Sci 38:1551–1578
Herzog GF, Alexander CMO'D, Berger EL, Delaney JS, Glass BP (2008) Potassium isotope abundances in Australasian tektites and microtektites. Meteorit Planet Sci 43:1641–1657
Hess J, Bender ML, Schilling J-G (1986) Evolution of the ratio of strontium-87 to strontium-86 in seawater from Cretaceous to present. Science 231:979–984
Hesselbo SP, Robinson SA, Surlyk F, Piasecki S (2002) Terrestrial and marine extinction at the Triassic-Jurassic boundary synchronized with major carbon-cycle perturbation: a link to initiation of massive volcanism? Geology 30:251–254
Heymann D, Chibante LP, Brooks RR, Wolbach WS, Smalley RE (1994) Fullerenes in the Cretaceous-Tertiary boundary layer. Science 265:645–647
Hicks JF, Johnson KR, Obradovich JD, Tauxe L, Clark D (2002) Magnetostratigraphy and geochronology of the Hell Creek and basal Fort Union Formations of southwestern North Dakota and a recalibration of the age of the Cretaceous-Tertiary boundary. In: Hartman JH, Johnson KR, Nichols DJ (eds) The Hell Creek Formation and the Cretaceous-Tertiary boundary in the northern great plains: an integrated continental record of the end of the Cretaceous. Geological Society of America, Special Paper 361, pp 35–55
Higgins AK (1970) The stratigraphy and structure of the Ketilidian rocks of Midternæs, South-West Greenland. Grønlands Geologiske Undersøgelse Bulletin 87, 96 pp
Hildebrand AR (1993) The Cretaceous/Tertiary boundary impact (or the dinosaurs didn't have a chance). J Roy Astron Soc Can 87:77–118
Hildebrand AR, Boynton WV (1988a) Provenance of the K/T boundary layers [abs]. In: Global catastrophes in Earth history: an interdisciplinary conference on impacts, volcanism, and mass mortality. Lunar Planetary Institute Contribution 673, Lunar and Planetary Institute, Houston, pp 78–79
Hildebrand AR, Boynton WV (1988b) Impact wave deposits at the Cretaceous/Tertiary boundary imply an oceanic impact site near North America [abs]. Meteoritics 23:274
Hildebrand AR, Boynton WV (1990) Proximal Cretaceous-Tertiary boundary impact deposits in the Caribbean. Science 248:843–847
Hildebrand AR, Stansberry JA (1992) K/T boundary ejecta distribution predicts size and location of Chicxulub crater [abs]. Lunar Planet Sci 23:537–538

Hildebrand AR, Penfield GT, Kring DA, Pilkington M, Camargo ZA, Jacobsen SB, Boynton WV (1991) Chicxulub crater: a possible Cretaceous/Tertiary boundary impact crater on the Yucatán Peninsula, Mexico. Geology 19:867–871

Hildebrand AR, Moholy-Nagy H, Koeberl C, Senftle F, Thorpe AN, Smith PE, York D (1994) Tektites found in the ruins of the Maya city of Tikal, Guatemala [abs]. Lunar Planet Sci 25:549–550

Hill AC, Grey K, Gostin VA, Webster LJ (2004) New records of Late Neoproterozoic Acraman ejecta in the Officer Basin. Aust J Earth Sci 51:47–51

Hill AC, Haines PW, Grey K, Willman S (2007) New records of Ediacaran ejecta in drillholes from the Stuart Shelf and Officer Basin, South Australia. Meteorit Planet Sci 42:1883–1891

Hill JC, Jimenez A (2010) The Haystacks sandstone: a proposed Devonian-Mississippian impact ejecta [abs]. Geol Soc Am Abstr Prog 42(5):306

Hinze WJ, Allen DJ, Braile LW, Mariano J (1997) The Midcontinent rift system: a major Proterozoic continental rift. In: Ojakangas RW, Dickas AB, Green JC (eds) Middle Proterozoic to Cambrian rifting, central North America. Geological Society of America, Special Paper 312, pp 7–35

Hirata T, Masuda A (1992) Rhenium and osmium systematics on iron and stony iron meteorites. Meteoritics 27:568–575

Ho K-S, Chen J-C (1996) Geochemistry and origin of tektites from the Pengli area, Hainan province, southern China. J SE Asian Earth Sci 13(1):61–72

Hodych JP, Dunning GR (1992) Did Manicouagan impact trigger end-of-Triassic mass extinction? Geology 29:51–54

Hoffman PF, Kaufman AJ, Halverson GP, Schrag DP (1998) A Neoproterozoic snowball Earth. Science 281:1342–1346

Hofmann A, Reimold WU, Koeberl C (2006) Archean spherule layers in the Barberton greenstone belt, South Africa: a discussion of problems related to the impact interpretation. In: Reimold WU, Gibson RL (eds) Processes on the early Earth. Geological Society of America, Special Paper 405, pp 33–56

Hollander DJ, McKenzie JA, Hsü KJ (1993) Carbon isotope evidence for unusual plankton blooms and fluctuations of surface water CO_2 in "Strangelove Ocean" after terminal Cretaceous event. Palaeogeogr Palaeoclimatol Palaeoecol 104:229–237

Hölker T, Deutsch A, Masaitis VL (1997) Nd-Sr isotope signatures of impactites from the Popigai crater (Russia) [abs]. Lunar Planet Sci 28: abstract no. 1356. pdf

Holser WT, Schönlaub H-P, Attrep M Jr, Boeckelmann K, Klein P, Magaritz M, Orth CJ, Fenninger A, Jenny C, Kralik M, Mauritsch H, Pak E, Schramm J-M, Stattegger K, Schmöller R (1989) A unique geochemical record at the Permian-Triassic boundary. Nature 337:39–44

Honda M, Yabuki S, Suzuki K, Ye W, Tatsumi Y (2002) Re-Os systematics in loess and paleosols from the Yili Basin, NW China: implications for the loess-paleosol. Frontier Res Earth Evol 1. http://w3.jamstec.go.jp/ifree/jp/05result/IFREE_Report_for_2001-2002/Data_and_Sample_Analyses?387

Hoppin RA, Dryden JE (1958) An unusual occurrence of Pre-Cambrian crystalline rocks beneath glacial drift near Manson, Iowa. J Geol 66:694–699

Horn P, Müller-Sohnius D, Köhler H, Graup G (1985) Rb-Sr systematic of rocks related to the Ries crater, Germany. Geochim Cosmochim Acta 49:384–392

Horn P, Müller-Sohnius D, Schaaf P, Kleinmann B, Storzer D (1997) Potassium-argon and fission-track dating of Libyan Desert Glass, and strontium and neodymium isotope constraints in its source rocks. In: de Michele V (ed) «Silica '96». Pyramids, Milano, Italy, pp 59–73

Hörz F, Quaide WL (1972) Debye-Scherrer investigations of experimentally shocked silicates. The Moon 6:45–82

Hough RM, Gilmour I, Pillinger CT, Arden JW, Gilkes KWR, Yuan J, Milledge HJ (1995) Diamond and silicon carbide in suevite from the Nördlinger Ries impact crater. Nature 378: 41–44

Hough RM, Gilmour I, Pillinger CT, Langenhorst F, Montanari A (1997) Diamonds from the iridium-rich K-T boundary layer at Arroyo el Mimbral, Tamaulipas, Mexico. Geology 25:1019–1022

Hough RM, Gilmour I, Pillinger CT (1998) Impact nanodiamonds in Cretaceous-Tertiary boundary fireball and ejecta layers: comparison with shock-produced diamond and search for lonsdaleite [abs]. Meteorit Planet Sci 33(Suppl 4):A70–A71

Hough RM, Lee MR, Bevan AWR (2003) Characterization and significance of shocked quartz from the Woodleigh impact structure, Western Australia. Meteorit Planet Sci 38:1341–1350

House MR (1985) Correlation of Mid-Paleozoic ammonoid evolution events with global sedimentary perturbations. Nature 313:17–22. doi:10.1038/313017a0

Howard KT (2008) Geochemistry of Darwin glass and target rocks from Darwin crater, Tasmania, Australia. Meteorit Planet Sci 43:479–496

Howard KT, Haines PW (2007) The geology of Darwin Crater, western Tasmania, Australia. Earth Planet Sci Lett 260:328–339

Hsü KJ, McKenzie JA (1990) Carbon-isotope anomalies at era boundaries; global catastrophes and their ultimate cause. In: Sharpton VL, Ward PD (eds) Global catastrophes in earth history; an interdisciplinary conference on impacts, volcanism, and mass mortality. Geological Society of America, Special Paper 247, pp 61–70

Huber MS, Crne AE, Lepland A, Melezhik VA, Koeberl C, and the FAR-DEEP Science Team (2011) Possible occurrence of distal impact ejecta from the Vredefort impact event in drill cores from the Onega Basin, Russia [abs], Lunar and Planetary Science 42: abstract no. 1487.pdf

Huber MS, Crne AE, Lepland A, McDonald I, Melezhik VA, Koeberl C, and the FAR-DEEP Science Team (2012) Chemical analysis of impact spherules from the Zaonega Formation, Karelia, Russia and implications for Vredefort origin [abs]. Lunar Planet Sci 43: abstract no. 1970.pdf

Huffman AR, Reimold WU (1996) Experimental constraints on shock-induced microstructures in naturally deformed silicates. Tectonophysics 256:165–217

Iasky RP, Mory AJ, Blundell KA (2001) A geophysical interpretation of the Woodleigh impact structure, southern Carnarvon Basin, Western Australia. Geological Survey of Western Australia Report 69, 48 pp

Imae N, Ikeda Y (2010) High-pressure polymorphs of magnesian orthopyroxene from a shock vein in the Yamato-000047 lherzolitic shergottite. Meteorit Planet Sci 45:43–54

Ingle S, Coffin MF (2004) Impact origin for the greater Ontong Java Plateau? Earth Planet Sci Lett 218:123–134

Inoue T, Irifune T, Higo Y, Sanehira T, Sueda Y, Yamada A, Shinmei T, Yamazaki D, Ando J, Funakoshi K, Utsumi W (2006) The phase boundary between wadsleyite and ringwoodite in Mg_2SiO_4 determined by in situ X-ray diffraction. Phys Chem Miner 33:106–114

Isozaki Y (2001) An extraterrestrial impact at the Permian-Triassic boundary? Science 293:2343a

Ito E, Matsui Y, Suito K, Kawai N (1972) High-pressure break-down of enstatite. Proc Jpn Acad 48:412–415

Ivanov BA (2005) Size-frequency distribution of asteroids and impact craters: Estimates of impact rates. In: Adushkin V, Nemchinov I (eds) Catastrophic events caused by cosmic objects. Springer, The Netherlands, pp 91–116

Ivanov BA, Melosh HJ (2003) Impacts do not initiate volcanic eruptions: eruptions close to the crater. Geology 31:869–872

Ivanov BA, Neukum G, Bottke WF Jr, Hartmann WK (2002) The comparison of size-frequency distributions of impact craters and asteroids and the planetary cratering rate. In: Bottke WF Jr, Cellino A, Paolicchi P, Binzel RP (eds) Asteroids III. Lunar and Planetary Institute, Houston, pp 89–101

Izett GA (1987) Authigenic "spherules" in K-T boundary sediments at Caravaca, Spain, and Raton Basin, Colorado and New Mexico, may not be impact derived. Geol Soc Am Bull 99: 78–86

Izett GA (1990) The Cretaceous/Tertiary boundary interval, raton basin, colorado and New Mexico, and its content of shock-metamorphosed minerals; evidence relevant to the K/T boundary impact-extinction theory. Geological Society of America, Special Paper 249, 100 pp

Izett GA (1991a) Are two comet or asteroid impacts recorded at Western North American K-T boundary sites? [abs]. EOS Trans Am Geophys Union 72, Fall Meeting, Program & Abstracts 278

Izett GA (1991b) Tektites in the Cretaceous-Tertiary boundary rocks on Haiti and their bearing on the Alvarez impact extinction hypothesis. J Geophys Res 96(E4):20879–20905

Izett GA, Obradovich JD (1992) Laser-fusion $^{40}Ar/^{39}Ar$ ages of Australasian tektites [abs]. Lunar Planet Sci 23:593–594

Izett GA, Obradovich JD (1994) $^{40}Ar/^{39}Ar$ age constraints for the Jaramillo normal subchron and the Matuyama-Brunhes geomagnetic boundary. J Geophys Res 99:2925–2934

Izett GA, Dalrymple GB, Snee LW (1991) $^{40}Ar/^{39}Ar$ age of Cretaceous-Tertiary tektites from Haiti. Science 252:1539–1542

Izett GA, Cobban WA, Obradovich JD, Kunk MJ (1993) The Manson impact structure: $^{40}Ar/^{39}Ar$ age and its distal impact ejecta in the Pierre Shale in southeastern South Dakota. Science 262:729–732

Izett GA, Cobban WA, Dalrymple GB, Obradovich JD (1998) $^{40}Ar/^{39}Ar$ age of the Manson impact structure, Iowa, and correlative impact ejecta in the Crow Creek Member of the Pierre Shale (Upper Cretaceous), South Dakota and Nebraska. Geol Soc Am Bull 110:361–376

Jackson JC, Horton JW Jr, Chou I-M, Belkin HE (2006) A shock-induced polymorph of anatase and rutile from the Chesapeake Bay impact structure, Virginia, U.S.A. Am Miner 91:604–608

Jahn BM, Simonson BM (1995) Carbonate Pb-Pb ages of the Wittenoom Formation and Carawine Dolomite, Hamersley Basin, Western Australia (with implications for their correlation with the Transvaal Dolomite of South Africa). Precambr Res 72:247–261

Jahn BM, Floran RJ, Simonds CH (1978) Rb-Sr isochron age of the Manicouagan melt sheet, Quebec, Canada. J Geophys Res 83:2799–2803

James HL, Dutton CE, Pettijohn FJ, Wier KL (1968) Geology and ore deposits of the Iron River-Crystal Falls District, Iron County, Michigan. United States Geological Survey, Professional Paper 570, 134 pp

Jansa LF, Aubry MP, Gradstein FM (1990) Comets and extinctions: cause and effects? In: Sharpton VL, Ward PD (eds) Global catastrophes in Earth history. Geological Society of America, Special Paper 247, pp 223–232

Javaux EJ, Marshall CP, Bekker A (2010) Organic-walled microfossils in 3.2-billion-year-old shallow-marine siliciclastic deposits. Nature 463:934–938

Jeffers SV, Manley SP, Bailey ME, Asher DJ (2001) Near-Earth object velocity distribution and consequences for the Chicxulub impactor. Mon Not R Astron Soc 327:126–132

Jéhanno C, Boclet D, Froget L, Lambert B, Robin E, Rocchia R, Turpin L (1992) The Cretaceous-Tertiary boundary at Beloc, Haiti: no evidence for an impact in the Caribbean Area. Earth Planet Sci Lett 109:229–241

Jessberger EK (1988) $^{40}Ar/^{39}Ar$ dating of the Haughton impact structure. Meteoritics 23:233–234

Jiang S, Bralower TJ, Patzkowsky ME, Kump LR, Schueth JD (2010) Geographic controls on nannoplankton extinction across the Cretaceous/Palaeogene boundary. Nat Geosci 3:280–285

Jin YG, Wang Y, Wang W, Shang QH, Cao CQ, Erwin DH (2000) Pattern of marine mass extinction near the Permian-Triassic boundary in South China. Science 289:432–436

Jirsa MA, Weiblen PW, Vislova T, McSwiggen PL (2008) Sudbury impactite layer near Gunflint Lake, NE Minnesota [abs], Institute on Lake Superior Geology Proceedings Part 1—Program and Abstracts 54:42–43

John C, Glass BP (1974) Clinopyroxene-bearing glass spherules associated with North American microtektites. Geology 2:599–602

Johnson BC, Melosh HJ (2012a) Formation of spherules in impact produced vapor plumes. Icarus 217:416–430

Johnson BC, Melosh HJ (2012b) Impact spherules as a record of ancient heavy bombardment of Earth. Nature 485:75–77

Johnston DT, Poulton SW, Fralick PW, Boswell AW, Canfield DE, Farquhar J (2006) Evolution of the oceanic sulfur cycle at the end of the Paleoproterozoic. Geochim Cosmochim Acta 70:5723–5739

Jolley D, Gilmour I, Gurov E, Kelley S, Watson J (2010) Two large impacts at the Cretaceous-Paleogene boundary. Geology 38:835–838

Jones AP, Price DG, DeCarli PS, Price N, Clegg R (2003a) Impact decompression melting: a possible trigger for impact induced volcanism and mantle hotspots? In: Koeberl C, Martínez-Ruiz F (eds) Impact markers in the stratigraphic record. Springer, Berlin, pp 91–119

Jones AP, Kearsley AT, Friend CRL, Robin E, Beard A, Tamura A, Trickett S, Claeys P (2005a) Are there signs of a large Paleocene impact, preserved around Disko Bay, West Greenland? Nuussuaq spherule beds origin by impact instead of volcanic eruption? In: Kenkmann T, Hörz F, Deutsch A (eds) Large meteoritie impacts III. Geological Society of America, Special Paper 384, pp 281–298

Jones AP, Wünnemann K, Price GD (2005b) Modeling impact volcanism as a possible origin for the Ontong Java Plateau. In: Foulger GR, Natland JH, Presnall DC, Anderson DC (eds) Plates, Plumes, and Paradigms. Geological Society of America, Special Paper 388, pp 711–720

Jones GO (1956) Glass. Methuen and Company, London, 119 pp

Jones JH, Neal CR, Ely JC (2003b) Signatures of highly siderophile elements in the SNC meteorites and Mars: a review and petrographic synthesis. Chem Geol 196:21–41

Jones WB (1985) Chemical analyses of Bosumtwi crater target rocks compared with Ivory Coast tektites. Geochim Cosmochim Acta 49:2569–2576

Jones-Zimberlin S, Simonson BM, Kreiss-Tomkins D, Garson D (2006) Using impact spherule layers to correlate sedimentary successions: a case study of the Neoarchean Jeerinah layer (Western Australia). S Afr J Geol 109:245–261

Jordanova D, Hoffmann V, Fehr KT (2004) Mineral magnetic characterization of anthropogenic magnetic phases in the Danube River sediments (Bulgarian part). Earth Planet Sci Lett 221:71–89

Joreau P, French BM, Doukhan J-C (1996) A TEM investigation of shock metamorphism in quartz from the Sudbury impact structure (Canada). Earth Planet Sci Lett 138:137–143

Jørgensen UG, Appel PWU, Hatsukawa Y, Frei R, Oshima M, Toh Y, Kimura A (2009) The Earth-Moon system during the late heavy bombardment period—geochemical support for impacts dominated by comets. Icarus 204:368–380

Jourdan F, Renne PR, Reimold WU (2009) An appraisal of the ages of terrestrial impact structures. Earth Planet Sci Lett 286:1–13

Jovane L, Florindo F, Sprovieri M, Pälike H (2006) Astronomical calibration of the late Eocene/early Oligocene Massignano section (central Italy). Geochem Geophy Geosyst 7:Q07012. doi: 10.1029/2005GC001195

Kaiho K, Kajiwara Y, Nakano T, Miura T, Kawahata H, Tazaki K, Ueshima M, Chen Z, Shi GR (2001) End-Permian catastrophe by bolide impact: evidence of a gigantic release of sulfur from the mantle. Geology 29:815–818

Kamo SL, Krogh TE (1995) Chicxulub crater source for shocked zircon crystals from Cretaceous-Tertiary boundary layer, Saskatchewan: evidence from new U-Pb data. Geology 23:281–284

Kamo SL, Reimold WU, Krogh TE, Colliston WP (1996) A 2.023 Ga age for the Vredefort impact event and a first report of shock metamorphosed zircons in pseudotachylitic breccias and granophyre. Earth Planet Sci Lett 144:369–388

Kamo SL, Lana C, Morgan JV (2011) U–Pb ages of shocked zircon grains link distal K–Pg boundary sites in Spain and Italy with the Chicxulub impact. Earth Planet Sci Lett 310: 401–408

Katongo C, Koeberl C, Witzke BJ, Hammond RH, Anderson RR (2004) Geochemistry and shock petrography of the Crow Creek Member, South Dakota, USA: Ejecta from the 74-Ma Manson impact structure. Meteorit Planet Sci 39:31–51

Kaufmann B (2006) Calibrating the Devonian time scale: a synthesis of U-Pb ID–TIMS ages and conodont stratigraphy. Earth-Sci Rev 76:175–190

Kawai N, Tachimori M, Ito E (1974) A high-pressure hexagonal form of $MgSiO_3$. Proc Jpn Acad 50:378–380

Keays R, Schaefer B, Wallace M, Lambert D (2004) The Acraman impact event horizon: relative contributions of meteoritic, diagenetic and host rock Cu and PGE from Re-Os isotopes [abs]. In: McPhie J, McGoldrick P (eds) Dynamic Earth; past, present and future. 17th Australian geological convention, Hobart, Tasmania; abstracts—Geological Society of Australia vol 73, p 238

Keller G (1986) Stepwise mass extinctions and impact events; late Eocene to early Oligocence. Mar Micropaleontol 10:267–293

Keller G, D'Hondt SL, Vallier TL (1983) Multiple microtektite horizons in Upper Eocene marine sediments: no evidence of mass extinctions. Science 221:150–152

Keller G, D'Hondt SL, Vallier TL (1984) Multiple microtektite horizons in upper Eocene marine sediments? Science 224:309–310

Keller G, D'Hondt SL, Orth CJ, Gilmore JS, Oliver PQ, Shoemaker EM, Molina E (1987) Late Eocene impact microspherules: stratigraphy, age, and geochemistry. Meteoritics 22:25–60

Keller G, Adatte T, Stinnesbeck W, Stueben D, Berner Z (2001) Age, chemo- and biostratigraphy of Haiti spherule-rich deposits: a multi-event K-T scenario. Can J Earth Sci 38:197–227

Keller G, Stinnesbeck W, Adatte T, Stüben D (2003) Multiple impacts across the Cretaceous-Tertiary boundary. Earth-Sci Rev 62:327–363

Keller G, Adatte T, Stinnesbeck W, Rebolledo-Vieyra M, Urrutia-Fucugauchi J, Kramar U, Stüben D (2004a) Chicxulub impact predates the K-T boundary mass extinction. Proc Natl Acad Sci U S A 101:3753–3758

Keller G, Adatte T, Stinnesbeck W, Stüben D, Berner Z, Harting M (2004b) More evidence that the Chicxulub impact predates the K-T mass extinctions. Meteorit Planet Sci 39:1127–1144

Keller G, Adatte T, Berner Z, Harting M, Baum G, Prauss M, Tantawy A, Stueben D (2007) Chicxulub impact predates K-T boundary: new evidence from Brazos, Texas. Earth Planet Sci Lett 255:339–356

Kelley SP, Gurov E (2002) Boltysh, another impact at the KT boundary. Meteorit Planet Sci 37:1031–1043

Kelly DC, Elkins-Tanton LT (2004) Bottle-green microtektites from the South Tasman Rise: deep-sea evidence for an impact event near the Miocene/Pliocene boundary. Meteorit Planet Sci 39:1921–1929

Kelly SP, Spray JG (1997) A late Triassic age for the Rochechouart impact structure, France. Meteorit Planet Sci 32:629–636

Kenkmann T, von Dalwigk I (2000) Radial transpression ridges: a new structural feature of complex impact craters. Meteorit Planet Sci 35:1189–1201

Kennett JP, Stott LD (1991) Abrupt deep-sea warming, paleoceanographic changes and benthic extinctions at the end of the Paleocene. Nature 353:225–229

Kennett DJ, Kennett JP, West A, Mercer C, Que Hee SS, Bement L, Bunch TE, Sellers M, Wolbach WS (2009) Nanodiamonds in the Younger Dryas boundary sediment layer. Science 323:94

Kent DV, Cramer BS, Lanci L, Wang D, Wright JD, Vander Voo R (2003) A case for a comet impact trigger for the Paleocene/Eocene thermal maximum and carbon isotope excursion. Earth Planet Sci Lett 211:13–26

Kepert DA (2001) Carbonate debris flows of the Joffre Member, Hamersley Province, Western Australia [abs]. In: 4th international Archaean symposium, extended abstracts, AGSO Geoscience Australia Record 2001/37, pp 238–240

Kettrup B, Deutsch A, Ostermann M, Agrinier P (2000) Chicxulub impactites: geochemical clues to the precursor rocks. Meteorit Planet Sci 35:1229–1238

Kettrup B, Deutsch A, Masaitis VL (2003) Homogeneous impact melts produced by heterogeneous target? Sr–Nd isotopic evidence from the Popigai crater, Russia. Geochim Cosmochim Acta 67:733–750

Kieffer SW (1971) Shock metamorphism of the Coconino Sandstone at Meteor Crater, Arizona. J Geophys Res 76:5449–5473

Kieffer SW, Phakey PP, Christie JM (1976) Shock processes in porous quartzite: transmission electron microscope observation and theories. Contrib Miner Petrol 59:41–93

Kimura M, Chen M, Yoshida Y, El Goresy A, Ohtani E (2003) Back-transformation of high-pressure phases in a shock melt vein of an H-chondrite during atmospheric passage: implications for the survival of high-pressure phases after decomposition. Earth Planet Sci Lett 217:141–150

King DT Jr, Petruny LW (2003) Cretaceous-Tertiary distal impact ejecta in Alabama—Shell Creek stratigraphic section [abs]. Geol Soc Am Abstr Prog 35(6):22

King DT Jr, Petruny LW (2008) Impact spherule-bearing, Cretaceous-Tertiary boundary sand body, Shell Creek stratigraphic section, Alabama, USA. In: Evans K, Horton JW Jr, King DT Jr, Morrow JR (eds) The sedimentary record of meteorite impact. Geological Society of America, Special Paper 437, pp 179–187

King EA Jr (1966) Comments on paper by F. Cuttitta, RS Clarke, Jr, MK Carron, and CS Annell, 'Martha's Vineyard and selected Georgia tektites: New chemical data'. J Geophys Res 73:2835–2836

Kirkham A (2002) Triassic microtektite pseudomorphs. Geoscientist 12:2–3

Kirkham A (2003) Glauconite spherules from the Triassic of the Bristol area, SW England: probable microtektite pseudomorphs. Proc Geol Assoc 114:11–21

Klaver GT, van Kempen TMG, Bianchi FR, van der Gaast SJ (1987) Green spherules as indicators of the Cretaceous-Tertiary boundary in Deep Sea Drilling Project Hole 603B. Init Rep Deep Sea Drilling Proj 93:1039–1053

Klein C (2005) Some Precambrian banded iron-formations (BIFs) from around the world: their age, geologic setting, mineralogy, metamorphism, geochemistry, and origin. Am Miner 90: 1473–1499

Kleinmann B (1969) The breakdown of zircon observed in the Libyan Desert Glass as evidence of its impact origin. Earth Planet Sci Lett 5:497–501

Kleinmann B, Horn P, Langenhorst F (2001) Evidence for shock metamorphism in sandstones from the Libyan Desert Glass strewn field. Meteorit Planet Sci 36:1277–1282

Klemm V, Levasseur S, Frank M, Hein JR, Halliday AN (2005) Osmium isotope stratigraphy of a marine ferromanganese crust. Earth Planet Sci Lett 238:42–48

Klöck W, Palme H, Tobschall HJ (1986) Trace elements in natural metallic iron from Disko Island, Greenland. Contrib Miner Petrol 93:273–282

Knoll AH (2003) Life on a young planet: the first three billion years of evolution on Earth. Princeton University Press, Princeton, 277 pp

Knoll AH, Beukes NJ (2009) Introduction: Initial investigations of a Neoarchean shelf margin-basin transition (Transvaal Supergroup, South Africa). Precambr Res 169:1–14

Knoll AH, Walter MR, Narbonne GM, Christie-Blick N (2006) The Ediacaran Period: a new addition to the geologic time scale. Lethaia 39:13–30

Koch PL, Zachos J, Gingerich PD (1992) Correlation between isotope records in marine and continental carbon reservoirs near the Paleocene/Eocene boundary. Nature 358:319–322

Koeberl C (1990) The geochemistry of tektites: an overview. Tectonophysics 171:405–422

Koeberl C (1992a) Geochemistry and origin of Muong Nong-type tektites. Geochim Cosmochim Acta 56:1033–1064

Koeberl C (1992b) Water content of glasses from the K/T boundary, Haiti: An indication of impact origin. Geochim Cosmochim Acta 56:4329–4332

Koeberl C (1993a) Extraterrestrial component associated with Australasian microtektites in a core from ODP Site 758B. Earth Planet Sci Lett 119:453–458

Koeberl C (1993b) Chicxulub crater, Yucatan: tektites, impact glasses, and geochemistry of target rocks and breccias. Geology 21:211–214
Koeberl C (1994) Tektite origin by hypervelocity asteroidal or cometary impact: Target rocks, source craters, and mechanisms. In: Dressler BO, Grieve RAF, Sharpton VL (eds) Large meteorite impacts and planetary evolution. Geological Society of America, Special Paper 293, pp 133–151
Koeberl C (1997) Libyan Desert Glass: geochemical composition and origin. In: de Michele V (ed) «Silica '96››. Pyramids, Milano, Italy, pp 121–132
Koeberl C (1998) Identification of meteoritical components in impactites. In: Grady MM, Hutchison R, McCall GJH, Rothery DA (eds) Meteorites: Flux with Time and Impact Effects. Geological Society of London, Special Publication 140, pp 133–152
Koeberl C (2000) Confirmation of meteoritic component in Libyan Desert Glass from osmium-isotopic data [abs]. Meteorit Planet Sci 35:A89–A90
Koeberl C (2002) Mineralogical and geochemical aspects of impact craters. Mineral Mag 66:745–768
Koeberl C (2004) The late heavy bombardment in the inner solar system: is there a connection to Kuiper Belt objects? Earth Moon Planets 92:79–87
Koeberl C (2007) The geochemistry and cosmochemistry of impacts. In: Davis A (ed) Treatise of Geochemistry, online edition, vol 1. Elsevier, Amsterdam, pp 1.28.1–1.28.52. doi: 10.1016/B978-008043751-4/00228-5
Koeberl C, Glass BP (1988) Chemical composition of North American microtektites and tektite fragments from Barbados and DSDP Site 612 on the continental slope off New Jersey. Earth Planet Sci Lett 87:286–292
Koeberl C, MacLeod KG (eds) (2002) Catastrophic events and mass extinctions: impacts and beyond. Geological Society of America, Special Paper 356, 746 pp
Koeberl C, Reimold WU (1995) Early Archaean spherule beds in the Barberton Mountain Land, South Africa: no evidence for impact origin. Precambr Res 74:1–33
Koeberl C, Reimold WU (2005) Bosumtwi impact crater: an updated and revised geological map, with explanations. Jahrbuch der Geologischen Bundesanstalt, Wien (Yearbook of the Austrian Geological Survey) vol 145, pp 31–70 (+ 1 map, 1:50,0000)
Koeberl C, Schultz PH (1992) Chemical composition of meteoritic and impactite samples from Rio Cuarto craters, Argentina [abs]. Lunar Planet Sci 23:707–708
Koeberl C, Shirey SB (1993) Detection of a meteoritic component in Ivory Coast tektites with rhenium-osmium isotopes. Science 261:595–598
Koeberl C, Shirey SB (1996) Re-Os isotope study of rocks from the Manson impact structure. In: Koeberl C, Anderson RR (eds) The manson impact structure, Iowa: anatomy of an impact crater. Geological Society of America, Special Paper 302, pp 331–339
Koeberl C, Sigurdsson H (1992) Geochemistry of impact glasses from the K/T boundary in Haiti: relation to smectites and a new type of glass. Geochim Cosmochim Acta 56:2113–2129
Koeberl C, Brandstaetter F, Niedermayr G, Kurat G (1988) Moldavites from Austria. Meteoritics 23:325–332
Koeberl C, Sharpton VL, Murali AV, Burke K (1990) The Kara and Ust-Kara impact structures (USSR) and their relevance to the K/T boundary event. Geology 18:50–53
Koeberl C, Reimold WU, Boer RH (1993) Geochemistry and mineralogy of Early Archaean spherule beds, Barberton Mountain Land, South Africa: evidence for origin by impact doubtful. Earth Planet Sci Lett 119:441–452
Koeberl C, Sharpton VL, Schuraytz BC, Shirey SB, Blum JD, Marin LE (1994) Evidence of a meteoritic component in melt rock from the Chicxulub structure. Geochim Cosmochim Acta 58:1679–1684
Koeberl C, Poag CW, Reimold WU, Brandt D (1996) Impact origin of Chesapeake Bay structure and the source of the North American tektites. Science 271:1263–1266
Koeberl C, Masaitis VL, Shafranovsky GI, Gilmour I, Langenhorst F, Schrauder M (1997a) Diamonds from the Popigai impact structure, Russia. Geology 25:967–970

Koeberl C, Bottomley R, Glass BP, Storzer D (1997b) Geochemistry and age of Ivory Coast tektites and microtektites. Geochim Cosmochim Acta 61:1745–1772

Koeberl C, Reimold WU, Blum JD, Chamberlain CP (1998) Petrology and geochemistry of target rocks from the Bosumtwi impact structure, Ghana, and comparison with Ivory Coast tektites. Geochim Cosmochim Acta 62:2179–2196

Koeberl C, Reimold WU, McDonald I, Rosing M (2000) Search for petrographic and geochemical evidence for the Late Heavy Bombardment on Earth in early Archaean rocks from Isua, Greenland. In: Gilmour I, Koeberl C (eds) Impacts and the early Earth. Lecture notes in earth sciences, vol 91. Springer, Berlin, pp 73–97

Koeberl C, Peucker-Ehrenbrink B, Reimold WU, Shukolyukov A, Lugmair GW (2002a) Comparison of osmium and chromium isotopic methods for the detection of meteoritic components in impactites: examples from Morokweng and Vredefort impact structures, South Africa. In: Koeberl C, McLeod KG (eds) Catastrophic events and mass extinction: impacts and beyond. Geological Society of America, Special Paper 356, pp 607–617

Koeberl C, Gilmour I, Reimold WU, Claeys P, Ivanov B (2002b) End-Permian catastrophe by bolide impact: evidence of a gigantic release of sulfur from the mantle: comment. Geology 30:855–856

Koeberl C, Huber H, Morgan M, Warme JW (2003) Search for an extraterrestrial component in the Late Devonian Alamo impact breccia (Nevada): Results of iridium measurements. In: Koeberl C, Martínez-Ruiz F (eds) Impact markers in the stratigraphic record. Impact Studies, vol 3. Springer, Heidelberg, pp 315–332

Koeberl C, Shukolyukov A, Lugmair G (2004a) An ordinary chondrite impactor composition for the Bosumtwi impact structure, Ghana, West Africa: Discussion of siderophile element contents and Os and Cr isotope data [abs]. Lunar Planet Sci 35: abstract no. 1256.pdf

Koeberl C, Farley KA, Peucker-Ehrenbrink B, Sephton MA (2004b) Geochemistry of the end-Permian extinction event in Austria and Italy: no evidence for an extraterrestrial component. Geology 32:1053–1056

Koeberl C, Shukolyukov A, Lugmair GW (2007a) Chromium isotopic studies of terrestrial impact craters: identification of meteoritic components at Bosumtwi, Clearwater East, Lappajärvi, and Rochechouart. Earth Planet Sci Lett 256:534–546

Koeberl C, Brandstätter F, Glass BP, Hecht L, Mader D, Reimold WU (2007b) Uppermost impact fallback layer in the Bosumtwi crater (Ghana): mineralogy, geochemistry, and comparison with Ivory Coast tektites. Meteorit Planet Sci 42:709–729

Kohl I, Simonson BM, Berke M (2006) Diagenetic alteration of impact spherules in the Neoarchean Monteville layer, South Africa. In: Reimold WU, Gibson RL (eds) Processes on the early Earth. Geological Society of America, Special Paper 405, pp 57–73

Kohl IE, Byerly GR, Lowe DR (2007) A reconnaissance study of rutile from the Barberton Greenstone Belt, South Africa: implications for a possible new Archean impact layer [abs]. EOS Trans Am Geophys Union 88(52) Fall Meeting supplement: abstract V23C-1557

Komarov AM, Masaitis VL, Yezerskiy VA (1991) Fission-track dating of the Urengoy tektites using an age standard. Geochim Cosmochim Acta 28:11–17

Kopp RE, Raub TD, Schumann D, Vali H, Smirnov AV, Kirschvink JL (2007) Magnetofossil spike during the Paleocene-Eocene thermal maximum: Ferromagnetic resonance, rock magnetic, and electron microscopy evidence from Ancora, New Jersey, USA. Paleoceanography 22: PA4103, doi:10.1029/2007PA001473

Koroteev VA, Loginov VN, Masaitis VL, Kozlov VS, Boriskov FF (1994) Tektite from Astaf Evskava placer deposit, Southern Urals (In Russian). Zapiski Vserossiĭskogo mineralogicheskogo obshchestva 123:44–48

Krapež B, Barley ME, Pickard AL (2003) Hydrothermal and resedimented origins of the precursor sediments to banded iron formation: sedimentological evidence from the Early Palaeoproterozoic Brockman Supersequence of Western Australia. Sedimentology 50:979–1011

Kring DA (1999) Ozone-depleting Cl and Br produced by the Chicxulub impact event [abs]. Meteorit Planet Sci 34:A67–A68

Kring DA (2000) Impact events and their effect on the origin, evolution, and distribution of life. GSA Today 10(8):2–7

Kring DA (2007) The Chicxulub impact event and its environmental consequences at the Cretaceous-Tertiary boundary. Palaeogeogr Palaeoclimatol Palaeoecol 255:4–21

Kring DA, Boynton WV (1992) Petrogenesis of an augite-bearing melt rock in the Chicxulub structure and its relationship to K/T impact spherules in Haiti. Nature 358:141–144

Kring DA, Durda DD (2002) Trajectories and distribution of material ejected from the Chicxulub: implications for postimpact wildfires. J Geophys Res 107(E8):6-1–6-22. doi:10.1029/2001JE001532

Kring DA, Wolbach WS, Patzer A, Goodwin D (2007) A test of the impact-mass extinction hyphothesis at the Triassic-Jurassic boundary [abs]. Meteorit Planet Sci 42(Suppl):A89

Krogh TE, Davis DW, Corfu F (1984) Precise U-Pb zircon and baddeleyite ages for the Sudbury area. In: Pye EG, Naldrett AJ, Giblin PE (eds) The geology and ore deposits of the Sudbury structure. Ontario Geological Survey, Special volume 1, pp 431–446

Krogh TE, Kamo SL, Bohor BF (1993a) Fingerprinting the K/T impact site and determining the time of impact by U-Pb dating of single shocked zircons from distal ejecta. Earth Planet Sci Lett 119:425–429

Krogh TE, Kamo SL, Sharpton VL, Marin LE, Hildebrand AR (1993b) U-Pb ages of single shocked zircons linking distal K/T ejecta to the Chicxulub crater. Nature 366:731–734

Kröner A, Byerly GR, Lowe DR (1991) Chronology of early Archaean granite-greenstone evolution in the Barberton Mountain Land, South Africa, based on precise dating by single zircon evaporation. Earth Planet Sci Lett 103:41–54

Kruge MA, Stankiewicz BA, Crelling JC, Montanari A, Bensley DF (1994) Fossil charcoal in the Cretaceous-Tertiary boundary strata: evidence for catastrophic firestorm and megawave. Geochim Cosmochim Acta 58:1393–1397

Krull ES, Lehrmann DJ, Druke D, Kessel B, Yu Y-Y, Li R (2004) Stable carbon isotope stratigraphy across the Permian–Triassic boundary in shallow marine carbonate platforms, Nanpanjiang Basin, south China. Palaeogeogr Palaeoclimatol Palaeoecol 204:297–315

Krull-Davatzes AE, Lowe DR, Byerly GR (2006) Compositional grading in an $\sim$3.24 Ga impact-produced spherule bed, Barberton greenstone belt, South Africa: a key to impact plume evolution. S Afr J Geol 109:233–244

Krull-Davatzes AE, Byerly GR, Lowe DR (2010) Evidence for a low-O_2 Archean atmosphere from nickel-rich chrome spinels in 3.24 Ga impact spherules, Barberton greenstone belt, South Africa. Earth Planet Sci Lett 296:319–328

Krull-Davatzes AE, Lowe DR, Byerly GR (2012) Mineralogy and diagenesis of 3.24 Ga meteorite impact spherules. Precambr Res 196–197:128–148

Kuiper KF, Deino A, Hilgren FJ, Krijgsman W, Renne PR, Wijbrans JR (2008) Synchronizing rock clocks of Earth history. Science 320:500–504

Kunk MJ, Izett GA, Haugerud RA, Sutter JF (1989) ^{40}Ar-^{39}Ar dating of the Manson impact structure: a Cretaceous-Tertiary boundary crater candidate. Science 244:1565–1568

Kunz J, Bollinger K, Jessberger EK, Storzer D (1995) Ages of Australasian tektites [abs]. Lunar Planet Sci 26:809–810

Kusaba K, Syono Y, Kikuchi M, Fukuoka K (1985) Shock behavior of zircon: phase transition to scheelite structure and decomposition. Earth Planet Sci Lett 72:433–439

Kutchko BG, Kim AG (2006) Fly ash characterization by SEM-EDS. Fuel 85:2537–2544

Kyte FT (1998) A meteorite from the Cretaceous/Tertiary boundary. Nature 396:237–239

Kyte FT (2002) Composition of impact melt debris from the Eltanin impact strewn field, Bellingshausen Sea. Deep Sea Res Part II: Top Stud Oceanogr 49:1029–1047

Kyte FT, Bohor BF (1995) Nickel-rich magnesiowüstite in Cretaceous/Tertiary boundary spherules crystallized from ultramafic, refractory silicate liquid. Geochim Cosmochim Acta 59:4967–4974

Kyte FT, Bostwick JA (1995) Magnesioferrite spinel in Cretaceous/Tertiary boundary sediments of the Pacific basin: Remnants of hot, early ejecta from the Chicxulub impact? Earth Planet Sci Lett 132:113–127

Kyte FT, Brownlee DE (1985) Unmelted meteorite debris in the Late Eocene iridium anomaly: evidence for the ocean impact of a nonchondritic asteroid. Geochim Cosmochim Acta 49:1095–1108

Kyte FT, Smit J (1986) Regional variations in spinel compositions: an important key to the Cretaceous/Tertiary event. Geology 14:485–487

Kyte FT, Wasson JT (1986) Accretion rate of extraterrestrial matter: iridium deposited 33 to 67 million years ago. Science 232:1225–1229

Kyte FT, Zhou Z, Wasson JT (1980) Siderophile-enriched sediments from the Cretaceous-Tertiary boundary. Nature 288:651–656

Kyte FT, Zhou Z, Wasson JT (1981) High noble metal concentrations in a late Pliocene sediment. Nature 292:417–420

Kyte FT, Zhou L, Wasson JT (1988) New evidence on the size and possible effects of a Late Pliocene oceanic impact. Science 241:63–65

Kyte FT, Zhou L, Lowe DR (1992) Noble metal abundances in an Early Archean impact deposit. Geochim Cosmochim Acta 56:1365–1372

Kyte FT, Bostwick JA, Zhou L (1995) Identification and characterization of the Cretaceous/Tertiary boundary at ODP Sites 886 and 803 and DSDP Site 576. In: Rea DK, Basov IA, Scholl DW, Allan JF (eds) Proceedings of the ocean drilling program 145, scientific results. Ocean drilling program, College Station, Texas, pp 427–434

Kyte FT, Bostwick JA, Zhou L (1996) The Cretaceous-Tertiary boundary on the Pacific plate: composition and distribution of impact debris. In: Ryder G, Fastovsky D, Gartner S (eds) The Cretaceous-Tertiary event and other catastrophes in Earth history. Geological Society of America, Special Paper 307, pp 389–401

Kyte FT, Shukolyukov A, Lugmair GW, Lowe DR, Byerly GR (2003) Early Archean spherule beds: chromium isotopes confirm origin from multiple impacts of projectiles of carbonaceous chondrite type. Geology 31:283–286

Kyte FT, Tanner LH, Walker AE (2008) Anomalous iridium at the palynological Triassic-Jurassic boundary in the Fundy Basin, Partridge Island, Nova Scotia [abs]. Lunar Planet Sci 29: abstract no. 2463.pdf

Kyte FT, Shukolyukov A, Hildebrand AR, Lugmair GW, Hanova J (2011) Chromium-isotopes in Late Eocene impact spherules indicate a likely asteroid belt provenance. Earth Planet Sci Lett 302:279–286

LaBerge GL (1966) Altered pyroclastic rocks in iron-formation in the Hamersley Range, Western Australia. Econ Geol 61:147–161

Lam J, Raunsgaard Pedersen K (1968) Precambrian organic compounds from the Ketilidian of South-West Greenland, Part II. Grønlands Geologiske Undersøgelse Bulletin 101, 15 pp

Lange JM (1996) Tektite glasses from Lusatia (Lausitz), Germany. Chemie der Erde 56:495–510

Langenhorst F (1994) Shock experiments on α- and β-quartz: II. X-ray investigations. Earth Planet Sci Lett 128:638–698

Langenhorst F (1996) Characteristics of shocked quartz in late Eocene impact ejecta from Massignano (Ancona, Italy): clues to shock conditions and source crater. Geology 24:487–490

Langenhorst F (2002) Shock metamorphism of some minerals: basic introduction and microstructural observations. Bull Czech Geochem Surv 77:265–282

Langenhorst F, Deutsch A (1994) Shock experiments on pre-heated α- and β-quartz; I. Optical and density data. Earth Planet Sci Lett 125:407–420

Langenhorst F, Deutsch A (1998) Minerals in terrestrial impact structures and their characteristic features. In: Marfunin AS (ed) Advances in mineralogy, vol 3, Mineral matter in space, mantle, ocean floor, biosphere, environmental management, and jewelry. Springer, Berlin, pp 95–119

Langenhorst F, Dressler B (2003) First observation of silicate hollandite in a terrestrial rock [abs]. Third international conference on large meteorite impacts, Nördlingen, Germany, August 5–7, 2003. Lunar and Planetary Institute, Houston, abstract no. 4046.pdf

Langenhorst F, Poirier J-P (2000) 'Eclogitic' minerals in a shocked basaltic meteorite. Earth Planet Sci Lett 176:259–265

Langenhorst F, Shafranovsky GI, Masaitis VL (1998) A comparative study of impact diamonds from the Popigai, Ries, Sudbury, and Lappajärvi craters [abs]. Meteorit Planet Sci 33:A90–A91

Langenhorst F, Shafranovsky GI, Masaitis VL, Koivisto M (1999) Discovery of impact diamonds in a Fennoscandian crater and evidence for their genesis by solid-state transformation. Geology 27:747–750

Langenhorst F, Kyte FT, Retallack GJ (2005) Reexamination of quartz grains from the Permian-Triassic section at Graphite Peak, Antarctica [abs]. Lunar Planet Sci 36: abstract no. 2358.pdf

Laurenzi MA, Bigazzi G, Balestrieri ML, Bouška V (2003) $^{40}Ar/^{39}Ar$ laser probe dating of the Central European tektite-producing impact event. Meteorit Planet Sci 38:887–893

Lawton TF, Shipley KW, Aschoff JL, Giles KA, Vega FJ (2005) Basinward transport of Chicxulub ejecta by tsunami-induced backflow, La Popa basin, northeastern Mexico, and its implications for distribution of impact-related deposits flanking the Gulf of Mexico. Geology 33:81–84

Lee M-Y, Wei K-Y (2000) Australasian microtektites in the South China Sea and the West Philippine Sea: implications for age, size, and location of the impact crater. Meteorit Planet Sci 35:1151–1155

Lee Y-T, Chen J-C, Ho K-S, Juang W-S (2004) Geochemical studies of tektites from East Asia. Geochem J 38:1–17

Lerbekmo JF, Sweet AR, Davidson RA (1999) Geochemistry of Cretaceous-Tertiary (K-T) boundary interval: south-central Saskatchewan and Montana. Can J Earth Sci 36:717–724

Leroux H, Reimold WU, Doukhan J-C (1994) A TEM investigation of shock metamorphism in quartz from the Vredefort dome, South Africa. Tectonophysics 230:223–239

Leroux H, Rocchia R, Froget L, Orue-Etxebarria X, Doukhan J-C, Robin E (1995a) The K/T boundary at Beloc (Haiti): compared stratigraphic distributions of the boundary markers. Earth Planet Sci Lett 131:255–268

Leroux H, Warme JE, Doukhan J-C (1995b) Shocked quartz in the Alamo breccias, southern Nevada; evidence for a Devonian impact event. Geology 23:1003–1006

Leroux H, Reimold WU, Koeberl C, Hornemann U, Doukhan J-C (1999) Experimental shock deformation in zircon: a transmission electron microscopic study. Earth Planet Sci Lett 169: 291–301

Levi BG (1992) Twelve-year trail of clues leads to impact crater from the K-T boundary. Physics Today 45(12):17–19

Levman BG, von Bitter PH (2002) The Frasnian-Famennian (mid-Late Devonian) boundary in the type section of the Long Rapids Formation, James Bay Lowlands, northern Ontario, Canada. Can J Earth Sci 39:1795–1818

Li C-H, Ouyang Z-Y, Liu D-S, An Z-S (1993) Microtektites and glassy microspherules in loess: their discoveries and implications. Sci China (Ser B) 36:1141–1152

Linde RK, DeCarli PS (1969) Polymorphic behavior of titania under dynamic loading. J Chem Phys 50:319–325

Liu L-G (1974a) Disproportionation of kyanite to corundum plus stishovite at high pressure and temperature. Earth Planet Sci Lett 24:224–228

Liu L-G (1974b) Silicate perovskite from phase transformations of pyrope-garnet at high-pressure and temperature. Geophys Res Lett 1:277–280

Liu L-G (1976) The high-pressure phases of $MgSiO_3$. Earth Planet Sci Lett 31:200–208

Liu L-G (1978) High-pressure phase transformations of albite, jadeite and nepheline. Earth Planet Sci Lett 37:438–444

Liu S (2006) Characterization, geographical distribution, and number of Upper Eocene impact ejecta layers and their correlations with source craters. Ph.D. dissertation, University of Delaware, Newark, Delaware, USA, 283 pp

Liu S, Papanastassiou DA, Ngo HH, Glass BP (2006) Sr and Nd analyses of upper Eocene spherules and their implications for target rock. Meteorit Planet Sci 41:705–714

Liu S, Glass BP, Kyte FT, Bohaty SM (2009) The upper Eocene clinopyroxene-bearing spherule layer: New sites, nature of the strewn field, Ir data, and discovery of coesite and shocked quartz. In: Koeberl C, Montanari A (eds) The late Eocene Earth—hothouse, icehouse, and impacts. Geological Society of America, Special Paper 452, pp 37–70

Lo C-H, Howard KT, Chung S-L, Meffre S (2002) Laser fusion argon-49/argon-39 ages of Darwin impact glass. Meteorit Planet Sci 37:1555–1562

Lodders K (2003) Solar system abundances and condensation temperatures of the elements. Astrophys J 591:12201247

Lodders K, Fegley B Jr (1998) The Planetary Scientist's Companion. Oxford University Press, New York, 371 pp

Lofgren G (1971a) Spherulitic textures in glassy and crystalline rocks. J Geophys Res 76:5635–5648

Lofgren G (1971b) Devitrified glass fragments from Apollo 11 and Apollo 12 lunar samples. In: Proceedings of the 2nd lunar science conference. Pergamon Press, New York, Geochim Cosmochim Acta, Suppl 2, pp 949–955

Lofgren G (1977) Dynamic crystallization experiments bearing on the origin of textures in impact-generated liquids. In: Proceedings of the 8th Lunar Science Conference. Pergamon Press, New York, Geochim Cosmochim Acta, Suppl 8:2079–2095

Lofgren GE (1980) Experimental studies on the dynamic crystallization of silicate melts. In: Hargraves RB (ed) Physics of magmatic processes. Princeton University Press, Princeton, pp 487–551

Lofgren G (1983) Effect of heterogeneous nucleation on basaltic textures: a dynamic crystallization study. J Petrol 24:229–255

Lofgren G, Donaldson CH (1975) Curved branching crystals and differentiation in comb-layered rocks. Contrib Miner Petrol 49:309–319

Longinelli A, Sighinolfi G, de Michele V, Selmo E (2011) $\delta^{18}O$ and chemical composition of Libyan Desert Glass, country rocks, sands: new considerations on target material. Meteorit Planet Sci 46:218–227

Lowe DR (1999) Petrology and sedimentology of cherts and related silicified sedimentary rocks in the Swaziland Supergroup. In: Lowe DR, Byerly GR (eds) Geological evolution of the Barberton Greenstone Belt, South Africa. Geological Society of America, Special Paper 329, pp 83–114

Lowe DR, Byerly GR (1986) Early Archean silicate spherules of probable impact origin, South Africa and Western Australia. Geology 14:83–86

Lowe DR, Byerly GR (1999) Stratigraphy of the west-central part of the Barberton Greenstone Belt, South Africa. In: Lowe DR, Byerly GR (eds) Geological evolution of the Barberton Greenstone Belt, South Africa. Geological Society of America, Special Paper 329, pp 1–36

Lowe DR, Byerly GR (2010) Did LHB end not with a bang but with a whimper? The geologic evidence [abs]. Lunar Planet Sci 41: abstract no. 2563.pdf

Lowe DR, Nocita BW (1986) Foreland basin sedimentation in the Mapepe Formation, southern-facies Fig Tree Group. In: Lowe DR, Byerly GR (eds) Geological evolution of the Barberton Greenstone Belt, South Africa. Geological Society of America, Special Paper 329, pp 233–258

Lowe DR, Byerly GR, Asaro F, Kyte FT (1989) Geological and geochemical record of 3400-million-year-old terrestrial meteorite impacts. Science 245:959–962

Lowe DR, Byerly GR, Heubeck C (1999) Structural divisions and development of the west-central part of the Barberton Greenstone Belt. In: Lowe DR, Byerly GR (eds) Geological evolution of the Barberton Greenstone Belt, South Africa. Geological Society of America, Special Paper 329, pp 37–82

Lowe DR, Byerly GR, Kyte FJ, Shukolyukov A, Asaro F, Krull A (2003) Spherule beds 3.47–3.24 billion years old in Barberton Greenstone Belt, South Africa: a record of large meteorite impacts and their influence on early crustal and biological evolution. Astrobiology 3:7–48

Luck JM, Turekian KK (1983) Osmium-187/osmium-186 in manganese nodules and the Cretaceous-Tertiary boundary. Science 222:613–615

Lugmair GW, Shukolyukov A (1998) Early solar system timescales according to ^{53}Mn-^{53}Cr systematics. Geochim Cosmochim Acta 63:2863–2886

Lyons JB, Officer CB (1992) Mineralogy and petrology of the Haiti Cretaceous/Tertiary section. Earth Planet Sci Lett 109:205–224

Ma P, Aggrey K, Tonzola C, Schnabel C, de Nicola P, Herzog GF, Wasson JT, Glass BP, Brown L, Tera F, Middleton R, Klein J (2004) Beryllium-10 in Australasian tektites: constraints on the location of the source crater. Geochim Cosmochim Acta 68:3883–3896

Ma XP, Bai SL (2002) Biological, depositional, microspherule, and geochemical records of the Frasnian/Famennian boundary beds, South China. Palaeogeogr Palaeoclimatol Palaeoecol 181:325–346

Maas MC, Anthony MRL, Gingerich PD, Grunnell GF, Krause DK (1995) Mammalian generic diversity and turnover in the late Paleocene and early Eocene of the Bighorn and Crazy Mountains Basins, Wyoming and Montana. Palaeogeogr Palaeoclimatol Palaeoecol 115: 181–207

MacDougall JD (1988) Seawater strontium isotopes, acid rain, and the Cretaceous-Tertiary boundary. Science 239:485–487

MacLeod KG, Huber BT, Fullagar PD (2001) Evidence for a small ($\sim$0.000030) but resolvable increase in the seawater ^{87}Sr/^{86}Sr ratios across the Cretaceous-Tertiary boundary. Geology 29: 303–306

MacLeod KG, Whitney DL, Huber BT, Koeberl C (2007) Impact and extinction in remarkably complete Cretaceous-Tertiary boundary sections from Demerara Rise, tropical western North Atlantic. Geol Soc Am Bull 119:101–115

Marchand E, Whitehead J (2002) Statistical evaluation of compositional differences between upper Eocene impact ejecta layers. Math Geol 34:555–572

Margolis SV, Claeys P, Kyte F (1991a) Microtektites, microkrystites, and spinels from late Pliocene asteroid impact in the Southern Ocean. Science 251:1594–1597

Margolis SV, Swinburne NHM, Asaro F, Swisher CC, McWilliams M, Hansen HJ, Pedersen AK (1991b) Possible impact ejecta in the Paleocene flood basalt province of West Greenland [abs]. EOS Trans Am Geophys Union 72, Fall Meeting, Program and Abstracts 278

Marlon JR, Bartlein PJ, Walsh MK, Harrison SP, Brown KJ, Edwards ME, Higuera PE, Power MJ, Anderson RS, Briles C, Brunelle A, Carcaillet C, Daniels M, Hu FS, Lavoie M, Long C, Minckley T, Richard PJH, Scott AC, Shafer DS, Tinner W, Umbanhowar CE Jr, Whitlocket C (2009) Wildfire responses to abrupt climate change in North America. Proc Natl Acad Sci U S A 106:2519–2524

Martin AJ (1969) Possible impact structure in southern Cyrenaica, Libya. Nature 223:940–941

Martin DM, Clendenin CW, Krapez B, McNaughton NJ (1998) Tectonic and geochronological constraints on late Archaean and Palaeoproterozoic stratigraphic correlation within and between the Kaapvaal and Pilbara cratons. J Geol Soc Lond 155:311–322

Martini JEJ (1978) Coesite and stishovite in the Vredefort Dome, South Africa. Nature 272:715–717

Martinez I, Schärer U, Guyot F (1993) Impact-induced phase transformations at 50–60 GPa in continental crust: an EPMA and ATEM study. Earth Planet Sci Lett 119:207–223

Martínez-Ruiz F, Ortega Huertas M, Palomo I, Acquafredda P (1997) Quench textures in altered spherules from the Cretaceous-Tertiary boundary layer at Agost and Caravaca, SE Spain. Sediment Geol 113:137–147

Martínez-Ruiz F, Ortega Huertas M, Palomo I, Smit J (2002) Cretaceous-Tertiary boundary at Blake Nose (Ocean Drilling Program Leg 171B): A record of the Chicxulub impact ejecta. In: Koeberl C, MacLeod KG (eds) Catastrophic events and mass extinctions: impacts and beyond. Geological Society of America, Special Paper 356, pp 181–199

Marzoli A, Bertrand H, Buratti N, Vérati C, Nomade S, Renne PR, Youbi N, Martini R, Allenbach K, Rapaille C, Zaninetti L, Bellieni G (2004) Synchrony of the Central Atlantic magmatic province and the Triassic-Jurassic boundary climatic and biotic crisis. Geology 32: 973–976

Masaitis VL (1998) Popigai crater: origin and distribution of diamond-bearing impactites. Meteorit Planet Sci 33:349–359

Masaitis VL (2003) Obscure-bedded ejecta facies from the Popigai impact structure, Siberia: lithological features and mode of origin. In: Koeberl C, Martínez-Ruiz F (eds) Impact markers in the stratigraphic record. Springer, Berlin, pp 137–162

Masaitis VL, Ivanov MA, Ezersky VG, Kozlov VS, Reshetnyak NB (1988) Finds of tektite glasses in West Siberia [abs]. Lunar Planet Sci 19:728–729

Masaitis VL, Shafranovsky GI, Federova IG (1995) The apographitic impact diamonds from astroblemes Ries and Popigai (in Russian). Proc Russ Miner Soc 4:12–18

Mason B, Nelen J, White JS Jr (1968) Olivine-garnet transformation in a meteorite. Science 160:66–67

Matamoros-Veloza Z, Rendón-Angeles JC, Yanagisawa K, Cisneros-Guerrero MM (2005) Densification of fly ash under alkaline hydrothermal hot pressing conditions. In: Nakahara M, Matubayasi N, Ueno M, Yasuka K, Watanabe K (eds) In: Proceedings of the 14th international conference on the properties of water and steam. Kyoto, Japan, pp 360–364

Maurette M, Jéhanno C, Robin E, Hammer C (1987) Characteristics and mass distribution of extraterrestrial dust from the Greenland ice cap. Nature 328:699–702

Maurrasse FJ-M, Sen G (1991) Impacts, tsunamis, and the Haitian Cretaceous-Tertiary boundary layer. Science 252:1690–1693

Maurrasse F, Pierre-Louis F, Rigaud J (1979) Upper Cretaceous to lower Paleocene pelagic deposits in the southern Peninsula of Haiti: Their bearing on the problem of the Cretaceous-Tertiary boundary. In: Transactions of the Fourth Latin American Geological Congress 1 (Port-of-Spain, Trinidad and Tobago, Ministry of Energy and Natural Resources), pp 328–337

McArthur JM, Thirlwall MF, Engkilde M, Zinsmeister WJ, Howarth RJ (1998) Strontium isotope profiles across K/T boundary sequences in Denmark and Antarctica. Earth Planet Sci Lett 160:179–192

McBride KM (2001) More Martians from Antarctica? A comparison of Antarctic meteorite abundances with falls [abs]. Meteorit Planet Sci 36(Suppl):A128

McCall GJH (2001) Tektites in the geological record: showers of glass from the sky. The Geological Society, London, 256 pp

McDonald I, Irvine GJ, de Vos E, Gale AS, Reimold WU (2006) Geochemical search for impact signatures in possible impact-generated units associated with the Jurassic-Cretaceous Boundary in southern England and northern France. In: Cockell C, Gilmour I, Koeberl C (eds) Biological processes associated with impact craters. Springer, Berlin, pp 257–286

McGetchin TR, Settle M, Head JW (1973) Radial thickness variation in impact crater ejecta: implications for lunar basin deposits. Earth Planet Sci Lett 20:226–236

McGhee GR (1996) The Late Devonian mass extinction. Columbia University Press, New York, 378 pp

McGhee GR (2001) The 'multiple impacts hypothesis' for mass extinction: a comparison of the Late Devonian and the late Eocene. Palaeogeogr Palaeoclimatol Palaeoecol 176:47–58

McGhee GR, Gilmore JS, Orth CJ, Olsen E (1984) No geochemical evidence for an asteroidal impact at late Devonian mass extinction horizon. Nature 308:629–631

McGhee GR, Orth CJ, Quintana LR, Gilmore JS, Olsen EJ (1986) Late Devonian "Kellwasser Event" mass-extinction horizon in Germany: no geochemical evidence for a large-body impact. Geology 14:776–779

McHone JF, Fries MC (2007) Raman detection of shock-metamorphosed rutile at Bosumtwi, Ghana [abs]. Meteorit Planet Sci 42(Suppl):A103
McHone JF, Nieman RA, Lewis CF, Yates AM (1989) Stishovite at the Cretaceous-Tertiary boundary, Raton, New Mexico. Science 243:1182–1184
McHone JG (2003) Volatile emissions from Central Atlantic Magmatic Province basalts; mass assumptions and environmental consequences. In: Hames WE, McHone JG, Renne PR, Ruppel C (eds) The Central Atlantic Magmatic Province: insights from fragments of Pangea, Geophysical Monogram, vol 136, pp 241–254
McHugh CMG, Snyder SW, Deconinck J-F, Saito Y, Katz ME, Aubry M-P (1996) Upper Eocene tektites of the New Jersey continental margin, Site 904. In: Mountain GS, Miller KG, Blum P, Poag CW, Twichell DC (eds) Proceedings of the ocean drilling Program 150. Scientific Results, Ocean drilling program, College Station, Texas, pp 241–265
McKirdy DM, Webster LJ, Arouri KR, Grey K, Gostin VA (2006) Contrasting sterane signatures in Neoproterozoic marine rocks of Australia before and after the Acraman asteroid impact. Org Geochem 37:189–207
McLaren DJ (1970) Presidential address; time, life and boundary. J Paleontol 44:801–815
McLaren DJ (1982) Frasnian-Famennian extinctions. In: Silver LT, Schultz PH (eds) Geological implications of impacts of large asteroids and comets on Earth. Geological Society of America, Special Paper 190, pp 477–484
McLaren DJ, Goodfellow WD (1990) Geological and biological consequences of giant impacts. Annu Rev Earth Planet Sci 18:123–171
McLean DM (1985) Deccan Traps mantle degassing in the terminal Cretaceous marine extinctions. Cretaceous Research 6:235–259
McQueen RG, Jamieson JC, Marsh SP (1967) Shock-wave compression and X-ray studies of titanium dioxide. Science 155:1401–1404
McSween HY (1987) Meteorites and their parent bodies. Cambridge University Press, New York, 237 pp
Meisel T, Koeberl C, Ford RJ (1990) Geochemistry of Darwin impact glass and target rocks. Geochim Cosmochim Acta 54:1463–1474
Meisel T, Krähenbühl U, Nazarov MA (1995) Combined osmium and strontium isotopic study of the Cretaceous-Tertiary boundary at Sumbar, Turmenistan: a test for an impact vs. a volcanic hypothesis. Geology 23:313–316
Melosh HJ (1989) Impact cratering: a geologic process. Oxford University Press, New York, 245 pp
Melosh HJ (2004) Impact ejecta sedimentation processes in the atmosphere and ocean [abs]. Meteorit Planet Sci 39(Suppl):A67
Melosh HJ, Artemieva N (2004) How does tektite glass lose its water? [abs]. Lunar Planet Sci 35: abstract no. 1723.pdf
Melosh HJ, Ivanov BA (1999) Impact crater collapse. Annu Rev Earth Planet Sci 27:385–415
Melosh HJ, Vickery AM (1991) Melt droplet formation in energetic impact events. Nature 350:494–497
Melosh HJ, Schneider NM, Zahnle KJ, Latham D (1990) Ignition of global wildfires at the K/T boundary. Nature 343:251–254
Melson WG, O'Hearn T, Fredriksson K (1988) Composition and origin of basaltic glass spherules in pelagic clay from the eastern Pacific. Mar Geol 83:253–271
Mendelson CV, Schopf JW (1992) Proterozoic and selected Early Cambrian microfossils and microfossil-like objects. In: Schopf JW, Klein C (eds) The Proterozoic biosphere: a multidisciplinary study. Cambridge University Press, Cambridge, pp 865–951
Michel HV, Asaro F, Alvarez W, Alvarez L (1985) Elemental profile of iridium and other elements near the Cretaceous/Tertiary boundary in Hole 577B. Init Rep Deep Sea Drilling Proj 86:533–538
Miller KG, Berggren WA, Zhang J, Palmer-Julson AA (1991) Biostratigraphy and isotope stratigraphy of Upper Eocene microtektites at Site 612: how many impacts? Palaios 6:17–38

Milton DJ (1977) Shatter cones—an outstanding problem in shock mechanics. In: Roddy DJ, Pepin RO, Merrill RB (eds) Impact and explosion cratering. Pergamon Press, New York, pp 703–714

Ming LC, Kim YH, Manghami MH, Usha-Devi S, Ito E, Xie H-S (1991) Back transformation and oxidation of $(Mg, Fe)_2SiO_4$ spinels at high temperatures. Phys Chem Miner 18:171–179

Minton DA, Malhotra R (2010) Dynamical erosion of the asteroid belt and implication for large impacts in the Solar System. Icarus 207:744–757

Miono S, Nakayama Y, Shoji M, Tsuji H, Nakanishi A (1993) Origin of microspherules in Paleozoic-Mesozoic bedded chert estimated by PIXE analysis. Nucl Instrum Methods Phys Res B75:435–439

Miono S, Chengzhi Z, Nakayama Y (1996) Study of microspherules in the Permian-Triassic bedded chert of Sasyama section, Southwest Japan by PIXE analysis. Nucl Instrum Methods Phys Res B 109:612–616

Misawa K, Kohno M, Tomiyama T, Noguchi T, Nakamura T, Nagao K, Mikouchi T, Nishiizumi K (2010) Two extraterrestrial dust horizons found in the Dome Fuji ice core, East Antarctica. Earth Planet Sci Lett 289:287–297

Miyahara M, El Goresy A, Ohtani E, Kimura M, Ozawa S, Nagase T, Nishijima M (2009) Fractional crystallization of olivine melt inclusion in shocked-induced chondritic melt vein. Phys Earth Planet Inter 177:116–121

Miyahara M, Ohtani E, Kimura M, El Goresy A, Ozawa S, Nagase T, Nishijima M, Hiraga K (2010) Coherent and subsequent incoherent ringwoodite growth in olivine of shocked L6 chondrites. Earth Planet Sci Lett 295:321–327

Moholy-Nagy H, Nelson F (1990) New data on sources of obsidian artifacts from Tikal, Guatemala. Ancient Mesoamerica 1:71–80

Molina E, Gonzalvo C, Keller G (1993) The Eocene-Oligocene planktic foraminiferal transition: extinctions, impacts and hiatuses. Geol Mag 130:483–499

Molina E, Alegret L, Arenillas I, Arz JA, Gallala N, Hardenbol J, von Salis K, Steurbaut E, Vandenberghe N, Zaghbib-Turki D (2006) The Global Boundary Stratotype Section and Point for the base of the Danian (Paleocene, Paleogene, "Tertiary", Cenozoic) at El Kef, Tunisia—original definition and revision. Episodes 29(4):263–273

Montanari A (1986) Spherules from the Cretaceous/Tertiary boundary clay at Gubbio, Italy: the problem of outcrop contamination. Geology 14:1024–1026

Montanari A, Koeberl C (2000) Impact stratigraphy: the Italian record. Springer, Heidelberg, 364 pp

Montanari A, Hay RL, Alvarez W, Asaro F, Michel HV, Alvarez LW, Smit J (1983) Spheroids at the Cretaceous-Tertiary boundary are altered impact droplets of basaltic composition. Geology 11:668–671

Montanari A, Claeys P, Asaro F, Bermudez J, Smit J (1994) Preliminary stratigraphy and iridium and other geochemical anomalies across the KT boundary in the Bochil section (Chiapas, southeastern Mexico) [abs]. In: New developments regarding the KT event and other catastrophes in Earth history. Lunar and Planetary Institute Contribution 825, Lunar and Planetary Institute, Houston, pp 84–85

Morey GB (1983) Animikie basin, Lake Superior region, U.S.A. In: Trendall AF, Morris RC (eds) Iron-formation: facts and problems. Elsevier, Amsterdam, pp 13–67

Morey GB, Southwick DL (1995) Allostratigraphic sequence relationships of Early Proterozoic iron-formations in the Lake Superior region. Econ Geol 90:1983–1993

Morgan JP, Reston TJ, Ranero CR (2004) Contemporaneous mass extinctions, continental flood basalts, and 'impact signals': are mantle plume-induced lithospheric gas explosions the causal link? Earth Planet Sci Lett 217:263–284

Morgan J, Lana C, Kearsley A, Coles B, Belcher C, Montanari S, Díaz-Martínez E, Barbosa A, Neumann V (2006) Analysis of shocked quartz at the global K-P boundary indicate an origin from a single, high-angle, oblique impact at Chicxulub. Earth Planet Sci Lett 251:264–279

Morgan JW (1978) Lonar crater glasses and high-magnesium australites: Trace element volatilization and meteoritic contamination. In: Proceedings of the 9th lunar planet science conference. Geochim Cosmochim Acta, Suppl 10, pp 2713–2730

Mori H (1990) Hollandite-type $NaAlSi_3O_8$ in shocked meteorites [abs]. In: Japan Society of High Pressure Science and Technology, 31st high pressure conference, Osaka, pp 134–135

Mori H (1994) Shock-induced phase transformations of Earth and planetary materials. J Miner Soc Jpn 23:171–178

Morrow JR, Sandberg CA, Harris AG (2005) Late Devonian Alamo impact, southern Nevada, USA: evidence of size, marine site, and widespread effects. In: Kenkmann T, Hörz F, Deutsch A (eds) Large meteorite impacts III. Geological Society of America, Special Paper 384, pp 259–280

Morrow JR, Sandberg CA, Malkowski K, Joachimski MM (2009) Carbon isotope chemostratigraphy and precise dating of middle Frasnian (lower Upper Devonian) Alamo Breccia, Nevada, USA. Palaeogeogr Palaeoclimatol Palaeoecol 282:105–118

Mory AJ, Iasky RP, Glikson AY, Pirajno F (2000a) Woodleigh, Carnarvon Basin, Western Australia: a new 120 km diameter impact structure. Earth Planet Sci Lett 177:119–128

Mory AJ, Iasky RP, Glikson AY, Pirajno F (2000b) Response to 'Critical comment on Mory et al., 2000, Woodleigh, Carnarvon Basin, Western Australia: a new 120 km diameter impact structure' by W.U. Reimold and C. Koeberl. Earth Planet Sci Lett 184:359–365

Mory AJ, Iasky RP, Ghori KAR (2003) A summary of the geological evolution and petroleum potential of Southern Carnarvon Basin, Western Australia. Geological Survey of Western Australia Report 86, 26 pp

Moser DE, Flower RM, Hart RJ (2001) Birth of the Kaapvaal tectosphere 3.08 billion years ago. Science 291:465–468

Mossman D, Eigendorf G, Tokaryk D, Gauthier-Lafaye F, Guckert KD, Melezhik V, Farrow CEG (2003) Testing for fullerenes in geological materials: Oklo carbonaceous substances, Karelian shungites, Sudbury Black Tuff. Geology 31:255–258

Mossman DJ, Grantham RG, Langenhorst F (1998) A search for shocked quartz at the Triassic-Jurassic boundary in the Fundy and Newark basins of the Newark Supergroup. Can J Earth Sci 35:101–109

Moynier F, Koeberl C, Quitté G, Telouk P (2009) A tungsten isotope approach to search for meteoritic components in terrestrial impact rocks. Earth Planet Sci Lett 286:35–40

Mukhopadhyay S, Farley KA, Montanari A (2001) A short duration of the Cretaceous-Tertiary boundary event: evidence from extraterrestrial helium-3. Science 291:1952–1955

Müller RD, Goncharov A, Kritski A (2005) Geophysical evaluation of the enigmatic Bedout basement high, offshore northwestern Australia. Earth Planet Sci Lett 237:264–284

Mundil R, Ludwig KR, Metcalfe I, Renne PR (2004) Age and timing of the Permian mass extinctions: U/Pb dating of closed-system zircons. Science 305:1760–1763

Mungall JE, Ames DE, Hanley JJ (2004) Geochemical evidence from the Sudbury structure for crustal redistribution by large bolide impacts. Nature 429:546–548

Muñoz-Espadas M-J, Martínez-Frías J, Lunar R (2003) Main geochemical signatures related to meteoritic impacts in terrestrial rock: a review. In: Koeberl C, Martínez-Ruiz F (eds) Impact markers in the stratigraphic record. Springer, Berlin, pp 65–90

Murali AV, Zolensky ME, Carr R, Underwood JR Jr, Giegengack RF (1988) Formation of the Libyan Desert Glass [abs]. Lunar Planet Sci 19:817–818

Murali AV, Linstrom EJ, Zolensky ME, Underwood JR Jr, Giegengack RF (1989) Evidence of extraterrestrial component in Libyan Desert Glass [abs]. EOS Trans Am Geophys Union 70(43):1178

Murali AV, Zolensky ME, Underwood JR Jr, Giegengack RF (1997) Chondritic debris in Libyan Desert Glass. In: de Michele V (ed) «Silica '96››. Pyramids, Milano, Italy, pp 133–142

Murayama JK, Nakai S, Kato M, Kumazawa M (1986) A dense polymorph of $Ca_3(PO_4)_2$: a high pressure phase of apatite decomposition and its geochemical significance. Phys Earth Planet Inter 44:293–303

Myers JS (1993) Precambrian history of the West Australian Craton and adjacent orogens. Annu Rev Earth Planet Sci 21:453–485
Nakano Y, Goto K, Matsui T, Tada R, Tajika E (2008) PDF orientations in shocked quartz grains around the Chicxulub crater. Meteorit Planet Sci 43:745–760
Naldrett AJ (2003) From impact to riches: evolution of geological understanding as seen at Sudbury, Canada. GSA Today 13:4–10
Narbonne GM (2005) The Ediacara biota: Neoproterozoic origin of animals and their ecosystems. Annu Rev Earth Planet Sci 33:421–442
Narcisi B, Petit JR, Engrand C (2007) First discovery of meteoritic events in deep Antarctic (EPICA-Dome C) ice cores. Geophys Res Lett 32:L15502. doi:10.1029/2007GL030801
Naslund HR, Officer CB, Johnson GD (1986) Microspherules in Upper Cretaceous and lower Tertiary clay layers at Gubbio, Italy. Geology 14:923–926
Nelson DR, Trendall AF, Altermann W (1999) Chronological correlations between the Pilbara and Kaapvaal cratons. Precambr Res 97:165–189
Neukum G, Ivanov BA (1994) Crater size distributions and impact probabilities on Earth from lunar, terrestrial-planet, and asteroid cratering data. In: Gehrels T (ed) Hazards due to comets and asteroids. University of Arizona, Tucson, pp 359–416
Ngo H, Wasserburg GJ, Glass BP (1985) Nd and Sr isotopic compositions of tektite material from Barbados and their relationship to North American tektites. Geochim Cosmochim Acta 49:1470–1485
Nichols DJ, Fleming RF (1990) Plant microfossil record of the terminal Cretaceous event in the western United States and Canada. In: Sharpton VL, Ward PD (eds) Global catastrophes in Earth history; an interdisciplinary conference on impacts, volcanism, and mass mortality. Geological Society of America, Special Paper 247, pp 445–455
Nicoll RS, Playford PE (1993) Upper Devonian iridium anomalies, conodont zonation and the Frasnian-Famennian boundary in the Canning Basin, Western Australia. Palaeogeogr Palaeoclimatol Palaeoecol 104:105–113
Nier AO, Schlutter DJ (1990) Helium and neon isotopes in stratospheric particles. Meteoritics 25:263–267
Nisbet EG (1987) The young Earth: an introduction to Archaean geology. Allen & Unwin, Boston, 402 pp
Nordenskiöld AE (1872) Account of an expedition to Greenland in the year 1870. Geol Mag 9:289
Norris RD, Huber BT, Self-Trail J (1999) Synchroneity of the K-T oceanic mass extinction and meteorite impact: Blake Nose, western North Atlantic. Geology 27:419–422
Nutman AP, Friend CRL (2009) New 1:20,000 scale geological maps, synthesis and history of investigation of the Isua supracrustal belt and adjacent orthogneisses, southern West Greenland: A glimpse of Eoarchaean crust formation and orogeny. Precambr Res 172:189–211
Nutman AP, Allaart JH, Bridgwater D, Dimroth E, Rosing MT (1984) Stratigraphic and geochemical evidence for the depositional environment of the early Archaean Isua supracrustal belt, southern West Greenland. Precambr Res 25:365–396
Nutman AP, Mojzsis SJ, Friend CRL (1997) Recognition of ≥3850 Ma water-lain sediments in West Greenland and their significance for the early Archaean Earth. Geochim Cosmochim Acta 61:2475–2484
Obradovich JD, Snee LW, Izett GA (1989) Is there more than one glassy impact layer in the Late Eocene? [abs]. Geol Soc Am Abstr Prog 21(6):A134
Oddone M, Vannucci R (1986) PGE and REE geochemistry at the B-W boundary in the Carnic and Dolomite Alps (Italy). Memorie della Societa Geologica Italiana 34:129–140
Officer CB, Drake CL (1985) Terminal Cretaceous environmental events. Science 227:1161–1167
Officer CB, Lyons JB (1993) A short note on the origin of the yellow glasses at the Haiti Cretaceous/Tertiary section. Earth Planet Sci Lett 118:349–351

Officer CB, Drake CL, Pindell JL, Meyerhoff AA (1992) Cretaceous-Tertiary events and the Caribbean caper. GSA Today 2:69–75

Ohtani E, Kimura Y, Kimura M, Takata T, Kondo T, Kubo T (2004) Formation of high-pressure minerals in shocked L6 chondrite Yamato 791384: constraints on shock conditions and parent body size. Earth Planet Sci Lett 227:505–515

Ojakangas RW (1983) Tidal deposits in the Early Proterozoic basin of the Lake Superior region—the Palms and Pokegama Formations: evidence for subtidal shelf deposition of Superior-type banded iron-formation. In: Medaris LG Jr (ed) Early Proterozoic geology of the Great Lakes region. Geological Society of America, Memoir 60, pp 49–66

Ojakangas RW, Morey GB, Green JC (2001a) Paleoproterozoic basin development and sedimentation in the Lake Superior region, North America. Sediment Geol 141–142:319–341

Ojakangas RW, Morey GB, Southwick DL (2001b) The Mesoproterozoic Midcontinent Rift System, Lake Superior region, USA. Sediment Geol 141–142:421–442

O'Keefe JA (ed) (1963) Tektites. University of Chicago Press, Chicago, 228 pp

O'Keefe JA (1976) Tektites and their origin. Elsevier, New York, 254 pp

O'Keefe JD, Ahrens TJ (1982) The interaction of the Cretaceous/Tertiary extinction bolide with the atmosphere, ocean, and solid Earth. In: Silver LT, Schultz PH (eds) Geological implications of impacts of large asteroids and comets on the Earth. Geological Society of America, Special Paper 190, pp 103–120

O'Keefe JD, Ahrens TJ (1983) Impact produced condensate and droplet size distributions [abs]. Lunar Planet Sci 19:883

O'Keefe JD, Ahrens TJ (1989) Impact production of CO_2 by the Cretaceous//Tertiary extinction bolide and the resultant heating of the Earth. Nature 338:247–249

Olsen PE, Shubin NH, Anders MH (1987) New early Triassic tetrapod assemblages constrain Triassic-Jurassic tetrapod extinction event. Science 237:1025–1029

Olsen PE, Fowell SJ, Cornet B (1990) The Triassic-Jurassic boundary in continental rocks of eastern North America; a progress report. In: Sharpton VL, Ward PD (eds) Global catastrophes in Earth history; an interdisciplinary conference on impacts, volcanism, and mass mortality. Geological Society of America, Special Paper 247, pp 585–593

Olsen PE, Koeberl C, Huber H, Montanari A, Fowell SJ, Et-Touhami M, Kent DV (2002a) Continental Triassic-Jurassic in central Pangea: Recent progress and discussion of an Ir anomaly. In: Koeberl C, McLeod KG (eds) Catastropic events and mass extinction: impacts and beyond. Geological Society of America, Special Paper 356, pp 505–522

Olsen PE, Kent DV, Sues H-D, Koeberl C, Huber H, Montanari A, Rainforth EC, Fowell SJ, Szajna MJ, Hartline BW (2002b) Ascent of dinosaurs linked to an iridium anomaly at the Triassic-Jurassic boundary. Science 296:1305–1307

Olson KR, Jones RL (2001) Use of fly ash as a time marker in soil erosion and sedimentation studies. In: Scott DE, Mohtar RH, Steinhart GC (eds) Sustaining the Global Farm. Selected papers from the 10th international soil conservation meeting, May 24–29, 1999, at Purdue University and the USDA-ARS National Soil Erosion Research Laboratory, pp 1059–1061

Olsson RK, Miller KG, Browning JV, Habib D, Sugerman PJ (1997) Ejecta layer at the Cretaceous-Tertiary boundary, Bass River, New Jersey (Ocean Drilling Program Leg 171AX). Geology 25:759–762

Olsson RK, Miller KG, Browning JV, Wright JV, Cramer BS (2002) Sequence stratigraphy and sea-level change across the Cretaceous-Tertiary boundary on the New Jersey passive margin. In: Koeberl C, MacLeod KG (eds) Catastrophic events and mass extinctions: impacts and beyond. Geological Society of America, Special Paper 356, pp 97–108

Omar G, Johnson KR, Hickey LJ, Roberstson PB, Dawson MR, Barnosky CW (1987) Fission-track dating of Haughton astrobleme and included biota, Devon Island, Canada. Science 237:1603–1605

Openshaw SC, Miller WL, Bolch WE, Bloomquist D (1992) Utilization of fly ash. Florida Center for Solid and Hazardous Waste Management Report #92-3. State University System of Florida, Gainesville, Florida, USA, 74 pp

O'Reilly TC, Haskin LA, King EA (1983) Element correlations among North American tektites [abs]. Lunar Planet Sci 14:580–581

Orth CJ, Attrep M, Quintana LR (1990) Iridium abundance patterns across bio-event horizons in the fossil record. In: Sharpton VL, Ward PD (eds) Global catastrophes in Earth history; an interdisciplinary conference on impacts, volcanism, and mass mortality. Geological Society of America, Special Paper 247, pp 45–59

Osinski GR, Grieve RAF, Spray JG (2004) The nature of the groundmass of surficial suevite from the Ries impact structure, Germany, and constraints on its origin. Meteorit Planet Sci 39:1655–1683

Osinski GR, Spray JG, Grieve RAF (2008) Impact melting in sedimentary target rocks: an assessment. In: Evans KR, Horton J W Jr, King DT Jr, Morrow JR (eds) The sedimentary record of meteorite impacts. The Geological Society of America, Special Paper 437, pp 1–18

Oskarsson N, Helgason O, Sigurdsson H (1996) Oxidation state of iron in tektite glasses from the Cretaceous/Tertiary boundary. In: Ryder G, Fastovsky D, Gartner S (eds) The Cretaceous-Tertiary event and other catastrophes in Earth history. Geological Society of America, Special Paper 307, pp 445–452

Over DJ, Conaway CA, Katz DJ, Goodfellow WD, Gregoire DC (1997) Platinum group element enrichments and possible chondritic Ru:Ir across the Frasnian–Famennian boundary, western New York State. Palaeogeogr Palaeoclimatol Palaeoecol 132:399–410

Pal DK, Tuniz C, Moniot RK, Kruse TH, Herzog GF (1982) Beryllium-10 in Australasian tektites: evidence for a sedimentary precursor. Science 218:787–789

Pálfy J, Demény A, Haas J, Hetényi M, Orchard MJ, Vető I (2001) Carbon isotope anomaly and other geochemical changes at the Triassic-Jurassic boundary from a marine section in Hungary. Geology 26:1047–1050

Pálfy J, Smith PL, Mortensen JK (2002) Dating the end-Triassic and Early Jurassic mass extinctions, correlative large igneous provinces, and isotope events. In: Koeberl C, McLeod KG (eds) Catastrophic events and mass extinctions: impacts and beyond. Geological Society of America, Special Paper 356, pp 523–532

Palme H (1982) Identification of projectiles of large terrestrial impact craters and some implications for the interpretation of Ir-rich Cretaceous-Tertiary boundary layers. In: Silver LT, Schultz PH (eds) Geological implications of impact of large asteroids and comets on Earth. Geological Society of America, Special Paper 190, pp 223–233

Palme H, Janssens M-J, Takahashi H, Anders E, Hertogen J (1978) Meteorite material at five large impact craters. Geochim Cosmochim Acta 42:313–323

Papanastassiou DA, Wasserburg GJ (1981) Microchrons: The ^{87}Rb–^{87}Sr dating of microscopic samples. In: Proceedings of the 12th lunar and planetary science conference, Part B. Pergamon Press, New York, Geochim Cosmochim Acta, Suppl 16, pp 1027–1038

Paquay FS, Ravizza GE, Dalai TK, Peucker-Ehrenbrink B (2008) Determining chondritic impactor size from the marine record. Science 320:214–218

Paquay FS, Goderis S, Ravizza G, Claeys P (2010) Reply to Bunch et al.: Younger Dryas impact proponents challenge new platinum group elements and osmium data unsupportive of their hypothesis. Proc Natl Acad Sci U S A 107: E59–E60. www.pnas.org/cgi/doi/10.1073/pnas.1001828107

Pati JK, Reimold WU (2007) Impact cratering—fundamental process in geosciences and planetary science. J Earth System Sci 116:81–98

Pearce TH (1974) Quench plagioclase from some Archean basalts. Can J Earth Sci 11:715–719

Pegram WJ, Turekian KK (1999) The osmium isotopic composition change of Cenozoic sea water as inferred from a deep-sea core corrected for meteoritic contribution. Geochim Cosmochim Acta 63:4053–4058

Peng H (1994) An extraterrestrial event at the Tertiary-Quaternary boundary [abs]. New developments regarding the KT event and other catastrophes in Earth history. Lunar and Planetary Institute Contribution 825, Lunar and Planetary Institute, Houston, pp 88–89

Perch-Nielsen K, McKenzie J, He Q (1982) Biostratigraphy and isotope stratigraphy and the 'catastrophic' extinction of calcareous nannoplankton at the Cretaceous/Tertiary boundary. In: Silver LT, Schultz PH (eds) Geological implications of impacts of large asteroids and comets on the Earth. Geological Society of America, Special Paper 190, pp 353–372

Pesonen LJ, Elming SÅ, Mertanen S, Pisarevsky S, D'Agrella-Filho MS, Meert JG, Schmidt PW, Abrahamsen N, Bylund G (2003) Palaeomagnetic configuration of continents during the Proterozoic. Tectonophysics 375:289–324

Petaev MI, Jacobsen SB, Basu AR, Poreda J (2003) Magnetic Fe,Si,Al-rich spherules from the P-T boundary layer at Graphite Peak, Antarctica [abs]. EOS Trans Am Geophys Union 84 (46): abstract B52B–1039

Petaev MI, Jacobsen SB, Basu AR, Becker L (2004) Magnetic Fe,Si,Al-rich impact spherules from the P-T boundary layer at Graphite Peak, Antarctica [abs]. Lunar Planet Sci 35: abstract no. 1216.pdf

Petaev MI, Jacobsen SB, Becker L (2006) Search for extraterrestrial materials in the P-T boundary samples from Graphite Peak, Antarctica [abs]. Lunar Planet Sci 37: abstract no. 2309.pdf

Peucker-Ehrenbrink B (1996) Accretion rate of extraterrestrial matter during the last 80 million years and its effect on the marine osmium isotope record. Geochim Cosmochim Acta 60:3187–3196

Peucker-Ehrenbrink B, Jahn B (2001) Rhenium-osmium isotope systematics and platinum group element concentrations: loess and the upper continental crust. Geochem Geophys Geosyst 2(10):1061. doi:10.1029/2001GC000172

Peucker-Ehrenbrink B, Bach W, Hart SR, Blusztajn JS, Abbruzzese T (2003) Rhenium-osmium isotope systematics and platinum group element concentrations in oceanic crust from DSDP/ODP Sites 504 and 417/418. Geochem Geophys Geosyst 4(7):8911. doi:10.1029/2002GC000414

Piasecki S, Larsen LM, Pedersen AK, Pedersen GK (1992) Palynostratigraphy of the lower Tertiary volcanic and marine clastic sediments in the southern part of the West Greenland basin: implications for the timing and duration of the volcanism. Rapport Grønlands Geologiske Undersøgelse 154:13–31

Pickard AL (2002) SHRIMP U-Pb zircon ages of tuffaceous mudrocks in the Brockman Iron Formation of the Hamersley Range, Western Australia. Aust J Earth Sci 49:491–507

Pickard AL (2003) SHRIMP U-Pb zircon ages for the Palaeoproterozoic Kuruman Iron Formation, Northern Cape Province, South Africa: evidence for simultaneous BIF deposition on Kaapvaal and Pilbara Cratons. Precambr Res 125:275–315

Pickard AL, Barley ME, Krapez B (2004) Deep-marine depositional setting of banded iron formation: sedimentological evidence from interbedded clastic sedimentary rocks in the early Palaeoproterozoic Dales Gorge Member of Western Australia. Sediment Geol 170:37–62

Pierazzo E, Collins G (2003) A brief introduction to hydrocode modeling of impact cratering. In: Dypvik H, Burchell M, Claeys P (eds) Cratering in marine environments and on ice. Springer, Berlin, pp 323–340

Pierazzo E, Melosh HJ (2000) Understanding oblique impacts from experiments, observations, and modeling. Annu Rev Earth Planet Sci 28:141–167

Pierazzo E, Kring DA, Melosh HJ (1998) Hydrocode simulation of the Chicxulub impact event and the production of climatically active gases. J Geophys Res 103:28607–28625

Pierazzo E, Hahmann AN, Sloan LC (2003) Chicxulub and climate: radiative perturbations of impact-produced S-bearing gases. Astrobiology 3:99–118

Pierrard O, Robin E, Rocchia R, Montanari A (1998) Extraterrestrial Ni-rich spinel in upper Eocene sediments from Massignano, Italy. Geology 26:307–310

Pigati JS, Latorre C, Rech JA, Betancourt JL, Martínez KE, Budahn JR (2012) Accumulation of impact markers in desert wetlands and implications for the Younger Dryas impact hypothesis. Proc Natl Acad Sci USA 109:7208–7212

Pinter N, Ishman SE (2008a) Impacts, mega-tsunami, and other extraordinary claims. GSA Today 18:37–38
Pinter N, Ishman SE (2008b) Reply. Impacts, mega-tsunami, and other extraordinary claims. GSA Today 18:e14. doi:10.1130/GSATG13Y.1
Pinter N, Scott AC, Daulton TL, Podoll A, Koeberl C, Anderson RS, Ishman SE (2011) The younger Dryas impact hypothesis: a requiem. Earth-Sci Rev 106:247–264
Pitakpaivan K, Byerly GR, Hazel JE (1994) Pseudomorphs of impact spherules from a Cretaceous-Tertiary boundary section at Shell Creek, Alabama. Earth Planet Sci Lett 124:49–56
Planavsky N, Rouxel O, Bekker A, Shapiro R, Fralick P, Knudsen A (2009) Iron-oxidizing microbial ecosystems thrived in late Paleoproterozoic redox-stratified oceans. Earth Planet Sci Lett 286:230–242
Playford PE, McLaren DJ, Orth CJ, Gilmore JS, Goodfellow JS (1984) Iridium anomaly in the Upper Devonian of the Canning Basin, Western Australia. Science 226:437–439
Poag CW (1997a) The Chesapeake Bay bolide impact: a convulsive event in Atlantic Coastal Plain evolution. Sediment Geol 108:45–89
Poag CW (1997b) Roadblocks on the kill curve: testing the Raup hypothesis. Palaios 12:582–590
Poag CW, Aubry M-P (1995) Upper Eocene impactites of the U.S. East Coast: depositional origins, biostratigraphic framework, and correlation. Palaios 10:16–43
Poag CW, Powars DS, Poppe LJ, Mixon RB (1994) Meteoroid mayhem in Ole Virginny: source of the North American tektite strewn field. Geology 22:691–694
Poag CW, Koeberl C, Reimold WU (2004) The Chesapeake Bay crater: geology and geophysics of a late Eocene submarine impact structure. Springer, Berlin, 522 pp
Pollack JB, Toon OB, Ackerman TP, McKay CP (1983) Environmental effects of an impact-generated dust cloud: implications for the Cretaceous-Tertiary extinctions. Science 219:287–289
Pollastro RM, Bohor BF (1993) Origin and clay-mineral genesis of the Cretaceous/Tertiary boundary unit, Western Interior of North America. Clays Clay Miner 41:7–25
Pope KO (2002) Impact dust not the cause of the Cretaceous-Tertiary mass extinction. Geology 30:99–102
Pope KO, Baines KH, Ocampo AC, Ivanov BA (1994) Impact winter and the Cretaceous-Tertiary extinctions: results of a Chicxulub asteroid impact model. Earth Planet Sci Lett 128:719–725
Poreda RJ, Becker L (2003) Fullerenes and interplanetary dust at the Permian-Triassic boundary. Astrobiology 3:75–90
Pospichal JJ (1996) Calcareous nannoplankton mass extinction at the Cretaceous/Tertiary boundary: an update. In: Ryder G, Fastovsky D, Gartner S (eds) The Cretaceous-Tertiary event and other catastrophes in Earth history. Geological Society of America, Special Paper 307, pp 335–360
Powell JL (2001) Mysteries of terra firma: the age and evolution of the world. The Free Press, New York, 256 pp
Poulton SW, Fralick PW, Canfield DE (2004) The transition to a sulphidic ocean 1.84 billion years ago. Nature 431:173–177
Prasad MS, Khedekar VD (2003) Impact microcrater morphology on Australasian microtektites. Meteorit Planet Sci 38:1351–1371
Prasad MS, Rao PS (1990) Tektites far and wide. Nature 347:340
Prasad MS, Sudhakar M (1996) Australasian microtektites from the central Indian basin: implications for ejecta distribution patterns. Current Science 70:74–77
Prasad MS, Sudhakar M (1998) Microimpact phenomena on Australasian microtektites: implications for ejecta plume characteristics and lunar surface processes. Meteorit Planet Sci 33:1271–1279
Prasad MS, Sudhakar M (1999) Australasian minitektites discovered in the Indian Ocean. Meteorit Planet Sci 34:179–184

Prasad MS, Mahale VP, Kodagali VN (2007) New sites of Australasian microtektites in the central Indian Ocean: implications for the location and size of source crater. J Geophys Res 112:E06007. doi:10.1029/2006JE002857
Prasad MS, Roy SK, Gupta A (2010) Processes in the Australasian impact ejecta revealed by interparticle collisions along a ~1300 km transect in the Indian Ocean. Meteorit Planet Sci 45:990–1006
Pratesi G, Giudice AL, Vishnevsky S, Manfredotti C, Cipriani C (2003) Cathodoluminescence investigations on the Popigai, Ries, and Lappajärvi impact diamonds. Am Miner 88:1778–1787
Preisinger A, Zobetz E, Gratz AJ, Lahodynsky R, Becke M, Mauritsch HJ, Eder G, Grass F, Rögl F, Stradner H, Surenian R (1986) The Cretaceous/Tertiary boundary in the Gosau Basin, Austria. Nature 322:794–799
Preiss WV (2000) The Adelaide Geosyncline of South Australia and its significance in Neoproterozoic continental reconstruction. Precambr Res 100:21–63
Premo WR, Izett GA (1992) Isotopic signatures of black tektites from the K-T boundary on Haiti: implications for the age and type of source material. Meteoritics 27:413–423
Price GD, Putnis A, Agrell O (1979) Electron petrography of shock-produced veins in the Tenham chondrite. Contrib Miner Petrol 71:211–218
Prinn RG, Fegley B Jr (1987) Bolide impacts, acid rain, biosphere traumas at the Cretaceous-Tertiary boundary. Earth Planet Sci Lett 83:1–15
Pufahl PK, Fralick PW (2004) Depositional controls on Palaeoproterozoic iron formation accumulation, Gogebic Range, Lake Superior region, USA. Sedimentology 51:791–808
Pufahl PK, Hiatt EE, Stanley CR, Morrow JR, Nelson GJ, Edwards CT (2007) Physical and chemical evidence of the 1850 Ma Sudbury impact event in the Baraga Group, Michigan. Geology 35:827–830
Pufahl PK, Hiatt EE, Kyser TK (2010) Does the Paleoproterozoic Animikie Basin record the sulfidic ocean transition? Geology 38:659–662
Pusz AE, Miller KG, Wright JD, Katz ME, Cramer BS, Kent DV (2009) Stable isotopic response to the late Eocene extraterrestrial impacts. In: Koeberl C, Montanari A (eds) The late Eocene earth—hothouse, icehouse, and impacts. Geological Society of America, Special Paper 452, pp 83–95
Quitté G, Robin E, Levasseur S, Capmas F, Rocchia R, Birck J-L, Allègre CJ (2007) Osmium, tungsten, and chromium isotopes in sediments and in Ni-rich spinel at the K-T boundary: signatures of a chondritic impactor. Meteorit Planet Sci 42:1567–1580
Racki G, Koeberl C (2004) Comment on "Impact ejecta layer from the Mid-Devonian: possible connection to global mass extinction". Science 303:471b
Rampino RM (1987) Impact cratering and flood-basalt volcanism. Nature 327:468
Rasmussen B, Fletcher IR (2010) Dating sedimentary rocks using in situ U-Pb geochronology of syneruptive zircon in ash-fall tuffs <1 mm thick. Geology 38:299–302
Rasmussen B, Koeberl C (2004) Iridium anomalies and shocked quartz in a Late Archean spherule layer from the Pilbara craton: new evidence for a major asteroid impact at 2.63 Ga. Geology 32:1029–1032
Rasmussen B, Blake TS, Fletcher IR (2005) U-Pb zircon age constraints on the Hamersley spherule beds: evidence for a single 2.63 Ga Jeerinah-Carawine impact ejecta layer. Geology 33:725–728
Raup DM (1979) Size of the Permo-Triassic bottleneck and its evolutionary implications. Science 206:217–218
Raup DM (1991) A kill curve for Phanerozoic marine species. Paleobiology 17:37–48
Raup DM (1992) Large-body impact and extinctions in the Phanerozoic. Paleobiology 18:80–88
Raup DM (1994) The role of extinction in evolution. Proc Natl Acad Sci U S A 91:6758–6763
Raup DM, Sepkoski JJ Jr (1984) Periodicity of extinctions in the geologic past. Proc Natl Acad Sci U S A 81:801–805
Raup DM, Sepkoski JJ Jr (1986) Periodic extinction of families and genera. Science 231:833–836

Reddy V, Emery JP, Gaffey MJ, Bottke WF, Cramer A, Kelley MS (2009) Composition of 298 Baptistina: implications for the K/T impactor link. Meteorit Planet Sci 44:1917–1927

Reddy V, Carvano JM, Lazzaro D, Michtchenko TA, Gaffey MJ, Kelley MS, Mothé-Diniz T, Alvarez-Candal A, Moskovitz NA, Cloutis EA, Ryan EL (2011) Mineralogical characterization of Baptistina family: implications for the K/T impactor source. Icarus 216:184–197

Reichow MK, Saunders AD, White RV, Pringle MS, Al'Mukhamedov AI, Medvedev AI, Kirda NP (2002) $^{40}Ar/^{39}Ar$ dates from the West Siberian Basin: Siberian flood basalt province doubled. Science 296:1846–1849

Reid AM, Cohen AJ (1962) Coesite in Darwin glass. J Geophys Res 67:1654

Reid AF, Ringwood AE (1969) Newly observed high pressure transformations in Mn_3O_4, $CaAl_2O_4$, and $ZrSiO_4$. Earth Planet Sci Lett 6:205–208

Reimold WU, Koeberl C (2000) Critical comment on: A.J. Mory et al. "Woodleigh, Carnarvon Basin, Western Australia: a new 120 km diameter impact structure". Earth Planet Sci Lett 184:353–357

Reimold WU, Koeberl C (2008) Catastrophes, extinctions and evolution: 50 years of impact cratering studies. Golden Jubilee Memoir of the Geological Society of India No. 66, pp 69–110

Reimold WU, Stöffler D (1978) Experimental shock metamorphism of dunite [abs]. In: Proceedings of the 9th lunar and planetary science conference. Pergamon Press, New York, Geochim Cosmochim Acta, Suppl 10, pp 2805–2824

Reimold WU, Koeberl C, Johnson S, McDonald I (2000) Early Archean spherule beds in the Barberton Mountain Land, South Africa: impact or terrestrial origin? In: Gilmour I, Koeberl C (eds) Impacts and the early Earth, Lecture Notes in Earth Sciences, vol 91. Springer, Berlin, pp 117–180

Reimold WU, Koeberl C, Hough RM, McDonald I, Bevan A, Amare K, French BM (2003) Woodleigh impact structure, Australia: shock petrography and geochemical studies. Meteorit Planet Sci 38:1109–1130

Reimold WU, Koeberl C, Gibson RL, Dressler BO (2005a) Economic mineral deposits in impact structures: a review. In: Koeberl C, Henkel H (eds) Impact tectonics. Springer, Berlin, pp 479–552

Reimold WU, Kelley SP, Sherlock SC, Henkel H, Koeberl C (2005b) Laser argon dating of melt breccias from the Siljan impact structure, Sweden: implications for a possible relationship to Late Devonian extinction events. Meteorit Planet Sci 40:591–607

Renne PR, Basu AR (1991) Rapid eruption of the Siberian Traps flood basalts at the Permo-Triassic boundary. Science 253:176–179

Renne PR, Reimold WU, Koeberl C, Hough R, Claeys P (2002) Comment on: "K–Ar evidence from illitic clays of a Late Devonian age for the 120 km diameter Woodleigh impact structure, Southern Carnarvon Basin, Western Australia" by Uysal et al. (2001) Earth Planet Sci Lett 201:247–252

Renne PR, Melosh HJ, Farley KA, Reimold WU, Koeberl C, Rampino MR, Kelly SP, Ivanov BA (2004) Is Bedout an impact crater? Take 2. Science 306:610–611

Retallack GJ, Seyedolali A, Krull ES, Holser WT, Ambers CP, Kyte FT (1998) Search for evidence of impact at the Permian-Triassic boundary in Antarctica and Australia. Geology 26:979–982

Ringwood AE (1958) Constitution of mantle-II: further data on the olivine-spinel transition. Geochim Cosmochim Acta 15:18–19

Ringwood AE, Major A (1966) Synthesis of Mg_2SiO_4-Fe_2SiO_4 spinel solid solution. Earth Planet Sci Lett 1:241–245

Ringwood AE, Major A (1970) The system Mg_2SiO_4-Fe_2SiO_4 at high pressures and temperatures. Phys Earth Planet Inter 3:89–108

Ringwood AE, Reid AF, Wadsley AD (1967) High-pressure $KAlSi_3O_8$, an aluminosilicate with sixfold coordination. Acta Crystallogr 23:1093–1095

Robb LJ, Knoll AH, Plumb KA, Shields GA, Strauss H, Veizer J (2004) The Precambrian: the Archean and Proterozoic Eons. In: Gradstein F, Ogg JG, Smith AG (eds) A geologic time scale 2004. Cambridge University Press, Cambridge, pp 129–140

Robertson DS, McKenna MC, Toon OB, Hope S, Lillegraven JA (2004) Survival in the first hours of the Cenozoic. Geol Soc Am Bull 116:760–768

Robertson PB (1975) Zones of shock metamorphism at the Charlevoix impact structure, Quebec. Geol Soc Am Bull 86:1630–1638

Robertson PB (1980) Anomalous planar feature development [abs]. Lunar Planet Sci 11:939–940

Robertson PB, Dence MR, Vos MA (1968) Deformation in rock-forming minerals from Canadian craters. In: French BM, Short NM (eds) Shock metamorphism of natural materials. Mono Book Corp, Baltimore, pp 433–452

Robin E, Molina E (2006) Chronostratigraphy, composition, and origin of Ni-Fe-rich spinel from the Late Eocene Fuente Caldera section in Spain: One impact or more? Meteorit Planet Sci 41:1231–1248

Robin E, Boclet D, Bonté P, Froget L, Jéhanno C, Rocchia R (1991) The stratigraphic distribution of Ni-rich spinels in Cretaceous-Tertiary boundary rocks at El Kef (Tunisia), Caravaca (Spain) and Hole 761C (Leg 122). Earth Planet Sci Lett 107:715–721

Robin E, Bonté P, Froget L, Jéhanno C, Rocchia R (1992) Formation of spinels in cosmic objects during atmospheric entry: a clue to the Cretaceous-Tertiary boundary event. Earth Planet Sci Lett 108:181–190

Robin E, Froget L, Jéhanno C, Rocchia R (1993) Evidence for a K/T impact event in the Pacific Ocean. Nature 363:615–617

Robin E, Swinburne NHM, Froget L, Rocchia R, Gayraud J (1996) Characteristics and origin of the glass spherules from the Paleocene flood basalt province of western Greenland. Geochim Cosmochim Acta 60:815–830

Robinson N, Ravizza G, Coccioni R, Peucker-Ehrenbrink B, Norris R (2009) A high-resolution marine $^{187}Os/^{188}Os$ record for the late Maastrichtian: distinguishing the chemical fingerprints of Deccan volcanism and the KP impact event. Earth Planet Sci Lett 281:159–168

Rocchia R, Boclet D, Bonté P, Froget L, Galbrun B, Jéhanno C, Robin E (1992) Iridium and other element distribution, mineralogy, and magnetostratigraphy near the Cretaceous-Tertiary boundary in Hole 761C. In: von Rad U, Haq BU et al (eds) Proceedings of the ocean drilling program 122. Scientific Results, Ocean drilling program, College Station, Texas, pp 753–762

Rocchia R, Robin E, Froget L, Gayraud J (1996) Stratigraphic distribution of extraterrestrial markers at the Cretaceous-Tertiary boundary in the Gulf of Mexico area: implication for the temporal complexity of the event. In: Ryder G, Fastovsky D, Gartner S (eds) The Cretaceous-Tertiary event and other catastrophes in Earth history. Geological Society of America, Special Paper 307, pp 279–286

Rocchia R, Robin E, Fröhlich F, Amossé J, Barrat J-A, Méon H, Froget L, Diemer E (1997) The impact origin of Libyan Desert Glass. In: de Michele V (ed) «Silica '96››. Pyramids, Milano, Italy, pp 143–149

Roddy DJ, Davis LK (1977) Shatter cones formed in large-scale experimental explosion craters. In: Roddy DJ, Pepin RO, Merrill RB (eds) Impact and explosion cratering: planetary and terrestrial implications. Pergamon, New York, pp 715–750

Rogers GC (1982) Oceanic plateaus as meteorite impact signatures. Nature 299:341–342

Rose NL (1996) Inorganic fly-ash spheres as pollution tracers. Enviro Pollut 91:245–252

Rost R, Nicht H, Wagner H (1979) Moldavite aus der Umgebung von Dresden, DDR. Časopsis pro Mineralogii a Geologii 25:263–271

Ruddiman WF, Jones GA, Peng T-H, Glover LK, Glass BP, Liebertz PJ (1980) Tests for size and shape dependency in deep-sea mixing. Sediment Geol 25:257–276

Ryder G. (2002) Mass flux in the ancient Earth-Moon system and benign implications for the origin of life on Earth. J Geophys Res 107(E4):5022. doi: 10.1029/2001JE001583

Ryder G, Fastovsky D, Gartner S (eds) (1996) The Cretaceous-Tertiary event and other catastrophes in Earth history. Geological Society of America, Special Paper 307, 569 pp

Salge T (2007) The ejecta blanket of the Chicxulub impact crater, petrographic and chemical studies of the K-P section of El Guayal, and of the UNAM boreholes [abs]. Lunar Planet Sci 38: abstract no. 1748.pdf

Salge T, Tagle R, Claeys P (2000) Accretionary lapilli from the Cretaceous-Tertiary boundary site of Guayal, Mexico: preliminary insights into expansion plume formation [abs]. Meteorit Planet Sci 35:A140–A141

Sandberg CA, Morrow JR (2007) Late Devonian 382 Ma Alamo impact: proximal and distal effects, Nevada and Utah [abs]. Geol Soc Am Abstr Prog 39(8):372

Sandberg CA, Ziegler W, Dreesen R, Butler JL (1988) Late Frasnian mass extinction: conodont event stratigraphy, global changes and possible causes. Courier Forschungsinstitut Senckenberg 102:267–307

Sandberg CA, Morrow JR, Ziegler W (2002) Late Devonian sea-level changes, catastrophic events and mass extinctions. In: Koeberl C, MacLeod KG (eds) Catastrophic events and mass extinctions: impacts and beyond. Geological Society of America, Special Paper 356, pp 473–487

Sanfilippo A, Reidel WR, Glass BP, Kyte FT (1985) Late Eocene microtektites and radiolarian extinctions on Barbados. Nature 314:613–615

Sankaran AV (2010) Extraterrestrial mega-impacts and continental growth on the early earth. Curr Sci 99:160–161

Sarna-Wojcicki AM, Pringle MS, Wijbrans J (2000) New age of the Bishop Tuff from multiple sites and sediment rate calibration for the Matuyama-Brunhes boundary. J Geophys Res 105(B9):21431–21443

Sato H, Endo S, Sugiyama M, Kikegawa T, Shimomura O, Kusaba K (1991) Baddeleyite-type high pressure phase of TiO_2. Science 251:786–788

Sawlowicz Z (1993) Iridium and other platinum-group elements as geochemical markers in sedimentary environments. Palaeogeogr Palaeoclimotol Palaeoecol 104:253–270

Saunders JB, Bernoulli D, Müller-Merz E, Oberhänsli H, Perch-Nielsen K, Riedel WR, Sanfilippo A, Torrini R Jr (1984) Stratigraphy of the late Middle Eocene to Early Oligocene in the Bath Cliff section, Barbados, West Indies. Micropaleontology 30:390–425

Saxena SK, Dubrovinsky LS, Lazor P, Cerenius Y, Häggkvist P, Hanfland M, Hu J (1996) Stability of perovskite ($MgSiO_3$) in the earth's mantle. Science 274:1357–1359

Scally A, Simonson BM (2005) Spherule textures in the Neoarchean Wittenoom impact layer, Western Australia: consistency in diversity. Aust J Earth Sci 52:773–783

Schaaf P, Müller-Sohnius D (2002) Strontium and neodymium isotope study of Libyan Desert Glass: inherited Pan-African age signatures and new evidence for target material. Meteorit Planet Sci 37:565–576

Schmidt G, Zhou L, Wasson JT (1993) Iridium anomaly associated with the Australasian-tektite-producing impact: masses of the impactor and the Australasian tektites. Geochim Cosmochim Acta 57:4851–4859

Schmidt MW, Poli S, Comodi P, Zanazzi PF (1997) High-pressure behavior of kyanite: decomposition of kyanite into stishovite and corundum. Am Miner 82:460–466

Schmidt PW, Williams GE (1991) Palaeomagnetic correlation of the Acraman impact structure and the Late Proterozoic Bunyeroo ejecta horizon, South Australia. Aust J Earth Sci 38:283–289

Schmidt PW, Williams GE (1996) Palaeomagnetism of the ejecta-bearing Bunyeroo Formation, late Neoproterozoic, Adelaide fold belt, and the age of the Acraman impact. Earth Planet Sci Lett 144:347–357

Schmidt RG (1980) The Marquette range supergroup in the Gogebic iron district, Michigan and Wisconsin. United States Geological Survey, Bulletin 1460, 96 pp

Schmieder M, Buchner E, Schwarz WH, Trieloff M, Lambert P (2010) A Rhaetian $^{40}Ar/^{39}Ar$ age for the Rochechouart impact structure (France) and implications for the latest Triassic sedimentary record. Meteorit Planet Sci 45:1225–1242

Schmitz B, Andersson P, Dahl J (1988) Iridium, sulfur isotopes and rare earth elements in the Cretaceous-Tertiary boundary clays at Stevns Klint, Denmark. Geochim Cosmochim Acta 52:229–236

Schmitz B, Asaro F, Molina E, Monechi S, von Salis K, Speijer RP (1997) High-resolution iridium, $\delta^{13}C$, $\delta^{18}O$, foraminifera and nannofossil profiles across the latest Paleocene benthic extinction event at Zumaya, Spain. Palaeogeogr Palaeoclimatol Palaeoecol 133:49–68

Schmitz B, Ellwood BB, Peucker-Ehrenbrink B, El Hassani A, Bultynck P (2006) Platinum group elements and $^{187}Os/^{188}Os$ in a purported impact ejecta layer near the Eifelian-Givetian stage boundary, Middle Devonian. Earth Planet Sci Lett 249:162–172

Schneider DA, Kent DV, Mello GA (1992) A detailed chronology of the Australasian impact event, the Brunhes-Matuyama geomagnetic polarity reversal, and global climate change. Earth Planet Sci Lett 111:395–405

Schneider DA, Bickford ME, Cannon WF, Schultz KJ, Hamilton MA (2002) Age of volcanic rocks and syndepositional iron formations, Marquette Range Supergroup: implications for the tectonic setting of Paleoproterozoic iron formations of the Lake Superior region. Can J Earth Sci 39:999–1012

Schneider H, Hornemann U (1977) The disproportionation of andalusite (Al_2SiO_5) to Al_2O_3 and SiO_2 under shock compression. Phys Chem Miner 1:257–264

Schnetzler CC (1970) The lunar origin of tektites R.I.P. Meteoritics 5:221–222

Schnetzler CC (1992) Mechanism of Muong Nong-type tektite formation and speculation on the source of the Australasian tektites. Meteoritics 27:154–165

Schnetzler CC, McHone JF (1996) Source of the Australasian tektites: investigating possible sites in Laos. Meteorit Planet Sci 31:73–76

Schnetzler CC, Pinson WH Jr (1963) The chemical composition of tektites. In: O'Keefe JA (ed) Tektites. University of Chicago Press, Chicago, pp 95–129

Schnetzler CC, Pinson WH Jr, Hurley PM (1966) Rubidium-strontium age of the Bosumtwi crater area, Ghana, compared with the age of the Ivory Coast tektites. Science 151:817–819

Schnetzler CC, Philpotts JA, Thomas HH (1967) Rare earth and barium abundances in Ivory Coast tektites and rocks from the Bosumtwi crater area, Ghana. Geochim Cosmochim Acta 31:1987–1993

Schnetzler CC, Walter LS, Marsh JG (1988) Source of the Australasian tektite strewn field: a possible off-shore impact site. Geophys Res Lett 15:357–360

Schoenberg R, Kamber BS, Collerson KD, Moorbath S (2002) Tungsten isotope evidence from ~3.8-Gy metamorphosed sediments for early meteorite bombardment of the Earth. Nature 418:403–405

Schröder S, Lacassie JP, Beukes NJ (2006) Stratigraphic and geochemical framework of the Agouron drill cores, Transvaal Supergroup (Neoarchean-Paleoproterozoic), South Africa. S Afr J Geol 109:23–54

Schulte P, Kontny A (2005) Chicxulub impact ejecta from the Cretaceous-Paleogene (K-P) boundary in northeastern Mexico. In: Kenkmann T, Hörz F, Deutsch A (eds) Large meteorite impacts III. Geological Society of America, Special Paper 384, pp 191–221

Schulte P, Stinnesbeck W, Stüben D, Kramar U, Berner Z, Keller G, Adatte T (2003) Fe-rich and K-rich mafic spherules from slumped and channelized Chicxulub ejecta deposits in the northern La Sierrita area, NE Mexico. Int J Earth Sci 92:114–142

Schulte P, Speijer R, Mai H, Kontny A (2006) The Cretaceous–Paleogene (K–P) boundary at Brazos, Texas: Sequence stratigraphy, depositional events and the Chicxulub impact. Sediment Geol 184:77–109

Schulte P, Speijer R, Brinkhuis H, Kontny A, Claeys P, Galeotti S, Smit J (2008) Comment on the paper "Chicxulub impact predates K-T boundary: new evidence from Brazos, Texas" by Keller et al. (2007). Earth Planet Sci Lett 269:614–620

Schulte P, Deutsch A, Salge T (2009) A dual-layer Chicxulub ejecta sequence with shocked carbonates from the Cretaceous-Tertiary (K/T) boundary, ODP Leg 207, western Atlantic [abs]. Lunar Planet Sci 40: abstract no. 1859.pdf

Schulte P, Alegret L, Arenillas I, Arz JA, Barton PJ, Bown PR, Bralower TJ, Christeson GL, Claeys P, Cockell CS, Collins GS, Deutsch A, Goldin TJ, Goto K, Grajales-Nishimura JM, Grieve RAF, Gulick SPS, Johnson KR, Kiessling W, Koeberl C, Kring DA, MacLeod KG, Matsui T, Melosh J, Montanari A, Morgan JV, Neal CR Nichols DJ, Norris RD, Pierazzo E, Ravizza G, Rebolledo-Vieyra M, Reimold WU, Robin E, Salge T, Speijer RP, Sweet AR, Urrutia-Fucugauchi J, Vajda V, Whalen M, Willumsen PS (2010) The Chicxulub asteroid impact and mass extinction at the Cretaceous-Paleogene boundary. Science 327:1214–1218

Schultz PH, Lianza RE (1992) Recent grazing impacts on the Earth recorded at the Rio Cuarto crater field, Argentina. Nature 355:234–237

Schultz PH, Orphal D, Miller B, Borden WF, Larson SA (1981) Multi-ring basin formation: possible clues from impact cratering calculations. In: Schultz PH, Merrill RB (eds) Multi-ring basins: formation and evolution. Proceedings of the lunar and planetary science conference 12A. Pergamon Press, New York, pp 181–195

Schultz PH, Koeberl C, Bunch T, Grant J, Collins W (1994) Ground truth for oblique impact processes: new insight from the Rio Cuarto, Argentina, crater field. Geology 22:889–892

Schultz PH, Zarate M, Hames W, Camilión C, King J (1998) A 3.3-Ma impact in Argentina and possible consequences. Science 282:2061–2063

Schultz PH, Zarate M, Hames W (2000) Pleistocene and Miocene impact glass layers in the Argentine Pampas [abs]. Meteorit Planet Sci 35(Suppl):A143–A144

Schultz PH, Zarate M, Hames W, Koeberl C, Bunch T, Storzer D, Renne P, Wittke J (2004) The Quaternary impact record from the Pampas, Argentina. Earth Planet Sci Lett 219:211–238

Schultz PH, Zarate M, Hames W, Harris SR, Bunch TE, Koeberl C, Renne P, Wittke J (2006) The record of Miocene impacts in the Argentine Pampas. Meteorit Planet Sci 41:749–771

Schulz KJ, Cannon WF (2007) The Penokean orogeny in the Lake Superior region. Precambr Res 157:4–25

Schwarz WH, Lippolt HJ (2002) Coeval argon-40/argon-39 ages of moldavites from Bohemia and Lusatian strewn fields. Meteorit Planet Sci 37:1757–1763

Scott ERD (1999) How were tektites formed and ejected? [abs]. Meteorit Planet Sci 34:A103

Senftle FE, Thorpe AN, Grant JR, Hildebrand A, Moholy-Nagy H, Evans BJ, May L (2000) Magnetic measurements of glass from Tikal, Guatemala: possible tektites. J Geophys Res 105:18921–18925

Sephton MA, Looy CV, Veefkind RJ, Brinkhuis H, De Keeuw JW, Visscher H (2002) Synchronous record of $\delta^{13}C$ shifts in the oceans and atmosphere at the end of the Permian. In: Koeberl C, McLeod KG (eds) Catastrophic events and mass extinctions: impacts and beyond. Geological Society of America, Special Paper 356, pp 455–462

Sepkoski JJ Jr (1982) Mass extinctions in the Phanerozoic oceans: A review. In: Silver LT, Schultz PH (eds) Geological implications of impacts of large asteroids and comets on the Earth. Geological Society of America, Special Paper 190, pp 283–289

Sepkoski JJ Jr (1996) Patterns of Phanerozoic extinctions: a perspective from global data bases. In: Walliser OH (ed) Global events and event stratigraphy in the phanerozoic. Springer, Berlin, pp 35–52

Serefidden F, Herzog GF, Koeberl C (2007) Beryllium-10 concentrations of tektites from the Ivory Coast and from Central Europe: evidence for near-surface residence of precursor materials. Geochim Cosmochim Acta 71:1574–1582

Sharp TG, Lingemann CM, Dupas C, Stöffler D (1997) Natural occurrence of $MgSiO_3$-ilmenite and evidence for $MgSiO_3$-perovskite in a shocked L chondrite. Science 277:352–355

Sharp TG, El Goresy A, Wopenka B, Chen M (1999) A post-stishovite SiO_2 polymorph in the meteorite Shergotty: implications for impact events. Science 284:1511–1513

Sharpton VL, Ward PD (eds) (1990) Global catastrophes in Earth history: an interdisciplinary conference on impacts, volcanism, and mass mortality. Geological Society of America, Special Paper 246, 631 pp

Sharpton VL, Schuraytz BC, Burke K, Murali AV, Ryder G (1990) Detritus in K/T boundary clays of western North America; evidence against a single oceanic impact. In: Sharpton VL, Ward PD (eds) Global catastrophes in Earth history: an interdisciplinary conference on impacts, volcanism, and mass mortality. Geological Society of America, Special Paper 246, pp 349–357

Sharpton VL, Dalrymple GB, Marin LE, Ryder G, Schuraytz BC, Urrutia-Fucugauchi J (1992) New links between the Chicxulub impact structure and the Cretaceous/Tertiary boundary. Nature 359:819–821

Sharpton VL, Dressler BO, Herrick RR, Schneiders B, Scott J (1996) New constraints on Slate Islands impact structure, Ontario, Canada. Geology 24:851–854

Shaw HF, Wasserburg GJ (1982) Age and provenance of the target materials for tektites and possible impactites as inferred from Sm-Nd and Rb-Sr systematics. Earth Planet Sci Lett 60:155–177

Sheehan PM, Fastovsky DE (1992) Major extinctions of land-dwelling vertebrates at the Cretaceous-Tertiary boundary, eastern Montana. Geology 20:556–560

Shipboard Scientitic Party (1992) Site 761. In: von Rad U, Haq BU et al. In: Proceedings of the ocean drilling program 122. Ocean drilling program, College Station, Texas, pp 161–211

Shoemaker EM (1977) Why study impact craters? In: Roddy DJ, Pepin RO, Merrill RB (eds) Impact and explosion cratering. Pergamon Press, New York, pp 1–10

Shoemaker EM, Chao ECT (1961) New evidence for the impact origin of the Ries Basin, Bavaria, Germany. J Geophys Res 66:3371–3378

Shoemaker EM, Izett GA (1992) Stratigraphic evidence from western North America for multiple impacts at the K/T boundary [abs]. Lunar Planet Sci 23:1293–1294

Short NM (1966) Shock processes in geology. J Geol Educ 14:149–166

Short NM, Gold DP (1996) Petrography of shocked rocks from the central peak at the Manson impact structure. In: Koeberl C, Anderson RR (eds) The Manson impact structure, Iowa: anatomy of an impact crater. Geological Society of America, Special Paper 302, pp 245–265

Shukolyukov A, Lugmair GW (1998) Isotopic evidence for the Cretaceous-Tertiary impactor and its type. Science 282:927–929

Shukolyukov A, Lugmair GW (2000) Extraterrestrial matter on Earth: evidence from the Cr isotopes. In: Catastrophic events and mass extinctions: impacts and beyond [abs]. Lunar and Planetary Institute Contribution 1053. Lunar and Planetary Institute, Houston, pp 197–198

Shukolyukov A, Kyte FT, Lugmair GW, Lowe DR, Byerly GR (2000) The oldest impact deposits on Earth—first confirmation of extraterrestrial component. In: Gilmour I, Koeberl C (eds) Impacts and the early Earth. Springer, Heidelberg, pp 99–116

Shukolyukov A, Lugmair GW, Becker L, Macisaac C, Poreda R (2004) Extraterrestrial chromium in the Permian-Triassic boundary at Graphite Peak, Antarctica [abs]. Lunar Planet Sci 35: abstract no. 1875.pdf

Shuvalov V (2003) Displacement of target material during impact cratering. In: Koeberl C, Martínez-Ruiz F (eds) Impact markers in the stratigraphic record. Springer, Berlin, pp 121–135

Sigurdsson H, D'Hondt S, Arthur MA, Bralower TJ, Zachos JC, van Fossen M, Channell JET (1991a) Glass from the Cretaceous/Tertiary boundary in Haiti. Nature 349:482–487

Sigurdsson H, Bonté P, Turpin L, Chaussidon M, Metrich N, Steinberg M, Pradel P, D'Hondt S (1991b) Geochemical constraints on source region of Cretaceous/Tertiary impact glasses. Nature 353:839–842

Silver LT, Schultz PH (eds) (1982) Geological implications of impacts of large asteroids and comets on the Earth. Geological Society of America, Special Paper 190, 528 pp

Simonson BM (1985) Sedimentological constraints on the origins of Precambrian iron-formations. Geol Soc Am Bull 96:244–252

Simonson BM (1987) Early silica cementation and subsequent diagenesis in arenites from four early Proterozoic iron-formations of North America. J Sediment Petrol 57:494–511

Simonson BM (1992) Geological evidence for a strewn field of impact spherules in the early Precambrian Hamersley Basin of Western Australia. Geol Soc Am Bull 104:829–839

Simonson BM (2003a) Petrographic criteria for recognizing certain types of impact spherules in well-preserved Precambrian successions. Astrobiology 3:49–65
Simonson BM (2003b) Origin and evolution of large Precambrian iron formations. In: Chan M, Archer A (eds) Extreme depositional environments: mega-end members in geologic time. Geological Society of America, Special Paper 370, pp 231–244
Simonson BM, Carney KE (1999) Roll-up structures: evidence of *in situ* microbial mats in late Archean deep shelf environments. Palaios 14:13–24
Simonson BM, Glass BP (2004) Spherule layers—records of ancient impacts. Annu Rev Earth Planet Sci 32:329–361
Simonson BM, Harnik P (2000) Have distal impact ejecta changed through geologic time? Geology 28:975–978
Simonson BM, Hassler SW (1996) Was the deposition of large Precambrian iron formation linked to major marine transgressions? J Geol 104:665–676
Simonson BM, Hassler SW (1997) Revised correlations in the early Precambrian Hamersley Basin based on a horizon of resedimented impact spherules. Aust J Earth Sci 44:37–48
Simonson BM, Hassler SW (2002) Revisiting an Archean impact layer (comment). Science 298:750
Simonson BM, Schubel KA, Hassler SW (1993a) Carbonate sedimentology of the early Precambrian Hamersley Group of Western Australia. Precambr Res 60:287–335
Simonson BM, Hassler SW, Schubel KA (1993b) Lithology and proposed revisions in stratigraphic nomenclature of the Wittenoom Formation (Dolomite) and overlying formations, Hamersley Group, Western Australia. Geological Survey of Western Australia, Report 34, Professional Papers, pp 65–79
Simonson BM, Davies D, Wallace M, Reeves S, Hassler SW (1998) Iridium anomaly but no shocked quartz from Late Archean microkrystite layer: oceanic impact ejecta? Geology 26:195–198
Simonson BM, Hassler SW, Beukes NJ (1999) Late Archean impact spherule layer in South Africa that may correlate with a layer in Western Australia. In: Dressler BO, Sharpton VL (eds) Large meteorite impacts and planetary evolution II. Geological Society of America, Special Paper 339, pp 249–262
Simonson BM, Davies D, Hassler SW (2000a) Discovery of a layer of probable impact melt spherules in the late Archean Jeerinah Formation (Fortescue Group, Western Australia). Aust J Earth Sci 47:315–325
Simonson BM, Hornstein M, Hassler SW (2000b) Particles in Late Archean Carawine Dolomite (Western Australia) resemble Muong Nong-type tektites. In: Gilmour I, Koeberl C (eds) Impacts and the early Earth, Lecture Notes in Earth Sciences, vol 91. Springer, Berlin, pp 181–214
Simonson BM, Koeberl C, McDonald I, Reimold WU (2000c) Geochemical evidence for an impact origin for a Late Archean spherule layer, Transvaal Supergroup, South Africa. Geology 28:1103–1106
Simonson BM, Byerly GR, Lowe DR (2004) The early Precambrian stratigraphic record of large extraterrestrial impacts. In: Eriksson PG, Altermann W, Nelson DR, Mueller WU, Catuneanu O (eds) The Precambrian Earth: tempos and events. Elsevier, Amsterdam, pp 27–45
Simonson BM, Sumner DY, Beukes NJ, Johnson S, Gutzmer J (2009a) Correlating multiple Neoarchean-Paleoproterozoic impact spherule layers between South Africa and Western Australia. Precambr Res 169:100–111
Simonson BM, McDonald I, Shukolyukov A, Koeberl C, Reimold WU, Lugmair GW (2009b) Geochemistry of 2.63-2.49 Ga impact spherule layers and implications for stratigraphic correlations and impact processes. Precambr Res 175:51–76
Simonson BM, Beukes NJ, Biller S (2009c) Monteville spherule layer (Neoarchean, Transvaal Supergroup, South Africa) looks familiar in three new cores that triple its areal extent boundary [abs]. Geological Society of America Abstracts with Program 41(7):531

Slack JF, Cannon WF (2009) Extraterrestrial demise of banded iron formations 1.85 billion years ago. Geology 37:1011–1014

Smit J (1990) Meteorite impact, extinctions and the Cretaceous-Tertiary boundary. Geologie en Mijnbouw 69:187–204

Smit J (1999) The global stratigraphy of the Cretaceous-Tertiary boundary impact ejecta. Annu Rev Earth Planet Sci 27:75–113

Smit J, Hertogen J (1980) An extraterrestrial event at the Cretaceous-Tertiary boundary. Nature 285:198–200

Smit J, Klaver G (1981) Sanidine spherules at the Cretaceous-Tertiary boundary indicate a large impact event. Nature 292:47–49

Smit J, Kyte FT (1984) Siderophile-rich magnetic spheroids from the Cretaceous-Tertiary boundary in Umbria, Italy. Nature 310:403–405

Smit J, Romein AJT (1985) A sequence of events across the Cretaceous-Tertiary boundary. Earth Planet Sci Lett 74:155–170

Smit J, van Eijden AJM, Troelstra SR (1991) Analysis of the Australasian microtektite event, the Toba Lake event, and the Cretaceous/Paleogene boundary, Eastern Indian Ocean. In: Weissel J, Peirce J, Taylor E, Alt J et al. (eds) Proceedings of the ocean drilling program 121, Scientific Results. Ocean Drilling Program, College Station, Texas, pp 489–495

Smit J, Montanari A, Swinburne NHM, Alvarez W, Hildebrand AR, Margolis SV, Claeys P, Lowrie W, Asaro F (1992a) Tektite-bearing, deep-water clastic unit at the Cretaceous-Tertiary boundary in northeastern Mexico. Geology 20:99–103

Smit J, Alvarez W, Montanari A, Swinburne N, Van Kempen TM, Klaver GT, Lustenhouwer WJ (1992b) "Tektites" and microkrystites at the Cretaceous Tertiary boundary: two strewn fields, one crater? In: Proceedings of the 22nd lunar and planetary science conference. Lunar and Planetary Institute, Houston, pp 87–100

Smit J, Roep TB, Alvarez W, Montanari A, Claeys P, Grajales-Nishimura JM, Bermudez J (1996) Coarse-grained, clastic sandstone complex at the K/T boundary around the Gulf of Mexico: deposition by tsunami waves induced by the Chicxulub impact? In: Ryder G, Fastovsky D, Gartner S (eds) The Cretaceous-Tertiary event and other catastrophes in Earth history. Geological Society of America, Special Paper 307, pp 151–182

Smit J, Simonson BM, Hassler SW, Sumner DY (2002) Large-impact triggered tsunami deposits in the deep sea: examples from the 65 Ma Chicxulub Crater and 2.5–2.6 Ga Hamersley Basin [abs]. Geol Soc Am Abstr Prog 34(6):401

Smit J, Van der Gaast S, Lustenhouwer W (2004) Is the transition impact to post-impact rock complete? Some remarks based on the XRF scanning, electron microprobe, and thin section analyses of the Yaxcopoil-1 core in the Chicxulub crater. Meteorit Planet Sci 39:1113–1126

Smith FC, Zullo JB, Glass BP (2006) The spherule layer in the Paleoproterozoic Grænsesø Formation in Midternæs, South Greenland [abs]. Geol Soc Am Abstr Prog 38(7):297

Smith FC, Zullo JB, Glass BP, Simonson BM (2010) Discovery of a shock-induced polymorph of rutile with α-PbO_2 structure (TiO_2II) in four Neoarchean spherule layers from Western Australia and South Africa [abs]. Meteorit Planet Sci 45:A192

Smith HJ, Smoluchowski R (1981) Hawaii as a consequence of an impact; precipitation driven magma convection [abs]. In: Papers presented in the conference on large body impacts and terrestrial evolution: geological, climatological, and biological implications. Lunar and Planetary Institute, Houston, Texas, p 53

Smith JV, Mason B (1970) Pyroxene-garnet transformation in Coorara meteorite. Science 168: 832–833

Smith RC, Berkheiser SW, Barnes JH, Hoff DT (1988) Strange clay baffles geologists. Pennsylvania Geology 19:8–13

Spencer LJ (1933) Answer to Fenner's "Origin of tektites". Nature 132:571

Spezzaferri S, Basso D, Coccioni R (2002) Late Eocene planktonic foraminiferal response to an extraterrestrial impact at Massignano GSSP (Northeastern Appennines, Italy). J Foramin Res 32(2):188–199

Spray JG, Butler HR, Thompson LM (2004) Tectonic influences on the morphology of the Sudbury impact structure: implications for terrestrial cratering and modeling. Meteorit Planet Sci 39:287–301

Spudis PD (1993) The geology of multi-ring impact basins: the moon and other planets. Cambridge University Press, New York, 263 pp

Squyres SW, Grotzinger JP, Arvidson RE, Bell JF III, Calvin W, Christensen PR, Clark BC, Crisp JA, Farrand WH, Herkenhoff KE, Johnson JR, Klingelhöfer G, Knoll AH, McLennan SM, McSween HY Jr, Morris RV, Rice JW Jr, Rieder R, Soderblom LA (2004) In situ evidence for an ancient aqueous environment at Meridiani Planum, Mars. Science 306:1709–1714

Stauffer PH (1978) Anatomy of the Australasian tektite strewnfield and the probable site of its source crater. In: 3rd regional conference on geology and mineral resources of Southeast Asia, Bangkok, pp 285–289

Stähle V (1973) Cordierite glass formed by shock in a cordierite-garnet-gneiss from the Ries crater, Germany. Earth Planet Sci Lett 18:385–390

Stähle V (1975) Natural shock behavior of almandite in metamorphic rocks from the Ries crater, Germany. Earth Planet Sci Lett 25:71–81

Stecher O, Ngo HH, Papanastassiou DA, Wasserburg GJ (1989) Nd and Sr isotopic evidence for the origin of tektite material from DSDP site 612 off the New Jersey coast. Meteoritics 24:89–98

Stinnesbeck W, Keller G (1996) K/T boundary coarse-grained siliciclastic deposits in northeastern Mexico and northeastern Brazil: evidence for a mega-tsunami or sea-level changes? In: Ryder G, Fastovsky D, Gartner S (eds) The Cretaceous-Tertiary event and other catastrophes in Earth history. Geological Society of America, Special Paper 307, pp 197–209

Stinnesbeck W, Barbarin JM, Keller G, Lopez-Oliva JG, Pivnik DA, Lyons JB, Officer CB, Adatte T, Graup G, Rocchia R, Robin E (1993) Deposition of channel deposits near the Cretaceous-Tertiary boundary in northeastern Mexico: catastrophic or "normal" sedimentary deposits? Geology 21:797–800

Stinnesbeck W, Keller G, Adatte T, Lopez-Oliva JG, MacLeod N (1996) The Cretaceous-Tertiary clastic deposition in NE Mexico: bolide impact or sealevel lowstand. In: MacLeod N, Keller G (eds) The Cretaceous-Tertiary boundary mass extinction: biotic and environmental events. Norton Press, New York, pp 471–517

Stinnesbeck W, Keller G, Adatte T, Stüben D, Kramar U, Berner Z, Desremaux C, Moliere E (2000) Beloc, Haiti, revisited: multiple impacts across the Cretaceous-Tertiary boundary in the Caribbean? Tera Nova 11:303–310

Stishov SM, Popova SV (1961) A new dense modification of silica. Geokhimiya 10:923–926

Stöckelmann D, Reimold WU (1989) The HMX mixing calculation program. Math Geol 21:853–860

Stöffler D (1966) Zones of impact metamorphism in the crystalline rocks at the Nördlinger Ries Crater. Contrib Miner Petrol 12:15–24

Stöffler D (1972) Deformation and transformation of rock-forming minerals by natural and experimental shock processes: 1. Behaviour of minerals under shock compression. Fortschritte der Mineralogie 49:50–113

Stöffler D (1974) Deformation and transformation of rock-forming minerals by natural and experimental processes: 2. Physical properties of shocked minerals. Fortschritte der Mineralogie 51:256–289

Stöffler D (1984) Glasses formed by hypervelocity impact. J Non-Cryst Solids 67:465–502

Stöffler D, Grieve RAF (2007) Impactites. In: Fettes D, Desmons J (eds) Metamorphic rocks, a classification and glossary of terms. Cambridge University Press, Cambridge, pp 82–92

Stöffler D, Langenhorst F (1994) Shock metamorphism of quartz in nature and experiment: I. Basic observations and theory. Meteoritics 29:155–181

Stöffler D, Gault DE, Wedekind J, Polkowski G (1975) Experimental hypervelocity impact into quartz sand: distribution and shock metamorphism of ejecta. J Geophys Res 80:4062–4077

Stöffler D, Keil K, Scott RD (1991) Shock metamorphism of ordinary chondrites. Geochim Cosmochim Acta 55:3845–3867

Stöffler D, Ryder G, Ivanov BA, Artemieva NA, Cintala MJ, Grieve RAF (2006) Cratering history and lunar geology. Rev Miner Geochem 60:519–596

Storey J (1987) Darwin glass: gift from the heavens. Aust Geogr 8:39–43

Störr M, Lange JM (1992) The occurrence of tektites northeast of Dresden, Germany. Geochim Cosmochim Acta 56:2937–2940

Storzer D (1985) The fission track age of high sodium/potassium australites revisited [abs]. Meteoritics 20:765–766

Storzer D (1992) Microtektite hunting and mineral wool shot [abs]. Lunar Planet Sci 23:1373–1374

Storzer D, Koeberl C (1991) Uranium and zirconium enrichments in Libyan Desert Glass [abs]. Lunar Planet Sci 22:1345–1346

Storzer D, Müller-Sohnius D (1986) The K/Ar age of high sodium/potassium australites [abs]. Meteoritics 21:518–519

Storzer D, Wagner GA (1977) Fission track dating of meteorite impacts. Meteoritics 12:368–369

Storzer D, Jessberger EK, Kunz J, Lange JM (1995) Synopsis von spaltspuren- und kalium-argon-datierungen an Ries-impactgläsern und moldaviten. Gesellschaft für Geowissenschaften 195:79–80

Sumner DY, Beukes NJ (2006) Sequence stratigraphic development of the Neoarchean Transvaal carbonate platform, Kaapvaal Craton, South Africa. S Afr J Geol 109:11–22

Sumner DY, Bowring SA (1996) U-Pb geochronologic constraints on deposition of the Campbellrand Subgroup, Transvaal Supergroup, South Africa. Precambr Res 79:25–35

Sun Y-Y, Chai C-F, Ma S-L, Mao X-X, Xu D-Y, Zhang Q-W, Chen C-Z, Yang Z-Z (1984) Ir anomaly in Permian-Triassic clay at Changxing, Zhejiang, China and its significance. In: Tu G (ed) Contributions to the 27th international geological congress on rare events in geology. Science Press, Beijing, pp 235–245

Surovell TA, Holliday VT, Gingerich JA, Ketron C, Haynes CV Jr, Hillman L, Wagner DP, Johnson E, Claeys P (2009) An independent evaluation of the Younger Dryas extraterrestrial impact hypothesis. Proc Natl Acad Sci U S A 106:18155–18158

Suzuki A, Ohtani E, Morishima H, Kubo T, Kanbe Y, Kondo T, Okada T, Terasaki H, Kato T, Kikegawa T (2000) In situ determination of the phase boundary between wadsleyite and ringwoodite in Mg_2SiO_4. Geophys Res Lett 27:803–806

Suzuki I, Ohtani E, Kumazawa M (1980) Thermal expansion of modified spinel, β-Mg_2SiO_4. J Phys Earth 28:273–280

Svensson NB (1971) Probable meteorite impact crater in central Sweden. Nature. Phys Sci 229(3):90–92

Sweeney D, Simonson BM (2008) Textural constraints on the formation of impact spherules: a case study from the Dales Gorge BIF, Paleoproterozoic Hamersley Group of Western Australia. Meteorit Planet Sci 43:2073–2087

Swisher CC III, Grajales-Nishimura JM, Montanari A, Margolis SV, Claeys P, Alvarez W, Renne P, Cedillo-Pardo E, Maurrasse FJ-MR, Curtis GH, Smit J, McWilliams MO (1992) Coeval $^{40}Ar/^{39}Ar$ ages of 65.0 million years ago from Chicxulub crater melt rock and Cretaceous-Tertiary boundary tektites. Science 257:954–958

Tada R, Nakano Y, Iturralde-Vinent MA, Yamamoto S, Kamata T, Tajika E, Toyoda K, Kiyokawa S, Delgado DG, Oji T, Goto K, Takayama H, Rojas-Consuegra R, Matsui T (2002) Complex tsunami waves suggested by the Cretaceous-Tertiary boundary deposit at the Moncada section, western Cuba. In: Koeberl C, Macleod KG (eds) Catastrophic events and mass extinctions: impacts and beyond. Geological Society of America, Special Paper 356, pp 109–123

Tagle R, Claeys P (2005) An ordinary chondrite as impactor for Popigai crater, Siberia. Geochim Cosmochim Acta 60:2877–2889

Tagle R, Hecht L (2006) Geochemical identification of projectiles in impact rocks. Meteorit Planet Sci 41:1721–1735
Tanaka KL, Hartmann WK (2008) Planetary time scale. In: Ogg JG, Ogg G, Gradstein F (eds) The concise geologic time scale. Cambridge University Press, Cambridge, pp 13–22
Tancredi G, Ishitsuka J, Schultz PH, Harris RS, Brown P, ReVelle DO, Antier K, Le Pichon A, Rosales D, Vidal E, Varela ME, Sánchez L, Benavente S, Bojorquez J, Cabezas D, Dalmau A (2009) A meteorite crater on Earth formed on September 15, 2007: the Carancas hypervelocity impact. Meteorit Planet Sci 44:1967–1984
Tanner LH, Kyte FT (2005) Anomalous iridium enrichment at the Triassic-Jurassic boundary, Blomidon Formation, Fundy basin, Canada. Earth Planet Sci Lett 240:634–641
Tanner LH, Lucas SG, Chapman MG (2004) Assessing the record and causes of the Late Triassic extinctions. Earth-Sci Rev 65:103–139
Taylor HP, Epstein SE (1969) Correlations between O^{18}/O^{16} ratios and chemical compositions of tektites. J Geophys Res 74:6834–6844
Taylor S, Brownlee DE (1991) Cosmic spherules in the geologic record. Meteoritics 26:203–211
Taylor S, Lever JH, Harvey RP (2000) Numbers, types, and compositions of an unbiased collection of cosmic spherules. Meteorit Planet Sci 35:651–666
Taylor SR (1962) The chemical composition of australites. Geochim Cosmochim Acta 26:685–722
Taylor SR, Kaye M (1969) Genetic significance of the chemical composition of tektites: a review. Geochim Cosmochim Acta 33:1083–1100
Taylor SR, Koeberl C (1994) The origin of tektites: comment on a paper by J. A. O'Keefe. Meteoritics 29:730–742
Taylor SR, McLennan SM (1979) Chemical relationships among irghizites, zhamanshinites, Australasian tektites and Henbury impact glasses. Geochim Cosmochim Acta 43:1551–1565
Taylor SR, McLennan SM (1985) The continental crust: its composition and evolution. Blackwell Scientific Publications, Oxford, 321 pp
Taylor SR, McLennan SM (2009) Planetary crusts: their composition, origin and evolution. Cambridge University Press, Cambridge, 378 pp
Taylor SR, Sachs M (1964) Geochemical evidence for the origin of australites. Geochim Cosmochim Acta 28:235–264
Taylor SR, Solomon M (1964) The geochemisty of Darwin glass. Geochim Cosmochim Acta 28:471–494
Thackrey G, Walkden G, Indares A, Horstwood M, Kelley S, Parrish R (2009) The use of heavy mineral correlation for determining the source of impact ejecta: a Manicouagan distal ejecta case study. Earth Planet Sci Lett 285:163–172
Thein J (1987) A tektite layer in upper Eocene sediments of the New Jersey continental slope (Site 612, Leg 95). Init Rep Deep Sea Drilling Proj 95:565–575
Therriault AM, Fowler AD, Grieve RAF (2002) The Sudbury igneous complex: a differentiated impact melt sheet. Econ Geol 97:1521–1540
Thiede J, Vallier TL et al (1981) Initial reports of the deep sea drilling project 62. U.S. Government Printing Office, Washington, 1120 pp
Thomas E, Shackleton NJ (1996) The Paleocene-Eocene benthic foramininferal extinction and stable isotope anomalies. In: Know RWOB, Corfield RM, Dunay RE (eds) Correlation of the early paleogene in Northwest Europe. Geological Society of London, Special Publication 101, pp 401–441
Thorne AM, Trendall AF (2001) Geology of the Fortescue Group, Pilbara Craton, Western Australia. Geological Survey of Western Australia, Bulletin 144, 249 pp
Thompson Stiegler M, Lowe DR, Byerly GR (2008) Abundant pyroclastic komatiitic volcanism in the 3.5–3.2 Ga Barberton greenstone belt. South Africa. Geology 36:779–782
Thompson Stiegler M, Lowe DR, Byerly GR (2010) The petrogenesis of volcaniclastic komatiites in the Barberton greenstone belt, South Africa: a textural and geochemical study. J Petrol 51:947–972

Thompson Stiegler M, Lowe DR, Byerly GR (2011) Fragmentation and dispersal of komatiitic pyroclasts in the 3.5–3.2 Ga Onverwacht Group, Barberton greenstone belt, South Africa. Geol Soc Am Bull 123:1112–1126

Tice MM, Lowe DR (2004) Photosynthetic microbial mats in the 3,416-Myr-old ocean. Nature 431:549–552

Timms NE, Reddy SM, Healy D, Nemchin AA, Grange ML, Pidgeon RT, Hart R (2012) Resolution of impact-related microstructures in lunar zircon: a shock-deformation mechanism map. Meteorit Planet Sci 47:120–141

Tomioka N, Fujino K (1997) Natural (Mg,Fe)SiO_3-ilmenite and -perovskite in the Tenham meteorite. Science 277:1084–1086

Tomioka N, Fujino K (1999) Akimotoite, (Mg,Fe)SiO_3, a new silicate mineral of the ilmenite group in the Tenham chondrite. Am Miner 84:267–271

Tomioka N, Mori H, Fujino K (2000) Shock-induced transition of $NaAlSi_3O_8$ feldspar into hollandite structure in a L6 chondrite. Geophys Res Lett 27:3997–4000

Toon OB, Pollack JB, Ackerman TP, Turco RP, McKay CP, Liu MS (1982) Evolution of an impact-generated dust cloud and its effects on the atmosphere. In: Silver LT, Schultz PH (eds) Geological implications of impacts of larger asteroids and comets on the Earth. Geological Society of America, Special Paper 190, pp 187–200

Toon OB, Zahnle K, Morrison D, Turco RP, Covey C (1997) Environmental perturbations caused by the impacts of asteroids and comets. Rev Geophys 35:41–78

Trendall AF (1983) The Hamersley Basin. In: Trendall AF, Morris RC (eds) Iron-formation: facts and problems. Elsevier, Amsterdam, pp 69–129

Trendall AF, Blockley JG (1970) the iron formations of the Precambrian Hamersley Group of Western Australia. Geological Survey of Western Australia, Bulletin 119, 366 pp

Trendall AF, Nelson DR, de Laeter JR, Hassler SW (1998) Precise zircon U-Pb ages from the Marra Mamba Iron Formation and Wittenoom Formation, Hamersley Group, Western Australia. Aust J Earth Sci 45:137–142

Trendall AF, Compston W, Nelson DR, de Laeter JR, Bennett VC (2004) SHRIMP zircon ages constraining the depositional chronology of the Hamersley Group, Western Australia. Aust J Earth Sci 51:621–644

Trepmann CA, Spray JG (2005) Planar microstructures and Dauphiné twins in shocked quartz from the Charlevoix impact structure, Canada. In: Kenkmann T, Hörz F, Deutsch A (eds) Large meteorite impacts III. Geological Society of America, Special Paper 384, pp 315–328

Trieloff M, Deutsch A, Jessberger EK (1998) The age of the Kara impact structure, Russia. Meteorit Planet Sci 33:361–372

Trieloff M, Bollinger K, Kunz J, Jessberger EK (2007) ^{40}Ar-^{39}Ar ages of Australasian tektites [abs]. Meteorit Planet Sci 42(Suppl):A150

Trinquier A, Birck J-L, Allègre CJ (2006) The nature of the KT impactor. A ^{54}Cr reappraisal. Earth Planet Sci Lett 241:780–788

Trnka M, Houzar S (2002) Moldavites: a review. Bull Czech Geol Surv 77(4):283–302

Trurnit P (1968) Pressure solution phenomena in detrital rocks. Sediment Geol 2:89–114

Tschermak G (1872) Die Meteorite von Shergotty und Gopalpur. Akademie der Wissenschaften in Wien. Sitzungsberichte. Mathematisch-naturwissenschaftliche Klasse 65:122–146

Tschudy RH, Pillmore CL, Orth CJ, Gilmore JS, Knight JD (1984) Disruption of the terrestrial plant ecosystem at the Cretaceous-Tertiary Boundary, Western Interior. Science 225:1030–1032

Tsuchida Y, Yagi T (1990) New pressure-induced transformations of silica at room temperature. Nature 347:267–269

Turgeon SC, Creaser RA, Algeo TJ (2007) Re–Os depositional ages and seawater Os estimates for the Frasnian-Famennian boundary: implications for weathering rates, land plant evolution, and extinction mechanisms. Earth Planet Sci Lett 261:649–661

Turtle EP, Pierazzo E, Collins GS, Osinski GR, Melosh HJ, Morgan JV, Reimold WU (2005) Impact structures: what does crater diameter mean? In: Kenkmann T, Hörz F, Deutsch A (eds) Large meteorite impacts III. Geological Society of America, Special Paper 384, pp 1–24

Twitchett RJ (2007) The Late Permian mass extinction event and recovery: biological catastrophe in a greenhouse world. In: Sammonds PR, Thompson JMT (eds) Advances in Earth science—from earthquakes to global warming. Royal Society Series on Advances in Science, vol 2. Imperial College Press, London, pp 69–90

Underwood JR Jr, Fisk EP (1980) Meteorite impact structures, Southeast Libya. In: Salem MJ, Busrewil MT (eds) The geology of Libya 3, 2. Symposium on the Geology of Libya 1978 (London), pp 893–900

Uysal IT, Golding SD, Glikson AY, Mory AJ, Glikson M (2001) K-Ar evidence from illitic clays of a Late Devonian age for the 120 km diameter Woodleigh impact structure, Southern Carnarvon Basin, Western Australia. Earth Planet Sci Lett 192:281–289

Uysal IT, Mory AJ, Golding SD, Bolhar R, Collerson SD (2005) Clay mineralogical, geochimical and isotopic tracing the evolution of the Woodleigh impact structure, Southern Carnarvon Basin, Western Australia. Contrib Miner Petrol 149:576–590

Vajda V, Raine JI, Hollis CJ (2001) Indication of global deforestation at the Cretaceous-Tertiary boundary by New Zealand fern spike. Science 294:1700–1702

Valentine GA (1998) Damage to structures by pyroclastic flows and surges, inferred from nuclear weapons effects. J Volcanol Geoth Res 87:117–140

Van Ginneken M, Folco L, Perchiazzi N, Rochette P, Bland PA (2010) Meteoritic ablation debris from the Transantarctic Mountains: evidence for a Tunguska-like impact over Antarctica ca. 480 ka ago. Earth Planet Sci Lett 293:104–113

van Hengstum PJ, Gröcke DR (2008) Stable isotope record of the Eifelian–Givetian boundary Kačák–*otomari* event (Middle Devonian) from Hungry Hollow, Ontario, Canada. Can J Earth Sci 45:353–366

Van Kranendonk MJ (2006) Volcanic degassing, hydrothermal circulation and the flourishing of early life on Earth: a review of the evidence from c. 3490–3240 Ma rocks of the Pilbara Supergroup, Pilbara Craton, Western Australia. Earth-Sci Rev 74:197–240

Van Kranendonk MJ (2010) Three and a half billion years of life on Earth: a transect back into deep time. Geological Survey of Western Australia, Record 2010/21, 93 pp

Van Kranendonk MJ, Smithies RH, Hickman AH, Champion DC (2007a) Review: secular tectonic evolution of Archean continental crust: interplay between horizontal and vertical processes in the formation of the Pilbara Craton, Australia. Terra Nova 19:1–38

Van Kranendonk MJ, Smithies RH, Hickman AH, Champion DC (2007b) Paleoarchean development of a continental nucleus: the East Pilbara Tarrane of the Pilbara Craton, Western Australia. In: Van Kranendonk MJ, Smithies RH, Bennett VC (eds) Earth's oldest rocks. Elsevier, Amsterdam, pp 307–367

Van Kranendonk MJ, Gehling J, Shields G (2008) Precambrian. In: Ogg JG, Ogg G, Gradstein F (eds) The concise geologic time scale. Cambridge University Press, Cambridge, pp 23–36

van Roermund HLM, Drury MR, Barhoorn A, De Ronde A (2001) Relict majoritic garnet microstructures from ultra-deep orogenic peridotites in Western Norway. J Petrol 42:117–130

van Soest MC, Wartho J-A, Monteleone BD, Hodges KV, Koeberl C, Schmieder M, Buchner E, Spray JG, Bezys RK, Reimold WU (2009) (U-Th)/He dating of single zircon and apatite crystals—a new tool for dating terrestrial impact structures [abs]. Lunar Planet Sci 40: abstract no. 2041.pdf

van Soest MC, Hodges KV, Wartho J-A, Biren MB, Monteleone BD, Ramezani J, Spray JG, Thompson LM (2011) (U-Th)/He dating of terrestrial impact structures: The Manicouagan example. Geochem Geophys Geosyst 12:Q0AA16. doi:10.1029/2010GC003465

van Westrenen W, Frank MR, Hanchar JM, Fei Y, Finch RJ, Zha C-S (2004) In situ compressibility of synthetic pure zircon ($ZrSiO_4$) and the onset of the zircon-reidite phase transition. Am Miner 89:197–203

Van Wyk CJ (1987) Die mineralogy en geochemie van sedimentere siklusse in die Kuruman en Griquatown-Ysterfomasies van die Transvaal-Supergroep in Griekwaland-Wes. M.Sc. thesis, Rand Afrikaans University, Johannesburg, 235 pp

Vassilev SV, Vassileva CG (1996) Mineralogy of combustion wastes from coal-fired power stations. Fuel Process Technol 47:261–280

Vassilev SV, Menendez R, Borrego AG, Diaz-Somoano M, Martinez-Tarazona MR (2004) Phase-mineralogy and chemical composition of coal fly ashes as a basis for their multicomponent utilization. 3. Characterization of magnetic and char concentrations. Fuel 83:1563–1583

Vazquez JA, Ort MH (2006) Facies variation of eruption units produced by passage of single pyroclastic surge currents, Hopi Buttes volcanic field, USA. J Volcanol Geoth Res 154: 222–236

Venkatesan MI, Dahl J (1989) Organic geochemical evidence for global fires at the Cretaceous/Tertiary boundary. Nature 338:57–60

Verati C, Rapaille C, Féraud G, Marzoli A, Betrand H, Youbi N (2007) $^{40}Ar/^{39}Ar$ ages and duration of the Central Atlantic Magmatic Province volcanism in Morocco and Portugal and its relation to the Triassic-Jurassic boundary. Palaeogeogr Palaeoclimatol Palaeoecol 244:308–325

Vickers-Rich P, Komarower P (eds) (2007) The rise and fall of the Ediacaran biota. Geological Society of London, Special Publication 286, 456 pp

Vickery AM (1993) The theory of jetting: application to the origin of tektites. Icarus 105: 441–453

Vickery AM, Melosh HJ (1990) Atmospheric erosion and impactor retention in large impacts, with applications to mass extinctions. In: Sharpton VL, Ward PD (eds) Global catastrophes in Earth history; an interdisciplinary conference on impacts, volcanism, and mass mortality. Geological Society of America, Special Paper 247, pp 289–300

Vickery AM, Kring DA, Melosh HJ (1992) Ejecta associated with large terrestrial impacts: implications for the Chicxulub impact and K/T boundary stratigraphy [abs]. Lunar Planet Sci 23:1473–1474

von der Borch CC (1970) Glassy objects in deep sea clays. Init Rep Deep Sea Drilling Proj 5:525–529

von der Borch CC (1971) Glassy objects in Tertiary deep-sea clays cored by the Deep Sea Drilling Project. Mar Geol 10:5–14

Vonhof HB, Smit J (1997) High-resolution late Maastrichtian—early Danian oceanic $^{87}Sr/^{86}Sr$ record: implications for Cretaceous-Tertiary events. Geology 25:347–350

Vonhof HB, Smit J (1999) Late Eocene microkrystites and microtektites at Maud Rise (Ocean Drilling Project Hole 689B; Southern Ocean) suggest a global extension of the approximately 35.5 Ma Pacific impact ejecta strewn field. Meteorit Planet Sci 34:747–755

Vonhof HB, Smit J, Brinkhuis H, Montanari A, Nederbragt AJ (2000) Global cooling accelerated by early late Eocene impact? Geology 28:687–690

Wacey D (2009) Early life on Earth: a practical guide. Topics in geobiology, vol 31. Springer, Berlin, 274 pp

Walkden G, Parker J, Kelley S (2002) A Late Triassic impact ejecta layer in southwestern Britain. Science 298:2185–2188

Walker JD, Geissman JW (compilers) (2009) Geologic time scale. Geological Society of America. doi: 10.1130/2009.CTS004R2C

Walker RJ, Horan MF, Morgan JW, Becker H, Grossman JN, Ruben AE (2002) Comparative ^{187}Re-^{187}Os systematics of chondrites: implications regarding early solar system processes. Geochim Cosmochim Acta 66:4187–4201

Wallace MW, Gostin VA, Keays RR (1989) Discovery of the Acraman impact ejecta blanket in the Officer Basin and its stratigraphic significance. Aust J Earth Sci 36:585–587

Wallace MW, Gostin VA, Keays RR (1990a) Spherules and shard-like clasts from the Late Proterozoic Acraman impact ejecta horizon, South Australia. Meteoritics 25:161–165

Wallace MW, Gostin VA, Keays RR (1990b) Acraman impact ejecta and host shales: evidence for low-temperature mobilization of iridium and other platinoids. Geology 18:132–135
Wallace MW, Keays RR, Gostin VA (1991) Stromatolitic iron oxides: evidence that sea-level changes can cause sedimentary iridium anomalies. Geology 19:551–554
Wallace MW, Gostin VA, Keays RR (1996) Sedimentology of the Neoproterozoic Acraman impact-ejecta horizon, South Australia. Australian Geological Survey Organization. J Aust Geol Geophys 16:443–451
Walliser OH (1996) Global events in the Devonian and Carboniferous. In: Walliser OH (ed) Global events and event stratigraphy. Springer, Berlin, pp 225–250
Walsh M, Lowe DR (1999) Modes of accumulation of carbonaceous matter in the early Archean: a petrographic and geochemical study of the carbonaceous cherts of the Swaziland Supergroup. In: Lowe DR, Byerly GR (eds) Geological evolution of the Barberton Greenstone Belt, South Africa. Geological Society of America, Special Paper 329, pp 213–232
Walter MR, Veevers JJ, Calver CR, Grey K (1995) Neoproterozoic stratigraphy of the Centralian Superbasin, Australia. Precambr Res 73:173–195
Walter MR, Veevers JJ, Calver CR, Gorjan P, Hill AC (2000) Dating the 840–544 Ma Neoproterozoic interval by isotopes of strontium, carbon, and sulfur in seawater, and some interpretative models. Precambr Res 100:371–433
Walton EL, Herd CDK (2007) Localized shock melting in lherzolitic shergottite Northwest Africa 1950: comparison with Allan Hills 77005. Meteorit Planet Sci 42:63–80
Wang J, Zhao Q, Cheng X, Wang R, Wang P (2000) Age estimation of the mid-Pleistocene microtektite event in the South China Sea: a case showing the complexity of sea-land correlation. Chin Sci Bull 45:2277–2280
Wang K (1992) Glassy microspherules (microtektites) from an Upper Devonian limestone. Science 256:1547–1550
Wang K, Attrep M Jr, Orth CJ (1993) Global iridium anomaly, mass extinction, and redox change at the Devonian-Carboniferous boundary. Geology 21:1071–1074
Wang K, Geldsetzer HHJ, Chatterton BDE (1994) A Late Devonian extraterrestrial impact and extinction in eastern Gondwana: geochemical, sedimentological, and faunal evidence. In: Dressler BO, Grieve RAF, Sharpton VL (eds) Large meteorite impacts and planetary evolution. Geological Society of America, Special Paper 293, pp 111–120
Wänke H, Dreibus G, Jagoutz E (1984) Mantle chemistry and accretion history of the Earth. In: Kröner A, Hanson GN, Goodwin AM (eds) Archaean geochemistry. Springer, Berlin, pp 1–24
Ward PD, Haggart JW, Carter ES, Wilbur D, Tipper HW, Evans T (2001) Sudden productivity collapse associated with the Triassic-Jurassic boundary mass extinction. Science 292:1148–1151
Warme JE, Kuehner H-C (1998) Anatomy of an anomaly: the Devonian catastrophic Alamo impact breccias of southern Nevada. Int Geol Rev 40:189–216
Warme JE, Sandberg CA (1995) The catastrophic Alamo breccias of southern Nevada: record of a Late Devonian extraterrestrial impact. Courier Forschungsinstitut Senckenberg 188:31–57
Warme JE, Sandberg CA (1996) Alamo megabreccia: record of Late Devonian impact in southern Nevada. GSA Today 6:1–7
Warme JE, Chamberlain AK, Ackman BW (1991) The Alamo event: Devonian cataclysmic breccia in southeastern Nevada [abs]. Geol Soc Am Abstr Prog 23(2):108
Warme JE, Morgan M, Kuehner H-C (2002) Impact-generated carbonate accretionary lapilli in the Late Devonian Alamo Breccia. In: Koeberl C, MacLeod KG (eds) Catastrophic events and mass extinctions: impacts and beyond. Geological Society of America, Special Paper 356, pp 489–50
Wasson JT (2003) Large aerial bursts: an important class of terrestrial accretionary events. Astrobiology 3:163–179
Wasson JT, Heins WA (1993) Tektites and climate. J Geophys Res 98(E2):3043–3052

Wasson JT, Mezger K (2007) Isotopic evidence of tektite formation [abs]. Meteorit Planet Sci 42(Suppl):A161
Waters AC, Fisher RV (1971) Base surges and their deposits: Capelinhos and Taal volcanoes. J Geophys Res 76:5596–5614
Watt N, Bouchet RA, Lee C-TA (2011) Exploration of tektite formation processes through water and metal content measurements. Meteorit Planet Sci 46:1025–1032
Wdowiak TJ, Armendarez LP, Agresti DG, Wade ML, Wdowiak SY, Claeys P, Izett G (2001) Presence of an iron-rich nanophase material in the upper layer of the Cretaceous-Tertiary boundary clay. Meteorit Planet Sci 36:123–133
Wedepohl KH (1995) The composition of the continental crust. Geochim Cosmochim Acta 59:1217–1232
Wedepohl KH, Muramatsu Y (1979) The chemical compositions of kimberlites compared with the average compositions of three basaltic magma types. In: Boyd FR, Meyer HOA (eds) Kimberlites, diatremes and diamonds: their geology, petrology and geochemistry. American Geophysical Union, Washington, pp 300–312
Weeks RA, Underwood JR Jr, Giegengack R (1984) Libyan Desert Glass: a review. J Non-Cryst Solids 67:593–619
Wei W (1995) How many impact-generated microspherule layers in the upper Eocene? Palaeogeogr Palaeoclimatol Palaeoecol 114:101–110
Weisberg MK, McCoy TJ, Krot AN (2006) Systematics and evaluation of meteorite classification. In: Lauretta DS, McSween HY Jr (eds) Meteorites and the early solar system II. University of Arizona Press, Tucson, pp 19–52
Wheatley CJV, Whitfield GG, Kenny KJ, Birch A (1986) The Pering carbonate-hosted zinc-lead deposit, Griqualand West. In: Anhaeusser CR, Maske S (eds) Mineral deposits of southern Africa, vol I. Geological Society of South Africa, Johannesburg, pp 867–874
White RV (2002) Earth's biggest 'whodunnit': unraveling the clues in the case of the end-Permian mass extinction. Philos Trans R Soc Lond A 360:2963–2985
White RV, Saunders AD (2005) Volcanism, impact and mass extinctions: incredible or credible coincidences? Lithos 79:299–316
Whitehead J, Papanastassiou DA, Spray JG, Grieve RAF, Wasserburg GJ (2000) Late Eocene impact ejecta: geochemical and isotopic connections with the Popigai impact structure. Earth Planet Sci Lett 181:473–487
Whitehead J, Spray JG, Grieve RAF (2002) Origin of "toasted" quartz in terrestrial impact structures. Geology 30:431–434
Whitehead J, Kelley S, Sherlock SC, Grieve RAF, Spray JG, Trepmann CA (2003) Structural and geochronologic constraints on the timing of the Charlevoix impact, Quebec, Canada [abs]. In: Third international conference on large meteorite impacts, nordlingen, Federal Republic of Germany, August 5–7, 2003. Lunar and Planetary Institute Contribution 1167, Lunar and Planetary Institute, Houston, abstract no. 4084
Whiteside JH, Olsen PE, Kent DV, Fowell SJ, Et-Touhami M (2007) Synchrony between the Central Atlantic magmatic province and the Triassic-Jurassic mass-extinction event? Palaeogeogr Palaeoclimatol Palaeoecol 244:345–367
Wichman RW, Schultz PH (1989) Loss of large craters in the terrestrial impact record [abs]. Lunar Planet Sci 20:1199–1200
Wieland F, Reimold WU, Gibson RL (2006) New observations on shatter cones in the Vredefort impact structure, South Africa, and evaluation of current hypotheses for shatter cone formation. Meteorit Planet Sci 41:1737–1759
Wignall P, Thomas B, Willink R, Watling J (2004) Is Bedout an impact crater? Take 1. Science 306:609
Wilkinson BH, Landing E (1978) "Eggshell diagenesis" and primary radial fabric in calcite ooids. J Sediment Petrol 48:1129–1138
Willbold W, Elliott E, Moorbath S (2011) The tungsten isotopic composition of the Earth's mantle before the terminal bombardment. Nature 477:195–198

Williams GE (1986) The Acraman impact structure: source of ejecta in Late Precambrian shales, South Australia. Science 233:200–203
Williams GE (1994a) Acraman, South Australia: Australia's largest meteorite impact structure. Proc R Soc Victoria 106:105–127
Williams GE (1994b) Acraman: a major impact structure from the Neoproterozoic of Australia. In: Dressler BO, Grieve RAF, Sharpton VL (eds) Large meteorite impacts and planetary evolution. Geological Society of America, Special Paper 293, pp 209–224
Williams GE, Gostin VA (2005) Acraman-Bunyeroo impact event (Ediacaran), South Australia, and environmental consequences: twenty-five years on. Aust J Earth Sci 52:607–620
Williams GE, Wallace MW (2003) The Acraman asteroid impact, South Australia: magnitude and implications for the late Vendian environment. J Geol Soc Lond 60:545–554
Williams GE, Schmidt PW, Boyd DM (1996) Magnetic signature and morphology of the Acraman impact structure, South Australia. Australian Geological Survey Organization. J Aust Geol Geophys 16:431–442
Williams GE, Gostin VA, McKirdy DM, Preiss WV (2008) The Elatina glaciation, late Cryogenian (Marinoan Epoch), South Australia: sedimentary facies and palaeoenvironments. Precambr Res 163:307–331
Williford KH, Ward PD, Garrison GH, Buick R (2007) An extended organic carbon-isotope record across the Triassic-Jurassic boundary in the Queen Charlotte Islands, British Columbia, Canada. Palaeogeogr Palaeoclimatol Palaeoecol 244:290–296
Willman S, Moczydlowska M, Grey K (2006) Neoproterozoic (Ediacaran) diversification of acritarchs—a new record from the Murnaroo 1 drillcore, eastern Officer Basin, Australia. Rev Palaeobot Palynol 139:17–39
Winslow FD III, Abbott D, Celestian AJ, Hemming SR, Olsen PE, Phillips BL, Rasbury ET, Smimov A, Whiteside JH (2006) Extra-basinal source for the Tr-J boundary clay layer in the Newark Basin [abs]. Geol Soc Am Abstr Prog 41(7):53
Wirth R, Vollmer C, Brenker F, Matsyuk S, Kaminsky F (2007) Inclusions of nanocrystalline hydrous aluminous silicate "Phase Egg" in superdeep diamonds from Juina (Mato Grosso State, Mexico). Earth Planet Sci Lett 259:384–399
Wittmann A, Kenkman T, Schmitt RT, Stöffler D (2006) Shock-metamorphosed zircon in terrestrial impact craters. Meteorit Planet Sci 41:433–454
Witzke BJ, Anderson RR (1996) Sedimentary-clast breccias of the Manson impact structure. In: Koeberl C, Anderson RR (eds) The Manson impact structure, Iowa: anatomy of an impact crater. Geological Society of America, Special Paper 302, pp 115–144
Witzke BJ, Hammond RH, Anderson RR (1996) Deposition of the Crow Creek Member, Campanian, South Dakota and Nebraska. In: Koeberl C, Anderson RR (eds) The Manson impact structure, Iowa: anatomy of an impact crater. Geological Society of America, Special Paper 302, pp 433–456
Wolbach WS, Lewis RS, Anders A (1985) Cretaceous extinctions: evidence for wildfires and search for meteoritic material. Science 230:167–170
Wolbach WS, Gilmour I, Anders E, Orth CJ, Brooks RR (1988) Global fire at the Cretaceous-Tertiary boundary. Nature 334:665–669
Wolbach WS, Gilmour I, Anders E (1990) Major wildfires at the Cretaceous-Tertiary boundary. In: Sharpton VL, Ward PD (eds) Global catastrophes in Earth history. Geological Society of America, Special Paper 247, pp 391–400
Wolfe JA, Upchurch GR Jr (1986) Vegetation, climatic and floral changes at the Cretaceous-Tertiary boundary. Nature 324:148–152
Woodhead JD, Hergt JM, Simonson BM (1998) Isotopic dating of an Archean bolide impact horizon, Hamersley Basin Western Australia. Geology 26:47–50
Wright FW, Hodge PW (1965) Studies of particles for extraterrestrial origin; Part 4, microscopic spherules from recent volcanic eruptions. J Geophys Res 70:3889–3898

Wrobel KE (2008) Computational modeling of impact-generated vapor and melt: implications for remnant products on Mars and Earth. Ph.D. thesis, Brown University, Providence, RI, USA, pp 215

Wrobel KE, Schultz PH (2003) The effect of rotation on the deposition of terrestrial impact ejecta [abs]. Lunar Planet Sci 34: abstract no.1190.pdf

Wu J (1995) Studies of impact ejecta associated with Australasian microtektites in deep-sea sediments: implications concerning the source region of the Australasian tektite strewn field. Ph.D. dissertation, University of Delaware, Newark, DE, USA, 218 pp

Wünnemann K, Lange MA (2002) Numerical modeling of impact-induced modification of the deep-sea floor. Deep-Sea Res II 49:969–981

Xie S, Pancost RD, Huang X, Jiao D, Lu L, Huang J, Yang F, Evershed RP (2007) Molecular and isotopic evidence for episodic environmental changes across the Permo/Triassic boundary at Meishan in South China. Global Planet Change 55:56–65

Xie X, Chao ECT (1985) The variation range of optical constants and distribution characteristics of shock lamellae in shock-metamorphosed quartz. Geochemistry 4:97–113

Xie X, Minitti ME, Chen M, Mao H, Wang D, Shu J, Fei Y (2002) Natural high-pressure polymorph of merrillite in the shock veins of the Suizhou meteorite. Geochim Cosmochim Acta 66:2439–2444

Xie X, Minitti ME, Chen M, Mao H-K, Wang D, Shu J, Fei Y (2003) Tuite, γ-$Ca_3(PO_4)_2$: a new mineral from the Suizhou L6 chondrite. Eur J Miner 15:1001–1005

Xie Z, Sharp TG (2004) High-pressure phases in shock-induced melt veins of the Umbarger L6 chondrite: Constraints of shock pressure. Meteorit Planet Sci 39:2043–2054

Xie Z, Sharp TG, DeCarli PS (2006) High pressure phases in a shock-induced melt vein of the Tenham L6 chondrite: constraints on shock pressure and duration. Geochim Cosmochim Acta 70:504–515

Xu D-Y, Yan Z (1993) Carbon isotope and iridium event markers near the Permian/Triassic boundary in the Meishan section, Zhejiang Province, China. Palaeogeogr Palaeoclimatol Palaeoecol 104:171–176

Xu D-Y, Ma S-L, Chai Z-F, Mao X-Y, Sun Y-Y, Zhang Q-W, Yang Z-Z (1985) Abundance variation of iridium and trace elements at the Permian/Triassic boundary at Shangsi in China. Nature 314:154–156

Xu GR, Zhang KX, Hunag SJ, Wu SB, Bi XM (1988) On the upper Permian and event stratigraphy of the Permo-Triassic boundary in Huangshi, Hubei. Earth Sci 13(5):521–527

Xu L, Lin Y, Shen W, Qi L, Xie L, Ouyang Z (2007) Platinum-group elements of the Meishan Permian-Triassic boundary section: evidence for flood basaltic volcanism. Chem Geol 246:55–64

Yagi A, Suzuki T, Akaogi M (1994) High pressure transitions in the system $KAlSi_3O_8$-$NaAlSi_3O_8$. Phys Chem Miner 21:12–17

Yamei H, Potts R, Baoylin Y, Zhengtang G, Deino A, Wei W, Clark J, Guangmao X, Weiwan H (2000) Mid-Pleistocene Acheulean-like stone technology of the Bose Basin, South China. Science 287:1622–1626

Yancey TE (1996) Stratigraphy and depositional environments of the Cretaceous-Tertiary boundary complex and basal Paleocene section, Brazos River, Texas. Trans Gulf Coast Assoc Geol Soc 46:433–442

Yancey TE, Guillemette RN (2008) Carbonate accretionary lapilli deposits of the Chicxulub impact event. Geol Soc Am Bull 120:1105–1118

Yerofeev MV, Lachinov PA (1888) About the Nova Urei meteorite (in Russian). Zhurnal Russlogo Physiko-Khimicheskogo Obstchestva 20:185–213

Yin HF, Zhang KX, Yang FQ (1988) A new scheme of biostratigraphic delimitation between marine Permian and Triassic. Earth Sci (J China Univ Geosci) 13(5):511–519

Yin H, Huang S, Zhang K, Hansen HJ, Yang F, Ding M, Bie X (1992) The effects of volcanism on the Permo-Triassic mass extinction in South China. In: Sweet WC, Zunyi Y, Dickins JM, Honfu Y (eds) Permo-Triassic events in the Eastern Tethys: stratigraphy, classification, and relations with the western Tethys. Cambridge University Press, Cambridge, pp 146–157

Yin H, Zhang Z, Tong J, Yang Z, Wu S (2001) The Global Stratotype Section and Point (GSSP) of the Permian-Triassic boundary. Episodes 24:102–114

Young GM, Long DGF, Fedo CM, Nesbitt HW (2001) Paleoproterozoic Huronian basin: product of a Wilson cycle punctuated by glaciations and a meteorite impact. Sediment Geol 141–142:233–254

Zachos JC, Lohmann KC, Walker JCG, Wise SW (1993) Abrupt climate change and transient climate during the Paleogene: a marine perspective. J Geol 101:191–213

Zahnle KJ (1990) Atmospheric chemistry by large impacts. In: Sharpton VL, Ward PD (eds) Global catastrophes in Earth history; an interdisciplinary conference on impacts, volcanism, and mass mortality. Geological Society of America, Special Paper 247, pp 271–288

Zähringer J (1963) K-Ar measurements of tektites. In: Radioactive dating. Proceedings IAEA symposium, international atomic energy agency Athens, Nov 19–23, 1962, Vienna, pp 289–305

Zajac IS (1974) The stratigraphy and mineralogy of the Sokoman Formation in the Knob Lake area, Quebec and Newfoundland. Geological Survey of Canada, Bulletin 220, 159 pp

Zhang A, Hsu W, Wang R, Ding M (2006a) Pyroxene polymorphs in melt veins of the heavily shocked Sixiangkou L6 chondrite. Eur J Miner 18:719–726

Zhang S, Peng Y, Yu J, Lei X, Gao Y (2006b) Characteristic of claystones across the terrestrial Permian-Triassic boundary: evidence from the Chahe section, western Guizhou, South China. J Asian Earth Sci 27:358–370

Zhou L, Kyte FT (1988) The Permian-Triassic boundary event: a geochemical study of three Chinese sections. Earth Planet Sci Lett 90:411–421

Zhou L, Kyte FT, Bohor B (1991) Cretaceous/Tertiary boundary of DSDP Site 596, South Pacific. Geology 19:694–697

Zieg MJ, Marsh BD (2005) The Sudbury Igneous Complex: viscous emulsion differentiation of a superheated impact melt sheet. Geol Soc Am Bull 117:1427–1450

Zullo JB III, Smith FC, Glass BP (2010) Searching for evidence of shock metamorphism in a 3.2 Ga spherule bed: preliminary results [abs]. Geol Soc Am Abstr Prog 42(1):161

Index

B. P. Glass and B. M. Simonson, *Distal Impact Ejecta Layers*, Impact Studies,
DOI: 10.1007/978-3-540-88262-6, © Springer-Verlag Berlin Heidelberg 2013

J

K

T